



Peter R. Lang
Frank S. Lombargo
Editors

Atmospheric Turbulence, Meteorological Modeling and Aerodynamics



ATMOSPHERIC TURBULENCE, METEOROLOGICAL MODELING AND AERODYNAMICS

No part of this digital document may be reproduced, stored in a retrieval system or transmitted in any form or by any means. The publisher has taken reasonable care in the preparation of this digital document, but makes no expressed or implied warranty of any kind and assumes no responsibility for any errors or omissions. No liability is assumed for incidental or consequential damages in connection with or arising out of information contained herein. This digital document is sold with the clear understanding that the publisher is not engaged in rendering legal, medical or any other professional services.

**ATMOSPHERIC TURBULENCE,
METEOROLOGICAL MODELING
AND AERODYNAMICS**

**PETER R. LANG
AND
FRANK S. LOMBARGO
EDITORS**

Nova Science Publishers, Inc.
New York

Copyright © 2010 by Nova Science Publishers, Inc.

All rights reserved. No part of this book may be reproduced, stored in a retrieval system or transmitted in any form or by any means: electronic, electrostatic, magnetic, tape, mechanical photocopying, recording or otherwise without the written permission of the Publisher.

For permission to use material from this book please contact us:

Telephone 631-231-7269; Fax 631-231-8175

Web Site: <http://www.novapublishers.com>

NOTICE TO THE READER

The Publisher has taken reasonable care in the preparation of this book, but makes no expressed or implied warranty of any kind and assumes no responsibility for any errors or omissions. No liability is assumed for incidental or consequential damages in connection with or arising out of information contained in this book. The Publisher shall not be liable for any special, consequential, or exemplary damages resulting, in whole or in part, from the readers' use of, or reliance upon, this material. Any parts of this book based on government reports are so indicated and copyright is claimed for those parts to the extent applicable to compilations of such works.

Independent verification should be sought for any data, advice or recommendations contained in this book. In addition, no responsibility is assumed by the publisher for any injury and/or damage to persons or property arising from any methods, products, instructions, ideas or otherwise contained in this publication.

This publication is designed to provide accurate and authoritative information with regard to the subject matter covered herein. It is sold with the clear understanding that the Publisher is not engaged in rendering legal or any other professional services. If legal or any other expert assistance is required, the services of a competent person should be sought. FROM A DECLARATION OF PARTICIPANTS JOINTLY ADOPTED BY A COMMITTEE OF THE AMERICAN BAR ASSOCIATION AND A COMMITTEE OF PUBLISHERS.

LIBRARY OF CONGRESS CATALOGING-IN-PUBLICATION DATA

Atmospheric turbulence, meteorological modeling, and aerodynamics / [edited by] Peter R. Lang and Frank S. Lombargo.
p. cm.

Includes index.

ISBN 978-1-61728-264-5 (E-Book)

1. Atmospheric turbulence--Mathematical models. 2. Reynolds analogy. 3. Aerodynamics. I. Lang, Peter R. II.

Lombargo, Frank S.

QC880.4.T8A86 2009

551.5501'5118--dc22

2009016571

Published by Nova Science Publishers, Inc. + New York

CONTENTS

Preface	vii
Research and Review Studies	1
Chapter 1 Climatology of the Arctic Planetary Boundary Layer <i>Igor Esau and Svetlana Sorokina</i>	3
Chapter 2 Nonequilibrium Thermodynamic Theory of Atmospheric Turbulence <i>Yinqiao Hu and Jinbei Chen</i>	59
Chapter 3 Generalized Scale Invariance of Edge Plasma Turbulence <i>V.P. Budaev</i>	111
Chapter 4 Turbulence, Turbulent Mixing and Diffusion in Shallow-Water Estuaries <i>Hubert Chanson and Mark Trevethan</i>	167
Chapter 5 Turbulent Scalar Transfer Modeling in Reacting Flows <i>Lei-Yong Jiang and Ian Campbell</i>	205
Chapter 6 The Research of the Solution Quality for the $k-\bar{\omega}$ Turbulence Method with Using Sensitivity Analysis of Flow Properties to Model Coefficients <i>Ewa Błazik-Borowa</i>	239
Chapter 7 Passive Air Sampler for the Determination of Atmospheric Nitrogen Dioxide Using Flat Porous Polyethylene Membrane as Turbulence Limiting Diffuser <i>Yoshika Sekine, Michio Butsugan and Simon F. Watts</i>	277
Chapter 8 Artificial Intelligence Technique for Modelling and Forecasting of Meteorological Data: A Survey <i>Adel Mellit</i>	293
Chapter 9 New Trends on Phenological Modelling <i>Herminia García Mozo</i>	329

Chapter 10	Time Dependent Shape Optimization Using Adjoint Variable Method for Reducing Drag <i>Kazunori Shinohara and Hiroshi Okuda</i>	343
Chapter 11	Numerical and Experimental Investigations of Fluid Dynamics of High Speed Flows <i>R. C. Mehta</i>	429
Chapter 12	Aerodynamic Research and Development of Vertical-Axis Wind Turbines with Rotary Blades <i>Victor V. Cheboxarov and Valery V. Cheboxarov</i>	469
Chapter 13	The Determination of Aerodynamic Forces on Sails – Challenges and Status <i>William C. Lasher</i>	487
Chapter 14	Large-Eddy Simulation of Free Shear and Wall-Bounded Turbulent Flows <i>Konstantin N. Volkov</i>	505
Chapter 15	Grand Computational Challenges for Prediction of the Turbulent Wind Flow and Contaminant Transport and Dispersion in the Complex Urban Environment <i>Fue-Sang Lien, Eugene Yee, Bing-Chen Wang and Hua-Ji</i>	575
Chapter 16	A Semi-Analytic Model of Fog Effects on Vision <i>Eric Dumont, Nicholas Hautiere and Romain Gallen</i>	635
Short Commentaries:		671
Short Commentary A	On Parameterizing Inclined Stable Boundary Layers <i>Branko Grisogono</i>	673
Short Commentary B	Ambient Air Temperature Interpolation in Inhomogeneous Regions <i>Klemen Zakšek and Daniel Joly</i>	679
Short Commentary C	Peat Moisture in Relation to Meteorological Factors: Monitoring, Modelling, and Implications for the Application of the Canadian Forest Fire Weather Index System <i>Vladimir Krivtsov, G. Matt Davies, Colin Legg, Teresa Valor and Alan Gray</i>	691
Index		705

PREFACE

Turbulence is a type of fluid (gas or liquid) flow in which the fluid undergoes irregular fluctuations, or mixing, in contrast to laminar flow, in which the fluid moves in smooth paths or layers. In turbulent flow the speed of the fluid at a point is continuously undergoing changes in both magnitude and direction. The flow of wind and rivers is generally turbulent in this sense, even if the currents are gentle. The air or water swirls and eddies while its overall bulk moves along a specific direction. This book will give the reader new insights into this natural phenomenon that occurs everyday yet is a puzzle that is not yet fully resolved in classical physics. Among the applications included are: fluid dynamics, aerodynamics, atmospheric and climatology research.

Chapter 1 - One of the central problems of the state-of-the-art climatology is to understand the relationship between the observed near-surface processes, first of all the processes dependent on such meteorological quantities as temperature, humidity and wind, and the general atmospheric circulation and its long-term variability. Complications arise from the fact that the near-surface processes are affected by the vertical turbulent exchange. This study provides climatological estimates of the turbulent exchange and quantifies aspects of the turbulent exchange important for the Arctic climate. By definition, the planetary boundary layer (PBL) is the lowermost atmospheric layer where the vertical turbulent exchange (mixing) is non-negligible in description of meteorological processes. The study focuses on the unique Arctic PBL features rarely observed at lower latitudes, namely, turbulence development and mixing under conditions of strong atmospheric static stability and under strongly negative surface radiation balance. The proposed reconstruction of the Arctic PBL climatology is based on episodic turbulence field campaigns as well as on regular radiosounding, reanalysis and satellite data. The authors found that the main difficulty of the data analysis appears not from data scarcity as it has been traditionally claimed but from data inconsistency and low quality. The reconstruction reveals that the Arctic PBL is stably stratified in 70% to 100% of observations. But the continues periods of stably stratified PBL (SBL) development are typically less than 100 hours (4 days). The Arctic PBL is shallow. Its depth is typically less than 200 m and frequently less than 50 m. But over the Arctic Ocean, this shallow PBL is often well mixed due to the conductive heat transport through ice and the convection over polynyas. The Arctic PBL can often dynamically decouple from the rest of the atmosphere. During the periods of decoupling the temperature variability within the PBL is much larger (in wintertime) or smaller (in summertime) than in the air aloft. Stability of the PBL and developing of the temperature inversions maintain high relative humidity (often

above 90%) and the Arctic haze and fog. Models are sensitive to the Arctic PBL dynamics. However the model resolution is usually inadequate to the requirements of the employed turbulence parameterization schemes.

Chapter 2 - Turbulence is one of the ubiquitous natural phenomena in everyday experience, and a puzzle that is not yet fully resolved in classical physics. A nonequilibrium thermodynamic theory of atmospheric turbulence is developed. The entropy equilibrium equation of atmospheric system with dynamic processes is advanced, and then Fourier's and Flick's laws, Newton's Law, and both the Dufour and the Soret effects—the cross coupling effect between the dynamic and turbulent transport processes in the atmosphere—and the turbulent intensity theorem are uniformly deducted by atmospheric nonequilibrium thermodynamics. These laws and theorem are partially validated by using observed data and, further, their phenomenological coefficients are determined. The turbulent intensity theorem reveals that the macroscopic cause of the development of fluid turbulence is a result of the shearing effects of velocity together with temperature and proves that both Reynolds turbulence and Rayleigh-Bénard turbulence coexist in the atmosphere. The discovery of the coupling effect phenomenon between the thermodynamic and dynamic processes breaks through the viewpoint of the theories of traditional turbulent transport, Fourier's and Flick's laws, and Newton's Law—i.e., the turbulent transport flux of one kind of macroscopic quantity is equivalent to the gradient transport flux of this macroscopic quantity. Moreover, the coupling principle between the thermodynamic and dynamic processes deems that the turbulent transport flux of one kind of macroscopic quantity should include the velocity coupling transport in addition to the gradient transport flux of this macroscopic quantity. Consequently, the vertical turbulent transport flux of energy and matter should count in the cross coupling effect of the vertical velocity, i.e., convergence and divergence motion, in addition to the turbulent transport flux caused by their vertical gradient. The earth's surface is characterized by spatial heterogeneity over a wide range of scales. The heterogeneity of underlying surface brings on the advection to lead the convergence and divergence motion. It may be an important cause of the imbalance of energy budget of the ground surface. The cross coupling principle of the vertical velocity and vertical turbulent transport may offer a possible clue to the development of the theory of atmospheric boundary layer with heterogeneous underlying surface and to overcome the difficulties encountered in the imbalance problem of ground energy budget and in the parameterization of the boundary layer with the heterogeneous underlying surface.

Chapter 3 - Experimental study of edge plasma turbulence in fusion devices such as tokamaks, stellarators and linear machines are presented. The fluctuations observed in the edge plasma of fusion devices are intermittent and self-similar. Non-Gaussian statistics, long-range correlation, superdiffusion and multifractality are observed in the edge plasma turbulence. The turbulence scalings display universal properties. Edge plasma turbulence exhibits a generalized (extended) self-similarity in an extended scale range. Such properties are predicted by the log-Poisson model of intermittent turbulence that considers a stochastic multiplicative cascade of energy and a strong effect of a dissipation range on an inertial range. Hidden statistical symmetries, hierarchy of moments and generalized scale invariance are behind the log-Poisson model. Experimental structure functions scalings have a nonlinear functional dependence on the order index. Such dependence is described by the log-Poisson model captured a topology of singular dissipative structures in case of strong anisotropy from a strong magnetic field. The experimental scalings are rather well fitted by the log-Poisson

model considering quasi-1D filament-like dissipative structures. It appears that the turbulence in the edge plasma of fusion devices is governed by cross-field motions similar to hydrodynamic turbulence. The experimental scalings from edge plasma are available for a comparison with experimental results from neutral fluids.

Chapter 4 - In natural waterways and estuaries, an understanding of turbulent mixing is critical to the knowledge of sediment transport, storm-water runoff during flood events, and release of nutrient-rich wastewater into ecosystems. The predictions of contaminant dispersion in estuaries can rarely be predicted analytically without exhaustive field data for calibration and validation. Why? In natural estuaries, the flow Reynolds number is typically within the range of 10^5 to 10^8 and more. The flow is turbulent, and there is an absence of fundamental understanding of the turbulence structure. Any turbulent flow is characterised by an unpredictable behaviour, a broad spectrum of length and time scales, and its strong mixing properties. In his classical experiment, Osborne Reynolds (1842-1912) illustrated this key feature with the rapid mixing of dye of a turbulent flow (Reynolds 1883). This is seen in Figure 1 showing the original Reynolds experiment and a modified Reynolds experiment. In turbulent flows, the fluid particles move in very irregular paths, causing an exchange of momentum from one portion of the fluid to another, as shown in Figure 1 where dye is rapidly dispersed in the turbulent flow regime ($Re = 2.3 \cdot 10^3$). In natural estuaries, strong momentum exchanges occur and the mixing processes are driven by turbulence. Interestingly Osborne Reynolds himself was involved in the modelling of estuaries (Reynolds 1887).

Relatively little systematic research was conducted on the turbulence characteristics in natural estuarine systems, in particular in relatively shallow-water systems. Long-duration studies of turbulent properties at high frequency are extremely limited. Most field measurements were conducted for short periods, or in bursts, sometimes at low frequency: e.g. Bowden and Ferguson (1980), Shiono and West (1987), Kawanisi and Yokosi (1994), Ham et al. (2001), Voulgaris and Meyers (2004). The data lacked spatial and temporal resolution to gain insights into the characteristics of fine-scale turbulence. It is believed that the situation derived partly from some limitation with suitable instrumentation for shallow-water estuaries.

Herein the turbulence characteristics of shallow-water estuaries with semi-diurnal tides are examined. It is shown that turbulence field measurements must be conducted continuously at high frequency for relatively long periods. Detailed field measurements highlight the large fluctuations in all turbulence characteristics during the tidal cycle. While the bulk parameters fluctuate with periods comparable to tidal cycles, the turbulence properties depend upon the instantaneous local flow properties, and the structure and temporal variability of turbulent characteristics are influenced by a variety of mechanisms.

Chapter 5 - Turbulence modeling is a major factor, affecting the precision of current numerical simulations, particularly for reacting flows. It is also one of the principal unsolved problems in physics today. In the last five decades, much effort has been devoted to the development of turbulent momentum transfer models. However, researches on turbulent scalar transportation issues are limited, particularly for reacting flows.

In almost all turbulent reacting flow RANS (Reynolds-averaged Navier-Stokes) simulations, the Reynolds analogy concept has been used to model turbulent scalar transfers since the 1970s. With this concept, the turbulent Prandtl/Schmidt number is used to calculate the turbulent scalar transfers in flow fields based on the momentum transfer that is modeled by a selected turbulence model. In this chapter, the rationale and limitation of the Reynolds

analogy are analyzed and validated against two benchmarking cases, a turbulent jet diffusion flame and a model diffusion flame combustor. The former represents a simple boundary-type flow, while the latter involves complex flow phenomena (shear layers, wall boundary layers, separations, recirculation zones, re-attachments and their interactions) which are relevant to many practical combustion systems.

The effects of turbulent Prandtl/Schmidt numbers on the flow fields of the jet flame and model combustor have been numerically studied with selected turbulence, combustion and radiation models. In comparison with comprehensive experimental databases, it is found that for both cases, the flow features and magnitudes of mean velocity fields are well predicted, particularly for the jet flame case, and the turbulent Prandtl/Schmidt number has insignificant effect on the velocity fields. In addition, for the combustor case, the turbulence kinetic energy and shear stress distributions are also reasonably well predicted. The proper prediction of velocity fields (or momentum transfers) provides a prerequisite for adequate evaluation of the Reynolds analogy concept or the effect of turbulent Prandtl/Schmidt numbers on the temperature fields of the reacting flows.

In contrast, the turbulent Prandtl/Schmidt number shows significant effects on the temperature fields, particularly for the temperature profiles in the outer layer region of the jet flame and the downstream region of the model combustor. This is also true for the temperature profile along the combustor wall.

Jet diffusion flames seem simple; however, they pose challenges to numerical simulations. The discrepancies of temperature distributions in the upstream outer layer region of the jet flame are observed by the authors and other researchers, and the anticipated reasons are three-fold, incapability to predict the local laminarization phenomenon, the limitations of Reynolds analogy, and insufficient effort in the development of turbulent scalar transfer models. For the Prandtl/Schmidt numbers considered, 0.45 – 1.2, the value of 0.85 can provide acceptable results for the temperature distributions along the jet centerline and at the downstream cross-sections.

For the model combustor configuration and operating conditions, the optimal Prandtl/Schmidt number for temperature prediction inside the combustor is 0.5 for all three combustion models, and it varies from 0.35 to 0.55 for the combustor wall temperature prediction. With the optimal value of 0.50, the velocity and temperature fields are reasonably well predicted, except in some local regions.

The present work suggests that for reliable temperature prediction in turbulent reacting flows without tuning turbulent Prandtl/Schmidt numbers, the Reynolds analogy concept should be improved and new approaches should be investigated.

Chapter 6 - The chapter will be devoted to the research of solution quality for the CFD problem, which is solved with use of the $k-\varepsilon$ standard turbulence method for the steady incompressible flow at a small velocity. The analyses are performed for the exemplary problem of the flow around square cylinder located at a ground. The research of solution quality can be made on the basis of comparison results calculations and measurements, whereas, in this chapter there is a proposal of the analysis for the solution on the basis of the sensitivity analysis of flow properties to model coefficients. The results of the sensitivity analysis have many applications but the most important feature of the sensitivity coefficients is the fact that they have higher values in the regions of high property gradients than in the others, it means in the region with the biggest calculation errors. In this case the analysis of problems with the same approximation degree of one flow property (for example, when the

pressure is constant in cells) and different degrees of polynomials for other properties, the higher sensitivity means the bigger errors. For the problems with different degrees of polynomials of the flow property (for example, the components of a flow velocity approximated by different method) the bigger sensitivity denotes that this property is better described. In this chapter the methods of determination of the sensitivity will be described. Next the assessment of the solution quality which is obtained by using different approximation methods will be introduced on the basis of values of these coefficients. The results of the research will be verified on the basis of comparison of the calculations results and own measurements of the 2D flow around square located at the ground. All calculations are made with use of FLUENT and own computer programs.

Chapter 7 - Atmospheric turbulence is a potential factor influencing on the sampling performance of passive air samplers. In this chapter, a new design of passive sampler named "Oxford sampler" is described which employs a flat type porous polyethylene membrane, made of sintered polyethylene particles, as a turbulence limiting diffuser. The flat diffuser controls mass transfer of the target analyte from ambient air to impregnated trapping filter. The new design is applicable to any analyte for which conventional Palmes' Tube method is applicable, e.g., H₂S, OCS, NO, SO₂, O₃, Organic Acids, NH₃ and so on. As an example, the sampler for the determination of ambient atmospheric nitrogen dioxide (NO₂), using a trapping filter impregnated with triethanolamine is described. Influence of external wind speed on the mass transfer of gas molecules was investigated in laboratory tests. The results showed the flat porous polyethylene membrane worked as an efficient draft baffle preventing over-sampling caused by eddy diffusion, whilst effect of boundary layer conductance was found when the sampling was conducted in a calm environment. The sampling rate of the passive sampler was measured directly at seven sites in Oxford, UK and Kanagawa, Niigata and Yamagata, Japan, by comparing measured concentrations from the samplers with co-located automated NO₂ monitors. The passive device had a relatively higher sampling rate than those of previous samplers and gave equivalent results on NO₂ concentrations to the automated NO₂ monitor at 24h or less sampling duration. This shows the Oxford sampler employing the flat porous polyethylene membrane is appropriate to reduce the sampling resolution of most formats of Palmes' Tubes from weeks to 24 hours or less. Uncertainty and sensitivity analysis of the new sampler indicated possible application of the device to sampling in urban intermediate, urban background and suburban areas.

Chapter 8 - Artificial intelligence (AI) techniques are becoming useful as alternate approaches to conventional techniques or as components of integrated systems. They have been used to solve complicated practical problems in various areas and are becoming popular more and more nowadays. AI techniques have the following features: can learn from examples; are fault tolerant in the sense that they are able to handle noise and incomplete data; are able to deal with non-linear problems; and once trained can perform prediction and generalization at high speed. AI-based systems are being developed and deployed worldwide in a myriad of applications, mainly because of their symbolic reasoning, flexibility and explanation capabilities. AI have been used and applied in different sectors, such as engineering, economic, medicine, military, marine, etc. They have also been applied for modeling, identification, optimization, prediction, forecasting, and control of complex systems. The main objective of this paper is to present an overview of the alternative approach and AI techniques for modeling and forecasting of meteorological data. Published literature works presented in this paper show the potential of AI as a design tool for prediction

and forecasting of meteorological data, these includes, solar radiation, mean temperature, wind speed, humidity, cleanliness index, etc. Additionally the advantage of using an AI-based prediction meteorological data in isolated areas where there no instrument for the measurement of this data, especially the parameters related to PV-systems such as solar radiation data. A new intelligent hardware based on neural network and FPGA (Fielded Programming Gate Array) implementation is proposed for estimating solar radiation from air temperature and sunshine duration.

Chapter 9 - Although phenology modelling has a long history, in recent years, given to the major impact of climate change on ecosystems, the number of studies modelling the response of plant phenology to climate has highly increased. Most of them have indicated the strong relationship between temperature and plant phenology, especially in woody plants. Nevertheless recent studies have also highlighted the influence of photoperiod on the flowering of late spring species and the importance of water availability for the herbaceous species. Mechanistic models describe reproductive phenology known cause-effect relationship of some driving factors in the plant environment. Recently process-based models allow including different bioclimatic factors and also the relationship among them in order to obtain a better description of the biological behaviour and therefore better prediction of phenological events. The reproductive phenology of plants is commonly assumed to be strongly related to local meteorology and also locally adapted to different climate ranges. Recent research suggests that local adaptation is not as great as expected, due to high levels of gene flow, marked year-on-year climate variation and the plasticity of phenology. Studies are showing that phenological models can be established for plant populations including individuals scattered over wide regional areas. Traditionally, plant flowering phenological studies have been concentrated on changes through time but patterns across space remains largely unexplored. In last years, the combined use of GIS and Geostatistics has been demonstrated as instrumental methods for spatial analysis in environmental studies and also plant distribution. Both tools applied on floral phenology studies will contribute to create phenological maps in base of a limited number of sampled locations. Finally, although the role of remote sensing in phenology studies, although is still under development, is increasingly regarded as a key on large areas studies. Given that remote sensing phenology is able to estimate start, peak, duration and end of growing season over large areas, the combined application of phenological models and remote sensing vegetative data can offer very valuable information about the evolution of reproductive phenology of large areas.

Chapter 10 - To obtain an optimal shape, a 3D shape optimization system based on the adjoint variable method is developed. The adjoint variable method is based on the variational principle (a conditional variational principle), and consists of the state equation, the adjoint equation and the sensitivity equation. The equations for reducing the fluid drag under a constant volume condition are formulated. This method was implemented using HEC-MW, and by doing so. The program was efficiently parallelized and the number of program lines was dramatically reduced. The automatic parallel library HEC-MW, running on a PC cluster (16 nodes), made possible the analysis of the optimal shape for a long time span. By using the proposed shape optimization system, the optimal shape under unsteady flow (RE100) could be obtained. Comparing to the initial shape, the drag on the optimal shape (teardrop) can be reduced by about 40% under unsteady flow.

Chapter 11 - The phenomenon of supersonic jets and their interaction with deflector surfaces is found in many engineering applications such as impingement of exhaust from a

rocket nozzle of launch vehicles during the liftoff phase, during stage separation of multistage rockets, and VTOL/STOL operation of aircraft etc. An interaction between a supersonic jet and a flat plate at atmospheric conditions has been studied as the fundamental problem to the impingement of a rocket exhaust plume on the deflector or plate that of a control jet on the rocket body, etc. Inviscid numerical models can offer a fairly good prediction of the impinging jet for moderate plate inclination. The impingement jet is characterized by many discontinuities such as barrel shock, exhaust gas jet boundary, Mach disk, reflected shock, plate shock. The flow structure of an under expanded supersonic jet impinging on an inclined plate has been numerically investigated using a numerical scheme for the Euler equations. The maximum pressure was found to be larger on the inclined plate than on the normal plate. Flow fields of the exit jet Mach number of 2.2 impinging on an inclined plate at various plate angles, nozzle-plate distance and pressure ratios are experimentally investigated using pressure-sensitive paints and schlieren flow visualization. The flow field patterns can be predicted without experiments if the shock cell length in the free jet for various pressure ratios is known in advance. Numerical study of under expanded jet impinging against the solid wall has been presented by Wu et al. The acoustic efficiency of deflected rocket exhaust is less than that of undeflected rockets. The differences are greatest when the exhaust impinges on a flat plate which is normal to the flow and are least for rockets that are deflected by smooth curved buckets.

Flow field features of supersonic free-jets as well as impinging jets over the axisymmetric and double wedge deflector are studied. The differences of the flow field behavior are obtained in the numerical simulations. An oscillating phenomena was noticed in the case of free jets operating at sonic exit Mach number and in another case of impinging of the under expanded jets on a flat plate. A non-dimensional parameter has been obtained to characterize the pressure distribution in the jet axis which makes them invariant of the exit to ambient pressure ratio.

Chapter 12 - Nowadays, offshore wind power engineering quickly grows and becomes the leading branch of renewable energy. However, offshore turbines differ from the onshore turbines essentially only in towers and foundations. So the well-known drawbacks and limitations of propellers still remain offshore. The authors note the limited unit power capacity, infrasound emission, and harmful effects on birds and animals. The following tasks were set: to increase substantially unit capacity of wind power plants, to work safely under extra wind loads, to enhance wind speed range, to reduce wind energy cost, to eliminate infra sound emission and fatal injury of birds due to turbine rotation. They can be reached with the recently suggested concept of wind turbines called Wind Energy Marine Unit (WEMU). All WEMU turbines feature large-scale (more than 100m in diameter) circular floating rotors. A circular pontoon bears vertical columns with a circular deck and rotary blades. In this way, water supports the rotor during slow rotation about vertical axis. Here the authors present approaches, methods, and important results of aerodynamic research of the WEMU turbines. Well-verified CFD-methods with full-scale domains are chosen for research. Flow through the turbine is described by RANS equations with chosen turbulent models. Numerical aerodynamic experiments are carried out using the finite volume method with several geometrical models of the rotor. Discretization, grid, and calculation conditions are described. As a rule, the computation domain is presented by a non-conformal grid of hexahedral elements and is divided into rotary and stationary zones. The vertical wind profile on the velocity-inlet boundary at height above 10 m is described according to the Monin-Obukhov

theory with parameters which are typical to sea surface. At first, several symmetric airfoils are analyzed. Slightly convex airfoil with two flaps is found out as optimal for rotary blades. Maximum of power capacity is achieved for nondimensional blade speed as $0.7 \sim 0.8$. Aerodynamic efficiency of the WEMU turbine about 50% is guaranteed by an optimal control of rotation of vertical blades. Vertical circulation in cross-flow turbines is described. Stiffened design of the turbine with two face rings is proposed and investigated. It is shown that a slope of the plane of the floating turbine's rotation cannot change the air flow significantly. Additionally, new design of cross-flow turbine with partially free rotating blades is investigated. Turbine's parameters are found out which provide positive torque for most blade positions.

Chapter 13 - It is important to be able to determine the forces on the sails of racing yachts and square-rigged historical vessels, as well as for potential commercial vessel applications. This problem is very complicated due to qualities of the sailing environment, viscous flow physics, and the need for accuracy. Three methods are currently being used to determine these forces – full-scale testing, wind tunnel testing, and computational fluid dynamics. Each of these methods has advantages and disadvantages relative to the sail aerodynamics problem, and these are discussed. Advances in our understanding of sail aerodynamics will require continued research using all three methods, and some suggestions for future research are presented.

Chapter 14 - The main objectives of the chapter are to show the possibilities of using large-eddy simulation to predict properties of free shear and wall-bounded turbulent flows, to test widely used sub-grid scale eddy viscosity models against selected benchmark problems identifying range of applicability and limitations of the models used, to help accurately predict flows in channels, mixing layers, free and impingement jets. The cases considered include fully developed turbulent flow in the channel, turbulent flow in the channel induced by wall injection, free mixing layer, free non-isothermal turbulent jet, unsteady-state heat transfer in the region of interaction of turbulent jet with a flat target. The data obtained from large-eddy simulation are used to predict aero-optical effects in the turbulent boundary layers and free shear turbulent flows. Comparisons are made with well-documented experimental data, benchmark cases and computations from other CFD codes.

Chapter 15 - A comprehensive overview of the prognostic physics-based urban microscale models for flow and dispersion that have been developed as part of a four-year research and development effort is described. The effort was funded by the Chemical, Biological, Radiological and Nuclear (CBRN) Research and Technology Initiative (CRTI) under a project entitled “An Advanced Emergency Response System for CBRN Hazard Prediction and Assessment for the Urban Environment”. The primary objective of this project was to develop an advanced, high-fidelity, fully validated, state-of-the-science modeling system for the prediction of urban flows and the dispersion of CBRN agents released in these highly disturbed flows. This chapter describes the progress on one of the components of the project. This component focuses on (1) the development and implementation of a computational fluid dynamics (CFD) model for the simulation of the aerodynamics of the extremely complex turbulent wind flow in an arbitrary cityscape; (2) the development of a grid generation capability for the automatic generation of grids in the computational domain when provided with detailed geometric information on the shapes and locations of buildings; and, (3) the provision of predictive models for transport and turbulent diffusion of contaminants released in an urban area. The predictive accuracy of the urban microscale

models for flow and dispersion have been validated by comparing model predictions with comprehensive experimental data obtained from laboratory studies of flow and dispersion over idealized obstacle arrays and from a full-scale urban field experiment conducted in Oklahoma City, Oklahoma in July 2003 (Joint Urban 2003, or JU2003 experiment).

Chapter 16 - Fog is often considered as a mere nuisance rather than a hazard. However, reduced meteorological visibility conditions cause accidents and transportation delays, with substantial financial consequences. The visibility loss results from minute airborne droplets which scatter light, causing drastic alterations in the image of the environment perceived by vision systems, both human and artificial. Modeling the visual effects of dense fog makes it possible to simulate foggy conditions, in order to design and test countermeasures for improved safety and mobility. First, the authors introduce basic notions about the nature of fog and they briefly review the microphysical models which usually serve to describe its droplet size distribution. Second, the authors explain how light interacts with fog droplets, and they present the optical descriptors which describe scattering and extinction phenomena. Third, the authors analyze how contrast is impaired by these phenomena in the image of the environment perceived by a vision system, and they propose and discuss a semi-analytic model of the visual effects of fog. Finally, the authors show applications of this model to the monitoring of the meteorological visibility through use of charge-coupled device cameras operating in the visible light range.

Short Commentary A – In this short commentary the author assesses the mixing length-scale for the SABL, i.e. that in the “z-less“ regime, as often parameterized in mesoscale models with higher-order closure turbulence parameterization schemes.

Short Commentary B - The importance of climatic data for the society increased in the last years due to the global climate change. But spatial representation of climatic data is also a key point in many applications. The estimation of the spatial distribution of ambient air temperature (AAT) measured 2 m above the ground is a GIS application that is especially problematic in mountainous countries with low autocorrelation among measurements. Kriging (usually optimal interpolation method) is not adapted to inhomogeneous areas, thus a statistical method based on multiple regression is proposed.

Within the presented case study, AAT was measured at 20 synoptic stations in Slovenia three times a day (7:00, 14:00 and 21:00) throughout 2005, which means that there are 1095 situations to be interpolated in total. The measurements were linked with the data stored in GIS: firstly, with the DEM and from it derived layers such as relief slope, relief aspect, etc., and secondly with the land cover including derived layers such as distance from the sea. Some of this data has a micro-local and some has a regional influence. Therefore, some explanatory variables were estimated within spatial analyses windows of seven different sizes and only the analysis window, where the attributes were the highest correlated to AAT, was considered in the following procedure.

The novelty of the presented study is inclusion of satellite data – MODIS is an instrument on board Terra and Aqua satellite that observes the land and sea surface from the polar orbit four times per day. Recorded images are used to derive land surface temperature, surface albedo, normalized difference vegetation index and enhanced vegetation index that were introduced into the case study and used within the multiple regression. Systematic correlations between temperature and explanatory variables introduced into the GIS showed that, next to the relief aspect, especially land surface temperature is a significant and easy

obtainable data for AAT interpolation. The standard deviation of all the results improved after MODIS data inclusion from 1.7 to the final 1.5 °C.

Short Commentary C - Underground fires in peatlands are relatively rare events but when active they can smoulder for very long periods and cause significant environmental damage. They emit large quantities of combustion products, including greenhouse gases, into the atmosphere causing deterioration in air quality and public health. These fires are fed by small but continuous quantities of air diffusing through the peat and flowing through fractured strata, cracks and soil pipes. Reduced heat losses and high thermal inertia of the ground, combined with the continual fuel availability and small oxidizer flow, promote long-term smouldering combustion and creeping propagation that can be extensive in both depth and area. These fires are difficult to detect and frustrate most efforts to extinguish them. Here the authors present a case study of variation in peat soil water potential in relation to changes in meteorological variables and indices of the Canadian Forest Fire Weather Index System (CFFWIS). Duff Moisture Code (DMC) values appeared to correspond relatively well to modelled changes in soil moisture deficit (SMD), as well as to the soil water potential (SWP), thus giving certain credibility to this component of the CFFWIS in relation to the probability of occurrence of an underground fire. It should be noted, however, that the fit between SWP and DMC was somewhat weaker than the fit between SWP and the modelled values of SMD ($r = 0.76$ and 0.85 respectively). It has previously been shown (Davies et al. 2006) that the CFFWIS is unable to predict the rate of fire spread in heather (*Calluna vulgaris*) stands, because the moisture content of live and dead *Calluna* was not accurately predicted by any of the moisture codes of the CFFWIS. Considering the results presented here, the standard method to estimate soil moisture deficit might be a good starting point for developing an index specifically catering for the British conditions.

RESEARCH AND REVIEW STUDIES

Chapter 1

CLIMATOLOGY OF THE ARCTIC PLANETARY BOUNDARY LAYER

Igor Esau* and Svetlana Sorokina

G.C. Rieber Climate Institute of
Nansen Environmental and Remote Sensing Center and
Bjerknes Center for Climate Research, Bergen, Norway

ABSTRACT

One of the central problems of the state-of-the-art climatology is to understand the relationship between the observed near-surface processes, first of all the processes dependent on such meteorological quantities as temperature, humidity and wind, and the general atmospheric circulation and its long-term variability. Complications arise from the fact that the near-surface processes are affected by the vertical turbulent exchange. This study provides climatological estimates of the turbulent exchange and quantifies aspects of the turbulent exchange important for the Arctic climate. By definition, the planetary boundary layer (PBL) is the lowermost atmospheric layer where the vertical turbulent exchange (mixing) is non-negligible in description of meteorological processes. The study focuses on the unique Arctic PBL features rarely observed at lower latitudes, namely, turbulence development and mixing under conditions of strong atmospheric static stability and under strongly negative surface radiation balance. The proposed reconstruction of the Arctic PBL climatology is based on episodic turbulence field campaigns as well as on regular radiosounding, reanalysis and satellite data. We found that the main difficulty of the data analysis appears not from data scarcity as it has been traditionally claimed but from data inconsistency and low quality. The reconstruction reveals that the Arctic PBL is stably stratified in 70% to 100% of observations. But the continues periods of stably stratified PBL (SBL) development are typically less than 100 hours (4 days). The Arctic PBL is shallow. Its depth is typically less than 200 m and frequently less than 50 m. But over the Arctic Ocean, this shallow PBL is often well mixed due to the conductive heat transport through ice and the convection over polynyas. The Arctic PBL can often dynamically decouple from the rest of the atmosphere. During the periods of decoupling the temperature variability within the PBL is much larger (in

* igore@nersc.no; tel: +47 55205876; fax: +47 55205801

wintertime) or smaller (in summertime) than in the air aloft. Stability of the PBL and developing of the temperature inversions maintain high relative humidity (often above 90%) and the Arctic haze and fog. Models are sensitive to the Arctic PBL dynamics. However the model resolution is usually inadequate to the requirements of the employed turbulence parameterization schemes.

1. INTRODUCTION

One of the central problems of the state-of-the-art climatology is to understand the relationship between the observed near-surface processes, first of all the processes dependent on such meteorological quantities as temperature, humidity and wind, and the general atmospheric circulation and its long-term variability. This dependence is often referred to as surface-to-atmosphere coupling. The strength of the coupling is one of the most important factors responsible for shaping the Earth's Climate System. In the Arctic, the coupling is achieved through a general atmospheric circulation pattern, the vertical turbulent mixing and radiation transfer processes. Due to generally low temperatures, elements of hydrological cycle, which are important at lower latitudes, do not play a significant role in the Arctic surface-to-atmosphere coupling [Koster et al., 2004; Guo et al., 2006]. Low temperatures however result in the intimate coupling between the atmosphere and different cryospheric components [Serreze et al., 2007] such as sea ice, snow, permafrost etc. These cryospheric components force the atmospheric response on a variety of scales from meter-scale radiation heating inversions near the surface [Savijarvi, 2006] to region-scale tele-connections in the atmospheric circulation patterns [Adachi and Yukimoto, 2006].

This study is focused on the climatological aspects of the coupling through the vertical turbulent mixing. The turbulent mixing is a dynamical process in the Earth's Climate System, which generally reduces differences in temperature, humidity and momentum between the surface and different layers in the atmosphere. The lowermost atmospheric layer where the vertical turbulent mixing is indispensable to description of the meteorological processes is known as the planetary boundary layer (PBL). There are some complications however. If the time scale of turbulent mixing is comparable with the time scale of a non-turbulent process, e.g. the radiation heating or horizontal temperature advection, the adjacent mixed and non-mixed layers may evolve independently. In result, the turbulent mixing may sharpen the meteorological gradients at the top and bottom of the PBL and may cause its mechanical decoupling from the adjacent layers.

The direction of the vertical turbulent mixing is an important question to be addressed in this study. The Arctic obtains on average 100 W m^{-2} of the heat flux through the atmospheric and 5 W m^{-2} through the oceanic meridional advection [Semmler et al., 2005; Serreze et al., 2007]. This is comparable in magnitude with the components of the radiation balance. Arguably, the meridional advection is the largest source of heat and moisture in the wintertime Arctic. The bulk amount of heat and moisture is transported in the mid-troposphere, [Chase, 2002] which makes it potentially warmer and more humid than the near-surface layer. This feature of the temperature and humidity profiles is reinforced by the negative surface radiation balance and the differential radiation cooling in the atmosphere below about 3 km. In result, the Arctic PBL is usually stably stratified or at least develops against the stably stratified non-turbulent atmosphere. The turbulence has to transport heat downward acting

against buoyancy force in a process called a top-down turbulent mixing. The top-down turbulent mixing is less effective than the bottom-up turbulent mixing (convection) as the stable stratification damps the vertical extend of turbulent eddies and their vertical velocities.

The Arctic PBL is shallow. The question arises whether the observed large temperature fluctuations on annual, decadal and century scales [Overpeck et al., 1997; Polyakov et al., 2003; Bengtsson et al., 2004] are the PBL confined feature, possibly skewed and magnified (damped), or accurate [Langen and Alexeev, 2005] reflection of the circulation variability. The recent surface temperature trend in the Arctic is about twice as large as the Northern Hemisphere trend [ACIA, 2004]. The trends are also the largest in the shallow near-surface layer [Serreze et al., 2008] while this feature is still disputable [Graversen et al., 2008]. Manabe and Wetherald [1975] suggested that one reason for the larger by magnitude and shallow by vertical extend Arctic temperature trends is the trapping of temperature anomalies in the Arctic PBL. Although, these PBL trapped anomalies often comprise less than 100 m of the atmosphere, their impact on the Arctic ecosystems and cryosphere could be pronounced [Serreze et al., 2000; Serreze and Francis, 2006]. Sophisticated turbulence observational campaigns, e.g. the Arctic Ocean Experiment [Tjernstroem et al., 2005], have demonstrated that the Arctic PBL isolation is asymmetric. It tends to insulate the surface from synoptic warming events. But the cooling events can effectively lower the SAT as the PBL stability reduces and the turbulent mixing enhances. This remarkable asymmetry in the PBL response favors considerably lower mean SAT than it could be observed under invariable PBL mixing.

Unfortunately, the Arctic PBL processes, effects and related feedbacks are difficult to study. Arctic is a remote, sparsely populated place with no or very limited available infrastructure. Direct turbulence measurements require stable platform, electricity supply for instruments and data storage, frequent outdoor work with tethered balloons and radiosoundings, temporary landing strips for research aircrafts to study the inversion and clouds. The turbulence observational campaigns are expensive, difficult to organize and therefore fragmentary. Moreover, the turbulence measurement campaigns tend to be organized in summertime and in a few preferable locations where the logistics is relatively easy. Thus, there is rather detailed turbulence data in the Atlantic region of the Arctic around Spitsbergen Archipelago (see Figure 1) and in the Beaufort Sea in the Central Arctic region. At the same time, the direct turbulence observations in inland Canadian, Greenland, and Siberian Arctic and sub-Arctic regions are scarce. In recent years, international efforts and advancement of the on-line data services, especially in the National Data Centers in USA, improved data availability and open possibility to combine data from different campaigns, satellite data and the regular meteorological measurements to obtain better reconstruction of the Arctic PBL climatology. The reconstruction in this study is based on a limited selection of the best available data sources. A more comprehensive reconstruction study will be developed in future.

The models (algorithms) help to reconstruct the PBL climatology. The models are however imperfect [Mahrt, 1998; Cuxart et al., 2006; Brunke et al., 2006] and sensitive to the turbulence parameterization [Dethloff et al., 1997; Byrkjedal et al., 2008] and numerical resolution [Roekner et al., 2006; Esau and Byrkjedal, 2007]. As essentially the same models are used in climate model simulations, their deficiency causes problems for the Arctic climate change projections. The largest discrepancy and the largest inter-model scatter in the Intergovernmental Panel for Climate Change (IPCC) model simulations were found in high-latitude regions, in particular over the Arctic Ocean [ACIA, 2004; Sorterberg et al., 2007;

Wang et al., 2007; Walsh, 2008]. At the same time the largest changes, mainly strong warming, are also projected in the Arctic north of 60°N. In several studies [e.g. Bengtsson et al., 2004; Lawrence et al., 2008; Serreze et al., 2008], these changes are linked to altering state of the surface, primarily to the reduction of the sea ice, and hence the strength of the surface-atmospheric coupling. In order to evaluate credibility of such projections as well as to assess the impact of the human activity, actual or potential, on the Arctic environment, the better understanding of the Arctic PBL climatology is needed.

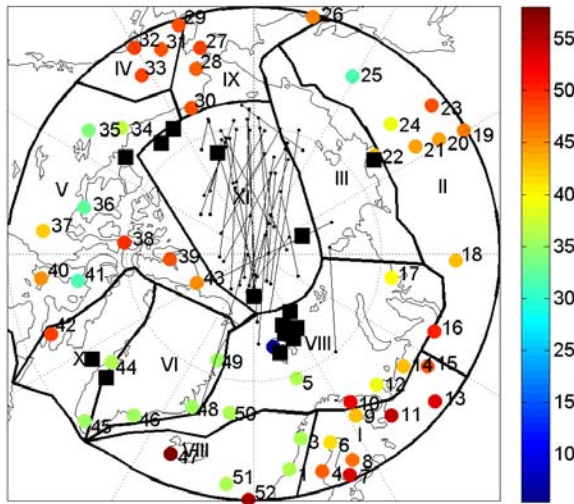


Figure 1. The Arctic region map. The map includes boundaries of the climate regions following the Atlas of the Arctic [Treshnikov, 1985]. The regions are identified by roman numbers I to IX according to Table 2. Geographical positions of 52 IGRA stations (Table 3) are marked with colour dots where colours (right colour bar) denote the total number of soundings in thousands. The station number is given near its location for each station. Geographical positions of the field turbulence campaigns (Table 4) are given by black squares. The black thin lines represent the Russian North Pole drift stations during 1979-2007.

In this study, we do not attempt to repeat or summarize the traditional aspects of the Arctic climatology that can be found elsewhere [e.g. Orvig, 1970; Fetterer and Radionov, 2000; Polyakov et al., 2003; Przybylak, 2003a, 2003b; ACIA, 2004; Serreze and Barry, 2005; Macdonald et al., 2005; IPCC, 2007; Walsh, 2008]. Web sites in Table 1 will help readers to obtain more detailed information on the Arctic climatology. It is worth to emphasize that even the traditional aspects of the Arctic climatology are established rather uncertainly. For instance, Overland et al. [2007] and Kuzmina et al. [2008] have demonstrated that the mean surface air temperature (SAT) patterns differ significantly from publication to publication and from database to database. In part this can be explained by scarcity and lower accuracy of the meteorological data in the Arctic as well as by interpolation and gap filling methods. But in part, this uncertainty should be also attributed to strong variability, both temporal and spatial, of the Arctic climate [Overpeck et al., 1997; Johannessen et al., 2003; Polyakov et al., 2003]. As the traditional climatology is largely based on the assessment of the surface meteorological characteristics, this enhanced variability may indicate the trapping and/or amplification of the anomalies in a shallow PBL and the other PBL related features.

Table 1. Web sites devoted to the Arctic climatology.

Web site title	URL
Arctic Climate Research at the University of Illinois. Leading authors: J. Walsh and W. Chapman	http://arctic.atmos.uiuc.edu/
"Greenland Climate" is part of the research project "Regional Climate Change in Greenland and Surrounding Seas". A data and knowledge base on the expected climate change in the Arctic, based on regional climate modeling, where the projections cover both meteorology and oceanography.	http://klimagroenland.dmi.dk/datauk.html
A special report on the Arctic climate research by the National Science foundation (USA)	http://www.nsf.gov/news/special_reports/arctic/index.jsp
Arctic Climate System Study (project finished in 2003)	http://acsy.npolar.no/
Arctic meteorology and climatology atlas	http://nsidc.org/arcticmet/basics/arctic_climate.html
A near real-time Arctic change indicators	http://www.arctic.noaa.gov/detect/
An international project of the Arctic Council and the International Arctic Science Committee (IASC), to evaluate and synthesize knowledge on climate variability, climate change, and increased ultraviolet radiation and their consequences.	http://www.acia.uaf.edu/
Arctic Monitoring and Assessment Programme (AMAP) is an international organization established in 1991 to implement components of the Arctic Environmental Protection Strategy (AEPS).	http://www.apmap.no/

Majority of published works on the PBL climatology attempted to assess the turbulent mixing in a limited spatial area and over very short, sometime just a few days, time interval. A pan-Arctic picture of the turbulent fluxes has been assembled in Russian publications [Treshnikov, 1985; Khrol, 1992] but this picture, based on fragmentary observations in the pre-satellite era, is somewhat inconsistent with more recent findings.

The Arctic consists of regions with very different physical and geographical conditions. There are several methods to classify the Arctic regions. For reference purposes, we adopt the classification of Arctic climate regions after the "*Atlas of the Arctic*" [Treshnikov, 1985]. We also include several sub-Arctic regions so that to complete the PBL climatology north of 60°N (see Figure 1). The regions are identified in Table 2. It should be noted however that the study

is organized following physical but not geographical principles. Therefore Treshnikov's geographical climate regions are grouped by similarity of the physical processes.

Table 2. Geographical climate regions according to the “*Atlas of the Arctic*” [Treshnikov, 1985] with recent modifications.

Continental regions:	Marine regions
I. European Sub-Arctic	VII. Atlantic Sub-Arctic region
II. Siberian Sub-Arctic	VIII. Atlantic region
III. Siberian	IX. Pacific region
IV. Alaska	X. Baffin Bay region
V. Canadian region	XI. Central Arctic region
VI. Greenland region	

The logical flow of this study is as follows. Section 2 describes the physical structure of the Arctic PBL obtained through the theoretical analysis and turbulence-resolving simulations. Also in this Section, the models (algorithms) are presented to relate the observable meteorological quantities with the turbulent characteristics such as fluxes. Section 3 characterizes data sets used in the study. Here, the special attention is paid to the data uncertainties and quality, in particular, to algorithms utilized to derive non observable quantities such as turbulent fluxes. Section 4 presents the reconstruction of the Arctic PBL climatology. The presentation consists of a general, pan-Arctic overview of the PBL climatology, more detailed discussions of the PBL features in each climatological region, and discussions of the cloud turbulence interaction and the PBL features over strongly heterogeneous surface. Section 5 presents the recent (1992-2007) trends in the PBL climatology and future projections for the Arctic PBL change. Section 6 summarizes the study.

2. THEORETICAL STRUCTURE OF THE ARCTIC PBL

Interpretation of often incomplete, inconsistent, noisy and biased observational data as well as time averaged data products requires certain physical understanding of the vertical structure and evolution of stratified boundary layers. This understanding is obtained from controllable laboratory experiments, theoretical considerations and, in recent years, from turbulence-resolving simulations. In particular, it has been understood that the dry, barotropic, statistically stationary PBL over homogeneous surface is controlled by a few external, relative to the PBL, parameters. The parameters are: the surface stability parameter $\mu = u_* (|f|L)^{-1}$; the imposed stability parameter $\mu_N = |f|^{-1} N$; the Rossby number $Ro = U (|f|z_{0u})^{-1}$; u_* [$m s^{-1}$] is the surface friction velocity or the square root of the amplitude of the vertical momentum flux; $f = 2\Omega \sin \varphi$ [s^{-1}] is the Coriolis parameter; $\Omega = 7.27 \cdot 10^{-5}$ [$rad s^{-1}$] is the Earth's angular velocity; φ [degrees] is the latitude; $L = -u_*^3 / (g\beta H / c_p \rho)$ [m] is the Monin-Obukhov length scale; H [$W m^{-2}$] is the sensible heat flux; $g = 9.81$ [$m s^{-1}$] is the

acceleration due to gravity; $\beta = 0.003$ [K] is the thermal expansion coefficient of air; $c_p = 1005$ [$\text{J kg}^{-1} \text{ K}^{-1}$] is the specific heat of air at constant pressure; ρ [kg] is the air density; $N = \sqrt{g\beta\partial\theta/\partial z}$ [s^{-1}] is the Brunt-Vaisala frequency; θ [K] is potential temperature; z [m] is the height above the surface; U [m s^{-1}] is the Geostrophic wind speed; and z_{0u} [m] is the aerodynamical roughness length for momentum. These parameters are related to each other through the PBL resistance laws [Zilitinkevich and Esau, 2005; Esau and Zilitinkevich, 2006]. In principal, the resistance laws give the relation between the climatological quantities, such as temperature, humidity, wind speed and direction, at any level within the PBL. However, the set of resistance laws consists of non-linear equations and therefore cannot be easily resolved with respect to observable surface and atmospheric parameters. The resistance laws read

$$\frac{\kappa}{C_g} \cos \alpha = \ln \frac{h}{z_{0u}} - A, \quad (1)$$

$$\frac{\kappa}{C_g} \sin \alpha = - \frac{|fh|}{u_*} B, \quad (2)$$

$$\frac{\kappa_T}{C_{TR}} = \ln \frac{h}{z_{0u}} - C, \quad \frac{\kappa_q}{C_{qR}} = \ln \frac{h}{z_{0u}} - D. \quad (3)$$

The coefficients A , B , C and D are considered as universal functions of h/L , where $\kappa=0.4$ is von Karman constant, h is the PBL depth. The geostrophic drag coefficient is $C_g = u_*/U$. In the limit of non-stratified, truly neutral PBL, the Rossby number and the geostrophic coefficient are related as $h/z_{0u} = C_g Ro$. The thermal and humidity resistance coefficients are $C_{TR} = \theta_*/(\theta_{z=h} - \theta_{z=0})$ and $C_{qR} = q_*/(q_{z=h} - q_{z=0})$. The theoretical approach becomes far less treatable if the atmospheric baroclinicity, microphysics, air subsidence and surface heterogeneity are taken into account.

The theoretical difficulties could be alleviated to some degree if the PBL depth is considered as the integral measure of the turbulent mixing [Zilitinkevich et al., 2002]. The prognostic PBL depth equation with the PBL entrainment rate w_h is usually formulated as a relaxation equation

$$dh/dt = w_h + (h_E - h)t_E^{-1} \quad (4)$$

The equilibrium PBL depth, h_E , is given for idealized stably stratified conditions [Zilitinkevich et al., 2007] as

$$h_E = C_R \frac{u_*}{|f|} (1 + C_{CN}\mu_N + C_{NS}\mu)^{-1/2}, \quad (5)$$

where $C_R = 0.6$, $C_{CN} = 1.3$ and $C_{NS} = 0.5$ are empirical constants fitted to the large-eddy simulations. For unstably stratified, convective conditions, the formulation reads [Fedorovich et al., 2004] as

$$h_E = (C' Ht / c_p \rho)^{1/2} N^{-1}, \text{ where } C' = 1.67. \quad (6)$$

Therefore, the theory suggests the following set of key parameters for the PBL climatology: the surface momentum flux, the sensible and latent heat fluxes, the stability of the free atmosphere above the PBL, and the PBL depth.

These parameters are often not observed, which makes necessary to invoke additional assumptions on the turbulent mixing. In this case, gradient measurements near the surface may help providing the required information through flux-gradient models, e.g. TOGA-COARE bulk flux model [Fairall et al. 2003],

$$\theta_* = -\tau_{\theta_s} / u_* = \rho c_p C_\theta U_z (\theta_s - \theta_a) / u_*, \quad (7)$$

$$q_* = -\tau_{qs} / u_* = \rho c_p L_q C_q U_z (q_s - q_a) / u_*, \quad (8)$$

$$u_* = \sqrt{|\tau_s|} = \sqrt{\rho C_M} |U_z|. \quad (9)$$

Here the lower index z denotes the height of measurements. The standard heights of 2 m and 10 m are often in use. The exchange coefficients C_M , C_θ , and C_q are determined utilizing Monin-Obukhov similarity theory as

$$C_M = \kappa^2 \left(\ln \frac{z}{z_{0u}} - \Psi_M(z/L) \right)^{-2}, \quad (10)$$

$$C_\theta = \sqrt{C_M} \frac{\kappa}{\ln \frac{z}{z_{0T}} - \Psi_T(z/L)}, \quad (11)$$

$$C_q = \sqrt{C_M} \frac{\kappa}{\ln \frac{z}{z_{0q}} - \Psi_q(z/L)}. \quad (12)$$

Here Ψ_M , Ψ_θ , Ψ_q are the universal Monin-Obukhov stability functions; z_{0T} , z_{0q} are the aerodynamic roughness lengths for temperature and moisture correspondingly. These functions and coefficients need to be determined empirically albeit several works have tried

to establish functional relationships for them [e.g. Andreas, 1987; Andreas et al., 2004]. The empirical Monin-Obukhov similarity functions in the integral form read

$$\Psi_M(z/L) = 2 \ln\left(\frac{1+x}{2}\right) + \ln\left(\frac{1+x^2}{2}\right) - 2 \arctan x + \pi/2, \text{ for } (13)$$

$$z/L < 0 \quad (14)$$

$$\Psi_M(z/L) = -\beta_M z/L, \text{ for } z/L > 0$$

$$\Psi_T(z/L) = \Psi_q(z/L) = 2 \ln\left(\frac{1+y}{2}\right), \text{ for } z/L < 0 \quad (15)$$

$$\Psi_T(z/L) = \Psi_q(z/L) = -\beta_T z/L, \text{ for } z/L > 0 \quad (16)$$

$$x = (1 - \gamma_M z/L)^{1/4}, \quad y = (1 - \gamma_T z/L)^{1/2} \quad (17)$$

And the constants are taken $\gamma_M = \gamma_T \approx 16$ and $\beta_M = \beta_T \approx 5$ in many applications.

As the vertical profiles of the turbulent fluxes are unavailable from the regular meteorological measurements as well as from the majority of the dedicated turbulence campaigns, indirect methods based on interpretation of coarse resolution vertical profiles of the wind speed and temperature have to be used in the PBL depth calculations. One of the most robust and popular methods is a bulk Richardson number algorithm proposed by Troen and Mahrt [1986]. In the method, h is defined as the lowest height $z = h$ at which the bulk Richardson number exceeds the critical Richardson number, i.e. $Ri_b > Ri_{cr}$.

$$Ri_b = \frac{g}{\theta_0} \frac{\theta(z) - \theta_s}{u^2(z)} z \quad (18)$$

The choice of Ri_{cr} is rather arbitrary and varies from 0.15 to 0.5.

3. DATA SETS AND PROXIES

Data coverage of the Arctic is rapidly improving in the satellite era. At the same time, snow, ice and low level cloud cover create significant difficulties for the satellite data retrieval. It may explain why many “global” satellite products practically do not present data north of 60 degrees [e.g. Chen et al., 2008].

The Arctic climatology also struggles from uneven geographical distribution of the observations as well as their tendency to be denser in summer and spring seasons and along coastal lines. Subsequent research publications tends to use springtime (April, May) observations as proxy for the winter season data and the summertime (July, August)

observations as proxy for the summer and autumn seasons. Although the use of summertime data to characterize the warm season is probably reasonable, especially over the permanently snow and ice covered surface, the still low springtime temperatures cannot justify the extrapolation toward the cold season due to significant differences in the atmospheric vertical structure and energy balance.

In this study, we characterize each group of climate regions with in situ direct turbulence measurements from at least one field campaign. The sources of information are presented in Figure 1. These measurements are combined with the gridded data, mainly with the reanalysis data, and satellite data products.

Pan-Arctic Data Sets

Pan-Arctic data sets are reanalysis and satellite products. They could be used to characterize general properties of the PBL climate as well as to outline regional specifics. The primary source of the in situ meteorological information is a network of stations, which carry out regular radio soundings of the atmosphere. We utilized the Integrated Global Radiosonde Archive (IGRA), [<ftp://ftp.ncdc.noaa.gov/pub/data/igra/data-por>] which comprises globally 1485 stations and includes over 28 million soundings of temperature, pressure, humidity and wind speed, with a total of 800 million levels [Gaffen, 1996]. Observations are available for the standard levels (1000, 925, 850, 700, 500, 400, 300, 250, 200, 150, 100 hPa), the surface, the tropopause and significant levels for temperature, geopotential height, dew point depression, and wind direction and speed. The period of record varies from station to station, with many extending from 1970 to 2008. All the soundings are processed with quality controls using the method described in [<http://www.ncdc.noaa.gov/oa/climate/igra>].

For the Arctic PBL climatology, the IGRA data were sampled at latitudes north of 60°N. There are 113 stations in the selected region. However, many records do not include a complete set of variables necessary to PBL climatology, namely, pressure, temperature, geopotential height, and wind speed for each sounding, at least at standard and surface levels. Those records were excluded from the data set. Table 3 lists the stations included in the presented analysis. Table 3 also provides information about the station number in this study (Number), their World Meteorological Organization index (WMO ID), latitude and longitude, period of data coverage (Time span), total number of launched soundings (Soundings), and the fraction of soundings with complete set of variables for this study. Totally, there are 52 IGRA stations to be used for PBL climatology reconstruction. The amount of data at every station is shown in Figure 1. The major problem with IGRA is its coarse vertical resolution. Many stations did not report 925 hPa level before 1992. As the Arctic PBL is expected to be shallow, 925 hPa level is of particular importance. Therefore, we reconstruct the IGRA PBL climatology only for 1992-2007. The exceptions are four stations with WMO ID (01028, 71043, 71925, 04270) where the complete data are available only for 1995-2007. Nevertheless, the vertical resolution of IGRA profiles is not sufficient to obtain the PBL depth with desired accuracy. We compromise on the PBL depth by setting it equal to the mean height of the level between two lowest standard isobaric levels where $Ri_b > Ri_{cr} = 0.5$.

This procedure is expected to exaggerate somewhat the PBL depth computed from IGRA soundings.

The regional PBL climatology is enhanced with short term turbulence campaigns. The campaigns are enlisted in Table 4. Although the campaigns do not provide climatologically significant data time series, they provide a deeper insight on the PBL structure and its short term variability thus constraining the errors and possible misinterpretation of the related information in the climatological data sets.

Satellite products are advantageous for the climatology reconstruction due to their regular and dense spatial data coverage. The disadvantage is their somewhat shorter time coverage and relative inaccuracy as they retrieve the requested meteorological quantities using proxy radiometer data and set of analytical bulk algorithms. There were several attempts to quantify uncertainties in the products, including studies related to the Arctic region [e.g. Chen et al., 2002] but more efforts are clearly needed. In particular Chen et al. [2002] found large temperature biases between the television-infrared observation satellite operational vertical sounder polar pathfinder (TOVS) and the International Arctic Buoy Program/Polar Exchange at the Sea Surface (IABP/POLES). TOVS temperatures were generally colder (up to -6 K) over snow/ice surfaces and warmer (up to +7 K) over tundra and open water surfaces. They recommended rejecting the TOVS retrievals in summer when the retrieved cloud cover is over 95%.

The third version of 49-year (1958-2006) analysis of latent and sensible heat fluxes, ocean evaporation, and flux-related surface meteorological variables was released by the Objectively Analyzed Air-Sea Heat Fluxes (OAFlux) project in January 2008 (Yu et al., 2008). The product is available from [<http://oaflux.whoi.edu/>]. The OAFlux products are an optimal blending of satellite retrievals and three atmospheric reanalyses. Daily fluxes are computed from the optimally estimated variables using the COARE bulk flux algorithm 3.0 [Fairall et al., 2003].

The Hamburg Ocean Atmosphere Parameters and Fluxes from Satellite Data set version 3 (HOAPS-3) contains basic state variables for the derivation of the fluxes [Grassl et al., 2000]. Except for the NODC/RSMAS Pathfinder sea surface temperature data set, all variables are derived from SSM/I passive microwave satellite data over the ice free global ocean. HOAPS-3 covers 18 complete years of data from July 1987 to December 2005. HOAPS provides data only for open ocean whereas OAFlux provides data for the whole Arctic.

There are several regional and global reanalysis products available to reconstruct the PBL climatology. In this study, only the European Centre for Medium-Range Weather Forecasts (ECMWF) reanalyses ERA-40 is utilized. As it has been announced, the Arctic Regional Reanalysis based on a polar version of the Weather Research and Forecast (WRF) model will be available by 2010. Up to date, only independent regional reanalysis are available and will be discussed in the regional data sections. ERA-40 is the second generation reanalysis [Uppala et al., 2005]. It assimilates data from the terrestrial global observational system, rawinsondes, including those in IGRA but with different quality control and correction procedures, and from the late 1970s the satellite observational system data. Temporal and spatial heterogeneity of observational sources creates difficulties in homogenization of the ERA-40 data over longer time periods. Bengtsson et al. [2004] questioned quality of trends computed from the ERA40 reanalysis for the period 1958–2001 in the context of changes to the global observing system. They found that changes in the observational system causes errors in the climate trends if calculated throughout 1979. Another known problem is a cold

temperature bias caused by HIRS satellite in 1979-1997. Both problems however have primary effect on the troposphere above the PBL.

Table 3. Information about IGRA stations north of 60°N, included into the present PBL climatology analysis. The stations are sorted by East longitudes.

Number	Station	WMO ID	East lon	North lat	Time span	Complete Soundings		Complete Soundings	
						Total period	%	1992-2007	%
1	ORLAND	01241	9,4	63,7	1963-2008	30929	33,9	11072	74,4
2	NY-ALESUND II	01004	11,9	78,9	1993-2008	5396	76,5	4997	79,4
3	BODO	01152	14,4	67,3	1963-2008	30809	28,9	10923	68,6
4	SUNDSVALL/HARNOSA ND	02365	17,5	62,5	1965-2008	42426	36,1	14380	77,0
5	BJORNOYA	01028	19	74,5	1963-2008	31223	25,1	11272	61,2
6	LULEA/KALLAX	02185	22,1	65,6	1964-2008	36400	35,6	12662	75,9
7	JOKIOINEN	02963	23,5	60,8	1957-2008	47880	16,6	11532	50,6
8	JYVASKYLA	02935	25,7	62,4	1964-2008	41577	12,7	11517	33,8
9	KANDALAKSA	22217	32,4	67,2	1957-2008	37947	24,5	8943	77,7
10	MURMANSK	22113	33,1	69	1946-2008	47540	11,0	10249	34,1
11	ARKHANGEL'SK	22550	40,5	64,5	1946-2008	49724	24,9	10382	83,6
12	KANIN NOS/SOJNA	22271	43,3	68,7	1962-2008	34169	21,3	6845	78,1
13	SYKTYVKAR	23804	50,9	61,7	1947-2008	47944	11,9	9906	46,1
14	NAR'JAN-MAR	23205	53,1	67,7	1963-2008	38046	25,9	8442	80,0
15	PECHORA	23418	57,1	65,1	1953-2008	43201	15,8	7391	68,3
16	SALEHARD	23330	66,7	66,5	1948-2008	45131	28,1	9137	82,6
17	OSTROV DIKSON	20674	80,2	73,5	1948-2008	34768	16,4	5869	69,4
18	TURUHANSK	23472	88,0	65,8	1963-2008	37833	31,5	9186	79,8
19	OLEKMINSK	24944	120,4	60,4	1950-2008	41131	15,2	6675	46,8
20	VILYUYSK	24641	121,6	63,8	1950-2008	39616	18,1	7015	52,6
21	ZHIGANSK	24343	123,4	66,8	1950-2008	39546	17,7	6659	67,6
22	TIKSI	21824	128,9	71,6	1948-2008	37858	30,1	7296	92,6

Table 3. Continued.

Number	Station	WMO ID	East lon	North lat	Time span	Complete Soundings		Complete Soundings	
						Total period	%	1992-2007	%
23	YAKUTSK	24959	129,8	62	1957-2008	42847	25,8	9997	53,6
24	VERKHOYANSK	24266	133,4	67,5	1963-2008	33885	17,7	8558	43,6
25	ZYRYANKA	25400	150,9	65,7	1954-2008	26952	29,6	6985	83,2
26	KORF	25954	166,0	60,4	1952-2006	40789	18,6	5097	86,3
27	NOME	70200	194,6	64,5	1948-2008	43612	35,5	11538	71,7
28	KOTZEBUE	70133	197,4	66,9	1948-2008	41997	38,9	11568	79,7
29	BETHEL	70219	198,3	60,8	1948-2008	43337	25,3	11480	60,0
30	BARROW	70026	203,2	71,3	1948-2008	43324	43,7	11698	87,4
31	MCGRATH	70231	204,4	63	1948-2008	43373	19,6	11415	34,4
32	ANCHORAGE	70273	210,2	61,2	1948-2008	44086	28,3	11688	57,0
33	FAIRBANKS	70261	212,3	64,8	1948-2008	43845	14,0	11605	24,1
34	INUVIK	71957	226,5	68,3	1963-2008	31686	28,7	11334	57,2
35	NORMAN WELLS	71043	233,2	65,3	1955-2008	28613	34,6	11141	53,6
36	CAMBRIDGE BAY	71925	254,9	69,1	1970-2008	27461	46,6	11484	80,9
37	BAKER LAKE	71926	264,0	64,5	1949-2008	37086	36,8	10966	72,6
38	RESOLUTE	71924	265,0	74,7	1948-2008	44862	32,2	11324	72,9
39	EUREKA	71917	273,8	80,2	1948-2008	43323	55,4	11468	88,3
40	CORAL HARBOUR	71915	276,6	64,2	1950-2008	40385	28,9	10597	69,7
41	HALL BEACH	71081	278,8	68,8	1957-2008	26982	46,8	11305	77,5
42	IQALUIT	71909	291,6	63,7	1946-2008	44049	36,4	11288	77,3
43	ALERT	71082	297,3	82,5	1950-2008	40312	40,4	11296	69,7
44	EGEDESMINDE	04220	307,3	68,7	1963-2008	31087	32,6	11305	66,5
45	NARSSARSSUAQ	04270	314,6	61,2	1963-2008	30159	38,2	11412	71,2
46	ANGMAGSSALIK	04360	323,3	65,9	1963-2008	30638	34,4	11159	58,5
47	KEFLAVIK	04018	337,4	64	1946-2008	53082	15,0	10924	46,9

Table 3. Continued.

Number	Station	WMO ID	East lon	North lat	Time span	Complete Soundings		Complete Soundings	
						Total period	%	1992-2007	%
48	SCORESBYSUND	04339	338,0	70,5	1963-2008	30722	37,7	11105	64,4
49	DANMARKSHAVN	04320	341,2	76,8	1963-2008	30180	46,8	11184	84,4
50	JAN MAYEN	01001	351,3	71	1963-2008	30981	33,4	11273	74,4
51	THORSHAVN	06011	353,2	62	1963-2008	31319	24,0	11473	58,2
52	LERWICK	03005	358,8	60,1	1963-2008	50548	17,3	16481	48,1

Table 4. The field turbulence and in-situ meteorological campaigns used in this study.

Name	Region	Period	latitude	longitude
AOE	Atlantic	2001	80°N-90°N	15°W-15°E
ARCTEX	Atlantic	2006	79°N	12°W
Arctic Stratus Experiment	Central Arctic/ Beaufort Sea	June 1980	73°N	140°W
ARK-XII	Siberian (Laptev, East Siberian, Chukchi Seas)	July-September 1996	77°N-87°N	60°E-160°E
ARTIST	Atlantic	1997-1998	79°N	12°W
BASE	Canadian region/ Mackenzie Basin, Beaufort sea	September-October 1994	60°N -75°N	117°W-147°W
CEAREX	Atlantic	Sep 1988-May 1989	60°N-80°N	25°W-25°E
GAME-Siberia	Siberian Sub-Arctic	1998-2000	72°N	128°E
KABEG	Greenland (Davis strait)	April-May 1997	67°N	49°W
LEADEX	Central Arctic	March-April 1992	65°N-80°N	180°W-120°W
PARCA	Greenland	2003-2007	67°N	48°W-50°W
REFLEX	Atlantic	1991, 1993, 1995	78°N	15°E
SHEBA	Central Arctic	October 1997-March 1998	75°N-80°N	142°W-166°W
SVALEX	Atlantic	2005	79°N	12°W
WARPS	Atlantic	2003	78°N	15°E

ERA-40 data contains considerable errors in the PBL too. Beesley et al. (2000) compared ECMWF forecast model with instrumental, lidar and radar measurements during the SHEBA field campaign for November and December of 1997. They found near-surface winds and

surface downward longwave irradiance in the model were in good agreement with SHEBA data. The largest discrepancies between the ECMWF model and the observations were in surface temperature (up to 15 K) and turbulent sensible heat fluxes (up to 60 W m^{-2}). This is due to slow response in the model of the air temperature to the cold advection and clear-sky radiative cooling. The slow response could be in part due to too deep PBL in the model [Cuxart et al., 2006]. Although ECMWF model stands behind the ERA-40 reanalysis, the PBL problem in the reanalysis may be less pronounced as it is constrained by observations. Nevertheless, ERA-40 to in situ data comparisons have revealed that discrepancies in ERA-40 could be also large. Renfrew et al. [2002] compared observations taken on board of the research vessel Knorr during the period 6 February to 13 March 1997 in the Labrador Sea Deep Convection Experiment with ECMWF and the National Centers for Environmental Prediction (NCEP) reanalysis. The PBL generally compares well with the reanalysis. The biases that exist are mainly related to discrepancies in the sea surface temperature or the relative humidity of the analyses. The bulk estimates of the turbulent surface fluxes were compared with the corresponding fluxes in reanalysis (see Table 5). ERA-40 overestimates the observationally derived convective fluxes only by about 10%. This result is much better than for the NCER reanalysis where fluxes were overestimated by 25% to 50%.

Table 5. Comparisons of surface turbulent flux data from research vessel *Knorr* and from ECMWF model. The *Knorr* data are calculated using bulk surface flux algorithm. In order to account for algorithmic difference in the ECMWF and *Knorr* data, the bulk fluxes (marked with *) were recalculated using the same *Knorr* algorithm. Data are taken from Renfrew et al. [2002]. In Table, SHF is the sensible heat flux, LHF – the latent heat flux, STRESS – the momentum flux. All heat fluxes are given in W m^{-2} , the momentum flux is given in N m^{-2} .

	SHF	LHF	STRESS	*Bulk SHF	*Bulk LHF	
Mean	183.8	136.2	0.28	-	-	<i>Knorr</i>
	208.0	150.4	0.37			ECMWF
RMS	100.0	56.5	0.16	-	-	<i>Knorr</i>
	129.8	74.3	0.24	-	-	ECMWF
Max	406.5	243.5	0.72	-	-	<i>Knorr</i>
	479.5	287.3	1.11	-	-	ECMWF
Min	-43.7	-8.9	0.01	-	-	<i>Knorr</i>
	-56.1	-22.2	0.01			ECMWF
Corr.	0.93	0.90	0.82	0.91	0.87	<i>Knorr</i>
						ECMWF
Slope	1.21	1.18	1.27	0.99	0.90	<i>Knorr</i>
						ECMWF
Bias	24.2	14.2	0.10	0.8	-7.5	<i>Knorr</i>
						ECMWF
Slope error	120.1	66.5	0.20	98.5	50.5	<i>Knorr</i>
						ECMWF
Rand. error	110.4	64.9	0.21	109.2	62.9	<i>Knorr</i>
						ECMWF
Total RMS	164.9	94.0	0.31	147.0	81.0	<i>Knorr</i>
						ECMWF

ERA-40 generally overestimates the surface turbulent flux both for open water and ice/snow covered surfaces. Moreover, ERA-40 overestimates the fluxes in the lower troposphere making the PBL considerably deeper than it was observed in the turbulent campaigns. Byrkjedal et al. [2008] suggested on the basis of general circulation simulations with a greatly refined vertical resolution that a part of this bias could be explained by too coarse resolution of ERA-40. A part of the bias should be also attributed to the turbulence closure in the ECMWF model as the first order turbulence closure schemes in combination with coarse vertical mesh tend to overestimate the surface fluxes [Cuxart et al., 2006; Esau and Byrkjedal, 2007]. At the same time, Bromwich and Wang [2005] work admonishes from overwhelming reliance on the in situ and campaign data as they also could be biased.

Maritime Arctic Regions

The maritime Arctic comprises the Atlantic Arctic and sub-Arctic regions, Baffin Bay and Pacific regions. These regions are ice free totally or over a large part of the year. Thus the PBL in those regions is mostly convective with active turbulent mixing in a deep atmospheric layer. The Atlantic regions are the most accessible and the most developed regions of the Arctic. The main physical surface feature in the Atlantic Arctic region is the permanent presence of the sea ice edge. The location of the edge is changing on inter- and intra-annual basis in some places by 1000 km. The ice is good isolator. Hence the vertical structures of the PBL over ice (mostly the SBL) and over open water (mostly the CBL) are contrasting. Error in determination of the ice margin, e.g. in climate models, leads to data misinterpretation and erroneous climatology. Thus, it is important to observe where relative to the ice edge the data were obtained.

Arctic Ocean Experiment (AOE-2001) can be used to characterize the PBL over sea ice. It was conducted from the icebreaker Oden [Tjernström et al., 2004; Tjernström, 2005]. Oden was moored to a 1.5 km by 3 km ice floe and drifted roughly southward with the ice. On Oden and on ice about 300 m from the ship several turbulence measuring instruments were deployed including two sodar systems, a tethered sounding system, micro-barographs and an 18-m instrumented mast. The Arctic Turbulence Experiment (ARCTEX-2006), the Arctic Radiation and Turbulence Interaction Study (ARTIST-1998) can be used to characterize the PBL over open water. The observations were done at Ny-Ålesund in the Kongsfjorden (78.933°N , 11.933°E , 11 m a.s.l.). The instrumentation employed in the field work included: a three-axis Doppler sodar, a tethersounding station, a micrometeorological station, a sensor to measure the ground flux, and three subsoil thermometers. The other experiments are listed in Table 4.

Central Arctic Regions

The central Arctic comprises the Central Arctic, Canadian and Siberian regions. Surprisingly, the Central Arctic region is relatively well covered with data (see Figure 1). In part this is because of the permanent sea ice cover, which provides a stable platform for measurements and simultaneously allows relatively easy logistics by ships and aircrafts throughout the year. But in part, this is because of the strategic importance of the region and

hence relatively large funding of scientific programme. The observations in the region are representative due to general homogeneity of the surface. The problems may appear however if the measurements were occasionally done near lee sides of open leads and polynyas where the transient convective plumes can significantly distort the representation of the turbulent mixing in the data [e.g. Makshtas, 1991].

The regular soundings were launched from the Russian drifting North Pole stations (NP). Over the period 1979-1991, there were continues coverage by at least one, usually two, stations deployed on the drifting ice. The NP program was renewed in 2003 but the data are to be processed yet. The NP data are available from the Arctic and Antarctic research institute in Sankt-Petersburg, Russia, as well as on a CD-ROM from the National Snow and Ice Data Center (NSIDC).

There were several dedicated field turbulence campaigns to study the structure of the Central Arctic PBL (see Table 4). One of the best sources of high quality PBL data in the Central Arctic region is the Surface Heat Budget of the Arctic Ocean (SHEBA) field experiment. SHEBA was conducted on drifting ice floe in Beaufort and Chukchi seas north of Alaska (75°N to 80°N and 142°E to 166°W) from 2 October 1997 to 11 October 1998 with an intensive observational period in May 1998. The data from the SHEBA experiment was taken from [<http://www.eol.ucar.edu/projects/sheba/>] and the experiment description has been published by Uttal et al. [2002]. Turbulent flux measurements were made at six levels on a 20 m tower in the main camp and at four remote portable automated stations.

Continental Sub-Arctic Regions

The continental Arctic regions comprise the European, Siberian, and Alaska sub-Arctic regions. Over the most of the year (9-10 months) those regions are covered with ice and snow. Low annual mean air temperatures maintain the permafrost in soil. The main feature of these regions is a short but warm summer where relatively deep convective PBL develops. Unlike the Arctic PBL, the PBL over continental sub-Arctic regions is less comprehensively studied. There are several permanent turbulence observing stations, e.g. Sodankyla in Finland. But the data are collected mostly for specific process studies over shorter periods of time. It is difficult to get access to the processed data from those studies. One of the most accessible experiments is the GEWEX Asian Monsoon Experiment (GAME) – Siberia. The experiment was performed during 1998-2000 in the vicinity of Yakutsk. The measurements characterize the northern taiga forest punctuated with large number of open water patches like bogs, marshes, lakes and rivers.

There is a relatively dense network of regular meteorological stations with available gradient measurements in the regions, especially in the Europe. Groisman et al. [1997], Groisman and Genikhovich [1997] and Groisman et al. [1999] used the network of 223 first order stations to compute the PBL climatology utilizing a modified bulk flux. The climatology covers 1960 through 1990 period. The approach is based on of the Monin-Obukhov similarity theory and the integral analysis of the eddy diffusivity. It utilizes the surface temperature, which is routinely observed, and the temperature observed at 2 m. As the surface temperature is not a good proxy for the aerodynamic surface temperature, the errors in the gradient and therefore flux estimations in the methods could be considerable. Their estimation could be found in Genikhovich and Osipova [1984].

Greenland Region

The Greenland surface is a high elevated ice plateau. It gives the Greenland PBL climate unique features combining those of the continental and central Arctic regions on the plateau but specific to the mountain valleys on the slopes. Interior of Greenland has become more accessible for observations and PBL studies over the recent years. In 1995, the Greenland Climate Network (GC-Net) [<http://cires.colorado.edu/science/groups/steffen/gcnet/>], coordinated by CIRES, has begun observations with more than 15 automatic meteorological stations. These stations do not provide regular data for the flux-gradient turbulent model so that the surface temperature should be inferred from the radiation data, e.g. utilizing the surface radiation balance and the Stefan-Boltzmann law, and the aerodynamic roughness should be introduced ad hoc. The approach could give only rough estimations as its errors can reach 1.5 K that is larger than the expected surface to air temperature difference.

Comprehensive and probably better quality turbulent fluxes could be extracted from the Greenland Climate Change (GCC) [<http://klimagroenland.dmi.dk/datauk.html>] data archive. GCC contains results of a transient climate simulation for the period 1950 to 2080 using a regional climate model HIRHAM4 covering Greenland and surrounding seas at a horizontal resolution of 25 km [Stendel et al., 2007].

Several field experiments were conducted on the slope of the ice sheet and on the summit (Tables 4). The slope data were collected during the aircraft-based experiment “Katabatic Wind and Boundary-Layer Front Experiment around Greenland” (KABEG-1997) in April/May 1997. Surface stations were deployed at five positions on the ice sheet and in tundra near Kangerlussuaq, West Greenland. In addition, a total of nine flights were performed. The measurements could be used for studies of the three dimensional structure of katabatic winds and shear-induced turbulent mixing. The summit data were collected during the “Investigation of the Greenland Boundary Layer over Summit” experiment (IGLOS). The main measurement platform was a research aircraft “Polar2” equipped with turbulence and radiation sensors METEOPOD. At the surface, the measurements of turbulent and radiation fluxes were made at Summit Camp, as well as with the turbulence measurements from the 50 m tower of the ETH Zurich.

It should be mentioned that measurements on the ice sheet in the ablation zone are complicated by the ice melt. Moreover, the ice is preferably melting under impurities. Masts can melt down into the ice by a few tens of cm, deviating from the upright position and changing the elevation of sensors.

4. ARCTIC PBL CLIMATOLOGY RECONSTRUCTION

The typical Arctic PBL is shallow, stably stratified and covered with low-level stratus (St) and stratocumulus (Sc) clouds. The Arctic PBL has usually enough time (10 to 20 hours and often longer) to equilibrate the turbulent mixing with the radiation balance and temperature, humidity profiles imposed by the general circulation. In result, the averaged cooling/warming rates in the atmosphere are low, which leads to a popular meteorological notion of the “coreless” winter/summer. The Arctic PBL is often thermo-dynamically decoupled from the lower atmosphere above and sometimes decoupled from the surface. The

decoupling means that wind and temperature variability within the PBL does not correspond closely to the variability outside the PBL. Over the Arctic Ocean, the shallow PBL is often well mixed due to conductive heat through thin ice and convective mixing over open water in leads and polynyas.

The depth of the PBL is readily available in ERA-40 reanalysis product (Figure 2a). Utilizing Serafin and Zardi [2005] algorithm based on Troen and Mahrt [1986] method, the PBL depth was also computed from IGRA data (Figure 2b). Generally both data sets agree on the geographical distribution of the PBL depth. It should be noted however that the PBL depth is likely overestimated here [Beare et al., 2006; Cuxart et al., 2006] as the vertical resolution of the radiosoundings is too coarse.

The interannual variation of the PBL depth for each region is presented in Figure 3 (continental regions) and 4 (maritime regions). For continental regions the PBL is the deepest during summer months when the amount of solar radiation maximizes and so does the surface radiative heating. For maritime regions the PBL is the deepest during winter and spring months when the air-sea temperature difference is the greatest.

The static stability and shallowness of the Arctic PBL are potent factor of the cold climate formation. The buoyancy force in the stably stratified PBL (SBL) damps the turbulent exchange so that the cold temperatures at the radiatively cooled surface cannot be effectively mixed with the warmer air advected from the lower latitudes at about 1 km to 3 km. As the near surface air is kept below the ice melting point, it initiates the non-turbulent climate feedbacks (ice-albedo and emissivity) that low the temperature even further. Large temperature gradients near the top of the Arctic PBL (the capping inversion) are favorable to the cloud formation especially in summertime, which also reduce the PBL heating rates.

In the Arctic, both the physical (radiation) and dynamical (meridional advection and subsidence in the polar circulation cell) atmospheric processes support the atmospheric stable re-stratification. The averaged vertical profiles of temperature and relative humidity are shown in Figure 5 for the entire Arctic. Figure 6 for the Atlantic Sub-Arctic and Figure 7 for the Siberian sub-Arctic regions contrast the transformation of the vertical structure of the troposphere during the advection across the Arctic.

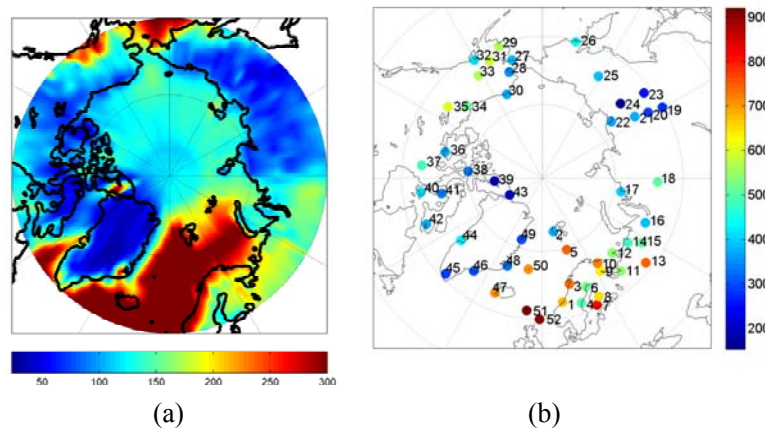


Figure 2. The mean annual PBL depth in (a) ERA40 during 1979-2001, and (b) IGRA during 1979-2007. The depth is given in meters. The depth larger than 300 m is not shown for the ERA-40.

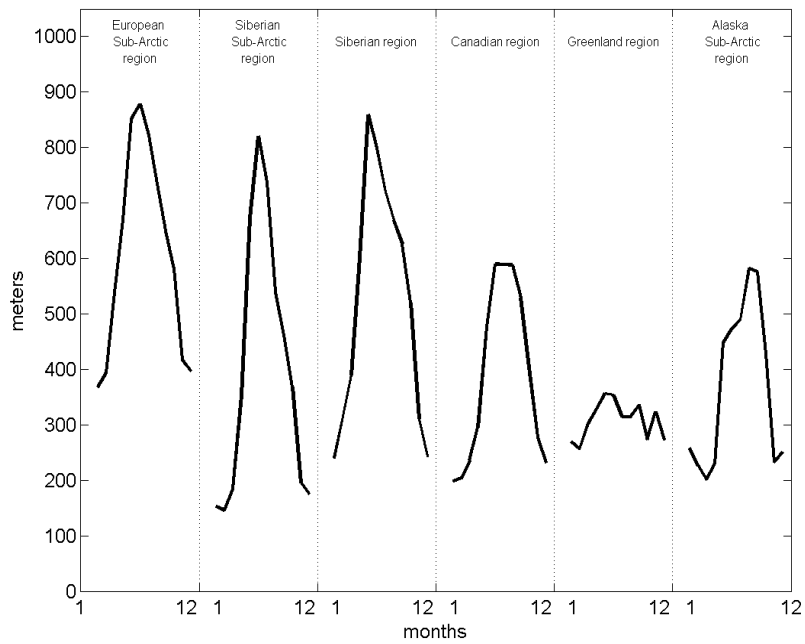


Figure 3. Average seasonal cycle of PBL depth over the climate regions. Continental zone.

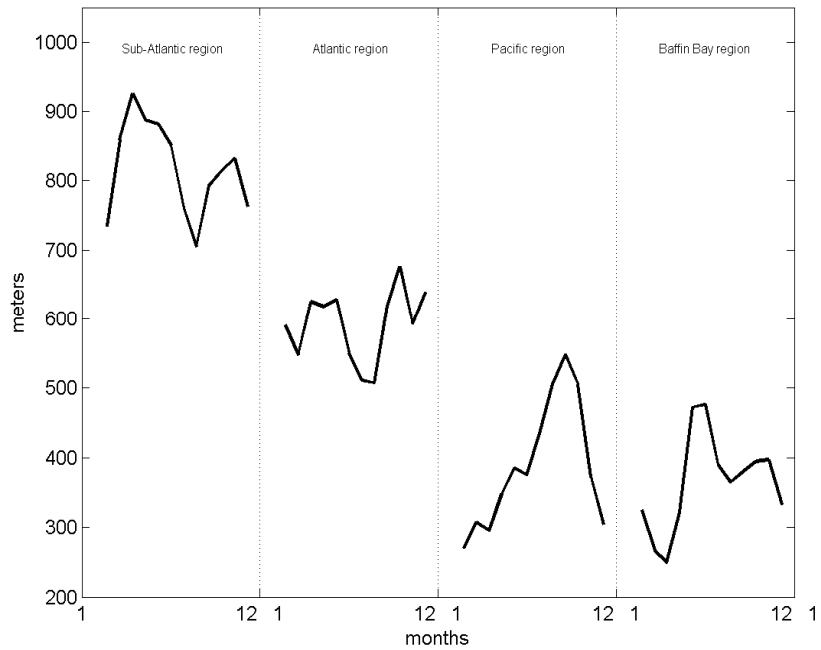


Figure 4. Average seasonal cycle of PBL depth over the climate regions. Marine zone.

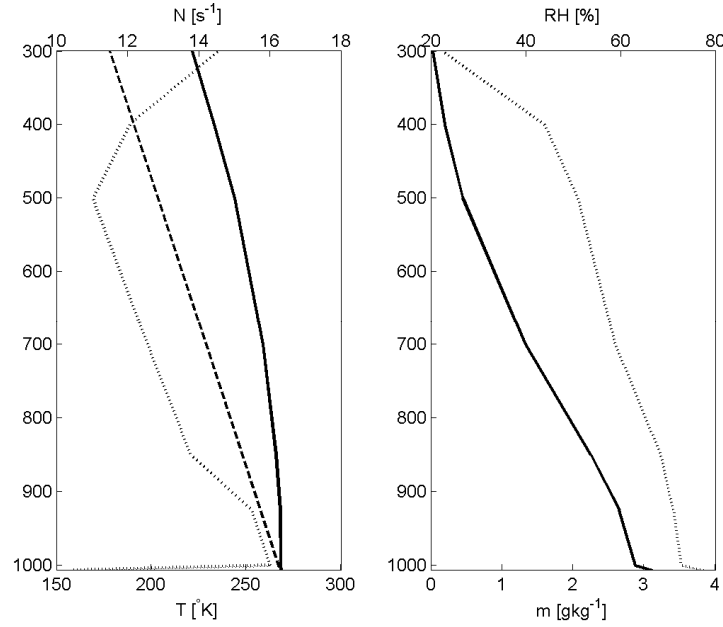


Figure 5. The annual mean vertical profiles from the IGRA data averaged over the entire data set during 1992-2007. Panel (a) shows the absolute temperature (solid line) in [K], the dry adiabate (dashed line), the Brunt – Vaisala frequency N (dotted line) in [1000s^{-1}]. Panel (b) shows The mixing ratio (solid line) in [g kg^{-1}], and relative humidity RH (dotted line) in [%].

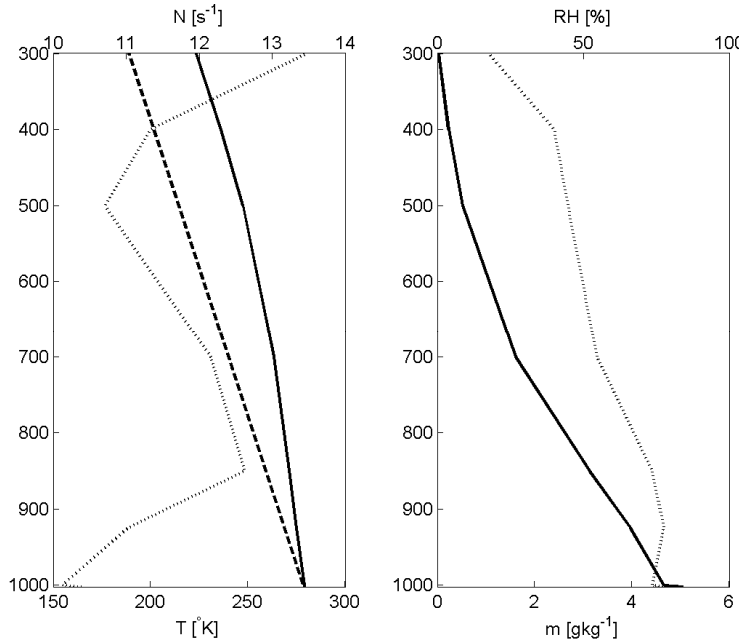


Figure 6. The same as in Figure 5 but for Atlantic sub-Arctic region only.

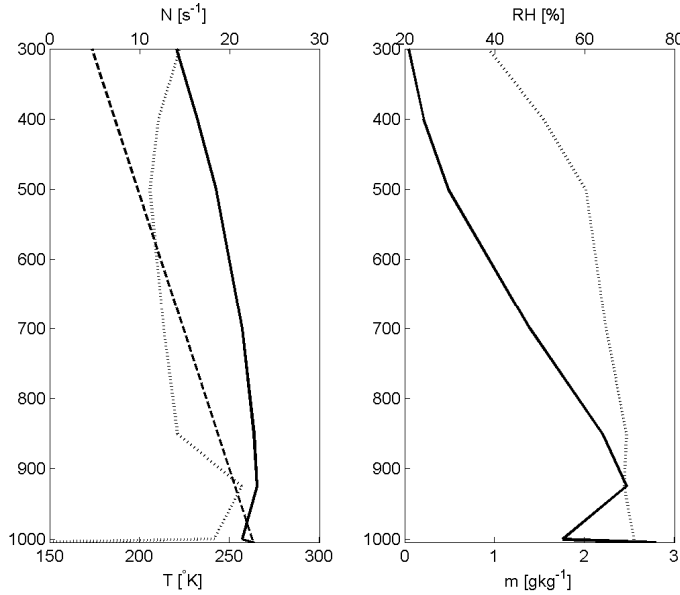


Figure 7. The same as in figure 5 but for Siberian sub Arctic region only.

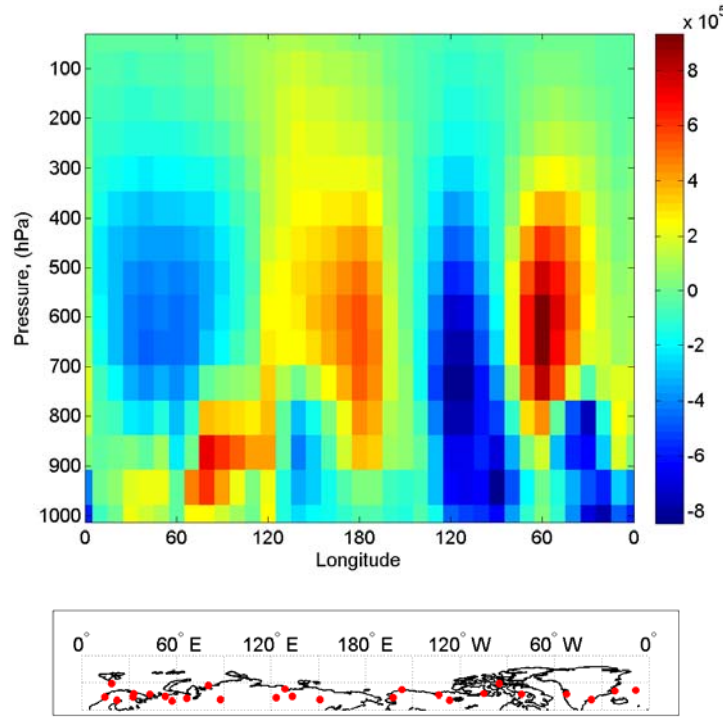


Figure 8. The annual mean meridional sensible heat flux across 70°N latitude. The flux is computed from IGRA data at standard isobaric levels as $H = \rho c_p (\bar{v} T)$ [W m^{-2}] where v is the meridional (positive direction in northward) component of the wind.

Dynamic Re-Stratification Processes

On average, the Arctic north of 70°N lacks about 100 W m⁻² (100 W m⁻² by Nakamura and Oort [1988] estimations, 100 W m⁻² in ERA-40 reanalysis, 103 W m⁻² in NCEP/NCAR reanalysis, and 99 W m⁻² in regional model REMO 5.1 reanalysis) in the radiation heat balance as incurred from the difference in the incoming and outgoing solar radiation at the top of the atmosphere [Serreze et al., 2007]. Even in summertime, the radiation balance at the top of the atmosphere remains negative of -15 W m⁻². The heat balance is maintained through the meridional heat transport from lower latitudes, which varies between 85 W m⁻² in summer and 111 W m⁻² in autumn according to Nakamura and Oort [1988] and between 85 W m⁻² and 121 W m⁻² according to Overland and Turet [1994]. The bulk of the advected atmospheric heat flux is spent to heat the Arctic Ocean, the permafrost, and to melt ice and snow.

The sensible and latent heat in the atmosphere is transported to the Arctic within a relatively well mixed layer between 900 mb and 700 mb (Figure 8) in the East Arctic regions and 700 mb to 300 mb in the West Arctic regions. Tsukernik et al. [2004] showed that the convection in the Atlantic and Buffin Bay sub-Arctic regions plays an important role in formation of the warm core of the advected air. The maximum convective heating is located between 900 mb and 700 mb, which is in good agreement with the observed depth of the convective PBL in those regions. The ocean transport is smaller [Trenberth and Caron, 2001] but the ocean role is probably more important than previously has been thought. The values of the sensible and latent meridional heat transport across 70°N are known with much less certainty. According to Vinogradova [2007] and the authors' data, the annual mean meridional sensible heat transport between surface and 6 km is southward of about -34 W m⁻². The heat flux is negative because the Central Arctic is generally warmer than the surrounding continents. Vinogradova calculated the positive, northward H only for April. Comparison with Overland and Turet [1994] data suggests that the positive, northward fluxes for all seasons are found mostly in mid- and high-troposphere above 3 km, which does not contradict the recent analysis in Graversen et al. [2008]. In wintertime, the H reaches 68 W m⁻² in the layer 0 to 10 km [Overland and Turet, 1994; Wunsch, 2005; Semmler et al., 2005; Serreze et al., 2007], whereas in the layer 0 to 3 km it is -29 W m⁻² [Vinogradova, 2007].

Radiation Re-Stratification Processes

Warm air, advected from mid-latitudes, remains warmer than the surface in the radiation equilibrium. Neglecting the heat storage, the surface radiation energy balance during the polar night could be written as

$$L_{W\downarrow} + L_{W\uparrow} = 0 . \quad (18)$$

The long wave thermal radiation (arrows indicate the upward and downward radiation flux correspondingly), L_W , is related to the gray body temperature through the Stefan-

Boltzmann law $L_w = \varepsilon\sigma T^4$ where ε is the gray body emissivity and σ is the constant. Then the surface, T_s , and air, T_a , temperatures could be related as

$$\varepsilon_{air}\sigma T_a^4 - \varepsilon_{surf}\sigma T_s^4 = 0, \text{ or} \quad (19)$$

$$T_a = (\varepsilon_{surf}/\varepsilon_{air})^{1/4} T_s. \quad (20)$$

Under radiative equilibrium, $T_a \geq T_s$ when $\varepsilon_{air} \geq \varepsilon_{surf}$. Table 7 gives the emissivity of air and of the different surfaces typical for the Arctic environment. Simple estimates give the air-surface temperature difference for the snow covered surface at 0°C of +3.5°K. This difference, distributed over the typical PBL of 100 m depth, corresponds to quite strong stable stratification.

Thus, the adiabatic (neutrally stratified) atmosphere would not be in radiative equilibrium with the radiatively cooled surface, especially covered with snow and ice [Overland and Guest, 1991]. The radiative imbalance results in intensive cooling of the surface and the near-surface air at the rate of about $-5^\circ\text{K day}^{-1}$, whereas the advected air aloft is cooled at much slower rate of $-1.8^\circ\text{K day}^{-1}$ [Savijarvi, 2006]. As the heat conduction in soil is much slower process than even weak turbulent mixing in air, the temperature of the surface will be slightly less than the near-surface air temperature. Such a discontinuity may have a big impact on the surface cooling rate. Raisanen [1996] demonstrated utilizing radio-soundings that the air-surface temperature difference of $+3^\circ\text{K}$, which is similar to the rough estimations above, increases the cooling rate to $-30^\circ\text{K day}^{-1}$ near the surface and up to $-12^\circ\text{K day}^{-1}$ at the PBL top.

Table 7. The gray body emissivity of air and of different type of the Arctic surfaces.
Adapted from Oke [1987].

Surface type	Emissivity, ε
Fresh snow	0.95 – 0.99
Old snow	0.82
Water	0.92 – 0.97
Sea ice / Glacier ice	0.92 – 0.97
Tundra	0.90 – 0.98
Coniferous forest (Taiga)	0.97 – 0.99
Air	0.9-0.95

Temperature Inversions

Together the dynamic and radiation re-stratification processes lead to formation of the pronounced and persistent temperature inversion. Although the absolute temperature increasing with height is important for a number of non-turbulent processes, e.g. the cloud formation, the turbulent mixing is controlled by the increase of the potential temperature or $N > 0$. From this point of view, the absolute temperature inversion is just an extreme case of

the potential temperature inversion. The atmospheric stability parameter corresponding to the isothermal stratification is $\mu_N|_{\partial T/\partial z=0} = N/|f| = 140$. Zilitinkevich et al. [2007] results suggest that at $\mu_N > 100$, the PBL depth and therefore the turbulent mixing is less dependent on μ_N . Thus the relatively well studied atmospheric inversions can be used as proxies to characterize the typical stability conditions on the background of the Arctic PBL development. Figure 9 shows the mean atmospheric stability in the layer 850 mb to 500 mb for winter (December through February) and summer (June through August) seasons.

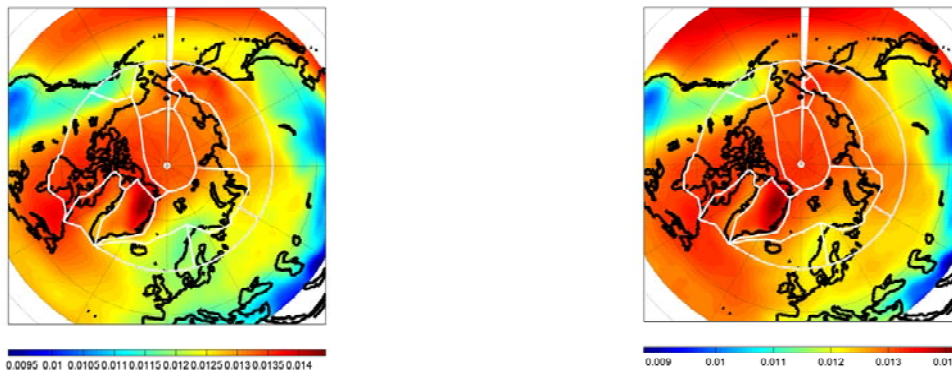


Figure 9. The mean atmospheric Brunt-Vaisala frequency N [s^{-1}] in the layer 850 mb to 500 mb for December through February (a) and June through August (b).

The background stability or the observed strong increase of the potential temperature with height strongly affects the near-surface climate. The equilibrium air temperature is significantly higher than the surface temperature. Therefore, even when the long wave radiation fluxes at the surface are in balance, the turbulent mixing will transport the sensible heat downward. Nkemdirim [1978] estimated that the turbulent mixing on average reduces the radiative cooling rate by factor of 2.5. The reduction factor is larger over grass than over snow.

The turbulent mixing interplays with the background stability. In the layer with vertical gradients of temperature and eddy viscosity such as the PBL, the better mixed sub-layer will have the sub-layer averaged temperature after a while. At the same time the temperature gradient remains in the worse mixed sub-layer. This simple reasoning [Nieuwstadt, 1984] explains sharpening of the temperature inversion at the top of the PBL. As this capping inversion strength depends upon time and the background stratification, the long-lived Arctic PBL can develop very strong capping inversions and decouple from the rest of the atmosphere. In some extreme cases, the gradient of potential temperature may reach $30^{\circ}\text{K m}^{-1}$ [Balsley et al., 2003]. However, generally the gradient in the capping inversion does not exceed 1°K m^{-1} [Bradley et al., 1992; Liu et al. 2006] and the total temperature jump across the capping inversion is between 5°K to 15°K .

Climatologically, the inversions are the dominant feature of the Arctic atmosphere throughout most of the year [Nagurny, 1995; Serreze et al., 1992; Liu et al., 2006]. Satellite data provide an opportunity to reconstruct the pan-Arctic inversion climatology. The clear-

sky temperature inversion strength during the cold season was derived from High Resolution Infrared Radiation Sounder (HIRS) data using a two-channel statistical method by Liu et al. [2006]. The satellite derived inversion statistics from a 17-yr time series over 1980–96 agree well with radiosonde data. The study revealed (see Figure 10) that the inversions with the strength between +10K to +15K are observed under clear-sky conditions in the Arctic excluding maritime regions where they are destroyed by the deep convection in the PBL. Both increasing and decreasing trends are found in the cold season for different areas. The changes in the inversion strength and the in surface temperature are strongly coupled.

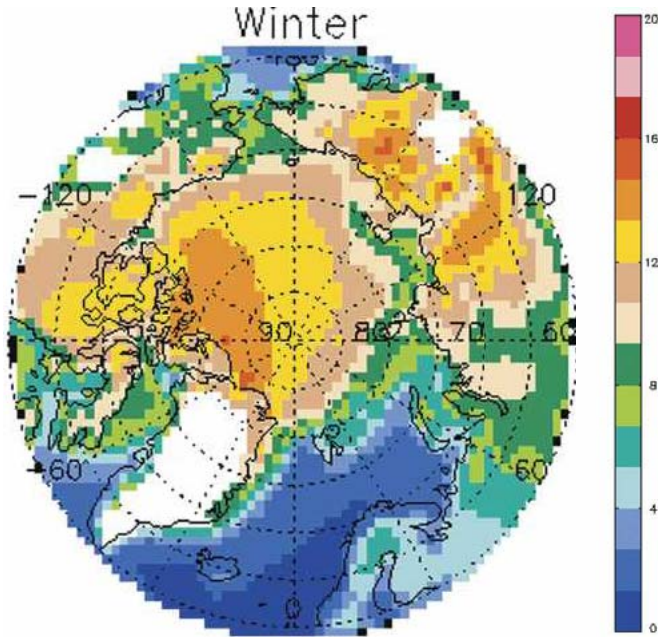


Figure 10. The mean wintertime (November through March, 1980-1996) absolute temperature inversion strength in [K] during clear-sky conditions. The plot adopted from Liu et al. [2006].

Clouds

Dynamic interactions between the low-level clouds and the Arctic PBL are still poorly understood. The turbulence-resolving models, which could provide a deeper insight into these interactions, were unable to simulate the strongly stratified PBL until very recently. Moreover, the description cloud micro-physics with ice crystals and sub-grid dynamic processes in clouds on scales less than a few meters remain yet imperfect [Bretherton et al., 1999]. The description of the radiation transfer processes in clouds on such scales remains seriously limited as well.

The characteristic feature of the Arctic PBL is often occurrence of the low-level cover of St and Sc. Figure 11 presents the typical view of this cloud cover. The cloudiness could be explained by availability of moisture. The source of the moisture is different in summer and winter seasons. In summer season, the surface snow, ice and permafrost is thawing so there are many open water sources (pools, lakes etc). The main source of the moisture is at the

ground during the melting season. In winter season, the surface is frozen and generally colder than the atmosphere (except the maritime Arctic regions). The main source of moisture is therefore the warm air advection from the lower latitudes. The moisture then entrained into the PBL from the atmosphere aloft. As the absolute temperature is generally increase with height and the main source of the moisture is the lateral advection, the air relative humidity is closer to saturation in downward motions at the PBL top. The mean annual meridional transport of the water vapor across 70°N is about 14 mm month^{-1} [Serreze et al., 1995; Semmler et al., 2005]. The high relative humidity of air is observed year around. In such conditions, the meridional flux of the water vapor closely follows the air temperature with the maximum of 17 mm month^{-1} in the late summer and the minimum of 10 mm month^{-1} in winter.

In addition, the upper cloud boundary is radiatively cooled that supports the downward air entrainment in the cloud layer. Wang and Wang [2004] studied boundary-layer properties in two regions, one with low-level cloud cover and the other free of clouds, using measurements from a research aircraft during the Beaufort and Arctic Storms Experiment (BASE). Unlike the clear sky regions, the cloudy region was characterized by strong horizontal heterogeneity in low-level temperature and moisture that varied with the cloud-top height. This is consistent with lidar data analysis in Shupe et al. [2008]. The later study found the horizontal heterogeneity on the scale of about 5 km, which strongly suggests self-organization of turbulent mixing in rolls. In the clear sky regions, the PBL was shallow and the maximum turbulent mixing was observed near the surface. In the cloudy region, turbulent mixing does not change significantly throughout the PBL or even reveals a local maximum near the cloud top.

Below the cloud layer the air remains nearly saturated as the downward humidity flux does not change much. It prevents evaporation of the cloud droplets and ice crystals. These three effects makes the Arctic clouds look like the upside-down picture of the stratus clouds in the mid-latitude. The Arctic clouds have sharp upper boundary and a hazy layer between the PBL top and the surface. This is clearly seen in Figure 12. The relative humidity near the surface stays almost always close to saturation [Andreas et al., 2002]. It is worth noticing that the saturation absolute humidity is lower with respect to ice than water. Hence the water cloud droplets evaporate in the PBL even when the relative humidity with respect to ice remains close to saturation. At very low temperatures, below -30°K , the high relative humidity with respect to the ice results in ice fog formation and precipitations of ice crystals from seemingly clear sky atmosphere.

Due to the lack of surface heating, the low-level cloud cover consists mainly of stratiform types of clouds such as St and Sc. In marginal ice zones and over summertime continents, convection is more intensive with occasional thunderstorms but the vertical development of the cumulus forms of clouds are still damped by the stability of the free atmosphere. The Arctic Stratus Experiment, conducted during June 1980 over the Beaufort Sea [Curry, 1986], provided data to determined the properties of the typical Arctic stratus layer. In the experiment, elevated humidity inversions were frequently observed which supports the hypothesis that the Arctic clouds are maintained through moisture entrainment at the PBL top and subsequent radiation cooling of the cloud top level. A portion of this radiative cooling drives the mixed layer convection, mixing the droplets downward and creating the Arctic haze. The mixing however remains shallow. The turbulent entrainment does not penetrate

beyond 50 m below mean cloud top. Thus the near-surface visibility improves significantly when the cloud top is higher than about 200 m as it has been found in AOE-2001.



Figure 11. Winter (19 April 2007) Arctic stratus layer at confluence 64°N 108°W (upper panel), photo by M. Sturm et al. Summer (9 August 2004) Arctic stratus layer at confluence 71°N 80°W, photo by P. Hundt. Both photos from the Degree Confluence Project web site [<http://www.confluence.org/index.php>].



Figure 12. The low-layer stratus cloudiness near Eastern Greenland cost in summer (left panel). The better visibility and sharp upper edge of the clouds are clearly seen. Photo by Knut Lisaeter from the Greenland Fjord Cruise 2007.

Due to the lack of surface heating, the low-level cloud cover consists mainly of stratiform types of clouds such as St and Sc. In marginal ice zones and over summertime continents, convection is more intensive with occasional thunderstorms but the vertical development of the cumulus forms of clouds are still damped by the stability of the free atmosphere. The Arctic Stratus Experiment, conducted during June 1980 over the Beaufort Sea [Curry, 1986], provided data to determine the properties of the typical Arctic stratus layer. In the experiment, elevated humidity inversions were frequently observed which supports the hypothesis that the Arctic clouds are maintained through moisture entrainment at the PBL top and subsequent radiation cooling of the cloud top level. A portion of this radiative cooling drives the mixed layer convection, mixing the droplets downward and creating the Arctic haze. The mixing however remains shallow. The turbulent entrainment does not penetrate beyond 50 m below mean cloud top. Thus the near-surface visibility improves significantly when the cloud top is higher than about 200 m as it has been found in AOE-2001.

Wind Speed and Aero-Dynamical Surface Roughness

In the stably stratified PBL, the wind shear or the vertical gradient of the wind speed is the only physical parameter contributing to the turbulence generation. Therefore, variations in the wind speed determine the PBL climatology to a large degree. Eq. (5) reveals strong dependence between the wind speed and the PBL depth. At the same time, the bulk surface flux approximations in Eq. (9) and the Monin-Obukhov functions in Eq. (13, 14) indicated the

importance of the wind speed for the vertical turbulent mixing. Excluding occasional passing of polar lows and cyclones, the wind speed in the Arctic is low. The continental regions are under anticyclone influence over the most of the year so that the mean wind speed there rarely exceeds 6 m s^{-1} [Przybylak, 2003a]. The mean surface (at 10 m height) wind speed in IGRA data is only 4 m s^{-1} . The minimum wind speed of 2.3 m s^{-1} is found in the Siberian sub-Arctic region and the maximum wind speed of 6.3 m s^{-1} is in the Atlantic sub-Arctic region. The slow surface winds are the direct consequence of the atmospheric stability and especially of the PBL stability that impede the vertical momentum transport to the surface. The dynamical decoupling between the PBL and the atmosphere aloft was demonstrated in the NOAA P-3 research aircraft studies on March 27 and 30, 1989, at 83°N , 10°E in the central Arctic. The surface winds were barely 2 to 3 m s^{-1} but the winds at 100 m were between 8 to 12 m s^{-1} . So that the geostrophic drag coefficient were 0.014 to 0.015 or about 50% larger than their typical values. Since the PBL was very shallow (estimations suggests the depth of 50 m to 75 m), the wind shear reached 0.1 s^{-1} and the ageostrophic angle 35° to 40° . The wind is stronger in coastal areas, where monsoon circulation is the most developed, and on mountain slopes, where katabatic drainage flow develops.

An important parameter in the flux gradient relationships is aero-dynamical surface roughness. In situ studies [e.g., Brunke et al., 2002] however have found a relative insignificance of the roughness magnitude and variability on the flux calculations. The observed roughness lengths for heat, z_{0t} , from the SHEBA data does not exhibit sounded dependence on surface temperature or u_* . A constant $z_{0t} \sim 5 \cdot 10^{-3} \text{ m}$ could be used in models. The observed z_0 at all four sites appear to be an exponential function of the friction velocity. Calculations of the wind stresses and sensible heat flux in model schemes demonstrated little sensitivity to the roughness variability of the observed magnitude.

Turbulent Surface Fluxes and the PBL Life-Time

The stably stratified and convective PBL can be distinguished by the sign of the surface sensible heat flux. Figure 13 gives the values of this flux for summer (June through August) and winter (December through February) months. In accord with the inter-annual variations of the PBL depth, $H \sim 20$ to 40 W m^{-2} is upward in the continental regions in summer but near-neutral or slightly negative in the maritime regions. In wintertime, H is strongly positive (50 to 100 W m^{-2}) only in maritime regions over open water whereas the Central Arctic and continents have nearly uniform negative H of - 20 to - 30 W m^{-2} .

The possible magnitude of the negative (downward) H is limited by the negative surface radiation balance and the turbulent intermittency [Derbyshire, 1999] and do not exceed 40 W m^{-2} over any longer period of time. On average, the negative surface sensible fluxes have considerably smaller magnitude than the positive fluxes. Hence, the straightforward averaging of the fluxes cannot provide meaningful information about the typical physical and dynamical conditions in the PBL. Figure 14 shows the mean annual fraction of the stably stratified PBL (SBL) in ERA-40 data. The SBL occurred 70% to 90% during the period of observations between 1979 and 2001. Figure 15 completes this climatology with the averaged persistence of the SBL. The SBL develops on average about 100 hours in the central Arctic without

changing stability. This persistence is in good correspondence with the mean duration of the synoptic cycle. Along the Atlantic storm track, the persistence significantly reduced to 30 hours and below. The persistence also reduced south of the polar cycle where changes of day and night make difference to the surface radiation heat balance.

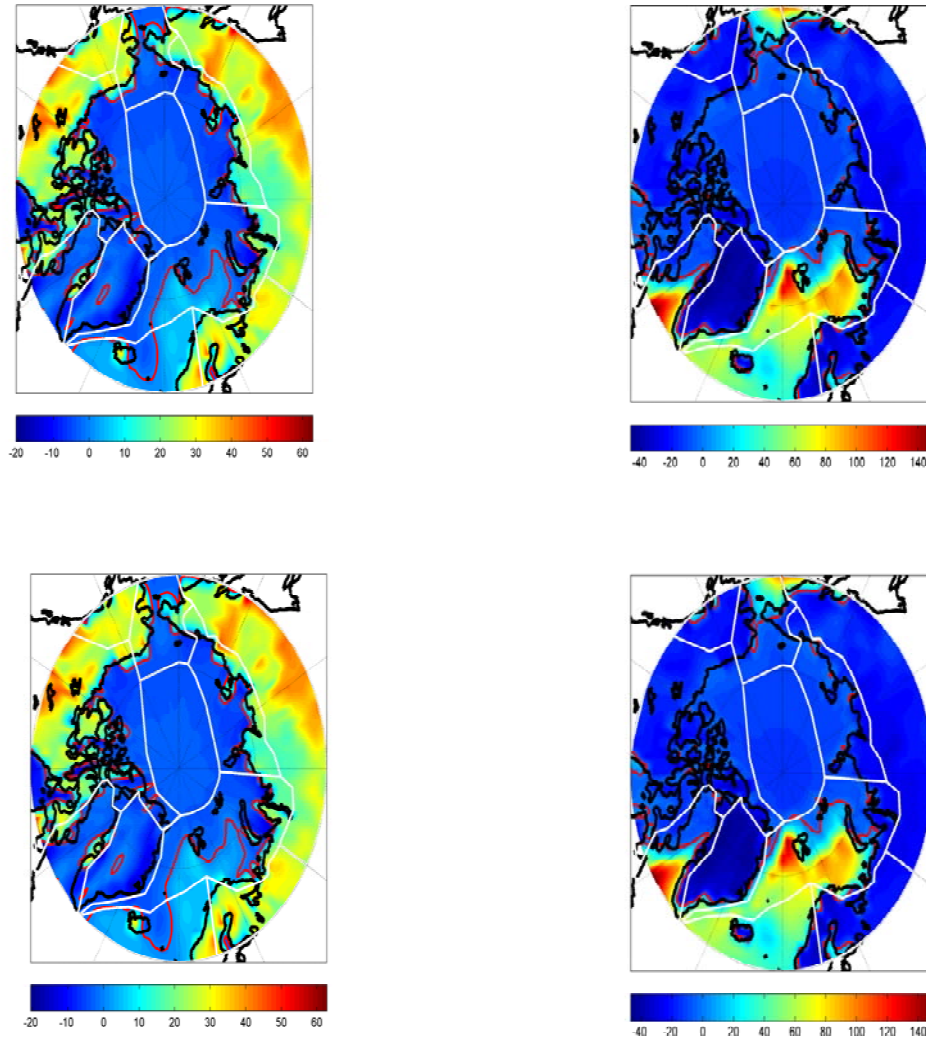


Figure 13. The mean seasonal sensible heat flux in ERA-40 at the surface in June through August (left) and December through February (right).

It is important to remember, that the PBL stability or instability have nothing to do with the absolute value of the SAT or the surface heat balance. If the SAT is near the radiation equilibrium, which means rather low temperatures of -50 C and below, even appearance of the sun for a few hours above horizon may cause initiation of the PBL convection. Such conditions were documented in Greenland data where the CBL frequencies are the highest in spring over the coldest parts of the plateau.

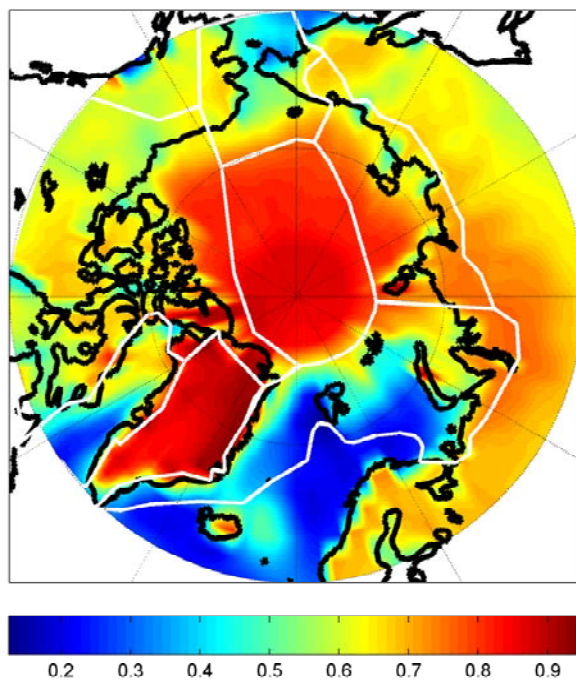


Figure 14. Mean annual fraction of SBL in ERA40.

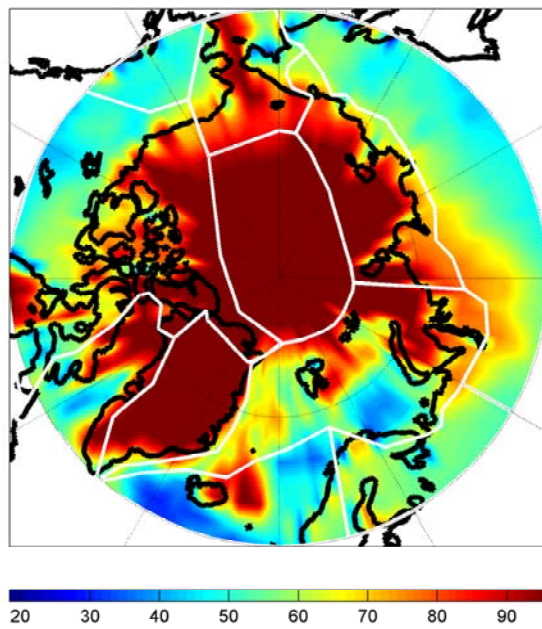


Figure 15. The annual averaged duration (in hours) of continues stably stratified PBL development in the ERA-40 data over 1979-2001.

Table 8. The annual mean wind speed for all selected stations and for each region separately

height (hPa)	Arctic	regions									
		I	II	III	IV	V	VI	VII	VIII	IX	X
Surface	4.0	2.9	2.3	5.1	3.1	4.3	3.4	6.3	5.5	5.0	4.0
1000	5.3	5.1	3.4	5.4	3.7	5.8	4.5	7.6	6.8	5.8	4.7
925	8.0	9.0	7.1	8.1	6.8	7.5	6.7	10.5	9.2	7.6	6.2
850	8.6	9.6	7.5	8.3	7.7	7.9	8.4	11.1	9.6	8.2	6.7
700	10.1	11.1	8.9	8.9	9.4	9.5	9.8	12.4	10.7	9.2	9.6
500	14.1	15.4	13.0	12.5	12.9	13.5	13.7	16.6	14.5	12.5	14.6
400	17.3	18.9	16.2	15.3	16.0	16.3	17.2	20.3	17.5	15.4	18.2
300	20.1	22.4	18.7	17.2	18.8	18.2	20.6	24.2	20.1	17.7	21.3

5. REGIONAL SPECIFICS OF THE ARCTIC PBL CLIMATOLOGY

Arctic and Sub-Arctic PBL over Continents (Canadian, Siberian and Alaska Regions)

The continents in the Northern Hemisphere extend up to approximately 70°N. At their northern edge, the continental PBL remain very much similar to the PBL in the maritime Arctic (the Siberian, Central Arctic and Atlantic regions), which it borders. This is due to the snow cover in the wintertime (about 9 to 10 months a year) and the large fraction of the open water surface in the summertime. At more southern latitudes, the continental PBL becomes significantly different.

In summertime, the continental PBL is affected by vegetation. The vegetation, especially taiga forest, has lower albedo, traps larger amount of the absorbed solar heat in an aerodynamically protected canopy layer, and has larger aero-dynamical roughness. Measurements (e.g. the Baseline Meteorological Data in Siberia Version 3) during the GAME-Siberia experiment at a larch forest site near Yakutsk (Siberian sub-Arctic region) showed that the latent heat flux is strongly affected by transpiration activity of larch trees [Yamazaki et al., 2007]. As transpiration increases toward summer, H drops. High correlation between the vegetation activity and the PBL structure were obtained using satellite normalized difference vegetation index (NDVI) data and the meteorological mast measurements. The averaged warm season (late April – early September) sensible and latent heat fluxes over 1986-2000 were about 50 W m^{-2} . The Bowen ratio remains about unity. In July and August, the latent heat flux can exceed the sensible flux by 20 W m^{-2} , while generally the difference is much smaller. By contrast, during the months with inactive vegetation and thus with no transpiration (April and May), the H was on average 75 W m^{-2} to 100 W m^{-2} and the latent heat flux remained less than 25 W m^{-2} . Thus, despite low forest albedo and strongly positive radiation balance, the continental CBL remains relatively shallow. The PBL climatology by Groisman et al. [1997] is summarized in Table 9.

Table 9. Examples of diurnal and seasonal changes of sensible heat fluxes over bare soil in Tundra zones, Nar'yan-Mar, 67.7°N, 53.1°E (Wm⁻²). Mean and standard deviations for the 25-yr period 1966–90. [Groisman et al, 1997].

Month	0000 LT		0300 LT		0600 LT		0900 LT		1200 LT		1500 LT		1800 LT		2100 LT	
	Avg.	Std.														
1	-9	17	-7	14	-7	14	-6	19	-7	13	-8	16	-7	15	-6	15
2	-9	21	-9	14	-8	14	-6	13	0	14	-8	13	-10	13	-9	14
3	-11	14	-10	13	-9	11	3	18	16	31	2	18	-12	14	-12	13
4	-6	15	-6	13	0	16	29	47	43	62	25	46	-2	20	-8	17
5	-2	13	0	14	12	24	44	59	64	81	51	71	17	39	0	16
6	-2	9	0	9	17	22	78	81	124	112	107	87	40	43	0	11
7	-2	9	-1	8	16	22	79	79	129	119	114	98	46	60	0	11
8	-4	7	-3	6	5	10	43	55	77	90	61	66	13	25	-3	8
9	-6	7	-5	7	-3	7	10	18	29	39	15	30	-5	8	-6	7
10	-4	13	-3	21	-3	13	0	15	1	17	-4	13	-6	12	-5	16
11	-3	17	-2	26	-2	17	-3	16	-2	15	-4	16	-3	16	-3	16
12	-5	19	-4	20	-5	15	-5	20	-5	12	-7	13	-5	16	-5	14

Arctic PBL over Ice-Covered Arctic Ocean (Central and Siberian Arctic Regions)

The ice cover is a good insulator. Hence, in many aspects, the PBL over the Arctic Ocean remains that over the sub-Arctic continents. There are however important differences too. The sensible heat flux at the surface is small all the year around. Therefore there is neither persistent strong cooling nor warming of the surface are observed. The lateral (both vertical and horizontal) convergence of heat in the region makes the wintertime SAT considerably higher than it would be under radiative equilibrium and higher than the SAT of surrounding continents at lower latitudes. At the same time the summertime SAT is colder than the surface radiation balance would allow as the available heat is spent on melting and evaporation. The SAT annual climatology is characterized by the coreless winter and summer when the SAT fluctuates near its minimum (-30°C to -35°C) and maximum (0°C to +2°C) values [Lindsay, 1998].

Until better and more sophisticated turbulence-resolving models appear, the relative importance of different physical processes at the ice surface and the PBL will probably remain controversial. It is unlikely that the ocean surface would reach temperatures significantly above 0°C even under clear sky conditions. But the Central Arctic is very cloudy place. In summertime, almost total thick low-level St cloudiness increases the earth's albedo. It creates an elevated layer of cooling at the cloud top, which preserve the cloud cover from dilution by the turbulent entrainment in the PBL.

In earlier publications [Budyko, 1969], the PBL processes in the central Arctic were thought to be insignificant for climatology as the vertical turbulent mixing in high latitudes was known to be weak. Later, numerical experiments [Overland and Guest, 1991; Groetzner et al., 1996; Vavrus, 1995] revealed significance of the convective turbulent exchange through open water patches. Groetzner et al. [1996] demonstrated that a few per cent of the open water rises the mean wintertime SAT in climate models by several degrees. In the

Atlantic and Central Arctic regions, the SAT rises by as much as 15 K. Vavrus [1995] demonstrated that not only the SAT but also the ice extent and thickness is not possible to simulate correctly without proper account for the convective heat exchange in the leads. Observational evidences support the model-based conclusions. Doronin [1974] argued that up to 50% of the ocean heat loss could occur through the turbulent mixing over the leads. However, the field studies in Weddell Sea (Antarctica) suggested even larger, up to 80%, fraction of the heat loss over the leads [Eisen and Kottmeier, 2000; Kottmeier et al., 2003]. Satellites [Lindsay and Rothrock, 1995] revealed that open water and thin ice cover 7% to 14% in summertime and 1% to 5% in wintertime of the Central Arctic region. At the same time, turbulence resolving simulations [Esau, 2007] and observations [Lüpkes et al., 2008] suggest the area averaged convective flux over 20% of the open water fraction is almost as strong as the flux over 100% open water fraction. Even 1% of open water causes 3.5 K increase in the area averaged SAT. Depending on the wind speed and air temperature, the mean wintertime H estimates of 50 to 150 W m⁻² over leads and thin ice.

The conductive heat flux through the multiyear ice is relatively small and remarkably stationary on the year to year basis as it is determined by ice thermodynamics [Lindsay, 1998]. Makshtas [1991] gives 5 to 10 W m⁻² for the winter months from the Russian North Pole stations analysis. In summer and autumn months, it could be slightly downward up to -3 W m⁻². Although small, the conductive heat flux plays an important role in mediation of the surface-based temperature inversions (See Figure 16).

Similar to the diurnal cycle of the marine PBL over the open water, the turbulent fluxes in the ice covered Central Arctic region do not show significant diurnal and seasonal variations [Brunke et al., 2006; see Figure 17]. This is due to polar day or night over the large part of the year. Some diurnal cycle could be seen in spring. However, synoptic variability still causes significantly stronger flux variations than it could be found on the diurnal scale. The heat flux is mostly directed toward the surface. Hence the atmosphere heats the surface even in summertime.

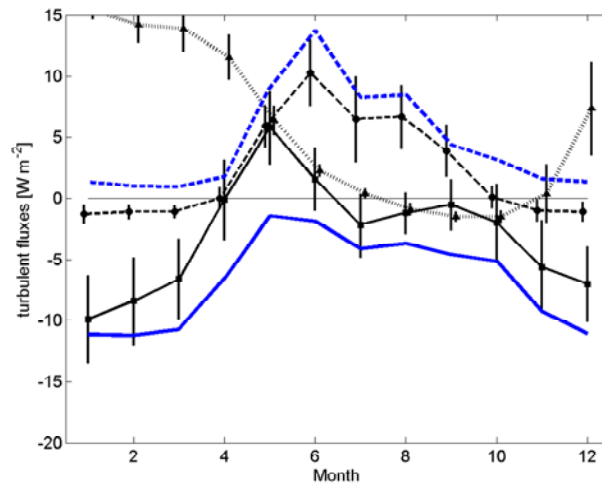


Figure 16. Mean annual cycle of sensible (solid lines), latent (dashed lines) and conductive (dotted line) fluxes for the Central Arctic region. The black lines are the averaged data for Russian North Pole stations over 1954-1992 after [Lindsay, 1998]; blue lines are the averaged ERA-40 reanalysis data over 1979-2001.

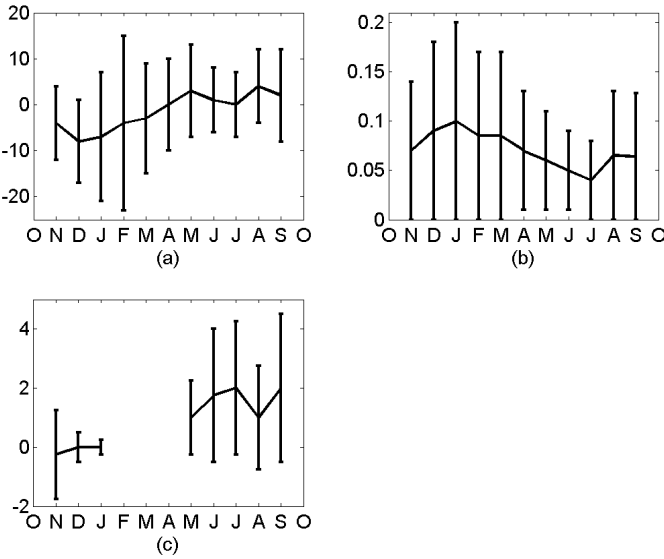


Figure 17. Monthly mean observed covariance (a) sensible heat flux, (b) wind stress, and (c) latent heat fluxes from SHEBA data. The thin vertical lines represent one standard deviation about the mean. [Brunke et al., 2006].

One important unresolved issue is related to the occurrence of convective conditions in the PBL. Observational data suggest that the PBL often becomes convectively unstable in spring and autumn months. Thus surface-atmosphere coupling could be much stronger than it is believed. Indirectly, a stronger degree of the coupling and its importance for Arctic climatology follows from Adachi and Yukimoto [2006] study of the effect of the conductive heat flux on the wintertime Arctic atmospheric circulation. The reanalysis does not support this conclusion.

The degree of the surface-atmospheric decoupling is seen in Figure 18. The SHEBA observations start from 30 October 1997 (day 300). Thus the period with days < 500 is corresponding to the winter months and with days > 500 to the summer months. In the former period, the temperature within the PBL is significantly more variable (maximum day to day fluctuation about 25 K) than the temperature above the PBL at 700 m (maximum day to day fluctuation about 9 K). The SAT cooling is not reflected in the free atmosphere temperature change. In the later period, the temperature within the PBL is significantly less variable (maximum day to day fluctuation about 2 K) than the temperature above the PBL at 700 m (maximum day to day fluctuation about 9 K). The temperature fluctuations in the free atmosphere (presumably of advective nature) are not reflected in the SAT changes. The similar conclusion about high degree of the PBL-to-atmosphere decoupling in summertime follows from the AOE-2001 data analysis [Tjernstroem et al., 2005]. During the early winter (November, days 320-340) and early spring (April, days 480-530), the potential temperature gradient is small. It indicates the presence of well mixed CBL and therefore high degree of the coupling.

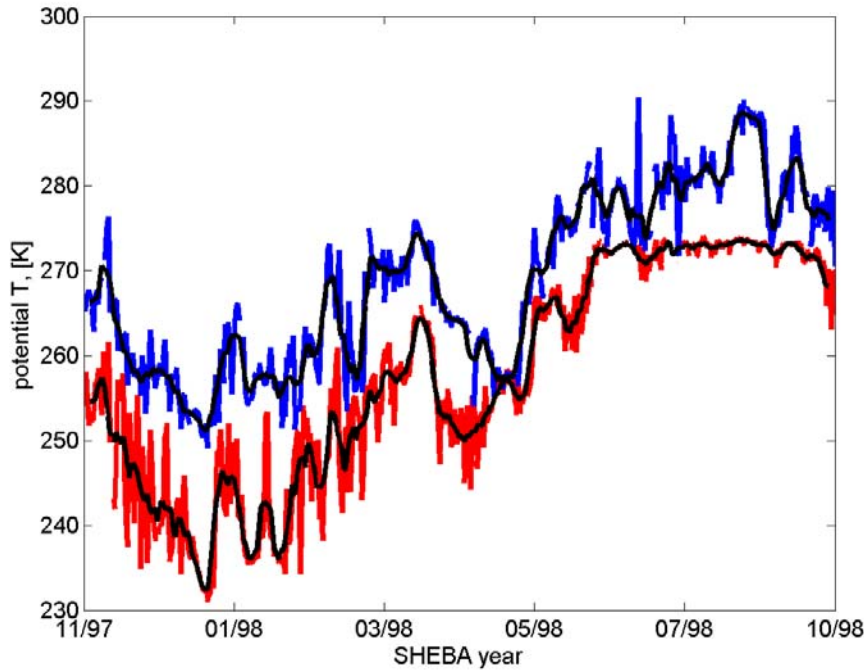


Figure 18. Variability of the SHEBA potential temperature within (at 2 m height – red line) and above (at 700 m height – blue line) the PBL. Black lines represent the 5 days' running averaging. The mean PBL depth at the site was 100 m (wintertime) to 250 m (summertime) with eventual extensions to 1500 m (spring and autumn).

Arctic PBL over Ice Sheets and Glaciers (Greenland Region)

As the Arctic Ocean in the Central Arctic region, Greenland is permanently covered with ice and snow. However, the Greenland ice sheet has high elevations, generally gentle slopes and no upward conductive and convective heat flux through the ice. The Greenland topography considerably modifies the PBL. The main feature of the PBL in the region is development of a katabatic flow. The katabatic flow is observed as down-slope winds, created by over-cooled air descending from higher elevation under the action of the gravity force. At lower elevations, the katabatic flow is adiabatically warmed and dried. It results in formation of a very stable PBL with unusually large downward H [Ball, 1956] and upward latent heat flux. The latter is responsible for annual sublimation of several cm of ice and snow in the lower ablation zone. A simple description of the vertical structure of the katabatic PBL is given in the model introduced by L. Prandtl in 1942. The governing equations are

$$\mu \sin \alpha - \frac{d}{dz} \left(K_h \frac{d\theta}{dz} \right) = 0 \quad (heat\ balance) \quad (21)$$

$$\frac{\theta}{T_0} g \sin \alpha + \frac{d}{dz} \left(K_m \frac{du}{dz} \right) = 0 \quad (22)$$

(momentum balance)

Where γ is the background potential temperature lapse rate, and α is the slope angle. The model solution for boundary conditions $\theta(z=0)=C$, $\theta(z \rightarrow \infty)=0$ and $u(z=0)=0$, $u(z \rightarrow \infty)=0$ reads

$$\theta(z/\lambda) = Ce^{-z/\lambda} \cos(z/\lambda) \text{ and } u(z/\lambda) = -C\mu e^{-z/\lambda} \sin(z/\lambda) \quad (23)$$

$$\lambda = \left(\frac{4T_0 K_m K_h}{\gamma g \sin^2 \alpha} \right)^{1/4} \text{ and } \mu = \left(\frac{g K_h}{T_0 \gamma K_m} \right) \quad (24)$$

Where λ the intrinsic length scale of the katabatic flow is, C is the surface temperature deficit. Figure 19 shows the solution and data for 22 April 1997 from KABEG-1997 experiment. This simple model describes the observations rather well. The bigger discrepancies could be observed the lower PBL where eddy viscosity and diffusivity coefficients vary strongly. Those variations could be accounted for in a more elegant but complicated solution of Grisogono and Oerlemans (2001) model.

The KABEG-1997 surface station data shows that in April/May the katabatic wind develops mostly in nighttime. It results in unusual diurnal cycle in the PBL with the strongest turbulent mixing over nights. The katabatic wind system is found to extend about 10 km over the tundra area and is associated with strong wind convergence and gravity waves [Heinemann, 1999]. The seasonal cycle in the PBL fluxes is also unusual, with the maximum downward sensible (the upward latent) heat flux in July/August when the katabatic flow is the strongest.

In spite of broadly spread expectations, the katabatic wind speed in West Greenland is moderate 5 m s^{-1} to 12 m s^{-1} [Oerlemans and Grisogono, 2002; van den Broeke et al, 2008]. The friction velocity is between 0.15 m s^{-1} and 0.4 m s^{-1} , which is rather large for the stably stratified PBL. GCC data in Figure 20 suggests that conclusion holds true for the East, North and West slopes. The mean slope wind speed between 1961 and 1990 is about 7 m s^{-1} . The typical observed wind speed in Greenland is given in Table 6. This moderate wind causes rather strong downward sensible (15 W m^{-2} in winter to 45 W m^{-2} in summer months) and upward latent (10 W m^{-2} in summer months) fluxes due to large (0.04 K m^{-1}) temperature gradient across the PBL. A strip of large turbulent fluxes over the Greenland slope is clearly visible in GCC data in Figure 21. The katabatic PBL is comparatively deep with typical depth of 200 m [Heinemann, 2002; Heinemann and Klein, 2002]. The slope PBL is stably stratified over 90% - 95% of time. The stable stratification is maintained by the katabatic flow and ultimately by the net negative radiation balance at higher elevations but also by the heat expenditure on melting at lower elevations. Thus, the CBL is less frequently observed on the slope where the temperature reaches the melting point than on the plateau.

Table 6. Typical wind speed at Greenland stations [Bromwich et al., 1996, van den Broeke, 2008].

Station	Coordinates	Elevation	Wind Direction	Wind Speed	Comments
S9	67°03'N, 48°14'W	1520	-	7.3	plateau/slope
S6	67°05'N, 49°13'W	1020	-	6.4	slope
S5	67°06'N, 50°07'W	490	-	5	slope
ETH/UC Camp	69°34'N, 49°17'W	1157	130°	13.8	slope
Barber	71°40'N, 38°10'W	3170	125°	3.6	plateau
Northice	78°04'N, 38°29'W	2342	270°	9.8	slope
Watkins	67°03'N, 41°49'W	2438	330°	6.0	plateau
Matt	73°29'N, 37°37'W	3100	170°	5.2	plateau
West Station	71°11'N, 51°07'W	954	113°	8.7	slope
Eismitte	70°55'N, 40°38'W	3025	98°	7.3	plateau
Century	77°10'N, 61°08'W	1923	128°	8.3	slope

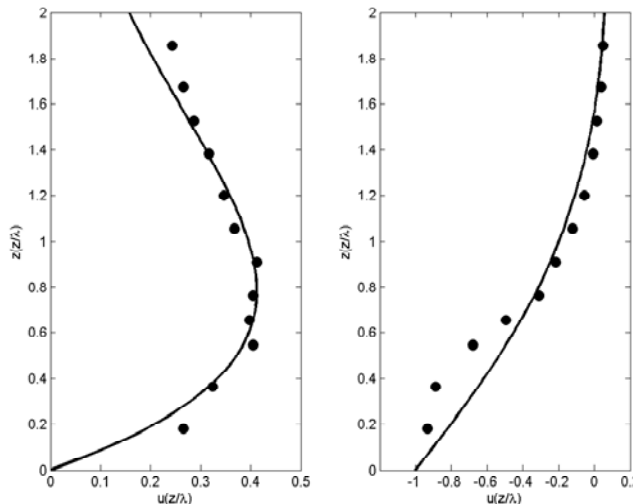


Figure 19. Non-dimensional profiles of wind speed (a) and temperature (b) from the Prandtl model of katabatic boundary layer (curves) and KABEG-1997 data on 22 April 1997 (dots). The following parameters are utilized: $\gamma = 0.04 \text{ K m}^{-1}$, $\alpha = 1^\circ$, $C = -1^\circ \text{ K}$. The eddy viscosity and diffusivity were unknown and hence tuned to the best fit to data.

On the Greenland plateau [e.g. IGLOS experiment; Drue and Heinemann, 2003], the katabatic winds are weak or not presented. The wintertime SBL reminds the SBL over other Arctic continental regions. The difference is that the plateau PBL remains stably stratified in summertime. During all six flights in IGLOS, well-developed SBL were found. Unlike the katabatic SBL, the plateau SBL is shallower with the PBL depth less than 100 m, typically between 30 m to 70 m according to P. Calanca (personal communication). In low-wind cases, radiative cooling dominates making the SBL intermittent. About 40% of the observations could be classified as non-stationary. During the periods of intermittency 50% of H was released in only 22% of the sampling time. The intermittency makes difficult recovery of the reliable flux climatology from gradient meteorological observations. Van den Broeke et al.

[2008] calculated the averaged plateau wintertime downward turbulent fluxes of 25 (sensible) and 15 (latent) W m^{-2} . These values seem to be unrealistically large and probably caused by oversimplification of the surface energy budget model utilized in the study. GCC data give the correspondent values of 15 (sensible) and ~ 0 (latent) W m^{-2} . At the same time, the plateau PBL is stably stratified only 80%. The CBL develops due to low summer air temperatures. The surface albedo (0.6-0.8) and cloudiness are low during summer. So the surface can absorb large amount of the solar radiation. The surface temperature rises and causes eventual daytime convection.

The surface roughness of the ice and its seasonal variations remain disputable. At least in ablation zone, the roughness can change significantly due to melting processes and crevasses in the ice. The typical roughness estimations vary from 10^{-3} m to 10^{-2} m, so that the roughness is generally lower than over the sea ice. The higher roughness value corresponds to 2 m to 3 m ice hills, which are often observed in summertime.

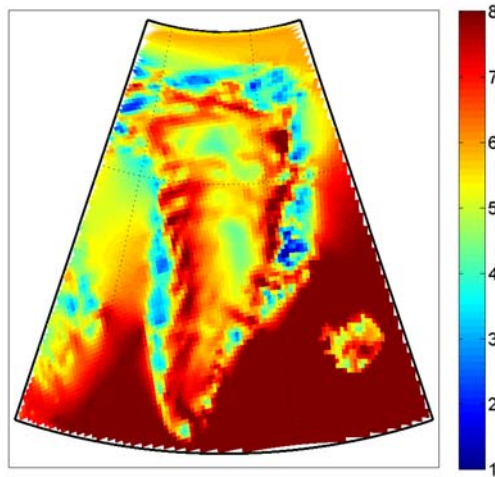


Figure 20. The mean 10 m wind speed (m s^{-1}) over 1961- 1990 from the Greenland Climate Change data archive.

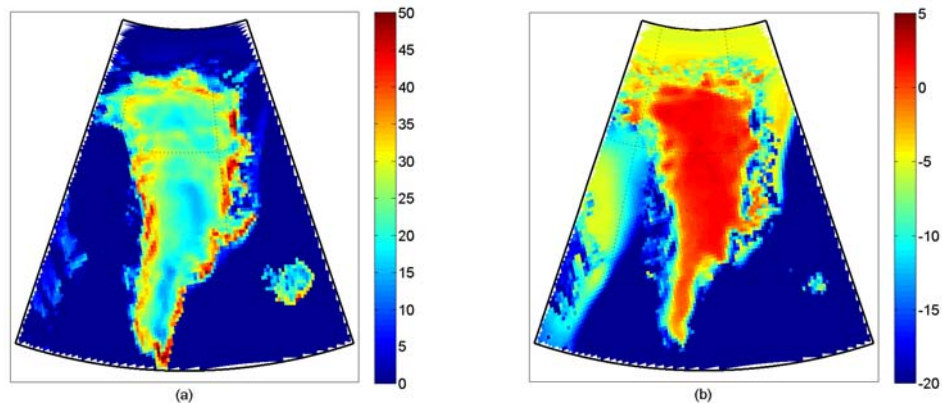


Figure 21. The mean sensible (a) and latent (b) heat flux (W m^{-2}) over 1961-1990 from the Greenland Climate Change data archive. The downward fluxes are positive.

The relative humidity remains rather high ($> 90\%$) throughout the year on the plateau. Often, the high humidity allows direct ice deposition on the surface. It is considerably smaller at lower elevations ($\sim 80\%$) due to the adiabatic heating and drying on the katabatic flows.

Arctic PBL near Ice Edge (Atlantic and Baffin Bay Regions)

The PBL near ice edge possesses many extreme properties not to be found elsewhere. Its vertical structure and stability may change rapidly as the direction of the wind is changing. Regularly, the open water has higher temperature than the air above it. It leads to statically unstable stratification within the PBL to enhanced turbulent mixing and to the deep PBL. The wintertime H can reach 500 W m^{-2} or briefly even larger values. Figure 22 shows the estimation of the mean flux from the satellite climatology HOAPS. The mean flux in March reaches $\sim 60 \text{ W m}^{-2}$ at the ice edge. The wintertime flux could be significantly underestimated in this data. Häkkinen and Cavalieri [1989] using the gridded Navy Fleet Numerical Oceanography Central surface analysis and the First GARP Global Experiment (FGGE) IIc data estimated the mean wintertime fluxes in the Barents sea to be as large as 400 W m^{-2} with uncertainty of about 30%. In September, the flux is much smaller (about 10 W m^{-2}) as the Arctic atmosphere has much higher summertime temperatures. Indeed the ARTIST data [Argentini et al., 2003] revealed that the PBL in the marginal ice zone remains surprisingly stable. The unstable conditions have been observed only during a small fraction of days characterized by easterly cold air outbreaks. Much more often the PBL is near-neutrally, slightly stably stratified, whereas its vertical structure remains well mixed up to 500 m to 700 m. As near-neutrality means a small surface H (typically downward between 15 W m^{-2} and 25 W m^{-2}), the comparison highlights an important contradiction between in situ and reanalysis (ERA-40) and satellite (HOAPS and AOFlux) data.

The satellite estimations are essentially the product of the bulk flux algorithms. The latter does not account for the development of the convective winds in the PBL. The convective winds are the highly variable surface layer air flows created through the self-organization of the turbulent convection into cell- and roll-like structures. Those structures are visualized by the convective clouds during cold outbreaks. The convective winds contribute significantly into the turbulent mixing. This contribution is missed in the bulk algorithms. In result, the satellite data locate the maximum heat flux right near the ice edge, whereas direct measurements from aircrafts found it at 50 km to 100 km from the ice edge and of considerably larger magnitude [Brown, 1992].

Figure 3 and 4 reveals that the annual cycle of the PBL depth and therefore stability in this region has an opposite phase to that in the rest of the Arctic. AOE-2001 observations [Tjernstroem et al., 2005] revealed essential asymmetry in the SAT distribution with the positive SAT much less frequent than the negative ones. The physical mechanism behind this asymmetry has been linked to the PBL dynamics. The warm air advected over colder surface creates more stable stratification of the PBL. As the PBL remains relatively well mixed with small surface H (the near-neutral PBL), the increased atmospheric stability strengthen the capping inversion. In result, the PBL becomes shallower and more insulated from the warmer atmosphere aloft. Just opposite, the cold air advection reduces the atmospheric stability, enhances the upward turbulent fluxes at the surface and increases the PBL depth.

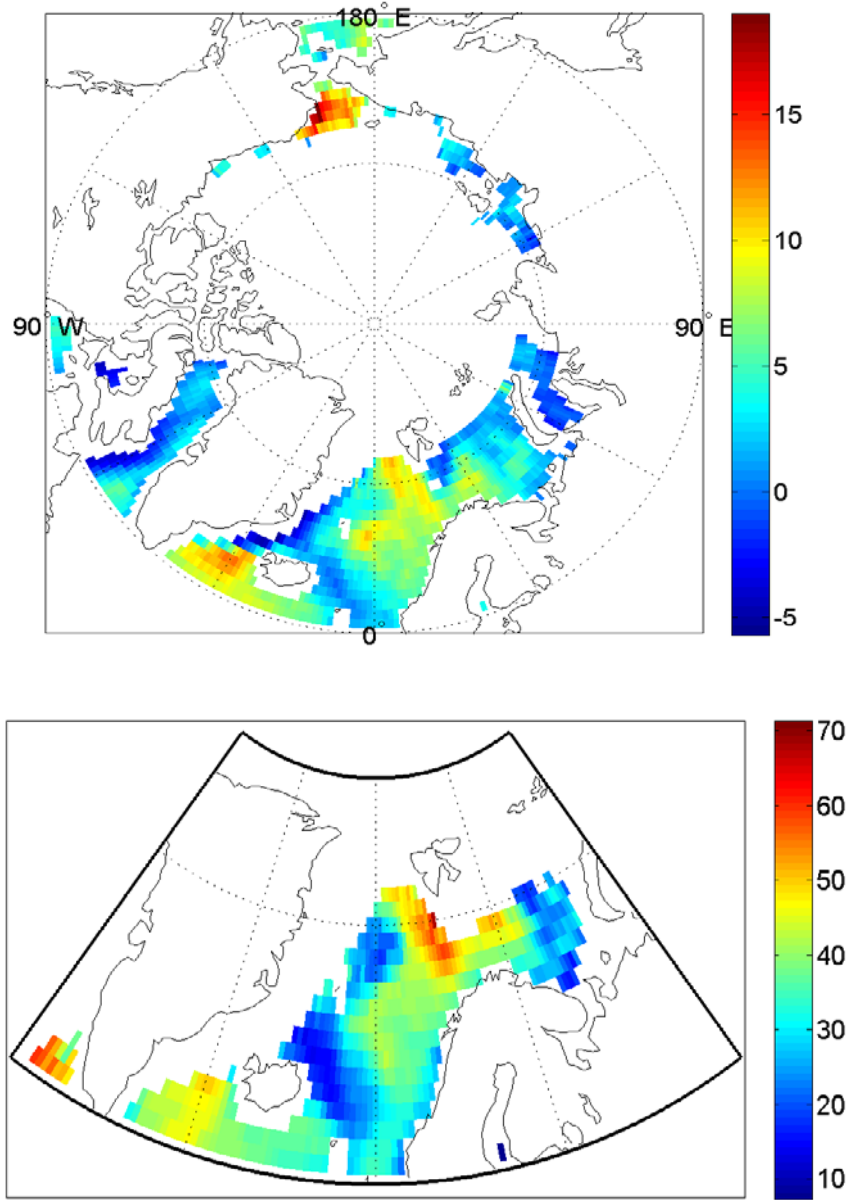


Figure 22. Sensible Heat Flux ($\text{W} \cdot \text{m}^{-2}$) from HOAPS satellite data set for September (a) and March (b) over 1987 - 2005. In March only the Atlantic region has enough open water for the flux evaluation.

The process of selective cooling maintains also high relative humidity of the PBL and the low-level cloudiness (mostly above 90%). During AOE-2001, the $\text{RH} > 95\%$ was in 85% cases. This high RH is maintained by large amount of droplets entrained into the PBL from the cloud layer so that the visibility was less than 1 km in more than 50% cases. But sometimes the visibility improved to 20 km and more. The mean cloud base was about 100 m. By contrast to mid-latitudes, the cloud base remains below 200 m even under good visibility conditions.

The mean summertime PBL depth is about 300 m in ERA-40 but lower, 200 m, depth was measured in AOE-2001. Better agreement between these data sources could be obtained if the cloud layer is included into the PBL. The inversion base height is 250 m in AOE-2001. The inversion thickness is from 100 m to 500 m (AOE-2001). Its stability fluctuates in a broad interval usually less than $5 \cdot 10^{-3} \text{ K m}^{-1}$. Over the inversion the temperature are often increased by 4°C to 5°C reaching its highest value at about 1 km. The wind mostly remains weak to moderate 3 m s^{-1} to 8 m s^{-1} . Although the low-level jet wasn't clearly observed, the wind oscillations are suggesting some inertial oscillation development due to turbulent drag reduction in advected warm air.

6. RECENT CHANGES IN THE PBL CLIMATOLOGY

The Arctic climate [Serreze et al., 2000; ACIA, 2005] and the Arctic PBL undergo significant changes. The atmospheric circulation may induce changes of opposite directions in the PBL. For example, the increased meridional heat advection in the polar cell should strengthen the atmospheric stability and therefore to damp the turbulent mixing and to decouple the dynamics of the surface processes in the even shallower PBL. Simultaneously, the increased advection means stronger winds, which enhance the mixing and deepen the PBL.

The first estimation of the dominant changes in the Arctic PBL could be obtained through analysis of the PBL depth changes. Figure 23 presents the geographical distribution of the PBL depth trends from IGRA. Generally, the PBL becomes deeper in the maritime Arctic and shallower in the continental sub-Arctic. The PBL depth trends in the continental Arctic from ERA-40 are in agreement with reduction of H during 1960-1992 [Groisman et al., 1999] (see Table 10). The above changes in turbulent heat fluxes have been supported by coherent wind reduction at the anemometer height and increase of the near-surface temperature inversions [Groisman et al., 1999] (Figure 24). These trends in near-surface winds, temperature gradients, and turbulent heat fluxes are not apparently linked to cloud cover variations.

The trends in the maritime Arctic cannot be explained so simple. Figure 25 shows decreasing the upward H in the maritime Arctic. Thus the PBL deepening here should be attributed to reduction of the atmospheric stability probably related to the increase of precipitations and to the more intensive cyclonic activity. At the same time the oceanic heat transport into the Arctic Ocean through Bering Strait and Fram Strait is also increasing [Woodgate et al., 2006; Schauer et al., 2004]. Intercomparisons between North Pole 4 (1956-57) and North Pole 23 (1976-77) stations suggests some decrease of the downward H in autumn and winter in the Central Arctic too [Makshtas, 1991]. Thus, the PBL changes at the ice edge could be related to the reduction of the ice extent, thickness and probably to the large part to increased fractures of the ice cover. The later factor would disproportionately enhance the convective heat flux through small scale surface features non-represented in the reanalysis models and satellite imagery. Vavrus [1995] demonstrated the larger heat flux through the open leads and polynyas can result in reduced extent of the ice cover and at the same time in thicker ice in the central Arctic.

Table 10. Estimates of mean daily turbulent heat fluxes area-averaged over tundra zones of Northern Eurasia and their linear trends. Period 1960-1990. Latent and Sensible heat flux. All trends are statistically significant at the 0.01 level (except latent heat flux, which is significant only at the 0.1 level) [Groisman et al., 1999].

Season	sensible heat flux		latent heat flux	
	Mean (W m ⁻²)	Linear trend (W m ⁻² / 30yrs)	Mean (W m ⁻²)	Linear trend (W m ⁻² / 30yrs)
Winter	-7	-5	0	-0,5
Spring	12	-15	-	-
Summer	37	-8	-	-
Autumn	0	-4	-	-

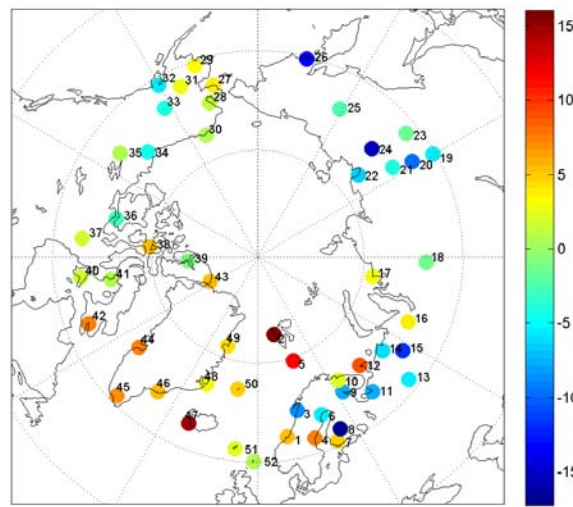


Figure 23. Annual trend of PBL depth (period 1992-2007), m yr⁻¹.

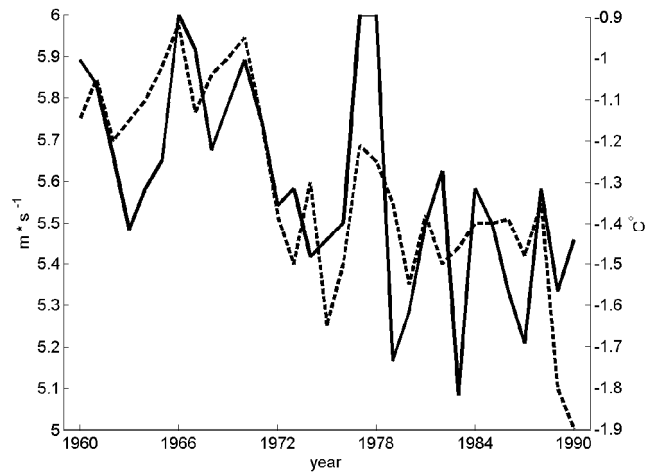


Figure 24. Winter wind speed, (m*s⁻¹) - solid line, and temperature inversion, (°C) - dashed line over the tundra zone of Northern Eurasia. [Groisman et al., 1999].

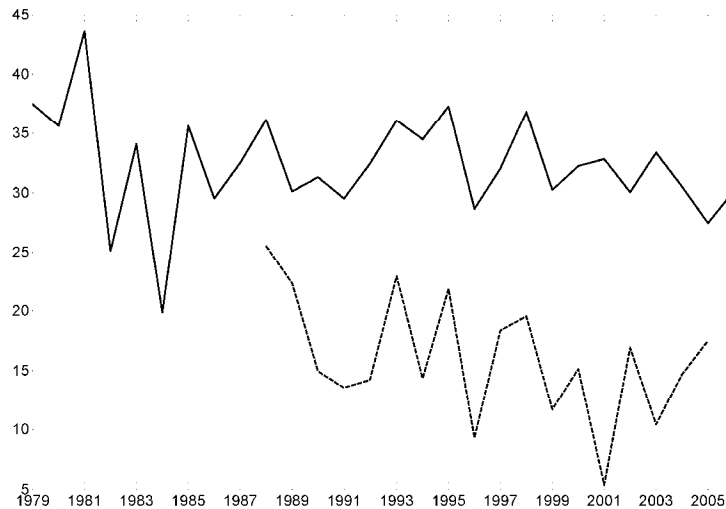


Figure 25. Sensible heat flux ($\text{W} \cdot \text{m}^{-2}$) from OAFlux (solid line) and HOAPS (dashed line) data set over 1979-2006. Atlantic region.

Representation of Arctic PBL in Meteorological Models

Since the long-term trends and projections in the Arctic are unavoidably rely on models, it is necessary to make some notions on the model representation of the Arctic PBL. Existing parameterizations of the Arctic PBL is still deficient [Mahrt, 1998]. The GABLS intercomparison study [www.gabls.org; Beare et al., 2006; Cuxart et al., 2006] concluded, perhaps unsurprisingly, that neither of 20 turbulence parameterizations from all actively used climate and weather prediction models were able to reproduce a rather weakly stable PBL case with tolerable accuracy. All parameterizations diagnosed 2 to 5 times too deep PBL and produced respectively too strong fluxes as compared to 11 turbulence-resolving models used as a reference in the study.

Further studies with SHEBA and AOE to be simulated in frameworks of Arctic Regional Climate Model Intercomparison Project (ARCMIP) disclosed important effects of the turbulence parameterization breakdown on the model climate. Rinke et al. [2006] published an evaluation of 8 different ARCMIP models (ARCSyM, COAMPS, CRCM, HIRLAM, RegCM, PolarMM5, RCA, REMO). The models had approximately the same horizontal resolution of about 50 km and 19 to 30 vertical levels. Thus, the model vertical resolution was clearly too coarse to resolve the thin Arctic PBL. The model discrepancy increases strongly below 800mb. Temperature, wind and humidity profiles in all models diverge from each other in the PBL, and differ considerably from what has been observed. The model surface fluxes exhibited very low correlation with the observed flux and often even sign of the flux was in opposition. Model latent fluxes as a rule were much larger than those observed. In other comparisons, the discrepancies were not so pronounced. Birch et al. [2007] compared observations from AOE-2001 to prognostics from another subset of the ARCMIP models (UM, COAMPS). The pressure, humidity and wind fields were found to be satisfactorily represented. The representation of cloud was unsatisfactory and the latent heat flux was found

too large. There were also problem with near-surface air temperature representation in the models.

Brunke et al. [2006] evaluated the turbulence parameterizations, namely in the part of the surface bulk aerodynamic schemes, in four climate and weather models: the National Center for Atmospheric Research's Community Climate System Model (CCSM), the European Centre for Medium-Range Weather Forecasts (ECMWF) model, the Arctic Regional Climate System Model (ARCSYM), and the National Center for Environmental Prediction's Global Forecasting System (GFS) model. The surface fluxes produced by these algorithms failed to reproduce the climatological annual and diurnal cycles. In summertime, H in all models were lower than observed. But the latent heat fluxes were much higher than observed. In particular, ECMWF, ARCSYM, and GFS produce H under stable conditions that are lower than observed ranges, particularly for the bulk Richardson number exceeding 0.05. ECMWF, ARCSYM, and GFS models have vertical profiles of H that are generally outside of the observed range. These conclusions are in general agreement with earlier Beesly et al. [2000] study of the ECMWF model versus SHEBA data. Byrkjedal et al. [2008] demonstrated using 90 levels model that the increasing of the model vertical resolution to an appropriate level leads to better reproduction of the radiative temperature inversion, surface heat budget and cloudiness.

The breakdown of the turbulence parameterizations in the models has more important effect on the Arctic climatology than just erroneous estimates of the turbulent mixing magnitude. It alters the physical and dynamical conditions in the PBL as diagnosed by the models. Although the best estimations of the annual mean H in the Central Arctic is 0 W m^{-2} to -4 W m^{-2} , which corresponds to the stably stratified PBL, the IPCC models with a few exceptions produce strongly positive (upward) fluxes, on average $+3.6 \text{ W m}^{-2}$, which corresponds to the convective PBL development. This error leads to significantly stronger air-surface coupling in the models and create a pronounced warm temperature bias in the Central Arctic with the effect on the ice cover and cloudiness. The largest spread between models and the largest errors are found in the marginal ice zones.

Projects for Arctic PBL in XXI Century

The projects of the Arctic climate should be considered accounting the specific properties of the Arctic PBL and general failure of the state-of-the-art climate models, leave alone “conceptual” climate models, to reproduce them. In particular, corrections must be done to the strength of the ice-albedo feedback as the ice reduction seem to be followed by increasing cloudiness and therefore cloud albedo. There are also many indirect signs that the observed apparent near-surface warming is largely a shallow feature trapped in the PBL. The significant heat spent on evaporation and evapo-transpiration and often decoupling of the PBL from the lower troposphere make it difficult to assess the real change of the Arctic heat balance on the basis of relatively dense surface measurements.

The IPCC models [Sorterberg et al., 2007] project the largest changes of the turbulent mixing in the marginal ice zone, notably, in Barents and Chukchi Seas (Atlantic and Pacific regions). As the sea ice affects the surface latent heat flux much stronger than the sensible heat flux, it is expected that the latent heat flux changes will be four times larger than the

corresponding changes in H . Over the Central Arctic, the projected change is 2 W m⁻² to 5 W m⁻² with the largest change in the autumn season. In the summer season, the IPCC predict increase of cloudiness and therefore some decrease in the sensible heat flux. It should be noted that a substantial fraction of the models simulate too much present-day sea ice in the Barents Sea.

The Arctic Ocean's summer warming is nearly zero because the mixture of melting snow/ice and open water is constrained to remain close to the freezing point. Thus changes in the summertime PBL will be marginal. The same is true for sub-Arctic seas where overturning circulation and deep sea convection transport the additional heat downward effectively preventing the temperature rise (Schweckendiek and Willebrand 2005). The predictions by the models generally show the largest variance in the regions and seasons of the largest changes. The wintertime standard deviations are largest near the ice margin, especially in the Atlantic sector, indicating that the North Atlantic marginal ice zone is the region of greatest uncertainty in the winter. By contrast, the standard deviations of the summer predictions are relatively small over the Arctic Ocean and sub-polar seas, as the large heat capacity of the water constrains the temperature rise in all models.

7. SUMMARY

The Arctic atmosphere, ocean and cryosphere are coupled through the vertical turbulent mixing in the interfacial layer – the PBL. The coupling is weak as the PBL is stably stratified with rather weak turbulent exchange during 70% to 90% of time. Low temperatures reduce the role of the hydrological cycle in the Arctic coupling with important reservation to still poorly understood St variability and effects on the PBL. Moreover, almost complete dynamical decoupling between the PBL and the surface or the atmosphere has been observed regularly. The decoupling is possible due to turbulent mixing suppression in very stably stratified surface and capping inversion layers.

The Arctic data coverage is still inadequate but improving rapidly in the satellite era, which gives hope for better PBL climatology reconstructions in future. The reconstructions have to overcome uneven geographical distribution of the observations as well as their tendency to be denser in summer and spring seasons and along coastal lines. In this study, in situ measurements are combined with the gridded data, mainly with the reanalysis data, and satellite data products. The study heavily relies upon the Integrated Global Radiosonde Archive (IGRA) with 52 stations used in the reconstruction. The next important source of data was the European Centre for Medium-Range Weather Forecasts (ECMWF) reanalysis ERA-40. ERA-40 is the second generation reanalysis [Uppala et al., 2005]. It assimilates data from the terrestrial global observational system, rawinsondes, including those in IGRA but with different quality control and correction procedures, and from the late 1970s the satellite observational system data. It should be remembered that temporal and spatial heterogeneity of observational sources creates difficulties in homogenization of the ERA-40 data over longer time periods. There are also several satellite products and in situ turbulence campaigns are included.

The typical Arctic PBL is shallow, stably stratified and covered with low-level stratus (St) and stratocumulus (Sc) clouds. The Arctic PBL develops typically 20 to 80 hours

between synoptic disruptions. The PBL depth is usually below 200 m, often even less than 50 m. But in maritime Arctic and over continents in summertime the PBL depth rises to 1.5 km and more. The PBL is the deepest in summer months in the continental regions but in winter and spring months in maritime regions when the air-sea temperature difference is the greatest. The static stability and shallowness of the PBL are potent factors of the cold climate formation. The buoyancy force in the stably stratified PBL (SBL) damps the turbulent exchange so that the cold temperatures at the radiatively cooled surface cannot be effectively mixed with the warmer air advected from the lower latitudes at about 1 km to 3 km. As the near surface air is kept below the ice melting point, it initiates the non-turbulent climate feedbacks (ice-albedo and emissivity) that low the temperature even further. Large temperature gradients near the top of the Arctic PBL (the capping inversion) are favorable to the cloud formation especially in summertime, which also reduce the PBL heating rates. In the Arctic, both the physical (radiation) and dynamical (meridional advection and subsidence in the polar circulation cell) atmospheric processes support the atmospheric stable re-stratification. The transpiration by vegetation in taiga also reduces the summertime convective instability of the PBL.

The sea ice fractures play important role in the Central Arctic climatology as up to 80% of the ocean heat loss goes through the turbulent mixing over the fractures. Satellites revealed open water and thin ice covering in the Arctic Ocean 7% to 14% in summertime and 1% to 5% in wintertime. The conductive heat flux through the multiyear ice is relatively small (5 to 10 W m⁻²) and remarkably stationary on the year to year basis as it is determined by ice thermodynamics.

The mean surface wind speed in the Arctic is low (about 4 m s⁻¹). The minimum wind speed of 2.3 m s⁻¹ is found in the Siberian sub-Arctic region and the maximum wind speed of 6.3 m s⁻¹ is in the Atlantic sub-Arctic region. The slow surface winds are the direct consequence of the atmospheric stability and especially of the PBL stability that impede the vertical momentum transport to the surface.

The presented Arctic PBL climatology does not encompass all aspects of the Arctic climate. There is still a lack of understanding of many key processes in the Arctic PBL. This reconstruction does not include information about a low-level jet, the development of the capping inversion, the PBL top entrainment rate, the convective plumes from the open water patches etc. In particular, in the case of the low-level jet the theoretical models are in odds with occasional observations [ReVelle and Nilsson, 2008]. The low-level jet is frequently observed in the Atlantic region. It is thought to be produced by the abrupt friction decay in on-ice air advection. However, the jet amplitude and frequency does not agree well with the proposed model. Models suggest the jet maximum amplitude should occur about 5 hours after crossing the ice edge by the flow. Taken the mean wind speed of the advection of 10 m s⁻¹, the maximum low-level jets should be observed at about 180 km from the ice edge. This development can be followed from ACSYS-1998 campaign [Brümmer and Thiemann, 2002].

ACKNOWLEDGMENTS

The authors want to emphasize utility of the scientific discussion in the Nansen Environmental and Remote Sensing Center, the Bjerknes Centre for Climate Research and the

Geophysical Institute of the University in Bergen to the content of this study. We also thank Prof. M. Tjernstroem, Prof. S. Zilitinkevich, Prof. V. Alexeev, Prof. I. Polyakov and Dr. A. Grachev for theoretical notions and making the data available. The study is prepared with financial support of the Norwegian Research Council projects PAACSIZ-178908/S30, POCAHONTAS-178345/S30, and NORCLIM-178245/S30.

REFERENCES

- [1] ACIA, 2004. Impacts of a Warming Arctic: Arctic Climate Impact Assessment. Cambridge University Press. (<http://www.acia.uaf.edu/>)
- [2] ACIA, 2005. Arctic Climate Impact Assessment. Cambridge University Press, 1042 p. (<http://www.acia.uaf.edu/>)
- [3] Adachi, Y.; Yukimoto, S. 2006, Influence of sea ice thickness on the atmosphere in the winter Arctic region in an atmospheric general circulation model, SOLA, 2, 76-79
- [4] Andreas, E. L. 1987, A theory for the scalar roughness and the scalar transfer coefficients over snow and sea ice, *Boundary Layer Meteorol.*, 38, 159–184.
- [5] Andreas, E. L.; Jordan, R. E.; Guest, P. S.; Persson, P. O. G.; Grachev A. A.; Fairall, C. W. 2004, Roughness lengths over snow, *Am. Meteorol. Soc.*, Seattle, Wash.
- [6] Andreas, E. L.; Guest, P. S.; Persson, P. O. G.; Fairall, C. W.; Horst, T. W.; Moritz, R. E.; Semmer, S. R. 2002, Near-surface water vapor over polar sea ice is always near ice saturation, *J. Geophys. Res.*, 107(C10), 8033.
- [7] Argentini, S.; Viola, A. P.; Mastrantonio, G.; Maurizi, A.; Georgiadis T.; Nardino M. 2003, Characteristics of the boundary layer at Ny-Ålesund in the Arctic during the ARTIST field experiment, *Annals of geophysics*, 46 (2), 185-196
- [8] Ball, F. K. 1956, The theory of strong katabatic winds. *Aust. J. Phys.*, 9, 373-386.
- [9] Balsley, B.B.; Frehlich, R.G.; Jensen, M.L.; Meillier, Y.; Muschinski, A. 2003: Extreme Gradients in the Nocturnal Boundary Layer: Structure, Evolution, and Potential Causes, *J. Atmos. Sci.*, 60, 2496-2507
- [10] Beare, R. J.; MacVean, M. K. Holtslag, A. A. M.; Cuxart, J.; Esau, I.; Golaz, J. C.; Jimenez, M. A.; Khairoudinov, M.; Kosovic, B.; Lewellen, D.; Lund, T. S.; Lundquist, J. K.; McCabe, A.; Moene, A. F.; Noh, Y.; Raasch, S.; Sullivan, P. 2006, An intercomparison of large eddy simulations of the stable boundary layer, *Boundary Layer Meteorol.* 118 (2), 247 – 272.
- [11] Beesley, J.A.; Bretherton, C.S.; Jakob, C.; Andreas, E.L.; Intrieri, J.M.; Uttal, T.A. 2000, A comparison of cloud and boundary layer variables in the ECMWF forecast model with observations at the Surface Heat Budget of the Arctic Ocean (SHEBA) ice camp. *J. Geophys. Res.*, 105, 337-349.
- [12] Beesley, John A. 2000, Estimating the effect of clouds on the arctic surface energy budget, *J. Geophys. Res.*, 105, 103-117.
- [13] Bengtsson, L.; Semenov, V. A.; Johannessen, O. M. 2004, The early twentieth-century warming in the Arctic – a possible mechanism, *J. Climate*, 17, 4045–4057.
- [14] Birch, C. E.; Brooks, I. M.; Tjernström, M.; Milton, S. F. 2007, *Turbulent exchange over the Arctic Icecap*, AMS 15th Conference on Air-Sea Interaction, August 20-24, Portland, Oregon.

- [15] Bradley, R. S.; Keimig, F. T.; Diaz H. F. 1992, Climatology of Surface-Based Inversions in the North American Arctic, *J. Geophys. Res.*, 97(D14), 699-712.
- [16] Bretherton, C.S.; Macvean, M. K.; Bechtold, P.; Chlond, A.; Cotton, W. R.; Cuxart, J.; Cuijpers, H.; Mhairoutdinov, M.; Kosovic, B.; Lewellen, D.; Moeng, C.-H.; Siebesma, P.; Stevens, B.; Stevens, D. E.; Sykes, I.; Wyant, M. C. 1999, An intercomparison of radiatively driven entrainment and turbulence in a smoke cloud, as simulated by different numerical models, *Quart. J. Royal Meteorol. Soc.*, 125(554), 391-423.
- [17] Brown, R.A., 1990, Meteorology, Chapter 1 in /Polar Oceanography, W.O. Smith, Ed., Academic Press, 406pp
- [18] Brunke, M. A.; Zhou, M.; Zeng, X.; Andreas, E. L. 2006, An intercomparison of bulk aerodynamic algorithms used over sea ice with data from the Surface Heat Budget for the Arctic Ocean (SHEBA) experiment. *Journal of Geophysical Research*, 111.
- [19] Bromwich, D.H.; Wang, S-H. 2005, Evaluation of the NCEP/NCAR and ECMWF 15/40-yr reanalyses using rawinsonde data from two independent Arctic field experiments, *Mon. Weath. Rev.*, 133, 3562-3578.
- [20] Brümmer, B.; Thiemann, S. 2002, The atmospheric boundary layer in an Arctic wintertime on-ice air flow, *Boundary Layer Meteorol.*, 104, 53-72.
- [21] Brunke, M. A.; Zeng, X.; Anderson, S. 2002, Uncertainties in sea surface turbulent flux algorithms and data sets, *J. Geophys. Res.*, 107(C10), 3141.
- [22] Brunke, M. A.; Zhou, J.; Zeng, X.; Andreas, E. L. 2006, An intercomparison of bulk aerodynamic algorithms used over sea ice with data from the Surface Heat Budget of the Arctic Ocean (SHEBA) experiment, *J. Geophys. Res.*, 111.
- [23] Budyko, M.I. 1969: Polar ice and climate, Gidrometeoizdat, Leningrad, Russia, 36 pp.
- [24] Byrkjedal, Ø; Esau, I; Kvamstø, N. G. 2008, Sensitivity of simulated wintertime Arctic atmosphere to vertical resolution in the ARPEGE/IFS model, *Climate Dynamics*, 30(7-8), 687-701.
- [25] Chase, T.N.; Herman, B.; Pielke Sr., R. A.; Zeng, X; Leuthold M. 2002, *J. Geophys. Res.*, 107(D14), 4193.
- [26] Chen, J.; del Genio, A.D.; Carlson, B.E.; Bosilovich, M.G. 2008: The Spatiotemporal Structure of Twentieth-Century Climate Variations in Observations and Reanalyses. Part I: Long-Term Trend. *J. Climate*, 21(11), 2611-2633.
- [27] Chen, Y.; Francis, J.A.; Miller, J.R. 2002, Surface Temperature of the Arctic: Comparison of TOVS Satellite Retrievals with Surface Observations, *J. Climate*, 15, 3698-3708
- [28] Curry, J.A. 1986, Interactions among Turbulence, Radiation and Microphysics in Arctic Stratus Clouds, *J. Atmos. Sci.* 43, 90–106.
- [29] Cuxart, J.; Holtslag, A.A.M.; Beare, R.J.; Bazile, E.; Beljaars, A.; Conangla, L.; Freedman, M. Ek, F.; Hamdi, R.; Kerstein, A.; Kitagawa, A.; Lenderink, G.; Lewellen, D.; Mailhot, J.; Mauritsen, T.; Perov, V.; Schayes, G.; Steeneveld, G.-J.; Svensson, G.; Taylor, P.; Weng, W.; Wunsch, S.; Xu, K.-M. 2006, Single-column model intercomparison for a stably stratified atmospheric boundary layer, *Bound.-Layer Meteor.*, 118, 273-303.
- [30] Derbyshire S. H. 1999, Boundary-layer decoupling over cold surfaces as a physical boundary instability. *Bound.-Layer Meteor.*, 90, 297–325.
- [31] Dethloff, K. , Rinke, A., Hebestadt, I., Christensen, J. H., Botzet, M., Machenhauer, B. (1997). High resolution climate simulations over the Arctic and its sensitivity to

- physical parameterizations, First SPARC General Assembly, Stratospheric Processes and their Role in Climate (SPARC) WMO/TD-NO 814, 1, 31-34.
- [32] Doronin, Y.P., 1974, Influence of ice cover on the heat exchange between the atmosphere and the ocean, *Problems of the Arctic and the Antarctic*, 43-44, 61-72.
 - [33] Drue, C.; Heinemann, G. 2003, Investigation of the Greenland Atmospheric Boundary Layer over Summit 2002 (IGLOS). Field Phase Report. Berichte zur Polarforschung Nr. 447, Alfred-Wegener-Institut fur Polar- und Meeresforschung, D-2751 Bremerhaven, Deutschland, 82 pp.
 - [34] Eisen O.; Kottmeier C. 2000, On the importance of leads in sea ice to the energy balance and ice formation in the Weddell Sea, *J. Geophys. Res.*, 105(C6), 14045-14060.
 - [35] Esau, I. N. 2007, Amplification of turbulent exchange over wide Arctic leads: Large-eddy simulation study, *J. Geophys. Res.*, 112.
 - [36] Esau, I.; Byrkjedal, Ø. 2007, Application of large eddy simulation database to optimization of first order closures for neutral and stably stratified boundary layers, *Boundary Layer Meteorol.*, 125(2), 207-225.
 - [37] Esau, I.; Zilitinkevich, S.S. 2006, Universal Dependences between Turbulent and Mean Flow Parameters in Stably and Neutrally Stratified Planetary Boundary Layers, *Nonlinear Processes in Geophysics (the special issue "Turbulent transport in Geosciences")*, 13, 122-144.
 - [38] Fairall, C.W.; Bradley, E.F.; Hare, J.E.; Grachev, A.A.; Edson, J.B. 2003, Bulk Parameterization of Air–Sea Fluxes: Updates and Verification for the COARE Algorithm. *J. Climate*, 16, 571–591.
 - [39] Fedorovich, E.; Conzemius, R.; Mironov, D. 2004, Convective entrainment into a shear free linearly stratified atmosphere: bulk models reevaluated through large eddy simulations, *J. Atmos. Sci.*, 61, 281–295.
 - [40] Fetterer, F.; Radionov, V. 2000, Arctic Climatology Project, *Environmental Working Group Arctic meteorology and climate atlas*, National Snow and Ice Data Center, CD-ROM, Boulder, CO, 2000.
 - [41] Gaffen, D.J. 1996, A Digitized metadata set of global upper-air station histories, NOAA, Technical Memorandum ERL-ARL 211, Silver Spring, MD, 38 pp.
 - [42] Genikhovich, E. L.; Osipova, G. I. 1984, Determination of the exchange coefficient using data of routine meteorological observations (in Russian), *Trans. Main Geophys. Observatory*, 479, 62-69.
 - [43] Grassl H.; Jost, V.; Kumar, R.; Schulz, J.; Bauer, P.; Schluessel, P. 2000, The Hamburg Ocean-Atmosphere Parameteres and Fluxes from Satellite Data (HOAPS): A Climatological Atlas of Satellite-Derived Air-Sea-Interaction Parameters over the Oceans. Report No. 312, ISSN 0937-1060, Max Planck Institute for Meteorology, Hamburg
 - [44] Graversen, R. G.; Mauritzen, T.; Tjernstrom, M.; Kallen, E.; Svensson, G. Vertical structure of recent Arctic warming, *Nature*, 451, 53-56, 2008.
 - [45] Grisogono, B.; Oerlemans, J. 2001, Katabatic flow: analytic solution for gradually varying eddy diffusivities, *J. Atmos. Sci.*, 58, 3349-3354.
 - [46] Groetzner, A.; Sausen, R.; Claussen, M. 1996, The impact of sub-grid scale sea-ice inhomogeneities on the performance of the atmospheric general circulation model ECHAM3, *Clim. Dyn.*, 12(7), 477-496

- [47] Groisman, P. Y.; Genikhovich, E. L. 1997, Assessing Surface-Atmosphere Interactions Using Former Soviet Union Standard Meteorological Network Data. Part I: Method, *J. Clim.*, 10, 2154-2183.
- [48] Groisman, P. Y.; Genikhovich, E. L.; Bradley, R.S.; Bomin, S. 1999, Trends in turbulent heat flux over Northern Eurasia, *Interaction Between the Cryosphere, Climate and Greenhouse Gases. IAHS Publ.*, 256, 19-25
- [49] Groisman, P. Y.; Genikhovich, E. L.; Bradley, R.S.; Ilyin B.M. 1997, Assessing Surface-Atmosphere Interactions Using Former Soviet Union Standard Meteorological Network Data. Part II: Cloud and Snow Cover Effects, *J. Clim.*, 10, 2184-2199.
- [50] Guo, Z.; Dirmeyer, P. A.; Koster, R. D.; Bonan, G.; Chan, E.; Cox, P.; Gordon, C. T.; et al. 2006, GLACE: The Global Land-Atmosphere Coupling Experiment. Part II: Analysis. *J. Hydrometeorology*, 7(4), 611-625.
- [51] Häkkinen, S.; Cavalieri, D. J. 1989, A Study of Oceanic Surface Heat Fluxes in the Greenland, Norwegian, and Barents Seas, *J. Geophys. Res.*, 94(C5), 6145-6157.
- [52] Heinemann G. 2002, Aircraft-Based Measurements Of Turbulence Structures In The Katabatic Flow Over Greenland, *Boundary Layer Meteorol.*, 103(1), 49-81.
- [53] Heinemann, G. 1999, The KABEG97 field experiment: An aircraft-based study of the katabatic wind dynamics over the Greenlandic ice sheet, *Boundary Layer Meteorol.* 93, 75-116.
- [54] Heinemann, G.; and Klein, T. 2002, Modelling and observations of the katabatic flow dynamics over Greenland, *Tellus*, 54 A, 542-554.
- [55] IPCC, 2007: *Climate Change 2007: The Physical Science Basis*. Contribution of Working Group I to the Fourth Assessment Report of the Intergovernmental Panel on Climate Change (Solomon, S., D. Qin, M. Manning, Z. Chen, M. Marquis, K.B. Averyt, M. Tignor and H.L. Miller (eds.)). Cambridge University Press, Cambridge, United Kingdom and New York, NY, USA, 996 pp. (<http://ipcc-wg1.ucar.edu/wg1/wg1-report.html>)
- [56] Johannessen, O.M.; Bengtsson, L.; Miles, M.W.; Kuzmina, S.I.; Semenov, V.A.; Alekseev, G.V; Nagurnyi, A.P.; Zakharov, V.F.; Bobylev, L.P.; Petterson, L.H.; Hasselmann K.; Cattle H. 2003, Arctic climate change – observed and modeled temperature and sea ice, *Tellus A*, 328-341.
- [57] Kanae, S.; Kowalczyk, E.; Lawrence, D.; Liu, P.; Lu, C.H.; Malyshev, S.; McAvaney, B.; McGregor, J.L; Mitchell, K.; Mocko, D.; Oki, T.; Oleson, K.W.; Pitman, A.; Sud, Y.C.; Taylor, C.M.; Verseghy, D.; Vasic, R.; Xue, Y.; Yamada, T. 2006, GLACE: The Global Land-Atmosphere Coupling Experiment. Part II: Analysis, *J. Hydrometeor*, 7, 611–625.
- [58] Khrol, V. P. (Ed.), 1992: *Atlas of the Energy Balance of the Northern Polar Area*, Arctic, and Antarctic. Res. Inst., p. 72, St. Petersburg, Russia.
- [59] Koster, R.; Suarez, M.; Liu, P.; Jambor, U.; Berg, A.; Kistler, M.; Reichle, R.; Rodell, M.; Famiglietti, J. 2004, Realistic initialization of land surface states: Impacts on subseasonal forecast skill, *J. Hydrometeorol.*, 5(6), 1049–1063.
- [60] Kottmeier, C.; Frey, K.; Hasel, M.; Eisen O. 2003, Sea ice growth in the eastern Weddell Sea in winter, *J. Geophys. Res.*, 108 (C4), 3125.
- [61] Kuzmina, S. I.; Johannessen, O. M.; Bengtsson, L. Aniskina, O.G.; Bobylev, L. P. 2008, High northern latitude surface air temperature: comparison of existing data and creation of a new gridded data set 1900-2000, *Tellus A*, 60 (2), 289-304.

- [62] Langen, P. L.; Alexeev V. A. 2005, Estimating $2 \times \text{CO}_2$ warming in an aquaplanet GCM using the fluctuation-dissipation theorem, *Geophys. Res. Lett.*, 32.
- [63] Lawrence, D. M.; Slater, A. G.; Tomas, R. A.; Holland, M. M.; Deser, C. 2008, Accelerated Arctic land warming and permafrost degradation during rapid sea ice loss, *Geophys. Res. Lett.*, 35.
- [64] Lindsay, R. W. 1998, Temporal variability of the energy balance of thick arctic pack ice, *J. Climate*, 11, 313–333.
- [65] Lindsay, R. W.; Rothrock, D. A. 1995, Arctic sea ice leads from advanced very high resolution radiometer images, *J. Geophys. Res.*, 100(C3), 4533- 4544.
- [66] Liu, Y.; Jeffrey R. Key; Axel Schweiger; Jennifer Francis 2006, Characteristics of Satellite-Derived Clear-Sky Atmospheric Temperature Inversion Strength in the Arctic, 1980–96, *J. Clim*, 19, 4902-4913.
- [67] Lüpkes, C.; Vihma, T.; Birnbaum, G.; Wacker U. 2008, Influence of leads in sea ice on the temperature of the atmospheric boundary layer during polar night, *Geophys. Res. Lett.*, 35.
- [68] Macdonald, R.W.; Harner, T.; Fyfe, J. 2005, Recent climate change in the Arctic and its impact on contaminant pathways and interpretation of temporal trend data, *Science of the Total Environment*, 342, 5- 86.
- [69] Mahrt L. 1998, Stratified atmospheric boundary layers and breakdown of models, *Theor. Comput. Fluid Dyn.*, 11, 263–279.
- [70] Makshtas, A. 1991, The heat budget of Arctic ice in the winter, Arctic and Antarctic Institute, Leningrad, U.S.S.R, 77 pp.
- [71] Manabe, S.; Wetherald, R. T. 1975, The effects of doubling CO_2 concentration on the climate of a general circulation model, *J. Atmos. Sciences*, 32(1), 3-15.
- [72] Nagurny, A. P. 1995, Space-time distribution of temperature inversions in the Arctic atmospheric boundary layer, *Ann. Geophysical*, 13, 1087-1092.
- [73] Nakamura, N.; Oort, A. 1988, Atmospheric heat budgets of the polar regions. *J. Geophys. Res.*, 93 (D8), 9510–9524.
- [74] Nieuwstadt, F. T. M. 1984, The turbulent structure of the stable, nocturnal boundary layer, *J. Atmos. Sciences*, 41, 2202-2216.
- [75] Nkemdirim, L.C. 1978, A comparison of radiative and actual nocturnal cooling rates over grass and snow, *J. Appl. Meteorol.*, 17, 1643-1646.
- [76] Oerlemans, J.; Grisogono, B. 2002, Glacier winds and parameterisation of the related surface heat fluxes, *Tellus*, 54, 440 – 452
- [77] Oke, T.R., 1987: Boundary Layer Climates. Routledge, New York.
- [78] Orvig, S. 1970, "Climates of the Polar Regions." *World Survey of Climatology*, 14, editor: H.E. Landsberg, Elsevier Publishing Company. Amsterdam-London-New York.
- [79] Overland, J. E.; Turet, P. 1994, Variability of the Atmospheric Energy Flux across 70°N computed from the GFDL data set. Nansen Centennial Volume, *Geophys. Monogr.*, No. 84, Amer. Geophys. Union, 313–325.
- [80] Overland, J.E.; Guest, P.S. 1991, The Arctic snow and air temperature budget over sea ice during winter, *J. Geophys. Res.*, 96, 4651-4662.
- [81] Overland, J.E.; Wang, M. 2007, The Recent Arctic Warm Period. Eos Trans. AGU, 88, Fall Meet. Suppl., Abstract U33B-02.
- [82] Overpeck, J.; Hughen, K.; Hardy, D.; Bradley, R.; Case, R.; Douglas, M.; Finney, B.; Gajewski, K.; Jacoby, G.; Jennings, A.; Lamoureux, S.; Lasca, A.; MacDonald, G.;

- Moore, J.; Retelle, M.; Smith, S.; Wolfe, A.; Zielinski, G. 1997, Arctic Environmental Change of the Last Four Centuries, *Science*, 278, 1251-1256.
- [83] Polyakov, I. ; Bekryaev, R. V.; Alekseev, G. V.; Bhatt, U. S.; Colony, R. L.; Johnson, M. A.; Makshtas, A. P.; Walsh, D. 2003, Variability and trends of air temperature and pressure in the maritime Arctic, 1875-2000, *Journal of Climate* 16 (12), 2067-2077.
- [84] Prandt, L., 1942: *Führer durch die Stromungslehre*. Vieweg und Sohn, 648 pp
- [85] Przybylak, R. 2003a, *The climate of the Arctic*, Kluwer Academic Publishers, Dordrecht, 270 pp.
- [86] Przybylak, R. 2003b, Variability of Air Temperature and Atmospheric Precipitation in the Arctic, Series: *Atmospheric and Oceanographic Sciences Library*, 25, 352 p.
- [87] Raisanen, P. 1996, The effect of vertical resolution on clear-sky radiation calculations: Tests with two schemes, *Tellus*, 48 A, 403-423.
- [88] Renfrew, I. A.; King, J. C.; Markus, T. 2002, Coastal polynyas in the southern Weddell Sea: variability of the surface energy budget, *J. Geophys. Res. (Oceans)*, 107 (C6), 3063.
- [89] ReVelle, D.O.; Nilsson, E.D. 2008, Summertime Low-Level Jets over the High-Latitude Arctic Ocean. *J. Appl. Meteor. Climatol.*, 47, 1770-1784
- [90] Rinke, A.; Dethloff, K.; Cassano, J.; Christensen, J.H.; Curry, J.A.; Du, P.; Girard, E.; Haugen, J.-E.; Jacob, D.; Jones, C.; Koltzow, M.; Laprise, R.; Lynch, A.H.; Pfeifer, S.; Serreze, M.C.; Shaw M.J., Tjernström M., Wyser K., Zgar M. 2006 Evaluation of an ensemble of Arctic regional climate models: spatial patterns and height profiles, *Clim. Dyn.* 26.
- [91] Roeckner, E.; Brokopf, R.; Esch, M.; Giorgi, M.; Hagemann, S., Kornblueh, L., Manzini, E., Schlese, U.; Schulzweida, U. 2006, Sensitivity of simulated climate to horizontal and vertical resolution in the ECHAM5 atmosphere model, *J. Climate*, 19, 3771–3791.
- [92] Savijarvi, H. 2006, Radiative and turbulent heating rates in the clear-air boundary layer, *Q. J. R. Meteorol. Soc.*, 132, 147-161.
- [93] Schauer, U.; Fahrbach, E.; Osterhus, S.; Rohardt G. 2004, Arctic warming through the Fram Strait: Oceanic heat transport from 3 years of measurements, *J. Geophys. Res.*, 109.
- [94] Schweckendiek, U.; Willebrand, J. 2005 Mechanisms Affecting the Overturning Response in Global Warming Simulations, *J. Climate*, 18(23), 4925-4936.
- [95] Semler, T.; Jacob, D.; Schlunzen, K.H.; Podzun R. 2005, The water and Energy budget of the Arctic atmosphere, *Bull. Amer. Meteor. Soc.* 18, 2515-2529.
- [96] Serafin, S.; Zardi, D. 2005, Critical evaluation and proposed refinement of the Troen and Marht (1986) boundary layer model. 28th International Conference on Alpine Meteorology – Mesoscale Alpine Programme Meeting, Zadar (HR), 23-27 May 2005; Proceedings, 464-467.
- [97] Serreze, M. C.; Barrett A. P.; Slater, A. G.; Steele, M.; Zhang, J.; Trenberth, K. E. 2007, The large-scale energy budget of the Arctic. *J. Geophys. Res.*, 112.
- [98] Serreze, M. C.; Barrett, A. P.; Stroeve, J. C.; Kindig, D. N.; Holland, M. M. 2008, The emergence of surface-based Arctic Amplification, *The Cryosphere Discuss.*, 2, 601-622.
- [99] Serreze, M. C.; Barry, R. G. 2005, The Arctic Climate System; Cambridge, England: Cambridge University Press.

- [100] Serreze, M. C.; Francis J. A. 2006, The arctic amplification debate, *Climatic Change* 76(3-4), 241-264.
- [101] Serreze, M. C.; Kahl, J. D.; Schnell, R. C. 1992, Low-level temperature inversions of the Eurasian Arctic and comparisons with Soviet drifting station data, *J. Climate*, 5 (6).
- [102] Serreze, M.C.; Barry, R. G.; Walsh, J. E. 1995, Atmospheric water vapor characteristics at 70°N, *J. Climate*, 8, 719-731.
- [103] Serreze, M.C.; Barry, R.G. 2000, Atmospheric components of the Arctic Ocean hydrologic budget assessed from rawinsonde data, in E.L. Lewis et al. (eds.) *The Freshwater Budget of the Arctic Ocean*, Kluwer Academic Press, Dordrecht, pp141-162.
- [104] Serreze, M.C.; Walsh, J.E.; Chapin F.S.; Osterkamp, T.; Dyurgerov, M.; Romanovsky, V.; Oechel, W.C.; Morison, J.; Zhang T.; Barry R.G. 2000, Observational evidence of recent change in the northern high-latitude environment, *Climatic Change* 46, 159-207.
- [105] Shupe, M.D.; Kollias, P.; Persson, P.O.G.; McFarquhar, G.M. 2008, Vertical Motions in Arctic Mixed-Phase Stratiform Clouds. *J. Atmos. Sci.*, 65, 1304–1322.
- [106] Sorteberg, A.; Kattsov, V.; Walsh, J. E.; Pavlova, T. 2007, The Arctic surface energy budget as simulated with the IPCC AR4 AOGCMs, *Climate Dynamics*, 29(2-3), 131-156
- [107] Stendel, M.; Christensen, J. H.; Aðalgeirsðóttir, G.; Kliem, N.; Drews, M. 2007, Regional climate change for Greenland and surrounding seas. Part I: Atmosphere and land surface. DMI Climate Centre Report, no. 07-02.
- [108] Tjernström, M. 2005, The Summer Arctic Boundary Layer during the Arctic Ocean Experiment 2001 (AOE-2001), *Bound Layer Meteorol.* 117, 5-36.
- [109] Tjernström, M.; Leck, C.; Persson, P. O. G.; Jensen, M. L. J.; Oncley, S. P.; Targino, A. 2004, The Summertime Arctic Atmosphere. Meteorological Measurements during the Arctic Ocean Experiment 2001. *Bull. Am. Meteorol. Soc.*, 1305-1321.
- [110] Trenberth, K.E.; Caron, J.M. 2001, Estimates of Meridional Atmosphere and Ocean Heat Transports, *J. Climate*, 14, 3433–3443.
- [111] Treshnikov, A. F., 1985: Atlas of the Arctic. Arctic and Antarctic Institute, USSR State Committee on Hydrometeorology and Environment, and The Arctic and Antarctic Research Institute, Central Administrative Board of Geodesy and Cartography of the Ministereal Council of the USSR, Moscow, 204 pp.
- [112] Troen, I.; Mahrt, L. 1986, A simple model of the atmospheric boundary layer; sensitivity to surface evaporation, *Boundary Layer Meteorol.*, 37, 129-148.
- [113] Tsukernik, M.; Chase, T.N.; Serreze M.C.; Barry R.G. 2004, On the regulation of minimum mid-tropospheric temperatures in the Arctic, *J. Geophys. Res. Lett.*, 31.
- [114] Uppala, S. M., and co-authors, 2005, The ERA-40 re-analysis, *QJRMS*, 131 Part B, 2961-3012.
- [115] Uttal, T.; Curry, J.A.; Mcphee, M.G.; Perovich, D.K.; Moritz, R.E.; Maslanik, J.A.; Guest, P.S.; Stern, H.L.; Moore, J.A.; Turenne, R.; Heiberg, A.; Serreze, M.C.; Wylie, D.P.; Persson, O.G.; Paulson, C.A.; Halle, C.; Morison, J.H.; Wheeler, P.A.; Makshtas, A.; Welch, H.; Shupe, M.D.; Intrieri, J.M.; Stamnes, K.; Lindsey, R.W.; Pinkel, R.; Pegau, W.S.; Stanton, T.P.; Grenfeld, T.C. 2002, Surface Heat Budget of the Arctic Ocean, *Bull. Amer. Meteor. Soc.*, 81, 255-275.
- [116] Van den Broeke, M.; Smeets, P.; Ettema, J.; 2008: Surface layer climate and turbulent exchange in the ablation zone of the west Greenland ice sheet, *Int. J. Climate.*, *in print*

- [117] Vavrus S. J. 1995; Sensitivity of the Arctic climate to leads in a coupled atmosphere-mixed layer ocean model, *J. Climate.*, 8(2), 158-171.
- [118] Vinogradova, A.A. 2007, Meridional mass and energy fluxes in the vicinity of the Arctic border, *Izvestia, Atmos. Oceanic Phys.*, 43(3), 281-293.
- [119] Walsh, J.E. 2008, Climate of the arctic marine environment, *Ecological Applications*, 18(Suppl.), 3-22.
- [120] Wang, M.; Overland, J.E.; Kattsov, V.; Walsh, J.E.; Zhang, X.; Pavlova, T. 2007, Intrinsic versus forced variation in coupled climate model simulations over the Arctic during the 20th Century, *J. Climate*, 20, 1084-1098.
- [121] Wang, Q.; Wang, S. 2004, Turbulent and thermodynamic structure of the autumnal Arctic boundary layer due to embedded clouds, *Boundary Layer Meteorol.*, 113, 225-247.
- [122] Woodgate, R. A.; Aagaard, K.; Weingartner, T. J. 2006, Interannual changes in the Bering Strait fluxes of volume, heat and freshwater between 1991 and 2004, *Geophys. Res.Lett.*, 33.
- [123] Wunsch, C. 2005, The Total Meridional Heat Flux and Its Oceanic and Atmospheric Partition, *J. Climate*, 18, 4374-4380
- [124] Yamazaki, T.; Ohta, T.; Suzuki, R.; Ohata, T. 2007, Flux variation in a Siberian taiga forest near Yakutsk estimated by a one-dimensional model with routine data, 1986-2000, *Hydrological Processes*, 21(15), 2009-2015.
- [125] Yu, L.; Jin, X.; Weller, R. A. 2008, Multidecade Global Flux Datasets from the Objectively Analyzed Air-sea Fluxes (OAFlux) Project: Latent and sensible heat fluxes, ocean evaporation, and related surface meteorological variables. Woods Hole Oceanographic Institution, OAFlux Project Technical Report. OA-2008-01, 64pp. Woods Hole. Massachusetts.
- [126] Zilitinkevich, S. S.; Esau, I. 2005, Resistance and Heat Transfer Laws for Stable and Neutral Planetary Boundary Layers: Old Theory, Advanced and Re-evaluated, *Quarterly J. Royal Meteorol. Soc.*, 131, 1863-1892.
- [127] Zilitinkevich, S.; Baklanov, A.; Rost, J.; Smedman, A.-S.; Lykosov, V.; Calanca, P. 2002, Diagnostic and prognostic equations for the depth of the stably stratified Ekman boundary layer, *Quart. J. Roy. Met. Soc.*, 128, 25-46.
- [128] Zilitinkevich, S.; Esau, I.; Baklanov, A. 2007, Further comments on the equilibrium height of neutral and stable planetary boundary layers, *Quart. J. Roy. Met. Soc.* 133, 265-271.

Chapter 2

NONEQUILIBRIUM THERMODYNAMIC THEORY OF ATMOSPHERIC TURBULENCE

Yinqiao Hu and Jinbei Chen

Gansu Province Key Laboratory of Arid Climatic Change and Reducing Disaster
Cold and Arid Regions Environment and Engineering Institute,
Chinese Academy of Sciences, Lanzhou, China

ABSTRACT

Turbulence is one of the ubiquitous natural phenomena in everyday experience, and a puzzle that is not yet fully resolved in classical physics. A nonequilibrium thermodynamic theory of atmospheric turbulence is developed. The entropy equilibrium equation of atmospheric system with dynamic processes is advanced, and then Fourier's and Flick's laws, Newton's Law, and both the Dufour and the Soret effects—the cross coupling effect between the dynamic and turbulent transport processes in the atmosphere—and the turbulent intensity theorem are uniformly deducted by atmospheric nonequilibrium thermodynamics. These laws and theorem are partially validated by using observed data and, further, their phenomenological coefficients are determined. The turbulent intensity theorem reveals that the macroscopic cause of the development of fluid turbulence is a result of the shearing effects of velocity together with temperature and proves that both Reynolds turbulence and Rayleigh-Bénard turbulence coexist in the atmosphere. The discovery of the coupling effect phenomenon between the thermodynamic and dynamic processes breaks through the viewpoint of the theories of traditional turbulent transport, Fourier's and Flick's laws, and Newton's Law—i.e., the turbulent transport flux of one kind of macroscopic quantity is equivalent to the gradient transport flux of this macroscopic quantity. Moreover, the coupling principle between the thermodynamic and dynamic processes deems that the turbulent transport flux of one kind of macroscopic quantity should include the velocity coupling transport in addition to the gradient transport flux of this macroscopic quantity. Consequently, the vertical turbulent transport flux of energy and matter should count in the cross coupling effect of the vertical velocity, i.e., convergence and divergence motion, in addition to the turbulent transport flux caused by their vertical gradient. The earth's surface is characterized by spatial heterogeneity over a wide range of scales. The heterogeneity of underlying surface brings on the advection to lead the convergence and divergence motion. It may be an

important cause of the imbalance of energy budget of the ground surface. The cross coupling principle of the vertical velocity and vertical turbulent transport may offer a possible clue to the development of the theory of atmospheric boundary layer with heterogeneous underlying surface and to overcome the difficulties encountered in the imbalance problem of ground energy budget and in the parameterization of the boundary layer with the heterogeneous underlying surface.

Keywords: atmospheric turbulence, nonequilibrium thermodynamics, turbulent transport flux, turbulent intensity, heterogeneous underlying surface

1. INTRODUCTION

Turbulence is one of the most common natural phenomena in everyday experience (Busse, 2004), and one of the most common examples of complex and disordered dynamic behaviors in nature (Hof et al., 2004). The turbulent flow exhibits a complex, chaotically-evolving structure over a broad range of space and time scales (Shraiman and Siggia, 2000), from atmospheric phenomena to revolving galaxy and cosmic dust and even the chemical and biology domains, all of which without exception exhibit turbulent phenomena. There exists a multifarious modality of the turbulence. In fluid turbulence, which is very well known, the presence of Reynolds turbulence with a high Reynolds number and heat convection turbulence with a high Rayleigh number (Glazier et al., 1999) is called Rayleigh-Bénard turbulence. These are vector turbulence in the velocity field, which correspond with the scale turbulence (Shraiman and Siggia, 2000); recently, the phenomena of “elastic turbulence” (Groisman, et al., 2000) and “magnetization turbulence” (Bramwell et al., 1998), etc. of the solid state have been discovered. Even as narrated in the article “Universality of Turbulence” (Victor S. L’vov, 1998), the length-scales vary from galactic distances of 10^{16} – 10^{18} km, through planetary distances of 1000–10000 km down to the human scales of 1 mm–10 m (in the atmosphere, ocean and rivers of habitation of human beings, as well as in the kitchen sink). Turbulence is a ubiquitous phenomenon that is not fully understood (Groisman et al., 2000) but in which scientists in the communities of science and engineering are interested.

As is well known, early in 1838 Hagen gave his attention to the fact that there exist two flow phenomena of the laminar flow and the turbulent flow with a distinct feature of the flow in a round pipe; after c. 50 years, O. Reynolds (1880) was the first to systematically investigate the transition from laminar to turbulent flow by injecting a dye streak into flow through a pipe having smooth transparent walls. His observations led to the identification of a single dimensionless parameter, now called the Reynolds number, and denoted (Reynolds, 1894):

$$R_e = \frac{\bar{U}d}{\nu}, \quad (1)$$

in which \bar{U} is the velocity scale of fluid, d the space scale, ν the molecular viscous coefficient of fluid kinematics. R_{ec} is the critical Reynolds number; the turbulence appears as $R_e > R_{ec}$ in general, the critical Reynolds number is $R_{ec} \sim 2000$. *Turbulence* (Hinze, J. O., 1959), a classical monograph edited by Hinze, systemically summarized the progress of

turbulence research in the first half of the twentieth century. At the very beginning, people recognized that turbulence is a vortex movement generated by the effect of fluid shear under the condition of external force. There is no commonly accepted unique definition of turbulent flow and it is usually identified by its main features (Groisman et al., 2000). The definition of turbulence given by Taylor (1935) and von Kármán (1937) is still the one applied most extensively in fluid turbulence: i.e., turbulence is a stochastically ruleless movement in space and time. In order to quantitatively describe the turbulence that is a stochastically ruleless movement, Dryden and Kuethe (Dryden et al., 1930) describe the mean movement state with the mean velocity \bar{U} and the intensity of turbulence with the velocity fluctuation mean square deviation $\sqrt{\bar{u}^2}$, in which the velocity fluctuation is the difference of the instantaneous velocity and mean velocity $u' = U - \bar{U}$. Half of velocity fluctuation variance $e = \frac{1}{2} \rho \bar{u}^2$ is the total energy of the turbulence, where ρ is the fluid density. Hence, the velocity fluctuation variance \bar{u}^2 is defined as the turbulent intensity, which essentially expresses the magnitude of the turbulent energy. Richardson (1922) proposed the cascade picture of turbulence as he investigated atmospheric turbulence in 1922. This cascade picture of turbulence indicates that the developed turbulence is structured by the vortices with a multifarious scale. The biggest vortex acquires energy from the mean movement to transfer the energy to a smaller vortex with a sublevel scale, whereafter the energy of this level of vortex is transferred again to a vortex with an even smaller scale, down to heat energy on the molecular scale. This is the cascade picture of turbulent energy. In 1941, Andrei Kolmogorov (1941, 1962) estimated the energy of turbulent vortex. The vortex energy $e_\lambda(\lambda)$ with scale λ equals $\rho(\varepsilon\lambda)^{2/3}$ and $\varepsilon = -d(\bar{u}^2)/dt$ is dissipation ratio of this level vortex. The energy of all levels in the system makes up of the energy spectrum $e_\lambda(\lambda)$, and the total turbulent energy in the system is namely $e = \int e_\lambda(\lambda) d\lambda$. No doubt, the turbulent intensity is a measurement of total turbulent energy of all vortices with various level scales, viz. $e = \frac{1}{2} \rho \bar{u}^2 = \int e_\lambda(\lambda) d\lambda$, because the turbulent energy in flow field is the contribution of the velocity fluctuation of vortices with multifarious scale. For the uniform isotropy turbulence without energy supply, the decay law was first extensively studied by Batchelor and Townsend (1948, 1953). The turbulence, which was nearly isotropic and homogeneous, was observed to have power-law decay in energy. The turbulent intensity is (Skrbek and Stalp, 2000)

$$\bar{u}^2 \propto (t - t^*)^{-n} \quad (2)$$

in which t is the time, t^* is a virtual origin and n is the decay exponent. This is an experimental relation of similarity. The decay law shows that the turbulent intensity of uniform isotropic turbulence without energy supply is inversely proportional to time t^n to decay until, finally, extinction. The decay exponents between $n = 6/5$ and $n = 2$ were found depending on the Reynolds number and on the size of the energy-containing eddies, i.e., behavior of the energy spectrum at low wavenumber. The decay law of an unbounded

homogeneous turbulence can be derived assuming a two-range model for the energy spectrum, $E(k) \propto Ak^2$ for small wavenumber k , followed by the Kolmogorov spectrum $E(k) \propto C\varepsilon^{2/3}k^{-5/3}$ at larger k . The total kinetic energy is $\frac{1}{2}\rho\overline{u^2} = \int_0^\infty E(k)dk$.

As early as 1900, French scholar Bénard discovered that the fluid starts the order structure, that is, up-down regular convection, when the temperature gradient reaches a definite “threshold” in the laminar fluid heated at the bottom (Bénard, 1900). This is called Bénard heat convection. Until 1916, Rayleigh (Rayleigh, 1916; Hu, 2002a) gave a theoretical explanation regarding the phenomenon of Bénard convection. If the physical parameter, Rayleigh Number

$$R_a = \frac{g\alpha d^3 \Delta T}{\tilde{\lambda} \nu} \quad (3)$$

reaches definite “threshold R_{ac} ”, the Bénard heat convection emerges. In the relation (3), α , $\tilde{\lambda}$, are the coefficient of thermal expansion and coefficient of heat conductivity, respectively, (d , ΔT , g) are the depth of laminar fluid, temperature difference and acceleration of gravity respectively. The threshold of Rayleigh number is $R_{ac} = 1700$. The convection presents itself as $R_a > R_{ac}$, thus it is sometimes also called Rayleigh-Bénard heat convection. Krishnamurti (1973) found out the transition to turbulent from Bénard convection; Swinney et al. (1978) found out that the turbulence emerges if the relative Rayleigh Number $R_c^* = R_a/R_{ac} \geq 65.4$, which makes it understood that the effect of temperature shear of fluid is also the mechanism causing the thermal turbulence. Consequently, the turbulence caused by the velocity shear is called the Reynolds turbulence, and then the turbulence caused by the temperature shear can be called Rayleigh-Bénard turbulence or the thermal turbulence. In 1922, Lewis Fry Richardson (1922) first found out the atmospheric turbulence. The atmospheric turbulence is three-dimensional, nonuniform, anisotropic, inhomogeneous, and controlled by the viscous stress and thermal stratification of the atmosphere. The three-dimensional turbulence should be described by the three velocity fluctuation components (u', v', w') in the space, so the turbulent intensity is the sum $(\overline{u'^2} + \overline{v'^2} + \overline{w'^2})$ of three velocity component variations. Both Reynolds number and Rayleigh number in the atmosphere are especially large, the Reynolds number in the atmosphere near earth surface generally reaches 10^7 , or even more; the relative Rayleigh number frequently exceeds far over its threshold $R_c^* = 65.4$ as well. The Bénard thermal turbulence is important for the atmospheric boundary layer. Hence the Reynolds turbulence and Bénard turbulence are both gained adequate development. The characteristics of atmospheric turbulence are more abundant and complex than that in the laboratory scale to offer an excellent platform for the research on the turbulent development.

The essential features of turbulence are the turbulent transport phenomena; it is the common name for processes involving transfer of mass, heat and momentum. There are two kinds of phenomena of the transport of energy and matter, i.e., the transport of molecular viscosity and the transport of turbulent viscosity. There is mature theory of molecular motion for the transport of molecular viscosity; however for the turbulent theory of the transport of

turbulent viscosity, there are still a lot of problems waiting for solving. Firstly, let us review the transient processes of molecular viscosity. Newton says that viscosity is due to molecular diffusion between layers in the fluid. A molecule leaves one layer and transfers its momentum to the adjoining layer. That transfer creates acceleration and that acceleration creates shear forces which is related to the viscosity. Newton's law of viscosity which says: When a shearing stress acts within a fluid moving in a streamlined motion, it sets up in the fluid a velocity gradient which is proportional to

$$\tau_{ij} = -\rho \tilde{\nu} \frac{\partial U_i}{\partial x_j} \quad (4)$$

where the constant, $\tilde{\nu}$, is called the coefficient of motion viscosity. Here the stress in the most basic forms, i.e., no simplifying assumptions, is a tensor. There are nine components, three normal stresses and 6 shear stresses, and for equilibrium, the six shear stresses are two groups of three that are equal, $\tau_{ij} = \tau_{ji}$.

The molecular transient processes of heat conduction (Fourier's law) described by a partial differential equation was first formulated by Jean Baptiste Joseph Fourier in 1807. Surprisingly, Fourier's work was met with resistance and would not become available to the general scientific community. Until some fifteen years later, this major contribution would be accessible to the general scientific community through publication of his classic monograph, *Théorie Analytique de la Chaleur* (Analytic Theory of Heat) (Fourier, 1822). From the formula of Fourier's law of thermal conduction, the flux of molecular thermal conduction is

$$\mathbf{J}_{qj} = -\rho \tilde{\lambda} \frac{\partial T}{\partial x_j} \quad (5)$$

$\tilde{\lambda}$ is the coefficient of thermal conductivity. Fourier's work developed to be one of the most important contributions of modern mathematical physics (Narasimhan, 1999). Fourier's method began to be applied to analyze problems in many fields besides heat transfer: electricity, chemical diffusion, fluids in porous media, genetics, and economics. Specifically, Fick (1855) were directly inspired by Fourier in formulating their equations for the diffusion of molecules in liquids (Fick's law). From Fick's law of molecular diffusion, the flux of matter transport is

$$\mathbf{J}_{nj} = -\rho \tilde{D}_n \frac{\partial c_n}{\partial x_j} \quad (6)$$

where \tilde{D}_n is the coefficient of Fick's molecular diffusion of unit mass for the n th component, c_n specific component. The form of Fourier's law and Fick's law are analogous to Newton's law, i.e., any transport flux is proportional to the gradient of relevant physical quantity. Fourier's law, Fick's law and Newton's law are three basic laws of the transport of molecular viscosity in the irreversible processes. A liquid at uniform temperature, but with a gradient in its concentration, develops a non-uniform temperature (the Dufour effect), this

was confirmed by Waldmann (1943). Thus, Fourier's law (Fourier, 1822) needs modification. If the density of a liquid is uniform, but the temperature is non-uniform, then there is a transport of matter (the Thompson effect) (Thompson, 1854) was also found, in 1856, by Ludwig. Thus, Fick's law (Fick, 1855) needs modification. The ratio of the molecular migration to the temperature gradient is called the Soret coefficient, after C. Soret, who studied the phenomenon in 1879–81. For gases, the Soret effect, under the name 'thermal diffusion', was obtained theoretically by Enskog (1911) using kinetic theory, and also by Chapman (1912). It was first observed experimentally in gas mixtures by Chapman and Dootson (1917). Streater (2000) finds that the model of statistical dynamics exhibits both the Dufour and the Soret effects, while obeying the first and second laws of thermodynamics.

In research on the turbulent transport phenomena, Reynolds introduced the random view of turbulence and proposed use of statistics to describe turbulent flows. The first major result was obtained by Prandtl (1925) in the form of a prediction of the eddy viscosity. In 1925, he developed the concept of mixing length to obtain eddy viscosity in turbulent flows. The mixing length is somewhat similar, as regards effect, to the mean free path in the kinetic theory of gases. In 1945, he modified the theory (Prandtl, 1945), which is now called the one-equation model of turbulence (Tulapurkara, 2005). Then the turbulent heat conduction obeys Fourier's law, the turbulent diffusion obeys Fick's law and the momentum transport of molecular viscosity obeys Newton's law. Both the Dufour and the Soret effects are crossed fluxes of the turbulent viscosity, two different approaches proposing the existence of turbulent crossed fluxes have been presented in the literature. In one of the approaches, which follow the thermodynamic analogy, these fluxes have been obtained for any type of flow whose energy distribution can be approximated by a Maxwell-type distribution (Sancho et al., 1995). In the other approach, based on the stochastic calculus, the effect is only present in compressible flows (Elperin et al., 1996; 1998; Sancho, 1999; 2000).

The research on turbulence should first develop the phenomenological model of turbulence, for which Kolmogorov (1941, 1962) did outstanding contribution. For the research on turbulence in atmospheric boundary layer, Monin-Obukhov (Monin et al., 1954) is the first who developed the phenomenological model of atmospheric turbulence to propose the similarity theory of atmospheric boundary layer. This theory establishes the base to develop the turbulence theory of the atmospheric boundary layer. In addition to the above phenomenological model in traditional description of the turbulence, the approximative truncation scheme in the closure theory and the statistical method were even developed, they are systematically summed up in the monographs by Monin, A. S. and Yaglom, A. M. (Monin et al., 1971; 1975). The turbulence is still a brainteaser that is difficult to understand in the classical physics. The description of multifarious characteristics of the turbulence and the explanation of its formation mechanism do not be faultlessly solved yet. The chaos theory proposed by Lorenz (Lorenz, 1963) urges to develop modern theory of the turbulent dynamics with an entirely new visual angle. The dynamic method of research on the turbulence is based on the physical concept of cascade picture of the turbulence. The theory of turbulent dynamics advances cognition of the essence of the turbulence. Bohr T. et al. (Bohr et al., 1998) systematically summarized the achievement of the turbulent dynamics in the latest 20 years to deem that the turbulence is a disorder structure, which results from the competition of endless stretch and fold of trajectory in the phase space and through development of the chaos, in the time and space. The turbulence is always developed in the chaos system with maximum freedom of motion; hence the turbulent dynamics defines refinedly the turbulence

as a chaos system that is disorder in the space starting from the concept of thermodynamic limit. The same as a system with huge degrees of freedom resulted from a great lot of molecules; a turbulent system made up of a great lot of vortexes has huge degrees of freedom. The original equation describing the turbulence should be Navier-Stokes equation. It is impractical to solve directly the Navier-Stokes equation of a fluid system with huge degrees of freedom for $R_e \gg 1$. For example, computation of flow at $R_e \approx 10^6$ requires at least 10^{14} degrees of freedom, which is more than enough to saturate the most powerful present-day computers (Chen et al., 2003). Consequently, one uses the spectrum truncation scheme of Navier-Stokes equation to decrease the degrees of freedom in the system studied. Lorenz (1963) found out the chaos phenomenon using the spectrum truncation model, and further opened up many characteristics, by which the fluid transforms from the chaos to the turbulence. The spectrum truncation model becomes a basic method of research on the turbulence. But the spectrum truncation model can generally take only 20—30 maximal modules, which result in the fact that it is difficult to reveal many characteristics of the turbulence because the immanent characteristics of fluid turbulence are lost excessively due to the oversimplified spectrum truncation model. Consequently, the shell model that can take higher than 100 modules in general; the ‘coupling lattice map’ model and ‘cellula automata’ model etc. are developed one after another in the turbulent dynamics. These modes are called the approach of dynamic system of the turbulence, they are expressly effective for research on such as the cascade property of turbulent energy, especially for constituting bridge between traditional statistic description of turbulence and dynamic behavior of phase space such as the structure function, probability distribution function, power spectrum, etc. (Bohr et al., 1998). Boltzmann equation established by the molecular dynamics is an important statistic method of research on the turbulence. Since Boltzmann equation is a differential-integral equation which results in the difficulty in its solving; hence its application to the research on turbulence is limited (Hu, 2002a). A lattice Boltzmann equation that was developed in recent years acquires tremendous success in research on the turbulence (Chen et al., 2003).

The above review about research on the turbulence illustrates history, characteristics, preponderances and limitation in the traditional research on turbulence. The traditional research on turbulence is mostly the dynamic method, viz. analytical method. The dynamic method of research on turbulence promotes the understanding of the microscopic structure and microscopic mechanism. No doubt, the turbulence is a phenomenon of the complexity. It is obligatory to study and understand this complex phenomenon from dissimilar level, especially to study from the microscopic and macroscopic levels. However, a lot of engineering problems that are closely related to people’s life are interested in the macroscopic structure and the macroscopic mechanism of the turbulence, especially as macroscopic causes of the turbulence, macroscopic transportation of the turbulence to the substance and energy. For example, the turbulence can dilute the pollution in atmosphere and the atmospheric turbulence can diffuse the contamination in atmosphere to pollute other location as well. The budget of the substance and energy in the climate system caused by macroscopic transports of the turbulence is one among the important physical processes that cause the climate change. The clear air turbulence is a fatally hidden trouble of aircraft navigation. Turbulence is expensive. By some estimates, overcoming the swirling drag that slows down submarines, boats, and airplanes costs billions of dollars annually in the United States (Dul et al., 2000). These series of the turbulent problems are all related to the macroscopic structure and mechanism of the turbulence, and the turbulent transport. Just as the above review,

original Navier-Stokes equation that describes the turbulent system is a system with huge degrees of freedom; however the nonequilibrium thermodynamics is just to study the system with galactic degrees of freedom (Prigogine, 1967). The nonequilibrium thermodynamics, which is an integrated method to hold the integrated property of the system, can deduce much new knowledge about the turbulence starting from the thermodynamic concept, and then its facticity is validated by using the experiments. Consequently, the development of the nonequilibrium thermodynamics offers a new avenue and vision to study the macroscopic structure and mechanism of the turbulence. Hu (2002a, 2002b, 2003) developed the atmospheric nonequilibrium thermodynamics and further proved the turbulent phenomenological relation, vortex theorem and turbulent intensity theorem starting from the atmospheric nonequilibrium thermodynamics (Hu, 2002c). Moreover, he proved that there exists certainly the linear phenomenological relation in the atmospheric boundary layer by using abundant data of the observed experiment in the atmospheric boundary layer (Hu, 2002d). Furthermore, a cross coupling effect between the dynamic and thermodynamic processes in the atmospheric system was proven theoretically (Hu and Zuo, 2003). This cross coupling effect results in the fact that the transport of energy and matter in the atmospheric boundary layer should include transport of energy and matter caused by the atmospheric convergent and divergent movement, in addition to the transports due to the gradient of energy and matter.

The transport of energy and matter is an important thermodynamic character in the nature, and is a basic content of the nonequilibrium thermodynamics study. The theory of nonequilibrium thermodynamics is at present one of the main tools to study the transport of energy and matter. The purpose of this article tries to prove the forms of turbulent intensity theorem and turbulent transportation of the momentum as concomitance of the Reynolds turbulence and Rayleigh-Bénard turbulence by using the atmospheric nonequilibrium thermodynamics, so as to testify coexistence of the Reynolds turbulence and the Rayleigh-Bénard turbulence in the atmospheric system and to reveal the macroscopic structure and mechanism of the turbulence. We will derivate uniformly Fourier's and Fick's law, Newton's Law and both the Dufour and the Soret effects, the cross coupling effect between the dynamic and thermodynamic processes in the atmospheric system from the atmospheric nonequilibrium thermodynamics. Furthermore, using the observed data of atmospheric field experiment validates the facticity of the above laws and turbulent intensity theorem, and further determines their phenomenological coefficient.

2. BASIC THEORY OF NONEQUILIBRIUM THERMODYNAMICS OF ATMOSPHERIC TURBULENCE

2.1. The Entropy Equilibrium Equation and the Linear Phenomenological Relations of Atmospheric System

Our analysis of classic nonequilibrium thermodynamics indicates that the dynamic processes controlled by the gravity field and the Coriolis force of earth rotation are very important for the environmental fluid of the atmosphere and marine bodies (Hu, 2002a,

2002b). The atmospheric entropy equilibrium equation of with the dynamic processes can be deduced from the principle of nonequilibrium thermodynamics as follows (Hu, 2002b, c, d):

$$\frac{\partial}{\partial t}(\rho s) = -\frac{\partial}{\partial x_j} \mathbf{J}_{sj} + \sigma + \sigma_g \quad (7)$$

in which the entropy flux \mathbf{J}_{sj} and the entropy production σ as well as the dynamic entropy production σ_g are respectively

$$\mathbf{J}_{sj} = \rho s \mathbf{U}_j + \frac{1}{\theta} \mathbf{J}_{\theta j} + \frac{\Delta\mu}{T} \mathbf{J}_{v_j} - \frac{\mathbf{U}_i}{T} \boldsymbol{\tau}_{ij} \quad (8)$$

$$\sigma = \mathbf{J}_{\theta j} \frac{\partial}{\partial x_j} \left(\frac{1}{\theta} \right) + \mathbf{J}_{v_j} \frac{\partial}{\partial x_j} \left(\frac{\Delta\mu}{T} \right) - \boldsymbol{\tau}_{ij} \frac{\partial}{\partial x_j} \left(\frac{\mathbf{U}_i}{T} \right) + \sum_{\alpha=1}^3 \omega_\alpha \lambda_\alpha \quad (9)$$

$$\sigma_g = \rho \frac{\mathbf{U}_i}{T} \left(\frac{1}{\rho} \frac{\partial p}{\partial x_j} \delta_{ij} + \mathbf{g} \delta_{i3} - f_c \mathcal{E}_{ij3} \mathbf{U}_j \right) = \rho \frac{\mathbf{U}_i}{T} \mathbf{F}_i \quad (10)$$

Moreover $\Delta\mu = \mu_d - \mu_v$ is the difference of chemical potential between the dry air and the moist air. The remainder of chemical potential $\Delta\mu$ is function of the (T, p and q)

$$\Delta\mu = \Delta c_p \left[T \ln \frac{T}{T_0} - (T - T_0) \right] - R_v T \ln q - T \Delta R \ln \frac{p}{p_0} \quad (11)$$

where θ, q, \mathbf{U}_i , and T are the atmosphere potential temperature, the specific humidity, the wind speed in the i direction and the absolute temperature respectively; p is the atmospheric pressure; $\mathbf{J}_{\theta j}, \mathbf{J}_{v_j}$ and $\boldsymbol{\tau}_{ij}$ are the heat flux, the vapor flux and the momentum flux of the turbulent transport respectively; ρ, c_p and R_v , the atmosphere density, the specific heat at the isopiestic pressure and the vapor gas constant; $\Delta c_p, \Delta R$ are the remainder of specific heat at the isopiestic pressure and gas constant between the dry air and the moist air; $\omega_\alpha, \lambda_\alpha$ are the rate and latent heat of phase change.

Each term in the entropy production (9) is the product of thermodynamic flow and thermodynamic force. The thermodynamic forces are the function of macroscopic parameter of the atmosphere system; the thermodynamic flows are the turbulent transport flux and the rate of phase change, respectively, if the molecule viscosity is neglected. Therefore the thermodynamic flows $\mathbf{J}_{\theta j}, \mathbf{J}_{v_j}, \boldsymbol{\tau}_{ij}$ and the thermodynamic forces $X_{\theta j}, X_{v_j}, X_{mij}$ of heat transport, vapor transport and momentum transport are, respectively,

$$\mathbf{J}_{\theta j} = \rho c_p \overline{\dot{\mathbf{u}}_j \theta}; \quad \mathbf{X}_{\theta j} = \frac{\partial}{\partial x_j} \left(\frac{1}{\theta} \right) \quad (12)$$

$$\mathbf{J}_{Vj} = \rho \overline{\dot{\mathbf{u}}_j q'}; \quad \mathbf{X}_{Vj} = \frac{\partial}{\partial x_j} \left(\frac{\Delta \mu}{T} \right)_{p,T} = - \frac{R_V}{q} \frac{\partial q}{\partial x_j} \quad (13)$$

$$\boldsymbol{\tau}_{ij} = \rho \overline{\dot{\mathbf{u}}_i \dot{\mathbf{u}}_j}; \quad \mathbf{X}_{mij} = \frac{\partial}{\partial x_j} \left(- \frac{\mathbf{U}_i}{T} \right) \quad (14)$$

The thermodynamic force is the driving force of irreversible processes in the nonequilibrium thermodynamics; the thermodynamic flow is the develop rate of irreversible processes. The nonequilibrium state is the character relative to the equilibrium state; the thermodynamic force and the thermodynamic flow are the characterization of measure deviating from the thermodynamic equilibrium state. The thermodynamic force is reason why the thermodynamic flow; hence we can consider that the thermodynamic flow \mathbf{J} is certain function $\mathbf{J}(\mathbf{X})$ of the thermodynamic force \mathbf{X} . Supposing this functional relation exists and tends to be continuous, the thermodynamic flow \mathbf{J} can be expanded as a Taylor function of the thermodynamic force \mathbf{X} according to the reference state, which is the equilibrium state (it is a state that both force and the flow are zero) (Groot and Mazur, 1962). For a single process, we have the Taylor function

$$\mathbf{J} = \mathbf{J}(\mathbf{X}) = \mathbf{J}_0(\mathbf{X}_0) + \left(\frac{\partial \mathbf{J}}{\partial \mathbf{X}} \right)_0 (\mathbf{X} - \mathbf{X}_0) + \frac{1}{2} \left(\frac{\partial^2 \mathbf{J}}{\partial \mathbf{X}^2} \right)_0 (\mathbf{X} - \mathbf{X}_0)^2 + \dots \quad (15)$$

Because both force and the flow are zero at the equilibrium state $\mathbf{X}_0 = 0$, $\mathbf{J}_0 = 0$, we have

$$\mathbf{J}(\mathbf{X}) = \sum_{n=1}^{\infty} \frac{1}{n!} L_n \mathbf{X}^n \quad L_n = \frac{\partial^n \mathbf{J}(\mathbf{X})}{\partial \mathbf{X}^n} \quad (16)$$

in which L_n is the Taylor coefficient. As the thermodynamic force very weak, it means the systematic state deviate equilibrium state a little. In the time, the terms of high power of \mathbf{X} in the formula (16) are far smaller than first term. Hens the high power terms can be neglected, and we have

$$\mathbf{J} = L \mathbf{X} \quad (17)$$

We can summarize also to get analogous some relations, similar to the formula (17) through direct observation of the irreversible process phenomena. These relationships are called the phenomenological relation between the thermodynamic force and the thermodynamic flow. The coefficient L of proportion is called the linear phenomenological coefficient. If the linear phenomenological coefficient is relative smaller to the

thermodynamic force, formula (17) represents that the thermodynamic force and the thermodynamic flow satisfy linear relation.

2.2. Turbulent Transport of the Atmospheric Heat and Vapor—Fourier’s Law, Fick’s Law, Dufour Effect and Soret Effect of the Atmospheric Turbulent Eddy Viscosity

Supposing only irreversible processes for the heat turbulent transportation and the vapor turbulent transportation exist in the atmosphere system, from formula (9) we can get the entropy production

$$\sigma = \mathbf{J}_{\theta j} \mathbf{X}_{\theta j} + \mathbf{J}_{Vj} \mathbf{X}_{Vj} = \mathbf{J}_{\theta j} \frac{\partial}{\partial x_j} \left(\frac{1}{\theta} \right)_p + \mathbf{J}_{Vj} \frac{\partial}{\partial x_j} \left(\frac{\Delta \mu}{T} \right)_{p,T} \quad (18)$$

If the turbulent fluxes, taken as the thermodynamic flow in the atmosphere system, are expanded as the Taylor series for the thermodynamic force, then we can find the turbulent transportation coefficient is the Taylor series of the gradient of systemic macroscopic parameter. According to the restriction of spatial symmetry of Curie’s principle (Curie, 1894), both the thermodynamic flow $\mathbf{J}_{\theta j}$ of heat and the thermodynamic flow \mathbf{J}_{Vj} of vapor are the vector. Both $\mathbf{J}_{\theta j}$ and \mathbf{J}_{Vj} satisfy not only the linear phenomenological relation, but also there are cross coupling between them. According to Onsager’s reciprocal relation principle in irreversible processes (Onsager, 1931a; b), the turbulent fluxes as the thermodynamic flow are expanded as the Taylor series for the thermodynamic force only keeping down linear term

$$\mathbf{J}_{\theta j} = L_{\theta\theta} \mathbf{X}_{\theta j} + L_{\theta V} \mathbf{X}_{Vj}, \quad \mathbf{J}_{Vj} = L_{VV} \mathbf{X}_{Vj} + L_{V\theta} \mathbf{X}_{\theta j} \quad (19)$$

Here $L_{\theta\theta}, L_{VV}, L_{\theta V} = L_{V\theta}$ are respectively defined as the phenomenological coefficient and the cross coupling phenomenological coefficient of heat and vapor. Substitute the thermodynamic force in (12) and (13) for the formula, (19), to get the turbulent flux of heat and vapor as follows:

$$\begin{array}{ll} \mathbf{J}_{\theta j} = \rho c_p \overline{w' \theta'} = -\rho c_p K_\theta \frac{\partial \theta}{\partial x_j} - \rho K_{\theta V} \frac{\partial q}{\partial x_j}, & \mathbf{J}_{Vj} = \rho \overline{w' q'} = -\rho K_V \frac{\partial q}{\partial x_j} - \rho c_p K_{V\theta} \frac{\partial \theta}{\partial x_j} \\ (I) & (II) \\ (III) & (IV) \end{array} \quad (20)$$

in which the turbulent transport coefficients of heat and vapor, K_θ and K_V , along with the turbulence coupling coefficients of them, $K_{\theta V}$ and $K_{V\theta}$, are respectively

$$K_\theta = \frac{K_{\theta\theta} - K_{V\theta} D_{\theta V}}{1 - D_{\theta V} D_{V\theta}}, \quad K_{\theta V} = \frac{K_{V\theta} D_{\theta V}}{1 - D_{\theta V} D_{V\theta}} \quad (21)$$

$$K_V = \frac{K_{VV}}{1 - D_{\theta V} D_{V\theta}}, \quad K_{V\theta} = \frac{K_{\theta\theta} D_{\theta V} - K'_{V\theta}}{1 - D_{\theta V} D_{V\theta}} \quad (22)$$

Here $K'_{V\theta}$ is

$$K'_{V\theta} = \frac{T}{\theta} \left(\Delta c_p \ln \frac{T_0}{T} - R_V \ln q - \Delta R \ln \frac{p}{p_0} - \frac{\Delta \mu}{T^2} \right) \left(L_{VV} - \frac{L_{\theta V}^2}{L_{\theta\theta}} \right) \quad (23)$$

And $K_{\theta\theta}$ and K_{VV} are, respectively,

$$K_{\theta\theta} = \frac{1}{\rho c_p \theta^2} \left(L_{\theta\theta} - \frac{L_{\theta V}^2}{L_{VV}} \right), \quad K_{VV} = \frac{R_V T}{\rho q} \left(L_{VV} - \frac{L_{\theta V}^2}{L_{\theta\theta}} \right) \quad (24)$$

The defines of the heat cross coupling coefficient $D_{V\theta}$ and the vapor cross coupling coefficient $D_{\theta V}$ are respectively

$$D_{\theta V} = \frac{L_{\theta V}}{L_{VV}}, \quad D_{V\theta} = \frac{L_{\theta V}}{L_{\theta\theta}} \quad (25)$$

When there is no cross coupling effect between heat and vapor

$$D_{\theta V} = 0, \quad D_{V\theta} = D_{\theta V} = 0 \quad (26)$$

We have

$$K_\theta = K_{\theta\theta} = \frac{1}{\rho c_p \theta^2} L_{\theta\theta}, \quad K_V = K_{VV} = \frac{R_V T}{\rho q} L_{VV}, \quad K_{V\theta} = K'_{V\theta} \quad (27)$$

Consequently, the formula (20) of the turbulent transport fluxes of heat and vapor has the following form

$$\mathbf{J}_{\theta j} = -\rho c_p K_\theta \frac{\partial \theta}{\partial x_j} \quad (28)$$

$$\mathbf{J}_{Vj} = -\rho K_V \frac{\partial q}{\partial x_j} - \rho c_p K_{V\theta} \frac{\partial \theta}{\partial x_j} \quad (29)$$

Comparing the formulae (20) with Fourier's law (5) and Fick's law (6) of the molecular viscosity, the (I),(II),(III) and (IV) terms in formulae (20) are Fourier's law of turbulent thermal conduction and Dufour effect of the crossed fluxes of the atmospheric turbulent eddy viscosity; Fick's law of turbulent eddy diffusion and Soret effect of the crossed fluxes of the

turbulent eddy viscosity, respectively. Fourier's law and Fick's law, Dufour effect and Soret effect of the atmospheric turbulence transport are deduced uniformly from the principle of atmospheric nonequilibrium thermodynamics. The formula (28) means that the vapor gradient has no influence on the heat transportation, when there is no cross coupling between the heat and the vapor. The heat turbulent flux (28) corresponds with the K turbulence closure; therefore the K turbulence closure is a special case for formula (20). But the vapor turbulent flux cannot be predigested to its brief form, similar to the formula (28), due to the entropy production formula (9) is not the immediate action of vapor specific humidity, but is the action of the gradient of chemical potential difference, $\Delta\mu$. Formula (11) shows that the chemical potential difference, $\Delta\mu$, is the function of atmospheric temperature, the pressure and the specific humidity. Therefore the potential temperature gradient still has influence to the vapor transportation. We call the coupling effect of the temperature to the vapor flux as "thermal coupling".

The coupling phenomenon between the heat turbulent transportation and the vapor turbulent transportation in the atmosphere has been discussed in research on the turbulent transport in the surface layer. The literature (Chang and Hu, 1995) shows influence between the heat turbulent flux and the vapor turbulent flux in the atmospheric surface layer. Although some results have given rise to a few controversies (Shashi et al., 1978; Chang and Hu, 1995), at present they mainly deal with the precision restrict of turbulence observations under the present technical conditions. Considering Curie principle (Curie, 1894) in the linear thermodynamics theory, the atmospheric entropy production (9) shows both the thermodynamic flow $\mathbf{J}_{\theta j}$ of heat transport and the thermodynamic flow \mathbf{J}_{Vj} of vapor transport are the vector, hence the cross coupling may exist between them.

2.3. The Turbulent Transport of Atmospheric Momentum and the Vortex Theorem

2.3.1. Linear Phenomenological Relation of the Atmospheric Momentum Transport

According to the restriction of spatial symmetry in the linear thermodynamics, i.e., the Curie's principle (Curie, 1894), the viscosity stress (including the molecular and turbulent viscosity) is a tensor. There is no cross coupling between it and the thermodynamic flows of vector type (such as heat flux or vapor flux) and scalar type (such as the rate of phase change). When the irreversible process related only with the momentum transport of viscosity stress is considered, the entropy production is

$$\sigma_m = \boldsymbol{\tau}_{ij} \mathbf{X}_{mij}, \quad \mathbf{X}_{mij} = -\frac{\partial}{\partial x_j} \left(\frac{\mathbf{U}_i}{T} \right) \quad (30)$$

Supposing the stress tensor has the symmetry character as following

$$\boldsymbol{\tau}_{ij} = \boldsymbol{\tau}_{ji} \quad (i \neq j) \quad (31)$$

Due to the viscosity stress is a tensor; the linear phenomenological relation should have following form

$$\tau_{ij} = L_{ijkl} X_{mkl} \quad (i,j,k,l=1,2,3) \quad (32)$$

The L_{ijkl} in (32) is the linear phenomenological coefficient of the momentum transport, and also a tetradic tensor with $3 \times 3 \times 3 \times 3 = 81$ components. Since the atmospheric turbulence is anisotropic, it is impossible to reduce the number of the phenomenological coefficients to two, as to the molecular viscosity. Nevertheless, it can be assumed that the momentum transport is independent with each other along different directions, and there is no cross coupling between different directions. Hence, the phenomenological coefficients will be contracted to a second-order tensor with only $3 \times 3 = 9$ components, and is represented by L_{ij} . Substitute the thermodynamic force in (30) for the formula (32) and using the definition of potential temperature, then (32) becomes the form

$$\tau_{ij} = -\rho K_{ij} \left(\frac{\partial \mathbf{U}_i}{\partial x_j} - \frac{\mathbf{U}_i}{\theta} \frac{\partial \theta}{\partial x_j} \right), \quad K_{ij} = \frac{L_{ij}}{\rho T}, \quad K_{ij} = K_{ji} \quad (33)$$

Here the turbulent coefficient of stress tensor is defined K_{ij} .

From the (33) two important conclusions can be obtained: (i) the stresses in the most basic forms, i.e. no simplifying assumptions, are second order tensors as the (33), not the scalar quantity. There are nine components, 3 normal stresses as the turbulent intensity and 6 shear stresses as the turbulent transport fluxes. Further more the 6 shear stresses have the symmetry to be 2 groups of 3 that are equal, $\tau_{ij} = \tau_{ji}$. (ii) There is also a thermal coupling effect in the turbulent transport process of momentum. In other words, the stress tensor τ_{ij} is not only related with the gradient of the velocity, but also related with the temperature gradient. This is, of course, because of that the thermodynamic force in (30), X_{mij} , in the irreversible process is related with temperature.

If the atmosphere system satisfies the condition

$$\left(\frac{1}{\theta} \frac{\partial \theta}{\partial x_j} \right) \left/ \left(\frac{1}{\mathbf{U}_i} \frac{\partial \mathbf{U}_i}{\partial x_j} \right) \right. \ll 1, \quad (34)$$

i.e., when the relative gradient of potential temperature is much smaller than that of the velocity, then the effect of thermal coupling can be neglected. Hence, (33) is simplified as the form

$$\tau_{ij} = -\rho K_{ij} \frac{\partial \mathbf{U}_i}{\partial x_j} \quad (35)$$

Comparing Newton's Law of molecular viscosity, (4), with the (35), this is Newton's Law of stresses of the turbulent eddy viscosity for atmospheric momentum transport, i.e., the traditional form of turbulent transport flux of momentum obtained through first order turbulence closure (K closure).

2.3.2. The Theorem of Turbulent Intensity and the Theorem of Turbulent Momentum Transport

If neglecting the effect of molecular viscosity, the relation of second order tensor (33) can be extended to the form of component matrix:

$$\tau_{ij} = \rho \begin{vmatrix} \bar{u^2} & \bar{uv'} & \bar{uw'} \\ \bar{vu'} & \bar{v^2} & \bar{vw'} \\ \bar{wu'} & \bar{wv'} & \bar{w^2} \end{vmatrix} = -\rho \begin{vmatrix} K_{11} \left(\frac{\partial U}{\partial x} - \frac{U}{\theta} \frac{\partial \theta}{\partial x} \right) & K_{12} \left(\frac{\partial U}{\partial y} - \frac{U}{\theta} \frac{\partial \theta}{\partial y} \right) & K_{13} \left(\frac{\partial U}{\partial z} - \frac{U}{\theta} \frac{\partial \theta}{\partial z} \right) \\ K_{21} \left(\frac{\partial V}{\partial x} - \frac{V}{\theta} \frac{\partial \theta}{\partial x} \right) & K_{22} \left(\frac{\partial V}{\partial y} - \frac{V}{\theta} \frac{\partial \theta}{\partial y} \right) & K_{23} \left(\frac{\partial V}{\partial z} - \frac{V}{\theta} \frac{\partial \theta}{\partial z} \right) \\ K_{31} \left(\frac{\partial W}{\partial x} - \frac{W}{\theta} \frac{\partial \theta}{\partial x} \right) & K_{32} \left(\frac{\partial W}{\partial y} - \frac{W}{\theta} \frac{\partial \theta}{\partial y} \right) & K_{33} \left(\frac{\partial W}{\partial z} - \frac{W}{\theta} \frac{\partial \theta}{\partial z} \right) \end{vmatrix} \quad (36)$$

where $\mathbf{U}_j = (U, V, W)$ are three components of velocity along the direction of $x_j = (x, y, z)$.

From the diagonal of the matrix (36), one obtains the turbulent intensities, respectively

$$\bar{u^2} = -K_{11} \left(\frac{\partial U}{\partial x} - \frac{U}{\theta} \frac{\partial \theta}{\partial x} \right), \quad \bar{v^2} = -K_{22} \left(\frac{\partial V}{\partial y} - \frac{V}{\theta} \frac{\partial \theta}{\partial y} \right), \quad \bar{w^2} = -K_{33} \left(\frac{\partial W}{\partial z} - \frac{W}{\theta} \frac{\partial \theta}{\partial z} \right) \quad (37)$$

or let $i=j$ in the tensor relation (33), one obtains the vector form of turbulent intensity

$$\overline{\mathbf{u}'^2} = -\mathbf{K}_{ii} \left(\nabla \cdot \vec{\mathbf{U}} - \frac{1}{\theta} \vec{\mathbf{U}} \cdot \nabla \theta \right) \quad (38)$$

This is called the theorem of turbulent intensity in the atmosphere. This theorem shows that the turbulent intensity is proportional to the summation of the velocity divergence and the scalar product of velocity and the temperature gradient. However the power-law decay of energy, (2), in the isotropic and homogeneous turbulence without energy supply indicates that the turbulent intensity is inversely proportional to time t^n to decay until extinction finally. Consequently the theorem of turbulent intensity, (38), reveals that the atmospheric turbulence roots the velocity gradient and the potential temperature gradient. And the (38) proves that the Reynolds and Rayleigh-Bénard turbulences coexist in the atmospheric system. In general, the atmosphere is assumed to be incompressible $\nabla \cdot \vec{\mathbf{U}} = 0$, and then the following important characters of the velocity variance of the atmosphere can be deduced

$$\overline{\mathbf{u}'^2} = \left(\bar{u^2} + \bar{v^2} + \bar{w^2} \right) = K_{m\theta} \frac{1}{\theta} \vec{\mathbf{U}} \cdot \nabla \theta, \quad K_{m\theta} = K_{ii} \quad (39)$$

This is the theorem of turbulent intensity of Rayleigh-Bénard turbulence. It shows that the Rayleigh-Bénard turbulence roots the potential temperature gradient. If the relative gradient of the potential temperature in the atmosphere is much smaller than that of the velocity, i.e., the condition (34) is held, the relation (38) becomes

$$\overline{\mathbf{u}'^2} = -K_{mm} \nabla \cdot \vec{\mathbf{U}}, \quad K_{mm} = K_{ii} \quad (40)$$

This is the theorem of turbulent intensity of Reynolds turbulence. It shows that the Reynolds turbulence roots the velocity gradient.

The turbulent fluctuation results in the turbulent transport of momentum, and if considering the symmetry condition of the viscose tensor of the turbulence in the (31) and (33), the covariance of the velocity of isotropic medium can be obtained, then from (36) the turbulent transport fluxes of the momentum are

$$\left. \begin{aligned} \tau_{xy} &= \rho \overline{u'v'} = \rho \overline{v'u'} = -\rho K_{xy} \left(\frac{\partial U}{\partial y} - \frac{U}{\theta} \frac{\partial \theta}{\partial y} \right), \\ \tau_{xz} &= \rho \overline{w'u'} = \rho \overline{u'w'} = -\rho K_{xz} \left(\frac{\partial U}{\partial z} - \frac{U}{\theta} \frac{\partial \theta}{\partial z} \right), \\ \tau_{yz} &= \rho \overline{w'v'} = \rho \overline{v'w'} = -\rho K_{yz} \left(\frac{\partial V}{\partial z} - \frac{V}{\theta} \frac{\partial \theta}{\partial z} \right) \end{aligned} \right\} \quad (41)$$

Here $K_{12}=K_{21}=K_{xy}$, $K_{13}=K_{31}=K_{xz}$, $K_{23}=K_{32}=K_{yz}$. The relations (41) are the formulas of the turbulent transport fluxes of the momentum along the horizontal and vertical directions deduced from the linear nonequilibrium thermodynamics, and can be called the theorem of turbulent transport of the momentum. The relations (41) show that the turbulent flux of momentum is not only related with the velocity gradient, but also related with the gradient of potential temperature. The (41) is the turbulent fluxes when the Reynolds and Rayleigh-Bénard turbulences coexist in the atmospheric system. Only when the relative gradient of the potential temperature is much smaller than that of the velocity, i.e., when the condition of (34) is held, (41) can become the well-known formula of the momentum flux of Reynolds turbulence, (42), i.e. under the condition of K closure

$$\tau_{xy} = \rho \overline{u'v'} = -\rho K_{xy} \frac{\partial U}{\partial y}, \quad \tau_{xz} = \rho \overline{w'u'} = -\rho K_{xz} \left(\frac{\partial U}{\partial z} \right), \quad \tau_{yz} = \rho \overline{w'v'} = -\rho K_{yz} \frac{\partial V}{\partial z} \quad (42)$$

The relations (37) and (41) reveal a very important fact that both the turbulent intensity and the turbulent transport flux of the momentum (generalized flow in the nonequilibrium thermodynamics) are the results of activities of shear effects (generalized force in the nonequilibrium thermodynamics) due to both the velocity and temperature gradient of the fluid field. The nonequilibrium thermodynamics deems the development of generalized flow is the result of generalized force (Prigogine, 1945, 1967; Groot et al., 1962), thus the shear effect of the speed and temperature of the fluid field is the cause of the turbulent development. Hence, it is proven from the nonequilibrium thermodynamics that both the

Reynolds and Rayleigh-Bénard turbulences coexist in the atmospheric system, and it is revealed that the macroscopic cause of the turbulence is the shear effect of velocity and temperature of the fluid field.

2.4. Vortex Theorem

The modern understanding of turbulence is that it is a collection of weakly correlated vorticity motions, which, despite their intermittent and chaotic distribution over a wide range of space and time scales, actually consist of local characteristic ‘eddy’ patterns that persist as they move around under the influences of their own and other ‘eddies’ vorticity fields (Hunt and Vassilicos, 2000). Numerical simulations and experimental observations have now identified some forms and elements of ‘life-cycles’ of some of these structures. The turbulence and vortex motion coexist and the turbulence is transition from the vortex motion. The following vortex theorem shows that the vortex results from the temperature gradient as the same of the turbulence.

Now one can deduce a vortex theorem from the nonequilibrium thermodynamics. When the gradient of relative potential temperature is big enough, the second term of (34) cannot be neglected

$$\frac{1}{U_i} \frac{\partial U_i}{\partial x_j} \sim \frac{1}{\theta} \frac{\partial \theta}{\partial x_j} \quad (43)$$

then the turbulent flux of momentum should use the form of (33). By using the symmetric condition of stress tensor (31), $\tau_{ij} = \tau_{ji}$ and the symmetry of the turbulent transport coefficient in the (33), $K_{ij} = K_{ji}$ one obtains

$$\left(\frac{\partial U_i}{\partial x_j} - \frac{U_i}{\theta} \frac{\partial \theta}{\partial x_j} \right) = \left(\frac{\partial U_j}{\partial x_i} - \frac{U_j}{\theta} \frac{\partial \theta}{\partial x_i} \right), \quad i \neq j \quad (44)$$

Or

$$\frac{\partial U_i}{\partial x_j} - \frac{\partial U_j}{\partial x_i} = \frac{1}{\theta} \left(U_i \frac{\partial \theta}{\partial x_j} - U_j \frac{\partial \theta}{\partial x_i} \right) \quad (45)$$

It can be written as the form of tensor

$$(-1)^k \varepsilon_{ijk} \frac{\partial U_i}{\partial x_j} = (-1)^k \varepsilon_{ijk} \frac{U_i}{\theta} \frac{\partial \theta}{\partial x_j} \quad (46)$$

or directly as the form of vector

$$\nabla \times \bar{\mathbf{U}} = \frac{1}{\theta} \bar{\mathbf{U}} \times \nabla \theta \quad (47)$$

The relation (46), or (47) shows that the vorticity of velocity is equal to the vector product of the velocity and the relative gradient of the potential temperature. It can be called the vortex theorem. The vortex theorem tells us that the gradient of potential temperature in the velocity field of atmosphere will form vortex motion. The vortex theorem is an approximate description of the atmospheric vortex motion in the linear region of thermodynamics.

Since

$$\nabla \times \bar{\mathbf{U}} = \begin{vmatrix} \bar{\mathbf{i}} & \bar{\mathbf{j}} & \bar{\mathbf{k}} \\ \frac{\partial}{\partial x} & \frac{\partial}{\partial y} & \frac{\partial}{\partial z} \\ U & V & W \end{vmatrix} = \left(\frac{\partial W}{\partial y} - \frac{\partial V}{\partial z} \right) \bar{\mathbf{i}} + \left(\frac{\partial U}{\partial z} - \frac{\partial W}{\partial x} \right) \bar{\mathbf{j}} + \left(\frac{\partial V}{\partial x} - \frac{\partial U}{\partial y} \right) \bar{\mathbf{k}} \quad (48)$$

However

$$\bar{\mathbf{U}} \times \nabla \theta = \begin{vmatrix} \bar{\mathbf{i}} & \bar{\mathbf{j}} & \bar{\mathbf{k}} \\ U & V & W \\ \frac{\partial \theta}{\partial x} & \frac{\partial \theta}{\partial y} & \frac{\partial \theta}{\partial z} \end{vmatrix} = \left(W \frac{\partial \theta}{\partial y} - V \frac{\partial \theta}{\partial z} \right) \bar{\mathbf{i}} + \left(V \frac{\partial \theta}{\partial z} - W \frac{\partial \theta}{\partial x} \right) \bar{\mathbf{j}} + \left(V \frac{\partial \theta}{\partial x} - U \frac{\partial \theta}{\partial y} \right) \bar{\mathbf{k}} \quad (49)$$

Let the velocity vorticity,

$$\bar{\boldsymbol{\Omega}} = \nabla \times \bar{\mathbf{U}} = (\xi, \eta, \zeta) \quad (50)$$

then the three components of the velocity vorticity

$$\xi = \frac{\partial W}{\partial y} - \frac{\partial V}{\partial z} = \frac{1}{\theta} \left(W \frac{\partial \theta}{\partial y} - V \frac{\partial \theta}{\partial z} \right) \quad (51)$$

$$\eta = \frac{\partial U}{\partial z} - \frac{\partial W}{\partial x} = \frac{1}{\theta} \left(U \frac{\partial \theta}{\partial z} - W \frac{\partial \theta}{\partial x} \right) \quad (52)$$

$$\zeta = \frac{\partial V}{\partial x} - \frac{\partial U}{\partial y} = \frac{1}{\theta} \left(V \frac{\partial \theta}{\partial x} - U \frac{\partial \theta}{\partial y} \right) \quad (53)$$

The two horizontal components of the vorticity of (51) and (52) represent the vortex motion caused by the vertical circulation in the atmosphere. It results from the horizontal gradient of the temperature and the vertical stratification. The vertical circulation is an

important circulation in the atmosphere, such as the land and sea breeze, mountain-valley wind, and land and lake breeze etc. (51) and (52) give a simple and direct mathematical description of such vertical circulation. The vertical vorticity of expression (53) describes the horizontal vortex motion. This expression shows the horizontal vortex motion formed by the horizontal gradient of the potential temperature. All the vortex motions in the atmosphere, such as cyclone, anticyclone, typhoon, tornado etc., belong to this category.

Further from the Stokes formula,

$$\iint_S (\nabla \times \vec{U}) \cdot d\vec{S} = \oint \vec{U} \cdot d\vec{r} \quad (54)$$

where $d\vec{S}$ is the vector of area element, and $d\vec{r}$ is the vector of line element, thus (47) can be written as

$$\oint \vec{U} \cdot d\vec{r} = \iint_S \frac{1}{\theta} (\vec{U} \times \nabla \theta) \cdot d\vec{S} \quad (55)$$

This is another expression of the vorticity theorem, i.e., the circulation theorem. The circulation theorem can be expressed as that the line integration of velocity should be equal to the area integration of the vector product of velocity and the relative gradient of potential temperature.

3. SIMILARITY THEORY AND DETERMINING LINEAR PHENOMENOLOGICAL COEFFICIENTS

Newton's Law, Fourier's law and Fick's law of the turbulent eddy viscosity for atmospheric transport are deduced uniformly from the principle of atmospheric nonequilibrium thermodynamics. These laws present the traditional form of turbulent transport flux of first order turbulence closure (K closure). Simultaneously the Dufour effect and Soret effect, as well as the cross coupling effect between the thermodynamic and dynamic processes of the atmospheric turbulence transport and the turbulent intensity theorem are also deduced. These laws and the theorem show that the turbulent transport coefficient is in proportion to the linear phenomenological coefficient; the properties of turbulent transport coefficient are decided entirely by the linear phenomenological coefficient. But the nonequilibrium thermodynamics cannot determine the linear phenomenological coefficients, which must be determined by the experiments. The well known relations of K turbulent closure in the atmosphere system, which are used extensively in the atmosphere, are the approximation relations to be proven by a great deal of experimental evidence as following. These experimental facts demonstrate also indirectly that the linear phenomenological relations of the atmospheric linear thermodynamics exist in the atmospheric thermodynamic system.

3.1. Coexistent Reynolds and Rayleigh-Bénard Turbulences and Monin-Obukhov Similarity Theory

The turbulent intensity theorem reveals that the atmospheric turbulence roots the velocity gradient and the potential temperature gradient, and that the Reynolds and Rayleigh-Bénard turbulences coexist in the atmospheric system. As result, the stress tensor τ_{ij} is not only related with the gradient of the velocity, but also related with the temperature gradient. From (41) the turbulent transport fluxes of the momentum along the vertical direction is

$$\tau_{xz} = \rho \overline{w' u'} = -\rho K_{xz} \left(\frac{\partial U}{\partial z} - \frac{U}{\theta} \frac{\partial \theta}{\partial z} \right) \quad (56)$$

It can write as

$$\tau_{xz} = -\rho K_m \frac{\partial U}{\partial z}, \quad K_m = K_{xz} \left(1 - \frac{U}{g} \frac{\partial U}{\partial z} R_i \right), \quad R_i = \frac{g}{\theta} \frac{\partial \theta}{\partial z} / \left(\frac{\partial U}{\partial z} \right)^2 \quad (57)$$

where K_m, R_i are the turbulent transport coefficient of momentum in the x direction and the gradient Richardson number, which is the dimensionless ratio of buoyant suppression of turbulence to shear generation of turbulence (Richardson, 1920). The (57) implies that the turbulent transport flux of momentum is in proportion to the gradient of velocity under the coexistence of Reynolds and Rayleigh-Bénard turbulences, but the turbulent transport coefficient is the function of the Richardson number describing the atmospheric stratification. The Richardson number includes the buoyant caused by the temperature gradient that generates Rayleigh-Bénard turbulence and the shear generation of turbulence that characters Reynolds turbulence. Richardson transcendently wake up to that the Reynolds and Rayleigh-Bénard turbulences coexist in the atmosphere to propose Richardson number as the criterion of development of the atmospheric turbulence. The critical Richardson number $R_c = 0.25$. The atmospheric condition is favorable for the occurrence of turbulence when $R_i < 0$ for unstable stratification, $R_i = 0$ for neutral stratification, and adverse for the occurrence of turbulence when $0 < R_c < 0.25$ for stable stratification.

Obukhov (1946) also transcendently wake up to the coexistence of Reynolds and Rayleigh-Bénard turbulences coexist in the atmosphere to propose an Obukhov Length as the criterion of development of the atmospheric turbulence. He assumed according to Buckingham's Π -theorem that the parameters $g/\bar{\theta}$, u_* friction velocity, and $H/\rho c_p$, with H (sensible heat flux), describe the atmospheric turbulence above the canopy. Here the friction velocity characters the Reynolds turbulence and the sensible heat flux characters the Rayleigh-Bénard turbulence. Only one parameter with the dimension of length is possible to describe these processes – the Obukhov Length

$$L = -\frac{u_*^3}{\kappa \frac{g}{\bar{\theta}} (\bar{\theta}' w')} \quad (58)$$

Here κ is the Kármán constant. $L < 0$ for unstable stratification, $L > 0$ for stable stratification and $L = 0$ for neutral stratification.

Further, A. S. Monin and A.M. Obukhov developed their famous similarity theory (Monin and Obukhov, 1954). According to Buckingham's Π -theorem, one can assume the dimensionless wind, temperature and humidity profiles

$$\frac{\kappa z}{u_*} \frac{\partial U}{\partial z}, \quad \frac{\kappa z}{\theta_*} \frac{\partial \theta}{\partial z}, \quad \frac{\kappa z}{q_*} \frac{\partial q}{\partial z}$$

are only a function of the parameters $g/\bar{\theta}$, u_* , $H/\rho c_p$, E/ρ , and the height z . There exists only one dimensionless length parameter z/L . In accordance with the dimensionless parameter z/L , the dimensionless wind, temperature and humidity profiles can be written with universal functions:

$$\frac{\kappa z}{u_*} \frac{\partial U}{\partial z} = \varphi_m \left(\frac{z}{L} \right), \quad \frac{\kappa z}{\theta_*} \frac{\partial \theta}{\partial z} = \varphi_\theta \left(\frac{z}{L} \right), \quad \frac{\kappa z}{q_*} \frac{\partial q}{\partial z} = \varphi_V \left(\frac{z}{L} \right) \quad (59)$$

Here the vertical momentum flux, τ_{xz} the vertical heat flux, $J_{\theta z}$ i.e. the sensible heat flux H , and the vertical vapor flux, J_{Vz} i.e. the evaporation E , are respectively

$$\tau_{xz} = -\rho K_m \frac{\partial U}{\partial z}, \quad J_{\theta z} = H = -\rho c_p K_\theta \frac{\partial \theta}{\partial z}, \quad J_{Vz} = E = -\rho K_V \frac{\partial q}{\partial z} \quad (60)$$

Their corresponding characteristic scalars are the friction velocity u_* , the dynamical temperature θ_* , and dynamical humidity q_* , are defined respectively

$$u_* = \left[\left(\overline{u'w'} \right)^2 + \left(\overline{v'w'} \right)^2 \right]^{1/4}, \quad \theta_* = -\frac{\overline{\theta'w'}}{u_*}, \quad q_* = -\frac{\overline{q'w'}}{u_*} \quad (61)$$

These universal functions in (59) are not predicted by theory and have to be determined through field experiments. Before the universal functions are determined, the Monin-Obukhov similarity theory was like a dogma and it was nearly impossible to publish in reviewed journals, and was applied. After the development of the similarity theory for the surface layer, a lot of experimental efforts were done to determine universal functions. The presently used universal functions by Businger et al. (1971) are based on the data of the 1968 KANSAS experiment (Izumi, 1971). The universal functions can be written the form

$$\varphi_m \left(\frac{z}{L} \right) = \begin{cases} \left(1 - \alpha_m \frac{z}{L} \right)^{-1/4}, & \text{for } \frac{z}{L} < 0 \\ 1 + \beta_m \frac{z}{L}, & \text{for } \frac{z}{L} > 0 \end{cases} \quad (62)$$

$$\varphi_\theta\left(\frac{z}{L}\right) = \begin{cases} a\left(1 - \alpha_\theta \frac{z}{L}\right)^{-1/2}, & \text{for } \frac{z}{L} < 0 \\ b + \beta_\theta \frac{z}{L}, & \text{for } \frac{z}{L} > 0 \end{cases} \quad (63)$$

$$\varphi_V\left(\frac{z}{L}\right) = \begin{cases} \left(1 - \alpha_V \frac{z}{L}\right)^{-1/2}, & \text{for } \frac{z}{L} < 0 \\ 1 + \beta_V \frac{z}{L}, & \text{for } \frac{z}{L} > 0 \end{cases} \quad (64)$$

In which, a , b , $\alpha_m, \alpha_\theta, \alpha_V$ and $\beta_m, \beta_\theta, \beta_V$ are experience constants determined from experiment, and distinct value for different author.

According to the similarity theory of atmospheric boundary layer and a large amount of observed data in the field experiment, a set of experimental relations of the velocity variance is obtained as follows:

$$\frac{\overline{u'^2}}{u_*^2} = \phi_{11}\left(\frac{z}{L}\right), \quad \frac{\overline{v'^2}}{u_*^2} = \phi_{22}\left(\frac{z}{L}\right), \quad \frac{\overline{w'^2}}{u_*^2} = \phi_{33}\left(\frac{z}{L}\right) \quad (65)$$

where $\phi_{ii}(z/L), (i=1,2,3)$ is Monin-Obukhov similarity function; and according to abundant observations of field experiment it has the following form:

$$\phi_{ii}\left(\frac{z}{L}\right) = C_{ii}\left(a_{ii} + b_{ii} \frac{z}{L}\right)^{\gamma_{ii}} \quad (66)$$

where $(C_{ii}, a_{ii}, b_{ii}, \gamma_{ii})$ are empirical constants, there may be different values of the empirical constants under different experimental conditions by different authors (see reference Panofsky, H. A. et al., 1983, pp160~162; Sorbjan, Z., 1989, pp70~76). A relatively consistent conclusion is that $\gamma_{33}=2/3$, then $\phi_{33} \sim (z/L)^{2/3}$; For the vertical component of the velocity variance, the average is $C_{33} \sim 1.5$ measured by different authors, that is $\phi_{33} = C_{33} \sim 1.5$ under the neutral stratification $z/L=0$. The introduction of the stability of thermal stratification of the atmospheric temperature implies that the effect of vertical shear of the temperature affects the atmospheric turbulence, i.e. the atmospheric turbulence comprises the component of Bénard thermal turbulence.

The Monin-Obukhov theory and the Richardson number provide a most successful tool in the analysis of turbulent flow in the atmospheric boundary layer. The physical sense of Richardson number in (57) is the dimensionless ratio of buoyant suppression of turbulence to shear generation of turbulence. The physical sense of Obukhov Length in (58) is the height above ground, where mechanically produced (by vertical shear) turbulence is in balance with the dissipative effect of negative buoyancy, thus where Richardson number equals to 1. Moreover the turbulent intensity theorem, (37), and the turbulent momentum transport

theorem, (41), predicate both Reynolds turbulence to be result from the velocity gradient and Rayleigh-Bénard turbulence to be result from temperature gradient coexist in the atmosphere. So, the Monin-Obukhov theory, the Richardson number and the turbulent intensity theorem are inherent coherence. Now, we can understand why the similarity theory and the Richardson number is triumphantly applied far and wide, it conceals oneself the important physical fact of coexistence of the Reynolds and Rayleigh-Bénard turbulences in the atmosphere.

3.2. Determining the Linear Phenomenological Coefficients of Atmospheric Turbulent Transports

In the above section, the phenomenological relationships of the atmospheric turbulence, (19) and (32), and the Fourier's law, Fick's law and Newton's Law of the turbulent eddy viscosity in the atmosphere, (20) and (33), are deduced from the atmospheric linear thermodynamics, but their phenomenological coefficients and the transport coefficients of turbulent eddy are not predicted by theory and have to be determined through field experiments.

The similarity relationships (59) and the universal functions should be the experiment relation. For the vertical direction, $i=j=3$ in (20) and (33), one can obtain the turbulent transport coefficients $\{K_\theta, K_V, K_m\}$ in (20) and (33) of the Fourier's law, Fick's law and Newton's Law, and corresponding linear phenomenological coefficients $\{L_\theta, L_V, L_m\}$ from the experiment relations (59) ~ (61), respectively

$$K_m = \frac{\kappa z u_*}{\varphi_m}, \quad K_\theta = \frac{\kappa z u_*}{\varphi_\theta}, \quad K_V = \frac{\kappa z u_*}{\varphi_V} \quad (67)$$

$$L_m = \rho K_m T = \rho \frac{\kappa z u_* T}{\varphi_m}, \quad L_\theta = \rho c_p K_\theta \theta^2 = \rho c_p \frac{\kappa z u_* \theta^2}{\varphi_\theta}, \quad L_V = \rho K_V \frac{q}{R_V} = \rho \frac{\kappa z u_*}{\varphi_V} \frac{q}{R_V} \quad (68)$$

The universal function, $\varphi_m, \varphi_\theta, \varphi_V$ in above relationships are determined from (62) ~ (64). These relationships show that the turbulent transport coefficient $\{K_m, K_\theta, K_V\}$ and the corresponding linear phenomenological coefficient $\{L_m, L_\theta, L_V\}$, all are the function of atmospheric stability. By all appearances, the linear phenomenological coefficients are not the constant in the atmospheric surface layer. Even though the neutral stratification $z/L=0$, $\varphi_m = \varphi_\theta = \varphi_V = 1$ they yet the function of the height z and friction velocity, u_* . (67) and (68) show that the linear phenomenological coefficients in (19) and (32) can be determined by the experiment, and the phenomenological relationships of the atmospheric turbulence, (19) and (32), are verified by the observational facts.

3.3. The Experimental Verification of the Theorem of Turbulent Intensity and the Determination of its Phenomenological Coefficients

The well-known formulae of the turbulent transport flux of the momentum have been proven by a lot of observational facts. The theorem of turbulent intensity is proven by firstly applying the atmospheric nonequilibrium thermodynamics; The theorem of turbulent intensity points out that the turbulent intensity, i.e., the turbulent kinetic energy is the function of the gradients of velocity and temperature; The theorem of turbulent intensity quantitatively describes the strength of the eddy motion or the extent of the disorder of the time and space of the eddy motion; and proves that the non-uniformity is the source of the turbulence, and reveals the macroscopic reason of the turbulent development from the viewpoint of thermodynamics. The theorem of turbulent intensity is deduced as a theoretical conclusion from the linear nonequilibrium thermodynamics, which must be verified by the observational experimental facts, and some of the phenomenological coefficients of the turbulent intensity must also be determined by observational experiment.

3.3.1. The Scheme for Experimental Verification of the Turbulent Intensity Theorem and the Materials

If experimentally the turbulent intensities $(\overline{u'^2}, \overline{v'^2}, \overline{w'^2})$ at height z in the relations (37), the corresponding velocity gradients $(\partial U / \partial x, \partial V / \partial y, \partial W / \partial z)$, the corresponding gradients of potential temperature, $(\partial \theta / \partial x, \partial \theta / \partial y, \partial \theta / \partial z)$, and the potential temperature, θ , have been observed, then the phenomenological coefficients K_{ii} ($i=1,2,3$) of the turbulent intensities can be obtained from the relations (37)

$$K_{11} = -\frac{\overline{u'^2}}{\left(\frac{\partial U}{\partial x} - \frac{U}{\theta} \frac{\partial \theta}{\partial x}\right)}, \quad K_{22} = -\frac{\overline{v'^2}}{\left(\frac{\partial V}{\partial y} - \frac{V}{\theta} \frac{\partial \theta}{\partial y}\right)}, \quad K_{33} = -\frac{\overline{w'^2}}{\left(\frac{\partial W}{\partial z} - \frac{W}{\theta} \frac{\partial \theta}{\partial z}\right)} \quad (69)$$

In order to determine the phenomenological coefficients of the turbulent intensities K_{ii} from the observed experimental data, it might be beneficial to apply the Π dimension principle of physical similarity to analyze the possible forms of K_{ii} ($i=1,2,3$). The characteristic quantity of the atmospheric velocity is the friction speed u_* ; The characteristic quantity of the length is the Monin-Obukhov length, which characterizes the stability of the thermal stratification, as shown in (58). The dimension analysis of relations (37) shows that the dimension of K_{ii} is $(m^2 \cdot s^{-1})$, and K_{ii} might be the function of the gradients of velocity and temperature; Hence, it can be defined for the dimensionless quantities that $\pi_1 = -K_{ii}/u_* L$ and $\pi_2 = \frac{L}{u_*} \left(\frac{\partial U_i}{\partial x_i} - \frac{U_i}{\theta} \frac{\partial \theta}{\partial x_i} \right)$, and according to Buckingham's Π -theorem, there is expression of similarity

$$\pi_1 = \varphi_{ii}(\pi_2), \text{ i.e. } K_{ii} = -u_* L \varphi_{ii}(\pi_2) \quad (70)$$

The related characteristic quantities u_* and L , and the specific form of the function of $\varphi_{ii}(\pi_2)$ in (70) can be determined by applying the observational experimental data of the atmospheric boundary layer. Since there are data of vertical average gradients of velocity available at present, there is no observational datum of horizontal average gradients of velocity available, the only relation that can be verified is the turbulent intensity of $\overline{w'^2}$, i.e., only K_{33} can be verified

$$K_{33} = -u_* L \varphi_{33}(\pi_2), \quad \pi_2 = \frac{L}{u_*} \left(\frac{\partial W}{\partial z} - \frac{W}{\theta} \frac{\partial \theta}{\partial z} \right) \quad (71)$$

By applying the above Monin-Obukhov similarity relation (59) of the surface layer and the Businger-dyer relation (Businger et al., 1971), the characteristic quantities u_* and L required in relationship (71) are calculated

$$u_* = \frac{\kappa(z-d)}{\varphi_m} \frac{\partial U}{\partial z} \quad (72)$$

$$\frac{z}{L} = \begin{cases} 1.0R_i & R_i < 0, \\ R_i/(1.0 - 5.0R_i) & R_i > 0. \end{cases} \quad R_i = \frac{g \partial \theta / \partial z}{\theta (\partial u / \partial z)^2} \quad (73)$$

where Kármán constant $\kappa = 0.40$, the parameters in which use the result by Businger et al (Businger et al, 1971), as $\alpha_M = 19.3, \beta_M = 6.0$ in (62). By applying the observational data of turbulent experiment of the surface layer in 1986 provided by Prof. Högström of Uppsala University, the phenomenological coefficient of turbulent intensity (69) is determined, and detail of the experimental data is described in detail in the reference (Högström, 1988).

3.3.2. The Properties of the Turbulent Intensity $\overline{w'^2}$ and Its Phenomenological Coefficient K_{33}

The normalized data are separately handled as stable, neutral and unstable stratifications, according to $z/L > 0.01, -0.01 \leq z/L \leq 0.01$, and $z/L < -0.01$, and φ_{33} is made diagrams as a function of π_2 . Figures 1(a) and (b) are the results of unstable and stable stratifications. The function φ_{33} is divided by the axes of the coordinate as two branches, located in the first and third quadrants, respectively; while when $\pi_2 \rightarrow 0, \varphi_{33} \rightarrow \pm\infty, \pi_2 \rightarrow \pm\infty, \varphi_{33} \rightarrow 0$; And the signs of π_2 and φ_{33} are the same.

It is assessed that this is a set of equiaxial hyperbolas, i.e., let $x = \pi_2$ and $y = \varphi_{33}(\pi_2) = -K_{33}/u_* L$, then $xy = C$ (constant), thus,

$$\varphi_{33}\pi_2 = C, \quad \text{i.e.,} \quad \varphi_{33} = C\pi_2^{-1} = C \left[\frac{L}{u_*} \left(\frac{\partial W}{\partial z} - \frac{W}{\theta} \frac{\partial \theta}{\partial z} \right) \right]^{-1} \quad (74)$$

where the constant C is a parameter of the function of hyperbola type, which is also a dimensionless parameter. Hence, the curve fit of the hyperbola type function of φ_{33} and $\pi_2 = \frac{L}{u_*} \left(\frac{\partial W}{\partial z} - \frac{W}{\theta} \frac{\partial \theta}{\partial z} \right)$, as well as the value of parameter C of the hyperbola type function are shown in figures; at the same time, the correlative coefficient R of the curve fit and the residual error S are also listed. The results of the two diagrams show that there is high correlation for the curve fits, the correlative coefficients of which can reach 0.93 and 0.99.

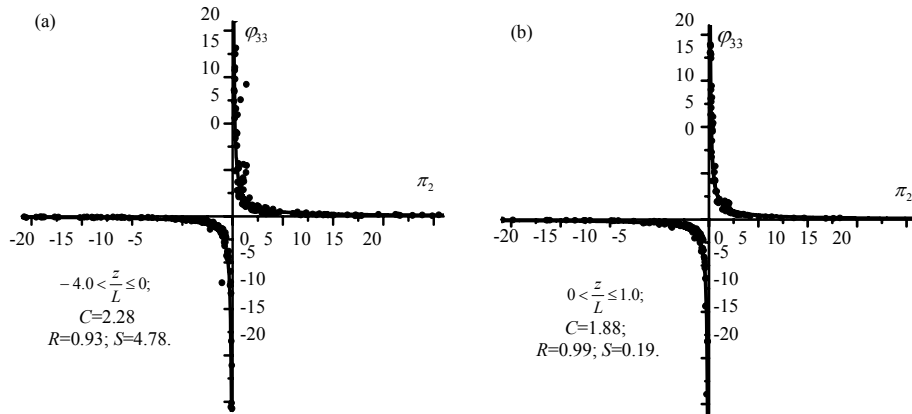


Figure 1. Function relation $\varphi_{33} = -\frac{K_{33}}{u_* L}$ vs. $\pi_2 = \frac{L}{u_*} \left(\frac{\partial W}{\partial z} - \frac{W}{\theta} \frac{\partial \theta}{\partial z} \right)$ (a) unstable stratification; (b) stable stratification.

The results show that the parameter C of the hyperbola function is a function of the stability of the thermal stratification, and it is predicted that the dimensionless parameter C might be a function of the Monin-Obukhov parameter z/L of the atmospheric stability, i.e.,

$$C = \phi\left(\frac{z}{L}\right), \text{ then } \varphi_{33} = \phi\left(\frac{z}{L}\right) \left[\frac{L}{u_*} \left(\frac{\partial W}{\partial z} - \frac{W}{\theta} \frac{\partial \theta}{\partial z} \right) \right]^{-1} \quad (75)$$

Such relation shows that the similarity function of the phenomenological coefficient of the turbulent intensity φ_{33} is not only a function of the velocity shear, but also a function of stability of the thermal stratification of the atmospheric temperature. From the similarity function of the phenomenological coefficient of the turbulent intensity φ_{33} (75), and relation (71), the expression of the phenomenological coefficient of the turbulent intensity K_{33} is

$$K_{33} = -u_*^2 \phi\left(\frac{z}{L}\right) \left[\left(\frac{\partial W}{\partial z} - \frac{W}{\theta} \frac{\partial \theta}{\partial z} \right) \right]^{-1} \quad (76)$$

On the other hand, substitute the above expression (76) of the phenomenological coefficient of the turbulent intensity, K_{33} , for the formula (37) of calculating the turbulent intensity, one obtains the relationship

$$\frac{\overline{w'^2}}{u_*^2} = C = \phi\left(\frac{z}{L}\right) \quad (77)$$

The relationship (77) is totally consistent with the similarity relation (65) of the velocity variance. It should be noted that the relation (65) is obtained as an empirical relation from the Monin-Obukhov similarity theory of the atmospheric boundary layer and a lot of field observational experiment; while the relation (77) is obtained from the theoretical relations (37) of the theorem of the turbulent intensity, which is proven by the nonequilibrium thermodynamics. Such a consistency means that the truth of the theorem of the turbulent intensity is proven by the facts of observational experiments; on the contrary, the Monin-Obukhov empirical relation of the velocity variance is theoretically and indirectly proved by the nonequilibrium thermodynamics. Hence, relation (77) is the similarity relation of the turbulent intensity, and $\phi(z/L)$ is the similarity function of the turbulent intensity.

The relations (75) ~ (77) show that as long as the form of the similarity function of the turbulent intensity $\phi(z/L)$ is determined, the similarity function of the phenomenological coefficient, φ_{33} , the phenomenological coefficient, K_{33} , and the turbulent intensity $\overline{w'^2}$ can be resolved.

3.3.3. The Form of the Similarity Function, $\phi(z/L)$, of the Turbulent Intensity

The specific form of the similarity function of the turbulent intensity $\phi(z/L)$ can further be determined by the similarity function of the phenomenological coefficient of the turbulent intensity determined by the above calculation. From the relation (77) and (37) the similarity function of the turbulent intensity is obtained as

$$\phi\left(\frac{z}{L}\right) = \varphi_{33} \frac{L}{u_*} \left(\frac{\partial W}{\partial z} - \frac{W}{\theta} \frac{\partial \theta}{\partial z} \right), \quad \varphi_{33} = -\frac{K_{33}}{u_* L} \quad (78)$$

The figure is drawn for ϕ of (78) as the function of z/L in Figure 2, which is obtained from the selected data. Finally, under the conditions of instable stratification ($-3 \leq z/L < -0.01$), near neutral stratification ($-0.01 \leq z/L \leq 0.01$), and stable stratification ($0.01 < z/L \leq 1$), the curve forms of the similarity functions of the turbulent intensity $\phi(z/L)$ are fitted as

$$\phi\left(\frac{z}{L}\right) = \begin{cases} 1.35 \left(1 - 1.9 \frac{z}{L}\right)^{2/3}, & -3 \leq \frac{z}{L} < -0.01 \\ 1.3, & -0.01 \leq \frac{z}{L} \leq 0.01 \\ 1.8 + \left(8.1 \frac{z}{L}\right)^{5/2}, & 0.01 < \frac{z}{L} \leq 1 \end{cases} \quad (79)$$

The result shows that the similarity function $\phi(z/L)$ of the turbulent intensity obtained has the similar form as the form, (66), of velocity variance. That is for the instable stratification

the similarity function $\phi \sim (z/L)^{2/3}$, for the near neutral stratification the similarity function is constant $\phi \sim 1.3$; while for the stable stratification situation is rather complicated $\phi \sim (z/L)^{5/2}$. The correlative coefficient R of the curve fit of the similarity function $\phi(z/L)$ of the turbulent intensity and residual error S are also listed in Figure 2.

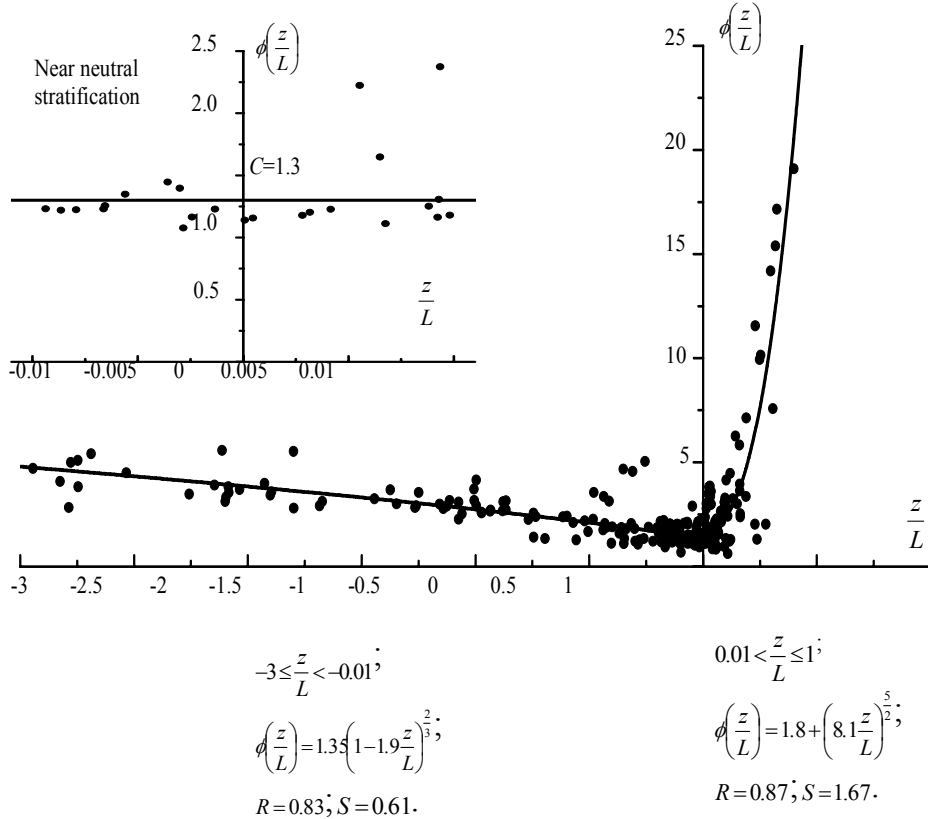


Figure 2. Function $\phi\left(\frac{z}{L}\right)$ vs. $\frac{z}{L}$.

3.3.4. The Verification of the Theorem of Turbulent Intensity

The practically measured velocity variance $\overline{w'^2}$ is compared with the turbulent intensity $\overline{w_c'^2}$, which is calculated by applying the similarity function of the turbulent intensity $\phi(z/L)$ (79) and the similarity relation (77), thus it is convenient to verify the trustiness and truth of the result of the phenomenological coefficient K_{33} of the turbulent intensity, that the theorem of turbulent intensity is proven by field observational experiments. Substitute relation (79) for relation (77), one obtains the formula to calculate the turbulent intensity from the theorem of turbulent intensity of nonequilibrium thermodynamics.

$$\overline{w'_c}^2 = \begin{cases} 1.35u_*^3 \left(1 - 1.9 \frac{z}{L}\right)^{\frac{2}{3}}, & -3 \leq \frac{z}{L} < -0.01; \\ 1.3u_*^3, & -0.01 < \frac{z}{L} \leq 0.01; \\ \left[1.8 + \left(8.1 \frac{z}{L}\right)^{\frac{5}{2}}\right] u_*^3, & 0.01 \leq \frac{z}{L} \leq 1. \end{cases} \quad (80)$$

Figure 3 shows the comparison between the practically measured velocity variance $\overline{w'^2}$ and the turbulent intensity $\overline{w'_c}^2$ calculated from the theorem of the turbulent intensity, in which Figures a, b, c represent the situations under the conditions of instable stratification ($-3 \leq z/L < -0.01$), stable stratification ($0.01 < z/L \leq 1$) and near neutral stratification respectively ($-0.01 \leq z/L \leq 0.01$). In the figures D represents the slope fitted from the data, which characterizes the extent of departure of the calculated turbulent intensity $\overline{w'_c}^2$ from the measure one $\overline{w'^2}$; R and S represent the correlative coefficient of the curve fit and the data, and the residual error. The result shows that there is quite good consistency between the calculated turbulent intensity $\overline{w'_c}^2$ and the measured one $\overline{w'^2}$, under the conditions of instable stratification and near neutral stratification the slope and correlative coefficient reach $D=1.01$, $R=0.92$ and $D=1.03$, $R=0.96$, respectively. Thus the truth of the turbulent intensity theorem is verified by the observational data.

3.3.5. Understanding of the Turbulence from the Theory of Linear Nonequilibrium Thermodynamics of the Atmosphere

The turbulence is still a puzzle hard to understand in the classic physics, the forming mechanism of which is still not perfectly resolved yet. The traditional theory of turbulence proves that in natural fluid there are Reynolds turbulence produced by the velocity shear, and Rayleigh-Bénard turbulence produced by temperature shear, these are two different kinds of turbulences. The modern turbulent dynamic theory developed by the modern chaotic theory teems that the turbulence is a chaotic structure of time and space produced through the development of chaos due to the competition of the uninterrupted stretches and folds of the trajectory of the phase space in the chaotic system with extremely large number of freedom. In essence, the nonequilibrium thermodynamics studies the system with extremely large number of freedom, here the Reynolds and Rayleigh-Bénard turbulences are united described in the theorems of the momentum transport and the turbulent intensity by applying the theory of linear nonequilibrium thermodynamics of the atmosphere, and it is proven that the Reynolds and Rayleigh-Bénard turbulences coexist in the atmospheric system. It is considered that the macroscopic cause of the turbulent development is the result of both the effects of the velocity shear and the temperature shear; the effects of velocity shear and temperature shear are also the macroscopic cause of the uninterrupted stretches and folds of the trajectory of the phase space. Further, the truth of the theorem of the turbulent intensity is proven by the field observational experimental data, and it is proven that the phenomenological coefficient of the turbulent intensity is not only the function of velocity

shear, but also the function of the atmospheric thermal stratification. Hence, the observational experimental facts prove that the macroscopic cause of the turbulent development is the result of both the effects of velocity shear and the temperature shear, which is the conclusion of the theory of linear nonequilibrium thermodynamics of the atmosphere.

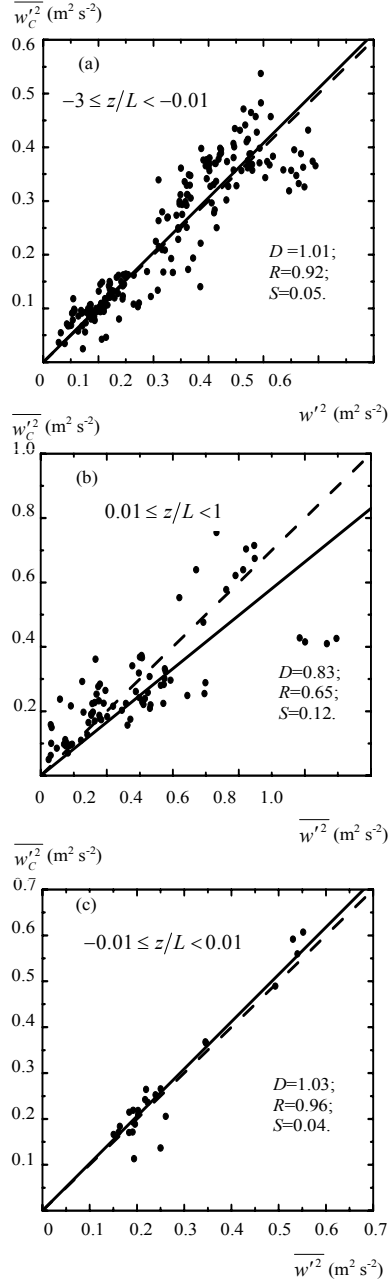


Figure 3. Comparison of turbulent intensity $\overline{w'_C}^2$ calculated by the turbulent intensity with observed turbulent intensity $\overline{w'}^2$

4. THE CROSS COUPLING BETWEEN THE THERMODYNAMIC AND DYNAMIC PROCESSES

4.1. The Principle of Cross Coupling of the Thermodynamic and Dynamic Processes

The entropy equilibrium equation of atmosphere, (7) ~ (10), in which the term of dynamic entropy production, σ_g , is introduced, is different from the traditional entropy equilibrium equation of nonequilibrium thermodynamics. Here, the dynamic entropy production is the work done by the Newton's force \mathbf{F}_i to the air micelle divided by temperature. This term is the contribution of the work by the driving force of airflow transport \mathbf{F}_i to the local entropy change of the system. In the nonequilibrium thermodynamics, both the turbulent heat flux $\mathbf{J}_{\theta j}$ and the airflow $\rho \mathbf{U}_i$ are called generalized flows, and the driving force of the generalized flow is called generalized force. In the atmospheric system, the gradient of temperature drives the heat turbulent flux, and the Newton's force drives the airflow. The generalized force $\mathbf{X}_{\theta j}$ of the turbulent flux of the heat, the generalized force \mathbf{X}_{Vj} of the turbulent flux of the vapor, and the generalized force \mathbf{X}_{gi} of the airflow are,

$$\mathbf{X}_{\theta j} = \frac{\partial}{\partial \mathbf{x}_j} \left(\frac{1}{\theta} \right), \quad \mathbf{X}_{Vj} = \frac{\partial}{\partial \mathbf{x}_j} \left(\frac{\Delta \mu}{T} \right) \quad (81)$$

$$\mathbf{X}_{gi} = \frac{1}{T} \left(\frac{1}{\rho} \frac{\partial p}{\partial \mathbf{x}_j} \delta_{ij} + g \delta_{ij} - f_c \varepsilon_{ij3} \mathbf{U}_j \right) \quad (82)$$

respectively. Relation (82) pointed out that the generalized force of the airflow is composed of three parts, the force of air pressure gradient, gravity, and the Coriolis force. Since both the heat flux and the airflow are vectors, according to the Curie-Prigogine principle of linear thermodynamics (Curie, 1894; Prigogine, 1967), there is cross coupling between them. By considering the Onsager reciprocal relation (Onsager, 1931a and b), the relation of linear thermodynamics between the heat flux and the airflow is as follows

$$\mathbf{J}_{\theta j} = L_{\theta j} \frac{\partial}{\partial \mathbf{x}_j} \left(\frac{1}{\theta} \right) + L_{\theta aj} \frac{1}{T} \left(\frac{1}{\rho} \frac{\partial p}{\partial \mathbf{x}_j} \delta_{ij} + g \delta_{ij} - f_c \varepsilon_{ij3} \mathbf{U}_j \right) \quad (83)$$

$$\rho \mathbf{U}_i = L_{aj} \frac{1}{T} \left(\frac{1}{\rho} \frac{\partial p}{\partial \mathbf{x}_j} \delta_{ij} + g \delta_{ij} - f_c \varepsilon_{ij3} \mathbf{U}_j \right) + L_{\theta aj} \frac{\partial}{\partial \mathbf{x}_j} \left(\frac{1}{\theta} \right) \delta_{ij} \varepsilon_{ij3} \quad (84)$$

In the above relations, $(L_{\theta j}, L_{aj}, L_{\theta aj})$, are defined as the thermodynamic phenomenological coefficient, the dynamic phenomenological coefficient, and corresponding cross coupling coefficient, respectively. The relation (83) shows that in addition to the gradient of potential temperature, any force of air pressure gradient, gravity, and Coriolis force all affect the heat flux of the turbulent transport. This means that the heat flux of the turbulent transport is not

only related with the potential temperature, but also related with the force of air pressure gradient, gravity and the Coriolis force, due to the existence of the cross coupling between the thermodynamic and dynamic processes. In addition, the relation (84) shows that the gradient of potential temperature also produces airflow. The geostrophic wind is namely resulting from the vertical temperature gradient of the atmosphere. The relations (83) and (84) can be called the principle of cross coupling between the thermodynamic and dynamic processes.

The following is mainly to discuss the cross coupling phenomenon of the airflow and the vertical heat flux of the turbulent transport. The left side of relation (84) is the airflow; its vertical component can be written as the following form,

$$\rho W = L_g \frac{1}{T} \left(\frac{1}{\rho} \frac{\partial p}{\partial z} + g \right) - L_{\theta p} \frac{1}{\theta^2} \frac{\partial \theta}{\partial z} \quad (85)$$

where W is the average vertical velocity; L_g and $L_{\theta p}$ are corresponding phenomenological coefficient and the cross coupling coefficient, respectively. Relation (85) proves that any departure from the static equilibrium $(1/\rho)\partial p/\partial z + g \neq 0$ or from the neutral stratification $\partial \theta/\partial z \neq 0$ will create a vertical velocity. On the other hand, to assume the atmosphere is an incompressible fluid, and then its continuity equation is

$$\frac{\partial U}{\partial x} + \frac{\partial V}{\partial y} + \frac{\partial W}{\partial z} = 0 \quad (86)$$

The vertical component of relation (83) can be written as,

$$J_{\theta z} = H|_z = \rho c_p \overline{w' \theta'} = -\rho c_p K'_{\theta 3} \frac{\partial \theta}{\partial z} + L_{\theta a 3} \frac{1}{T} \left(\frac{1}{\rho} \frac{\partial p}{\partial z} + g \right), \quad K'_{\theta 3} = \frac{L_{\theta 3}}{\rho c_p \theta^2} \quad (87)$$

where the turbulent transport coefficient K'_{θ} is the linear function of phenomenological coefficient L_{θ} . In the following, the subscripts $j=3$ of the turbulent transport coefficient and phenomenological coefficient in the vertical direction are omitted. By using relation (85), the second term of the right side of relation (87) can be eliminated

$$J_{\theta z} = H|_z = \rho c_p \overline{w' \theta'} = -\rho c_p K'_{\theta} \frac{\partial \theta}{\partial z} + \rho \frac{L_{\theta a}}{L_g} W + \frac{L_{\theta p}}{L_g} \frac{1}{\theta^2} \frac{\partial \theta}{\partial z} \quad (88)$$

By using the continuity equation (86) and vertical velocity of relation (85), the vertical component of the heat flux of turbulent transport is

$$\left. \begin{aligned} J_{\theta z} &= H|_z = \rho c_p \overline{w' \theta'} = -\rho c_p K_{\theta} \frac{\partial \theta}{\partial z} - \rho c_p K_{\theta w} W \\ W &= \int_0^z (\nabla|_h \cdot \vec{V}) dz, \quad \nabla|_h \cdot \vec{V} = \frac{\partial U}{\partial x} + \frac{\partial V}{\partial y} \end{aligned} \right\} \quad (89)$$

Here, the coefficient of vertical turbulent transport of the heat K_θ caused by the gradient of the potential temperature and the corresponding cross coupling coefficient $K_{\theta W}$ are defined as,

$$K_\theta = \left(L_\theta - \frac{L_{\theta a} L_{\theta p}}{L_g} \right) \frac{1}{\rho c_p \theta^2}, \quad K_{\theta W} = \frac{L_{\theta a}}{c_p L_g} \quad (90)$$

respectively. In formula (89), $J_{\theta z}$ is the vertical component of the turbulent transport flux of the heat; $H|z$ is the vertical component of the turbulent transport flux at height z ; w' is the fluctuate of vertical velocity; and θ' is the fluctuate of potential temperature. The relation (89) of heat flux of vertical turbulent transport concludes that the vertical heat flux of turbulence is composed of two parts, the transport of vertical gradient of potential temperature and the transport of vertical velocity or the transport of the horizontal velocity divergent. This is the cross coupling principle between the vertical velocity and the vertical turbulent transport of the heat.

Similarly, the flux of vapor is also a vector, and according to Curie-Prigogine principle of the linear thermodynamics, there should also be cross coupling between the vapor flux and the airflow, and for the vapor transport the cross coupling relation,

$$\mathbf{J}_{Vj} = L_V \frac{\partial}{\partial x_j} \left(\frac{\Delta \mu}{T} \right) + L_{Va} \frac{1}{T} \left(\frac{1}{\rho} \frac{\partial p}{\partial x_j} \delta_{ij} + g \delta_{i3} - f_c \varepsilon_{ij3} \mathbf{U}_j \right) \quad (91)$$

where L_V , L_{aV} and L_{Va} are the phenomenological coefficient of vapor turbulent transport and its corresponding phenomenological coefficients of cross coupling. Relation (91) shows that the gradient of difference of the chemical potentials of dry air and vapor, and any gradient force of air pressure, gravity and Coriolis force, all will also produce the vapor flux of turbulent transport. From (13), $\partial(\Delta \mu/T)_{p,T}/\partial x_j = -(R_v/q)(\partial q/\partial x_j)$, the gradient of difference of the chemical potentials of dry air and vapor equals the gradient of atmospheric specific humidity. This means that the vapor flux of the turbulent transport is not only related with the vapor gradient, but also related with the force of pressure gradient, gravity and the Coriolis force, due to the existence of the cross coupling of the thermodynamic and dynamic processes. Similar to the deduction of relation (89), by considering the relation of vertical velocity (85) and the equation of continuity of the incompressible fluid (86), the vertical component of the flux vapor of turbulent transport is deduced from relation (91) as

$$\left. \begin{aligned} J_{Vz} &= E|z = \rho \overline{w'q'} = -\rho K_V \frac{\partial q}{\partial z} - \rho K_{VW} W, \\ W &= \int_0^z (\nabla|_h \cdot \bar{V}) dz, \quad \nabla|_h \cdot \bar{V} = \frac{\partial U}{\partial x} + \frac{\partial V}{\partial y} \end{aligned} \right\} \quad (92)$$

$$K_V = \left(L_V + \frac{L_{Va} L_{pV}}{L_g} \right) \frac{1}{\theta^2}; \quad K_{VW} = \frac{L_{Va}}{L_g} \quad (93)$$

The relation (92) of the vapor flux of turbulent transport concludes that the vertical component of the vapor flux of turbulent transport is also composed of two parts, i.e., the turbulent transport of vertical vapor gradient and the vertical velocity transport or the divergent transport of horizontal velocity. This is the principle of cross coupling between the transport of vertical velocity and the vertical turbulent transport of the vapor.

The turbulent transport is the thermodynamically irreversible transport processes of matter and energy, i.e., thermodynamic processes; the airflow is dynamically reversible transport processes of matter and energy. The traditional theory of turbulent transport deems that any turbulent transport of macroscopic quantity is proportional to the gradient of this macroscopic quantity. While, the principle of cross coupling between the vertical velocity and the vertical turbulent transport proves that the airflow also produces coupling effect to the turbulent transport, the turbulent transport has the component proportional to the gradient of the macroscopic quantity, and has the component of the additional coupling effect of the airflow, as well. Expression (89) and (92) show that for the fluxes of heat and vapor of the heterogeneous underlying surface, in addition to the well-known turbulent flux, there is vertical turbulent transport of heat and vapor caused by the divergence or convergence of the flow field. The convergence or divergence of the flow field is the dynamically reversible processes, while the transport of turbulent flux is the thermodynamically irreversible processes. Hence, the above fact proves the cross coupling effect between the thermodynamic and dynamic processes from the theory of nonequilibrium thermodynamics.

4.2. The Experimental Verification of the Cross Coupling of the Thermodynamic and Dynamic Processes and the Determination of its Coefficient of Cross Coupling

The coupling effect caused by the airflow on the turbulent transport in the cross coupling of the thermodynamic and dynamic processes proven in the above section is first proven by the theory of the nonequilibrium thermodynamics, and must be proven further by the observational facts, as well as the coupling coefficient of the cross coupling between the airflow and turbulent transport must also be determined by the observational experiments.

4.2.1. The Method of Experimental Verification and the Determination of the Coupling Coefficient

The relations (89) and (92) of the vertical turbulent fluxes of the heat and vapor are obtained as a theoretical conclusion deduced from the linear nonequilibrium thermodynamics, which has to be proven by the observational experimental facts; and the coefficients of turbulent transport and the coefficients of cross coupling have to be determined by observational experiment in order to realize the practical application.

Now, the vertical turbulent transport of the heat is taken as example, to prove the principle of cross coupling of the thermodynamic and dynamic processes by the observational facts. In the relation (89), if all the vertical component of the turbulent flux of heat

$H|^z = \rho c_p \overline{w' \theta'}$, the temperature gradient $\partial \theta / \partial z$ and the average vertical velocity $W|_z$ at the height z , are observed from the experiment; then according to the classic theory of the atmospheric boundary layer, the coefficient of turbulent transport K_θ can be determined, thus the coupling coefficient of vertical velocity $K_{\theta w}$ can be obtained from the experiment as

$$K_{\theta w} = \frac{\overline{H|^z} + \rho c_p K_\theta \partial \theta / \partial z}{\rho c_p W|_z} = \frac{\overline{w' \theta'} + K_\theta \partial \theta / \partial z}{W|_z} \quad (94)$$

In order to determine the coupling coefficient of the vertical velocity $K_{\theta w}$ from the observational data, first the possible forms of $K_{\theta w}$ are analyzed by applying the Π dimension principle of the physical similarity. The analysis to the dimension of relation (89) shows that $K_{\theta w}$ holds the dimension of temperature (K), hence it is assumed that a parameter T_{w0} with temperature dimension (K) as the characterized quantity of temperature; By considering that the vertical velocity W is an important parameter of the cross coupling between the vertical velocity and the vertical turbulent transport of heat, then the friction velocity characterizing the property of the turbulent momentum might be the characteristic quantity of velocity of the airflow coupling; it is considered that the ground surface as a boundary also affects the $K_{\theta w}$, and cannot be neglected, i.e., $K_{\theta w}$ might be related with height z , thus there is a coupling roughness z_{w0} , characterizing the property of the underlying surface. According to the Π dimension principle, the dimensionless quantities can be defined as $\pi_1 = K_{wT} / T_{w0}$, $\pi_2 = z / z_{w0}$ and $\pi_3 = W / u_*$, then $\pi_1 = \phi(\pi_2, \pi_3)$, i.e., the dimensionless similarity expression can be obtained as

$$K_{\theta w} = T_{w0} \phi \left(\frac{z}{z_{w0}}, \frac{W}{u_*} \right) \quad (95)$$

The expression (95) might be the similarity relation of the coupling coefficient of the vertical velocity and the characteristic quantities of the atmospheric boundary layer, and the related characteristic quantities u_*, T_{w0}, z_{w0} and the specific forms of functions of the relation (95) can be determined by applying the experiment data of the atmospheric boundary layer.

4.2.2. The Method and Materials Determining the Coupling Coefficient

In order to determine the coupling coefficient of the vertical velocity from relation (95) by applying the experimental data, the observational data at height z include not only the vertical component of the turbulent flux of heat, the temperature gradient, and the average vertical velocity, but also are required a high accuracy. Hence, the experimental data of the turbulence of surface layer in 1986 provided by Högström (1988) of Uppsala University are chosen. The detail of the experimental data is described in detail in the reference (Högström, 1988). The observational data include the turbulent fluctuation of three level wind velocities,

temperature, humidity, and the vertical velocity; six level average wind velocities, temperature, and humidity. The wind velocity error by the tunnel calibration is within 0.05m/s; the accuracy of temperature gradient from the laboratory calibration is 0.01°C , the predicted error of field observation is not larger than 0.02°C; In case the average wind velocity is larger than 3m/s, the relative error of turbulent wind velocity is within 2%-3%. These data provide all the parameters required in this study, and with qualified accuracy, satisfy basic requirement of this study.

In order to estimate the coupling coefficient $K_{\theta W}$ of the vertical velocity from relation (95), first according to the classic Monin-Obukhov similarity theory of surface layer, from the (59) and (60) one can obtain the formula to calculate the vertical turbulent transport coefficient of the heat, K_θ

$$K_\theta = \frac{\kappa^2(z-d)^2}{\varphi_m \varphi_\theta} \frac{\partial U}{\partial z} \quad (96)$$

Where, $\varphi_m, \varphi_\theta$ are calculated by the Businger-Dyer similarity relation, (62) and (63), in which Kármán constants $\kappa = 0.41$, parameters $a=b=0.95$, $\alpha_m = 19.3, \beta_m = 6.0$, $\alpha_\theta = 11.6, \beta_\theta = 7.8$; the parameter of atmospheric stability z/L is calculated by the (73); the friction velocity, u_* , is calculated by the (72). The roughness $z_0=0.01$ m and the formula of displacement height $d=0.75h$ are used, respectively, where h is the height of the plant cover.

Finally, all the data are normalized according to the relation of (95), and further the relations of all the normalized quantities are analyzed, thus the form and property of the specific function of the coupling coefficient $K_{\theta W}$ of the vertical speed are analyzed

4.2.3. The Properties of the Coupling Coefficient of the Vertical Velocity

It is discovered from the preliminary analysis to the normalized data that when $|W/u_*| \rightarrow 1$, $z/z_{w0} \rightarrow 1$ and $K_{\theta W}/T_{w0} \rightarrow 0$; and for the two situations of $W>0$ and $W<0$, there will be upper and lower branches at $|W/u_*|=1$. According to these properties, it is predicted that the coupling coefficient of the vertical velocity $K_{\theta W}$ should have the following characters

$$K_{\theta W} = T_W \left[\ln \left(\frac{W}{u_*} \right)^2 \right]^\beta \quad (97)$$

$$T_W = T_{w0} \ln \left(\frac{z}{z_{w0}} \right)^\alpha \quad (98)$$

The $K_{\theta W}$ of relation (95) is obtained from the normalized data as the function of $\ln(W/u_*)^2$ and $\ln(z/z_{w0})$, as well as is shown in Figure 4.

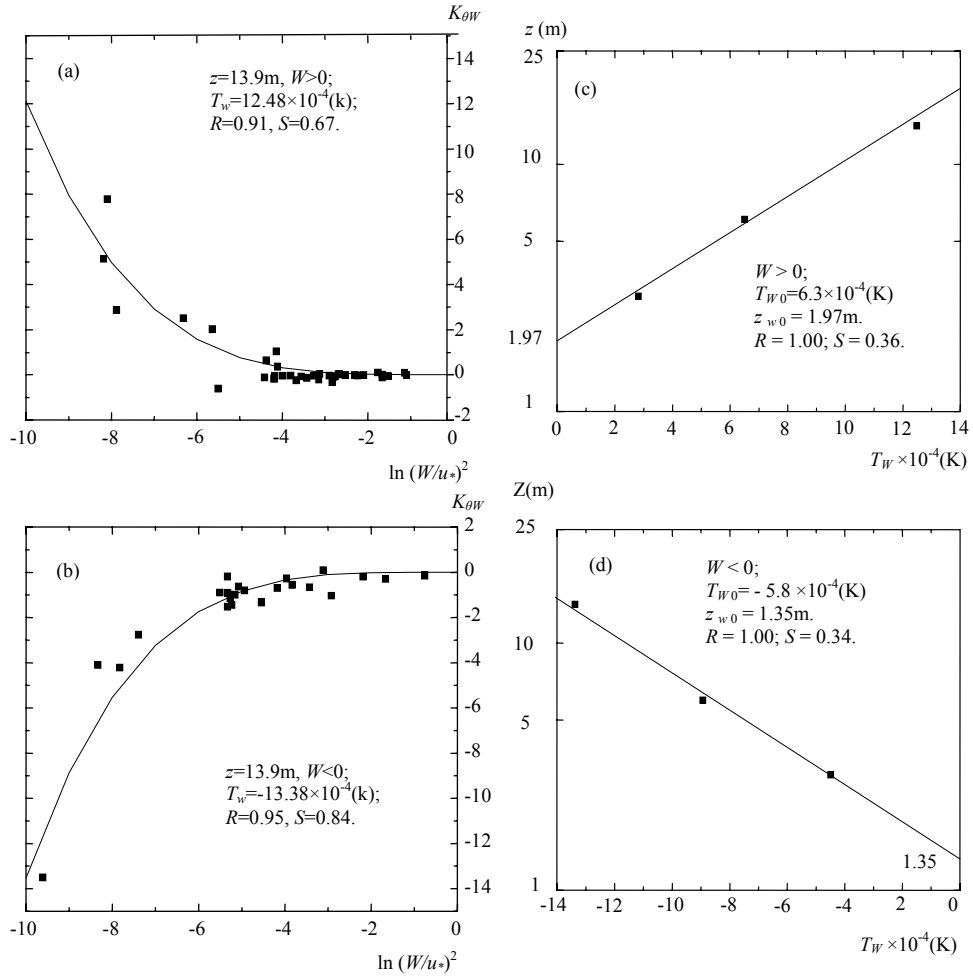


Figure 4. The coupling coefficient of the vertical velocity $K_{\theta W}$ as function of $\ln(W/u_*^2)$ and $\ln(z/z_{w0})$.

The left (a) and (b) of Figure 4 are the $K_{\theta W}$ at level $z=13.9\text{m}$ (the rest of the heights are omitted) as the function of $\ln(W/u_*^2)$ predicted by relation (97). The β values of fitting curves at different heights are all close to 4, hence to adopt $\beta=4$. As predicted by relation (98), the result shows that T_W is logarithmically related with height, as shown in Table 1. In Table 1, the function relation between T_W and $\ln(z/z_{w0})$ is shown in the right (c) and (d) of Figure 4, which displays $\alpha=1$ in relation (98), i.e., there is linear function relation between T_W and $\ln(z/z_{w0})$. The upper Figures 4(a) and (c) are the situation for updraft $W>0$; the lower Figures 4 (b) and (d) are the situation for downdraft $W<0$. The correlation coefficient of the fitting curve and the residual error are separately listed in the corresponding figures as R and S , and the correlation coefficient of the fitting curve is quite high. The intercept of the height of the ordinate in the right figures (c) and (d) is just the height characterized quantity of the coupling coefficient of vertical velocity, z_{w0} , and the slope of the logarithmic fitting straight

line is the temperature characteristic quantity of the coupling coefficient of vertical velocity T_{w0} . The height characteristic quantity, z_{w0} , is defined as the roughness height of the vertical velocity coupling. The roughness height z_{w0} of vertical velocity coupling and the temperature characteristic quantity, T_{w0} , of the vertical velocity coupling characterize the statuses of the dynamic and thermodynamic character of the underlying surface.

Table 1. The relation of T_w ($\times 10^4$ K) and level

level	$W>0$	$W<0$
3m	2.82	-4.49
6m	6.74	-8.93
13.9m	12.48	-13.38

Finally, the coupling coefficient between the vertical velocity and the vertical heat turbulent flux is obtained as the following form

$$K_{\theta w} = T_{w0} \ln\left(\frac{z}{z_{w0}}\right) \left[\ln\left(\frac{W}{u_*}\right)^2 \right]^4 \quad (99)$$

This is the function form of coupling coefficient, $K_{\theta w}$, of the vertical velocity for the vertical heat flux. In summing up the above results, there are following important properties of the coupling coefficient of vertical velocity for the vertical heat turbulent flux:

- [1] The coupling coefficient of vertical velocity of the heat flux $K_{\theta w}$ is a logarithmic function of the height and vertical velocity, i.e., the function of $\ln(z/z_{w0})$ and $\ln(W/u_*)^2$. The relation (99) means that the coupling coefficient of the vertical velocity is increasing logarithmically with the height, and increasing with the 4th power of the logarithm of the vertical velocity.
- [2] The coupling coefficient of vertical velocity, $K_{\theta w}$, is also related with the velocity characteristic quantity, friction velocity u_* ; height characteristic quantity, the roughness height of the vertical velocity coupling, z_{w0} , and the temperature characteristic quantity of the vertical velocity coupling T_{w0} . All the friction velocity, the roughness height of the vertical velocity coupling, and the temperature characteristic quantity are characteristic quantities determined by the dynamic and thermodynamic states of the underlying surface.

Once the characteristic quantities of underlying surface are determined, the coupling coefficient of vertical velocity is totally determined by formula (99). Hence, for a specific underlying surface, as long as the observational data of vertical gradient of the temperature, the vertical gradient of wind velocity, and the vertical wind velocity are available, the coupling coefficient of vertical velocity can be calculated from formula (99), and further, the

terms of turbulent transport of the temperature gradient, and the coupling transport of vertical velocity can be calculated from the relation (89), and finally the vertical heat turbulent flux is obtained.

4.2.4. The Experimental Verification of the Coupling Effect of Vertical Velocity on the Vertical Heat Flux

The above relation (89) has pointed out that the coupling term of vertical velocity is a modification to the transport term of temperature gradient of the turbulent heat flux. Now, the modification term is estimated by applying the coupling coefficient of vertical velocity, as well as the coupling effect of vertical velocity to the vertical heat flux is analyzed, thus provide verification to the trustiness of the result from the coupling coefficient of vertical velocity. The each term in the relation (89) is separately signed as

$$\left. \begin{array}{l} H_T = \rho c_p \overline{w' \theta'}, \quad H_K = -\rho c_p K_\theta \frac{\partial \theta}{\partial z}, \quad H_W = \rho c_p K_{\theta W} W; \\ \text{Without vertical velocity coupling:} \\ H_T = \rho c_p \overline{w' \theta'} = -\rho c_p K_\theta \frac{\partial \theta}{\partial z}, \quad \text{i.e. } H_T = H_K; \\ \text{With vertical velocity coupling:} \\ H_T = \rho c_p \overline{w' \theta'} = -\rho c_p K_\theta \frac{\partial \theta}{\partial z} - \rho c_p K_{\theta W} W, \quad \text{i.e. } H_T = H_K + H_W. \end{array} \right\} \quad (100)$$

Now, the above each term of heat fluxes is calculated separately by applying the observational data of the above parameters of characterized quantities of the underlying surface, temperature gradient, wind velocity gradient and the vertical velocity. The result is shown in Figure 5. The ordinate is the heat flux value observed directly, the abscissa is the heat flux value calculated according to the above theory of turbulent transport, and the void discontinues line is the fitting straight line. The left (a) and (c) in the Figure 5 is the situation modified by the vertical velocity coupling, the right (b) and (d) in the Figure 5 is the situation modified by the vertical velocity coupling; the upper Figures (a) and (b) are the situation for the updraft $W > 0$, and the lower Figures (c) and (d) are the situation for the downdraft $W < 0$. The correlation coefficient of fitting straight line, R , and residual error, S , are also listed in the figure. The C_D in the figure is the slope of linear fitting without the modification of the vertical velocity coupling, while C_{DW} is the slope after the modification to show the effect of the modification, $C_{DW}=1$ is the perfect modification.

The classic theory of turbulent transport in the atmospheric boundary layer deems that the vertical turbulent transport flux of the heat is equivalent to the transport flux of the vertical temperature gradient, i.e., $H_T = H_K$, that is the slope of the linear fitting in the figure should be $C_D=1$. But, in Figures 5(a) and (c), it is shown that for the situation without the modification from the vertical velocity coupling, when $W > 0$ the slope of linear fitting is $C_D=0.81$; when $W < 0$ the slope $C_D=0.70$. This means that the calculated values from the transport flux of vertical temperature gradient are all departing and larger than the directly measured values of the vertical turbulent transport flux of the heat. While Figures 5 (b) and (d) show that after the modification of the vertical speed coupling, when $W > 0$, the slope of linear fitting is

$C_{DW}=0.98$; when $W < 0$, the slope $C_{DW}=0.87$. The result shows that after the modification of the vertical velocity coupling, not only the calculated value of vertical turbulent transport flux of the heat is closer to the directly measured value of vertical turbulent transport flux, but also the correlation coefficient of fitting straight line, R , increases, and the residual error S decreases. The result of the modification from the vertical speed coupling is significant. This fact shows that the coupling effect of vertical velocity on the vertical turbulent transport flux of heat proven by the observational experimental data is true.

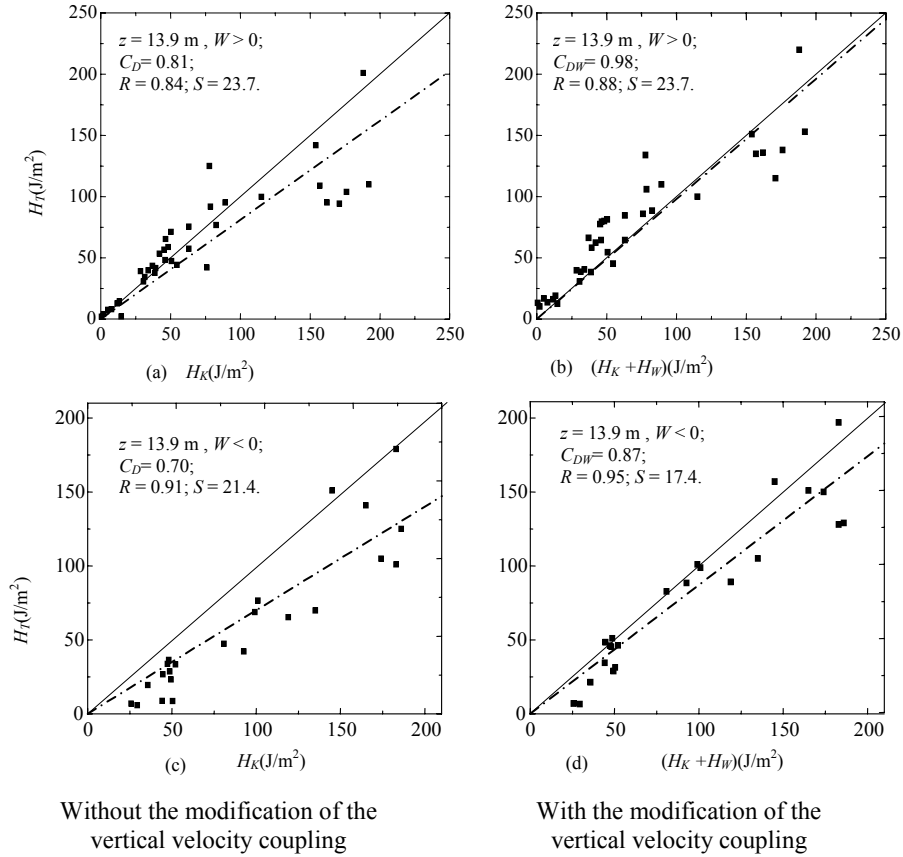


Figure 5. The modification of the vertical velocity coupling to the turbulent heat transport.

The coupling effect of the vertical velocity upon the vertical turbulent transport of the heat is proven above by the available observational experimental data of the atmospheric boundary layer, the cross coupling coefficient of the vertical velocity to the vertical turbulent transport of the heat is specifically determined by the observational experimental data, and further, a series of important properties of the cross coupling coefficient are obtained. The result shows that the coupling coefficient of vertical velocity is a logarithmic function of the height and the vertical velocity; it also related with the characteristic quantities determined by the character state of underlying surface, such as the friction velocity u_* , the roughness height of the vertical velocity coupling z_{w0} , and the temperature characteristic quantity of the vertical velocity coupling T_{w0} , etc. The important properties of cross coupling coefficient

establish the foundation to the practical application of the theory of cross coupling between the vertical velocity and the vertical turbulent transport.

4.3. Some Problems of the Turbulent Transport of the Atmospheric Boundary Layer and the Application of Cross Coupling Principle between the Vertical Velocity and Vertical Turbulent Transport

The classic theory of turbulent transport considers that the turbulent transport flux of a macroscopic quantity is equivalent to the gradient transport flux of this macroscopic quantity. The similarity theory of Monin-Obukhov obtained under the assumed condition of homogeneous underlying surface of the atmospheric boundary deems that the surface layer is a layer of constant flux, in which the average vertical velocity is always zero. While the conclusion of the theory of cross coupling between the dynamic process and the turbulent transport deems that it cannot be simply assumed that the surface layer is a constant flux layer without the vertical velocity, since there are always multifarious non-uniformities on the underlying surface or there are always convergence or divergence of horizontal motion during the development of thermal convection, i.e., there are the upward or downward vertical motion; the vertical turbulent transport flux of energy and matter is not fully equivalent to its vertical gradient transport flux, and is the sum of turbulent transport flux of its vertical gradient and the coupling transport flux of the vertical velocity. Though the coupling transport of vertical velocity is only a small modification to the vertical gradient transport flux, such a modification cannot be neglected in the atmospheric boundary layer with heterogeneous underlying surface and the convective boundary layer. This theory provides important clues to overcome the difficulty in the present theory of the atmospheric boundary layer with heterogeneous underlying surface.

It has been one century since the application of the theory of K turbulent transport in the atmosphere, and about half a century since the application of the similarity theory of Monin-Obukhov in the atmospheric boundary layer; these are still the theoretical bases in the study of the atmospheric turbulent transport. The theoretical and experimental results of the cross coupling between the dynamic process and the turbulent transport is a challenging problem to the theory of traditional turbulent transport and Monin-Obukhov similarity theory. For the theory of cross coupling between the dynamic process and the turbulent transport, it is at the stage of exploration and not matures. It is an urgent task to develop the theory of cross coupling between the dynamic process and the turbulent transport in the linear nonequilibrium thermodynamics of the atmosphere, and to operate observational and experimental study in this field. These will be beneficial to understand the turbulent transport, and to overcome the difficulties in the present study of the atmospheric boundary layer of heterogeneous underlying surface. The following is to discuss several problems of the turbulent transport of the atmospheric boundary layer by using the results of the theory of the cross coupling between the dynamic process and the turbulent transport.

4.3.1. The Convective Transport of Large Eddy in the Mixture Layer

When the convection in the atmospheric boundary layer develops sufficiently into a mixed layer (James et al., 1999)

$$\frac{\partial \theta}{\partial z} = 0, \quad \frac{\partial U}{\partial z} = 0, \quad \frac{\partial V}{\partial z} = 0 \quad (101)$$

By considering the above relation, the transports of the heat, vapor, and momentum are obtained respectively from the expressions (89), (92) and (42), as

$$J_{\theta z} = \rho c_p \overline{w' \theta'} = -\rho c_p K_{\theta W} \int_0^z (\nabla|_h \cdot \vec{V}) dz \quad (102)$$

$$J_{Vz} = \rho \overline{w' q'} = -\rho K_V \frac{\partial q}{\partial z} - \rho K_{VW} \int_0^z (\nabla|_h \cdot \vec{V}) dz \quad (103)$$

$$\tau_{13} = \rho \overline{w' u'} = 0; \quad \tau_{23} = \rho \overline{w' v'} = 0 \quad (104)$$

It is obvious that the heat transports in the mixed layer are proportional to the integral of the convergence or divergence in the air column. The heat transport flux observed in the mixed layer is actually the contribution from the convergence or divergence. The vapor transport flux should contain the contribution of the vapor transport resulted from the convergence or divergence, in addition to the turbulent transport flux caused by vapor vertical gradient. While the momentum transport in the mixed layer is zero to lead often windless during the development of convection.

The convection will inevitably create the atmospheric motion of convergence or divergence, and the development of convective boundary layer to the convection of large eddy is essentially a series of convergent or divergent motion. It is proven by the atmospheric linear thermodynamics that the processes of atmospheric convergence or divergence will certainly affect the processes of turbulent transport that an additional term of the heat and vapor transport by the convergence and divergence should be calculated in the turbulent transport of heat and vapor in the mixed layer. There is even only the contribution of convergence and divergence in the local turbulent transport of heat in the mixed layer. In the traditional atmospheric boundary physics, the flux of the heat transport, $J_{\theta z} = \rho c_p \overline{w' \theta'} = -\rho c_p K_{\theta} \partial \theta / \partial z$. However the observational fact shows that both the vertical gradient of the potential temperature and velocity in the convective boundary layer are zero in the convective boundary layer due to the strong mixing effect, $\partial \theta / \partial z = 0, \partial U / \partial z = 0, \partial V / \partial z = 0$. On the other hand, the observation of turbulent flux in the maiming layer shows that the $J_{\theta z} = \rho c_p \overline{w' \theta'}$ is limited to come into conflict with $\partial \theta / \partial z = 0$. Thus, an unreasonable result is obtained whereby the turbulent transport coefficient, K_{θ} , of the heat in the convective boundary layer is infinite. However the atmospheric thermodynamics reveals that the turbulent transport coefficient of the heat is not infinite in the mixing layer, as well as the heat transport flux is equal to the amount of heat transport caused by the atmospheric convergence and divergence motion, as shown in expression (102). Hence, such a contradiction in the convective boundary layer is resolved.

4.3.2. The Balance of Ground Surface Energy

Energy balance closure on the ground surface as a formulation of the first law of thermodynamics requires that the sum of the latent heat flux (LE) and sensible (H) heat flux estimated is equivalent to all other energy sinks and sources. The conventional expression is as follows:

$$LE + H = R_n - G - S - Q \quad (105)$$

where R_n is the net radiation, G the heat flux into the soil substrate, S the rate of change of heat storage (air and biomass) between the level of the eddy covariance instrumentation and the soil surface, and Q the sum of all additional energy sources and sinks. Typically, Q is neglected as a small term. During the late 1980s it became obvious that the energy balance at the earth's surface could not be closed with experimental data (Foken et al., 2006; Culf et al., 2000). Surface energy fluxes ($LE + H$) are frequently (but not always) underestimated by about 10–30% relative to estimates of available energy ($R_n - G - S$). The imbalance is often present, though often to a lesser extent, even over flat, homogeneous surfaces and short vegetation, which are presumably ideal conditions for the eddy covariance method.

The most common point of discussion is measurement errors of the eddy covariance method. Improvements of the sensors and the more stringent control of the data quality (Foken et al., 2004) have made this method much more reliable in the past ten years (Moncrieff, 2004). However the theoretical assumptions for the extrapolation algorithm in the above energy balance, for example, homogeneity of the meteorological fields in the horizontal direction and stationarity of the observed processes during the averaging time, may be important cause of imbalance of the ground surface energy. This involves applicability of the Taylor hypothesis of frozen turbulence (Taylor 1938) as well as the Monin–Obukhov similarity theory (Monin and Obukhov 1954) that assumes the surface layer as constant flux without the vertical velocity under the condition of homogeneity and stationarity.

The different balance layers and scales of diverse measuring methods (the measurements of surface net radiation is approx. 2m, and turbulent fluxes approx. 5m above the surface, as well as the soil heat flux is approx. 10 cm below the surface) are cause of energy imbalance. The observation of turbulent fluxes at approximate 5m above the surface vs. the corresponding observation of net radiation at surface requires that the surface layer is constant flux. In fact, the earth's surface is characterized by spatial heterogeneity over a wide range of scales, as can be seen by examining soil and topographic maps. This heterogeneity affects the exchange of momentum, heat, and water between the land surface and atmosphere, and results in the no constant flux of surface layer. The energy balance closure problem is also closely connected with the horizontal turbulent fluxes (Raabe, et al., 2002), and the advection and fluxes due to longer wavelengths (Finnigan et al., 2003; Sakai et al., 2001) or organized turbulence structures (Inagaki et al., 2006; Kanda et al., 2004). These heterogeneity effects, advection and fluxes due to longer wavelengths effects or organized turbulence structures may all behave the vertical convection velocity to result also in the exchange of energy and mass between both levels of turbulent fluxes observation above the surface and the observation of net radiation at surface. Kukharets et al. (2000) found also that the soil heat flux and the energy balance closure are closely related due to the energy storage in the upper soil layer. In the following text, we will discuss that the vertical convection velocity, as an important source of the energy imbalance, affects the balance closure.

The balance of ground surface energy is the continuity condition of the transport of ground surface energy, the net radiation of the ground surface $R_n|_0$ is equal to the sensitive heat flux of upward transport $H = -\left(\rho c_p K_\theta \partial \theta / \partial z\right)|_{0+}$, the latent heat flux of the vapor $LE = -\left(\rho \lambda_v K_v \partial q / \partial z\right)|_{0+}$, and the downward heat flux of the soil thermal conduction $G = \left(\rho \lambda c_g \partial T / \partial z\right)|_{0-}$. Here, the subscript ‘ $0+$ ’ and ‘ $0-$ ’ represent the ground surface, the positive sign indicates above the ground surface, and negative sign represents below the ground surface; λ_v is the latent heat of water vaporization; λ and c_g represent the thermal conductivity and specific heat of the soil, respectively. The budget equation of the ground surface energy, (105), can be written as the following form

$$R_n|_0 = -\left(\rho c_p K_\theta \frac{\partial \theta}{\partial z}\right)|_{0+} - \left(\rho \lambda_v K_v \frac{\partial q}{\partial z}\right)|_{0+} + \left(\rho \lambda c_g \frac{\partial T}{\partial z}\right)|_{0-} \quad (106)$$

In which, Q and S in (105) neglected as a small term. Substitute (89) and (92) and eliminate the gradient term in (106), one obtains

$$R_n|_0 - G|_{0-} = H|^z + LE|^z + \rho K_w \int_0^z (\nabla|_h \cdot \vec{V}) dz \quad (107)$$

where $K_w = c_p K_{\theta w} + \lambda_v K_{v w}$, $G|_{0-} = \left(\rho \lambda c_g \partial T / \partial z\right)|_{0-}$, the superscript z represents the measured value of the turbulence at that level. The budget equation of the ground surface energy can be written as the following customarily using form

$$R_n - G = H + LE + \rho K_w \int_0^z (\nabla|_h \cdot \vec{V}) dz \quad (108)$$

This expression shows that the balance of the ground surface energy must contain the contribution proportional to the integral term of the convergence or divergence in the air column. For the heterogeneous underlying surface or the convective boundary layer the effect of the energy transport by convergence or divergence is more significant. The reason of the imbalance of the ground surface energy measured by the turbulent flux for the heterogeneous underlying surface or convective boundary layer may be that the effect of the energy transport resulted from convergence or divergence is not considered.

The balance of ground surface energy is importance in the land surface processes. The traditional energy budget equation of the ground surface is established under the condition of homogeneous underlying surface. While the real ground surface is often heterogeneous to lead that there often is imbalanced phenomenon in the energy budget equation of ground surface in practical observation. This is the result of the vertical transport of the energy and matter (vapor) from the atmospheric convergence or divergence under the condition of heterogeneous underlying surface. Even if under the homogeneous underlying surface, due to the development of the convection, the atmospheric motion of convergence and divergence is

created, and the appearance of which will also affect the vertical transport of the energy and matter, that has been proven theoretically by the atmospheric linear thermodynamics. It should be pointed out that the energy budget equation of the ground surface of the heterogeneous underlying surface and the convective boundary layer must be supplemented by the contribution of the vertical transport of the energy and matter caused by the atmospheric convergence and divergence.

4.3.3. The Parameterization of the Boundary Layer in the Land Surface Processes

Basically, three methods, the “tile” approach (e.g., Li and Avissar 1994), the “mosaic” approach (e.g., Koster and Suarez 1992) and the “effective parameter” approach (e.g., Arain et al. 1996) have been developed for spatial heterogeneity effects in the parameterization of the boundary layer in the land surface processes. Because of the highly nonlinear interaction among the soil, the vegetation, and the atmosphere, there is no general rule for the derivation of suitable parameters and averaging procedures. However the spatial heterogeneity effects in the land surface processes may behave the vertical velocity effects due to horizontal convergence and divergence discussed in the above section. So here, a possible scheme of parameterization with the vertical velocity effects is developed.

The parameterization of the boundary layer in the land surface processes can start from the sensible heat flux and the latent heat flux transporting from the bottom of the atmospheric boundary layer to the free atmosphere, as shown in (89) and (92), as well as the momentum flux transporting from the free atmosphere through the top of the atmospheric boundary layer into the boundary layer, as (42), i.e.,

$$J_{\theta z}|^{z_i} = \rho c_p \overline{w' \theta'}|^{z_i} = -\rho c_p K_\theta \frac{\partial \theta}{\partial z}|^{z_i} + \rho c_p K_{\theta w} \int_0^{z_i} (\nabla|_h \cdot \vec{V}) dz \quad (109)$$

$$J_{Vz}|^{z_i} = \rho \overline{w' q'}|^{z_i} = -\rho K_V \frac{\partial q}{\partial z}|^{z_i} + \rho K_{Vw} \int_0^{z_i} (\nabla|_h \cdot \vec{V}) dz \quad (110)$$

$$\tau_{13}|^{z_i} = \rho \overline{w' u'}|^{z_i} = -\rho K_{13} \left(\frac{\partial U}{\partial z} \right)|^{z_i}; \quad \tau_{23}|^{z_i} = \rho \overline{w' v'}|^{z_i} = -\rho K_{23} \left(\frac{\partial V}{\partial z} \right)|^{z_i} \quad (111)$$

respectively. The superscripts of the above expressions z_i are the related values at the top of the boundary layer. The parameterization of the boundary layer in the land surface processes is essentially by using the heat, vapor and the momentum transport fluxes, which can be measured at the ground surface at the level z , to estimate the values of fluxes at the top of the boundary layer, at the level z_i , with simple methods.

$$J_{\theta z}|^{z_i} = \alpha_H \left(-\rho c_p K_\theta \frac{\partial \theta}{\partial z}|^z + \rho c_p K_{Hw} \int_0^z (\nabla|_h \cdot \vec{V}) dz \right) \quad (112)$$

$$J_{Vz}|^{z_i} = \alpha_V \left(-\rho \beta K_V \frac{\partial q}{\partial z}|^z + \rho K_{Vw} \int_0^z (\nabla|_h \cdot \vec{V}) dz \right) \quad (113)$$

$$\tau|^{zi} = -\rho \alpha_D K_{13} \left(\frac{\partial U}{\partial z} \right)^z \quad (114)$$

where α_H , α_V and α_D are the ratio coefficients of parameterization. These can be written as the following traditionally frequently used forms

$$H = -\rho c_p C_H (U - U_0)(T - T_0) + \rho c_p C_{HW} \int_0^z (\nabla|_h \cdot \vec{V}) dz \quad (115)$$

$$E = -\rho C_V (U - U_0)(q - q_0) + \rho C_{vW} \int_0^z (\nabla|_h \cdot \vec{V}) dz \quad (116)$$

$$\tau = -\rho C_D (U - U_0)^2 \quad (117)$$

The C_D , C_H and C_V in the above expressions are the traditionally frequently used drag coefficients. The above expressions show that there should be an additional term proportional to the convergent or divergent integral in the air column in the parameterization of the transport flux of heat and vapor of the boundary layer. The transport of heat and vapor due to convergence or divergence is of importance for the thermally heterogeneous underlying surface or convective boundary layer.

The traditional approach of the parameterization of the boundary layer in the land surface processes is also established on the base of the atmospheric boundary layer theory with homogeneous underlying surface. Such an approach is reasonable under homogeneous underlying surface, while for the heterogeneous underlying surface such an approach is open to question. It is pointed out by the conclusion of the atmospheric linear thermodynamics that in addition to the turbulent transport, the contribution of the vertical transport of energy by the atmospheric convergence and divergence should also be included in the transport of energy and matter from the atmospheric boundary layer to the free atmosphere. Such a consideration is especially important to the heterogeneous underlying surface and the convective boundary layer. At present, the area weighted mean method is generally used to handle the parameterization of the land surface process of the heterogeneous underlying surface. This is, of course, a method that has to be taken without alternative, and which makes handling the problem much more complicated and loses the original meaning of the parameterization. As everyone knows, the parameterization of climate is to simply estimate the transport flux of energy and matter from the ground surface to the free atmosphere by using the routine meteorological observational data of the ground surface. It seems more reasonable and accurate in physics to estimate the transport flux of energy and matter from the ground surface to the free atmosphere for the parameterization of boundary layer of land surface processes under heterogeneous underlying surface that the turbulent transport fluxes of vertical gradient of energy and matter supplement by the vertical transport resulted from the atmospheric convergence and divergence.

5. CONCLUSION

Turbulence is one of the most common natural phenomena in everyday experience, and one of the most common examples of complex and disordered dynamic behavior in nature. It is a ubiquitous phenomenon that is not fully understood but in which scientists in the communities of science and engineering are interested. The dynamic method of research on turbulence promotes the understanding of the microscopic structure and microscopic mechanism. However, a lot of engineering problems that are closely related to human life are focused on the turbulent macroscopic structure and mechanism, especially as macroscopic causes of the turbulence and macroscopic transportation of matter and energy. Nonequilibrium thermodynamics, an integrated method to hold the integrated property of the system, can deduce much new knowledge about turbulence. Consequently, the development of nonequilibrium thermodynamics offers a new tool to study the macroscopic structure and mechanism of the turbulence. The essential features of turbulence are the turbulent transport phenomena involving transfer of mass, energy and momentum. There are two kinds of phenomena in the transport of energy and matter—molecular viscosity and turbulent viscosity. The transport of molecular viscosity has a mature theory from molecular dynamics; however, for the transport theory of turbulent viscosity, there are still a lot of problems awaiting a solution.

The atmospheric nonequilibrium thermodynamics derives uniformly the Fourier's and Fick's law, Newton's Law and both the Dufour and the Soret effects, the cross coupling effect between the dynamic velocity and turbulent transport processes in the atmosphere, and the turbulent intensity theorem. The above laws and theorem are partially validated by using the observed data and, further, their phenomenological coefficients are determined.

The turbulent intensity theorem shows that the turbulent intensity is proportional to the summation of the velocity divergence resulting in the Reynolds turbulence and scalar product of velocity and the temperature gradient resulting in the Rayleigh-Bénard turbulence. It reveals that the atmospheric turbulence roots the velocity gradient and the potential temperature gradient and proves that both Reynolds turbulence and Rayleigh-Bénard turbulence coexist in the atmosphere. It emerges that the atmospheric turbulence is anisotropic and inhomogeneous, because that isotropic and homogeneous turbulence without energy supply decays with time to until extinction finally.

The discovery of the coupling effect phenomenon between the dynamic and thermodynamic processes breaks through the viewpoint of the theories of traditional turbulent transport, Fourier's and Fick's law, and Newton's Law—i.e., the turbulent transport flux of one kind of macroscopic quantity is equivalent to the gradient transport flux of this macroscopic quantity. Moreover, the coupling principle between the thermodynamic and dynamic processes deems that the turbulent transport flux of one kind of macroscopic quantity should include the velocity coupling transport in addition to the gradient transport flux of this macroscopic quantity. It means that the vertically turbulent transport of matter and energy should be composed of two parts: the vertical gradient transport of this macroscopic quantity and the coupling transport of vertical velocity. The principle of the cross coupling between the dynamic and thermodynamic process is proven by the theory of nonequilibrium thermodynamics. Though such a phenomenon is proven by the observational fact in the atmosphere, such a principle might universally exist in nature, or especially in the

environmental fluid. Hence, such knowledge is theoretically very important in understanding turbulent transport.

The classic Monin–Obukhov similarity, which is the basic theory of atmospheric boundary layer in the present age, assumes the surface layer as a constant flux without the vertical velocity under the condition of homogeneity and stationarity. The extrapolation algorithm in the energy budget and the parameterization scheme of the boundary layer in the land surface processes are based on Monin–Obukhov similarity theory with the homogeneity and stationarity of meteorological field. In fact, the earth's surface is characterized by spatial heterogeneity over a wide range of scales. The heterogeneity of underlying surface brings on the advection to lead the convergence and divergence motion. It may be an important cause of the imbalance of energy budget of the ground surface. The cross coupling principle of the vertical velocity and vertical turbulent transport may offer a possible clue to develop the theory of atmospheric boundary layer with heterogeneous underlying surface and to overcome the difficulties encountered in the imbalance problem of ground energy budget and in the parameterization of the boundary layer with the heterogeneous underlying surface. Consequently, the ground energy budget and the parameterization of the boundary layer should count the coupling transport of vertical velocity in addition to the turbulent transport of vertical gradient of energy and matter.

The non-equilibrium thermodynamic theory of atmospheric turbulence is at the stage of exploration and has not matured. Some theoretical results await experimental validation; for example, both the Dufour and the Soret effects are not verified by the experiment due to a lack of sufficient accurate data on humidity in the atmosphere. The cross coupling of vertical velocity to vapor turbulent transport awaits experimental validation with enough accurate data on humidity. It is an urgent task to operate observational and experimental study in this field.

ACKNOWLEDGMENTS

This work was supported by the National Natural Science Foundation of China (Grant Nos. 40705007, 40775017, 40633014).

The authors would like to thank Prof. Högström for kindly providing the accurate and detailed observed data that enabled the successful implementation of this work.

REFERENCES

- Batchelor, G. K. and Townsend, A. A., 1948, *Proc. Roy. Soc. London, A* 194.; 1948. Decay of turbulence in the final period. *Proc. Roy. Soc. London, A* 194.; 1948c. *Proc. Roy. Soc. A* 190.
- Batchelor, G. K., 1953, *The Theory of Homogeneous Turbulence*, London: Cambridge Univ. Press.
- Bénard, H., 1900, *Rev. Gén. Sci.*, 11, 1261-1271 & 1309-1328; *Ann. Chim. Phys.* 23, 62 (1901).
- Bohr, T.; Jensen, M. H., 1998, Paladin G, et al. *Dynamical Systems Approach to Turbulence*, London: Cambridge Uni. Press, pp350

- Bramwell, S. T. ; Holdsworth, C. W. ; Pinton, J. F., 1998, *Nature*, 396, 552.
- Busse, F. H., 2004, *Science*, 305, 1574—1575.
- Businger, J. A.; Wyngaard, J. C.; Izumi, Y., et al., 1971, *J. Atoms. Sci.*, 28, 181—189.
- Chapman, S., 1912, *Phil. Trans. Roy. Soc., Lond. A*, 211, 433-483, *ibid*, A217, 115.
- Chapman, S. & Dootson, F. W., 1917, *Phil. Mag.*, 33, 248-256.
- Chen, H.; Satheesh, K.; Steven, O., et al., 2003, *Science*, 301, 633–636.
- Culf, A. D.; Foken, T.; Gash, J. H. C., 2004, *The energy balance closure problem, in: Vegetation, water, humans and the climate. A new perspective on an interactive system*, edited by: Kabat, P., Claussen, M., Dirmeyer, P. A., et al., Springer, Berlin, Heidelberg, 159–166.
- Curie, P., 1894, *Journal de Physique* 3, 393–415.
- Du1, Y., George, E. K., 2000, *Science*, 288: 1230.
- Dryden, H. L.; Kuethe, A. M., 1930, *NACA-report-320*, 357-382; *Nat. Adv. Ctee. Aero., Report No. 320* (1929). 213.
- Elperin, T.; Kleeorin, N.; Rogachevskii, I., 1996, *Phys. Rev. Lett.*, 76, 224-227.
- Elperin, T.; Kleeorin, N.; Rogachevskii, I., 1998, *Phys. Rev. Lett.*, 80, 69-72.
- Enskog, D., 1911, *Phys. Z.*, 12(56), 533.
- Finnigan, J. J., Clement, R., Malhi, Y., Leuning, R., and Cleugh, H. , 2003, *Boundary-Layer Meteorol.*, 107, 1–48.
- Foken, T., 2006, *Boundary-Layer Meteorology*, 119(3), 431-447.
- Foken, T.; Göckede, M.; Mauder, M.; Mahrt, L.; Amiro, B. D.; Munger, J. W., 2004, *Post-field data quality control, in: Handbook of Micrometeorology: A Guide for Surface Flux Measurement and Analysis*, edited by: Lee, X., Massman, W. J., and Law, B., Kluwer, Dordrecht, 181–208.
- Foken, T.; Wimmer, F.; Mauder, M.; Thomas, C.; Liebethal, C., 2006, *Atmos. Chem. Phys.*, 6, 4395–4402
- Fourier, J. B. J., 1822, *Théorie Analytique de la Chaleur*, F. Didot, Paris.
- Fick, A., 1855a, *Ann. Phys. Chem.*, 94, 59–86.
- Fick, A., 1855b, *Phil. Msg. and Jour. Sci.*, 10, 31–39.
- Glazier, J. A.; Segawa, T., et al., 1999, *Nature*, 398, 307–310.
- Groisman A.; Steinberg V., 2000, *Nature*, 405, 53–55.
- Groot, S. R. De. and Mazur, P., 1962, *Non-equilibrium Thermodynamics*, chapter 6, North-Holland Publishing Company-Amsterdam, 441pp.
- Heslot, F.; Castaing, B.; Libchaber, A., 1987, *Phys Rell A*, 36, 5870–5873
- Hinze, J. O., 1959, *Turbulence*, New York: McGRAW-HILL Company, Inc, 1959, pp.586
- Hof, B.; van Doorne, Casimir W. H., et al., 2004, *Science*, 305, 1594–1598.
- Högström U., 1988, *Boundary-Layer Meteorology*, 42: 55–78.
- Hu, Yinqiao, 2002a, *Progress in Natural Science*, 12(3), 180–164.
- Hu, Yinqiao, 2002b, *Introduction to Atmospheric Thermodynamic-dynamics*. Beijing: Geological Publishing House. 406. (in Chinese)
- Hu, Yinqiao, 2002c, *Adv. Atmos. Sci.*, 19 (3), 448–458.
- Hu, Yinqiao, 2002d, *Adv. Atmos. Sci.*, 19(5), 767–776.
- Hu, Yinqiao; Zuo, Hongchao, 2003, *Adv. Atmos. Sci.*, 20(5): 794–798.
- Hu, Yinqiao, 2003, *Acta. Phys. Sin.*, 52, (I), 1379–1384; (II), 1354–1359. (in Chinese)
- Hunt, J. C. R.; Vassilicos, J. C., 2000, *Turbulence Structure and Vortex Dynamics* , London: Cambridge University Press.

- Inagaki, A.; Letzel, M. O.; Raasch, S.; Kanda, M., 2006, *J. Meteorol. Soc. Japan*, 84, 187–198.
- Izumi, Y., 1971. *Kansas 1968 field program data report. Air Force Cambridge Research Papers*, No. 379, Air Force Cambridge Research Laboratory, Bedford, MA.
- James, A. G.; Takehiko, S.; Antoine, N.; Masaki, S., *Nature*, 1999, 398, 307–310.
- Kanda, M.; Inagaki, A.; Letzel, M. O.; Raasch, S.; Watanabe, T., 2004, *Boundary-Layer Meteorol.*, 110, 381–404.
- von Kármán, T., 1937, *Proc. Nat. Acad. Sci.*, Wash. 23, 98.
- Kukharets, V. P.; Nalbandyan, H. G.; Foken, T., 2000, *Izv., Atmos. & Oceanic Phys.*, 36, 318–325.
- Krishnamurti, R., 1973, *J. Fluid Mech.* 60, 285–303.
- Lorenz, E. N., 1963, *J. Atoms. Sci.*, 28, 130–141.
- Moncrieff, J., 2004, *Surface turbulent fluxes, in: Vegetation, water, humans and the climate. A new perspective on an interactive system*, edited by: Kabat, P., Claussen, M., Dirmeyer, P. A., et al., Springer, Berlin, Heidelberg, 173–182.
- Monin, A. S.; Obukhov A. M., 1954, *Tr. Akad. Nauk. SSSR Geofiz. Inst.*, 24 (151), 163–187.
- Monin, A. S., Yaglom, A. M., 1971, *Statistical Fluid Mechanics*, Vol. 1. London: MIT Press Cambridge Mass.
- Monin, A. S., Yaglom, A. M., 1975, *Statistical Fluid Mechanics*, Vol. 2. London: MIT Press Cambridge Mass.
- Narasimhan, T. N., 1999, *Rev. Geophys.*, 37(1), 151–172.
- Obukhov, A. M., 1946, *Tr. Geofiz. Inst. AN SSSR*, 1, 95–115 (in Russian).
- Onsager, L., 1931a, *Phys. Rev.*, 37, 405–426.
- Onsager, L., 1931b, *Phys. Rev.*, 38, 2265–2279.
- Panofsky, H. A.; Dutton, J. A., 1983, *Atmospheric Turbulence*. New York: John Wiley & Sons, Inc., 160–162.
- Pedro Sancho, 1999, *Phys. Rev. E* 60, 1762–1766.
- Pedro Sancho, 2000, *Phys. Rev. E* 61, 2111–2113.
- Prandtl, L., 1925, *ZAMM* 5: 136–139; Prandtl, L., *Zs. angew. Math. Mech.*, 5, 136–139.
- Prandtl, L. 1945, *Nachr. Akad. Wiss. Göttingen, Math. Phys.* 6–19.
- Prigogine, I., 1945, *Bull. Classe Sci., Acad. Roy. Belg.*, 31, p.600.
- Prigogine, I., 1967, *Introduction to Thermodynamics of Irreversible Processes*, 3rd ed. New York: Interscience Pub.
- Raabe, A.; Arnold, K.; Ziemann, A., 2002, *Journal of Atmospheric and Oceanic Technology*, 19, 1225–1230.
- Rayleigh, L., 1916, *Phil. Mag.* 32, 529–546.
- Reynolds O., 1894, *Phil. Trans. R. Soc. London*, A186: 123–161.
- Richardson, L.F., 1920. *Proceedings Royal Society*, A 97, 354–373.
- Richardson, L. F., 1922, *Weather Prediction by Numerical Process*, London: Cambridge University Press.
- Sancho, P., 1999, *Phys. Rev. E* 60, 1762–1766.
- Sancho, P., 2000, *Phys. Rev. E* 61, 2111–2113.
- Shashi, B. V.; Rosenherg, N. J.; Blad, B. L., 1978, *J. Appl. Met.*, 17, 330–338.
- Shraiman, B. I.; Siggia, E. D., 2000, *Nature*, 405: 639–646.
- Skrbek, L.; S. R. Stalp, 2000, *Phys. Fluids*, 12 (8), 1997–2019.

- Sorbian, Z., 1989, *Structure of the Atmospheric Boundary layer*. London: Prentice-Hall, Inc., 70–76.
- Soret, C., 1879, *Arch. Sci. Phys. Nat.*, 2, 48.
- Streater, R. F., 2000, *Mathematical Physics (math-ph)*, KCL-MTH-98-32, arXiv:math-ph/9910043v1
- Swinney, H. L.; Gollub, J. P., 1978, *Physics Today* (August 1978).
- Taylor, G. I., 1935, *Proc. Roy. Soc. A* 151, 421–478.
- Taylor, G. I., 1938, *Proc. Roy. Soc.*, A164, 476–490.
- Thompson, W., 1854, reprinted in *Mathematical and Physical Papers*, I, Cambridge University Press, p. 232, 1882.
- Tulapurkara, E. G., 2005, *Sādhanā*, Vol. 30, Part 4, August 2005, 499–512.
- Victor S. L'vov, 1998, *Nature*, 396, 519–520.
- Waldmann, L., 1943, *Die Naturwissenschaften*, Volume 31, Issue 16-18, pp. 204–204.

Chapter 3

GENERALIZED SCALE INVARIANCE OF EDGE PLASMA TURBULENCE

V.P. Budaev*

Nuclear Fusion Institute, RRC Kurchatov Institute, Moscow, Russia

ABSTRACT

Experimental study of edge plasma turbulence in fusion devices such as tokamaks, stellarators and linear machines are presented. The fluctuations observed in the edge plasma of fusion devices are intermittent and self-similar. Non-Gaussian statistics, long-range correlation, superdiffusion and multifractality are observed in the edge plasma turbulence. The turbulence scalings display universal properties. Edge plasma turbulence exhibits a generalized (extended) self-similarity in an extended scale range. Such properties are predicted by the log-Poisson model of intermittent turbulence that considers a stochastic multiplicative cascade of energy and a strong effect of a dissipation range on an inertial range. Hidden statistical symmetries, hierarchy of moments and generalized scale invariance are behind the log-Poisson model. Experimental structure functions scalings have a nonlinear functional dependence on the order index. Such dependence is described by the log-Poisson model captured a topology of singular dissipative structures in case of strong anisotropy from a strong magnetic field. The experimental scalings are rather well fitted by the log-Poisson model considering quasi-1D filament-like dissipative structures. It appears that the turbulence in the edge plasma of fusion devices is governed by cross-field motions similar to hydrodynamic turbulence. The experimental scalings from edge plasma are available for a comparison with experimental results from neutral fluids.

1. INTRODUCTION

Turbulence is a natural state of laboratory [1] and space [2] plasmas. Numerous experimental investigations in fusion devices (see, e.g., [3–7]) show that the plasma in the

* email: budaev@mail.ru

central and peripheral parts of the confinement region is highly turbulent. Turbulence in the frequency range of drift instabilities, from about 0.1 kHz to about 1 MHz, drives enhanced plasma transport across the confining magnetic field, thereby deteriorating confinement and raising heat loads to the material elements of the vacuum chamber that are in contact with the plasma. The turbulence level—the ratio of the amplitude of fluctuations to their mean amplitude—is higher in the peripheral discharge region. This effect is observed in devices of various scales with different plasma heating methods [8]. Although there are several reasons that are considered to cause such an increase in the turbulence intensity, the dominant factor is presumably the universal behavior of turbulent processes under the influence of boundary effects. The most important question to be answered is that of whether the magnetic-field-related anisotropy on intermediate and small scales is as high as that on large scales. Despite a considerable theoretical research on the topic, the question of whether the small-scale plasma turbulence is isotropic or not remains open and is being actively discussed. Solving this problem requires relevant experimental data. In turbulence research, very efficient and effective analytic methods have been developed, such as the quasilinear approximation [9, 10], the weak turbulence theory or direct interaction approximation [1, 11], and renormalization-group (RG) methods (see review [12] and other related works). But existing analytic models are yet incapable of providing as detailed and exact descriptions as do semi-empirical cascade models based on statistical methods. This especially concerns the description of intermittent turbulence. In analytic models, the RG methods in fact consist in the renormalization of viscosity and of a random force (which, in most of the models, is assumed to obey Gaussian statistics) in order to account for how the processes occurring on a given spatial scale are influenced by longrange correlations on other scales. Since this description is made in the mean-field approach, it cannot give a detailed description of intermittency. The intermittency results from turbulent activity; but this activity is itself distributed nonuniformly. In such process, the distribution function is described not by exponential but by power laws. The turbulence of hydrodynamic flows and plasma turbulence in laboratory devices and astrophysics are described by nontrivial algebraic, fractional stable (see [13, 14] and other related papers), log-normal [15], log-Poisson [16,17], log-Levy[18], and other statistics known in probability theory (see [19]).

The fundamental principles for investigating developed turbulence were laid by A.N. Kolmogorov [20]. Fully developed turbulence is characterized by such features as a large number of degrees of freedom, many nonlinearly interacting modes, a small-scale structure, and random fluctuations of the velocities and fields. Consequently, it can be best described by the methods of statistical physics and probability theory. In order to describe a random process, it is necessary to determine its distribution function or, equivalently, all the moments of the distribution function. The distribution function and statistical averages (moments) can be measured in experiments and the results can then be compared with theoretical predictions. In the simplest case, the probability distribution of the amplitudes of fluctuations in a random process obeys a Gaussian (so called normal) law. Gaussian statistics is used to describe, e.g., the classical Brownian motion (see [19]), in which correlations decrease exponentially. In probability theory, other distribution laws are known [19] with which to describe random processes with memory and long-range correlations. The distributions of such processes are not always described by the known mathematical functions, and what is known for many types of random processes is only an approximation of their distribution functions. Experimental investigations (see [5, 21–24] and other related papers) show that the

distribution function of fluctuations in tokamak scrape-off-layer (SOL) plasmas is highly non-Gaussian, so it is necessary to analyze the moments of the distribution function. In the inertial range $\eta \ll l \ll L$ (where η and L are the dissipative and global spatial scales, respectively), for high Reynolds numbers, the Kolmogorov theory [20] (published in 1941 and known as K41) assumes Gaussian statistics for velocity fluctuations and predicts a power-law dependence of the structure function (the q th-order moment) on the spatial scale l ,

$$S_q(l) \sim l^{\zeta(q)} \quad (1)$$

with a linear functional exponent, $\zeta(q) = q/3$. Assuming a local dependence of the structure functions only on the spatial scale and on the energy dissipation rate ϵ , from dimensionality considerations A.N. Kolmogorov derived the well known scaling $E_k \sim k^{-5/3}$ (the so-called five-thirds law) for the energy flux spectrum of developed isotropic turbulence in the inertial range. This law provides a relatively good description of the spectrum of developed isotropic hydrodynamic turbulence. More precise measurements of the uniform turbulence spectrum showed that the exponent in the law $E_k \sim k^{-\gamma}$ differs from five-thirds $\gamma = 1.71 \pm 0.02$ (see, e.g., [25]). This slight difference from five-thirds is of fundamental importance because it arises from the structural inhomogeneity and special statistical symmetries of the turbulent process. Experimental investigations and computer simulations of turbulent hydrodynamic flows showed that the scaling for structure functions of high orders ($q > 3$) deviates from that predicted by the K41 theory; the reason is the intermittent nature of turbulence [26].

Intermittency—a local breaking of the inhomogeneity of turbulence, when active regions coexist with passive (quasi-laminar) ones—was first considered by Novikov and Stewart [27]. The intermittency phenomenon is observed in turbulent hydrodynamic flows in neutral media [26] and in turbulent magnetized plasmas (see, e.g., [5] and other related papers), both with high and moderate Reynolds numbers. Random fluctuations in the velocity, field, and other parameters of a turbulent flow in an intermittent medium obey a non-Gaussian statistics; i.e., they cannot be described in terms of a classical (normal) diffusion law. Turbulent transport in an SOL plasma can possess several types of symmetries, including the scale invariance symmetry. In real intermittent turbulence, the simplest (trivial) scale invariance is observed on very limited spatial scales. Theoretical studies predict generalized scale invariance laws associated with hidden statistical symmetries. The extended self-similarity (ESS) criterion (which was proposed phenomenologically by Benzi et al. [28] and was later considered in log-Poisson turbulence statistics in [16, 17]) assumes a scaling of the form $S_q(l) \sim S_3(l)^{\zeta(q)/\zeta(3)}$ for an extended scale of $l \geq 5\eta$. The ESS property is observed on the scales up to those on which dissipation occurs [17]. It is thought that this self-similarity results from hidden statistical symmetries of equations. The equations describing the edge plasma in tokamaks and other fusion devices (for discussion of this issue, see [29]) are similar in structure to the Navier–Stokes (NS) equation. The scalings for turbulent plasma flows in a magnetic field are related to scale invariance symmetries of turbulence and therefore to the scalings for the statistical moments of the probability distribution function. Information on turbulence scalings can be obtained by investigating the statistical symmetries of turbulence, as well as its self-similarity and fractal properties, without considering the details of the particular conditions under which turbulence is excited. An analysis of the self-similarity properties of turbulence (or equivalently a search for statistical symmetries and a study of the fractal

properties of turbulence [26]) led to the models of fully developed turbulence for hydrodynamic systems, such as the log-normal Kolmogorov model [15] (published in 1962 and known as K62), the multifractal [25, 30] and log-Poisson [16, 17] models. In the K62 model, Kolmogorov proposed to account for the local inhomogeneity of turbulence. A.N. Kolmogorov originated the similarity hypothesis (power laws) for the moments of the dissipation energy and formulated the normal law for the logarithm of the dissipation energy (the log-normal law). The hypothesis of the log-normal distribution was confirmed neither experimentally nor theoretically. But in accordance with Kolmogorov's approach, studies of the similarity laws for the moments led to the development of later turbulence models, in particular, of the most common one—the log-Poisson model.

All models of intermittent turbulence have adjustable parameters that are difficult to determine from the first principles and physical arguments and that provide enough freedom to account for the experimentally determined values of $\zeta(q)$, the scaling exponent of structure functions.

The log-Poisson model [16, 17], in which a stochastic multiplicative cascade is considered and the logarithm of the dissipation energy is described by a Poisson distribution, provides the most complete and detailed description of intermittent turbulence. This model makes use of a hierarchy of moments, the existence of limiting dissipative structures, and power laws. Such characteristics agree with the most common turbulence properties that are observed in experiments, in particular, with the ESS property. The log-Poisson model is advantageous in that it takes into account the dissipative range of turbulence—a case in which boundary effects play an important role in a system with a relatively low Reynolds number and a limited (in the classical sense) inertial range. The ESS property accounts for boundary effects and implies that self-similarity occurs on a finite spatial and temporal scale rather than in infinite space, thereby providing a natural means of analyzing the viscosity (dissipation) effects and the properties of limiting dissipative structures (in particular, their dimension). For instance, the log-Poisson model of three-dimensional (3D) isotropic hydrodynamic turbulence assumes a filamentary geometry of limited (singular) dissipative structures [16, 17]. The log-Poisson model that accounts for two-dimensional (2D) Iroshnikov–Kraichnan (IK) empirics describes 2D singular dissipative structures [31, 32]. The ESS of the log-Poisson process establishes long-range correlations, which give rise to an anomalous process—superdiffusion. In edge plasma of fusion devices, this property leads to enhanced plasma losses and degrades plasma confinement.

Incompressible hydrodynamic turbulence in K41 is considered as a hierarchical energy cascade from the largest scales (where energy is injected) to smaller scales, where viscosity becomes substantial and leads to dissipation. At large Reynolds numbers, $Re \gg 1$, a statistical quasi-equilibrium of fluctuations is established in the process of energy transfer from large turbulent eddies towards smaller ones within the inertial range l ($\eta \ll l \ll L$, where L is the largest eddy/structure scale and η is the dissipation scale).

Turbulence in neutral fluids is approximately isotropic in a reference frame moving at mean velocity. The magnetic field in a turbulent plasma induces an anisotropy of the dynamics, since field lines can easily be shifted but resist bending. In a plasma with a strong magnetic field small scale fluctuations occur mainly in planes perpendicular to the magnetic field, making the turbulence anisotropic [2]. Iroshnikov and Kraichnan (IK) [34,35] include the influence of a magnetic field via mutual scattering of Alfvén waves triggered by velocity fluctuations, the IK fluctuations having the energy spectrum $E_k \sim k^{-3/2}$. An essential

assumption of the IK phenomenology is that the eddy size is the same parallel and perpendicularly to the magnetic field (isotropic and incompressible approach). The validity of the K41 and IK paradigms in MHD turbulence and plasma confined in fusion devices is still under discussion (see, i.e., debates in [36-37,2]).

Plasmas may be modeled most accurately by using the kinetic theory. Many plasma simulation codes are based on magnetohydrodynamic (MHD) models generated by taking the moments of the Vlasov equation and averaging over velocity space for each plasma species. MHD is the convenient framework to describe magnetic turbulence in astrophysical systems [2].

Edge plasma turbulence in fusion devices is treated by models starting from the Braginskii fluid equations [38]. Reduced equations of various subsets of the Braginskii equations have been derived by many authors (see, e.g., [39-42] and references therein) neglecting either electron or ion dynamics, assuming adiabatic electron response etc. The magnetic field contributes to make the turbulent wave-field anisotropic and allows different types of waves to coexist. Equations describing the edge plasma turbulence in fusion devices are nonlinear (see, e.g. [39-42]). In the edge plasma of tokamaks, the pure situation of drift wave turbulence is a slab geometry in a sheared magnetic field, and all its basic processes can be found in simplified two dimensional models (e.g. the Hasegawa–Mima model [43]). A competition between drift wave and interchange physics (in general $E \times B$ drift turbulence), and nonlinear vorticity advection are the processes in edge plasma turbulence of fusion devices [41]. Edge turbulence is characterized by anomalous cross-field transport, strong intermittency, long-range correlation, non-Gaussian statistics. Although 2D models of plasma turbulence predict some typical features of edge turbulence, they cannot treat all properties, especially, as regards intermittency, spectral energy cascades and scale invariance. This limitation of 2D electrostatic models (as well as of other 2D models of magnetized plasma) stems from the treatment of equations with a truncated symmetry reducing the real 3D scale invariance symmetry. Manipulations of 2D models violate a fundamental symmetry of nonlinear motion equations: scale invariance. The alternative approach that is discussed below is based on a fundamental property of the nonlinear motion equations: real scale invariance.

In a neutral fluid the turbulence properties in 2D and 3D differ fundamentally (see, e.g., [26]). In both cases there are three quadratic ideal invariants [2, 44, 36]. The energy $E=1/2\int(v^2+B^2) dV$ and the cross-helicity $H_v=\int v \cdot B dV$, where the spectral densities $E(k)$ and $H_v(k)$ exhibit a direct cascade (the cascade of $H_v(k)$ seems to be of a mixed type). The magnetic helicity $H=\int A \cdot B dV$ in 3D and the mean-square magnetic potential $H_\psi=\int \psi^2 dV$ in 2D, both $H(k)$ and $H_\psi(k)$ are characterized by an inverse cascade. Because of this similarity, many theoretical approaches do not distinguish between 2D and 3D as far as the velocity-magnetic field alignment and the energy spectrum are concerned. Despite this formal similarity, however, there is a substantial difference. While in 2D MHD there are always two ideal invariants, in 3D for $H=H_v=0$ the energy only is ideally conserved. Hence 3D is more hydrodynamic than 2D. Incompressible MHD equations, in the terms of the Elsässer variables (defined as $z^\pm = v \pm (4\pi\rho)^{-1/2}b$, where v and b are the velocity and magnetic field relative disturbance and ρ is the mass density) have the same structure as the Navier-Stokes equations (see, [45]). The governing equations used for a treatment of the edge plasma in fusion devices and astrophysics have similar structure [41,42,2]. This similarity justifies the scale invariance

studying and explains the similar character of energy cascades in plasma turbulence to those of neutral fluid.

Numerical and experimental data indicate that in MHD turbulence the energy transfer occurs predominantly perpendicularly to the magnetic field (see, e.g., [45]). Therefore, the question arises as to whether anisotropy is crucial for the energy cascade, and whether it changes the spectrum of turbulence. The two-dimensional digital numerical simulations (DNS) support the IK picture [32, 46], while three-dimensional simulations exhibit a K41 scaling behavior [36]. Experimental studies of the interplanetary turbulent plasma (solar wind, SW) have demonstrated that the SW turbulence is anisotropic with multi-scale structure and scalings close to those of the IK model [47]. On the contrary, analytical results [31,2] suggest K41 energy spectra, also measured in the solar wind [48]. SW plasma exploration is going on (see e.g. [49]) that might renew the results of Ref. [47]. The Kolmogorov model K41 assumes that the dominating nonlinear cascade process is eddy scrambling (with the energy spectrum $\sim k^{-5/3}$). Conversely, the Iroshnikov-Kraichnan model introduces the Alfvén wave collisions (with the energy spectrum $\sim k^{-3/2}$). The IK phenomenology (that was the dominating candidate for describing of strong MHD turbulence) leads to a reduction of problem symmetry. Reducing a 3D problem to a 2D problem leads to neglecting important effects related to the geometry of singular dissipative structures in 3D space. A Kolmogorov-type energy spectrum, with wave vectors perpendicular to the local magnetic field, can also be derived from Alfvén wave collisions under the assumption of a critical balance proposed by Goldreich and Sridhar [50].

Goldreich and Sridhar [50] have postulated a balance between K41 and IK energy cascades and have accounted for the local anisotropy induced by a magnetic field. Goldreich and Sridhar have also suggested that anisotropy increases with k_{\perp} and that the energy cascading along k_{\perp} is more effective than along $k_{||}$. The field-parallel and field perpendicular scales are found from a critical balance condition. The field-parallel scale of an eddy is found from a balance of linear and nonlinear terms in the MHD equations. The field-perpendicular scale of an eddy can be obtained from the requirement that the eddy size perpendicularly to the magnetic field is comparable with the magnetic field line displacement. The GS model assumes that eddies are filamentary. The GS model considers “intermediate” turbulence [2]. Direct numerical simulation (DNS) claims to support this picture in MHD turbulence [51, 52]. Using the same approach Boldyrev [53] has assumed that eddies have a current sheet like shape.

In the edge of a fusion device, the inertial range of turbulence is rather limited. Large scale (a scale of boundary layer) and small scales (ion gyroradius or Debye length) are close, unlike in the 3D isotropic fluid turbulence considered by the K41 model. Turbulent fluctuations on the smallest scales depend on the character of the dissipation processes. A direct interaction between large and small scales is possible, without a need for passing sequentially through the full cascade. The boundary conditions of this problem include large-scale motion and dissipation properties at small scales. These boundary effects are related not only with geometrical limitations of the flow, but also with bounds of the energy cascade. Such effects discriminate the intermittent turbulence of edge plasma in fusion devices from other turbulent flows.

To quantify whether boundary conditions influence the statistical properties of turbulence a multifractal formalism was proposed (see [26]). Stochastic multifractal fields overcome the

strong limitations of traditional approaches for the exploration of extremely variable fields. The multifractal theory uses a saddle point evaluation in determining the power-law behavior of structure functions. It is clear now that a very general outcome of stochastic cascades is multifractal measures. A multifractal approach advance is that it can treat and analyze the turbulence self-similarity from the largest to the smallest scales considering large scales (e.g., structures, blobs, jets etc.) coupled with intermediate and small scales. A log-Poisson multifractality proposal is in fact a weak hypothesis of turbulent cascades universality [54].

In this review article, edge plasma turbulence in fusion devices tokamaks, stellarator and linear machine are described. Experimental results obtained in edge plasma regions with open magnetic field lines – scrape-off-layer (SOL) – are discussing in the next Sections. The SOL region is characterized by enhanced turbulent transport leading to the anomalous losses of plasma from confining volume. We focus on the scale invariance property of the turbulence and test several analytical fits.

2. EDGE PLASMA IN FUSION DEVICES

Experimental results obtained last decade have shown that intermittent turbulence of plasma in edge of tokamaks, stellarators and linear devices has similar properties supposing universality of the phenomenon. Despite the different magnetic topology of tokamaks, stellarators and linear devices parameters of intermittency in boundary layer of plasma discharge (SOL) are similar. In this article, analysis of experimental data from T-10 tokamak (Kurchatov Institute, Moscow) [55, 56, 57], Large Helical Devise (NIFS, Toki) [55,4], HYBTOK-II tokamak (Nagoya University, Nagoya) [55,4] and NAGDIS-II linear device (Nagoya University, Nagoya) [55,57] are reviewed.

The T-10 tokamak [4,55] has a major radius of $R=1.5$ m, a minor radius of $r=0.4$ m and operates typically at plasma currents of 200-300 kA, toroidal magnetic field of 2-2.2 T, central chord-averaged plasma density and electron temperature of $\sim 1\text{-}2 \times 10^{13} \text{ cm}^{-3}$ and $\sim 1\text{-}2 \text{ keV}$, respectively. A rail limiter was positioned at 30 cm producing a scrape-off layer (SOL) at $r>30$ cm. A natural shear of poloidal rotation (shear layer) is observed at $r\approx29$ cm in the vicinity of the last closed magnetic flux surface (LCFS). Langmuir probe signals [4,55] have been analyzed: ion saturation current I_{sat} , that is essentially plasma density n_e , and cross-field particle flux Γ estimated from poloidal electric field and I_{sat} . The reference potential for the probe characteristics is the ground potential of the tokamak vacuum vessel. No evidence of probe-induced plasma perturbation on the fluctuations has been observed in these experiments. It was studied the radial range of $29 < r < 36$ cm through a sequence of repetitive ohmic discharges with no large scale MHD activity in the tokamak. The plasma parameters in the SOL region substantially change, demonstrating strong plasma fluctuations and anomalously high transport across the magnetic field. Average plasma parameters and statistical measures demonstrate a strong variation in space (along poloidal and radial extension) [4]. Cross-field pressure gradients in SOL drive strong turbulence. Fluctuations of plasma density, poloidal electric field and radial plasma flux exhibit intermittent behaviors [4,55]. Such behaviors are typical for SOL plasma in tokamaks and stellarators [3-8].

The linear divertor plasma simulator NAGDIS-II has a plasma column of 2.5 m in length and about 30 mm in diameter and can generate high density helium plasma with electron

densities up to 10^{20} m^{-3} , electron temperatures of 1-3 eV, and magnetic field $B= 0.25 \text{ T}$ in a steady state [58]. The plasma column simulates a scrape-off layer with a variation of plasma turbulence properties from the centre of the plasma column to the edge [55]. By increasing the neutral gas pressure in the divertor test region, the detached plasma condition can be achieved. The detached plasma (observed as well in tokamak experiments) is characterized by a decreasing of plasma heat load on the wall. A bifurcation from the attached to the detached state is characterized by a reconstruction of a spatial structure of turbulent plasma transport and turbulence property. Statistical measures of detached plasma turbulence are deviated from that of attached plasma [55]. The turbulence signals from attached and detached plasma are available for a comparative analysis of different states of plasma turbulence. The ion saturation current I_{sat} has been measured by Langmuir probes in the radial range $0 < r < 36 \text{ mm}$ in the upstream and downstream region.

Large Helical Device has a set of $l = 2/ m = 10$ continuous helical coil and three sets of poloidal coils, producing a heliotron-type magnetic configuration [59]. The major radius R is 3.9 m and the averaged minor radius a is 0.65 m . The edge magnetic structure is more complicated than that in the SOL of divertor tokamaks. An intrinsic divertor exists without additional coils, and four plasma legs reach the divertor plates. The natural island layers overlap and the stochastic field structure (stochastic layer) appear between the LCFS and the residual X-point [59]. This magnetic configuration is a natural helical divertor. Ion particle flux to the divertor plates follows the deposition profile of the magnetic field lines. Ion saturation current I_{sat} was measured with the Langmuir probe array (16 channels) embedded in the divertor plate. The Langmuir probe graphite electrodes (of a dome-type with a diameter of 1 mm) were separated by 6 mm . The probe electrodes are numbered from 1 to 16 starting from the lower right. The lower numbered probes are located in a low field side and the higher numbered ones are in a high field side, because the magnetic field strength near the helical coils is always strong. It were analyzed signals from probes on the inboard-side divertor plate, the operating magnetic axis and field strength were $R_{\text{ax}}=3.6 \text{ m}$ and 2.75 T , respectively. The magnetic field line with large connection length L_c reaches the ergodic layer surrounding the core plasma region. L_c varies from less than a few meters to over a few kilometres. The probe connected to the field line with a large L_c has a large ion particle flux.

In HYBTOK-II small tokamak it was investigated the boundary plasma with the movable Langmuir probe installed at a mid-plane of the tokamak [60]. It is composed of 4 tungsten tips with 0.5 mm in a diameter and 0.5 mm in a length. We have measured I_{sat} in the experiment with Rotating Helical Magnetic Fields (RHMF) [61], [62] that produces a dynamic ergodic divertor. The RHMF can drive a modification of the edge plasma structure and the turbulence. Measurements in the SOL and inside the LCFS at the region of a maximal effect of the RHMF ($r/a \approx 0.75$) have been done. The data were collected during 10 ms at a steady state phase.

Experimental signals are digitized with a sampling rate of 1 MHz by 12 bit ADC, and with the sample number of $10^5 - 10^6$.(in HYBTOK-II tokamak the sample number of $2 \cdot 10^4$)

Data from fusion devices used in this article were obtained in plasma regions with open magnetic field lines. An estimation of kinetic (Re) and magnetic (Re_m) Reynolds numbers for turbulence in the SOL of fusion devices is a complicated issue. From the plasma velocity data and theoretical estimations [55] Re , Re_m could be in the range from 10 to 1000, the magnitudes are much less than for a strong MHD turbulence in the hot plasma core in large-scale fusion devices and in the interplanetary plasma, where Re , $\text{Re}_m > 10^5 - 10^7$.

The understanding of intermittency relates to a problem of chaotic motion description of individual fluid particles and characteristics of mixing flows. Most of the experimental work has been obtained in the Eulerian framework. Lagrangian measurements are challenging because they involve the tracking of particle trajectories. For a detailed introduction to the statistical mechanics of Eulerian and Lagrangian turbulence see reviews [62], [26]. In neutral fluid turbulence and MHD turbulence of interplanetary plasmas, Lagrangian information has been extracted following Taylor's approach of frozen flux in the wide range of scales. This hypothesis is widely used for a description of homogeneous and isotropic turbulence. In the edge plasma of fusion devices, the boundary effects and a strong anisotropy may eliminate a validity of the frozen flux approximation in the intermediate scales. To characterize an intermittency of the developed turbulence in the Eulerian framework we may consider a mixing and a chaotic motion due to Lagrangian chaos phenomenon [63]. The chaotic motion means an exponential separation of close trajectories. In presence of Lagrangian chaos it is expected that relative separation between an advected tracer $l(t)$ typically growth exponentially in time only for a separation $l \ll \eta$, where η is the characteristic scale of the smallest Eulerian structures (i.e., dissipative eddies in plasma turbulence). In 3D homogeneous fully developed turbulence in the inertial range $\eta \ll l \ll L$ the Richardson law $\langle l^2 \rangle \sim t^3$ and standard diffusive regime $\langle l^2 \rangle \sim t$ for very large separations $l > L$, are assumed to treat the scaling property. In order to keep in the Eulerian framework considering anisotropic and intermittent turbulence, we may assume power laws $\langle l^2 \rangle \sim t^h$ (i.e., index h may depend on a scale) being more general than the Richardson law. To overcome the difficulties a multifractal approach may be used. The intermittency can be described quantitatively in terms of a multifractal formalism that is a bridge between Eulerian and Lagrangian descriptions (see, e.g., [33]). To investigate a time intermittency we constructed the high-order structure functions from the time-dependent signals of the ion saturation current $I_{\text{sat}}(t)$ (related to a local plasma density) and cross-field particle flux Γ by ensemble averaging,

$$S_q(\tau) \equiv \langle |I_{\text{sat}}(t+\tau) - I_{\text{sat}}(t)|^q \rangle \quad \text{or} \quad S_q(\tau) \equiv \langle |\Gamma(t+\tau) - \Gamma(t)|^q \rangle.$$

3. POWER SPECTRUM AND CORRELATIONS

Typical time traces of the density $n(t)$ fluctuations in edge of fusion devices are shown in figure 1a. The signals possess a high frequency part and the peaks of total intensity (referred as the bursts) caused by the intermittent structures. There exist fluctuations in each burst (figure 1b) and maxima are separated by a time greater than the auto-correlation time. The characteristic time scale of the bursts is of 40-200 μs . The fraction of time spent by signal in the bursts (that are defined as the peaks of total intensity with amplitude above a certain threshold of 3 times the standard deviation) is of $\sim 10\%$.

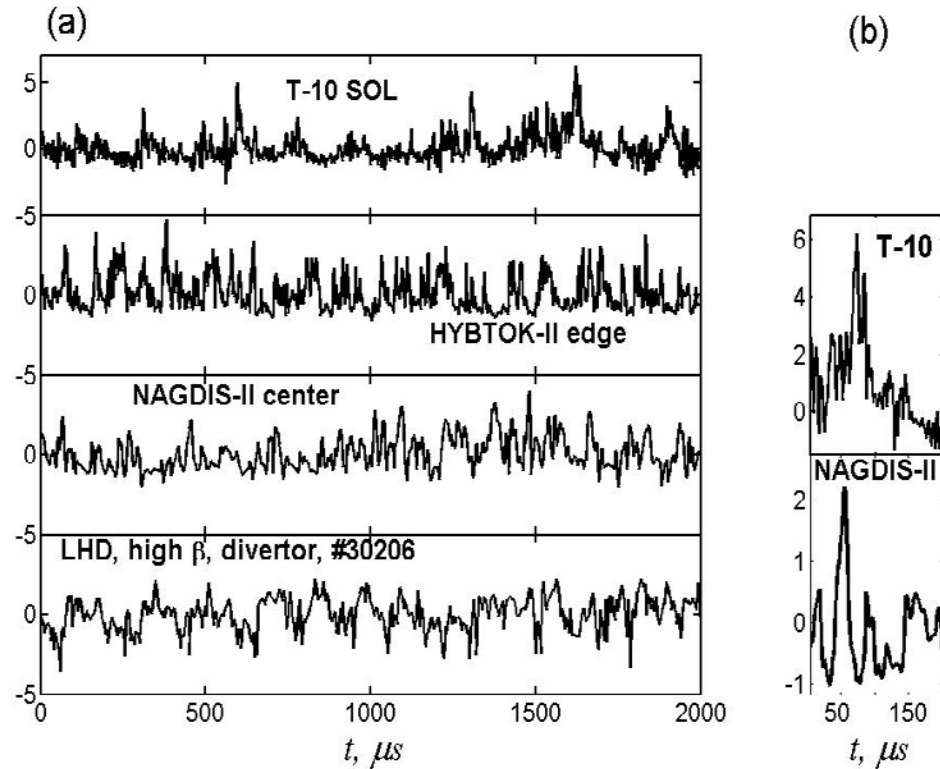


Figure 1. (a) Time traces of density fluctuations (subtracted by mean value and normalized by standard deviation) in magnetized edge plasmas: in the T-10 tokamak SOL plasma at $r=34$ cm, edge plasma in HYBTOK-II at $r=10$ cm, in the NAGDIS-II attached plasma at $r=0$ cm, divertor probe in the LHD shot# 30206. (b) Typical burst's shape in the T-10 SOL and NAGDIS-II.

The scaling features of complex processes can be studied by means of various numerical approaches such as Fourier and correlation analyses. The shapes of the spectral density $S(f)$ and the correlation function $C(l)$ allow one to conclude whether the scaling behavior of a time series can be described by power-law dependences of the type $S(f) \sim f^{-\gamma}$ and $C(l) \sim l^b$ with the single exponents γ or b .

The power spectrum, $S(f)=|n(f)|^2$, of the turbulent fluctuations quantifies the properties of the process. In the developed turbulence of incompressible fluid, Kolmogorov theory (K41) predicts the so-called inertial subrange, with self-similar properties leading to a power law dependence, $S(f) \sim f^{-\gamma}$, $\gamma=1$. In our experiments, several scaling ranges with respect to the frequency are registered in the frequency spectra of density fluctuation (figure 2) with no $1/f$ behaviour. Similar behaviour of power spectra was obtained in another experiment using Langmuir probes in edge plasmas [5-8]. Typical value of scaling exponent of the power spectra in the high frequency range above ~ 100 kHz is in the range of $\gamma \approx 1.2 \div 2.5$ (figure 2). The spectra scaling exponent γ is highly nontrivial and demands theoretical understanding.

Auto-correlation function quantifies the correlation properties and correlation time. Typical auto-correlation function is shown in figure 3. The tails of auto-correlation function oscillate demonstrating long-range “memory” effect in the process. In log-log plot the auto-correlation function exhibits highly nontrivial decay, there exist several ranges fitted by

power law $C(l) \sim l^{-b}$ demonstrating inhomogeneous and nontrivial process. Only in very narrow range of lags fittings with exponents $b=2.4 \pm 1.3$ and 3.3 ± 1.1 are shown in figure 3. Non-trivial self-similarity of the turbulent process with long-range correlation is discussed in next Sections.

From the correlation and Fourier analysis there is no trivial self-similarity in the turbulent process. One of the disadvantages of the above approach of traditional correlation and Fourier analyses arises from their restriction to stationary data. Since processes in fusion plasmas are highly inhomogeneous and non-stationary, we need a technique that possesses the lack of restrictions with respect to the homogeneity and the stationarity of the data series. Such rather universal and effective tool for signal processing are the probabilistic approach and struture function method. Application of this methods to the experimental data is described in the next section.

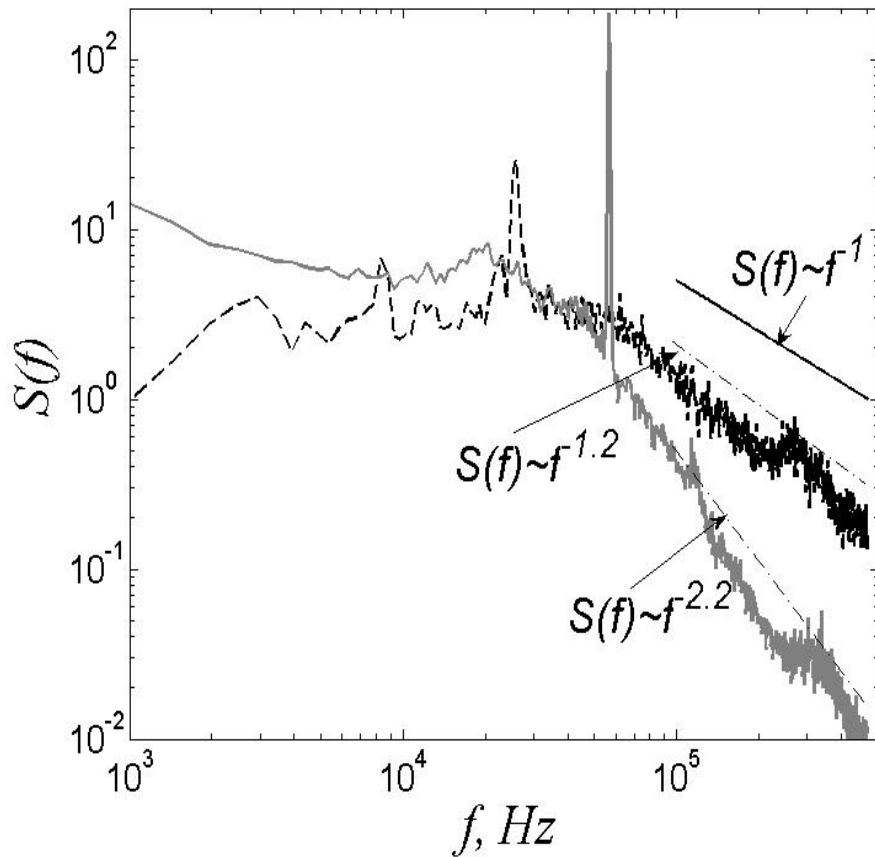


Figure 2. Power spectra $S(f) = |n(f)|^2$ of the density fluctuations. Dashed line – T-10 shear layer $r/a=0.95$, solid grey line –NAGDIS-II detached plasma. The power-law fits with corresponding values of exponent (slightly shifted for better visibility) are shown by dashed-dot lines. For comparison, a power-law fit of $1/f$ spectrum is shown by solid line.

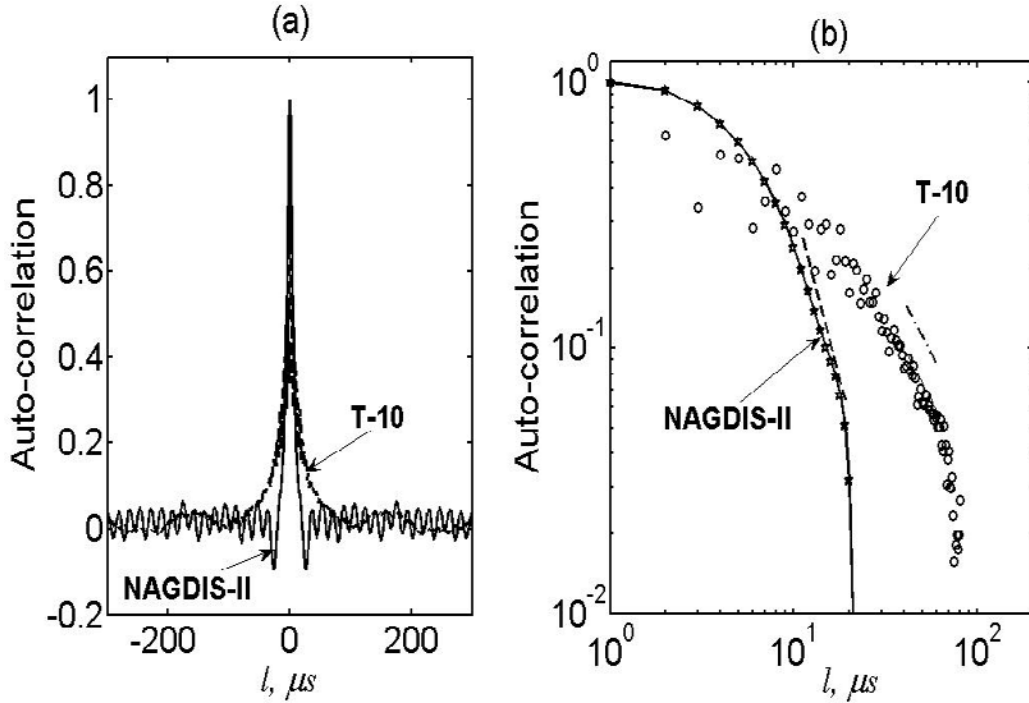


Figure 3. (a) Typical auto-correlation function of the density fluctuations. Dashed line – the T-10 SOL, solid line –NAGDIS-II attached plasma. (b) Auto-correlation function in log-log plot. The doted lines are the power-law fits for the narrow region (slightly shifted for better visibility), $C(l) \sim l^v$, $v=2.4$ the T-10 and $v=3.3$ for the NAGDIS-II.

4. PROBABILISTIC APPROACH AND THE MULTIFRACTAL STATISTICS

The fluctuations observed in tokamaks, stellarators and linear machines are self-similar suggesting the universality of self-similarity properties in the edge of magnetized plasmas [4-8,13,14,23]. The detailed features of edge plasma turbulence and transport can be investigated by focusing on a probabilistic approach.

In understanding of plasma turbulence we compare the dynamics of plasma with neutral fluid turbulence [26,33]. There are some differences between plasma turbulence and fluid turbulence: plasma turbulence has more distributed driving and dissipation ranges. Approach based on the probability density function prediction, development of probabilistic theory of anomalous transport and superdiffusion in fusion devices, is one of the perspective way to describe intermittent anomalous transport observed in fusion plasmas. Particular interest is the open question of how “non-locality” and fast bursty transport (superdiffusion) are linked to self-similarity (fractality).

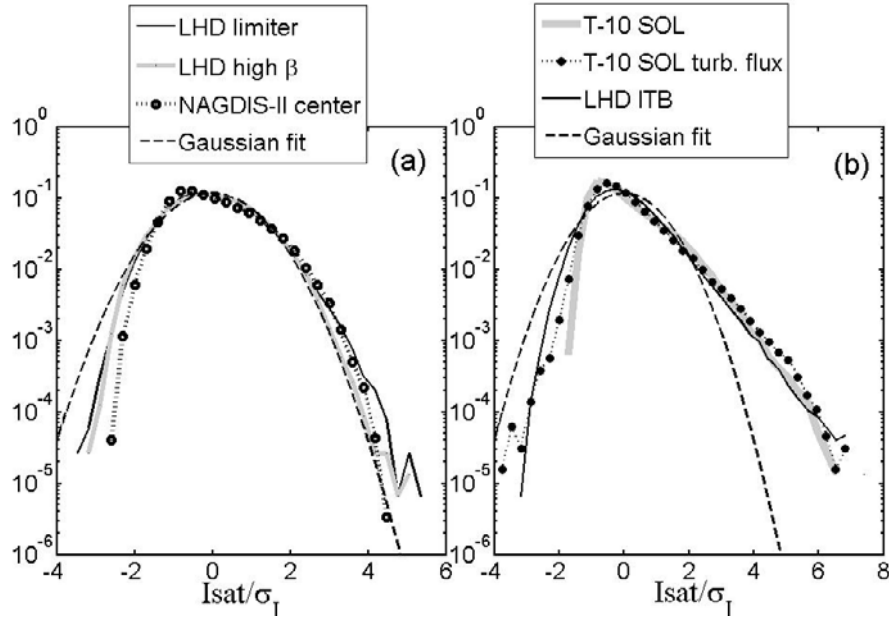


Figure 4. Log-log plots of typical probability density functions of fluctuations in edge plasmas. Density fluctuation signals from (a) divertor probes on the LHD in limiter and high β shots , centre of NAGDIS-II. (b) divertor probes on the LHD in ITB shot and T-10 tokamak SOL plasma. Gaussian fits of the pdf's are shown in solid lines.

Monofractal Kolmogorov's cascade model K41 is now significantly reconsidered. It has been argued that the effects of boundary conditions influence large-scale motion and direct interaction between large and small scales is possible by means other than passing sequentially through the full cascade. In the developed turbulence of incompressible fluids, Kolmogorov (1962) [64] formulated hypothesis invoking some statistical independence in the cascading process, which led to the log-normal model for the rate of dissipation of turbulent kinetic energy. To quantify whether boundary conditions influence the statistical properties in turbulence it was proposed multifractal formalism [26,26]. The multifractal theory uses a saddle-point evaluation in determining the power-law behaviour of structure functions. Using multifractal formalism, we analyse the probability density function (pdf) and self-similarity of the plasma turbulence over time scales, from $1\ \mu\text{s}$ (less than the auto-correlation time) up to $\sim 10^4\ \mu\text{s}$ (the magnitude of the energy confinement time).

Probability Density Function

The probability density function (pdf) $P(x)$ is an important statistical quantity for turbulence research. It is a powerful characteristics for comparative analysis: if pdf's for two processes have the same profile, the turbulence quantities computed from such pdf's have the same values. In order to obtain the pdf function, we construct a histogram of the experimental signal. The bin size is set at 0.1σ in this analysis, where σ is a standard deviation of the fluctuation. For fully random signal, the pdf has Gaussian profile. In fully developed turbulence the deviation from Gaussian is called intermittency where

inhomogeneous distribution of the fluctuations leads to a coherent structure formation. In edge plasmas of fusion devices, pdf's of density fluctuations are typically non-Gaussian and positively skewed (see, f.e. [8,29]). For edge plasma turbulence, typical pdf's are shown in figure 4, illustrating intermittent character of the process. Non-Gaussian statistics of density fluctuations transforms in the same statistics of cross-field turbulent particle flux ([29]).

Scale Symmetry of Generating Equations

The reduced magnetohydrodynamic equations (Kadomtsev–Pogutse equations [65], and others) are frequently used to describe plasmas embedded in a very strong magnetic field of fusion devices. Equations described the edge plasma turbulence are nonlinear (see, e.g. [41] and references therein). The pure situation of drift wave turbulence is slab geometry in a sheared magnetic field, and all of its basic processes can be found in the simplified two-dimensional models (Hasegawa-Mima model [43]). Reach properties of the edge turbulence should be considered in three-dimensional models. In edge turbulence, the competition between drift wave and interchange physics in general $E \times B$ drift turbulence and the nonlinear vorticity advection (see, e.g., [41], [42]) derive a turbulent motion with strong intermittency. Generally, the governing equation can respect (more or less formal) scale symmetries. This is known as “self-similarity”. Governing equations described neutral fluid turbulence are the Navier-Stokes equations:

$$\partial_t \mathbf{v} + \mathbf{v} \cdot \nabla \mathbf{v} = -\nabla p/\rho + \nu \Delta \mathbf{v} + \mathbf{f} \quad (2)$$

(where \mathbf{v} is the velocity field describing a turbulent flow, p is the pressure, ρ is the density, ν is the kinematics viscosity, \mathbf{f} is the forcing density).

The edge plasma turbulence is treated by models starting from Braginskii fluid equations [38]. Reduced equations of various subsets of Braginskii equations have been derived by many authors ([40], [41], [39],[42],[66] and references therein) neglecting either electron or ion dynamics, assuming adiabatic electron response and applying other approximations. Governing equations are more complicated than the Navier-Stokes equations. At the same time, all these governing equations remain formally invariant (same as the Navier-Stokes equations) under any affine contraction of the time-space $x \rightarrow x/\lambda$, $t \rightarrow t/\lambda^{1-h}$, (of scale ratios λ). As well, the dependent variables are suitably renormalized:

$$\mathbf{v} \rightarrow \mathbf{v}/\lambda^h ; \quad \rho \rightarrow \rho/\lambda^h ; \quad \nu \rightarrow \nu/\lambda^{1+h} ; \quad \mathbf{f} \rightarrow \mathbf{f}/\lambda^{2h-1} \quad (3)$$

Governing equations are often treated as associated with advection-diffusion equations for a scalar field θ (see, e.g., in neutral fluids [67] , and in edge plasma [68]):

$$\frac{\partial \theta}{\partial t} + (\mathbf{v} \cdot \nabla) \theta = \chi \nabla^2 \theta + f_0 , \quad (4)$$

(f_0 – forcing density for the scalar, χ - diffusivity), they remain invariant under above transforms, as well, $\theta \rightarrow \theta \lambda^h$.

The basic mathematical properties of their solutions (e.g. existence and uniqueness) are unsolved “Hilbert problems”. The Lie symmetry method [69] is generally capable of detecting both simple geometric symmetries of systems of partial differential equations (e.g., rotations, scaling transforms and translations), and more complicated ones. When the Lie transformations are found, they can be used to build particular solutions of the system under consideration, to reduce the order and to obtain invariants. Self-similar solutions can be constructed from Lie symmetries [70]. Considering a symmetry classification problem, the symmetry properties of the MHD equations [71], [72], [73] have general peculiarities equivalent to the symmetries of the Navier-Stokes equations (see, e.g., [74],[75]). A particular solution depends on the concrete boundary conditions imposing topology of electric and magnetic fields and admitting a symmetry (i.e., scale invariance) property of governing equations.

A similar scale invariance of velocity and density variables Eq. (3) may be an argument to analyze the scaling laws (dilatation group) of time intermittency by a treatment of plasma density fluctuations. From this scale invariance property we may expect that non-linear scaling laws of density fluctuation related with scaling laws of velocity field. A proof of this assumption is needed in future plasma experiments.

Multifractal Description of Intermittent Turbulence

Monofractal Kolmogorov’s cascade model K41 is now significantly reconsidered. It has been argued that the effects of boundary conditions influence the large-scale motion and direct interaction between large and small scales is possible by means other than a passing sequentially through the full cascade. In the developed turbulence of incompressible fluids, Kolmogorov (1962, K62) formulated hypothesis involving some statistical independence in the cascading process, which led to the log-normal model for the rate of dissipation of turbulent kinetic energy. To quantify whether boundary conditions influence the statistical properties in turbulence it was proposed a multifractal formalism (see review [26]). The multifractal theory uses a saddle-point evaluation in determining the power-law behaviour of structure functions. The multifractal formalism for turbulent flows has been introduced in order to describe the anomalous scaling for structure functions (moments of velocity increments) of turbulence at large Reynolds numbers [26].

Kolmogorov assumed that at large Reynolds numbers ($v \rightarrow 0$) the rate of energy dissipation is constant and exponent of scale invariance in Eq. (3) $h = 1/3$. Involving statistical independence in the cascade and developing Kolmogorov’s theory , Parisi and Frisch assumed [26], [30] that the velocity field is local scale-invariance with continuous spectrum exponents h , each of them belongs to a given fractal set Ω_h with dimension $D(h)$:

$$\delta v l(x,t) \sim (l/L)^h , \text{ for } x \in \Omega_h \quad (5)$$

for h ranges in $h \in [h_{\min}, h_{\max}]$

The probability to have a given δv in a sphere of radius l (on the set with dimension $D(h)$) is $P_h(l) \sim (l/L)^{3-D(h)}$. So, the structure function assumes the form:

$$S_q(l) = \langle |\delta v_l|^q \rangle \propto \int_{h_{min}}^{h_{max}} \left(\frac{l}{L}\right)^{hq} \left(\frac{l}{L}\right)^{3-D(h)} \mu(h) dh \sim \left(\frac{l}{L}\right)^{\zeta(q)} \quad (6)$$

where $\mu(h)$ is a smooth function independent of l . If $l/L \ll 1$, using a saddle point estimate one obtains :

$$\zeta(q) \equiv \min_h \{hq + 3 - D(h)\} = h^* q + 3 - D(h^*) , \quad (7)$$

where h^* is a solution of the equation $D'(h^*(q))=q$ and $D''(h^*(q))<0$. The scaling $\zeta(q)$ depends on the shape of $D(h)$ that has a convex shape. $D(h)$ is called the singularity spectrum. From the analogy [76-78] between the multifractal formalism and statistical thermodynamics, $\zeta(q)$ plays a role of a thermodynamical potential which intrinsically contains only some degenerate information about the Hamiltonian of the problem, i.e., the underlying cascading process. Therefore experimental determination of the $\zeta(q)$ spectrum may provide a test for various cascade models of intermittent turbulence.

The above reinterpretation of the Kolmogorov's theory naturally opens the way to describe intermittent fluctuations in turbulent flows. The space-time scaling is a crucial and delicate issue considering multifractal fields for the governing equations. The goal is to compute the function $D(h)$ starting or from the equation of motions or from an experimental investigation of a turbulent process. One of the key issue in the multifractal language of the turbulence is to understand in a more constructive way what is a multifractal field and how the fluctuations of h are related to the dynamics of the system. In order to develop any systematic theory for computing $D(h)$ starting from the equation of motions, one has to handle a complex non-linear problem: the way in which a perturbative scheme may be developed strongly depending on reasonable assumptions on the time-space properties of the probability distribution. It is therefore crucial to understand how we can formulate the most general form of a multifractal random field which is consistent with the time and space scaling properties of the governing equations described edge turbulence.

Multifractal Statistics

In fluid turbulence, it is traditional [33] to study the inertial scales and intermittency (as a measure of energy dissipation rate) by looking at the statistics of velocity differences between two times on the same probe. In our analysis of plasma turbulence, we are looking for the self-similarity properties in the signal $X(t)$ (that is time series of plasma density or cross-field particle flux) by consideration of differences (increments) $\delta_t X = X(t+l) - X(t)$.

In the mathematics, a process $X(t)$ is called self-similar of exponent H if for $\forall \lambda > 0$, $\lambda^H X(\lambda t)$ is the same process as $X(t)$. Stochastic homogeneous signals are characterized by single global Hurst exponent H and have the same scaling properties at all time intervals.

Widely used examples of such process are fractional Brownian motion (fBm) and Lévy walks. The Brownian motion is self-similar with an exponent $H=1/2$. The definition above describes only monofractal process.

For monofractal process being self-similar with an exponent H the probability density function (pdf) $P_l(\delta X)$ of increments $\delta_l X$ at scales l and $L=\lambda l$ are related by

$$P_l(\delta X) = \lambda^H P_L(\lambda \delta X) \quad (8)$$

The q th-order moments $S(q, l) = \langle |\delta_l X|^q \rangle$ at scales l and $L=\lambda l$ are related by

$$S(q, l) = S(q, L) \cdot (l/L)^q \quad (9)$$

This is a "monofractal" process with exponent $\zeta_q = qH$.

Another class of stochastic process includes multifractal signals that are described by many local Hurst exponents (or Hölder exponents) quantifying the local singular behaviour and local scaling in time series. According to the definition, the Hölder exponent $h(t_0)$ of a function f at the point t_0 is the greatest h so that f is Lipschitz at t_0 , i.e., there exist a constant A and a polynomial $Q_n(t)$ of order n so that for all t in the neighbourhood of t_0 we have,

$$|f(t) - Q_n(t-t_0)| \approx A |t-t_0|^h \quad (10)$$

It measures the degree of irregularity of f at the point t_0 .

In order to account for multifractality, one has to generalize the classical definition of self-similarity. It was originally proposed in the field of fully developed turbulence [26]. According to definition of self-similarity, a process is self-similar if the increment pdf's at scales l and $L=\lambda l$ ($\lambda > 1$) are related by the relationship,

$$P_l(\delta X) = \int G_{l,L}(u) P_L(e-u \delta X) du \quad (11)$$

where the self-similarity kernel $G_{l,L}(u)$ depends only on L/l . This definition generalizes classical definition. The pdf $P_l(\delta X)$ can be obtained through a "geometrical convolution" between the kernel $G_{l,L}$ and the pdf P_L . In case of self-similar process of exponent H (monofractal), $G_{l,L}$ has a Dirac function low $G_{l,L}(u) = \delta(u - H \ln(l/L))$. In the non-linear case, the moments at scales l and $L=\lambda l$ are related by

$$S(q, l) = S(q, L) \cdot (l/L)^{\zeta(q)} \quad (12)$$

with nonlinear spectrum $\zeta(q)$.

Thus, as far as the pdf of increments $\delta_l X(t)$ at different time scales l are concerned, they will satisfy an evolution equation from "quasi-Gaussian" at very large scale L to fat tailed pdf's at small scales. This transformation of the pdf's for edge plasma turbulence is illustrated in figure 5 where are plotted, in logarithmic scale, the standardized pdf's for different time scales in the range $l=1,2,4,8,16,32,128,256,512,1024$ microseconds.

Multifractal Cascade Process

The study of anisotropic multiplicative random processes in a turbulence has a long history (see, e.g. [79]). A multifractal model originated from the phenomenological assumptions that the successive cascade steps define the fraction of the flux transmitted to smaller scales and that a cascade from scale ratio λ to scale ratio $\Lambda=\lambda\lambda'$ is a rescaled version (by scale ratio λ) of a cascade from ratio 1 to λ' .

One possible interpretation of the multifractal formalism is the multiplicative cascade paradigm, that for any $l < L$, the multifractal theory predicts:

$$\delta v(l) = W(l,L)\delta v(L), \quad \delta v(l) = v(x+l)-v(x), \quad (13)$$

Then, according to the scaling properties of velocity, the generator $W(l,L)$ is a random quantity proportional to $(l/L)^h$. It turns out that for $l_1 < l_2 < l_3$ we have

$$W(l_1, l_3) = W(l_1, l_2) \bullet W(l_2, l_3). \quad (14)$$

The property of the generator W defines a statistics of the process. The scaling function $\zeta(q)$ is nothing other than the characteristic function of the generator $W(l_1, l_3)$ (see, e.g., [80], [81]). So, scaling functions $\zeta(q)$ obtained from experiments help to determine cascading model parameters. The hypothesis on universal multifractal process [80] establishes renormalized nonlinear mixing over finite range of scales. It opens a way for the continuous scale cascade paradigm to overcome a problem of discrete scales in models.

Although stochastic multifractal cascade models of turbulence respect various symmetries of the dynamical equations, namely, the scaling and the energy flux conservation, there is nonetheless a large gap between the deterministic (i.e., Navier-Stokes) equations for the vector velocity field and phenomenological cascades for the scalar energy flux. In order to bridge the gap an extension to vector cascades called "Lie cascades" (see, e.g., [80]), has been considered. However, in this framework, the extra symmetries which must be respected are not yet known.

Multiplicative cascading process has «coarse» time scale L from that iterating towards finer scales. This time scale L is refereed as correlation scale that characterizes coherent event scale in the turbulent plasma. As shown in figure 5, typical scale L is of $\sim 50-100$ μs for the edge plasma.

Multifractal process is described by a set of Holder exponents $\{h\}$ and the spectrum. To determine the whole singularity spectrum $D(h)$ and q th-order moments from an experimental

signal we follow the methods developed for the multifractal analysis of fluid turbulence [55]. It is considered the wavelet transform which has proven very powerful in characterizing the scaling properties of multifractal measures.

One can consider the increments of the process $\delta_l X = X(t+l) - X(t)$. or more generally its wavelet transform $T_\Psi(t, l)$. It allows analyze the process $X(t)$ both in physical space and in scale space. Wavelet analysis is available to analyse scale invariance properties of the signal. The wavelet transform (WT) of the function $X(t)$ is defined as

$$T_\Psi(t, l) = \frac{1}{l} \int_{-\infty}^{+\infty} \Psi\left(\frac{t'-t}{l}\right) X(t') dt' \quad (15)$$

where Ψ is the analyzing wavelet , $l \in R^+$ is a scale parameter and $t \in R$ is a space parameter.

As was proven by [82-83] the WT modulus maxima (local maxima of $T_\Psi(t, l)$ at a given scale l) detect all the singularities of a signal under investigation. The skeleton from the modulus maxima lines contains all information about the hierarchical distribution of the singularities in the signal. Wavelet Transform Modulus Maxima (WTMM) method consists of the space-scale partitioning given by this skeleton to define a partition function which scales , in the limit $l \rightarrow 0^+$, as :

$$Z(q, l) = \sum_{\{t_i(l)\}_i} |T_\Psi(t_i(l), l)|^q \sim l^{\zeta(q)} \quad (16)$$

where $\{t_i\}_i$ are the WT modulus maxima and $q \in R$. . Scaling exponent $\zeta(q)$ of the structure function of order q one can get the Hausdorff dimension $D(h)$ of the subset of R for which the increments behaves as $\delta_l X \sim l^h$. According to the theorem proved in [82-83] , $D(h)$, the singularity spectrum of the function X , is obtained by Legendre transformation of the function ζ_q defined above,

$$D(h) = \min_q (qh - \zeta(q)) \quad (17)$$

The variables h and $D(h)$ play the same role as the energy and entropy in the thermodynamics, whereas instead of the inverse of temperature and free energy we have q and $\zeta(q)$ [82,83]. From a numerical point of view, it is more conveniently to calculate at first the scaling exponents:

$$h(q) = \lim_{l \rightarrow 0} \frac{1}{\ln l} \sum_{\{t_i(l)\}_i} \tilde{T}_\Psi(q, t_i(l), l) \ln |T_\Psi(t_i(l), l)| \quad (18)$$

And

$$D(h(q)) = \lim_{l \rightarrow 0} \frac{1}{\ln l} \sum_{\{t_i(l)\}_i} \tilde{T}_\Psi(q, t_i(l), l) \ln |T_\Psi(q, t_i(l), l)| \quad (19)$$

$$\text{where } \tilde{T}_\Psi(q, t_i(l), l) = |T_\Psi(t_i(l), l)|^q / \left(\sum_{t_i} |T_\Psi(t_i(l), l)| \right)^q \quad (20)$$

We extract the set of Hölder exponent and corresponding singularity spectrum $D(h)$ from log-log plot of $h(q)$ and $D(h(q))$ [82,83]. When increasing $|q|$, oscillations become larger in the logarithmic presentation of $Z(q,l)$ vs. l , which very quickly deteriorate the power-low scaling behavior observed for $q=0$. To make easier and more reliable the regression linear fit estimate of $\zeta(q)$ we analyze $\log_2(Z(q,l)/Z(0,l))$ as a function of $\log_2(l)$. To test the analysis code used for the multifractal analysis, we have used test signal of fractional Brownian motion. It has linear behaviour of $\zeta(q)$ with q .

From the analogy [82,83] between the multifractal formalism and statistical thermodynamics, scaling of structure function $\zeta(q)$ plays a role of a thermodynamical potential which intrinsically contains only some degenerate information about the Hamiltonian of the problem, i.e., the underlying cascading process. Therefore experimental determination of the $\zeta(q)$ spectrum may provide a test for various cascade models of turbulence. The scaling function $\zeta(q)$ is nothing other than the characteristic function of the generator $W(l_1, l_3)$ (see, e.g., [82,83]). So, scaling functions $\zeta(q)$ obtained from experiments help to select a cascading model parameters.

Multifractal Spectra

Using the wavelet technique described we estimate singularity spectra $D(h)$ of experimental data. The signals are characterized by the broadened $D(h)$ spectra being of a convex shape (Figure 6). This is the typical shape of singularity spectra observed in multifractal fields (cf. examples in [78]). $D(h)$ spectra estimated by the WTMM method are plotted in Figure 6 against the Hölder exponent $h^* = l + (h - h_{Dmax})$ (where h_{Dmax} is the Hölder exponent at a maximum of the $D(h)$ spectrum). In this frame, the spectra are centered around 1. Such presentation avoids problems of the WTMM result interpretation (see discussion in Ref. [60]). Because the most important properties of the singularity spectrum $D(h)$ are a convex shape and its broadness (a difference $h_{max} - h_{min}$), the Figure 6 is representative of the multifractality characterization.

For a monofractal process the $D(h)$ spectrum collapses into a point. The maximum of $D(h)$ is in the range of 0.8-1 for all signals. A value close to 1 suggests that the experimental signal is singular almost everywhere. The Hölder exponents exceed that of Brownian signal with $h=1/3$. The broadness of the $D(h)$ singularity spectrum provides a measure of multifractality (deviation from the monofractal K41 model) and lies in the range of 0.5-1.2. This range is typical for the strong intermittency observed in numerical models and experiments in fluids and magnetofluids [78,26,84].

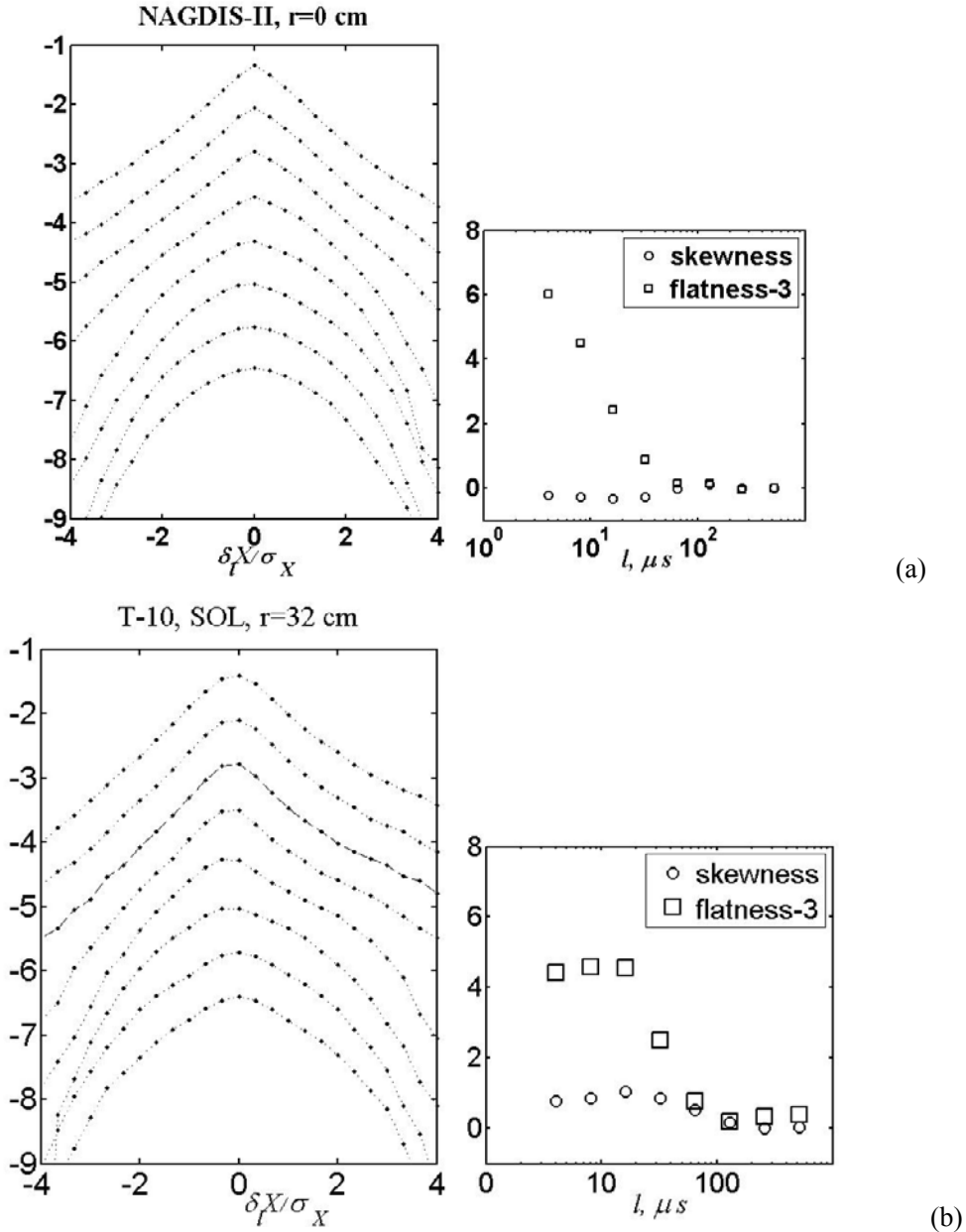


Figure 5. Scaling properties of magnetized plasma density fluctuations as an evidence of multifractality for NAGDIS-II (a) Standardized estimated pdf's of increments $\delta_t X(t)$ (normalized to its standard deviation σ_X) for different time scales (from top to bottom) $l=4, 8, 16, 32, 64, 128, 256, 512 \mu s$ (from top to bottom). Plots have been arbitrary shifted for illustration. One can see continuous deformation from "quasi-Gaussian" at very large scale to fat tailed pdf's at small scales. Third (skewness) and fourth (flatness) moments of the increment pdf's for different time scales l . The appearance of fat tails at the scale related the "coarse" time scale $T \sim 50 \mu s$. (b) the same for the T-10 data, SOL, $r=32$ cm.

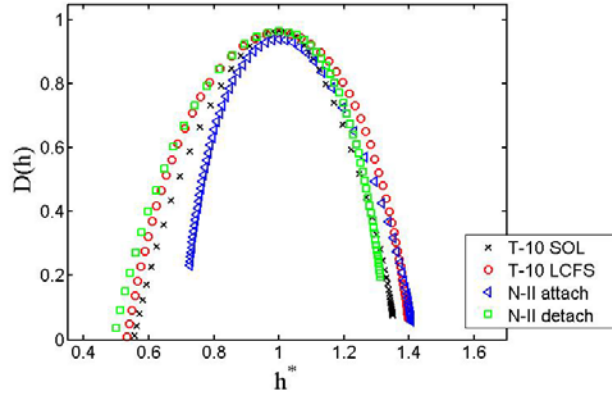


Figure 6. Singularity spectra $D(h)$ plotted against the Hölder exponent $h^* = 1 + (h - h_{D\max})$ (centered around 1 by subtracting $h_{D\max}$). Edge plasma turbulence in tokamak T-10 (T-10 SOL), near the last closed magnetic surface (T-10 LCFS); in NAGDIS-II for attached plasma (N-II attach) and for detached plasma (N-II detach).

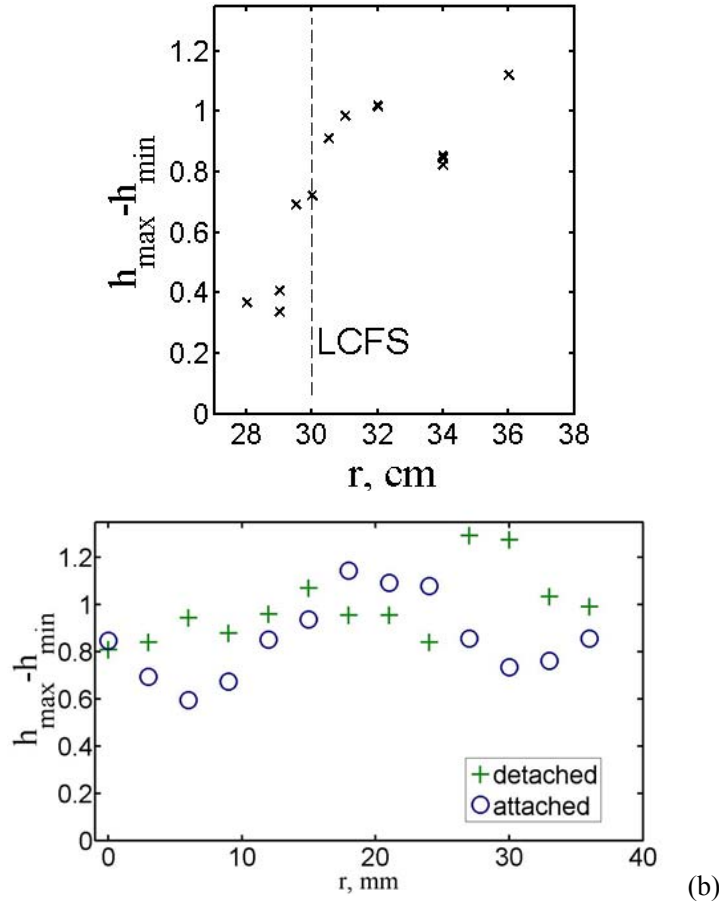


Figure 7. Broadness of the singularity spectrum $D(h)$ (a difference $h_{\max} - h_{\min}$) as a measure of a multifractality (a deviation from monofractal K41 model) vs. radius. (a) Edge of T-10 tokamak; (b) NAGDIS-II in attached and detached plasmas.

The difference between the maximal and minimal Hölder exponents belonging to the same singularity spectrum $D(h)$, was proposed in [85] to characterize a degree of multifractality. Such parameter was computed for data from T-10 tokamak and NAGDIS-II device, Figure 7. This width has a radial dependence in the devices decreasing in the regions where turbulent eddies are likely destroyed or by shear of poloidal velocity (T-10, near LCFS) or by other mechanisms led to a decorrelation effect (in the edge of NAGDIS-II), Figure 7.

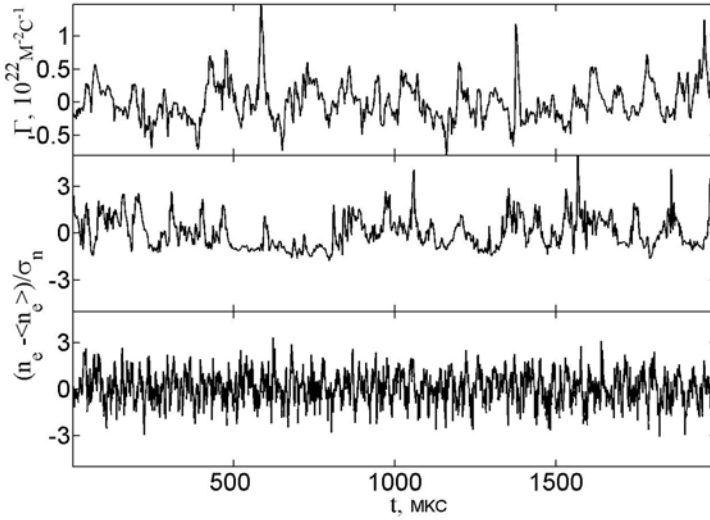


Figure 8. Fluctuating parameters in the SOL plasma in the T-10 tokamak: signal from a cross-field particle flux Γ in the SOL plasma at the radius $r = 36$ cm (top) and signals from a plasma with the density n_e at the radii $r = 32$ cm (middle) and $r = 29$ cm (bottom). The density is normalized by subtracting the mean value $\langle n \rangle$ and by dividing the difference by the root-mean-square deviation σ_n from this mean value.

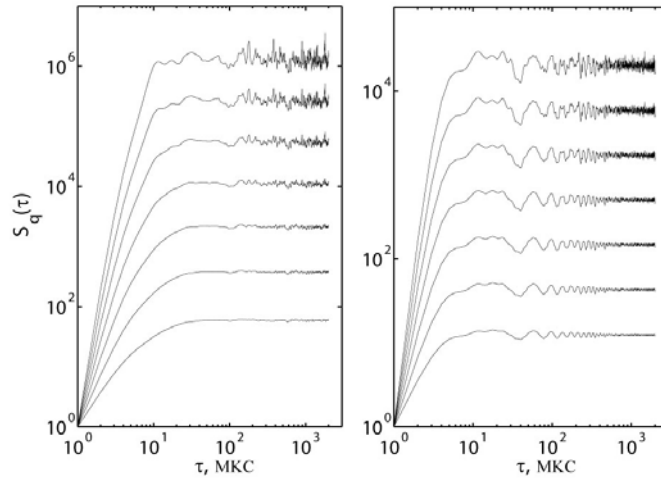


Figure 9. Structure functions of the $q = 2, 3, 4, 5, 6, 7$, and 8 orders (from top to bottom) for signals from a particle flux at $r = 36$ cm (left) and from T-10 tokamak plasma at $r = 29$ cm in the shear layer (right). The functions are normalized to their minimum value.

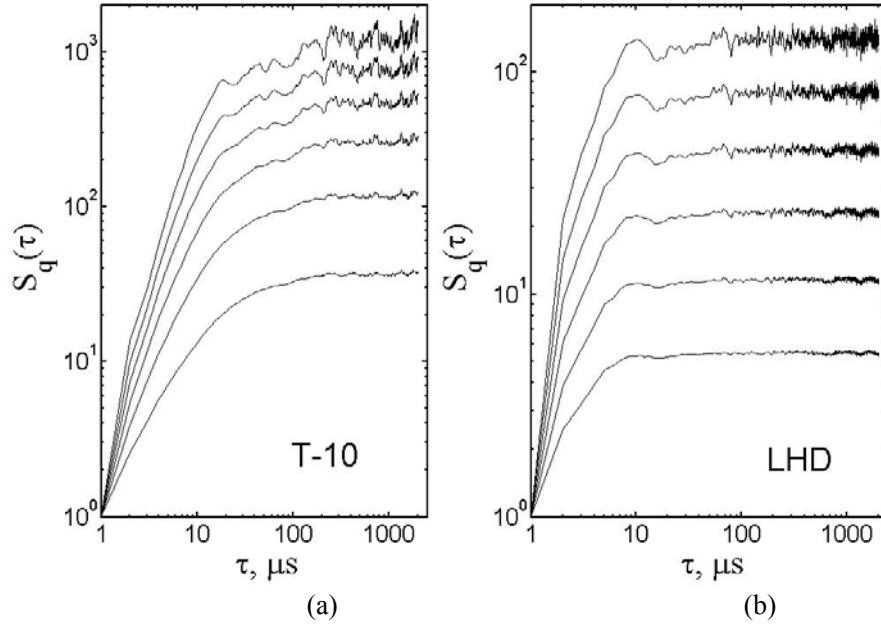


Figure 10 . The high-order structure functions *vs.* time scale τ in log-log plot. (a) T-10 tokamak; (b) heliotron LHD, probe 10 of divertor plate. Linear behavior in the log-log plot is observed in the limited time scale of $\tau < 30 \mu\text{s}$.

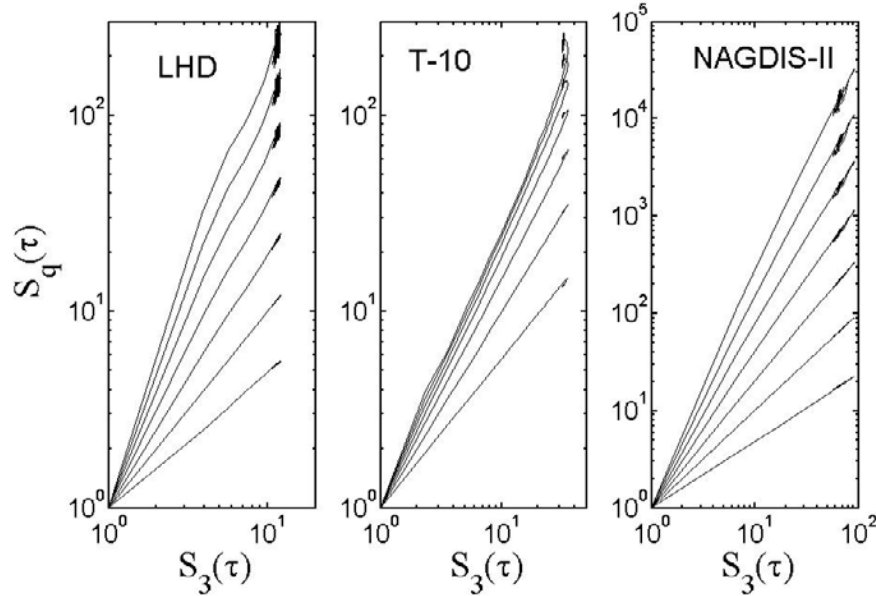


Figure 11. Plot of the high-order structure functions *vs.* third-order structure function for LHD SOL, T-10 SOL, NAGDIS-II detached edge plasmas. A linear behavior is interpreted that the ESS holds.

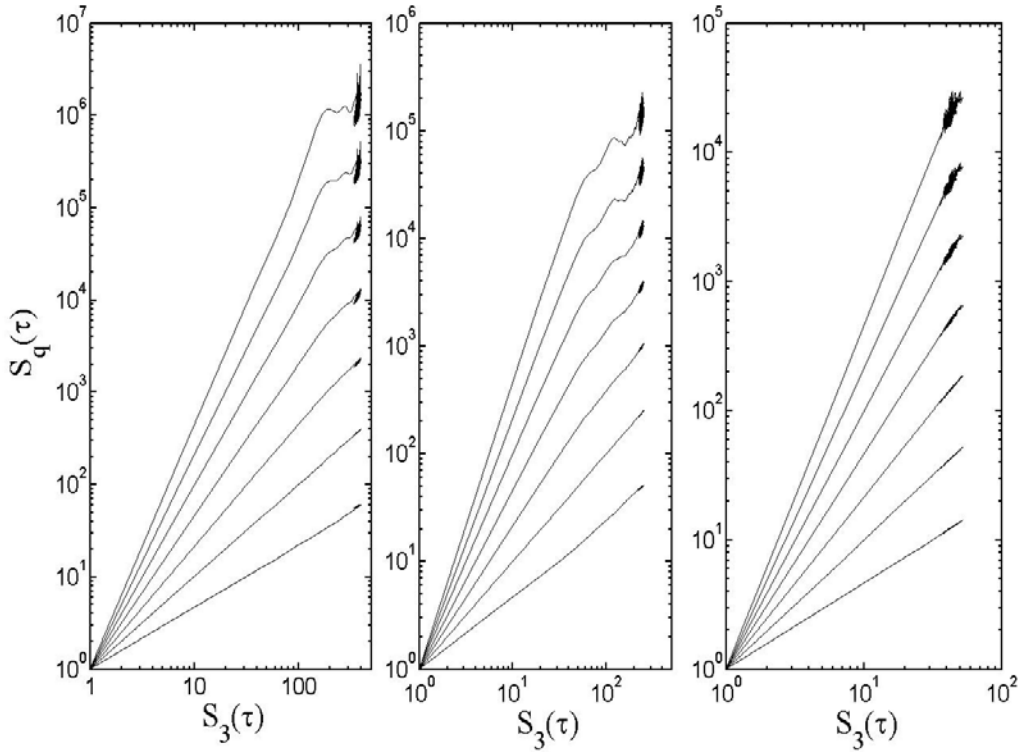


Figure 12. The ESS plot for structure functions of the $q = 2, 3, 4, 5, 6, 7$, and 8 orders (from top to bottom) for signals from T-10 tokamak. Particle flux at $r = 36$ cm (left), from the SOL plasma at $r = 32$ cm (center), and from a plasma at $r = 29$ cm in the shear layer (right). The functions are normalized to their minimum value.

6. GENERALIZED SCALE INVARIANCE OF EDGE PLASMA TURBULENCE

The issue of a scale invariance (a self-similarity or a dilatational symmetry) is important for a turbulence study. The symmetries are presented in the equations of motion. A random motion and the presence of a large number of modes make turbulence amenable for statistical analysis. Turbulence is characterized by the probability density function (PDF) of a fluctuating quantity. The departure of the PDF from the Gaussian shape leads to a break of the trivial self-similarity. It drives non-trivial self-similarity and the intermittency. The intermittency and scale invariance are studied by analyzing the structure functions $S_q(\tau) = \langle |\delta_\tau X(t)|^q \rangle$ (moments of the PDF, see, e.g., [33]) of different orders versus space or time separation (Eulerian statistics). Structure functions are sensitive to correlation via dependence on the differences and are weighted to events of greater intensity as the order q increases.

Statistical self-similarity of the type $S_q(\tau) \sim \tau^{\zeta(q)}$ can be expected in an inertial range. For the isotropic fully developed 3D turbulence (described by Kolmogorov's K41 model), the scaling exponents are $\zeta(q) = q/3$. Introduction of an imposed anisotropy, such as an external magnetic field, modifies the symmetries of the underlying equations (i.e. describing edge

plasma physics in fusion devices) of motion that are reflected in the statistical properties of the flow. In this case, expected a nonlinear function of q for intermittent turbulence is expected.

In a neutral fluid turbulence, Benzi et al. [28] have showed that scaling properties of the velocity increments can be extended up to a dissipative range: $S_q(l)$ has a power-law dependence on $S_3(l)$, $S_q(l) \sim S_3(l)^{\zeta(q)/\zeta(3)}$, over a range which is substantially longer (for long ranges of scale $l \geq 5\eta$, η – dissipation scale) than the scaling range obtained by plotting $S_q(l)$ as a function of l . This behavior holds even at a moderate Reynolds number. It was named an extended self-similarity (ESS). Hidden statistical symmetries of the equations of motion, hierarchy of moments, multifractality are behind the property of the ESS. The ESS corresponds to the considering of the scaling in a turbulent cascade not with respect to the usual distance, but with respect to an effective scale defined by the third order moment of the velocity field.

We estimate the high-order structure functions $S_q(\tau) = \langle \square \square \tau X(t) \square^q \rangle$ as a function of time lag τ , $\square \tau X(t) = X(t+\tau) - X(t)$, from the time signals $X(t)$ from the ion saturation current to Langmuir probes and from the ExB radial particle flux across the magnetic field. See typical intermittent behaviour of experimental data from edge plasma in Figure 8.

The power dependence $S_q(\tau) \sim \tau^{\zeta(q)}$ is observed only on a limited time scale of about 10 μ s (Figures 9,10). The structure functions exhibit a saturation and oscillations over time scale $> 10-30 \mu$ s. Such behaviour is typical and observed for all data from tokamak (Figure 10), stellarator (Figure 9) and linear machine.

The ESS property is illustrated in the log-log plots: the dependence of $S_q(t)$ on $S_3(t)$ is seen to be linear almost over three orders of magnitude in time, up to 1 ms (Figure 11,12). All data from edge plasma in fusion devices (tokamaks T-10 [55], HYBTOK-II [55], JT-60U [86], stellarator LHD [55,86], linear NAGDIS-II [55]) that were analyzed, demonstrate such ESS property as for density fluctuation as for particle flux fluctuation confirming universality of this property in edge magnetized plasmas

The ESS property is observed in hydrodynamic turbulence [28], in SOL plasmas in magnetic fusion systems [55], and in the MHD turbulence of interplanetary plasmas [87, 88]. The ESS shows evidence of the presence of statistical symmetry that ensures the invariance of the process over a broad scale, up to the dissipative one. Our observations of the ESS in the intermittent turbulence of the tokamak SOL plasma, where the boundary effects (caused by a limited range of typical spatial and temporary scales) play an important role, can be interpreted in terms of the log-Poisson turbulence model (see below).

In practice, the ESS property can be used to improve the accuracy of determining the scaling for the structure functions in an analysis of the experimental data. From the exact result $\zeta(3) = 1$ [26] and by using the ESS property, one can obtain rather accurate values of $\zeta(q)$ considering $\zeta(q) / \zeta(3)$ in experiments. An example of structure scaling is in Figure 13-15. Non-linear behavior of the scaling is observed in the edge plasma of fusion devices demonstrating deviation from Kolmogorov's model prediction. The experimental scaling will be compared with prediction of intermittent turbulent models in the next section.

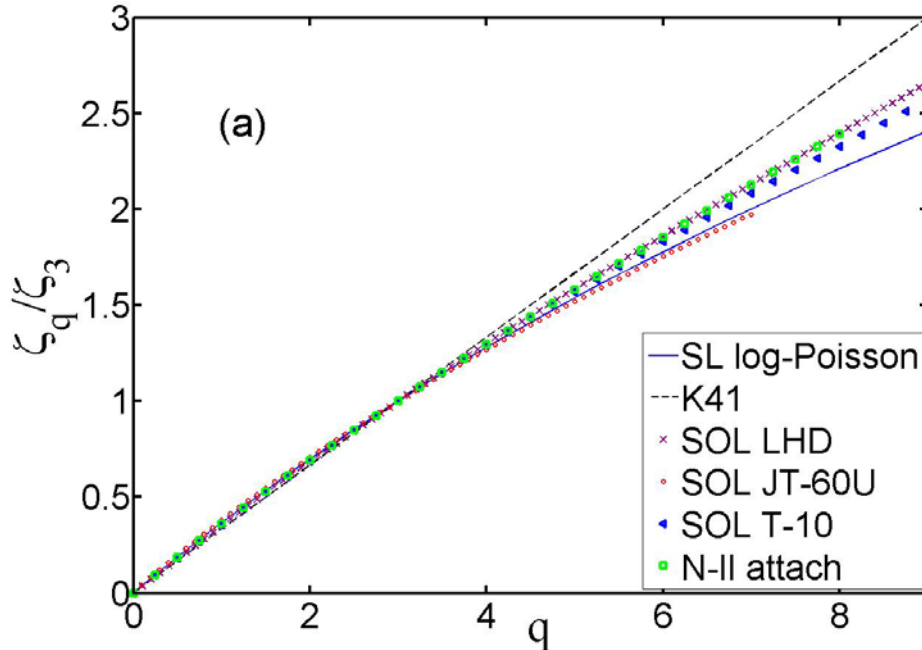


Figure 13. Structure function scaling $\zeta(q)$ vs. order q . Edge plasma in scrape-off-layer of T-10 (SOL T-10) and JT-60U (SOL JT-60U) tokamaks, stellarator LHD (SOL LHD) and linear plasma device NAGDIS-II attached mode (N-II attach). Kolmogorov K41 (a dashed line) and She-Leveque (SL) log-Poisson (a solid line) models are for the reference (from Ref. []).

7. LOG-POISSON MODEL OF INTERMITTENT TURBULENCE

Any analytic theory of plasma turbulence is linear if it does not make use of non-Gaussian distribution functions. Direct numerical solution of equations describing an actual plasma faces a fundamental problem: because of the cascade nature of the process, the number of degrees of freedom increases algebraically for increasingly small spatial scales. This is why cascade turbulence models are better suited for describing intermittent turbulence. With a stochastic cascade, many properties of such turbulence can be described, in particular, its multiscale and multifractal nature. By incorporating an anisotropic multiplicative cascade, it became possible to develop a multifractal turbulence model [26], i.e., to consider how the self-similarity depends on the local spatial scale.

For hydrodynamic turbulence, the study of the phenomenology of scalar turbulent cascade dates back to the paper by Richardson. In phenomenological turbulence models [15, 20, 33], the main assumption is that the energy flux is distributed among the smaller scale cells at each next stage of the cascade process. Small cells serve merely to model the energy cascade from larger scales (of course, an analogous scheme can be considered for an inverse cascade as well). Consideration is given to the hierarchy of turbulent cells in a turbulent medium, which becomes increasingly inhomogeneous on smaller scales.

The turbulence intermittency property is described by the β -model [26]. A hierarchy of spatial scales is considered such that, at each scale n , the initial region (a cube of side l_0) is divided into smaller cubes of side $l_n = l_0^{-n}$, the total number of which is $N = 2^{3n}$. It is assumed

that, in a cascade to smaller scales in the hierarchy, only a given relative fraction of the cubes, β , remains active and that this fraction is constant, thereby being a parameter of the model. The β -model yields a correction to the Kolmogorov scaling but does not satisfy the condition for the scaling to be zero for the zeroth moment. Log-Poisson models generalize the β -model [26]. They began to be developed in the middle of 1990s as a generalization of the previous fractal turbulence models, which in turn were constructed after, and based on, phenomenological observations of the ESS property [28] in hydrodynamic turbulence.

The She–Leveque–Dubrulle model [16, 17] assumes the existence of a limiting value ε_l^∞ associated with the most dissipative structures. This model makes use of the

dimensionless dissipation energy $\pi_l = \frac{\varepsilon_l}{\varepsilon_l^\infty}$ and of the following three similarity hypotheses:

- [I] The scaling for the structure function is the same as that in the K62 model, with the mutually dependent exponents, $\zeta(q) = q/3 + \tau(q/3)$, specifically, $\langle \varepsilon_l^q \rangle \sim l^{\zeta(q)}$, where ε_l is the mean dissipation rate measured within the cells (say, spheres, or cubes) of size l . This scaling describes a local inhomogeneity (intermittency).
- [II] The hierarchy of the moments of the mean dissipation rate is described by a power dependence,

$$\frac{\langle \pi_l^{q+1} \rangle}{\langle \pi_l^q \rangle} = A_q \left(\frac{\langle \pi_l^q \rangle}{\langle \pi_l^{q-1} \rangle} \right)^\beta \quad (21)$$

It is assumed that this property arises from the hidden symmetries of dynamic equations, such as the NS equation in hydrodynamics and MHD equations in plasma physics. The exponent β characterizes the degree of intermittency (for nonintermittent homogeneous developed turbulence in, e.g., the K41 model, we have $\beta = 1$).

- [III] The scaling for singular ($l \rightarrow 0$) dissipative structures has the form $\varepsilon_l \sim l^{-\Delta}$, where the parameter Δ is associated with the geometry of dissipative structures and also with boundary effects [16, 26].

These three hypotheses assume the existence of power laws associated with the self-similar symmetries of a turbulent process. By analyzing hypotheses (I)–(III), one can derive the scaling for the structure functions. Let us outline this derivation (see, e.g., [25]).

Dependence (3) yields

$$\langle \pi_l^{q+1} \rangle = \langle \pi_l^q \rangle^{\beta+1} \langle \pi_l^{q-1} \rangle^{-\beta} \quad (22)$$

Let us write the hierarchy in expanded form,

$$\begin{aligned}\langle \pi_l^2 \rangle &= \langle \pi_l \rangle^{\beta+1} \\ \langle \pi_l^3 \rangle &= \langle \pi_l^2 \rangle^{\beta+1} \langle \pi_l \rangle^{-\beta} \\ \langle \pi_l^q \rangle &= \langle \pi_l \rangle^\psi\end{aligned}\tag{23}$$

Where

$$\psi = \sum_{m=0}^{q-1} \beta^m = \sum_{m=0}^{\infty} \beta^m - \sum_{m=q}^{\infty} \beta^m = \frac{1}{1-\beta} - \frac{\beta^q}{1-\beta} = \frac{1-\beta^q}{1-\beta}\tag{24}$$

In shortcut form, we have

$$\langle \pi_l^q \rangle = \langle \pi_l \rangle^{\frac{1-\beta^q}{1-\beta}} \sim (\delta_l v)^{\Delta \frac{1-\beta^q}{1-\beta}}\tag{25}$$

In terms of the third-order moments, the q th-order scaling for the velocity can then be written as

$$\langle \delta_l v^q \rangle \sim (\delta_l v^3)^{q/3} \frac{\langle \pi_l^{q/3} \rangle}{\langle \pi_l \rangle^{q/3}} = (\delta_l v^3)^{\frac{q}{3}(1-\Delta)+\Delta \frac{1-\beta^{q/3}}{1-\beta}}\tag{26}$$

$$\langle \delta v_l^q \rangle = \langle \delta v_l^3 \rangle^{\zeta(q)}\tag{27}$$

$$\zeta(q) = (1-\Delta) \frac{q}{3} + \frac{\Delta}{1-\beta} \left[1 - \beta^{\frac{q}{3}} \right]\tag{28}$$

For 3D isotropic turbulence, She and Leveque [16] proposed that $\Delta = \beta = 2/3$, which gives the scaling

$$\zeta(q) = \frac{q}{9} + 2 \left[1 - \left(\frac{2}{3} \right)^{\frac{q}{3}} \right]\tag{29}$$

The hierarchy of the moments can be explained by considering invariance under the generalized scale transformation, in which case the scaling should be considered with respect to the generalized scale determined by the third moment of the distribution function.

Let us briefly describe the hierarchy in the log-Poisson model. Consider a multiplicative cascade turbulent energy process in a system with hierarchical turbulent cells or with velocity fluctuations of different amplitudes on different scales. Let us divide the entire region into small cubic cells of side l_0 and introduce the energy dissipation rate ε_l for each of the cells. In the steady state, the energy dissipation flux is the same as the energy influx into the system on the largest scales. In the K41 model, this energy dissipation flux is constant. Let us then divide each of the cells into smaller cubic cells of side λl_0 , where $0 < \lambda < 1$, and repeat this procedure with the same λ for all smaller scales. As a result, we arrive at a hierarchy of cells like that shown in Figure 16. Let us consider two hierarchical levels: the levels l with the flux ε_l and the level $l' = \lambda l$ with the new cells. Assume that the dissipation energy flux through a fraction y of these new cells is $1-y$ and that the dissipation energy flux through the remaining fraction of the same cells is $\varepsilon'_1 = \beta_1 \varepsilon_l$. Provided that the energy flux along the cascade is conserved, we have $y\beta_1 + (1-y)\beta_2 = 1$. Assume then that the division into cells is random, i.e., that a fixed observation point can occur in any of the new, smaller scale cells with equal probability. A large number m of divisions ends with the spatial scale $l_m = l_0 \lambda^m$. The energy moment $\langle \varepsilon_l^q \rangle \sim l^{q(\tau)}$, averaged over the entire large initial region, obeys the scaling law

$$\tau(q) = \log(Wq) / \log \lambda \quad (30)$$

where $W = \varepsilon_{i+1}/\varepsilon_i$ is the cascade factor that describes the process and is defined by

$$W = \begin{cases} 0 & \text{with probability } 1 - y\beta_1 - (1-y)\beta_2 \\ |1/\beta_1| & \text{with probability } y\beta_1 \\ |1/\beta_2| & \text{with probability } (1-y)\beta_2 \end{cases} \quad (31)$$

Accordingly, we can find the β_1 value with probability y and the β_2 value with probability $(1-y)$. Assume that the fraction y is small and that the parameter of the cascade is also small, $\lambda = 1 - C_0/y$. For a small y value, we

have $\beta_1 < 1$ and $\beta_2 > 1$, in which case the structures with β_2 are the most intense, singular structures. Using definition (13), we obtain

$$\tau(q) = C_0(\beta_1 - 1)q + C_0(1 - \beta_1^q) \quad (32)$$

The parameter C_0 is related to the fractal dimension of structures with the fraction of energy β_2 . The number of such cells is $N_m = N_0((1-y)/\lambda)^m$, the side of a cubic cell at the m th

hierarchical level being $l_n = l_0 \lambda^m$. The fractal dimension calculated for a small y value by the boxcounting method is

$$D = -\lim_{m \rightarrow \infty} \log(N_m) / \log(l_m/l_0) = 3 - C_0 \quad (33)$$

That is, the parameter C_0 is the codimension of the structure that involves only cells characterized by the parameter β_2 : for one-dimensional (1D), or filamentary, structures, we have $C_0 = 2$ and, for 2D sheetlike structures, we have $C_0 = 1$. We can then use the Kolmogorov formula for the dissipation rate, $\varepsilon_l \approx \delta_l v^3/l$, so the scaling for the structure velocity function is

$$\zeta(q) = (1 - C_0(1 - \beta))q/3 + C_0(1 - \beta q)/3 \quad (34)$$

This scaling coincides with scaling (10). The parameter $\beta = \beta_1$, which characterizes the degree of intermittency, can be determined from numerical or laboratory experiments (for nonintermittent turbulence, we have $\beta = 1$).

Under the additional assumption that velocity fluctuations near the most dissipative structures are nonintermittent, we can reduce scaling (15) to She–Leveque (SL) scaling (11).

The logarithm of the dissipation energy ε_l obeys the Poisson distribution,

$$P(y, \mu) = \frac{\mu^y e^{-\mu}}{\Gamma(y+1)}, \quad (35)$$

for $y = \ln \varepsilon_l / \ln \beta$; here $\mu > 0$ is the parameter of the distribution, $\Gamma(y)$ is the Gamma function.

Recall that the Poisson distribution is one of the most important distributions of the probabilities of random quantities that take on integer values. For instance, such a distribution provides a good description of radioactive decay processes and many other physical phenomena. In theoretical probabilistic models, the Poisson distribution is used both as an approximating and as an exact distribution. The Poisson distribution is a limiting form of a binomial distribution. For $\mu > 9$, the Poisson distribution can be approximated by a normal distribution with the mean and the dispersion both equal to μ .

She and Waymire [41] considered a stochastic multiplicative cascade in which complicated topological structures, namely, dissipative structures of different dimensions (in particular, those having fractal dimensions), can form simultaneously. In probability theory, such a process is described by the Khintchine–Levy approach [89]. The results of applying this approach are important for interpretation of the experimental data when experimental scalings deviate insignificantly from scaling (11) with fixed Δ and β values. The deviation can arise from the complicated geometry of the dissipative structures or from the fact that structures of different dimensions are present in the process simultaneously. This is why the process can be characterized by the fitting values of Δ and β .

Table 1. Indexes Δ and β obtained from the best nonlinear fitting of the experimental scaling to the log-Poisson scaling Eq. (28) .

Experimental data	Δ	β
T-10 SOL, $r=34$ cm	0.43	0.33
T-10 LCFS, $r=30.5$ cm	0.41	0.36
T-10 shear layer, $r=29.5$ cm	0.28	0.5
NAGDIS-II attached, $r=18$ mm	0.23	0.36
NAGDIS-II detached, $r=18$ mm	0.35	0.3
LHD limiter , shot 33355	0.15	0.62
LHD high beta, shot 30206	0.57	0.48
LHD ITB, shot 32982	1.0	0.87
LHD, short magnetic connection length	0.73	0.72
LHD, long magnetic connection length	0.43	0.83
HYBTOK-II, with RHMF of 7 kHz	0.3	0.4
HYBTOK-II SOL	0.26	0.11

The results of calculating the scalings for the structure functions of the experimental signals are illustrated in Figure 14,15, which also shows the scalings in the K41 and log-Poisson (for $\beta=\Delta=2/3$ [16]) turbulence models for comparison. Note that the experimental spectra deviate substantially from the Kolmogorov spectrum. The experimental curves can be described by spectrum (10) with the fitting parameters β and Δ . Figure 17 shows the parameters β and Δ calculated for the experimental scalings by the method of nonlinear adjustment to scaling (10). The parameters β and Δ are seen to vary only slightly, except in the velocity shear layer ($r \approx 29$ cm), where the turbulent cells are supposed to be destroyed [55].

We can see that there are deviations from the values $\beta=\Delta = 2/3$, which are characteristic of 3D isotropic turbulence [16, 17, 26]. Observations show that the parameter Δ in the main SOL region falls in the range from 0.2 to 0.4 (Figure 17), which can be interpreted as evidence that quasi-1D dissipative structures make a dominant contribution to intermittent turbulence. The values of the parameter Δ at $r \approx 36$ cm in the far SOL region differ from those at $30 < r < 35$ cm in the main SOL region. A possible reason for this is that there may be dissipative structures of different topology in comparison with that of the structures in the main SOL plasma.

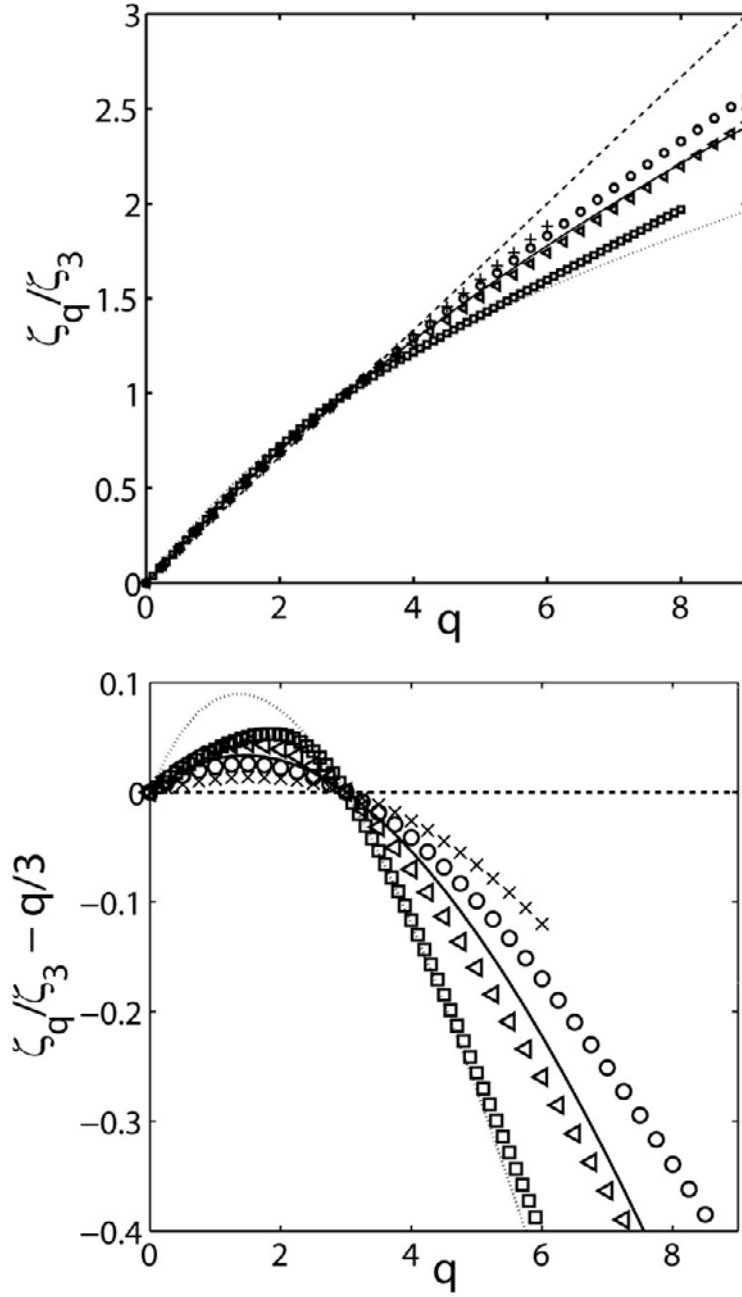


Figure 14. (a) Scaling for the structure function and (b) its deviation from the K41 spectrum. Edge plasma of T-10 tokamak. Shown are the plasma density in the shear layer (crosses), near the LCFS $r = 30$ cm (circles) and at $r = 34$ cm in the SOL region (triangles) and the density of the cross-field particle flux Γ_1 at $r = 36$ cm in the far SOL region (squares). Also shown are the spectra in the K41 model (dashed curves), in the SL model (solid curves) and in the MB model for 2D dissipative structures (dotted curves).

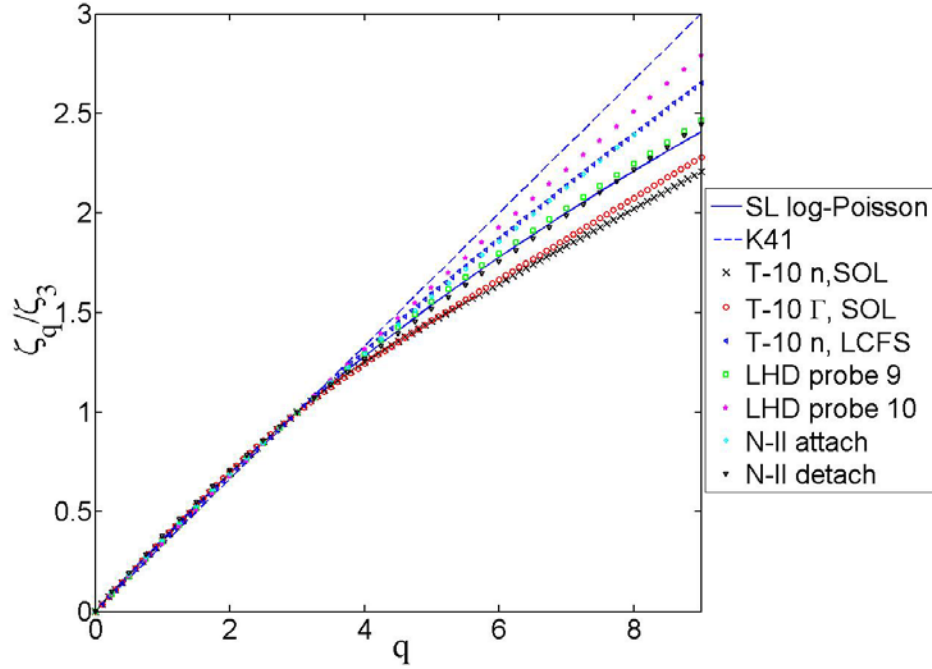


Figure 15. Nonlinear scaling of the high-order structure function $\zeta(q) / \zeta(3)$ for edge plasma fluctuations in fusion devices: T-10 tokamak, LHD stellarator and linear device NAGDIS-II (N-II). The dashed line shows the Kolmogorov K41 scaling $q/3$, the solid line shows the log-Poisson model prediction for $\beta=\Delta=2/3$, She-Leveque model (SL).

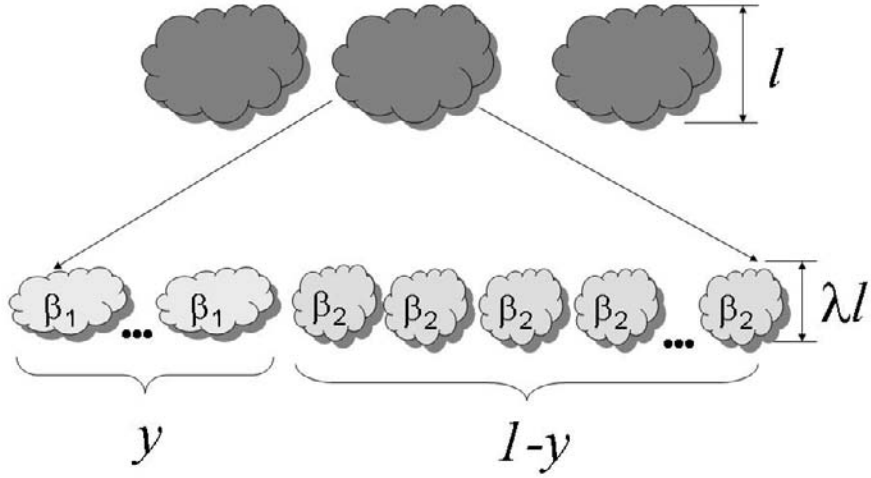


Figure 16. Scheme of a random anisotropic multiplicative cascade in the log-Poisson model.

For different devices the indexes are obtained by fitting experimental scalings to theoretical prediction of the log-Poisson model (28). They are in the range $\beta=0.11 \div 0.9$, $\Delta=0.25 \div 0.7$ (Table 1). In some cases we observed non-intermittent signals with $\beta \approx 1$. The value of index Δ can be interpreted in frame of results from isotropic developed turbulence [16,17] and numerical simulation of MHD [36,37]. Values of Δ between 1/3 and 2/3 are found in our analysis; these cases can be interpreted that the most intermittent dissipative structures are likely filament structures. Such dissipative structures have likely not a trivial geometrical topology but a fractal one.

This issue can be investigated in detail by considering an anisotropic stochastic cascade (see below). In order to check the hypotheses about the power laws in the log-Poisson model

$$(see [25]), we can analyze the scalings for the relative moments \(\Pi_q(\tau) = \frac{S_{q+1}(\tau)}{S_q(\tau)}$$

and examine the dependence

$$\Pi_{q+1} = (\Pi_q)^{\delta_q} \quad (36)$$

Figure 18 displays a representative hierarchical dependence of Π_{q+1} on Π_q for $q \in [1, 8]$ on a logarithmic scale. All the data are seen to lie on the same straight line—a fact in support of the hierarchical nature of the moments in accordance with scaling (9), predicted by the log-Poisson model; moreover, all the constants A_q are the same. If there were no such a law, groups of points would lie on nonparallel segments or would not lie on the same straight line.

A comment is in order regarding revealing the contributions of the direct and inverse cascades to the parameters of the scalings. The quantities $\langle \varepsilon_i \rangle$, $\square(q)$, and Π_q characterize the intensity of the energy cascade processes regardless of their direction. Consequently, the inverse cascade, too, can be described by the scaling of the structure function. In order to calculate the contribution of the inverse cascade to the process, it is necessary to invoke additional investigation methods (see [47]).

The ESS of the log-Poisson process establishes long-range correlations, which give rise to an anomalous process—superdiffusion. In tokamaks, this property can lead to enhanced plasma losses and can degrade plasma confinement.

The intermittency phenomenon similar to edge turbulence in fusion plasma is observed in other natural systems, like heliosphere [47]. Scalings for plasma turbulence in the magnetosheath near the Earth magnetopause demonstrate non-linear behaviour (Figure 19). Fit to log-Poisson scaling yields the parameters $\Delta=0.2 - 0.24$ and $\beta=0.3-0.41$ of the same range as for edge plasma in fusion devices (see Table I) supposing universality of the property. It is contrary to non-intermittent plasma turbulence of sun wind (interplanetary turbulence) out of the turbulent boundary layer of the Earth magnetosphere (Figure 19).

It should be noted that scalings close to those in the log-Poisson model were also observed in turbulent flows in anisotropic neutral media [26]. Presumably, the similarity in the scalings for different turbulent media implies that the structure of developed anisotropic

turbulence and of intermittent turbulence near the boundaries of a turbulent flow is of a universal nature.

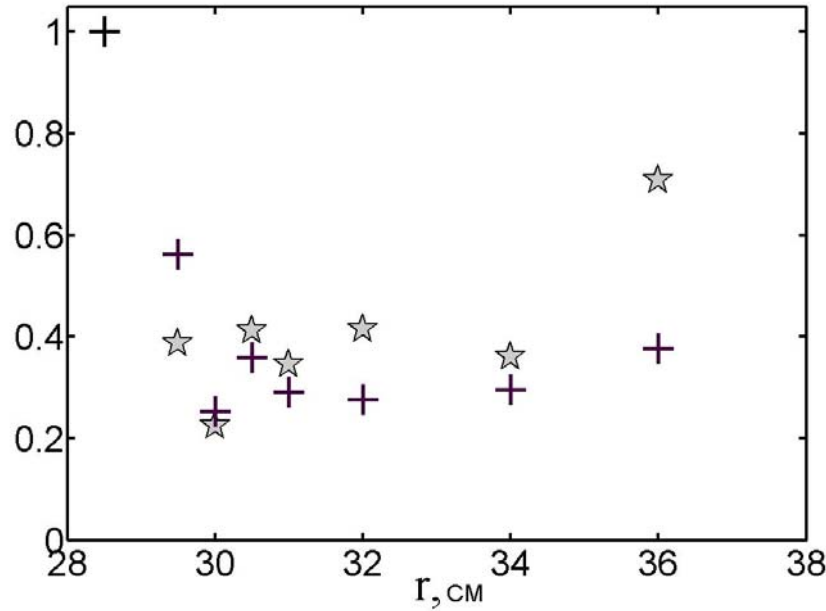


Figure 17. Radial profiles of the parameters Δ (asterisks) and β (crosses) of the log-Poisson model.

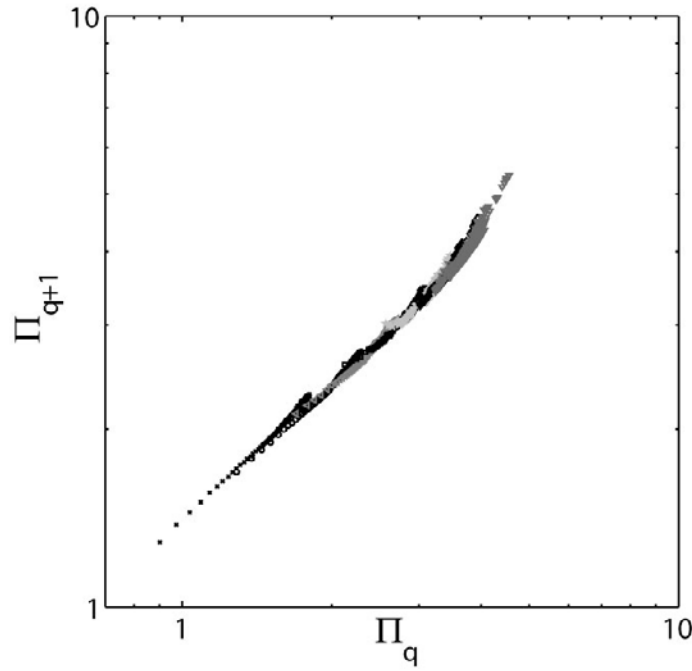


Figure 18. Relative moments Π_{q+1} vs. Π_q for the plasma density at $r = 36$ cm in the far SOL region. Each group of points corresponds to a certain value of q from the interval [1, 8].

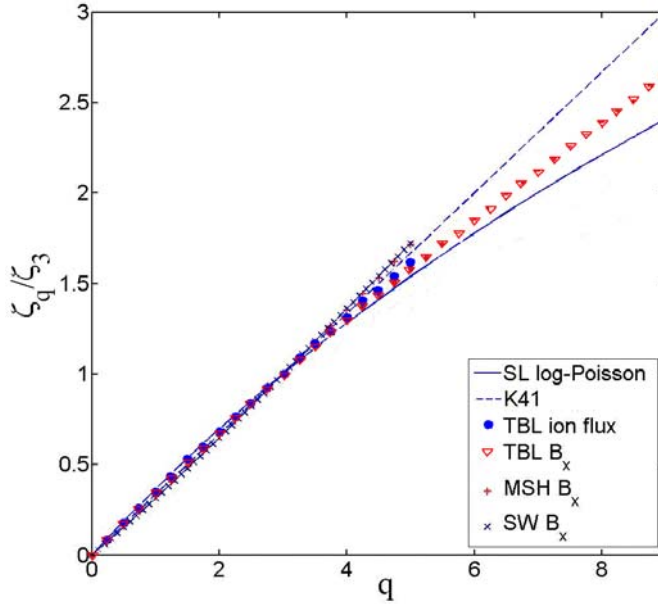


Figure 19. Intermittency scaling for plasma turbulence in the magnetosheath near the Earth magnetopause. Dependence of the scaling ratio $\zeta(q)/\zeta(3)$ on its order q versus that of Kolmogorov K41 (a dashed line) and that of the log-Poisson She-Leveque model (SL), describing the developed 3D turbulence (a solid line). Magnetic field fluctuations in B_x and particle flux. The symbols in the right bottom corner mark different experimental signals from satellites: Interball-I (turbulent boundary layer - TBL ion flux, magnetosheath - MSH B_x , TBL B_x) and Geotail (B_x , sun wind - SW) data.

The intermittency property is not observed to depend on local plasma density. On LHD stellarator, the substantial increasing of the plasma density at internal density barrier (IDB) phase do not lead to a detectable change of intermittency property in the edge plasma and scaling (Figure 20).

A dependence of intermittency level with the different magnetic topology was investigated in the series of LHD experiments. Intermittent behaviour is different depending on the magnetic field line length (Figure 21). At different magnetic axis position R_{ax} (from 3.6 m to 4 m) magnetic topology is changed in LHD. It allows to make probe measurement in edge plasma at magnetic field line with different magnetic field line length L_c . The parameter β of the log-Poisson scaling is estimated from the analysis of a stable period of discharges at super dense core phase with minimal plasma current (less than 5 kA). It was observed a degradation of the intermittency at large L_c (Figure 22). At short L_c a tendency of parameter to be in the range $0 < \beta < 1$ is observed, that is a case of the intermittent turbulence. We stress that this result is obtained in the series of experiments with different magnetic topology and edge plasma profiles. Despite a scattering data for the short L_c , a clear degradation for the long L_c could be interpreted in favor of hypothesis considered a dependence of the intermittency property on a magnetic connection length.

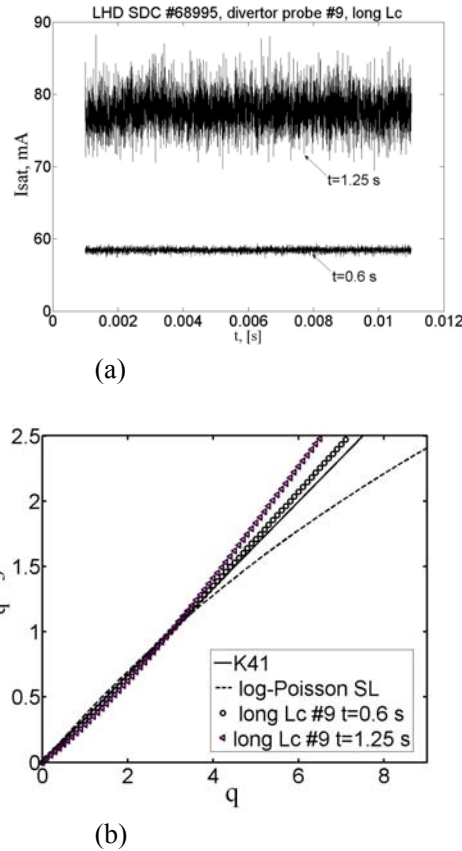


Figure 20. The substantial increasing of the plasma density at LHD IDB phase (a) keeps the scaling close to K41 (b), I_{sat} on probe #9 at long L_c . The K41(line) and She-Leveque log-Poisson (dashed line) scalings are shown for the reference.

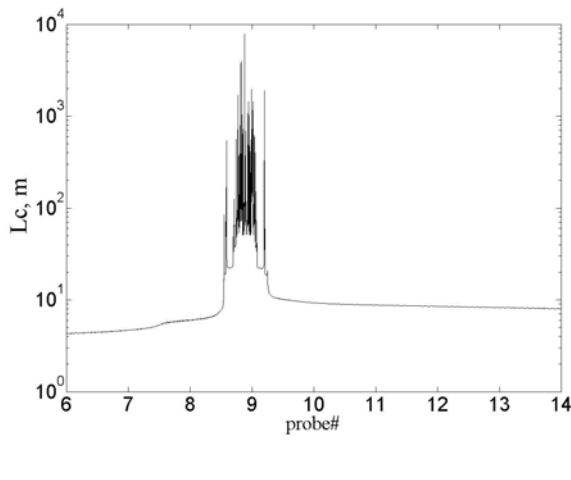


Figure 21. (Continued)

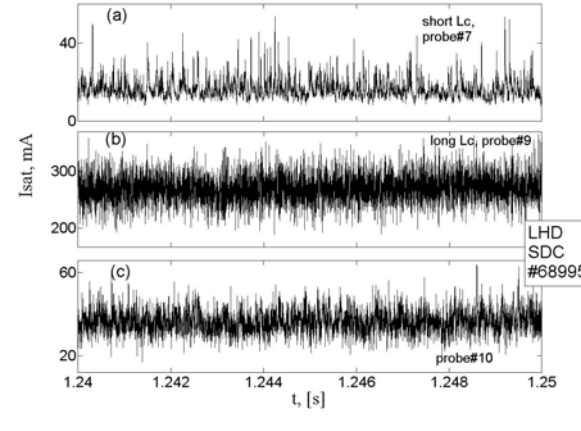


Figure 21. (a) Connection length L_c profile on the divertor probes plane regarding the probes numbering. (b) Signals of I_{sat} on divertor probes in LHD Super Dense Core mode. Bursty behaviour is different depending on L_c .

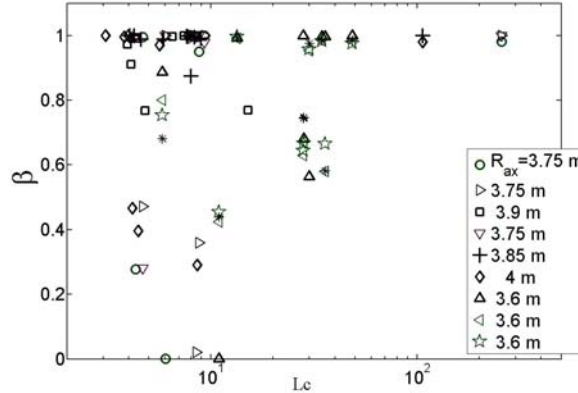


Figure 22 . Intermittency characterization β vs. connection magnetic length L_c on divertor probes. $\beta = 1$ corresponds to a non-intermittent behaviour. Intermittency is degraded at large L_c . Divertor probe measurements on LHD in shots with different magnetic axis position $R_{ax}=3.6 \text{ m} \div 4 \text{ m}$ at ITB phase.

5. MODIFIED SCALING OF THE LOG-POISSON MODEL WITH ANISOTROPIC TURBULENT CASCADE

To consider a geometry of the most singular dissipative structures we have to treat a scaling of energy dissipation $\varepsilon_l \sim l^\Delta$ and the scaling of velocity $v_l \sim l^{1/g}$ [36] (with the parameter $g=3$ for K41, $g=4$ for IK). In a random cascade model a non-intermittency index β relates with Δ and co-dimension C_0 of the most singular dissipative structures: $\beta=1-\Delta/C_0$ (see [90], [91]). $C_0=3-D$, where D is the dimension of dissipative structures. In three dimensions $C_0=2$ for filaments ($D=1$), $C_0=1$ for micro-sheets ($D=2$). Therefore, log-Poisson model scaling (Eq.5) could be rewritten as

$$\zeta(q) = (1-\Delta)q/g + C_0(1-[1-\Delta/C_0] q/g) \quad (37)$$

Usually Δ and g are related assuming an equal scaling for the time scale t_l^∞ of the $\varepsilon_l^\infty \sim E^\infty / t_l^\infty$ (E^∞ is an amount of the energy dissipated in the most singular structures) and for the nonlinear transfer time t_l^{NL} of the energy cascade $\varepsilon \sim \delta v_l^2 / t_l^{\text{NL}}$. From $\varepsilon_l^\infty \sim l^\Delta$ and $v_l \sim l^{1/g}$, we obtain $\Delta=2/g$. The hydrodynamic SL formula results from $C_0=2$, $g=3$, $\Delta=2/3$. The IK MHD model assumes $g=4$, $\Delta=1/2$, and $C_0=1$ with dissipative structures interpreted as two-dimensional current sheets. In DNS of three-dimensional isotropic MHD turbulence (the Biskamp–Mueller model (BM) [15]) scalings are reproduced well with the combination $g=3$, $\Delta=2/3$, and $C_0=1$ implying hydrodynamic scaling and sheet-like dissipative structures. To consider an anisotropy statistics of the cascade strength we may follow a phenomenological interpretation of Biskamp and Mueller in [36] by dropping the scaling equality of t_l^{NL} and t_l^∞ . Instead, t_l^∞ is fixed to the K41 time scale, $t_l^\infty \sim l/\delta v_l \sim l^{1-1/g}$, $\Delta=1-1/g$, which with $C_0=1$ leads to [36] :

$$\zeta(q) = q/g^2 + 1 - (1/g)^{q/g} \quad (38)$$

As an alternative we can consider the same scaling $t_l^\infty \sim l/\delta v_l \sim l^{1-1/g_f}$ with $C_0=2$ of one-dimensional filament-like structures. On this basis, we propose an anomalous scaling that captures one-dimensional filament-like structures:

$$\zeta_f(q) = \frac{q}{g_f^2} + 2 \left(1 - \left(\frac{1+g_f}{2g_f} \right)^{\frac{q}{g_f}} \right) \quad (39)$$

The quantity $g_f/3$ expresses the cascade strength relative to the isotropic K41 case. As proposed in [36], the modified transfer time

$$t^{\text{NL}} \sim (l/l_0)\theta (l/\delta v_l) \quad (40)$$

can be considered detaching t_l^{NL} and t_l^∞ to characterize the strength of field-perpendicular and field-parallel polarized fluctuations. Here, l_0 is an arbitrary reference length, and θ is a dimensionless efficiency parameter. Assuming a constant energy cascade

$$\varepsilon \sim \delta v_l^2 / t^{\text{NL}} = \text{const}, \quad (41)$$

$$t^{\text{NL}} \sim l(1+\theta)/2/3 \quad (42)$$

In a standard phenomenology $t_l^{\text{NL}} \sim l^{2/g}$. In a such approach (12), the cascade efficiency is controlled by the $(l/l_0)^\theta$ factor.

- [i] $\theta=0$ ($g=3$) yields the isotropic K41 cascade,
- [ii] $\theta<0$ ($g>3$) corresponds to a cascade enhancement,
- [iii] $\theta>0$ ($g<3$) corresponds to a cascade depletion.

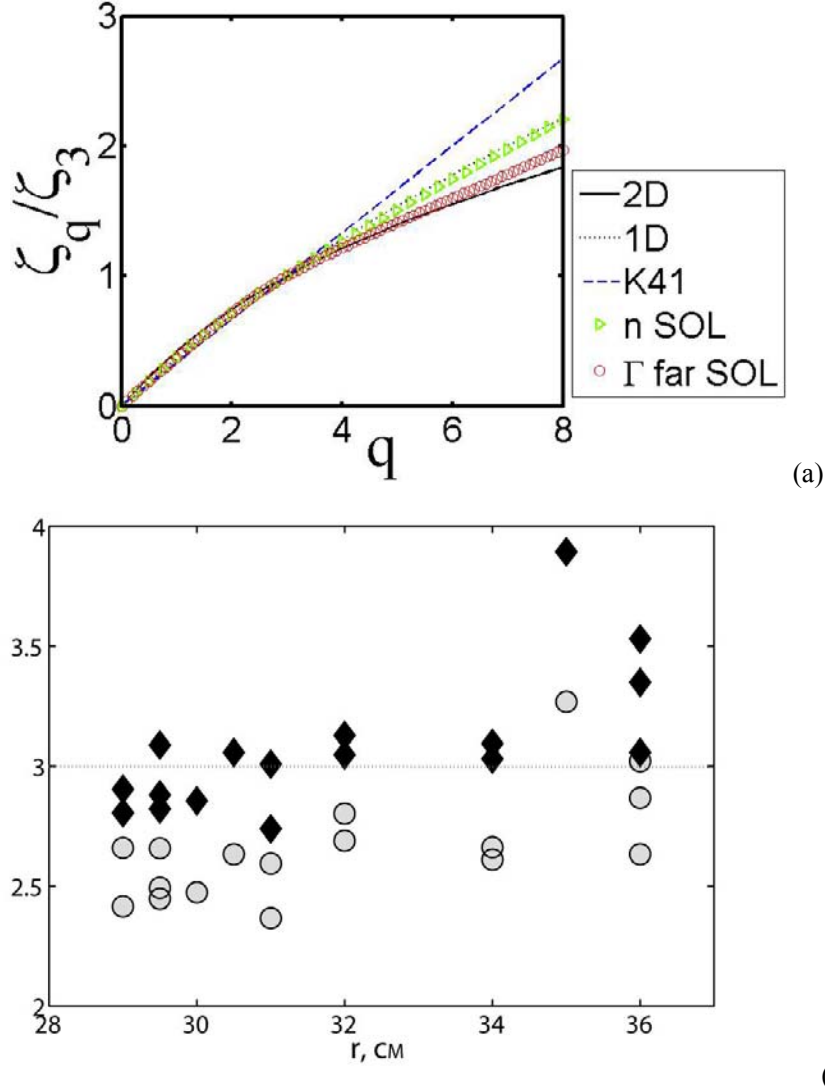


Figure 23. (a) Scaling for the structure function - its deviation from the K41 spectrum. Edge plasma of T-10 tokamak. Shown are the plasma density in the shear layer (crosses), near the LCFS $r = 30$ cm (circles) and at $r = 34$ cm in the SOL region (triangles) and the density of the cross-field particle flux Γ_t at $r = 36$ cm in the far SOL region (squares). The K41 model (dashed curves), log-Poisson model with two-dimension 2D (solid curves) and one-dimension 1D (dotted curves) dissipative structures in three dimensions with anisotropy from magnetic field. (b) Parameters g (circles) and g_f (diamonds) for SOL turbulence in the T-10 tokamak. Over almost the entire SOL region, the parameter g_f is close to 3.

A comparison of the experimental scalings with scaling (Eq.39) and the log-Poisson scaling is illustrated in Figure 23a. In the main SOL region, the scaling is described by relationship (20) in the model with 1D dissipative structures and, in the far SOL region, the scaling is illustrated in Figure 23. In the main SOL region, the scaling is given by relationship (Eq.39) in the model with 1D dissipative structures, and, in the far SOL region, the scaling at large q values is close to scaling (Eq.38) in the model with 2D dissipative structures.

Figure 23b shows radial profiles of the parameters g and g_f for SOL plasma turbulence in the T-10 tokamak. The uniform norm of the difference (the relative error in determining the parameters in the fitting process) was in the range from $5 \cdot 10^{-2}$ to $5 \cdot 10^{-5}$, so the approximation was good. Almost over the entire region of the SOL plasma and of the sheared poloidal plasma rotation ($28 < r < 29.5$ cm), the parameter g_f is close to 3. As was already mentioned, this result gives evidence of the presence of 1D singular dissipative structures, because the experimental scaling is closer to scaling (Eq.39). At the minor radius $r = 36$ cm in the far SOL region, the cascade is closer in properties to that described by scaling (Eq.38) in the model with 2D dissipative structures ($g \geq 3$). Presumably, in this case, we deal with the dominant contribution of 2D vortex structures. Similar processes with vortex structures were observed in numerical experiments based on more or less complicated models developed for SOL plasmas in fusion devices (see, e.g., [42, 66]). In experiments on T-10 [55, 22] and other tokamaks (see, e.g., [8]), large-scale structures were observed to occur in the SOL plasma that were referred to as blobs in the literature. In the probe signals under analysis, the radial motion of the blobs is recorded as large-amplitude bursts of irregular shape. Other structures—such as vortices and spatiotemporal modes with different degrees of coherence—were also recorded. All such structures result from the strong nonlinearity of the process. From their spectral parameters against the turbulent flow background it cannot be concluded that they exist independently of the whole turbulent motion. Thus, the existing blobs contribute at frequencies of about $\sim 1\text{--}30$ kHz to the low-frequency part of the Fourier spectrum and on time scales of about $\sim 40\text{--}1000$ μs to the structure functions. But there are no monochromatic peaks in the spectra and structure functions and the spectra are broadened. All this goes to show that it is incorrect to interpret the spectra as supporting the existence of the structures in isolation from turbulence. The results of numerous experimental studies that have been carried out on T-10 and other tokamaks allow us to draw the conclusion about the strong nonlinear mutual interdependence of all the structures and modes in the SOL plasma—a situation that is considered in modern theoretical models (see [41, 42]). The approach applied in the present paper makes it possible to utilize the language of the scalings of structure functions in order to characterize the degree to which structures and modes occurring on different spatial scales are nonlinearity coupled to each other. The results of the above analysis in the log-Poisson model provide insight into the topology of the structures responsible for dissipation in SOL turbulence. Such structures can be attributed to the previously discussed coherent phenomena that were clearly observed in tokamak experiments and also to the structures that are indistinguishable from the strong turbulence background in the SOL plasma. Note that there may also coexist dissipative structures of different geometries (topologies)—a possibility that is discussed in the log-Poisson model [41]. In order to provide a detailed investigation of the geometry of dissipative structures and to confirm the analytic results obtained here on the basis of the log-Poisson phenomenological model, special experiments are required. The author is unaware of any theoretical studies of

the geometry of dissipative structures in tokamak SOL plasmas. A theoretical analysis [89] of a stochastic multiplicative cascade (such as is the log-Poisson cascade) shows that the process can involve generating dissipative structures of different (in particular, fractal) geometries. As was discussed above, the properties of the experimental scalings for 1D dissipative structures are adequately described by the log-Poisson model (Figure 23b). The approach used here does not provide information on the particular spatial shape of quasi-1D dissipative structures. The symmetry properties of MHD flows (such as helicity conservation) may indicate that the flows have a complicated helical shape, stretched predominantly along the magnetic field. In a tokamak, the magnetic field at the edge of the plasma discharge has a complicated topology, sometimes with many magnetic islands, some of which can overlap. This may lead to percolation effects (including those across the magnetic field; see, e.g., [92]) and may influence the topology (according to the above results, the fractal topology) of the limiting dissipative structures. A possible consequence is an additional contribution to isotropization on microscales, a situation in which SOL turbulence becomes closer in properties to hydrodynamic turbulence. The properties of the scaling depend on the dissipation scale length, on which viscosity effects become important and the nonlinear interaction time is on the order of the diffusion time. It is therefore expedient to compare the dissipative scale lengths λ in turbulence models for a conventional fluid and for a plasma described by the MHD equations. For a conventional fluid, we have [93]

$$\lambda v \sim L Re^{-3/4} \quad (43)$$

where L is the macroscopic spatial scale of motion with the velocity U , $Re = UL/v$, is the Reynolds number, and v is the viscosity. In a plasma in a strong magnetic field, the dissipation scale length is far larger because of the cascade anisotropy [94]:

$$\lambda B \sim L Re^{-2/3} \quad (44)$$

Such a great difference between the dissipation scale lengths in comparison with that in hydrodynamic turbulence plays an important role only at very high Reynolds numbers (for instance, in hot plasma cores in large tokamaks or in interplanetary plasmas, the Reynolds number is as high as $Re \sim 10^5 - 10^{10}$). For tokamak SOL plasmas, the Reynolds number is difficult to estimate because the viscosity can vary over a very broad range. Approximate estimates yield comparatively low Re values for a tokamak SOL plasma (possibly, from about ~ 10 [5] to about ~ 1000). That is, for relatively low Reynolds numbers, the extent to which the functional dependence of the dissipation scale length is altered by the magnetic field effects is not too large: for $Re \sim 1000$, the dissipation length merely doubles. Presumably, this is one of the reasons for the similarity in the properties of the energy cascade in a conventional turbulent fluid and in a tokamak SOL plasma.

Log-Poisson Statistics of Waiting-Time

Multifractal nature of the edge plasma turbulence suggests subordinated process in some stochastic time. To investigate a subordinated process of plasma turbulence as Markov one,

the waiting-time statistics has to be analysed. The waiting-time is defined as the time interval between two consecutive maxima in burst intensity (Figure 24) selected above a threshold (e.g., of 2÷3 standard deviation in amplitude).

If the triggering of the turbulent bursts are not correlated, such process may follow a the Poisson process, and the probability density function of the waiting times, Δt , should be an exponential law: $P(\Delta t)=\gamma^{-1} e^{-\Delta t/\gamma}$. Such law [95] is sometimes known as the law of rare events, although this name may be misleading because the events in a Poisson process need not be rare. This exponential pdf is considered in frame of self-organized criticality (SOC) hypothesis [96]. However, power law in the waiting-time pdf's observed in some experiments and studied in [97], [98], [99]. It is needed the detailed study of dominant underlying dynamics of the edge plasma turbulence in fusion devices.

Typical waiting-times series constructed from intervals between successive bursts in the signal is shown in Figure 25. Waiting-time series demonstrate intermittency and the fractal nature of the hierarchy of scales in the wavelet decomposition (Figure 11). Typically, the PDF's of these series are not decayed exponentially (Figure 26). Typical power law exponent of the pdf's $P(\Delta t) \sim (\Delta t)^\gamma$, derived from the slope of log-log plot (see example in Figure 27), is of $\gamma \approx -3 \div -2$. Power-law behavior of the waiting-time PDF's does not depend strongly on the parameters of the analysis such as threshold of the burst amplitude. Only in the vicinity of the last closed flux surface in T-10, where a shear of poloidal velocity is observed, the PDF exhibits close to Poisson statistics and monofractality. The lack of an exponential law for PDF's and multifractal statistics of waiting-time allows considering the problem of subordinated process. Our analysis shows a general lack of exponential decay of PDF's for waiting-time in the edge plasma and has raised criticism about the applicability of the simple SOC concept to the edge plasma.

Multifractal analysis has shown that the waiting-time has multifractal statistics, i.e. the scaling behavior of structure function $S(q,l)$ of increments, $\delta \Delta t = \Delta t(N+l) - \Delta t(N)$, $S(q,l) = \langle |\delta \Delta t|^q \rangle \sim l^{\xi(q)}$, has nonlinear scaling. In Figure 28, scaling of waiting-time is shown in the same plot with scaling of original signal of flux (in the plot of deviation from Kolmogorov's K41 scaling of $q/3$). They fully coincide illustrating similar statistics. It is very remarkable observation.

From this, we may consider a conception of the edge plasma turbulence modelling. We have to consider an idea of the stochastic time in the process. The idea of modelling stochastic process as a Brownian motion in a “fractal time” can be found in many approaches. The multifractal nature of the developed turbulence has been modelled [100] by a fractional Brownian motion subordinated with a multifractal stochastic measure. Subordinated processes are Markov processes in a time variable $\mu(t)$ that is itself an (increasing) random process [101]. It can be constructed a stochastic measure $\mu(dt) = e^{w(t)} dt$, $w(t)$ – normal random process, with multifractal spectrum ξ defined by $\langle \mu([0,t])^q \rangle \sim t^{\xi(q)}$. In this construction, the subordinated process $X(t) = B_m(\langle \mu([0,t]) \rangle)$ with stochastic time, where $B_m(t)$ is the standard Brownian motion. Despite the question of well-definiteness of this construction is still open problem, this example of the construction with multifractal time in the stochastic process may be considered as a model of edge plasma turbulence in fusion devices.

Another possible tool for the description of anomalous diffusion is kinetic equations with fractional space and time derivatives. The power-law distribution of waiting times is

predicted by the Continuous-Time Random Walk theory which is described by the fractional diffusion equations with a given order fractional time derivative [102]. Space-time models should satisfy the correct space-time stratification. The main feature of such models should be a conservation of causality: artificial time mirror-symmetry (statistically symmetric with the past) should be broken. To treat this problem a (generalized) diffusion equation (of fractional spatial and temporal order) for the singularities (i.e. for the cascade generator) should be considered. Order of fractional derivatives are related to the parameters of multiplicative multifractal cascade that could be derived from experimental data (e.g., the parameters Δ and β of the log-Poisson scaling).

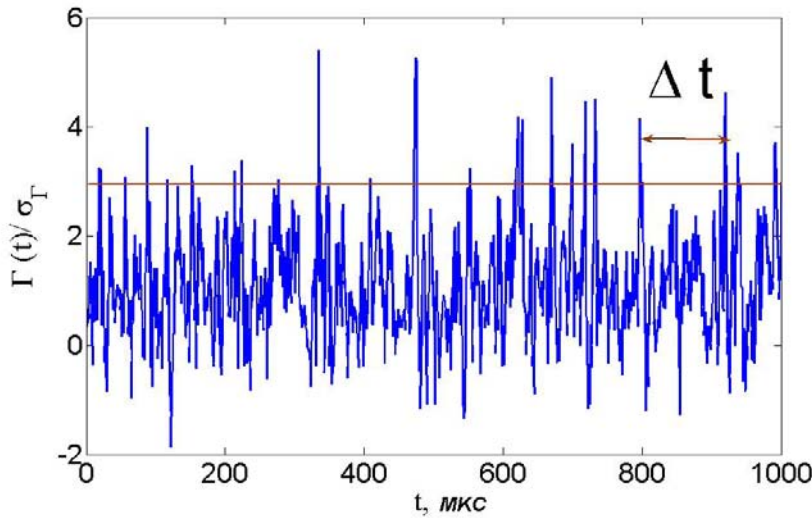


Figure 24 . Example of raw flux signal in T-10 normalized by a standard deviation. Waiting-time Δt is defined as a period between successive bursts with an amplitude above some levels (red line).

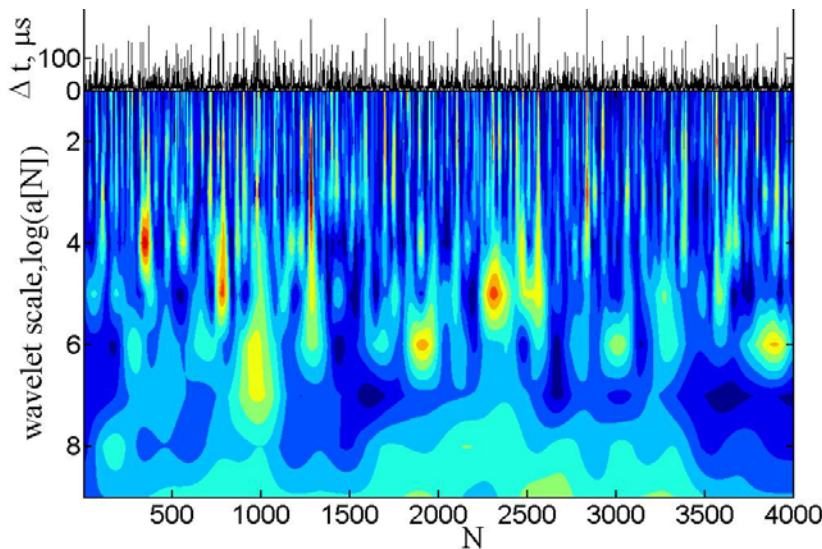


Figure 25 . Intermittent waiting-time series Δt and its wavelet decomposition. Hierarchy of scales is observed as an evidence of fractality and long-term correlation. T-10 tokamak flux signal, SOL.

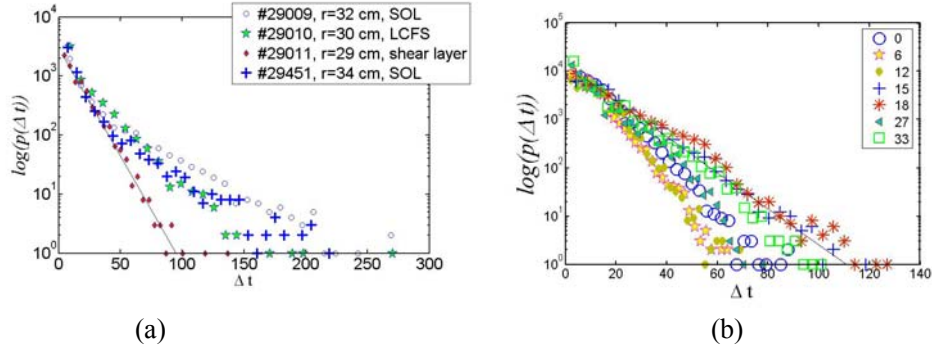


Figure 26 . PDF of waiting-time in semi-logarithmic plots. (a) T-10 tokamak density signals at different radial position. Only at $r=29$ cm in a shear layer the PDF exhibits an exponential law. (b) NAGDIS-II radial flux at different radial position from 0 mm to 33 mm, attached plasma.

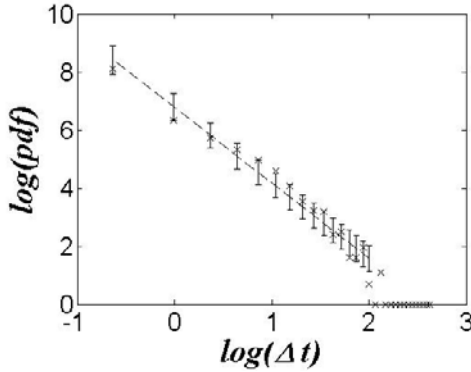


Figure 27 . Log-log plot of waiting-time PDF, flux in SOL of T-10 tokamak.

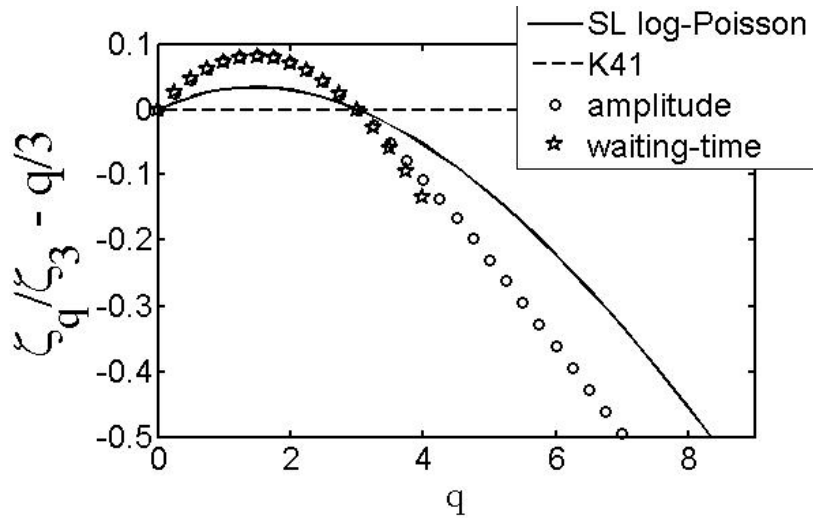


Figure 28. The structure function scaling for the signal amplitude and the waiting-time series in the same signal. Plot of a deviation from Kolmogorov's K41 model. NAGDIS-II detached plasma, $r=27$ mm.

Test of the Iroshnikov-Kraichnan Phenomenology

Although phenomenological cascade models of intermittent turbulence do not follow directly from the equations of motion (e.g., the equations describing tokamak SOL plasma or the hydrodynamic turbulence of a neutral fluid), the properties of a cascade are associated with the structure and symmetries of the motion equations. The assumptions of the log-Poisson model concern the scaling properties of structures of different intensities (see hierarchy (3)). These properties can be attributed to, e.g., the quadratic nonlinearity in the motion equations [26]. In particular, these arguments are considered in analyzing the Burgers equation, which describes strong intermittency. One more assumption concerns the nature of limiting dissipative structures. In a 3D turbulent flow of an incompressible neutral fluid, such structures are considered to be filamentary: it is likely that only filaments are mechanically stable on small scales. In 2D incompressible fluid models, as well as in the Iroshnikov-Kraichnan (IK) model, which describes plasma turbulence in a strong magnetic field, the corresponding limiting structures may be vortices and, accordingly, the predictions for the spectra will differ from those in 3D models. Therefore, in order to check the validity of 2D models and of traditional approaches to describing plasma turbulence in a strong magnetic field, it is important to compare the scalings for the structure functions with those given by the IK model. Several important assumptions of the IK model ought to be carefully checked in practice. This is an incompressible MHD model in which the magnetic field is represented as $B(x, t) = B_0 + b(x, t)$, where B_0 is the mean (quasi-uniform) magnetic field, $B_0 = \langle B \rangle$, and $b(x, t)$ is the fluctuating field component. It is assumed that the size of the system exceeds the correlation length of the random forces acting upon a conducting fluid (plasma) and that the viscosity and conductivity of the fluid are low. The velocity of motion on large scales can be made zero by a Galilean transformation, so the plasma can be considered in a coordinate system moving with the flow. But the magnetic field of the large scale eddies cannot be made zero by passing over to a coordinate system moving with these eddies. In other words, small-scale turbulent eddies are always subject to the large-scale magnetic field. The IK model considers nonlinear energy transfer to small scales, thereby describing weak turbulence. An important assumption of the model is that the cells have the same size along and across the magnetic field. That this assumption is valid for all possible cases has not yet been proved.

Numerical MHD simulations show that energy is transferred predominantly in a direction across the field [46]. The question therefore arises as to whether anisotropy on small scales plays an important role in energy transfer along the cascade. The IK spectrum implies that there is no correlation between the magnetic field and velocity fluctuations. In the IK theory, the scaling for the structure function is of the fourth order, $\zeta(4) = 1$ (in contrast to the third-order scaling $\zeta(3) = 1$ in the K41 model). This is why we can compare the experimental scalings $\zeta(q)/\zeta(4)$, normalized to $\zeta(4)$, with the scaling $\zeta(4) =$

$q/4$, predicted in the IK model. A comparison of the experimentally measured scalings with the IK scaling is given in Figure 29 for T-10 tokamak. The experimental curves are seen to deviate substantially from the IK predictions. Consequently, in order to interpret these experimental results, it is necessary to refer to other models.

The IK phenomenology was used in the next generations of MHD turbulence models. The Goldreich–Sridhar moderately strong MHD turbulence model (published in 1995 and known as GS95) provides the most detailed description of anisotropy and mixing on microscales in a turbulent magnetic field. The GS95 turbulence model considers the balance

of the nonlinear terms in the MHD equation. This model, which came to be called moderate or intermediate, differs from the weak MHD turbulence model and describes observed energy spectra that are close to the Kolmogorov spectrum. In the GS95 model, the moving cells mix the lines of the magnetic field across its local direction. As in the case of a hydrodynamic turbulence, the correlation time for coherent structures is comparable to $(k_{\perp}v_k)^{-1}$ for any spatial scale. This mixing motion is closely related to the wave motion with the correlation time $(k_{\parallel}v_A)^{-1}$. GS95 is based on the concept of “critical balance” between these two time scales, $(k_{\perp}v_k)^{-1} \sim (k_{\parallel}v_A)^{-1}$. The resulting anisotropy depends on the spatial scale $k_{\parallel} \propto k_{\perp}^{-2/3}$; i.e., all the cells on smaller scales are longer. In the global coordinate system, the turbulent magnetic field changes the orientation of the cells and mixes them only across its local direction. This is why the GS95 model makes use of a coordinate system oriented along the local magnetic field. In this coordinate system, the spectrum of the cascade across the field is close to the Kolmogorov spectrum and the turbulence becomes local in nature, like hydrodynamic turbulence. In MHD turbulence theory, the GS95 model came to be used instead of the IK model [50]. The question of whether the predictions and conclusions of the GS95 model can be used to describe tokamak SOL plasmas remains open and requires experimental verification. The anisotropy effects associated with the distinctive features of MHD turbulence can also be incorporated in the log-Poisson model [16, 17]. Numerical simulations of MHD turbulence [36,37] capture the ESS property and dissipative structures predicted by the log- Poisson model, possibly because the MHD equations possess the same ESS symmetries (the Lie symmetries) as the NS equation [71-73].

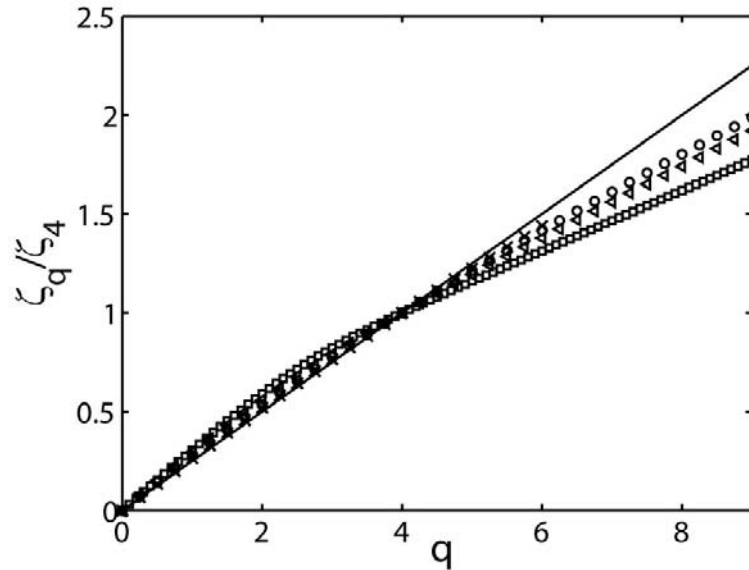


Figure 29 . Scalings $\zeta(q)/\zeta(4)$, for the plasma density in the shear layer (crosses), near the LCFS $r = 30$ cm (circles), and at $r = 34$ cm in the SOL region (triangles) and for the density of the cross-field particle flux Γ at $r = 36$ cm in the far SOL region (squares). The nonlinear dependence demonstrates the deviation from the IK scaling $q/4$ (solid line).

8. TRANSPORT SCALING LAWS AND SUPERDIFFUSION IN EDGE PLASMA

The statistical description of transport processes in fusion plasmas is an alternative approach to the traditional characterization of a transport based on the computation of effective transport diffusion coefficients assuming Einstein law of the diffusion. Traditionally, a displacement of particles across a magnetic field with time τ is considered as $\langle \delta x^2 \rangle \propto D\tau$ with a constant (or independent on time scale) diffusion coefficient D . In these models, D is estimated from some assumptions supposing some dominant physical mechanism and eliminating other contributions. In such approach, effects of a non-linear coupling of modes with different scales (large and small) is excluded that could lead to a significant deviation of the model properties from the real plasma properties. It relates especially to the SOL plasmas where many mechanisms (such as pressure gradient driven instabilities, stochastic magnetic structure, flow shearing, neutral drag, radiation instabilities, effect of the boundaries etc.) can contribute to the transport process. Statistical approach is based on a general consideration of turbulent fluctuations suggesting some universal properties of intermittent turbulence. It allows skipping a consideration of concrete mechanisms driven the turbulent and transport process. Because a plasma transport in edge of fusion devices is a multi-scale process consisting of events of different scales (e.g. large scale blobs and small scale coherent events etc.), the statistical approach is most appropriate for a self-consistent description of turbulence and transport phenomena.

The log-Poisson model could be used to estimate a transport scaling based on the self-similarity indexes β and Δ that responsible for percolation effect in the turbulence. In a simplified approach [55], the diffusion scaling depends on the structure function scaling as $D \propto \tau^{K(-1)}$, the exponent $K(q)$ relates with the scaling of the high-order structure function $\zeta(q)$ as $K(q)=q-\zeta(3q)$. Index $K(-1)$ is defined by fractal dimensions. A displacement of particles across a magnetic field with time τ is scaled as

$$\langle \delta x^2 \rangle \propto D\tau \propto \tau^\alpha \quad (45)$$

with an exponent $\alpha \approx 1 + K(-1)$. This index was estimated from experimental scalings. From Table 1 and Eq. (5) for the log-Poisson scalings one can get the time scaling for the D_f across the magnetic field with $K(-1) \approx 0.4 \div 0.87$. Experimental measurements in edge of fusion devices (in T-10, HYBTOK-II, JT-60U tokamaks, LHD stellarator, linear device NAGDIS-II) [55] shown that $\alpha \approx 1.4 \div 1.87 > 1$, i.e. such scaling invokes the superdiffusion (as classic diffusion implies that $\alpha = 1$).

Index α varies with a radius in edge plasma. In tokamak JT-60U SOL (Figure 30a) scaling exponents α exhibit a scattering behaviour between 1 and 1.5 [86]. This area is characterized by a specific behaviour of the SOL parameters [4]. In Large Helical Device edge plasma (Figure 30b) the superdiffusion process ($\alpha > 1$) is observed at vertical distance 0.97-1.15 m [86].

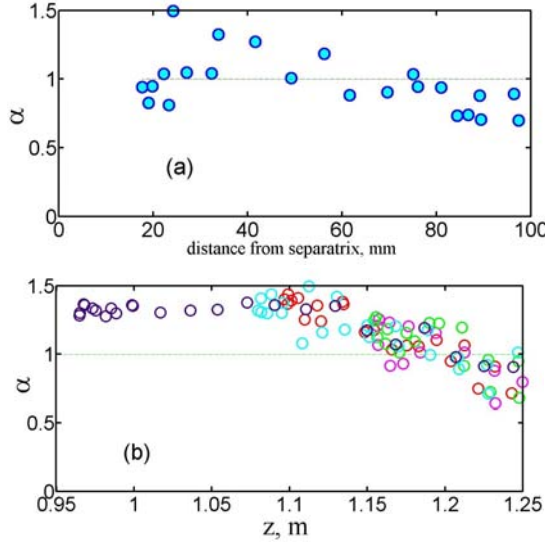


Figure 30. Diffusion scaling index $\langle \delta x^2 \rangle \propto \tau^\alpha$ in edge plasma of (a) JT-60U tokamak; (b) LHD stellarator .

6. CONCLUSION

In this review article, results of the analysis of experimental data from the edge plasma of fusion devices are presented. The fluctuations observed in plasma are intermittent and self-similar. Edge plasma turbulence is characterized by a non-Gaussian probability density function of the fluctuation amplitudes. The intermittency and scale invariance of the turbulence are studied by analyzing the structure functions (moments of the PDF) of different orders versus time lag .

The structure function method, which makes use of the statistical moments of the distribution function of the density fluctuation amplitudes and thereby provides an effective means of analyzing the self-similarity properties of the turbulent process. The high-order moments (structure functions) characterize the nonuniformity of the process on small scales. The structure function scalings are non-linear. Intermittent turbulence exhibits an extended self-similarity (ESS). While a power-law scaling of the structure functions $S_q(\tau) \sim \tau^{\zeta(q)}$ can be found only in a limited time interval (over 1÷1,5 decades of time scales), the generalized scale invariance (ESS), when $S_q(\tau)$ has a power-law dependence on $S_3(\tau)$, $S_q(\tau) \sim S_3(\tau)^{\zeta(q)/\zeta(3)}$, can be extended over 2÷3 decades of time scales. The ESS (a generalized scale invariance) observation is very important for further studies of non-trivial symmetries. Hidden statistical symmetries of the equations of motion, a hierarchy of moments, and multifractality are behind the ESS. The multifractality is confirmed by the experimental singularity (multifractal) $D(h)$ spectra, which are broadened indicating a strong intermittency.

Using the ESS property of the turbulence and the wavelet technique, the experimental scaling exponents $\zeta(q)$ up to the order $q=9$ have been got rather accurately. The scaling exponent $\zeta(q)$ is a nonlinear function of the index q for all data. The experimental data are fitted in the full scale range to the log-Poisson model, considering a stochastic cascade process. The fitting demonstrates a reasonable agreement with the log-Poisson model of

intermittent turbulence with dominant contribution from quasi-1D filament-like structures. 2D dissipative structures conform to the far SOL in tokamaks. They have been compared with the predictions of the K41 turbulence model and log-Poisson model. In most cases, the scalings deviate substantially from the Kolmogorov spectrum and can be described by scaling (Eq.28) with two fitting parameters in the log- Poisson model. One of the parameters characterizes the power law for the hierarchy of the moments and qualitatively describes the degree of intermittency. The second fitting parameter of the model is associated with the geometry of the limited dissipative structures, which are responsible for the generalized scale invariance property on spatial scales close to the dissipation length. In the literature, the log-Poisson model is treated as the most general model for describing a random cascade process of energy transfer between the turbulent cells. This model makes use of the generalized scale invariance property, which is observed in experiments as the hierarchical dependence of the moments of different orders. Generalized scale invariance is observed on time scales much longer than the linear correlation time, thereby providing evidence of distinctive symmetry (self-similarity) properties of the turbulent process. In theoretical studies (see [16, 17, 26] and other related papers), the generalized scale invariance property is attributed to the hidden statistical symmetries of the equations describing turbulent processes. In hydrodynamics, these are the NS equations, and, in SOL plasma physics, these are MHD equations that possess self-similar symmetries equivalent to the symmetries of the NS equations. The log-Poisson model provides a description of the experimentally observed multiscale and multifractal nature of turbulence.

The log-Poisson model proposes different functional dependences of the scaling on the geometry of the limiting dissipative structures. A study has been made of 1D (filamentary) and 2D (sheetlike) structures that arise on increasingly small spatial scales in a cascade process. The experimental scalings can be compared with these theoretical predictions. Many of the experimentally obtained scalings have been found to be close to the model scalings for 1D dissipative structures. The experimental data have been tested against modified scaling (Eq.39). It is only for the far SOL region that the experimental scalings are found to be close to the model scalings for 2D dissipative structures. This result can be interpreted as evidence of the dominant contribution of the vortices that are discussed in different theoretical studies (see [41] and other related papers).

It seems that the turbulence in the edge plasma of fusion devices is similar to hydrodynamic turbulence and is governed by cross-field motions. Most experimental data that we analyzed, demonstrate the statistical features to be closer to hydrodynamic flows than to flows in the standard IK phenomenology. The Goldreich and Sridhar phenomenology, proposed the critical balance and anisotropy of fluctuation structures in 3D, is one of the best concepts, which can be implemented for the interpretation of experimental data.

The question of whether the SOL turbulence in tokamaks can be dominated by the presence of 1D dissipative structures require additional theoretical investigations. It should be kept in mind that the same properties are observed in 3D turbulence in a neutral fluid [26]. The scale invariance properties of a turbulent process are related to the correlation properties. The nontrivial self-similarity establishes long-range correlations in a random process and makes it a process with memory. Long-range correlations in turbulent SOL plasma give rise to turbulent plasma transport across the magnetic field. This transport is more intense than that predicted by a classical diffusion law. The ESS of the log-Poisson process establishes long-scale correlations, which give rise to an anomalous process—superdiffusion. In fusion

devices, this property deteriorates confinement—an effect that is well known from experimental observations—and leads to enhanced plasma losses. The experimentally obtained exponents in the scale invariance laws can be used to estimate scalings for turbulent transport.

Turbulent transport scalings can be evaluated using the log-Poisson fitted parameters. The average squared displacement of a particle can be evaluated as : $\langle \delta x^2 \rangle \propto D_f \tau \propto \tau^\alpha$, with $\alpha \approx 1.4 \div 1.87$. In conclusion, as the α values are > 1 supposing superdiffusion.

Finally, it can be concluded that edge plasma turbulence in fusion devices is characterized by intermittency and multifractality, the generalized scale invariance. The scalings for the statistical moments are well described by the log-Poisson model with a random anisotropic cascade.

REFERENCES

- [1] B.B. Kadomtsev *Plasma Turbulence* (London: Academic) (1965)
- [2] A. A. Schekochihin, S. C. Cowley, *Turbulence and Magnetic Fields in Astrophysical Plasmas*, in "Magnetohydrodynamics: Historical Evolution and Trends", S. Molokov et al., Eds, Springer, pp. 85-115 (2007)
- [3] S. J. Zweben, J. McChesney, and R. W. Gould, Nucl. Fusion 23, 825 (1983).
- [4] V. P. Budaev, S. Takamura, N. Ohno, and S. Masuzaki, Nucl. Fusion 46, 181 (2006).
- [5] G. Y. Antar, S. I. Krasheninnikov, P. Devynck, et al., Phys. Rev. Lett. 87, 065 001 (2001).
- [6] V. Budaev, G. Fuchs, R. Ivanov, and U. Samm, Plasma Phys. Controlled Fusion 3, 4 29 (1993).
- [7] B. A. Carreras, V. E. Lynch, and B. LaBombard, Phys. Plasmas 8, 3702 (2001).
- [8] S. J. Zweben, J. A. Boedo, O. Grulke, et al., Nucl. Fusion 49, S1 (2007).
- [9] M. D. Millionschikov, Dokl. Akad. Nauk. SSSR 32, 611 (1941).
- [10] A. A. Vedenov, E. P. Velikhov, and R. Z. Sagdeev, Yad. Sintez 1, 82 (1961).
- [11] R. H. Kraichnan, J. Fluid Mech. 5, 497 (1959).
- [12] A. M. Bykov and I. N. Toptygin, Usp. Fiz. Nauk 163 (11), 19 (1993) [Phys. Usp. 36, 1020 (1993)].
- [13] G. M. Batanov, V. E. Bening, V. Yu. Korolev, et al., Pis'ma Zh. Eksp. Teor. Fiz. 78, 974 (2003) [JETP Lett. 78, 502 (2003)].
- [14] N. N. Skvortsova, V. Yu. Korolev, G. M. Batanov, et al., Plasma Phys. Controlled Fusion 48, A393 (2006).
- [15] A. N. Kolmogorov, J. Fluid Mech. 13, 82 (1962).
- [16] Z. S. She and E. Leveque, Phys. Rev. Lett. 72, 336 (1994).
- [17] B. Dubrulle, Phys. Rev. Lett. 73, 959 (1994).
- [18] D. Schertzer, S. Lovejoy, and P. Hubert, in *Mathematical Problems in Environmental Science and Engineering*,
- [19] Ed. by A. Ern and Liu Weiping (Higher Education Press, Beijing, 2002), Vol. 4, p. 106.
- [20] I. Guikhman and A. Skorokhod, *Introduction to the Theory of Random Processes* (W. B. Saunders, Philadelphia, 1969).
- [21] A. N. Kolmogorov, Dokl. Akad. Nauk SSSR, 30, 299 (1941).

- [22] V. Budaev, Y. Kikuchi, Y. Uesugi, and S. Takamura, Nucl. Fusion 44, 108 (2004).
- [23] G. S. Kirnev, V. P. Budaev, S. A. Grashin, et al., Nucl. Fusion 45, 459 (2005).
- [24] E. O. Vekshina, P. R. Goncharov, S. V. Shatalin, et al., Pis'ma Zh. Tekh. Fiz. 26 (19), 52 (2000).
- [25] S. V. Shatalin, A. V. Pavlov, A. Yu. Popov, et al., Fiz. Plazmy 33, 195 (2007) [Plasma Phys. Rep. 33, 169(2007)].
- [26] P. G. Frick, *Turbulence: Approaches and Models* (Inst. Komp. Issled., Izhevsk, 2003) [in Russian].
- [27] U. Frisch, *Turbulence: The Legacy of A.N. Kolmogorov* (Cambridge University Press, Cambridge, 1995).
- [28] E. A. Novikov and R. V. Styuart, Izv. Akad. Nauk SSSR, Ser. Geofiz. 3, 408 (1964).
- [29] R. Benzi, S. Ciliberto, R. Tripiccione, et al., Phys. Rev. E 48, R29 (1993).
- [30] V. P. Budaev, N. Ohno, S. Masuzaki, et al., Nucl. Fusion 48, 024 014 (2008).
- [31] Parisi G. and Frish U.// in *Turbulence and Predictability*. North-Holland, Amsterdam, 1985.
- [32] H. Politano and A. Pouquet, Geophys. Rev. Lett. 25, 273 (1998).
- [33] H. Politano, A. Pouquet, and V. Carbone, Europhys. Lett. 43, 516 (1998).
- [34] A. S. Monin and A. M. Yaglom, *Statistical Fluid Mechanics* (Nauka, Moscow, 1967; MIT Press, Cambridge, MA, 1971,1975), Vols. 1, 2.
- [35] P.S. Iroshnikov *Astron. Zh.* 40 742 (1963) (reprinted 1964 Sov. Astron. 7 566)
- [36] R.H. Kraichnan *Phys. Fluids* 8 1385 (1965)
- [37] D Biskamp W Mueller *Phys. Rev E* 67, 066302 2000 (2003)
- [38] D. Biskamp, W Mueller *Phys. Plasmas* 7, 12 4889 (2000)
- [39] S.I. Braginskii *Reviews of Plasma Physics* vol I, ed M A Leontovich (New York: Consultants Bureau) , 205 (1965)
- [40] I.A. Zeiler et al *Phys. Plasmas* 4 2134 (1997)
- [41] W. Horton *Phys. Rep.* 192 177 (1990)
- [42] B.D. Scott *Phys. Plasmas* 12 062314 (2005)
- [43] V.P. Pastukhov *Plasma Phys. Rep.* 31 577 (2005)
- [44] A. Hasegawa and K. Mima *Phys. Rev. Lett.* 39 205 (1977)
- [45] U. Frisch, A. Pouquet, J. Leorat, and A. Mazure, *J. Fluid Mech.* 68, 769 (1975)
- [46] D. Biskamp, *Magnetohydrodynamic Turbulence* (Cambridge University Press, Cambridge, 2003).
- [47] D. Biskamp and E. Schwarz, *Phys. Plasmas* 8, 3282 (2001)
- [48] V. Carbone, P. Veltry, R. Bruno, *Nonlinear Processes in Geophysics* 3, 247 (1996).
- [49] R.J. Leamon et al., *J. Geophys. Res., @Space Phys.* 103, 4775 (1998).
- [50] S.P. Savin, E. Amata, L. Zelenyi et al., *JETP Letters*, submitted, (2008)
- [51] P. Goldreich and S. Sridhar *Astrophys. J.* 438 763 (1995)
- [52] J. Maron and P. Goldreich, *Astrophys. J.* 554, 1175 (2001)
- [53] J. Cho, A. Lazarian, and E.T. Vishniac, *Astrophys. J.* 564, 291 (2002).
- [54] S. Boldyrev *Phys. Rev. Lett.* 96, 115002 (2006)
- [55] D. Schertzer, S. Lovejoy and F. Schmitt, in *Small-scale structures in 3D hydro and MHD turbulence*, eds. M. Meneguzzi et al. (Springer-Verlag, Berlin, 1995).
- [56] V P Budaev et al., *Nucl. Fusion* 48 024014 (2008)
- [57] Budaev CPP 2008
- [58] Budaev PPCF 2008

- [59] N. Ohno et al *Nucl. Fusion* 41 1055 (2001)
- [60] Masuzaki S. et al 2002 *Nucl. Fusion* 42 750
- [61] Takamura S. et al 2003 *M. Nucl. Fusion* 43 393
- [62] Budaev V.P. et al 2004 *Nucl. Fusion* 44 S108
- [63] Budaev V.P. et al 2002 *J. Plasma Fusion Res. Ser.* 5 418
- [64] Ottino J.M. 1989 *The kinematic of mixing: stretching, chaos and transport* (Cambridge University Press, Cambridge).
- [65] A.N. Kolmogorov, *J. Fluid Mech.* 13, 82 (1962).
- [66] Kadomtsev B.B. and Pogutse O.P. 1984 *Soviet JETP Lett.* 39 269
- [67] Shurygin R.V. 2004 *Plasma Physics Reports* 30 353
- [68] Falkovich G. et al 2001 *Rev. Mod. Phys.* 73 913
- [69] Naulin V. 2005 *Phys. Rev. E* 71 015402
- [70] Olver P.J. 1993 *Applications of Lie Groups to Differential Equations* Springer-Verlag New York Bogoyavlenskij O.I. 2002 *Phys. Rev. E* 66 056410
- [71] Ciocogna G. et al 2006 *Symmetry, Integrability and Geometry: Methods and Applications* 2 17
- [72] Gusyatnikova V.N. et al 1989 *Acta Appl. Math.* 15 23
- [73] Gridnev I. P. 1968 *Journal of Applied Mechanics and Technical Physics* 9 718
- [74] Ames W.F. and M.C. Nucci 1985 *J. Eng. Math.* 20 181
- [75] Ibragimov N.H. (Editor) 1994 *CRC Handbook of Lie group analysis of differential equations*, Boca Raton CRC Press 1 - 3
- [76] Arneodo A. et al 1997 *J. Phys. II France* 7 363
- [77] Arneodo A. et al 1998 *J. Math. Phys.* 39 4142
- [78] J. F. Muzy , E. Bacry and Arneodo A. *Phys. Rev. Lett.* 67 3515 (1991)
- [79] Schertzer D . et al 1997 *Fractals* 5 427
- [80] Schertzer D. and Lovejoy S. 2004 *Physica A* 338 173
- [81] Lovejoy S. et al 1998 *Water Resources Research* 34 3283
- [82] J. F. Muzy, E. Bacry, and A. Arneodo, *Int. J. BifurcationChaos* 4, 245 (1994).
- [83] A. Arneodo, E. Bacry, and J. F. Muzy, *Physica A* (Amsterdam) 213, 232 (1995).
- [84] Yordanova, E., A. Vaivads, M. Andre, S. C. Buchert, Z. Voros, *Phys. Rev. Lett.* (2007)
- [85] Silchenko A. and Hu C.-K. 2001 *Phys. Rev. E* 63 041105
- [86] Budaev PFR 2008
- [87] H. Politano, A. Pouquet, and V. Carbone, *Europhys. Lett.* 43, 516 (1998).
- [88] V. Carbone, R. Bruno, and P. Veltri, *Geophys. Rev. Lett.* 23, 121 (1996).
- [89] Z. S. She and E. Waymire, *Phys. Rev. Lett.* 74, 262 (1995).
- [90] S. Boldyrev *The Astrophysical Journal*, 569 841 (2002)
- [91] H. Politano and A. Pouquet *Phys. Rev. E* 52, 636 (1995)
- [92] L. M. Zelenyi and A. V. Milovanov, *Usp. Fiz. Nauk* 174,809 (2004) [*Phys. Usp.* 47, 749 (2004)].
- [93] L. D. Landau and E. M. Lifshitz, *Fluid Mechanics* (Nauka, Moscow, 1986; Pergamon, Oxford, 1987).
- [94] S. Boldyrev, *Phys. Rev. Lett.* 97, 255 002 (2006).
- [95] B. V. Gnedenko, B. V. Gnedenko, *Theory of Probability*
- [96] (Gostekhizdat, Moscow, 1956; Central Books, London,1970).
- [97] Bak P. et al 1988 *Phys. Rev. A* 38 364
- [98] Spada E. et al 2001 *Phys. Rev. Lett.* 86 3032

- [99] Sanches R. *et al* 2002 *Phys. Rev. Lett.* 88 068302
- [100] Sanches R. *et al* 2003 *Phys. Rev. Lett.* 90 185005
- [101] Mandelbrot B.B. 1999 *Scientific American* 280 70
- [102] Feller W. 1971 *An introduction to probability theory and its applications* Vol 2 (John Wiley & Sons New York)
- [103] Chechkin A. V. *et al.* 2002 *Physical Review E* 66 046129

Chapter 4

TURBULENCE, TURBULENT MIXING AND DIFFUSION IN SHALLOW-WATER ESTUARIES

Hubert Chanson^{1*} and Mark Trevethan²

¹The University of Queensland, Brisbane, Australia

²MARUM, The University of Bremen, Germany (formerly Ph.D. graduate in Civil Engineering. The University of Queensland, Brisbane Australia)

1. INTRODUCTION

In natural waterways and estuaries, an understanding of turbulent mixing is critical to the knowledge of sediment transport, storm-water runoff during flood events, and release of nutrient-rich wastewater into ecosystems. The predictions of contaminant dispersion in estuaries can rarely be predicted analytically without exhaustive field data for calibration and validation. Why? In natural estuaries, the flow Reynolds number is typically within the range of 10^5 to 10^8 and more. The flow is turbulent, and there is an absence of fundamental understanding of the turbulence structure. Any turbulent flow is characterised by an unpredictable behaviour, a broad spectrum of length and time scales, and its strong mixing properties. In his classical experiment, Osborne REYNOLDS (1842-1912) illustrated this key feature with the rapid mixing of dye of a turbulent flow (REYNOLDS 1883). This is seen in Figure 1 showing the original Reynolds experiment and a modified Reynolds experiment. In turbulent flows, the fluid particles move in very irregular paths, causing an exchange of momentum from one portion of the fluid to another, as shown in Figure 1 where dye is rapidly dispersed in the turbulent flow regime ($Re = 2.3 \cdot 10^3$). In natural estuaries, strong momentum exchanges occur and the mixing processes are driven by turbulence. Interestingly Osborne REYNOLDS himself was involved in the modelling of estuaries (REYNOLDS 1887).

Relatively little systematic research was conducted on the turbulence characteristics in natural estuarine systems, in particular in relatively shallow-water systems. Long-duration

* Email: h.chanson@uq.edu.au - Url: <http://www.uq.edu.au/~e2hchans/> - Ph.: +61 7 3365 3516 - Fax: +61 7 3365 4599

studies of turbulent properties at high frequency are extremely limited. Most field measurements were conducted for short periods, or in bursts, sometimes at low frequency: e.g. BOWDEN and FERGUSON (1980), SHIONO and WEST (1987), KAWANISI and YOKOSI (1994), HAM et al. (2001), VOULGARIS and MEYERS (2004). The data lacked spatial and temporal resolution to gain insights into the characteristics of fine-scale turbulence. It is believed that the situation derived partly from some limitation with suitable instrumentation for shallow-water estuaries.

Herein the turbulence characteristics of shallow-water estuaries with semi-diurnal tides are examined. It is shown that turbulence field measurements must be conducted continuously at high frequency for relatively long periods. Detailed field measurements highlight the large fluctuations in all turbulence characteristics during the tidal cycle. While the bulk parameters fluctuate with periods comparable to tidal cycles, the turbulence properties depend upon the instantaneous local flow properties, and the structure and temporal variability of turbulent characteristics are influenced by a variety of mechanisms.

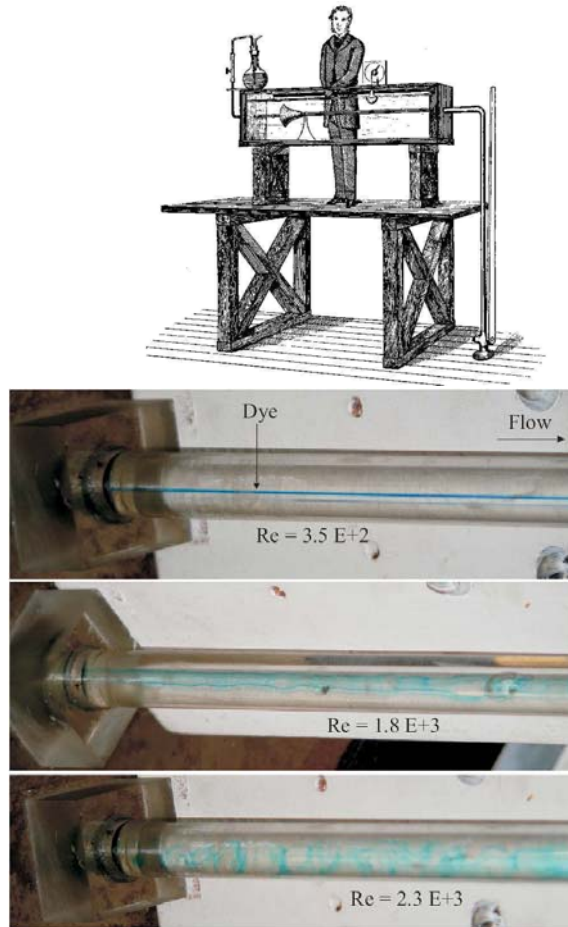


Figure 1. Dye dispersion in laminar and turbulent flows (Left) Gravure of the experimental apparatus of Osborne REYNOLDS (1883) (Right) Dye injection in a circular pipe for $Re = 3.5 \times 10^2$, 1.8×10^3 and 2.3×10^3 .

2. TURBULENCE MEASUREMENTS IN SMALL ESTUARIES

2.1. Presentation

Since "turbulence is a three-dimensional time-dependent motion in which vortex stretching causes velocity fluctuations to spread to all wavelengths between a minimum determined by viscous forces and a maximum determined by the boundary conditions of the flow" (BRADSHAW 1971, p. 17), turbulence measurements must be conducted at high frequency to characterise the small eddies and the viscous dissipation process. They must also be performed over a sampling period significantly larger than the characteristic time of the largest vortical structures to capture the "random" nature of the flow and its deviations from Gaussian statistical properties. Turbulence in natural estuaries is neither homogeneous nor isotropic. Basically detailed turbulence measurements are almost impossible in unsteady estuarine flows unless continuous sampling at high frequency is performed over a full tidal cycle. The estuarine flow conditions and boundary conditions may vary significantly with the falling or rising tide. In shallow-water estuaries and inlets, the shape of the channel cross-section changes drastically with the tides as shown in Figures 2 and 3. Figures 2 and 3 illustrate two sampling sites in a small subtropical estuary at high and low tides. Figure 2 presents the cross-section at the mid-estuary sampling site with more than 3 m depth at high tide and less than 0.6 m of water at low tide. Figure 3 shows a narrower section in the upper estuary at both high and low tides.



(A) End of flood tide on 16 May 2005 with poles supporting the instrumentation visible across the creek.



(B) Low tide on 23 November 2003 - The water depth was less than 0.6 m in the deepest channel next to the ADV poles during spring tidal conditions.

Figure 2. Sampling site in the mid-estuarine zone of Eprapah Creek, Australia (site 2B, AMTD 2.1 km) looking upstream.



(A) High tide in 28 August 2006 looking downstream (Courtesy of CIVL4120 student Group 3) - The water depth was about 2 m.



(B) Low tide on 8 June 2006 looking upstream (Courtesy of Clive BOOTH).

Figure 3. Sampling site in the upper estuarine zone of Eprapah Creek, Australia (site 3, AMTD 3.1 km).

All these constraints affect the selection of a suitable, rugged instrumentation for field deployment. Traditional propellers and electro-magnetic current meters are adequate for time-averaged velocity measurements and some large-scale turbulence measurements, but these instruments lack temporal and spatial resolution for fine-scale turbulence measurements. Velocity profilers do not work in shallow waters (e.g., less than 0.6 m) while lacking spatial and temporal resolution. A suitable instrumentation for turbulence measurements in shallow-water estuaries is limited to the acoustic Doppler velocimeters (ADV), although the signal can be adversely affected by "spikes", noises and instabilities.

2.2. Turbulence Properties

Turbulent flows have a great mixing potential involving a wide range of eddy length scales (HINZE 1975). Although the turbulence is a "random" process, the small departures from a Gaussian probability distribution constitute some key features. For example, the skewness and kurtosis give some information on the temporal distribution of the turbulent velocity fluctuation around its mean value. A non-zero skewness indicates some degree of temporal asymmetry of the turbulent fluctuation: e.g., acceleration versus deceleration, sweep versus ejection. The skewness retains some sign information and it can be used to extract basic information without ambiguity. An excess kurtosis larger than zero is associated with a peaky signal: e.g., produced by intermittent turbulent events.

In turbulence studies, the measured statistics include usually (a) the spatial distribution of Reynolds stresses, (b) the rates at which the individual Reynolds stresses are produced, destroyed or transported from one point in space to another, (c) the contribution of different sizes of eddy to the Reynolds stresses, and (d) the contribution of different sizes of eddy to the rates mentioned in (b) and to rate at which Reynolds stresses are transferred from one range of eddy size to another (BRADSHAW 1971). The Reynolds stress is a transport effect resulting from turbulent motion induced by velocity fluctuations with its subsequent increase of momentum exchange and of mixing (PIQUET 1999). The turbulent transport is a property of the flow. The turbulent stress tensor, or Reynolds stress tensor, includes the normal and tangential stresses, although there is no fundamental difference between normal stress and tangential stress. For example, $(v_x + v_y)/\sqrt{2}$ is the component of the velocity fluctuation along a line in the xy-plane at 45° to the x-axis; hence its mean square $(v_x^2 + v_y^2 + 2 v_x v_y)/2$ is the component of the normal stress over the density in this direction although it is a combination of normal and tangential stresses in the x- and y-axes.

2.3. Field Experiments in Shallow-Water Estuaries with Semi-Diurnal Tides

A series of detailed turbulence field measurements were conducted in two shallow-water estuaries with a semi-diurnal tidal regime (Table 1).

Table 1. - Turbulence field measurements in Australia (Eprapah Creek, QLD) and Japan (Hamana Lake).

Ref.	Dates	Tidal range (m)	ADV system(s)	Sampling rate (Hz)	Sampling duration	Sampling volume
(1)	(2)	(3)	(4)	(5)	(6)	(7)
<u>Series E</u>						<u>Eprapah Creek, QLD Australia</u>
E1	4/04/03	1.84	10 MHz	25	9 × 25 min	Site 2B, AMTD 2.1 km, 14.2 m from left bank, 0.5 m below surface.
E2	17/07/03	2.03	10 MHz	25	8 hours	Site 2, AMTD 2.0 km, 8.0 m from left bank, 0.5 m below surface.
E3	24/11/03	2.53	10 MHz	25	7 hours	Site 2B, AMTD 2.1 km, 10.7 m from left bank, 0.5 m below surface.
E4	2/09/04	1.81	10 MHz	25	6 & 3 hours	Site 2B, AMTD 2.1 km, 10.7 m from left bank, 0.052 m above bed.
E5	8-9/03/05	2.37	10 MHz	25	25 hours	Site 2B, AMTD 2.1 km, 10.7 m from left bank, 0.095 m above bed.
E6	16-18/05/05	1.36	2 ADVs (10 & 16 MHz)	25	49 hours	Site 2B, AMTD 2.1 km, 10.7 m from left bank, 0.2 & 0.4 m above bed.
E7	5-7/06/06	1.58	2 ADVs (10 & 16 MHz)	25 & 50	50 hours	Site 3, AMTD 3.1 km, 4.2 m from right bank, 0.2 & 0.4 m above bed.
E8	18/06/06	2.10	--	--	12 hours	Sites 1, 2B & 3, AMTD 1.0, 2.1 and 3.1 km
E9	2-4/10/06 & 11-13/10/06	1.89 & 1.81	--	--	50	Six sampling sites: AMTD 1.0 to 3.4 km
E10	6-8/06/07	1.76	3 ADVs (16 MHz)	50	50 hours	Site 2B, AMTD 2.1 km, 10.7 m from left bank, 0.13 & 0.38 m above bed.
<u>Series HL</u>						<u>Hamana Lake, Japan</u>
J1	24-25/11/05	0.39	3D-Vector field ADV	32	28 hours	Site 1, 0.25 m above bed, 454 m from left bank.
J2	30/11-1/12/05	0.56	3D-Vector field ADV	32	25 hours	Site 1, 0.25 m above bed, 454 m from left bank.
J3	10-21/12/05	0.6	3D-Vector field ADV	32	30 hours	Site 1, 0.25 m above bed, 454 m from left bank.

Note: AMTD: Adopted Middle Thread Distance measured upstream from the river mouth; Tidal range: maximum tidal range observed at sampling site.

At Eprapah Creek (Australia), the estuarine zone was 3.8 km long, about 1 to 2 m deep mid-stream (Fig. 2 & 3). This was a relatively small estuary with a narrow, elongated and meandering channel (CHANSON et al. 2005, TREVETHAN et al. 2007a, 2008). It is a drowned river valley (coastal plain) type with a small, sporadic freshwater inflow, a cross-section which deepens and widens towards the mouth, and surrounded by extensive mud flats. This type of estuary is very common in Australia. It is also called an alluvial estuary (SAVENIJE 2005) and can be classified as a wet and dry tropical/subtropical estuary (DIGBY et al. 1999). Although the tides are semi-diurnal, the tidal cycles have slightly different periods and amplitudes indicating that a diurnal inequality exists. Table 1 summarises ten field studies conducted between 2003 and 2007. A range of field conditions were tested: tidal conditions from neap tides (Studies E6, E7, E10) to spring tides (Studies E3, E5, E8), and different bathymetry from mid-estuary (Studies E5, E6, E10) to upper estuary (Study E7) (Table 1).

Another series of field studies were undertaken at Hamana Lake, Japan in late 2005 (TREVETHAN 2008). Hamana Lake is a relatively large tidal lake with a small opening to the Pacific Ocean (Fig. 4). It extends approximately 15 km inland and has a surface area of $7.4 \times 10^7 \text{ m}^2$. The width of the entrance is approximately 200 m and is controlled by man made structures (Fig. 4A). The depth of Hamana Lake increases landwards, from less than 1 m near the entrance to more than 12 m further inland. The field investigations were conducted under neap and spring tidal forcing, collecting continuous high frequency turbulence data over a 25 hour period. The sampling site was located in a shallow area near the estuary mouth (Fig. 4). This type of shallow region is typical of restricted entrance (bar-built) type estuaries (DYER 1997). It was located approximately 600 m North-East of the main navigation channel, 450 m South of the nearest bank and approximately 3.5 km NNW of the estuary mouth seen in Figure 4A. The mean depth was approximately 0.9 m during the two field studies and the maximum tidal range during the field studies were 0.39 and 0.56 m.



(A) Estuary mouth in 1999 (Courtesy of Mr. KATO, Omotehama network).

Figure 4. (Continued)



(B) Hamana Lake sampling site on 24 November 2005, looking North to nearest bank about 450 m away.



(C) Wind waves on 24 November 2005 with the poles holding the ADV system on the far left.

Figure 4. Photographs of Hamana Lake (Japan).

2.4. Instrumentation

Turbulent velocities were measured with acoustic Doppler velocimetry. That is, a Sontek™ UW 3D ADV (10 MHz) and some Sontek™ 2D micro-ADV (16 MHz) in Australia (Erapah Creek), and a Nortek™ 3D-Vector field ADV in Japan (Hamana Lake). The turbulent velocity measurements were performed continuously at high frequency for between 8 to 50 hours during various tide conditions (Table 1, columns 5 & 6). All ADV units were synchronised carefully within 20 ms for the entire duration of the studies.

The acoustic backscatter intensity of some ADV signals was also analysed. The backscatter intensity is a function of the ADV signal amplitude that is proportional to the number of particles within the sampling volume :

$$I_b = 10^{-5} 10^{0.043 \text{ Ampl}} \quad (1)$$

where the backscatter intensity I_b is dimensionless and the average amplitude Ampl is in counts. (The coefficient 10^{-5} is a value introduced to avoid large values of backscatter intensity.) The backscatter intensity may be used as a proxy for the instantaneous suspended sediment concentration (SSC) within the sampling volume because of the strong relationship between I_b and SSC (THORNE et al. 1991, FUGATE and FRIEDRICHES 2002, CHANSON et al. 2008a). The terms $V_x I_b$ is proportional to the suspended sediment flux per unit area, where V_x is the longitudinal velocity component.

A thorough post-processing technique was developed and applied to remove electronic noise, physical disturbances and Doppler effects (CHANSON et al. 2008b). The field experience demonstrated that the gross ADV signals were unsuitable, and led often to inaccurate time-averaged flow properties and turbulent characteristics. Herein only post-processed data are discussed.

2.5. Calculations of Turbulence Properties

The post-processed data sets included the three instantaneous velocity components V_x , V_y and V_z , and the backscatter intensity I_b , where x is the longitudinal direction positive downstream, y is the transverse direction positive towards the left bank and z is the vertical direction positive upwards. The turbulent fluctuations were defined as : $v = V - \bar{V}$ and $i_b = I_b - \bar{I}_b$, where V was the instantaneous (measured) velocity component, \bar{V} was the variable-interval time average (VITA) velocity and \bar{I}_b was the VITA backscatter intensity. A cut-off frequency was selected with an averaging time greater than the characteristic period of turbulent fluctuations, and smaller than the characteristic period for the time-evolution of the mean tidal properties. An upper limit of the filtered signal was the Nyquist frequency. The selection of the cut-off frequency was derived from a sensitivity analysis (CHANSON et al. 2008b, TREVETHAN 2008). Herein all turbulence data, including the turbulent flux events, were processed using samples that contain 5,000 to 10,000 data points and calculated every 10 s along the entire data sets. In a study of boundary layer flows, FRANSSON et al. (2005) proposed a cut-off frequency that was consistent with the selected sample size.

A basic turbulence analysis yielded the first four statistical moments of each velocity component, the tensor of instantaneous Reynolds stresses, and the statistical moments of the tangential stresses. An auto-correlation analysis yielded further the Eulerian dissipation and integral time scales, τ_E and T_E respectively, for each velocity component (Fig. 5). Herein τ_E was calculated using the method of HALLBACK et al. (1989) extended by FRANSSON et al. (2005) and KOCH and CHANSON (2005).

Note that the turbulence calculations were not conducted when more 20% of the (5,000 to 10,000) sample points within a data sample were corrupted/repaired during the ADV data post-processing.

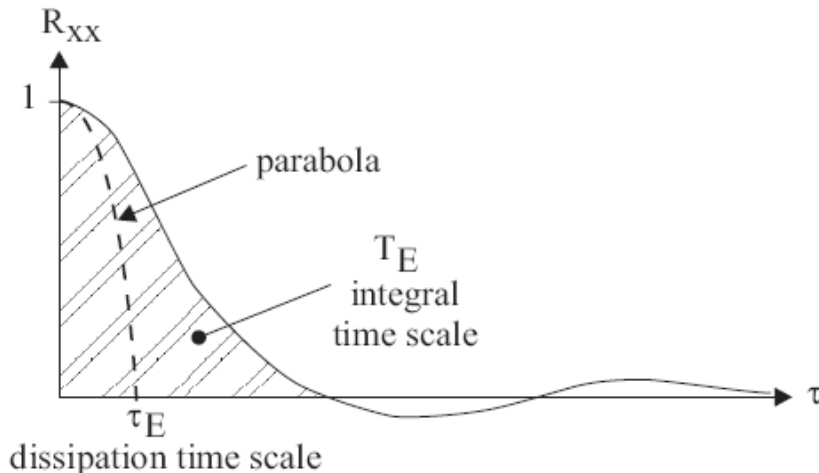


Figure 5. Definition sketch of a velocity component autocorrelation function.

2.6. Turbulent Event Detection Technique

A detection of turbulence bursting events was derived from the technique of NARASIMHA et al. (2007) that was adapted and extended. While this approach differs from more traditional event detection techniques (e.g. JOHANSSON and ALFREDSSON 1982, BAUER et al. 1998, OSTERLUND et al. 2003), it was found to be a robust method well-suited to the study of unsteady estuarine flow (TREVETHAN et al. 2007b).

A turbulent event is basically defined as a series of turbulent fluctuations that contain more energy than the average turbulent fluctuations within a data section. The method detects bursting events within a data section by comparing the absolute value of an instantaneous turbulent flux q (e.g. $q = v_x v_z$) with the standard deviation q' of that flux over the data section. A turbulent event occurs if :

$$|q| > k q' \quad (2)$$

where k is a positive constant setting the threshold and q' is the standard deviation of the flux q over the data sample section. NARASIMHA et al. (2007) conducted a sensitivity analysis on the positive multiplier threshold (k). They obtained $k = 1$ to provide good results

in atmospheric boundary layer studies and a similar result was obtained in an estuarine system (TREVETHAN et al. 2007b). Herein $k = 1$ and consecutive data sections of 10,000 data sample points (200 s at 50 Hz) were used.

For each data section, the information of each detected event encompassed the event start/finish times, duration τ , dimensionless flux amplitude A and relative magnitude m . The event properties were used to compare individual turbulent events within a data set and between synchronised data sets collected simultaneously. Figure 6A introduces the definition of the duration and amplitude of an isolated event. The duration τ of the event is the time interval between the "zeroes" in momentum flux (e.g. $q = v_x v_z$) nearest to the sequence of data points satisfying Equation (2) (Fig. 6A). Practically, the event duration is calculated from the first data point with the same sign as the event to the first data point after the change in sign in momentum flux. The method provides an accurate estimate of the event duration within the limitations of the sampling frequency. The dimensionless amplitude A of an event is the ratio of the averaged flux amplitude during the event to the long-term mean flux of the entire data section :

$$A = \frac{1}{\bar{q}} \int_{t=0}^{\tau} \frac{q}{\tau} dt \quad (3)$$

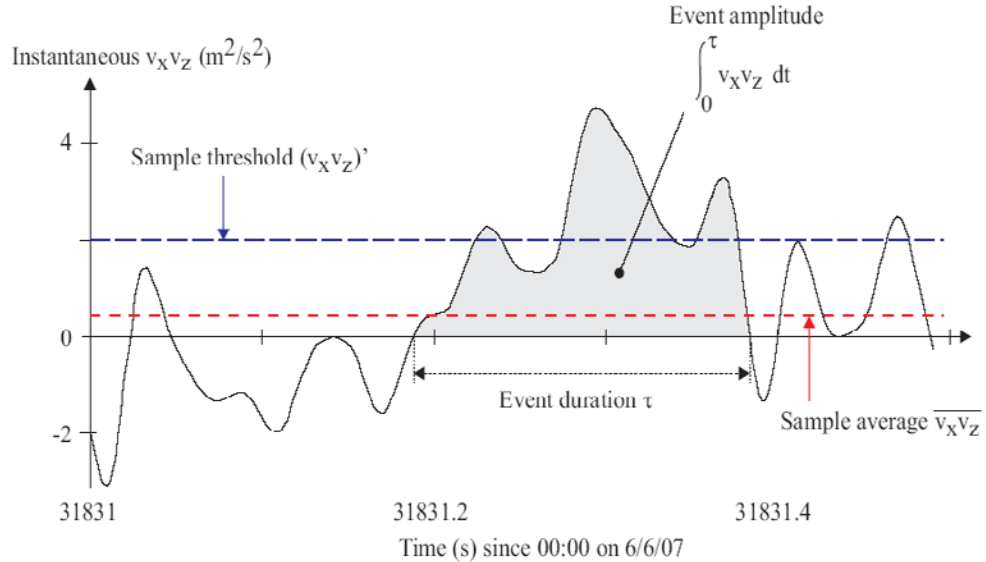
where \bar{q} is the averaged value of q over the data section, τ is the event duration and $dt = 1/f_{\text{scan}}$ (e.g. $f_{\text{scan}} = 50$ Hz). The relative contribution of an event to the total momentum flux of the data section is called the relative magnitude m defined as:

$$m = \frac{A \tau}{T} \quad (4)$$

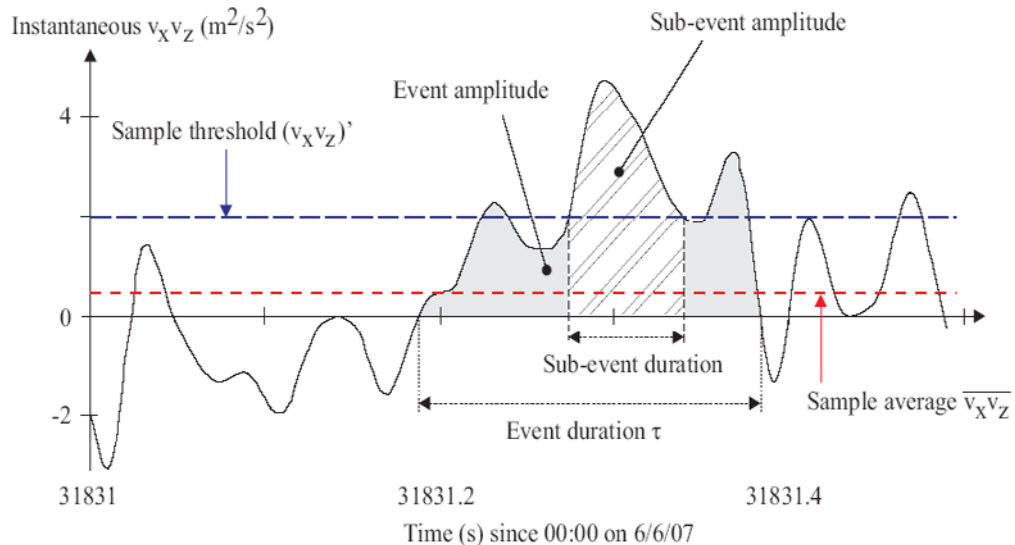
where T is the total duration of the data section : i.e., $T = 200$ s for 10,000 samples collected at 50 Hz. This technique was applied to the momentum fluxes $v_x v_y$ and $v_x v_z$, and to the "pseudo" longitudinal suspended sediment flux $v_x i_b$, where i_b is the instantaneous fluctuation in the ADV backscatter intensity.

The method was extended to investigate turbulent sub-events within a large event. For example, in Figure 6A, the turbulent event is characterised by three distinct peaks in momentum flux and the entire event may be represented as a succession of three consecutive "turbulent sub-events". The second sub-event is highlighted with hatching in Figure 6B. A turbulent sub-event was defined when the instantaneous momentum flux within the main turbulent event was greater than the momentum flux threshold (Eq. (2)) of the data section. In Figure 6B, the definition of duration and amplitude of the sub-event are shown. For each sub-event, its start/finish times, duration, dimensionless flux amplitude and relative magnitude were calculated within a given event. The duration of a sub-event is that time interval during which the momentum flux was equal to or greater than the threshold value. For each sub-event, the dimensionless sub-event amplitude is the ratio of the averaged sub-event amplitude to the sub-event duration to the mean flux over the data section. The sub-event properties were calculated for consecutive data sections containing 10,000 data points (200 s at 50 Hz)

along each data set with the same technique used to analyse turbulence events, including the number of sub-events that occurred in each individual event.



(A) Definition sketch of flux event and event parameters.



(B) Definition sketch of turbulent sub-events within a turbulent event.

Figure 6. Turbulent flux event definitions and momentum flux data in terms of $v_x v_z$ (study E10, Erapah Creek, data collected at 0.38 m above bed).

3. TURBULENT FLOW PROPERTIES AT THE MACROSCOPIC SCALES: BASIC PATTERNS

3.1. Basic Flow Properties

The estuarine flow was an unsteady process. The bulk parameters including the water depth and time-average longitudinal velocity were time-dependant and they fluctuate with periods comparable to tidal cycles and other large-scale processes. This is illustrated in Figures 7 and 8 showing the water depth, water conductivity and time-averaged velocities recorded mid-estuary for two field studies in Australia (Erapah Creek). Figure 7 presents the water depth and conductivity data recorded about mid-estuary during neap tide conditions. The results highlighted some tidal asymmetry during a 24 hours 50 minutes period with a smaller (minor) tidal cycle followed by a larger (major) tidal amplitude. The water conductivity variations were driven primarily by the ebb and flood tides. The moderate range of specific conductivity seen in Figure 7 was typical of a small subtropical estuary under neap tidal conditions in absence of freshwater runoff.

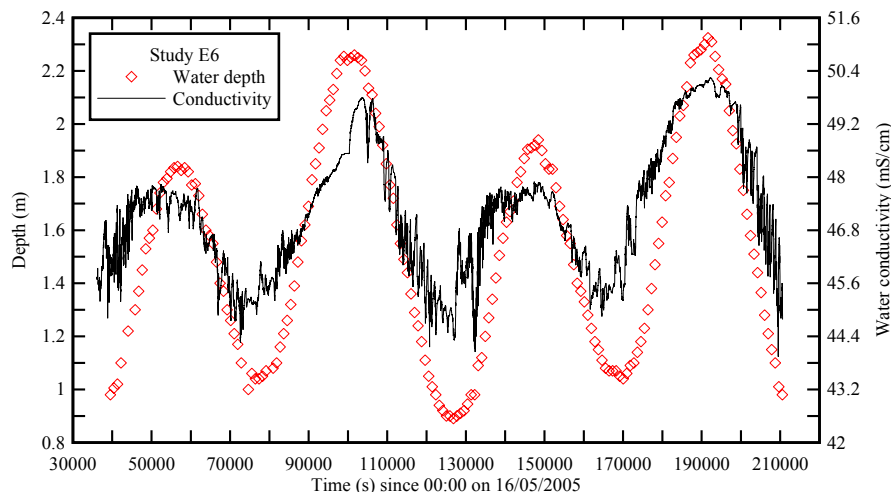
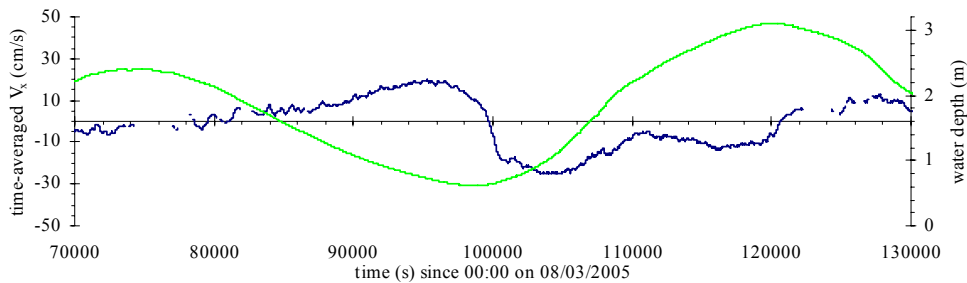


Figure 7. Time variations of the water depth and conductivity in the mid-estuary zone of Erapah Creek (Australia) during neap tide conditions (study E6).

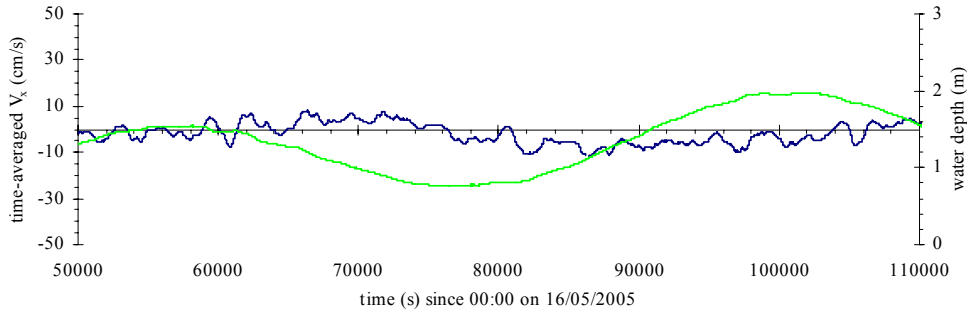
Figures 8 and 9 present the time-averaged longitudinal velocities in Australia (Fig. 8) and in Japan (Fig. 9). Figure 8 shows data collected in the middle of the deepest channel during spring and neap tides. For all mid-estuary field studies, the largest velocity magnitude occurred just before and after the low tide, with the flood velocities always larger than ebb velocities. KAWANISI and YOKOSI (1994) observed similarly maximum flood and ebb velocities around low tide and larger flood velocities, during some field works in an estuarine channel in Japan. The velocity data showed some multiple flow reversal events around high tides and some long-period oscillations in water elevation and velocity around mid-tide. Figure 8A shows an example of long-period velocity oscillations during the flood tide between $t = 105,000$ and $125,000$ s where the time t is counted since midnight (00:00) on the first day of the study. Figure 8B presents an illustration of multiple flow reversals about high

tide between $t = 50,000$ and $65,000$ s. These low frequency velocity oscillations were possibly generated by some resonance caused by the tidal forcing interacting with the estuary topography and the outer bay system (CHANSON 2003, TREVETHAN 2008). These effects were more noticeable during neap tide conditions and seemed more pronounced in the upper estuary (TREVETHAN et al. 2007a).

At Hamana Lake, the tidal range was small during both spring and neap tidal conditions because the restricted entrance (Fig. 4C) reduced the tidal range observed in the estuary by dampening the ocean tidal oscillations. The difference in tidal range was less than 0.2 m between neap and spring tide studies (Fig. 9). The response of the time-averaged streamwise velocity to the tidal forcing was different between Erapah Creek and Hamana Lake. Figure 9 shows the time-averaged streamwise velocity and water depth as functions of time in Japan. The maximum flood and ebb velocities at Hamana Lake were observed in the middle of the tide under spring and neap tidal forcing. HAM et al. (2001) observed a similar tidal trend in a shallow semi-enclosed bay. During neap tidal conditions, the maximum flood and ebb velocity suggested a neutral tidal bias (Fig. 9B). However, under spring tidal forcing, the maximum ebb velocity at Hamana Lake was larger than the maximum flood velocity (Fig. 9A).

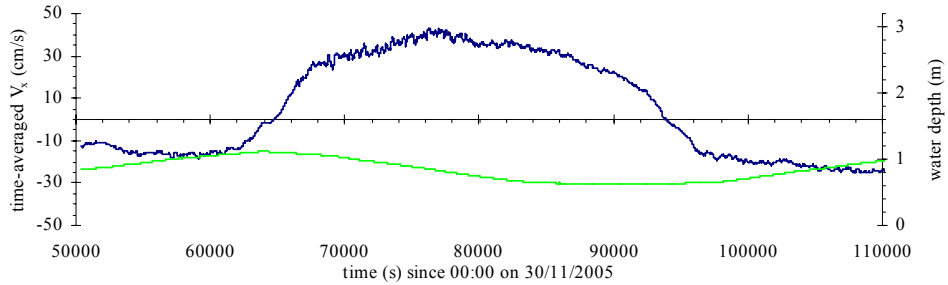


(A) Longitudinal velocity data collected at 0.1 m above the bed during spring tides (study E5).

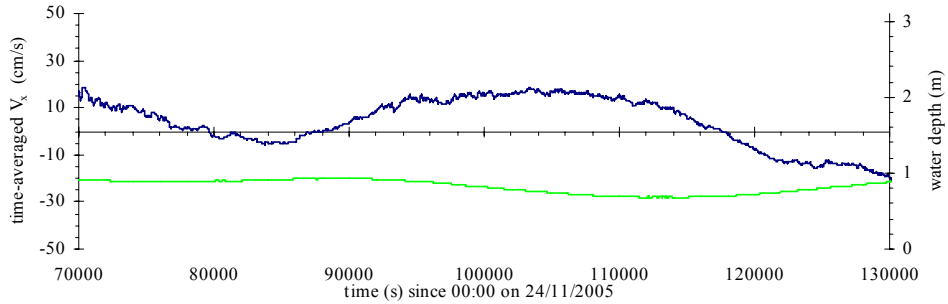


(B) Longitudinal velocity data collected at 0.4 m above the bed during neap tides (study E6).

Figure 8. Time variations of the time-averaged longitudinal velocity $\overline{V_x}$ (positive downstream) and water depth for a full tidal cycle at Erapah Creek (Australia), mid-estuary zone (site 2B) - Legend: [—] time-averaged longitudinal velocity (cm/s); [—] water depth.



(A) Longitudinal velocity data collected at 0.25 m above the bed during spring tides (study J2).



(B) Longitudinal velocity data collected at 0.25 m above the bed during neap tides (study J1).

Figure 9. Time variations of the time-averaged longitudinal velocity $\overline{V_x}$ (positive downstream) and water depth for a full tidal cycle at Hamana Lake (Japan) - Legend: [—] time-averaged longitudinal velocity (cm/s); [—] water depth (m).

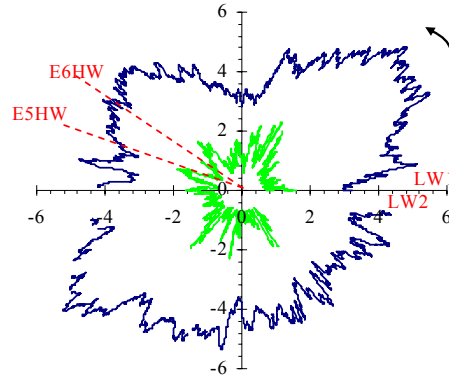
3.2. Turbulence Properties

The field observations showed systematically large standard deviations of all velocity components at the beginning of the flood tide for all tidal cycles. Typical field measurements of standard deviations for the longitudinal velocity v_x' are shown in Figure 10 for two tidal cycles in spring and neap tides in Australia and Japan. Figure 10 shows the magnitude of v_x' from a low water (LW1) to the next low water (LW2), and the data are presented in a circular plot. In such a circular plot, the radial coordinate is the turbulent property v_x' and the angular coordinate is the time relative to the next low water. From the first low water, the time variations of the data progress anticlockwise until the next low water. The high and low waters are indicated: the low waters are the positive horizontal axis, and the high waters are the dotted lines. The upper half of the graph corresponds roughly to the flood tide while the lower half represents the ebb tide.

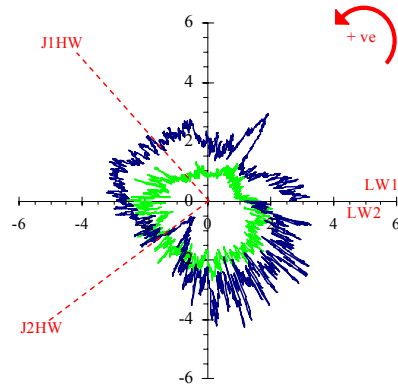
In Australia, the standard deviations of all velocity components were two to four times larger in spring tides than during neap tides. Figure 10A highlights the large velocity standard deviations in spring tide conditions. The presentation illustrates that v_x' was systematically larger during the flood tide than during the ebb tide, while there were significant fluctuations

in velocity standard deviations during the entire tidal cycle. KAWANISI and YOKOSI (1994) observed similarly larger measured velocity standard deviations during flood tide in a large tidal channel.

At Hamana Lake, the tidal trends of all velocity standard deviations were about the same for spring and neap tidal conditions, but the median values were twice as large during spring tides (Fig. 10B). The observation tended to indicate that the largest velocity standard deviations occurred about the time of maximum longitudinal velocity as noted in TREVETHAN (2008).



(A) Eprapah Creek (Australia), mid-estuary zone (site 2B), study E5 (0.1 m above bed), and study E6 (0.4 m above bed).



(B) Hamana Lake (Japan).

Figure 10. Time variations of the standard deviations of the longitudinal velocity v_x' (cm/s) during a major tidal cycle in spring and neap tidal conditions: [•] spring tide, and [•] neap tide - Circular plot from a low water to the next low water - Dotted line: high water.

The horizontal turbulence intensity v_y'/v_x' was approximately equal to 1 for spring and neap tide conditions at both Eprapah Creek and Hamana Lake, indicating that turbulence fluctuations in the longitudinal and transverse directions were of similar magnitude. They were larger than laboratory observations in straight prismatic rectangular channels which yielded $v_y'/v_x' = 0.5$ to 0.7 (NEZU and NAKAGAWA 1993, KOCH and CHANSON 2005),

but the findings were close to recent LES computations in a shallow water channel with similar Reynolds number conditions (HINTERBERGER et al. 2008). The vertical turbulence intensities v_z'/v_x' were similar to the observations of SHIONO and WEST (1987) and KAWANISI and YOKOSI (1994) in estuaries, and of NEZU and NAKAGAWA (1993) and XIE (1998) in laboratory open channels. For all estuarine studies in Australia and Japan, v_z'/v_x' was always smaller than the horizontal turbulence intensity v_y'/v_x' and the result implied some form of turbulence anisotropy.

The skewness and kurtosis gave some information on the temporal distribution of the turbulent velocity fluctuation around its mean value. For all studies, the skewness and kurtosis of all velocity components fluctuated significantly during each tidal cycle. They exhibited some characteristics that differed from the expected skewness and kurtosis for a Gaussian distribution. The normalised third (skewness) and fourth (kurtosis) moments of the velocity fluctuations appeared to be close to the observations of SHIONO and WEST (1987) in an estuary. They were also comparable with the LDV data of NIEDERSCHULTZE (1989) and TACHIE (2001) in developing turbulent boundary layers in laboratory channels.

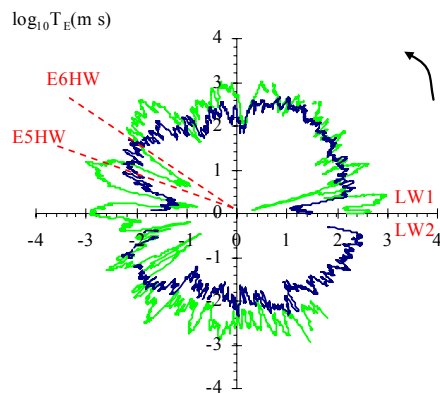
All tangential Reynolds stresses showed significant fluctuations over the tidal cycles of all field studies undertaken at both estuaries. The turbulent stress $\rho \overline{v_x v_z}$ close to the bed varied with the tides, being predominantly positive during the flood tide and negative during the ebb tide. This trend was consistent with the earlier data of OSONPHASOP (1983), KAWANISI and YOKOSI (1994) and HAM et al. (2001) in tidal channels. The negative correlation between $\rho \overline{v_x v_z}$ and $\overline{V_x}$ was also consistent with traditional boundary layer results (XIE 1998, TACHIE 2001, NEZU 2005). At Erapah Creek the magnitudes of all tangential Reynolds stresses were at least an order of magnitude larger during spring tides than those observed for neap tidal conditions. The larger magnitude of all Reynolds stresses derived from the increased tidal forcing interacting with the local bathymetry. However, at Hamana Lake, the difference in the magnitude of all Reynolds stresses under spring and neap tidal forcing was not as significant, with Reynolds stress magnitudes being up to twice as large under spring tidal forcing. The smaller difference in spring and neap turbulent stress magnitudes at Hamana Lake was conceivably related to the small difference in tidal amplitude between the field investigations (Table 1).

The standard deviations of all tangential Reynolds stresses increased with increasing longitudinal velocity magnitude. At Erapah Creek (Australia), the magnitude of all tangential Reynolds stress standard deviations were one order of magnitude greater under spring tidal forcing than those observed during neap tides. At Hamana Lake (Japan), the spring tidal tangential Reynolds stress standard deviations were approximately twice as large as those measured under neap tidal conditions. The results obtained in both estuaries showed that the probability distribution functions of all tangential Reynolds stresses were not Gaussian.

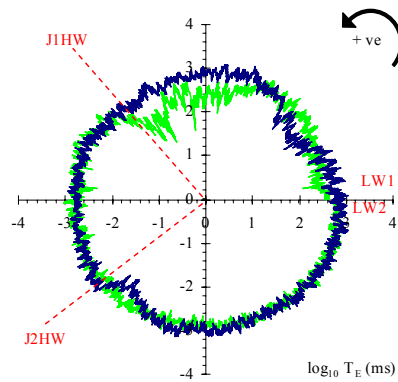
3.3. Turbulence Time Scales

The integral time scale of a velocity component is a measure of the longest connection in the turbulent behaviour of that velocity component. Some variations of longitudinal integral time scales T_{Ex} are shown in Figure 11 for a major tidal cycle during neap and spring tide

conditions. Note that the axes have a logarithmic scale and the units are milliseconds. At Erapah Creek significant fluctuations in the horizontal integral time scales were observed throughout the tidal cycles, with the integral time scales observed under neap tidal conditions being larger than those for spring tides (Figure 11). The horizontal integral times at Erapah Creek ranged between 0.06 s and 1.0 s with a median value of approximately 0.15 s under spring tides and between 0.06 s and 2.40 s (median value: 0.31 s) during neap tidal conditions. In Hamana Lake, the fluctuations in horizontal integral time scales over the tidal cycle were relatively small. The horizontal integral time scales ranged between 0.2 s and 1.5 s under both spring and neap tides (Figure 11). The median values of longitudinal and transverse integral time scales at Hamana Lake were approximately 0.75 a and 0.58 s under spring and neap tidal conditions respectively.

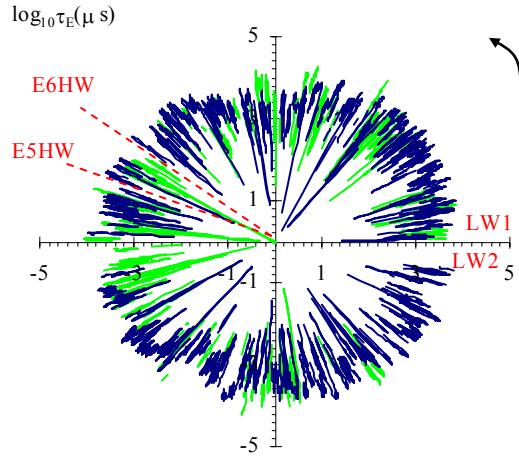


(A) Erapah Creek (Australia), mid-estuary zone (site 2B), study E5 (0.1 m above bed), and study E6 (0.4 m above bed).

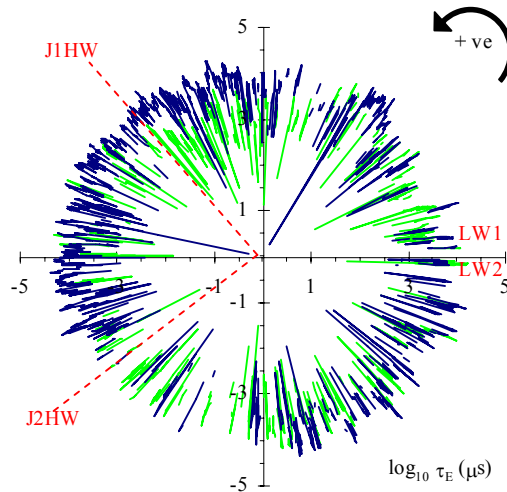


(B) Hamana Lake (Japan), 0.28 m above the bed.

Figure 11. - Time variations of the integral time scale T_{Ex} (units: ms) for V_x during a major tidal cycle for neap and spring tidal conditions - The axes have a logarithmic scale - Legend: [•] spring tide; [•] neap tide.



(A) Eprapah Creek (Australia), mid-estuary zone (site 2B), study E5 (0.1 m above bed), and study E6 (0.4 m above bed).



(B) Hamana Lake (Japan), 0.28 m above the bed.

Figure 12. Time variations of the dissipation time scale τ_{Ex} (units μs) for V_x during a major tidal cycle for neap and spring tidal conditions - The axes have a logarithmic scale - Legend: [•] spring tide; [•] neap tide.

The dissipation time scale, also called Taylor micro scale, is a measure of the most rapid changes that occur in the fluctuations of a velocity component. It is a characteristic time scale of the smaller eddies which are primary responsible for the dissipation of energy. Figure 12 shows the variations of longitudinal dissipation time scales τ_{Ex} for a major tidal cycle during neap and spring tide conditions in Australia and in Japan. The axes have a logarithmic scale

and the units are in microseconds. At both estuaries, the dissipation time scale data seemed independent of the tidal phase with horizontal dissipation time scales between 0.0001 s and 0.03 s for all field studies (Fig. 12). The dissipation time scales at Erapah Creek seemed independent of the tidal conditions, vertical and longitudinal sampling locations, with median values typically between 0.002 s and 0.003 s. At Hamana Lake, the median values of the horizontal dissipation time scales (τ_{Ex} and τ_{Ey}) were between 0.007 s and 0.011 s for spring tidal conditions, and between 0.004 s and 0.006 s during neap tidal conditions. The horizontal dissipation time scales were slightly different, and the median values of transverse dissipation time scales τ_{Ey} were larger than the median values of longitudinal dissipation time scales τ_{Ex} under spring and neap tidal forcing. Note that the dissipation time scales were consistently smaller than the time between two consecutive samples: e.g., $1/f_{\text{scan}} = 0.04$ s for $f_{\text{scan}} = 25$ Hz in Figure 12. The findings highlighted that a high frequency sampling is required and the sampling rates must be at least 20 to 30 Hz to capture a range of eddy time scales relevant to the dissipation processes.

The analysis of the integral and dissipation time scales of all velocity components showed no obvious trend with tidal phase under both neap and spring tidal forcing. During the present field studies at Hamana Lake and Erapah Creek, the dimensionless transverse and vertical dissipation time scales were respectively: $T_{Ey}/T_{Ex} \sim 1$ and $T_{Ez}/T_{Ex} \sim 1$ to 3. In a tidal channel in Southern Australia, OSONPHASOP (1983) observed $T_{Ey}/T_{Ex} \sim 1.7$ and $T_{Ez}/T_{Ex} \sim 2.2$.

3.4. Dimensionless Turbulence Parameters

For most turbulence properties, the spring tidal data at Erapah Creek were larger and showed a more asymmetrical tidal response. For example, the standard deviations of longitudinal velocity under spring tidal conditions were larger at Erapah Creek than at Hamana Lake, despite the larger longitudinal velocity observed at Hamana Lake (Fig. 8, 9 and 10). The ratio of local tidal amplitude and local mean depth at the experimental site a_1/h_1 may assist with the understanding of this phenomenon (TREVETHAN 2008).

Dimensionless turbulence parameters are commonly used in turbulence investigations to compare the relative turbulence characteristics of different systems under distinct flow conditions. Table 2 regroups the median values of basic dimensionless turbulence properties in Australia and Japan. The dimensionless turbulence parameters include the turbulent intensity ratios (v_y'/v_x' , v_z'/v_x'), the relative turbulence intensities of the longitudinal, transverse and vertical velocity fluctuations ($v_x'/|V_x|$, $v_y'/|V_x|$, $v_z'/|V_x|$), the normalized tangential Reynolds stresses ($|v_x v_z|/\overline{|V_x|^2}$, $|v_x v_y|/\overline{|V_x|^2}$, $|v_y v_z|/\overline{|V_x|^2}$), the magnitude of correlation coefficients of Reynolds stresses ($|R_{vxvz}|$, $|R_{vxvy}|$, $|R_{vyvz}|$) and the dimensionless integral time scales ($T_{Ex}\sqrt{g/h_1}$, $T_{Ey}\sqrt{g/h_1}$, $T_{Ez}\sqrt{g/h_1}$).

Table 2. Median values of dimensionless turbulence parameters over the full investigation periods for the field studies undertaken in Australia (Erapah Creek) and Japan (Hamana Lake).

Estuary	Erapah Creek		Hamana Lake	
Field Study	E5	E6	J1	J2
Tidal Conditions	Spring	Neap	Neap	Spring
Tidal range (m)	2.37	1.36	0.39	0.56
a_l/h_l	0.76	0.43	0.22	0.31
$v_y'/ V_x' $	1.00	0.89	0.83	0.86
$v_z'/ V_x' $	0.39	0.51	0.52	0.56
$v_x'/ V_x' $	0.42	0.21	0.15	0.13
$v_y'/ V_x' $	0.44	0.19	0.15	0.13
$v_x'/ V_x' $	0.16	0.11	0.07	0.07
$ v_x v_z / V_x ^2$	0.014	0.005	0.004	0.004
$ v_x v_y / V_x ^2$	0.014	0.004	0.003	0.002
$ v_y v_z / V_x ^2$	0.004	0.002	0.001	0.001
$ R_{vxvy} $	0.08	0.13	0.20	0.27
$ R_{vxvz} $	0.23	0.17	0.31	0.30
$ R_{vyvz} $	0.07	0.10	0.13	0.20
$T_{Ex} \sqrt{g/h_l}$	0.43	0.59	2.45	2.50
$T_{Ey} \sqrt{g/h_l}$	0.30	0.93	1.86	1.94
$T_{Ez} \sqrt{g/h_l}$	0.72	2.06	1.98	1.39

The dimensionless turbulence data suggested a different set of turbulence and mixing properties when $a_l/h_l > 0.5$ (Table 2), while the magnitudes of relative turbulence intensities and normalised Reynolds stresses were similar for $a_l/h_l < 0.5$. Previous turbulence studies in

large estuarine systems (e.g. BOWDEN and HOWE 1963, OSONPHASOP 1983, WEST and ODUYEMI 1989) yielded results of $v_x' / \overline{|V_x|} < 0.15$ and $\overline{|v_x v_z|} / \overline{V_x}^2 < 0.004$, that were similar to those observed at Hamana Lake and Erapah Creek when $a_1/h_1 < 0.5$. The findings indicated that the turbulence properties of estuaries with $a_1/h_1 < 0.5$ could not be applied to shallow-water estuaries where $a_1/h_1 > 0.5$.

3.5. Suspended Sediment Fluxes

For some field studies in Australia (Erapah Creek), an acoustic Doppler velocimeter (ADV) was calibrated in terms of the backscatter intensity versus suspended sediment concentration (SSC) (CHANSON et al. 2008a). The results enabled a characterisation of the fluctuations in suspended sediment concentrations for two field studies (E6 and E7).

The instantaneous suspended sediment concentration (SSC) showed some large fluctuations throughout the entire field studies, including during the tidal slacks (high and low tides). The data tended to indicate larger suspended loads during the early flood tides. The data showed also some low frequency oscillation patterns in terms of the SSC that may be linked with the low frequency fluctuations of the streamwise velocity. In the middle and upper estuarine zones, the ratio $\overline{SSC}' / \overline{SSC}$ was respectively 0.66 and 0.57 on average, where \overline{SSC} is the time-averaged suspended sediment concentration and SSC' is its standard deviation.

The instantaneous advective suspended sediment flux per unit area q_s was calculated as :

$$q_s = SSC V_x \quad (5)$$

where q_s and V_x are positive in the downstream direction, and the suspended sediment concentration SSC is in kg/m^3 . q_s is a local measure of the suspended sediment flux at the ADV sampling site. Typical instantaneous suspended sediment flux per unit area results are presented in Figure 13. The data characterise the advective suspended sediment flux per unit area in a sampling volume located at 0.2 m above the bed.

The sediment flux per unit area data showed typically an upstream, negative suspended sediment flux during the flood tide and a downstream, positive suspended sediment flux during the ebb tide. The instantaneous suspended sediment flux per unit area data q_s showed considerable time-fluctuations that derived from a combination of velocity and suspended sediment concentration fluctuations. The data demonstrated further some high frequency fluctuation with some form of suspended sediment flux bursts that were likely linked to and caused by some turbulent bursting phenomena next to the bed. Some low frequency fluctuations in suspended sediment flux were also observed. In the middle estuary, the magnitude of suspended sediment fluxes were about one order of magnitude larger than those observed in the upper estuary.

For each tidal period of 24 hour 50 min., the suspended sediment flux per unit area data were integrated with respect of time. The results gave the net sediment mass transfer per unit area at the sampling volume:

$$m_s = \int_{24\text{h}50\text{ min}} q_s dt \quad (6)$$

For both field studies E6 and E7, the net sediment mass transfer per area was negative (i.e. upstream). In the middle estuary, Equation (6) yielded $m_s = -22.3$ and -20.8 kg/m^2 for each 24 h 50 min tidal period, while Equation (6) gave $m_s = -6.66$ and -1.81 kg/m^2 in the upper estuary. That is, the net sediment flux over a full tidal cycle corresponded on average to an upstream net suspended sediment transfer. Several researchers investigated the net suspended sediment flux in estuaries of subtropical and tropical river estuaries during similar dry conditions and tidal ranges. Previous results showed a similar net upstream sediment transfer in dry weather: e.g., LARCOMBES and RIDD (1992), HOSSAIN et al. (2001), KAWANISI et al. (2006). However, during rain storms and wet weather the net sediment mass flux is positive in the downstream direction in such estuarine systems.

A striking feature of the analysed data sets is the large fluctuations in the suspended sediment fluxes during the tidal cycles. This feature was rarely documented, but an important feature of the data sets is that the present data were collected continuously at high frequency (25 and 50 Hz) during relatively long periods. It is however acknowledged that the data were point measurements. Any extrapolation would imply that the sampling volume was representative of the entire channel cross-section.

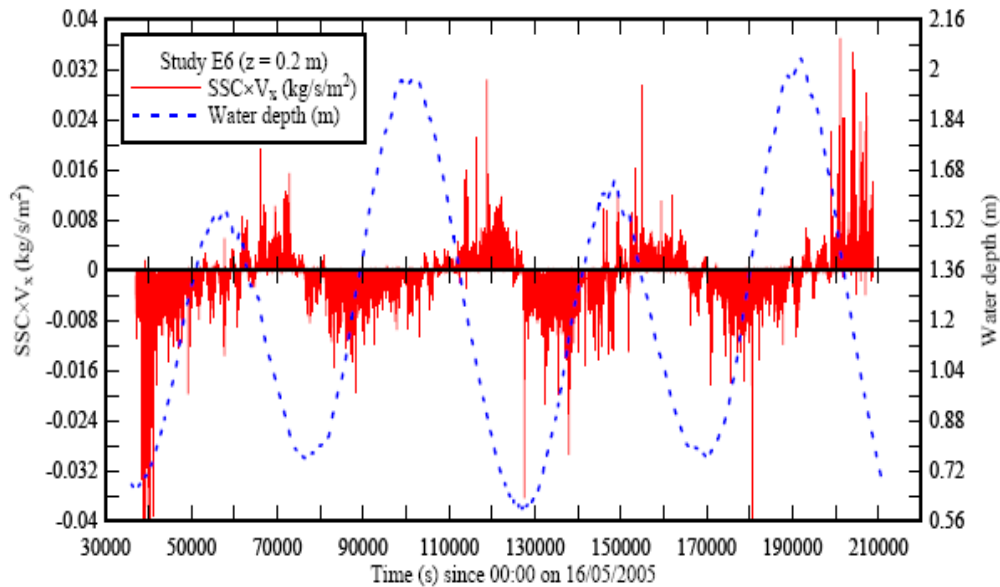


Figure 13. Time variations of the instantaneous suspended sediment flux per unit surface area ($\text{SSC} \times V_x$, positive downstream) and measured water depth during the study E6 (neap tide) at 0.2 m above bed.

The integral time scale of the suspended sediment concentration (SSC) data represents a characteristic time of turbid suspensions in the creek. Calculations were performed for two field studies in Australia (E6 and E7). The SSC integral time scale data seemed relatively independent of the tidal phase and yielded median SSC integral time scales T_{ESSC} of about 0.06 s.

A comparison between the turbulent and SSC integral time scales showed some difference especially during the ebb tide. In the mid-estuarine zone, the ratio of SSC to turbulent integral time scales was on average $T_{ESSC}/T_{EX} = 0.21$ and 0.14 during the flood and ebb tides respectively. In the upper estuary, the ratio T_{ESSC}/T_{EX} was about $T_{ESSC}/T_{EX} = 1$ and 0.18 during the flood and ebb tides respectively. Basically the ratio T_{ESSC}/T_{EX} was about 2 to 5 times lower during ebb tide periods. The findings tended to suggest that the sediment suspension and suspended sediment fluxes were dominated by the turbulent processes during the flood tide, but not during the ebb tide. The experimental results showed further some fluctuations in SSC integral time scales during the tidal cycle.

These data sets provided simultaneous turbulence and suspended sediment concentration measurements recorded continuously at high frequency for 50 hours per investigation. The data analyses yielded an unique characterisation of the turbulent mixing processes and suspended sediment fluxes. The integral time scales for turbulence and suspended sediment concentration were about equal during flood tides, but differed significantly during ebb tides. The same pattern might take place with other scalars and be pertinent to the turbulent mixing modelling in shallow-water subtropical estuaries under dry-weather conditions.

3.6. Discussion

The boundary shear stress may be estimated from the velocity gradient next to the bed, although other techniques may be used (SCHLICHTING 1979, MONTES 1998, KOCH and CHANSON 2005). The near-bed velocity shear stress is calculated as:

$$\tau_o = \rho \left(\frac{\kappa (V_x)_1}{\ln \frac{z_1}{k_s}} \right)^2 \quad (7)$$

where ρ is the fluid density, $(V_x)_1$ is the time-averaged longitudinal velocity of the ADV unit located closest to the bed ($z_1 = 0.13$ m, study E10), κ is the von Karman constant ($\kappa = 0.4$) and k_s is the equivalent roughness height. At Erapah Creek (Australia), the river bed in the middle estuarine zone consisted of gravels and sharp rocks corresponding to $k_s \approx 10$ mm. Experimental results indicated that the boundary shear stress was maximum during the early flood tide and end of ebb tide when the measured longitudinal velocity amplitude was the largest. For the entire field study E10, the median shear stress was $\tau_o = 0.0052$ Pa. For the same study, the boundary shear stress data may be compared with the tangential Reynolds stress $\rho \overline{v_x v_z}$ measured simultaneously at $z_2 = 0.38$ m, as well as with the velocity gradient shear stress measured between $z_1 = 0.13$ m and $z_2 = 0.38$ m :

$$\tau_{12} = \rho \left(\frac{\kappa((V_x)_2 - (V_x)_1)}{\ln \frac{z_2}{z_1}} \right)^2 \quad (8)$$

For the entire study E10, the tangential Reynolds stress and the median velocity gradient shear stress (Eq. (8)) were respectively: $\rho \overline{v_x v_z} = 0.02 \text{ Pa}$ and $\tau_{12} = 0.052 \text{ Pa}$. For comparison, the median tangential shear stresses $\rho \overline{v_x v_y}$ measured at $z = 0.13 \text{ m}$ and 0.38 m were 0.024 Pa and 0.031 Pa respectively.

The findings implied that the turbulent shear between $0.13 \text{ m} \leq z \leq 0.38 \text{ m}$ was one order of magnitude larger than the boundary shear stress (Eq. (7)). The observation differed from turbulence data collected in a laboratory channel, but a key feature of natural estuary flows was the significant three-dimensional effects associated with strong secondary currents.

During several field studies, some anomalies were observed in terms of the transverse velocity data. For example, during the study E10, the time-averaged transverse velocities \overline{V}_y recorded at $z = 0.13 \text{ m}$ and 0.38 m flowed at times in opposite directions for relatively long durations (e.g. Fig. 14). These anomalies were observed during the flood and ebb tides, and around low tides for the entire study.

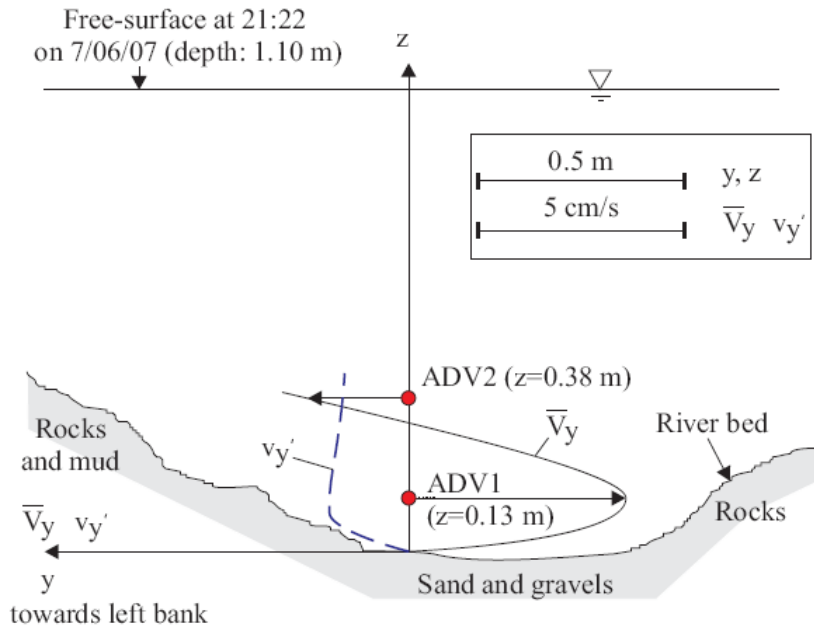


Figure 14. Transverse shear flow pattern in the mid-estuarine zone of Eprapah Creek: dimensioned sketch of the vertical profiles of transverse velocity \overline{V}_y and turbulent velocity v_y' at the sampling site during the early flood tide in Australia (study E10).

These observations highlighted the occurrence of some secondary currents associated with strong transverse shear and large tangential stresses $\rho \overline{v_x v_y}$ at the sampling location. An example of transverse velocity anomaly is presented in Figure 14. The flow pattern sketched in Figure 14 shows the vertical profiles of transverse velocity $\overline{V_y}$ and of turbulent velocity v_y' next to the channel bed, where v_y' is the standard deviation of the transverse velocity. The transverse shear pattern sketched in Figure 14 was associated with large normal and tangential stresses $\rho \overline{v_y v_y}$ and $\rho \overline{v_x v_y}$ at both $z = 0.13$ m and 0.38 m for that study.

TREVETHAN (2008) discussed the formation the transverse velocity anomalies in Erapah Creek, their collapse and reformation in the opposite direction. He suggested that the alternance in transverse shear anomalies was linked with the long-period oscillations induced by seiching resonance in the outer bay system (Moreton Bay).

4. TURBULENT FLOW PROPERTIES AT THE MICROSCOPIC SCALES: TURBULENT EVENTS

4.1. Presentation

While the turbulence is often characterised by its statistical moments, it is not a Gaussian process. Turbulent flows are dominated by coherent structure activities and turbulent events. A turbulent event may be defined as a series of turbulent fluctuations containing more energy than the average turbulent fluctuations. The turbulent events are often associated with coherent flow structures such as eddies and bursting (KLINE et al. 1967, RAO et al. 1971). These events play a major role in terms of sediment scour, transport and accretion as well as contaminant mixing and dispersion (NIELSEN 1992, NEZU and NAKAGAWA 1993, CHANSON 2004). Turbulent event analyses were successfully applied to laboratory open channel flows (NEZU and NAKAGAWA 1993), wind tunnel studies (OSTERLUND et al. 2003) and atmospheric boundary layer flows (FINNIGAN 2000, NARASIMHA et al. 2007). They were however rarely applied to unsteady open channel flows and estuaries.

For a field study (study E10, Erapah Creek), a detailed turbulent event analysis was conducted (section 2.6). Figure 15 illustrates a time series of the dimensionless flux amplitude of $v_x v_z$ from a data set as a function of time for a 10 s sample during the early flood tide. The data presentation shows the duration and dimensionless amplitude of each event in a simplified format. It is seen that the time series includes both positive and negative turbulent events, each event corresponding to a rectangular pulse. The pulse width is the duration τ and the height is the dimensionless amplitude A , while the area beneath is proportional to the event magnitude m .

The turbulent events and sub-events were investigated specifically for the turbulent fluxes $v_x v_z$, $v_x v_y$, and $v_x i_b$, for the study E10 conducted mid-estuary in Erapah Creek (Australia). Table 3 summarises the number of events and sub-events detected by the ADV units for the entire study (50 hours). For the whole data set, the histograms of event duration, event amplitude, sub-event duration and sub-event amplitude were calculated. Figure 16

shows the normalised probability distribution functions of event duration τ and dimensionless event amplitude A for the momentum fluxes $v_{xi} \dot{v}_b$.

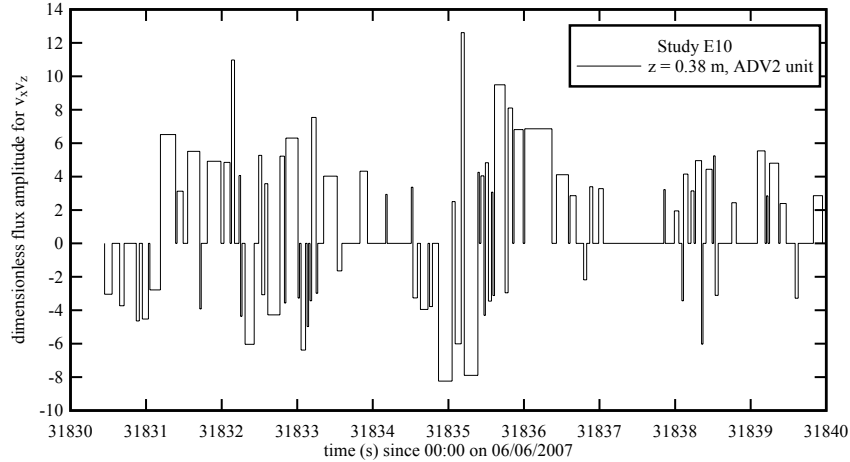


Figure 15. Dimensionless amplitude of detected turbulent events in terms of $v_x v_z$ (Study E10, 0.38 m above the bed).

During the field study, the majority of turbulent events had a duration between $0.08 < \tau < 0.3$ s for all momentum fluxes. On average, the turbulent event duration was about 0.2 s. The distributions of event amplitude presented a similar shape for the fluxes $v_x v_z$ and $v_x v_y$. For the entire study and all fluxes, the median amplitude magnitude was between $3 \leq |A| \leq 14$. For each turbulent flux, the event amplitude distribution tended to indicate a larger proportion of positive events than of negative events for all ADV units. Next to a boundary, the turbulent bursting process is composed of a quasi-periodic cycle of ejections and sweep motions (NEZU and NAKAGAWA 1993, PIQUET 1999). Ejections and sweeps corresponded to a negative amplitude in Figure 16B, while a positive event amplitude implied a wallward or outward interaction. The data sets for the field study E10 suggested comparatively a larger number of interaction events than sweep and ejection events. However, for all the fluxes, the positive events ($A > 0$) were on average longer and of smaller amplitude than the negative events ($A < 0$), with a similar event magnitude overall (Table 4). Table 4 summarises the median values of number of events per sample, event duration, dimensionless event amplitude, and relative event magnitude for each ADV unit. (The exact location of each sampling volume is given in Table 3, column 1.) Although there were some differences between the three velocimeters (Table 4), the statistical results were relatively close and tended to show little effect of the sampling volume location.

4.2. Turbulence Event and Sub-Event Statistics

The turbulent event statistics were collected over a 200 s sample (10,000 data points) every 10 s along the entire ADV data sets. The event statistics including the number of events per sample, median event duration, amplitude and relative magnitude were sampled in a

similar fashion to all turbulence properties, thereby allowing for observations of any tidal trend.

For the entire study, there were on average 1 to 4 turbulent events per second for all the fluxes (Table 4). This result was close for all ADV units and somehow consistent with the early results of RAO et al. (1971). For all momentum fluxes and all ADV units, the number of events per sample varied in a similar pattern with the tides. The number of events per sample increased about low tide when the water column was shallower and the effects of bed shear stress were stronger, while it decreased about high tide.

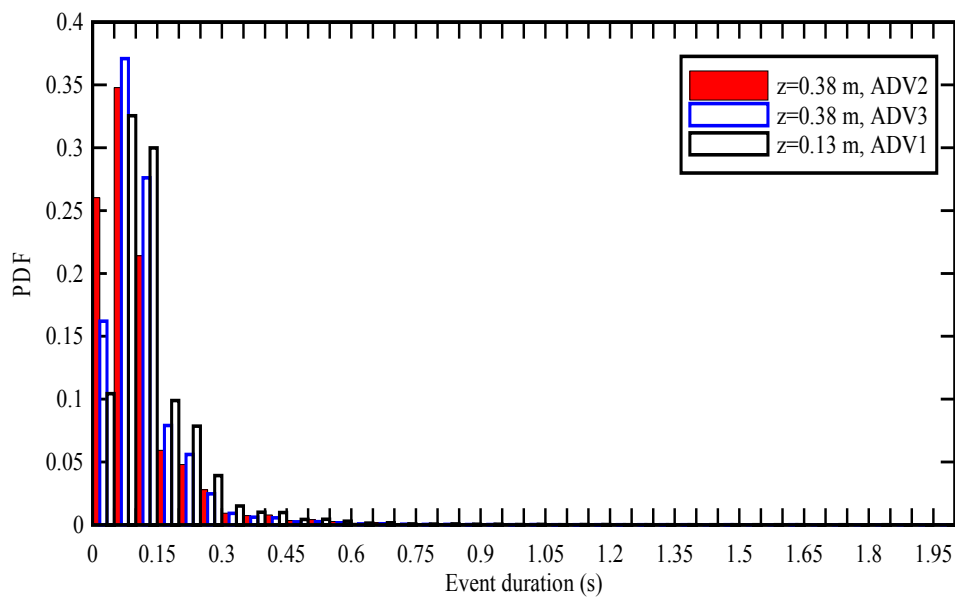
Table 3. Total number of turbulent events and sub-events detected in the ADV data sets for the entire study E10 (Erapah Creek, Australia).

ADV unit (1)	Flux (2)	Number of events (3)	Number of sub-events (4)
ADV1 ($z=0.13$ m, 10.70 m from left bank)	$v_x v_y$	164,706	479,376
	$v_x \dot{i}_b$	640,046	741,963
ADV2 ($z=0.38$ m, 10.70 m from left bank)	$v_x v_z$	389,113	712,283
	$v_x v_y$	762,090	982,352
	$v_x \dot{i}_b$	889,305	743,320
ADV3 ($z=0.38$ m, 10.78 m from left bank)	$v_x v_z$	542,861	829,317
	$v_x v_y$	242,939	588,094
	$v_x \dot{i}_b$	885,940	902,951

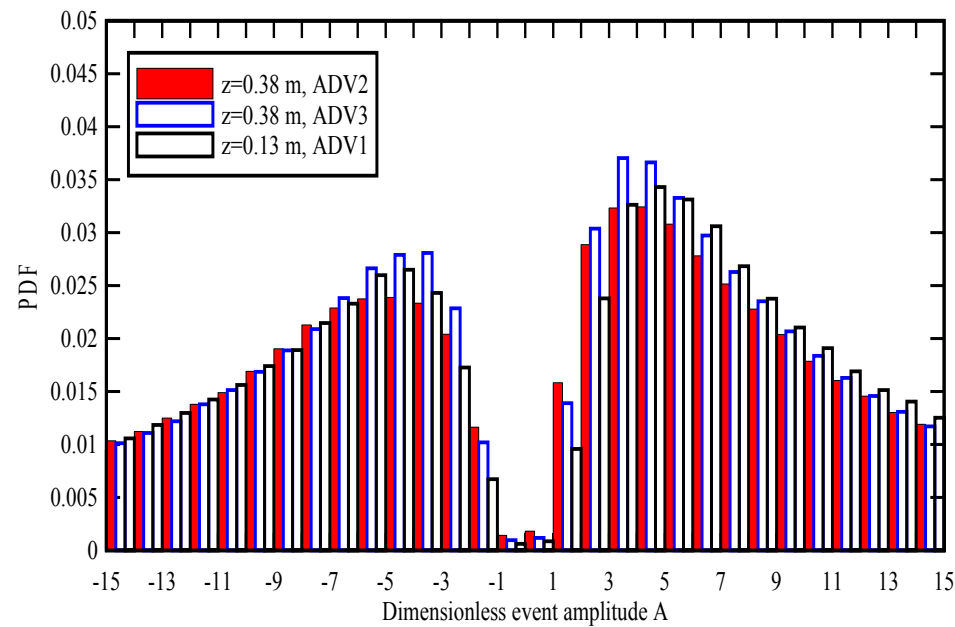
Table 4. Turbulent event characteristics for all ADV units during the entire study E10.

Parameter (1)	ADV1 unit		ADV2 unit			ADV3 unit		
	$v_x v_y$ (2)	$v_x \dot{i}_b$ (3)	$v_x v_z$ (4)	$v_x v_y$ (5)	$v_x \dot{i}_b$ (6)	$v_x v_z$ (7)	$v_x v_y$ (8)	$v_x \dot{i}_b$ (9)
Nb of events per data sample	154	743	389	912	988	614	221	1,050
Event duration τ (s)								
Median duration of positive events ($A > 0$) (s)	0.26	0.10	0.12	0.10	0.08	0.10	0.16	0.40
Median duration of negative events ($A < 0$) (s)	0.18	0.10	0.10	0.08	0.06	0.08	0.12	0.08
Event amplitude A								
Median amplitude of positive events ($A > 0$)	3.34	11.87	3.44	3.87	11.9	3.56	3.26	11.04
Median amplitude of negative events ($A < 0$)	-4.21	-13.34	-4.06	-4.67	-13.3	-4.31	-4.08	-12.19
Relative magnitude m								
Median magnitude of positive events ($A > 0$)	0.0048	0.0069	0.0026	0.0021	0.0055	0.0023	0.0033	0.0055
Median magnitude of negative events ($A < 0$)	-0.0045	-0.0067	-0.0023	-0.0020	-0.0052	-0.0023	-0.0030	-0.0053

Note: data sample length = 200 s (10,000 data points).



(A) Event duration with histogram intervals of 0.05 s.



(B) Dimensionless event amplitude with histogram intervals of 1.

Figure 16. Normalised probability distribution functions of event duration and dimensionless amplitude for the suspended sediment flux $v_x i_b$ - Data collected by all ADV units (study E10).

The event duration for the momentum fluxes $v_x v_z$ and $v_x v_y$ seemed to vary with the tides for all the ADV systems, while the pseudo suspended sediment flux data $v_x i_b$ showed no discernable tidal pattern. The magnitude of dimensionless event amplitude for the momentum flux $v_x v_z$ tended to be larger about low water and smaller about high water. No discernable tidal patterns in terms of event amplitude of $v_x v_y$ and $v_x i_b$ fluxes were observed for all ADV units.

For the turbulent sub-events, the median values of the number of sub-events per sample, the sub-event duration, dimensionless sub-event amplitude, and the relative sub-event magnitude are summarized in Table 5. The median sub-event duration was 0.04 s for all fluxes and ADV units, implying that most sub-events had a short life span. The dimensionless sub-event amplitudes for the fluxes $v_x v_z$ and $v_x v_y$ were typically between 2.8 and 6.4, but the sub-event amplitudes for the suspended sediment flux $v_x i_b$ were larger, between 11 and 16 (Table 5).

Table 5. Median sub-event characteristics for all ADV units during the entire study E10.

Parameter (1)	ADV1 unit		ADV2 unit			ADV3 unit		
	$v_x v_y$ (2)	$v_x i_b$ (3)	$v_x v_z$ (4)	$v_x v_y$ (5)	$v_x i_b$ (6)	$v_x v_z$ (7)	$v_x v_y$ (8)	$v_x i_b$ (9)
Nb of sub-events per data sample	540	982	910	1,375	1,195	1,107	707	1,284
Sub-event duration (s)								
Median duration of positive sub-events ($A > 0$) (s)	0.04	0.04	0.04	0.04	0.04	0.04	0.04	0.04
Median duration of negative sub-events ($A < 0$) (s)	0.04	0.04	0.04	0.04	0.04	0.04	0.04	0.04
Sub-event amplitude A								
Median amplitude of positive sub-events ($A > 0$)	2.83	12.67	3.18	4.09	11.81	3.57	2.76	11.55
Median amplitude of negative sub-events ($A < 0$)	-5.28	-15.98	-4.84	-6.37	-15.38	-5.41	-5.08	-14.65
Sub-event magnitude m								
Median magnitude of positive sub-events ($A > 0$)	0.0009	0.0033	0.0009	0.0010	0.0029	0.0010	0.0008	0.0029
Median magnitude of negative sub-events ($A < 0$)	-	-	-	-	-	-	-	-
	0.0014	0.0038	0.0012	0.0015	0.0035	0.0013	0.0013	0.0034

For all fluxes and all ADV units, the number of sub-events per sample varied in a similar fashion with the tides. That is, the number of sub-events increased about low tide and decreased about high tide. Altogether the variation of the number of sub-events per sample exhibited a similar tidal pattern to that of the number of events per sample. For the entire field study (50 hours), the events durations showed no obvious tidal trend while, for the sub-event amplitude, only those of the momentum flux $v_x v_z$ seemed to vary with the tide. The sub-event

amplitude of the flux $v_x v_z$ showed a similar tidal trend to that of the event amplitude for $v_x v_z$, being largest about low tide and smallest about high tide. On average over the entire study, the results showed 1 to 3 sub-events per turbulent event and the finding was independent of the tidal period.

4.3. Discussion

The turbulent event results in the small estuary of Erapah Creek may be compared with the field data of RUDRA KUMAR et al. (1995) in an atmospheric boundary layer, re-analysed by NARASIMHA et al. (2007). That study was based upon data collected at Jodhpur with an acoustic anemometer located 4 m above the ground. The comparative results are discussed herein in terms of the momentum flux events for $v_x v_z$ and the basic results are summarised in Table 6.

Table 6. Momentum flux event analyses in terms of $v_x v_z$: comparative results.

Parameters	Erapah Creek (study E10)	Jodhpur, India
	TREVETHAN et al. (2007b)	NARASIMHA et al. (2007)
(1)	(2)	(3)
z (m)	0.38	4
Mean momentum flux (m^2/s^2)	$2.1 \cdot 10^{-5}$	0.191
Ratio r.m.s/mean	2.98	3.04
Sweep ejection period	40%	36%
Wallward/inward interaction period	16.6%	15%
Idle/passive period	43.4%	49%
Average duration of positive events ($A > 0$) (s)	0.12	1.71
Average duration of negative events ($A < 0$) (s)	0.10	1.12
Outer time scale (s)	~ 15 (mode)	~ 30

The experimental data showed that the duration of the events was of the order of 0.11 s and 1.4 s respectively for the estuary and atmospheric studies, compared to an outer time scale of the order of 15 s and 30 s respectively. In the small estuary, the outer time scale was based upon the measured water depth and the velocity magnitude recorded at $z = 0.38$ m. Hence the outer time scale estimate was a very rough average and could vary over a wide range from as low as 3 s to over 100 s. Overall the differences between turbulent event durations and outer time scales were comparable for both environmental flow studies.

The probability distribution functions of event duration tended to follow a log-normal distribution for both studies. But the probability distribution functions of event magnitude presented some marked difference between estuarine flow data and atmospheric flow results,

with a much narrower event magnitude distribution, as well as a different PDF shape, in the estuarine system.

The relationship between turbulent event amplitude and duration illustrated little correlation between the event amplitude and the event duration. That is, there were a wide range of event amplitudes for any given event duration, and conversely. The observation was valid for both studies and implied that the size of an event, represented by its dimensionless amplitude, and its duration may be considered as two independent parameters.

In the estuarine turbulent flow, the probability distribution functions of the number of turbulent sub-events per burst event were skewed with a very large proportion of events having between 1 and 2 sub-events for all fluxes. The probability distribution functions had however a long tail of small numbers of turbulent events with large numbers of sub-events. This is illustrated in Figure 17 presenting the normalised PDF for the number of sub-events per events for all fluxes at $z = 0.38$ m. For the momentum flux $v_x \times v_z$, the average number of sub-events per event was 1.21 for that data set, and the maximum number of sub-events per event was 440, with 5,420 turbulent events having 40 sub-events or more for the entire study. Overall the distribution of "extreme" numbers of sub-events per turbulent event showed no tidal trend or correlation with the longitudinal velocity V_x .

The data analyses demonstrated the significance of turbulent events in environmental flows and showed the complex nature of bursting events consisting of consecutive sub-events.

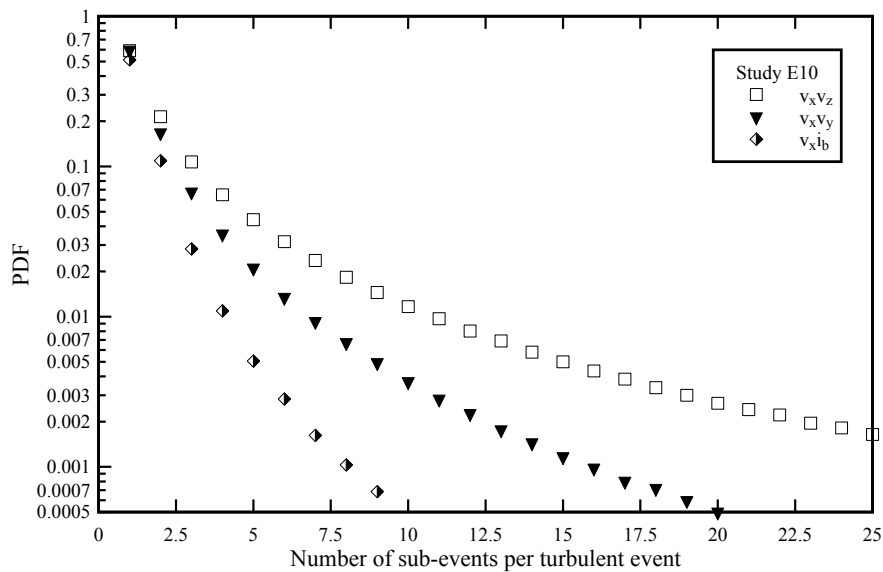


Figure 17. Normalised probability distribution function of the number of turbulent sub-events per turbulent event for the momentum flux v_xv_z , v_xv_y and v_xi_b - Data collected at $z = 0.38$ m (ADV2 unit) for the entire field study E10 (Erapah Creek, Australia).



(A) Field work in a small estuary in Australia (Eprapah Creek) at low tide (study E10) (Courtesy of Dr S. FURUYAMA).



(B) Field work in a shallow-water saltwater lake in Japan (Hamana Lake) in December 2005 (Courtesy of Professor S. AOKI).

Figure 18. Field measurements in shallow water estuaries.

5. CONCLUSION

In small estuaries, the predictions of scalar dispersion can rarely be estimated accurately because of a lack of fundamental understanding of the turbulence structure. Detailed turbulent velocity and suspended sediment concentration measurements were performed simultaneously and continuously at high frequency for between 25 and 50 hours per investigation in shallow-water estuaries with semi-diurnal tides in Australia and Japan (Fig. 18). The detailed analyses provided a unique characterisation of the turbulent mixing processes and suspended sediment fluxes.

Continuous turbulent velocity sampling at high frequency allowed a detailed characterisation of the turbulence field in estuarine systems and its variations during the tidal cycle. The turbulence was neither homogeneous nor isotropic. It was not a purely Gaussian process, and the small departures from Gaussian probability distribution were an important feature of the turbulent processes. A striking feature of the present data sets was the large and rapid fluctuations in all turbulence characteristics and of the suspended sediment fluxes during the tidal cycles. This was rarely documented, but an important characteristic of the newer data sets is the continuous high frequency sampling over relatively long periods. The findings showed that the turbulent properties, and integral time and length scales should not be assumed constant in a shallow estuary. The integral time scales for turbulence and suspended sediment concentration were similar during flood tides, but differed significantly during ebb tides. It is believed that the present results provided a picture general enough to be used, as a first approximation, to characterise the flow field in similar shallow-water estuaries with semi-diurnal tides. It showed in particular a different response from that observed in larger, deep-water estuaries.

A turbulent flux event analysis was performed for a 50 hour long field study. The results showed that the large majority of turbulent events had a duration between 0.04 s and 0.3 s, and there were on average 1 to 4 turbulent events per second. A number of turbulent bursting events consisted of consecutive sub-events, with between 1 and 3 sub-events per event on average for all turbulent fluxes. A comparison with atmospheric boundary layer results illustrated a number of similarities between the two types of turbulent flows. Both studies implied that the amplitude of an event and its duration were nearly independent.

Overall the present research highlighted some turbulent processes that were rarely documented in previous studies. However, an important feature of the present analysis was the continuous high frequency sampling data sets collected during relatively long periods, as well as the simultaneous sampling of both turbulent velocities and suspended sediment concentrations.

ACKNOWLEDGMENTS

The writers acknowledge the assistance of and inputs from Prof. Shin-ichi AOKI (Toyohashi University of Technology), Dr Richard BROWN (Q.U.T.), John FERRIS (Queensland E.P.A.), and Dr Ian RAMSAY (Queensland E.P.A.). They acknowledge further the contribution of the numerous people involved in the field works.

REFERENCES

- [1] Bauer B.O., Yi, J., Namikas, S.L., and Sherman, D.J. (1998). "Event Detection and Conditional Averaging in Unsteady Aeolian Systems." *Jl of Arid Env.*, Vol. 39, pp. 345-375.
- [2] Bowden, K.F., and Ferguson, S.R. (1980). "Variations with Height of the Turbulence in a Tidally-Induced Bottom Boundary Layer." *Marine Turbulence*, J.C.J. NIHOUL, Ed., Elsevier, Amsterdam, The Netherlands, pp. 259-286.
- [3] Bowden, K.F. and Howe, M.R. (1963). "Observations of turbulence in a tidal current." *Journal of Fluid Mechanics*, Vol. 17, No. 2, pp. 271-284.
- [4] Bradshaw, P. (1971). "An Introduction to Turbulence and its Measurement." *Pergamon Press*, Oxford, UK, The Commonwealth and International Library of Science and technology Engineering and Liberal Studies, Thermodynamics and Fluid Mechanics Division, 218 pages.
- [5] Chanson, H. (2003). "A Hydraulic, Environmental and Ecological Assessment of a Sub-tropical Stream in Eastern Australia: Eprapah Creek, Victoria Point QLD on 4 April 2003." *Report No. CH52/03*, Dept. of Civil Engineering, The University of Queensland, Brisbane, Australia, June, 189 pages.
- [6] Chanson, H. (2004). "Environmental Hydraulics of Open Channel Flows." *Elsevier Butterworth-Heinemann*, Oxford, UK, 483 pages.
- [7] Chanson, H., Brown, R., Ferris, J., Ramsay, I., and Warburton, K. (2005). "Preliminary Measurements of Turbulence and Environmental Parameters in a Sub-Tropical Estuary of Eastern Australia." *Environmental Fluid Mechanics*, Vol. 5, No. 6, pp. 553-575 (DOI: 10.1007/s10652-005-0928-y).
- [8] Chanson, H., Takeuchi, M., and Trevethan, M. (2008a). "Using Turbidity and Acoustic Backscatter Intensity as Surrogate Measures of Suspended Sediment Concentration in a Small Sub-Tropical Estuary." *Journal of Environmental Management*, Vol. 88, No. 4, Sept., pp. 1406-1416 (DOI: 10.1016/j.jenvman.2007.07.009).
- [9] Chanson, H., Trevethan, M., and Aoki, S. (2008b). "Acoustic Doppler Velocimetry (ADV) in Small Estuary : Field Experience and Signal Post-Processing." *Flow Measurement and Instrumentation*, Vol. 19, No. 5, pp. 307-313 (DOI: 10.1016/j.flowmeasinst.2008.03.003).
- [10] Digby, M.J., Saenger, P., Whelan, M.B., Mcconchie, D., Eyre, B., Holmes, N., Bucher, D. (1999). "A Physical Classification of Australian Estuaries." *Report No. 9*, LWRRDC, Australia, National River Health Program, Urban sub-program, Occasional Paper, 16/99.
- [11] Dyer, K.R. (1997). "Estuaries. A Physical Introduction." *John Wiley*, New York, USA, 2nd edition, 195 pages.
- [12] Finnigan, J. (2000). "Turbulence in Plant Canopies." *Ann. Rev. Fluid Mech.*, Vol. 32, pp. 519-571.
- [13] Fransson, J.H.M., Matsubara, M., and Alfredsson, P.H. (2005)." Transition Induced by Free-stream Turbulence." *Jl of Fluid Mech.*, Vol. 527, pp. 1-25.
- [14] Fugate, D.C., and Friedrichs, C.T. (2002). "Determining Concentration and Fall Velocity of Estuarine Particle Populations using ADV, OBS and LISST." *Continental Shelf Research*, Vol. 22, pp. 1867-1886.

- [15] Hallbeck, M., Groth, J., and Johansson, A.V. (1989). "A Reynolds Stress Closure for the Dissipation in Anisotropic Turbulent Flows." *Proc. 7th Symp. Turbulent Shear Flows*, Stanford University, USA, Vol. 2, pp. 17.2.1-17.2.6.
- [16] Ham, R. van der, Fromtijn, H.L., Kranenburg, C., and Winterwerp, J.C. (2001). "Turbulent Exchange of Fine Sediments in a Tidal Channel in the Ems/Dollard Estuary. Part I: Turbulence Measurements." *Continental Shelf Research*, Vol. 21, pp. 1605-1628.
- [17] Hinterberger, C., Fröhlich, J., and Rodi, W. (2008). "2D and 3D Turbulent Fluctuations in Open Channel Flow with $Re_\tau = 590$ studied by Large Eddy Simulation." *Flow Turbulence Combustion*, Vol. 80, No. 2, pp. 225-253 (DOI: 10.1007/s10494-007-9122-2).
- [18] Hinze, J.O. (1975). "Turbulence." *McGraw-Hill Publ.*, 2nd Edition, New York, USA.
- [19] Hossain, S., Eyre, B., and Mcconchie, D. (2001). "Suspended Sediment Transport Dynamics in the Subtropical Micro-tidal Richmond River Estuary, Australia." *Estuarine, Coastal and Shelf Science*, Vol. 52, pp. 529–541.
- [20] Johansson, A.V., and Alfredsson, P.H. (1982). "On the Structure of Turbulent Channel Flow." *Jl of Fluid Mech.*, Vol. 122, pp. 295-314.
- [21] Kawanisi, K., and Yokosi, S. (1994). "Mean and Turbulence Characteristics in a Tidal River." *Continental Shelf Research*, Vol. 17, No. 8, pp. 859-875.
- [22] Kawanisi, K., Tsutsui, T., Nakamura, S., and Nishimaki, H. (2006). "Influence of Tidal Range and River Discharge on Transport of Suspended Sediment in the Ohta Flood-way." *Jl of Hydroscience and Hyd. Eng.*, JSCE, Vol. 24, No. 1, May, pp. 1-9.
- [23] Kline, S.J., Reynolds, W.C., Schraub, F.A. and Runstaller, P.W. (1967)."The structure of turbulent boundary layers." *Journal of Fluid Mechanics*, Vol. 30, No. 4, pp. 741-773.
- [24] Koch, C., and Chanson, H. (2005). "An Experimental Study of Tidal Bores and Positive Surges: Hydrodynamics and Turbulence of the Bore Front." *Report No. CH56/05*, Dept. of Civil Engineering, The University of Queensland, Brisbane, Australia, July, 170 pages.
- [25] Larcombe, P. and Ridd, P.V. (1992). "Dry Season Hydrodynamics and Sediment Transport in a Mangrove Creek." *Proceedings 6th International Biennial Conf on Physics of Estuaries and Coastal Seas*, Margaret River WA, Australia, Paper 23. (Also *Mixing in Estuaries and Coastal Seas*, Coastal and Estuarine Studies Vol. 50, AGU, New York, USA, 1996, pp. 388-404.)
- [26] Montes, J.S. (1998). "Hydraulics of Open Channel Flow." *ASCE Press*, New-York, USA, 697 pages.
- [27] Narasimha, R., Kumar, S.R., Prabhu, A., and Kailas, S.V. (2007). "Turbulent Flux Events in a Nearly Neutral Atmospheric Boundary Layer." *Phil. Trans. Royal Soc., Series A*, Vol. 365, pp. 841-858.
- [28] Nezu, I. (2005). "Open-Channel Flow Turbulence and its Research prospect in the 21st Century." *Jl of Hyd. Engrg.*, ASCE, Vol. 131, No. 4, pp. 229-246.
- [29] Nezu, I., and Nakagawa, H. (1993). "Turbulence in Open-Channel Flows." *IAHR Monograph*, IAHR Fluid Mechanics Section, Balkema Publ., Rotterdam, The Netherlands, 281 pages.
- [30] Niederschulte, M.A. (1989). "Turbulent Flow Through a Rectangular Channel." *Ph.D. thesis*, Dept. of Chem. Eng., University of Illinois, Urbana-Champaign, USA, 417 pages.

-
- [31] Nielsen, P. (1992). "Coastal Bottom Boundary Layers and Sediment Transport." *Advanced Series on Ocean Eng.*, Vol. 4, World Scientific Publ., Singapore.
 - [32] Nikora, V., Goring, D., and Ross, A. (2002). "The Structure and Dynamics of the Thin Near-Bed Layer in a Complex Marine Environment: A Case Study in Beatrix Bay, New Zealand." *Estuarine, Coastal and Shelf Science*, Vol. 54, pp. 915-926.
 - [33] Osonphasop, C. (1983). "The Measurements of Turbulence in Tidal Currents." *Ph.D. thesis*, Dept of Mech. Eng., Monash Univ., Australia.
 - [34] Osterlund, J.M., Lindgren, B., and Johansson, A.V. (2003). "Flow Structures in Zero Pressure-Gradient Turbulent Boundary Layers at High Reynolds Numbers." *Eur. Jl Mechanics B. Fluids*, Vol. 22, pp. 379-390 (DOI: 10.1016/S0997-7546(03)00034-7).
 - [35] Piquet, J. (1999). "Turbulent Flows. Models and Physics." *Springer*, Berlin, Germany, 761 pages.
 - [36] Rao, K.N., Narasimha, R., and Narayanan, A.A.B. (1971). "The "Bursting" Phenomena in a Turbulent Boundary Layer." *Jl of Fluid Mech.*, Vol. 48, Part 2, pp. 339-352.
 - [37] Reynolds, O. (1883). "An Experimental Investigation of the Circumstances which Determine whether the Motion of Water shall be Direct or Sinuous, and the Laws of Resistance in Parallel Channels." *Phil. Trans. Roy. Soc. Lond.*, Vol. 174, pp. 935-982.
 - [38] Reynolds, O. (1887) "On Certain Laws Relating to the Regime of Rivers and Estuaries, and on the Possibility of Experiments on a Small Scale." *British Association Report*, UK.
 - [39] Rudra Kumar, S., Ameenulla, S., and Prabhu, A. (1995). "MONTBLEX Tower Observations: Instrumentation, Data Acquisition and Data Quality." *Proc. Indian Acad. Science (Earth Planet Science)*, Vol. 104, No. 2, pp. 221-248.
 - [40] Savenije, H.H.G. (2005). "Salinity and Tides in Alluvial Estuaries." *Elsevier*, Amsterdam, The Netherlands, 194 pages.
 - [41] Schlichting, H. (1979). "Boundary Layer Theory." *McGraw-Hill*, New York, USA, 7th edition.
 - [42] Shiono, K., and West, J.R. (1987). "Turbulent Perturbations of Velocity in the Conwy Estuary." *Estuarine, Coastal and Shelf Science*, Vol. 25, pp. 533-553.
 - [43] Tachie, M.F. (2001). "Open Channel Turbulent Boundary Layers and wall Jets on Rough Surfaces." *Ph.D. thesis*, Dept. of Mech. Eng., Univers. of Saskatchewan, Canada, 238 pages.
 - [44] Thorne, P.D., Vincent, C.E., Hardcastle, P.J., Rehman, S., and Pearson, N. (1991). "Measuring Suspended Sediment Concentrations using Backscatter Devices." *Marine Geology*, Vol. 98, pp. 7-16.
 - [45] Trevethan, M. (2008). "A Fundamental Study of Turbulence and Turbulent Mixing in a Small Subtropical Estuary." *Ph.D. thesis*, Div. of Civil Engineering, The University of Queensland, 342 pages.
 - [46] Trevethan, M., Chanson, H., and Takeuchi, M. (2007a). "Continuous High-Frequency Turbulence and Sediment Concentration Measurements in an Upper Estuary." *Estuarine Coastal and Shelf Science*, Vol. 73, No. 1-2, pp. 341-350 (DOI:10.1016/j.ecss.2007.01.014).
 - [47] Trevethan, M., Chanson, H., and Brown, R.J. (2007b). "Turbulence and Turbulent Flux Events in a Small Subtropical Estuary." *Report No. CH65/07*, Hydraulic Model Report series, Div. of Civil Engineering, The University of Queensland, Brisbane, Australia, November, 67 pages.

-
- [48] Trevethan, M., Chanson, H., and Brown, R. (2008). "Turbulence Characteristics of a Small Subtropical Estuary during and after some Moderate Rainfall." *Estuarine Coastal and Shelf Science*, Vol. 79, No. 4, pp. 661-670 (DOI: 10.1016/j.ecss.2008.06.006).
- [49] Voulgaris, G., and Meyers, S.T. (2004). "Temporal Variability of Hydrodynamics, Sediment Concentration and Sediment Settling in a Tidal Creek." *Continental Shelf Research*, Vol. 24, pp. 1659-1683.
- [50] West, J.R. and Oduyemi, K.O.K. (1989). "Turbulence measurements of suspended solids concentration in estuaries." *Journal of Hydraulic Engineering*, ASCE, Vol. 115, No. 4, pp. 457-473.
- [51] Xie, Q. (1998). "Turbulent Flows in Non-Uniform Open Channels : Experimental Measurements and Numerical Modelling." *Ph.D. thesis*, Dept. of Civil Eng., University Of Queensland, Australia, 339 pages.

INTERNET REFERENCES

A Hydraulic, Environmental and Ecological Assessment of a Sub-tropical Stream in Eastern Australia: Erapah Creek, Victoria Point QLD on 4 April 2003	{ http://www.uq.edu.au/~e2hchans/eprapa.html }
Queensland EPA water quality monitoring	{ http://www.epa.qld.gov.au/environmental_management/water/water_quality_monitoring/ }
Erapah Creek Catchment Landcare Association Inc. (ECCLA)	{ http://erapah.scouting.net.au/index/projects/landcare.htm }
Research publications in hydraulic engineering and applied fluid mechanics	{ http://espace.library.uq.edu.au/list/author_id/193/ }

OPEN ACCESS REPOSITORIES

OAIster	{ http://www.oaister.org/ }
UQeSpace	{ http://espace.library.uq.edu.au/ }

Reviewed by Professor Michele MOSSA, Politecnico di Bari (Italy)

Chapter 5

TURBULENT SCALAR TRANSFER MODELING IN REACTING FLOWS

Lei-Yong Jiang* and Ian Campbell

Gas Turbine Laboratory, Institute for Aerospace Research, National Research Council
Canada, Ottawa, Ontario, Canada

ABSTRACT

Turbulence modeling is a major factor, affecting the precision of current numerical simulations, particularly for reacting flows. It is also one of the principal unsolved problems in physics today. In the last five decades, much effort has been devoted to the development of turbulent momentum transfer models. However, researches on turbulent scalar transportation issues are limited, particularly for reacting flows.

In almost all turbulent reacting flow RANS (Reynolds-averaged Navier-Stokes) simulations, the Reynolds analogy concept has been used to model turbulent scalar transfers since the 1970s. With this concept, the turbulent Prandtl/Schmidt number is used to calculate the turbulent scalar transfers in flow fields based on the momentum transfer that is modeled by a selected turbulence model. In this chapter, the rationale and limitation of the Reynolds analogy are analyzed and validated against two benchmarking cases, a turbulent jet diffusion flame and a model diffusion flame combustor. The former represents a simple boundary-type flow, while the latter involves complex flow phenomena (shear layers, wall boundary layers, separations, recirculation zones, re-attachments and their interactions) which are relevant to many practical combustion systems.

The effects of turbulent Prandtl/Schmidt numbers on the flow fields of the jet flame and model combustor have been numerically studied with selected turbulence, combustion and radiation models. In comparison with comprehensive experimental databases, it is found that for both cases, the flow features and magnitudes of mean velocity fields are well predicted, particularly for the jet flame case, and the turbulent Prandtl/Schmidt number has insignificant effect on the velocity fields. In addition, for the combustor case, the turbulence kinetic energy and shear stress distributions are also reasonably well predicted. The proper prediction of velocity fields (or momentum

* Contact author: leiyong.jiang@nrc-cnrc.gc.ca

transfers) provides a prerequisite for adequate evaluation of the Reynolds analogy concept or the effect of turbulent Prandtl/Schmidt numbers on the temperature fields of the reacting flows.

In contrast, the turbulent Prandtl/Schmidt number shows significant effects on the temperature fields, particularly for the temperature profiles in the outer layer region of the jet flame and the downstream region of the model combustor. This is also true for the temperature profile along the combustor wall.

Jet diffusion flames seem simple; however, they pose challenges to numerical simulations. The discrepancies of temperature distributions in the upstream outer layer region of the jet flame are observed by the authors and other researchers, and the anticipated reasons are three-fold, incapability to predict the local laminarization phenomenon, the limitations of Reynolds analogy, and insufficient effort in the development of turbulent scalar transfer models. For the Prandtl/Schmidt numbers considered, 0.45 – 1.2, the value of 0.85 can provide acceptable results for the temperature distributions along the jet centerline and at the downstream cross-sections.

For the model combustor configuration and operating conditions, the optimal Prandtl/Schmidt number for temperature prediction inside the combustor is 0.5 for all three combustion models, and it varies from 0.35 to 0.55 for the combustor wall temperature prediction. With the optimal value of 0.50, the velocity and temperature fields are reasonably well predicted, except in some local regions.

The present work suggests that for reliable temperature prediction in turbulent reacting flows without tuning turbulent Prandtl/Schmidt numbers, the Reynolds analogy concept should be improved and new approaches should be investigated.

NOMENCLATURE

symbol	definition
$C\mu$	empirical constant
C_p	specific heat at constant pressure
D	molecular diffusivity
f	mixture fraction
f''	fluctuating component of mixture fraction
H	enthalpy
K	turbulence kinetic energy
Le	Lewis number
Pr_t	turbulent Prandtl number
Re	Reynolds number
S	source term
Sc_t	turbulent Schmidt number
T	temperature
\mathbf{T}	viscous stress tensor

symbol	definition
U	mean axial velocity
U_i	ith mean velocity component
u_i''	ith fluctuating velocity component
$\overline{u''u''}$ or $u''u''$	stream-wise turbulence normal stress
\mathbf{V}	velocity vector
$\mathbf{v''}$	fluctuating velocity vector
$\overline{v''v''}$ or $v''v''$	radial turbulence normal stress
$\overline{w''w''}$ or $w''w''$	circumferential turbulence normal stress
$\overline{u''v''}$ or $u''v''$	turbulence shear stress
x_i	ith Cartesian coordinate
X	coordinate along the combustor axis of symmetry
Y	species mass fraction
y^+	non-dimensional parameter, $\sqrt{\tau_w/\rho} y/\nu$
Γ_t	turbulence Prandtl or Schmidt number
δ_{ij}	Kronecker delta function ($\delta_{ij} = 1$ if $i = j$; $\delta_{ij} = 0$ if $i \neq j$)
ε	turbulence dissipation rate
Ω	specific turbulence dissipation rate
μ	laminar viscosity
μ_t	turbulent viscosity
ρ	density
ϕ	species mole fraction, mixture fraction, density or temperature

1. INTRODUCTION

Turbulence modeling is one of the major issues, which affects the precision of current numerical simulations, particularly for reacting flows. Turbulence is characterized with irregularity or randomness, diffusion, vortices fluctuation and viscous dissipation, and involves a wide range of time and length scales. It is one of the principal unsolved problems in physics today (Tennekes & Lumley, 1983). Despite the rapid development of computing power, direct numerical simulations of turbulent flows remain practical only at low Reynolds numbers, while large eddy simulations are limited to benchmarking cases with relatively simple geometries (Wilcox 2001 & 2002). This is particularly true for turbulent reacting flows. Combustion, even without turbulence, is an intrinsically complex process, and can

involve hundreds of species and thousands of reactions, which cause numerical difficulties (Dagaut et al., 1994). For these reasons, it is necessary to utilize turbulence models in numerical simulations for the development of advanced combustion systems.

Much effort has been devoted to the development of turbulent momentum transfer models in the last five decades. Progresses focused on constant density flows have been reviewed or described by many researchers, such as Reynolds and Cebeci (1976), Marvin (1983), Lauder (1989) and Wilcox (2002), and brought up to date for the second momentum closure in reacting flows by Jones (1994). Various algebraic, one- and two-equation turbulence models were systematically evaluated by Wilcox (2001 & 2002) against a number of well-documented non-reacting flows, including free-shear, boundary-layer and separated flows. Some guidelines regarding application of these turbulence models were provided.

In contrast to turbulent momentum transfer modeling, studies on turbulent scalar transfer modeling particularly in reacting flows are limited, but are of great engineering interest. For example, accurate prediction of temperature distribution is critical in the development of gas turbine combustors. Poor temperature profiles on the combustor liner and at the combustor exit can significantly reduce lifetime of the combustor and turbine vanes & blades behind. In extreme cases, devastating structural damage to engine components can occur.

After reviewing the progresses and challenges in experimental understanding and numerical methods for turbulent jet diffusion flames, Bilger (1976 & 1989) pointed out that much of the interest in turbulent mixing was not yet resolved, and interactive investigation of modeling techniques and simple experimental flows was required. The same topics were revisited by Eickhoff (1982), and it was suggested that the wrinkled laminar flamelet method combined with the conserved scalar approach could predict turbulent jet diffusion flames with satisfactory accuracy. In terms of turbulent scalar transfer modeling, as mentioned by Jones (1994), the closure adopted for the scalar field was often not as influential as that for the velocity field, although clearly an accurate representation of the velocity field was an essential prerequisite for the accurate prediction of the scalar field.

From the pioneering CFD work of the 1970's up to the present, turbulent scalar transfers (mixture fraction, species and energy or temperature) in turbulent reacting flow RANS (Reynolds-averaged Navier-Stokes) simulations have usually been based on the Reynolds analogy concept. In this approach, the turbulent Prandtl (Pr_t) and Schmidt (Sc_t) numbers are used to link the turbulent scalar transfers in flow fields to the momentum transfer that is determined by a selected turbulence model. The main advantage of this approach is that the turbulent scalar transfers can be effectively computed from the modeled momentum transfer without solving a full second moment closure for both momentum and scalar transports. Consequently, the computing time to reach a converged solution is much reduced.

The Reynolds analogy concept was first postulated by Osborne Reynolds (1874) over a century ago by studying the similarity between the wall shear and heat flux in boundary layers. This original hypothesis has been considerably amended and applied to general turbulent heat and species transfers (Hinze 1987 & White 1988). Recently, its application to high-Mach-number boundary layers (Suraweera et al. 2006), turbine flows (Bons 2005) and film cooling (Jones & Walton 1991) have been studied. The Reynolds analogy factors for flow parameters related to hypersonic propulsion and turbines have been determined (Suraweera et al. 2006 & Bons 2005).

The suitability of Reynolds analogy to disturbed turbulent thermal boundary flows has been reported by a number of authors. Choi and Orchard (1997) investigated the heat transfer characteristics over a triangular-profiled riblet surface, while de Souza et al. (1999) studied the large scale organization of a boundary layer disturbed by a cylinder wake flow. They all pointed out that this concept did not hold in these disturbed boundary flows. Vogel and Eaton (1985) carried out heat transfer and fluid dynamic measurements downstream of a backward-facing step. It was found that Reynolds analogy failed in the recovering boundary layer region, and it was only valid far downstream of the reattachment point. Time-resolved gas temperature in the oscillating turbulent flow of a pulse combustor tail pipe was studied by John and Keller (1990). The results indicated that the analogy between momentum and thermal transport at the tail pipe wall was no longer valid.

Numerous experimental studies on Pr_t and Sc_t have been carried out in the last century, particularly in the period of 1930s - 1980s (Hinze 1987 and White 1988). Hinze (1987) reviewed a large number of experimental measurements in pipe and 2-D channel flows, and concluded that the overall Pr_t or Sc_t varied from 0.6 to 0.8. More recently, based on their velocity and concentration half-width measurements in axi-symmetric jets of air and helium, Panchapakesan and Lumley (1993) obtained an average value of 0.7 for Sc_t .

In most turbulent reacting or mixing flow simulations, it has become a common practice to set $Le \equiv Sc_t / Pr_t = 1$ or $Pr_t = Sc_t$ (Libby & Williams 1994). Traditionally a constant value of $Pr_t = Sc_t = 0.7 - 0.85$ has been used in jet flows (Lubbers et al. 2001 and Spalding 1971) and gas turbine combustor modeling (Bai & Fuchs 1995 and Lai 1997). However, low Pr_t and Sc_t numbers from 0.20 to 0.5 have been used by a number of authors for simulating gas turbine combustors. Much effort was made by Syed & Sturgess (1980) to validate a two-dimensional finite difference (TEACH) code against a number of isothermal and reacting flow measurements. A value of $Pr_t = Sc_t = 0.5$ was recommended for recirculation zone simulations, and an accuracy of ~80% was reported in terms of the recirculation zone size and strength. Kaaling et al. (1997) systematically studied five RQL (rich burn, quick quench, lean burn) low-emission combustor designs. The CFD calculations were calibrated against CARS (coherent anti-Stokes Raman spectroscopy) temperature measurements, and good agreement was found by using $Pr_t = Sc_t = 0.2$. Crocker et al. (1998) successfully modeled an entire combustor from the compressor diffuser exit to the turbine inlet, including air split and liner wall temperature prediction. A low value of 0.25 was used for Pr_t and Sc_t since it consistently demonstrated better agreement with the combustor fuel/air mixing results. Moreover, the effect of Schmidt number on turbulent scalar mixing of a gaseous jet issued into a cross airflow was investigated by He et al. (1999). By comparison with the available experimental data, $Pr_t = Sc_t = 0.2$ was recommended.

The objectives of the present work are to assess the Reynolds analogy concept currently used in turbulent reacting flow RANS simulations and to find out if such a low value of Pr_t and Sc_t is a real physical fact in combustor modeling. These objectives are substantiated by two benchmarking cases: a free-jet turbulent diffusion flame and a model diffusion-flame combustor. The jet flame is a simple basic boundary-type flow, and the validation against a well-defined experimental database may highlight some challenges in turbulent reacting flow simulations. In the model combustor case, complex flow phenomena such as wall boundary layers, shear layers, separations and reattachments as well as recirculation zones are involved. Since the model combustor geometry is much simpler than practical combustors, its boundary

conditions are well defined and a comprehensive experimental database is also available, hence the assessment of the above issues is relevant.

In the following sections, the governing equations and Reynolds analog are discussed first; the turbulence, combustion and other physical models used in this work are briefly described, followed by the two benchmarking cases and discussions. Finally, some conclusions are highlighted.

2. GOVERNING EQUATIONS AND REYNOLDS ANALOGY

2.1. Governing Equations

The first-moment Favre-averaged conservation equations for mass, momentum, species, mixture fraction and total enthalpy, may be expressed in a coordinate-free form as (Ferziger & Peric 2002, Moores 2006 and Fluent 2006)

$$\nabla \cdot (\bar{\rho} \tilde{\mathbf{V}}) = 0 \quad (1)$$

$$\nabla \cdot (\bar{\rho} \tilde{\mathbf{V}} \tilde{\mathbf{V}}) = -\nabla \bar{p} + \nabla \cdot \mathbf{T} - \nabla \cdot (\overline{\rho \mathbf{v}' \mathbf{v}'}) \quad (2)$$

$$\nabla \cdot (\bar{\rho} \tilde{\mathbf{V}} \tilde{Y}_i) = \nabla \cdot (\rho D_i \nabla \tilde{Y}_i) - \nabla \cdot (\overline{\rho \mathbf{v}' Y'_i}) + \omega_i \quad (3)$$

$$\nabla \cdot (\bar{\rho} \tilde{\mathbf{V}} \tilde{f}) = \nabla \cdot (\rho D \nabla \tilde{f}) - \nabla \cdot (\overline{\rho \mathbf{v}' f'}) \quad (4)$$

$$\nabla \cdot (\bar{\rho} \tilde{\mathbf{V}} \tilde{H}) = \nabla \cdot \left(\frac{\mu}{Pr_l} \nabla \tilde{H} \right) - \nabla \cdot (\overline{\rho \mathbf{v}' H'}) + S_H \quad (5)$$

In the above equations, $\bar{\rho}$ represents mean density, $\tilde{\mathbf{V}}$ is the mean velocity vector, \mathbf{v}' stands for fluctuation velocity vector, the viscous stress tensor $\mathbf{T} = \mu \left[\nabla \tilde{\mathbf{V}} + (\nabla \tilde{\mathbf{V}})^T \right] - \frac{2}{3} \mu \nabla \cdot \tilde{\mathbf{V}} \mathbf{I}$ with \mathbf{I} a unit tensor and μ the molecular viscosity, $\overline{\rho \mathbf{v}' \mathbf{v}'}$ denotes Reynolds stresses, Y_i is the mass fraction of the i th species, f stands for mixture fraction, H denotes total enthalpy, and D and Pr_l represent molecular diffusivity and Prandtl number respectively.

For closure of the above equations, the species source term, ω_i in Eq. (3) is obtained from a selected combustion model. The energy source term, S_H in Eq. (5) includes viscous heating and radiation heat transfer that is obtained from a radiation model. As mentioned earlier, Reynolds stresses, $\overline{\rho \mathbf{v}' \mathbf{v}'}$ or turbulent momentum transfer in Eq. (2) are modeled by a selected turbulence model, while $\overline{\rho \mathbf{v}' Y'}$, $\overline{\rho \mathbf{v}' f'}$, $\overline{\rho \mathbf{v}' H'}$ or turbulent scalar transfers in Eqs. (3-5) are computed based on Reynolds analogy. That is,

$$-\nabla \bullet \overline{\rho v'' \phi''} \cong \nabla \bullet \left(\frac{\mu_t}{\Gamma_t} \nabla \tilde{\phi} \right) \quad (6)$$

where ϕ stands for species, mixture fraction or enthalpy, μ_t is turbulent viscosity which is computed from the selected turbulence model, and Γ_t represents turbulent Prandtl (Pr_t) or Schmidt (Sc_t) numbers. Note that in Eq. (6), the turbulent scalar transfer coefficients, μ_t/Γ_t , are simply the products of the turbulent momentum transfer coefficient (μ_t) and $1/\Gamma_t$.

2.2. Reynolds Analogy

The rationale and limitation of the Reynolds analogy can be revealed by reducing the conservation equations (2-5) to two-dimensional steady boundary flows and neglecting the streamwise pressure gradient, molecular viscous terms, and source terms. Then the following equations are obtained,

$$\widetilde{\rho u} \frac{\partial \widetilde{u}}{\partial x} + \widetilde{\rho v} \frac{\partial \widetilde{u}}{\partial y} \approx \frac{\partial}{\partial y} \left(\mu_t \frac{\partial \widetilde{u}}{\partial y} \right) \quad (7)$$

$$\widetilde{\rho u} \frac{\partial \widetilde{\phi}}{\partial x} + \widetilde{\rho v} \frac{\partial \widetilde{\phi}}{\partial y} \approx \frac{\partial}{\partial y} \left(\frac{\mu_t}{\Gamma_t} \frac{\partial \widetilde{\phi}}{\partial y} \right) \quad (8)$$

where the turbulent viscosity concept is applied to both streamwise momentum and scalar transfers. With $\Gamma_t = 1$, the two equations become identical. That is, under appropriate boundary conditions, the solution of all these flow parameters can be obtained from a single partial differential equation or the momentum and scalar fields are similar. For wall boundary flows, the original form of the Reynolds analogy can be deduced (Incropera & DeWitt 2002),

$$\frac{2St}{c_f} = \frac{(h/\rho C_p U_\infty)}{(\tau_w / \rho U_\infty^2)} \approx 1 \quad (9)$$

where $St = h/(\rho C_p U_\infty)$ is the Stanton number and $c_f = \tau_w/(0.5\rho U_\infty^2)$ is the wall friction coefficient. From this equation, the turbulent heat transfer coefficient can be estimated from the measurement of pressure loss due to friction in the flow.

The above analysis suggest that the Reynolds analogy method can be used to adequately calculate turbulent scalar transfers in boundary type of flows, such as free jets, wall boundary layers, and shear layers, etc., where the effects of the streamwise pressure gradient, viscous and source terms are minor. However, its application to general complex three-dimensional flows is questionable.

3. PHYSICAL MODELS

3.1. Turbulence Models

Two turbulence models, the standard $k-\omega$ two-equation model with a low-Reynolds-number correction and the Reynolds stress model (RSM), were used in the present work. The former was used to model turbulent momentum transfer in the free-jet flame, while the latter was used to account for turbulent momentum transfer in the model combustor. The major features of these two models are outlined below, and detailed descriptions and formations can be found in references (Wilcox 2002, Launder et al. 1975, Jones 1994 and Fluent 2006).

Wilcox (2001) pointed out that the $k-\omega$ model is superior over other popular two-equation turbulence models for free shear flows, attached boundary layers and mildly separated flows, after a systematic validation against a number of well-documented non-reacting flow measurements.

As for all two-equation eddy-viscosity turbulence models, the Boussinesq hypothesis is adopted to model Reynolds stresses in equation (2),

$$-\overline{\rho u_i'' u_j''} = \mu_t \left(\frac{\partial U_i}{\partial x_j} + \frac{\partial U_j}{\partial x_i} \right) - \frac{2}{3} \delta_{ij} \left(\mu_t \frac{\partial U_k}{\partial x_k} + \rho \bar{k} \right) \quad (10)$$

With this approach, the turbulent viscosity, μ_t is given by the expression,

$$\mu_t = \alpha^* \bar{\rho} k / \omega \quad \alpha^* = [0.024 + (\bar{\rho} k / \mu \omega / 6)] / [1 + (\bar{\rho} k / \mu \omega / 6)] \quad (11)$$

where the values of the turbulence kinetic energy, k , and the specific turbulence dissipation rate, ω , are calculated from a pair of transport differential equations.

The RSM is a second-moment closure. It is more "general" than the eddy-viscosity turbulence models where the isotropic eddy-viscosity and the linear relations between Reynolds stresses and mean rate of strain are assumed, as shown in Eq. (10). For the RSM, all Reynolds stress components in the flow field are directly computed from their corresponding transport differential equations. In principle, this model is likely to have a wider range of applicability than the eddy-viscosity concept models.

In a previous benchmarking on turbulence modeling in the model combustor (Jiang & Campbell 2007), the RSM produced better results than three popular two-equation eddy-viscosity models. Therefore, it was chosen to model turbulent momentum transfer in the combustor flow, where the complex flow phenomena and their interactions are involved.

For axi-symmetric flows as in the present model combustor, only four components of Reynolds stresses, $\overline{\rho u_i'' u_j''}$, need to be considered. The four transportation equations of these components along with the turbulence dissipation rate equation are solved in the combustor flow field. From the solutions of Reynolds stresses and dissipation rate, the turbulent viscosity (momentum transfer coefficient) is then computed,

$$\mu_t = \bar{\rho} C_\mu k^2 / \varepsilon \quad (12)$$

where $C_\mu = 0.09$, and k and ε are turbulent kinetic energy and dissipation rate respectively.

For both cases, the turbulent scalar transfers are modeled by the Reynolds analogy concept and computed by Eq. (6). It should be mentioned that for the RSM case, the isotropic turbulent transfer (coefficient) assumption is abandoned in momentum transfer; however, it is still used for turbulent scalar transfers.

3.2. Combustion Models

Two combustion models, the eddy-dissipation (EDS) and probability density function (PDF) models, were applied to the jet flame and model combustor respectively. The EDS model is based on the work of Magnussen and Hjertager (1976), which has been widely accepted in diffusion flame modeling (Bilger 1989). For this model, the reaction rate is governed by turbulent mixing, or the large-eddy mixing time scale, k/ε . The net rate of reaction of species “i” is given by the smaller of the two following expressions in $\text{kg/m}^3\text{-s}$,

$$R_i = \nu_i M_i A \rho \frac{\varepsilon}{k} \min \left[\frac{Y_{C_3H_8}}{\nu_{C_3H_8} M_{C_3H_8}}, \frac{Y_{O_2}}{\nu_{O_2} M_{O_2}} \right] \quad (13)$$

$$R_i = \nu_i M_i AB \rho \frac{\varepsilon}{k} \frac{(Y_{CO_2} + Y_{H_2O})}{(\nu_{CO_2} M_{CO_2} + \nu_{H_2O} M_{H_2O})} \quad (14)$$

where Y is the mass fraction, ν stands for the stoichiometric coefficient, M represents the molecular weight, and A and B are empirical constants equal to 4.0 and 0.5 respectively (Magnussen & Hjertager, 1976).

The PDF combustion model is based on the mixture fraction approach with an assumption of fast chemistry (Jones & Whitelaw 1982). The comparisons between the numerical and experimental results (Jiang & Campbell 2005) suggest that this combustion model combined with other selected physical models can provide adequate simulations for the model combustor. It offers many advantages over the EDS or EDS-finite-rate models. It allows intermediate (radical) species prediction, dissociation effect, and more rigorous turbulence-chemistry coupling. The mixture fraction can be written in terms of atomic mass fraction as,

$$f = \frac{Z_i - Z_{i,ox}}{Z_{i,fuel} - Z_{i,ox}} \quad (15)$$

where Z_i stands for the elemental mass fraction of element, “i”, $Z_{i,ox}$ and $Z_{i,fuel}$ denote the elemental mass fraction of “i” at the oxidizer and fuel inlets respectively. It is a common practice to assume that all species have the same diffusivity in turbulent flows. As a result, the mixture fraction becomes a conserved quantity, and the transport equations for the mean mixture fraction and its variance can be simplified as,

$$\frac{\partial}{\partial t} \left(\rho \bar{f} \right) + \nabla \bullet \left(\rho \vec{v} \bar{f} \right) = \nabla \bullet \left(\frac{\mu_t}{\sigma_t} \nabla \bar{f} \right) \quad (16)$$

and

$$\frac{\partial}{\partial t} \left(\rho \bar{f}^{\prime \prime 2} \right) + \nabla \bullet \left(\rho \vec{v} \bar{f}^{\prime \prime 2} \right) = \nabla \bullet \left(\frac{\mu_t}{\sigma_t} \nabla \bar{f}^{\prime \prime 2} \right) + C_g \mu_t (\nabla^2 \bar{f}) - C_d \rho \frac{\varepsilon}{k} \bar{f}^{\prime \prime 2} \quad (17)$$

where $f'' = f - \bar{f}$, and the constants σ_t , C_g and C_d take the values of 0.85, 2.86 and 2.0 respectively (Jones & Whitelaw 1982, and Fluent 2006).

With the fast chemistry assumption, the chemical equilibrium calculation based on the minimization of Gibbs free energy can be used to determine the combustion system. For a defined combustion system, the instantaneous mole fractions of individual species, density and temperature at each point in the flow-field can be exclusively determined from the instantaneous mixture fraction at the adiabatic condition. When heat loss is considered, as in the present study, the relationship may be generalized as,

$$\phi_i = \phi_i(f, H) \quad (18)$$

where ϕ represents the instantaneous species mole fraction, density or temperature, and H is the instantaneous enthalpy.

Eighteen species were considered for the PDF model, including C_3H_8 , CO_2 , H_2O , O_2 , N_2 , CO , HO , H , O , H_2 , C_3H_6 , C_2H_6 , C_2H_4 , CH_4 , CH_3 , CH_2 , CH , and $C(s)$. The selection of these species was based on the basic chemical kinetics and requirements for pollutant predictions (Glassman 1987). As pointed by Bilger (1989) and Sivathanu & Faeth (1990), full chemical equilibrium gives considerable errors in temperature on the rich side of hydrocarbon flames. To avoid this, a partial equilibrium approach was applied in the rich flame region. When the instantaneous equivalence ratio exceeded 1.75, the combustion reaction was considered extinguished and unburned fuel coexisted with reacted products, where the value of 1.75 was suggested by Fluent (2006).

3.3. Other Physical Models and Numerical Methods

To account for heat radiation between the hot gas mixture and surroundings, the discrete ordinates radiation model (Raithby et al., 1990) was employed. The absorption coefficient of gaseous mixture was determined from the local species mass fractions in the flow. For the wall boundaries in the combustor case, an enhanced wall boundary treatment was applied, where the traditional two-layer zonal model was enhanced by smoothly blending the viscous sub-layer and fully turbulent regions.

Polynomials were used to calculate the specific heat of species as a function of temperature. For the case of the PDF model, the polynomials were determined from the JANAF tables (NIST 1998); while in the case of the EDS model the polynomials from Rose et al. (1977) were used, where the chemical dissociation was considered. For other thermal

properties such as molecular viscosity, thermal conductivity and diffusivity, the values of air at 900 K were used.

A segregated solver with a second-order accurate scheme from a commercial software, Fluent, was used to resolve the flow-fields. At convergence, the normalized residual was less than 10^{-6} for the energy equation, and about 10^{-5} for the rest of the flow variables in all test cases. The monitored axial velocities in shear layers of the flow fields remained unchanged at least for the first four digits. A LINUX PC server with eight Pentium 2.8-GHz CPUs and 32-GB RAM was used to perform all numerical simulations.

4. APPLICATION OF REYNOLDS ANALOGY TO A TURBULENT JET DIFFUSION FLAME

4.1. Some Previous RANS Studies

In contrast to numerical RANS simulations of non-reacting jet flows, RANS studies on jet flames where numerical results are compared with well-defined experiments are rare. Lockwood and Naguid (1975) methodically studied and validated a two-equation $k-\epsilon$ turbulence model and a proposed pdf (probability density function) equilibrium combustion model against three well-documented round turbulent jet flows: inert & isothermal, inert & non-isothermal, and jet diffusion flame. Ten constants for the turbulence kinetic energy, dissipation rate and variance of mixture fraction were adjusted to fit the above experimental data. Due to the lack of comprehensive experimental data, for the jet flame case, only the predicted temperature distributions were validated, including the axial temperature profiles at $Re = 24,000$ and $43,000$ and the radial profile at $Re = 24,000$. At the end, they pointed out that new experimental data were urgently required to evaluate these physical models. In their study, the turbulent Prandtl/Schmidt number of 0.7 was used, which was consistent with Spalding's work (1971) where a turbulent jet mixing was simulated and good agreements with experiments were illustrated for the radial profiles of mean axial velocity, mean and fluctuation (species) concentrations.

Recently, Zhou et al. (2000) studied a hydrogen/air jet diffusion flame ($Re = 10,000$) with a modified $k-\epsilon$ turbulence model (with Rodi's correction), detailed chemistry and an algebraic correlation closure for turbulence and chemistry coupling. The turbulent Prandtl/Schmidt number was set to 0.75. Their methods were successfully validated against a well-documented isothermal jet flow before being applied to the jet flame. The predicted temperature and major species distributions were presented and compared with the experimental data. It was found that the predicted temperature profile along the jet centerline was in good agreement with the experimental data. However, the radial temperature profiles at upstream sections $x/d = 5$ and 20 were considerably different from the measurements, and the predicted spraying rate was wider and the peaks shifted away from the jet centerline. At two downstream sections, $x/d = 40$ and 80 , the predicted trends or spreading rates were consistent with the measurements although the predicted temperature profiles were higher than the experimental results. It was anticipated that the disagreements were caused by the inaccurate prediction in turbulent mixing of chemical species.

The well-known Sandia National Laboratory Flame C, a confined piloted turbulent jet flame, was studied by Wang et al. (2008) and Zhou et al. (2002) to validate their new combustion and unified turbulence-chemistry models, where a turbulent Prandtl/Schmidt number of 0.7 was used. The predicted temperature and species distributions were quantitatively compared with the experimental data, and various degrees of satisfaction were observed. It should be mentioned that in the above jet flame studies, the velocity validation was performed with experimental data different from those for temperature validation, or no direct velocity validation was given.

In order to predict the upstream local laminarization phenomena of jet diffusion flames, Torii (2001) recently developed a pair of transportation equations of temperature variance and its dissipation rate, as well as a modified $k-\varepsilon$ model where the coefficients of production and dissipation terms of ε were replaced by functions of turbulence Reynolds number and dimensionless distance y^+ . These models were implemented into a boundary-layer solver to simulate a hydrogen/air jet diffusion flame ($Re = 4,200$). Good agreement between the numerical and experimental results was shown at two downstream sections $x/d = 18$ and 32 for axial velocity, turbulence kinetic energy and temperature. However, upstream validations were not presented.

4.2. Simulation of a Turbulent Jet Diffusion Flame

4.2.1. Experimental Measurements

To study the influence of combustion process on the turbulence structure of combustible jet flows and to provide a comprehensive database to validate various turbulence and combustion models, measurements of mean velocity components, turbulence intensities, velocity probability density functions, power spectra and autocorrelation functions of axial velocity fluctuation, spatial turbulence macro-scales as well as mean temperature were performed in a turbulent jet diffusion flame (Sislian et al. 1988). The test apparatus and rig are shown in Fig. 1. The test rig was mounted on a three-dimensional traversing mechanism with a positioning accuracy of 0.125 mm in the horizontal directions and approximately 1 mm in the vertical direction. The jet nozzle was made of brass with an area contraction ratio of 26:1 and a throat diameter of 10mm. The contraction contour of the nozzle was designed for uniform exit velocity following Smith & Wang (1944). In order to minimize room disturbances, the test rig was placed within a screened enclosure having dimensions of 1.4-m \times 1.2-m \times 2.7-m high. A one-dimensional laser velocimeter operating in a forward scattering mode was used to obtain the velocity measurements. Gas temperatures were measured by thermocouples. For the flow visualization, schlieren photography was conducted.

The fuel mixture density was chosen to be equal to the cold flow mixture density in order to minimize the effects of density difference between cold fuel mixture and cold flow mixture on measured turbulence properties. The fuel flow was a mixture of methane and argon, whose volume ratio was 2.33. In the cold flow case, the jet flow was a mixture of 21.4% helium and 78.6% air by volume. The flow velocity in the central region of the nozzle exit was 17.2 m/s for both reacting and non-reacting cases, and the Reynolds numbers (based on the nozzle diameter) were 7,850 and 1,020 respectively. The flame was stabilized and attached to the rim of the nozzle exit all the time. No external flame holder was used during

the experiments. Details of the experimental setup, instrumentation, measurements, error analyses and results are available from Sislian et al. (1988).

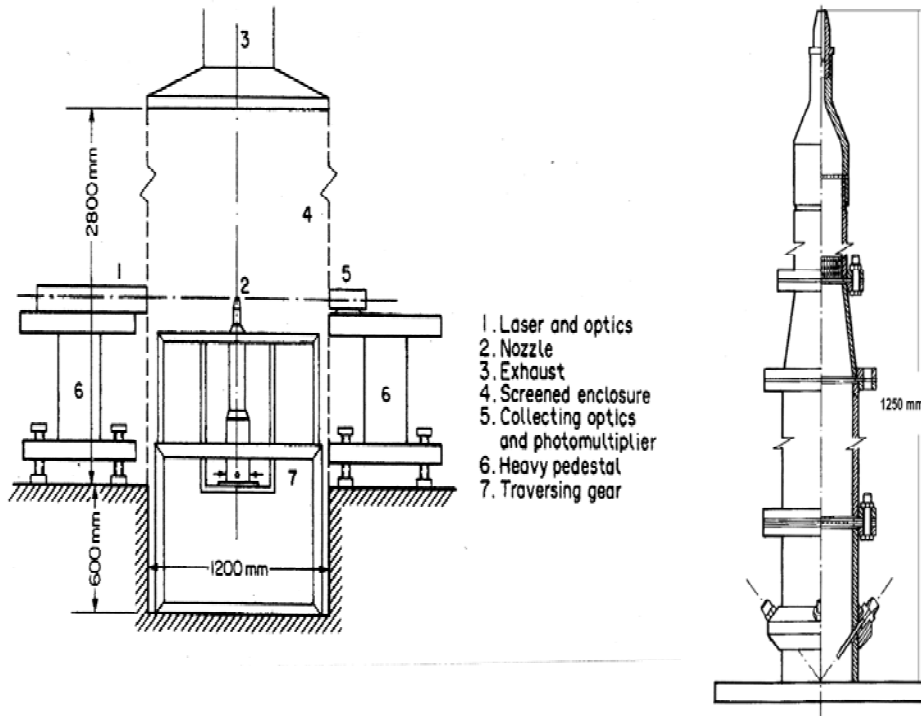


Figure 1. Schematic of the test apparatus and rig.

4.2.2. Computational Domain, Mesh and Boundary Conditions

A rectangular axi-symmetric computational domain was considered in this study, which had a width of 100 mm ($R/d = 10$) and a length of 500 mm ($X/d = 50$). A mesh with 140 nodes in the radial direction, 400 in the axial direction and a total of 56,000 cells was used for most of the simulations. Fine grids were laid over the shear layer between the jet and ambient air, and upstream regions. A number of meshes were tested to ensure mesh-independence of the numerical results.

The profiles of axial velocity, turbulence kinetic energy and temperature at the nozzle boundary are shown in Fig. 2, which were obtained from the experimental measurements at sections $X/d = 0.3$ and 0.2 respectively. The nozzle boundary specific turbulence dissipation rate was calculated by $\omega = k^{0.5} / l$ (Wilcox 2002), where k is the turbulence kinetic energy and l is the measured macro-length scale (Sislian et al. 1988).

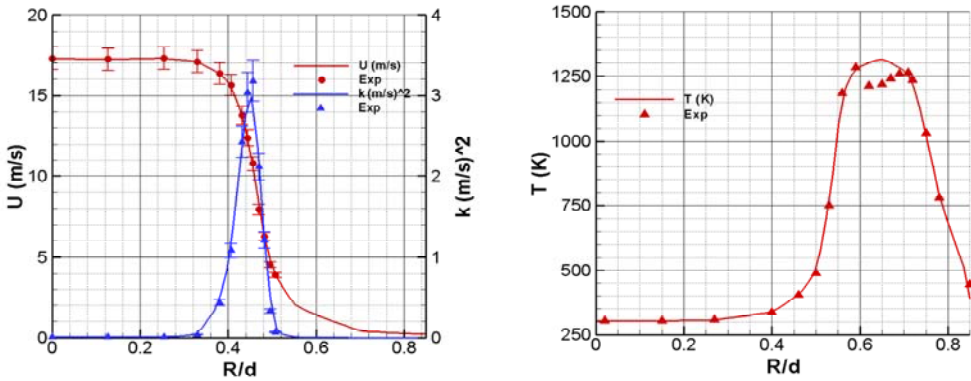
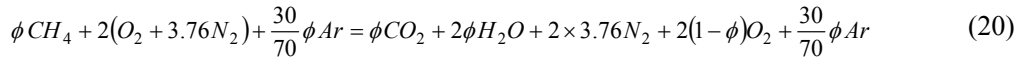
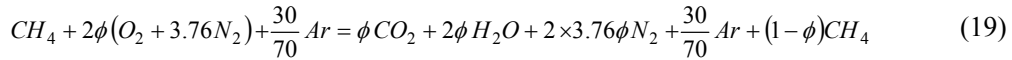


Figure 2. Nozzle exit boundary (inlet of the computational domain) conditions.

The nozzle boundary species profiles were determined from the temperature profile in Fig. 2. In the inner layer (the left side of the peak temperature) of the flame, the fuel was rich and the complete consumption of oxidizer was assumed, while in the outer layer (the right side of the peak temperature) the fuel was lean and the complete burning was considered. The species profiles were calculated by the following equations for the fuel rich and lean zones respectively,



At the downstream outlet boundary, the static pressure was set to the atmospheric pressure. For the side and upstream ambient boundaries, a total pressure of one atmosphere and temperature of 298 K were defined. A turbulence intensity of 2% and hydraulic diameters were used to estimate turbulence kinetic energy and specific turbulence dissipation rate at these ambient boundaries. A sensitivity study was performed with turbulence intensities of 5% and 1% respectively, and the computed velocity and temperature distributions were almost identical.

4.2.3. Results and Discussion

The predicted axial velocity profiles along the centerline are illustrated in Fig. 3 and quantitatively compared with the experimental measurements. Error bars in the figure represent the measurement accuracy of 4%. Detailed quantitative comparisons between the numerical and experimental results at six cross-sections, $x/d = 5, 10, 20, 30, 40$ and 50 are given in Fig. 4. In these two figures, the numerical results for three turbulent Prandtl/Schmidt numbers, $\Gamma_t = 0.45, 0.85$ and 1.2, are displayed. It is obvious that the velocity flow field or turbulent momentum transfer is extremely well predicted, particularly at upstream sections. The effect of turbulent Prandtl/Schmidt number on the velocity field is minor or insignificant. Figures 3 and 4 clearly demonstrate that the $k-\omega$ turbulence model with the low Reynolds number correction can properly predict the momentum field of jet diffusion flames.

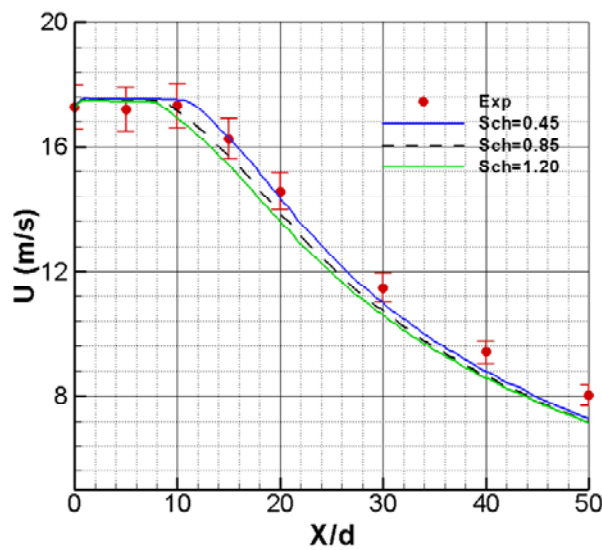


Figure 3. Axial velocity profiles along the jet centerline.

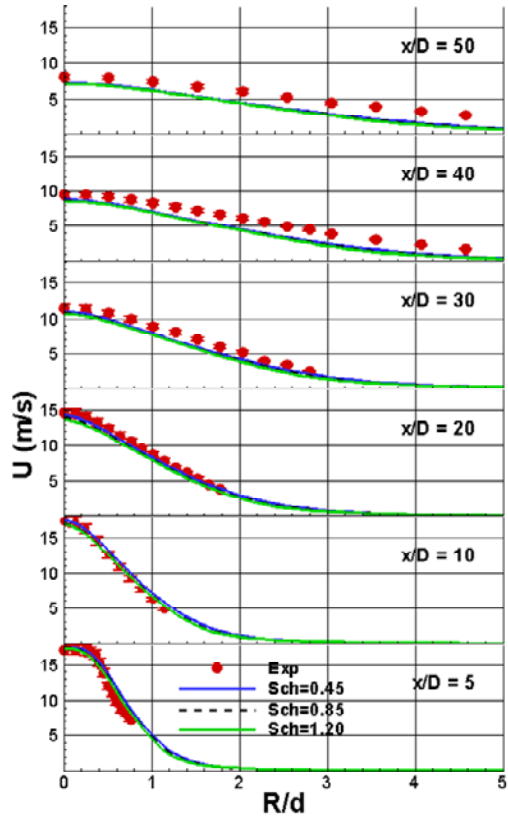


Figure 4. Axial velocity profiles at six cross-sections, $x/d = 5 - 50$.

As mentioned earlier, the proper prediction of velocity field (or momentum transfer) is a prerequisite for an adequate evaluation of Reynolds analogy or Γ_t effect on the temperature field of turbulent reacting flows. This is because the turbulent scalar transfers (and then the temperature field) in the flow are computed from the modeled momentum transfer using Reynolds analogy. Based on the well-predicted velocity field, the Reynolds analogy concept is assessed with added confidence.

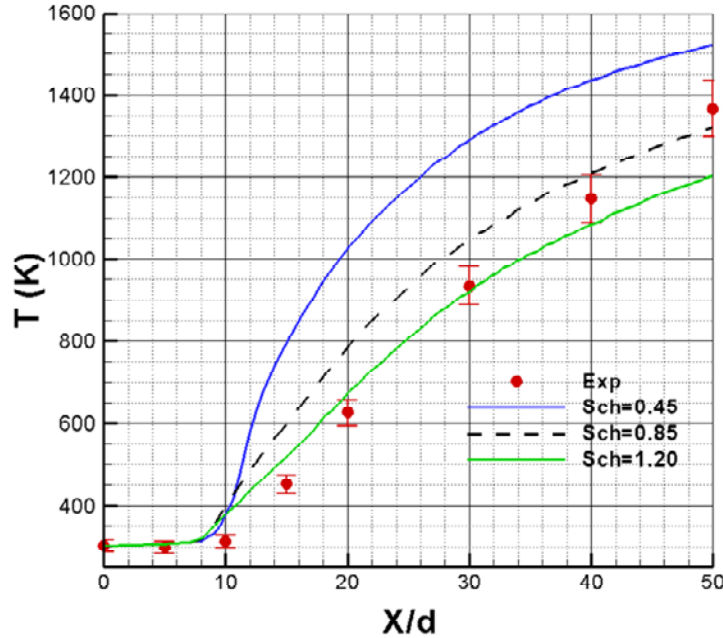


Figure 5. Temperature profiles along the jet centerline.

Figure 5 presents the predicted temperature distributions along the centerline for $\Gamma_t = 0.45, 0.85$ and 1.2 , and the results are compared with the experimental results with an estimated measurement error of 5% . The temperature profiles are reasonably predicted with $\Gamma_t = 0.85$ and 1.2 , while for $\Gamma_t = 0.45$ the centerline temperature is considerably overpredicted. A strong effect of Γ_t on the temperature field is obvious in Fig. 5. Shown in Fig. 6 are the predicted and experimental temperature profiles at six cross-sections for $\Gamma_t = 0.45, 0.85$ and 1.2 . In general, the quality of temperature prediction is inferior to that of the velocity field. At upstream sections, $X/d = 5, 10$ and 20 , although the peak temperatures are consistent with the experimental values for $\Gamma_t = 0.85$ and 1.2 , the predicted temperature spreading rates are much wider than the measurements in the outer layers of the flame. At downstream sections, $X/d = 40$ and 50 , the trends and magnitudes are reasonably predicted with $\Gamma_t = 0.85$ and 1.2 . As observed in Fig. 5, the turbulent Prandtl/Schmidt number has great effect on the temperature distributions, particularly in the outer layers of the flame. Note that similar trends and deviations of temperature distributions between the simulation and experiment are also observed by Zhou et al. (2000) for the hydrogen/air jet diffusion flame, as mentioned earlier, where a modified $k-\epsilon$ turbulence model was used. The challenge of modeling the upstream region of a turbulent jet flame is also recognized by Eickhoff (1982).

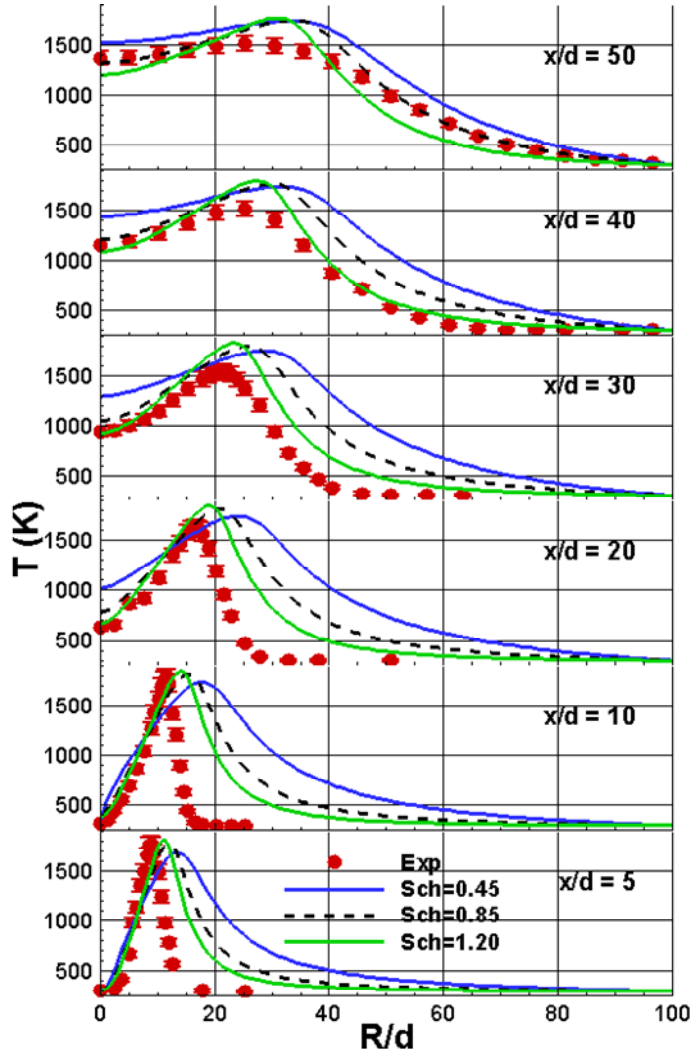


Figure 6. Temperature profiles at six cross-sections, $x/d = 5 - 50$.

Jet diffusion flames look simple; however they pose challenges for numerical simulations. The anticipated reasons for the above discrepancies may be three-fold. First, the existence of a flame suppresses turbulence in the upstream local region and enhances turbulence in the downstream region, which is an important feature of turbulent jet diffusion flames. This phenomenon has been successfully studied by Takagi et al. (1980). Their laser Doppler anemometer (LDA) measurements clearly indicate the existence of local laminarization near the nozzle exit ring at $Re = 4,200$, which is consistent with the observation from Sislian et al. (1988). The measurements show that in the outer layer of the jet flame near the nozzle exit, the flame suppression on turbulence is significant although the central part of the jet is fully turbulent; however, it is insignificant in the inner layer in comparison with the measurements without flame. Their experimental results also indicate that in the strong suppression outer layer of the flame, the axial velocity magnitudes and gradients are low and flat, while the temperature magnitudes and gradients are high. These

may explain why the velocity profiles are well predicted (Figs. 3 - 4) and why the thermal spreading is over-predicted in this outer layer region of the flame, where the turbulent transfer predictions are based on the gradient-type viscosity concept.

Second, the current turbulent scalar transfer modeling based on the Reynolds analogy concept needs to be improved in order to properly predict turbulent scalar transports in flows. This example clearly demonstrates that the flow velocity and temperature fields cannot be simply linked by a constant Prandtl/Schmidt number, and the strong viscous suppression effect on turbulence in the upstream outer layer of the jet flame cannot be neglected, which is against the application requirements of the Reynolds analogy (see Eqs. 7-9). Third, as pointed out by many researchers (Bilger 1989, Jones 1994, etc.), in comparison with constant-density flows for which turbulence models have been widely tested, the effects of heat release on the flow turbulence and more importantly the interaction of turbulence and chemistry are not well understood.

5. APPLICATION OF REYNOLDS ANALOGY TO A MODEL COMBUSTOR

5.1. Experimental Measurements

To provide a benchmarking database for the evaluation and development of various physical models, a series of experiments were performed on a diffusion flame model combustor at the National Research Council of Canada (NRCC). The comprehensive results include mean and fluctuating velocity components, mean temperature, wall temperature, radiation heat flux, as well as species concentrations (Campbell & Logan 1997).

The test apparatus and model combustor are shown in Fig. 7. The model combustor is composed of the fuel and air inlets, combustion chamber and contracted exhaust section (all dimensions in mm). Air entered the combustion chamber around a disc flame-holder, while fuel was fed through the center of the bluff body. The test rig was mounted on a three-axis traversing unit with a resolution of $\pm 100 \mu\text{m}$. Fuel used in the experiments was commercial grade propane, and dry air was delivered from a shop air supply. Both air and fuel flows were controlled by Sierra Side-Trak mass-flow controllers with 2% accuracy of full scale (fuel 100 l/min and air 2550 l/min).

To reduce the heat losses through walls, a 25.4-mm thick fibre blanket of Al_2O_3 was wrapped around the combustion chamber. Four narrow slots were cut into the blanket to allow appropriate physical and optical access to the chamber interior. Interchangeable sets of stainless steel and fused silica windows were used, the former for physical probing with gas sampling probes, radiometers and thermocouples, and the latter for optical probing with a laser Doppler anemometer (LDA). The viewing area of the windows measured 17 mm in width and 344 mm in length.

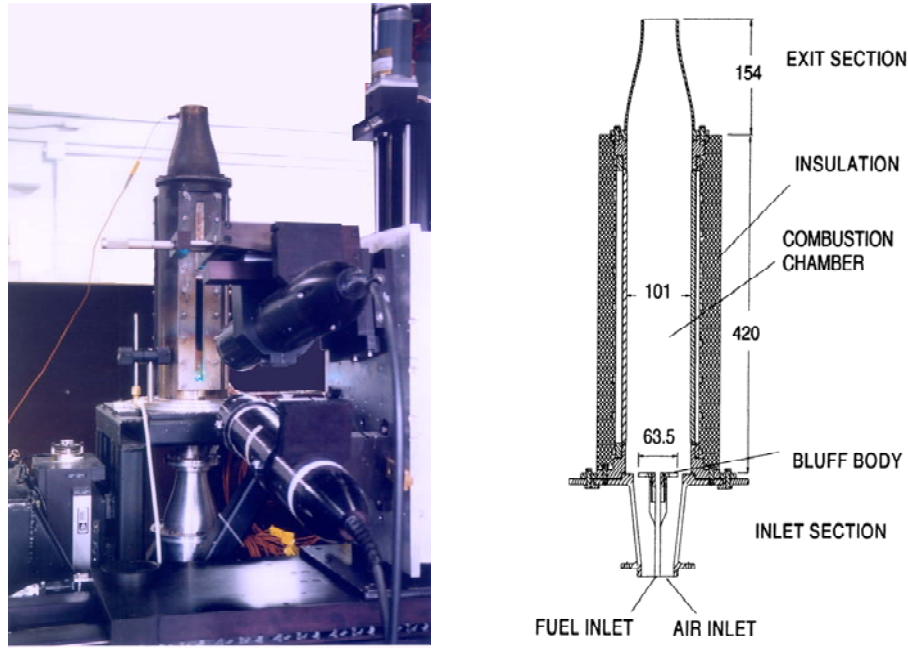


Figure 7. The test apparatus and model combustor

Measurements of velocity were made using both a 2- and 3-component LDA system operating in a back scattering mode. In the lower section of the combustion chamber, limited optical access forced the use of a single fibre optic head to measure axial and tangential velocities. In the upper section of the chamber, a complete 3-component LDA system was used. Gas temperatures were acquired using an uncoated 250- μm diameter, type "S" thermocouple supported by a twin-bore ceramic tube. Thermocouples embedded in and flush with the combustor wall were used to measure the wall temperature. Gas species measurements were made with a sampling probe connected to a Varian Model 3400 Gas Chromatograph. The major species measured were CO, CO₂, H₂O and C₃H₈.

5.2. Numerical Simulations

5.2.1. Computational Domain

The computational domain covers the entire combustor flow field from the fuel and air inlets to the exhaust exit, and includes the internal and external conjugate heat transfers from the combustion mixture to the flame-holder body and insulation walls, as shown in Fig. 8.

Since the flow field was axi-symmetric, 2-D quadrilateral meshes were used. Fine grids were laid behind the flame-holder in the combustion chamber in order to resolve the recirculation region. Fine grids were also generated in the shear layers between the recirculation region and fuel and air jets, as well as in the gap between the flame-holder edge and air inlet chamber wall. Coarse grids were used in the stainless steel walls and ceramic blanket. A total of 74,100 elements were used for most of the simulations. The skewness was less than 0.2 in the flow-field domain and the aspect ratio was less than 12 for 99.5% of

elements. Efforts were made to keep the wall parameter, $y^+ (\sqrt{\tau_w/\rho} y/\nu)$, in the desired range (30 to 60). A number of meshes were generated and tested to ensure mesh independence of the numerical results.

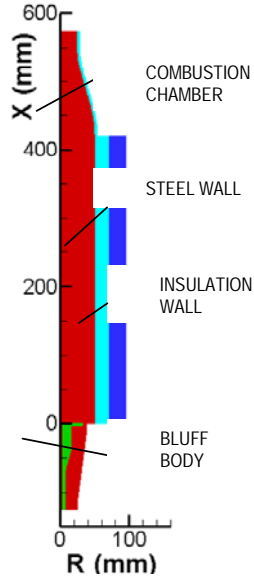


Figure 8. Computational domain.

5.2.2. Boundary Conditions and Solution Methods

The fuel mass flow rate was 16.2 g/s and the airflow rate was 550 g/s, for a corresponding overall equivalence ratio of 0.46. For both flows, the inlet temperature was 293K. The Reynolds number based on the air entry velocity and flame-holder diameter was 1.9×10^5 . An estimated turbulence intensity of 10% and hydraulic diameters were used to estimate Reynolds stress components and turbulence dissipation rate at the fuel and air inlets. A sensitivity study was performed with the inlet turbulence intensity of 5% and 2% respectively. The difference in computed turbulence kinetic energy along the combustor centerline is observable only in the fuel inlet passage and a small region near $x = 80$ mm, and the maximum deviation between case 2% and case 10% is only 2.3%. The difference is even smaller for the mean axial velocity and temperature along the combustor centerline.

The external wall temperatures were defined based on the experimental measurements. A room temperature of 293 K was assigned to the walls of the inlet section, and the upstream edges of the combustion chamber and ceramic insulation walls. A linear temperature profile from 294 K to 405 K was specified along the outer boundary of the ceramic insulation wall. The temperature of the outer boundary of the exit section was set to 960 K. The same temperature was assigned to the downstream edge of the combustion chamber wall because its heat resistance was much smaller than the ceramic insulation. A linear temperature profile from 960 K to 405 K was assigned to the downstream edge of the insulation wall. Finally, the pressure at the combustor exit was set to the atmospheric value.

5.3. Results and Discussion

5.3.1. Velocity Distributions

Numerical simulations were performed with Γ_t varying from 0.25 to 0.85, and a large amount of data were processed and analyzed. Only some of the results are presented here. The upper half of Fig. 9 shows the axial velocity contours and flow path-lines for $\Gamma_t = 0.85$. The lower half of the figure presents the experimental data with the zero axial velocity lines specified. The flow patterns in the combustion chamber are excellently predicted. Two recirculation zones are formed behind the flame-holder although, in the experimental case, the central recirculation zone is not completely resolved and no flow path-lines are drawn due to the limited data points. It is significant that both reattachment points or lengths of the two recirculation zones are well predicted. The central recirculation zone created by the fuel jet is completely confined within the annular recirculation zone generated by the annular air jet. This implies that the transportation of fuel into the flow field is realized by laminar and turbulent diffusion only through the annular recirculation zone.

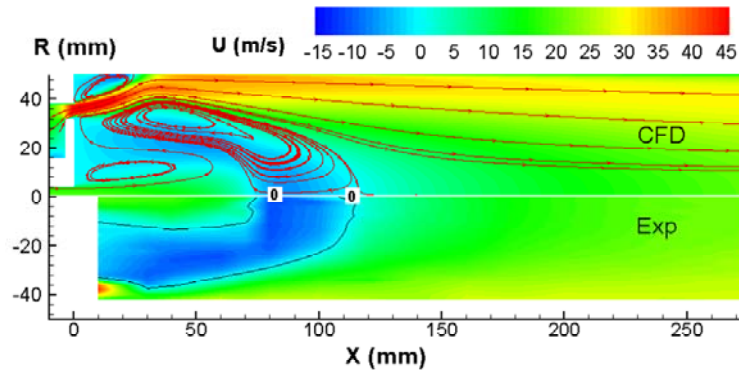


Figure 9. Axial velocity contours and flow path-lines, $\Gamma_t = 0.85$.

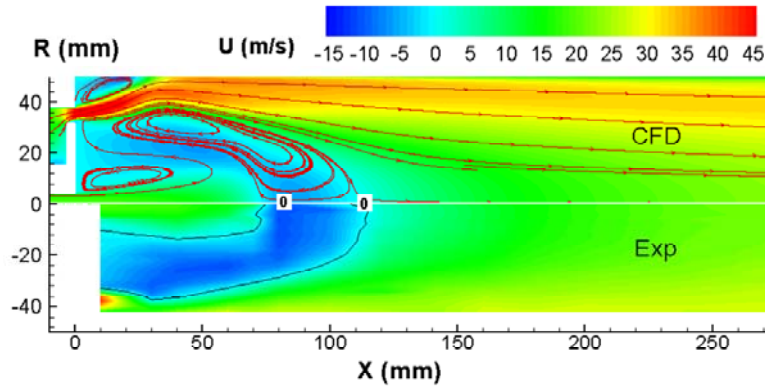


Figure 10. Axial velocity contours and flow path-lines, $\Gamma_t = 0.50$.

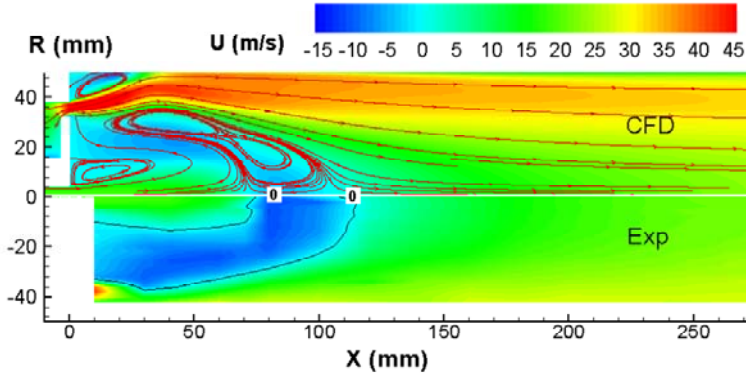


Figure 11. Axial velocity contours and flow path-lines, $\Gamma_t = 0.25$.

Although turbulent scalar transfers are calculated based on the modeled turbulent momentum transfer, the former also affects the latter since they are coupled. The effect of Γ_t on velocity field is illustrated in Figs. 10 and 11 for $\Gamma_t = 0.50$ and 0.25 respectively. The differences in the flow fields between $\Gamma_t = 0.85$ and $\Gamma_t = 0.50$ are minor. For $\Gamma_t = 0.25$, the length and volume of the annular recirculation zone are slightly reduced in comparison with those in Figs. 9 and 10. The numerical results indicate that in the range of Γ_t studied, the effect of Γ_t on velocity field is limited, particularly for $\Gamma_t > 0.35$.

Figure 12 gives axial velocity profiles along the combustor centerline, and compares the results with the experimental measurements. Superimposed in the figure, in red, are the estimated error bars of 2%. The numerical results show good agreement with the experimental data, except that the peak value of negative velocity is under-predicted. The effect of Γ_t variation from 0.85 to 0.25 on the centerline velocity profile is small.

The predicted axial velocity profiles at five cross-sections, two inside the recirculation region, one close to the stagnation point, and the last two located downstream of the recirculation region, are presented in Fig. 13, and quantitatively compared with the experimental results. In general, the profiles are reasonably predicted except in the local regions at three middle sections, where the discrepancies increase as Γ_t decreases. At these three sections, the flow field is complex, which is a challenging task in numerical simulations.

Figure 14 shows quantitative comparisons of turbulence kinetic energy between the numerical and experimental results at four cross-sections from $x = 60$ to 240 mm. In the figure, error bars show the measurement accuracy of $\pm 8\%$. The trends and magnitudes are reasonably well predicted, except for the magnitudes at some local regions.

Figure 15 compares the numerical results of turbulence shear stress, $\overline{\rho u'' v''} / \bar{\rho}$ with the measured experimental data at four cross-sections. Here the estimated measurement accuracy is about 12%. The shear stress is of primary interest for momentum transport in turbulent flows, particularly in shear flows. Again, the trends and magnitudes are reasonably well predicted at all sections, except for some local regions. The effect of Γ_t variation is insignificant, particularly in comparison with the measurement error.

The above numerical results indicate that the effect of Γ_t variation on the predicted velocity field is limited, and the velocity fields predicted by the RSM turbulence model agree reasonably well with the experimental data for $\Gamma_t > 0.35$.

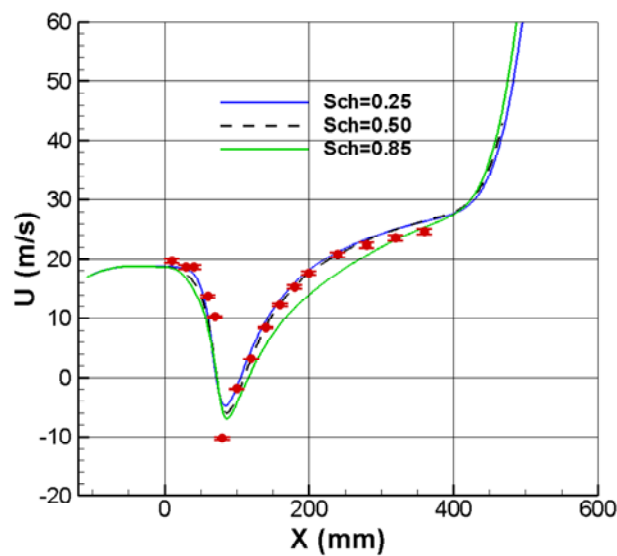


Fig. 12 Axial velocity profiles along the combustor centerline.

Figure 12. Axial velocity profiles along the combustor centerline.

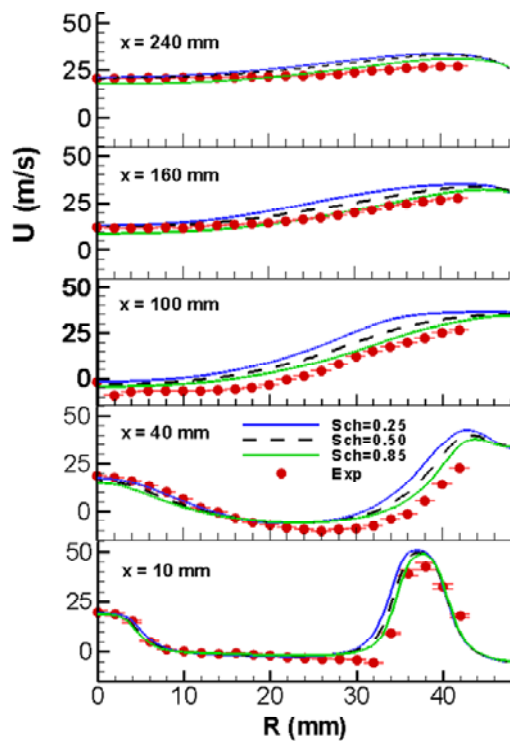


Figure 13. Axial velocity profiles at sections, $x = 10$ to 240 mm.

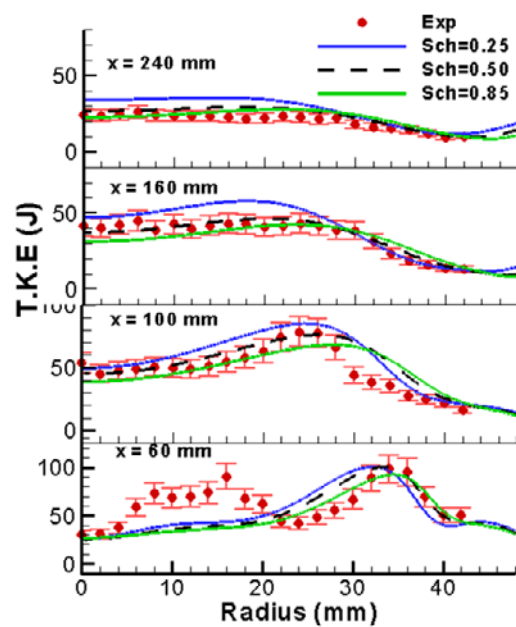


Figure 14. Turbulence kinetic energy profiles at sections, $x = 60$ to 240 mm.

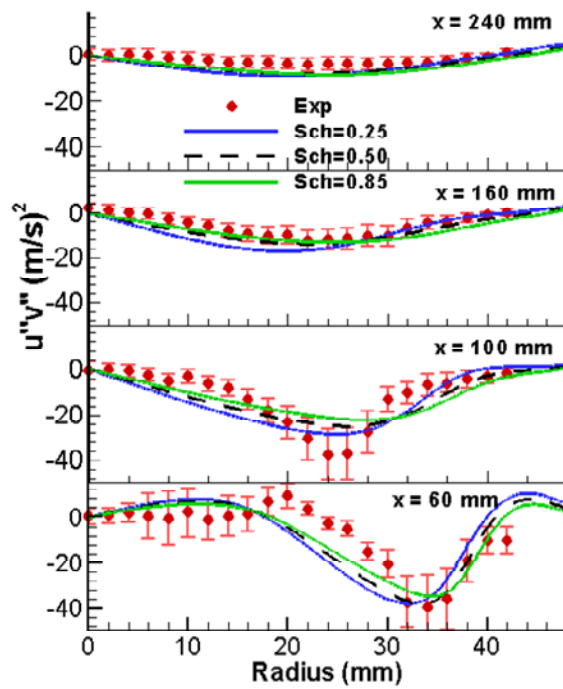


Figure 15. Turbulence shear stress profiles at sections $x = 60$ to 240 mm.

5.3.2. Temperature Distributions

The temperature contours for $\Gamma_t = 0.85$, 0.50 and 0.25 are presented and compared with the experimental database in Figs. 16-18, respectively. As expected, the temperature in the recirculation region is relatively uniform due to strong turbulent mixing. Intense chemical reaction takes place around the envelope of the annular recirculation zone. In comparison with the experimental data, the high temperature region is shifted downstream for $\Gamma_t = 0.85$, significantly reduced and shifted upstream for $\Gamma_t = 0.25$, and best predicted with $\Gamma_t = 0.50$. In short, the high temperature region moves upstream and becomes smaller with decreasing Γ_t . This is because the turbulence transfer of fuel into the airflow and then the chemical reaction are accelerated as Γ_t decreases.

In Figs. 16-18, it is found that the predicted temperature in the high temperature region is higher than the measured values. The maximum difference is about 200 K. The main reason may be that the temperature was measured by a 0.25-mm diameter thermocouple, as mentioned earlier. Owing to the radiation and conduction losses from the thermocouple, the measurement error could exceed 100 K over regions where the gas temperature was high and the flow velocity was low (Sislian et al. 1988).

The effect of Γ_t on the predicted flame length is illustrated in Fig. 19. The flame region is represented by the stoichiometric line of the mean mixture fraction ($\tilde{f} = 0.0603$) in the upper half of the figure, and by the OH mole fraction contour lines in the lower half. The effect of Γ_t on the flame length and region is obvious. As Γ_t decreases from 0.85 to 0.25, both the flame length and region are significantly reduced, and the flame length decreases more than three times from 365mm to 110mm.

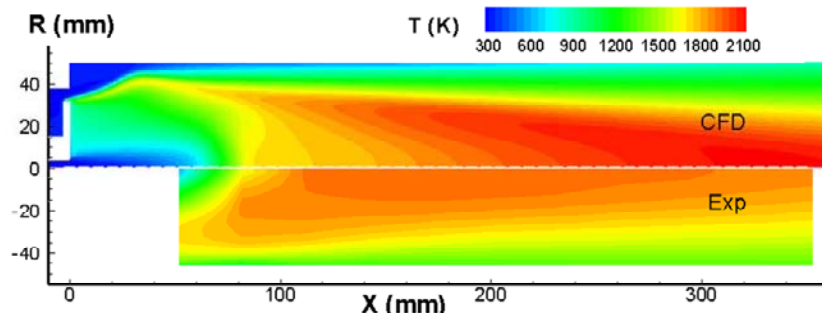


Figure 16. Temperature contours, $\Gamma_t = 0.85$.

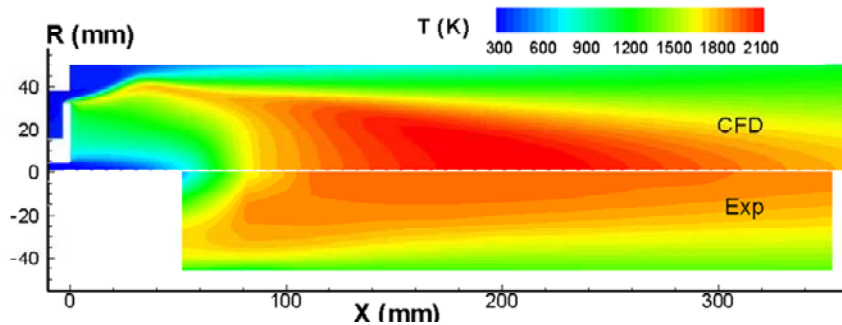


Figure 17. Temperature contours, $\Gamma_t = 0.50$.

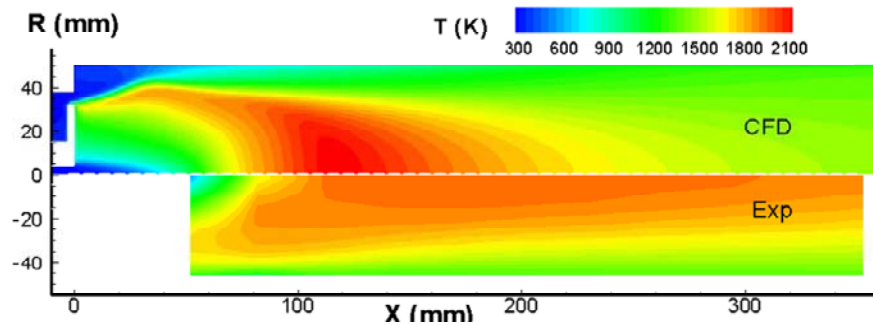


Figure 18. Temperature contours, $\Gamma_t = 0.25$.

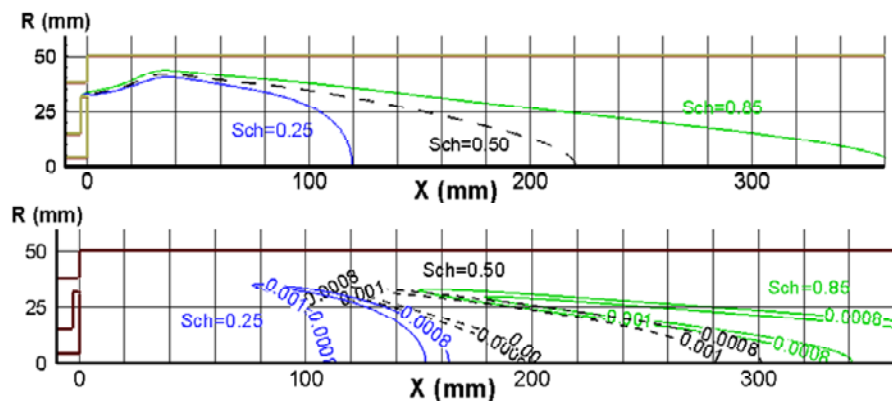


Figure 19. Variation of predicted flame length with Γ_t .

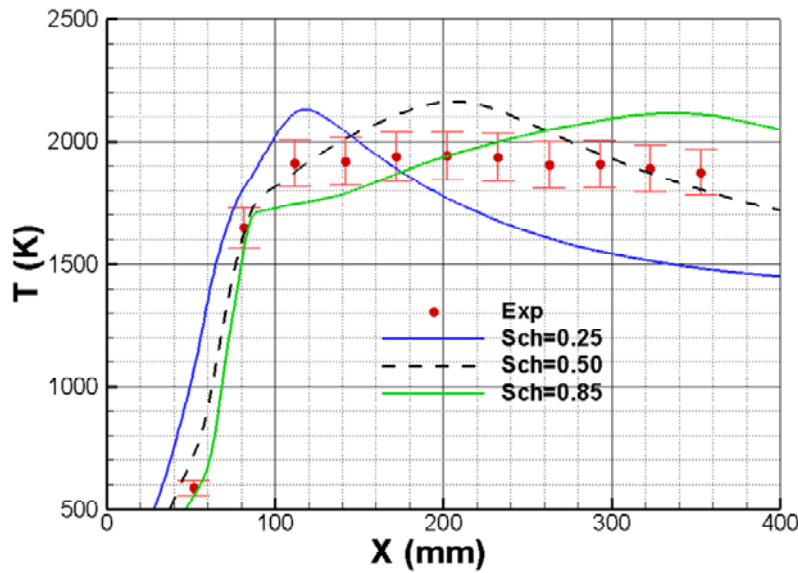


Figure 20. Temperature profiles along the combustor centerline.

The predicted temperature profiles along the combustor centerline are compared with the experimental data in Fig. 20, where the experimental measurement error is about 5%. In the upstream region ($x < \sim 80\text{mm}$), the effect of Γ_t is limited; the numerical results for $\Gamma_t = 0.50$ and 0.85 agree well with the experimental data. In contrast, the effect of Γ_t is apparent in the downstream region. It is because in the upstream region the fuel distribution or chemical reaction is mainly determined by the location and size of the annular recirculation zone, which is formed by complex flow interactions among the central fuel jet, annular airflow and two recirculation zones. That is, the flow is convection-dominated. However, in the downstream region, the turbulent diffusion or transfer plays a dominant role in the fuel spreading away from the axis of symmetry, where the flow path-lines are almost parallel to each other as shown in Figs. 9-11. In Fig. 20, $\Gamma_t = 0.50$ gives the best results although the predicted profile shows a peak in the middle portion, while the measurements tend to be flat. The predicted maximum temperature reaches 2150K, while the measured value is 1950K.

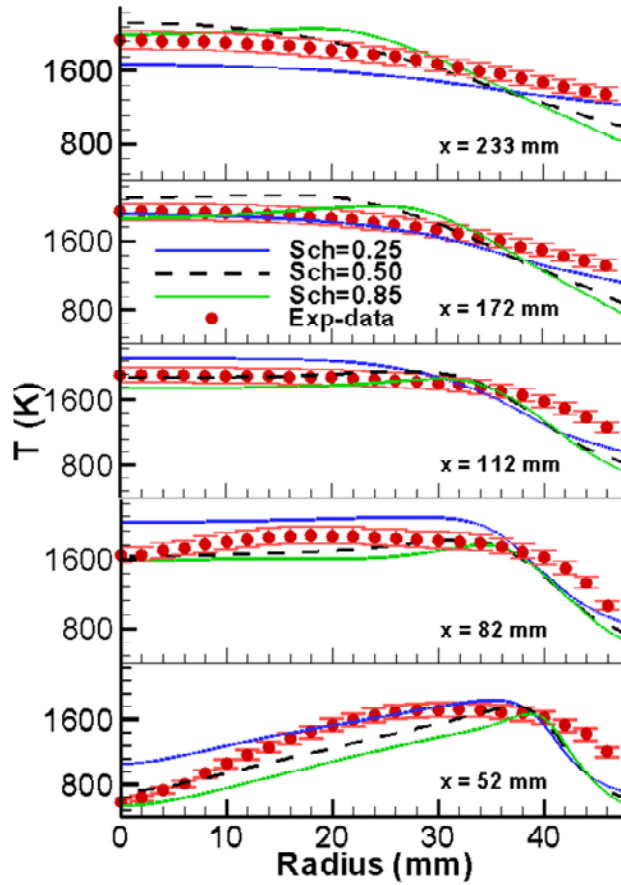


Figure 21. Temperature profiles at sections $x = 52 - 233\text{ mm}$.

Figure 21 presents the temperature profiles for $\Gamma_t = 0.85$, 0.50 and 0.25 at five cross-sections, $x = 52 - 233\text{ mm}$. As expected, at all sections, with Γ_t decreasing the temperature profiles become flatter, i.e., the fuel spreading becomes faster. In general, the numerical results from $\Gamma_t = 0.50$ are consistent with the experimental results, except for the regions near

the combustor wall. In these near-wall regions, the temperature is under-predicted, which may suggest that the fuel spreading is under-predicted in these local regions. Poor performance is observed for $\Gamma_t = 0.25$ at $x = 82$ and 233mm , and $\Gamma_t = 0.85$ at $x = 52\text{ mm}$. A strong effect of Γ_t is observed at all sections.

Variation of combustor wall temperature with Γ_t is shown in Fig. 22. The numerical results are compared with the experimental data that have a measurement error of $\sim 2.5\%$. Unsurprisingly, the predicted wall temperature increases as Γ_t decreases. The results of $\Gamma_t = 0.35$ show best agreement with the measurements, although the wall temperature is slightly over-predicted in the upstream region and under-predicted in the downstream region. As noticed, this Γ_t value does not agree with the preferred value of 0.50 for the temperature prediction inside the combustor. This may suggest that varying Γ_t , instead of a constant value, should be used in turbulent reacting flow simulations.

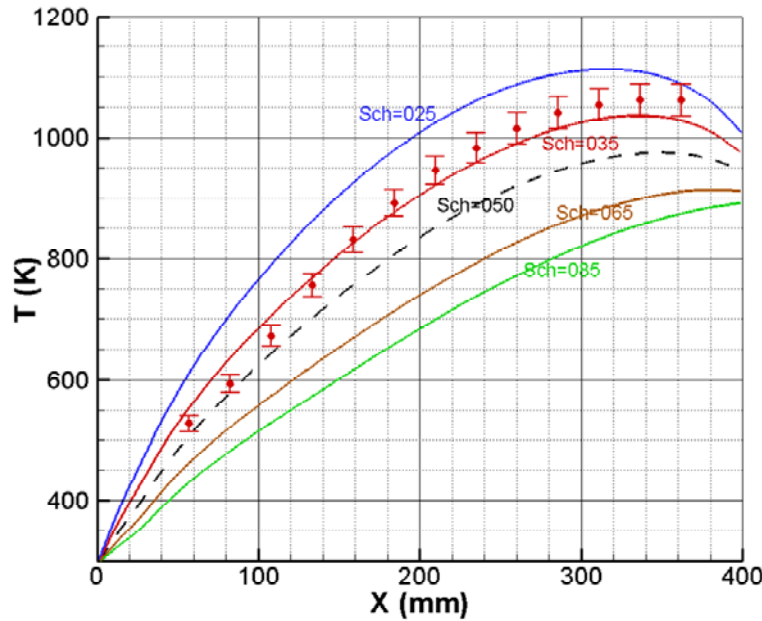


Figure 22. Temperature profiles along the combustor wall.

Finally, it should be mentioned that in order to thoroughly assess the Reynolds analogy issue, numerical simulations were also carried out with the eddy-dissipation (EDS) and laminar flamelet combustion models. A large amount of numerical results and figures were generated. The trends and magnitudes of velocity, turbulence kinetic energy, Reynolds stresses, and temperature distributions are similar to those obtained from the flamelet and EDS combustion models (Jiang & Campbell 2007, 2008). Although the results are not presented in this paper, the optimized Γ_t numbers are given in Table 1 for the purpose of comparison. During optimization, Γ_t number gradually decreased from 0.85 to 0.25 with an interval of 0.1 in general. Near the optimal value, an interval of 0.05 or even 0.01 was used. For temperature prediction inside the combustor, the numerical results were compared with and judged by the same experimental datasets, including velocity and temperature

distributions. For wall temperature prediction, the optimal Γ_t number was judged mainly by the experimental temperature profile along the combustor wall.

As shown in Table 1, the optimal Γ_t for the temperature prediction inside the combustion chamber (line 1) is the same for all three combustion models; however, it (line 2) is different for the wall temperature prediction. This indicates that the combustion model has some effect on the near-wall temperature distribution.

Table 1. Optimal Prandtl and Schmidt number.

	flamelet	PDF	EDS
T-chamber	0.50	0.50	0.50
T-wall	0.40	0.35	0.5-0.55

5.3.3. Discussion

As shown in the above results, the optimal Γ_t number for the temperature prediction inside the combustor is 0.50 for all three combustion models. This number is different from 0.25 by Crocker et al. (1998), 0.20 by Kaaling et al. (1997) for gas turbine combustors, and 0.20 for a cross-jet flow simulation (He et al. 1999). However, it is the same as recommended by Syed & Sturgess (1980) for recirculation zone simulations.

All these examples reveal two important facts. First, the optimized value of Γ_t is lower than the traditionally used value of 0.7 - 0.85. Second, the optimal value of Γ_t is most likely dependent on the combustor configuration and possibly the operating conditions. That is, a priori optimization of Γ_t is required in order to reasonably predict temperature and species distributions inside combustors. Obviously, this type of prior optimization is not practical in the real world.

The above observations may be attributed to the following reasons. First, theoretically, equations (7-9) are only valid for boundary layer flows where the streamwise pressure gradient, viscous and source terms can be neglected. Certainly, its application to complex turbulent reacting flows is questionable. As stated earlier, a number of authors (Choi & Orchard 1997, de Souza et al. 1999, Vogel & Eaton 1985, and John & Keller 1990) have experimentally found that this analogy cannot apply to disturbed turbulent boundary flows.

Second, the experimental values of Γ_t (~0.7) are obtained from fully developed boundary or pipe flows (Hinze 1987, White 1988, and Panchapakesan & Lumley 1993), and they may not be suitable for practical turbulent reacting flows. Therefore, in the sense of the average relative strength between the turbulent momentum and scalar transfers, a low value of Γ_t is a true fact and it may vary with flow configurations.

Third, equations (7-9) are based on the gradient-type diffusion assumption which has been questioned by a number of researchers, particularly for turbulent energy and heat transfer. Hinze (1987) pointed out that both the gradient-type diffusion caused by small-scale turbulence and the convective action of large-scale turbulent motion should be considered in turbulent scalar transports. It may be expected that the gradient-type diffusion approach is suitable for turbulent boundary flows; however, it is not suitable for complex flow fields inside combustion systems.

In summary, although the Reynolds analogy concept has been extended to flow-field simulations since the 1970s, for accurate prediction of scalar transfers in turbulent reacting flows without prior optimization, this concept should be improved and new approaches should be developed.

CONCLUSIONS

The current modeling approach for turbulent scalar transfers in reacting flows, Reynolds analogy, is discussed in this chapter. Its rationale and limitation are analyzed and validated by two benchmarking cases, a turbulent jet diffusion flame and a diffusion flame model combustor. The former represents a simple boundary-type flame, while the latter involves complex flow phenomena (shear layers, wall boundary layers, separations, reattachments, recirculation zones and their interactions) which are relevant to many practical combustion systems.

The effects of the turbulent Prandtl/Schmidt number on the flow fields of the jet flame and model combustor have been numerically studied with the selected turbulence, combustion and radiation models. In comparison with comprehensive experimental databases, it is found that for both cases, the flow features and magnitudes of mean velocity fields are excellently predicted, particularly for the jet flame case. These results indicate that the $k-\omega$ turbulence model with the low Reynolds number correction together with other selected physical models can properly predict the velocity field of jet diffusion flames. For complex flows such as the model combustor, the Reynolds stress model (RSM) is able to successfully predict the lengths of both recirculation zones, turbulence kinetic energy and shear stress distributions in the combustor chamber in addition to the mean axial velocity.

The benchmarking cases indicate that the turbulent Prandtl/Schmidt number has insignificant effect on the velocity fields. In contrast, it shows significant effects on the temperature fields, particularly for the temperature profiles in the outer layer region of the jet flame and the downstream region of the model combustor case. This is also true for the temperature profile along the combustor wall.

Jet diffusion flames seem simple; however they pose challenges to numerical simulations. The discrepancies of temperature distributions in the upstream outer layer region of the flame, observed by the authors and other researchers, may be attributed to the local labialization phenomenon, the limitations of Reynolds analogy, and less effort in the development of turbulent scalar transfer models. For the Prandtl/Schmidt numbers considered in the present work, $\Gamma_t = 0.45 - 1.2$, the value of 0.85 can provide acceptable results for the temperature distributions along the jet centerline and at the downstream cross-sections.

For the model combustor configuration and operating conditions, the optimal Γ_t for temperature prediction inside the combustor is 0.5 for all three combustion models, and it varies from 0.35 to 0.55 for the combustor wall temperature prediction. With $\Gamma_t = 0.50$, the velocity and temperature fields are reasonably well predicted, except in some local regions.

Finally, for reliable temperature prediction in turbulent reacting flows without tuning turbulent Pr_t and Sc_t numbers, the Reynolds analogy concept should be improved and new approaches should be studied. The authors hope that this work will stimulate further

investigation on turbulent scalar transfer modeling, and eventually industrial problems such as temperature pattern factors at the exit of gas turbine combustors can be accurately predicted.

ACKNOWLEDGMENTS

The authors are grateful to Dr. Bill Wallace for his valuable comments and suggestions during the preparation of this chapter. Also the authors want to express many thanks to Mr. Youliang Cheong (co-op student) for his assistance in the post-processing of numerical and experimental results.

REFERENCES

- [1] Bai, X.S. and Fuchs, L., Sensitivity Study of Turbulent Reacting Flow Modeling in Gas Turbine Combustors, *AIAA Journal* 33 (10) (1995) 1857-1864.
- [2] Bilger, R.W., Turbulent Diffusion Flames, Annular Review, *Fluid Mechanics*, 1989, Vol. 21, pp. 101-135.
- [3] Bilger, R.W., Turbulent Jet Diffusion Flames, *Progress in Energy and Combustion Science*, 1976, Vol. 1, pp. 87-109.
- [4] Bons, J., A Critical Assessment of Reynolds Analogy for Turbine Flows, Transactions of the ASME, *Journal of Heat Transfer* 127 (2005) 472-485.
- [5] Campbell, I. and Logan, D.L., An Experimental Study of a Combusting Flow past a Confined Bluff Body, Combustion Institute - Canadian Section, Halifax, Canada, 1997.
- [6] Choi, K.S. and Orchard, D.M., Turbulence Management using Riblets for Heat and Momentum Transfer, *Experimental Thermal and Fluid Science* 15 (1997) 109-124.
- [7] Crocker, D.S., Nickolaus, D., Smith, C.E., CFD Modeling of a Gas Turbine Combustor from Compressor Exit to Turbine Inlet, the IGTI Expo 1998, Stockholm, Sweden, 1998, 1998-GT-184.
- [8] Dagaut, P., Reuillon, M., Boettner, J.C. and Cathonnet, M., Kerosene Combustion at Pressures up to 40 atm: Experimental Study and Detailed Chemical Kinetic Modeling, 25th Symp. (Int.) on Combustion, 1994, pp. 919-926.
- [9] de Souza, F., Delville, J., Lewalle, J. and Bonnet, J.P., Larger Scale Coherent Structures in a Turbulent Boundary Layer Interacting with a Cylinder Wake, *Experimental Thermal and Fluid Science* 19 (1999) 204-213.
- [10] Eickhoff, H., Turbulent Hydrocarbon Jet Flames, *Progress in Energy and Combustion Science*, 1982, Vol. 8, pp. 159-168.
- [11] Ferziger, J.H. and Peric, M., Computational Methods for Fluid Dynamics, Springer-Verlag, New York, 2002, pp. 1-10.
- [12] Fluent Inc., Fluent 6.2 Documentation, 10 Cavendish Court, Lebanon, NH 03766, USA, 2006.
- [13] Glassman, I., 1987, Combustion, Academic Press Inc., New York.
- [14] He, G., Guo, Y. and Hsu, A.T., The Effect of Schmidt Number on Turbulent Scalar Mixing in a Jet-in-Crossing Flow, *International Journal of Heat and Mass Transfer* 42 (1999) 3727-3738.

- [15] Hinze, J.O., *Turbulence*, the McGraw-Hill Book Company Inc., New York, 1987, pp.372 - 753.
- [16] Incropera, F.P. and DeWitt, D.P., *Fundamentals of Heat and Mass Transfer*, Fifth Edition, 2002, John Wiley & Sons Inc., New York.
- [17] Jiang, L.Y. and Campbell, I., Application of Three Combustion Models to a Model Combustor, *Canadian Aeronautics and Space Journal*, 2005, Vol. 51, No. 1, pp.1-11.
- [18] Jiang, L.Y. and Campbell, I., Prandtl/Schmidt Number Effect on Temperature Distribution in a Generic Combustor, The XVIII International Symposium Air Breathing Engine Conference, ISABE-2007-0178, Sept. 2-7, 2007, Beijing, China.
- [19] Jiang, L.Y. and Campbell, I., Reynolds Analogy in Combustor Modeling, *International Journal of Heat and Mass Transfer*, 2008, Vol 51/5-6, pp. 1251-1263.
- [20] Jiang, L.Y. and Campbell, I., Turbulence Modeling in a Model Combustor, *Canadian Aeronautics and Space Journal*, 2007, Vol. 53, No. 2, pp. 47-57.
- [21] John, E.D. and Keller, J.O., Time-Resolved Gas Temperature in the Oscillating Turbulent Flow of a Pulse Combustor Pipe, *Combustion and Flame* 80 (1990) 358-370.
- [22] Jones, T.V. and Walton, T.W., Reynolds Analogy in Film Cooling, 10th International Symposium on Air Breathing Engines, Nottingham, England, 1991, pp. 1263-1268.
- [23] Jones, W.P. and Whitelaw, J.H., Calculation Methods for Reacting Turbulent Flows: A Review, *Combustion and Flame*, 1982, Vol. 48, pp.1-26.
- [24] Jones, W.P., Turbulence Modeling and Numerical Solution Methods for Variable Density and Combustion Flows, *Turbulent Reacting Flows*, Libby, P.A. and Williams, F.A (Eds.), 1994, Academic Press, New York.
- [25] Kaaling, H., Ryden, R., Bouchie, Y., Ansart, D., Magre, P., and Guin, C., RQL Combustor Development including Design, CFD Calculations, CARS Measurements and Combustion Tests, the 13th International Symposium Air Breathing Engines, Chattanooga, TN, USA, 1997, ISABE 97-7069.
- [26] Lai, M.K., CFD Analysis of Liquid Spray Combustion in a Gas Turbine Combustor, the IGTE Expo, Orlando, FL, 1997, 1997-GT-309.
- [27] Launder, B.E., Second-Moment Closure: Present and Future? *International Journal of Heat and Fluid Flow*, Vol. 10, 1989, pp. 282-299.
- [28] Launder, B.E., Reece, G.J. and Rodi, W., Progress in the Development of a Reynolds-Stress Turbulence Closure, *J. Fluid Mech.* 68 (1975) 537-566.
- [29] Libby, P.A. and Williams, F.A., Fundamental Aspects and a Review, *Turbulent Reacting Flows*, Libby, P.A. and Williams, F.A (Eds.), 1994, Academic Press, New York, pp. 1-61.
- [30] Lockwood, F.C. and Naguib, A.S., The Prediction of the Fluctuations in the Properties of Free, Round-Jet, Turbulent, Diffusion Flames, *Combustion and Flame* 1975, Vol. 24, pp. 109-124.
- [31] Lubbers, C.L., Brethouwer, G. and Boersma, B.J., Simulation of the Mixing of a Passive Scalar in a Round Turbulent Jet, *Fluid Dynamics Research* 28 (2001) 189-208.
- [32] Magnussen B.F. and Hjertager, B.H., On Mathematical Models of Turbulent Combustion with Special Emphasis on Soot Formation and Combustion, In 16th Symposium on Combustion (International), 1976, pp. 719-729.
- [33] Marvin, J.G., Turbulence Modeling for Computational Aerodynamics, *AIAA Journal*, 21, 1983, pp. 941-955.

- [34] Moore, J.G. and Moore, J., Functional Reynolds Stress Modeling, 2006, Pocahontas Press Inc., Blacksburg, Virginia, USA.
- [35] NIST, NIST-JANAF Thermochemical Tables, 4th edition, Washington, DC, 1998.
- [36] Panchapakesan, N.R. Lumley, J.L., Turbulence Measurements in Axi-Symmetric Jets of Air and Helium, Part 2, Helium Jet, *Journal of Fluid Mechanics* 246 (1993) 225-247.
- [37] Raithby, G.D. and Chui, E.H., A Finite-Volume Method for Predicting a Radiant Heat Transfer in Enclosures with Participating Media, *Journal of Heat Transfer* 112 (1990) 415-423.
- [38] Reynolds O., On the Extent and Action of the Heating Surface for Steam Boilers, Manchester Lit. Phil. 14 (1874) 7-12.
- [39] Reynolds, W.C. and Cebeci, T., Calculation of Turbulent Flows, *Topics in Applied Physics*, 1976, Vol. 12, pp. 193-229, Springer-Verlag.
- [40] Rose, J.W. and Cooper, J.R., 1977, *Technical Data on Fuel*, John Wiley & Sons, New York.
- [41] Sislian, J.P., Jiang, L.Y. and Cusworth, R.A., Laser Doppler Velocimetry Investigation of the Turbulence Structure of Axi-Symmetric Diffusion Flames, *Prog. in Energy and Combustion Science* 14 (2) (1988) 99-146.
- [42] Sivathanu, Y.R. and Faeth, G.M., 1990, "Generalized State Relationships for Scalar Properties in Non-Premixed Hydrocarbon/Air Flames," *Combustion and Flame*, 82:211-230.
- [43] Smith, R.H. and Wang, C.T., Contracting Cones Giving Uniform Throat Speeds, *J. Aero. Sci.*, 1944, No. 11, pp. 356-380.
- [44] Spalding, D.B., Concentration Fluctuations in a Round Turbulent Free Jet, *Chem. Eng. Sci.* 26 (1971) 95-107.
- [45] Suraweera, M.V., Mee, D.J., Stalker, R.J., Reynolds Analogy in High-Enthalpy and High-Mach-Number Turbulent Flows, *AIAA Journal* 44 (4) (2006) 917-919.
- [46] Syed, S.A. and Sturgess, G.J., Validation Studies of Turbulence and Combustion Models for Aircraft Gas Turbine Combustors, Proceeding of Momentum and Heat Transfer Processes in Recirculating Flows, Edited by B.E. Lauder and J.A.C. Humphrey, ASME HTD-Vol. 13, ASME Winter Annual Meeting, Chicago, Illinois, USA, 1980, pp. 71-89.
- [47] Takagi, T., Shin H.D. and Ishio, A., Local Laminarization in Turbulent Diffusion Flames, *Combustion and Flame*, 1980. Vol. 37, pp. 163-170.
- [48] Tennekes, H. and Lumley, J.L., *A First Course in Turbulence*, the MIT Press, 1983, Cambridge, Mass.
- [49] Torii, S., Numerical Simulation of Turbulent Jet Diffusion Flames by means of Two-Equation Heat Transfer Model, *Energy Conversion and Management*, 2001, Vol. 42, pp. 1953-1962.
- [50] Vogel, J.C. and Eaton, L.K., Combined Heat Transfer and Fluid Dynamic Measurements Downstream of a Backward-Facing Step, *Journal of Heat Transfer* 107 (1985) 922-929.
- [51] Wang, F., Zhou, L.X., Xu, C.X. and Goldin, G.M., Comparison between a Composition PDF Transport Equation Model and an ASOM Model for Simulating a Turbulent Jet Flame, *International Journal of Heat and Mass Transfer*, 2008, Vol. 51, pp. 136-144.

- [52] White, F.M., *Heat and Mass Transfer*, Addison-Wesley Publishing Company, New York, 1988, pp. 320 - 641.
- [53] Wilcox, D.C., *Turbulence Modeling for CFD*, Second edition, 2002, DCW Industries, Inc., La Canada California.
- [54] Wilcox, D.C., Turbulence Modeling: an Overview, 2001, AIAA paper 2001-0724.
- [55] Zhou, L.X., Liao, L., Chen, X.L. and Zhang, J., A USM Turbulence-Chemistry Model for Simulating NOx Formation in Turbulent Combustion, *Fuel*, 2002, Vol. 81, pp. 1703-1709.
- [56] Zhou, X., Sun, Z., Brenner, G. and Durst, F., Combustion Modeling of Turbulent Jet Diffusion H₂/Air Flame with Detailed Chemistry, *International Journal of Heat and Mass Transfer*, 2000, Vol. 43, pp. 2075-2088.

Chapter 6

THE RESEARCH OF THE SOLUTION QUALITY FOR THE $k-\varepsilon$ TURBULENCE METHOD WITH USING SENSITIVITY ANALYSIS OF FLOW PROPERTIES TO MODEL COEFFICIENTS

Ewa Blazik-Borowa*

Lublin University of Technology, Lublin, Poland

ABSTRACT

This chapter will be devoted to the research of solution quality for the CFD problem, which is solved with use of the $k-\varepsilon$ standard turbulence method for the steady incompressible flow at a small velocity. The analyses are performed for the exemplary problem of the flow around square cylinder located at a ground. The research of solution quality can be made on the basis of comparison results calculations and measurements, whereas, in this chapter, there is a proposal of the analysis for the solution on the basis of the sensitivity analysis of flow properties to model coefficients. The results of the sensitivity analysis have many applications but the most important feature of the sensitivity coefficients is the fact that they have higher values in the regions of high property gradients than in the others, it means in the region with the biggest calculation errors. In this case the analysis of problems with the same approximation degree of one flow property (for example, when the pressure is constant in cells) and different degrees of polynomials for other properties, the higher sensitivity means the bigger errors. For the problems with different degrees of polynomials of the flow property (for example, the components of a flow velocity approximated by different method) the bigger sensitivity denotes that this property is better described. In this chapter the methods of determination of the sensitivity will be described. Next the assessment of the solution quality which is obtained by using different approximation methods will be introduced on the basic values of these coefficients. The results of the research will be verified on the basis of comparison of the calculations results and own measurements of the 2D flow around square located at the ground. All calculations are made with use of FLUENT and own computer programs.

* e-mail:e.blazik@pollub.pl

INTRODUCTION

The computer calculations have great importance at present both in industry and in science. However, it should be remembered that the quality of numeric analysis depends on the quality of applied mathematical models, use of numeric methods as well as user's experience. From among the mentioned tools, the most important meaning has the mathematical model. There have been developed quite precise models for complex problems which cannot be applied in computer programs. Simplified mathematical equations, including empirical and semi-empirical coefficients in the reference to such problems came into being. The influence in such cases on solution quality has additionally the correct selection of these coefficients. The problems of fluid mechanics with the turbulent flow belong to the group of such issues. The solution of problems of computer fluid mechanics depends on the solution of the set of differential equations, which are the simplification of considerably more compiled mathematical issues.

The basic equations which occur in every task of fluid mechanics are equations describing the field of the pressure and the velocity for flow that is the equation of continuity and the Navier-Stokes equations. As the effect of the solution of such set we should receive the field of a velocity and a pressure in calculation domain which models fluid. The direct solution of such set is possible in reference to simple problems with the small Reynolds numbers only. If the Reynolds number is just big enough that the flow has the turbulent character (comp. Schlichting (1979), Hinze (1975)), additional equations should be used. These additional equations differ between themselves in mathematical models and depend on the way of averaging of flow properties or the choice (sometimes intuitive) of them, which helps to describe the flow turbulence. Since the forties of the XX century several methods of description of the turbulent flow came into being (comp. works of Kołmogorow (1942), Chou (1945), Prandtl (1945), Smagorinsky (1963), Dradshaw (1967), Hanjalic (1970), Launder and Spalding (1972) and many others). With computer development in the eighties of the last century the growth of number of methods using computer fluid mechanics became higher.

This work is devoted to the research of the qualities of solutions of the incompressible turbulent flows obtained by calculations based upon the $k-\varepsilon$ model. This model besides the continuity and Navier-Stokes equations contains two equations: the turbulence kinetic energy and the dissipation rate of the kinetic turbulence energy equations. Additional relationships described by Launder and Spalding (1972), Launder and Spalding (1974) serve to modeling the turbulence of the flow. This model is, at present, the most popular model among the users of commercial CFD programs. This is not the effect of its perfection, because the model has many faults, but just that the shortcomings of the model are known and tested. One of the main and unfortunately probably still not solved problems of the $k-\varepsilon$ model is the selection of semi-empirical coefficients. Getting the correct solution by the turbulent model $k-\varepsilon$ in standard version depends, among others, on the selection of five "constants": C_μ , $C_{\varepsilon 1}$, $C_{\varepsilon 2}$, σ_k and σ_ε . These values are the result of nondimensional theoretical analyses and much research, among others in the wind tunnels, and that is why they are called "semi-empirical coefficients" or "constants". The process of choosing their values is called the calibration of the model and it is described in such works as: Launder and Spalding (1972), Shih et al. (1995), Johansson (2001), and Błazik-Borowa (2008). In literature, they are called "constants" of model $k-\varepsilon$, but it seems to be the incorrect name, because studying the

literature (e.g. Launder and Spalding (1972), Jones and Launder (1972), So et al. (1991), Hrenya et al. (1995), Sajjagi and Waywell (1997), Johansson (2001)) it can be found the various values of these parameters.

The best way to check the results quality is the comparison of the results of calculations and measurements e.g. in the wind tunnel. However this is not always possible because of the lack of the access to suitable equipments or because of the economic reasons. The numeric tool will be proposed in this work to estimate the solution quality and its usefulness will be verified by comparisons with the results of research in the tunnel, which are accessible in the literature and the ones known by own research. The sensitivity analysis of the flow properties will be the proposed research tool of the solution quality, being the result of computer calculations, with regard to the value of the coefficients of the $k-\varepsilon$ model. These coefficients will not be called "constants" in this work, but they will be treated as variables. Since they are the subject of the sensitivity analysis they will be called the sensitivity analysis parameters.

The problem of the solution quality will be presented for the calculations of the incompressible steady two-dimensional flow around the square arranged near ground, obtained by the finite volume method. However in order to present the full possibility of application of the sensitivity analysis, checking the quality of the calculation results for chosen numeric methods will be shown, especially the way of solving the set of equations and of approximation of the flow property in the volume, and the application of the sensitivity analysis to check the quality of the mesh at various Reynolds numbers.

Computer calculations, presented in this work, have been made with use of FLUENT program and own programs.

THE SENSITIVITY ANALYSIS

The aim of this chapter is the presentation of problems connected with using of the $k-\varepsilon$ method and, if it is possible, to propose their solutions to avoid or to minimize the calculation errors. The basis of the research of the solutions quality is the sensitivity analysis of the $k-\varepsilon$ turbulence model to its parameters. The sensitivity analysis serves to check the influence of the small changes of the model parameters on the problem solution. The method is applied in the solid mechanics and often used in a design process. Many papers (comp. Hang et al. (1986), Kleiber et al. (1997)) describe the usage of the sensitivity analysis for evaluation of influence of geometrical parameters or materials parameters on the efficiency of industrial processes. The sensitivity analysis is also applied in the fluid mechanics. This application occurs more rarely, because the problems of the fluid mechanics are non-linear ones. However in the last years you can find in the literature the sensitivity analysis as the tool for the design of channels geometry (Mohammadi et al. (2003)) or for research of influence of a body motion in a flow on properties (pressure, velocity etc.) of this flow (Fernández i Moubachir (2002)).

The sensitivity analysis is used here in this chapter for the $k-\varepsilon$ turbulence model evaluation in the standard version in the reference to the incompressible and steady flow. The proposal conception of the use of the sensitivity analysis and led out dependencies have been made by the author herself, who had presented her results for the first time in the paper of Blazik-Borowa (2006), but also in her later works e.g. Blazik-Borowa (2008). In the same

time Colin et al. (2005) have presented similar way of the use of sensitivity analysis in the reference to thermal flows.

THE DETERMINATION OF THE SENSITIVITY COEFFICIENTS FOR THE k - ε STANDARD METHOD

The determination of the sensitivity coefficients is presented in the reference to the set of differential equations of the k - ε method in the standard version for the incompressible flow with large Reynolds numbers. The equations of the k - ε model take the following form for incompressible flow without the influence of external forces:

$$\frac{\partial u_i}{\partial x_i} = 0, \quad (1a)$$

$$\rho \left(\frac{\partial u_i}{\partial t} + u_j \frac{\partial u_i}{\partial x_j} \right) = - \frac{\partial p}{\partial x_i} + 2 \frac{\partial}{\partial x_m} [(\mu + \mu_t) s_{im}] \quad (1b)$$

$$\rho \left(\frac{\partial k}{\partial t} + u_j \frac{\partial k}{\partial x_j} \right) = \frac{\partial}{\partial x_m} \left[\left(\mu + \frac{\mu_t}{\sigma_k} \right) \frac{\partial k}{\partial x_m} \right] + \rho P_k - \rho \varepsilon \quad (1c)$$

$$\rho \left(\frac{\partial \varepsilon}{\partial t} + u_j \frac{\partial \varepsilon}{\partial x_j} \right) = \frac{\partial}{\partial x_m} \left[\left(\mu + \frac{\mu_t}{\sigma_\varepsilon} \right) \frac{\partial \varepsilon}{\partial x_m} \right] + C_{\varepsilon 1} \rho P_k \frac{\varepsilon^2}{k} - \rho C_{\varepsilon 2} \frac{\varepsilon^2}{k} \quad (1d)$$

$$\mu_t = \rho C_\mu \frac{k^2}{\varepsilon}. \quad (1e)$$

where: p – pressure, u_i – velocity vector component, k – kinetic turbulence energy, ε – dissipation rate of the kinetic turbulence energy, P_k – production of the kinetic turbulence energy, x_i – co-ordinate of the global co-ordinates system, t – time, ρ – density of a fluid, μ – dynamic viscosity coefficient, μ_t – turbulence dynamic viscosity coefficient, $C_{\varepsilon 1}$, $C_{\varepsilon 2}$, C_μ , σ_k and σ_ε – parameters of the k - ε model.

The production of the kinetic turbulence energy is described by formula:

$$\rho P_k = \mu_t S^2 \quad (2)$$

where: S – modulus of the mean rate-of-strain tensor, defined as $S \equiv \sqrt{2s_{ij}s_{ij}}$ and

$$s_{ij} = \frac{1}{2} \left(\frac{\partial u_i}{\partial x_j} + \frac{\partial u_j}{\partial x_i} \right)$$

As the result of computer calculations there are fields of: the pressure p , the velocity components u_i , the turbulence kinetic energy k , the dissipation rate of turbulence kinetic energy ε and the turbulence dynamic viscosity coefficient μ_t in the individual cells of the mesh FVM (the Finite Volume Method). All mentioned flow properties are the functions of the parameters of the $k-\varepsilon$ turbulence model. The coefficients of the sensitivity analysis of the model in the whole computational domain are calculated as the derivatives of these properties in relation to the given parameter. The coefficients of the sensitivity analysis in relation to parameters $C_{\varepsilon 1}$, $C_{\varepsilon 2}$, C_μ , σ_k and σ_ε in one point may be set into the matrix:

$$\mathbf{J} = \begin{bmatrix} \tilde{p}_{C_{\varepsilon 1}} & \tilde{p}_{C_{\varepsilon 2}} & \tilde{p}_{C_\mu} & \tilde{p}_{\sigma_k} & \tilde{p}_{\sigma_\varepsilon} \\ \tilde{u}_{1C_{\varepsilon 1}} & \tilde{u}_{1C_{\varepsilon 2}} & \tilde{u}_{1C_\mu} & \tilde{u}_{1\sigma_k} & \tilde{u}_{1\sigma_\varepsilon} \\ \tilde{u}_{2C_{\varepsilon 1}} & \tilde{u}_{2C_{\varepsilon 2}} & \tilde{u}_{2C_\mu} & \tilde{u}_{2\sigma_k} & \tilde{u}_{2\sigma_\varepsilon} \\ \tilde{k}_{C_{\varepsilon 1}} & \tilde{k}_{C_{\varepsilon 2}} & \tilde{k}_{C_\mu} & \tilde{k}_{\sigma_k} & \tilde{k}_{\sigma_\varepsilon} \\ \tilde{\varepsilon}_{C_{\varepsilon 1}} & \tilde{\varepsilon}_{C_{\varepsilon 2}} & \tilde{\varepsilon}_{C_\mu} & \tilde{\varepsilon}_{\sigma_k} & \tilde{\varepsilon}_{\sigma_\varepsilon} \\ \tilde{\mu}_{C_{\varepsilon 1}} & \tilde{\mu}_{C_{\varepsilon 2}} & \tilde{\mu}_{C_\mu} & \tilde{\mu}_{\sigma_k} & \tilde{\mu}_{\sigma_\varepsilon} \end{bmatrix} = \begin{bmatrix} \frac{\partial p}{\partial C_{\varepsilon 1}} & \frac{\partial p}{\partial C_{\varepsilon 2}} & \frac{\partial p}{\partial C_\mu} & \frac{\partial p}{\partial \sigma_k} & \frac{\partial p}{\partial \sigma_\varepsilon} \\ \frac{\partial u_1}{\partial C_{\varepsilon 1}} & \frac{\partial u_1}{\partial C_{\varepsilon 2}} & \frac{\partial u_1}{\partial C_\mu} & \frac{\partial u_1}{\partial \sigma_k} & \frac{\partial u_1}{\partial \sigma_\varepsilon} \\ \frac{\partial u_2}{\partial C_{\varepsilon 1}} & \frac{\partial u_2}{\partial C_{\varepsilon 2}} & \frac{\partial u_2}{\partial C_\mu} & \frac{\partial u_2}{\partial \sigma_k} & \frac{\partial u_2}{\partial \sigma_\varepsilon} \\ \frac{\partial k}{\partial C_{\varepsilon 1}} & \frac{\partial k}{\partial C_{\varepsilon 2}} & \frac{\partial k}{\partial C_\mu} & \frac{\partial k}{\partial \sigma_k} & \frac{\partial k}{\partial \sigma_\varepsilon} \\ \frac{\partial \varepsilon}{\partial C_{\varepsilon 1}} & \frac{\partial \varepsilon}{\partial C_{\varepsilon 2}} & \frac{\partial \varepsilon}{\partial C_\mu} & \frac{\partial \varepsilon}{\partial \sigma_k} & \frac{\partial \varepsilon}{\partial \sigma_\varepsilon} \\ \frac{\partial \mu_t}{\partial C_{\varepsilon 1}} & \frac{\partial \mu_t}{\partial C_{\varepsilon 2}} & \frac{\partial \mu_t}{\partial C_\mu} & \frac{\partial \mu_t}{\partial \sigma_k} & \frac{\partial \mu_t}{\partial \sigma_\varepsilon} \end{bmatrix} \quad (3)$$

The sensitivity coefficients, used in the following part of the chapter, are determined by the method of the direct differentiating. Two versions of this method (Kleiber et al. (1997)) exist:

- semi-analytic (the finite difference approximation to the sensitivities coefficients),
- analytic (forward sensitivity analysis).

The first of these methods consists in the realization of calculations in the reference to two neighboring values of the studied parameter and the sensitivity calculation from the formula:

$$\tilde{w}_{C_m} = \frac{w_2 - w_1}{\Delta C_m} \quad (4)$$

where: w_1 , w_2 – results of calculations at $C_m - \Delta C_m / 2$ and $C_m + \Delta C_m / 2$, respectively, ΔC_m – increment of the C_m parameter.

The ΔC_m value depends on the complexity of the problem. It can be checked the correctness of acceptance of this increment through the realization of many calculations having various values of ΔC_m , but it requires much effort. Therefore the verification of the curvature of the graph of the function $w = w(C_m)$ is proposed by the checking how much the

w property is moved away from the line connecting the points $(C_m + \Delta C_m / 2, w_2)$ and $(C_m - \Delta C_m / 2, w_1)$ on the basis of the following formula:

$$\xi = \left| \frac{w - \frac{w_2 + w_1}{2}}{\frac{w_2 - w_1}{2}} \right| \quad (5)$$

The second method of determination of the sensitivity coefficients consists in differentiation of suitable equations describing the problem (in our case the set of equations (1)). Next it should be solved the obtained set of equations supplemented by suitable boundary conditions of the finite volume or finite element methods. It should be preceded the solution of this problem by calculation of the flow properties, that is to solve the set of equations (1).

The equations of the set (1) after the differentiation with regard to the C_m parameter take the following forms:

$$\frac{\partial \tilde{u}_{iC_m}}{\partial x_i} = 0 \quad (6a)$$

$$\rho \left(\tilde{u}_{jC_m} \frac{\partial u_i}{\partial x_j} + u_j \frac{\partial \tilde{u}_{iC_m}}{\partial x_j} \right) = - \frac{\partial \tilde{p}_{C_m}}{\partial x_i} + 2 \frac{\partial}{\partial x_r} \left[\tilde{\mu}_{C_m} s_{ir} + (\mu + \mu_t) \frac{\partial s_{ir}}{\partial C_m} \right] \quad (6b)$$

$$\rho \left(\tilde{u}_{jC_m} \frac{\partial k}{\partial x_j} + u_j \frac{\partial \tilde{k}_{C_m}}{\partial x_j} \right) = \frac{\partial}{\partial x_r} \left[\frac{\tilde{\mu}_{C_m}}{\sigma_k} \frac{\partial k}{\partial x_r} + \left(\mu + \frac{\mu_t}{\sigma_k} \right) \frac{\partial \tilde{k}_{C_m}}{\partial x_r} \right] + \rho \frac{\partial P_k}{\partial C_m} - \rho \tilde{\varepsilon}_{C_m} + q_{km} \quad (6c)$$

$$\begin{aligned} \rho \left(\tilde{u}_{jC_m} \frac{\partial \varepsilon}{\partial x_j} + u_j \frac{\partial \tilde{\varepsilon}_{C_m}}{\partial x_j} \right) &= \\ &= \frac{\partial}{\partial x_r} \left[\frac{\tilde{\mu}_{C_m}}{\sigma_\varepsilon} \frac{\partial \varepsilon}{\partial x_r} + \left(\mu + \frac{\mu_t}{\sigma_\varepsilon} \right) \frac{\partial \tilde{\varepsilon}_{C_m}}{\partial x_r} \right] + \end{aligned} \quad (6d)$$

$$+ \rho C_{\varepsilon 1} \frac{\varepsilon}{k} \frac{\partial P_k}{\partial C_m} + \frac{\rho P_k C_{\varepsilon 1} - 2\rho \varepsilon}{k} \tilde{\varepsilon}_{C_m} - \frac{\rho P_k C_{\varepsilon 1} \varepsilon - \rho \varepsilon^2}{k^2} \tilde{k}_{C_m} +$$

$$+ q_{\varepsilon n}$$

$$\tilde{\mu}_{C_m} - \rho C_\mu \frac{2k}{\varepsilon} \tilde{k}_{C_m} + \rho C_\mu \frac{k^2}{\varepsilon^2} \tilde{\varepsilon}_{C_m} = q_{\mu m}. \quad (6e)$$

The terms of the right-hand side, which are non-zero ones, are described with the following formulae:

- for $C_{\varepsilon 1}$:

$$q_{\varepsilon 1} = P_k \frac{\varepsilon}{k} \quad (7)$$

- for $C_{\varepsilon 2}$:

$$q_{\varepsilon 2} = -\rho \frac{\varepsilon^2}{k} \quad (8)$$

- for C_μ :

$$q_{\mu 3} = \rho \frac{k^2}{\varepsilon}, \quad (9)$$

- for σ_k :

$$q_{k4} = -\frac{\partial}{\partial x_r} \left(\frac{\mu_t}{\sigma_k^2} \frac{\partial k}{\partial x_r} \right), \quad (10)$$

- for σ_ε :

$$q_{\varepsilon 5} = -\frac{\partial}{\partial x_r} \left(\frac{\mu_t}{\sigma_\varepsilon^2} \frac{\partial \varepsilon}{\partial x_r} \right). \quad (11)$$

The use of the finite difference approximation to the sensitivities coefficients requires the solution of ten problems, but it does not require the additional computer program. In the case of the forward sensitivity analysis, at the first, the flow properties should be calculated and then the sensitivity coefficients can be obtained by solving the set of differential equations (6). Sets of the five equations which will come into being after the discretization of the differential equations by the finite element or the finite volume methods, will be sparse asymmetrical sets. Methods of solving such problems have been described among others by Chung (2002).

The comparison of both methods of obtaining the sensitivity coefficients and the sensitivity analyses of exemplary problems have been the subject among others of such papers like: Błazik-Borowa (2006), Błazik-Borowa (2007a), Błazik-Borowa (2007b), Błazik-

Borowa (2007c), Błazik-Borowa (2008). The results of calculations introduced in the following part of this chapter have been found by of the finite difference approximation to the sensitivity coefficients.

THE INTERPRETATION OF SENSITIVITY ANALYSIS RESULTS

The basic importance of the sensitivity coefficients is to show the influence of the selection of the k - ε model parameters on the results of calculations. It will be shown in the chapter that the sensitivity may be also used to determine the area with the largest computational errors in the domain, to check quality of solutions, to choose the mesh of the domain and to chose the approximation methods. The parameters of the model are the factors of derivatives in the set of equations (1). It causes that when the term with the given parameter is quite enough large then also the value of this parameter, being only the factor, have the larger influence on the solution, as well. If we analyze problems with the same degree of the approximation of the function, then the larger sensitivity means larger computational errors, because it shows areas with the largest gradients of the flow property function. If we have various orders of approximation of the function (the density of the mesh, functions approximation the flow properties) then the largest sensitivity will show us the best from the applied methods of approximation. The more exact the approximation causes the larger values of the derivative flow properties and their sensitivity to the parameters of the model.

THE METHODS OF THE ANALYSES OF CALCULATIONS ERRORS AND THE SENSITIVITY ANALYSIS COEFFICIENTS

The flow properties and also their sensitivities get the values of various orders, that is why the comparison of the sensitivity coefficients of various properties ought to be executed on relative values. Calculating relative sensitivities in individual volumes on the basis of following dependences is proposed in this part of work:

- relative sensitivity coefficients of the pressure p :

$$p \geq 0.5\rho u_o^2 \Rightarrow \check{p}_m = \frac{\tilde{p}_m}{p}; \quad p < 0.5\rho u_o^2 \Rightarrow \check{p}_m = \frac{\tilde{p}_m}{0.5\rho u_o^2}; \quad (12)$$

- relative sensitivity coefficients of the component velocity u_1 :

$$u_1 \geq u_o \Rightarrow \check{u}_{1m} = \frac{\tilde{u}_{1m}}{u_1}; \quad u_1 < u_o \Rightarrow \check{u}_{1m} = \frac{\tilde{u}_{1m}}{u_o}; \quad (13)$$

- relative sensitivity coefficients of the component velocity u_2 :

$$u_2 \geq u_o \Rightarrow \bar{u}_{2m} = \frac{\tilde{u}_{2m}}{u_2}; \quad u_2 < u_o \Rightarrow \bar{u}_{2m} = \frac{\tilde{u}_{2m}}{u_o}; \quad (14)$$

- relative sensitivity coefficients of the kinetic turbulence energy k :

$$k \geq k_o \Rightarrow \bar{k}_m = \frac{\tilde{k}_m}{k}; \quad k < k_o \Rightarrow \bar{k}_m = \frac{\tilde{k}_m}{k_o}; \quad (15)$$

- relative sensitivity coefficients of dissipation rate of the turbulence kinetic energy ε :

$$\varepsilon \geq \varepsilon_o \Rightarrow \bar{\varepsilon}_m = \frac{\tilde{\varepsilon}_m}{\varepsilon}; \quad \varepsilon < \varepsilon_o \Rightarrow \bar{\varepsilon}_m = \frac{\tilde{\varepsilon}_m}{\varepsilon_o}; \quad (16)$$

- relative sensitivity coefficients of the turbulence dynamic viscosity μ_t :

$$\mu_t \geq \mu_{t_o} \Rightarrow \bar{\mu}_m = \frac{\tilde{\mu}_m}{\mu_t}; \quad \mu_t < \mu_{t_o} \Rightarrow \bar{\mu}_m = \frac{\tilde{\mu}_m}{\mu_{t_o}}; \quad (17)$$

where p , u_1 , u_2 , k , ε , μ_t are the values of the properties in given volume and u_o , k_o , ε_o , μ_{t_o} the values of the properties on the inflow edge.

The problems analysed in this chapter are quite enough difficult so the limitation to show the sensitivity analysis coefficients in form of fields or graphs in the intersections of the computational domain does not allow to make correct analyses. The fields of coefficients show the relation only for one coefficient and one computational situation and graphs are very complicated so they lose their transparency. Hence, the analysis of the results quality will be performed not only on basis of fields of the sensitivity coefficients but also on the basis of errors described by the formula:

$$\varphi_w = \frac{w_o - w_b}{w_b}, \quad (18)$$

where: w_b – result of measurements, w_o – result of calculations.

However, the estimation of dependence between sensitivity and the methods of approximation will be executed on the basis of the changes of the relative average sensitivity coefficient in the transverse intersection of the domain according to the formula:

$$\hat{w}_m = \bar{w}_m \cdot C_m \quad (19)$$

and the average sensitivity coefficient described by the formula:

$$\bar{\tilde{w}}_m = \frac{1}{H} \sum_{i=1}^n |\tilde{w}_{mi}| dx_{2i} \quad (20)$$

where: \tilde{w}_{mi} – value of sensitivity in i volume; dx_{2i} – dimension of i volume along the axis x_2 ; n – number of the volume in the intersection along the axis x_2 .

Also the total influence of all five parameters of the $k-\varepsilon$ models on the solution will be determined in this chapter. The total sensitivity in the given volume will be calculated on the basis of the formula:

$$\tilde{w}_c = C_{\varepsilon 1} |\tilde{w}_{C_{\varepsilon 1}}| + C_{\varepsilon 2} |\tilde{w}_{C_{\varepsilon 2}}| + C_{\mu} |\tilde{w}_{C_{\mu}}| + \sigma_k |\tilde{w}_{\sigma_k}| + \sigma_{\varepsilon} |\tilde{w}_{\sigma_{\varepsilon}}|. \quad (21)$$

THE DESCRIPTION OF THE EXAMPLE

The research of the solutions quality presented in the next section consists of the comparison of the calculation result with the measurement results based on the analysis of the sensitivity coefficients and the dependence between the calculations errors appointed in relation to measurements and the level of the sensitivity.

THE RESEARCH IN THE WIND TUNNEL

In this part of the chapter the results described in the papers of Noda et al. (1995a, 1995b), of Noda and Nakayama (2003) and the results of own research (Błazik-Borowa et al. (2008)) are used. These external researches are related to the measurement of the pressure distribution on the surface of the model, while own research of measurement has been made for average velocities and their fluctuation around the model shown in Figure 1.

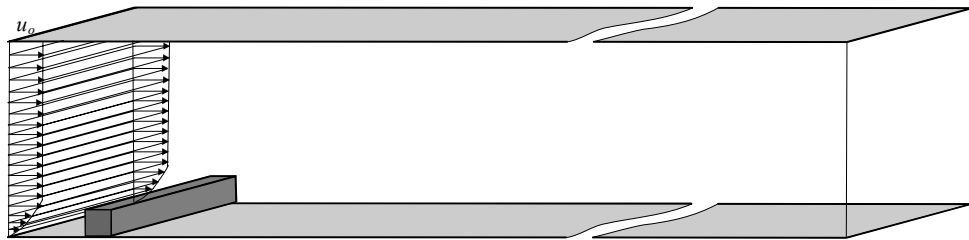


Figure 1. The scheme of the square cylinder in the wind tunnel.

Own research has been performed in the wind tunnel of the Wind Engineering Laboratory of the Cracow University of Technology directed by prof. Andrzej Flaga. The model with square intersection 200x200 mm had been constructed and set in the tunnel so the flow in its central intersection can be treated as two dimensional.

The pressure distribution on the surface of the model, the approximate average values of pressures on ground in front and behind the model and the field of velocity in the space of the

wind tunnel are results of measurements. The measurements of the pressure distribution have been made by using the pressure scanner which is made of piezoresistive transducers, two-directional pressure sensors of Motorola MPX 2010 and of the battery of manometers. The measurements by the pressures scanner have been carried in 30 points of the model and 63 tubes have been connected to the battery of manometers, located on the model and the ground. The pressure scanner measured the voltages which with the frequency 500 Hz have been passed to the computer where the program DaqView collected data, transformed them on the value of pressure and then archived on the hard disc. The results of measurements by the battery of manometers have been taken to the archives in the form of photos, after the processing of which the average values of pressure have been received with the precision of 10 Pa.

The measurements of velocities have been carried with the help of hotwire anemometers with the frequency of the measurement 500 Hz. The probes of anemometer, the measuring system ATU 2001 and software for collection of data had been made at The Strata Mechanics Research Institute in Cracow. The measurements have been performed with use of two single-wire probes and four X-wire probes. The measurements made by the single-wire probes served to determine the average velocity and that is why their sensors had been placed before the model. The measurement of the average velocity made by hot-wire anemometers has been verified by using the pressure scanner, to which one tube located in the free flow in front of the model had been connected. The X-wire probes had been placed on a mobile carriage with the help of which they can be move to any point of the measuring space. The measurements have been made in two rounds:

- measurement I – the wires of probes have been arranged so that one was parallel to the average direction of the flow.
- measurement II – the wires of the probes have been arranged so that the angle between the wires and average direction of the flow was about $\pi/4$

The modules of velocities, their components and fluctuations of the flow are determined on the basis of measured time series. Final velocities are calculated on the basis of recommendations from such works like: Evans (1974), Hinze (1975) and Shabbir et al. (1996).

THE NUMERIC MODELS

Two computational domains have been used in calculations, modeling flows around squares with sides of 0.06 m which had been the subject of research of Noda et al. (1995) and 0.2 m corresponding to model of own research. Data for these models are juxtaposition in Table 1. Calculations have been made on the following set of turbulence model parameters: $C_{\varepsilon 1}=1.44$, $C_{\varepsilon 2}=1.92$, $C_\mu=0.09$, $\sigma_k=1.0$, $\sigma_\varepsilon=1.3$.

Table 1. The data for the flow models around the cross-section of building.

Model	L_n [m]	L_z [m]	H [m]	a [m]	Number of volumes	Number of nodes	Number of edges	Remarks
No 1	0.7	4.1	1.425	0.2	12 775	13 056	25 830	Figure 2, upper surface as the wall (own research)
No 2	0.3	1.8	0.9	0.06	7 710	7 939	15 648	Figure 2, The upper surface as the inflow

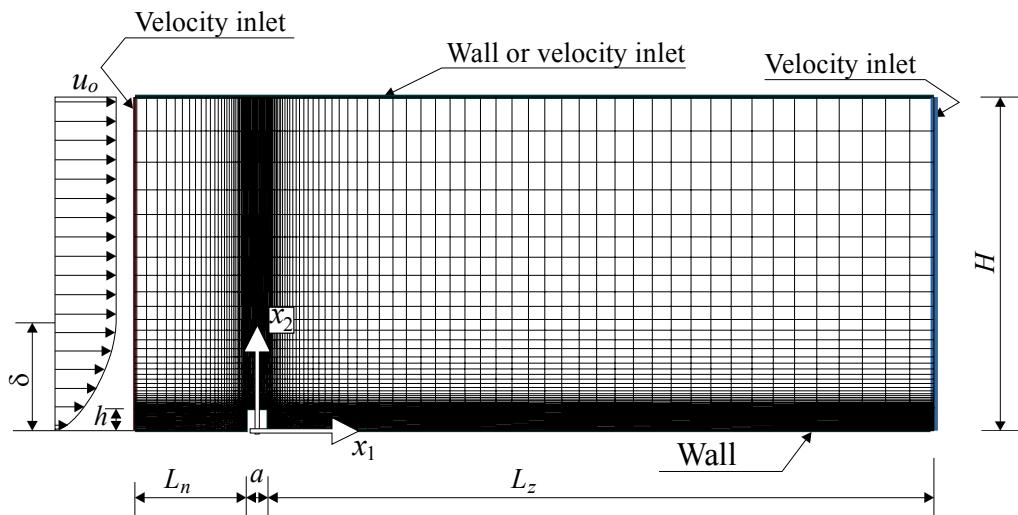


Figure 2. The scheme of the computational domain with notations.

The inflow at the upstream edge of computational domain is modeled by using the uniform value of the turbulence scale length, the turbulence intensity and a velocity which is described by the formulae:

$$\begin{aligned} u_1(x_2) &= u_h \left(\frac{x_2}{h} \right)^\alpha \quad \text{for } x_2 < \delta, \\ u_1(x_2) &= u_o \quad \text{for } x_2 \geq \delta, \end{aligned} \tag{22}$$

where: u_h – velocity on the height of the upper edge of the model, u_o – velocity beyond the boundary layer, h – height of the model.

Data of the applied model of velocity are juxtaposition in Table 2. The smooth surface of model and terrain around the model has been assumed in all calculations. The majority of analyses has been made in the reference to own research that is performed for the model No 1 and profile p7.

**Table 2. The information about the inflow velocity profiles
(according to Noda et al. (1995a)).**

Profile	u_o [m/s]	u_h [m/s]	I_u [%] (above the boundary layer)	δ [m] (the height of boundary layer)	α [/]	l [m] (turbulence length scale)	Research of
p1	25	15.4	15.3	0.3	0.30	0.054	Noda et al.. (1995a)
p2	25	18.7	10.2	0.3	0.18	0.054	
p3	25	21.0	6.6	0.3	0.11	0.066	
p4	25	22.3	7.4	0.1	0.22	0.018	
p5	25	19.7	9.5	0.2	0.20	0.048	
p6	25	18.1	10.4	0.4	0.17	0.054	
p7	10.0	9.7	6.0	0.25	0.15	H	own research

THE SENSITIVITY ANALYSIS OF THE FLOW AROUND THE MODEL AT THE GROUND

The sensitivity analysis of the flow properties around the model, described in point 3, is performed in this section. The sensitivity analysis coefficients used here and in the next points are calculated by the method of finite differences at $\Delta C_{\varepsilon 1}=0.02$, $\Delta C_{\varepsilon 2}=0.02$, $\Delta \sigma_k=0.02$, $\Delta \sigma_\varepsilon=0.02$ and $\Delta C_\mu=0.002$. The increments are well-chosen so that the error ξ , calculated from formula (5), does not exceed 10% on 80% surface of the computational domain. The exception is the component of velocity u_2 , which values are close to zero. In this case even small differences of property at $C_m + \Delta C_m / 2$ and $C_m - \Delta C_m / 2$ related to the value in the cell achieve significant values. The changes of the surface on which the assumed error ξ is not exceeded for individual coefficients are juxtaposition in Table 3–Table 7.

Table 3. The surface percentage of the computational domain where the error ξ of determination of the sensitivity coefficients in relation to the parameter $C_{\varepsilon 1}$ is smaller than the value given in the first column.

100ξ	$\tilde{P}_{C_{\varepsilon 1}}$	$\tilde{u}_{1C_{\varepsilon 1}}$	$\tilde{u}_{2C_{\varepsilon 1}}$	$\tilde{k}_{C_{\varepsilon 1}}$	$\tilde{\varepsilon}_{C_{\varepsilon 1}}$	$\tilde{\mu}_{C_{\varepsilon 1}}$
5.0%	56.88	93.02	24.31	82.80	60.53	83.75
10.0%	94.38	97.71	36.03	88.16	81.85	94.89
15.0%	100.00	100.00	45.66	95.36	87.62	98.81
20.0%	100.00	100.00	51.62	98.74	93.15	100.00
25.0%	100.00	100.00	56.25	100.00	97.03	100.00
30.0%	100.00	100.00	59.40	100.00	99.41	100.00
35.0%	100.00	100.00	62.56	100.00	100.00	100.00
40.0%	100.00	100.00	65.60	100.00	100.00	100.00
45.0%	100.00	100.00	67.23	100.00	100.00	100.00
50.0%	100.00	100.00	71.06	100.00	100.00	100.00

Table 4. The surface percentage of the computational domain where the error ξ of determination of the sensitivity coefficients in relation to the parameter $C_{\varepsilon 2}$ is smaller than the value given in the first column.

100ξ	$\tilde{p}_{C_{\varepsilon 2}}$	$\tilde{u}_{1C_{\varepsilon 2}}$	$\tilde{u}_{2C_{\varepsilon 2}}$	$\tilde{k}_{C_{\varepsilon 2}}$	$\tilde{\varepsilon}_{C_{\varepsilon 2}}$	$\tilde{\mu}_{C_{\varepsilon 2}}$
5.0%	59.42	92.33	23.21	83.29	71.09	83.11
10.0%	93.87	95.85	29.32	88.07	82.29	95.01
15.0%	100.00	98.35	37.51	94.06	87.48	98.47
20.0%	100.00	100.00	45.32	99.29	93.13	100.00
25.0%	100.00	100.00	55.25	100.00	97.47	100.00
30.0%	100.00	100.00	61.22	100.00	100.00	100.00
35.0%	100.00	100.00	66.31	100.00	100.00	100.00
40.0%	100.00	100.00	73.34	100.00	100.00	100.00
45.0%	100.00	100.00	91.16	100.00	100.00	100.00
50.0%	100.00	100.00	98.56	100.00	100.00	100.00

Table 5. The surface percentage of the computational domain where the error ξ of determination of the sensitivity coefficients in relation to the parameter C_μ is smaller than the value given in the first column.

100ξ	\tilde{p}_{C_μ}	\tilde{u}_{1C_μ}	\tilde{u}_{2C_μ}	\tilde{k}_{C_μ}	$\tilde{\varepsilon}_{C_\mu}$	$\tilde{\mu}_{C_\mu}$
5.0%	95.11	100.00	51.74	95.10	94.12	94.39
10.0%	100.00	100.00	63.94	97.87	97.78	98.33
15.0%	100.00	100.00	67.76	99.41	99.32	99.99
20.0%	100.00	100.00	72.95	100.00	99.95	100.00
25.0%	100.00	100.00	73.89	100.00	100.00	100.00
30.0%	100.00	100.00	77.98	100.00	100.00	100.00
35.0%	100.00	100.00	80.14	100.00	100.00	100.00
40.0%	100.00	100.00	85.41	100.00	100.00	100.00
45.0%	100.00	100.00	95.69	100.00	100.00	100.00
50.0%	100.00	100.00	100.00	100.00	100.00	100.00

The error ξ is considerably smaller in the case of simpler problem but in the problem, where the clear vortices appear, the violent growth of the curvature of the graph describing the dependence of the flow propriety from the model parameters is observed around the kernel of the vortex. Unfortunately in such areas the errors of the sensitivity coefficients calculated by the method of finite differences grow considerably.

Table 6. The surface percentage of the computational domain where the error ξ of determination of the sensitivity coefficients in relation to the parameter σ_k is smaller than the value given in the first column.

100ξ	\tilde{p}_{σ_k}	$\tilde{u}_{1\sigma_k}$	$\tilde{u}_{2\sigma_k}$	\tilde{k}_{σ_k}	$\tilde{\varepsilon}_{\sigma_k}$	$\tilde{\mu}_{\sigma_k}$
5.0%	89.39	98.57	29.23	84.70	82.31	87.09
10.0%	100.00	100.00	41.36	91.65	89.76	93.63
15.0%	100.00	100.00	51.74	99.05	95.67	100.00
20.0%	100.00	100.00	63.35	100.00	100.00	100.00
25.0%	100.00	100.00	71.28	100.00	100.00	100.00
30.0%	100.00	100.00	85.78	100.00	100.00	100.00
35.0%	100.00	100.00	95.77	100.00	100.00	100.00
40.0%	100.00	100.00	99.60	100.00	100.00	100.00
45.0%	100.00	100.00	100.00	100.00	100.00	100.00
50.0%	100.00	100.00	100.00	100.00	100.00	100.00

Table 7. The surface percentage of the computational domain where the error ξ of determination of the sensitivity coefficients in relation to the parameter σ_ε is smaller than the value given in the first column.

100ξ	$\tilde{p}_{\sigma_\varepsilon}$	$\tilde{u}_{1\sigma_\varepsilon}$	$\tilde{u}_{2\sigma_\varepsilon}$	$\tilde{k}_{\sigma_\varepsilon}$	$\tilde{\varepsilon}_{\sigma_\varepsilon}$	$\tilde{\mu}_{\sigma_\varepsilon}$
5.0%	64.43	93.33	24.69	82.14	76.28	74.50
10.0%	90.69	96.32	28.78	86.52	81.44	92.58
15.0%	100.00	98.73	34.96	89.85	85.76	97.52
20.0%	100.00	100.00	38.49	96.16	89.60	99.31
25.0%	100.00	100.00	43.52	100.00	94.29	100.00
30.0%	100.00	100.00	50.52	100.00	98.42	100.00
35.0%	100.00	100.00	57.77	100.00	100.00	100.00
40.0%	100.00	100.00	63.06	100.00	100.00	100.00
45.0%	100.00	100.00	66.83	100.00	100.00	100.00
50.0%	100.00	100.00	80.51	100.00	100.00	100.00

The sensitivity coefficients can be presented in the form of graphs or bitmaps for the whole computational domain. The distributions of the pressure sensitivity on walls of model No 2 are shown in Figure 3 and in the next figures there are presented: the field of the sensitivity coefficients of the component velocity u_1 (Figure 4), the kinetic turbulence energy (Figure 5), rate dissipation (Figure 6) and the turbulence dynamic viscosity (Figure 7) for model No 1. The areas of large sensitivity are visible on these figures and therefore they can be used to point the location of significant errors. Whereas the fields of sensitivity coefficients cannot be used in comparisons of the coefficients of the sensitivity of various properties. More useful are relative values to obtain this aim. They are determined on the basis of formulae (12)÷(17) and presented in Table 8 and Figure 8.

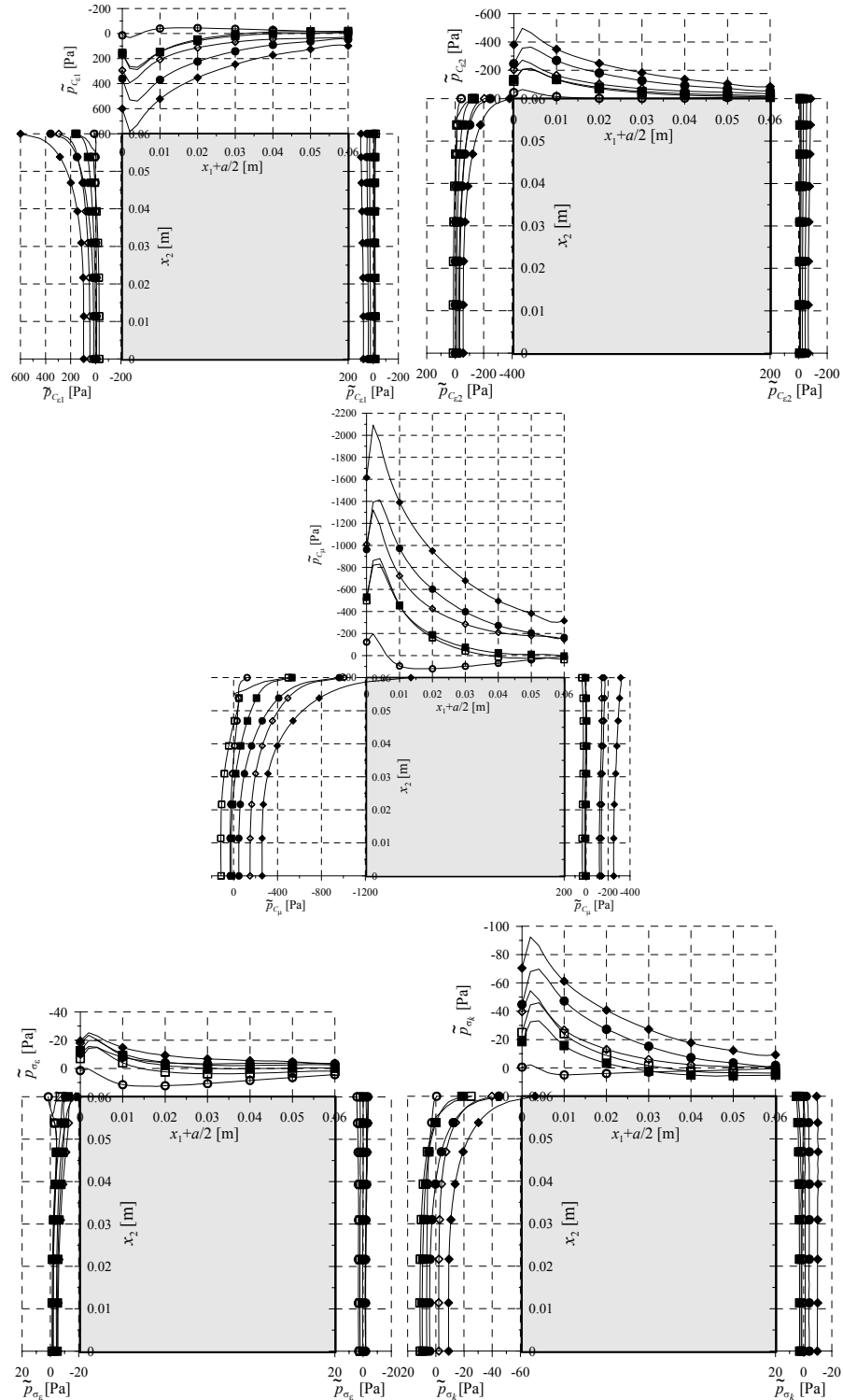


Figure 3. The distribution of pressure sensitivity on the walls of the model No 2 received for the set of methods S0 (comp.) in reference to various profiles: \circ - p1; \diamond - p2; \blacklozenge - p3; \bullet - p4; \square - p5; \blacksquare - p6.

As it can be seen in Figure 3 the largest pressure sensitivities are obtained in the upstream part of the upper edge. The sensitivity diminishes along this edge but the coefficients of the sensitivity on the whole length are nevertheless larger than on remaining walls. The values of pressure sensitivity on the ground behind the model reach very high values, comparable to the ones on the upper wall of the model, but it is of the opposite sign.

In Figure 4 there have been shown the fields of the velocity sensitivity coefficients. It can be seen two clear areas of large sensitivities on all parts of this figure: behind the model and on the border of the aerodynamic wake. Such area also exists over the upper surface of the model No 2. The sensitivity of the kinetic energy, shown in Figure 5, reaches quite considerable values in the upper upstream corner, but it achieves extreme values behind the model. The location of this area agrees with the area of the large velocity sensitivities.

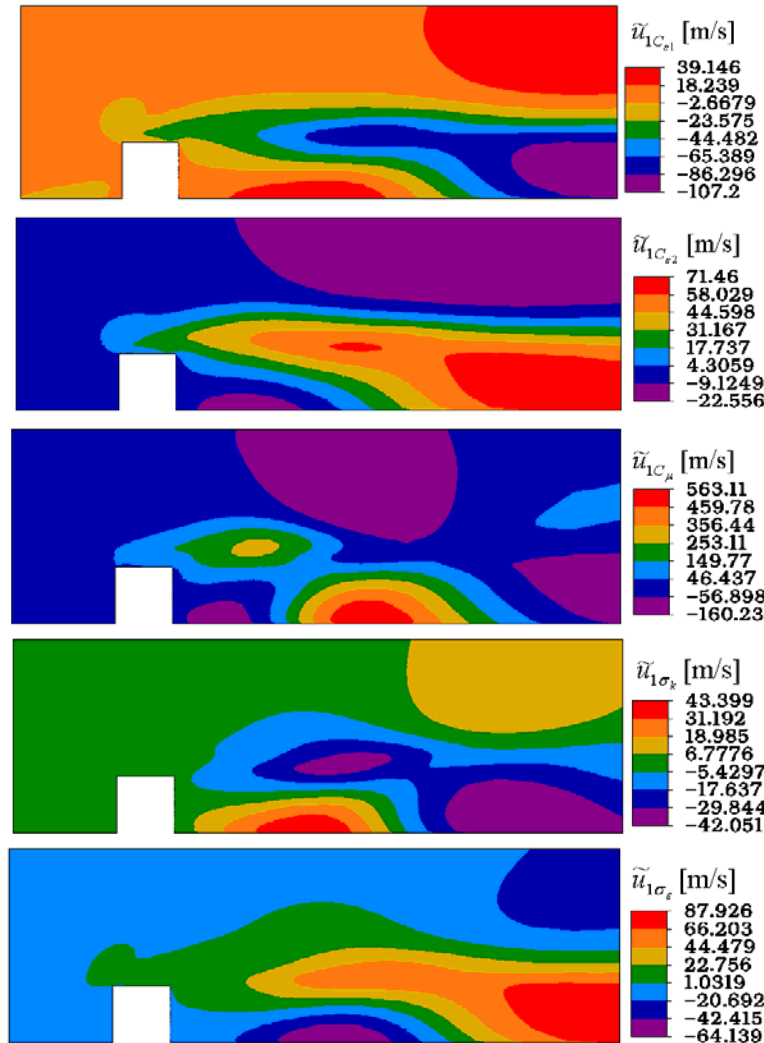


Figure 4. The fields of the velocity sensitivity for the model No 1 received for the set of methods S0 (comp.)

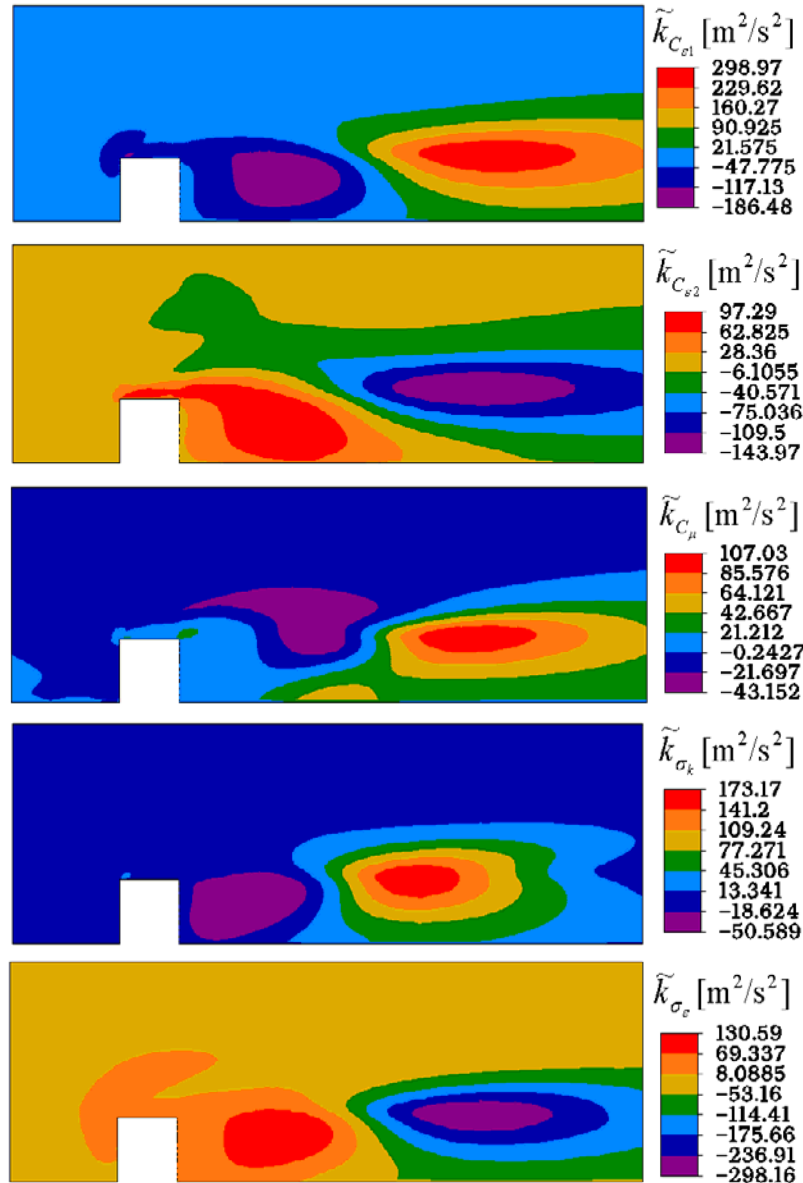


Figure 5. The fields of the sensitivity of turbulence kinetic energy for model No 1 received for the set of methods S0 (comp.).

The dissipation sensitivity achieves the largest values but the area of these larger values placed near upper upstream corner is small. Among others that is why in Figure 6 there is shown only small fragment of the field of the sensitivity around the upper part of the model.

The extreme sensitivity values of the turbulence dynamic viscosity also occur behind the model. In Figure 7 two areas of the large values are visible and they are situated similarly as areas of the large sensitivities of the turbulence kinetic energy.

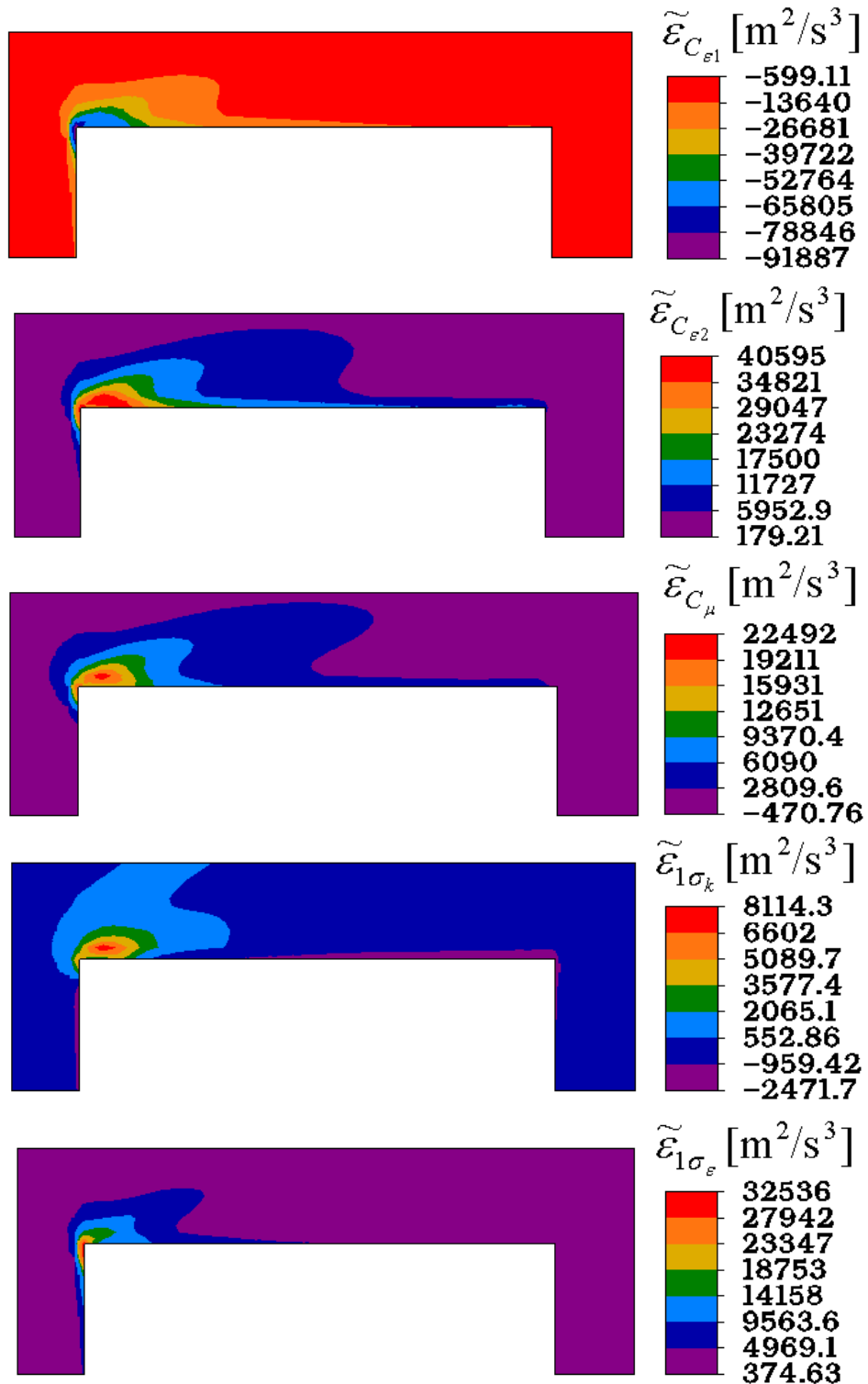


Figure 6. The fields of the sensitivity of rate dissipation of the kinetic turbulence energy around the top edge of the model No 1 received for the set of method S0 (comp. Tab. 9).

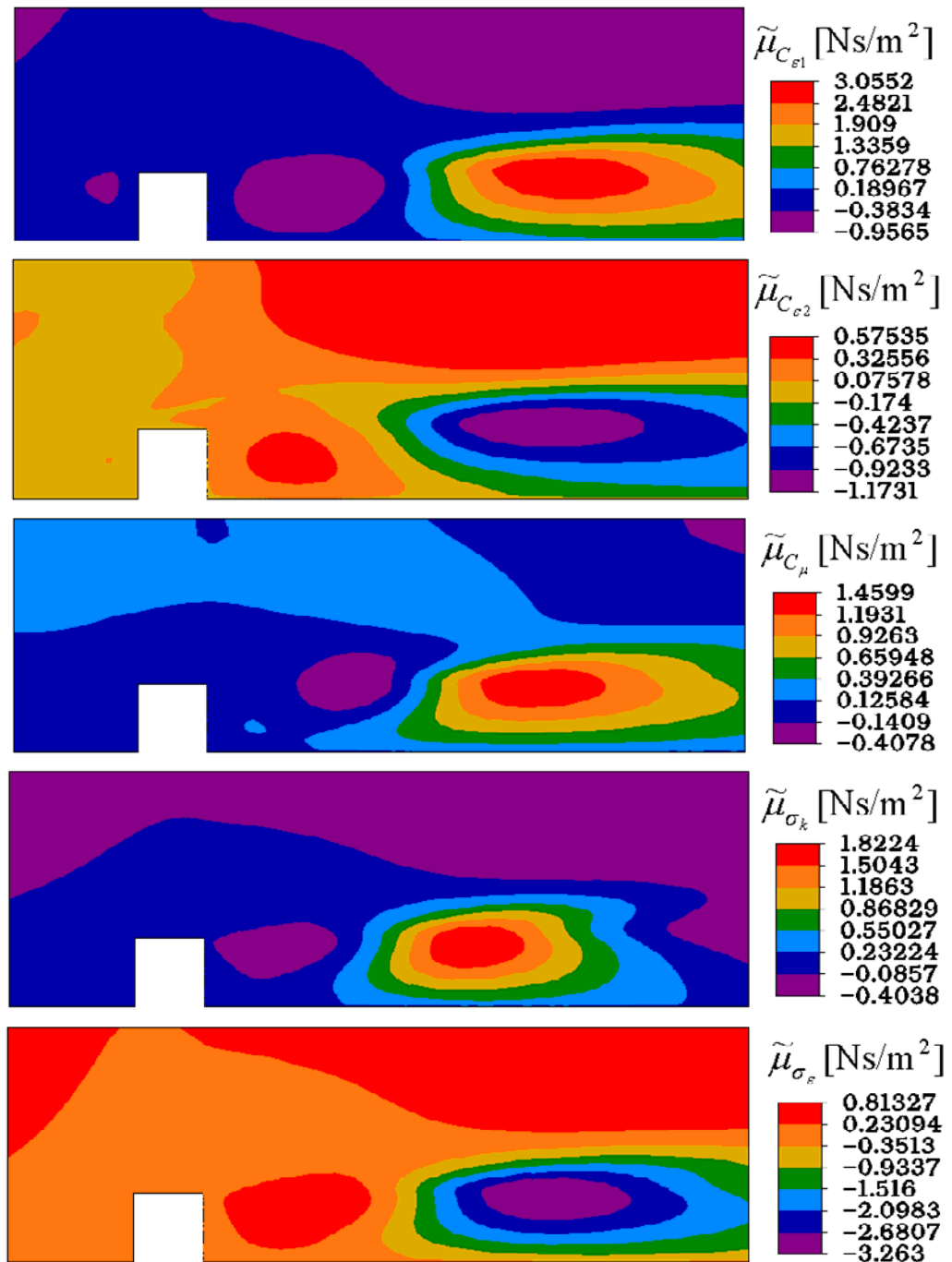


Figure 7. The fields of the sensitivity of turbulence dynamic viscosity for the model No 1 received for the set of method S0 (comp. Tab. 9).

Table 8. The extreme sensitivity coefficients of all parameter in reference to model No 2.

	$C_{\varepsilon 1}$		$C_{\varepsilon 2}$		C_{μ}		σ_k		σ_{ε}	
	min	max	min	max	min	max	min	max	min	max
\tilde{p}_m [Pa]	-199.7	383.17	-296.1	135.08	-1521.1	728.21	-63.914	45.441	-28.131	84.226
\check{p}_m	-0.664	0.480	-0.452	0.513	-1.969	2.635	-0.100	0.119	-0.069	0.220
$C_m \tilde{p}_m$ [Pa]	-287.568	551.7648	-568.512	259.3536	-136.899	65.5389	-63.914	45.441	-36.5703	109.4938
\tilde{u}_{1m} [m/s]	-16.568	4.499	-4.439	14.175	-15.601	71.59	-0.848	4.398	-2.998	2.776
\check{u}_{1m}	-0.663	0.180	-0.178	0.567	-0.624	2.864	-0.034	0.176	-0.120	0.111
$C_m \tilde{u}_{1m}$ [m/s]	-23.8579	6.47856	-8.52288	27.216	-1.40409	6.4431	-0.848	4.398	-3.8974	3.6088
\tilde{u}_{2m} [m/s]	-5.095	6.940	-4.444	5.063	-27.088	20.831	-0.856	1.014	-1.726	1.449
\check{u}_{2m}	-0.204	0.278	-0.178	0.203	-1.083	0.833	-0.034	0.041	-0.069	0.058
$C_m \tilde{u}_{2m}$ [m/s]	-0.29376	0.40032	-0.34176	0.38976	-0.09747	0.07497	-0.034	0.041	-0.0897	0.0754
\tilde{k}_m [m ² /s ²]	-144.5	0.085	-0.016	83.846	-185.76	291.11	-22.694	39.769	-0.459	44.959
\check{k}_m	-3.106	0.004	-0.0007	3.066	-6.019	6.577	-0.754	0.535	-0.021	0.955
$C_m \tilde{k}_m$ [m ² /s ²]	-208.08	0.1224	-0.03072	160.9843	-16.7184	26.1999	-22.694	39.769	-0.5967	58.4467
$\tilde{\varepsilon}_m$ [m ² /s ³]	-404671	10899	-6408.24	231215	-10971.1	1565491	-35359	59939.3	-584.872	118918

Table 8. Continued.

	$C_{\varepsilon 1}$		$C_{\varepsilon 2}$		C_μ		σ_k		σ_ε	
	min	max	min	max	min	max	min	max	min	max
$\check{\varepsilon}_m$	-5.733	0.570	-0.532	6.447	-4.742	19.730	-2.613	0.586	-0.260	2.321
$C_m \check{\varepsilon}_m$ [m^2/s^3]	-582726	15694.56	-12303.8	443932.8	-987.399	140894.2	-35359	59939.3	-760.334	154593.4
$\tilde{\mu}_m$ [Ns/m ²]	-0.176	0.0003	0	0.155	-0.020	0.581	-0.054	0.025	-0.0056	0.078
$\check{\mu}_m$	-1.036	0.0018	0	0.916	-0.116	3.416	-0.320	0.145	-0.033	0.460
$C_m \tilde{\mu}_m$ [Ns/m ²]	-0.25344	0.000432	0	0.2976	-0.0018	0.05229	-0.054	0.025	-0.00728	0.1014

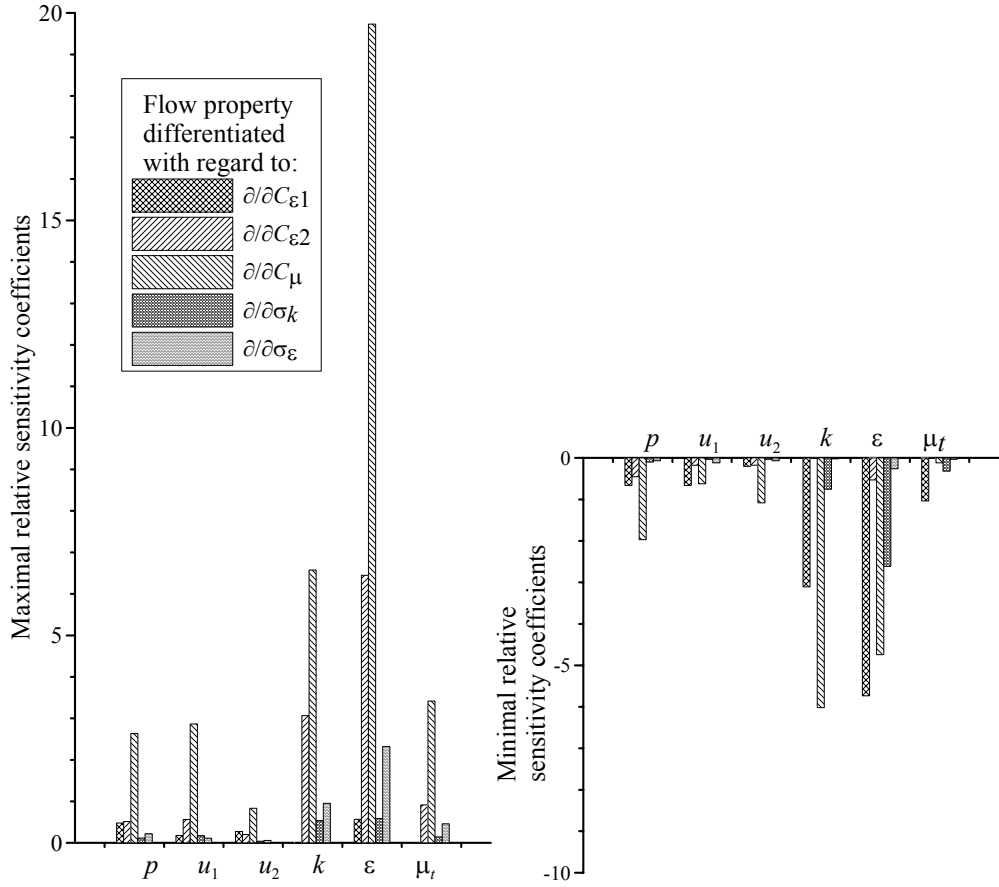


Figure 8. The comparison of extreme relative sensitivity coefficients of all parameters in the reference to model No 2.

The comparison of the sensitivity of various flow properties to the various model parameters should be made on the basis of the relative sensitivity coefficients. The values of such coefficients are set against each other in Table 8 and in Figure 8. The rate dissipation is the most sensitive flow property to model parameters. The turbulence kinetic energy is the next property because of the magnitude of the sensitivity. The velocity and pressure are less sensitive to the choice of parameters than the remaining flow properties. The sensitivity for other sets of parameters can considerably differ, but the mentioned order of parameters is always kept in the sensitivity analysis. It is confirmed by the research presented in such papers as Błazik-Borowa (2007c) and Błazik-Borowa (2008).

It comes from the comparison of the sensitivity of flow properties to the various model parameters that the largest sensitivities occur for the C_μ parameter. However it should be noted that this parameter is one order smaller than the remaining ones and if we compare the sensitivity coefficients received after multiplying the sensitivity coefficients by the suitable model parameter (comp. Table 8), then it can be found that the parameters $C_{\varepsilon 1}$ and $C_{\varepsilon 2}$ have the largest influence on calculations.

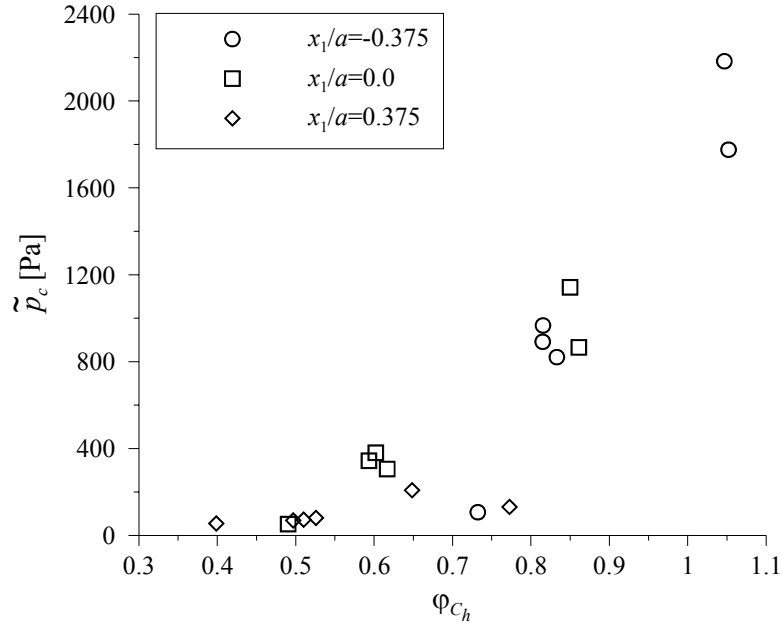


Figure 9. The dependence between the calculations error φ_{ch} (equation (18)) and the total pressure sensitivity \tilde{p}_c (equation (21)) on the upper wall of the model No 2.

The sensitivity analysis shows not only mutual relationships between the individual sensitivity coefficients, but large sensitivities also show the areas of domain where computational errors are the largest. The model parameters are the factors of terms of the set of equations (1) which contain derivatives with regard to co-ordinates. If the values of these terms are large, then the influence of such factor on the result of the solutions is larger, as well. Taking into consideration the fact that the largest errors occur in areas where the largest gradients of the flow properties are, it can be noted that the areas of the largest sensitivities coincide with the areas of the largest errors. This fact also confirms Figure 9, in which the dependence between the calculation errors and total influence of the model parameters on pressure \tilde{p}_c on upper wall of model in three points is shown. The calculation results in three points of the upper edge presented in the figure in the reference to the model No 2 performed for six profiles of the wind velocity (comp. Table 2). In Figure 9 you can see not only the growth of the errors together with the growth of sensitivity in one point, but such visible tendency is on the whole graph. The lack of the exact regularity of dependence among errors and sensitivity coefficients comes from the various conditions of making calculations, the errors of the measurements and the errors of reading the results of the measurement from literature.

THE ANALYSIS OF THE INFLUENCE OF SELECTED NUMERICAL METHODS ON QUALITY OF THE SOLUTION

In previous section the general sensitivity analysis of the flow properties to the $k-\varepsilon$ model parameters is made and the dependence between the sensitivity and the calculations errors has

been presented. In this section the sensitivity analysis is applied to determine the numerical methods used in approximation of flow properties in the mesh volumes and to solve the set of equations.

THE DESCRIPTION OF ANALYSED NUMERICAL METHODS

Before starting the analysis of results the short description of examined numerical methods (the methods of solving the set of the equations and the flow properties approximation) is presented. Two methods of solving the set of equations are used in presented calculations:

- the *segregated* method, in which velocity is calculated as first, the next determined property is pressure and, finally, other parameters are calculated based on known the velocity and pressure values,
- the *coupled* method, in which velocity and pressure are simultaneously calculated as first and other parameters are determined based on them.

Using the finite volume method average values in cells are obtained as the calculation results. However, the flow properties are variously approximated in the volume during the calculations which depend, among the others, on the determination of curvilinear and surface integrals. The most often way is to assume that properties are constant or vary linearly. The additional methods of the pressure approximation are applied because of the difficulties which occur at the determination of the pressure in the *segregated* method. The following methods are used in Fluent 6.1 program (2003):

- *standard* - the values of pressure in the middle of the edge are calculated from Navier-Stokes motion equations prepared in the reference to these points, but also by using the velocity values from the volume centres, this method is called the Rhie-Chow method (comp. Rhie and Chow(1983)),
- *linear* - the pressure value is constant in the volume and the values on the edge are average values from neighbouring elements,
- *second* - the pressure varies linearly in the volume, and the value on the edge is taken from the upstream edge (according to the flow direction),
- *presto!* - two meshes are used in calculations and one of them is moved in such a way that its volumes centres would be placed on the edges of second mesh; the pressure values are calculated on the edges of the first mesh which include the centres of the volume of second mesh and the other flow parameters are calculated inside the volumes of the first mesh,
- *body force weighted* – in this method it is assumed that the gradient of the difference between the pressure and mass forces is constant in the volume.

Table 9. The variants of methods used in calculations.

Variant	Method of solving the set of equations	Assumption of constant parameter value	Linear approximation of parameter	Method of pressure approximation
C0	<i>coupled</i>	k, ε	$u_1, u_2,$	-----
C1	<i>coupled</i>	ε	u_1, u_2, k	-----
C2	<i>coupled</i>	-----	u_1, u_2, k, ε	-----
C3	<i>coupled</i>	u_1, u_2, k, ε	-----	-----
C4	<i>coupled</i>	u_1, u_2	k, ε	-----
C5	<i>coupled</i>	k	u_1, u_2, ε	-----
S0	<i>segregated</i>	k, ε	$u_1, u_2,$	<i>Standard</i>
S1	<i>segregated</i>	k, ε	$u_1, u_2,$	<i>Presto!</i>
S2	<i>segregated</i>	k, ε	$u_1, u_2,$	<i>Linear</i>
S3	<i>segregated</i>	k, ε	$u_1, u_2,$	<i>Second</i>
S4	<i>segregated</i>	k, ε	$u_1, u_2,$	<i>Body force weighted</i>
S5	<i>segregated</i>	u_1, u_2, k, ε	-----	<i>Linear</i>
S6	<i>segregated</i>	ε	u_1, u_2, k	<i>Linear</i>
S7	<i>segregated</i>	-----	u_1, u_2, k, ε	<i>Linear</i>
S8	<i>segregated</i>	u_1, u_2	k, ε	<i>Linear</i>
S9	<i>Segregated</i>	k	u_1, u_2, ε	<i>Linear</i>

The detailed description of mentioned methods, concerning both solving the set of equations and approximation of flow properties, can be found in papers of such authors as: Patankar (1980), Rhee and Chow (1983), Chung (2002) and in Fluent 6.1 program documentation (2003). Whereas, here, the influence of these methods on solutions is presented on the basis of comparisons of measurements in wind tunnel and calculations and of the sensitivity analysis of the flow properties to the model parameters. Therefore sixteen tasks which differ from one another in applied methods have been analysed, and data for the set of used methods is placed in Table 9.

The calculations usually require the use of various methods of both solving the set of equations and the approximation of flow properties. In case of complex problems or the large-sized tasks it is impossible to solve such problem by simultaneously solving all differential equations describing the flow. Therefore solution of the problem begins with methods which solve individual equations separately. In case of FLUENT 6.1 program it is the *segregated* method. Moreover, in the first step the method of the flow properties approximation, which also causes simplification of the problem, can be applied. Then, having first approximate solution, not necessarily obtained with large accuracy, more appropriate methods of properties approximation and solving the set of equations can be used. The reason of application of the methods depends on the analysed problem. Sometimes the *coupled* method can be applied already in the first step of calculations, but there are cases that task cannot be solved with this method at once regarding its size. Sometimes if it is not preceded by the *segregated* method it can result with the divergence of iterative process. The problem analysed in this chapter is a simple enough task to be solved with similar number of iterations and the same accuracy of calculations with use of any of the methods juxtaposition presented in Tab. 9.

The problem of the influence of approximation methods on quality of solutions is presented in reference to the model No 1 with wind profile p7. The research includes three parts:

- analysis of influence of pressure approximation methods;
- analysis of influence of velocity, kinetic energy and dissipation approximation methods;
- analysis of influence of solving the set of equations methods.

THE EVALUATION OF THE QUALITY OF RESULTS ON THE BASIS OF THE COMPARISON OF THE MEASUREMENTS AND CALCULATIONS RESULTS

Figure 10÷Figure 13 show the comparison of calculation results, obtained with methods listed in Tab. 9, with results of own research in the wind tunnel. The used numerical methods and the way of their application in calculations strongly influence on the obtained results and their quality and it is clearly seen on example of the flow around the model located at the ground. Often the same methods, in this case methods of solving the set of equations and the approximation, together with different numerical methods can cause the obtained results to be completely different. Therefore it is difficult to evaluate mathematical models applied in computer programs because results obtained from them depend on their numeric description.

The comparison of the pressure distribution which are obtained by using different approximation methods of this property has been shown in Figure 10. The differences between the graphs are not visible. The exception is the graph for the set of methods C0 where method used to solve the set of equations is different from the other cases. The differences between graphs of the pressure are not clear as well as these differences are not clearly visible on graphs of the velocity obtained with different methods of the pressure approximation. This means that the methods of pressure approximation have negligible influence on pressure distributions and velocity fields.

However, in case of approximation methods of other flow properties there are bigger differences between calculation results. The graphs of pressure shown in Figure 11 differ most of all from each other on upstream side of model, and the least on upper edge. The graphs of velocity shown in Figure 12 and Figure 13 are almost the same, over model as well, but there are clear differences between them in aerodynamic wake of the model. Both the results presented for the pressure and for the velocity show that the worst results are obtained by applying sets of methods S5, S8, C3 and C4 that is when the velocity of flow is approximated as constant in the volume. The selection of the best results is not so unambiguous, but it seems, that it can be assumed, that the graphs, obtained with the sets of methods S0 and C0 are the best, it is for the situation when the turbulence kinetic energy and the rate dissipation are constant in the volume and the velocity is approximated by the linear function.

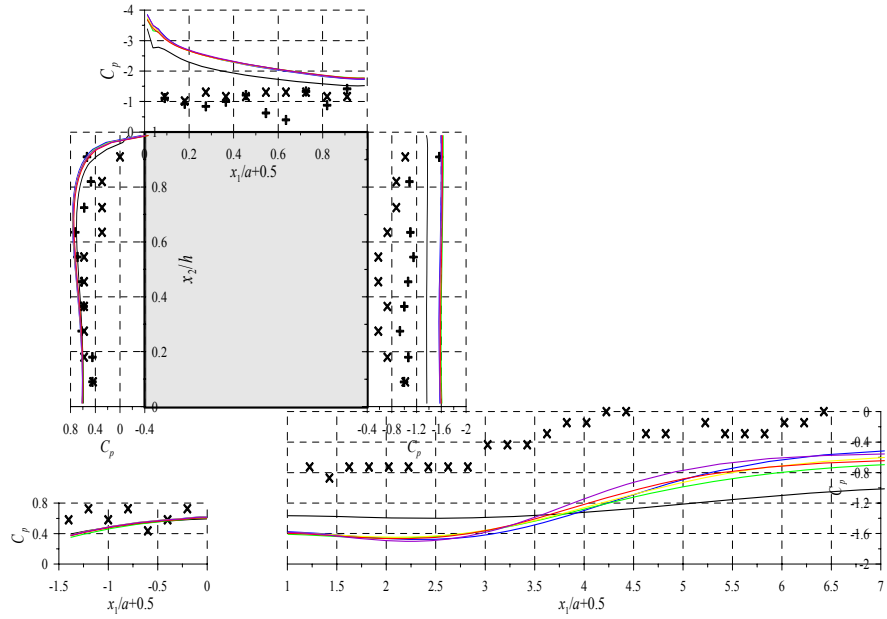


Figure 10. The graphs of the pressure coefficient C_p (where $C_p = \frac{P}{0.5\rho u_o^2}$) with regard to different methods of pressure approximation for model No 1 and the profile p7 obtained with use of the *segregated* method: \times own research from the battery of manometers; $+$ own research from the pressure scanner; — - C0; — - S0; — - S1; — - S2; — - S3; — - S4.

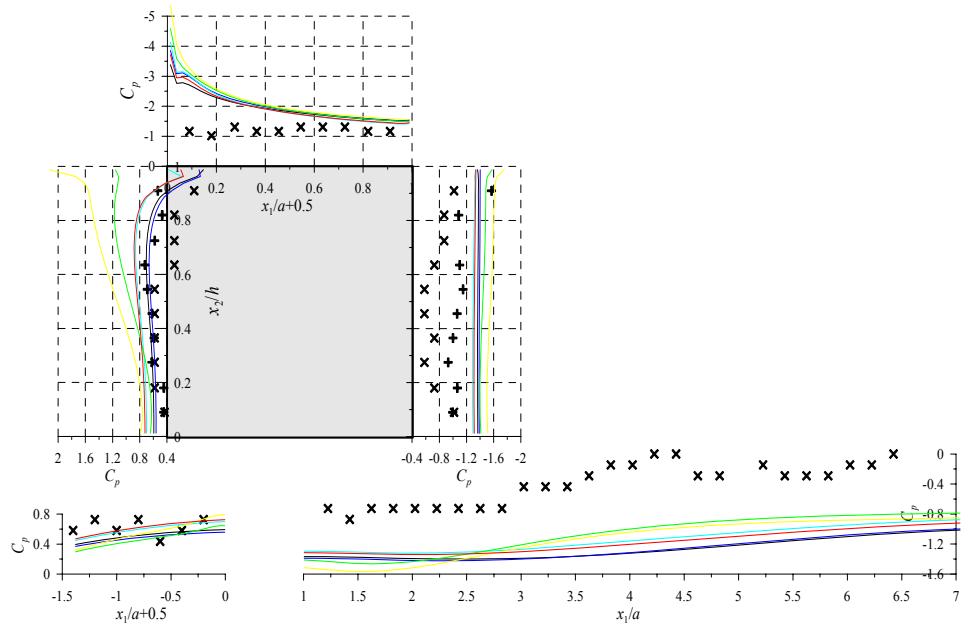


Figure 11. The graphs of pressure coefficient C_p with regard to different methods of pressure approximation for model No 1 and the profile p7 obtained with use of the *coupled* method: \times own research from battery of manometers; $+$ own research from the pressure scanner; — - C0; — - C1; — - C2; — - C3; — - C4; — - C5.

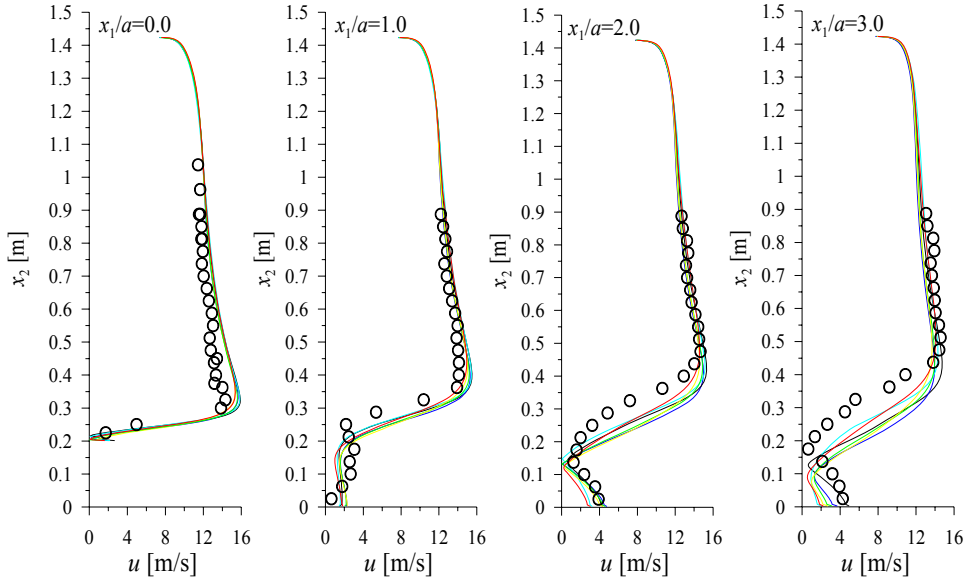


Figure 12. The graphs of velocities obtained with use of the *segregated* method and the different methods of flow parameters approximation with regard to model No 1 and the profile p7: \circ - own research; — - S0; — - S5; — - S6; — - S7; — - S8; — - S9.

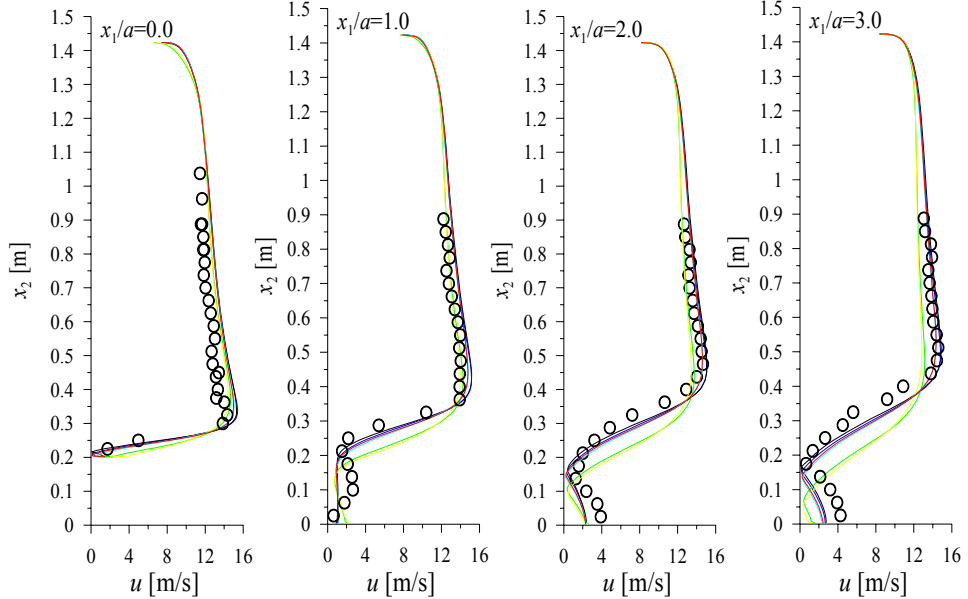


Figure 13. The graphs of resultant velocities u obtained with usu of the *coupled* method and the different methods of flow parameters approximation with regard to model No 1 and the profile p7: \circ - own research; — - C0; — - C1; — - C2; — - C3; — - C4; — - C5.

All the figures presented in this subsection show that the best results are obtained by simultaneously solving the biggest number of equations of the k - ε model that is in FLUENT program by the *coupled* method. Obviously this statement relates to these tasks only where the obtaining the results with both analysed here methods of solving the set of equations is possible. Often the more complex problems must be first solved with the *segregated* method and then, if this is possible, corrected with the *coupled* method.

THE SENSITIVITY ANALYSIS OF THE SOLUTION WITH REGARD TO APPLIED NUMERICAL METHODS

The results of comparison of measurements and calculations allow to find out which sets of numerical methods are the best. Using the sensitivity analysis these conclusions will be confirmed and additionally supplemented by new dependences between the quality of results and the used numerical methods. At the beginning the possibility of different interpretations of sensitivity analyses results to the parameters of the k - ε method should be reminded. In case of the comparison of the task solutions which have been obtained with different methods of approximation, the bigger sensitivity means the more exact description of the problem.

The areas of different levels of the results conformity are visible in figures containing comparison of calculations and measurements. This is why the average sensitivities of the flow properties to the model parameters, appointed according to formula (20), are presented in Figure 14 and Figure 15. The pressure sensitivity is averaged with regard to following areas: in front of the model, on the walls of model and on the ground behind the model. The velocity sensitivity is averaged in the individual cross-sections of the computational domain, starting with the cross-section in front of the model in the distance about 0.1m from its upstream side that is $0.5a$ from it.

The first conclusions concern the choice of modelling methods based on pressure sensitivity. In Figure 14 the sensitivities of pressure approximated with different methods are presented, i.e. bigger sensitivity on this figure means better quality of the solution. Unfortunately the pattern of averaged pressure sensitivity is not the same for all the parameters, which makes the analysis results more complicated. However, if we estimate the total influence of all parameters on the pressure, shown in the form of the average sensitivity in Figure 14, and if we consider the fact that parameters $C_{\varepsilon 1}$ and $C_{\varepsilon 2}$, have the biggest influence on solutions, then it can be stated that *standard* and *linear* methods are the best among methods used together with the *segregated* method.

The solutions obtained by two methods of solving the set of equations are compared in Figure 15. Since these methods do not influence on the level of the flow property approximation, it seems that the principle that the bigger sensitivity coefficients values mean bigger computational errors should be applied. Hence, on the basis of the comparison of parts a) and b) from Figure 15 it can be denoted that results obtained with the *coupled* method are less sensitive to the model parameters and the method is more effective than the *segregated* one.

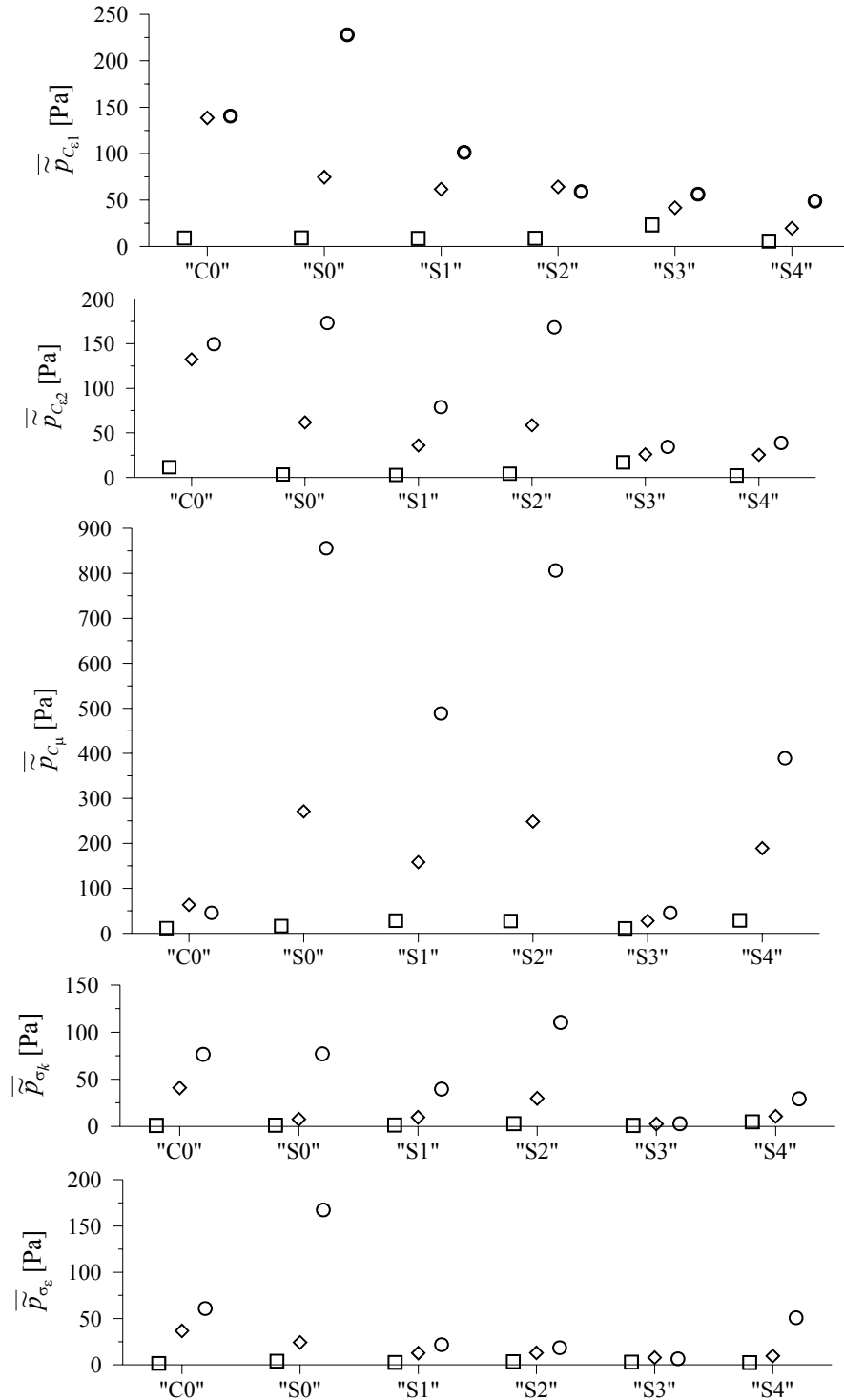


Figure 14. The average sensitivity pressure for the different methods of the pressure approximation; \square - the sensitivity in front of the model; \diamond - on the walls of the model, \circ - behind the model.

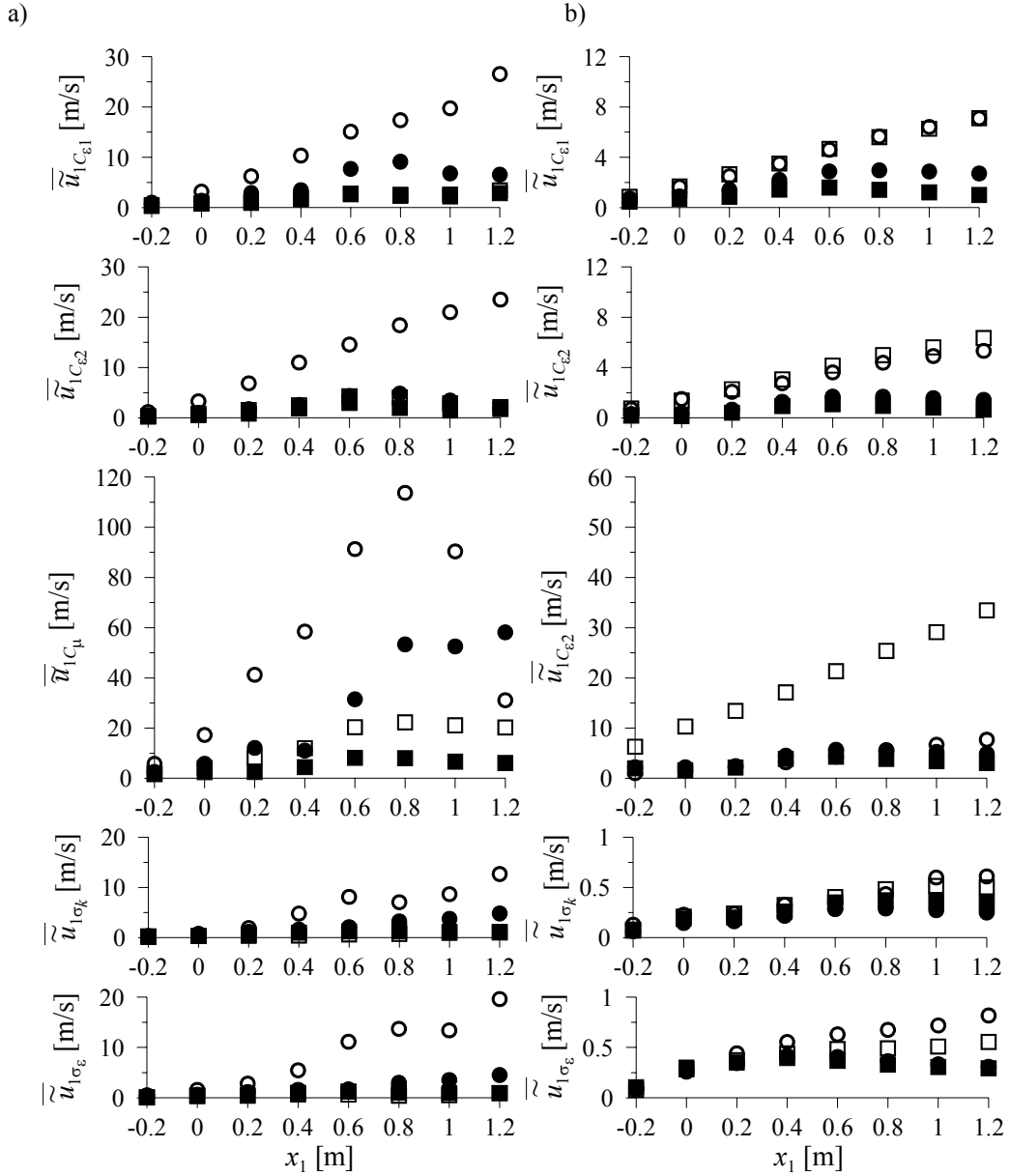


Figure 15. The graphs of the average velocity sensitivities along computational domain for the various methods of the approximation of a velocity, the kinetic turbulence energy and its dissipation (see: Tab. 9): a) segregated method, b) coupled method; ● $[u_1, u_2, k, \varepsilon]$ [-]; ○ $[k, \varepsilon] [u_1, u_2]$; ■ $[u_1, u_2] [k, \varepsilon]$; □ [-] $[u_1, u_2, k, \varepsilon]$.

THE RESEARCH OF SOLUTIONS WITH VARIOUS NUMERICAL METHODS

In this subsection the evaluation of the solutions quality based on applied methods is made. In section 5.2 the results of calculations and measurements in the wind tunnel have

been compared and in section 5.3 the sensitivity analysis of the individual solutions has been made. The conclusions from both of these methods are the same, what confirms the usefulness of the sensitivity analysis for the research of solutions quality. Whereas the results of presented research are the following statements:

- *coupled* method of solving the equations guarantees better results, but unfortunately it cannot be applied in each of the cases;
- methods which assume that the pressure is constant in the volume should be applied to model the pressure;
- velocity should be approximated by the polynomial of at least the same degree as the turbulence kinetic energy and its dissipation, however, the best results are obtained by approximation of the velocity with the linear function, and the kinetic turbulence energy and its dissipation with the constant or linear function.

At the selection of the calculations methods it should be also remembered that the calculations results do not depend only on the method itself, but also on the accuracy of its description in the computer program. Therefore, conclusions presented in this section may be untrue in reference to the other program which is not tested well enough, in which numeric methods are incorrectly applied, or which is not optimised regarding the used computer processor and memory.

THE CHOICE OF THE FVM MESH BASED ON THE SENSITIVITY ANALYSIS

The density of the FVM mesh depends on the character of the flow, which subsequently depends on the flow geometry around the objects and on the level of the turbulence represented by the Reynolds number Re .

It is very difficult to estimate the influence of Reynolds number on the quality of results, because parameters which are used to calculate the Reynolds number influence the kinetic energy and farther on the value of nondimensional distance x_n^* (defined as $x_n^* = \frac{\rho C_\mu^{1/4} k^{1/2} x_n}{\mu}$).

This variable is used to calculate the thickness of laminar sublayer near the wall, and so it determines the profile of the velocity function. Growth of the Reynolds number of one order causes the one-order growth of the x_n^* distance. In case of too large nondimensional distance value the viscosity layer of the flow is too wide and in the case of too small number x_n^* it is too narrow. In effect velocity values in the boundary layer are incorrectly evaluated.

In the following research the change of the Reynolds number has been modelled by the change of the air viscosity. The analysis of results consists of the comparison of the tasks solutions with the same mesh and different Reynolds numbers. The comparison of problems with different meshes and Reynolds numbers, but with the same x_n^* values is impossible, because density of the mesh is too influential on the quality of solution and the sensitivity of the $k-\varepsilon$ model to its parameters. Moreover, too dense mesh can cause numerical errors, but too

coarse mesh must give completely incorrect results, even if the correct value of the x_n^* distance is kept. This last situation appears at low Reynolds numbers with regard to which the $k-\varepsilon$ model should not be applied. The information about the analysed tasks is listed in Table . The bolded numbers represent the correct or the acceptable the x_n^* values.

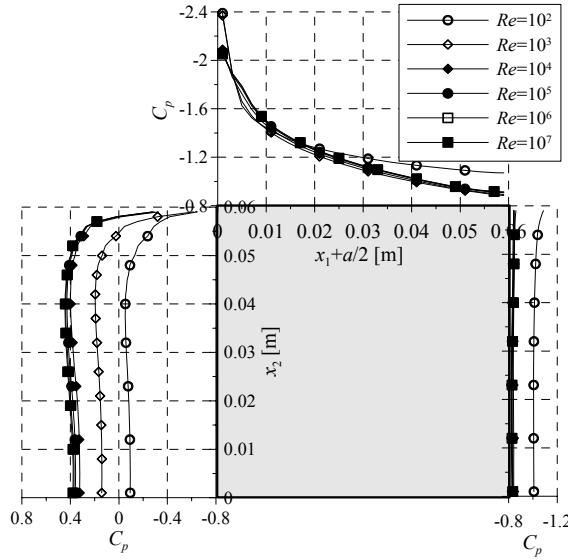


Figure 16. The distribution of the pressure coefficient on the surface of model No 2 with the same meshes and various Re .

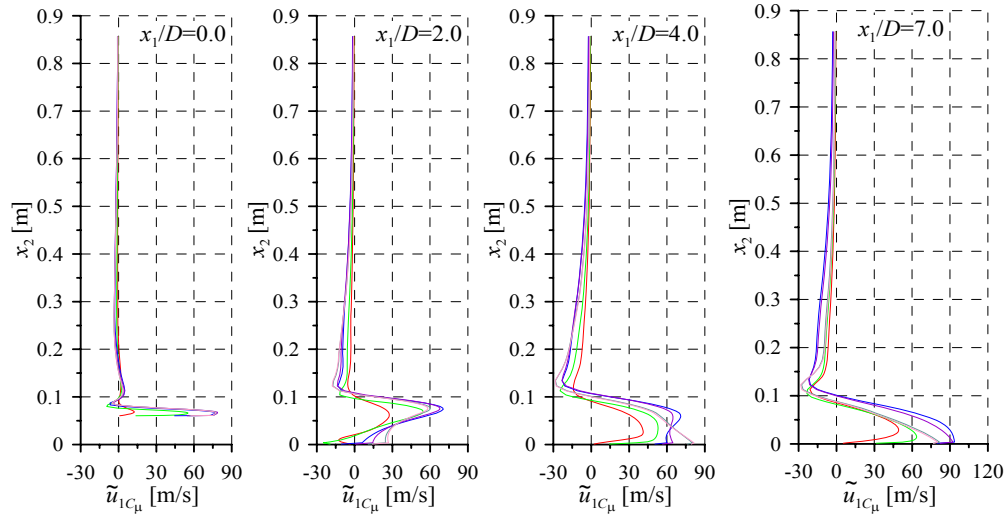


Figure 17. The exemplary graphs of the velocity sensitivity \tilde{u}_{1C_μ} behind the square with the same calculation models: — $Re=1 \cdot 10^2$, — $Re=1 \cdot 10^3$, — $Re=1 \cdot 10^4$, — $Re=1 \cdot 10^5$, — $Re=1 \cdot 10^6$, — $Re=1 \cdot 10^7$.

Table 10. The tasks with Reynolds numbers and the nondimensional distance x_n^* .

$Re [~]$	$x_n^* [~] (\text{maximum})$	Number of volumes
$1.0 \cdot 10^2$	0.3	7830
$1.0 \cdot 10^3$	2.4	7830
$1.0 \cdot 10^4$	5.0	7830
$1.0 \cdot 10^5$	50	7830
$1.0 \cdot 10^6$	490	7830
$1.0 \cdot 10^7$	4970	7830

The distributions of pressures and their sensitivities obtained at various Reynolds numbers and shown in Figure 16 almost do not differ, except from the results with $Re = 100$. Whereas the differences are visible on the velocity sensitivity graphs (Figure 17). The simple dependence between Reynolds number and sensitivity cannot be noticed in Figure 17. The change of the sensitivity is connected with the correctness of the velocity approximation here and so is with the quality of the mesh. The meshes are correct at the Reynolds numbers order of 10^4 and 10^5 and for these calculations the obtained sensitivity is the biggest. In other cases the meshes are too coarse at bigger Reynolds numbers or too dense at smaller Reynolds numbers. The sensitivity decreases for more coarse meshes because non-linear functions are „straightened” as the result of the wrong approximation. Too dense mesh causes the velocity and other flow properties to be described by correct curvilinear functions only in small part of boundary layer. In other parts they are assumed as constants in cells, and it also reduces the gradients in boundary layer.

The above described dependence can be applied to check the quality of the mesh with regard to the given Reynolds number, i.e. if we make several meshes of the finite volume method, and next we analyse the sensitivity coefficients then the best mesh gives the biggest sensitivities for the given Reynolds number.

CONCLUSION

This chapter is devoted to the sensitivity analysis of calculation results to the parameters of the $k-\varepsilon$ turbulence model. The sensitivity analysis is presented as the research tool of the solutions quality, but first of all its results allow us to bring attention to the problem of the selection of $k-\varepsilon$ model coefficients.

The examples of the sensitivity analysis application presented in the chapter are: the solutions quality research at different numerical methods and suggestion of method for checking the FVM mesh. The aim of presented research is not only to show the problem of the choice of the FVM meshes, though these are quite important problems, but to prove that the analysis can be applied in practice.

The author has presented the sensitivity analysis on one example, but all analyses conclusions have been also confirmed by the channel flow research, which is presented in the paper Błazik-Borowa (2008) and by the research of the flow around the free square which is presented in the paper Błazik-Borowa (2007c).

REFERENCES

- [1] Błazik-Borowa, E. *The sensitivity analysis of CFD problems with using the k-ε model on “constants” of the Turbulence Model*, Systems, Journal of Transdisciplinary Systems Science, 2006, 11, 1 (Appendix), 145-152.
- [2] Błazik-Borowa, E. *The application of the sensitivity analysis of flow properties to parameters of the k-ε method*, Proc. of the 17th International Conference on Computer Methods in Mechanics, 2007a, 91-92.
- [3] Błazik-Borowa, E. *The influence of input flow properties on the quality of the solution obtained with using the k-ε turbulence model* in Environmental Effects on Buildings, Structures, Materials and People, Flaga, A., Lipecki, T., Lublin University of Technology Printing Services, Lublin, 2007b, 151-160.
- [4] Blazik-Borowa, E. *The sensitivity analysis of the flow around a square cylinder to parameters of the k-ε method*, Proc. of the 12th International Conference on Wind Engineering, 2007c, Vol. II, 1919-1926.
- [5] Blazik-Borowa, E. *Analysis of the channel flow sensitivity to the parameters of the k-ε method*, International Journal for Numerical Methods in Fluids, 2008, 58, 1257-1286.
- [6] Błazik-Borowa, E., Bęc, J., Nowicki, T., Lipecki, T., Szulej, J. *Measurements of 2-D flow parameters around rectangular prosms arranged at the ground*, Budownictwo i Architektura, 2008, 3, 33-51.
- [7] Bradshaw, P., Ferriss, D.H., Atwell, N.P. *Calculation of boundary layer development using the turbulent energy equation*, Journal of Fluid Mechanics, 1967, 28, 593-616.
- [8] Chou, P. Y. *On velocity correlations and the solutions of the equations of turbulent motion*, Quart. of Applied Math., 1945, 3, 38-54.
- [9] Chung, T.J. Computational fluid dynamics, Cambridge University Press, 2002.
- [10] Colin, E., Etienne, S., Pelletier, D., Borggaard, J. *Application of a sensitivity equation method to turbulent flows with heat transfer*, Int. Journal of Thermal Science, 2005, 44, 1024-1038.
- [11] European Research Community on Flow, Turbulence and Combustion, Best practice guidelines, Special Interest Group on „Quality and Trust in Industrial CFD”, 2000.
- [12] Evans, R.L. Free stream turbulence effects on the turbulent boundary layer, report No 1282 for Procurement Executive, Ministry of Defence, 1974.
- [13] Fernández, M.A., Moubachir, M. *Sensitivity analysis for an incompressible aeroelastic system*, Mathematical Model and Methods in Applied Sciences, 2002, vol. 12, 8, 1109-1130.
- [14] FLUENT: FLUENT 6.1 Documentation, Fluent Inc, 2003.
- [15] Hanjalić, K. Two-dimensional asymmetric turbulent flow in duct, PhD thesis, University of Londyn, 1970.
- [16] Haug, H. J., Choi, K. K., Komkov, V. Design sensitivity analysis of structural systems, Academic Press, Orlando, 1986.
- [17] Hinze, J.O. Turbulence, the second edition, McGraw-Hill, Nowy York, 1975.
- [18] Hrenya, C. M., Bolio, E. J., Chakrabarti, D., Sinclair J. L. *Comparison of low Reynolds number k-ε turbulence models in predicting fully developed pipe flow*, Chemical Engineering Science, 1995, Vol. 50, No. 12, 1923-1941.

- [19] Johansson, A. V. Engineering turbulence models and their development, with emphasis on explicit algebraic reynolds stress models, course “Theories of Turbulence” organized by of CISM,Udine, 2001.
- [20] Jones, W.P. Launder, B.E. *The prediction of laminarization with a two-equation model turbulence*, Int. Journal Heat Mass Transfer, 1972, 15, 301-314.
- [21] Kleiber, M., Antúnez, H., Hien, T. D., Kowalczyk, P. Parameter Sensitivity in Nonlinear Mechanics, John Wiley & Sons, 1997.
- [22] Kołmogorow, A.N. *Equations of turbulent motion of an incompressible turbulent fluid*, Wykłady Akademii Nauk SSSR, 1942, VI, nr 1-2.
- [23] Launder, B.E, Spalding, D.B. Mathematical models of turbulence, Academic Press, London and New York, 1972.
- [24] Launder, B.E, Spalding, D.B. *The numerical computation of turbulent flows*, Computer Methods in Applied Mechanics and Engineering, 1974, 3, 269-289.
- [25] Mohammadi, B., Molho, J. I., Santiago, J. G. *Incomplete sensitivities for the design of minimal dispersion fluidic channels*, Comput. Methods Appl. Mech. Engineering, 2003, 192, 4131-4145.
- [26] Noda, M., Nakayama, A. *Reproducibility of flow past two-dimensional rectangular cylinders in a homogeneous turbulent flow by LES*, Journal of Wind Engineering and Industrial Aerodynamics, 2003, 91, 265-278.
- [27] Noda, M., Utsunomiya, H., Nagao, F., Takenaka, K. *Effects of the wind velocity profile on the aerostatic forces*, Proc. of the 9ICWE'95, 1995a, Vol. 1, 249-260.
- [28] Noda, M., Utsunomiya, H., Nagao, F. *Basic study on blockage effects in turbulent boundary layer flows*, Journal of Wind Engineering and Industrial Aerodynamics, 1995b, 54/55, 645-656.
- [29] Patankar, S.V. Numerical heat transfer and fluid flow, McGraw-Hill Book Company, 1980.
- [30] Prandtl, L. *Über ein neues Formelsystem für die ausgebildete Turbulenz*, Nachrichten von der Akademie der Wissenschaft in Göttingen, 1945.
- [31] Rhee, C. M., Chow, W. L. *Numerical study of the turbulent flow past an airfoil with trailing edge separation*, AIAA Journal, 1983, 21(11), 1525-1532.
- [32] Sajjadi, S.G., Waywell, M. N. *Application of roughness-dependent boundary conditions to turbulent oscillatory flows*, Int. Journal Heat and Fluid Flow, 1997, 18, 368-375.
- [33] Schlichting, H. Boundary layer theory, McGraw-Hill Book Company, 1979.
- [34] Shabbir, A., Beuther, P. D., George, W. K. *X-wire response in turbulent flows of high-intensity turbulence and low mean velocity*, Experimental Thermal and Fluid Science, 1996, 12, 52-56.
- [35] Shih, T. H., Liou, W.W., Shabbir, A., Yang, Z., Zhu, J. *A new $k-\varepsilon$ eddy-viscosity model for high Reynolds number turbulent flows*, Computers Fluid, 1995, vol. 24, 3, 227-238.
- [36] Smagorinsky, J. General circulation experiments with the primitive equation, Part 1. Basic experiments, Mon. Weather Rev., 1963, 99-164.
- [37] So, R. M. C., Zhang, H. S., Speziale, C.G. *Near-wall modeling of the dissipation rate equation*, AIAA Journal, 1991, 29, 2069-2076.

Chapter 7

PASSIVE AIR SAMPLER FOR THE DETERMINATION OF ATMOSPHERIC NITROGEN DIOXIDE USING FLAT POROUS POLYETHYLENE MEMBRANE AS TURBULENCE LIMITING DIFFUSER

Yoshika Sekine^{1*}, Michio Butsugan² and Simon F. Watts³

¹School of Science, Tokai University, Hiratsuka, Kanagawa, Japan

²Hitachi Chemical Co., Ltd., Hitachi, Ibaraki, Japan

³School of Geography, Environment and Earth Sciences, Victoria University of Wellington, Wellington, New Zealand

ABSTRACT

Atmospheric turbulence is a potential factor influencing on the sampling performance of passive air samplers. In this chapter, a new design of passive sampler named “Oxford sampler” is described which employs a flat type porous polyethylene membrane, made of sintered polyethylene particles, as a turbulence limiting diffuser. The flat diffuser controls mass transfer of the target analyte from ambient air to impregnated trapping filter. The new design is applicable to any analyte for which conventional Palms’ Tube method is applicable, e.g. H₂S, OCS, NO, SO₂, O₃, Organic Acids, NH₃ and so on. As an example, the sampler for the determination of ambient atmospheric nitrogen dioxide (NO₂), using a trapping filter impregnated with triethanolamine is described. Influence of external wind speed on the mass transfer of gas molecules was investigated in laboratory tests. The results showed the flat porous polyethylene membrane worked as an efficient draft baffle preventing over-sampling caused by eddy diffusion, whilst effect of boundary layer conductance was found when the sampling was conducted in a calm environment. The sampling rate of the passive sampler was measured directly at seven sites in Oxford, UK and Kanagawa, Niigata and Yamagata, Japan, by comparing measured concentrations from the samplers with co-located automated NO₂ monitors. The passive device had a relatively higher sampling rate than those of previous samplers and gave equivalent results on NO₂ concentrations to the automated NO₂ monitor at 24h or less sampling duration. This shows the Oxford sampler

* email: sekine@tsc.u-tokai.ac.jp, Phone: +81-463-58-1211

employing the flat porous polyethylene membrane is appropriate to reduce the sampling resolution of most formats of Palmes' Tubes from weeks to 24 hours or less. Uncertainty and sensitivity analysis of the new sampler indicated possible application of the device to sampling in urban intermediate, urban background and suburban areas.

INTRODUCTION

Passive air samplers, which employ molecular diffusion process based on Fick's law and hence do not require power supply or other services, have been recognized as effective alternative to pumped samplings. The samplers are widely used for air quality monitoring for purposes ranging from occupational exposure [Vinzents, 1996] and outdoor air pollution monitoring [Kirby et al., 2001] to indoor pollution monitoring for the conservation of cultural heritage [Ankersmit et al., 2005] and prevention of Sick Building/House Syndrome. Atmospheric turbulence is however a potential factor influencing on the sampling performance of the passive air samplers. Therefore, use of a good turbulence baffle as a diffuser, where molecular diffusion process takes place, is essential way to prepare sensitive passive samplers with significant analytical liability.

One particular type of passive sampler, originally developed by Palmes et al. (1976) for workplace monitoring, is used extensively in UK, EU and USA primarily for atmospheric nitrogen dioxide (NO_2). The "Palmes' Tube" is routinely used to determine the extent of polluted zones [Kirby et al., 1998, Glasius et al., 1999] and for comparison of national and international air quality standards [Reeuwijk, et al., 1998] according to its ubiquitous, cost-effective and robust properties. Although there are different formats and methodologies of preparation which each bring difficulties in intercomparisons, all agree that these tubes over-sample in the outdoor environment [AQEG, 2004; Kirby et al., 2001; Ridge et al., 2005]. Two potential sources of such enhancement have been identified. Firstly, eddy diffusion caused by air turbulence at the entrance of the sampling tube can lead to a shortening of the diffusion path length [Campbell et al., 1994, Gair and Penkett, 1995, Ridge et al. 2005, Koutrakis, et al., 1993]. Various approaches involving the use of turbulence baffles have been tried, but with mixed results [Gair & Penkett, 1995, Shooter et al., 1995]. In essence, the root of this problem lies in the use of a column of air as the diffusion path, and could only be resolved if this were not used. The second source of positive bias is the disruption of the photo-stationary steady-state in samplers not transparent to light ($\lambda \sim 315 \text{ nm}$). In Palmes' Tube type samplers, the time that the co-diffusing NO_2 , ozone (O_3) and nitrogen monoxide (NO) are in the tube is similar to, or greater than the residence time for reaction between the NO and O_3 molecules. Hence this reaction causes excess NO_2 formation, without the corresponding NO_2 loss from photolysis within the tube [Heal and Cape, 1999]. This issue is effectively one of kinetics, and could be resolved if the sampling rate of the passive sampler was much higher than the rate of the NO and O_3 reaction.

Porous polyethylene (PE) membrane, made of sintered PE particles, has been used for diffuser of reactive passive samplers for the determination of carbonyl compounds [Uchiyama et al., 2004, Sekine et al., 2001, Onishi et al., 2007], and volatile organic compounds (VOCs) such as benzene, toluene, xylene, ethylbenzene, limonene and p-dichlorobenzene [Sekine et al., 2002, 2004] in indoor air at ppb levels. The diffuser, whose shape is cylinder or tube, also serves as container of powder-like adsorbents; spherical silica gel impregnated with 2,4-

dinitrophenylhydrazine (DNPH) or O-(4-cyano-2-ethoxybenzyl)hydroxylamine (CNET) for carbonyl compounds and carbon molecular sieves for VOCs. Performance of the passive samplers were evaluated by laboratory and field experiments and found the sampling rate of the samplers was high enough to realize short term sampling and was independent on the wind speed between 0.2 to 4 m s⁻¹ (cylinder type: 89 mL min⁻¹ for formaldehyde, approx. 35 mL min⁻¹ for VOCs, tube type: 74 mL min⁻¹ for formaldehyde). The work showed that the porous PE membrane not only had a high gas permeability, but also worked as a good turbulence baffle.

Then, the authors prepared a flat type porous PE membrane to suit the trapping filter of the Palmes' Tube and proposed the alternation of the diffuser from "tube" to "flat porous PE filter" [Sekine et al., 2008]. The new passive sampler named Oxford sampler is applicable to any analyte for which Palmes' Tube method is applicable, e.g. hydrogen sulphide (H₂S), carbonyl sulphide (OCS), sulphur dioxide (SO₂), organic acids, ammonia (NH₃), NO, O₃, and so on. However, ambient air movement on the exposed surface of the flat type diffuser can affect the mass transfer of gas molecules by producing standstills that increase effective diffusion length [Ballesta et al., 1993, Underhill et al., 1991]. Under conditions of low external wind speeds, the effect is produced by the formation of a laminar boundary layer on the diffuser surface. This leads to an extra length of static air which increases transfer residence and a decrease in overall sampling rate. The aim of this chapter is to discuss a potential alternation of the flat diffuser from the view point of influence of air movement on the surface of the flat porous PE membrane on the mass transfer of an analyte and to demonstrate the use of the new design sampler for the determination of atmospheric concentrations of NO₂.

EXPERIMENTAL

Sampler Construction

Figure 1 shows an overview of the Oxford sampler (c), alongside other samplers (a, b, d, e) as reference. Passive samplers employing the porous PE membrane were a) cylinder type for VOC collection (VOC-SD, commercially available from Sigma-Aldrich, Japan) [Sekine et al., 2002], b) tube type for carbonyls collection (CNET-P, available from Sumika Chemical Analysis Service, Japan) [Onishi et al., 2007] and c) flat type applied to Oxford sampler for NO₂ collection (this work). The area of porous PE membrane used for construction of the Oxford sampler was smallest among three samplers. Ogawa sampler (d) [Hirano et al., 1985, Koutrakis et al., 1993] and Palmes' Tube (e) have been previously used for atmospheric NO₂ monitoring. Whilst both the Palmes' Tube and Ogawa samplers have tubes, the new sampler has a rod – it is simply a support for the trapping media as shown in Figure 2.

The trapping filter for NO₂ was prepared by dipping Whatman#1, 13mmφ filter into 10% v/v triethanolamine (TEA) in acetone solution. A 13mmφ of the flat Porous PE membrane was prepared by sintering spherical polyethylene powders. The filter has a thickness of 1.0 mm with average pore size of 43 μm. The filter retains aerosol particles with larger than 20 μm of aerodynamic diameter in air. Pressure drop of the filter was measured at an air flow of 100 m³ m⁻² min⁻¹ and resulted in 58 mm Hg (7730 Pa). Figure 3 shows a scanning electron microscope image of the porous PE membrane whose porosity was approximately 34.5%.

Molecular diffusion of gas takes place through the air cavities. The trapping filter and diffuser were retained by open centre cap on the solid support made of polyolefin. The solid support is a straight rod, so both sides can be used for sampling purposes. Therefore, simultaneous measurements of NO₂ and another gaseous component such as NO, H₂S, OCS, O₃, SO₂, NH₃, organic acids, or any other analyte for which there is a working Palmes' Tube could be conducted using the one sampler.

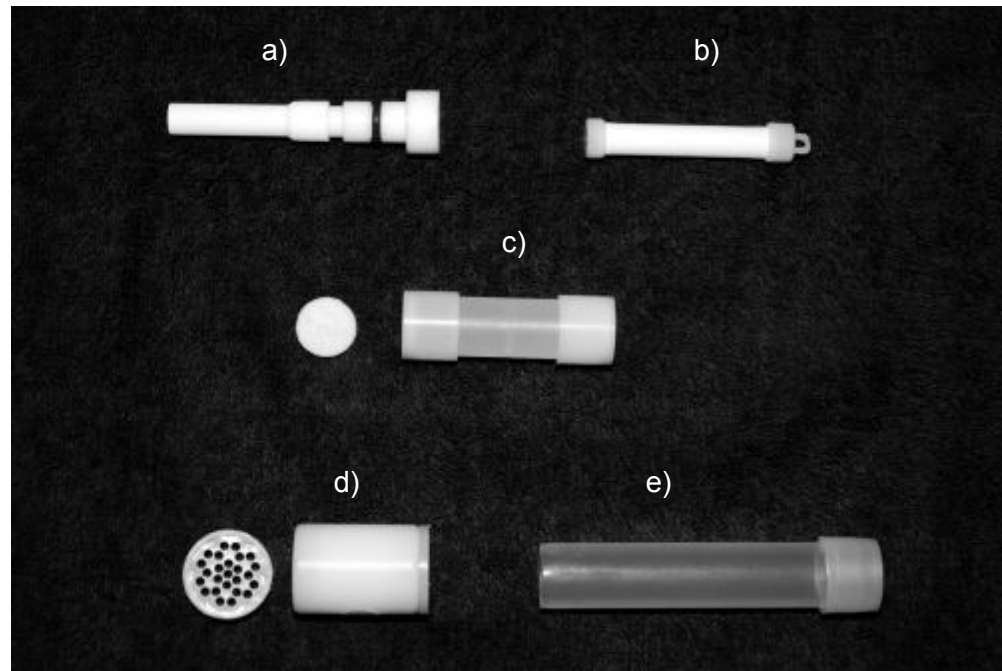


Figure 1. Schematic view of the passive samplers. a) VOC-SD employing cylinder type porous PE membrane, b) CNET-P employing tube type porous PE membrane, c) Oxford sampler with a flat type porous PE membrane (this work), d) Ogawa sampler with a diffuser of multi-tube structure and e) Palmes' Tube (This differs from the original Palmes' Tube [Palmes et al., 1976], in that the sampler body consists of a fluoroethylene polymer (FEP) tube, and a stainless steel wire mesh holds a NO₂ trapping filter impregnated with TEA. This has been fully described elsewhere [Ankersmit et al., 2005]).

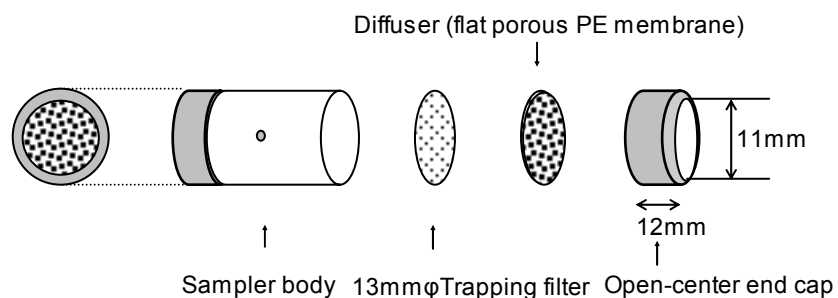


Figure 2. Schematic view of the Oxford sampler, employing a flat porous PE membrane as turbulent limiting diffuser.

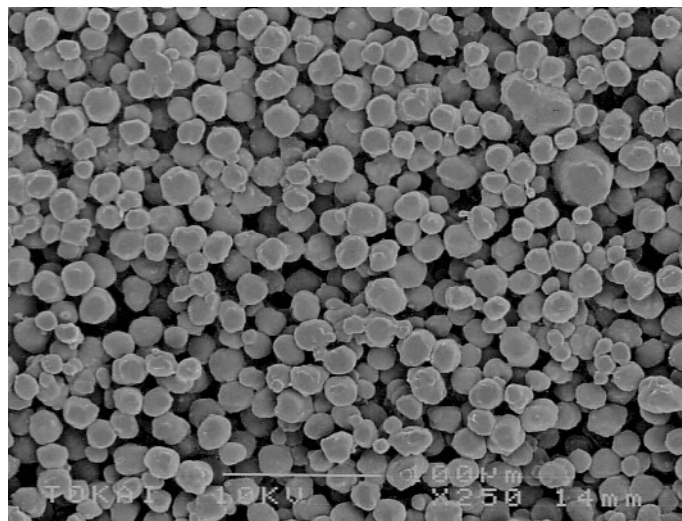


Figure 3. SEM image of the porous PE membrane (Porosity:34.5%).

Influence of Wind-Speed

Influence of wind speed on the rate of mass transfer of gas molecules by diffusion within the diffuser was investigated using the evaporation method according to Ridge *et al.*(2005). A glass test tube (13mm OD and 12mm ID) was filled with diethyl ether (AR grade). The open end was covered by the flat diffusion filter with open centre cap and subsequently set in a downstream of a wind tunnel. A head space between diffuser and bulk liquid was set constant at the beginning of each run because diffusion rate within glass tube affected the overall mass transfer rate. The wind tunnel was made as follows: a blade of a Microtec 30cm fan was fitted with 38cm collar such to produce a decrease in cross-sectional area from the blade face to the end of the collar of 50%. Measurements were conducted in the centre of the exit of the collar where the flow characteristics were very turbulent. The face of the diffusion filter was set parallel to the air-flow. The tube was weighed at various intervals between the beginning and end of placement. The change of mass with time, M (g h^{-1}) was normalized by those at static mode, M_0 and plotted against the wind speed measured by flow monitor. Diffuser end cap of Ogawa sampler, which has 25 holes of 2 mm ID and 6 mm depth, was also tested in the same manner.

The boundary layer effect was separately investigated using naphthalene (Kanto Chemical, reagent grade) instead of diethyl ether by rotating evaporation method, referring Uchiyama *et al.* (2004). A glass vial (13mm OD and 12mm ID) was filled with naphthalene. The open end of the vial was covered by the flat porous PE membrane with open centre cap. The prepared units were subsequently fixed at certain intervals of 2 m rod in parallel to the air flow and then rotated by an electric motor at 15 ~ 23 rpm for 45 hrs. After rotating, the loss of weight of naphthalene was measured.

The influence of wind speed on NO_2 collection amount was also investigated in the laboratory. The Oxford samplers were deployed downstream of the fan for 24 hours. Collected NO_2 on the trapping filter was determined by the sulfanilamide/NEDA methodology, see below. Repeatability of NO_2 uptake was investigated in turbulent

environment. The oxford samplers ($n=8$) were deployed outdoors of the laboratory for 24 hours and variations of collected NO_2 on the trapping filter were subsequently determined.

DETERMINATION OF SAMPLING RATE

The overall sampling rate of the Oxford sampler was derived from relationships between air concentrations monitored by automated NO_2 monitor and collected amounts of NO_2 on the sampler. A set of three passive samplers were deployed for 24hours alongside a calibrated auto-analyzer. The passive samplers were deployed 2 cm from each other beneath a rain shield. Exposure heights were kept as close as possible to the sampling nozzle of the automated monitors. The parallel measurements were carried out at kerbside sites (within 5m of roadside) at Carfax and High street in Oxford, UK from 11 to 19 September 2004 and Hadano and Isehara in Kanagawa, Japan from 10 to 18 November 2004. Similar measurements were also conducted at suburban site at Niigata, Japan from 28 December 2004 to 1 January 2005, and at background sites at Hiyoriyama and Sakaicho in Yamagata, Japan from 31 May to 29 June 2005. Air concentration data of NO_2 by automated NO_2 monitors were cited from public sources operated by Oxford Air Watch, Oxford City Council and Atmospheric Environmental Regional Observation System (AEROS), Ministry of Environment, Japan. The Oxford chemiluminescence auto-monitors for $\text{NO}_x - \text{NO} - \text{NO}_2$ were conducted as a part of the UK Automatic Urban Network and as such were checked fortnightly for noise, linearity and conversion efficiency by comparing the site standard cylinder to a stable inter-site standard. The automated NO_2 monitors based on Saltzman method in Japan were calibrated every three months using zero and span gases following the national guidelines.

Sampler Analysis

Collected NO_2 on the trapping filter was determined by colorimetry, the sulphanilamide/NEDA (N-1-naphthylethylenediamine dihydrochloride) methodology [Campbell,1988] implemented on an AMS AA II auto-analyzer at the Oxford site, after extraction in 2 mL of 18 M Ω deionized water [Ridge et al., 2005]. At Japanese sites, collected NO_2 was also determined by the sulfanilamide/NEDA methodology described in Hirano et al. (1983) and Sekine and Kagawa (1997). Briefly, the trapping filters were transferred to 15ml of centrifuge tube and nitrate ions were extracted in 8ml of de-ionized distilled water with vigorous shaking for 2min. After addition of 2 mL of a combined reagent, 10parts sulfanilamide solution to 1part NEDA, to each sample, the tube was mildly shaken and stand to allow for full colour deployment. Aliquot of the contents was transferred to a quartz cell with 1cm of path length for the measurements of the optical absorbance at 540nm. Nitrate ion concentrations were determined by comparison with a reference calibration graph derived from standard nitrate solutions (from sodium nitrate dried in oven at 100°C before use) in the range from 0 to 1.0 $\mu\text{g mL}^{-1}$ NO_2^- . For each exposure set, the mean blank absorbance from two unexposed samplers was substituted from the readings of exposed samples.

RESULTS AND DISCUSSION

Influence of Wind Speed

Figure 4 shows the results of typical runs on diethyl ether evaporation studies on the flat porous PE membrane diffuser at 272K. All the runs had a similar linear nature as this sample. The rate of mass loss, M was measured from the slope of these plots and plotted against wind speed after normalized by M_0 , measured at zero wind-speed, as shown in Figure 5. Results on the Palmes tube at 298K were cited from Ridge *et al.* (2005) and plotted together. M/M_0 of the Palmes' Tube increased with an increase of wind speed. This means over-sampling of the order of 50% is predicted even at low wind speed with less than 1.5 m s^{-1} [Ridge *et al.*, 2005] probably due to eddy diffusion caused by air movement at the entrance of the sampling tube. As previously reported [Koutrakis, et al., 1993], influence of wind speed exponentially increased on M/M_0 of the Ogawa sampler diffuser. It should be remembered that this is a wind tunnel experiment, rather than a natural environmental exposure – hence it might be expected to be considerably more laminar and uniform than the often changeable wind speeds and direction encountered in the outdoor environment. This in mind, the measured mass transfer coefficients (in this case of diethyl ether) might be expected to be maximal, and probably greater than those found in the natural environment. In spite of that, no significant influence was found on the M/M_0 for the flat porous PE membrane diffuser of the Oxford sampler. This means that wind speed within the range $0 - 2 \text{ m s}^{-1}$ does not change mass transfer of diethyl ether within the diffuser and the porous PE membrane acts as a draft shielding baffle to prevent the eddy diffusion.

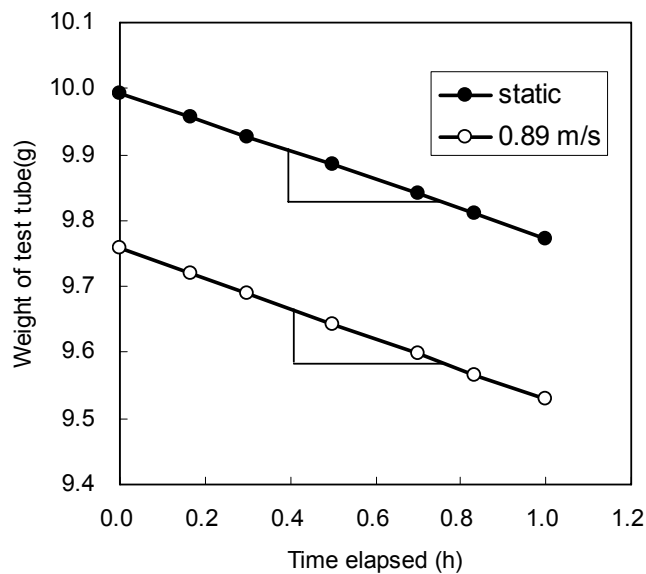


Figure 4. Typical change of loss of mass with time of diethyl ether from glass tubes covered with a flat porous PE membrane in a static and with a wind speed of 0.89 m s^{-1} at 272K.

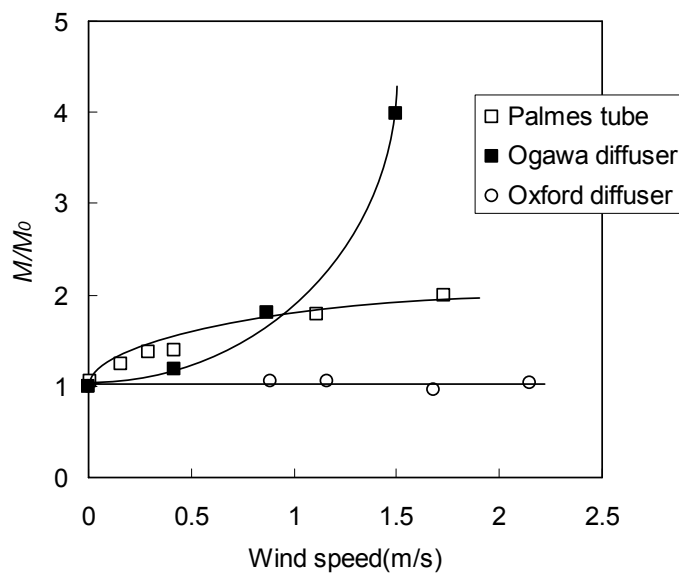


Figure 5. Comparison of influence of wind speed on the evaporation rate of diethyl ether from glass test-tubes without (Palmes' Tube format) and with diffusion filter of Ogawa sampler and Oxford sampler. Temperature: Palmes tube: 298K [Ridge *et al.*,2005], Ogawa diffuser :297K, Oxford diffuser: 272K.

On the other hand, there was a possibility that the evaporation rate of diethyl ether was too high to detect the boundary layer conductance of the draft shielding diffuser in low wind region. Then, the boundary layer effect on the flat porous PE membrane was closely investigated by using naphthalene whose evaporation rate was much smaller than that of diethyl ether. Figure 6 shows loss of naphthalene filled in vials end-capped with the flat porous PE membrane as a function of wind speed at 298K. The results showed the amounts of vaporized naphthalene, M' (mg day^{-1}) slightly increased with air velocity, v (ml min^{-1}): $M' = 0.00086 \ln(v) + 0.00813$ ($R^2 = 0.93$). This means there potentially exists the boundary layer effect on the sampling performance of the Oxford sampler when the air velocity is very low (approximately $< 0.15\text{m/s}$). Figure 7 shows influence of wind speed on the amount of NO_2 collected by the passive samplers deployed in the indoor air of the laboratory for 24 hours with varying wind speed from 0 (static) to 2.0 m s^{-1} . Significant changes of NO_2 quantity were not found in the range of 0.5 to 2.0 m s^{-1} , whilst the NO_2 quantity collected at static mode was significantly reduced due to the boundary layer effect (t -test, $p=0.001$).

The Oxford samplers were then deployed outside, in the turbulent environment, for 24 hours. The average wind speed at the surface of the samplers was not available due to a lack of appropriate measurement methods in our laboratory. Relative standard deviation of eight samplers was 8.5% (collected NO_2 : $0.24 \pm 0.020\text{ }\mu\text{g}$) when measured by the auto-analyser employing sulfanilamide/NEDA methodology. No outlier value was found in the readings of optical absorbance. These results show that the flat porous PE membrane works as a very efficient turbulence baffle and diffusion resistance to the NO_2 gas molecule with good repeatability in ambient air. However, we have to mind the effect of boundary layer conductance when sampling in a calm environment.

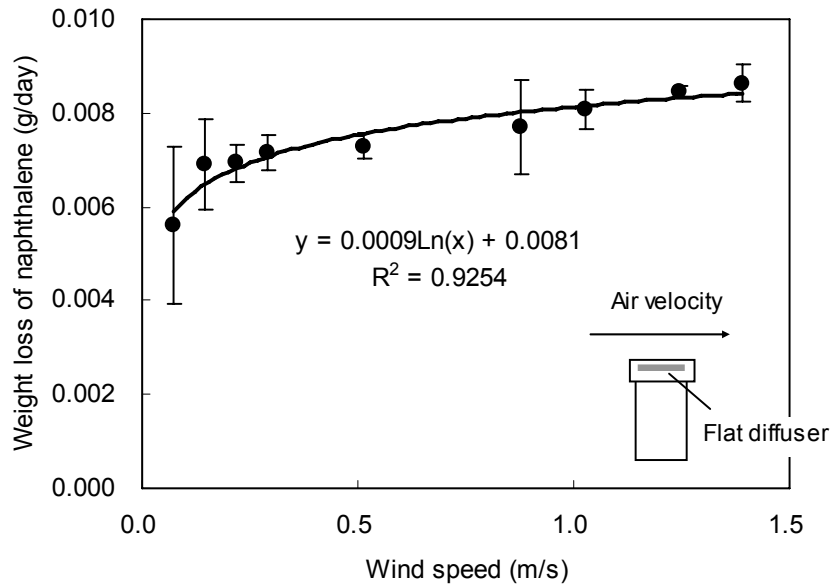


Figure 6. Influence of wind speed on the evaporation rate of naphthalene from glass vials with a flat porous PE membrane (diffuser of the Oxford sampler) at 298K. Bars show standard deviations of quartet measurements.

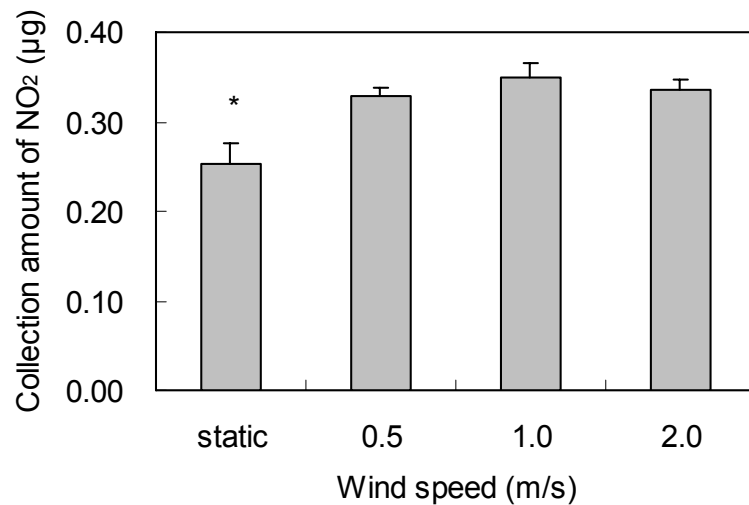


Figure 7. Influence of wind speed on the NO_2 collection amount by the Oxford sampler deployed in indoor air of a laboratory for 24 hours. Bars show standard deviations of triplicate measurements. * Significantly different with others at $p=0.001$.

Estimation of the Boundary Layer Conductance

Using such passive samplers, the sampling rate, S (mL min^{-1}) is a dominant factor that affects analytical reliability. As shown in Eq.(1), the collected amount of NO_2 on the TEA impregnated filter, W could be converted to air concentration, C using exposure time, t and

the sampling rate, S , if the adsorbent reduces the concentration of the given analyte at the end of diffusion layer ideally to zero due to sorption [Brown, 2000].

$$C = \frac{W}{St} \quad (1)$$

The sampling rate, S for an analyte depends on the conductance across two regimes placed in series: across the external boundary layer, and the internal air gap of a diffuser [Underhill et al., 1991]. The sampling rate is a harmonic mean of the both conductances. Thus,

$$\frac{I}{S} = \frac{I}{S_i} + \frac{I}{S_b} \quad (2)$$

where S_i is the internal conductance of a diffuser (mL min^{-1}) and S_b is the conductance of the boundary layer (mL min^{-1}). Rearranging equation (2) provides equation (2)' which permits S_b to be calculated from S and S_i , which are both determinable parameters.

$$S_b = \frac{S_i S}{S_i - S} \quad (2)$$

The overall sampling rate, S is practically obtained from a relationship (or ratio) between atmospheric air concentrations measured by standard methods and collection amount of an analyte on the passive sampler.

$$S = \frac{W}{tC} \quad (3)$$

The internal conductance, S_i is calculated from

$$S_i = D \frac{A}{L} \quad (4)$$

where D is a diffusion coefficient of a gas molecule in air ($\text{m}^2 \text{ min}^{-1}$), A is a cross section area of diffusion path(m^2), L is a diffusion path length (m). Then, the boundary layer conductance was estimated for the Oxford sampler.

Figure 8 shows relationship between air concentrations measured by the NO_2 auto-analyzer (24h-mean) and collected amounts of NO_2 on the TEA impregnated filter of the passive sampler (mean of triplicate 24h-measurements by each sampler). Sampling duration was set at 24 hours. Even though there seemed to be systematic errors in automated NO_2 monitoring data by each site, the collected amounts of NO_2 by the passive sampler showed good linearity against air concentrations at seven sites in UK and Japan. By using Eq.(3), the sampling rate of the Oxford sampler can be derived from the slope of a linear regression

analysis and resulted in $S = 1.2 \pm 0.032 \mu\text{g ppm}^{-1} \text{ h}^{-1}$ for NO_2 . Alternatively, the sampling rate was also written in $S = 11 \text{ mL min}^{-1}$. This rate was approximately 1.2 times greater than that of Ogawa sampler and 10 times greater than that of Palmes' Tube ($\sim 1.2 \text{ mL min}^{-1}$).

On the other hand, the factors A and L were determined by direct measurement using geometry, SEM image and porosity of the porous PE membrane. The A/L resulted in 2.09 cm. The diffusion process consists of both molecular diffusion (D_m) and Knudsen flow (D_k) [Ruthven, 1984] within a diffuser. The D_k is expressed as,

$$D_k = 9700r\sqrt{\frac{T}{M}} \quad (5)$$

where, r is the mean pore radius of the porous PE membrane (0.00215cm), T is in Kelvin and M is the molecular weight of the diffusing species (46 for NO_2). However, by Eq (5) the calculated D_k became $53 \text{ cm}^2 \text{ s}^{-1}$ at 295K and much greater than D_m ($0.154 \text{ cm}^2 \text{ s}^{-1}$ for NO_2). According to Eq.(6), contribution of D_k is hence negligible for overall diffusion coefficient, D .

$$\frac{1}{D} = \frac{1}{D_m} + \frac{1}{D_k} \quad (6)$$

Then, the internal conductance, S_i resulted in 19.3 ml min^{-1} using A/L and D_m for the calculation. The conductance across the boundary layer, S_b was 26 ml min^{-1} for the Oxford sampler as calculated from equation (2'). We have to mind the experimental error of the conductance was relatively high, because it was determined from the difference between S and S_i . However, in simple comparison, the calculated S_b is smaller than those of VOCs for 3M Model Diffusive Sampler from 63 to 163 ml min^{-1} [Underhill et al., 1991].

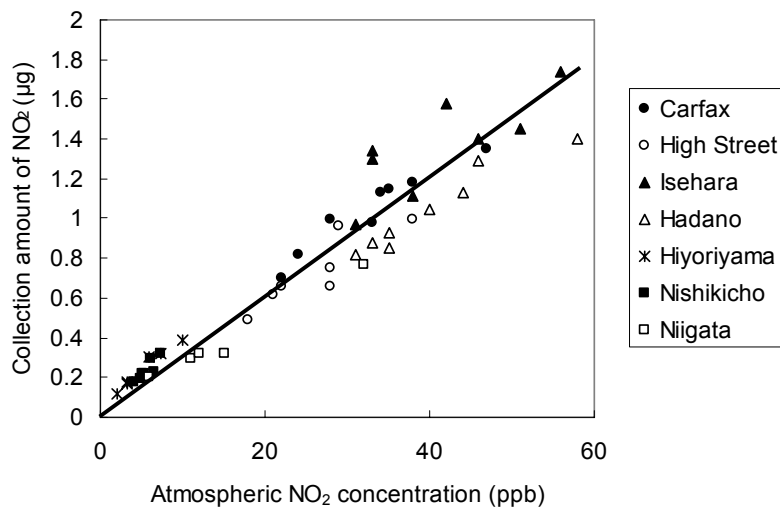


Figure 8. Relationship between atmospheric concentration of NO_2 measured by automated NO_2 monitors and quantity of NO_2 collected by the Oxford sampler in Oxford (Carfax and High street), UK, Kanagawa (Hadano and Isehara), Niigata and Yamagata (Hiyoriyama and Nishikicho), Japan. Linear regression analysis; $y=0.0295 \pm 0.00063x$ (intercept was forced to zero), $r=0.95(n=50)$.

Field Tests of the Oxford Sampler

Performance of the Oxford sampler with the derived overall sampling rate, S was demonstrated in field tests. To evaluate the uncertainty of the new passive sampler, additional parallel measurements were conducted at both Hadano and Isehara sites from April to December 2005 ($n=75$). The orthogonal linear regression based method described in the Guide for the Demonstration of Equivalence [EC, 2005], Buzica, D. et al. [2005] and Plaisance et al. [2007] were refereed and used for the evaluation. Briefly, the method allows computing the relationship between atmospheric NO_2 concentrations measured by new passive sampler (candidate methods), y_i and those of automated NO_2 monitor (reference method), x_i , by a linear regression.

$$y_i = b + ax_i \quad (7)$$

The uncertainty will be a function of the concentration of the measured. The relative expanded uncertainty of the results of the new passive sampler, $U(y_i)$ (%) can be evaluated by

$$U(y_i) = k \sqrt{\frac{RSS / (n-2) - u^2(x_i) + [b + (a-1)x_i]^2}{y_i^2}} \quad (8)$$

where RSS is the sum of squares of residuals resulting from the regression (Eq(9)), $u(x_i)$ is a random uncertainty of the reference method and k is a coverage factor (a bias between the values of automated NO_2 monitor and Oxford sampler).

$$RSS = \sum (y_i - b - ax_i)^2 \quad (9)$$

The random uncertainty of the automated NO_2 monitor was set to 5 % at the NO_2 concentration measured and the coverage factor of 2 was used because of large number of freedom in this case.

The atmospheric NO_2 concentrations measured the Oxford sampler were plotted in Figure 9 a) versus the auto-monitor measurements. The use of the derived sampling rate gave a coefficient of correlation $r = 0.89$ by the linear regression analysis resulting in $y = 0.0048 + 0.84x$. Figure 9 b) shows the relative expanded uncertainties of an individual 24h-measurement calculated for the new passive sampler. Since the expanded uncertainty of the sampler was 25% around the target values, 50 ppb for UK and 40 ppb for Japan, the data quality of the passive sampler could be satisfied for practical uses.

The sampling rate was then applied for sampling deployments of various exposure times: 3 for five runs, 6, 12 and 30 hours at Hadano site from 29 November to 1 December 2004. Figure 10 shows comparison of atmospheric concentrations of NO_2 in ppb measured by Saltzman-type automated NO_2 monitor and Oxford sampler coupled with the manual analysis. No significant differences between the two methods were observed for every exposure time. This work shows that there is now the opportunity to be able to use passive sampling (with its concomitant economic and wide area monitoring advantages) reliably at these short (3 hour) sampling times. Given the framing of air quality standards in many parts of the world are

based on short term averages, this has serious implications for the practice of air quality monitoring.

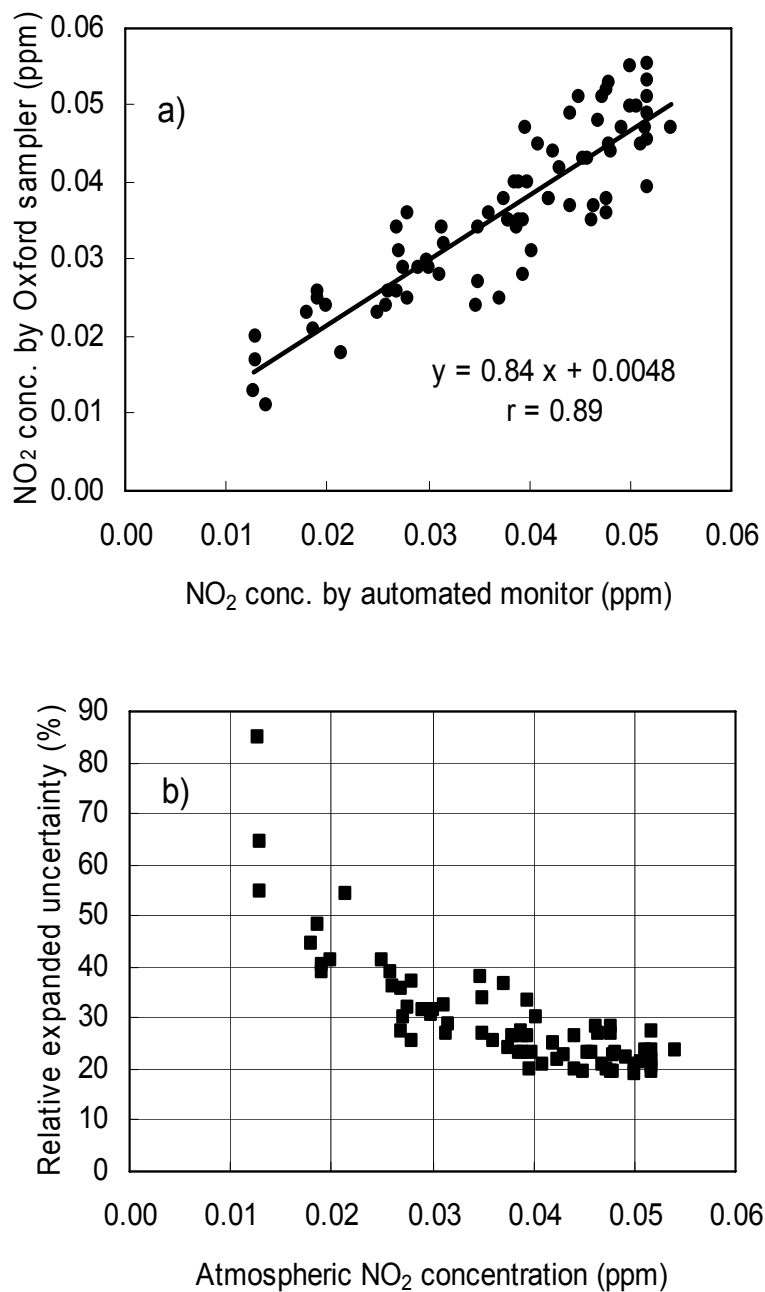


Figure 9a). Atmospheric NO_2 concentration given by the Oxford sampler versus automated NO_2 monitor. b) Relative expanded uncertainty of the Oxford sampler versus daily mean NO_2 concentrations at Hadano and Isehara sites, Kanagawa, Japan from April to December 2005 ($n=75$).

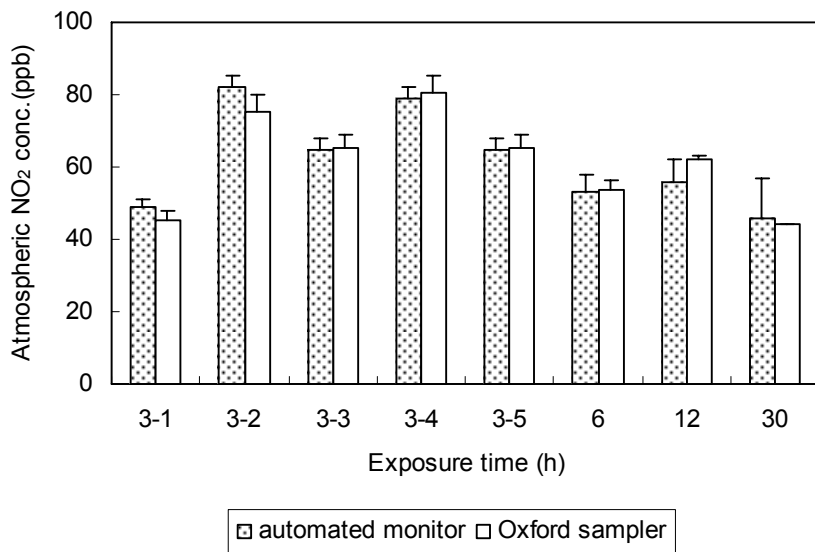


Figure 10. Comparison of atmospheric concentrations of NO₂ measured by automated NO₂ monitor and Oxford sampler at various exposure times (3 for five runs, 6, 12 and 30), using the sampling rate derived (Hadano site, 29 November - 1 December 2004). Bars of automated NO₂ monitor show standard deviations of 1h-measurements during the exposure. Those of passive sampler show standard deviations of triplicate measurements. No significant difference was found between two methods (*t*-test).

Since significant contamination by trapping filter preparation, field handling and during storage was detected in transport and storage blanks, limit of detection (LOD) of the passive sampler was defined as blank reading + 3σ_B of multiple deployment blank samples obtained by either auto-analysis used in UK site and manual analysis used in Japanese site. Similarly, limit of quantitation (LOQ) was defined as blank reading + 10σ_B of multiple deployment blank samples. Table 1 summarized LOD and LOQ of the Oxford sampler at 3 hour and 24 hour exposure time, using the overall sampling rate obtained above. These values indicate possible application of the passive device to atmospheric sampling in urban intermediate (20-30m from roadside), urban background (>50m) and suburban areas.

Table 1. LOD and LOQ of the Oxford sampler for the determination of atmospheric concentrations of NO₂ using the overall sampling rate derived in this study and sulfanilamide/NEDA technology with auto and manual analytical procedures (unit: ppb).

	Auto analysis			Manual analysis		
	<i>n</i> *	24h-sampling	3h-sampling	<i>n</i>	24h-sampling	3h-sampling
LOD**	8	1.9	15	10	3.2	25
LOQ***	8	3.7	29	10	4.1	33

* number of deployment blanks used for calculation

** defined as blank reading + 3σ_B, *** defined as blank reading + 10σ_B

CONCLUSION

A new passive sampler, employing a flat porous polyethylene membrane as a diffuser, had a relatively higher sampling rate than extant passive samplers thus far used for this purpose, and gave equivalent results on NO₂ concentration to the automated NO₂ monitor even at 3h sampling duration. These results shows that the flat porous PE membrane is a possible alternative to tube diffuser of the Palmes' Tube preventing over-sampling caused by the eddy diffusion and reaction between NO and O₃ molecules. It should be however noted that the sampling rate of the passive sampler is potentially influenced by the boundary layer effect when sampling in a calm environment. An extended program on the full evaluation of the sampling rate is being carried out and will be served to improve the uncertainty of the passive sampler measurements.

ACKNOWLEDGMENTS

Authors would like to thank Prof. Andrew Rendell and Ms. Marien Perez, Oxford Brookes University, Prof. Toshihiko Otoshi, Tohoku University of Community Service and Science, Ms. Ayumi Kawamura, Ms. Yuko Mitsui and Mr. Yoshiaki Takahashi, Tokai University for their great advices and assistances. Authors also thank Oxford City Council, Kanagawa Environmental Research Center and Technical Service Coordination Office Tokai University for their kind helps in field and laboratory tests.

REFERENCES

- [1] Air Quality Expert Group *Nitrogen Dioxide in the United Kingdom*; DEFRA, UK, 2004.
- [2] Ankersmit, H.; Tennant, N. ; Watts, S.F. *Atmos. Environ.* 2005, 39, 695-707.
- [3] Ballesta, P.P.; Ferradas, E.G.; Aznar, M. *Environ. Sci. Tech.* 1993, 27, 2031-2034.
- [4] Brown, R. H. *J. Environ. Monit.* 2000, 2000 (2), 1-9.
- [5] Buzica, D.; Gerboles, M.; Amantini,L.; Ballesta, P.P.; de Saeger, E. *J. Environ. Minit.* 2005, 7, 169-174.
- [6] Campbell, G. W. *Environ. Pollut.* 1998, 55, 251-270.
- [7] Campbell, G. W.; Stedman, J. R.; Stevenson, K. J. *Atmos. Environ.* 1994, 28, 468-477.
- [8] European Commission *Demonstration of Equivalence of Ambient Air Monitoring Methods*, EC Working Group, 2005.
- [9] Gair, A. J.; Penkett, S. A. *Atmos. Environ.* 1995, 29, 2529-2533.
- [10] Gair, A.J.; Penkett, S.A.; Oyola, P. *Atmos. Env. Part A*, 1991, 25 (9), 1927–1939.
- [11] Glasius, M.; Carlsen, M. F.; Hansen, T. S. ; Lohse, C. *Atmos. Environ.*,1999, 33,1177-1185.
- [12] Heal, M.R. ; Cape, J. N. *Atmos. Environ.* 1997, 31 , 1911-1923
- [13] Hirano,K.; Maeda, T.; Ishii,T. ; Yoneyama, E. *Environ. Measurement Tech.* 1985, 2, 32-39.
- [14] Kirby, C.; Fox, M.; Waterhouse, J. ; Dyre, T. *J. Environ. Monit.* 2001, 3, 150-158.

- [15] Kirby, C.; Greig, A.; Drye, T. *Environ. Monit. Assess.*, 1998, 52, 65-82.
- [16] Koutrakis, P.; Wolfson, J.M.; Bunyaviroch, A.; Forehlich, S.E.; Hirano, K.; Mulik, J. D. *Anal. Chem.* 1993, 65, 209-214.
- [17] Onishi, M.; Sekine, Y.; Sugihara, K.; Kitasaka, K.; Shimajiri, H. *J. Health Sci.* 2007, 53(4), 413-422.
- [18] Palmes, E. D.; Gunnison, A. F.; Dimattio, J.; Tomczyk, C. *Am. Ind. Hyg. Assoc. J.* 1976, 37, 570-577.
- [19] Plaisance; H., Gerboles, M.; Piechoki,A.; Detimmerman, F.; de Saeger, E. *Environ. Pollut.* 2007, 148, 1-9.
- [20] Ridge, L. J.; Rendell, A.R.; Watts, S. F.; Grebenik, P. D.; Miller, A.; Perez, M.; Reid, A. J. *Proc. of The fourth international conference on urban air quality - measurement, modelling and management*; Institute of Physics Publishing, Prague, 2005.
- [21] Ruthven, D. M. *Principles of Adsorption and Adsorption Process*; John Wiley & Sons, USA, 1984, pp136-137.
- [22] Sekine, Y.; Kagawa, J. *J. Resource and Environ.* 1997, 33(15), 41-45.
- [23] Sekine, Y.; Butsugan, M.; Usuki, H.; Kitahara,T. *J. Environ. Chem.*, 2001, 11, 511-516.
- [24] Sekine, Y.; Hirota, C.; Butsugan, M. *J. Environ. Chem.* 2002, 12, 847-854.
- [25] Sekine, Y.; Matsuo, A.; Butsugan, M. *J. Environ. Chem.* 2004, 14, 343-350.
- [26] Sekine, Y.; Watts, S.F.; Rendell, A.; Butsugan, M. *Atmos. Environ.* 2008, 42, 4079-4088
- [27] Shooter, D.; Watts, S.F.; Hayes, A.J. *Env. Mon. and Assess* 1995, 38, 11-23.
- [28] Uchiyama, S.; Aoyagi,S.; Ando, M. *Atmos. Environ.* 2004, 38(37), 6319-6326.
- [29] Underhill, D. W.; Feigley, C. E. *Anal. Chem.* 1991, 63, 1011-1013.
- [30] Van Reeuwijk, H.; Fischer, P. H.; Harssema, H.; Briggs, D. J.; Smallbone, K.; Lebret, E. *Environ. Monit. Assess.*, 1998, 50, 37-51.
- [31] Vinzents, P. S. *Ann. Occup. Hygiene*, 1996, 40 (3), 261-280.

Chapter 8

ARTIFICIAL INTELLIGENCE TECHNIQUE FOR MODELLING AND FORECASTING OF METEOROLOGICAL DATA: A SURVEY

Adel Mellit*

Department of LMD & Electronics, Faculty of Sciences Engineering, LAMEL,
Jijel University, Ouled-aissa, Algeria

ABSTRACT

Artificial intelligence (AI) techniques are becoming useful as alternate approaches to conventional techniques or as components of integrated systems. They have been used to solve complicated practical problems in various areas and are becoming popular more and more nowadays. AI techniques have the following features: can learn from examples; are fault tolerant in the sense that they are able to handle noise and incomplete data; are able to deal with non-linear problems; and once trained can perform prediction and generalization at high speed. AI-based systems are being developed and deployed worldwide in a myriad of applications, mainly because of their symbolic reasoning, flexibility and explanation capabilities. AI have been used and applied in different sectors, such as engineering, economic, medicine, military, marine, etc. They have also been applied for modeling, identification, optimization, prediction, forecasting, and control of complex systems. The main objective of this paper is to present an overview of the alternative approach and AI techniques for modeling and forecasting of meteorological data. Published literature works presented in this paper show the potential of AI as a design tool for prediction and forecasting of meteorological data, these includes, solar radiation, mean temperature, wind speed, humidity, cleanness index, etc. Additionally the advantage of using an AI-based prediction meteorological data in isolated areas where there no instrument for the measurement of this data, especially the parameters related to PV-systems such as solar radiation data. A new intelligent hardware based on neural network and FPGA (Filed Programming Gate Array) implementation is proposed for estimating solar radiation from air temperature and sunshine duration.

* The present address: International Centre of Theoretical Physics (ICTP), Strada-Costiera 1134014, Trieste, Italy.
E-mail: a.mellit@yahoo.co.uk or amellit@ictp.it. Phone: +213551998982, Fax: +21334501189.

Keywords: Meteorological data, artificial intelligence, conventional approach, modeling, forecasting, VHDL, FPGA.

1. INTRODUCTION

Meteorological data such as solar radiation, ambient temperature, relative humidity, wind speed, clearness index and sunshine duration, are accepted as dependable and widely variable renewable energy sources. It is therefore required to be able to formulate forecasting and estimation models of these meteorological data. These data play very important role for many applications, such as atmospheric energy-balance studies, analysis of the thermal load on buildings, designing, sizing, operation and economic assessment of energy and renewable energy system.

This chapter is organized as follows: A brief review of conventional methods (empiric, analytic, numeric simulation and statistic approaches such as AR, ARMA, ARIMA, Markov chain, etc.) for estimation and modeling of the meteorological data is presented in the next section, followed by an extensive overview on the application of artificial intelligence techniques for modeling and forecasting of meteorological data. In section 4, a new intelligent hardware based on neural network and FPGA (Filed Programming Gate Array) implementation is proposed for estimating solar radiation from air temperature and sunshine duration.

2. OVERVIEW ON THE CONVENTIONAL METHODS FOR MODELING AND PREDICTION OF METEOROLOGICAL DATA

Bendt et al. [1] analyzed 20 years of data from 90 US locations and developed expression for the clearness index (K_t) distribution based on these data, while Hollands and Huget [2] developed an implicit expression for the Liu and Jordan distributions presented in [3]. Collares-Pereira and Rabl [4] studied the average distribution of solar radiation-correlations between diffuse insolation and between daily and hourly insolation values. Mustacchi et al. [5] developed a stochastic model for simulation of the hourly global irradiation sequences.

Olseth and Skartveit [6] developed a probability density function for daily insolation within the temperate storm belts. The application of Markov chain and Fourier analysis for daily solar radiation data was investigated by Amato et al. [7]. In Ref [8], the authors had developed a modified solar radiation model to determine solar irradiance from sunshine hours for a number of stations located in hot dry arid climates. Graham et al. [9] designed a time series model for K_t with application to global synthetic weather generation. A simplified model for generating sequences of global solar radiation data was developed by Aguiar et al. [10]. Maafi and Adane [11] proposed a method for estimating solar radiation data in Algeria based on a two states Markovian model.

A further comparison and discussion of sunshine-based models to estimate global solar radiation had been developed by Akinoslu and Ecevit [12]. Shuichi et al. [13] developed adequate statistical models for the solar radiation (ARMA) and outdoor air temperature (ARMAX) time series and their correlations. Hokoi et al. [14] developed a stochastic model

of hourly solar radiation time series for the summer months. After a series of transformations, the authors found that an ARMA(3,3) model gave the best results. Aguiar et al. [15] developed a model for generating synthetic daily sequences of hourly radiation values, on the horizontal plane, for any location, with the daily clearness index K_t as input. The model assumes that for each K_t and solar hour the probability density of the hourly clearness index K_t is simply a truncated Gaussian function. The actual data for the direct, diffuse and global radiations were measured by Eppley Precision Pyranometers.

The correlation between estimated and measured hourly and daily solar fluxes over Bahrain is presented in Ref [16]. Dincer et al. [17] presented a simplified technique for estimating solar radiation parameters and its application for Gebze. Gopinathan and Soler [18] developed a diffuse radiation model to predict monthly average, daily diffuse radiation for a wide range of latitudes. Several years of measured data on global and diffuse radiation and sunshine duration for 40 widely spread locations in the latitude range 36°S to 60°N have been used to develop the model. The Box-Jenkins approach is applied to daily solar radiation data from four different locations in Malaysia [19]. A procedure has been formulated by Parishwad et al. [20] to estimate the direct, diffuse and global hourly solar radiation on a horizontal surface for any location in India; the authors used three statistical indicators to compare the accuracy of the developed procedure.

Rehmann and Halawani [21] used their own adaptation of the model to estimate the mean daily global solar irradiation for 52 cities in 11 countries, which apart from the Italian locations, were all between 40°N and 40°S. According to the authors, the model of Rehman and Halawani is capable of giving estimates within an acceptable mean percentage error of 5% and less for 33% of cities and between 5-10% for 50% of cities.

Mora-Lopez and Sidrach-de-Cardona [22] proposed the use of ARIMA(1,0,0)(0,1,1) for the modeling of the global solar irradiance as a percentage of the maximum available value. David et al. [23] used several expressions to estimate global solar radiation from sunshine hours for weather stations in Oman; these include linear, modified linear algorithm, Angstrom black type regression, a quadratic function and a new Angstrom-Black type algorithm.

A number of years of data relating the solar radiation on a horizontal surface, sunshine duration and wind speed in Sudan have been compiled, evaluated and presented by Omer [24]. The author used Angstrom formula to correlate relative global solar irradiance to the corresponding relative duration of bright sunshine. The monthly average wind speed and average power has been determined for 70 stations of Sudan by analyzing the routine wind data of these stations. In addition, a wind map of Sudan has been prepared in the same paper. In Ref [25] a univariate stochastic modeling, using SARIMA (Seasonal Autoregressive Moving Average) models, is carried out for horizontal and south facing vertical solar irradiance. This model presented good results and has been applied for a number of UK locations.

Badescu [26] formulated a correlation to estimate the monthly mean daily global solar irradiation with bright sunshine hour number or fractional total cloud amount as input for Romania. Sekai and Sahin [27] proposed a regional procedure for estimating the solar irradiation value of any point from sites where measurements of solar global irradiation already exist. The spatial weights are deduced through the regionalized variables theory and the cumulative semi-variogram approach; this method is applied for a Turkish location. Rehman [28] developed an empirical correlation for the estimation of global solar radiation in

Saudi Arabia. In addition, he had presented the comparison between the present correlation and other models developed under different geographical and varied meteorological conditions. A linear model for estimating clear-sky beam irradiation from observed irradiation and sunshine duration is proposed by Helen [29]. Meyer and Van Dyk [30] developed an energy model based on total daily irradiation and maximum ambient temperature.

To predict the energy produced by photovoltaic modules under certain meteorological conditions, an energy model can be used. Batlles et al. [31] analyzed the results provided by different models in the estimation of hourly direct irradiance values. Chegaar and Chibani [32] proposed two models for estimating monthly daily solar in horizontal surface; these models were applied for four locations in Algeria. Sen and Tan [33] developed a simple parabolic model with three parameters to estimate the hourly, daily and monthly global or diffuse radiation for Northwestern part of Turkey.

Geiger et al. [34] developed a new technique for the control of quality of solar radiation data based on Web service. Though data are usually controlled by meteorological offices, the sources are so numerous that the user often faces time-series of measurements containing questionable values. Wong and Chow [35] reviewed the solar radiation models for predicting the average daily and hourly global radiation, beam radiation and diffuse radiation. A general methodology was presented by Celik [36] and used for estimating the monthly average daily energy output from photovoltaic energy systems. Energy output is estimated from synthetically generated solar radiation data. Oliveira et al. [37] formulated a correlation model to estimate hourly, daily and monthly values of diffuse solar radiation on horizontal surfaces, applied to the city of Sao Paulo, Brazil. Safi et al. [38] used higher order statistics to predict the global solar radiation by means of two different procedures. The synthetic solar radiation data are generated based on the cumulative frequency distribution of the daily clearness index, given as a function of the monthly clearness index. Santos et al. [39] proposed a suitable model (ARIMA) for generating sequences of daily clearness index based on hourly clearness index.

A methodology for calculating on hourly basis the solar diffuse irradiation from global data for horizontal surfaces in Ajaccio was developed by Notton [40]. Ravinder and Umanand [41] proposed a methodology for developing a simple theoretical model for calculating global insolation on a horizontal surface. The input parameters to the model are the latitude of the desired location and the amount of total precipitable water content in the vertical column at that location. Both parameters are easily measurable with an inexpensive instrument such as a global positioning system (GPS). Jain [42] developed stochastic models using Box and Jenkins technique for sunshine duration and solar irradiation measured at Sebele, Botswana. The data used consists of the monthly averages and the Julian-days averages of sunshine duration and solar irradiation sequences.

A critical review on the estimation of daily global solar radiation from sunshine duration was discussed and reviewed by Yorukoglu and Celik [43]. Jebaraj and Iniyan [44] reviewed several energy models. An improved approach for estimation of the mean expected hourly global solar radiation and the estimation of stochastically fluctuating values, based on only one morning measurement of a day was investigated by Kaplani and Kaplani [45]. Gabriel López et al. [46] developed a new simple parameterization of daily clear-sky global solar radiation including horizon effect. This new model has also been shown to improve daily estimates against those obtained using the clear-sky model from the European Solar Radiation Atlas and other accurate parameterized daily irradiation models. Sen [47] proposed a simple

nonlinear model with three parameters for global solar irradiation estimation from sunshine duration ratio measurements. The suggested model is similar to the Angstrom equation but with the power term of the sunshine duration. The authors in Ref [48] demonstrated the applicability of localized spectral analysis for the analysis of cloud-induced fluctuations in solar irradiance. Their study was based on empirical data from several years recorded at three different sites.

Several solar radiation models are reviewed and discussed in [49]. In Ref [50], the authors reviewed both time-series and stochastic approaches to model prices and settles on time-series models to forecast the Sydney accumulated cooling degree day (CDD) and heating degree day (HDD) index levels. Two daily and one intraday models are proposed based on a Fourier Transformation of temperature, as well as a wavelet reconstructed Fourier Transformation. All models are compared to a current weather index pricing model and a naïve benchmark model. According to the author, the results suggest that, overall, the HDD index forecast is superior to the CDD index forecast and that the proposed models show forecast improvement over the current model and benchmark for the CDD index.

Sen and Murat [51] proposed a more efficient approach in terms of physical interpretations and mathematical convenience in modeling solar irradiation and sunshine duration relationship. An approach to estimate the solar radiation on inclined planes using solar geometry and measured sunshine hours was proposed by [52]. According to the authors, The proposed approach can provide a simple and reliable alternative for predicting the annual global solar radiation incident on various inclined surfaces facing different orientations.

These are some of the models that have been developed to estimate meteorological data by considering several parameters. These models are based an analytic formula, numeric simulation, or statistical approaches such as Markov chain, AR, ARMA, ARIMA, etc. The measurement of some of these meteorological parameters requires very expensive equipment making the whole process expensive. For a preliminary design of a stand-alone PV system, spending enormous amount of money in collecting meteorological data is not justified. The majority of these models may not be suitable for forecasting purposes because of the large amount of empirically determined parameters which results in higher prediction errors. In addition, these models need to acknowledge some behavior of the data. However, these models cannot be used in the following problems:

- Forecasting and modeling the data in long term
- Missing data in the database
- Prediction of the data in the location, where the measurement instruments are not available

A way to solve these problems based on AI techniques will be presented in the next section.

3. APPLICATION OF ARTIFICIAL INTELLIGENCE TECHNIQUES FOR THE PREDICTION OF METEOROLOGICAL DATA

This section deals with an overview on the application of AI techniques in meteorological data. This includes modeling of the daily, monthly and hourly solar radiation, wind speed prediction, daily clearness index modeling, temperature prediction, weather and insolation forecasting. An alternative way to avoid the problems outlined in the previous section is to employ AI techniques and emphasis is given to their growing use for data analysis, offering an effective alternative to more traditional statistical techniques in many scientific fields.

In the meteorological and solar energy resource fields, the numbers of applications presented for each AI field are summarized in Table 1. As can be seen the majority of applications deal with ANNs.

Table 1. Summary of numbers of applications presented in meteorological data.

AI technique	Area	Number of applications
Neural networks	Modeling and prediction of solar radiation Wind speed forecasting Temperature forecasting Weather forecasting (temperature, humidity, etc.) Clearness index forecasting Insolation modeling and prediction	52
Fuzzy logic	Modeling and prediction of solar radiation	3
Neuro-fuzzy (ANFIS)	Prediction of clearness index K_t	3
Wavelet and neural network	Forecasting of solar radiation (for missing data) Generation of hourly wind speed	5
ANN with Markov chain	Prediction of daily global solar radiation	2

3.1. Application of Neural Network for Solar Radiation Prediction .

There are several applications of ANN for modeling, prediction and forecasting of monthly, daily and hourly global solar radiation. Table 2 lists several representative examples of the use of ANNs in solar radiation estimation and prediction.

Elizondo et al. [53] formulated a neural network for predicting daily solar radiation. The daily observed values of minimum and maximum air temperature and precipitation, together with daily calculated values for day-length and clear sky radiation, were used as inputs for the neural network model. According to the authors, the RMSE varied from 2.92 to 3.64 MJ/m² and the coefficient of determination varied from 0.52 to 0.74 for the individual years used to test the accuracy of the model. The proposed neural network model was developed and tested for a limited number of sites, the results suggest that it can be used to estimate daily

solar radiation when measurements of only daily maximum and minimum air temperature and precipitation are available.

Table 2. Summary of applications of artificial neural networks in solar radiation estimation.

Number	Authors	References	Year	Subject
1	Senkal and Kuleli	[88]	In	Estimation of solar radiation
2	Bosch et al.	[87]	In	Daily solar radiation estimation
3	Moustrisa et al.	[86]	2008	Creation of hourly global and diffuse solar
4	Rehman, Mohandes	[85]	2008	Estimation of global solar radiation
5	Mubiru and Banda	[84]	2008	Estimating of average monthly solar radiation
6	Gabriel and Christian	[83]	2008	Clear-sky solar luminous efficacy determination
7	Elminir et al.	[82]	2007	Prediction of diffuse fraction K_D
8	Alama et al.	[81]	2006	Computation of beam solar radiation at normal incidence
9	Zarzalejo and Ramirez	[80]	2006	Estimating of hourly radiation from satellite
10	López et al.	[79]	2005	Estimation of a direct irradiation
11	Mellit et al.	[78]	2005	Prediction of daily solar radiation
12	Tymvios et al.	[77]	2005	Global solar radiation estimation
13	Adnan et al.	[76]	2005	Mean monthly solar irradiation
14	Hontoria et al.	[75]	2005	Generating of solar radiation synthetic series
15	Mellit et al.	[74]	2004	Estimation of solar radiation from sunshine duration
16	Sozen et al.	[72, 73]	2004	Estimation the solar potential
17	Reddy and Manish	[71]	2003	Estimating monthly and daily global solar radiation
18	Kalogirou et al.	[70]	2002	Prediction of maximum irradiation
19	Tymvios et al.	[69]	2002	Total solar energy on a horizontal level
20	Dorvio et al.	[68]	2002	Estimate solar radiation and clearness index
21	Hontoria et al.	[66,67]	2001	Generation of solar radiation maps
22	Kalogirou	[65]	2001	Generating of solar radiation synthetic series AI for renewable energy systems , includes meteorological data
23	Mihalakakou et al.	[64]	2000	Simulation of total solar radiation
24	Sfetsos and Coonick	[63]	2000	Forecasting of solar radiation
25	Hontoria et al.	[62]	2000	Generation of solar radiation map
26	Mohandes et al.	[61]	2000	Monthly mean of daily values of global solar radiation on horizontal surfaces
27	Zufiria et al.	[60]	1999	Generating series of solar radiation
28	Hontoria et al.	[59]	1999	Generating series of solar radiation
29	Guessoum et al.	[58]	1998	Prediction and forecasting of daily solar radiation
30	Alawi and Hinai	[57]	1998	Solar radiation in areas not covered by direct measurement instrumentation
31	Mohandes et al.	[56]	1998	Prediction of mean monthly global solar radiation data
32	Williams et al.	[54,55]	1994 1996	Estimation of daily solar radiation
33	Elizondo et al.	[53]	1994	Prediction of daily solar radiation

Williams et al. [54,55] proposed the use of feed-forward neural networks to estimate the daily solar radiation. The authors used as inputs other meteorological parameters such as precipitation, temperature, clear sky radiation, day length and day of the year. Mohandes et al. [56] used data from 41 collection stations in Saudi Arabia. From these, the data for 31 stations

were used to train a neural network and the data for the other 10 for testing the network. The input values to the network are latitude, longitude, altitude and sunshine duration. The results for the testing stations obtained are within 16.4% and indicate the viability of this approach for spatial modeling of solar radiation.

Alawi and Hinai [57] used ANNs to predict global solar radiation in areas not covered by direct measurement instrumentation. The input data to the network are the location, month, mean pressure, mean temperature, mean vapor pressure, mean relative humidity, mean wind speed and mean duration of sunshine. The ANN model predicts solar radiation with an accuracy of 93% and mean absolute percentage error of 7.3. In addition, the model was tested to predict global radiation values for the Seeb location over a 12-month period. The monthly-predicted values of the ANN model compared to the actual global radiation values for Seeb produced an accuracy of 95% and a mean absolute percentage error of 5.43.

A radial basis function network has been used for the prediction of daily solar radiation data in Algeria [58]. The proposed model has been tested and compared with the measured global solar radiation for Algiers; the RMSE is 0.000325 and the correlation coefficient is 97%. Hontoria et al. [59] improved the generation of hourly solar radiation artificial series using neural networks. A neural network approach for generating solar radiation artificial series has been proposed by Zufiria [60].

Mohandes et al. [61] used RBF networks for modeling monthly mean daily values of global solar radiation on horizontal surfaces and compared its performance with that of a MLP model and a classical regression model. The proposed network employs as inputs the latitude, longitude, altitude and sunshine duration. According to the authors, the results on locations that are not included in the modeling indicate viability of the neural network methods to solve such problems when compared with a classical regression model. Although the data sample is relatively small, representing only 1 year from each of 32 locations, it demonstrates the concept. The average MAPE for the MLP network is 12.6 and the average MAPE for RBF networks is 10.1.

Hontoria et al. [62] applied a recurrent ANN for modeling the global solar radiation. The proposed model has been applied and tested in Spanish locations with good accuracy. Sfetsos and Coonick [63] introduced a simple approach for the forecasting of hourly solar radiation using various artificial intelligence based techniques (ANNs and ANFIS). They also investigated other meteorological variables such as temperature, wind speed and pressure. A comparison between the various models in terms of prediction error and training time indicated the LM network as the optimum prediction model. The performance of the LM and the ANFIS forecasting methods is enhanced when a wind direction is included in the input list. Overall, the best prediction results are found from the multivariate LM case, which exhibits 74% improvement in the RMS error when compared with that of the benchmark persistent approach.

Mihalakakou et al. [64] developed a total solar radiation time series simulation model based on ANN and applied it in Athens. The Neural Logic Network was identified as the model with least error. It incorporates Logic Rules that produced an RMS error of 4.9% lower than the persistent approach. Artificial neural networks in renewable energy systems applications were reviewed and discussed by Kalogirou [65]. Hontoria et al. [66, 67] proposed a recurrent neural network and MLP network for generating solar radiation synthetic series. A comparison between the MLP and other two models was carried out and according to the authors, the values of the annual irradiation of the synthetic year obtained by

the MLP method were closer to the real data than the values of the years obtained by the other two methods. Dorvio et al. [68] used radial basis functions and multi-layer perception methods to estimate solar radiation by using long-term data from eight stations in Oman. It is shown that both the RBF and MLP models performed well, based on the RMSE between the observed and estimated solar radiation values. However, the RBF is preferred because it requires less computing power and time. The RMSE value of $0.83 \text{ MJ/m}^2\text{-day}$ is obtained for the RBF and $1.01 \text{ MJ/m}^2\text{-day}$ for the MLP. Tymbios et al. [69], used an artificial neural network for estimating the total solar energy on a horizontal surface. Kalogirou et al. [70] used an ANN model for prediction of maximum solar radiation from relative humidity and temperature. The results obtained indicate that the correlation coefficient varied between 98.58% and 98.75%.

An ANN based model for estimation of monthly daily and hourly values of solar global radiation were proposed by Reddy and Manish [71]. Solar radiation data from 13 stations spread over India have been used for training and testing the ANN. The maximum mean absolute error between predicted and measured hourly global radiation is 4.07%. The results indicate that the ANN model show promise for predicting solar global radiation at places where monitoring stations are not established. Sozen et al. [72, 73] used a neural network for the estimation of solar potential based on geographical and meteorological data (latitude, longitude, altitude, month, mean sunshine duration and mean temperature) as input of the network. The measured data from seventeen stations in Turkey collected between the years 2000 and 2002 were used. One set with data for 11 stations was used for training a neural network and the other dataset from six stations was used for testing. According to the authors, the maximum mean absolute percentage error was found to be less than 6.7% and R^2 values to be about 99.89% for the testing stations. The predictions from the ANN models could enable scientists to locate and design solar-energy systems in Turkey and determine the appropriate solar technology. Mellit et al. [74] used the radial basis function network for estimating total daily solar radiation data from measured daily sunshine duration. The correlation coefficient obtained for the validation data set is 97.0%.

Hontoria et al. [75] used a MLP for developing a solar radiation map for Spain. The inputs are the previous irradiation, clearness index and the hour order number of the K_t . Figure 1 shows the proposed ANN for clearness index prediction. The classical methods are unable to generate solar radiation series in places where no solar information is available. Nevertheless, the methodology proposed is able to do the generation; it is more versatile than the classical methods and so is able to draw maps of the zone. This methodology is easily extendable to other places. The only requirement is the knowledge of the hourly solar radiation from only one site of the zone where the map is going to be drawn.

Sozen et al. [76] proposed an ANN for forecasting mean monthly solar radiation in Turkey. The proposed model has as input the geographical coordinates, mean sunshine duration, mean temperature and month. According to the authors, the results indicate that the ANN model seems promising for evaluating the solar resource potential at the places where there are no monitoring stations in Turkey. Figure 2 shows the proposed ANN for solar radiation forecasting. According to the authors, the best value of R^2 is 99.55% for Siirt (location in Turkey); similarly, maximum MAPE value is 5.28% for Sakarya (location in Turkey) and R^2 is 99.898% for Artvin. The predicted solar resource values are very close to the actual values for the all months.

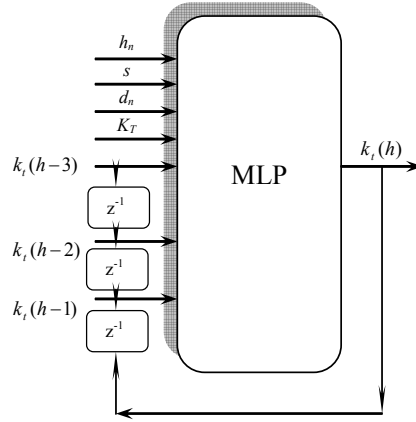


Figure 1. MLP architecture for clearness indexes prediction [75].

A comparative study of Angstroms and artificial neural network methodologies in estimating global solar radiation was presented by Tymvios et al. [77], where several models have been proposed. The parameters used as input were the daily values of measured sunshine duration, theoretical sunshine duration, maximum temperature and the month number. The period of data collection was 1986–1992 at Athalassa, Cyprus situated at latitude 35°08' N, longitude 33°23'E, altitude 161 m. According to the authors, the best ANN model was the one with all inputs except the month number and the results showed a MBE and RMSE of 0.12% and 0.67%, respectively. The ANN methodology is a promising alternative to the traditional approach for estimating global solar radiation, especially in cases where radiation measurements are not readily available.

Mellit et al. [78] proposed an ANN for prediction of daily solar radiation and this model has been applied for sizing a PV system. The correlation coefficient obtained for the validation data set is 98.0% and the mean relative error was less than 1.5%. The developed RBF has been applied in an Algiers location. López et al. [79] proposed the selection of input parameters to model direct solar irradiance by using artificial neural networks. The Bayesian framework ANN, named as automatic Relevance Determination Method (ARD), was employed to obtain the relative relevance of a large set of atmospheric and radiometric variables used for estimating hourly direct solar irradiance. The proposed novel methodology can be used in unfavorable conditions, in terms of limited amount of available data, giving accurate results.

Artificial intelligence techniques, such as fuzzy logic and neural networks, have been used for estimating hourly global radiation from satellite images [80]. The models have been fitted to measured global irradiance data from 15 Spanish terrestrial stations. The accuracy of the different models proposed is similar but artificial intelligence models (FL & NN) provide much better results. Despite the statistical analysis of the likelihood of the models not showing a definitive good fit with 95% confidence, the results seem to point to fuzzy and neural network models as better than regression models.

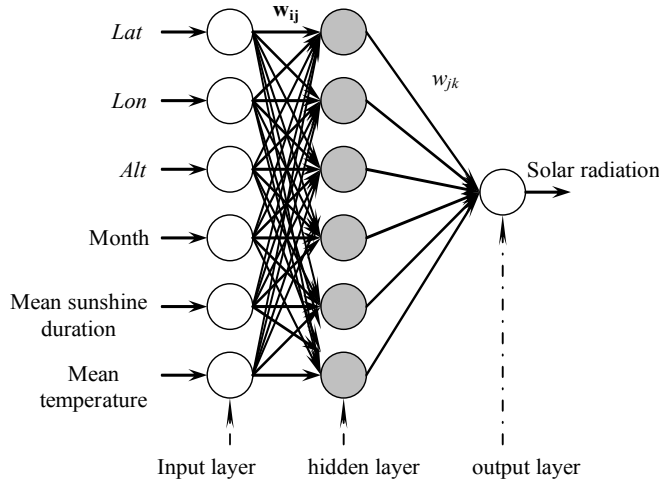


Figure 2. ANN architecture used incorporating six neurons in a single hidden layer [76].

Alam et al. [81] proposed an ANN model for estimating beam solar radiation. A new defined parameter, known as Reference Clearness Index (RCI), is introduced. Computation of monthly mean daily beam solar radiation at normal incidence has been carried out. According to the authors, the results of ANN model were compared with measured data based on Root Mean Square Error (RMSE) and Mean Bias Error (MBE). The RMSE obtained for the ANN model varied between 1.65-2.79% for an Indian region. Figure 3 shows the proposed ANN used for estimating the beam solar radiation.

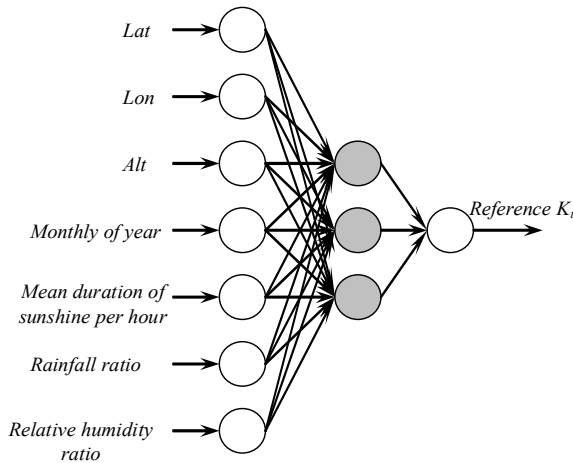


Figure 3. ANN architecture used for the estimation of beam solar radiation [81].

Elminir et al. [82] proposed an ANN model to predict diffuse fraction in hourly and daily scale. A comparison between the performances of the ANN model with that of two linear regression models has been reported. The results show that the ANN model is more suitable to predict diffuse fraction in hourly and daily scales than the regression models in the plain areas of Egypt. The predicted values were compared with the actual values and presented in

terms of usual statistics. According to the authors, the ANN model predicted infrared, ultraviolet and global insolation with a good accuracy of approximately 95%, 93% and 96%, respectively. In addition, ANN model was tested to predict the same components for Aswan over an 11-month period. The predicted values of the ANN model compared to the actual values for Aswan produced an accuracy of 95%, 91% and 92%, respectively. Data for Aswan were not included as a part of ANN training set. Hence, these results demonstrate the generalization capability of this approach over unseen data and its ability to produce accurate estimates.

Gabriel and Christian [83] used artificial neural networks for clear-sky solar luminous efficacy determination. The proposed ANN model can thus be used worldwide, avoiding the need of using detailed atmospheric information or empirical models if radiometric measurements and perceptible water data (or temperature and relative humidity data) are available. Relative errors, which are larger than 5%, are due to shortcomings in the ANN model that only occur when solar elevation, irradiance and illuminance are all very low and therefore are of marginal significance. The average RMS errors induced by the overall ANN model are found to be 1.8%, 2.4% and 1.7% for the direct, diffuse and global illuminances, respectively. These numbers decrease only slightly, to 1.6%, 2.3% and 1.6%, if zenith angles $>85^\circ$ are excluded, confirming that the incidence of the efficacy outliers indicated above is not significant when the end result (illuminance) of the overall method is considered.

Mubiru and Banda [84] used an artificial neural network for estimating the monthly average global solar irradiation on the horizontal surface in Uganda. The comparison between the ANN and empirical method emphasized the superiority of the proposed ANN prediction model. Estimates obtained for the validation site (Kampala), from the proposed ANN model were correlated with the measured values giving a correlation coefficient of 0.974. The corresponding MBE was 0.059 MJ/m² and the RMSE was 0.385 MJ/m². These results indicate an acceptable fitting between the estimated and measured global solar irradiation values.

Table 3 summarizes the Mean Absolute Percentage Error (MAPE) for estimating the average monthly global solar radiation in different location of the world by using different ANN architectures.

Table 3. MAPE for estimating the average monthly solar radiation by different ANNs architecture.

Model by author	Refs.	Year	MAPE
Mubiru and Banda	[84]	2007	0.3
Tymvios et al.	[77]	2005	0.12
Sozen et al.,	[76]	2004	6.7
Reddy et Manish	[71]	2003	4.07
Mohandes et al.	[61]	2000	10.1
Mihalakakou et al.	[64]	2000	0.2
Alawi and hinaï	[57]	1998	7.3
Mohandes et al.	[88]	1998	16.4

Rehman and Mohandes [85] used an ANN for estimation of daily solar radiation from air temperature and relative humidity at Abha City (Sausi Arabia). A set of 4 years has been used for training the network, while a set of one year is used for testing and validating the model. Results show that using the relative humidity along with daily mean temperature outperforms the other cases with absolute mean percentage error of 4.49%. The absolute mean percentage error for the case when only day of the year and mean temperature were used as inputs was 11.8% while when maximum temperature is used instead of mean temperature is 10.3%.

Moustrisa [86] employed neural network for creating missing mean, maximum and minimum global and diffuse solar irradiance hourly data, the meteorological data such as hourly data of air temperature, relative humidity, sunshine duration, clouds, as well as local latitude are used with regard to these sites, these data have been recorded during 1991–2000 at certain Greek locations. Following the same scheme, the produced hourly global and diffuse mean hourly solar irradiance values are in a very good agreement ($p<0.01$) with actual measurements.

A methodology for estimating of daily global irradiation on station located in complex terrain is proposed by Bosch [87], the proposed technique is based on the using of neural network. The ANN model developed provides a satisfactory performance with an RMSE of 6.0% when comparing the estimated values with the measured ones over the whole validation data set. On the other hand, model performance for each station has presented no dependence with the distance to the reference station or with the altitude, with RMSE below 7.5% and MBE lower than 1% for most of the stations. In addition, this methodology can be applied to other areas with a complex topography

Sosan [88], they used an ANN for the estimation of solar radiation in Turkey (26–45 E and 36–42 N). Meteorological and geographical data (latitude, longitude, altitude, month, mean diffuse radiation and mean beam radiation) are used in the input layer of the network, and solar radiation is the output. Additionally, the authors used a physical method for estimating solar radiation from Meteosat-6 satellite C3 D data. The RMS between the estimated and ground values for monthly mean daily sum with ANN and Physical method values have been found as 2.32 MJ m⁻² (54 W/m²) and 2.75 MJ/ m² (64 W/m²) (training cities), 3.94 MJ /m² (91 W/m²) and 5.37 MJ /m² (125 W/m²) (testing cities), respectively.

3.2. Application of Neural Network and Wavelet for Wind-Speed Prediction

Table 4 lists the application of ANN-based prediction on wind speed. A neural network approach is formulated for the wind speed prediction and compares its performance with an autoregressive model, after observing the statistical characteristics of mean monthly and daily wind speed in Jeddah, Saudi Arabia [89]. The autocorrelation coefficients are computed and are found compatible with the real diurnal variation of mean wind speed. In addition, the stochastic time series analysis is found to be suitable for the description of autoregressive model that involves a time lag of one month for the mean monthly prediction and 1 day for the mean daily wind speed prediction.

Table 4. Summary of applications of artificial neural networks and wavelet in wind speed prediction.

Number	Authors	References	Year	Subject
1	Bilgili et al.	[93]	2007	Prediction of wind speed based on references stations
2	Cadenasa and Riverab	[94]	2007	Prediction of wind speed
3	Barbounis et al.	[91,92]	2006,2007	Long-term wind speed and power forecasting
4	Flores et al.	[95]	2005	Application of a control algorithm for wind speed and active generation
5	Aksoy et al.	[96]	2004	Generation of hourly wind sped based on stochastic and wavelet analysis
6	Sfetsos	[90]	2000	Application of various forecasting techniques applied to mean hourly wind speed time series
7	Mohandes et al.,	[89]	1998	Wind speed prediction

The comparison of various time series forecasting approaches on mean hourly wind speed data had been proposed by Sfetsos [90]. The model with the least error was identified as a neural logic network that incorporates logic rules that produced an RMS error of 4.9% lower than that of the persistent approach. Table 5 summarizes a comparison between different models.

Table 5. Forecasting results [90].

Model	RMSE	% improvement from persistent	Architecture	Ct(%)
Persistent	1.2587	--	--	--
AR(2)	1.2383	1.62	--	--
ARIMA 1	1.2303	2.25	(2,1,2)	--
ARIMA 2	1.2607	-0.15	(0,1,0)	--
Linear NN	1.2161	3.37	No	79
BPNN	1.2111	3.78	6 Hidden neurones	532
LM NN	1.1999	4.67	4 Hidden neurones	5
RBF	1.2121	3.70	35 Hidden neurones	39
ELM	1.2250	2.67	3 Hidden neurones	331
ANFIS	1.2062	4.17	9 rules	7
NLN	1.2048	4.28	No Hidden neurones	22
NLN+LR	1.1971	4.89	3 Hidden neurones	141

Barbounis et al. [91, 92] proposed a recurrent ANN for long-term wind speed and power forecasting. Two novel learning algorithms are introduced for the training of the recurrent forecast models, the Global Recursive Prediction Error (GRPE) and the Decoupled Recursive Prediction Error (DRPE), that have considerably smaller computational and storage requirements. Figure 4 shows the proposed RNN for wind speed and power forecasting. Bilgili et al. [93] used an artificial neural network for the wind speed prediction of a target station using reference stations' data; the maximum mean absolute percentage error was found to be 14.13% for Antakya meteorological station and the best result was found to be 4.49% for Mersin meteorological station.

Comparison of two techniques for wind speed forecasting in the South Coast of the state of Oaxaca, Mexico was presented in Ref [94]. Autoregressive Integrated Moving Average (ARIMA) and the ANN methods are applied to a time series of 7 years of wind speed measurements. Six years were used in the formulation of the models and the last year was used to validate and compare the effectiveness of the generated prediction by the techniques mentioned above. Particularly for this case, seasonal ARIMA models present a better sensitivity to adjustment and prediction of wind speed. Nevertheless, it is probable that when increasing the number of training vectors for the ANN model, its performance will improve. A control algorithm based on neural network has been proposed in Ref [95]. This algorithm has been used for wind speed and active generation power. According to the authors, if the ANN is used to predict the wind speed at a wind farm, the active and reactive power generation policies can be established in order to obtain the maximum economic benefits for both producers and utilities.

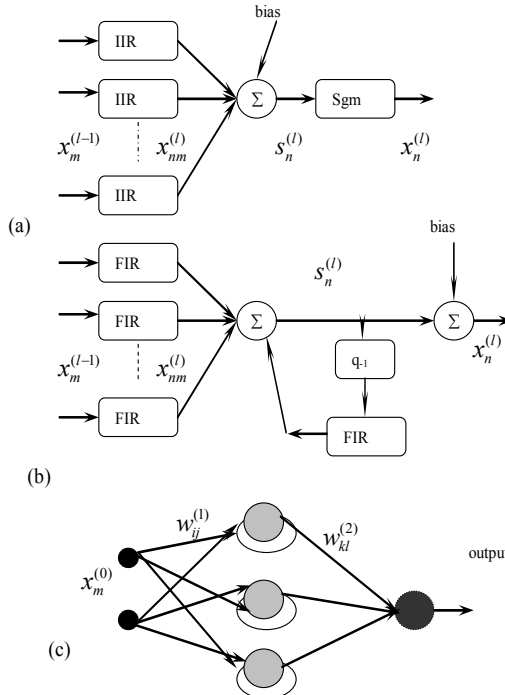


Figure 4. Local recurrent NNs used for wind forecasting. (a) Neuron model for IIR-MLP. (b) Neuron model for Local Activation Feedforward-Multilayer Network (LAF-MLN). (c) Dynamic Recurrent Neural Network (DRNN) configuration [91,92].

In ref [96], a new wind speed data generation scheme based on wavelet transformation is introduced and compared to the existing wind speed generation methods namely normal and Weibull distributed independent random numbers. The results obtained prove that the wavelet-based approach, as a wind speed data generation scheme, is better than the existing methods. For example, the wavelet method is the best in preserving the correlation structure of the sequence. Additionally, this method is as good at preserving other statistical features of the series as the other methods. Therefore, it can be concluded that the wavelet method proposed can be used as a tool to substitute the classical generation schemes for the simulation of hourly mean wind speed data.

3.3. Application of Neural Network for Mean Temperature Prediction

Imran et al. [97] utilized artificial neural networks for the prediction of hourly mean values of ambient temperature 24 hours in advance. Full year hourly values of ambient temperature are used to train a neural network model for the coastal location of Jeddah, Saudi Arabia. The mean percent deviation between the predicted and measured values is found to be 3.16, 4.17 and 2.83 for three different years.

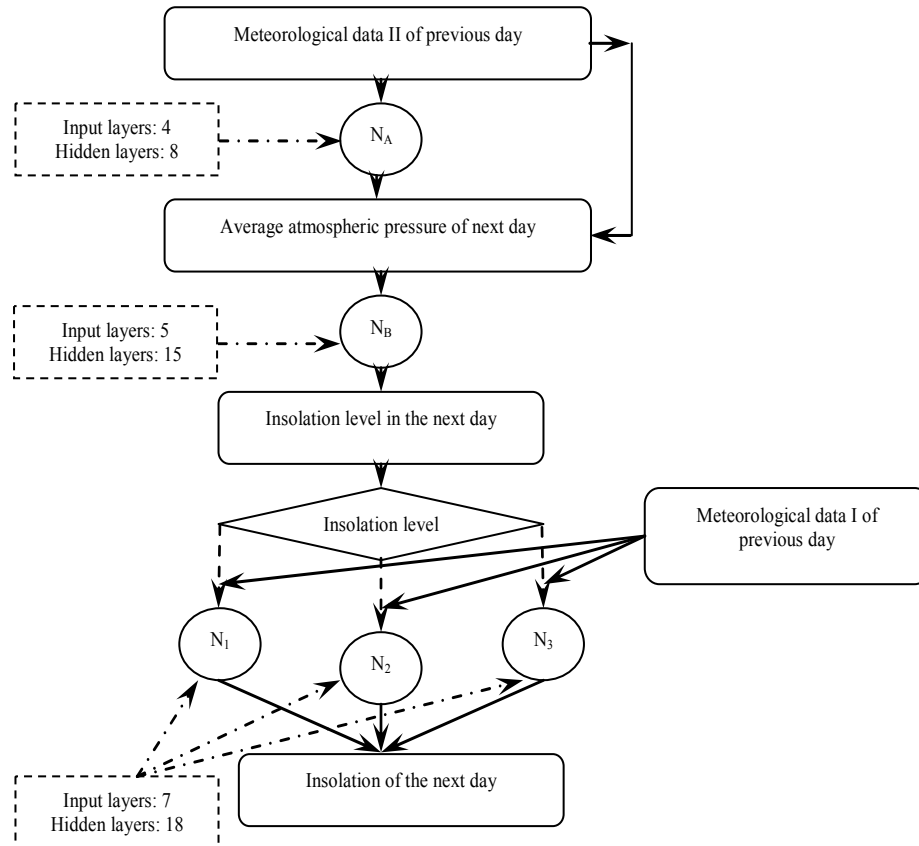


Figure 5. Flowchart for insolation forecast using a multi-stage neural network [98].

3.4. Application of Neural Network for Forecasting Insolation And Diffuse Fraction

Two applications concern the application of neural network for forecasting insolation (see Table 6). Kemmoku et al. [98] used a multistage ANN to predict the insolation of the next day. The input data to the network are the average atmospheric pressure, predicted by another ANN and various weather data of the previous day. The results obtained show a prediction accuracy of 20%. Authors propose to use a multi-stage NN method for forecasting the insolation of the next day. Figure 5 shows the block diagram of the multi-stage NN used for forecasting the insolation.

Table 6. Summary of applications of artificial neural networks for forecasting of insolation.

Number	Authors	References	Year	Subject
1	Elminir et al.	[99]	2005	Prediction of diffuse fraction
2	Kemmoku et al.	[98]	1999	Insolation forecasting

Elminir [99] used an ANN for estimating the diffuse fraction, Estimation of solar radiation components incident on Helwan site using neural networks. The results indicates that, the ANN model predicted infrared, ultraviolet, and global insolation with a good accuracy of approximately 95%, 93% and 96%, respectively.

3.5. Application of Fuzzy Logic for Solar Radiation and Sunshine Duration

Table 7 illustrates two applications of fuzzy logic for solar radiation and sunshine estimation. Sen [100] used a fuzzy logic for estimating solar radiation from sunshine duration measurements. The fuzzy approach is applied for three sites with monthly average of daily irradiances in the western part of Turkey. According to the authors, the necessary fuzzy rule bases of the solar irradiation estimation from available sunshine duration are given and applied to some stations on the western part of Turkey at different latitudes. The application of the proposed fuzzy subsets and rule bases is straightforward for any irradiation and sunshine duration measurements in any part of the world.

A fuzzy model of solar irradiance on inclined surfaces has been developed by Gomez and Casanovas [101]. The fuzzy model includes concepts from earlier models, though unlike these, it considers non-disjunctive sky categories. The proposed model offers performance similar to that of the models with the best results in the comparative analysis of the literature, such as the Perez model.

Table 7. Summary of applications fuzzy logic for estimating of solar radiation and sunshine duration.

Number	Authors	References	Year	Subject
1	Iqdour and zeroual	[102]	2005	Prediction of global solar radiation
2	Gomez and Casanovas	[101]	2003	Solar radiation model
3	Sen	[100]	1998	Estimation of solar radiation and sunshine duration

Iqdour and zeroual [102], used the Takagi-Sugeno (TS) fuzzy systems, for modeling daily global solar radiation recorded in Marrakesh, Morocco. The results obtained from the proposed model have been compared with two models based on higher order statistics; the fuzzy model provides better results in the prediction of the daily solar radiation in terms of statistical indicators. The Normalized RMSE is 13.97% for the fuzzy model, while about 19.96% and 16.72 % for the models based on the higher order statistics.

3.6. Application of Neuro-Fuzzy for Solar Radiation, Sunshine Duration and Clearness Index

Table 8 reviews the application of ANFIS for estimating total solar radiation. A Neuro-Fuzzy approach has been developed for prediction of clearness index (K_t) in isolated sites for Algeria [103]. The inputs of this model are the geographical coordinates and the outputs are the mean monthly K_t .

Table 8. Summary of applications of neuro-fuzzy solar radiation, sunshine duration and clearness index.

Number	Authors	References	Year	Subject
1	Mellit et al.	[103,105]	2006, 2007	Estimation of K_t and H in isolated area
2	Mellit et al.	[104]	2007	Estimation of solar radiation from sunshine duration and mean temperature

A new model for the prediction of daily solar radiation is proposed by Mellit et al. [104]. This model combines neural network and fuzzy logic (ANFIS). The input of this model is the mean temperature and sunshine duration. Figure 6 illustrates the ANFIS-model used for estimating the irradiation from the mean temperature and the sunshine duration. Table 9 presents a comparison between different ANNs and the proposed ANFIS.

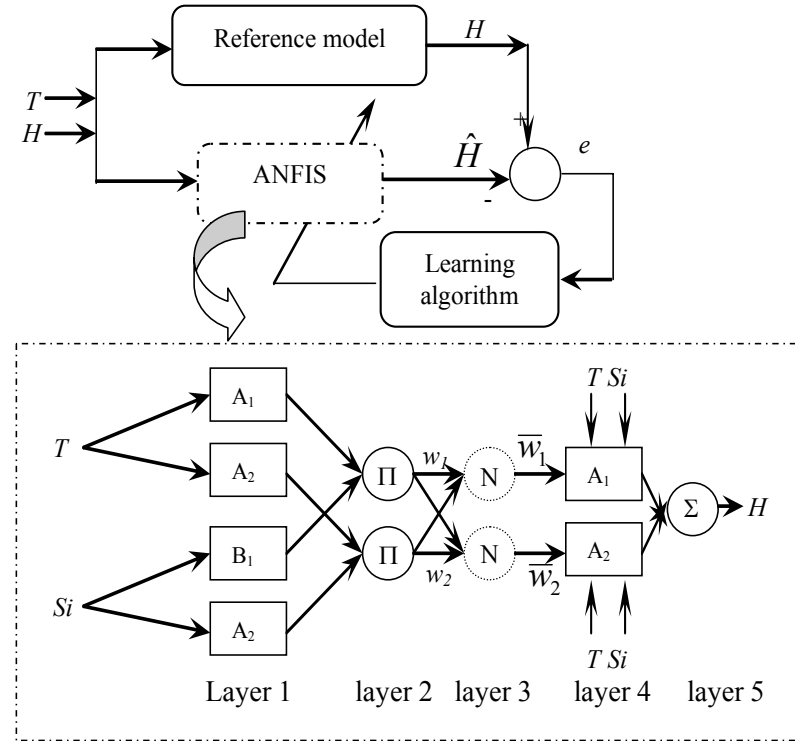


Figure 6. The ANFIS-model used for estimating of the irradiation from the mean temperature and the sunshine duration .[104]

Table 9. Training results from each network structure [104].

Artificial neural network structure	# of iterations	MSE for test set	R ² (%)
MLPN (2x15x1)	2112	0.00997	96
RBFN(2x15x1)	1846	0.00995	96.6
RNN (2x15x1)	1439	0.00990	97.4
ANFIS (2x15x1)	319	0.00912	98

Mellit et al. [105] also proposed a new model based on neuro-fuzzy for predicting the sequences of monthly clearness index and proposed it for generating solar radiation, which has been used for the sizing of a PV-system. The authors proposed a hybrid model for estimating sequences of daily clearness index by using an ANFIS and Markov chain; the proposed model has been used for estimating the daily solar radiation. An application of sizing a PV-system is presented based on the data generated by this model. Figure 7 shows the proposed ANFIS-based prediction for monthly clearness index.

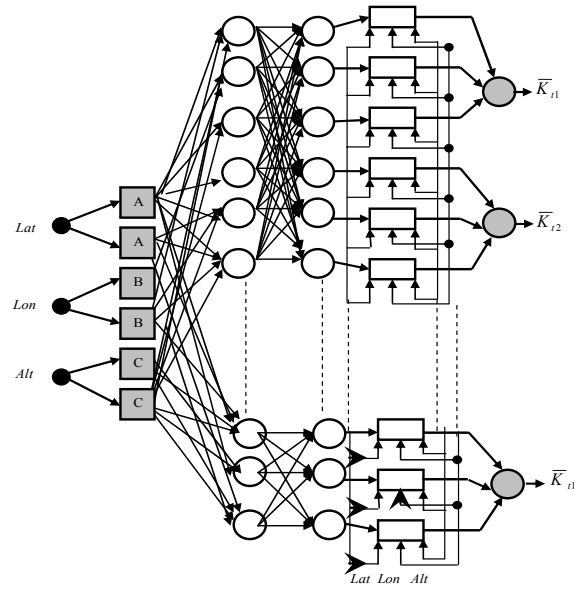


Figure 7. The proposed ANFIS-based prediction for monthly clearness index [105].

3.7. Application of Neural Network and Markov Chain for Solar Radiation Prediction

Mellit et al. [106, 107] proposed a simplified hybrid model for generating sequences of total daily solar radiation, which combine a neural network and Markov chain. This model is called ANN-MTM (Markov Transition Matrix). The inputs of the proposed model are the geographical coordinates while the outputs are the daily total solar radiation. It can be used for generating sequences of solar radiation at long term and it was applied for Algeria. Figure 8 shows the hybrid configuration for generating sequences of daily solar radiation data. The unknown validation data set produced very accurate prediction with an RMSE error not exceeding 8% between the measured and predicted data. A correlation coefficient ranging from 90% and 92% has been obtained.

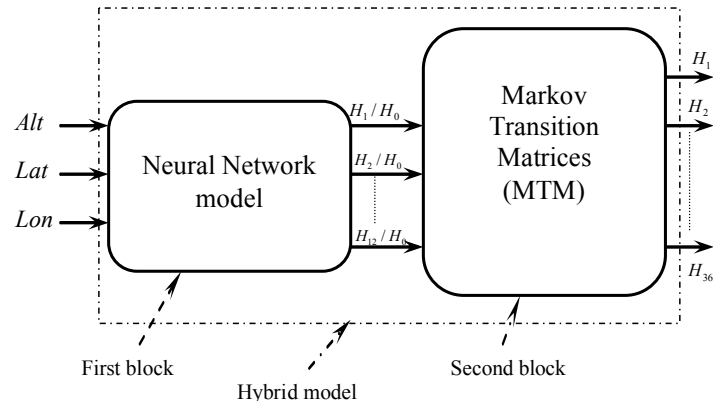


Figure 8. Block diagram of hybrid model ANN-MTM [107].

3.8. Application of Neural Networks and Wavelet Analysis for Forecasting Solar Radiation

Table 10 lists the applications of neural networks and wavelet analysis for forecasting of solar radiation. Cao and Cao [108] developed a hybrid model for forecasting sequences of total daily solar radiation, which combines artificial neural network with wavelet analysis. The characteristics of this method is the pre-processing of data using wavelet transformation, i.e., the data sequence of solar irradiance is first mapped into several time-frequency domains and then a recurrent Back-Propagation network is established for each domain. According to the authors, the results showed that the accuracy of the method is more satisfactory than that of the methods reported before (see Fig. 9). An example of solar irradiance shows that the RMSE of the training and the forecast with wavelet analysis are 0.8997 and 0.9277 MJ/m²-day respectively. The MRE of the forecast with wavelet analysis accounts for 7.83%, which is about one fourth of the forecast without wavelet analysis.

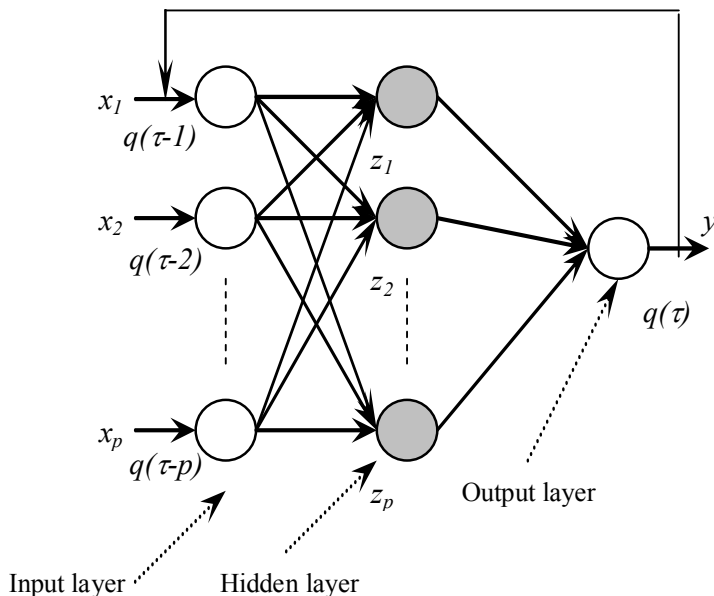


Figure 9. Flowchart of RBPN (Recurrent Network Back Propagation Network) training [108].

Table 10. Summary of applications of artificial neural networks and wavelet analysis for forecasting of solar radiation.

Number	Authors	References	Year	Subject
1	Shuanghua and Jiacong	[108, 110]	2005, 2006	Estimation of total daily solar radiation
2	Mellit et al.	[109, 111]	2006, 2006	Estimation of total daily solar radiation Time series prediction

Mellit et al. [109] also proposed an artificial neural network with discrete wavelet transforms for time series prediction. This model has been used for the prediction of solar radiation based on sunshine duration and mean temperature; the proposed architecture is shown in Figure 10. Table 11 displays the statistical features (mean, variance, RMSE and the Kolmogorov-Smirnov test [KS]) between the measured daily global solar radiation data and those predicted by the model. It is found that there is no significant difference between the predicted and the measured data from the statistical features point of view. The correlation coefficient obtained for the validation data set is 96.2%. Cao and Cao [110] used neural network and wavelet analysis for prediction of solar radiation. According to the authors, this method presents remarkable improvement in the accuracy of the forecast for the day-by-day solar irradiance of a year compared with that without combining wavelet transformation. The mean error of the forecast is 7.83%, which is one fourth of the forecast without wavelet analysis.

Mellit et al. [111] proposed an adaptive wavelet-network model for forecasting daily total solar radiation. In this study, several structures have been investigated for resolving the missing data problem. In this particular estimation process, the model consists of an adaptive neural-network topology with the wavelet transformation embedded in the hidden units. In cascade with the network is a local IIR (Infinite Impulse Response) block structure, as shown in Figure 11.

Table 11. comparison between measured and predicted daily solar radiation [109] (statistical test).

Solar radiation (Wh/m ² /day)	Mean	Variance	RMSE	Kolmogorov-Smirnov test (KS)
Measured	3652	0.2531	96.2	0.0013
Predicted	3645	0.2635		

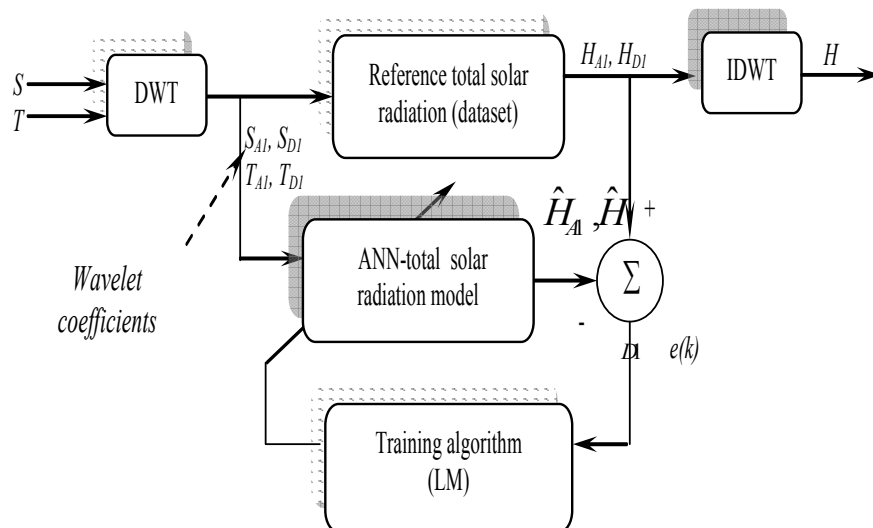


Figure 10. Flowchart of discrete wavelet transform (DWT) with ANN for estimating the solar radiation from sunshine duration and mean temperature [109].

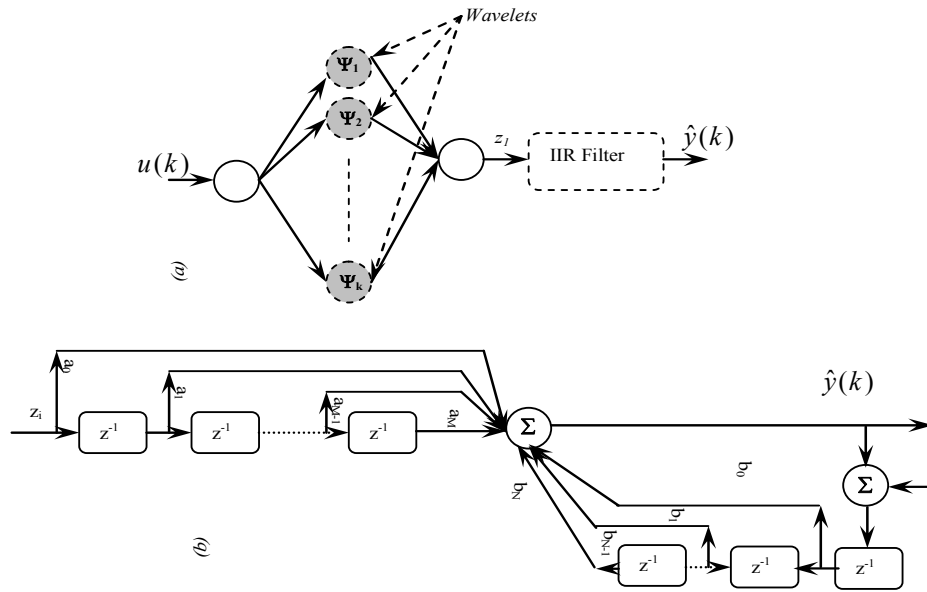


Figure 11. IIR adaptive wavelet-network structure: (a) neural-network architecture, (b) IIR model [111].

3.9. Application of ANN for Weather Forecasting

Table 12 presents the application of the ANN in the weather forecasting. Maqsood et al. [112, 113] used connectionist-learning paradigms for Canadian weather analysis. An intelligent weather monitoring systems using connectionist models was also developed by Khan and Abraham [114]. Maqsood et al. [115] presented a soft computing model based on a radial basis function network (RBFN) for 24-hour weather forecasting of southern Saskatchewan, Canada. The model is trained and tested using hourly weather data of temperature, wind speed and relative humidity for 2001. The results indicate that the RBFN produces the most accurate forecasts compared to the MLP, ERNN and HFM.

Table 12. Summary of applications of artificial neural networks in weather forecasting.

Number	Authors	References	Year	Subject
1	Maqsood et al.	[112, 113]	2002, 2002	Weather analysis and forecasting
2	Khan and Abraham	[114]	2002	Intelligent weather monitoring systems
3	Maqsood and Ajith	[115]	2007	Weather forecasting (include, air temperature, humidity, irradiation, etc)
4	Maqsood et al.	[116]	2005	Weather forecasting

Maqsood and Abraham [116] presented a comparative analysis of different connectionist and statistical models for forecasting the weather of Vancouver, Canada. For developing the models, one year's of data comprising daily temperature and wind speed were used. A MLPN

and an Elman recurrent neural network (ERNN) were trained using the one-step-secant and Levenberg–Marquardt algorithm. Radial basis function network was employed as an alternative to examine its applicability for weather forecasting. According to the authors, the proposed ensemble approach produced the most accurate forecast, while the statistical model was relatively less accurate for the weather forecasting problem considered.

3.10. Evolving Polynomial Neural Network for Forecasting of Meteorological Data

Recently, an application of Evolving Polynomial Neural Network (EPNN) for predicting meteorological time-series data (Solar irradiance, ambient temperature, relative humidity, and wind speed) is developed by Mellit [117]. The problem of time series prediction is formulated as a system identification problem, where the input to the system is the past values ($y(t-1), y(t-2), y(t-3), \dots$) of a time series and its desired output ($y(t), y(t+1), y(t+2), \dots$) are the future of a time series. Dataset of meteorological time series for five years collected from Algiers (Algeria) has been used. The Group Method of Data Handling (GMDH) and Genetic Algorithm (GA) are combined in order to obtain a hybrid model called Genetic-based Self-Organizing Network (GBSON).

Firstly, the data were normalized to take values from zero to one [0,1], before using them as input data to the polynomial neural networks. Subsequently, the input pattern was assigned as $x(t-1), x(t-2)$ and $x(t-3)$ and the desired output was $x(t)=f(x(t-1), x(t-2), x(t-3))$. Therefore, from the 1825 available data points, 1460 points were used for training the network while 365 data points were used for validation of potential models for each parameter (i.e. H, G, T and W). A soft computing program is developed on the Matlab (Ver. 7.5) environment. The number of generation is 500, the crossover probability (P_{cross}) is 0.8 and the mutation probability (P_{mut}) of 0.01. The different step of the used GBSON is summarized as follows:

Step 1. Determine system input variables, form training, and the testing data (normalized data)

Step 3. Determine initial information for constructing the PNN structure

Step 4. Apply genetic algorithm for determining the PN structure using.

- Representation
- Fitness Evaluation
- Selection
- Crossover & Mutation
- Elitism

Step 5. Estimate the coefficients of the polynomial corresponding to the selected node (PN)

Step 6. Select nodes (PNs) with the best predictive capability, and construct their corresponding layer. All nodes of the corresponding layer of PNN architecture are constructed by genetic optimization.

Step 7. Check the termination criterion

Step 8. Determine new input variables for the next layer. The PNN algorithm is carried out by repeating steps 4-8 consecutively

The results show a good agreement between both the series (measured meteorological data) and those predicted by GBSON model. The correlation coefficient (R) is between 98.54% and 99.23%, and the mean relative error also is between 3.44×10^{-4} and 1.54×10^{-3} . from obtained results the proposed model provides more accurate results than other ANNs architecture (feed forward neural network, Radial Basis Function network, recurrent neural network locally feedback), wavenet and adaptive neuro-fuzzy inference scheme. Figure 12 a comparison between measured and estimated.

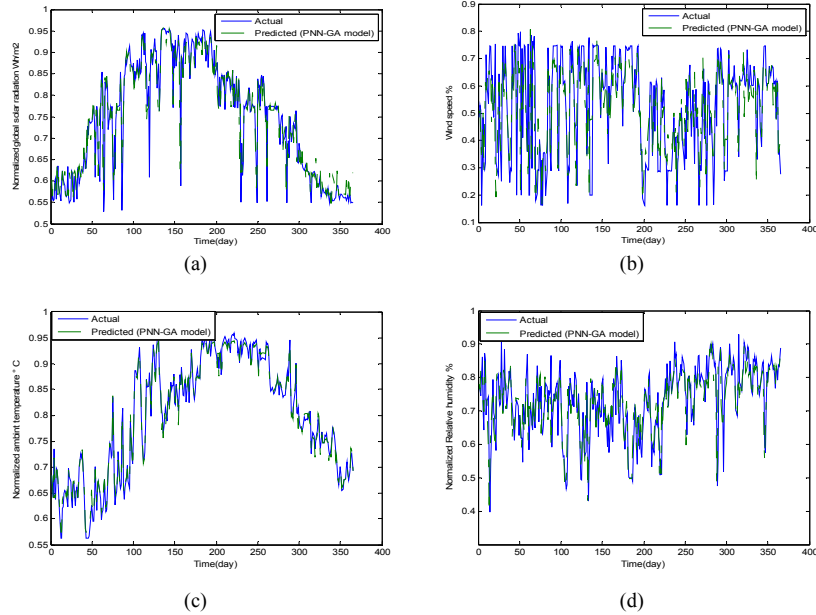


Figure 12. Comparison between measured and estimated meteorological data by using the GBSON (PNN-GA) model: (a) Solar radiation, (b) Wind speed, (c) Ambient temperature and (d) Relative humidity.

As can be seen, good agreement between both series (measured and predicted) for the different parameters used in this simulation (wind speed, relative humidity, air temperature and irradiation).

4. FPGA-BASED IMPLEMENTATION OF SOLAR RADIATION MODEL

The technology of field programming gate arrays (FPGA) was introduced in the mid-1980s. Its success was mainly due to its capability for implementing significantly more logic, and they could be programmed by a completely electrical process. The main feature of FPGAs is that they can be reprogrammed by user unlimited number of times. A hardware description language (HDL) used to design electronic systems at the component, board and system level. VHDL allows models to be developed at a very high level of abstraction. Initially conceived as a documentation language only, most of the language can today be used for simulation and logic synthesis.

According to the above applications, we note that the AI-technique has been demonstrated for modeling, and forecasting of solar radiation, insolation, cleanliness index and weather data. While software implementation is useful for investigating the capabilities of models based on AI-technique. Relatively they are not adequate for real-time processing in the context of large networks or on-line learning, number class of Fuzzy logic etc. In order to overcome these drawbacks an application of VHDL and neural network for solar radiation forecasting is developed in [18].

The proposed intelligent configuration will be used for implementing in the reconfigurable hardware architecture FPGA. The architecture exploits the inherent parallelism of neural networks. Once the designed model is validated and tested, the circuit can be easily implemented using hardware description language (HDLs), and the FPGA is used for realization of our circuit for forecasting the daily solar radiation.

The designed integrated circuit called TS-Irrad, can be used with other compounds for estimating the daily solar radiation based on ambient temperature and sunshine duration. To our knowledge, this is the first real time proposed application in solar radiation estimation. Figure 13 shows the proposed global architecture of the neural network based on VHDL.

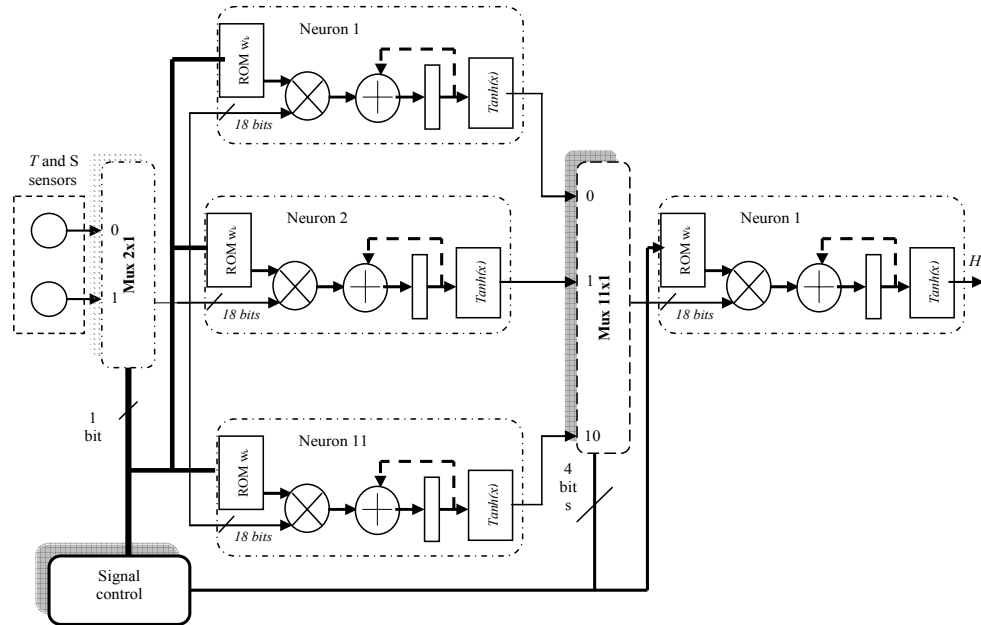


Figure 13. Global architecture of the neural network.

The simulation result based on VHDL is presented in figure 13 (a), where X_1 is the sunshine duration and X_2 is the mean average temperature, Y_1 is the daily total solar radiation. The ModelSim has been used for simulating the proposed architecture based on the VHDL. Comparison between MATLAB and VHDL estimation of the daily solar radiation is illustrated in Figure 13 (b), while figure 13 (c) presents the hardware FPGA-device used in this subject.

A simplified schema of the proposed circuit is presented in figure 15. This circuit can be used for estimating of the daily solar radiation data form T and S. The designed circuit

contains: two sensors for sunshine duration and ambient temperature, memory (RAM), converter (CAN-CNA), multiplexer (MUX), supply load and the designed integrated circuit.

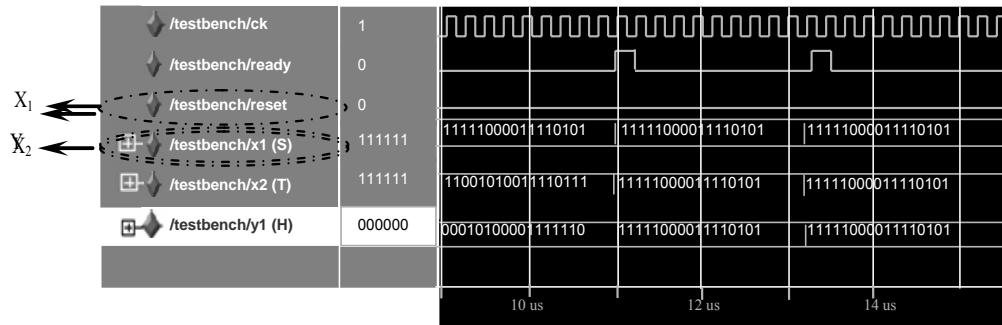


Figure 14a. Simulation results based on VHDL for prediction of solar radiation data from sunshine duration and mean temperature.

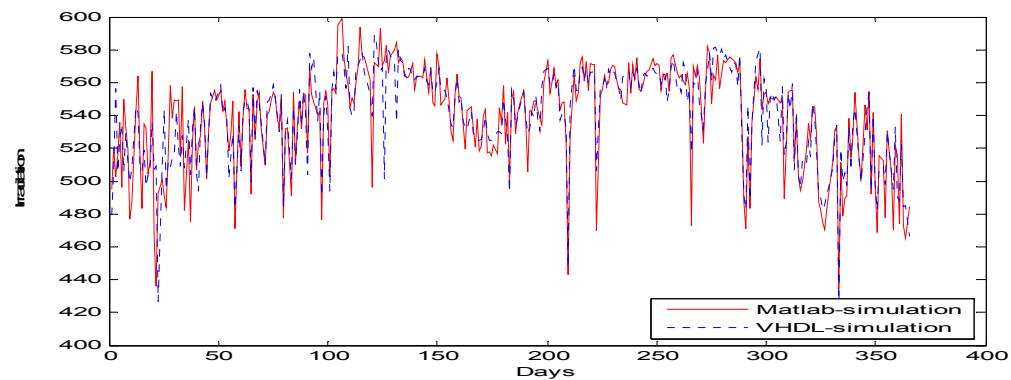


Figure 14b. Comparison between MATLAB and VHDL estimation of the daily solar radiation.

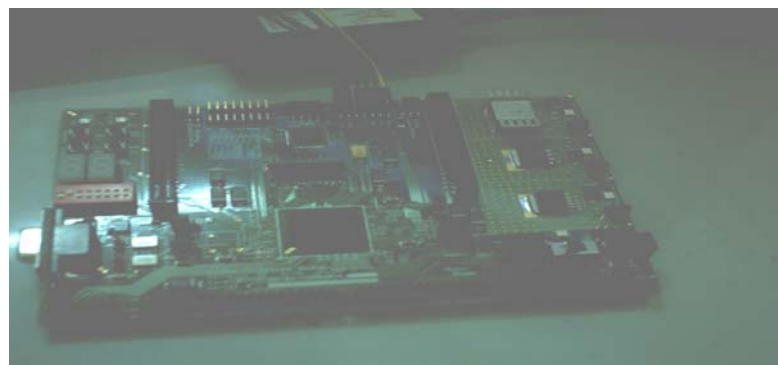


Figure 14c. FPGA Hardware used for solar radiation implementation, XILINX Virtex II.

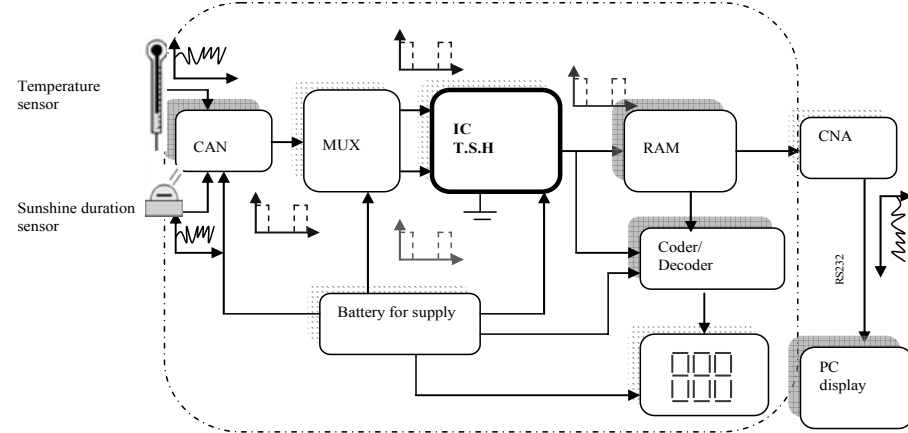


Figure 15. The designed circuit for estimating solar radiation based on sunshine duration and ambient temperature.

4. CONCLUSION

In this paper, various conventional and AI techniques used for modeling, forecasting and prediction of meteorological data have been reviewed. Based on to the above applications, the following remarks can be concluded:

- Artificial neural network-based models have been successfully developed to model solar radiation, wind speed, mean air temperature, relative humidity, insolation and cleanliness index (in different time scale, i.e. monthly, daily, hourly, etc.), thus improving the existing statistical approaches. These have been used for estimating data in sites where measurement instruments are not available.
- AI techniques differ from the traditional ones in that no transformations of the data are required (e.g. neural networks, fuzzy logic and neuro-fuzzy).
- It should be noted that some models have been applied for specific location, but they can be generalized to be used in different sites around the word.

Based on the work presented here it is believed that AI offers an alternative method, which should not be underestimated. Additionally, the reprogrammable hardware such as FPGA can offer a way for implementing intelligent meteorological model based on neural networks or hybrid neural networks (neuron-fuzzy, wavenet, etc.).

ACKNOWLEDGMENTS

The author would like to thank Pof. S.A. Kalogirou (Cyprus University of Technology) for their interesting remarks and helpful. Also, I wish to thank the ICTP for providing the necessary equipment for achieving the present work.

REFERENCES

- [1] Bendt P., Collares-Pereira M., Rabl A. The frequency distribution of daily insolation values. *Solar Energy*, 1981;27(1):1–5.
- [2] Hollands K.G.T., Huget R.G. A probability density function for the clearness index, with applications. *Solar Energy*, 1983;30(3):195–209.
- [3] Liu B.Y.H., Jordan R.C. The interrelationship and characteristic distribution of direct, diffuse and total solar radiation. *Solar Energy*, 1960;4(1):1–19.
- [4] Collares-Pereira M., Rabl A. The average distribution of solar radiation-correlations between diffuse and hemispherical and between daily and hourly insolation values. *Solar Energy*, 1979;22:155–65.
- [5] Mustacchi C., Cena V., Rocchi M. Stochastic simulation of hourly global radiation sequences. *Solar Energy*, 1979;23 (1): 47-51.
- [6] Olseth J.A., Skartveit A. A probability density function for daily insolation within the temperate storm belts. *Solar Energy*, 1984, 33 (6), 533-542.
- [7] Amato U., Andretta A., Bartolli B., Coluzzi B., Cuomo V., Fontana F., Serio C. Markov processes and Fourier analysis as a tool to describe and simulate daily solar irradiance. *Solar Energy*, 1986;37 (3):179-194.
- [8] Habbane A.Y., McVeigh J.C., Cabawe S.O.I. Solar radiation model for hot dry arid climates. *Applied Energy*, 1986;23:269-79.
- [9] Graham V.A., Hollands K.G.T., Unny T.E. A time series model for K_t with application to global synthetic weather generation. *Solar Energy*, 1988;40(2):83–92.
- [10] Aguiar R.J., Collares-Perrira M., Conde J.P. Simple procedure for generating sequences of daily radiation values using library of Markov transition matrices. *Solar Energy*, 1988;40 (3):269-279.
- [11] Maafi A., Adane A. A two state Markovian model of global irradiation suitable for photovoltaic conversion. *Solar Wind Technol.* 1989; 6:247–252.
- [12] Akinoslu B.G., Ecevit A. A further comparison and discussion of sunshine-based models to estimate global solar radiation. *Energy*, 1990;15:865–72.
- [13] Shuichi H., Mamoru M., Toshikazu I. Statistical time series models of solar radiation and outdoor temperature identification of seasonal Models by Kalman Filter, *Energy and Buildings*, 1990;15-16 : 373-383
- [14] Hokoi S., Matsumoto M. and Kagawa M. Stochastic models of solar radiation and outdoor temperature. *ASHRAE Trans.*, 1990; 2:245–252.
- [15] Aguiar R.J., Collares-Perreira M., T.A.G. A time dependent autoregressive Gaussian model for generating synthetic hourly radiation. *Solar Energy*, 1992;49 (3):167-174.
- [16] Ragab F.M., Som A.K. Correlation between estimated and measured hourly and daily solar fluxes over Bahrain. *Applied Energy*, 1991;40:83-99.
- [17] Dincer I., Dilmac S., Ture I.E., Edin M. A simple technique for estimating solar radiation parameters and its application for Gebze. *Energy Conversion and Management*, 1996;37(2):183-98.
- [18] Gopinathan K.K., Soler A. Diffuse radiation models and monthly-average, daily, diffuse data for a wide latitude range. *Energy*, 1995;20:657–67.
- [19] Yusof M.S., Hlaing W.M., Mahdi O.O., Wahab A. and Sulaiman A. Analysis of residuals in daily solar radiation time series. *Renewable Energy*, 1997;11(1): 9-105.

- [20] Parishwad G.V., Bhardwaj R.K., Nema V.K. Estimation of hourly solar radiation for India. *Renewable Energy*, 1997;12:303-313.
- [21] Rehman S., Halawani T.O. Global solar radiation estimation. *Renewable Energy*, 1997;12(4):369-85.
- [22] Mora-Lopez L.L. and Sidrach-de-Cardona M. Multiplicative ARMA models to generate hourly series of global irradiation. *Solar Energy*, 1998 ;63:283-291.
- [23] David B.A., Atsu S.S.D. Estimation of solar radiation from the number of sunshine hours. *Applied Energy*, 1999; 63:161-167.
- [24] Omer AM. Compilation and evaluation of solar and wind energy resources in Sudan. *Renew Energy* 1997; 12:39-69.
- [25] Craggsa C., Conwaya E., Pearsall N.M. Stochastic modeling of solar irradiance on horizontal and vertical planes at a northerly location. *Renewable Energy*, 1999; 18:445-463.
- [26] Badescu V. Correlations to estimate monthly mean daily solar global irradiation: application to Romania. *Energy*, 1999;24:883-93.
- [27] Sen Z., Sahin A.D. Spatial interpolation and estimation of solar irradiation by cumulative semivariograms. *Solar Energy*, 2001;71(1):11-21.
- [28] Rehman S. Empirical model development and comparison with existing correlations. *Applied Energy*, 1999; 64:369-78.
- [29] Helen C. Power estimating clear-sky beam irradiation from sunshine duration *Solar Energy*, 2001;71(4):217-224.
- [30] Meyer E.L., Vandyk E.E.. Development of energy model based on total daily irradiation and maximum ambient temperature. *Renewable Energy*, 2000 :21(1, 1) :37-47.
- [31] Batlles F.J., Rubio M.A., Tovar J., Olmo F.J., Alados-Arboledas L., Empirical modeling of hourly direct irradiance by means of hourly global irradiance. *Energy*, 2000;25:675-88.
- [32] Chegaar M., Chibani A., Global solar radiation estimation in Algeria. *Energy conversion and Management*, 2001;42: 967-973.
- [33] Sen Z., Tan E., Simple models of solar radiation data for north-western part of Turkey. *Energy Conversion and Management*, 2001;42:587-98.
- [34] Geiger M., Diabate L., Menard L. and Wald L., A web service for controlling the quality of measurements of global solar irradiation. *Solar Energy*, 2002;73(6): 475-480.
- [35] Wong L.T., Chow W.K., Solar radiation model. *Applied Energy*, 2001;69:191-224.
- [36] Celik A.N., Long-term energy output estimation for photovoltaic energy systems using synthetic solar irradiation data. *Energy*, 2003;28:479-493
- [37] Oliveira A. P., Escobedo J.F., Machado A.J., Soaresa J. Correlation models of diffuse solar-radiation applied to the city of Sao Paulo, Brazil. *Applied Energy*, 2002;71:59-73.
- [38] Safi S., Zeroual A., Hassani M. Prediction of global daily solar radiation using higher order statistics. *Renew Energy*, 2002;27:647-66.
- [39] Santos J.M., Pinazo J.M., Canada J., Methodology for generating daily clearness index values Kt starting from the monthly average daily value Kt. Determining the daily sequence using stochastic models. *Renewable Energy*, 2003;28:1523-1544.
- [40] Notton G., Cristofari C., Muselli M, Poggi P. Calculation on an hourly basis of solar diffuse irradiations from global data for horizontal surfaces in Ajaccio. *Energy Conversion and Management*, 2004;45:2849-2866.

- [41] Ravinder K., Umanand L. Estimation of global radiation using clearness index model for sizing photovoltaic system. *Renewable Energy*, 2005;30:2221-2233
- [42] Jain P.K., Lungu E.M. Stochastic models for sunshine duration and solar irradiation. *Renewable Energy*, 2002;27: 197-209.
- [43] Yorukoglu M., Celik A.N. A critical review on the estimation of daily global solar radiation from sunshine duration. *Energy Conversion and Management*, 2006;47:2441-2450
- [44] Jebara S., Iniyab S. A review of energy models. *Renewable and Sustainable Energy Reviews*, 2006; 10:281-311.
- [45] Kaplanis S., Kaplanis E. A model to predict expected mean and stochastic hourly global solar radiation $I(h;n)$ values. *Renewable Energy*, 2007; 32:1414–1425.
- [46] Gabriel L., Batlles J.F., Joaquín T.P. A new simple parameterization of daily clear-sky global solar radiation including horizon effects. *Energy Conversion and Management*, 2007;48:226-233.
- [47] Sen Z., Simple nonlinear solar irradiation estimation model. *Renewable Energy*, 2007;32342-350.
- [48] Achim W., Ronnie B., Nijs J. Fluctuations in instantaneous clearness index: Analysis and statistics. *Solar Energy*, 2007;81:195–206.
- [49] Loutzenhier P.G., Manz H., Felsmann C., Strachan P.A., Frank T. and Maxwell G.M., Empirical validation of models to compute solar irradiance on inclined surfaces for building energy simulation, *Solar Energy*, In press 2007.
- [50] Svec J., Stevenson M. Modelling and forecasting temperature based weather derivatives. *Global Finance Journal*, In press 2007.
- [51] Zekai Sen , Sükrü Murat Cebeci Solar irradiation estimation by monthly principal component analysis, *Energy Conversion and Management*. in press
- [52] Li D.H.W., Lam T.N.T, Chu V.W.C. Relationship between the total solar radiation on tilted surfaces and the sunshine hours in Hong Kong, solar energy, In press.
- [53] Elizondo D., Hoogenboom G. Mcclendon R.W. Development of a neural network model to predict daily solar radiation. *Agricultural and Forest Meteorology*, 1994;71:115-132.
- [54] Williams D.B., Zazueta F.S. Solar radiation estimation via neural network. In: ASAE, Editor. Sixth internationalconference on Computers in Agriculture, Cancun, Mexico. 1994:140-146.
- [55] Williams D. and Zazueta F. Solar radiation estimation via neural network. In 6th International Conference on radiation. Computers in Agriculture, Cancun ,Mexico, 1996: 1143–1149.
- [56] Mohandes M., Rehman S. and Halawani T.O. Estimation of global solar radiation using artificial neural networks. *Renewable Energy*, 1998;14,(1-4):179-184.
- [57] Alawi S.M., Hinai H.A., An ANN-based approach for predicting global radiation in locations with no direct measurement instrumentation. *Renewable Energy*, 1998;14(1-4):199-204.
- [58] Guessoum A., Boubkeur S., Maafi A., A global irradiation model using radial basis function neural network. WREC, UK, 1998. p.332–336.
- [59] Hontoria L., Riesco J., Zufiria P., Aguilera J. Improved generation of hourly solar radiation artificial Series using neural networks. EANN99. Warsaw. 1999.

- [60] Zufiria P., Vázquez A., Riesco J., Aguilera J., Hontoria L. A neural network approach for generating solar radiation artificial series. In: Proceedings of the IWANN099. 4-5 June. Alicante, Spain. 1999.
- [61] Mohandes M., Balghonaim A., Kassas M., Rehman S. and Halawani T.O. Use of radial basis functions for estimating monthly mean daily solar radiation. *Solar Energy*, 2000;68(2):161-168.
- [62] Hontoria L., Riesco J., Zufiria P., Aguilera J. Application of neural networks in the solar radiation field. Obtainment of solar radiation maps. 16th European Photovoltaic for Chemical Engineers. Elsevier, 2000;3:385-408.
- [63] Sfetsos A., Coonick A.H. Univariate and Multivariate forecasting of hourly solar radiation with artificial intelligence techniques. *Solar Energy*, 2000;68(2):169-78.
- [64] Mihalakakou G. Santamouris M., Asimakopoulos D.N. The total solar radiation time series simulation in Athens, using neural networks. *Theor. Appl. Climatol.*, 2000;66:185-197.
- [65] Kalogirou S.A. Artificial neural networks in renewable energy systems applications: a review. *Renewable and Sustainable Energy Reviews*, 2001; 373-401.
- [66] Hontoria L., Aguilera J. Riesco J., Zufiria P. Recurrent neural supervised models for generating solar radiation synthetic series. *Journal of Intelligent and Robotic Systems*, 2001; 31: 201-221.
- [67] Hontoria L., Aguilera J. and Zufiria P. Generation of hourly irradiation synthetic series using the neural network multilayer Perceptron. *Solar Energy*, 2002;72(5): 441-446.
- [68] Dorvio A.S.S., Jervase J.A., Al-Lawati A. Solar radiation estimation using artificial neural networks. *Applied Energy*, 2002;74:307-19.
- [69] Tymvios F., Jacovides C.P., Michaelides S.C. The total solar energy on a horizontal level with the use of artificial neural networks. In: 6th Hellenic Conference of Meteorology, Climatology and Atmospheric Physics, Ioannina, Greece, 26.28 September. 2002.
- [70] Kalogirou S., Michaelides S.C., Tymvios F.S. Prediction of maximum solar radiation using artificial neural networks. World Renewable Energy Congress VII (WREC 2002) on CD-ROM, 2002.
- [71] Reddy K.S., Manish R. Solar resource estimation using artificial neural networks and comparison with other correlation models. *Energy Conversion and Management*, 2003; 44:2519-2530.
- [72] Sozen A., Arcaklıyoglu E., Ozalp M., Kanýt E.G. Use of artificial neural networks for mapping the solar potential in Turkey. *Applied Energy*, 2004;77:273-286.
- [73] Sozen A., Arcaklıyoglu E., Ozalp M. Estimation of solar potential in Turkey by artificial neural networks using meteorological and geographical data. *Energy Conversion and Management*, 2004;45(18-19):3033-3052.
- [74] Mellit A., Benghanem M., Hadj Arab A., Guessoum A. Modeling of global solar radiation data from sunshine duration and temperature using the Radial Basis Function networks, The IASTED, MIC, February 22 - 25, 2004, in Grindelwald, Switzerland (on CD-ROM) 2004.
- [75] Hontoria L. Aguilera J. Zufiria P. An application of the multilayer perceptron: Solar radiation maps in Spain. *Solar Energy*, 2005; 79:523-530.
- [76] Sozen A., Arcaklıyoglu E., Ozalp M., Agclar N.C. Forecasting based on neural network approach of solar potential in Turkey. *Renewable Energy*, 2005;30:1075-1090.

- [77] Tymvios F.S., Jacovides C.P., Michaelides S.C., Scouteli C. Comparative study of Angstroms and artificial neural networks methodologies in estimating global solar radiation. *Solar Energy*, 2005;78:752-762.
- [78] Mellit A., Benghanem M., Bendekhis M. Artificial neural network model for prediction solar radiation data: application for sizing stand-alone photovoltaic power system. In proceedings of IEEE Power Engineering Society, General Meeting, 2005;1:40-44 , June 12-16, 2005, USA.
- [79] López G., Batlles F.J., Tovar-Pescador J. Selection of input parameters to model direct solar irradiance by using artificial neural networks. *Energy*, 2005;30:1675-1684.
- [80] Zarzalejo L.F. Ramirez L.J. Artificial intelligence techniques applied to hourly global irradiance estimation from satellite-derived cloud index. *Energy*, 2005;30:1685-1697.
- [81] Alam S., Kaushik S.C., Garg S.N. Computation of beam solar radiation at normal incidence using artificial neural network. *Renewable Energy*, 2006;31:1483-1491.
- [82] Elminir H.K., Azzam Y.A., Younes F.I. Prediction of hourly and daily diffuse fraction using neural network, as compared to linear regression models. *Energy*, 2007;32:1513-1523.
- [83] Gabriel L. and Christian A.G. Clear-sky solar luminous efficacy determination using artificial neural networks. *Solar Energy*, 2007; 81(7):929-939
- [84] Mubiru, E.J., Banda, K.B. Estimation of monthly average daily global solar irradiation using artificial neural networks, *Solar Energy* 2008;82(2):181-187
- [85] S Rehmana, M Mohandesb Artificial neural network estimation of global solar radiation using air temperature and relative humidity. *Energy Policy* 2008;36:571-576
- [86] Moustrisa K., Paliatsos A.G., Bloutsos A., Nikolaidis K., Koronaki I., Kavadias K., Use of neural networks for the creation of hourly global and diffuse solar irradiance data at representative locations in Greece. *Renewable Energy* 2008;33:928-932
- [87] Bosch J.L., Lopez G., Batllesa F.J., Daily solar irradiation estimation over a mountainous area using artificial neural networks Renewable Energy in press
- [88] Sozan Senkal , Tuncay Kuleli Estimation of solar radiation over Turkey using artificial neural network and satellite data. Applied energy, in press
- [89] Mohandes M.A., Rehman S., Halawani T.O. A neural networks approach for wind speed prediction. *Renewable Energy*, 1998;13(3):345-54.
- [90] Sfetsos A., A comparison of various forecasting techniques applied to mean hourly wind speed time series. *Renewable Energy*, 2000;21:23-35.
- [91] Barbounis T.G., Theocharis J.B. Alexiadis M.C. and Dokopoulos P.S., Long-term wind speed and Power Forecasting Using Local Recurrent Neural Network Models. *IEEE Transactions on Energy Conversion*, 2006;21(1):273-284.
- [92] Barbounis T.G., Theocharis J.B. Locally recurrent neural networks for wind speed prediction using spatial correlation. *Information Sciences*, 2007;177: 5775-5797.
- [93] Bilgili M., Sahin B., Yasar A. Application of artificial neural networks for the wind speed prediction of target station using reference stations data. *Renewable Energy*, In press. 2007.
- [94] Cadenasa E., Riverab W. Wind speed forecasting in the South Coast of Oaxaca, Mexico. *Renewable Energy*, 2007;32:2116-2128.
- [95] Flores P., Tapia A., Tapia G. Application of a control algorithm for wind speed prediction and active power generation. *Renewable Energy*, 2005;305:23-536.

- [96] Aksoy H., Fuat Z.T., Aytek A., Unal E.N. Stochastic generation of hourly mean wind speed data. *Renewable Energy*, 2004;29:2111–2131
- [97] Tasadduq I., Rehman S., Bubshait K. Application of neural networks for the prediction of hourly mean surface temperatures in Saudi Arabia. *Renewable Energy*, 2002;25:545–554.
- [98] Kemmoku Y., Orita S., Nakagawa S., Sakakibara T. Daily insolation forecasting using a multi-stage neural network. *Solar Energy*, 1999;66(3):193-199.
- [99] Elminir H. K., Areed F.F., Elsayed S.T. Estimation of solar radiation components incident on Helwan site using neural networks. *Solar Energy*, 2005;79:270-279.
- [100] Sen Z. Fuzzy algorithm for estimation of solar irradiation from sunshine duration. *Solar Energy*, 1998;63(1):39-49.
- [101] Gomez V., Casanovas A. Fuzzy modeling of solar irradiance on inclined surfaces. *Solar Energy*, 2003;75:307-315.
- [102] Iqdour R. and Zeroual A., Prediction of daily global solar radiation using fuzzy systems, *International Journal of Sustainable Energy* 2005;26 (1): 19-29.
- [103] Mellit A. and Guessoum A., Application of an adaptive Neuro-Fuzzy inference (ANFIS) for prediction of clearness index (K_t) in isolated sites , in 19th international Conference on Efficiency, Cost, Optimization, Simulation and Environment Impact of Energy System 12-14- July 2006, Greece.
- [104] Mellit A., Hadj Arab A., Khorissi N., Salhi H. An ANFIS-based forecasting for solar radiation data from sunshine duration and ambient temperature IEEE Power Engineering Society General Meeting Florida, USA. p.1-6; 24-28-June 2007.
- [105] Mellit A., Kalogirou S.A., Shaari S., Salhi H. and Hadj Arab A. Methodology for predicting sequences of mean monthly clearness index and daily solar radiation data in remote areas: Application for sizing a stand-alone PV system. *Renewable Energy*, In press.2007.
- [106] Mellit A., Benghanem M., Hadj Arab A., Guessoum A. Hybrid model for prediction sequences of global solar radiation data using artificial neural network and Markov Transitions Matrices, The IASTED, ASM, June 28-30 2004 Greece (on CD-ROM).
- [107] Mellit A., Benghanem M., Hadj Arab A. and Guessoum A. A simplified model for generating sequences of global radiation data for isolated sites: using artificial neural network and a library of Markov transition Matrices. *Solar Energy*, 2005;79 (5):468-482.
- [108] Cao S., Cao J., Forecast of solar irradiance using recurrent neural networks combined with wavelet analysis. *Applied Thermal Engineering*, 2005;25: 161-172.
- [109] Mellit A., Artificial neural network with discrete wavelet transforms for time series prediction: Application for solar radiation data. In proceedings of European modeling and simulation symposium, Greece, June 20-23, 2006.
- [110] Cao J.C., Cao S.H. Study of forecasting solar irradiance using neural networks with preprocessing sample data by wavelet analysis. *Energy*, 2006;3:13435-3445.
- [111] Mellit A., Benghanem M., Kalogirou S.A. An adaptive wavelet-network model for forecasting daily total solar radiation. *Applied Energy*, 2006; 83(7):705-722.
- [112] Maqsood I., Khan M.R., Abraham A. Canadian weather analysis using connectionist learning paradigms. The Seventh Online World Conference on Soft Computing in Industrial Application, On the Internet, Springer, Germany, 2002.

- [113] Maqsood I., Khan M.R., Abraham A. Neuro-computing based Canadian weather analysis, The 2nd International Workshop on Intelligent Systems Design and Applications, Computational Intelligence and Applications. Dynamic Publishers, Atlanta, Georgia, 2002;39-44.
- [114] Khan M.R., Abraham A., Intelligent weather monitoring systems using connectionist models. International Journal of Neural, Parallel and Scientific Computations, 2002;10:157-178.
- [115] Maqsood I., Abraham A. Weather analysis using ensemble of connectionist learning paradigms. *Applied Soft Computing*, 2007;7:995-1004
- [116] Maqsood I., Riaz M.K., Huang G.H., Abdalla R. Application of soft computing models to hourly weather analysis in southern Saskatchewan, Canada Engineering, *Applications of Artificial Intelligence*, 2005;18:115–125.
- [117] Mellit A. Application of evolving polynomial neural network for predicting meteorological time-series, submitted to Theoretical and applied climatology 2008
- [118] Mellit A. Shaari S. and Mekki H., FPGA-based artificial neural network for prediction of solar radiation data from sunshine duration and air temperature”, IEEE International Conference on Computational Technologies in Electrical and Electronics Engineering, Novosibirsk, Russia, July 21-25, 2008.

Chapter 9

NEW TRENDS ON PHENOLOGICAL MODELLING

Herminia García Mozo

Dpto. Botánica, Ecología y Fisiología Vegetal, University of Cordoba, Cordoba, Spain

ABSTRACT

Although phenology modelling has a long history, in recent years, given to the major impact of climate change on ecosystems, the number of studies modelling the response of plant phenology to climate has highly increased. Most of them have indicated the strong relationship between temperature and plant phenology, especially in woody plants. Nevertheless recent studies have also highlighted the influence of photoperiod on the flowering of late spring species and the importance of water availability for the herbaceous species. Mechanistic models describe reproductive phenology known cause-effect relationship of some driving factors in the plant environment. Recently process-based models allow including different bioclimatic factors and also the relationship among them in order to obtain a better description of the biological behaviour and therefore better prediction of phenological events. The reproductive phenology of plants is commonly assumed to be strongly related to local meteorology and also locally adapted to different climate ranges. Recent research suggests that local adaptation is not as great as expected, due to high levels of gene flow, marked year-on-year climate variation and the plasticity of phenology. Studies are showing that phenological models can be established for plant populations including individuals scattered over wide regional areas. Traditionally, plant flowering phenological studies have been concentrated on changes through time but patterns across space remains largely unexplored. In last years, the combined use of GIS and Geostatistics has been demonstrated as instrumental methods for spatial analysis in environmental studies and also plant distribution. Both tools applied on floral phenology studies will contribute to create phenological maps in base of a limited number of sampled locations. Finally, although the role of remote sensing in phenology studies, although is still under development, is increasingly regarded as a key on large areas studies. Given that remote sensing phenology is able to estimate start, peak, duration and end of growing season over large areas, the combined application of phenological models and remote sensing vegetative data can offer very valuable information about the evolution of reproductive phenology of large areas.

INTRODUCTION

In last years it has been a great progress in the transmission of phenology perspectives, especially related to the needs of global change research (Schwartz, 2003). Phenology models are important tools in a wide range of issues: prediction of the impact of global warming on the phenology, improvement of primary productivity models, prediction of the occurrence of pollen in the atmosphere, and thus the occurrence of pollen allergies and support of foresters and farmers in management decisions. Firstly, new forms of data collection such as remote sensing, cloned indicator species and model output must be accepted. In the case of phenology modelling, integrative models combine different aspects of the environment and plant characteristics should be developed. Moreover, the results of a long-term investment are the considerable progress that it has been made in understanding the workings of the earth's climate systems.

At present, one of the main scopes of phenology is the statistic analysis of the data for the attainment of modelling and therefore forecasting formulas and models of prognosis of the biological behaviour of plants. These models are of great interest for elaborating forecasts to build more trustworthy prognoses with a greater advance in the time (Leventin et al., 2001). The precision in these forecasts especially helps to environmental authorities and ecologists (Beggs, 2004), but also to doctors and patients with problems related to pollen allergies, since it allows to an anticipated planning of the activities and the treatments, priority factor in success of the same (D'amato et al., 2007). As well, the phenological models are also interesting for the study and development of models of harvest forecast where data of flowering are used as a forecast tool (Frenguelli, 1998; Garcia-Mozo et al., 2007; Galan et al., 2008).

FLOWERING INTENSITY MODELS

Although numerous works that study the relation between daily pollen concentrations and different parameters, mainly meteorological factors, few works deal with the start of flowering of the peak of the pollen season. These forecast models are based on ample series of pollen and meteorological data, being the latter ones used as independent variables to predict the pollen concentrations. Since the pollen sampling of the atmosphere is a recent technique, in many of the works series of about a 5-10 years are used, which we could denominate "short series", there are other works where of around 15-20 years of data are available, "long series" (Fornaciari et al., 1997; Clot 1998; Emberlin et al., 1999). Forecast models are scarce in the case of predicting the intensity of the flowering. Also in these models the forecast parameters vary according to the species and zones. (Reiss & Kostic, 1976; Dahl & Strandhede, 1996; Galan et al., 1998). Most of these models are multiple regression models. Exist other models based on different physical applications such as temporary series (Moseholm et al., 1987; Bianchi et al., 1992; Comtois, 2000), the fractal analysis (Toro, 1997) and neural networks (Arizmendi et al., 1993; Ranzi et al., 2000; Sánchez-Mesa et al., 2002).

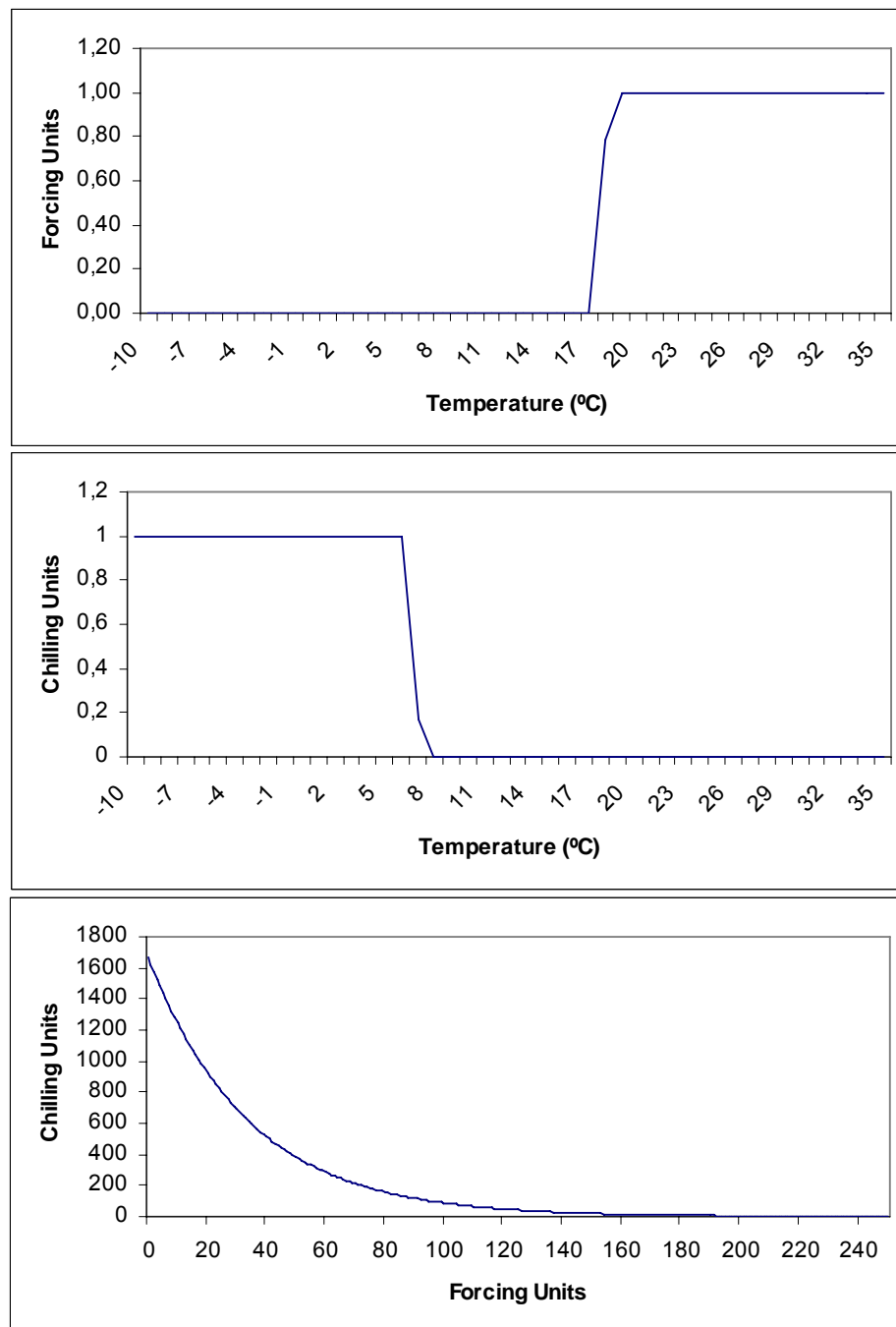


Figure 1. Graphic representation of a model to forecast the Start and Peak flowering dates of *Quercus* in Spain a) Relationship between temperature and heat units b) Relationship between temperature and Chilling Units. c) Relationship between Heat Units and Chilling requirements.

FORECASTING PHENOLOGY DATES

In the majority of the plant species exists a great variability in the beginning of flowering station, strongly influenced by the climatology. The forecast of this beginning is very useful since the pollen curves in a given site have own characteristics that are usually repeated throughout the time. The accumulated temperature is the determining factor of the beginning of flowering of many species of temperate, and mainly of arboreal species. The models proposed in bibliography determine the needs of temperature of the different species before their flowering (Larsson et al., 1993; Alba & Diaz de la Guardia, 1998; García-Mozo et al., 2000; Galán et al., 2001). The common base to all of them is the use of a threshold temperature for the determination of the amount of "useful" temperature for the growth and development of the floral buds (Arnold et al., 1959; García-Mozo et al., 2001). In numerous species the temperature of 5°C like optimum threshold (Frenguelli & Bricchi, 1998; Jato ET al., 2000). Although in colder regions the certain threshold has been 0°C (Gerad-Peeters, 1998; Clot, 1998). Other authors have proposed thresholds (12,5°) in species of warm higher climates (Alcalá & Barranco, 1992; Galan et al., 2001) The estimation of the date of accumulation beginning varies according to the climatology and the species studied in each zone. Diverse models of accumulation propose as the date of beginning of accumulation that one in which the arboreal species have exceeded their stage of dormancy because they have completed his requirements of cold (Jato et al., 2000; García-Mozo et al., 2000). On the other hand, other models use dates of reference that indicate the average date of beginning of heat accumulation, varying according to species and localities of study. , In works thus carried out in Europe it has been determined, for example, 1 January in species of early flowering (Frenguelli & Bricchi, 1998; Dawn & Diaz de la Guardia, 1998) or the 1 of March in species of later flowering (Alba & Diaz de la Guardia, 1998; Clot, 1998).

On the other hand, in the last years models have settled down that combine weather data and phonological data from previous flowering species ("indicator plants") can be of a great interest and it can improve the forecasts of beginning (Driessen & Moelands, 1985; Driessen et al., 1989; Frenguelli & Bricchi, 1998; Norris-Hill, 1998).

MODELLING IN HERBACEOUS SPECIES

Grasses are all anemophilous species, in which pollen release is favoured by a number of environmental factors. The development of grasses is positively influenced by water availability, especially in Mediterranean areas (Clary et al., 2004). Recent studies have also highlighted the influence of photoperiod on the flowering of late spring species and the importance of water availability for the herbaceous species, especially in the Mediterranean Region. High temperatures, a critical photoperiod and low relative humidity contribute to high atmospheric levels of airborne Poaceae pollen (Sánchez-Mesa et al., 2005). A number of studies report that reproduction patterns in this family vary according to latitude, ecology and climatology (Raju et al., 1985; Connor, 1986). Grass flowering is greatly influenced by weather conditions. Prior to flowering, the primary factors – temperature, photoperiod and water availability – influence plant growth and development. During flowering, other, secondary weather-related factors, such as rainfall and relative humidity, influence pollen

release (Laidii, 2001). Although various authors have developed models for predicting daily grass-pollen concentrations (Moseholm et al., 1987; Emberlin et al., 1999; Sánchez-Mesa, 2005), few papers have addressed the development of models to forecast the main pollen-season dates, i.e. start date and peak date (Clot, 1998; Chuine and Belmonte, 2004; Laaidi, 2001, Stach et al., 2008; García-Mozo et al., 2009). The main difficulty in developing forecasting models for this taxon is that grass pollen counts are an amalgam of pollen from many species, and pollen release dynamics prompt a large number of peaks (Fernández-González et al., 1999; Emberlin et al., 1999).

Recently process-based models allow including different bioclimatic factors and also the relationship among them in order to obtain a better description of the biological behaviour and therefore better prediction of phenological events. García-Mozo et al. (2009) developed process-based models to predict the start-date and the peak-date of the grass pollen season. Models take into account the effects of temperature, photoperiod and water availability on the timing of grass flowering in Spain. Apart from predicting the pollen-season start and peak dates, process-based models provide information on (i) the Poaceae response to weather-related factors, (ii) the period during which these factors affect grass growth, and (iii) the relationship between photoperiod, temperature and water availability for flowering grasses.

MODELLING AND CLIMATE CHANGE

A number of authors have used these models to predict the consequences of increasing temperatures on the phenology of temperate-zone trees, in order to determine whether species would break bud or flower later or earlier (Walther et al., 2002; Galán et al., 2005). The reproductive phenology of temperate tree species is commonly assumed to be strongly related to temperature and also locally adapted to different climate ranges. Climate change has already modified the phenology of numerous plant species over recent years (Parmesan and Yohe, 2003) and models suggest that these changes will increase in magnitude (Osborne et al. 2000; García-Mozo et al., 2006). One of the most widely-expected consequences of climate change will be an increase in minimum temperatures, especially in winter and early spring (Ahmad, 2001); it is during this period that the reproductive structures of early-spring-flowering species are developed, while late-spring-flowering species are still in the undifferentiated-bud phase (Galán et al., 2001b).

The response of trees will depend largely on the species, the latitude and the intensity of change (Taiz & Zeiger, 1998). There is evidence of an advance in flowering dates of wild plants across Europe, apparent in almost 80% of species. The mean advance of spring flowering dates has been calculated at 2.5 days per decade (Menzel et al., 2006). *Quercus* phenology has been reported as a good indicator of future climate change, due to its dependence on temperature and its geographical distribution over the high-risk warming area of the Mediterranean basin (García-Mozo et al., 2006). In this area, late spring temperatures are not expected to increase as much as winter and early spring temperatures.

REGIONAL MODELS

The reproductive phenology of plants is commonly assumed to be strongly related to local meteorology and also locally adapted to different climate ranges. Numerous studies have proposed local phenological models adapted to different climatic areas. However, recent research suggests that local adaptation is not as great as expected, due to high levels of gene flow, marked year-on-year climate variation and the plasticity of phenology. Studies are showing that phenological models can be established for plant populations including individuals scattered over wide regional areas. Recent research suggests that local adaptation is not as great as expected, due to high levels of gene flow, marked year-on-year climate variations and the plasticity of phenology. Studies have shown that phenological models can be established for tree populations including individuals scattered over wide regional areas. Chuine et al. (2000) reported a common response to temperature in natural populations of *Alnus glutinosa*, *Ulmus minor* and *Carpinus betulus* distributed throughout central Europe.

García-Mozo et al (2008) developed a regional temperature-based model to explain and forecast the main *Quercus* reproductive phenological phases in the Iberian Peninsula: flowering start and flowering peak. The prior hypothesis to test the effectiveness of a regional model for *Quercus* took into account the anemophilous nature of these species, which prompts a high potential gene flow due to wide pollen dispersal (up to hundreds of kilometres) (Faegri & Iversen, 1989); moreover, the marked ability of Iberian *Quercus* species to adapt to different climate ranges has been amply demonstrated, especially in the evergreen *Quercus ilex* subsp. *ballota* Desf. (Samp) (Faust, 1989; Larcher, 1995). Therefore, the selective force attributed to climate-related variables such as temperature is partially reduced in these species. It was hypothesized that the balance between factors contributing to local adaptation would not lead to significant genetic variations in phenology between close populations.

The study sought to achieve the broadest possible spatial and temporal predictions by examining genetic variations in the timing of flowering between populations of the Iberian *Quercus* species using pollen data from 15 sites in Spain. The influence of genetic patterns in the phenological response was also taken into account in order to use the minimum number of validated models to predict *Quercus* reproductive phenology in the Iberian Peninsula to optimise real application.

SPATIAL ANALYSIS

Traditionally, plant flowering phenological studies have been concentrated on changes through time but patterns across space remains largely unexplored. Only few works have developed models in terms of both space and time (Puppi & Zanotti, 1992; Kawashima & Takahashi, 1995; Hidalgo et al. 2002).

Geographic Information Systems (GIS) are computer-based methodologies conceived for spatial data collection, storage, retrieval, transformation, display and analysis. They can be very useful for a visual analysis of phenological variations in a given area. Georeferenced data, such as floral phenology of a population, can be incorporated into a GIS to produce map layers. While the advent of GIS allows for compiling and manipulating spatially referenced

data, modelling spatial patterns from areas where no data are available is difficult without an adequate set of statistical tools (Liebhold et al., 1993). Also orthophotos can be used even for measure plant density in a given area. This data joint to a knowledge of pollen production per plant can offer information about the potential pollen emission in a given area.

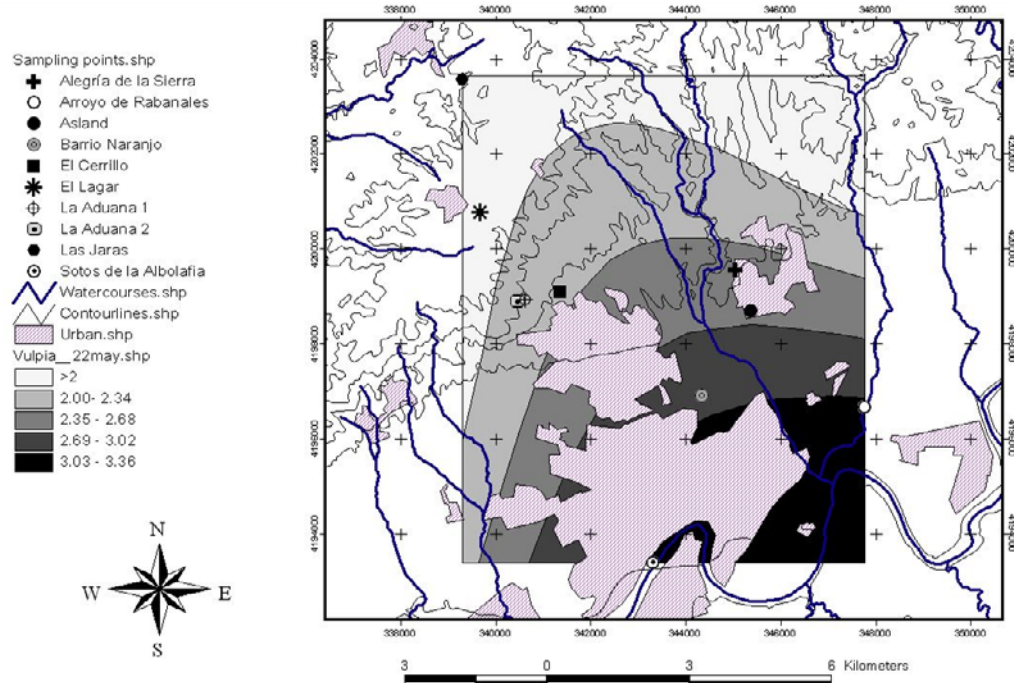


Figure 2. Phenological stages of grasses around the city of Cordoba. Map elaborated by using combined geostatistic and GIS analysis (León et al., in press).

Geostatistics designs a group of tools and techniques that are useful to analyze spatial patterns and predict the values of a continuous variable distributed in space or in time at unsampled locations (Moral García, 2003). Geostatistics is a family of statistical methods that describe correlations through space/time and that can be used for quantifying the spatial correlation and interpolating sample points via Kriging or other related procedures. Although there are no surface limits for applying Geostatistic analysis, validity of the estimated data increase in reduced areas. A high number of co-variables: altitude, temperature, land cover, etc... And a detailed statistic analysis: descriptive statistical analysis, variogram determination and interpolation (i.e. kriging) and also an external validation of data are recommended before mapping.

Most phenomena show, as an inherent feature, a high degree of spatial continuity (Moral García., 2003). In ecological research, there are many instances where it is necessary to interpolate among spatially stratified samples which is the reason because in last years GIS and Geostatistics are being applied to environmental studies such as entomology (Liebhold et al., 1993), plant distribution (Legendre & Fortin, 1989), and general ecology (Robertson, 1987) with excellent results. The combined use of GIS and Geostatistics has been demonstrated as a very instrumental method for spatial analysis in environmental studies and

also plant distribution (Robertson, 1987; Legendre & Fortin, 1989; Burrough 2001). Both tools applied on floral phenology studies will contribute to create phenological maps in base of a limited number of sampled locations (Garcia Mozo et al., 2005)

REMOTE SENSING IN PHENOLOGY STUDIES

The role of remote sensing in phenology studies, although is still under development, is increasingly regarded as a key on large areas studies (Schwartz, 2003). The use of remote sensing methods such as Normalized Difference Vegetation Index (NDVI) measures by means of satellite observations the different stages of phenology. Observations from satellite sensors provide a mechanism for regional scale studies of phenology. The need for large area measures to support global change studies is growing.

Satellite maps of vegetation show the density of plant growth over the entire globe. The most common measurement is NDVI, which uses of the spectral reflection/absorption characteristics of plants to describe the colour of each pixel in a satellite observation image.

Very low values of NDVI (0.1 and below) correspond to barren areas of rock, sand, or snow. Moderate values represent shrub and grassland (0.2 to 0.3), while high values indicate temperate and tropical rainforests (0.6 to 0.8).

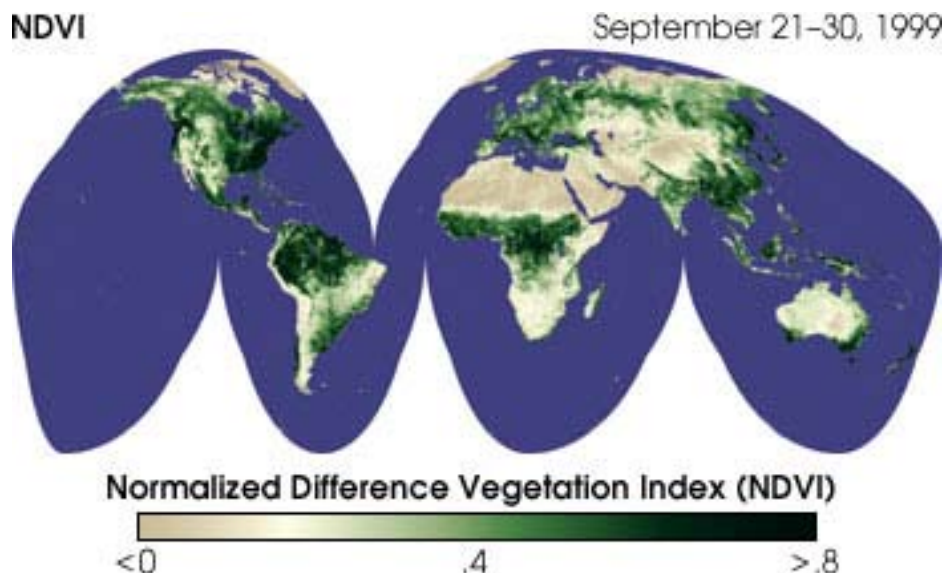


Figure 3. Satellite maps of vegetation show the density of plant growth over the entire globe. The most common measurement is called the Normalized Difference Vegetation Index (NDVI). Image from <http://earthobservatory.nasa.gov/Library/MeasuringVegetation>.

NDVI is calculated from the visible and near-infrared light reflected by vegetation. Healthy vegetation (left) absorbs most of the visible light that hits it, and reflects a large portion of the near-infrared light. The key phenological variables that can be estimated by means of satellite control are the time of the start of growing season and the end.

It can be used for measuring reproductive but mainly vegetative phenological indexes by detecting the color changes on vegetation.

In an effort to monitor major fluctuations in vegetation and understand how they affect the environment, 20 years ago Earth scientists began using satellite remote sensors to measure and map the density of green vegetation over the Earth. Using NOAA's Advanced Very High Resolution Radiometer (AVHRR), scientists have been collecting images of our planet's surface. By carefully measuring the wavelengths and intensity of visible and near-infrared light reflected by the land surface back up into space, scientists use an algorithm called a "Vegetation Index" to quantify the concentrations of green leaf vegetation around the globe. Then by combining the daily Vegetation Indices into 8-, 16-, or 30-day composites, scientists create detailed maps of the Earth's green vegetation density that identify where plants are thriving and where they are under stress (i.e., due to lack of water).

Given that remote sensing phenology is able to estimate start, peak, duration and end of growing season over large areas, the combined application of phenological models and remote sensing vegetative data can offer very valuable information about the evolution of reproductive phenology of large areas.

REFERENCES

- [1] Ahmad, Q.K. (ed) 2001. Climate Change 2001: Impacts, Adaptation, and Vulnerability. In: Summary for Policymakers, (ed. IPCC Working Group II).
- [2] Alba, F. & Díaz de la Guardia, C. 1998. The effect of air temperature on the starting dates of the *Ulmus*, *Platanus* and *Olea* pollen season in the SE Iberian Peninsula. *Aerobiologia* 14:191-194.
- [3] Alcalá, A.R. & Barranco, D. 1992. *HortScience* 27(11):1205-1207.
- [4] Arizmendi, C.M., Sanchez, J.R., Ramos, N.E. & Ramos, G.I. 1993. Time-series prediction with neural nets- applications to airborne pollen forecasting. *Int. J. Biometeorol.* 37(3):139-144.
- [5] Arnold, C. 1959. The development and significance of the base temperature in a linear H.U. system. *Proc. Am. Soc. Hort. Sci.* 74:430-445.
- [6] Beggs, P.J. 2004. Impacts of climate change on aeroallergens: past and future. *Clin Exp Allergy* 34(10), 1507-1513.
- [7] Bianchi, M.M., Arizmendi, C.M. & Sanchez, J.R. 1992. Detection of chaos: new approach to atmospheric pollen time-series analysis. *Int. J. Biometeorol.* 36(3):172-175.
- [8] Burrough P.A. 2001. GIS and geostatistics; essential partners for spatial analysis. *Environmental and Ecological Statistics* 8, 361-377.
- [9] Chuine, I., Belmonte, J. 2004. Improving prophylaxis for pollen allergies: Predicting the time course of the pollen load of the atmosphere of major allergenic plants in France and Spain. *Grana* 43, 65-80.
- [10] Chuine, I., Belmonte, J., Mignot, A. 2000. A modelling analysis of the genetic variation of phenology between tree populations. *Journal of Ecology* 80, 561-570.
- [11] Clary, J., Savé, R., Biel, C., de Herralde, F. 2004. Water relations in competitive interactions of Mediterranean grasses and shrubs. *Ann. Appl. Biol.* 144 (2), 149–155.

- [12] Clot, B. 1998. Forecast of the Poaceae pollination in Zurich and Basle (Switzerland). *Aerobiologia* 14:267-268.
- [13] Comtois, P. 2000. Time-series analysis applications in Aerobiology. Second European Symposium on Aerobiology. September 2000, Vienna, Austria.
- [14] Connor, H.E., 1986. Grass systematics and evolution. Systematics and evolution. Smithsonian Institution Press, Washington, D.C., London.
- [15] D'Amato G., Cecchi L., Bonini S., Nunes C., Annesi-Maesano I., Behrendt H., Liccardi G., Popov T., van Cauwenberge P. 2007. Allergenic pollen and pollen allergy in Europe. *Allergy* 62(9), 976–990.
- [16] Dahl, A. & Strandhede, S. 1996. Predicting the intensity of the birch pollen season. *Aerobiologia* 12:97-106.
- [17] Driessen, M. & Moelands, M. 1985. Estimation of the commencement of the grass pollen season and its prediction by means of the phonological method. *Acta Bot. Neerl.* 34 Abstract 131.
- [18] Driessen, M., Van Herpen, A., Moelands, M. & Spiekma, M. 1989. Prediction of the start of the grass pollen season for the western part of the Netherlands. *Grana* 28:37-44.
- [19] Emberlin, J., Mullins, J., Corden, J., Jones, S., Millington, W., Brooke, M. & Savage, M. 1999. Regional variations in grass pollen seasons in the U.K., long-term trends and forecast models. *Clin. and Exp. Allergy* 29:347-356.
- [20] Emberlin, J., Mullins, J., Corden, J., Jones, S., Savage, J., Millington, W., Brooke, M., Savage, M., 1999. Regional variations in grass pollen seasons in the UK, long term trends and forecasts models. *Clin. Exp. Allergy* 29, 347-356.
- [21] Faegri, K., Iversen J., 1989. Textbook of pollen analysis. Wiley and Sons, New York. 328 pp.
- [22] Faust, M., 1989. Time of bloom. En: Faust, M. (ed.). Physiology of temperate zone fruit trees. J. Wiley & Sons, New York. pp.188-199.
- [23] Fernández-González, D., Valencia-Barrera, R.M., Vega, A., Díaz de la Guardia, C., Trigo, M.M, Cariñanos, P., Guardia, A., Pertíñez, C., Rodríguez-Rajo, F.J., 1999. Analysis of grass pollen concentrations in the atmosphere of several spanish sites. *Polén* 10, 123-132.
- [24] Fornaciari, M., Pieroni, L., Ciuchi, P. & Romano, B. 1997. A statistical model for correlating airborne pollen grains (*Olea europaea* L.) with some meteorological parameters. *Agr. Med.* 127:134-137.
- [25] Frenguelli, G. & Bricchi, E. 1998. The use of the pheno-climatic model for forecasting the pollination of some arboreal taxa. *Aerobiologia* 14:39-44.
- [26] Frenguelli, G. & Bricchi, E. 1998. The use of the pheno-climatic model for forecasting the pollination of some arboreal taxa. *Aerobiologia* 14:39-44.
- [27] Galán, C., Fuillerat, M.J., Comtois, P. & Domínguez, E. 1998. A predictive study of Cupressaceae pollen season onset, severity, maximum value and maximum value date. *Aerobiologia* 14:145-199.
- [28] Galán, C., García-Mozo, H., Cariñanos, P., Alcázar, P., Domínguez, E. 2001. The role of temperature in the onset of the *Olea europaea* L. pollen season in southwestern Spain. *Int. J. Biometeorol.* 45(1):8-12.
- [29] Galán, C., García-Mozo, H., Vázquez, L., Ruiz, L., Díaz de la Guardia, C. & Domínguez, E. Modelling olive (*Olea europaea* L.) crop yield in Andalusia Region, Spain 2008. *Agronomy Journal*. Vol 100(1); 98-104.

- [30] Galán, C., García-Mozo, H., Vazquez, L., Ruiz-Valenzuela, L., Díaz de la Guardia, C., Trigo-Perez, M., 2005. Heat requirement for the onset of the *Olea europaea* L. Pollen season in several places of Andalusia region and the effect of the expected future climate change. *Int. J. Biometeorol.* 49(3), 184 – 188.
- [31] García-Mozo, H., Galán, C., Gómez-Casero, M.T. & Dominguez, E. 2000. A comparative study of different temperature accumulation methods for predicting the *Quercus* pollen season start in Córdoba (Southwest Spain). *Grana* 39:194-199.
- [32] García-Mozo, H., Galán, C., Aira, M.J., Belmonte, J., Díaz DE LA Guardia, C. Fernández, D. Gutierrez, A.M., Rodriguez, F.J., Trigo, M.M., & Dominguez-Vilches, E. 2002. Modelling start of oak pollen season in different climatic zones in Spain. *Agricultural and Forest Meteorology* 110: 247-257.
- [33] García-Mozo, H., Galán C.& Vazquez, L. 2005. The reliability of geostatistic interpolation in olive field phenology. *Aerobiologia* 2006, 22:97-108.
- [34] García-Mozo, H., Galán, C., Jato, V., Belmonte, J., Díaz de la Guardia, C., Fernández D., Gutiérrez, M., Aira, M.J., Roure, J.M., Ruiz, L., Trigo, M.M., Domínguez-Vilches, E. 2006. *Quercus* pollen season dynamics in the Iberian Peninsula: response to meteorological parameters and possible consequences of climate change. *Annals of Agricultural and Environmental Medicine* 13, 209-224.
- [35] García-Mozo, H., Gómez-Casero, M.T., Dominguez, E. Galán, C. 2007. Influence of pollen emission and weather-related factors on variations in holm-oak (*Quercus ilex* subsp. *ballota*) acorn production. *Environmental and Experimental Botany* 61:35-40.
- [36] García-Mozo H., Chuine I., Aira M.J., Belmonte J., Bermejo D., Díaz de la Guardia C., Elvira B., Gutiérrez M., Rodríguez-Rajo J., Ruiz L., Trigo M.M., Tormo R., Valencia R., Galán C. 2008. Regional phenological models for forecasting the start and peak of the *Quercus* pollen season in Spain. *Agricultural and Forest Meteorology* 148:372-380.
- [37] García-Mozo H., Galán, C., Belmonte, J., Bermejo. D., Candau, P., Díaz de la Guardia., C., Elvira, B., Gutiérrez, M., Jato, V., Silva, I. , Trigo, M.M., Valencia, R. & Chuine, I. 2009. Predicting the start and peak dates of the Poaceae pollen season in Spain using process-based models. *Agriculture and Forest Meteorology*, 149: 256-262.
- [38] Gerard-Peeters, A. 1998. Cumulative temperatures for prediction of the beginning of ash (*Fraxinus excelsior* L.) pollen season. *Aerobiologia* 14: 375-381.
- [39] Hidalgo P.J., A. Mangin, C. Galán, O. Hembisse, L.M. Vazquez & O. Sanchez. 2002. An automated system for surveying and forecasting *Olea* pollen dispersion. *Aerobiologia*, 18:23-31.
- [40] Jato, V., Frenguelli, G. Rodríguez, F.J. & Aira, M.J. 2000. Temperature requirements of *Alnus* pollen in Spain. *Grana* 39: 240-245.
- [41] Kawashima, S. and Takahashi, Y. 1995. Modelling and simulation of mesoscale dispersion processes for airborne cedar pollen. *Grana* 34, 142-150.
- [42] Laaidi, M., 2001. Forecasting the start of the pollen season of Poaceae: evaluation of some methods based on meteorological factors. *Int. J. Biometeorol.* 45(1), 1-7.
- [43] Larcher, W. 1995. Physiological plant ecology. 3th edn. Springer, Berlin
- [44] Larsson, K.A. 1993. Prediction of the pollen season with a cumulated activity method. *Grana* 32: 111-114.
- [45] Legendre P. and Fortin M.J. 1989. Spatial pattern and ecological analysis. *Vegetatio* 80,107-138.

- [46] Leventin, E., Van de Water, P.K., Main, C.E. & Keever, T. 2001. Assesment of Mt. Cedar forecasting. *Aerobiology* 2001. Annual Symposium of the Pan-American Aerobiology Association. Junio 2001, North-Caroline, USA
- [47] Liebhold A.M., Rossi R.E. & Kemp W.P. 1993. Geostatistics and Geographic Information Systems in Applied Insect Ecology. *Annual Review of Entomology* 38: 303-327
- [48] Menzel, A., Tim, H., Sparks, T., Estrella, N., Koch, E., Aasa, A., Ahas, R., Alm-Kübler, K., Bissolli, P., Braslavská, O., Briede, A., Chmielewski, F.M., Crepinsek, Z., Curnel, Y., Dahl, Å., Defila, C., Donnelly, A., Filella, Y., Jatczak, K., Måge, F., Mestre, A., Nordli, Ø., Peñuelas, J., Pirinen, P., Remišová, V., Scheifinger, H., Striz, M., Susnik, A., Van Vliet, A. J.H., Wielgolaski, F., Zach, S. & Zust, A. 2006. European phenological response to climate change matches the warming pattern. *Global Change Biology* 12 (10), 1969–1976.
- [49] Moral García, F.J. 2003. La representación gráfica de las variables regionalizadas. Geoestadística Lineal. Servicio de publicaciones de la Universidad de Extremadura. Cáceres (Spain).
- [50] Moseholm, L., Weeke, E. R., Petersen, B.N. 1987. Forecast of pollen concentrations of Poaceae (grasses) in the air by time series analysis. *Pollen et Spores* 29, 305-322.
- [51] Norris-Hill, J. 1998. A method to forecast the start of the *Betula*, *Platanus* and *Quercus* pollen seasons in North London. *Aerobiology* 14: 165-170.
- [52] Osborne, C.P., Chuine, I., Viner, D., Woodward, F.I. 2000. Olive phenology as a sensitive indicator of future climatic warming in the Mediterranean. *Plant, Cell and Environment* 23, 701-710
- [53] Parmesan C., Yohe G., 2003. A globally coherent fingerprint of climate change impacts across natural systems. *Nature* 421(2), 37-42.
- [54] Puppi G., Zanotti A.L. 1992. Estimate and mapping of the activity of airborne pollen sources. *Aerobiologia* 8 (1): 69-74
- [55] Raju, M.V.S., Jones, E.J., Ledingham, G.F., 1985. Floret anthesis and pollination in wild oats (*Avena fatua*). *Can. J. Bot.* 63:2187-2195.
- [56] Ranzi, A., Lauriola, P., Marletto, F. & Zinoni, F. 2000. Forecasting airborne pollen concentrations: development of local models. Second European Symposium on Aerobiology. September 5-9, 2000. Vienna-Austria.
- [57] Reiss, N. & Kostic, S. 1976. Pollen season severity and meteorologic parameters in central New Jersey. *J. Allergy Clin. Immunol.* 57(6): 609-614.
- [58] Robertson G.P. 1987, Geostatistics in Ecology: interpolating with known variance. *Ecology* 68, 744-748.
- [59] Sánchez Mesa J. A., Galán C., Hervás C. 2005. The use of discriminant analysis and neural networks to forecast the severity of the Poaceae pollen season in a region with a typical Mediterranean climate. *Int. J. Biometeorol.* 49:355-362.
- [60] Sánchez-Mesa, J.A., C. Galán, J.A. Martínez-Heras, & C. Hervás-Martínez. 2002. The use of an neural network to forecast daily grass pollen concentration in a Mediterranean region: the southern part of the Iberian Peninsula. *Clinical and Experimental Allergy*, 32:1-7.
- [61] Schwartz, H.J. (ed.), 2003. Phenology: an integrative environmental science. Kluwer Academic Publishers. Netherlands.

-
- [62] Stach, A., Smith, M., Prieto-Baena, J.C., Emberlin, J. 2008. Long-term and short-term forecast models for Poaceae (grass) pollen in Poznan, Poland, constructed using regression analysis. *Environ. Exp. Botany* 62, 323-332.
 - [63] Taiz, L., Zeiger, E. 1998. The control of flowering. En: (Taiz, L. & Zeiger, E. (eds). Plant Physiology, 2nd edition. Sinaeur Associates, Inc. Sunderland. Massachusetts, pp 691-724.
 - [64] Toro, F.J. 1997. Estudio aerobiológico de la costa del sol occidental: Málaga y Estepona (1995-1997). Análisis comparativo y de pronóstico. Tesis Doctoral. Departamento de Biología Vegetal. Facultad de Ciencias. Universidad de Málaga.
 - [65] Walther, G.R., Post, E., Convey, P., Menzel, A., Parmesan C., Beebee T. J. C., J. M. Fromentin, Guldberg O. H. & F. Bairlein. 2002. Ecological responses to recent climate change. *Nature* 416, 389-395.

Chapter 10

TIME DEPENDENT SHAPE OPTIMIZATION USING ADJOINT VARIABLE METHOD FOR REDUCING DRAG

Kazunori Shinohara^{1,*} and Hiroshi Okuda²

¹Intelligent Modeling Laboratory (IML), The University of Tokyo, Tokyo, Japan

²Research into Artifacts, Center for Engineering (RACE), The University of Tokyo,
Tokyo, Japan

To obtain an optimal shape, a 3D shape optimization system based on the adjoint variable method is developed. The adjoint variable method is based on the variational principle (a conditional variational principle), and consists of the state equation, the adjoint equation and the sensitivity equation. The equations for reducing the fluid drag under a constant volume condition are formulated. This method was implemented using HEC-MW, and by doing so. The program was efficiently parallelized and the number of program lines was dramatically reduced. The automatic parallel library HEC-MW, running on a PC cluster (16 nodes), made possible the analysis of the optimal shape for a long time span. By using the proposed shape optimization system, the optimal shape under unsteady flow (RE100) could be obtained. Comparing to the initial shape, the drag on the optimal shape (teardrop) can be reduced by about 40% under unsteady flow.

Keywords: Shape optimization; CFD; FEM; HEC-MW; Adjoint variable method; Navier - Stokes equation; Calculus of variations; Drag reduction.

1. INTRODUCTION

In the design of new industrial products added value is always demanded. Added value means increased economical performance, which depends on various consumer and supplier criteria, usually related to low production and end-user cost, high performance and high reliability. Therefore, the optimization analysis technology used to develop a high-quality design becomes important. In the case that this added value depends on the shape of the

* Corresponding author. Email: shinohara@nihonbashi.race.u-tokyo.ac.jp.

object, shape optimization techniques make effective tools in developing a good design compromise.

The algorithm used in the proposed shape optimization system is shown in Fig.1. The algorithm consists of the making of the initial shape, the analysis of the governing equations, the sensitivity analysis, the search for the optimum, the control of the design variables and the mesh deformation. First, the mesh data of the initial shape is made using CAD software. Second, the governing equations (the heat equation, the fluid equation, the stress equation, the vibration equation and the electromagnetic equation) are solved using a specialized solver. Third, the variation of the objective function with respect to the variation of the control variables (such as the nodal points on the surface of an object) is analysed and the sensitivities are obtained. These sensitivities represent the direction and the amount of the deformation applied to the respective nodal points. Next, the optimal value is searched based on the previously computed sensitivities using an optimization method (e.g. gradient method [1][2] or BFGS method [3][4] etc.). Following, the control points on the surface are modified to construct a smooth surface using methods like the basis vector method [5][6], the traction method [7][8], using Response Surface Methodology [9][10] etc. Last, the node points in the mesh are relocated (using the Laplace or the biharmonic equation etc.) and the optimal shape is constructed.

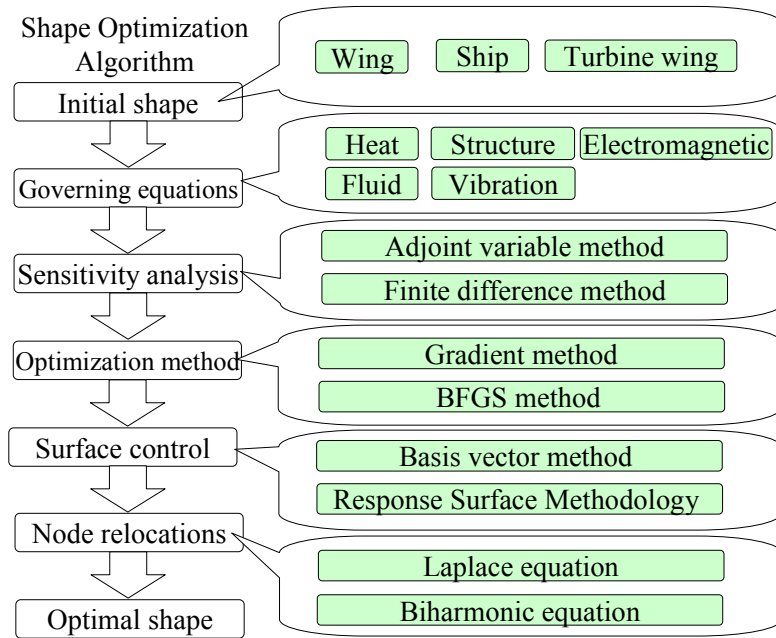


Figure 1. The shape optimization algorithm.

Shape optimization methods can be roughly divided into two categories. The former contains deterministic methods, like the adjoint variable method [11][12], the finite difference method [13][14] or the direct differential method [15][16]. The latter contains probabilistic methods, like genetic algorithms (GA) [17], simulated annealing (SA) [18] and so on. The largest advantage of probabilistic methods is that sensitivity analysis is not needed therefore the equations used to obtain those sensitivities are not required. As such, one can obtain the

optimal shape even for cases where writing the sensitivity equations is very hard or impossible to do. On the other hand, as opposed to the deterministic methods, where the governing equations have to be solved only once for each analysis step, in the case of probabilistic methods the number of evaluations is greatly increased. Besides, due to the non-deterministic nature, the optimality of the final solution cannot be guaranteed. Therefore, we chose to base our analysis on a deterministic method, the adjoint variable method, using which we developed an improved shape optimization system able to construct the optimal shape for reducing drag. Such kind of analysis is important in optimizing designs such as airplane and turbine wings, etc.

The adjoint variable method is a sensitivity analysis method based on the Lagrange-Multiplier Method. The Lagrange-Multiplier Method is based on the calculus of variations under constraints, which is based on the variational principle. In the stationary point of the action I , the first variation δI produces no change even if the variables of the functional (I) would change. In the adjoint variable method, the Lagrange function L is similarly formulated and the optimal shape can be constructed by obtaining the stationary point ($\delta L=0$) based on the variational principle [19][20].

Using optimization techniques based on the variational principle, many optimization problems in industry, such as obtaining minimum drag for a given lift or obtaining minimum drag for a given surface area, have been approached [4][11][12][21][22].

In Stokes flow, the development of shape optimization algorithms for minimizing drag on an object in viscous flow, under a constant volume, has started since 1968 [23]. Tuck and Watson investigated the minimum drag problem for a symmetric body in Stokes flow [23][24]. In 1973, Pironneau [25], aided by earlier work by Lion [26], presented the mathematical theory behind a drag minimization algorithm. The calculations needed for optimization were partly performed by hand. Bourot made a numerical computation of the optimum profile by making use of Pironneau's theoretical results [27]. John constructed asymmetric bodies having low drag in incompressible flow [28]. In the 1980's, Sano constructed a 2D optimal shape that minimized the cost function under a constant area by using Stokes equation [29]. Bessho and Himeno presented an inverse procedure for the minimization of the hydrodynamic drag [30]. Taseli et al. employed geometrical shape functions to tackle the problem by using the simplex method [31]. In 1990's, Ganesh used Pironneau's algorithm to reduce the drag on an object and obtained the optimal shape by using Stokes flow [32]. Wagner et al developed numerical shape optimization tool of asymmetric minimum-drag bodies using evolution strategies [33]. Richardson considered the problem of designing the section of a cylinder for minimizing drag [34]. Kim et al. carried out optimizations for low Reynolds numbers ($RE \ll 40$) by using Navier-Stokes equations[35]. In the 2000's, Datta constructed the maximum drag profile under Stokes flow [36]. Guest presented topology optimization in Stokes flow [37].

In unsteady flow, Glowinski and Pironneau (1975) presented a numerical algorithm to compute the minimum-drag profile of a two-dimensional body, although with a boundary layer approximation [38]. Huan and Modi investigated two-dimensional minimum drag bodies for a range of Reynolds numbers [39]. Makino et all. presented a shape optimization problem for minimizing unsteady viscous resistance of a 2-dimensional body by combination with CFD[40]. Using the traction method, Katamine and Azegami proposed a numerical analysis method under viscous flow [41]. Neittaanmaki et al. tackled the problem of finding the optimal shape for a body surrounded by a Navier-Stokes flow [42]. At Reynolds number

500, Ghattas et al. obtained the optimal shape in viscous energy dissipation[43]. Lund et al. presented a gradient based shape optimization method for strongly coupled stationary fluid-structure interaction problems[44]. Using the adjoint variable method, Yagi, Kawahara and Okumura solved steady and unsteady flow problems after a careful comparison of the optimal shape that they obtained with Pironneau's result [45][58]. Matsumoto used the bubble function in his shape optimization algorithm and solved unsteady flow problems [46]. Using a stabilized finite element formulation, Srinath and Mittal solved the adjoint equations[47]. Zhiming G. et all presented a gradient - type algorithm for time dependent cost functionals [48].

In unsteady viscous flow, one of the problems is how to choose the time span. In steady flow, the optimal shape for reducing drag can be constructed by arbitrary choosing the time span, because the surface force on an object doesn't change with respect to time. However, unsteady flow causes the change of the surface force. As such, the resulting optimal shape will depend on the particular choice of the time span (that is the choice of the start test time and of the end test time) so not choosing the right time span will generally lead to obtaining a sub-optimal shape. The flow field changes the shape by deforming it from initial form to the optimal one. Because of this, the time span may have to be changed in correspondence with the modified shape as well.

We propose a practical shape optimization method based on the unsteady adjoint variable method and using the parallel library HEC-MW (HPC-MW) [49][50]. We verify what kind of optimal shapes are constructed for various time spans. We then discuss which time spans are appropriate.

2. ADJOINT VARIABLE METHOD

2.1. Definition

The computational domain is shown in Fig.2. We denote by Ω the computational domain. We denoted by Γ , γ and Ψ the boundaries of the computational domain. We defined Γ as follows:

$$\psi = \Gamma_E + \Gamma_W + \Gamma_S + \Gamma_N + \Gamma_U + \Gamma_L + \gamma = \Gamma + \gamma \quad (2.1)$$

where subscripts E , W , S , N , U and L indicate the boundary parts. The domain Π shows the internal domain in the object. We denote time and the three dimensional spatial coordinate vector as follows:

$$t \in R^1 \quad (2.2)$$

$$\mathbf{x} = (x_1, x_2, x_3)^T \in R^3 \quad \text{in } \Omega \quad (2.3)$$

The variable χ also represents the spatial coordinates in the integrand.

$$\chi = (\chi_1, \chi_2, \chi_3)^T \in R^3 \quad \text{in } \Omega \quad (2.4)$$

A unit normal vector on the boundary is defined as follows:

$$n(\mathbf{x}) = (n_1(\mathbf{x}), n_2(\mathbf{x}), n_3(\mathbf{x}))^T \in R^3 \quad \text{on } \psi \quad (2.5)$$

We define the velocity vector as follows:

$$\mathbf{u}(t, \mathbf{x}) = (u_1(t, \mathbf{x}), u_2(t, \mathbf{x}), u_3(t, \mathbf{x}))^T \in R^3 \quad \text{in } \Omega \quad (2.6)$$

and the state variable vector as:

$$\begin{aligned} \mathbf{w}(t, \mathbf{x}) &= (w_1(t, \mathbf{x}), w_2(t, \mathbf{x}), w_3(t, \mathbf{x}), w_4(t, \mathbf{x}))^T \\ &= (p(t, \mathbf{x}), u_1(t, \mathbf{x}), u_2(t, \mathbf{x}), u_3(t, \mathbf{x}))^T \in R^4 \quad \text{in } \Omega \end{aligned} \quad (2.7)$$

where p denotes the pressure. The adjoint variable vector depending on time and spatial coordinates is defined as follows:

$$\lambda(t, \mathbf{x}) = (\lambda_1(t, \mathbf{x}), \lambda_2(t, \mathbf{x}), \lambda_3(t, \mathbf{x}), \lambda_4(t, \mathbf{x}))^T \in R^4 \quad \text{in } \Omega \quad (2.8)$$

where λ_1 represents the adjoint pressure, and $\lambda_2\text{-}\lambda_4$ represents the adjoint velocity vectors. The superscript (n) shows the n^{th} time step. The subscript $[i]$ shows the node number. The subscript $<m>$ shows the element number. The subscript (k) shows the k^{th} shape step. The shape step represents the number of shape modifications from the initial step to the optimal one. For example, the k^{th} velocity of both the node $[i]$ and the element $<m>$ in the time step (n) is defined as follows:

$$\mathbf{u}_{(k)}^{(n)} = \left(u_{1,(k),[i]}^{(n)}, u_{2,(k),[i]}^{(n)}, u_{3,(k),[i]}^{(n)} \right)^T \quad n, k, i = 0, 1, \dots \in R^3 \quad \text{in } \Omega \quad (2.9)$$

$$\mathbf{u}_{(k)}^{(n)} = \left(u_{1,(k),<m>}^{(n)}, u_{2,(k),<m>}^{(n)}, u_{3,(k),<m>}^{(n)} \right)^T \quad n, k, m = 0, 1, \dots \in R^3 \quad \text{in } \Omega \quad (2.10)$$

The subscripts $i, j, m, \alpha, \beta, \gamma$ and δ represent dummy indices like in the following:

$$a_j b_j = a_1 b_1 + a_2 b_2 + a_3 b_3 = \sum_{j=1}^3 a_j b_j \quad (2.11)$$

The subscript l, n is defined as the free index.

$$a_l b_l = \begin{cases} a_1 b_1 & l = 1 \\ a_2 b_2 & l = 2 \\ a_3 b_3 & l = 3 \end{cases} \quad (2.12)$$

2.2. Problem

To minimize the cost function under constraints, we formulated the Lagrange function by introducing the adjoint variables. The adjoint variable method is based on the variational method. By introducing Lagrange multipliers called adjoint variables, the constrained optimization of the cost function is transformed to the unconstrained optimization of the Lagrange function. A circular cylinder is placed in the computational domain Ω , as shown in Fig.2. Γ is the *N-S-E-W-U-L* boundary at the north side, the south side, the east side, the west side, the upper side and the lower side. γ represents the surface of the object under optimization. A fluid flows in on the boundary Γ_w and flows out on the boundary Γ_E . The origin of coordinates is at the centre of the cylinder.

In this paper, as the cost function, the traction force on the surface γ is defined as:

$$\begin{aligned} J &= - \int_{t_s}^{t_e} \int_{\gamma(x)} \left\{ -p \eta + \frac{1}{Re} \left(\frac{\partial u_1}{\partial x_1} + \frac{\partial u_1}{\partial x_1} \right) n_1 + \frac{1}{Re} \left(\frac{\partial u_2}{\partial x_1} + \frac{\partial u_1}{\partial x_2} \right) n_2 + \frac{1}{Re} \left(\frac{\partial u_3}{\partial x_1} + \frac{\partial u_1}{\partial x_3} \right) n_3 \right\} d\gamma dt \\ &= - \int_{t_s}^{t_e} \int_{\gamma(x)} T d\gamma dt \in \mathbf{R}^1 \end{aligned} \quad (2.13)$$

The domain $\gamma(x)$ depends on x . The constant t_s and t_e show the start of the test time and the end of the test time in the optimization. The constant Re represents the Reynolds number as follows:

$$Re = \frac{\rho L U_1}{\mu} \quad (2.14)$$

The constant L , U_1 , ρ and μ represents the representative length and the representative flow, the density and the viscosity coefficient respectively. The equations are dimensionless in this paper. We formulated the Lagrange function by introducing the adjoint variable as follows:

$$L = J + B + V + F \in \mathbf{R}^1 \quad (2.15)$$

$$\begin{aligned} F &= \int_{t_s}^{t_e} \int_{\Omega(x)} \lambda_1(t, \chi) f_1(t, \chi, \mathbf{W}(t, \chi)) d\Omega dt + \int_{t_s}^{t_e} \int_{\Omega(x)} \lambda_2(t, \chi) f_2(t, \chi, \mathbf{W}(t, \chi)) d\Omega dt \\ &\quad + \int_{t_s}^{t_e} \int_{\Omega(x)} \lambda_3(t, \chi) f_3(t, \chi, \mathbf{W}(t, \chi)) d\Omega dt + \int_{t_s}^{t_e} \int_{\Omega(x)} \lambda_4(t, \chi) f_4(t, \chi, \mathbf{W}(t, \chi)) d\Omega dt \in \mathbf{R}^1 \end{aligned} \quad (2.16)$$

$$\begin{aligned}
B = & \int_{t_s}^{t_e} \int_{\Gamma_N(\mathbf{x}) + \Gamma_S(\mathbf{x})} \lambda_5(t, \chi) T_1(t, \chi, \mathbf{W}(t, \chi)) d\gamma dt + \int_{t_s}^{t_e} \int_{\Gamma_N(\mathbf{x}) + \Gamma_S(\mathbf{x})} \lambda_6(t, \chi) u_2(t, \chi) d\gamma dt \\
& + \int_{t_s}^{t_e} \int_{\Gamma_N(\mathbf{x}) + \Gamma_S(\mathbf{x})} \lambda_7(t, \chi) T_3(t, \chi, \mathbf{W}(t, \chi)) d\gamma dt + \int_{t_s}^{t_e} \int_{\Gamma_U(\mathbf{x}) + \Gamma_L(\mathbf{x})} \lambda_8(t, \chi) T_1(t, \chi, \mathbf{W}(t, \chi)) d\gamma dt \\
& + \int_{t_s}^{t_e} \int_{\Gamma_U(\mathbf{x}) + \Gamma_L(\mathbf{x})} \lambda_9(t, \chi) T_2(t, \chi, \mathbf{W}(t, \chi)) d\gamma dt + \int_{t_s}^{t_e} \int_{\Gamma_U(\mathbf{x}) + \Gamma_L(\mathbf{x})} \lambda_{10}(t, \chi) u_3(t, \chi) d\gamma dt \\
& + \int_{t_s}^{t_e} \int_{\Gamma_E(\mathbf{x})} \lambda_{11}(t, \chi) T_1(t, \chi, \mathbf{W}(t, \chi)) d\gamma dt + \int_{t_s}^{t_e} \int_{\Gamma_E(\mathbf{x})} \lambda_{12}(t, \chi) T_2(t, \chi, \mathbf{W}(t, \chi)) d\gamma dt + \int_{t_s}^{t_e} \int_{\Gamma_E(\mathbf{x})} \lambda_{13}(t, \chi) T_3(t, \chi, \mathbf{W}(t, \chi)) d\gamma dt \\
& + \int_{t_s}^{t_e} \int_{\Gamma_H(\mathbf{x})} \lambda_{14}(t, \chi) \{u_1(t, \chi) - 1\} d\gamma dt + \int_{t_s}^{t_e} \int_{\Gamma_H(\mathbf{x})} \lambda_{15}(t, \chi) u_2(t, \chi) d\gamma dt + \int_{t_s}^{t_e} \int_{\Gamma_H(\mathbf{x})} \lambda_{16}(t, \chi) u_3(t, \chi) d\gamma dt \\
& + \int_{t_s}^{t_e} \int_{\gamma(\mathbf{x})} \lambda_{17}(t, \chi) u_1(t, \chi) d\gamma dt + \int_{t_s}^{t_e} \int_{\gamma(\mathbf{x})} \lambda_{18}(t, \chi) u_2(t, \chi) d\gamma dt + \int_{t_s}^{t_e} \int_{\gamma(\mathbf{x})} \lambda_{19}(t, \chi) u_3(t, \chi) d\gamma dt \in \mathbf{R}^1
\end{aligned} \tag{2.17}$$

$$V = \kappa \int_{t_s}^{t_e} \int_{\Pi(\mathbf{x})} d\Pi dt \in \mathbf{R}^1 \tag{2.18}$$

where the variable F shows the constraint function by the governing equation and the variable B shows the constraint function by the boundary condition for the governing equation. The variable λ_1 shows the adjoint pressure corresponding to the pressure p and $\lambda_2 \square \lambda_4$ show the adjoint velocity corresponding to the flow velocity $u_1 \square u_3$. The variable $\lambda_5 \square \lambda_{19}$ represents the undetermined adjoint variables. For example, the variables λ_5, λ_6 and λ_7 show the introduced adjoint variable to set the boundary condition $T_1=0, u_2=0$ and $T_3=0$ on the boundary Γ_N and boundary Γ_S in Fig.1, respectively. The control variables used to deform the shape are the coordinates of the node points on the surface in the analytical model. The objective function consists of the cost function (J) and the function (V) which represents the constant volume constraint on the object. The shape is deformed to minimize this objective function. The function $f(t, \mathbf{x}, \mathbf{w}(t, \mathbf{x}))$ consists of the continuity equation $f_1(t, \mathbf{x}, \mathbf{w}(t, \mathbf{x}))$ and the Navier-Stokes equation $f_2(t, \mathbf{x}, \mathbf{w}(t, \mathbf{x})), f_3(t, \mathbf{x}, \mathbf{w}(t, \mathbf{x}))$ and $f_4(t, \mathbf{x}, \mathbf{w}(t, \mathbf{x}))$. The stationary conditions (the state equation, the adjoint equation and the sensitivity equation) are derived by using the first variation. The Lagrange function is formulated as follows:

$$\begin{aligned}
L = & J + B + V + \int_{t_s}^{t_e} \int_{\Omega(\mathbf{x})} \lambda_1 \left(\frac{\partial \hat{u}_1}{\partial \hat{x}_1} + \frac{\partial \hat{u}_2}{\partial \hat{x}_2} + \frac{\partial \hat{u}_3}{\partial \hat{x}_3} \right) d\Omega dt \\
& + \int_{t_s}^{t_e} \int_{\Omega(\mathbf{x})} \lambda_2 \left[-\frac{\partial \hat{u}_1}{\partial t} - \frac{\partial \hat{p}}{\partial \hat{x}_1} - u_1 \frac{\partial \hat{u}_1}{\partial \hat{x}_1} - u_2 \frac{\partial \hat{u}_1}{\partial \hat{x}_2} - u_3 \frac{\partial \hat{u}_1}{\partial \hat{x}_3} + \frac{1}{Re} \left\{ 2 \frac{\partial}{\partial \hat{x}_1} \frac{\partial \hat{u}_1}{\partial \hat{x}_1} + \frac{\partial}{\partial \hat{x}_2} \left(\frac{\partial \hat{u}_2}{\partial \hat{x}_1} + \frac{\partial \hat{u}_1}{\partial \hat{x}_2} \right) + \frac{\partial}{\partial \hat{x}_3} \left(\frac{\partial \hat{u}_3}{\partial \hat{x}_1} + \frac{\partial \hat{u}_1}{\partial \hat{x}_3} \right) \right\} \right] d\Omega dt \\
& + \int_{t_s}^{t_e} \int_{\Omega(\mathbf{x})} \lambda_3 \left\{ -\frac{\partial \hat{u}_2}{\partial t} - \frac{\partial \hat{p}}{\partial \hat{x}_2} - u_1 \frac{\partial \hat{u}_2}{\partial \hat{x}_1} - u_2 \frac{\partial \hat{u}_2}{\partial \hat{x}_2} - u_3 \frac{\partial \hat{u}_2}{\partial \hat{x}_3} + \frac{1}{Re} \left\{ \frac{\partial}{\partial \hat{x}_1} \left(\frac{\partial \hat{u}_1}{\partial \hat{x}_1} + \frac{\partial \hat{u}_2}{\partial \hat{x}_1} \right) + 2 \frac{\partial}{\partial \hat{x}_2} \frac{\partial \hat{u}_2}{\partial \hat{x}_1} + \frac{\partial}{\partial \hat{x}_3} \left(\frac{\partial \hat{u}_3}{\partial \hat{x}_1} + \frac{\partial \hat{u}_2}{\partial \hat{x}_3} \right) \right\} \right\} d\Omega dt \\
& + \int_{t_s}^{t_e} \int_{\Omega(\mathbf{x})} \lambda_4 \left\{ -\frac{\partial \hat{u}_3}{\partial t} - \frac{\partial \hat{p}}{\partial \hat{x}_3} - u_1 \frac{\partial \hat{u}_3}{\partial \hat{x}_1} - u_2 \frac{\partial \hat{u}_3}{\partial \hat{x}_2} - u_3 \frac{\partial \hat{u}_3}{\partial \hat{x}_3} + \frac{1}{Re} \left\{ \frac{\partial}{\partial \hat{x}_1} \left(\frac{\partial \hat{u}_1}{\partial \hat{x}_3} + \frac{\partial \hat{u}_3}{\partial \hat{x}_1} \right) + \frac{\partial}{\partial \hat{x}_2} \left(\frac{\partial \hat{u}_2}{\partial \hat{x}_3} + \frac{\partial \hat{u}_3}{\partial \hat{x}_2} \right) + 2 \frac{\partial}{\partial \hat{x}_3} \frac{\partial \hat{u}_3}{\partial \hat{x}_1} \right\} \right\} d\Omega dt \in \mathbf{R}^1
\end{aligned} \tag{2.19}$$

The integral domain depends on spatial coordinates. However, the domain $\gamma(\mathbf{x})$ etc. are often abbreviated to γ etc.

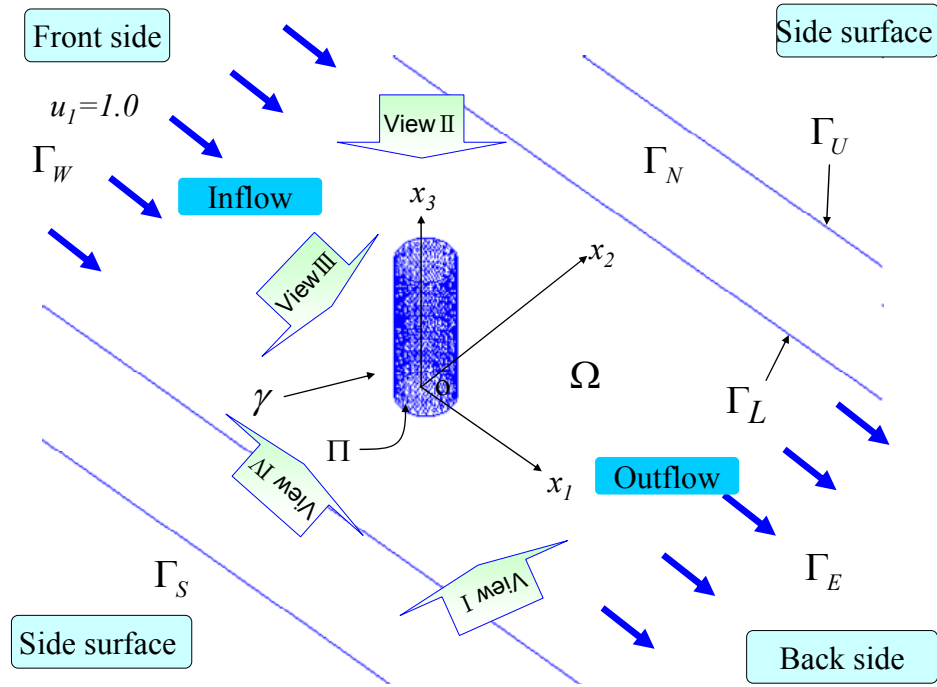


Figure 2. The computational domain.

2.3. State Equations

We denote the function that minimizes the Lagrange function (Eq.(2.19)) by the adjoint variables $\lambda_l(t, \mathbf{x})$. The comparison function $\Lambda_l(t, \mathbf{x})$ is defined as follows [19][20]:

$$\Lambda_l(\alpha, t, x_1, x_2, x_3) = \lambda_l(t, x_1, x_2, x_3) + \alpha \eta_l(x_1, x_2, x_3) \quad l=1,2,3,4 \quad \text{in } \Omega \quad (2.20)$$

where α is the parameter of the family and $\eta_l(\mathbf{x})$ is an arbitrary differentiable function[19]. The comparison function $\Lambda_l(t, \mathbf{x})$ represents the domain around the variable λ_l by changing the parameter α . Replacing the variable λ_l by the variable Λ_l , Eq.(2.19) becomes $L(\lambda_l + \alpha \eta_l)$. When the parameter α in $L(\lambda_l + \alpha \eta_l)$ is zero, it becomes equivalent with the Eq.(2.19). When the variable λ_l gives the stationary condition with respect to the Lagrange function L , the function $L(\lambda_l + \alpha \eta_l)$ should satisfy the stationary condition with respect to the arbitrary function η_l . To derive the variable λ_l which gives the extremal value with respect to the function $L(\lambda_l + \alpha \eta_l)$, the function $L(\lambda_l + \alpha \eta_l)$ is differentiated with respect to the parameter α and the parameter α in $L(\lambda_l + \alpha \eta_l)$ is set to zero as follows:

$$\delta L = \left\{ \lim_{\alpha \rightarrow 0} \frac{L(\lambda_l + \alpha \eta_l) - L(\lambda_l)}{\alpha} \right\}_{\alpha=0} = \left[\frac{\partial L(\lambda_l + \alpha \eta_l)}{\partial \alpha} \right]_{\alpha=0} = 0 \quad l=1 \sim 19 \quad (2.21)$$

The integral (Eq.(2.19)) is minimized with respect to α for the value $\alpha=0$ and $\lambda(t,x)$ is the actual minimizing function. All three variables α , t and x are independent. By using the fundamental lemma of the calculus of variations, the state equation is derived from the above equation as follows:

$$\begin{aligned} \left[\frac{\partial L(\lambda_l + \alpha \eta_l)}{\partial \alpha} \right]_{\alpha=0} &= \left[\frac{\partial J(\lambda_l + \alpha \eta_l)}{\partial \alpha} \right]_{\alpha=0} + \left[\frac{\partial B(\lambda_l + \alpha \eta_l)}{\partial \alpha} \right]_{\alpha=0} \\ &+ \left[\frac{\partial V(\lambda_l + \alpha \eta_l)}{\partial \alpha} \right]_{\alpha=0} + \left[\frac{\partial F(\lambda_l + \alpha \eta_l)}{\partial \alpha} \right]_{\alpha=0} \quad l=1 \sim 19 \end{aligned} \quad (2.22)$$

The state equations consist of the continuum and the Navier-Stokes equations. The Navier-Stokes consists of the time derivative term, the convective term, the pressure term, and the diffusion term as follows:

$$\frac{\partial u_1}{\partial x_1} + \frac{\partial u_2}{\partial x_2} + \frac{\partial u_3}{\partial x_3} = 0 \quad (= f_1) \quad \text{in } \Omega \quad (2.23)$$

$$\begin{aligned} -\frac{\partial u_1}{\partial t} - \frac{\partial p}{\partial x_1} - \left(u_1 \frac{\partial u_1}{\partial x_1} + u_2 \frac{\partial u_1}{\partial x_2} + u_3 \frac{\partial u_1}{\partial x_3} \right) \\ + \frac{1}{Re} \left\{ \frac{\partial}{\partial x_1} \left(\frac{\partial u_1}{\partial x_1} + \frac{\partial u_1}{\partial x_2} \right) + \frac{\partial}{\partial x_2} \left(\frac{\partial u_2}{\partial x_1} + \frac{\partial u_2}{\partial x_2} \right) + \frac{\partial}{\partial x_3} \left(\frac{\partial u_3}{\partial x_1} + \frac{\partial u_3}{\partial x_3} \right) \right\} = 0 \quad (= f_2) \quad \text{in } \Omega \end{aligned} \quad (2.24)$$

$$\begin{aligned} -\frac{\partial u}{\partial t} - \frac{\partial p}{\partial x_2} - \left(u_1 \frac{\partial u_2}{\partial x_1} + u_2 \frac{\partial u_2}{\partial x_2} + u_3 \frac{\partial u_2}{\partial x_3} \right) \\ + \frac{1}{Re} \left\{ \frac{\partial}{\partial x_1} \left(\frac{\partial u_1}{\partial x_2} + \frac{\partial u_2}{\partial x_1} \right) + \frac{\partial}{\partial x_2} \left(\frac{\partial u_2}{\partial x_2} + \frac{\partial u_2}{\partial x_3} \right) + \frac{\partial}{\partial x_3} \left(\frac{\partial u_3}{\partial x_2} + \frac{\partial u_2}{\partial x_3} \right) \right\} = 0 \quad (= f_3) \quad \text{in } \Omega \end{aligned} \quad (2.25)$$

$$\begin{aligned} -\frac{\partial u_3}{\partial t} - \frac{\partial p}{\partial x_3} - \left(u_1 \frac{\partial u_3}{\partial x_1} + u_2 \frac{\partial u_3}{\partial x_2} + u_3 \frac{\partial u_3}{\partial x_3} \right) \\ + \frac{1}{Re} \left\{ \frac{\partial}{\partial x_1} \left(\frac{\partial u_1}{\partial x_3} + \frac{\partial u_3}{\partial x_1} \right) + \frac{\partial}{\partial x_2} \left(\frac{\partial u_2}{\partial x_3} + \frac{\partial u_3}{\partial x_2} \right) + \frac{\partial}{\partial x_3} \left(\frac{\partial u_3}{\partial x_1} + \frac{\partial u_3}{\partial x_3} \right) \right\} = 0 \quad (= f_4) \quad \text{in } \Omega \end{aligned} \quad (2.26)$$

In the state equation, the boundary condition is shown in Table 1.

Table 1. Boundary conditions.

Domains	State equations	Adjoint equations
Γ_w	$u_1=1, u_2=0, u_3=0$	$\lambda_2=0, \lambda_3=0, \lambda_4=0$
Γ_E	$\mathbf{T}=0$	$\mathbf{S}=0$
Γ_N, Γ_S	$u_2=0, T_1=0, T_3=0$	$\lambda_3=0, S_1=0, S_3=0$
Γ_U, Γ_L	$u_3=0, T_1=0, T_2=0$	$\lambda_4=0, S_1=0, S_2=0$
γ	$u_1=0, u_2=0, u_3=0$	$\lambda_2=1, \lambda_3=0, \lambda_4=0$

2.4. Adjoint Equations

In analyzing unsteady flow, the convective term is needed. However, the first variation in the convective term is impossible to derive. Millikan gave the necessary condition for the existence of a variational principle for the Navier-Stokes equation. He concluded that a variational principle could not be found unless $u \cdot \nabla u = 0$ or $u \times (\nabla \times u) = 0$ [51][52][53]. Finlayson improved on Millikan's proof by using Frechet derivatives [54]. By Eq.(2.19), the state variables cannot be eliminated from the convective term of the adjoint equations [55][56][57].

$$\begin{aligned} & -\frac{\partial \lambda_2}{\partial t} - \frac{\partial \lambda_1}{\partial x_1} - u_1 \frac{\partial \lambda_2}{\partial x_1} - u_2 \frac{\partial \lambda_2}{\partial x_2} - u_3 \frac{\partial \lambda_2}{\partial x_3} + \lambda_2 \frac{\partial u_1}{\partial x_1} + \lambda_3 \frac{\partial u_2}{\partial x_1} + \lambda_4 \frac{\partial u_3}{\partial x_1} \\ & + \frac{1}{Re} \left\{ \frac{\partial}{\partial x_1} \left(\frac{\partial \lambda_2}{\partial x_1} + \frac{\partial \lambda_2}{\partial x_1} \right) + \frac{\partial}{\partial x_2} \left(\frac{\partial \lambda_3}{\partial x_1} + \frac{\partial \lambda_2}{\partial x_2} \right) + \frac{\partial}{\partial x_3} \left(\frac{\partial \lambda_4}{\partial x_1} + \frac{\partial \lambda_2}{\partial x_3} \right) \right\} = 0 \quad \text{in } \Omega \end{aligned} \quad (2.27)$$

$$\begin{aligned} & -\frac{\partial \lambda_3}{\partial t} - \frac{\partial \lambda_1}{\partial x_2} - u_1 \frac{\partial \lambda_3}{\partial x_1} - u_2 \frac{\partial \lambda_3}{\partial x_2} - u_3 \frac{\partial \lambda_3}{\partial x_3} + \lambda_2 \frac{\partial u_1}{\partial x_2} + \lambda_3 \frac{\partial u_2}{\partial x_2} + \lambda_4 \frac{\partial u_3}{\partial x_2} \\ & + \frac{1}{Re} \left\{ \frac{\partial}{\partial x_1} \left(\frac{\partial \lambda_2}{\partial x_2} + \frac{\partial \lambda_3}{\partial x_1} \right) + \frac{\partial}{\partial x_2} \left(\frac{\partial \lambda_3}{\partial x_2} + \frac{\partial \lambda_3}{\partial x_2} \right) + \frac{\partial}{\partial x_3} \left(\frac{\partial \lambda_4}{\partial x_2} + \frac{\partial \lambda_3}{\partial x_3} \right) \right\} = 0 \quad \text{in } \Omega \end{aligned} \quad (2.28)$$

$$\begin{aligned} & -\frac{\partial \lambda_4}{\partial t} - \frac{\partial \lambda_1}{\partial x_3} - u_1 \frac{\partial \lambda_4}{\partial x_1} - u_2 \frac{\partial \lambda_4}{\partial x_2} - u_3 \frac{\partial \lambda_4}{\partial x_3} + \lambda_2 \frac{\partial u_1}{\partial x_3} + \lambda_3 \frac{\partial u_2}{\partial x_3} + \lambda_4 \frac{\partial u_3}{\partial x_3} \\ & + \frac{1}{Re} \left\{ \frac{\partial}{\partial x_1} \left(\frac{\partial \lambda_2}{\partial x_3} + \frac{\partial \lambda_4}{\partial x_1} \right) + \frac{\partial}{\partial x_2} \left(\frac{\partial \lambda_3}{\partial x_3} + \frac{\partial \lambda_4}{\partial x_2} \right) + \frac{\partial}{\partial x_3} \left(\frac{\partial \lambda_4}{\partial x_3} + \frac{\partial \lambda_4}{\partial x_3} \right) \right\} = 0 \quad \text{in } \Omega \end{aligned} \quad (2.29)$$

Since the state variables and the adjoint variables are independent, the stationary condition in the adjoint equations with respect to the state variables alone cannot be obtained.

In the shape optimization algorithm, the values for the variable $u_i (i=1 \sim 3)$ are undetermined. Besides, the sensitivity equations are also impossible to derive as the first variation of the convective term produces an inconsistency (the $\partial \eta_{24} / \partial x_1$ term in appendix C) in the stationary condition of the sensitivity equation. In other words, in order to derive a stationary condition, some kind of approximation is demanded for the convection term.

In this study, the stationary conditions under unsteady flow are derived by using Oseen's approximation. The non-linear equation in the convective term is linearized using Oseen's approximation as follows:

$$\begin{aligned} L = J + B + V + \int_{t_1}^{t_e} \int_{\Omega(x)} \lambda_1 \left(\frac{\partial u_1}{\partial x_1} + \frac{\partial u_2}{\partial x_2} + \frac{\partial u_3}{\partial x_3} \right) d\Omega dt \\ + \int_{t_1}^{t_e} \int_{\Omega(x)} \lambda_2 \left[-\frac{\partial u_1}{\partial t} - \frac{\partial p}{\partial x_1} - U_1 \frac{\partial u_1}{\partial x_1} - U_2 \frac{\partial u_1}{\partial x_2} - U_3 \frac{\partial u_1}{\partial x_3} + \frac{1}{Re} \left\{ 2 \frac{\partial}{\partial x_1} \frac{\partial u_1}{\partial x_1} + \frac{\partial}{\partial x_2} \left(\frac{\partial u_2}{\partial x_1} + \frac{\partial u_1}{\partial x_2} \right) + \frac{\partial}{\partial x_3} \left(\frac{\partial u_3}{\partial x_1} + \frac{\partial u_1}{\partial x_3} \right) \right\} \right] d\Omega dt \\ + \int_{t_1}^{t_e} \int_{\Omega(x)} \lambda_3 \left\{ -\frac{\partial u_2}{\partial t} - \frac{\partial p}{\partial x_2} - U_1 \frac{\partial u_2}{\partial x_1} - U_2 \frac{\partial u_2}{\partial x_2} - U_3 \frac{\partial u_2}{\partial x_3} + \frac{1}{Re} \left\{ \frac{\partial}{\partial x_1} \left(\frac{\partial u_1}{\partial x_2} + \frac{\partial u_2}{\partial x_1} \right) + 2 \frac{\partial}{\partial x_2} \frac{\partial u_2}{\partial x_2} + \frac{\partial}{\partial x_3} \left(\frac{\partial u_3}{\partial x_2} + \frac{\partial u_2}{\partial x_3} \right) \right\} \right\} d\Omega dt \\ + \int_{t_1}^{t_e} \int_{\Omega(x)} \lambda_4 \left\{ -\frac{\partial u_3}{\partial t} - \frac{\partial p}{\partial x_3} - U_1 \frac{\partial u_3}{\partial x_1} - U_2 \frac{\partial u_3}{\partial x_2} - U_3 \frac{\partial u_3}{\partial x_3} + \frac{1}{Re} \left\{ \frac{\partial}{\partial x_1} \left(\frac{\partial u_1}{\partial x_3} + \frac{\partial u_3}{\partial x_1} \right) + \frac{\partial}{\partial x_2} \left(\frac{\partial u_2}{\partial x_3} + \frac{\partial u_3}{\partial x_2} \right) + 2 \frac{\partial}{\partial x_3} \frac{\partial u_3}{\partial x_3} \right\} \right\} d\Omega dt \quad \in \mathbf{R}^1 \end{aligned}$$

(2.30)

The constants U_1, U_2 and U_3 denote the representative flow (constants). In order to derive the adjoint equation and the sensitivity equation, Eq.(2.30) can be transformed as follows: (see appendix A for details regarding this transformation):

$$\begin{aligned}
 L = & -\int_{t_s}^{t_e} \int_{\gamma} T_i d\gamma dt + \int_{t_s}^{t_e} \int_{\Omega} P \frac{\partial \lambda_{k+1}}{\partial x_k} d\Omega dt + \int_{t_s}^{t_e} \int_{\Omega} u_i \left\{ \frac{\partial \lambda_{i+1}}{\partial t} - \frac{\partial \lambda_i}{\partial x_i} + U_j \frac{\partial \lambda_{i+1}}{\partial x_j} + \frac{1}{\text{Re}} \frac{\partial}{\partial x_i} \left(\frac{\partial \lambda_{j+1}}{\partial x_i} + \frac{\partial \lambda_{i+1}}{\partial x_j} \right) \right\} d\Omega dt \\
 & + \int_{t_s}^{t_e} \int_{\psi} \lambda_{i+1} T_i d\psi dt - \int_{t_s}^{t_e} \int_{\psi} u_i S_i d\psi dt + \int_{t_s}^{t_e} \int_{\Gamma_N + \Gamma_S} \lambda_S T_i d\gamma dt + \int_{t_s}^{t_e} \int_{\Gamma_N + \Gamma_S} \lambda_6 u_2 d\gamma dt \\
 & + \int_{t_s}^{t_e} \int_{\Gamma_N + \Gamma_S} \lambda_7 T_3 d\gamma dt + \int_{t_s}^{t_e} \int_{\Gamma_U + \Gamma_L} \lambda_8 T_1 d\gamma dt + \int_{t_s}^{t_e} \int_{\Gamma_U + \Gamma_L} \lambda_9 T_2 d\gamma dt + \int_{t_s}^{t_e} \int_{\Gamma_U + \Gamma_L} \lambda_{10} u_3 d\gamma dt \\
 & + \int_{t_s}^{t_e} \int_{\Gamma_E} \lambda_{11} T_1 d\gamma dt + \int_{t_s}^{t_e} \int_{\Gamma_E} \lambda_{12} T_2 d\gamma dt + \int_{t_s}^{t_e} \int_{\Gamma_E} \lambda_{13} T_3 d\gamma dt + \int_{t_s}^{t_e} \int_{\Gamma_W} \lambda_{14} u_1 d\gamma dt + \int_{t_s}^{t_e} \int_{\Gamma_W} \lambda_{15} u_2 d\gamma dt \\
 & + \int_{t_s}^{t_e} \int_{\Gamma_W} \lambda_{16} u_3 d\gamma dt + \int_{t_s}^{t_e} \int_{\gamma} \lambda_{17} u_1 d\gamma dt + \int_{t_s}^{t_e} \int_{\gamma} \lambda_{18} u_2 d\gamma dt + \int_{t_s}^{t_e} \int_{\gamma} \lambda_{19} u_3 d\gamma dt - \int_{\Omega} [\lambda_{i+1} u_i]_{s^*}^{t_e} d\Omega + \kappa \int_{t_s}^{t_e} \int_{\Pi} d\Pi dt
 \end{aligned} \tag{2.31}$$

The functions S_I - S_3 are as follows:

$$S_l = \lambda_{l+1} U_j n_j - \lambda_l n_l + \frac{1}{\text{Re}} \left(\frac{\partial \lambda_{l+1}}{\partial x_j} + \frac{\partial \lambda_{j+1}}{\partial x_l} \right) n_j = 0 \quad l = 1, 2, 3 \tag{2.32}$$

The comparison function $W_l(\alpha, t, x_1, x_2, x_3)$ is defined as follows:

$$W_l(\alpha, t, x_1, x_2, x_3) = w_l(t, x_1, x_2, x_3) + \alpha \eta_{l+19}(x_1, x_2, x_3) \quad l = 1, 2, 3, 4 \quad \text{in } \Omega \tag{2.33}$$

The adjoint variable is calculated by solving the adjoint equation, the stationary condition which is obtained by taking the first variation of the Lagrange function with respect to the state variable \mathbf{w} as follows:

$$\begin{aligned}
 \left[\frac{\partial L(w_l + \alpha \eta_{l+19})}{\partial \alpha} \right]_{\alpha=0} &= \left[\frac{\partial J(w_l + \alpha \eta_{l+19})}{\partial \alpha} \right]_{\alpha=0} + \left[\frac{\partial B(w_l + \alpha \eta_{l+19})}{\partial \alpha} \right]_{\alpha=0} \\
 &+ \left[\frac{\partial V(w_l + \alpha \eta_{l+19})}{\partial \alpha} \right]_{\alpha=0} + \left[\frac{\partial F(w_l + \alpha \eta_{l+19})}{\partial \alpha} \right]_{\alpha=0} \quad l = 1, 2, 3, 4
 \end{aligned} \tag{2.34}$$

The adjoint equation is derived as follows (see appendix B for details regarding this transformation):

$$\frac{\partial \lambda_2}{\partial x_1} + \frac{\partial \lambda_3}{\partial x_2} + \frac{\partial \lambda_4}{\partial x_3} = 0 \quad \text{in } \Omega \tag{2.35}$$

$$\begin{aligned}
 & -\frac{\partial \lambda_2}{\partial t} - \frac{\partial \lambda_1}{\partial x_1} + U_1 \frac{\partial \lambda_2}{\partial x_1} + U_2 \frac{\partial \lambda_2}{\partial x_2} + U_3 \frac{\partial \lambda_2}{\partial x_3} \\
 & + \frac{1}{\text{Re}} \left\{ \frac{\partial}{\partial x_1} \left(\frac{\partial \lambda_2}{\partial x_1} + \frac{\partial \lambda_2}{\partial x_2} \right) + \frac{\partial}{\partial x_2} \left(\frac{\partial \lambda_3}{\partial x_1} + \frac{\partial \lambda_2}{\partial x_2} \right) + \frac{\partial}{\partial x_3} \left(\frac{\partial \lambda_4}{\partial x_1} + \frac{\partial \lambda_2}{\partial x_3} \right) \right\} = 0 \quad \text{in } \Omega
 \end{aligned} \tag{2.36}$$

$$\begin{aligned} & -\frac{\partial \lambda_3}{\partial \tau} - \frac{\partial \lambda_1}{\partial x_2} + U_1 \frac{\partial \lambda_3}{\partial x_1} + U_2 \frac{\partial \lambda_3}{\partial x_2} + U_3 \frac{\partial \lambda_3}{\partial x_3} \\ & + \frac{1}{\text{Re}} \left\{ \frac{\partial}{\partial x_1} \left(\frac{\partial \lambda_2}{\partial x_2} + \frac{\partial \lambda_3}{\partial x_1} \right) + \frac{\partial}{\partial x_2} \left(\frac{\partial \lambda_3}{\partial x_2} + \frac{\partial \lambda_4}{\partial x_2} \right) + \frac{\partial}{\partial x_3} \left(\frac{\partial \lambda_4}{\partial x_2} + \frac{\partial \lambda_3}{\partial x_3} \right) \right\} = 0 \quad \text{in } \Omega \end{aligned} \quad (2.37)$$

$$\begin{aligned} & -\frac{\partial \lambda_4}{\partial \tau} - \frac{\partial \lambda_1}{\partial x_3} + U_1 \frac{\partial \lambda_4}{\partial x_1} + U_2 \frac{\partial \lambda_4}{\partial x_2} + U_3 \frac{\partial \lambda_4}{\partial x_3} \\ & + \frac{1}{\text{Re}} \left\{ \frac{\partial}{\partial x_1} \left(\frac{\partial \lambda_2}{\partial x_3} + \frac{\partial \lambda_4}{\partial x_1} \right) + \frac{\partial}{\partial x_2} \left(\frac{\partial \lambda_3}{\partial x_3} + \frac{\partial \lambda_4}{\partial x_2} \right) + \frac{\partial}{\partial x_3} \left(\frac{\partial \lambda_4}{\partial x_3} + \frac{\partial \lambda_4}{\partial x_3} \right) \right\} = 0 \quad \text{in } \Omega \end{aligned} \quad (2.38)$$

In the adjoint equation, the boundary condition is shown in Table 1.

2.5 Sensitivity equations

Adjoint formulations can employ either a discrete or a continuous approach. In the discrete approach, the sensitivity, the gradient of the Lagrange function, must be calculated using only nodal information. Therefore, programming techniques for computing the sensitivities, such as automatic differentiation [59], are demanded. In this study, the adjoint formulation is based on the continuous approach so such methods are not needed. The comparison function $X_l(\alpha, x_1, x_2, x_3)$ is defined as follows:

$$X_l(\alpha, x_1, x_2, x_3) = x_l(x_1, x_2, x_3) + \alpha \eta_{l+23}(x_1, x_2, x_3) \quad l=1,2,3 \quad \text{in } \Omega \quad (2.39)$$

The first variation of the Lagrange function with respect to x represents the sensitivity equation. The first variation is as follows:

$$\begin{aligned} & \left[\frac{\partial L(x_l + \alpha \eta_{l+23})}{\partial \alpha} \right]_{\alpha=0} = \left[\frac{\partial J(x_l + \alpha \eta_{l+23})}{\partial \alpha} \right]_{\alpha=0} + \left[\frac{\partial B(w_l + \alpha \eta_{l+23})}{\partial \alpha} \right]_{\alpha=0} \\ & + \left[\frac{\partial F(x_l + \alpha \eta_{l+23})}{\partial \alpha} \right]_{\alpha=0} + \left[\frac{\partial V(x_l + \alpha \eta_{l+23})}{\partial \alpha} \right]_{\alpha=0} \quad l=1,2,3 \in R^3 \end{aligned} \quad (2.40)$$

The above equation is as following (see appendix C for details regarding this transformation):

$$\begin{aligned} & \left\{ \lambda_2 (U_1 n_1 + U_2 n_2 + U_3 n_3) + \left(-\lambda_1 + 2\mu \frac{\partial \lambda_2}{\partial x_1} \right) n_1 + \mu \left(\frac{\partial \lambda_2}{\partial x_2} + \frac{\partial \lambda_3}{\partial x_1} \right) n_2 + \mu \left(\frac{\partial \lambda_2}{\partial x_3} + \frac{\partial \lambda_4}{\partial x_1} \right) n_3 \right\} \frac{\partial u_1}{\partial x_1} \\ & + \left\{ \lambda_3 (U_1 n_1 + U_2 n_2 + U_3 n_3) + \mu \left(\frac{\partial \lambda_3}{\partial x_1} + \frac{\partial \lambda_2}{\partial x_2} \right) n_1 + \left(-\lambda_1 + 2\mu \frac{\partial \lambda_3}{\partial x_2} \right) n_2 + \mu \left(\frac{\partial \lambda_3}{\partial x_3} + \frac{\partial \lambda_4}{\partial x_2} \right) n_3 \right\} \frac{\partial u_2}{\partial x_1} \\ & + \left\{ \lambda_4 (U_1 n_1 + U_2 n_2 + U_3 n_3) + \mu \left(\frac{\partial \lambda_4}{\partial x_1} + \frac{\partial \lambda_2}{\partial x_3} \right) n_1 + \mu \left(\frac{\partial \lambda_4}{\partial x_2} + \frac{\partial \lambda_3}{\partial x_3} \right) n_2 + \left(-\lambda_1 + 2\mu \frac{\partial \lambda_4}{\partial x_3} \right) n_3 \right\} \frac{\partial u_3}{\partial x_1} \\ & - \kappa n_1 = 0 \quad (= G_1) \quad \text{on } \gamma \end{aligned} \quad (2.41)$$

$$\begin{aligned}
& \left\{ \lambda_2(U_1 n_1 + U_2 n_2 + U_3 n_3) + \left(-\lambda_1 + 2\mu \frac{\partial \lambda_2}{\partial x_1} \right) n_1 + \mu \left(\frac{\partial \lambda_2}{\partial x_2} + \frac{\partial \lambda_3}{\partial x_1} \right) n_2 + \mu \left(\frac{\partial \lambda_2}{\partial x_3} + \frac{\partial \lambda_4}{\partial x_1} \right) n_3 \right\} \frac{\partial u_1}{\partial x_1} \\
& + \left\{ \lambda_3(U_1 n_1 + U_2 n_2 + U_3 n_3) + \mu \left(\frac{\partial \lambda_3}{\partial x_1} + \frac{\partial \lambda_2}{\partial x_2} \right) n_1 + \left(-\lambda_1 + 2\mu \frac{\partial \lambda_3}{\partial x_2} \right) n_2 + \mu \left(\frac{\partial \lambda_3}{\partial x_3} + \frac{\partial \lambda_4}{\partial x_2} \right) n_3 \right\} \frac{\partial u_2}{\partial x_2} \\
& + \left\{ \lambda_4(U_1 n_1 + U_2 n_2 + U_3 n_3) + \mu \left(\frac{\partial \lambda_4}{\partial x_1} + \frac{\partial \lambda_2}{\partial x_3} \right) n_1 + \mu \left(\frac{\partial \lambda_4}{\partial x_2} + \frac{\partial \lambda_3}{\partial x_3} \right) n_2 + \left(-\lambda_1 + 2\mu \frac{\partial \lambda_4}{\partial x_3} \right) n_3 \right\} \frac{\partial u_3}{\partial x_3} \\
& - \kappa n_2 = 0 \quad (= G_2) \quad \text{on } \gamma
\end{aligned} \tag{2.42}$$

$$\begin{aligned}
& \left\{ \lambda_2(U_1 n_1 + U_2 n_2 + U_3 n_3) + \left(-\lambda_1 + 2\mu \frac{\partial \lambda_2}{\partial x_1} \right) n_1 + \mu \left(\frac{\partial \lambda_2}{\partial x_2} + \frac{\partial \lambda_3}{\partial x_1} \right) n_2 + \mu \left(\frac{\partial \lambda_2}{\partial x_3} + \frac{\partial \lambda_4}{\partial x_1} \right) n_3 \right\} \frac{\partial u_1}{\partial x_3} \\
& + \left\{ \lambda_3(U_1 n_1 + U_2 n_2 + U_3 n_3) + \mu \left(\frac{\partial \lambda_3}{\partial x_1} + \frac{\partial \lambda_2}{\partial x_2} \right) n_1 + \left(-\lambda_1 + 2\mu \frac{\partial \lambda_3}{\partial x_2} \right) n_2 + \mu \left(\frac{\partial \lambda_3}{\partial x_3} + \frac{\partial \lambda_4}{\partial x_2} \right) n_3 \right\} \frac{\partial u_2}{\partial x_3} \\
& + \left\{ \lambda_4(U_1 n_1 + U_2 n_2 + U_3 n_3) + \mu \left(\frac{\partial \lambda_4}{\partial x_1} + \frac{\partial \lambda_2}{\partial x_3} \right) n_1 + \mu \left(\frac{\partial \lambda_4}{\partial x_2} + \frac{\partial \lambda_3}{\partial x_3} \right) n_2 + \left(-\lambda_1 + 2\mu \frac{\partial \lambda_4}{\partial x_3} \right) n_3 \right\} \frac{\partial u_3}{\partial x_3} \\
& - \kappa n_3 = 0 \quad (= G_3) \quad \text{on } \gamma
\end{aligned} \tag{2.43}$$

3. TECHNIQUES USED IN A SHAPE OPTIMIZATION ALGORITHM

3.1. Shape Modification

The variables G_1-G_3 of Eqs.(2.41)-(2.43) make the sensitivity. When the surface takes extremal values, this sensitivity equals to zero. By using the gradient method, the shape is modified so that the sensitivity becomes zero.

$$x_{l,(k+1)} = x_{l,(k)} + \beta \int_{t_s}^{t_e} G_{l,(k)} dt \quad l=1,2,3 \quad k=0,1,\dots \in R^3 \quad \text{on } \gamma \tag{3.1}$$

The value of the coefficient β should be small enough in order to robustly converge to the optimal coordinates and to avoid collapse of the mesh topology. The value is decided based on a heuristic search method [11][59].

3.2. Smoothing

In shape optimization, meshes have been mainly analysed by using 2D low resolution models. Shapes were optimized by controlling the nodes located on the surface. This approach is called the mesh point approach [61]. Unfortunately, in the case of 3D high resolution unstructured grid (especially once using tetrahedral elements), the mesh point approach does not work so well. As a node on the boundary in a finite element is moved along the sensitivity, the smooth shape is lost and an irregular shape is constructed as shown in Fig.3[62]. As the surface becomes irregular, it partly causes a numerical vibration in the fluid analysis and negative volumes of mesh elements. In this study, the smoothing method is applied to the surface shape, as this method can be easily implemented [63]-[64].

$$\bar{g}_{<j>,(l)} = \frac{g_{[i],(l)} + g_{[k],(l)} + g_{[m],(l)}}{3} \quad l = 1, 2, 3, \dots \quad \text{on } \gamma \quad (3.2)$$

$$g_{[i],(l+1)} = \frac{\sum_j \bar{g}_{<j>,(l)} A_{<j>}}{\sum_j A_{<j>}} \quad l = 1, 2, 3, \dots \quad \text{on } \gamma \quad (3.3)$$

The surface is shown in Fig.2. $[i]$, $[k]$, $[m]$ show the node number. The smoothing method is one of the methods where the averaged movement amount of an element is converted to the movement amount of a node. The variable $g_{[i]}$ shows the movement amount of a node point $[i]$ (in Fig.4). The variable $\bar{g}_{<j>}$ represents the movement amount at gravity position of element $<j>$. The variable $A_{<j>}$ stands for the area of an element $<j>$. The lower subscript (l) is the iteration number. By updating the movement amount iteratively ($l=l+1$), the deformed surface mesh is constructed. We noticed the following:

Point A : In the case that some elements turned inside out when a node $[i]$ moved to a new node position, this node does not execute the move.

Point B : The smoothing method is sequential. The number of necessary iterations cannot be known in advance. If the number of iteration (l) is relatively large, the sharp edges will be smoothed out. On the contrary, if only a small number of iterations (l) is applied, the awkward shape of the surface will make the optimization calculations impossible. The number of iterations (l) has to increase as the Reynolds number increases as follows:

$$l \propto \text{Re} \quad (3.4)$$

One can empirically interpret the aforementioned behavior as a tendency of the mesh deformation by sensitivities to create negative volumes as the Reynolds number increased.

In calculation using the high resolution mesh and in the high Reynolds number cases, more robust smoothing methods are often demanded. In literature [67], two types of the smoothing methods were presented. One type is segment springs, where Hook's Law is applied to the displacement of the nodes. These springs are defined as in Eq.(3.3). Another type is vertex springs, where Hook's Law is applied to the coordinates of the nodes. In this case, two approaches are considered. In the first one, the springs are connected between the nodes in the shape step(k). While in the second one, the springs are connected between the nodes in the shape step(k) and the nodes in the shape step($k+1$). By using the latter approach, robust smoothing can be realized by attaching the springs on the surface nodes. The equations describing this method are as follows:

$$\begin{aligned} & \left\{ \lambda_{2,(k)} \left(U_{1,(k)} n_{1,(k)} + U_{2,(k)} n_{2,(k)} + U_{3,(k)} n_{3,(k)} \right) + \left(-\lambda_{1,(k)} + 2\mu \left(\frac{\partial \lambda_{2,(k)}}{\partial x_1} + \frac{\partial \lambda_{3,(k)}}{\partial x_1} \right) \right) n_{1,(k)} + \mu \left(\frac{\partial \lambda_{2,(k)}}{\partial x_1} + \frac{\partial \lambda_{4,(k)}}{\partial x_1} \right) n_{3,(k)} \right\} \frac{\partial u_{1,(k)}}{\partial x_1} \\ & + \left\{ \lambda_{3,(k)} \left(U_{1,(k)} n_{1,(k)} + U_{2,(k)} n_{2,(k)} + U_{3,(k)} n_{3,(k)} \right) + \mu \left(\frac{\partial \lambda_{3,(k)}}{\partial x_1} + \frac{\partial \lambda_{2,(k)}}{\partial x_2} \right) n_{1,(k)} + \left(-\lambda_{1,(k)} + 2\mu \frac{\partial \lambda_{3,(k)}}{\partial x_2} \right) n_{2,(k)} + \mu \left(\frac{\partial \lambda_{3,(k)}}{\partial x_2} + \frac{\partial \lambda_{4,(k)}}{\partial x_2} \right) n_{3,(k)} \right\} \frac{\partial u_{2,(k)}}{\partial x_1} \\ & + \left\{ \lambda_{4,(k)} \left(U_{1,(k)} n_{1,(k)} + U_{2,(k)} n_{2,(k)} + U_{3,(k)} n_{3,(k)} \right) + \mu \left(\frac{\partial \lambda_{4,(k)}}{\partial x_1} + \frac{\partial \lambda_{2,(k)}}{\partial x_3} \right) n_{1,(k)} + \mu \left(\frac{\partial \lambda_{4,(k)}}{\partial x_2} + \frac{\partial \lambda_{3,(k)}}{\partial x_3} \right) n_{2,(k)} + \left(-\lambda_{1,(k)} + 2\mu \frac{\partial \lambda_{4,(k)}}{\partial x_3} \right) n_{3,(k)} \right\} \frac{\partial u_{3,(k)}}{\partial x_1} \\ & - \kappa n_{1,(k)} - \omega(x_{1,(k)} - x_{1,(0)}) = 0 \quad (= G_{1,(k)}) \quad \text{on } \gamma \end{aligned} \quad (3.5)$$

$$\begin{aligned}
& \left\{ \lambda_{2,(k)}(U_{1,(k)}n_{1,(k)} + U_{2,(k)}n_{2,(k)} + U_{3,(k)}n_{3,(k)}) + \left(-\lambda_{1,(k)} + 2\mu \frac{\partial \lambda_{2,(k)}}{\partial x_1} \right) n_{1,(k)} + \mu \left(\frac{\partial \lambda_{2,(k)}}{\partial x_2} + \frac{\partial \lambda_{3,(k)}}{\partial x_1} \right) n_{2,(k)} + \mu \left(\frac{\partial \lambda_{2,(k)}}{\partial x_3} + \frac{\partial \lambda_{4,(k)}}{\partial x_1} \right) n_{3,(k)} \right\} \frac{\partial u_{1,(k)}}{\partial x_1} \\
& + \left\{ \lambda_{3,(k)}(U_{1,(k)}n_{1,(k)} + U_{2,(k)}n_{2,(k)} + U_{3,(k)}n_{3,(k)}) + \mu \left(\frac{\partial \lambda_{3,(k)}}{\partial x_1} + \frac{\partial \lambda_{2,(k)}}{\partial x_2} \right) n_{1,(k)} + \left(-\lambda_{1,(k)} + 2\mu \frac{\partial \lambda_{3,(k)}}{\partial x_2} \right) n_{2,(k)} + \mu \left(\frac{\partial \lambda_{3,(k)}}{\partial x_3} + \frac{\partial \lambda_{4,(k)}}{\partial x_2} \right) n_{3,(k)} \right\} \frac{\partial u_{2,(k)}}{\partial x_2} \\
& + \left\{ \lambda_{4,(k)}(U_{1,(k)}n_{1,(k)} + U_{2,(k)}n_{2,(k)} + U_{3,(k)}n_{3,(k)}) + \mu \left(\frac{\partial \lambda_{4,(k)}}{\partial x_1} + \frac{\partial \lambda_{2,(k)}}{\partial x_3} \right) n_{1,(k)} + \mu \left(\frac{\partial \lambda_{4,(k)}}{\partial x_2} + \frac{\partial \lambda_{3,(k)}}{\partial x_3} \right) n_{2,(k)} + \left(-\lambda_{1,(k)} + 2\mu \frac{\partial \lambda_{4,(k)}}{\partial x_3} \right) n_{3,(k)} \right\} \frac{\partial u_{3,(k)}}{\partial x_3} \\
& - \kappa n_{2,(k)} - \omega(x_{2,(k)} - x_{2,(0)}) = 0 \quad (= G_{2,(k)}) \quad \text{on } \gamma
\end{aligned} \tag{3.6}$$

$$\begin{aligned}
& \left\{ \lambda_{2,(k)}(U_{1,(k)}n_{1,(k)} + U_{2,(k)}n_{2,(k)} + U_{3,(k)}n_{3,(k)}) + \left(-\lambda_{1,(k)} + 2\mu \frac{\partial \lambda_{2,(k)}}{\partial x_1} \right) n_{1,(k)} + \mu \left(\frac{\partial \lambda_{2,(k)}}{\partial x_2} + \frac{\partial \lambda_{3,(k)}}{\partial x_1} \right) n_{2,(k)} + \mu \left(\frac{\partial \lambda_{2,(k)}}{\partial x_3} + \frac{\partial \lambda_{4,(k)}}{\partial x_1} \right) n_{3,(k)} \right\} \frac{\partial u_{1,(k)}}{\partial x_1} \\
& + \left\{ \lambda_{3,(k)}(U_{1,(k)}n_{1,(k)} + U_{2,(k)}n_{2,(k)} + U_{3,(k)}n_{3,(k)}) + \mu \left(\frac{\partial \lambda_{3,(k)}}{\partial x_1} + \frac{\partial \lambda_{2,(k)}}{\partial x_2} \right) n_{1,(k)} + \left(-\lambda_{1,(k)} + 2\mu \frac{\partial \lambda_{3,(k)}}{\partial x_2} \right) n_{2,(k)} + \mu \left(\frac{\partial \lambda_{3,(k)}}{\partial x_3} + \frac{\partial \lambda_{4,(k)}}{\partial x_2} \right) n_{3,(k)} \right\} \frac{\partial u_{2,(k)}}{\partial x_2} \\
& + \left\{ \lambda_{4,(k)}(U_{1,(k)}n_{1,(k)} + U_{2,(k)}n_{2,(k)} + U_{3,(k)}n_{3,(k)}) + \mu \left(\frac{\partial \lambda_{4,(k)}}{\partial x_1} + \frac{\partial \lambda_{2,(k)}}{\partial x_3} \right) n_{1,(k)} + \mu \left(\frac{\partial \lambda_{4,(k)}}{\partial x_2} + \frac{\partial \lambda_{3,(k)}}{\partial x_3} \right) n_{2,(k)} + \left(-\lambda_{1,(k)} + 2\mu \frac{\partial \lambda_{4,(k)}}{\partial x_3} \right) n_{3,(k)} \right\} \frac{\partial u_{3,(k)}}{\partial x_3} \\
& - \kappa n_{3,(k)} - \omega(x_{3,(k)} - x_{3,(0)}) = 0 \quad (= G_{3,(k)}) \quad \text{on } \gamma
\end{aligned} \tag{3.7}$$

The parameter ω represents the stiffness of the springs. The center of an object is set to the origin of the coordinate system. The last term is the added term, which shows the spring connections between the nodes of the initial shape and the nodes of the deformed shape. In the case that a node displacement is extremely larger than another one, the spring of this node is stronger than that of the other node and the spring pulls back this node to the surface.

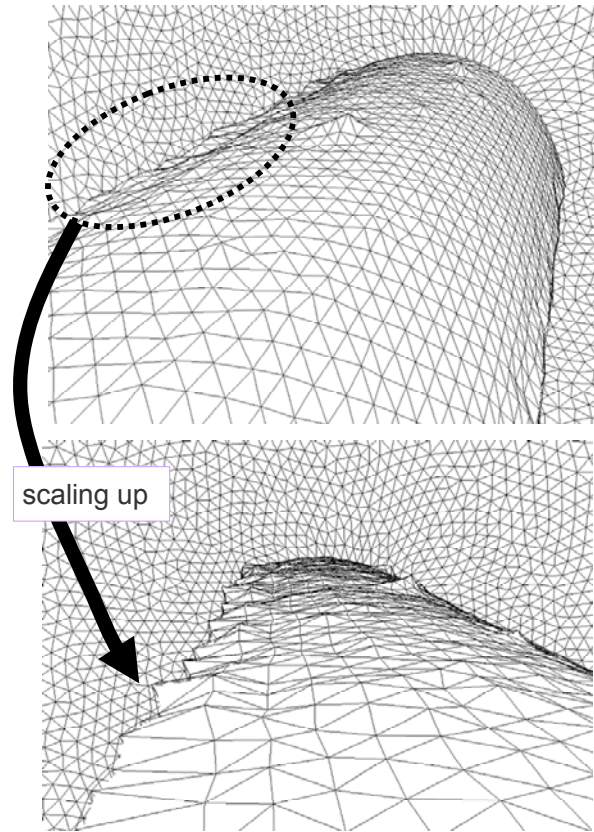


Figure 3. The irregular surface without smoothing techniques.

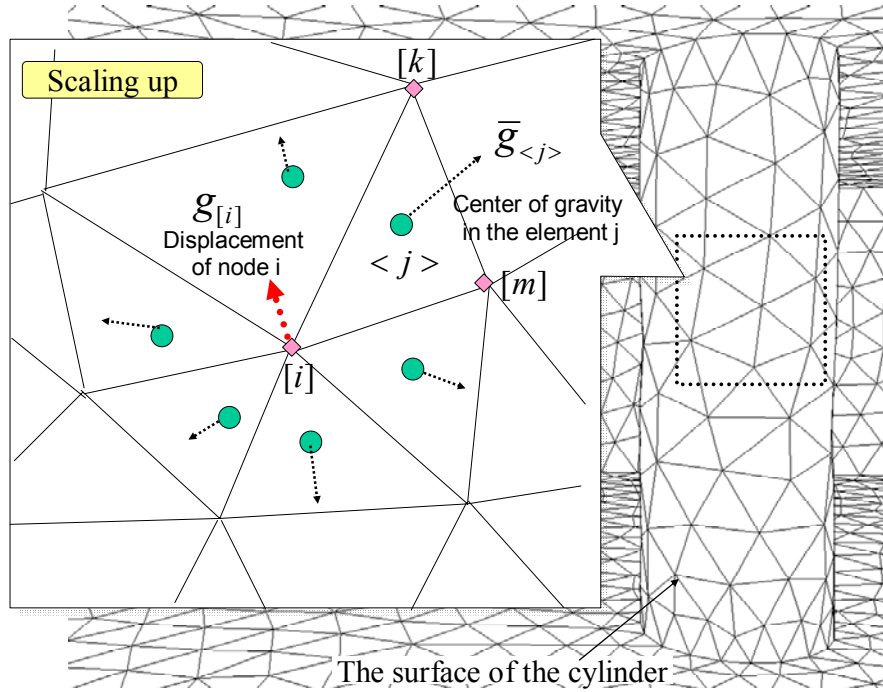


Figure 4. Smoothing on the surface of the object.

3.3. Constant Volume Constraint

By using only the sensitivity from the initial shape to the optimal shape, due to the volume becoming negative, the object may cause an unrealistic deformation. This problem can be overcome by considering constraints. In this research, a constant volume constraint is implemented. Two approaches are considered.

Process A : By introducing a new adjoint variable, the constant volume constraint is added to the Lagrange function. The sensitivity is modified to satisfy the constant volume constraint.

Process B : After constructing the optimal shape with respect to the cost function, this shape is iteratively modified to satisfy the constant volume constraint.

In the former approach, the sensitivity at every shape step includes the constant volume constraint. The constant volume condition could not be sufficiently satisfied by this approach [65]. In this study, the latter approach is implemented. Line search method is applied to the constant volume constraint. The function $h(\mathbf{x})$ is defined as follows:

$$h(\mathbf{x}_{(k)}) = V(\mathbf{x}_{(k)}) - V(\mathbf{x}_{(0)}) \quad k = 0, 1, \dots \in \mathbb{R}^I \quad (3.8)$$

where $V(\mathbf{x}_{(k)})$ represents the volume with respect to the shape step (k) . Minimizing the function $h(\mathbf{x})$ means satisfying the constant volume constraint. To minimize $h(\mathbf{x})$ with

maintaining the surface shape, the surface shape is deformed along an outward normal vector of the object as follows:

$$x_{(k),(l+1)} = x_{(k),(l)} + \alpha h(x_{(k),(l)}) \mathbf{n}(x_{(k)}) \quad l = 0, 1, \dots \in \mathbf{R}^3 \quad \text{on } \gamma \quad (3.9)$$

The lower subscript (l) is the iteration number of the mesh deformation. As this (l) is increased, the volume of the deformed shape gets closer to the volume of the initial shape. $\mathbf{n}(x_{(k)})$ remains constant while the subscript (l) is increased. The deformation amount is set to be small by multiplying a coefficient α in the second term. The constant volume mechanism is shown in Fig.5. In the beginning, the shape is deformed using sensitivity analysis based on the adjoint variable method. In case the deformed volume is smaller than the initial volume, the volume is slowly increased along an outward normal vector of the object surface by expanding the shape. In case that the deformed volume is larger than the initial volume, the deformed volume is slowly decreased along an inward normal vector of the object surface by suppressing the shape. In other words, this algorithm is repeated until the deformed shape is in good agreement with the initial volume.

To avoid generating elements with negative volume, smoothing is executed after node reallocations. An increased number of iterations (l) performed under the constant volume condition results in excess smoothing; therefore the sharp edge in the optimal shape can not be obtained. To solve this problem, the volume is increased before constructing the optimal shape. The nodal points in the mesh are reallocated by according to the biharmonic equations (Eq.(3.13) etc.). As deforming from the enlarged initial shape to the optimal one, the volume in the optimal shape naturally returns to the volume in the initial shape.

3.4. Robust Mesh Deformation

In the field of shape optimization, the mesh is mainly deformed by using the Laplace equation, as the deformation of shape is rather small. Laplace equation is as follows:

$$\nabla^2 \Theta(\mathbf{x}) = 0 \quad \in \mathbf{R}^3 \quad \text{in } \Omega \quad (3.10)$$

$$\Theta(\mathbf{x}) = \beta \int_{t_s}^{t_e} \mathbf{G}_{(k)} dt \left(= \beta g_{(k)} \right) \quad \in \mathbf{R}^3 \quad \text{on } \gamma \quad (3.11)$$

$$\Theta(\mathbf{x}) = 0 \quad \in \mathbf{R}^3 \quad \text{on } \Gamma_W, \Gamma_N, \Gamma_E, \Gamma_S \quad (3.12)$$

The variables $\Theta(\mathbf{x})$ represent the amount of the node displacement from the initial mesh to the deformed mesh in the domain Ω . β is a small coefficient. In this approach, the object's surface is deformed to satisfy the Dirichlet boundary condition. However, some elements might have partially negative volumes causing the calculation to fail. To robustly relocate nodes, the biharmonic equation consisting of the fourth derivative is applied to deforming the mesh [68].

$$\nabla^4 \Theta(\mathbf{x}) = 0 \quad \in \mathbf{R}^3 \quad \text{in } \Omega \quad (3.13)$$

$$\Theta(x) = \beta \int_{t_s}^{t_e} G(k) dt \in \mathbf{R}^3 \quad \text{on } \gamma \quad (3.14)$$

$$\Theta(x) = 0 \in \mathbf{R}^3 \quad \text{on } \Gamma_W, \Gamma_N, \Gamma_E, \Gamma_S \quad (3.15)$$

In the approaches above, the value of the stiffness for all elements in the mesh is equal to a constant. The stiffness of an element shows the resistance of the element to deformation (e.g. large stiffness means hard to deform). By using the stiffness, Masud A. and Thomas J.R. Hughes presented a more robust mesh deformation [69]. In this method, the stiffness in a small volume of elements is increased while the stiffness in another large volume of elements is decreased. Therefore, while deforming the large volume is easy, deforming the small volume becomes hard. This approach prevents the generation of negative volumes.

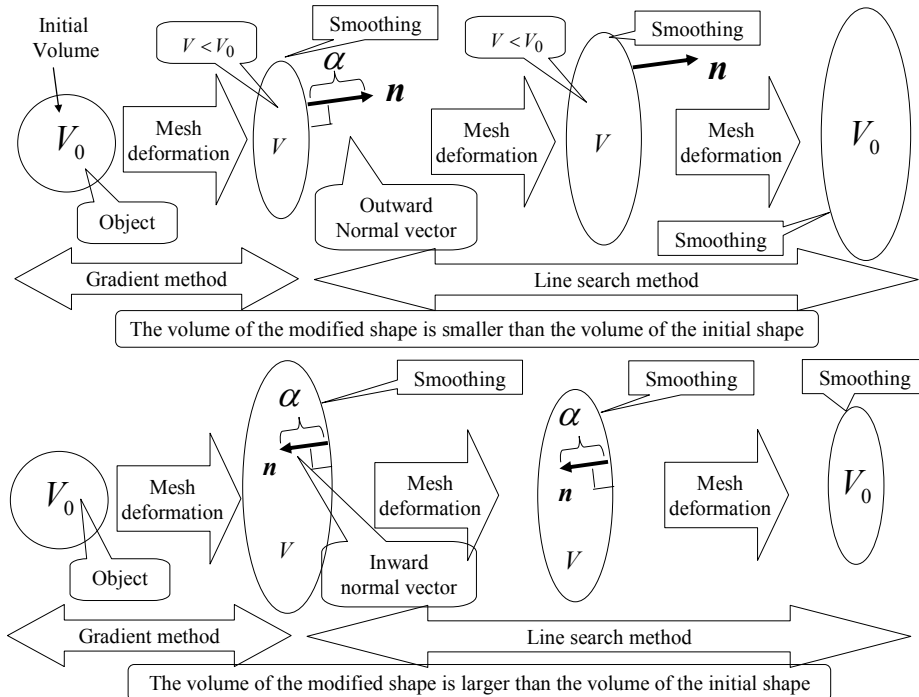


Figure 5. Volume constant.

4. DISCRETIZATION

4.1. Fluid Algorithms

In this study, we base the fluid algorithm on an approach which uses the fractional step method, presented for the numerical simulation of time-dependent incompressible flows [70]. In the fractional step, the velocity analysis and the pressure analysis are decoupled by using the continuum equation [71]. The Navier-Stoke equation with respect to time is discretized as follows:

$$\frac{u_l^{(n+1)} - u_l^{(n)}}{\Delta t} + u_j^{(n)} \frac{\partial u_l^{(n)}}{\partial x_j} = -\frac{\partial p^{(n+1)}}{\partial x_i} + \frac{1}{\text{Re}} \frac{\partial}{\partial x_j} \left(\frac{\partial u_l^{(n)}}{\partial x_j} + \frac{\partial u_j^{(n)}}{\partial x_l} \right) \quad l=1,2,3 \quad (4.1)$$

$$\frac{\partial u_i^{(n+1)}}{\partial x_i} = 0 \quad (4.2)$$

Assuming the total time interval is divided into many short time increments, denoted by Δt , the intermediate velocity \tilde{u}_l is defined as follows:

$$\tilde{u}_l = u_l^{(n)} - \Delta t \left\{ u_j^{(n)} \frac{\partial u_l^{(n)}}{\partial x_j} - \frac{1}{\text{Re}} \frac{\partial}{\partial x_j} \left(\frac{\partial u_l^{(n)}}{\partial x_j} + \frac{\partial u_j^{(n)}}{\partial x_l} \right) \right\} \quad l=1,2,3 \quad (4.3)$$

By the divergence of Eq.(4.3), Eq.(4.1) and Eq.(4.2), the following Poisson equation is derived:

$$\frac{\partial^2 p^{(n+1)}}{\partial x_1^2} + \frac{\partial^2 p^{(n+1)}}{\partial x_2^2} + \frac{\partial^2 p^{(n+1)}}{\partial x_3^2} = \frac{1}{\Delta t} \frac{\partial \tilde{u}_i}{\partial x_i} \quad (4.4)$$

By subtracting Eq.(4.3) from Eq.(4.1), the velocity fields are obtained as follows:

$$u_l^{(n+1)} = \tilde{u}_l - \Delta t \frac{\partial p^{(n+1)}}{\partial x_l} \quad l=1,2,3 \quad (4.5)$$

4.2. Weighted Residual Method

To obtain a weak form, arbitrary weighting functions are introduced as follows;

$$p^*, u_1^*, u_2^*, u_3^* \quad (4.6)$$

Using these functions, we can get the following:

$$\int_{\Omega} u_l^* \tilde{u}_l d\Omega = \int_{\Omega} u_l^* u_l^{(n)} d\Omega - \Delta t \left[\int_{\Omega} u_l^* u_j^{(n)} \frac{\partial u_l^{(n)}}{\partial x_j} d\Omega - \frac{1}{\text{Re}} \int_{\Omega} u_l^* \frac{\partial}{\partial x_j} \left(\frac{\partial u_l^{(n)}}{\partial x_j} + \frac{\partial u_j^{(n)}}{\partial x_l} \right) d\Omega \right] \quad l=1,2,3 \quad (4.7)$$

$$\int_{\Omega} p^* \left(\frac{\partial^2 p^{(n+1)}}{\partial x_1^2} + \frac{\partial^2 p^{(n+1)}}{\partial x_2^2} + \frac{\partial^2 p^{(n+1)}}{\partial x_3^2} \right) d\Omega = \frac{1}{\Delta t} \int_{\Omega} p^* \frac{\partial \tilde{u}_i}{\partial x_i} d\Omega \quad (4.8)$$

$$\int_{\Omega} u_l^* u_l^{(n+1)} d\Omega = \int_{\Omega} u_l^* \tilde{u}_l d\Omega - \Delta t \int_{\Omega} u_j^* \frac{\partial p^{(n+1)}}{\partial x_j} d\Omega \quad l=1,2,3 \quad (4.9)$$

Using the Gauss Green theorem, Eq.(4.7) and Eq.(4.8) become as follows:

$$\begin{aligned} \int_{\Omega} u_l^* \tilde{u}_l d\Omega &= \int_{\Omega} u_l^* u_l^{(n)} d\Omega - \Delta t \left[\int_{\Omega} u_l^* u_j^{(n)} \frac{\partial u_l^{(n)}}{\partial x_j} d\Omega \right. \\ &\quad \left. - \frac{1}{\text{Re}} \int_{\Gamma} u_l^* \left(\frac{\partial u_l^{(n)}}{\partial x_j} + \frac{\partial u_l^{(n)}}{\partial x_l} \right) n_j d\Gamma + \frac{1}{\text{Re}} \int_{\Omega} \frac{\partial u_l^*}{\partial x_j} \left(\frac{\partial u_l^{(n)}}{\partial x_j} + \frac{\partial u_l^{(n)}}{\partial x_l} \right) d\Omega \right] \quad l=1,2,3 \end{aligned} \quad (4.10)$$

$$\int_{\Gamma} p^* \frac{\partial p^{(n+1)}}{\partial x_j} n_j d\Gamma - \int_{\Omega} \frac{\partial p^*}{\partial x_j} \frac{\partial p^{(n+1)}}{\partial x_j} d\Omega = \frac{1}{\Delta t} \int_{\Omega} p^* \frac{\partial \tilde{u}_j}{\partial x_j} d\Omega \quad (4.11)$$

In the natural boundary condition, the integral domain Γ is zero. The weighted residual equation is summarized as follows:

$$\int_{\Omega} u_l^* \tilde{u}_l d\Omega = \int_{\Omega} u_l^* u_l^{(n)} d\Omega - \Delta t \left[\int_{\Omega} u_l^* u_j^{(n)} \frac{\partial u_l^{(n)}}{\partial x_j} d\Omega + \frac{1}{\text{Re}} \int_{\Omega} \frac{\partial u_l^*}{\partial x_j} \left(\frac{\partial u_l^{(n)}}{\partial x_j} + \frac{\partial u_l^{(n)}}{\partial x_l} \right) d\Omega \right] \quad l=1,2,3 \quad (4.12)$$

$$\int_{\Omega} \frac{\partial p^*}{\partial x_i} \frac{\partial p^{(n+1)}}{\partial x_i} d\Omega = -\frac{1}{\Delta t} \int_{\Omega} p^* \frac{\partial \tilde{u}_i}{\partial x_i} d\Omega \quad (4.13)$$

$$\int_{\Omega} u_l^* u_l^{(n+1)} d\Omega = \int_{\Omega} u_l^* \tilde{u}_l d\Omega - \Delta t \int_{\Omega} u_j^* \frac{\partial p^{(n+1)}}{\partial x_j} d\Omega \quad l=1,2,3 \quad (4.14)$$

4.3. SU (Stream Upwind) Method

Using a decoupled approach based on the fractional step method, the fluid can be simulated for a Reynolds number of around 100. As the Reynolds number increases, the convective term in the Navier-Stokes equation causes numerical vibrations in the velocity field and the pressure field. Although in such cases the stabilization technique of choice is SUPG [72], this cannot be used for decoupled-type CFD algorithms [73]. Therefore, the streamline-upwind (SU) stabilization technique is applied to this method in order to prevent numerical oscillations [74][75]. In the SU method, the streamline upwind term is directly added to the intermediate velocity calculation (Eq.(4.12)) as follows [76]:

$$\int_{\Omega} u_l^* \tilde{u}_l d\Omega = \int_{\Omega} u_l^* u_l^{(n)} d\Omega - \Delta t \left[\int_{\Omega} u_l^* u_j^{(n)} \frac{\partial u_l^{(n)}}{\partial x_j} d\Omega + \frac{1}{Re} \int_{\Omega} \frac{\partial u_l^*}{\partial x_j} \left(\frac{\partial u_l^{(n)}}{\partial x_j} + \frac{\partial u_l^{(n)}}{\partial x_l} \right) d\Omega + \int_{\Omega} \tau \left(u_j^{(n)} \frac{\partial u_l^*}{\partial x_j} \right) \left(u_m^{(n)} \frac{\partial u_l^{(n)}}{\partial x_m} \right) d\Omega \right] \quad l=1,2,3 \quad (4.15)$$

The variable τ is as follows [72]:

$$\tau = \frac{h}{2\|\mathbf{u}\|} Z(Re) \quad (4.16)$$

Here Re denote element Reynolds numbers which are based on the local velocity \mathbf{u} .

$$Re = \frac{\|\mathbf{u}\| h}{2\nu} \quad (4.17)$$

where ν represents the kinematic viscosity. The parameter h represents the element length as follows (in this study, the element type in a mesh is the $P1/P1$ element):

$$h = 2 \left(\sum_{i=1}^4 |\mathbf{s} \cdot \nabla N_{[i]}| \right)^{-1} \quad (4.18)$$

where \mathbf{s} is the unit vector in the direction of the local velocity. The function $z(Re)$ is defined as:

$$Z(Re) = \begin{cases} Re/3 & 0 \leq Re \leq 3 \\ 1 & 3 \leq Re \end{cases} \quad (4.19)$$

While applying the SU method, there is the possibility of the NS equation not being satisfied, as the computed values for velocity and pressure tend to contain strong numerical viscosity by the parameter τ . Therefore, one has to check the calculation results (e.g. the drag on the surface) by comparing them to the literature [77].

4.4. Derivation of the Finite Element Equations

Using the shape function of the first order triangular elements, the intermediate velocity, the interpolation function of the velocity and pressure, respectively, are defined as follows:

$$\tilde{u}_l = N_{[1]} \tilde{u}_{l,[1]} + N_{[2]} \tilde{u}_{l,[2]} + N_{[3]} \tilde{u}_{l,[3]} + N_{[4]} \tilde{u}_{l,[4]} \quad l=1,2,3 \quad (4.20)$$

$$u_l = N_{[1]} u_{l,[1]} + N_{[2]} u_{l,[2]} + N_{[3]} u_{l,[3]} + N_{[4]} u_{l,[4]} \quad l=1,2,3 \quad (4.21)$$

$$p = N_{[1]} p_{[1]} + N_{[2]} p_{[2]} + N_{[3]} p_{[3]} + N_{[4]} p_{[4]} \quad (4.22)$$

where the shape function is as follows:

$$N_{[i]} = a_{[i]} + b_{[i]}x_1 + c_{[i]}x_2 + d_{[i]}x_3 \quad (4.23)$$

with

$$6V = \det \begin{vmatrix} 1 & x_{1,[i]} & x_{2,[i]} & x_{3,[i]} \\ 1 & x_{1,[j]} & x_{2,[j]} & x_{3,[j]} \\ 1 & x_{1,[k]} & x_{2,[k]} & x_{3,[k]} \\ 1 & x_{1,[l]} & x_{2,[l]} & x_{3,[l]} \end{vmatrix} \quad i, j, k, l = 1, 2, 3, 4 \quad (4.24)$$

where V represents the volume of the tetrahedron. By expanding the other relevant determinants into their cofactors we have

$$a_{[i]} = \frac{1}{6V_{<\epsilon>}} \det \begin{vmatrix} x_{1,[j]} & x_{2,[j]} & x_{3,[j]} \\ x_{1,[k]} & x_{2,[k]} & x_{3,[k]} \\ x_{1,[l]} & x_{2,[l]} & x_{3,[l]} \end{vmatrix} \quad i, j, k, l = 1, 2, 3, 4 \quad (4.25)$$

$$b_{[i]} = -\frac{1}{6V_{<\epsilon>}} \det \begin{vmatrix} 1 & x_{2,[j]} & x_{3,[j]} \\ 1 & x_{2,[k]} & x_{3,[k]} \\ 1 & x_{2,[l]} & x_{3,[l]} \end{vmatrix} \quad i, j, k, l = 1, 2, 3, 4 \quad (4.26)$$

$$c_{[i]} = -\frac{1}{6V_{<\epsilon>}} \det \begin{vmatrix} x_{1,[j]} & 1 & x_{3,[j]} \\ x_{1,[k]} & 1 & x_{3,[k]} \\ x_{1,[l]} & 1 & x_{3,[l]} \end{vmatrix} \quad i, j, k, l = 1, 2, 3, 4 \quad (4.27)$$

$$d_{[i]} = -\frac{1}{6V_{<\epsilon>}} \det \begin{vmatrix} x_{1,[j]} & x_{2,[j]} & 1 \\ x_{1,[k]} & x_{2,[k]} & 1 \\ x_{1,[l]} & x_{2,[l]} & 1 \end{vmatrix} \quad i, j, k, l = 1, 2, 3, 4 \quad (4.28)$$

with the other constants obtained by cyclic interchange of the subscripts in the order i, j, k, l . [78]. The variables \tilde{u}_l , u_l and p represent the value of the unknown function. We use the Galerkin method by which the weight function takes the same form in the interpolation function. Therefore, the weight functions are defined as follows:

$$u_l^* = N_{[1]} u_{l,[1]}^* + N_{[2]} u_{l,[2]}^* + N_{[3]} u_{l,[3]}^* + N_{[4]} u_{l,[4]}^* \quad l = 1, 2, 3 \quad (4.29)$$

$$p^* = N_{[1]} p_{[1]}^* + N_{[2]} p_{[2]}^* + N_{[3]} p_{[3]}^* + N_{[4]} p_{[4]}^* \quad (4.30)$$

Using Eq.(4.29) and Eq.(4.30), Eq.(4.15) becomes as follows:

$$\begin{aligned}
\int_{\Omega} N_{[\alpha]} N_{[\beta]} d\Omega \tilde{u}_{l,[\beta]} &= \int_{\Omega} N_{[\alpha]} N_{[\beta]} d\Omega \tilde{u}_{l,[\beta]}^{(n)} - \Delta t \int_{\Omega} N_{[\alpha]} N_{[\beta]} \frac{\partial N_{[\gamma]}}{\partial x_j} d\Omega u_{l,[\gamma]}^{(n)} \\
&- \Delta t \frac{1}{\text{Re}} \left\{ \int_{\Omega} \left(\frac{\partial N_{[\alpha]}}{\partial x_j} \frac{\partial N_{[\beta]}}{\partial x_l} \right) d\Omega u_{l,[\beta]}^{(n)} + \int_{\Omega} \left(\frac{\partial N_{[\alpha]}}{\partial x_j} \frac{\partial N_{[\beta]}}{\partial x_l} \right) d\Omega u_{j,[\beta]}^{(n)} \right\} \\
&- \Delta t \int_{\Omega} \tau \left(N_{[\gamma]} u_{j,[\gamma]}^{(n)} \right) \frac{\partial N_{[\alpha]}}{\partial x_j} \left(N_{[\delta]} u_{k,[\delta]}^{(n)} \right) \frac{\partial N_{[\beta]}}{\partial x_k} d\Omega u_{l,[\beta]}^{(n)} \quad l = 1,2,3 \quad \alpha, \beta, \gamma, \delta = 1,2,3,4
\end{aligned} \tag{4.31}$$

Using Eq.(4.30), Eq.(4.13) becomes as follows:

$$\int_{\Omega} \frac{\partial N_{[\alpha]}}{\partial x_j} \frac{\partial N_{[\beta]}}{\partial x_i} d\Omega p_{[\beta]}^{(n+1)} = -\frac{1}{\Delta t} \int_{\Omega} N_{[\alpha]} \frac{\partial N_{[\beta]}}{\partial x_i} d\Omega \tilde{u}_{i,[\beta]} \quad \alpha, \beta = 1,2,3,4 \tag{4.32}$$

Using Eq.(4.29) and Eq.(4.30), Eq.(4.14) becomes as follows:

$$\int_{\Omega} N_{[\alpha]} N_{[\beta]} d\Omega u_{l,[\beta]}^{(n+1)} = \int_{\Omega} N_{[\alpha]} N_{[\beta]} d\Omega \tilde{u}_{l,[\beta]}^{(n+1)} - \frac{\Delta t}{\rho} \int_{\Omega} N_{[\alpha]} \frac{\partial N_{[\beta]}}{\partial x_l} d\Omega p_{[\beta]}^{(n+1)} \quad l = 1,2,3 \quad \alpha, \beta = 1,2,3,4 \tag{4.33}$$

The previous equations are summarized as follows:

$$M \tilde{u}_{l,[\beta]} = M \tilde{u}_{l,[\beta]}^{(n)} - \Delta t \left[K_{lj} u_{j,[\beta]}^{(n)} + \frac{1}{\text{Re}} S_{lj} u_{j,[\beta]}^{(n)} \right] - \Delta t E u_{l,[\beta]}^{(n)} \quad l = 1,2,3 \quad \beta = 1,2,3,4 \tag{4.34}$$

$$A p_{[\beta]}^{(n+1)} = -\frac{1}{\Delta t} H_j \tilde{u}_{j,[\beta]} \quad \beta = 1,2,3,4 \tag{4.35}$$

$$M u_{l,[\beta]}^{(n+1)} = M \tilde{u}_{l,[\beta]}^{(n+1)} - \Delta t H_l p_{[\beta]}^{(n+1)} \quad l = 1,2,3 \quad \alpha, \beta = 1,2,3,4 \tag{4.36}$$

where

$$M = \int_{\Omega} N_{[\alpha]} N_{[\beta]} d\Omega \quad \alpha, \beta = 1,2,3,4 \tag{4.37}$$

$$A = \int_{\Omega} \frac{\partial N_{[\alpha]}}{\partial x_j} \frac{\partial N_{[\beta]}}{\partial x_j} d\Omega \quad \alpha, \beta = 1,2,3,4 \tag{4.38}$$

$$K_{lj} = \int_{\Omega} N_{[\alpha]} N_{[\beta]} \frac{\partial N_{[\gamma]}}{\partial x_j} d\Omega u_{l,[\gamma]}^{(n)} \quad l, j = 1,2,3 \quad \alpha, \beta, \gamma = 1,2,3,4 \tag{4.39}$$

$$S_{lj} = \int_{\Omega} \frac{\partial N_{[\alpha]}}{\partial x_m} \frac{\partial N_{[\beta]}}{\partial x_m} d\Omega \cdot \delta_{lj} + \int_{\Omega} \frac{\partial N_{[\alpha]}}{\partial x_j} \frac{\partial N_{[\beta]}}{\partial x_l} d\Omega \quad l, j = 1,2,3 \quad \alpha, \beta = 1,2,3,4 \tag{4.40}$$

$$H_l = \int_{\Omega} N_{[\alpha]} \frac{\partial N_{[\beta]}}{\partial x_l} d\Omega \quad l = 1,2,3 \quad \alpha, \beta = 1,2,3,4 \tag{4.41}$$

$$\mathbf{E} = \mathbf{e}_{11} + \mathbf{e}_{12} + \mathbf{e}_{13} + \mathbf{e}_{21} + \mathbf{e}_{22} + \mathbf{e}_{23} + \mathbf{e}_{31} + \mathbf{e}_{32} + \mathbf{e}_{33} \quad (4.42)$$

where \mathbf{e}_{nl} is as follows:

$$\mathbf{e}_{nl} = \int_{\Omega} \tau \left(N_{[\gamma]} u_{n,[\gamma]}^{(n)} \right) \frac{\partial N_{[\alpha]}}{\partial x_n} \left(N_{[\delta]} u_{l,[\delta]}^{(n)} \right) \frac{\partial N_{[\beta]}}{\partial x_l} d\Omega \quad n,l=1,2,3 \quad \alpha,\beta,\gamma,\delta=1,2,3,4 \quad (4.43)$$

The indexes n,l represents the free indices. The function δ_{nl} represents the Kronecker delta, which is defined as follows:

$$\delta_{nl} = \begin{cases} 1 & (n=l) \\ 0 & (n \neq l) \end{cases} \quad (4.44)$$

4.5. Coefficient Matrix

The coefficient matrices in the finite element equations are discretized by using the integration formula for area coordinates as follows [79]:

$$\int_{\Omega} N_{[\alpha]}^i N_{[\beta]}^j N_{[\gamma]}^k N_{[\delta]}^l d\Omega = \frac{3!i!j!k!l!V_{<\epsilon>}}{(3+i+j+k+l)!} \quad (4.45)$$

The variable $V_{<\epsilon>}$ represents the volume of the element number $<\epsilon>$. The mass matrix (Eq.(4.37)) is as follows:

$$\mathbf{M} = \int_{\Omega} N_{[\alpha]} N_{[\beta]} d\Omega = \int_{\Omega} \begin{bmatrix} N_{[1]}N_{[1]} & N_{[1]}N_{[2]} & N_{[1]}N_{[3]} & N_{[1]}N_{[4]} \\ N_{[2]}N_{[1]} & N_{[2]}N_{[2]} & N_{[2]}N_{[3]} & N_{[2]}N_{[4]} \\ N_{[3]}N_{[1]} & N_{[3]}N_{[2]} & N_{[3]}N_{[3]} & N_{[3]}N_{[4]} \\ N_{[4]}N_{[1]} & N_{[4]}N_{[2]} & N_{[4]}N_{[3]} & N_{[4]}N_{[4]} \end{bmatrix} d\Omega = \frac{V_{<\epsilon>}}{20} \begin{bmatrix} 2 & 1 & 1 & 1 \\ 1 & 2 & 1 & 1 \\ 1 & 1 & 2 & 1 \\ 1 & 1 & 1 & 2 \end{bmatrix} \quad (4.46)$$

In this study, the mass matrix is transformed to the lumped mass matrix as follows:

$$\overline{\mathbf{M}} = \frac{V_{<\epsilon>}}{4} \begin{bmatrix} 1 & 0 & 0 & 0 \\ 0 & 1 & 0 & 0 \\ 0 & 0 & 1 & 0 \\ 0 & 0 & 0 & 1 \end{bmatrix} \quad (4.47)$$

The convective matrix ($l=1, j=1$) in Eq.(4.39) is as follows:

$$\begin{aligned}
\mathbf{K}_{11} &= \int_{\Omega} N_{[\alpha]} N_{[\beta]} \frac{\partial N_{[\gamma]}}{\partial x_1} d\Omega u_{l,[\gamma]}^{(n)} \\
&= (b_{[1]} u_{1,[1]} + b_{[2]} u_{1,[2]} + b_{[3]} u_{1,[3]} + b_{[4]} u_{1,[4]}) \int_{\Omega} \begin{bmatrix} N_{[1]} N_{[1]} & N_{[1]} N_{[2]} & N_{[1]} N_{[3]} & N_{[1]} N_{[4]} \\ N_{[2]} N_{[1]} & N_{[2]} N_{[2]} & N_{[2]} N_{[3]} & N_{[2]} N_{[4]} \\ N_{[3]} N_{[1]} & N_{[3]} N_{[2]} & N_{[3]} N_{[3]} & N_{[3]} N_{[4]} \\ N_{[4]} N_{[1]} & N_{[4]} N_{[2]} & N_{[4]} N_{[3]} & N_{[4]} N_{[4]} \end{bmatrix} d\Omega \\
&= \frac{V_{e>}}{20} (b_{[1]} u_{1,[1]} + b_{[2]} u_{1,[2]} + b_{[3]} u_{1,[3]} + b_{[4]} u_{1,[4]}) \begin{bmatrix} 2 & 1 & 1 & 2 \\ 1 & 2 & 1 & 1 \\ 1 & 1 & 2 & 1 \\ 1 & 1 & 1 & 2 \end{bmatrix} = b_{[\alpha]} u_{1,[\alpha]} \mathbf{M}
\end{aligned} \tag{4.48}$$

The convective matrix ($l=1, j=2$) in Eq.(4.39) is as follows:

$$\begin{aligned}
\mathbf{K}_{12} &= \int_{\Omega} N_{[\alpha]} N_{[\beta]} \frac{\partial N_{[\gamma]}}{\partial x_2} d\Omega u_{l,[\gamma]}^{(n)} \\
&= (c_{[1]} u_{1,[1]} + c_{[2]} u_{1,[2]} + c_{[3]} u_{1,[3]} + c_{[4]} u_{1,[4]}) \int_{\Omega} \begin{bmatrix} N_{[1]} N_{[1]} & N_{[1]} N_{[2]} & N_{[1]} N_{[3]} & N_{[1]} N_{[4]} \\ N_{[2]} N_{[1]} & N_{[2]} N_{[2]} & N_{[2]} N_{[3]} & N_{[2]} N_{[4]} \\ N_{[3]} N_{[1]} & N_{[3]} N_{[2]} & N_{[3]} N_{[3]} & N_{[3]} N_{[4]} \\ N_{[4]} N_{[1]} & N_{[4]} N_{[2]} & N_{[4]} N_{[3]} & N_{[4]} N_{[4]} \end{bmatrix} d\Omega \\
&= \frac{V_{e>}}{20} (c_{[1]} u_{1,[1]} + c_{[2]} u_{1,[2]} + c_{[3]} u_{1,[3]} + c_{[4]} u_{1,[4]}) \begin{bmatrix} 2 & 1 & 1 & 2 \\ 1 & 2 & 1 & 1 \\ 1 & 1 & 2 & 1 \\ 1 & 1 & 1 & 2 \end{bmatrix} = c_{[\alpha]} u_{1,[\alpha]} \mathbf{M}
\end{aligned} \tag{4.49}$$

The convective matrix ($l=1, j=3$) in Eq.(4.39) is as follows:

$$\begin{aligned}
\mathbf{K}_{13} &= \int_{\Omega} N_{[\alpha]} N_{[\beta]} \frac{\partial N_{[\gamma]}}{\partial x_3} d\Omega u_{l,[\gamma]}^{(n)} \\
&= (d_{[1]} u_{1,[1]} + d_{[2]} u_{1,[2]} + d_{[3]} u_{1,[3]} + d_{[4]} u_{1,[4]}) \int_{\Omega} \begin{bmatrix} N_{[1]} N_{[1]} & N_{[1]} N_{[2]} & N_{[1]} N_{[3]} & N_{[1]} N_{[4]} \\ N_{[2]} N_{[1]} & N_{[2]} N_{[2]} & N_{[2]} N_{[3]} & N_{[2]} N_{[4]} \\ N_{[3]} N_{[1]} & N_{[3]} N_{[2]} & N_{[3]} N_{[3]} & N_{[3]} N_{[4]} \\ N_{[4]} N_{[1]} & N_{[4]} N_{[2]} & N_{[4]} N_{[3]} & N_{[4]} N_{[4]} \end{bmatrix} d\Omega \\
&= \frac{V_{e>}}{20} (d_{[1]} u_{1,[1]} + d_{[2]} u_{1,[2]} + d_{[3]} u_{1,[3]} + d_{[4]} u_{1,[4]}) \begin{bmatrix} 2 & 1 & 1 & 2 \\ 1 & 2 & 1 & 1 \\ 1 & 1 & 2 & 1 \\ 1 & 1 & 1 & 2 \end{bmatrix} = d_{[\alpha]} u_{1,[\alpha]} \mathbf{M}
\end{aligned} \tag{4.50}$$

In the others indexes $l=2,3$ and $j=1,2,3$, the coefficient matrixes are as follows:

$$\mathbf{K}_{21} = b_{[\alpha]} u_{2,[\alpha]} \mathbf{M} \tag{4.51}$$

$$\mathbf{K}_{22} = c_{[\alpha]} u_{2,[\alpha]} \mathbf{M} \tag{4.52}$$

$$\mathbf{K}_{23} = d_{[\alpha]} u_{3,[\alpha]} \mathbf{M} \tag{4.53}$$

$$\mathbf{K}_{31} = b_{[\alpha]} u_{3,[\alpha]} \mathbf{M} \quad (4.54)$$

$$\mathbf{K}_{32} = c_{[\alpha]} u_{3,[\alpha]} \mathbf{M} \quad (4.55)$$

$$\mathbf{K}_{33} = d_{[\alpha]} u_{3,[\alpha]} \mathbf{M} \quad (4.56)$$

The viscous matrix ($l=1, j=1$) in Eq.(4.40) is as follows:

$$\begin{aligned} \mathbf{S}_{11} = & 2V_{<\epsilon>} \begin{bmatrix} b_{[1]}b_{[1]} & b_{[1]}b_{[2]} & b_{[1]}b_{[3]} & b_{[1]}b_{[4]} \\ b_{[2]}b_{[1]} & b_{[2]}b_{[2]} & b_{[2]}b_{[3]} & b_{[2]}b_{[4]} \\ b_{[3]}b_{[1]} & b_{[3]}b_{[2]} & b_{[3]}b_{[3]} & b_{[3]}b_{[4]} \\ b_{[4]}b_{[1]} & b_{[4]}b_{[2]} & b_{[4]}b_{[3]} & b_{[4]}b_{[4]} \end{bmatrix} + V_{<\epsilon>} \begin{bmatrix} c_{[1]}c_{[1]} & c_{[1]}c_{[2]} & c_{[1]}c_{[3]} & c_{[1]}c_{[4]} \\ c_{[2]}c_{[1]} & c_{[2]}c_{[2]} & c_{[2]}c_{[3]} & c_{[2]}c_{[4]} \\ c_{[3]}c_{[1]} & c_{[3]}c_{[2]} & c_{[3]}c_{[3]} & c_{[3]}c_{[4]} \\ c_{[4]}c_{[1]} & c_{[4]}c_{[2]} & c_{[4]}c_{[3]} & c_{[4]}c_{[4]} \end{bmatrix} \\ & + V_{<\epsilon>} \begin{bmatrix} d_{[1]}d_{[1]} & d_{[1]}d_{[2]} & d_{[1]}d_{[3]} & d_{[1]}d_{[4]} \\ d_{[2]}d_{[1]} & d_{[2]}d_{[2]} & d_{[2]}d_{[3]} & d_{[2]}d_{[4]} \\ d_{[3]}d_{[1]} & d_{[3]}d_{[2]} & d_{[3]}d_{[3]} & d_{[3]}d_{[4]} \\ d_{[4]}d_{[1]} & d_{[4]}d_{[2]} & d_{[4]}d_{[3]} & d_{[4]}d_{[4]} \end{bmatrix} \end{aligned} \quad (4.57)$$

The viscous matrix ($l=1, j=2$) in Eq.(4.40) is as follows:

$$\mathbf{S}_{12} = V_{<\epsilon>} \begin{bmatrix} b_{[1]}c_{[1]} & b_{[1]}c_{[2]} & b_{[1]}c_{[3]} & b_{[1]}c_{[4]} \\ b_{[2]}c_{[1]} & b_{[2]}c_{[2]} & b_{[2]}c_{[3]} & b_{[2]}c_{[4]} \\ b_{[3]}c_{[1]} & b_{[3]}c_{[2]} & b_{[3]}c_{[3]} & b_{[3]}c_{[4]} \\ b_{[4]}c_{[1]} & b_{[4]}c_{[2]} & b_{[4]}c_{[3]} & b_{[4]}c_{[4]} \end{bmatrix} \quad (4.58)$$

The viscous matrix ($l=1, j=3$) in Eq.(4.40) is as follows:

$$\mathbf{S}_{13} = V_{<\epsilon>} \begin{bmatrix} b_{[1]}d_{[1]} & b_{[1]}d_{[2]} & b_{[1]}d_{[3]} & b_{[1]}d_{[4]} \\ b_{[2]}d_{[1]} & b_{[2]}d_{[2]} & b_{[2]}d_{[3]} & b_{[2]}d_{[4]} \\ b_{[3]}d_{[1]} & b_{[3]}d_{[2]} & b_{[3]}d_{[3]} & b_{[3]}d_{[4]} \\ b_{[4]}d_{[1]} & b_{[4]}d_{[2]} & b_{[4]}d_{[3]} & b_{[4]}d_{[4]} \end{bmatrix} \quad (4.59)$$

The viscous matrix ($l=2, j=1$) in Eq.(4.40) is as follows:

$$\mathbf{S}_{21} = V_{<\epsilon>} \begin{bmatrix} q_{[1]}b_{[1]} & q_{[1]}b_{[2]} & q_{[1]}b_{[3]} & q_{[1]}b_{[4]} \\ q_{[2]}b_{[1]} & q_{[2]}b_{[2]} & q_{[2]}b_{[3]} & q_{[2]}b_{[4]} \\ q_{[3]}b_{[1]} & q_{[3]}b_{[2]} & q_{[3]}b_{[3]} & q_{[3]}b_{[4]} \\ q_{[4]}b_{[1]} & q_{[4]}b_{[2]} & q_{[4]}b_{[3]} & q_{[4]}b_{[4]} \end{bmatrix} \quad (4.60)$$

The viscous matrix ($l=2, j=2$) in Eq.(4.40) is as follows:

$$\begin{aligned}
S_{22} = & V_{<\epsilon>} \begin{bmatrix} b_{[1]}b_{[1]} & b_{[1]}b_{[2]} & b_{[1]}b_{[3]} & b_{[1]}b_{[4]} \\ b_{[2]}b_{[1]} & b_{[2]}b_{[2]} & b_{[2]}b_{[3]} & b_{[2]}b_{[4]} \\ b_{[3]}b_{[1]} & b_{[3]}b_{[2]} & b_{[3]}b_{[3]} & b_{[3]}b_{[4]} \\ b_{[4]}b_{[1]} & b_{[4]}b_{[2]} & b_{[4]}b_{[3]} & b_{[4]}b_{[4]} \end{bmatrix} + 2V_{<\epsilon>} \begin{bmatrix} q_{[1]}q_{[1]} & q_{[1]}q_{[2]} & q_{[1]}q_{[3]} & q_{[1]}q_{[4]} \\ q_{[2]}q_{[1]} & q_{[2]}q_{[2]} & q_{[2]}q_{[3]} & q_{[2]}q_{[4]} \\ q_{[3]}q_{[1]} & q_{[3]}q_{[2]} & q_{[3]}q_{[3]} & q_{[3]}q_{[4]} \\ q_{[4]}q_{[1]} & q_{[4]}q_{[2]} & q_{[4]}q_{[3]} & q_{[4]}q_{[4]} \end{bmatrix} \\
& + V_{<\epsilon>} \begin{bmatrix} d_{[1]}d_{[1]} & d_{[1]}d_{[2]} & d_{[1]}d_{[3]} & d_{[1]}d_{[4]} \\ d_{[2]}d_{[1]} & d_{[2]}d_{[2]} & d_{[2]}d_{[3]} & d_{[2]}d_{[4]} \\ d_{[3]}d_{[1]} & d_{[3]}d_{[2]} & d_{[3]}d_{[3]} & d_{[3]}d_{[4]} \\ d_{[4]}d_{[1]} & d_{[4]}d_{[2]} & d_{[4]}d_{[3]} & d_{[4]}d_{[4]} \end{bmatrix}
\end{aligned} \tag{4.61}$$

The viscous matrix ($l=2, j=3$) in Eq.(4.40) is as follows:

$$S_{23} = V_{<\epsilon>} \begin{bmatrix} q_{[1]}d_{[1]} & q_{[1]}d_{[2]} & q_{[1]}d_{[3]} & q_{[1]}d_{[4]} \\ q_{[2]}d_{[1]} & q_{[2]}d_{[2]} & q_{[2]}d_{[3]} & q_{[2]}d_{[4]} \\ q_{[3]}d_{[1]} & q_{[3]}d_{[2]} & q_{[3]}d_{[3]} & q_{[3]}d_{[4]} \\ q_{[4]}d_{[1]} & q_{[4]}d_{[2]} & q_{[4]}d_{[3]} & q_{[4]}d_{[4]} \end{bmatrix} \tag{4.62}$$

The viscous matrix ($l=3, j=1$) in Eq.(4.40) is as follows:

$$S_{31} = V_{<\epsilon>} \begin{bmatrix} d_{[1]}b_{[1]} & d_{[1]}b_{[2]} & d_{[1]}b_{[3]} & d_{[1]}b_{[4]} \\ d_{[2]}b_{[1]} & d_{[2]}b_{[2]} & d_{[2]}b_{[3]} & d_{[2]}b_{[4]} \\ d_{[3]}b_{[1]} & d_{[3]}b_{[2]} & d_{[3]}b_{[3]} & d_{[3]}b_{[4]} \\ d_{[4]}b_{[1]} & d_{[4]}b_{[2]} & d_{[4]}b_{[3]} & d_{[4]}b_{[4]} \end{bmatrix} \tag{4.63}$$

The viscous matrix ($l=3, j=2$) in Eq.(4.40) is as follows:

$$S_{32} = V_{<\epsilon>} \begin{bmatrix} d_{[1]}q_{[1]} & d_{[1]}q_{[2]} & d_{[1]}q_{[3]} & d_{[1]}q_{[4]} \\ d_{[2]}q_{[1]} & d_{[2]}q_{[2]} & d_{[2]}q_{[3]} & d_{[2]}q_{[4]} \\ d_{[3]}q_{[1]} & d_{[3]}q_{[2]} & d_{[3]}q_{[3]} & d_{[3]}q_{[4]} \\ d_{[4]}q_{[1]} & d_{[4]}q_{[2]} & d_{[4]}q_{[3]} & d_{[4]}q_{[4]} \end{bmatrix} \tag{4.64}$$

The viscous matrix ($i=3, j=3$) in Eq.(4.40) is as follows:

$$\begin{aligned}
S_{33} = & V_{<\epsilon>} \begin{bmatrix} b_{[1]}b_{[1]} & b_{[1]}b_{[2]} & b_{[1]}b_{[3]} & b_{[1]}b_{[4]} \\ b_{[2]}b_{[1]} & b_{[2]}b_{[2]} & b_{[2]}b_{[3]} & b_{[2]}b_{[4]} \\ b_{[3]}b_{[1]} & b_{[3]}b_{[2]} & b_{[3]}b_{[3]} & b_{[3]}b_{[4]} \\ b_{[4]}b_{[1]} & b_{[4]}b_{[2]} & b_{[4]}b_{[3]} & b_{[4]}b_{[4]} \end{bmatrix} + V_{<\epsilon>} \begin{bmatrix} q_{[1]}q_{[1]} & q_{[1]}q_{[2]} & q_{[1]}q_{[3]} & q_{[1]}q_{[4]} \\ q_{[2]}q_{[1]} & q_{[2]}q_{[2]} & q_{[2]}q_{[3]} & q_{[2]}q_{[4]} \\ q_{[3]}q_{[1]} & q_{[3]}q_{[2]} & q_{[3]}q_{[3]} & q_{[3]}q_{[4]} \\ q_{[4]}q_{[1]} & q_{[4]}q_{[2]} & q_{[4]}q_{[3]} & q_{[4]}q_{[4]} \end{bmatrix} \\
& + 2V_{<\epsilon>} \begin{bmatrix} d_{[1]}d_{[1]} & d_{[1]}d_{[2]} & d_{[1]}d_{[3]} & d_{[1]}d_{[4]} \\ d_{[2]}d_{[1]} & d_{[2]}d_{[2]} & d_{[2]}d_{[3]} & d_{[2]}d_{[4]} \\ d_{[3]}d_{[1]} & d_{[3]}d_{[2]} & d_{[3]}d_{[3]} & d_{[3]}d_{[4]} \\ d_{[4]}d_{[1]} & d_{[4]}d_{[2]} & d_{[4]}d_{[3]} & d_{[4]}d_{[4]} \end{bmatrix}
\end{aligned} \tag{4.65}$$

The matrix A in the Poisson equation (Eq.(4.38)) is as follows:

$$\begin{aligned}
 A = & V_{\langle e \rangle} \begin{bmatrix} b_{[1]}b_{[1]} & b_{[1]}b_{[2]} & b_{[1]}b_{[3]} & b_{[1]}b_{[4]} \\ b_{[2]}b_{[1]} & b_{[2]}b_{[2]} & b_{[2]}b_{[3]} & b_{[2]}b_{[4]} \\ b_{[3]}b_{[1]} & b_{[3]}b_{[2]} & b_{[3]}b_{[3]} & b_{[3]}b_{[4]} \\ b_{[4]}b_{[1]} & b_{[4]}b_{[2]} & b_{[4]}b_{[3]} & b_{[4]}b_{[4]} \end{bmatrix} + V_{\langle e \rangle} \begin{bmatrix} q_{[1]}q_{[1]} & q_{[1]}q_{[2]} & q_{[1]}q_{[3]} & q_{[1]}q_{[4]} \\ q_{[2]}q_{[1]} & q_{[2]}q_{[2]} & q_{[2]}q_{[3]} & q_{[2]}q_{[4]} \\ q_{[3]}q_{[1]} & q_{[3]}q_{[2]} & q_{[3]}q_{[3]} & q_{[3]}q_{[4]} \\ q_{[4]}q_{[1]} & q_{[4]}q_{[2]} & q_{[4]}q_{[3]} & q_{[4]}q_{[4]} \end{bmatrix} \\
 & + V_{\langle e \rangle} \begin{bmatrix} d_{[1]}d_{[1]} & d_{[1]}d_{[2]} & d_{[1]}d_{[3]} & d_{[1]}d_{[4]} \\ d_{[2]}d_{[1]} & d_{[2]}d_{[2]} & d_{[2]}d_{[3]} & d_{[2]}d_{[4]} \\ d_{[3]}d_{[1]} & d_{[3]}d_{[2]} & d_{[3]}d_{[3]} & d_{[3]}d_{[4]} \\ d_{[4]}d_{[1]} & d_{[4]}d_{[2]} & d_{[4]}d_{[3]} & d_{[4]}d_{[4]} \end{bmatrix}
 \end{aligned} \tag{4.66}$$

The matrix H₁ in the Poisson equation (Eq.(4.41)) is as follows:

$$H_1 = \frac{V_{\langle e \rangle}}{4} \begin{bmatrix} b_{[1]} & b_{[2]} & b_{[3]} & b_{[4]} \\ b_{[1]} & b_{[2]} & b_{[3]} & b_{[4]} \\ b_{[1]} & b_{[2]} & b_{[3]} & b_{[4]} \\ b_{[1]} & b_{[2]} & b_{[3]} & b_{[4]} \end{bmatrix} \tag{4.67}$$

The matrix H₂ in the Poisson equation (Eq.(4.41)) is as follows:

$$H_2 = \frac{V_{\langle e \rangle}}{4} \begin{bmatrix} c_{[1]} & c_{[2]} & c_{[3]} & c_{[4]} \\ c_{[1]} & c_{[2]} & c_{[3]} & c_{[4]} \\ c_{[1]} & c_{[2]} & c_{[3]} & c_{[4]} \\ c_{[1]} & c_{[2]} & c_{[3]} & c_{[4]} \end{bmatrix} \tag{4.68}$$

The matrix H₃ in the Poisson equation (Eq.(4.41)) is as follows:

$$H_3 = \frac{V_{\langle e \rangle}}{4} \begin{bmatrix} d_{[1]} & d_{[2]} & d_{[3]} & d_{[4]} \\ d_{[1]} & d_{[2]} & d_{[3]} & d_{[4]} \\ d_{[1]} & d_{[2]} & d_{[3]} & d_{[4]} \\ d_{[1]} & d_{[2]} & d_{[3]} & d_{[4]} \end{bmatrix} \tag{4.69}$$

The matrix (n=1, l=1) in Eq.(4.43) is as follows:

$$\begin{aligned}
e_{11} &= \int_{\Omega} \tau \left(N_{[\gamma]} u_{1,[\gamma]}^{(n)} \right) \frac{\partial N_{[\alpha]}}{\partial x_1} \left(N_{[\delta]} u_{1,[\delta]}^{(n)} \right) \frac{\partial N_{[\beta]}}{\partial x_1} d\Omega = b_{[\alpha]} b_{[\beta]} \int_{\Omega} \tau \left(N_{[\gamma]} u_{1,[\gamma]}^{(n)} \right) \left(N_{[\delta]} u_{1,[\delta]}^{(n)} \right) d\Omega \\
&= b_{[\alpha]} b_{[\beta]} \int_{\Omega} \tau \left(N_{[1]} u_{1,[1]}^{(n)} + N_{[2]} u_{1,[2]}^{(n)} + N_{[3]} u_{1,[3]}^{(n)} + N_{[4]} u_{1,[4]}^{(n)} \right) \left(N_{[1]} u_{1,[1]}^{(n)} + N_{[2]} u_{1,[2]}^{(n)} + N_{[3]} u_{1,[3]}^{(n)} + N_{[4]} u_{1,[4]}^{(n)} \right) d\Omega \\
&= b_{[\alpha]} b_{[\beta]} \tau_{<e>} \left\{ \int_{\Omega} N_{[1]} N_{[1]} d\Omega u_{1,[1]}^{(n)} u_{1,[1]}^{(n)} + \int_{\Omega} N_{[2]} N_{[1]} d\Omega u_{1,[2]}^{(n)} u_{1,[1]}^{(n)} + \int_{\Omega} N_{[3]} N_{[1]} d\Omega u_{1,[3]}^{(n)} u_{1,[1]}^{(n)} + \int_{\Omega} N_{[4]} N_{[1]} d\Omega u_{1,[4]}^{(n)} u_{1,[1]}^{(n)} \right. \\
&\quad + \int_{\Omega} N_{[1]} N_{[2]} d\Omega u_{1,[1]}^{(n)} u_{1,[2]}^{(n)} + \int_{\Omega} N_{[2]} N_{[2]} d\Omega u_{1,[2]}^{(n)} u_{1,[2]}^{(n)} + \int_{\Omega} N_{[3]} N_{[2]} d\Omega u_{1,[3]}^{(n)} u_{1,[2]}^{(n)} + \int_{\Omega} N_{[4]} N_{[2]} d\Omega u_{1,[4]}^{(n)} u_{1,[2]}^{(n)} \\
&\quad + \int_{\Omega} N_{[1]} N_{[3]} d\Omega u_{1,[1]}^{(n)} u_{1,[3]}^{(n)} + \int_{\Omega} N_{[2]} N_{[3]} d\Omega u_{1,[2]}^{(n)} u_{1,[3]}^{(n)} + \int_{\Omega} N_{[3]} N_{[3]} d\Omega u_{1,[3]}^{(n)} u_{1,[3]}^{(n)} + \int_{\Omega} N_{[4]} N_{[3]} d\Omega u_{1,[4]}^{(n)} u_{1,[3]}^{(n)} \\
&\quad + \int_{\Omega} N_{[1]} N_{[4]} d\Omega u_{1,[1]}^{(n)} u_{1,[4]}^{(n)} + \int_{\Omega} N_{[2]} N_{[4]} d\Omega u_{1,[2]}^{(n)} u_{1,[4]}^{(n)} + \int_{\Omega} N_{[3]} N_{[4]} d\Omega u_{1,[3]}^{(n)} u_{1,[4]}^{(n)} + \int_{\Omega} N_{[4]} N_{[4]} d\Omega u_{1,[4]}^{(n)} u_{1,[4]}^{(n)} \Big\} \\
&= b_{[\alpha]} b_{[\beta]} \tau_{<e>} \left\{ 2u_{1,[1]}^{(n)} u_{1,[1]}^{(n)} + u_{1,[2]}^{(n)} u_{1,[1]}^{(n)} + u_{1,[3]}^{(n)} u_{1,[1]}^{(n)} + u_{1,[4]}^{(n)} u_{1,[1]}^{(n)} + u_{1,[1]}^{(n)} u_{1,[2]}^{(n)} + 2u_{1,[2]}^{(n)} u_{1,[2]}^{(n)} + u_{1,[3]}^{(n)} u_{1,[2]}^{(n)} + u_{1,[4]}^{(n)} u_{1,[2]}^{(n)} \right. \\
&\quad + u_{1,[1]}^{(n)} u_{1,[3]}^{(n)} + u_{1,[2]}^{(n)} u_{1,[3]}^{(n)} + 2u_{1,[3]}^{(n)} u_{1,[3]}^{(n)} + u_{1,[4]}^{(n)} u_{1,[3]}^{(n)} + u_{1,[1]}^{(n)} u_{1,[4]}^{(n)} + u_{1,[2]}^{(n)} u_{1,[4]}^{(n)} + u_{1,[3]}^{(n)} u_{1,[4]}^{(n)} + 2u_{1,[4]}^{(n)} u_{1,[4]}^{(n)} \Big\} \\
&= \frac{V_{<e>}}{20} \tau_{<e>} \left\{ (u_{1,[1]}^{(n)} + u_{1,[2]}^{(n)} + u_{1,[3]}^{(n)} + u_{1,[4]}^{(n)}) (u_{1,[1]}^{(n)} + u_{1,[2]}^{(n)} + u_{1,[3]}^{(n)} + u_{1,[4]}^{(n)}) + u_{1,[1]}^{(n)} u_{1,[1]}^{(n)} + u_{1,[2]}^{(n)} u_{1,[2]}^{(n)} + u_{1,[3]}^{(n)} u_{1,[3]}^{(n)} + u_{1,[4]}^{(n)} u_{1,[4]}^{(n)} \right\} b_{[\alpha]} b_{[\beta]} \\
&= \frac{V_{<e>}}{20} \tau_{<e>} \left\{ \left(\sum_{i=1}^4 u_{1,[i]}^{(n)} \right) \left(\sum_{i=1}^4 u_{1,[i]}^{(n)} \right) + \sum_{i=1}^4 u_{1,[i]}^{(n)} u_{2,[i]}^{(n)} \right\} \begin{bmatrix} b_{11} b_{11} & b_{11} b_{12} & b_{11} b_{13} & b_{11} b_{14} \\ b_{12} b_{11} & b_{12} b_{12} & b_{12} b_{13} & b_{12} b_{14} \\ b_{13} b_{11} & b_{13} b_{12} & b_{13} b_{13} & b_{13} b_{14} \\ b_{14} b_{11} & b_{14} b_{12} & b_{14} b_{13} & b_{14} b_{14} \end{bmatrix} \\
&= \frac{V_{<e>}}{20} \tau_{<e>} \left\{ \left(\sum_{i=1}^4 u_{1,[i]}^{(n)} \right) \left(\sum_{i=1}^4 u_{1,[i]}^{(n)} \right) + \sum_{i=1}^4 u_{1,[i]}^{(n)} u_{1,[i]}^{(n)} \right\} \begin{bmatrix} b_{11} b_{11} & b_{11} b_{12} & b_{11} b_{13} & b_{11} b_{14} \\ b_{12} b_{11} & b_{12} b_{12} & b_{12} b_{13} & b_{12} b_{14} \\ b_{13} b_{11} & b_{13} b_{12} & b_{13} b_{13} & b_{13} b_{14} \\ b_{14} b_{11} & b_{14} b_{12} & b_{14} b_{13} & b_{14} b_{14} \end{bmatrix} \quad (4.70)
\end{aligned}$$

The variable $\tau_{<e>}$ represents the stabilization parameter of the element number $<e>$. The matrix ($i=1, j=2$) in Eq.(4.43) is as follows:

$$e_{12} = \frac{V_{<e>}}{20} \tau_{<e>} \left\{ \left(\sum_{i=1}^4 u_{1,[i]}^{(n)} \right) \left(\sum_{i=1}^4 u_{2,[i]}^{(n)} \right) + \sum_{i=1}^4 u_{1,[i]}^{(n)} u_{2,[i]}^{(n)} \right\} \begin{bmatrix} b_{11} c_{11} & b_{11} c_{12} & b_{11} c_{13} & b_{11} c_{14} \\ b_{12} c_{11} & b_{12} c_{12} & b_{12} c_{13} & b_{12} c_{14} \\ b_{13} c_{11} & b_{13} c_{12} & b_{13} c_{13} & b_{13} c_{14} \\ b_{14} c_{11} & b_{14} c_{12} & b_{14} c_{13} & b_{14} c_{14} \end{bmatrix} \quad (4.71)$$

The matrix ($i=1, j=3$) in Eq.(4.43) is as follows:

$$e_{13} = \frac{V_{<e>}}{20} \tau_{<e>} \left\{ \left(\sum_{i=1}^4 u_{1,[i]}^{(n)} \right) \left(\sum_{i=1}^4 u_{3,[i]}^{(n)} \right) + \sum_{i=1}^4 u_{1,[i]}^{(n)} u_{3,[i]}^{(n)} \right\} \begin{bmatrix} b_{11} d_{11} & b_{11} d_{12} & b_{11} d_{13} & b_{11} d_{14} \\ b_{12} d_{11} & b_{12} d_{12} & b_{12} d_{13} & b_{12} d_{14} \\ b_{13} d_{11} & b_{13} d_{12} & b_{13} d_{13} & b_{13} d_{14} \\ b_{14} d_{11} & b_{14} d_{12} & b_{14} d_{13} & b_{14} d_{14} \end{bmatrix} \quad (4.72)$$

The matrix ($i=2, j=1$) in Eq.(4.43) is as follows:

$$e_{21} = \frac{V_{<e>}}{20} \tau_{<e>} \left\{ \left(\sum_{i=1}^4 u_{2,[i]}^{(n)} \right) \left(\sum_{i=1}^4 u_{1,[i]}^{(n)} \right) + \sum_{i=1}^4 u_{2,[i]}^{(n)} u_{1,[i]}^{(n)} \right\} \begin{bmatrix} c_{11} b_{11} & c_{11} b_{12} & c_{11} b_{13} & c_{11} b_{14} \\ c_{12} b_{11} & c_{12} b_{12} & c_{12} b_{13} & c_{12} b_{14} \\ c_{13} b_{11} & c_{13} b_{12} & c_{13} b_{13} & c_{13} b_{14} \\ c_{14} b_{11} & c_{14} b_{12} & c_{14} b_{13} & c_{14} b_{14} \end{bmatrix} \quad (4.73)$$

The matrix ($i=2, j=2$) in Eq.(4.43) is as follows:

$$e_{22} = \frac{V_{<e>}}{20} \tau_{<e>} \left\{ \left(\sum_{i=1}^4 u_{2,[i]}^{(n)} \right) \left(\sum_{i=1}^4 u_{2,[i]}^{(n)} \right) + \sum_{i=1}^4 u_{2,[i]}^{(n)} u_{2,[i]}^{(n)} \right\} \begin{bmatrix} c_{11} c_{11} & c_{11} c_{12} & c_{11} c_{13} & c_{11} c_{14} \\ c_{12} c_{11} & c_{12} c_{12} & c_{12} c_{13} & c_{12} c_{14} \\ c_{13} c_{11} & c_{13} c_{12} & c_{13} c_{13} & c_{13} c_{14} \\ c_{14} c_{11} & c_{14} c_{12} & c_{14} c_{13} & c_{14} c_{14} \end{bmatrix} \quad (4.74)$$

The matrix ($i=2, j=3$) in Eq.(4.43) is as follows:

$$e_{23} = \frac{V_{\text{ee}}}{20} \tau_{\text{ee}} \left\{ \left(\sum_{i=1}^4 u_{2,i}^{(n)} \right) \left(\sum_{i=1}^4 u_{3,i}^{(n)} \right) + \sum_{i=1}^4 u_{2,i}^{(n)} u_{3,i}^{(n)} \right\} \begin{bmatrix} c_{[1]}d_{[1]} & c_{[1]}d_{[2]} & c_{[1]}d_{[3]} & c_{[1]}d_{[4]} \\ c_{[2]}d_{[1]} & c_{[2]}d_{[2]} & c_{[2]}d_{[3]} & c_{[2]}d_{[4]} \\ c_{[3]}d_{[1]} & c_{[3]}d_{[2]} & c_{[3]}d_{[3]} & c_{[3]}d_{[4]} \\ c_{[4]}d_{[1]} & c_{[4]}d_{[2]} & c_{[4]}d_{[3]} & c_{[4]}d_{[4]} \end{bmatrix} \quad (4.75)$$

The matrix ($i=3, j=1$) in Eq.(4.43) is as follows:

$$e_{31} = \frac{V_{\text{ee}}}{20} \tau_{\text{ee}} \left\{ \left(\sum_{i=1}^4 u_{3,i}^{(n)} \right) \left(\sum_{i=1}^4 u_{1,i}^{(n)} \right) + \sum_{i=1}^4 u_{3,i}^{(n)} u_{1,i}^{(n)} \right\} \begin{bmatrix} d_{[1]}b_{[1]} & d_{[1]}b_{[2]} & d_{[1]}b_{[3]} & d_{[1]}b_{[4]} \\ d_{[2]}b_{[1]} & d_{[2]}b_{[2]} & d_{[2]}b_{[3]} & d_{[2]}b_{[4]} \\ d_{[3]}b_{[1]} & d_{[3]}b_{[2]} & d_{[3]}b_{[3]} & d_{[3]}b_{[4]} \\ d_{[4]}b_{[1]} & d_{[4]}b_{[2]} & d_{[4]}b_{[3]} & d_{[4]}b_{[4]} \end{bmatrix} \quad (4.76)$$

The matrix ($i=3, j=2$) in Eq.(4.43) is as follows:

$$e_{32} = \frac{V_{\text{ee}}}{20} \tau_{\text{ee}} \left\{ \left(\sum_{i=1}^4 u_{3,i}^{(n)} \right) \left(\sum_{i=1}^4 u_{2,i}^{(n)} \right) + \sum_{i=1}^4 u_{3,i}^{(n)} u_{2,i}^{(n)} \right\} \begin{bmatrix} d_{[1]}c_{[1]} & d_{[1]}c_{[2]} & d_{[1]}c_{[3]} & d_{[1]}c_{[4]} \\ d_{[2]}c_{[1]} & d_{[2]}c_{[2]} & d_{[2]}c_{[3]} & d_{[2]}c_{[4]} \\ d_{[3]}c_{[1]} & d_{[3]}c_{[2]} & d_{[3]}c_{[3]} & d_{[3]}c_{[4]} \\ d_{[4]}c_{[1]} & d_{[4]}c_{[2]} & d_{[4]}c_{[3]} & d_{[4]}c_{[4]} \end{bmatrix} \quad (4.77)$$

The matrix ($i=3, j=3$) in Eq.(4.43) is as follows:

$$e_{33} = \frac{V_{\text{ee}}}{20} \tau_{\text{ee}} \left\{ \left(\sum_{i=1}^4 u_{3,i}^{(n)} \right) \left(\sum_{i=1}^4 u_{3,i}^{(n)} \right) + \sum_{i=1}^4 u_{3,i}^{(n)} u_{3,i}^{(n)} \right\} \begin{bmatrix} d_{[1]}d_{[1]} & d_{[1]}d_{[2]} & d_{[1]}d_{[3]} & d_{[1]}d_{[4]} \\ d_{[2]}d_{[1]} & d_{[2]}d_{[2]} & d_{[2]}d_{[3]} & d_{[2]}d_{[4]} \\ d_{[3]}d_{[1]} & d_{[3]}d_{[2]} & d_{[3]}d_{[3]} & d_{[3]}d_{[4]} \\ d_{[4]}d_{[1]} & d_{[4]}d_{[2]} & d_{[4]}d_{[3]} & d_{[4]}d_{[4]} \end{bmatrix} \quad (4.78)$$

The parameter $\|u\|_{\text{ee}}$ in Eq.(4.16) is as follows[72]:

$$\|u\|_{\text{ee}} = \sqrt{\sum_{i=1}^4 u_{1,i}^2 + \sum_{i=1}^4 u_{2,i}^2 + \sum_{i=1}^4 u_{3,i}^2} \quad (4.79)$$

The parameter h_{ee} in Eq.(4.16) is as follows:

$$\begin{aligned} h_{\text{ee}} &= \frac{2}{|\mathbf{s} \cdot \nabla N_{[1]} + \mathbf{s} \cdot \nabla N_{[2]} + \mathbf{s} \cdot \nabla N_{[3]} + \mathbf{s} \cdot \nabla N_{[4]}|} \\ &= \frac{2}{\sqrt{\sum_{i=1}^4 u_{1,i}^2 + \sum_{i=1}^4 u_{2,i}^2 + \sum_{i=1}^4 u_{3,i}^2}} \left[\begin{bmatrix} b_{[1]} \\ c_{[1]} \\ d_{[1]} \end{bmatrix} + \begin{bmatrix} u_{1,[2]} & u_{2,[2]} & u_{3,[2]} \\ c_{[2]} \\ d_{[2]} \end{bmatrix} + \begin{bmatrix} b_{[2]} \\ c_{[2]} \\ d_{[2]} \end{bmatrix} + \begin{bmatrix} u_{1,[3]} & u_{2,[3]} & u_{3,[3]} \\ c_{[3]} \\ d_{[3]} \end{bmatrix} + \begin{bmatrix} b_{[3]} \\ c_{[3]} \\ d_{[3]} \end{bmatrix} + \begin{bmatrix} u_{1,[4]} & u_{2,[4]} & u_{3,[4]} \\ c_{[4]} \\ d_{[4]} \end{bmatrix} \right] \\ &= \frac{2\sqrt{\sum_{i=1}^4 u_{1,i}^2 + \sum_{i=1}^4 u_{2,i}^2 + \sum_{i=1}^4 u_{3,i}^2}}{\sum_{i=1}^4 b_{[i]}u_{1,[i]} + \sum_{i=1}^4 c_{[i]}u_{2,[i]} + \sum_{i=1}^4 d_{[i]}u_{3,[i]}} \quad (4.80) \end{aligned}$$

The finite element equation in Eq.(4.34)(l=1) under Z(Re)=1 is summarized as follows:

$$\begin{aligned}
& \frac{V_{<\epsilon>}}{4} \begin{bmatrix} 1 & 0 & 0 & 0 \\ 0 & 1 & 0 & 0 \\ 0 & 0 & 1 & 0 \\ 0 & 0 & 0 & 1 \end{bmatrix} \begin{bmatrix} \tilde{u}_{1,[1]} \\ \tilde{u}_{1,[2]} \\ \tilde{u}_{1,[3]} \\ \tilde{u}_{1,[4]} \end{bmatrix} = \frac{V_{<\epsilon>}}{4} \begin{bmatrix} 1 & 0 & 0 & 0 \\ 0 & 1 & 0 & 0 \\ 0 & 0 & 1 & 0 \\ 0 & 0 & 0 & 1 \end{bmatrix} \begin{bmatrix} u_{1,[1]}^{(n)} \\ u_{1,[2]}^{(n)} \\ u_{1,[3]}^{(n)} \\ u_{1,[4]}^{(n)} \end{bmatrix} - \Delta t \begin{bmatrix} V_{<\epsilon>} b_{[f]} u_{1,[j]}^{(n)} \\ 20 \\ 1 & 2 & 1 & 1 \\ 1 & 1 & 2 & 1 \\ 1 & 1 & 1 & 2 \end{bmatrix} \begin{bmatrix} u_{1,[1]}^{(n)} \\ u_{1,[2]}^{(n)} \\ u_{1,[3]}^{(n)} \\ u_{1,[4]}^{(n)} \end{bmatrix} \\
& + \frac{V_{<\epsilon>}}{20} c_{[J]} u_{1,[J]}^{(n)} \begin{bmatrix} 2 & 1 & 1 & 2 \\ 1 & 2 & 1 & 1 \\ 1 & 1 & 2 & 1 \\ 1 & 1 & 1 & 2 \end{bmatrix} \begin{bmatrix} u_{2,[1]}^{(n)} \\ u_{2,[2]}^{(n)} \\ u_{2,[3]}^{(n)} \\ u_{2,[4]}^{(n)} \end{bmatrix} + \frac{V_{<\epsilon>}}{20} d_{[J]} u_{1,[J]}^{(n)} \begin{bmatrix} 2 & 1 & 1 & 2 \\ 1 & 2 & 1 & 1 \\ 1 & 1 & 2 & 1 \\ 1 & 1 & 1 & 2 \end{bmatrix} \begin{bmatrix} u_{3,[1]}^{(n)} \\ u_{3,[2]}^{(n)} \\ u_{3,[3]}^{(n)} \\ u_{3,[4]}^{(n)} \end{bmatrix} + \frac{1}{\text{Re}} \begin{bmatrix} 2V_{<\epsilon>} \\ b_{[1]} b_{[1]} & b_{[1]} b_{[2]} & b_{[1]} b_{[3]} & b_{[1]} b_{[4]} \\ b_{[2]} b_{[1]} & b_{[2]} b_{[2]} & b_{[2]} b_{[3]} & b_{[2]} b_{[4]} \\ b_{[3]} b_{[1]} & b_{[3]} b_{[2]} & b_{[3]} b_{[3]} & b_{[3]} b_{[4]} \\ b_{[4]} b_{[1]} & b_{[4]} b_{[2]} & b_{[4]} b_{[3]} & b_{[4]} b_{[4]} \end{bmatrix} \begin{bmatrix} u_{1,[1]}^{(n)} \\ u_{1,[2]}^{(n)} \\ u_{1,[3]}^{(n)} \\ u_{1,[4]}^{(n)} \end{bmatrix} \\
& + V_{<\epsilon>} \begin{bmatrix} c_{[1]} c_{[1]} & c_{[1]} c_{[2]} & c_{[1]} c_{[3]} & c_{[1]} c_{[4]} \\ c_{[2]} c_{[1]} & c_{[2]} c_{[2]} & c_{[2]} c_{[3]} & c_{[2]} c_{[4]} \\ c_{[3]} c_{[1]} & c_{[3]} c_{[2]} & c_{[3]} c_{[3]} & c_{[3]} c_{[4]} \\ c_{[4]} c_{[1]} & c_{[4]} c_{[2]} & c_{[4]} c_{[3]} & c_{[4]} c_{[4]} \end{bmatrix} \begin{bmatrix} u_{1,[1]}^{(n)} \\ u_{1,[2]}^{(n)} \\ u_{1,[3]}^{(n)} \\ u_{1,[4]}^{(n)} \end{bmatrix} + V_{<\epsilon>} \begin{bmatrix} d_{[1]} d_{[1]} & d_{[1]} d_{[2]} & d_{[1]} d_{[3]} & d_{[1]} d_{[4]} \\ d_{[2]} d_{[1]} & d_{[2]} d_{[2]} & d_{[2]} d_{[3]} & d_{[2]} d_{[4]} \\ d_{[3]} d_{[1]} & d_{[3]} d_{[2]} & d_{[3]} d_{[3]} & d_{[3]} d_{[4]} \\ d_{[4]} d_{[1]} & d_{[4]} d_{[2]} & d_{[4]} d_{[3]} & d_{[4]} d_{[4]} \end{bmatrix} \begin{bmatrix} u_{1,[1]}^{(n)} \\ u_{1,[2]}^{(n)} \\ u_{1,[3]}^{(n)} \\ u_{1,[4]}^{(n)} \end{bmatrix} \\
& + V_{<\epsilon>} \begin{bmatrix} b_{[1]} c_{[1]} & b_{[1]} c_{[2]} & b_{[1]} c_{[3]} & b_{[1]} c_{[4]} \\ b_{[2]} c_{[1]} & b_{[2]} c_{[2]} & b_{[2]} c_{[3]} & b_{[2]} c_{[4]} \\ b_{[3]} c_{[1]} & b_{[3]} c_{[2]} & b_{[3]} c_{[3]} & b_{[3]} c_{[4]} \\ b_{[4]} c_{[1]} & b_{[4]} c_{[2]} & b_{[4]} c_{[3]} & b_{[4]} c_{[4]} \end{bmatrix} \begin{bmatrix} u_{2,[1]}^{(n)} \\ u_{2,[2]}^{(n)} \\ u_{2,[3]}^{(n)} \\ u_{2,[4]}^{(n)} \end{bmatrix} + V_{<\epsilon>} \begin{bmatrix} b_{[1]} d_{[1]} & b_{[1]} d_{[2]} & b_{[1]} d_{[3]} & b_{[1]} d_{[4]} \\ b_{[2]} d_{[1]} & b_{[2]} d_{[2]} & b_{[2]} d_{[3]} & b_{[2]} d_{[4]} \\ b_{[3]} d_{[1]} & b_{[3]} d_{[2]} & b_{[3]} d_{[3]} & b_{[3]} d_{[4]} \\ b_{[4]} d_{[1]} & b_{[4]} d_{[2]} & b_{[4]} d_{[3]} & b_{[4]} d_{[4]} \end{bmatrix} \begin{bmatrix} u_{3,[1]}^{(n)} \\ u_{3,[2]}^{(n)} \\ u_{3,[3]}^{(n)} \\ u_{3,[4]}^{(n)} \end{bmatrix} \\
& - \Delta t \frac{V_{<\epsilon>}}{20} \frac{1}{\sum_{i=1}^4 b_{[i]} u_{1,[i]} + \sum_{i=1}^4 c_{[i]} u_{2,[i]} + \sum_{i=1}^4 d_{[i]} u_{3,[i]}} \left[\left\{ \left(\sum_{i=1}^4 u_{1,[i]}^{(n)} \right) \left(\sum_{i=1}^4 u_{1,[i]}^{(n)} \right) + \sum_{i=1}^4 u_{1,[i]}^{(n)} u_{1,[i]}^{(n)} \right\} \begin{bmatrix} b_{[1]} b_{[1]} & b_{[1]} b_{[2]} & b_{[1]} b_{[3]} & b_{[1]} b_{[4]} \\ b_{[2]} b_{[1]} & b_{[2]} b_{[2]} & b_{[2]} b_{[3]} & b_{[2]} b_{[4]} \\ b_{[3]} b_{[1]} & b_{[3]} b_{[2]} & b_{[3]} b_{[3]} & b_{[3]} b_{[4]} \\ b_{[4]} b_{[1]} & b_{[4]} b_{[2]} & b_{[4]} b_{[3]} & b_{[4]} b_{[4]} \end{bmatrix} \right. \\
& \quad \left. + \left\{ \left(\sum_{i=1}^4 u_{1,[i]}^{(n)} \right) \left(\sum_{i=1}^4 u_{2,[i]}^{(n)} \right) + \sum_{i=1}^4 u_{1,[i]}^{(n)} u_{2,[i]}^{(n)} \right\} \begin{bmatrix} b_{[1]} c_{[1]} & b_{[1]} c_{[2]} & b_{[1]} c_{[3]} & b_{[1]} c_{[4]} \\ b_{[2]} c_{[1]} & b_{[2]} c_{[2]} & b_{[2]} c_{[3]} & b_{[2]} c_{[4]} \\ b_{[3]} c_{[1]} & b_{[3]} c_{[2]} & b_{[3]} c_{[3]} & b_{[3]} c_{[4]} \\ b_{[4]} c_{[1]} & b_{[4]} c_{[2]} & b_{[4]} c_{[3]} & b_{[4]} c_{[4]} \end{bmatrix} \right. \\
& \quad \left. + \left\{ \left(\sum_{i=1}^4 u_{1,[i]}^{(n)} \right) \left(\sum_{i=1}^4 u_{3,[i]}^{(n)} \right) + \sum_{i=1}^4 u_{1,[i]}^{(n)} u_{3,[i]}^{(n)} \right\} \begin{bmatrix} b_{[1]} d_{[1]} & b_{[1]} d_{[2]} & b_{[1]} d_{[3]} & b_{[1]} d_{[4]} \\ b_{[2]} d_{[1]} & b_{[2]} d_{[2]} & b_{[2]} d_{[3]} & b_{[2]} d_{[4]} \\ b_{[3]} d_{[1]} & b_{[3]} d_{[2]} & b_{[3]} d_{[3]} & b_{[3]} d_{[4]} \\ b_{[4]} d_{[1]} & b_{[4]} d_{[2]} & b_{[4]} d_{[3]} & b_{[4]} d_{[4]} \end{bmatrix} \right. \\
& \quad \left. + \left\{ \left(\sum_{i=1}^4 u_{2,[i]}^{(n)} \right) \left(\sum_{i=1}^4 u_{1,[i]}^{(n)} \right) + \sum_{i=1}^4 u_{2,[i]}^{(n)} u_{1,[i]}^{(n)} \right\} \begin{bmatrix} c_{[1]} b_{[1]} & c_{[1]} b_{[2]} & c_{[1]} b_{[3]} & c_{[1]} b_{[4]} \\ c_{[2]} b_{[1]} & c_{[2]} b_{[2]} & c_{[2]} b_{[3]} & c_{[2]} b_{[4]} \\ c_{[3]} b_{[1]} & c_{[3]} b_{[2]} & c_{[3]} b_{[3]} & c_{[3]} b_{[4]} \\ c_{[4]} b_{[1]} & c_{[4]} b_{[2]} & c_{[4]} b_{[3]} & c_{[4]} b_{[4]} \end{bmatrix} \right. \\
& \quad \left. + \left\{ \left(\sum_{i=1}^4 u_{2,[i]}^{(n)} \right) \left(\sum_{i=1}^4 u_{2,[i]}^{(n)} \right) + \sum_{i=1}^4 u_{2,[i]}^{(n)} u_{2,[i]}^{(n)} \right\} \begin{bmatrix} c_{[1]} q_{[1]} & c_{[1]} q_{[2]} & c_{[1]} q_{[3]} & c_{[1]} q_{[4]} \\ c_{[2]} q_{[1]} & c_{[2]} q_{[2]} & c_{[2]} q_{[3]} & c_{[2]} q_{[4]} \\ c_{[3]} q_{[1]} & c_{[3]} q_{[2]} & c_{[3]} q_{[3]} & c_{[3]} q_{[4]} \\ c_{[4]} q_{[1]} & c_{[4]} q_{[2]} & c_{[4]} q_{[3]} & c_{[4]} q_{[4]} \end{bmatrix} \right. \\
& \quad \left. + \left\{ \left(\sum_{i=1}^4 u_{2,[i]}^{(n)} \right) \left(\sum_{i=1}^4 u_{3,[i]}^{(n)} \right) + \sum_{i=1}^4 u_{2,[i]}^{(n)} u_{3,[i]}^{(n)} \right\} \begin{bmatrix} c_{[1]} d_{[1]} & c_{[1]} d_{[2]} & c_{[1]} d_{[3]} & c_{[1]} d_{[4]} \\ c_{[2]} d_{[1]} & c_{[2]} d_{[2]} & c_{[2]} d_{[3]} & c_{[2]} d_{[4]} \\ c_{[3]} d_{[1]} & c_{[3]} d_{[2]} & c_{[3]} d_{[3]} & c_{[3]} d_{[4]} \\ c_{[4]} d_{[1]} & c_{[4]} d_{[2]} & c_{[4]} d_{[3]} & c_{[4]} d_{[4]} \end{bmatrix} \right.
\end{aligned}$$

$$\begin{aligned}
& + \left\{ \left(\sum_{i=1}^4 u_{3,[i]}^{(n)} \right) \left(\sum_{i=1}^4 u_{1,[i]}^{(n)} \right) + \sum_{i=1}^4 u_{3,[i]}^{(n)} u_{1,[i]}^{(n)} \right\} \begin{bmatrix} d_{[1]} b_{[1]} & d_{[1]} b_{[2]} & d_{[1]} b_{[3]} & d_{[1]} b_{[4]} \\ d_{[2]} b_{[1]} & d_{[2]} b_{[2]} & d_{[2]} b_{[3]} & d_{[2]} b_{[4]} \\ d_{[3]} b_{[1]} & d_{[3]} b_{[2]} & d_{[3]} b_{[3]} & d_{[3]} b_{[4]} \\ d_{[4]} b_{[1]} & d_{[4]} b_{[2]} & d_{[4]} b_{[3]} & d_{[4]} b_{[4]} \end{bmatrix} \\
& + \left\{ \left(\sum_{i=1}^4 u_{2,[i]}^{(n)} \right) \left(\sum_{i=1}^4 u_{3,[i]}^{(n)} \right) + \sum_{i=1}^4 u_{2,[i]}^{(n)} u_{3,[i]}^{(n)} \right\} \begin{bmatrix} c_{[1]} d_{[1]} & c_{[1]} d_{[2]} & c_{[1]} d_{[3]} & c_{[1]} d_{[4]} \\ c_{[2]} d_{[1]} & c_{[2]} d_{[2]} & c_{[2]} d_{[3]} & c_{[2]} d_{[4]} \\ c_{[3]} d_{[1]} & c_{[3]} d_{[2]} & c_{[3]} d_{[3]} & c_{[3]} d_{[4]} \\ c_{[4]} d_{[1]} & c_{[4]} d_{[2]} & c_{[4]} d_{[3]} & c_{[4]} d_{[4]} \end{bmatrix} \\
& + \left\{ \left(\sum_{i=1}^4 u_{3,[i]}^{(n)} \right) \left(\sum_{i=1}^4 u_{3,[i]}^{(n)} \right) + \sum_{i=1}^4 u_{3,[i]}^{(n)} u_{3,[i]}^{(n)} \right\} \begin{bmatrix} d_{[1]} d_{[1]} & d_{[1]} d_{[2]} & d_{[1]} d_{[3]} & d_{[1]} d_{[4]} \\ d_{[2]} d_{[1]} & d_{[2]} d_{[2]} & d_{[2]} d_{[3]} & d_{[2]} d_{[4]} \\ d_{[3]} d_{[1]} & d_{[3]} d_{[2]} & d_{[3]} d_{[3]} & d_{[3]} d_{[4]} \\ d_{[4]} d_{[1]} & d_{[4]} d_{[2]} & d_{[4]} d_{[3]} & d_{[4]} d_{[4]} \end{bmatrix} \begin{bmatrix} u_{1,[1]}^{(n)} \\ u_{1,[2]}^{(n)} \\ u_{1,[3]}^{(n)} \\ u_{1,[4]}^{(n)} \end{bmatrix} \tag{4.81}
\end{aligned}$$

The finite element equation in Eq.(4.35) is summarized as follows:

$$\begin{aligned}
V_{<\epsilon>} & \begin{bmatrix} b_{[1]} b_{[1]} & b_{[1]} b_{[2]} & b_{[1]} b_{[3]} & b_{[1]} b_{[4]} \\ b_{[2]} b_{[1]} & b_{[2]} b_{[2]} & b_{[2]} b_{[3]} & b_{[2]} b_{[4]} \\ b_{[3]} b_{[1]} & b_{[3]} b_{[2]} & b_{[3]} b_{[3]} & b_{[3]} b_{[4]} \\ b_{[4]} b_{[1]} & b_{[4]} b_{[2]} & b_{[4]} b_{[3]} & b_{[4]} b_{[4]} \end{bmatrix} + \begin{bmatrix} c_{[1]} q_{[1]} & c_{[1]} q_{[2]} & c_{[1]} q_{[3]} & c_{[1]} q_{[4]} \\ c_{[2]} q_{[1]} & c_{[2]} q_{[2]} & c_{[2]} q_{[3]} & c_{[2]} q_{[4]} \\ c_{[3]} q_{[1]} & c_{[3]} q_{[2]} & c_{[3]} q_{[3]} & c_{[3]} q_{[4]} \\ c_{[4]} q_{[1]} & c_{[4]} q_{[2]} & c_{[4]} q_{[3]} & c_{[4]} q_{[4]} \end{bmatrix} \\
& + \begin{bmatrix} d_{[1]} d_{[1]} & d_{[1]} d_{[2]} & d_{[1]} d_{[3]} & d_{[1]} d_{[4]} \\ d_{[2]} d_{[1]} & d_{[2]} d_{[2]} & d_{[2]} d_{[3]} & d_{[2]} d_{[4]} \\ d_{[3]} d_{[1]} & d_{[3]} d_{[2]} & d_{[3]} d_{[3]} & d_{[3]} d_{[4]} \\ d_{[4]} d_{[1]} & d_{[4]} d_{[2]} & d_{[4]} d_{[3]} & d_{[4]} d_{[4]} \end{bmatrix} \begin{bmatrix} p_{[1]}^{(n+1)} \\ p_{[2]}^{(n+1)} \\ p_{[3]}^{(n+1)} \\ p_{[4]}^{(n+1)} \end{bmatrix} = -\frac{1}{\Delta t} \frac{V_{<\epsilon>}}{4} \begin{bmatrix} b_{[1]} & b_{[2]} & b_{[3]} & b_{[4]} \\ b_{[1]} & b_{[2]} & b_{[3]} & b_{[4]} \\ b_{[1]} & b_{[2]} & b_{[3]} & b_{[4]} \\ b_{[1]} & b_{[2]} & b_{[3]} & b_{[4]} \end{bmatrix} \begin{bmatrix} \tilde{u}_{1,[1]} \\ \tilde{u}_{1,[2]} \\ \tilde{u}_{1,[3]} \\ \tilde{u}_{1,[4]} \end{bmatrix} \\
& + \begin{bmatrix} c_{[1]} & c_{[2]} & c_{[3]} & c_{[4]} \\ c_{[1]} & c_{[2]} & c_{[3]} & c_{[4]} \\ c_{[1]} & c_{[2]} & c_{[3]} & c_{[4]} \\ c_{[1]} & c_{[2]} & c_{[3]} & c_{[4]} \end{bmatrix} \begin{bmatrix} \tilde{u}_{2,[1]} \\ \tilde{u}_{2,[2]} \\ \tilde{u}_{2,[3]} \\ \tilde{u}_{2,[4]} \end{bmatrix} + \begin{bmatrix} d_{[1]} & d_{[2]} & d_{[3]} & d_{[4]} \\ d_{[1]} & d_{[2]} & d_{[3]} & d_{[4]} \\ d_{[1]} & d_{[2]} & d_{[3]} & d_{[4]} \\ d_{[1]} & d_{[2]} & d_{[3]} & d_{[4]} \end{bmatrix} \begin{bmatrix} \tilde{u}_{3,[1]} \\ \tilde{u}_{3,[2]} \\ \tilde{u}_{3,[3]} \\ \tilde{u}_{3,[4]} \end{bmatrix} \tag{4.82}
\end{aligned}$$

The finite element equation in Eq.(4.36)(l=1) is summarized as follows:

$$\frac{V_{<\epsilon>}}{4} \begin{bmatrix} 1 & 0 & 0 & 0 \\ 0 & 1 & 0 & 0 \\ 0 & 0 & 1 & 0 \\ 0 & 0 & 0 & 1 \end{bmatrix} \begin{bmatrix} u_{1,[1]}^{(n+1)} \\ u_{1,[2]}^{(n+1)} \\ u_{1,[3]}^{(n+1)} \\ u_{1,[4]}^{(n+1)} \end{bmatrix} = \frac{V_{<\epsilon>}}{4} \begin{bmatrix} 1 & 0 & 0 & 0 \\ 0 & 1 & 0 & 0 \\ 0 & 0 & 1 & 0 \\ 0 & 0 & 0 & 1 \end{bmatrix} \begin{bmatrix} \tilde{u}_{1,[1]} \\ \tilde{u}_{1,[2]} \\ \tilde{u}_{1,[3]} \\ \tilde{u}_{1,[4]} \end{bmatrix} - \Delta t \frac{V_{<\epsilon>}}{4} \begin{bmatrix} b_{[1]} & b_{[2]} & b_{[3]} & b_{[4]} \\ b_{[1]} & b_{[2]} & b_{[3]} & b_{[4]} \\ b_{[1]} & b_{[2]} & b_{[3]} & b_{[4]} \\ b_{[1]} & b_{[2]} & b_{[3]} & b_{[4]} \end{bmatrix} \begin{bmatrix} p_{[1]}^{(n+1)} \\ p_{[2]}^{(n+1)} \\ p_{[3]}^{(n+1)} \\ p_{[4]}^{(n+1)} \end{bmatrix} \tag{4.83}$$

For l=2,3 of Eq.(4.34) and Eq.(4.36), the discretization is performed in the same way. The local matrices in the finite element equations are converted to a global matrix, which is solved using the HEC-MW solver [80]. We take the same approach for the adjoint equations.

4.6. Discretization of Sensitivity Equation

In this section, the algorithm to obtain the sensitivity is shown in a 9-step procedure.

Step 1: According to HEC-MW text format, the connectivity with respect to the boundary γ is made [49]. The mesh data structure contains a list of nodes and a list of elements. The former contains nodal coordinates, while the latter contains node indices, in order to describe the connectivity of the mesh.

Step 2: Both an element (four nodes [1],[2],[3],[4]) and a surface are selected by using the connectivity data.

Step 3: The coefficients $a_{[i]}, b_{[i]}, c_{[i]}, d_{[i]}$ (Eq.(4.25)-Eq.(4.28)) are calculated.

Step 4: Partial differentiations in the sensitivity equations are computed. The partial differentiation of u_1 with respect to x_1 , for example, is determined as follows:

$$\left(\frac{\partial u_1}{\partial x_1} \right)_{<m>} = b_{[1]}u_{1,[1]} + b_{[2]}u_{1,[2]} + b_{[3]}u_{1,[3]} + b_{[4]}u_{1,[4]} = b_{[4]}u_{1,[4]} \quad (4.84)$$

where $<m>$ shows the element number and [1],[2],[3],[4] show the node numbers. The state variable u_1 has been already obtained using the state equations. As shown in Fig.6, the nodes [1],[2],[3] are on the surface γ and the node [4] is in the space. By using the boundary condition in Table 1, $u_{[1]}, u_{[2]}, u_{[3]}$ become zero. Eq.(4.84) shows the value of the element $< m >$, which needs to be converted to the value of a node to calculate the sensitivity.

Step 5: The value of the partial differentiation at each element is divided into the three nodal values [1],[2],[3], in proportion to the surface area. In the data structure of HEC-MW, the value (sensitivity eq.) of the node and the cell area (as shown in Fig.6) can not be obtained directly, while the value of the node can be partly calculated by using the value of the element. The node [1], for example, is connected to six elements as shown in Fig.6. The sixth part of the value corresponding to the node [1],[2],[3] can be obtained as follows:

$$\left(\frac{\partial u_1}{\partial x_1} \right)_{<m>} \cdot \frac{A_{<m>}}{3} \quad (4.85)$$

where $A_{<m>}$ indicates the surface area in element $<m>$. If the area of element $<m>$ is large, the value of the partial differentiation for element $<m>$ is dominant at node [1].

Step 6: The area for element $<m>$ is divided into three cells.

$$\frac{A_{<m>}}{3} \quad (4.86)$$

Step 7: Steps 2-6 are repeated for all surfaces.

Step 8: The partial differentiation of u_1 with respect to x_1 is obtained as follows:

$$\left(\frac{\partial u_1}{\partial x_1} \right)_{[1]} = \frac{\sum_{n=0}^5 \left(\frac{\partial u_1}{\partial x_1} \right)_{<m+n>} \frac{A_{<m+n>}}{3}}{\sum_{n=0}^5 \frac{A_{<m+n>}}{3}} \quad (4.87)$$

where the value of the node [1] can be obtained by summing parts of the value after finishing step 7. The other terms in the sensitivity equations are obtained in a similar way.

Step 9: The sensitivity G at every node is calculated. G_1 , for example, is determined as follows:

$$\begin{aligned} G_{1,[1]} = & \left\{ -\lambda_{1,[1]} n_{1,[1]} + 2\mu \left(\frac{\partial \lambda_2}{\partial x_1} \right)_{[1]} n_{1,[1]} + \mu \left\{ \left(\frac{\partial \lambda_2}{\partial x_2} \right)_{[1]} + \left(\frac{\partial \lambda_3}{\partial x_1} \right)_{[1]} \right\} n_{2,[1]} + \mu \left\{ \left(\frac{\partial \lambda_2}{\partial x_3} \right)_{[1]} + \left(\frac{\partial \lambda_4}{\partial x_1} \right)_{[1]} \right\} n_{3,[1]} \right\} \left(\frac{\partial u_1}{\partial x_1} \right)_{[1]} \\ & + \left\{ -\lambda_{1,[1]} n_{2,[1]} + \mu \left\{ \left(\frac{\partial \lambda_2}{\partial x_2} \right)_{[1]} + \left(\frac{\partial \lambda_3}{\partial x_1} \right)_{[1]} \right\} n_{1,[1]} + 2\mu \left(\frac{\partial \lambda_3}{\partial x_2} \right)_{[1]} n_{2,[1]} + \mu \left\{ \left(\frac{\partial \lambda_3}{\partial x_3} \right)_{[1]} + \left(\frac{\partial \lambda_4}{\partial x_2} \right)_{[1]} \right\} n_{3,[1]} \right\} \left(\frac{\partial u_2}{\partial x_1} \right)_{[1]} \\ & + \left\{ -\lambda_{1,[1]} n_{3,[1]} + \mu \left\{ \left(\frac{\partial \lambda_2}{\partial x_3} \right)_{[1]} + \left(\frac{\partial \lambda_4}{\partial x_1} \right)_{[1]} \right\} n_{1,[1]} + \mu \left\{ \left(\frac{\partial \lambda_4}{\partial x_2} \right)_{[1]} + \left(\frac{\partial \lambda_3}{\partial x_3} \right)_{[1]} \right\} n_{2,[1]} + 2\mu \left(\frac{\partial \lambda_4}{\partial x_3} \right)_{[1]} n_{3,[1]} \right\} \left(\frac{\partial u_3}{\partial x_1} \right)_{[1]} \end{aligned} \quad (4.88)$$

The adjoint variables $\lambda_{1,[1]}$ etc. are calculated by using the saved files containing the adjoint and state variables. This approach is also applied to the drag on the surface and the normal vector on the surface.

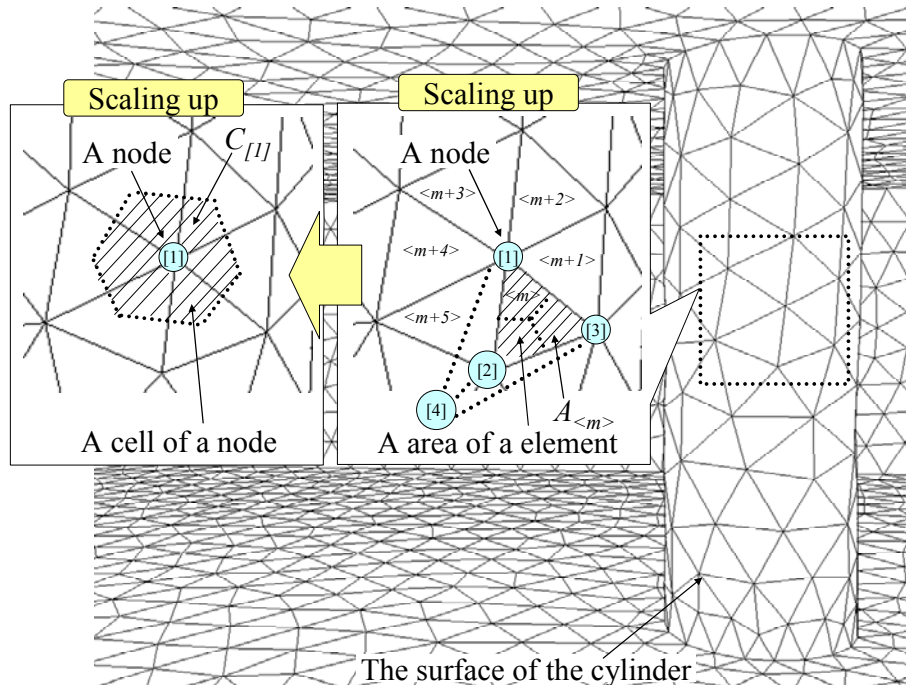


Figure 6. An element (four node tetrahedron) in the mesh.

4.7. Discretization in the Shape Modification

Variables G_1-G_3 from Eqs.(2.41)-(2.43) represent the sensitivity. The shape is modified so that the sensitivity becomes zero. The superscripts (1) and (n) show the start of the test time and the end of test time, respectively. The surface in the shape step ($k+1$) can be obtained as follows:

$$\begin{bmatrix} x_{l(k+1)[1]} \\ x_{l(k+1)[2]} \\ \vdots \\ x_{l(k+1)[i]} \end{bmatrix} = \begin{bmatrix} x_{l(k)[1]} \\ x_{l(k)[2]} \\ \vdots \\ x_{l(k)[i]} \end{bmatrix} + \begin{bmatrix} \beta(G_{l(k)[1]}^{(1)} + G_{l(k)[1]}^{(2)} + \dots + G_{l(k)[1]}^{(n)}) \\ \beta(G_{l(k)[2]}^{(1)} + G_{l(k)[2]}^{(2)} + \dots + G_{l(k)[2]}^{(n)}) \\ \vdots \\ \beta(G_{l(k)[i]}^{(1)} + G_{l(k)[i]}^{(2)} + \dots + G_{l(k)[i]}^{(n)}) \end{bmatrix} = \begin{bmatrix} x_{l(k)[1]} \\ x_{l(k)[2]} \\ \vdots \\ x_{l(k)[i]} \end{bmatrix} + \beta \begin{bmatrix} g_{l(k)[1]} \\ g_{l(k)[2]} \\ \vdots \\ g_{l(k)[i]} \end{bmatrix} \quad l=1,2,3 \quad k=0,1,\dots \quad \text{on } \gamma \quad (4.89)$$

The value β is decided based on a heuristic search method [11][59]. The value β is empirically decided as follows:

$$\beta \propto \frac{1}{t_e - t_s} \frac{1}{\text{Re}} \cdot H \quad (4.90)$$

where Re and H represents the Reynolds number and the element size respectively. In high Reynolds number cases, the value of the sensitivity (G) becomes large. When using a high resolution mesh, due to mesh deformations, the volumes of small elements easily become negative. Therefore, the coefficient β is inverse proportional to the Reynolds number Re and proportional to the element size H .

4.8. Discretization of the Biharmonic Equation

In this subsection we describe how to solve the biharmonic equation. Eq.(3.13) can be decomposed as follows [68]

$$-\frac{\partial^2 \tilde{\Theta}}{\partial x_1^2} - \frac{\partial^2 \tilde{\Theta}}{\partial x_2^2} - \frac{\partial^2 \tilde{\Theta}}{\partial x_3^2} = 0 \quad \text{in } \Omega \quad (4.91)$$

$$-\frac{\partial^2 \Theta}{\partial x_1^2} - \frac{\partial^2 \Theta}{\partial x_2^2} - \frac{\partial^2 \Theta}{\partial x_3^2} = \tilde{\Theta} \quad \text{in } \Omega \quad (4.92)$$

where $\tilde{\Theta}$ indicates the intermediate displacement. The present implementation follows a Galerkin finite-element procedure. The discrete equations are given by

$$\int_{\Omega} \left(\frac{\partial \tilde{\Theta}^*}{\partial x_1} \frac{\partial \tilde{\Theta}}{\partial x_1} + \frac{\partial \tilde{\Theta}^*}{\partial x_2} \frac{\partial \tilde{\Theta}}{\partial x_2} + \frac{\partial \tilde{\Theta}^*}{\partial x_3} \frac{\partial \tilde{\Theta}}{\partial x_3} \right) d\Omega - \int_{\Gamma} \left(\tilde{\Theta}^* \frac{\partial \tilde{\Theta}}{\partial x_1} n_1 + \tilde{\Theta}^* \frac{\partial \tilde{\Theta}}{\partial x_2} n_2 + \tilde{\Theta}^* \frac{\partial \tilde{\Theta}}{\partial x_3} n_3 \right) d\Gamma = 0 \quad (4.93)$$

$$\int_{\Omega} \left(\frac{\partial \Theta^*}{\partial x_1} \frac{\partial \Theta}{\partial x_1} + \frac{\partial \Theta^*}{\partial x_2} \frac{\partial \Theta}{\partial x_2} + \frac{\partial \Theta^*}{\partial x_3} \frac{\partial \Theta}{\partial x_3} \right) d\Omega - \int_{\Gamma} \left(\Theta^* \frac{\partial \Theta}{\partial x_1} n_1 + \Theta^* \frac{\partial \Theta}{\partial x_2} n_2 + \Theta^* \frac{\partial \Theta}{\partial x_3} n_3 \right) d\Gamma = \int_{\Omega} \Theta^* \tilde{\Theta} d\Omega \quad (4.94)$$

Assuming the second terms on the left hand side of Eqs. (4.93) and (4.94) to be zero, the equations are transformed as follows (by using the same form as in Eq.(4.20) etc.):

$$\int_{\Omega} (b_{[\alpha]} b_{[\beta]} + c_{[\alpha]} c_{[\beta]} + d_{[\alpha]} d_{[\beta]}) d\Omega \Theta_{[\beta]} d\Gamma = \int_{\Omega} N_{[\alpha]} N_{[\beta]} d\Omega \tilde{\Theta}_{[\beta]} \quad \alpha, \beta = 1, 2, 3, 4 \quad (4.95)$$

$$\int_{\Omega} (b_{[\alpha]} b_{[\beta]} + c_{[\alpha]} c_{[\beta]} + d_{[\alpha]} d_{[\beta]}) d\Omega \tilde{\Theta}_{[\beta]} d\Gamma = 0 \quad \alpha, \beta = 1, 2, 3, 4 \quad (4.96)$$

The two equations above become as follows:

$$\begin{aligned} & \frac{V_{ce}}{20} \begin{bmatrix} b_{[1]} b_{[1]} & b_{[1]} b_{[2]} & b_{[1]} b_{[3]} & b_{[1]} b_{[4]} \\ b_{[2]} b_{[1]} & b_{[2]} b_{[2]} & b_{[2]} b_{[3]} & b_{[2]} b_{[4]} \\ b_{[3]} b_{[1]} & b_{[3]} b_{[2]} & b_{[3]} b_{[3]} & b_{[3]} b_{[4]} \\ b_{[4]} b_{[1]} & b_{[4]} b_{[2]} & b_{[4]} b_{[3]} & b_{[4]} b_{[4]} \end{bmatrix} \begin{bmatrix} \tilde{\Theta}_{[1]} \\ \tilde{\Theta}_{[2]} \\ \tilde{\Theta}_{[3]} \\ \tilde{\Theta}_{[4]} \end{bmatrix} + \frac{V_{ce}}{20} \begin{bmatrix} c_{[1]} c_{[1]} & c_{[1]} c_{[2]} & c_{[1]} c_{[3]} & c_{[1]} c_{[4]} \\ c_{[2]} c_{[1]} & c_{[2]} c_{[2]} & c_{[2]} c_{[3]} & c_{[2]} c_{[4]} \\ c_{[3]} c_{[1]} & c_{[3]} c_{[2]} & c_{[3]} c_{[3]} & c_{[3]} c_{[4]} \\ c_{[4]} c_{[1]} & c_{[4]} c_{[2]} & c_{[4]} c_{[3]} & c_{[4]} c_{[4]} \end{bmatrix} \begin{bmatrix} \tilde{\Theta}_{[1]} \\ \tilde{\Theta}_{[2]} \\ \tilde{\Theta}_{[3]} \\ \tilde{\Theta}_{[4]} \end{bmatrix} \\ & + \frac{V_{ce}}{20} \begin{bmatrix} d_{[1]} d_{[1]} & d_{[1]} d_{[2]} & d_{[1]} d_{[3]} & d_{[1]} d_{[4]} \\ d_{[2]} d_{[1]} & d_{[2]} d_{[2]} & d_{[2]} d_{[3]} & d_{[2]} d_{[4]} \\ d_{[3]} d_{[1]} & d_{[3]} d_{[2]} & d_{[3]} d_{[3]} & d_{[3]} d_{[4]} \\ d_{[4]} d_{[1]} & d_{[4]} d_{[2]} & d_{[4]} d_{[3]} & d_{[4]} d_{[4]} \end{bmatrix} \begin{bmatrix} \tilde{\Theta}_{[1]} \\ \tilde{\Theta}_{[2]} \\ \tilde{\Theta}_{[3]} \\ \tilde{\Theta}_{[4]} \end{bmatrix} = \begin{bmatrix} 0 \\ 0 \\ 0 \\ 0 \end{bmatrix} \end{aligned} \quad (4.97)$$

$$\begin{aligned} & \frac{V_{ce}}{20} \begin{bmatrix} b_{[1]} b_{[1]} & b_{[1]} b_{[2]} & b_{[1]} b_{[3]} & b_{[1]} b_{[4]} \\ b_{[2]} b_{[1]} & b_{[2]} b_{[2]} & b_{[2]} b_{[3]} & b_{[2]} b_{[4]} \\ b_{[3]} b_{[1]} & b_{[3]} b_{[2]} & b_{[3]} b_{[3]} & b_{[3]} b_{[4]} \\ b_{[4]} b_{[1]} & b_{[4]} b_{[2]} & b_{[4]} b_{[3]} & b_{[4]} b_{[4]} \end{bmatrix} \begin{bmatrix} \Theta_{[1]} \\ \Theta_{[2]} \\ \Theta_{[3]} \\ \Theta_{[4]} \end{bmatrix} + \frac{V_{ce}}{20} \begin{bmatrix} q_{[1]} q_{[1]} & q_{[1]} q_{[2]} & q_{[1]} q_{[3]} & q_{[1]} q_{[4]} \\ q_{[2]} q_{[1]} & q_{[2]} q_{[2]} & q_{[2]} q_{[3]} & q_{[2]} q_{[4]} \\ q_{[3]} q_{[1]} & q_{[3]} q_{[2]} & q_{[3]} q_{[3]} & q_{[3]} q_{[4]} \\ q_{[4]} q_{[1]} & q_{[4]} q_{[2]} & q_{[4]} q_{[3]} & q_{[4]} q_{[4]} \end{bmatrix} \begin{bmatrix} \Theta_{[1]} \\ \Theta_{[2]} \\ \Theta_{[3]} \\ \Theta_{[4]} \end{bmatrix} \\ & + \frac{V_{ce}}{20} \begin{bmatrix} d_{[1]} d_{[1]} & d_{[1]} d_{[2]} & d_{[1]} d_{[3]} & d_{[1]} d_{[4]} \\ d_{[2]} d_{[1]} & d_{[2]} d_{[2]} & d_{[2]} d_{[3]} & d_{[2]} d_{[4]} \\ d_{[3]} d_{[1]} & d_{[3]} d_{[2]} & d_{[3]} d_{[3]} & d_{[3]} d_{[4]} \\ d_{[4]} d_{[1]} & d_{[4]} d_{[2]} & d_{[4]} d_{[3]} & d_{[4]} d_{[4]} \end{bmatrix} \begin{bmatrix} \Theta_{[1]} \\ \Theta_{[2]} \\ \Theta_{[3]} \\ \Theta_{[4]} \end{bmatrix} = \frac{V_{ce}}{4} \begin{bmatrix} 1 & 0 & 0 & 0 \\ 0 & 1 & 0 & 0 \\ 0 & 0 & 1 & 0 \\ 0 & 0 & 0 & 1 \end{bmatrix} \begin{bmatrix} \tilde{\Theta}_{[1]} \\ \tilde{\Theta}_{[2]} \\ \tilde{\Theta}_{[3]} \\ \tilde{\Theta}_{[4]} \end{bmatrix} \end{aligned} \quad (4.98)$$

The integral on the right hand side of Eq.(4.97) is mass-lumped (off-diagonal matrix entries are added to the mass diagonal and then set to zero). Eq. (4.97) under the boundary condition expressed by Eqs.(3.11)-(3.12) is first solved by using the HEC-MW solver and the intermediate displacement $\tilde{\Theta}$ at each x_1, x_2, x_3 is obtained. Then, Eq.(4.98) under Eqs.(3.14)-(3.15) is also solved by the HEC-MW solver to obtain the displacement Θ at each x_1, x_2, x_3 . Using the obtained displacement values, the coordinates of all nodes are updated.

For a more robust mesh deformation, ζ_{ce} is added to Eq.(4.97) and Eq.(4.98) as follows [69]:

$$\begin{aligned} & \frac{V_{\text{e}}}{20} (1 + \zeta_{\text{e}}) \begin{bmatrix} b_{[1]}b_{[1]} & b_{[1]}b_{[2]} & b_{[1]}b_{[3]} & b_{[1]}b_{[4]} \\ b_{[2]}b_{[1]} & b_{[2]}b_{[2]} & b_{[2]}b_{[3]} & b_{[2]}b_{[4]} \\ b_{[3]}b_{[1]} & b_{[3]}b_{[2]} & b_{[3]}b_{[3]} & b_{[3]}b_{[4]} \\ b_{[4]}b_{[1]} & b_{[4]}b_{[2]} & b_{[4]}b_{[3]} & b_{[4]}b_{[4]} \end{bmatrix} \begin{bmatrix} \tilde{\Theta}_{[1]} \\ \tilde{\Theta}_{[2]} \\ \tilde{\Theta}_{[3]} \\ \tilde{\Theta}_{[4]} \end{bmatrix} + \frac{V_{\text{e}}}{20} (1 + \zeta_{\text{e}}) \begin{bmatrix} c_{[1]}c_{[1]} & c_{[1]}c_{[2]} & c_{[1]}c_{[3]} & c_{[1]}c_{[4]} \\ c_{[2]}c_{[1]} & c_{[2]}c_{[2]} & c_{[2]}c_{[3]} & c_{[2]}c_{[4]} \\ c_{[3]}c_{[1]} & c_{[3]}c_{[2]} & c_{[3]}c_{[3]} & c_{[3]}c_{[4]} \\ c_{[4]}c_{[1]} & c_{[4]}c_{[2]} & c_{[4]}c_{[3]} & c_{[4]}c_{[4]} \end{bmatrix} \begin{bmatrix} \tilde{\Theta}_{[1]} \\ \tilde{\Theta}_{[2]} \\ \tilde{\Theta}_{[3]} \\ \tilde{\Theta}_{[4]} \end{bmatrix} \\ & + \frac{V_{\text{e}}}{20} (1 + \zeta_{\text{e}}) \begin{bmatrix} d_{[1]}d_{[1]} & d_{[1]}d_{[2]} & d_{[1]}d_{[3]} & d_{[1]}d_{[4]} \\ d_{[2]}d_{[1]} & d_{[2]}d_{[2]} & d_{[2]}d_{[3]} & d_{[2]}d_{[4]} \\ d_{[3]}d_{[1]} & d_{[3]}d_{[2]} & d_{[3]}d_{[3]} & d_{[3]}d_{[4]} \\ d_{[4]}d_{[1]} & d_{[4]}d_{[2]} & d_{[4]}d_{[3]} & d_{[4]}d_{[4]} \end{bmatrix} \begin{bmatrix} \tilde{\Theta}_{[1]} \\ \tilde{\Theta}_{[2]} \\ \tilde{\Theta}_{[3]} \\ \tilde{\Theta}_{[4]} \end{bmatrix} = \begin{bmatrix} 0 \\ 0 \\ 0 \\ 0 \end{bmatrix} \end{aligned} \quad (4.99)$$

$$\begin{aligned} & \frac{V_{\text{e}}}{20} (1 + \zeta_{\text{e}}) \begin{bmatrix} b_{[1]}b_{[1]} & b_{[1]}b_{[2]} & b_{[1]}b_{[3]} & b_{[1]}b_{[4]} \\ b_{[2]}b_{[1]} & b_{[2]}b_{[2]} & b_{[2]}b_{[3]} & b_{[2]}b_{[4]} \\ b_{[3]}b_{[1]} & b_{[3]}b_{[2]} & b_{[3]}b_{[3]} & b_{[3]}b_{[4]} \\ b_{[4]}b_{[1]} & b_{[4]}b_{[2]} & b_{[4]}b_{[3]} & b_{[4]}b_{[4]} \end{bmatrix} \begin{bmatrix} \Theta_{[1]} \\ \Theta_{[2]} \\ \Theta_{[3]} \\ \Theta_{[4]} \end{bmatrix} + \frac{V_{\text{e}}}{20} (1 + \zeta_{\text{e}}) \begin{bmatrix} c_{[1]}c_{[1]} & c_{[1]}c_{[2]} & c_{[1]}c_{[3]} & c_{[1]}c_{[4]} \\ c_{[2]}c_{[1]} & c_{[2]}c_{[2]} & c_{[2]}c_{[3]} & c_{[2]}c_{[4]} \\ c_{[3]}c_{[1]} & c_{[3]}c_{[2]} & c_{[3]}c_{[3]} & c_{[3]}c_{[4]} \\ c_{[4]}c_{[1]} & c_{[4]}c_{[2]} & c_{[4]}c_{[3]} & c_{[4]}c_{[4]} \end{bmatrix} \begin{bmatrix} \Theta_{[1]} \\ \Theta_{[2]} \\ \Theta_{[3]} \\ \Theta_{[4]} \end{bmatrix} \\ & + \frac{V_{\text{e}}}{20} (1 + \zeta_{\text{e}}) \begin{bmatrix} d_{[1]}d_{[1]} & d_{[1]}d_{[2]} & d_{[1]}d_{[3]} & d_{[1]}d_{[4]} \\ d_{[2]}d_{[1]} & d_{[2]}d_{[2]} & d_{[2]}d_{[3]} & d_{[2]}d_{[4]} \\ d_{[3]}d_{[1]} & d_{[3]}d_{[2]} & d_{[3]}d_{[3]} & d_{[3]}d_{[4]} \\ d_{[4]}d_{[1]} & d_{[4]}d_{[2]} & d_{[4]}d_{[3]} & d_{[4]}d_{[4]} \end{bmatrix} \begin{bmatrix} \Theta_{[1]} \\ \Theta_{[2]} \\ \Theta_{[3]} \\ \Theta_{[4]} \end{bmatrix} = \begin{bmatrix} 1 & 0 & 0 & 0 \\ 0 & 1 & 0 & 0 \\ 0 & 0 & 1 & 0 \\ 0 & 0 & 0 & 1 \end{bmatrix} \begin{bmatrix} \tilde{\Theta}_{[1]} \\ \tilde{\Theta}_{[2]} \\ \tilde{\Theta}_{[3]} \\ \tilde{\Theta}_{[4]} \end{bmatrix} \end{aligned} \quad (4.100)$$

where ζ_{e} is as follows:

$$\zeta_{\text{e}} = \frac{1 - \frac{V_{\min}}{V_{\max}}}{\frac{V_{\text{e}}}{V_{\max}}} = \frac{V_{\max} - V_{\min}}{V_{\text{e}}} \quad (4.101)$$

ζ_{e} is designed to apply this condition stronger over the smaller elements, thereby preserving their shapes and preventing mesh inversion. V_{\max} and V_{\min} represent the volume of the largest and the smallest element in the mesh, respectively and V_{e} represents the volume of the element e [69].

When a more robust mesh deformation is needed, we have to choose the remeshing approach [89]

4.9. Superposition of the Finite Element Equations

In this section, we describe the superposition of the finite element equations (see section 4.5 and 4.8) from the local matrix to the global matrix. Two elements ($<1>$ and $<2>$) are shown in Fig.7. The local numbers ([I], [II], [III], [IV]) at each element are connected to the global numbers ([1], [2], [3], [4]), as shown in Table 2. The finite element equations are as follows:

$$\begin{bmatrix} R_{11,<1>} & R_{12,<1>} & R_{13,<1>} & R_{14,<1>} \\ R_{21,<1>} & R_{22,<1>} & R_{23,<1>} & R_{24,<1>} \\ R_{31,<1>} & R_{32,<1>} & R_{33,<1>} & R_{34,<1>} \\ R_{41,<1>} & R_{42,<1>} & R_{34,<1>} & R_{44,<1>} \end{bmatrix} \begin{bmatrix} u_{[I],<1>} \\ u_{[II],<1>} \\ u_{[III],<1>} \\ u_{[IV],<1>} \end{bmatrix} = \begin{bmatrix} F_{[I],<1>} \\ F_{[II],<1>} \\ F_{[III],<1>} \\ F_{[IV],<1>} \end{bmatrix} \quad (4.102)$$

where the vectors \mathbf{u} and \mathbf{F} denote the unknown and the known right hand side at nodes in an element, respectively. R_{ij} represents an element in the coefficient matrix (in Eq.(4.81) etc.). For two elements, these are combined as follows:

$$\begin{bmatrix} R_{11}, <1> & R_{12}, <1> & R_{13}, <1> & R_{14}, <1> & \vdots \\ R_{21}, <1> & R_{22}, <1> & R_{23}, <1> & R_{24}, <1> & \vdots \\ R_{31}, <1> & R_{32}, <1> & R_{33}, <1> & R_{34}, <1> & \vdots \\ R_{41}, <1> & R_{42}, <1> & R_{34}, <1> & R_{44}, <1> & \vdots \\ \cdots & \cdots & \cdots & \cdots & \cdots \\ & & & & \vdots \\ & & & & R_{11}, <2> & R_{12}, <2> & R_{13}, <2> & R_{14}, <2> \\ & & & & R_{21}, <2> & R_{22}, <2> & R_{23}, <2> & R_{24}, <2> \\ & & & & R_{31}, <2> & R_{32}, <2> & R_{33}, <2> & R_{34}, <2> \\ & & & & R_{41}, <2> & R_{42}, <2> & R_{34}, <2> & R_{44}, <2> \end{bmatrix} = \begin{bmatrix} u_{[1]}, <1> \\ u_{[II]}, <1> \\ u_{[III]}, <1> \\ u_{[IV]}, <1> \\ \vdots \\ u_{[1]}, <2> \\ u_{[II]}, <2> \\ u_{[III]}, <2> \\ u_{[IV]}, <2> \end{bmatrix} = \begin{bmatrix} F_{[1]}, <1> \\ F_{[II]}, <1> \\ F_{[III]}, <1> \\ F_{[IV]}, <1> \\ \cdots \\ F_{[1]}, <2> \\ F_{[II]}, <2> \\ F_{[III]}, <2> \\ F_{[IV]}, <2> \end{bmatrix} \quad (4.103)$$

As shown in Table 2, the relation between the unknown in the local matrix and the unknown in the global matrix is as follows:

$$\begin{aligned} u_{[1]}, <1> &= u_{[1]} & , \quad u_{[1]}, <2> &= u_{[2]} \\ u_{[II]}, <1> &= u_{[4]} & , \quad u_{[II]}, <2> &= u_{[3]} \\ u_{[III]}, <1> &= u_{[3]} & , \quad u_{[III]}, <2> &= u_{[4]} \\ u_{[IV]}, <1> &= u_{[2]} & , \quad u_{[IV]}, <2> &= u_{[5]} \end{aligned} \quad (4.104)$$

The global vector \mathbf{F} is computed as the sum of the local vector \mathbf{F} as follows:

$$\begin{aligned} F_{[1]}, <1> &= F_{[1]} \\ F_{[IV]}, <1> + F_{[1]}, <2> &= F_{[2]} \\ F_{[III]}, <1> + F_{[II]}, <2> &= F_{[3]} \\ F_{[II]}, <1> + F_{[III]}, <2> &= F_{[4]} \\ F_{[IV]}, <2> &= F_{[5]} \end{aligned} \quad (4.105)$$

Eq.(4.105) are summarized as follows:

$$\begin{bmatrix} u_{[1]}, <1> \\ u_{[II]}, <1> \\ u_{[III]}, <1> \\ u_{[IV]}, <1> \\ \cdots \\ u_{[1]}, <2> \\ u_{[II]}, <2> \\ u_{[III]}, <2> \\ u_{[IV]}, <2> \end{bmatrix} = \begin{bmatrix} 1 & 0 & 0 & 0 & 0 \\ 0 & 0 & 0 & 1 & 0 \\ 0 & 0 & 1 & 0 & 0 \\ 0 & 1 & 0 & 0 & 0 \\ \cdots & \cdots & \cdots & \cdots & \cdots \\ 0 & 1 & 0 & 0 & 0 \\ 0 & 0 & 1 & 0 & 0 \\ 0 & 0 & 0 & 1 & 0 \\ 0 & 0 & 0 & 0 & 1 \end{bmatrix} \begin{bmatrix} u_{[1]} \\ u_{[2]} \\ u_{[3]} \\ u_{[4]} \\ u_{[5]} \end{bmatrix} \quad (4.106)$$

Eq.(4.106) are summarized as follows:

$$\begin{bmatrix} 1 & 0 & 0 & 0 & \vdots & 0 & 0 & 0 & 0 \\ 0 & 0 & 0 & 1 & \vdots & 1 & 0 & 0 & 0 \\ 0 & 0 & 1 & 0 & \vdots & 0 & 1 & 0 & 0 \\ 0 & 1 & 0 & 0 & \vdots & 0 & 0 & 1 & 0 \\ 0 & 0 & 0 & 0 & \vdots & 0 & 0 & 0 & 1 \end{bmatrix} \begin{bmatrix} F_{[I],<1>} \\ F_{[II],<1>} \\ F_{[III],<1>} \\ F_{[IV],<1>} \\ \vdots \\ F_{[I],<2>} \\ F_{[II],<2>} \\ F_{[III],<2>} \\ F_{[IV],<2>} \end{bmatrix} = \begin{bmatrix} F_{[1]} \\ F_{[2]} \\ F_{[3]} \\ F_{[4]} \\ F_{[5]} \end{bmatrix} \quad (4.107)$$

Eq.(4.106) and Eq.(4.107) are substituted into Eq.(4.103) as follows:

$$\begin{bmatrix} 1 & 0 & 0 & 0 & \vdots & 0 & 0 & 0 & 0 \\ 0 & 0 & 0 & 1 & \vdots & 1 & 0 & 0 & 0 \\ 0 & 0 & 1 & 0 & \vdots & 0 & 1 & 0 & 0 \\ 0 & 1 & 0 & 0 & \vdots & 0 & 0 & 1 & 0 \\ 0 & 0 & 0 & 0 & \vdots & 0 & 0 & 0 & 1 \end{bmatrix} \begin{bmatrix} R_{11,<1>} & R_{12,<1>} & R_{13,<1>} & R_{14,<1>} & \vdots \\ R_{21,<1>} & R_{22,<1>} & R_{23,<1>} & R_{24,<1>} & \vdots \\ R_{31,<1>} & R_{32,<1>} & R_{33,<1>} & R_{34,<1>} & \vdots \\ R_{41,<1>} & R_{42,<1>} & R_{34,<1>} & R_{44,<1>} & \vdots \\ \vdots & \vdots & \vdots & \vdots & \ddots \end{bmatrix} \begin{bmatrix} R_{11,<2>} & R_{12,<2>} & R_{13,<2>} & R_{14,<2>} \\ R_{21,<2>} & R_{22,<2>} & R_{23,<2>} & R_{24,<2>} \\ R_{31,<2>} & R_{32,<2>} & R_{33,<2>} & R_{34,<2>} \\ R_{41,<2>} & R_{42,<2>} & R_{34,<2>} & R_{44,<2>} \end{bmatrix} \\ \begin{bmatrix} 1 & 0 & 0 & 0 & 0 \\ 0 & 0 & 0 & 1 & 0 \\ 0 & 0 & 1 & 0 & 0 \\ 0 & 1 & 0 & 0 & 0 \\ 0 & 0 & 0 & 0 & 1 \end{bmatrix} \begin{bmatrix} u_{[1]} \\ u_{[2]} \\ u_{[3]} \\ u_{[4]} \\ u_{[5]} \end{bmatrix} = \begin{bmatrix} F_{[1]} \\ F_{[2]} \\ F_{[3]} \\ F_{[4]} \\ F_{[5]} \end{bmatrix} \quad (4.108)$$

where Eq.(4.108) is as follows:

$$\begin{bmatrix} R_{11,<1>} & R_{14,<1>} & R_{13,<1>} & R_{12,<1>} & 0 \\ R_{41,<1>} & R_{44,<1>} + R_{11,<2>} & R_{43,<1>} + R_{12,<2>} & R_{42,<1>} + R_{13,<2>} & R_{14,<2>} \\ R_{31,<1>} & R_{34,<1>} + R_{21,<2>} & R_{33,<1>} + R_{22,<2>} & R_{32,<1>} + R_{23,<2>} & R_{24,<2>} \\ R_{21,<1>} & R_{24,<1>} + R_{31,<2>} & R_{23,<1>} + R_{32,<2>} & R_{22,<1>} + R_{33,<2>} & R_{34,<2>} \\ 0 & R_{41,<2>} & R_{42,<2>} & R_{43,<2>} & R_{44,<2>} \end{bmatrix} \begin{bmatrix} u_{[1]} \\ u_{[2]} \\ u_{[3]} \\ u_{[4]} \\ u_{[5]} \end{bmatrix} = \begin{bmatrix} F_{[1]} \\ F_{[2]} \\ F_{[3]} \\ F_{[4]} \\ F_{[5]} \end{bmatrix} \quad (4.109)$$

These operations to obtain the global matrix from the local matrices are executed for all elements.

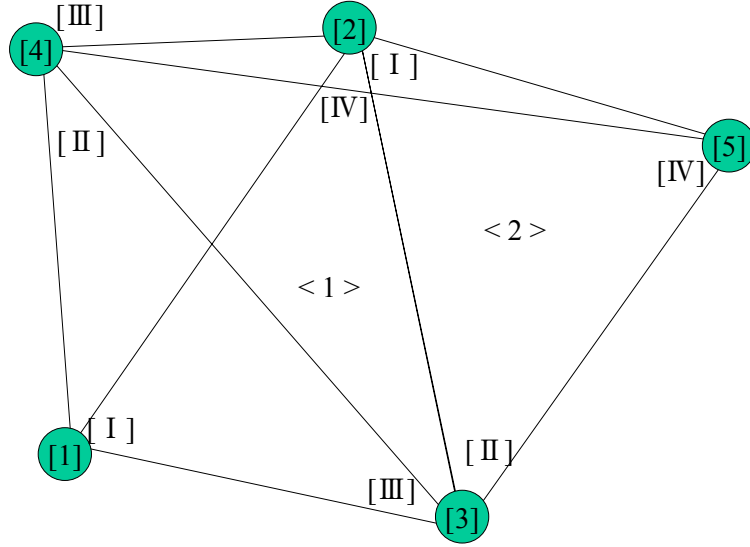


Figure 7. Finite elements in a mesh.

Table 2. Relation of two elements (Figure 7.).

• Element number	• Node [I]	• Node [II]	• Node[III]	• Node[IV]
• < 1 >	• [1]	• [4]	• [3]	• [2]
• < 2 >	• [2]	• [3]	• [4]	• [5]

4.10. Setting of the Boundary Conditions

In the above section, we described the construction of the global matrix. In this section, we describe the setting of the boundary conditions (Dirichlet boundary condition) in the global matrix by using the example shown in Eq.(4.109). The boundary condition $u_{[2]}=a$ (a is a constant) is assumed.

Step 1. The known parameter $F_{[2]}$ is set to the constant "a" in the left hand side vector (the second line) as follows:

$$\begin{bmatrix} R_{11,<1>} & R_{14,<1>} & R_{13,<1>} & R_{12,<1>} & 0 \\ R_{41,<1>} & R_{44,<1>} + R_{11,<2>} & R_{43,<1>} + R_{12,<2>} & R_{42,<1>} + R_{13,<2>} & R_{14,<2>} \\ R_{31,<1>} & R_{34,<1>} + R_{21,<2>} & R_{33,<1>} + R_{22,<2>} & R_{32,<1>} + R_{23,<2>} & R_{24,<2>} \\ R_{21,<1>} & R_{24,<1>} + R_{31,<2>} & R_{23,<1>} + R_{32,<2>} & R_{22,<1>} + R_{33,<2>} & R_{34,<2>} \\ 0 & R_{41,<2>} & R_{42,<2>} & R_{43,<2>} & R_{44,<2>} \end{bmatrix} \cdot \begin{bmatrix} u_{[1]} \\ u_{[2]} \\ u_{[3]} \\ u_{[4]} \\ u_{[5]} \end{bmatrix} = \begin{bmatrix} F_{[1]} \\ a \\ F_{[3]} \\ F_{[4]} \\ F_{[5]} \end{bmatrix} \quad (4.110)$$

Step 2. All elements of left hand side vector but for the second one are modified by using the matrix element R_{ij} as follows:

$$\begin{bmatrix} R_{11,<1>} & R_{14,<1>} & R_{13,<1>} & R_{12,<1>} & 0 \\ R_{41,<1>} & R_{44,<1>} + R_{11,<2>} & R_{43,<1>} + R_{12,<2>} & R_{42,<1>} + R_{13,<2>} & R_{14,<2>} \\ R_{31,<1>} & R_{34,<1>} + R_{21,<2>} & R_{33,<1>} + R_{22,<2>} & R_{32,<1>} + R_{23,<2>} & R_{24,<2>} \\ R_{21,<1>} & R_{24,<1>} + R_{31,<2>} & R_{23,<1>} + R_{32,<2>} & R_{22,<1>} + R_{33,<2>} & R_{34,<2>} \\ 0 & R_{41,<2>} & R_{42,<2>} & R_{43,<2>} & R_{44,<2>} \end{bmatrix} \cdot \begin{bmatrix} u[1] \\ u[2] \\ u[3] \\ u[4] \\ u[5] \end{bmatrix} = \begin{bmatrix} F_{[1]} - aR_{14,<1>} \\ a \\ F_{[3]} - a(R_{34,<1>} + R_{21,<2>}) \\ F_{[4]} - a(R_{24,<1>} + R_{31,<2>}) \\ F_{[5]} - aR_{41,<2>} \end{bmatrix} \quad (4.111)$$

Step 3. The elements in the second line and the second column are set to the zero. The element at the intersection between the two is set to 1.

$$\begin{bmatrix} R_{11,<1>} & 0 & R_{13,<1>} & R_{12,<1>} & 0 \\ 0 & 1 & 0 & 0 & 0 \\ R_{31,<1>} & 0 & R_{33,<1>} + R_{22,<2>} & R_{32,<1>} + R_{23,<2>} & R_{24,<2>} \\ R_{21,<1>} & 0 & R_{23,<1>} + R_{32,<2>} & R_{22,<1>} + R_{33,<2>} & R_{34,<2>} \\ 0 & 0 & R_{42,<2>} & R_{43,<2>} & R_{44,<2>} \end{bmatrix} \cdot \begin{bmatrix} u[1] \\ u[2] \\ u[3] \\ u[4] \\ u[5] \end{bmatrix} = \begin{bmatrix} F_{[1]} - aR_{14,<1>} \\ a \\ F_{[3]} - a(R_{34,<1>} + R_{21,<2>}) \\ F_{[4]} - a(R_{24,<1>} + R_{31,<2>}) \\ F_{[5]} - aR_{41,<2>} \end{bmatrix} \quad (4.112)$$

Step 4. The variable $u_{[ij]}$ ($i=1 \sim n$) is calculated by using the HEC-MW solver [49].

In a similar way, the same operations are applied to the general matrix. In the pressure-Poisson equation (Eq.(4.82)), a solver for the linear simultaneous system of linear equations is used afterwards. In this study, we used the parallel library HEC-MW to solve the Poisson equation [49]. By using the mass-lumped matrix in the calculation of the unknown parameter \mathbf{u} (Eq.(4.81) etc.) we avoid the calculation of the inverse matrix.

5. IMPLEMENTATION

5.1. Shape Optimization Algorithm

The algorithm of the shape optimization method is shown in Fig.8. As described before, we used Oseen's approximation to derive the first variation in the convective term. For computing of the fluid analysis, the Navier-Stokes equations are used. Before executing the algorithm, the Navier-Stokes equations are solved until the flow field reaches steady state.

In the first phase of the algorithm, the state variables (W) are calculated by using the state equations. The state equations are solved from the test of start time to the test of end time. All the nodal values of the state variables (W) are stored at every time step.

In the second phase of the algorithm, the adjoint variables (λ) are calculated by Eq.(2.35)-(2.38) from the test of end time to the test of start time. The adjoint equations, which include the time derivative, are also solved until the adjoint flow field reaches the steady state. All the nodal values of the adjoint variables (λ) are saved at every time step. This data is stored as files.

In the third phase, the sensitivity at every time step is calculated by using the saved files containing the adjoint and state variables. The sensitivity represents the displacement of the nodes on the surface of the object and must have a small value in order to robustly converge to the optimal coordinates and to avoid collapse of the mesh topology.

In the fourth phase, the shape is modified by using the time integral sensitivity. The optimization method is the gradient method. After that, the nodes of the mesh are relocated

according to the time integral sensitivity. The node relocation is performed by using the biharmonic equation.

In the fifth phase, the shape is modified in order to satisfy the constraint of constant volume.

In case the shape converges to the optimum, the result is outputted. In the case that the shape doesn't converge to the optimum, the algorithm returns to the first phase.

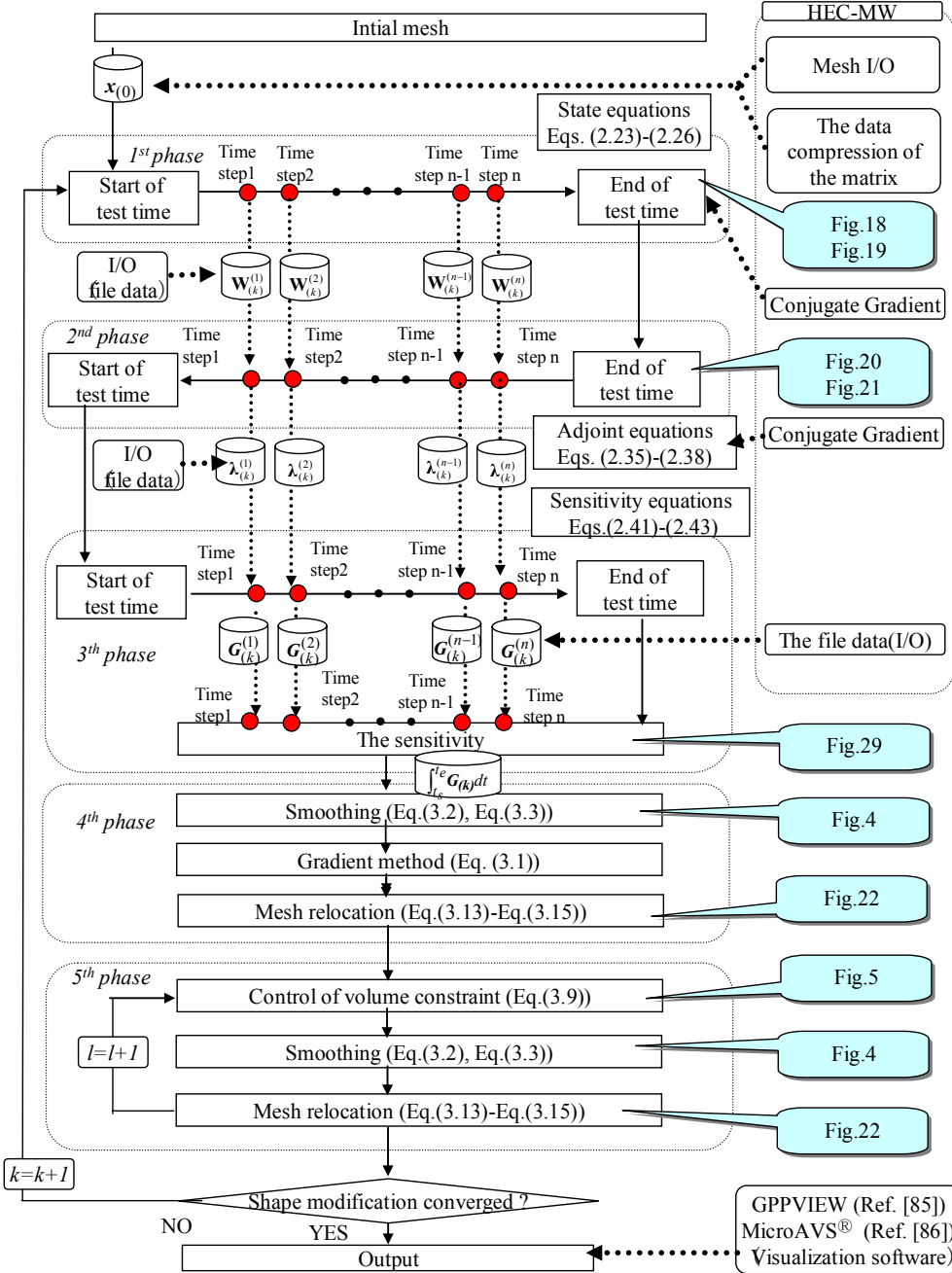


Figure 8. Shape optimization algorithm by the adjoint variable method.

(Note)

The setting of the initial conditions after the deformed shape (the shape step (k)) is one of the important problems. We can consider that the values of the nodes are modified by using the interpolation function. In this study, the values of the nodes for the test of the start time(t_s) and the end time(t_e) in the shape step (k) are used as the ones in the shape step (k). In the fluid analysis, the state variables for the test of the start time in the shape step(k) are used as the ones for the test of the start time in the shape ($k+1$). In the adjoint analysis, the adjoint variables for the test of the end time in the shape step(k) are used as the ones for the test of the end time in the shape step($k+1$). As other initial conditions, we can use the same initial conditions in the shape step one (the state variables and the adjoint variables) for every shape steps. However, the deformed shape becomes dull and the sharp edge can not be constructed in this conditions.

5.2. HEC-MW

Parallel computing requires some unique techniques, such as the domain decomposition, message passing, vectorization etc. This extra work is very burdensome for application developers; the implementation is very time-consuming and often causes numerous bugs. In addition, since recently available architectures vary from PC-clusters to SMP clusters, the optimization strategies to make the best use of the hardware are no longer unique. Therefore, parallel software such as HEC Middleware(HPC-MW) [49][50], WARP3D[91], FEAST (Finite Element Analysis & Solutions Tools) [92] , Adventure[90], PCP (Parallel Computing Platform) [93] , Salinas (a scalable software for high-performance structural and solid mechanics simulations) [94] and so on where developed in order to enable the user to easily implement the algorithm of the calculation and efficiently handle and distribute the computation load. For developing the parallel finite element fluid analysis code, the present study employs the “HEC Middleware”, which has been developed within the project named “Frontier Simulation Software for Industrial Science” at the Institute of Industrial Science (IIS), The University of Tokyo, as a research project of the IT-program under Research Revolution 2002 organized by Ministry of Education, Culture, Sport, Science and Technology, Japan.

The HEC Middleware (HEC-MW) is a hardware-independent platform, which extracts patterns of calculation processes and common interfaces of unstructured grid simulations. A program developed on a PC is automatically optimized for each high-end machine by plugging-in the installed HEC-MW (Fig.9).

By simply installing HEC-MW and calling the appropriate subroutine, complex computations can be performed. Thus, HEC-MW enables the development of portable and highly reliable simulation code.

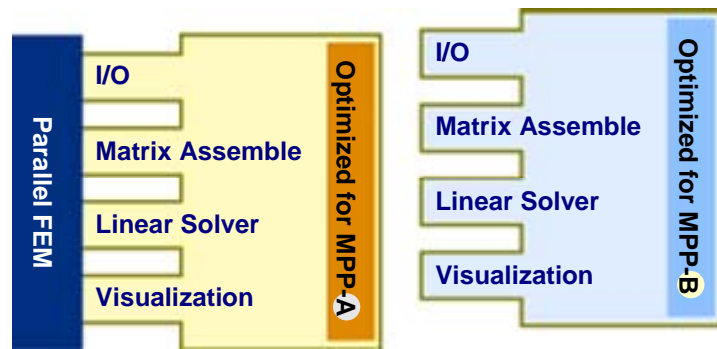


Figure 9. Utilization of HEC-MW.

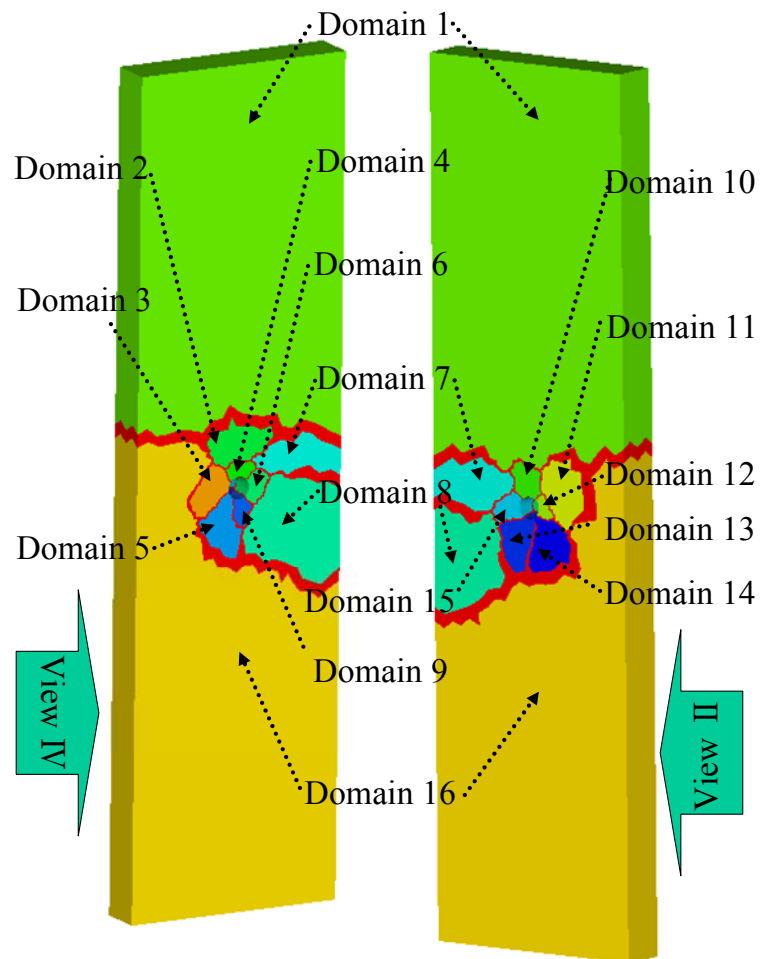


Figure 10. Domain decomposition.

5.3. Parallel Computing by Using Domain Decomposition and CRS Format

By using HEC-MW, the calculation load is processed in parallel, on a PC cluster environment consisting of 16 CPUs. As shown in Fig.10, the computational domain is divided in 16 parts which enable distributed processing on 16 CPUs in the PC cluster environment.

The "hecmw-part" from HEC-MW is used as partitioner for domain decomposition. From the decomposition method, it provides METIS [81] (based on graph theory and RCB (based on recursive coordinate bisection). We selected the former.

From the point of view of memory organization, parallel computers can be either of shared memory type, where all processors share the same memory, or of distributed memory type, where each processor uses a different memory. The shared memory type organization may perform slower due to processors competing for reading or writing. Because of this fact, the distributed memory type has been adopted. Data for different domain is stored in different memories. In order to minimize memory requirements and maximize performance, unnecessary data and communication have to be removed. HEC-MW extracts non-zero elements from two dimensional matrices and compresses them to one dimensional vectors which do not include zero elements. This matrix storage format is known as CRS (Compressed Row Storage).

The conversion algorithm to the CRS format is shown in Fig.11. In HEC-MW, the 2D matrix is divided into an upper triangular matrix, a lower triangular matrix and a diagonal matrix. First, the two dimensional matrix is made from the mesh data (the node coordinates and the connectivities). Following, the location information of the nonzero elements in the 2D matrix are selected. Last, this location information is stored as a 1D array. The algorithm in Fig.11 mainly consists of eight steps.

- 1 • for i=1,2, ... ,n_elem
- 2 • iS = elem_index(i)
- 3 •
- 4 • for j=1,2,3,4
- 5 • c(j)=Connectivity(iS+j)
- 6 • end
- 7 •
- 8 • for j=1,2,3,4
- 9 •
- 10 • for k=1,2,3,4
- 11 • if k≠j
- 12 • if c(j) > c(k)
- 13 •
- 14 • for m=1,2, ... ,INL(c(j))
- 15 • If c(k)=IAL(c(j) , m) goto line 10
- 16 • end
- 17 • INL(c(j))=INL(c(j))+1
- 18 • IAL(c(j) ,INL(c(j)))=c(k)
- 19 • endif
- 20 •

- 21 • If $c(k) > c(j)$
- 22 • for $m=1, 2, \dots, INU(c(j))$
- 23 • If $c(k) = IAL(c(j), m)$ goto line 10
- 24 • end
- 25 • $INU(c(j)) = INU(c(j)) + 1$
- 26 • $IAU(c(j), INU(c(j))) = c(k)$
- 27 • endif
- 28 •
- 29 • endif
- 30 •
- 31 • for $i=1, 2, \dots, n_node$
- 32 • for $k=1, 2, \dots, INL(i)$
- 33 • $NC(k) = IAL(i, k)$
- 34 • end
- 35 •
- 36 • for $ii=1, 2, \dots, INL(i)$
- 37 • $IN(ii) = ii$
- 38 • end
- 39 •
- 40 • for $ii=1, 2, \dots, INL(i)-1$
- 41 • for $jj=1, 2, \dots, INL(i)-ii$
- 42 • if $NC(IN(jj)) < NC(IN(jj+1))$
- 43 • $IT = IN(jj+1)$
- 44 • $IN(jj+1) = IN(jj)$
- 45 • $IN(jj) = IT$
- 46 • endif
- 47 • end
- 48 • end
- 49 •
- 50 • for $k=INL(i), \dots, 1$
- 51 • $IAL(i, INL(i)-k+1) = NC(IN(k))$
- 52 • end
- 53 •
- 54 • for $k=1, 2, \dots, INU(i)$
- 55 • $NC(k) = IAU(i, k)$
- 56 • end
- 57 •
- 58 • for $ii=1, 2, \dots, INU(i)$
- 59 • $IN(ii) = ii$
- 60 • end
- 61 •
- 62 • for $ii=1, 2, \dots, INU(i)-1$
- 63 • for $jj=1, 2, \dots, INU(i)-ii$
- 64 • if $NC(IN(jj)) < NC(IN(jj+1))$
- 65 • $IT = IN(jj+1)$
- 66 • $IN(jj+1) = IN(jj)$
- 67 • $IN(jj) = IT$

```

• 68      • endif
• 69      • end
• 70      • end
• 71      •
• 72      • for k=INU(i) , ...,2 ,1
• 73      • IAU(i,INU(i)-k+1)=NC(IN(k))
• 74      • end
• 75      •
• 76      • end
• 77      •
• 78      • for i=1,2, .... , n_node
• 79      • indexL(i)=indexL(i-1)+INL(i)
• 80      • indexU(i)=indexU(i-1)+INU(i)
• 81      • end
• 82      •
• 83      • for i=1,2, ... ,n_node
• 84      • for k=1,2, ... , INL(i)
• 85      •   kk=k+indexL(i-1)
• 86      •   itemL(kk)=IAL(i,k)
• 87      • end
• 88      • for k=1,2, ... , INU(i)
• 89      •   kk=k+indexU(i-1)
• 90      •   itemU(kk)=IAU(i,k)
• 91      • end
• 92      • end

```

Figure 11. The algorithm to extract the nonzero elements in a matrix.

Step 1. (1 line ~ 2 line): The index (iS) of the element number is extracted from the mesh data.

Step 2. (4 line ~ 6 line): The four node numbers are extracted from the index (iS). (A tetrahedral element is used in this study)

Step 3. (8 line ~ 11 line): Two node numbers out of the total four are selected (the node numbers do not overlap)

Step 4. (12 line ~ 19 line): For the lower triangular matrix, the location information of non-zero elements is stored.

Step 4-1. (17 line ~ 18 line)

The node numbers correspond to both rows and columns in the matrix. In the diagonal position, a non-zero element always exists. For the lower triangular matrix, the $INL(c(j))$ shows the number of non-zero elements under the $c(j)$ row. For example, the element number <2> in Fig.7 is assumed to be extracted. The node numbers for the element number <2> are [2],[3],[4],[5], by the connectivity information. The element locations under the lower triangular matrix are [3] row [2] column, [4] row [2] column, [4] row [3] column, [5] row [2] column, [5] row [3] column and [5] row [4] column. As shown in Fig.12, the first of the

nonzero elements is in the third row ($INL([3])=1$), the second in the fourth row ($INL([4])=2$) and the third in the fifth row ($INL([5])=3$) etc. The column numbers are stored according to the small number order at each row number (18 line in Fig.11).

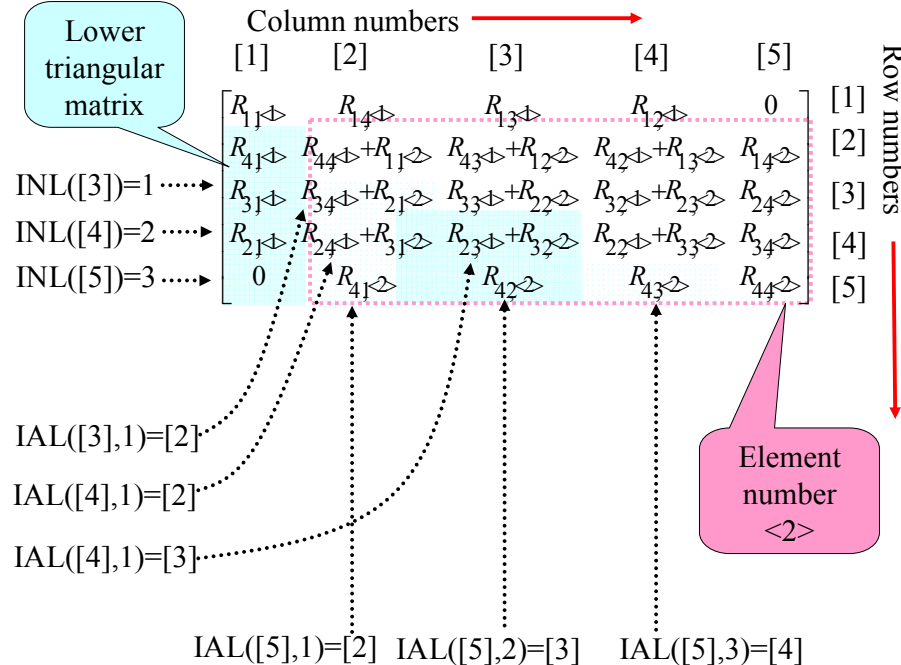


Figure 12. Matrix.

Step 4-2. (14 line ~ 16 line)

The overlaps in the array IAL are checked.

Step 5. (21 line ~ 27 line): For the upper triangular matrix, step 5 of the algorithm is carried out in the similar manner to step 4.

Step 6. (31 line ~ 48 line): According to the small column number with respect to the i row number, the number $NC(k)$ in the equation ($IAL(i,j)=NC(k)$) is ordered according to the small number. The bandwidth of the resulting matrix depends on how the node numbering is done. In this step, we use an algorithm to reduce the bandwidth and also do preprocessing for the Solver.

Step 6-1. (31 line ~ 34 line)

For the lower triangle line, the column number corresponding to nonzero elements with respect to the row i are extracted in order and stored in the array $NC(k)$.

Step 6-2. (40 line ~ 48 line)

Two neighboring column numbers are selected. The larger of the two moves to the right side in the matrix while the smaller one moves to the left side. For example, the order of the array $NC(k)$ is assumed to be $NC(1)=4, NC(2)=2, NC(3)=1, NC(4)=3$ and $NC(5)=5$, as shown in Fig.13. As the indexes ii and jj advance, the column numbers are ordered.

Step 7. (62 line ~ 76 line): In step 6, the nonzero elements are stored for the lower triangular matrix. In this step, the same operations are applied to the upper triangular one.

Step 8. (78 line ~ 92 line): A 1D array containing only nonzero elements stores all the needed information from the previous 2D matrix (which contained zero elements as well). The vector $itemL(kk)$ stores the summarized nonzero elements at each row in the lower triangle matrix. By using the array $indexL$, the location information of the nonzero elements can be extracted from the array $itemL(kk)$. For example in Eq.(4.109), the relation between the $itemL$ and the $indexL$ is shown in Fig.14. The relation of the [5] row and the [4] column in the matrix is $itemL(indexL(3)+3)=R_{43,<2>}=4$.

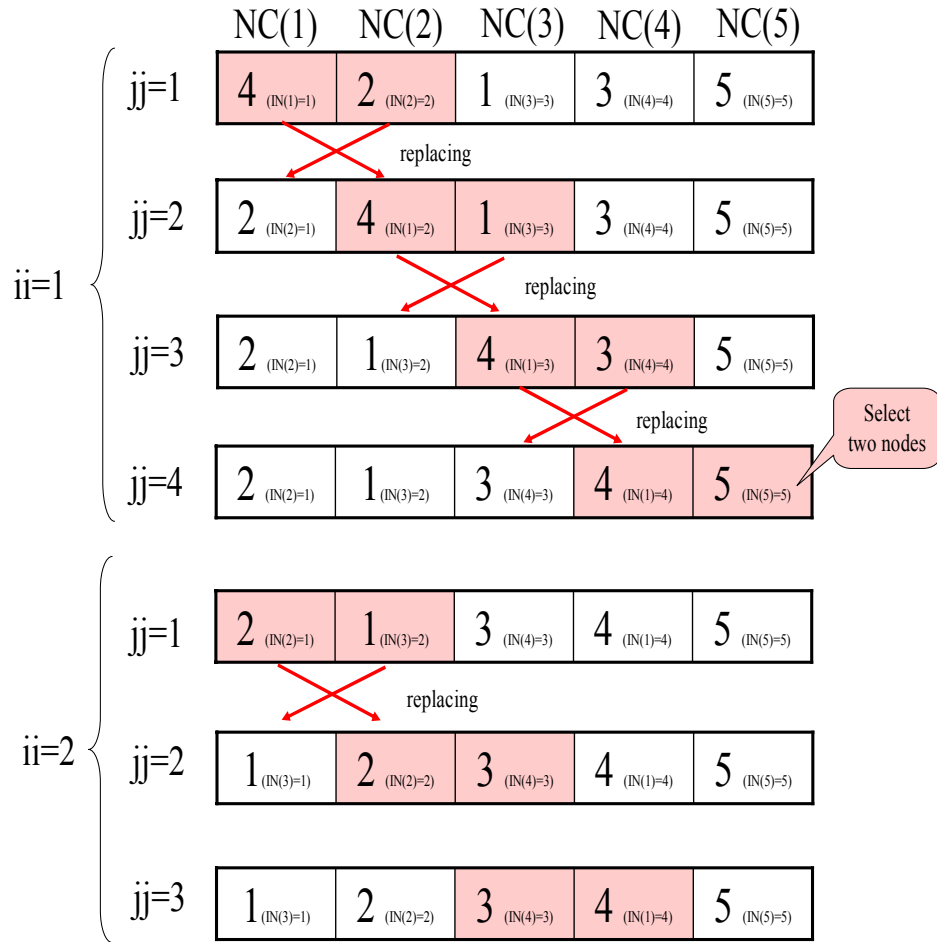


Figure 13. Ordering.

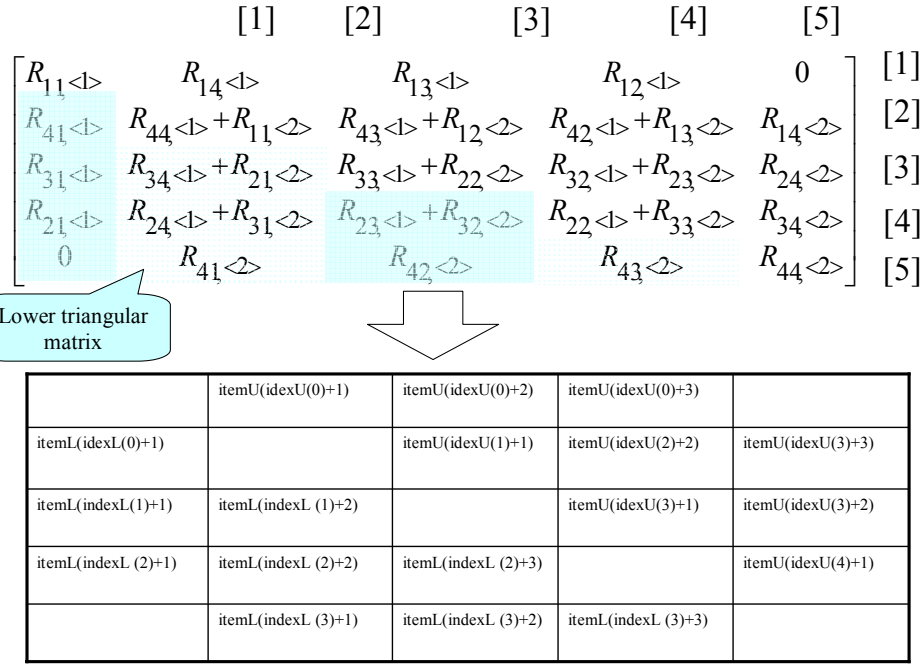


Figure 14. Ordering.

Table 3. Variables in Figure 11 and Figure 15.

• n_elem	• The number of the element in the mesh
• n_node	• The number of the node in the mesh
• Conectivity	• The node connectivity
• INL(i)	• The number of the nonzero elements with respect to the row i under the lower triangular matrix.
• IAL(i,j)	• The nonzero elements at the number j^{th} with respect to the row i
• INU(i)	• The number of the nonzero elements with respect to the column i under the upper triangular matrix.
• IAU(i,j)	• The nonzero elements at the number j^{th} with respect to the column i
• indexU	• The index in the array "itemU" to divide at each row number.
• indexL	• The index in the array "itemL" to divide at each row number.
• itemU	• The column number with respect to the row number i for the upper triangular matrix.
• itemL	• The column number with respect to the row number i for the lower triangular matrix.
• AU	• The 1D array for the upper triangular matrix
• AL	• The 1D array for the lower triangular matrix
• D	• The 1D array for the diagonal matrix
• ALD	• The 1D array for the diagonal inverse matrix

5.4. Operations Using the CRS Format

Now that the matrix is stored in compressed format, all operations involving the matrix (e.g. matrix \times vector) have to be able to use the matrix in this form. Once again, we have to obtain the line number and the column number with respect to the nonzero-elements. In Fig.15, we show the algorithm for assembling the global matrix from local matrices, in compressed format, used before the solver process. This algorithm is based on the first order tetrahedron elements.

```

• 1           •      for i= 1, 4
• 2           •      for j= 1, 4
• 3           •      if c(j) > c(i)
• 4           •      S=indexU(c(i)-1) + 1
• 5           •      E=indexU(c(i) )
• 6           •      do k= S, E
• 7           •      if itemU(k)=c(j)
• 8           •          kk= k
• 9           •      endif
• 10          •      end
• 11          •      endif
• 12          •      if c(j) < c(i)
• 13          •      S= indexL(c(i)-1) + 1
• 14          •      E= indexL(c(i) )
• 15          •      do k= S, E
• 16          •      if itemL(k)=c(j)
• 17          •          kk= k
• 18          •      endif
• 19          •      end
• 20          •      endif
• 21          •      if c(j) > c(i)
• 22          •          AU(9×kk-8)=AU(9×kk-8)+s11
• 23          •          AU(9×kk-7)=AU(9×kk-7)+s12
• 24          •          AU(9×kk-6)=AU(9×kk-6)+s13
• 25          •          AU(9×kk-5)=AU(9×kk-5)+s21
• 26          •          AU(9×kk-4)=AU(9×kk-4)+s22
• 27          •          AU(9×kk-3)=AU(9×kk-3)+s23
• 28          •          AU(9×kk-2)=AU(9×kk-2)+s31
• 29          •          AU(9×kk-1)=AU(9×kk-1)+s32
• 30          •          AU(9×kk )=AU(9×kk )+s33
• 31          •      endif
• 32          •      if c(j) < c(i)
• 33          •          AL(9×kk-8)=AL(9×kk-8)+s11
• 34          •          AL(9×kk-7)=AL(9×kk-7)+s12
• 35          •          AL(9×kk-6)=AL(9×kk-6)+s13
• 36          •          AL(9×kk-5)=AL(9×kk-5)+s21
• 37          •          AL(9×kk-4)=AL(9×kk-4)+s22

```

```

• 38      •          AL(9×kk-3)=AL(9×kk-3)+s23
• 39      •          AL(9×kk-2)=AL(9×kk-2)+s31
• 40      •          AL(9×kk-1)=AL(9×kk-1)+s32
• 41      •          AL(9×kk )=AL(9×kk )+s33
• 42      •          endif
• 43      •          if c(j)=c(i)
• 44      •              D(9×c(i)-8)=D(9×c(i)-8)+s11
• 45      •              D(9×c(i)-7)=D(9×c(i)-7)+s12
• 46      •              D(9×c(i)-6)=D(9×c(i)-6)+s13
• 47      •              D(9×c(i)-5)=D(9×c(i)-5)+s21
• 48      •              D(9×c(i)-4)=D(9×c(i)-4)+s22
• 49      •              D(9×c(i)-3)=D(9×c(i)-3)+s23
• 50      •              D(9×c(i)-2)=D(9×c(i)-2)+s31
• 51      •              D(9×c(i)-1)=D(9×c(i)-1)+s32
• 52      •              D(9×c(i) )=D(9×c(i) )+s33
• 53      •          endif
• 54      •          enddo
• 55      •          enddo
• 56      •          enddo
• 57      •          enddo

```

Figure 15. The algorithm of making the global matrix (Eq.(4.109)).

This algorithm mainly consists of the two step process.

Step 1. (1 line ~ 20 line): The index is extracted to construct the global matrix.

Step 1-1. The index of the upper triangular matrix is extracted (4 line ~ 11 line)

The global matrix is constructed by using the 1D array which stores the data in the upper triangular matrix, the lower triangular matrix and the diagonal matrix. First, the array *indexU* is extracted as shown in Fig.16. The coefficient a_{ij} is the element at i row and j column. The two node number ($c(i)$, $c(j)$) by using the connectivity information(in Fig.11 at 5 line) is selected. $c(i)$ is the row number. $c(j)$ is the column number. In the case $c(j)>c(i)$, the element in the $c(i)$ row and the $c(j)$ column is the element in the upper triangular matrix. The 1D array *itemU* have the row number of the nonzero-elements from the small line number to the large number in order. By using the 1D array *indexU*, the column number *itemU* with respect to the row number can be extracted as shown in Fig.16. *S* shows the start number in the array *indexU* with respect to the row number i . *E* shows the end number in the array *indexU* with respect to the row number i . The array *itemU* in the interval between *S* and *E* store the column number information with respect to $c(i)$ row number.

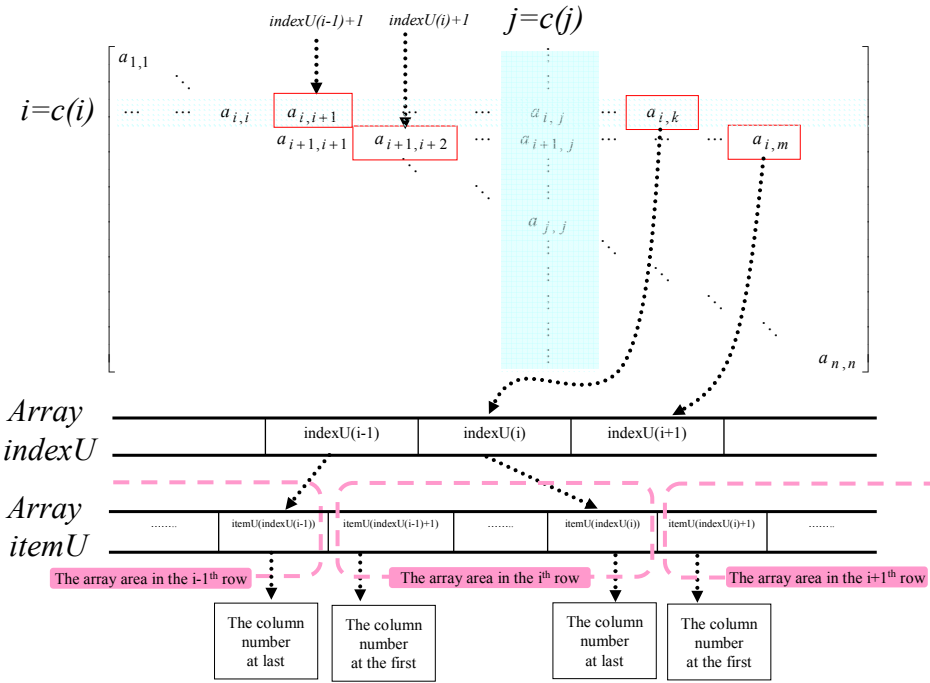


Figure 16. Matrix and array.

Step 1-2. The index of the lower triangular matrix is extracted in a similar way to the previous step (12 line ~ 20 line)

Step 2. (21 line ~ 57 line): The local matrix is added to the global matrix. (see section 4.9) The "Line" represents the line number in Fig.15. The operations in step 2 are an example for the viscous term in Navier-Stokes equations.

Step 2-1. The upper triangular matrix

22 line : S_{11} (Eq.(4.57)) is added to the global matrix in Eq.(2.24).

23 line : S_{12} (Eq.(4.58)) is added to the global matrix in Eq.(2.24).

24 line : S_{13} (Eq.(4.59)) is added to the global matrix. in Eq.(2.24)

25 line : S_{21} (Eq.(4.60)) is added to the global matrix in Eq.(2.25).

26 line : S_{22} (Eq.(4.61)) is added to the global matrix in Eq.(2.25).

27 line : S_{23} (Eq.(4.62)) is added to the global matrix in Eq.(2.25).

28 line : S_{31} (Eq.(4.63)) is added to the global matrix in Eq.(2.26).

29 line : S_{32} (Eq.(4.64)) is added to the global matrix in Eq.(2.26).

30 line : S_{33} (Eq.(4.65)) is added to the global matrix in Eq.(2.26).

Step 2-2. The lower triangular matrix

33 line : S_{11} (Eq.(4.57)) is added to the global matrix in Eq.(2.24).

34 line : S_{12} (Eq.(4.58)) is added to the global matrix in Eq.(2.24).

35 line : S_{13} (Eq.(4.59)) is added to the global matrix in Eq.(2.24).

-
- 36 line : S_{21} (Eq.(4.60)) is added to the global matrix in Eq.(2.25).
 37 line : S_{22} (Eq.(4.61)) is added to the global matrix in Eq.(2.25).
 38 line : S_{23} (Eq.(4.62)) is added to the global matrix in Eq.(2.25).
 39 line : S_{31} (Eq.(4.63)) is added to the global matrix in Eq.(2.26).
 40 line : S_{32} (Eq.(4.64)) is added to the global matrix in Eq.(2.26).
 41 line : S_{33} (Eq.(4.65)) is added to the global matrix in Eq.(2.26).

Step 2-3. The diagonal matrix

In the diagonal matrix, there are the nonzero elements except for the coefficient zero. Therefore, the index is not needed. The selected row and column are directly used.

- 44 line : S_{11} (Eq.(4.57)) is added to the global matrix in Eq.(2.24).
 45 line : S_{12} (Eq.(4.58)) is added to the global matrix in Eq.(2.24).
 46 line : S_{13} (Eq.(4.59)) is added to the global matrix in Eq.(2.24).
 47 line : S_{21} (Eq.(4.60)) is added to the global matrix in Eq.(2.25).
 48 line : S_{22} (Eq.(4.61)) is added to the global matrix in Eq.(2.25).
 49 line : S_{23} (Eq.(4.62)) is added to the global matrix in Eq.(2.25).
 50 line : S_{31} (Eq.(4.63)) is added to the global matrix in Eq.(2.26).
 51 line : S_{32} (Eq.(4.64)) is added to the global matrix in Eq.(2.26).
 52 line : S_{33} (Eq.(4.65)) is added to the global matrix in Eq.(2.26).

The coefficients ($b_{ij}, c_{ij}, d_{ij}, V_{<e>} , etc.$) in the matrix are needed before Step 2. In the detailed version of the algorithm, we can obtain the "static_LIB_3d1.f" [49]. The above operations are an example for the viscous term. Similarly, the same operations are applied to the time derivative term, the convective term and the pressure term. First, the left side in Eq.(4.109) is constructed. Next, the right hand side vector in Eq.(4.109) is constructed. Last, the boundary condition is set as shown in Eq.(4.112). In the detailed version, we **can** obtain something similar to the program "psan_mat_ass_main.f" [49]. By using the array in Fig.15, the system of linear equations is solved. In HEC-MW, only one line is added to the previously written code, as follows::

```
call hpcmw_solver_33(hpcMESH, hpcMAT)
```

The hpcMESH, hpcMAT show the structure in the hpcmw[50]. By this subroutine, the following three operations are executed:

$$\begin{aligned} & S_{11} \times u_1 + S_{12} \times u_2 + S_{13} \times u_3 \text{ (in the Eq.(4.81))} \\ & S_{21} \times u_1 + S_{22} \times u_2 + S_{23} \times u_3 \\ & S_{31} \times u_1 + S_{32} \times u_2 + S_{33} \times u_3 \end{aligned}$$

where $u_1 \sim u_3$ show the velocity vector. By using the subroutine from *HEC-MW*, the calculation load in the operation is automatically distributed in the PC cluster environment. One can obtain the full version of the algorithm from *hpcmw_solver_33.f* from the following address:

URL : http://www.ciss.iis.u-tokyo.ac.jp/rss21/en/result/download_fsis/index.php

The algorithm in section 5.3 is described in the *psan_mat_con0.f* and the *psan_mat_con1.f* (The folder name : *pSAN-hpcmw-2.00*). The algorithm to construct the finite element equation by CRS format is described in the *psan_mat_ass_main.f* in the *pSAN-hpcmw-2.00*. The solver based on the finite element equation by CRS format is described in the folder name : *hpcmw-2.00*.

6. SHAPE OPTIMIZATION OBJECTS IN FLOW

6.1. Calculation Model and Conditions

The calculation conditions are shown in Table 4. The mesh is shown in Fig. 17. The mesh resolution is 44,039 nodes and 246,343 elements. Using the low resolution mesh, the sharpened ends of the optimal shape can not be constructed; the resulting shape is rather rounded at the ends. Therefore, a high resolution mesh is required. We chose the element type to be a 4-node tetrahedron. The *P1-P1* element with linear shape functions for velocity and pressure is used. Therefore, the tractions on the boundary Γ_E are treated as " $p=0$ " and the adjoint tractions on the boundary Γ_E are treated as " $\lambda_i=0$ " while computing the shape optimization. The inflow velocity in the boundary Γ_E is 1.0 and the Reynolds number is 100. The representative flow is set as $(U_1, U_2, U_3)=(0, 0, 0)$ in the adjoint and sensitivity equations. The parameter ω (Eq.(3.5)-Eq.(3.7)) is set as $\omega=0.1$. The cylinder surface is shown in Fig. 17. The cylinder is divided into about 70 sections along circumferential direction and about 60 sections along the longitudinal direction. The time step size is 0.001 as shown in Table 4. Because of the mesh deformation, the element size around the optimal shape is smaller than the one from the initial shape. The fluid analysis often causes numerical oscillation because the CFL condition is not satisfied. Therefore, the time step size Δt has to be smaller than the one of the initial shape in the optimization calculation.

We used Adventure CAD [90] to make the mesh and GppView[85], MiroAVS[®][86] and Meshman Viewer[96] to visualize the calculation results.

Table 4. Analysis conditions.

Parameter	Value (Dimensionless)
Density	100.0
Viscosity	1.0
Inlet velocity	1.0
Cylinder diameter	1.0
Cylinder volume	1.57
Number of elements	246343
Number of nodes	44039
Time step size	0.001
The representative flow	$(U_1, U_2, U_3)=(0, 0, 0)$

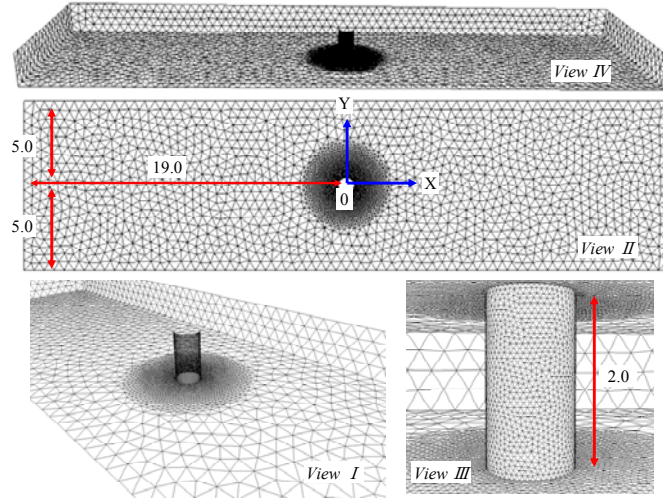


Figure 17. Mesh.

6.2. Flow fields

In Fig.18 and Fig.19, the velocity vector and the pressure contour at 300(s) are shown. In Fig.23, we show the drag coefficient (the x axis). This coefficient is calculated as follows:

$$C_D = \frac{2F}{\rho U_1^2 (L \cdot d)} \quad (6.1)$$

where L , d and F represents the height ($L=2.0$), the diameter ($d=1.0$) and the drag respectively. Comparing the calculation of the drag coefficients and of the Strouhal Number to the ones found in literature [72][77], the accuracy of the solver can be checked.

The accuracy of the drag coefficient generally depends on the distance between the cylinder and the boundary [95], the mesh resolution, the height of the cylinder and the scheme of the fluid. The calculations are performed until the flow field converges to a periodic state.

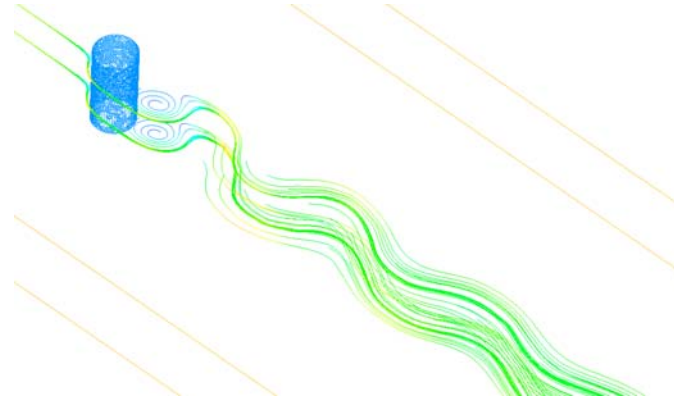


Figure 18. Streamline of initial shape (Streamline (View I in Fig.2)) (300(s)) (the initial shape).

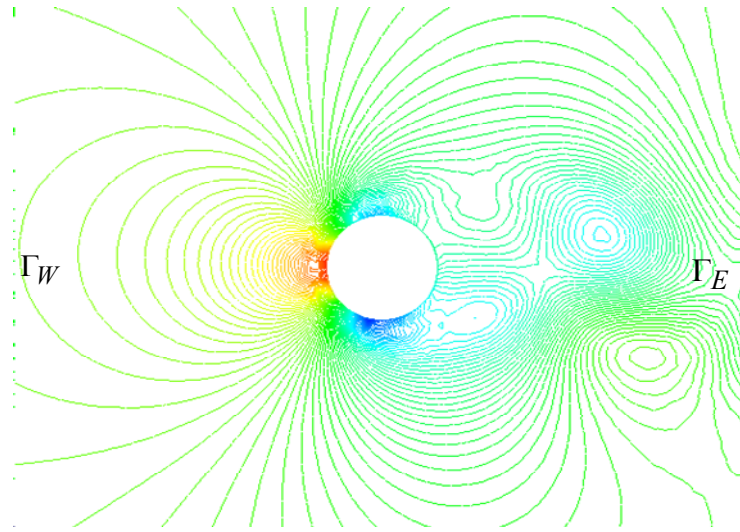


Figure 19. Pressure contour (View \square in Fig.2) (300(s)) (the initial shape).

In Fig.20 and Fig.21, we show the adjoint velocity vector and the adjoint pressure contour at time 200(s). The flow speed (the state variable) decreases behind the downstream cylinder, while the adjoint flow speed (the adjoint variable) increases behind the upstream cylinder. The fluid flows from the inlet Γ_w to the outlet Γ_E . The adjoint fluid flows from the inlet behind the cylinder (the boundary Γ_E side), turns in the computational domain and finally reaches the outlet in front of the cylinder (the boundary Γ_w side).

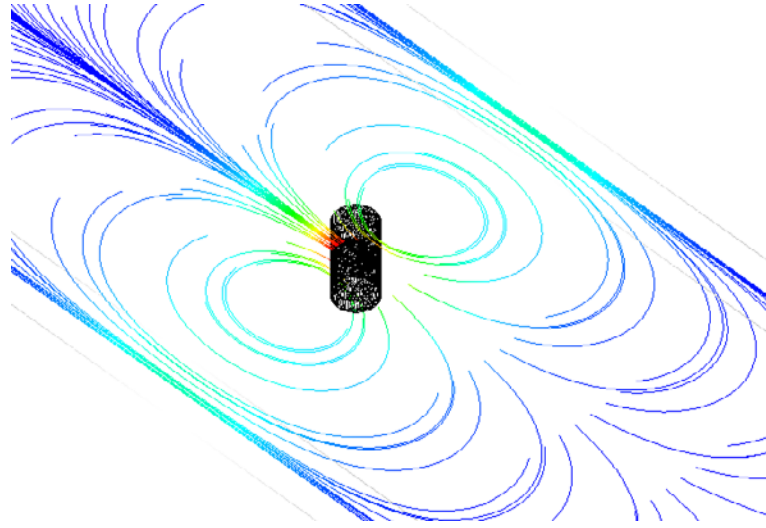


Figure 20. Adjoint streamline of initial shape (Streamline (View \square in Fig.2)) (200(s)) (the initial shape).

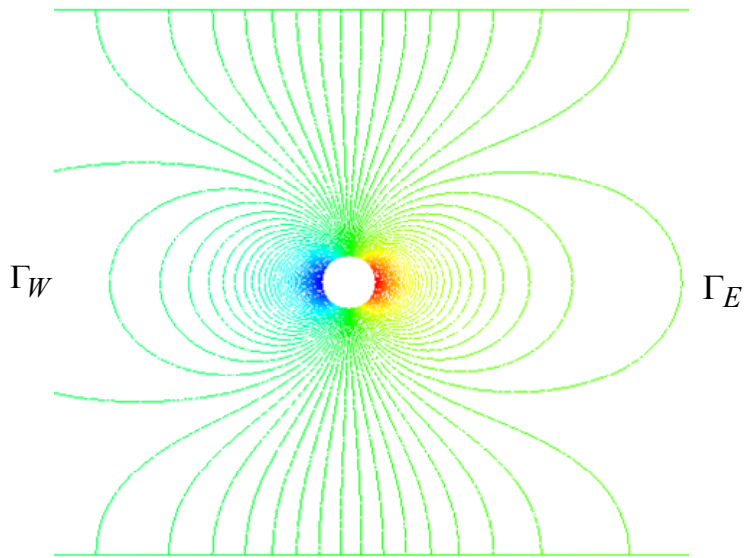


Figure 21. Adjoint pressure contour (View □ in Fig.2) (200(s)) (the initial shape).

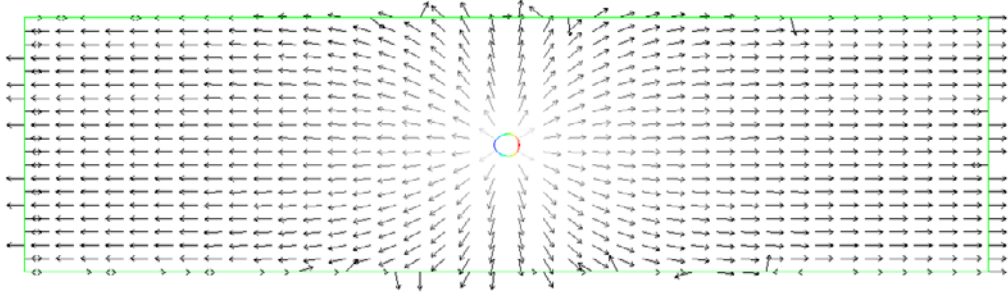


Figure 22. The directions of movement of nodes (View □ in Fig.2) (the initial shape).

6.3. Calculation Results

For Eq.(B23), we take two cases (denoted by case □ and case □) to check the effectiveness of the adjoint variable with respect to the optimal shape. The drag coefficient for the initial shape is shown in Fig.23, Fig.25 and Fig.27. This coefficient is almost in agreement with the coefficients reported in literature [72][77]. The time history of the adjoint drag is shown in Fig.24, Fig.26 and Fig.28. In the time 300(s), the adjoint variable λ is zero. In the case□, the test of the start time is 280(s) and the test of the end time is 300(s), therefore $\lambda(t_e) \neq \lambda(t_s)$. In the case□, the test of the start time is 100(s) and the test of the end time is 120(s), therefore $\lambda(t_e) = \lambda(t_s)$. The streamline of the initial shape is shown in Fig.18. We confirm that Karman vortices are generated in the computational domain. The sensitivity distribution in case □ is shown in Fig.29. As the shape step advances, the sensitivity distribution reaches zero and the initial shape reaches the optimal shape. Intermediate shapes with respect to the shape step are shown in Fig.30. The cylinder deforms like a teardrop and

the optimal shape is constructed. The streamline of the optimal shape is shown in Fig.31 (case □). Karman vortices obtained for the optimal shape are smaller than the ones for the initial shape.

The normalized cost function is shown in Fig.32. The horizontal axis represents the shape step and the vertical axis represents the normalized cost function with respect to the initial cost function. Comparing case □ to case □, it can be seen that the reduction speeds are different. However, the same optimal shape is constructed. Although Eq.(B23) is needed for the formulation of the adjoint variable method, in practice, one can successfully conduct optimization even if this equation is not satisfied. The directions of movement of nodes by using Eq.(3.13) is shown in Fig.22.

(Note)

In this study, the cost function is defined as Eq.(2.13). In the case the cost function is defined as the drag coefficient Eq.(6.1), the project area $L \cdot d$ are needed. We notice that there are difference between the reduction of Eq.(2.13) and the reduction of Eq.(6.1) by the variation of the project area.

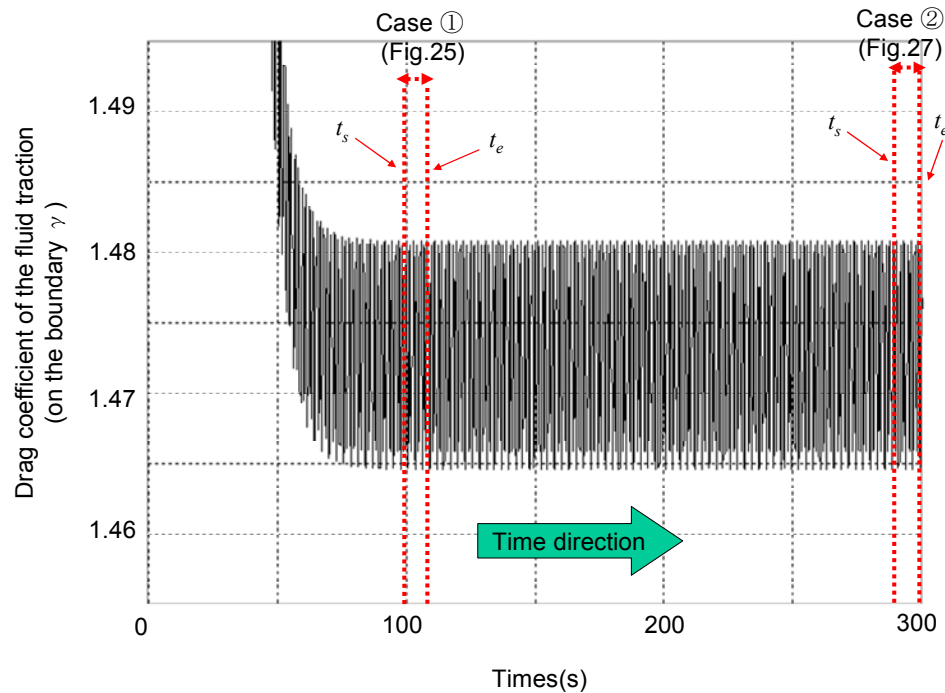


Figure 23. History of drag coefficient (the initial shape).

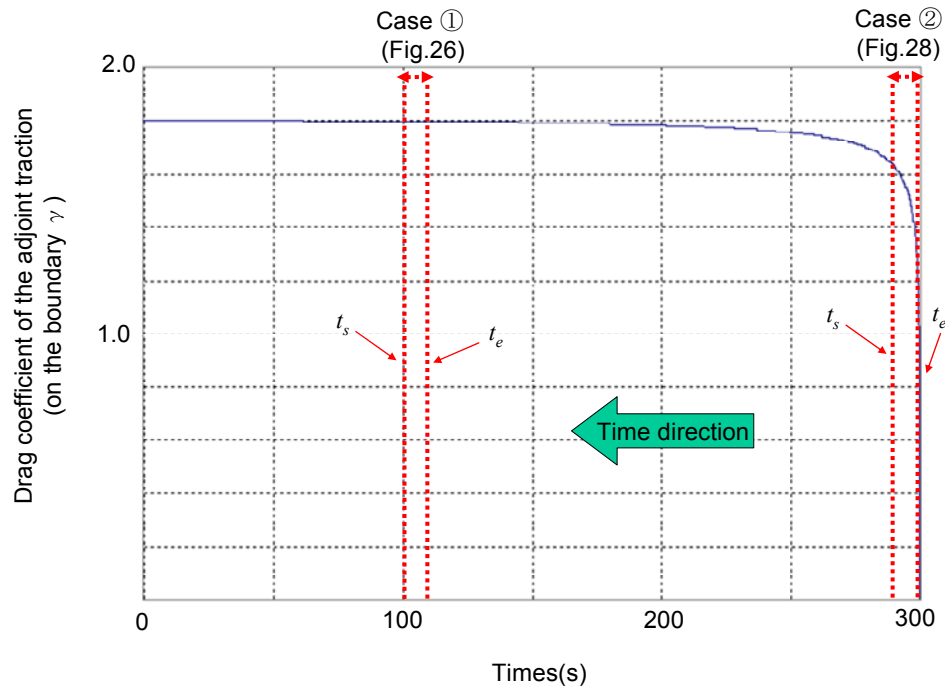


Figure 24. History of the drag coefficient of the adjoint traction (the initial shape).

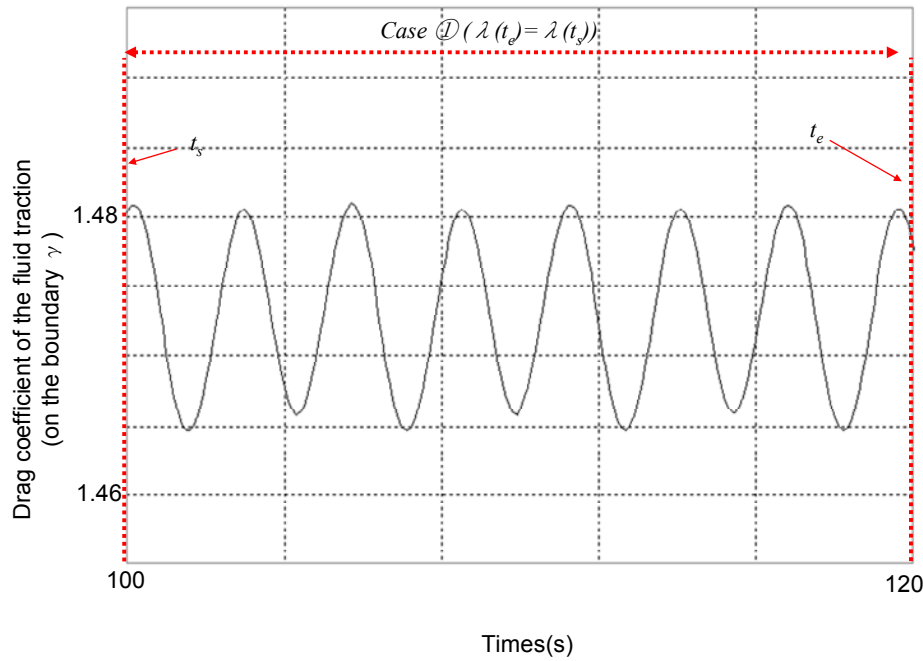


Figure 25. History of the drag coefficient of the traction for the initial shape (The case □ (the time span between the time 100(s) and 120(s))).

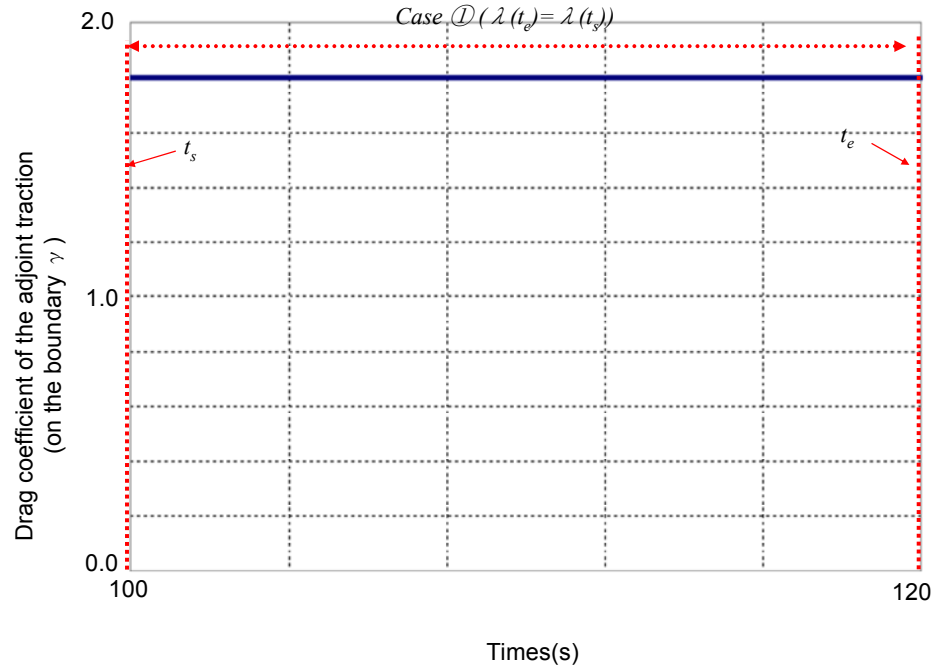


Figure 26. History of the drag coefficient of the adjoint traction for the initial shape (The case ① (the time span between the time 100(s) and 120(s))).

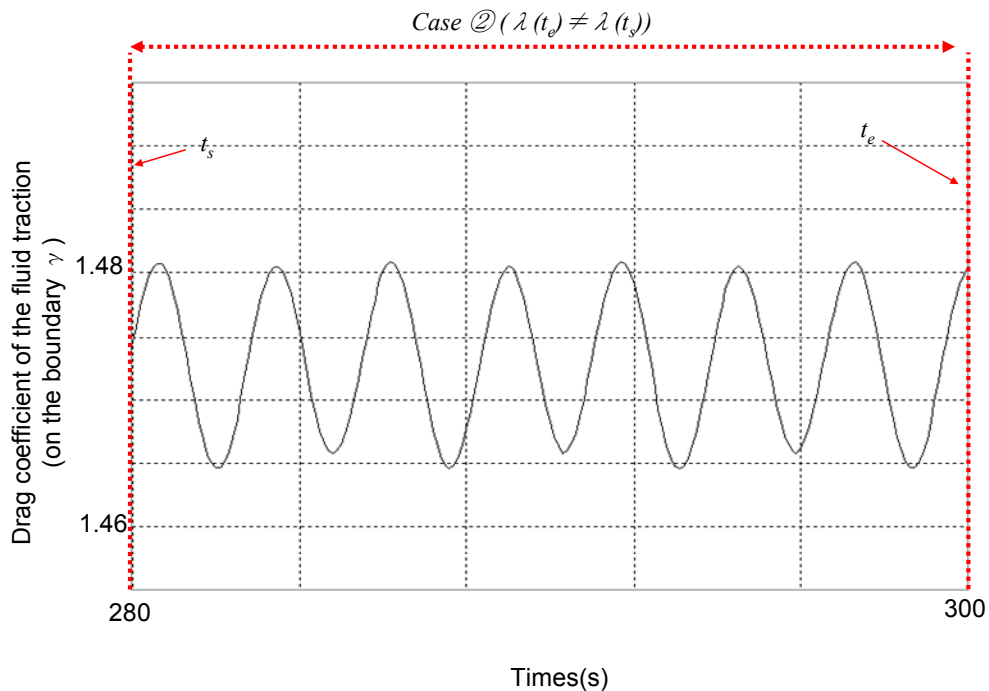


Figure 27. History of the drag coefficient of the traction for the initial shape (The case ② (the time span between the time 280(s) and 300(s))).

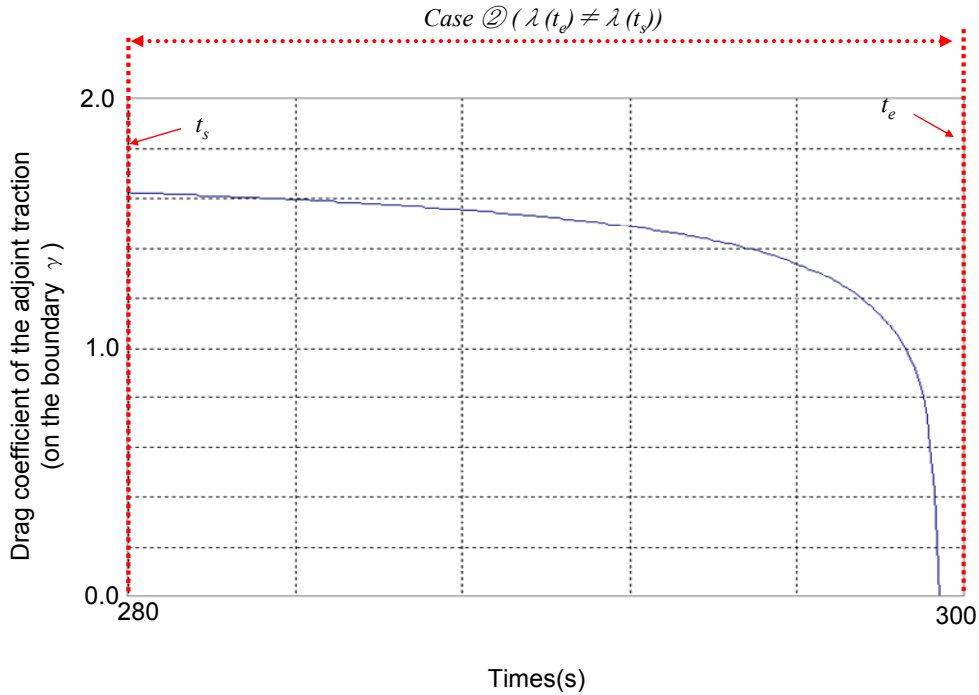


Figure 28. History of the drag coefficient of the adjoint traction for the initial shape (The case \square (the time span between the time 280(s) and 300(s))).

6.4. Shape Optimality

In Fig.30 we show the teardrop-like optimal shape, which has a protuberance with respect to the upstream side. This type of optimal shape is also found in literature [41][45]. However, a few cases where the result of the optimization procedure has the protuberance with respect to the downstream side have been reported as well [87]. In the following paragraphs we show that for the conditions considered here, the drag on such shape is larger than on the result obtained in this study.

To compute the drag generated by the inverse flow (i.e. on the shape with the protuberance on the downstream side), the optimal shape as obtained in this study is subjected to inverse flow from the boundary Γ_E to the boundary Γ_W . The streamline in the inverse flow is shown in Fig.33. As compared average drag on the optimal shape, in Fig.31, the average drag of the inverse flow as shown in Fig.33 is larger. This proves that such shape (Fig.31) is not optimal for this kind of flow.

(Note)

The streamline of the optimal shape is shown in Fig.31. The pressure at point A rises rapidly. In the case the non-slip condition holds, like in our current situation, the pressure

difference between points A and B cannot be maintained therefore the integrand of the surface soon becomes close to zero. On the other hand, in the case the non-slip condition does not hold (i.e. detachment phenomenon on the surface), the pressure difference between the two points is sustained. Therefore, total pressure on the object raise by the pressure difference.

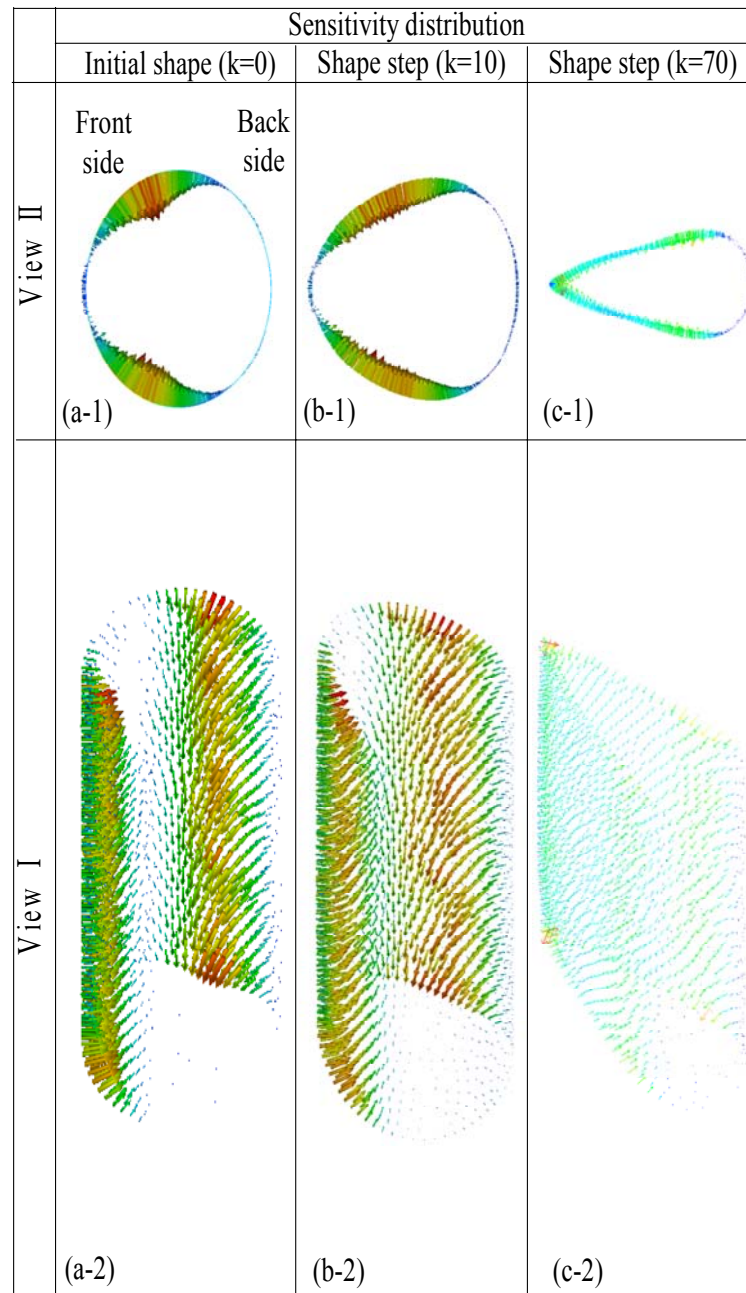


Figure 29. History of cost function and sensitivity distribution with respect to shape step.

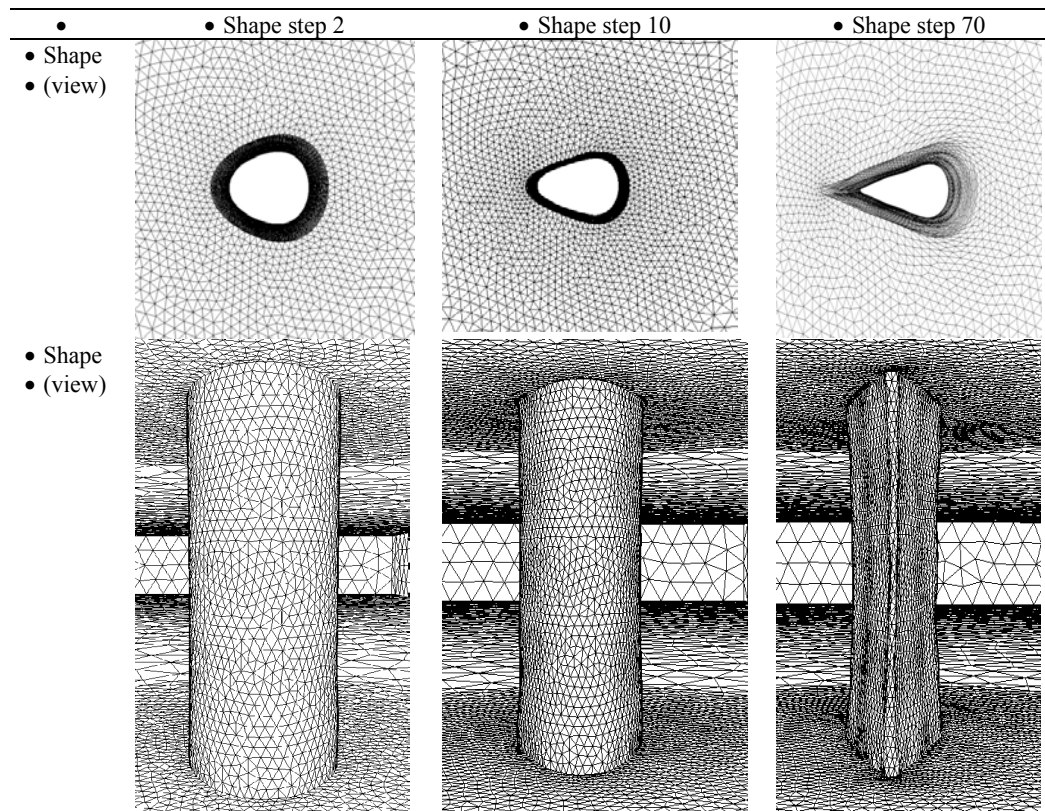


Figure 30. Shape deformation (case □).

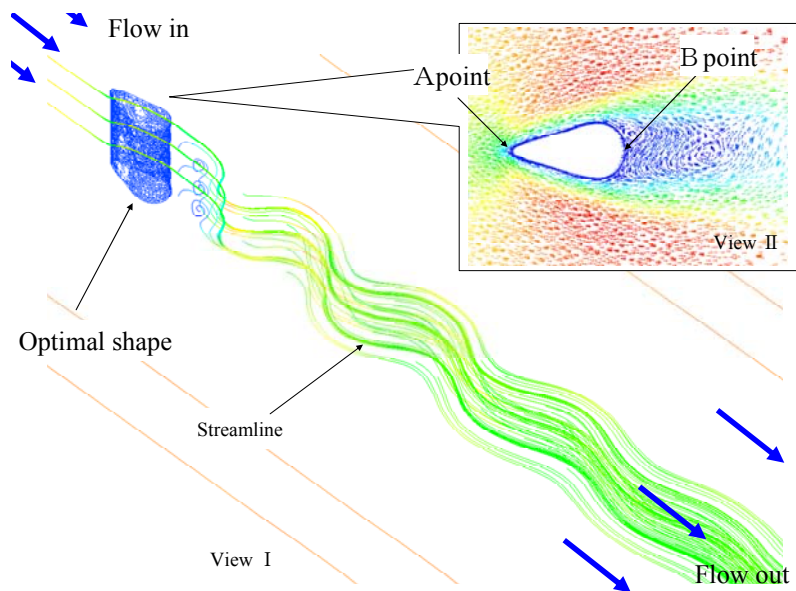


Figure 31. The streamline and the flow velocity vector distribution of the optimal shape.

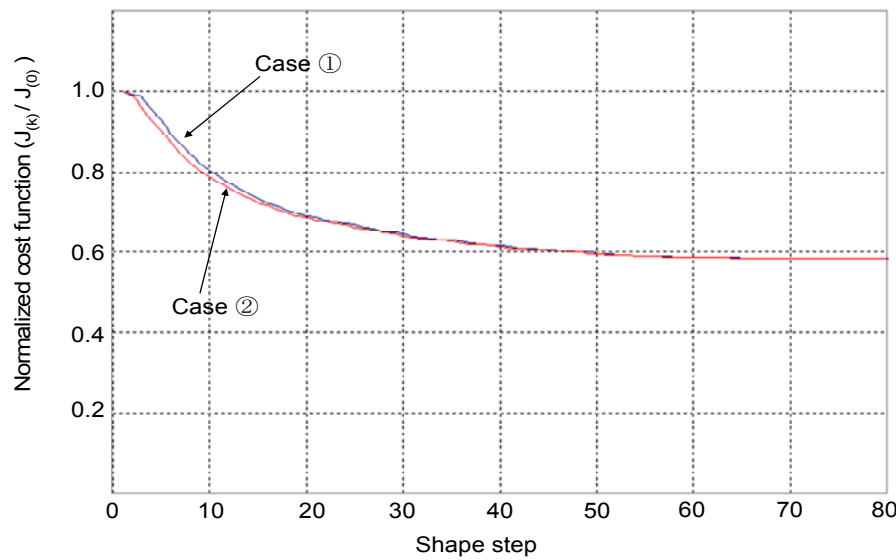


Figure 32. History of normalized cost function.

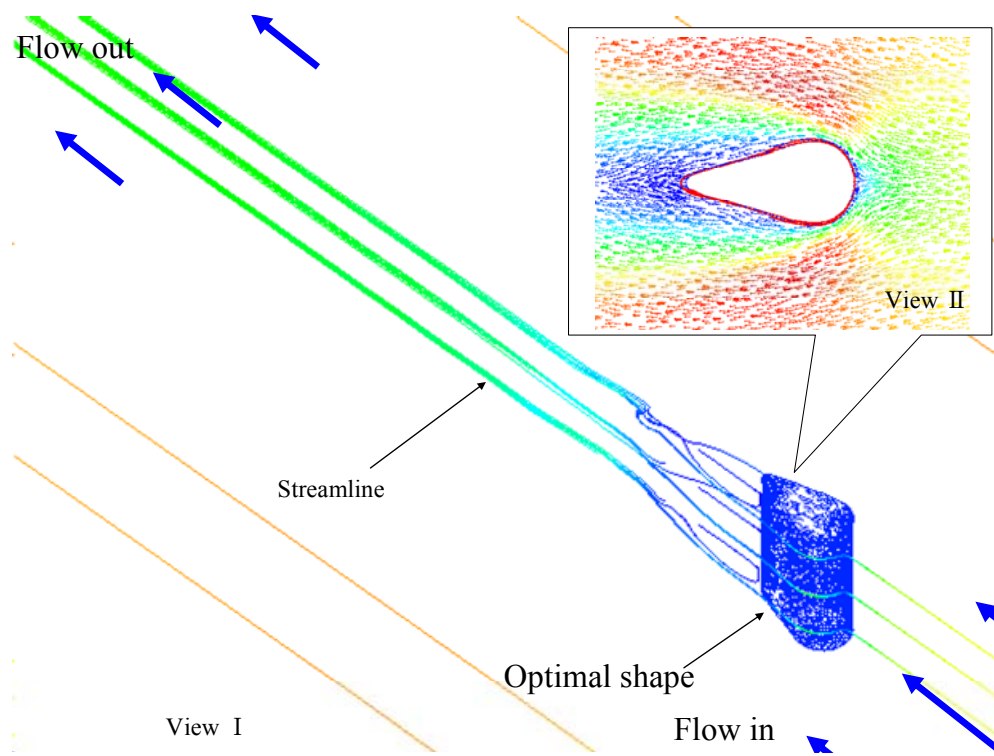


Figure 33. The streamline of the optimal shape (the inverse flow).

7. CONCLUSION

Under unsteady flow, a high-resolution mesh is needed to analyze complex flows with high accuracy. Such mesh contains a large amount of data, so a large amount of storage is demanded for saving the values of both state variables and adjoint variables at every time step, especially for long time spans. Therefore, parallel techniques for distributing the data are naturally required.

In this study, the automatic parallel library HEC-MW used on a 16-node PC cluster made possible the computation of the optimal shape for a long time span. By using the improved shape optimization system, the optimal shape under unsteady flow (RE100) could be obtained. We concluded the following:

- By applying the Oseen approximation to the convective term (the non-linear term), in which the first variation can't be derived, the adjoint variable method containing the boundary condition was formulated.
- Comparing the sensitivities in an unsteady flow to those in a stokes flow, the sensitivity distribution slants toward the upstream side on the cylinder. A teardrop shape with protuberance toward the upstream side was constructed.
- The optimal shape depends on the time span between the test of the start time and the test of the end time. By taking a long time span, robust convergence of the cost function can be produced, and the axis-symmetric optimal shape can be naturally derived. This optimal shape reduces drag by about 40% as compared to the initial shape.

To summarize, a shape optimization method based on the adjoint variable method for reducing drag under unsteady flow was presented. By taking a long time span, the cost function could robustly converge even under unsteady flow. Therefore, this method can be widely applied to both simple and complex shapes. We believe the proposed method to be more efficient and robust than the conventional techniques currently used in shape optimization.

A. TRANSFORMATION OF LAGRANGE FUNCTION

The Lagrange function (Eq.(2.30)) is transformed to derive the adjoint equation and the sensitivity equation. By applying the Gauss green theorem, Eq.(2.30) becomes as follows:

$$\int_{t_s}^{t_e} \int_{\Omega} \lambda_1 \frac{\partial u_k}{\partial x_k} d\Omega dt = \int_{t_s}^{t_e} \int_{\psi} \lambda_1 u_j n_j d\psi dt - \int_{t_s}^{t_e} \int_{\Omega} \frac{\partial \lambda_1}{\partial x_j} u_j d\Omega dt \quad (\text{A1})$$

The other term of Eq.(2.30) is as follows:

$$\begin{aligned}
& \int_{t_s}^{t_e} \int_{\Omega} \lambda_{i+1} \left\{ -\frac{\partial u_i}{\partial t} - \frac{\partial p}{\partial x_i} - U_j \frac{\partial u_i}{\partial x_j} + \frac{1}{Re} \frac{\partial}{\partial x_j} \left(\frac{\partial u_j}{\partial x_i} + \frac{\partial u_i}{\partial x_j} \right) \right\} d\Omega dt = - \int_{t_s}^{t_e} \int_{\Omega} \lambda_{i+1} \frac{\partial u_i}{\partial t} d\Omega dt - \int_{t_s}^{t_e} \int_{\gamma} \lambda_{i+1} p n_i d\gamma dt \\
& + \int_{t_s}^{t_e} \int_{\Omega} \frac{\partial \lambda_{k+1}}{\partial x_k} p d\Omega dt - \int_{t_s}^{t_e} \int_{\gamma} \lambda_{i+1} U_j u_i n_j d\gamma dt + \int_{t_s}^{t_e} \int_{\Omega} \frac{\partial \lambda_{i+1}}{\partial x_j} U_j u_i d\Omega dt + \frac{1}{Re} \int_{t_s}^{t_e} \int_{\gamma} \lambda_{i+1} \left(\frac{\partial u_j}{\partial x_i} + \frac{\partial u_i}{\partial x_j} \right) n_j d\gamma dt \quad (A2) \\
& - \frac{1}{Re} \int_{t_s}^{t_e} \int_{\Omega} \frac{\partial \lambda_{i+1}}{\partial x_j} \left(\frac{\partial u_j}{\partial x_i} + \frac{\partial u_i}{\partial x_j} \right) d\Omega dt = - \int_{\Omega} [\lambda_{i+1} u_i]_{t_s}^{t_e} d\Omega + \int_{t_s}^{t_e} \int_{\Omega} \frac{\partial \lambda_{i+1}}{\partial t} u_i d\Omega dt + \int_{t_s}^{t_e} \int_{\Omega} \frac{\partial \lambda_{k+1}}{\partial x_k} p d\Omega dt \\
& + \int_{t_s}^{t_e} \int_{\gamma} \lambda_{i+1} \left\{ -p n_i + \frac{1}{Re} \left(\frac{\partial u_j}{\partial x_i} + \frac{\partial u_i}{\partial x_j} \right) n_j \right\} d\gamma dt - \int_{t_s}^{t_e} \int_{\gamma} \lambda_{i+1} U_j u_i n_j d\gamma dt + \int_{t_s}^{t_e} \int_{\Omega} \frac{\partial \lambda_{i+1}}{\partial x_j} U_j u_i d\Omega dt \\
& - \frac{1}{Re} \int_{t_s}^{t_e} \int_{\gamma} \frac{\partial \lambda_{i+1}}{\partial x_j} (u_j n_i + u_i n_j) d\gamma dt + \frac{1}{Re} \int_{t_s}^{t_e} \int_{\Omega} \left(\frac{\partial}{\partial x_j} \frac{\partial \lambda_{i+1}}{\partial x_j} u_i + \frac{\partial}{\partial x_i} \frac{\partial \lambda_{i+1}}{\partial x_j} u_j \right) d\Omega dt
\end{aligned}$$

The p term, the u term, the v term and the w term in the integrand of Ω term are arranged by using the following equation:

$$\begin{aligned}
& -\frac{1}{Re} \int_{t_s}^{t_e} \int_{\gamma} \frac{\partial \lambda_{i+1}}{\partial x_j} (u_i n_j + u_j n_i) d\gamma dt = -\frac{1}{Re} \int_{t_s}^{t_e} \int_{\gamma} \left(\frac{\partial \lambda_{i+1}}{\partial x_j} u_i n_j + \frac{\partial \lambda_{j+1}}{\partial x_i} u_i n_j \right) d\gamma dt \quad (A3) \\
& = -\frac{1}{Re} \int_{t_s}^{t_e} \int_{\gamma} \left(\frac{\partial \lambda_{i+1}}{\partial x_j} + \frac{\partial \lambda_{j+1}}{\partial x_i} \right) u_i n_j d\gamma dt
\end{aligned}$$

$$\begin{aligned}
& \frac{1}{Re} \int_{t_s}^{t_e} \int_{\Omega} \left(\frac{\partial}{\partial x_j} \frac{\partial \lambda_{i+1}}{\partial x_j} u_i + \frac{\partial}{\partial x_i} \frac{\partial \lambda_{i+1}}{\partial x_j} u_j \right) d\Omega dt = \frac{1}{Re} \int_{t_s}^{t_e} \int_{\Omega} \left(\frac{\partial}{\partial x_j} \frac{\partial \lambda_{i+1}}{\partial x_j} u_i + \frac{\partial}{\partial x_j} \frac{\partial \lambda_{j+1}}{\partial x_i} u_i \right) d\Omega dt \quad (A4) \\
& = \frac{1}{Re} \int_{t_s}^{t_e} \int_{\Omega} u_i \frac{\partial}{\partial x_j} \left(\frac{\partial \lambda_{i+1}}{\partial x_j} + \frac{\partial \lambda_{j+1}}{\partial x_i} \right) d\Omega dt
\end{aligned}$$

Eq.(2.31) is derived after the transformation and the arrangement.

B. DERIVATION OF ADJOINT EQUATIONS

Using the first variation with respect to the state variable $\mathbf{w}=(p, u_1, u_2, u_3)$, equations are derived. These equations are called as adjoint equations. The index $l=1$ in Eq.(2.33) is as follows:

$$W_1(\alpha, t, x_1, x_2, x_3) = p(t, x_1, x_2, x_3) + \alpha \eta_{20}(x_1, x_2, x_3) \quad (B1)$$

To derive the first variation L with respect to p , the function η_{20} is introduced. This function is the continuity condition, an arbitrary differentiable function which is defined on the set of spatial coordinates over the analytical domain. Its boundary depends on the boundary p . Arbitrary functions are defined with respect to each state variable. The left side first term in The Lagrange function (Eq.(2.31)) is as follows:

$$\left[-\frac{\partial}{\partial \alpha} \int_{t_s}^{t_e} \int_{\gamma} T_1(p + \alpha \eta_{20}) d\gamma dt \right]_{\alpha=0} = \left[-\frac{\partial}{\partial \alpha} \int_{t_s}^{t_e} \int_{\gamma} \left\{ -(p + \alpha \eta_{20}) n_1 + \frac{1}{Re} \left(\frac{\partial u_1}{\partial x_j} + \frac{\partial u_j}{\partial x_1} \right) n_j \right\} d\gamma dt \right]_{\alpha=0} \quad (B2)$$

Each variable is independent. Exchange of the order between the integral domain x and the differential α is possible.

$$\left[-\frac{\partial}{\partial \alpha} \int_{t_s}^{t_e} \int_{\gamma} T_1(p + \alpha \eta_{20}) d\gamma dt \right]_{\alpha=0} = \left[- \int_{t_s}^{t_e} \int_{\gamma} \frac{\partial}{\partial \alpha} \left\{ -(p + \alpha \eta_{20}) n_1 + \frac{1}{\text{Re}} \left(\frac{\partial u_1}{\partial x_j} + \frac{\partial u_j}{\partial x_1} \right) n_j \right\} d\gamma dt \right]_{\alpha=0} = \int_{t_s}^{t_e} \int_{\gamma} n_1 \eta_{20} d\gamma dt \quad (\text{B3})$$

The second term in Eq.(2.31) is as follows:

$$\left[\frac{\partial}{\partial \alpha} \int_{t_s}^{t_e} \int_{\Omega} (p + \alpha \eta_{20}) \frac{\partial \lambda_{k+1}}{\partial x_k} d\Omega dt \right]_{\alpha=0} = \left[\int_{t_s}^{t_e} \int_{\Omega} \frac{\partial \lambda_{k+1}}{\partial x_k} \eta_{20} d\Omega dt \right]_{\alpha=0} = \int_{t_s}^{t_e} \int_{\Omega} \frac{\partial \lambda_{k+1}}{\partial x_k} \eta_{20} d\Omega dt \quad (\text{B4})$$

The sixth term in Eq.(2.31) is as follows:

$$\begin{aligned} \left[\frac{\partial}{\partial \alpha} \int_{t_s}^{t_e} \int_{\Gamma_N + \Gamma_S} \lambda_5 T_1(p + \alpha \eta_{20}) d\gamma dt \right]_{\alpha=0} &= \left[\frac{\partial}{\partial \alpha} \int_{t_s}^{t_e} \int_{\Gamma_N + \Gamma_S} \lambda_5 \left\{ -(p + \alpha \eta_{20}) n_1 + \frac{1}{\text{Re}} \left(\frac{\partial u_1}{\partial x_j} + \frac{\partial u_j}{\partial x_1} \right) n_j \right\} d\gamma dt \right]_{\alpha=0} \\ &= - \int_{t_s}^{t_e} \int_{\Gamma_N + \Gamma_S} \lambda_5 n_1 \eta_{20} d\gamma dt \end{aligned} \quad (\text{B5})$$

The other term in Eq.(2.31) are also a similar approach. Eq.(B1)-Eq.(B5) are summarized as follows:

$$\begin{aligned} \left[\frac{\partial L(p + \alpha \eta_{20})}{\partial \alpha} \right]_{\alpha=0} &= \int_{t_s}^{t_e} \int_{\gamma} n_1 \eta_{20} d\gamma dt - \int_{t_s}^{t_e} \int_{\Omega} \frac{\partial \lambda_{k+1}}{\partial x_k} \eta_{20} d\Omega dt - \int_{t_s}^{t_e} \int_{\psi} \lambda_{i+1} n_i \eta_{20} d\Gamma dt \\ &- \int_{t_s}^{t_e} \int_{\Gamma_N + \Gamma_S} \lambda_5 n_1 \eta_{20} d\Gamma dt - \int_{t_s}^{t_e} \int_{\Gamma_N + \Gamma_S} \lambda_7 n_3 \eta_{20} d\Gamma dt - \int_{t_s}^{t_e} \int_{\Gamma_U + \Gamma_L} \lambda_8 n_1 \eta_{20} d\Gamma dt - \int_{t_s}^{t_e} \int_{\Gamma_U + \Gamma_L} \lambda_9 n_2 \eta_{20} d\Gamma dt \\ &- \int_{t_s}^{t_e} \int_{\Gamma_E} \lambda_{11} n_1 \eta_{20} d\Gamma dt - \int_{t_s}^{t_e} \int_{\Gamma_E} \lambda_{12} n_2 \eta_{20} d\Gamma dt - \int_{t_s}^{t_e} \int_{\Gamma_E} \lambda_{13} n_3 \eta_{20} d\Gamma dt = 0 \end{aligned} \quad (\text{B6})$$

By the fundamental lemma of the calculus of variations, Eq.(B6) becomes as follows:

$$\frac{\partial \lambda_2}{\partial x_1} + \frac{\partial \lambda_3}{\partial x_2} + \frac{\partial \lambda_4}{\partial x_3} = 0 \quad \text{in } \Omega \quad (\text{B7})$$

$$-\lambda_1 + \lambda_2 n_1 + \lambda_3 n_2 + \lambda_4 n_3 = 0 \quad \text{on } \gamma \quad (\text{B8})$$

The above equation should be consistently satisfied with respect to the arbitrary surface. Therefore, the boundary γ is set as follows:

$$(\lambda_2 \quad \lambda_3 \quad \lambda_4) = (1 \quad 0 \quad 0) \quad \text{on } \gamma \quad (\text{B9})$$

Similarly, the boundary Γ_E and Γ_S are as follows:

$$(\lambda_2 + \lambda_5) n_1 + \lambda_3 n_2 + (\lambda_4 + \lambda_7) n_3 = 0 \quad \text{on } \Gamma_N, \Gamma_S \quad (\text{B10})$$

The above equation is also as follows:

$$\lambda_3 = 0, \quad \lambda_5 = -\lambda_2, \quad \lambda_7 = -\lambda_4 \quad \text{on} \quad \Gamma_N, \Gamma_S \quad (\text{B11})$$

The other boundary condition is similarly derived as follows:

$$\lambda_8 = -\lambda_2 \quad \lambda_9 = -\lambda_3 \quad \lambda_4 = 0 \quad \text{on} \quad \Gamma_U, \Gamma_L \quad (\text{B12})$$

$$\lambda_{11} = -\lambda_2 \quad \lambda_{12} = -\lambda_3 \quad \lambda_{13} = -\lambda_4 \quad \text{on} \quad \Gamma_E \quad (\text{B13})$$

The first variation with respect to u_l is derived. Eq.(2.33) in the index $l=2$ is as follows:

$$W_2(a, x_1, x_2, x_3) = u_1(t, x_1, x_2, x_3) + \alpha \eta_{21}(x_1, x_2, x_3) \quad \text{in} \quad \Omega \quad (\text{B14})$$

The function η_{21} is the arbitrary function to take the first variation. However, the function η_{21} has to satisfy $u_l=0$ on the boundary γ , Γ_w . In the boundary γ , the velocity u_l has to be zero. Therefore, $u_l + \alpha \eta_{21}$ (the perturbation $\alpha \eta_{21}$ is added to u_l) has to be zero as well. In this boundary, W_2 and u_l are zero and the function η_{21} is naturally derived as follows[19][20]:

$$\eta_{21}(x_1, x_2, x_3) = 0 \quad \text{on} \quad \gamma, \Gamma_W \quad (\text{B15})$$

Using the above equation, the first term in Eq.(2.31) is as follows:

$$\left[\frac{\partial J(u_l + \alpha \eta_{21})}{\partial \alpha} \right]_{\alpha=0} = \left[\frac{\partial J(u_l + \alpha \cdot 0)}{\partial \alpha} \right]_{\alpha=0} = 0 \quad \text{on} \quad \gamma \quad (\text{B16})$$

The third term in Eq.(2.31) is as follows:

$$\begin{aligned} & \left[\frac{\partial}{\partial \alpha} \int_{t_s}^{t_e} \int_{\Omega} (u_l + \alpha \eta_{21}) \left\{ \frac{\partial \lambda_2}{\partial t} - \frac{\partial \lambda_1}{\partial x_i} + U_j \frac{\partial \lambda_2}{\partial x_j} + \frac{1}{\text{Re}} \frac{\partial}{\partial x_j} \left(\frac{\partial \lambda_{j+1}}{\partial x_i} + \frac{\partial \lambda_2}{\partial x_j} \right) \right\} d\Omega dt \right]_{\alpha=0} \\ & + \left[\frac{\partial}{\partial \alpha} \int_{t_s}^{t_e} \int_{\Omega} u_2 \left\{ \frac{\partial \lambda_3}{\partial t} - \frac{\partial \lambda_1}{\partial x_2} + U_j \frac{\partial \lambda_3}{\partial x_j} + \frac{1}{\text{Re}} \frac{\partial}{\partial x_j} \left(\frac{\partial \lambda_{j+1}}{\partial x_2} + \frac{\partial \lambda_3}{\partial x_j} \right) \right\} d\Omega dt \right]_{\alpha=0} \\ & + \left[\frac{\partial}{\partial \alpha} \int_{t_s}^{t_e} \int_{\Omega} u_3 \left\{ \frac{\partial \lambda_4}{\partial t} - \frac{\partial \lambda_1}{\partial x_3} + U_j \frac{\partial \lambda_4}{\partial x_j} + \frac{1}{\text{Re}} \frac{\partial}{\partial x_j} \left(\frac{\partial \lambda_{j+1}}{\partial x_3} + \frac{\partial \lambda_4}{\partial x_j} \right) \right\} d\Omega dt \right]_{\alpha=0} \\ & = \int_{t_s}^{t_e} \int_{\Omega} \left\{ \frac{\partial \lambda_2}{\partial t} - \frac{\partial \lambda_1}{\partial x_i} + U_j \frac{\partial \lambda_2}{\partial x_j} + \frac{1}{\text{Re}} \frac{\partial}{\partial x_j} \left(\frac{\partial \lambda_{j+1}}{\partial x_i} + \frac{\partial \lambda_2}{\partial x_j} \right) \right\} \eta_{21} d\Omega dt \end{aligned} \quad (\text{B17})$$

The fifth term is as follows:

$$-\left[\frac{\partial}{\partial \alpha} \int_{t_s}^{t_e} \int_{\psi(x)} (u_l + \alpha \eta_{21}) S_1 d\Omega dt \right]_{\alpha=0} = -\int_{t_s}^{t_e} \int_{\psi(x)} S_1 \eta_{21} d\Omega dt \quad (\text{B18})$$

The function S_1 represents the adjoint traction. The twenty-first in Eq.(2.31) is as follows:

$$\begin{aligned} & \left[\frac{\partial}{\partial \alpha} \int_{\Omega} [\lambda_2(t, x_1, x_2, x_3) u_1(t, x_1, x_2, x_3) + \alpha \eta_2(x_1, x_2, x_3)] + \lambda_3(t, x_1, x_2, x_3) u_2(t, x_1, x_2, x_3) + \lambda_4(t, x_1, x_2, x_3) u_3(t, x_1, x_2, x_3)] \right]_{\alpha=0}^{t_e} d\Omega \\ & = \left[\int_{\Omega} [\lambda_2(t, x_1, x_2, x_3) \eta_2(x_1, x_2, x_3)] \right]_{\alpha=0}^{t_e} d\Omega = \int_{\Omega} [\lambda_2(t_e, x_1, x_2, x_3) - \lambda_2(t_s, x_1, x_2, x_3)] \eta_2(x_1, x_2, x_3) d\Omega \end{aligned} \quad (\text{B19})$$

In the similar way, the other term is obtained by taking the first variation. Using Eqs.(B15)-(B19), Eq.(2.31) is as follows:

$$\begin{aligned} & \left[\frac{\partial L(u_1 + \alpha \eta_{21})}{\partial \alpha} \right]_{\alpha=0}^{t_e} = \int_{t_s}^{t_e} \int_{\Omega} \left\{ \frac{\partial \lambda_2}{\partial t} - \frac{\partial \lambda_1}{\partial x_j} + U_j \frac{\partial \lambda_2}{\partial x_j} + \frac{1}{\text{Re}} \frac{\partial}{\partial x_j} \left(\frac{\partial \lambda_{j+1}}{\partial x_i} + \frac{\partial \lambda_2}{\partial x_j} \right) \right\} \eta_{21} d\Omega dt \\ & - \int_{\Omega} \{ \lambda_2(t_e, x_1, x_2, x_3) \eta_{21}(x_1, x_2, x_3) - \lambda_2(t_s, x_1, x_2, x_3) \eta_{21}(x_1, x_2, x_3) \} d\Omega \\ & - \int_{t_s}^{t_e} \int_{\gamma} \left\{ \lambda_2 U_j n_j - \lambda_1 n_j + \frac{1}{\text{Re}} \left(\frac{\partial \lambda_{j+1}}{\partial x_1} + \frac{\partial \lambda_2}{\partial x_j} \right) n_j \right\} \eta_{21} d\psi dt + \int_{t_s}^{t_e} \int_{\Gamma_W} \lambda_{14} \eta_{21} d\psi dt + \int_{t_s}^{t_e} \int_{\gamma} \lambda_{17} \eta_{21} d\psi dt \end{aligned} \quad (\text{B20})$$

By the fundamental lemma of the calculus of variations, the domain Ω is as follows:

$$\frac{\partial \lambda_2}{\partial t} - \frac{\partial \lambda_1}{\partial x_j} + U_j \frac{\partial \lambda_2}{\partial x_j} + \frac{1}{\text{Re}} \frac{\partial}{\partial x_j} \left(\frac{\partial \lambda_j}{\partial x_1} + \frac{\partial \lambda_2}{\partial x_j} \right) = 0 \quad \text{on } \Omega \quad (\text{B21})$$

Eq.(B21) causes inverse diffusion problems because the viscosity term in Eq.(B21) has the same positive sign as the time derivative[82][83]. Inverse diffusion problems cause numerical oscillations and can not converge. For stability reasons [84], the backward time is defined as follows:

$$t = -\tau \quad \text{on } \Omega \quad (\text{B22})$$

The second term is as follows:

$$\lambda_2(t_e, x_1, x_2, x_3) - \lambda_2(t_s, x_1, x_2, x_3) = 0 \quad \text{in } \Omega \quad (\text{B23})$$

Using Eq.(B15), the third term in Eq.(B20) is as follows:

$$\begin{aligned} S_1 &= \lambda_2 U_i n_i - \lambda_1 n_1 + \frac{1}{\text{Re}} \left\{ \left(\frac{\partial \lambda_2}{\partial x_1} + \frac{\partial \lambda_2}{\partial x_1} \right) n_1 + \left(\frac{\partial \lambda_2}{\partial x_2} + \frac{\partial \lambda_3}{\partial x_1} \right) n_2 + \left(\frac{\partial \lambda_2}{\partial x_3} + \frac{\partial \lambda_4}{\partial x_1} \right) n_3 \right\} \\ &= 0 \quad \text{on } \Gamma_N, \Gamma_S, \Gamma_U, \Gamma_L, \Gamma_E \end{aligned} \quad (\text{B24})$$

The other term is derived as follows:

$$\lambda_{14} = 0 \quad \text{on } \Gamma_W, \quad \lambda_{17} = 0 \quad \text{on } \gamma \quad (\text{B25})$$

The adjoint equation in the domain and the boundary with respect to the variable u_1 is derived. Adjoint equations with respect to the variable u_2 and u_3 are also derived in similar approach.

C. DERIVATION OF SENSITIVITY EQUATION

By using Eq.(B11)-Eq.(B13),(B.25) etc., the Lagrange function (Eq.(2.31)) is as follows:

$$\begin{aligned}
 L = & -\int_{t_s}^{t_e} \int_{\gamma} T_i d\gamma dt + \int_{t_s}^{t_e} \int_{\Omega} p \frac{\partial \lambda_{k+1}}{\partial x_k} d\Omega dt + \int_{t_s}^{t_e} \int_{\Omega} u_i \left\{ \frac{\partial \lambda_{i+1}}{\partial t} - \frac{\partial \lambda_i}{\partial x_i} + U_j \frac{\partial \lambda_{i+1}}{\partial x_j} + \text{Re} \frac{\partial}{\partial x_j} \left(\frac{\partial \lambda_{j+1}}{\partial x_i} + \frac{\partial \lambda_{i+1}}{\partial x_j} \right) \right\} d\Omega dt \\
 & - \int_{t_s}^{t_e} \int_{\psi} u_i S_i d\psi dt + \int_{t_s}^{t_e} \int_{\Gamma_w + \gamma} \lambda_2 T_1 d\gamma dt + \int_{t_s}^{t_e} \int_{\Gamma_w + \Gamma_N + \Gamma_S + \gamma} \lambda_3 T_2 d\gamma dt \\
 & + \int_{t_s}^{t_e} \int_{\Gamma_U + \Gamma_L + \gamma} \lambda_4 T_3 d\gamma dt - \int_{\Omega} [\lambda_{i+1} u_i]_{t_s}^{t_e} d\Omega + \kappa \int_{t_s}^{t_e} \int_{\Pi} d\Pi dt \in \mathbf{R}^1
 \end{aligned} \quad (\text{C1})$$

The sensitivity is calculated by solving the sensitivity equations, the stationary conditions which are obtained by taking the first variation of the Lagrange function with respect to the spatial coordinate x . In the beginning, the first variation is derived with respect to x_1 as follows:

$$X_1(\alpha, x_1, x_2, x_3) = x_1 + \alpha \eta_{24}(x_1, x_2, x_3) \quad X_2(\alpha, x_1, x_2, x_3) = x_2 \quad X_3(\alpha, x_1, x_2, x_3) = x_3 \quad \text{in } \Omega \quad (\text{C2})$$

The boundary Γ is fixed as $X_1=x_1$. Therefore, the function η_{24} is as follows:

$$\eta_{24}(x_1, x_2, x_3) = 0 \quad \text{on } \Gamma \quad (\text{C3})$$

The first term in Eq.(C1) is as follows:

$$\begin{aligned}
 \left[-\frac{\partial}{\partial \alpha} \int_{t_s}^{t_e} \int_{\gamma(X_1(\alpha, x_1, x_2, x_3))} T_i(X_1(\alpha, x_1, x_2, x_3)) d\gamma dt \right]_{\alpha=0} = & \left[-\frac{\partial}{\partial \alpha} \int_{t_s}^{t_e} \int_{\gamma(X_1(\alpha, x_1, x_2, x_3))} \{-p(X_1(\alpha, x_1, x_2, x_3))n_i(X_1(\alpha, x_1, x_2, x_3)) \right. \\
 & \left. + \frac{1}{\text{Re}} \left(\frac{\partial u_i(X_1(\alpha, x_1, x_2, x_3))}{\partial x_1} + \frac{\partial u_i(X_1(\alpha, x_1, x_2, x_3))}{\partial x_i} \right) n_i(X_1(\alpha, x_1, x_2, x_3)) \} d\gamma dt \right]_{\alpha=0}
 \end{aligned} \quad (\text{C4})$$

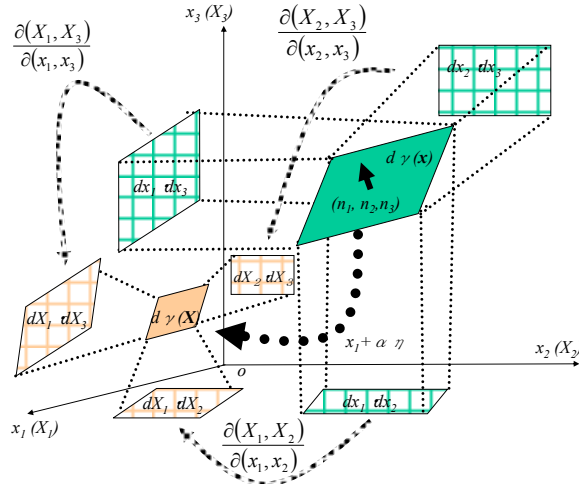


Figure 34. The small surface area γ and the projected area

The integral domain $\gamma(X)$, $\Omega(X)$, $\Psi(X)$ shows the domain with respect to X . The boundary $\gamma(X)$ depends on the parameter α . Exchange of the order between the integral domain x and the differential α is impossible. Therefore, an integral domain is converted. The surface domain $d\gamma$ on the object, and the projected areas with respect to the x_1x_2 -plane, the x_2x_3 -plane and the x_1x_3 -plane are shown in Fig.34. The surface domain $d\gamma(X)$ containing the perturbation, and the projected areas with respect to the X_1X_2 -plane, the X_2X_3 -plane and the X_1X_3 -plane are shown in Fig.34.

The unit normal vector (n_1, n_2, n_3) on the domain $d\gamma$ is defined. The relation becomes as follows:

$$n_1(x_1, x_2, x_3)d\gamma = dx_2dx_3 \quad n_2(x_1, x_2, x_3)d\gamma = dx_3dx_1 \quad n_3(x_1, x_2, x_3)d\gamma = dx_1dx_2 \quad (C5)$$

$$n_1(x_1 + \alpha\eta_{24}, x_2, x_3)d\gamma = dX_2dX_3 \quad n_2(x_1 + \alpha\eta_{24}, x_2, x_3)d\gamma = dX_3dX_1 \quad n_3(x_1 + \alpha\eta_{24}, x_2, x_3)d\gamma = dX_1dX_2 \quad (C6)$$

The Jacobian to transform the coordinate from the projected area on the x_3x_1 -plane to the X_3X_1 -plane is as follows [19][20][88]:

$$\left| \frac{\partial(X_3, X_1)}{\partial(x_3, x_1)} \right| = \begin{vmatrix} \frac{\partial X_3}{\partial x_1} & \frac{\partial X_1}{\partial x_1} \\ \frac{\partial X_3}{\partial x_3} & \frac{\partial X_1}{\partial x_3} \end{vmatrix} = \begin{vmatrix} 0 & 1 + \alpha \frac{\partial \eta_{24}}{\partial x_1} \\ 1 & \alpha \frac{\partial \eta_{24}}{\partial x_3} \end{vmatrix} = 1 + \alpha \frac{\partial \eta_{24}}{\partial x_1} \quad (C7)$$

The Jacobian to transform the coordinate from the projected area on the x_1x_2 -plane to the X_1X_2 -plane is as follows :

$$\left| \frac{\partial(X_1, X_2)}{\partial(x_1, x_2)} \right| = \begin{vmatrix} \frac{\partial X_1}{\partial x_1} & \frac{\partial X_2}{\partial x_1} \\ \frac{\partial X_1}{\partial x_2} & \frac{\partial X_2}{\partial x_2} \end{vmatrix} = \begin{vmatrix} 1 + \alpha \frac{\partial \eta_{24}}{\partial x_1} & 0 \\ \alpha \frac{\partial \eta_{24}}{\partial x_2} & 1 \end{vmatrix} = 1 + \alpha \frac{\partial \eta_{24}}{\partial x_1} \quad (C8)$$

The Jacobian to transform the coordinate from the projected area on the x_2x_3 -plane to the X_2X_3 -plane is as follows :

$$\left| \frac{\partial(X_2, X_3)}{\partial(x_2, x_3)} \right| = \begin{vmatrix} \frac{\partial X_2}{\partial x_2} & \frac{\partial X_3}{\partial x_2} \\ \frac{\partial X_2}{\partial x_3} & \frac{\partial X_3}{\partial x_3} \end{vmatrix} = \begin{vmatrix} 1 & 0 \\ 0 & 1 \end{vmatrix} = 1 \quad (C9)$$

By using Eq.(C.5) and Eq.(C.6), Eq.(C4) is as follows:

$$\begin{aligned}
& \left[-\frac{\partial}{\partial \alpha} \int_{t_1}^{t_2} \int_{\gamma(x)} T_1(X_1(\alpha, x_1, x_2, x_3)) d\gamma dt \right]_{\alpha=0} = \left[-\frac{\partial}{\partial \alpha} \int_{t_1}^{t_2} \int_{\gamma(x)} \left\{ -p(X_1(\alpha, x_1, x_2, x_3)) + \frac{2}{\text{Re}} \frac{\partial u_1(X_1(\alpha, x_1, x_2, x_3))}{\partial x_1} \right\} dX_2 dX_3 dt \right. \\
& - \frac{\partial}{\partial \alpha} \int_{t_1}^{t_2} \int_{\gamma(x)} \frac{1}{\text{Re}} \left(\frac{\partial u_2(X_1(\alpha, x_1, x_2, x_3))}{\partial x_1} + \frac{\partial u_1(X_1(\alpha, x_1, x_2, x_3))}{\partial x_2} \right) dX_3 dX_1 dt \\
& - \frac{\partial}{\partial \alpha} \int_{t_1}^{t_2} \int_{\gamma(x)} \frac{1}{\text{Re}} \left(\frac{\partial u_3(X_1(\alpha, x_1, x_2, x_3))}{\partial x_1} + \frac{\partial u_1(X_1(\alpha, x_1, x_2, x_3))}{\partial x_3} \right) dX_1 dX_2 dt \Big]_{\alpha=0} \\
& = \left[-\frac{\partial}{\partial \alpha} \int_{t_1}^{t_2} \int_{\gamma(x)} \left\{ -p(X_1(\alpha, x_1, x_2, x_3)) + \frac{2}{\text{Re}} \frac{\partial u_1(X_1(\alpha, x_1, x_2, x_3))}{\partial x_1} \right\} \left| \frac{\partial(X_2, X_3)}{\partial(x_2, x_3)} \right| dx_2 dx_3 dt \right. \\
& - \frac{\partial}{\partial \alpha} \int_{t_1}^{t_2} \int_{\gamma(x)} \frac{1}{\text{Re}} \left(\frac{\partial u_2(X_1(\alpha, x_1, x_2, x_3))}{\partial x_1} + \frac{\partial u_1(X_1(\alpha, x_1, x_2, x_3))}{\partial x_2} \right) \left| \frac{\partial(X_3, X_1)}{\partial(x_3, x_1)} \right| dx_3 dx_1 dt \\
& - \frac{\partial}{\partial \alpha} \int_{t_1}^{t_2} \int_{\gamma(x)} \frac{1}{\text{Re}} \left(\frac{\partial u_3(X_1(\alpha, x_1, x_2, x_3))}{\partial x_1} + \frac{\partial u_1(X_1(\alpha, x_1, x_2, x_3))}{\partial x_3} \right) \left| \frac{\partial(X_1, X_2)}{\partial(x_1, x_2)} \right| dx_1 dx_2 dt \Big]_{\alpha=0} \\
& = \left[-\frac{\partial}{\partial \alpha} \int_{t_1}^{t_2} \int_{\gamma(x)} \left\{ -p(X_1(\alpha, x_1, x_2, x_3)) + \frac{2}{\text{Re}} \frac{\partial u_1(X_1(\alpha, x_1, x_2, x_3))}{\partial x_1} \right\} n_1 d\gamma dt \right. \\
& - \frac{\partial}{\partial \alpha} \int_{t_1}^{t_2} \int_{\gamma(x)} \frac{1}{\text{Re}} \left(\frac{\partial u_2(X_1(\alpha, x_1, x_2, x_3))}{\partial x_1} + \frac{\partial u_1(X_1(\alpha, x_1, x_2, x_3))}{\partial x_2} \right) \left(1 + \alpha \frac{\partial \eta_{24}}{\partial x_1} \right) n_2 d\gamma dt \\
& - \frac{\partial}{\partial \alpha} \int_{t_1}^{t_2} \int_{\gamma(x)} \frac{1}{\text{Re}} \left(\frac{\partial u_3(X_1(\alpha, x_1, x_2, x_3))}{\partial x_1} + \frac{\partial u_1(X_1(\alpha, x_1, x_2, x_3))}{\partial x_3} \right) \left(1 + \alpha \frac{\partial \eta_{24}}{\partial x_1} \right) n_3 d\gamma dt \Big]_{\alpha=0} \tag{C10}
\end{aligned}$$

The first term in Eq.(C10) is as follows:

$$\begin{aligned}
& \left[-\frac{\partial}{\partial \alpha} \int_{t_1}^{t_2} \int_{\gamma} \left\{ -p(X_1(\alpha, x_1, x_2, x_3)) + \frac{2}{\text{Re}} \frac{\partial u_1(X_1(\alpha, x_1, x_2, x_3))}{\partial x_1} \right\} n_1(X_1(\alpha, x_1, x_2, x_3)) d\gamma dt \right]_{\alpha=0} \\
& = \left[- \int_{t_1}^{t_2} \int_{\gamma} \left\{ -\frac{\partial p(X_1(\alpha, x_1, x_2, x_3))}{\partial X_1} \frac{\partial X_1(\alpha, x_1, x_2, x_3)}{\partial \alpha} + \frac{2}{\text{Re}} \frac{\partial}{\partial x_1} \left(\frac{\partial u_1(X_1(\alpha, x_1, x_2, x_3))}{\partial X_1} \frac{\partial X_1(\alpha, x_1, x_2, x_3)}{\partial \alpha} \right) \right\} n_1(X_1(\alpha, x_1, x_2, x_3)) d\gamma dt \right]_{\alpha=0} \\
& + \left[- \int_{t_1}^{t_2} \int_{\gamma} \left\{ -p(X_1(\alpha, x_1, x_2, x_3)) + \frac{2}{\text{Re}} \frac{\partial u_1(X_1(\alpha, x_1, x_2, x_3))}{\partial x_1} \right\} \frac{\partial n_1(X_1(\alpha, x_1, x_2, x_3))}{\partial X_1} \frac{\partial X_1(\alpha, x_1, x_2, x_3)}{\partial \alpha} d\gamma dt \right]_{\alpha=0} \tag{C11}
\end{aligned}$$

The second term in Eq.(C10) is as follows:

$$\begin{aligned}
& \left[-\frac{\partial}{\partial \alpha} \int_{t_1}^{t_2} \int_{\gamma} \frac{1}{\text{Re}} \left(\frac{\partial u_2(X_1(\alpha, x_1, x_2, x_3))}{\partial x_1} + \frac{\partial u_1(X_1(\alpha, x_1, x_2, x_3))}{\partial x_2} \right) \left(1 + \alpha \frac{\partial \eta_{24}(X_1(\alpha, x_1, x_2, x_3))}{\partial x_1} \right) n_2(X_1(\alpha, x_1, x_2, x_3)) d\gamma dt \right]_{\alpha=0} \\
& = \left[- \int_{t_1}^{t_2} \int_{\gamma} \frac{1}{\text{Re}} \left\{ \frac{\partial}{\partial x_1} \left(\frac{\partial u_2(X_1(\alpha, x_1, x_2, x_3))}{\partial X_1} \frac{\partial X_1(X_1(\alpha, x_1, x_2, x_3))}{\partial \alpha} \right) + \frac{\partial}{\partial x_2} \left(\frac{\partial u_1(X_1(\alpha, x_1, x_2, x_3))}{\partial X_1} \frac{\partial X_1(X_1(\alpha, x_1, x_2, x_3))}{\partial \alpha} \right) \right\} \left(1 + \alpha \frac{\partial \eta_{24}}{\partial x_1} \right) n_2 d\gamma dt \right]_{\alpha=0} \\
& + \left[- \int_{t_1}^{t_2} \int_{\gamma} \frac{1}{\text{Re}} \left(\frac{\partial u_2(X_1(\alpha, x_1, x_2, x_3))}{\partial x_1} + \frac{\partial u_1(X_1(\alpha, x_1, x_2, x_3))}{\partial x_2} \right) \left(1 + \alpha \frac{\partial \eta_{24}(X_1(\alpha, x_1, x_2, x_3))}{\partial x_1} \right) \frac{\partial n_2(X_1(\alpha, x_1, x_2, x_3))}{\partial X_1} \frac{\partial X_1(\alpha, x_1, x_2, x_3)}{\partial \alpha} d\gamma dt \right]_{\alpha=0} \\
& + \left[- \int_{t_1}^{t_2} \int_{\gamma} \frac{1}{\text{Re}} \left(\frac{\partial u_2(X_1(\alpha, x_1, x_2, x_3))}{\partial x_1} + \frac{\partial u_1(X_1(\alpha, x_1, x_2, x_3))}{\partial x_2} \right) \frac{\partial \eta_{24}(X_1(\alpha, x_1, x_2, x_3))}{\partial x_1} n_2(X_1(\alpha, x_1, x_2, x_3)) d\gamma dt \right]_{\alpha=0} \tag{C12}
\end{aligned}$$

The third term in Eq.(C10) is as follows:

$$\begin{aligned}
& \left[-\frac{\partial}{\partial \alpha} \int_{t_1}^{t_2} \int_{\gamma} \frac{1}{\operatorname{Re}} \left(\frac{\partial u_3(X_1(\alpha, x_1, x_2, x_3))}{\partial x_1} + \frac{\partial u_1(X_1(\alpha, x_1, x_2, x_3))}{\partial x_3} \right) \left(1 + \alpha \frac{\partial \eta_{24}(X_1(\alpha, x_1, x_2, x_3))}{\partial x_1} \right) n_3(X_1(\alpha, x_1, x_2, x_3)) d\gamma dt \right]_{\alpha=0} \\
& = \left[- \int_{t_1}^{t_2} \int_{\gamma} \frac{1}{\operatorname{Re}} \left(\frac{\partial}{\partial x_1} \left(\frac{\partial u_3(X_1(\alpha, x_1, x_2, x_3))}{\partial x_1} \right) \frac{\partial X_1(X_1(\alpha, x_1, x_2, x_3))}{\partial \alpha} \right) + \frac{\partial}{\partial x_3} \left(\frac{\partial u_1(X_1(\alpha, x_1, x_2, x_3))}{\partial x_3} \right) \frac{\partial X_1(X_1(\alpha, x_1, x_2, x_3))}{\partial \alpha} \right) \left(1 + \alpha \frac{\partial \eta_{24}}{\partial x_1} \right) n_3 d\gamma dt \right]_{\alpha=0} \\
& + \left[- \int_{t_1}^{t_2} \int_{\gamma} \frac{1}{\operatorname{Re}} \left(\frac{\partial u_3(X_1(\alpha, x_1, x_2, x_3))}{\partial x_1} + \frac{\partial u_1(X_1(\alpha, x_1, x_2, x_3))}{\partial x_3} \right) \left(1 + \alpha \frac{\partial \eta_{24}(X_1(\alpha, x_1, x_2, x_3))}{\partial x_1} \right) \frac{\partial n_3(X_1(\alpha, x_1, x_2, x_3))}{\partial X_1} \frac{\partial X_1(X_1(\alpha, x_1, x_2, x_3))}{\partial \alpha} d\gamma dt \right]_{\alpha=0} \\
& + \left[- \int_{t_1}^{t_2} \int_{\gamma} \frac{1}{\operatorname{Re}} \left(\frac{\partial u_3(X_1(\alpha, x_1, x_2, x_3))}{\partial x_1} + \frac{\partial u_1(X_1(\alpha, x_1, x_2, x_3))}{\partial x_3} \right) \frac{\partial \eta_{24}(X_1(\alpha, x_1, x_2, x_3))}{\partial x_1} n_3(X_1(\alpha, x_1, x_2, x_3)) d\gamma dt \right]_{\alpha=0}
\end{aligned} \tag{C13}$$

Using Eq.(C2), it is derived as follows:

$$\frac{\partial X_1(\alpha, x_1, x_2, x_3)}{\partial \alpha} = \frac{\partial}{\partial \alpha} (x_1 + \alpha \eta_{24}(x_1, x_2, x_3)) = \eta_{24}(x_1, x_2, x_3) \quad \text{in } \Omega \tag{C14}$$

Eq.(C2) at $\alpha=0$ is as follows:

$$X_l(0, x_1, x_2, x_3) = x_l \quad l = 1, 2, 3 \quad \text{in } \Omega \tag{C15}$$

Eq.(C11) is as follows:

$$\begin{aligned}
& \left[-\frac{\partial}{\partial \alpha} \int_{t_1}^{t_2} \int_{\gamma} \left\{ -p(X_1(\alpha, x_1, x_2, x_3)) + \frac{2}{\operatorname{Re}} \frac{\partial u_1(X_1(\alpha, x_1, x_2, x_3))}{\partial x_1} \right\} n_1(X_1(\alpha, x_1, x_2, x_3)) d\gamma dt \right]_{\alpha=0} \\
& = - \int_{t_1}^{t_2} \int_{\gamma} \left\{ -\frac{\partial p}{\partial x_1} \eta_{24} + \frac{2}{\operatorname{Re}} \frac{\partial}{\partial x_1} \left(\frac{\partial u_1}{\partial x_1} \eta_{24} \right) \right\} n_1 d\gamma dt - \int_{t_1}^{t_2} \int_{\gamma} \left\{ -p + \frac{2}{\operatorname{Re}} \frac{\partial u_1}{\partial x_1} \right\} \frac{\partial n_1}{\partial x_1} \eta_{24} d\gamma dt
\end{aligned} \tag{C16}$$

Eq.(C12) is as follows:

$$\begin{aligned}
& \left[-\frac{\partial}{\partial \alpha} \int_{t_1}^{t_2} \int_{\gamma} \frac{1}{\operatorname{Re}} \left(\frac{\partial u_2(X_1(\alpha, x_1, x_2, x_3))}{\partial x_1} + \frac{\partial u_1(X_1(\alpha, x_1, x_2, x_3))}{\partial x_2} \right) \left(1 + \alpha \frac{\partial \eta_{24}(X_1(\alpha, x_1, x_2, x_3))}{\partial x_1} \right) n_2(X_1(\alpha, x_1, x_2, x_3)) d\gamma dt \right]_{\alpha=0} \\
& = - \int_{t_1}^{t_2} \int_{\gamma} \frac{1}{\operatorname{Re}} \left\{ \frac{\partial}{\partial x_1} \left(\frac{\partial u_2}{\partial x_1} \eta_{24} \right) + \frac{\partial}{\partial x_2} \left(\frac{\partial u_1}{\partial x_1} \eta_{24} \right) \right\} n_2 d\gamma dt - \int_{t_1}^{t_2} \int_{\gamma} \frac{1}{\operatorname{Re}} \left(\frac{\partial u_2}{\partial x_1} + \frac{\partial u_1}{\partial x_2} \right) \frac{\partial n_2}{\partial x_1} \eta_{24} d\gamma dt - \int_{t_1}^{t_2} \int_{\gamma} \frac{1}{\operatorname{Re}} \left(\frac{\partial u_2}{\partial x_1} + \frac{\partial u_1}{\partial x_2} \right) \frac{\partial \eta_{24}}{\partial x_1} n_2 d\gamma dt
\end{aligned} \tag{C17}$$

Eq.(C13) is as follows:

$$\begin{aligned}
& \left[-\frac{\partial}{\partial \alpha} \int_{t_1}^{t_2} \int_{\gamma} \frac{1}{\operatorname{Re}} \left(\frac{\partial u_3(X_1(\alpha, x_1, x_2, x_3))}{\partial x_1} + \frac{\partial u_1(X_1(\alpha, x_1, x_2, x_3))}{\partial x_3} \right) \left(1 + \alpha \frac{\partial \eta_{24}(X_1(\alpha, x_1, x_2, x_3))}{\partial x_1} \right) n_3(X_1(\alpha, x_1, x_2, x_3)) d\gamma dt \right]_{\alpha=0} \\
& = - \int_{t_1}^{t_2} \int_{\gamma} \frac{1}{\operatorname{Re}} \left\{ \frac{\partial}{\partial x_1} \left(\frac{\partial u_3}{\partial x_1} \eta_{24} \right) + \frac{\partial}{\partial x_3} \left(\frac{\partial u_1}{\partial x_1} \eta_{24} \right) \right\} n_3 d\gamma dt - \int_{t_1}^{t_2} \int_{\gamma} \frac{1}{\operatorname{Re}} \left(\frac{\partial u_3}{\partial x_1} + \frac{\partial u_1}{\partial x_3} \right) \frac{\partial n_3}{\partial x_1} \eta_{24} d\gamma dt - \int_{t_1}^{t_2} \int_{\gamma} \frac{1}{\operatorname{Re}} \left(\frac{\partial u_3}{\partial x_1} + \frac{\partial u_1}{\partial x_3} \right) \frac{\partial \eta_{24}}{\partial x_1} n_3 d\gamma dt
\end{aligned} \tag{C18}$$

Therefore, the first term in Eq.(C1) is as follows:

$$\begin{aligned} & \left[-\frac{\partial}{\partial \alpha} \int_{t_s}^{t_e} \int_{\gamma(x)} T_1(X_1(\alpha, x_1, x_2, x_3)) d\gamma dt \right]_{\alpha=0} = - \int_{t_s}^{t_e} \int_{\gamma(x)} \left\{ -\frac{\partial p}{\partial x_1} n_i + \frac{1}{\text{Re}} \frac{\partial}{\partial x_1} \left(\frac{\partial u_i}{\partial x_1} + \frac{\partial u_i}{\partial x_i} \right) n_i \right\} \eta_{24} d\gamma dt \\ & - \int_{t_s}^{t_e} \int_{\gamma(x)} \left\{ -p \frac{\partial n_i}{\partial x_1} + \frac{1}{\text{Re}} \left(\frac{\partial u_i}{\partial x_1} + \frac{\partial u_i}{\partial x_i} \right) \frac{\partial n_i}{\partial x_1} \right\} \eta_{24} d\gamma dt - \int_{t_s}^{t_e} \int_{\gamma(x)} \frac{1}{\text{Re}} \left(\frac{\partial u_i}{\partial x_1} \frac{\partial \eta_{24}}{\partial x_1} + \frac{\partial u_i}{\partial x_1} \frac{\partial \eta_{24}}{\partial x_i} \right) n_i d\gamma dt \\ & - \int_{t_s}^{t_e} \int_{\gamma(x)} \frac{1}{\text{Re}} \left(\frac{\partial u_2}{\partial x_1} + \frac{\partial u_1}{\partial x_2} \right) n_2 \frac{\partial \eta_{24}}{\partial x_1} d\gamma dt - \int_{t_s}^{t_e} \int_{\gamma(x)} \frac{1}{\text{Re}} \left(\frac{\partial u_3}{\partial x_1} + \frac{\partial u_1}{\partial x_3} \right) n_3 \frac{\partial \eta_{24}}{\partial x_1} d\gamma dt \end{aligned} \quad (\text{C19})$$

The second term in Eq.(C1) is expanded. The domain Ω is as follows:

$$\frac{\partial X_1, X_2, X_3}{\partial (x_1, x_2, x_3)} = \begin{vmatrix} \frac{\partial X_1}{\partial x_1} & \frac{\partial X_2}{\partial x_1} & \frac{\partial X_3}{\partial x_1} \\ \frac{\partial X_1}{\partial x_2} & \frac{\partial X_2}{\partial x_2} & \frac{\partial X_3}{\partial x_2} \\ \frac{\partial X_1}{\partial x_3} & \frac{\partial X_2}{\partial x_3} & \frac{\partial X_3}{\partial x_3} \end{vmatrix} = \begin{vmatrix} \frac{\partial}{\partial x_1} (x_1 + \alpha \eta_{24}(x_1, x_2, x_3)) & \frac{\partial x_2}{\partial x_1} & \frac{\partial x_3}{\partial x_1} \\ \frac{\partial}{\partial x_2} (x_1 + \alpha \eta_{24}(x_1, x_2, x_3)) & \frac{\partial x_2}{\partial x_2} & \frac{\partial x_3}{\partial x_2} \\ \frac{\partial}{\partial x_3} (x_1 + \alpha \eta_{24}(x_1, x_2, x_3)) & \frac{\partial x_2}{\partial x_3} & \frac{\partial x_3}{\partial x_3} \end{vmatrix} = \begin{vmatrix} 1 + \alpha \frac{\partial \eta_{24}(x_1, x_2, x_3)}{\partial x_1} & 0 & 0 \\ \alpha \frac{\partial \eta_{24}(x_1, x_2, x_3)}{\partial x_2} & 1 & 0 \\ \alpha \frac{\partial \eta_{24}(x_1, x_2, x_3)}{\partial x_3} & 0 & 1 \end{vmatrix} = 1 + \alpha \frac{\partial \eta_{24}(x_1, x_2, x_3)}{\partial x_1} \quad (\text{C20})$$

The second term in Eq.(C1) is as follows:

$$\begin{aligned} & \left[\frac{\partial}{\partial \alpha} \int_{t_s}^{t_e} \int_{\Omega(x)} p(X_1) \frac{\partial \lambda_{j+1}(X_1)}{\partial x_j} d\Omega dt \right]_{\alpha=0} = \left[\frac{\partial}{\partial \alpha} \int_{t_s}^{t_e} \int_{\Omega(x)} p(X_1) \frac{\partial \lambda_{j+1}(X_1)}{\partial x_j} \left(1 + \alpha \frac{\partial \eta_{24}}{\partial x_1} \right) d\Omega dt \right]_{\alpha=0} \\ & = \left[\int_{t_s}^{t_e} \int_{\Omega(x)} \frac{\partial p(X_1)}{\partial \alpha} \frac{\partial X_1}{\partial x_1} \frac{\partial \lambda_{j+1}(X_1)}{\partial x_j} \left(1 + \alpha \frac{\partial \eta_{24}}{\partial x_1} \right) d\Omega dt \right]_{\alpha=0} + \left[\int_{t_s}^{t_e} \int_{\Omega(x)} p(X_1) \frac{\partial}{\partial x_j} \left(\frac{\partial \lambda_{j+1}(X_1)}{\partial x_1} \frac{\partial X_1}{\partial \alpha} \right) \left(1 + \alpha \frac{\partial \eta_{24}}{\partial x_1} \right) d\Omega dt \right]_{\alpha=0} \\ & + \left[\int_{t_s}^{t_e} \int_{\Omega(x)} p(X_1) \frac{\partial \lambda_{j+1}(X_1)}{\partial x_j} \frac{\partial \eta_{24}}{\partial x_1} d\Omega dt \right]_{\alpha=0} \\ & = \int_{t_s}^{t_e} \int_{\Omega(x)} \frac{\partial p}{\partial x_1} \frac{\partial \lambda_{j+1}}{\partial x_j} \eta_{24} d\Omega dt + \int_{t_s}^{t_e} \int_{\Omega(x)} p \frac{\partial}{\partial x_j} \left(\frac{\partial \lambda_{j+1}}{\partial x_1} \eta_{24} \right) d\Omega dt + \int_{t_s}^{t_e} \int_{\Omega(x)} p \frac{\partial \lambda_{j+1}}{\partial x_j} \frac{\partial \eta_{24}}{\partial x_1} d\Omega dt \\ & = \int_{t_s}^{t_e} \int_{\Omega(x)} \frac{\partial p}{\partial x_1} \frac{\partial \lambda_{j+1}}{\partial x_j} \eta_{24} d\Omega dt + \int_{t_s}^{t_e} \int_{\psi(x)} p \frac{\partial \lambda_{j+1}}{\partial x_1} n_j \eta_{24} d\psi dt - \int_{t_s}^{t_e} \int_{\Omega(x)} \frac{\partial p}{\partial x_j} \frac{\partial \lambda_{j+1}}{\partial x_1} \eta_{24} d\Omega dt + \int_{t_s}^{t_e} \int_{\Omega(x)} p \frac{\partial \lambda_{j+1}}{\partial x_j} \frac{\partial \eta_{24}}{\partial x_1} d\Omega dt \end{aligned} \quad (\text{C21})$$

Using Eq.(2.35), Eq.(C21) is as follows:

$$\left[\frac{\partial}{\partial \alpha} \int_{t_s}^{t_e} \int_{\Omega(x)} p(X_1) \frac{\partial \lambda_{j+1}(X_1)}{\partial x_j} d\Omega dt \right]_{\alpha=0} = \int_{t_s}^{t_e} \int_{\psi} p \frac{\partial \lambda_{j+1}}{\partial x_1} n_j \eta_{24} d\psi dt - \int_{t_s}^{t_e} \int_{\Omega} \frac{\partial p}{\partial x_j} \frac{\partial \lambda_{j+1}}{\partial x_1} \eta_{24} d\Omega dt \quad (\text{C22})$$

The domain $X_I(\alpha, x_1, x_2, x_3)$ are abbreviated to X_I . This abbreviation is same in the other equation. The time derivation in the third term is as follows:

$$\begin{aligned}
& \int_{t_1}^{t_e} \int_{\Omega} u_i \left\{ \frac{\partial \lambda_{j+1}}{\partial \alpha} - \frac{\partial \lambda_j}{\partial \alpha_i} + U_j \frac{\partial \lambda_{j+1}}{\partial \alpha_j} + \frac{1}{\text{Re}} \frac{\partial}{\partial \alpha_j} \left(\frac{\partial \lambda_{j+1}}{\partial \alpha_i} + \frac{\partial \lambda_{j+1}}{\partial \alpha_j} \right) \right\} d\Omega dt = \int_{t_1}^{t_e} \int_{\Omega} \frac{\partial u_j}{\partial \alpha} \left\{ \frac{\partial \lambda_{j+1}}{\partial \alpha} - \frac{\partial \lambda_j}{\partial \alpha_i} + U_i \frac{\partial \lambda_{j+1}}{\partial \alpha_i} + \frac{1}{\text{Re}} \frac{\partial}{\partial \alpha_i} \left(\frac{\partial \lambda_{j+1}}{\partial \alpha_i} + \frac{\partial \lambda_{j+1}}{\partial \alpha_j} \right) \right\} \eta_{24} d\Omega dt \\
& + \int_{t_1}^{t_e} \int_{\Omega} \frac{\partial \lambda_{j+1}}{\partial \alpha_i} \left\{ - \frac{\partial u_j}{\partial \alpha} - \frac{\partial u_i}{\partial \alpha_j} U_j + \frac{1}{\text{Re}} \frac{\partial}{\partial \alpha_i} \left(\frac{\partial u_i}{\partial \alpha_j} + \frac{\partial u_j}{\partial \alpha_i} \right) \right\} \eta_{24} d\Omega dt + \int_{t_1}^{t_e} \int_{\Omega} u_i \left\{ \frac{\partial \lambda_{j+1}}{\partial \alpha} - \frac{\partial \lambda_j}{\partial \alpha_j} + U_i \frac{\partial \lambda_{j+1}}{\partial \alpha_i} + \frac{1}{\text{Re}} \frac{\partial}{\partial \alpha_i} \left(\frac{\partial \lambda_{j+1}}{\partial \alpha_i} + \frac{\partial \lambda_{j+1}}{\partial \alpha_j} \right) \right\} \frac{\partial \eta_{24}}{\partial \alpha_i} d\Omega dt \\
& + \int_{t_1}^{t_e} \int_{\Omega} \frac{\partial u_j}{\partial \alpha_j} \frac{\partial \lambda_j}{\partial \alpha_i} \eta_{24} d\Omega dt + \int_{\Omega} \left[u_j \frac{\partial \lambda_{j+1}}{\partial \alpha_i} \eta_{24} \right]_{t_1}^{t_e} d\Omega + \int_{t_1}^{t_e} \int_{\gamma} u_i \left\{ U_j \frac{\partial \lambda_{j+1}}{\partial \alpha_i} n_j - \frac{\partial \lambda_j}{\partial \alpha_i} n_i + \frac{1}{\text{Re}} \left(\frac{\partial}{\partial \alpha_i} \frac{\partial \lambda_{j+1}}{\partial \alpha_i} + \frac{\partial}{\partial \alpha_j} \frac{\partial \lambda_{j+1}}{\partial \alpha_i} \right) n_j \right\} \eta_{24} d\Gamma dt \\
& - \int_{t_1}^{t_e} \int_{\gamma} \left\{ -p\eta + \frac{1}{\text{Re}} \left(\frac{\partial u_j}{\partial \alpha_i} + \frac{\partial u_i}{\partial \alpha_j} \right) n_j \right\} \frac{\partial \lambda_{j+1}}{\partial \alpha_i} \eta_{24} d\gamma dt + \frac{1}{\text{Re}} \int_{t_1}^{t_e} \int_{\gamma} u_i \left\{ \frac{\partial \lambda_{j+1}}{\partial \alpha_i} \frac{\partial \eta_{24}}{\partial \alpha_i} + \frac{\partial \lambda_{j+1}}{\partial \alpha_i} \frac{\partial \eta_{24}}{\partial \alpha_j} \right\} n_j d\Gamma dt
\end{aligned} \tag{C27}$$

Using Eq.(2.35)~Eq.(2.38), Eq.(2.23)~Eq.(2.26), Eq.(B23), Table 1, Eq.(C27) becomes as follows:

$$\begin{aligned}
& \int_{t_1}^{t_e} \int_{\Omega} u_i \left\{ \frac{\partial \lambda_{j+1}}{\partial \alpha} - \frac{\partial \lambda_j}{\partial \alpha_i} + U_j \frac{\partial \lambda_{j+1}}{\partial \alpha_j} + \frac{1}{\text{Re}} \frac{\partial}{\partial \alpha_j} \left(\frac{\partial \lambda_{j+1}}{\partial \alpha_i} + \frac{\partial \lambda_{j+1}}{\partial \alpha_j} \right) \right\} d\Omega dt = \int_{t_1}^{t_e} \int_{\gamma} u_i \left\{ U_j \frac{\partial \lambda_{j+1}}{\partial \alpha_i} n_j - \frac{\partial \lambda_j}{\partial \alpha_i} n_i + \frac{1}{\text{Re}} \left(\frac{\partial}{\partial \alpha_i} \frac{\partial \lambda_{j+1}}{\partial \alpha_i} + \frac{\partial}{\partial \alpha_j} \frac{\partial \lambda_{j+1}}{\partial \alpha_i} \right) n_j \right\} \eta_{24} d\Gamma dt \\
& + \int_{\Omega} \left[u_j \frac{\partial \lambda_{j+1}}{\partial \alpha_i} \eta_{24} \right]_{t_1}^{t_e} d\Omega - \int_{t_1}^{t_e} \int_{\gamma} \left\{ -p\eta + \frac{1}{\text{Re}} \left(\frac{\partial u_j}{\partial \alpha_i} + \frac{\partial u_i}{\partial \alpha_j} \right) n_j \right\} \frac{\partial \lambda_{j+1}}{\partial \alpha_i} \eta_{24} d\gamma dt + \frac{1}{\text{Re}} \int_{t_1}^{t_e} \int_{\gamma} u_i \left\{ \frac{\partial \lambda_{j+1}}{\partial \alpha_i} \frac{\partial \eta_{24}}{\partial \alpha_i} + \frac{\partial \lambda_{j+1}}{\partial \alpha_i} \frac{\partial \eta_{24}}{\partial \alpha_j} \right\} n_j d\Gamma dt
\end{aligned} \tag{C28}$$

The fourth term in Eq.(C1) is as follows:

$$\begin{aligned}
& - \left[\frac{\partial}{\partial \alpha} \int_{t_1}^{t_e} \int_{\gamma(\mathbf{x})} u_i S_i d\gamma dt \right]_{\alpha=0} = - \int_{t_1}^{t_e} \int_{\gamma(\mathbf{x})} \frac{\partial u_j}{\partial \alpha_i} \left\{ \lambda_{j+1} U_i n_i - \lambda_i n_j + \frac{1}{\text{Re}} \left(\frac{\partial \lambda_{j+1}}{\partial \alpha_i} + \frac{\partial \lambda_{j+1}}{\partial \alpha_{j+1}} \right) n_i \right\} \eta_{24} d\gamma dt \\
& - \int_{t_1}^{t_e} \int_{\gamma} u_j \left\{ \frac{\partial \lambda_{j+1}}{\partial \alpha_i} U_i n_i - \frac{\partial \lambda_i}{\partial \alpha_i} n_j + \frac{1}{\text{Re}} \left(\frac{\partial}{\partial \alpha_i} \frac{\partial \lambda_{j+1}}{\partial \alpha_i} + \frac{\partial}{\partial \alpha_{j+1}} \frac{\partial \lambda_{j+1}}{\partial \alpha_i} \right) n_i \right\} \eta_{24} d\gamma dt \\
& - \int_{t_1}^{t_e} \int_{\gamma} u_j \left\{ \lambda_{j+1} U_i \frac{\partial n_i}{\partial \alpha_i} - \lambda_i \frac{\partial n_j}{\partial \alpha_i} + \frac{1}{\text{Re}} \left(\frac{\partial \lambda_{j+1}}{\partial \alpha_i} + \frac{\partial \lambda_{j+1}}{\partial \alpha_j} \right) \frac{\partial n_i}{\partial \alpha_i} \right\} \eta_{24} d\gamma dt - \int_{t_1}^{t_e} \int_{\gamma} u_j \frac{1}{\text{Re}} \left(\frac{\partial \lambda_{j+1}}{\partial \alpha_i} \frac{\partial \eta_{24}}{\partial \alpha_i} + \frac{\partial \lambda_{j+1}}{\partial \alpha_i} \frac{\partial \eta_{24}}{\partial \alpha_j} \right) n_i \eta_{24} d\gamma dt \\
& - \int_{t_1}^{t_e} \int_{\gamma} u_i \left\{ \lambda_{j+1} U_2 n_2 + \frac{1}{\text{Re}} \left(\frac{\partial \lambda_{j+1}}{\partial \alpha_2} + \frac{\partial \lambda_3}{\partial \alpha_i} \right) n_2 \right\} \frac{\partial \eta_{24}}{\partial \alpha_1} d\gamma dt + \int_{t_1}^{t_e} \int_{\gamma} u_2 \lambda_2 n_2 \frac{\partial \eta_{24}}{\partial \alpha_1} d\gamma dt \\
& - \int_{t_1}^{t_e} \int_{\gamma} u_i \left\{ \lambda_{j+1} U_3 n_3 + \frac{1}{\text{Re}} \left(\frac{\partial \lambda_{j+1}}{\partial \alpha_3} + \frac{\partial \lambda_4}{\partial \alpha_i} \right) n_3 \right\} \frac{\partial \eta_{24}}{\partial \alpha_1} d\gamma dt + \int_{t_1}^{t_e} \int_{\gamma} u_3 \lambda_3 n_3 \frac{\partial \eta_{24}}{\partial \alpha_1} d\gamma dt
\end{aligned} \tag{C29}$$

The calculation condition becomes $u_i=0$ on the boundary γ . It becomes $n_2=n_3=0$ on the boundary Γ_W , Γ_E . It becomes $n_1=n_3=0$, $u_2=0$, $S_1=0$ and $S_3=0$ on the boundary Γ_N , Γ_S . It becomes $n_1=n_2=0$, $u_3=0$, $S_1=0$ and $S_2=0$ on the boundary Γ_U , Γ_L . Therefore, the fifth - eighth terms become zero. Eq.(C29) is as follows:

$$\begin{aligned}
& - \left[\frac{\partial}{\partial \alpha} \int_{t_1}^{t_e} \int_{\gamma(\mathbf{x})} u_i S_i d\gamma dt \right]_{\alpha=0} = - \int_{t_1}^{t_e} \int_{\gamma(\mathbf{x})} \frac{\partial u_j}{\partial \alpha_i} \left\{ \lambda_{j+1} U_i n_i - \lambda_i n_j + \frac{1}{\text{Re}} \left(\frac{\partial \lambda_{j+1}}{\partial \alpha_i} + \frac{\partial \lambda_{j+1}}{\partial \alpha_{j+1}} \right) n_i \right\} \eta_{24} d\gamma dt \\
& - \int_{t_1}^{t_e} \int_{\gamma} u_j \left\{ \frac{\partial \lambda_{j+1}}{\partial \alpha_i} U_i n_i - \frac{\partial \lambda_i}{\partial \alpha_i} n_j + \frac{1}{\text{Re}} \left(\frac{\partial}{\partial \alpha_i} \frac{\partial \lambda_{j+1}}{\partial \alpha_i} + \frac{\partial}{\partial \alpha_{j+1}} \frac{\partial \lambda_{j+1}}{\partial \alpha_i} \right) n_i \right\} \eta_{24} d\gamma dt \\
& - \int_{t_1}^{t_e} \int_{\gamma} u_j \left\{ \lambda_{j+1} U_i \frac{\partial n_i}{\partial \alpha_i} - \lambda_i \frac{\partial n_j}{\partial \alpha_i} + \frac{1}{\text{Re}} \left(\frac{\partial \lambda_{j+1}}{\partial \alpha_i} + \frac{\partial \lambda_{j+1}}{\partial \alpha_j} \right) \frac{\partial n_i}{\partial \alpha_i} \right\} \eta_{24} d\gamma dt - \int_{t_1}^{t_e} \int_{\gamma} u_j \frac{1}{\text{Re}} \left(\frac{\partial \lambda_{j+1}}{\partial \alpha_i} \frac{\partial \eta_{24}}{\partial \alpha_i} + \frac{\partial \lambda_{j+1}}{\partial \alpha_i} \frac{\partial \eta_{24}}{\partial \alpha_j} \right) n_i \eta_{24} d\gamma dt
\end{aligned} \tag{C30}$$

The fifth term in Eq.(C1) is as follows:

$$\begin{aligned} & \left[\frac{\partial}{\partial \alpha} \int_{t_s}^{t_e} \int_{\Gamma_W(\mathbf{x})+\gamma(\mathbf{x})} \lambda_2 T_i d(\Gamma_W + \gamma) dt \right]_{\alpha=0} = \int_{t_s}^{t_e} \int_{\Gamma_W(\mathbf{x})+\gamma(\mathbf{x})} \frac{\partial \lambda_2}{\partial \hat{\alpha}_1} \left\{ -pn_i + \frac{1}{\text{Re}} \left(\frac{\partial u_i}{\partial \hat{\alpha}_1} + \frac{\partial u_i}{\partial \hat{\alpha}_2} \right) n_i \right\} \eta_{24} d(\Gamma_W + \gamma) dt \\ & + \int_{t_s}^{t_e} \int_{\Gamma_W+\gamma} \lambda_2 \left\{ \frac{\partial p}{\partial \hat{\alpha}_1} n_i + \frac{1}{\text{Re}} \left(\frac{\partial \partial u_i}{\partial \hat{\alpha}_1 \partial \hat{\alpha}_1} + \frac{\partial \partial u_i}{\partial \hat{\alpha}_1 \partial \hat{\alpha}_2} \right) n_i \right\} \eta_{24} d(\Gamma_W + \gamma) dt + \int_{t_s}^{t_e} \int_{\Gamma_W+\gamma} \lambda_2 \left\{ -p \frac{\partial n_i}{\partial \hat{\alpha}_1} + \frac{1}{\text{Re}} \left(\frac{\partial u_i}{\partial \hat{\alpha}_1} + \frac{\partial u_i}{\partial \hat{\alpha}_2} \right) \frac{\partial n_i}{\partial \hat{\alpha}_1} \right\} \eta_{24} d(\Gamma_W + \gamma) dt \quad (\text{C31}) \\ & + \int_{t_s}^{t_e} \int_{\Gamma_W+\gamma} \lambda_2 \frac{1}{\text{Re}} \left(\frac{\partial u_i}{\partial \hat{\alpha}_1} \frac{\partial \eta_{24}}{\partial \hat{\alpha}_1} + \frac{\partial u_i}{\partial \hat{\alpha}_1} \frac{\partial \eta_{24}}{\partial \hat{\alpha}_2} \right) n_i d(\Gamma_W + \gamma) dt + \int_{t_s}^{t_e} \int_{\Gamma_W+\gamma} \lambda_2 \frac{1}{\text{Re}} \left(\frac{\partial u_i}{\partial \hat{\alpha}_1} + \frac{\partial u_i}{\partial \hat{\alpha}_2} \right) \frac{\partial \eta_{24}}{\partial \hat{\alpha}_1} n_i d(\Gamma_W + \gamma) dt \\ & + \int_{t_s}^{t_e} \int_{\Gamma_W+\gamma} \lambda_2 \frac{1}{\text{Re}} \left(\frac{\partial u_i}{\partial \hat{\alpha}_1} + \frac{\partial u_i}{\partial \hat{\alpha}_2} \right) \frac{\partial \eta_{24}}{\partial \hat{\alpha}_1} n_i d(\Gamma_W + \gamma) dt \end{aligned}$$

Using the boundary condition $\lambda_2=0$ on Γ_W and $\lambda_2=1$ on γ , Eq.(C31) is as follows:

$$\begin{aligned} & \left[\frac{\partial}{\partial \alpha} \int_{t_s}^{t_e} \int_{\Gamma_W(\mathbf{x})+\gamma(\mathbf{x})} \lambda_2(X_1) T_i(X_1) d(\Gamma_W + \gamma) dt \right]_{\alpha=0} = \int_{t_s}^{t_e} \int_{\Gamma_W(\mathbf{x})+\gamma(\mathbf{x})} \frac{\partial \lambda_2}{\partial \hat{\alpha}_1} \left\{ -pn_i + \frac{1}{\text{Re}} \left(\frac{\partial u_i}{\partial \hat{\alpha}_1} + \frac{\partial u_i}{\partial \hat{\alpha}_2} \right) n_i \right\} \eta_{24} d\gamma dt \\ & + \int_{t_s}^{t_e} \int_{\gamma} \left\{ -\frac{\partial p}{\partial \hat{\alpha}_1} n_i + \frac{1}{\text{Re}} \left(\frac{\partial \partial u_i}{\partial \hat{\alpha}_1 \partial \hat{\alpha}_1} + \frac{\partial \partial u_i}{\partial \hat{\alpha}_1 \partial \hat{\alpha}_2} \right) n_i \right\} \eta_{24} dy dt + \int_{t_s}^{t_e} \int_{\gamma} \left\{ -p \frac{\partial n_i}{\partial \hat{\alpha}_1} + \frac{1}{\text{Re}} \left(\frac{\partial u_i}{\partial \hat{\alpha}_1} + \frac{\partial u_i}{\partial \hat{\alpha}_2} \right) \frac{\partial n_i}{\partial \hat{\alpha}_1} \right\} \eta_{24} dy dt \quad (\text{C32}) \\ & + \int_{t_s}^{t_e} \int_{\gamma} \frac{1}{\text{Re}} \left(\frac{\partial u_i}{\partial \hat{\alpha}_1} \frac{\partial \eta_{24}}{\partial \hat{\alpha}_1} + \frac{\partial u_i}{\partial \hat{\alpha}_1} \frac{\partial \eta_{24}}{\partial \hat{\alpha}_2} \right) n_i dy dt + \int_{t_s}^{t_e} \int_{\gamma} \frac{1}{\text{Re}} \left(\frac{\partial u_i}{\partial \hat{\alpha}_1} + \frac{\partial u_i}{\partial \hat{\alpha}_2} \right) \frac{\partial \eta_{24}}{\partial \hat{\alpha}_1} n_i dy dt + \int_{t_s}^{t_e} \int_{\gamma} \frac{1}{\text{Re}} \left(\frac{\partial u_i}{\partial \hat{\alpha}_1} + \frac{\partial u_i}{\partial \hat{\alpha}_2} \right) \frac{\partial \eta_{24}}{\partial \hat{\alpha}_1} n_i dy dt \end{aligned}$$

The sixth term in Eq.(C1) is as follows:

$$\begin{aligned} & \left[\frac{\partial}{\partial \alpha} \int_{t_s}^{t_e} \int_{\Gamma_W(\mathbf{x})+\Gamma_N(\mathbf{x})+\Gamma_S(\mathbf{x})+\gamma(\mathbf{x})} \lambda_3(X_1) T_2(X_1) d(\Gamma_W + \Gamma_N + \Gamma_S + \gamma) dt \right]_{\alpha=0} \\ & = \int_{t_s}^{t_e} \int_{\Gamma_W(\mathbf{x})+\Gamma_N(\mathbf{x})+\Gamma_S(\mathbf{x})+\gamma(\mathbf{x})} \frac{\partial \lambda_3}{\partial \hat{\alpha}_1} \left\{ -pn_2 + \frac{1}{\text{Re}} \left(\frac{\partial u_i}{\partial \hat{\alpha}_2} + \frac{\partial u_i}{\partial \hat{\alpha}_3} \right) n_i \right\} \eta_{24} d(\Gamma_W + \Gamma_N + \Gamma_S + \gamma) dt \\ & + \int_{t_s}^{t_e} \int_{\Gamma_W+\Gamma_N+\Gamma_S+\gamma} \lambda_3 \left\{ -\frac{\partial p}{\partial \hat{\alpha}_1} n_2 + \frac{1}{\text{Re}} \left(\frac{\partial \partial u_i}{\partial \hat{\alpha}_1 \partial \hat{\alpha}_1} + \frac{\partial \partial u_i}{\partial \hat{\alpha}_1 \partial \hat{\alpha}_2} \right) n_i \right\} \eta_{24} d(\Gamma_W + \Gamma_N + \Gamma_S + \gamma) dt \\ & + \int_{t_s}^{t_e} \int_{\Gamma_W+\Gamma_N+\Gamma_S+\gamma} \frac{1}{\text{Re}} \lambda_3 \left(\frac{\partial u_i}{\partial \hat{\alpha}_1} \frac{\partial \eta_{24}}{\partial \hat{\alpha}_2} + \frac{\partial u_i}{\partial \hat{\alpha}_1} \frac{\partial \eta_{24}}{\partial \hat{\alpha}_3} \right) n_i d(\Gamma_W + \Gamma_N + \Gamma_S + \gamma) dt \\ & + \int_{t_s}^{t_e} \int_{\Gamma_W+\Gamma_N+\Gamma_S+\gamma} \lambda_3 \left\{ -p + \frac{1}{\text{Re}} \left(\frac{\partial u_i}{\partial \hat{\alpha}_2} + \frac{\partial u_i}{\partial \hat{\alpha}_3} \right) \right\} \frac{\partial n_i}{\partial \hat{\alpha}_1} \eta_{24} d(\Gamma_W + \Gamma_N + \Gamma_S + \gamma) dt \\ & + \int_{t_s}^{t_e} \int_{\Gamma_W+\Gamma_N+\Gamma_S+\gamma} \lambda_3 \left\{ -p + \frac{1}{\text{Re}} \left(\frac{\partial u_i}{\partial \hat{\alpha}_2} + \frac{\partial u_i}{\partial \hat{\alpha}_3} \right) \right\} n_2 \frac{\partial \eta_{24}}{\partial \hat{\alpha}_1} d(\Gamma_W + \Gamma_N + \Gamma_S + \gamma) dt \\ & + \int_{t_s}^{t_e} \int_{\Gamma_W+\Gamma_N+\Gamma_S+\gamma} \lambda_3 \frac{1}{\text{Re}} \left(\frac{\partial u_i}{\partial \hat{\alpha}_2} + \frac{\partial u_i}{\partial \hat{\alpha}_3} \right) n_3 \frac{\partial \eta_{24}}{\partial \hat{\alpha}_1} d(\Gamma_W + \Gamma_N + \Gamma_S + \gamma) dt \quad (\text{C33}) \end{aligned}$$

Using the boundary condition $\lambda_3=0$ on γ , Γ_W , Γ_N and Γ_S , Eq.(C33) is as follows:

$$\begin{aligned} & \left[\frac{\partial}{\partial \alpha} \int_{t_s}^{t_e} \int_{\Gamma_W(\mathbf{x}) + \Gamma_N(\mathbf{x}) + \Gamma_S(\mathbf{x}) + \gamma(\mathbf{x})} \lambda_3(X_1) T_2(X_1) d(\Gamma_W + \Gamma_N + \Gamma_S + \gamma) dt \right]_{\alpha=0} \\ &= \int_{t_s}^{t_e} \int_{\Gamma_W(\mathbf{x}) + \Gamma_N(\mathbf{x}) + \Gamma_S(\mathbf{x}) + \gamma(\mathbf{x})} \frac{\partial \lambda_3}{\partial \dot{x}_1} \left\{ -pn_2 + \frac{1}{\text{Re}} \left(\frac{\partial u_i}{\partial x_2} + \frac{\partial u_2}{\partial x_i} \right) n_i \right\} \eta_{24} d(\Gamma_W + \Gamma_N + \Gamma_S + \gamma) dt \end{aligned} \quad (\text{C34})$$

The seventh term in Eq.(C1) is as follows:

$$\begin{aligned} & \left[\frac{\partial}{\partial \alpha} \int_{t_s}^{t_e} \int_{\Gamma_W(\mathbf{x}) + \Gamma_U(\mathbf{x}) + \Gamma_L(\mathbf{x}) + \gamma(\mathbf{x})} \lambda_4(X_1) T_3(X_1) d(\Gamma_W + \Gamma_U + \Gamma_L + \gamma) dt \right]_{\alpha=0} \\ &= \int_{t_s}^{t_e} \int_{\Gamma_W(\mathbf{x}) + \Gamma_U(\mathbf{x}) + \Gamma_L(\mathbf{x}) + \gamma(\mathbf{x})} \frac{\partial \lambda_4}{\partial \dot{x}_1} \left\{ -pn_3 + \frac{1}{\text{Re}} \left(\frac{\partial u_i}{\partial x_3} + \frac{\partial u_3}{\partial x_i} \right) n_i \right\} \eta_{24} d(\Gamma_W + \Gamma_U + \Gamma_L + \gamma) dt \\ &+ \int_{t_s}^{t_e} \int_{\Gamma_W + \Gamma_U + \Gamma_L + \gamma} \lambda_4 \left\{ -\frac{\partial p}{\partial \dot{x}_1} n_3 + \frac{1}{\text{Re}} \left(\frac{\partial}{\partial x_3} \frac{\partial u_i}{\partial x_1} + \frac{\partial}{\partial x_i} \frac{\partial u_3}{\partial x_1} \right) n_i \right\} \eta_{24} d(\Gamma_W + \Gamma_U + \Gamma_L + \gamma) dt \\ &+ \int_{t_s}^{t_e} \int_{\Gamma_W + \Gamma_U + \Gamma_L + \gamma} \lambda_4 \left\{ -p \frac{\partial n_3}{\partial \dot{x}_1} + \frac{1}{\text{Re}} \left(\frac{\partial u_i}{\partial x_3} + \frac{\partial u_3}{\partial x_i} \right) \right\} \frac{\partial n_i}{\partial \dot{x}_1} \eta_{24} d(\Gamma_W + \Gamma_U + \Gamma_L + \gamma) dt \\ &+ \int_{t_s}^{t_e} \int_{\Gamma_W + \Gamma_U + \Gamma_L + \gamma} \frac{1}{\text{Re}} \lambda_4 \left(\frac{\partial u_i}{\partial x_1} \frac{\partial \eta_{24}}{\partial x_3} + \frac{\partial u_3}{\partial x_1} \frac{\partial \eta_{24}}{\partial x_i} \right) n_i d(\Gamma_W + \Gamma_U + \Gamma_L + \gamma) dt \\ &+ \int_{t_s}^{t_e} \int_{\Gamma_W + \Gamma_U + \Gamma_L + \gamma} \lambda_4 \frac{1}{\text{Re}} \left(\frac{\partial u_2}{\partial x_3} + \frac{\partial u_3}{\partial x_2} \right) n_2 \frac{\partial \eta_{24}}{\partial \dot{x}_1} d(\Gamma_W + \Gamma_U + \Gamma_L + \gamma) dt \\ &+ \int_{t_s}^{t_e} \int_{\Gamma_W + \Gamma_U + \Gamma_L + \gamma} \lambda_4 \left\{ -p + \frac{2}{\text{Re}} \frac{\partial u_3}{\partial x_1} \right\} n_3 \frac{\partial \eta_{24}}{\partial \dot{x}_1} d(\Gamma_W + \Gamma_U + \Gamma_L + \gamma) dt \end{aligned} \quad (\text{C35})$$

Using the boundary condition $\lambda_4=0$ on γ , Γ_U , Γ_L and Γ_W , Eq.(C35) is as follows:

$$\begin{aligned} & \left[\frac{\partial}{\partial \alpha} \int_{t_s}^{t_e} \int_{\Gamma_W(\mathbf{x}) + \Gamma_U(\mathbf{x}) + \Gamma_L(\mathbf{x}) + \gamma(\mathbf{x})} \lambda_4(X_1) T_3(X_1) d(\Gamma_W + \Gamma_U + \Gamma_L + \gamma) dt \right]_{\alpha=0} \\ &= \int_{t_s}^{t_e} \int_{\Gamma_W(\mathbf{x}) + \Gamma_U(\mathbf{x}) + \Gamma_L(\mathbf{x}) + \gamma(\mathbf{x})} \frac{\partial \lambda_4}{\partial \dot{x}_1} \left\{ -pn_3 + \frac{1}{\text{Re}} \left(\frac{\partial u_i}{\partial x_3} + \frac{\partial u_3}{\partial x_i} \right) n_i \right\} \eta_{24} d(\Gamma_W + \Gamma_U + \Gamma_L + \gamma) dt \end{aligned} \quad (\text{C36})$$

The eighth in Eq.(C1) is as follows:

$$\begin{aligned} & - \left[\frac{\partial}{\partial \alpha} \int_{\Omega(\mathbf{x})} [\lambda_{i+1} u_i]_{t_s}^{t_e} d\Omega \right]_{\alpha=0} = - \left[\frac{\partial}{\partial \alpha} \int_{\Omega(\mathbf{x})} [\lambda_{i+1} u_i]_{t_s}^{t_e} \left(1 + \alpha \frac{\partial \eta_{24}(x_1, x_2, x_3)}{\partial x_1} \right) d\Omega \right]_{\alpha=0} = - \left[\int_{\Omega} \left[\frac{\partial \lambda_{i+1}}{\partial X_1} \frac{\partial X_1}{\partial \alpha} u_i + \lambda_{i+1} \frac{\partial u_i}{\partial X_1} \frac{\partial X_1}{\partial \alpha} \right]_{t_s}^{t_e} d\Omega \right]_{\alpha=0} \\ & - \left[\int_{\Omega} [\lambda_{i+1} u_i]_{t_s}^{t_e} \frac{\partial \eta_{24}(x_1, x_2, x_3)}{\partial x_1} d\Omega \right]_{\alpha=0} = - \int_{\Omega} \left[\frac{\partial \lambda_{i+1}}{\partial x_1} u_i + \lambda_{i+1} \frac{\partial u_i}{\partial x_1} \right]_{t_s}^{t_e} \eta_{24}(x_1, x_2, x_3) d\Omega - \int_{\Omega} [\lambda_{i+1} u_i]_{t_s}^{t_e} \frac{\partial \eta_{24}(x_1, x_2, x_3)}{\partial x_1} d\Omega \end{aligned} \quad (\text{C37})$$

The ninth term in Eq.(C1) is as follows:

$$\begin{aligned} & \kappa \left[\frac{\partial}{\partial \alpha} \int_{t_s}^{t_e} \int_{\Pi(\mathbf{x})} d\Pi dt \right]_{\alpha=0} = \kappa \left[\frac{\partial}{\partial \alpha} \int_{t_s}^{t_e} \int_{\Pi(\mathbf{x})} \left(1 + \alpha \frac{\partial \eta_{24}}{\partial x_1} \right) d\Pi dt \right]_{\alpha=0} \\ &= \kappa \int_{t_s}^{t_e} \int_{\Pi} \frac{\partial \eta_{24}}{\partial x_1} d\Pi dt = \kappa \int_{t_s}^{t_e} \int_{\gamma} n_1 \eta_{24} d\gamma dt - \kappa \int_{t_s}^{t_e} \int_{\Pi} 0 \cdot \eta_{24} d\Pi dt = \kappa \int_{t_s}^{t_e} \int_{\gamma} n_1 \eta_{24} d\gamma dt \end{aligned} \quad (\text{C38})$$

Using Eq.(C20)-(C38), the first variation with respect to x_1 is summarized. Using Eqs.(2.23)-(2.26), Eqs.(2.35)-(2.38), Eq.(B23) and Table 1 (the boundary condition) is as follows:

$$\left[\frac{\partial L(x_1 + \alpha\eta_{24})}{\partial \alpha} \right]_{\alpha=0} = - \int_{t_s}^{t_e} \int_{\gamma} \frac{\partial u_i}{\partial x_i} \left\{ \lambda_{i+1} U_j n_j - \lambda_i n_i + \frac{1}{Re} \left(\frac{\partial \lambda_{i+1}}{\partial x_j} + \frac{\partial \lambda_{j+1}}{\partial x_i} \right) n_j \right\} \eta_{24} d\Gamma dt + \kappa \int_{t_s}^{t_e} \int_{\gamma} n_i \eta_{24} d\gamma dt = 0 \quad (C39)$$

The sensitivity equation with respect to x_1 is derived as shown in Eq.(2.41). The sensitivity equation with respect to x_2 and x_3 is also derived in the same operation.

ACKNOWLEDGMENTS

This work was supported by the IML (Intelligent Modeling Laboratory). The first author is grateful to the IML for the financial support as a postdoctoral fellow. This work was also supported by the HEC-MW group (Frontier Simulation Software for Industrial Science (FSIS) project, which started in 2002 and has been driven for more than three years, has developed and released more than 60 pieces of most-advanced simulation software in the field of computational mechanics). This program, based on HEC-MW, was improved by useful advice from a large number of people, who also helped debug it. The first author gratefully acknowledges useful advice received from Dr. Serban Georgescu.

REFERENCES

- [1] Carpentieri G, Koren B, van Tooren, MJL. Adjoint-based aerodynamic shape optimization on unstructured meshes. *Journal of Computational Physics* 2007; 224; 267-287.
- [2] Fazzolari A, Gauger NR, Brezillon J. Efficient aerodynamic shape optimization in MDO context. *Journal of Computational and Applied Mathematics* 2007; 203; 548-560.
- [3] Tafreshi A, Fenner RT. General-purpose computer-program for shape optimization of engineering structures using the boundary-element method. *Computers & Structures* 1995; 56; 713-720.
- [4] Bangtsson E, Noreland D, Berggren M. Shape optimization of an acoustic horn. *Computer Methods in Applied Mechanics and Engineering* 2003; 192: 1533-1571.
- [5] Kenji N, Zhiqiang W, Yuji S, Yutaka A. A study of thickness optimization of golf club heads to maximize release velocity of balls. *Communications in Numerical Methods in Engineering* 2004; 20; 747-755.
- [6] Matsumori T, Yamazaki K and Matsui Y. Optimization of Cooling Pipe System of Plastic Molding. *IFIP International Federation for Information Processing* 2006; 199; 161-168.
- [7] Katamine E, Azegami H, Tsubata T, Itoh S. Solution to Shape Optimization Problems of Viscous Flow Fields. *International Journal of Computational Fluid Dynamics* 2005; 19; 45-51.

- [8] Inzarulfaisham AR, Azegami H. Solution to boundary shape optimization problem of linear elastic continua with prescribed natural vibration mode shapes. *Structural And Multidisciplinary Optimization* 2004; 27; 210-217.
- [9] Erik G, Niclas S. Shape optimization of castings by using successive response surface methodology. *Structural and Multidisciplinary Optimization* 2008; 35;11-28.
- [10] Marjavaara BD, Lundstrom TS. Redesign of a sharp heel draft tube by a validated CSD-optimization. *International Journal for Numerical Methods in Fluids* 2006; 50; 911-924.
- [11] Jameson A. Aerodynamic design via control theory. *Journal of Scientific Computing* 1988; 3: 233-260.
- [12] Ragab SA. Shape optimization of surface ships in potential flow using an adjoint formulation. *AIAA Journal* 2004; 42: 296-304.
- [13] Bedair OK, Thompson JC. Shape sensitivity analysis using the indirect boundary element method, *Structural Optimization* 1993; 6; 116-122.
- [14] Afonso SMB, Hinton E. Free vibration analysis and shape optimization of variable thickness plates and shells, *Computing Systems in Engineering* 1995; 6; 47-66.
- [15] Zi-Xian W, Daniel AT, Jonathan AD. Sensitivity analysis and optimization of coupled thermal and flow problems with applications to contraction design. *International Journal for Numerical Methods in Fluids* 1996; 23; 991-1020.
- [16] Balagangadhar D, Roy S, Design sensitivity analysis and optimization of steady fluid-thermal systems, *Computer Methods in Applied Mechanics and Engineering* 2001; 190; 5465-5479.
- [17] Nejati V, Matsuuchi K. Aerodynamics Design and Genetic Algorithms for Optimization of Airship Bodies. *International Journal Series B-Fluids and Thermal Engineering* 2003; 46; 610-617.
- [18] Ghaly WS, Mengistu T, Optimal Geometric Representation of Turbomachinery Cascades using NURBS, *Journal of Inverse Problems in Engineering* 2003; 5; 359-373.
- [19] Robert W. Calculus of variations with applications to physics and engineering. *Dover* 1974.
- [20] Gelfand IM, Fomin SV. Calculus of variations. *Courier Dover Publications* 1963.
- [21] Campobasso AS, Duta MC, Giles MB. Adjoint calculation of sensitivities of turbomachinery objective functions. *Journal of Propulsion and Power* 2003; 19: 693-703.
- [22] Burgreen GW, Antaki JF, Griffith BP. CFD-based design optimization of a three-dimensional rotary blood pump. *AIAA* 1996; 96-4185.
- [23] Tuck EO. Toward the calculation and minimization of stokes drag on bodies of arbitrary shape. *Proceedings Australasian Conference on Hydrodynamics and Fluid Mechanics* 1968; 3; 29-32.
- [24] Watson SR. Toward the minimum drag on a body of given volume in slow viscous flow. *Institute of Mathematics and its Applications* 1971; 7; 367-376.
- [25] Pironneau O. On optimum design in fluid mechanics. *Journal of Fluid Mechanics* 1973; 59; 117-128.
- [26] Lions JL. Controle optimal de systemes governes par des equations aux derivees partielles. *Paris Dunod* 1968.
- [27] Bourot JM. On the numerical computation of the optimum profiles in stokes flow. *International Journal for Numerical Methods in Engineering*. 1974; 65; 1007-1021.

- [28] John HL. On the problem of shaping an asymmetric body to obtain low drag at large Reynolds numbers, *Journal of Ship Research* 1976; 20; 51-60.
- [29] Sano M, Sakai, H. Numerical determination of minimum drag profile in stokes flow, *Journal of the Japan Society for Aeronautical and Space Sciences* 1983; 26; 1-9.
- [30] Bessho M, Himeno Y. On optimum profiles in two-dimensional stokes flow. *The Japan Society of Naval Architects and Ocean Engineers Kansai Division*. 1983; 193 ; 115-125.
- [31] Taseli, H. and Demiralp, M.: Drag minimization in stokes flow, *International Journal of Engineering Science*, 27(1989), pp.633-640.
- [32] Ganesh RK. The minimum drag profile in laminar flow. *Journal of Fluids Engineering* 1994; 116: 456-462.
- [33] Schveyher H, Lutz Th and Wagner S. An Optimization tool for asymmetric bodies of minimum drag. *Proceedings 2nd International Airship Conference* 1996; 3-4.
- [34] Richardson S. Optimum profiles in two-dimensional stokes flow, *Proceedings of The Royal Society of London Series A-Mathematical and Physical Sciences* 1995; 450: 603-622.
- [35] Kim DW, Kim MU. Minimum drag shape in 2-dimensional viscous-flow. *International Journal For Numerical Methods In Fluids* 1995; 21: 93-111.
- [36] Datta S, Srivastava DK. Optimum drag profile in asymmetric stokes flow. *Indian Journal of Pure & Applied Mathematics* 2002; 33: 409-426.
- [37] Guest JK, Prevost JH. Topology optimization of creeping fluid flows using a darcy-stokes finite element. *International Journal for Numerical Methods in Engineering* 2006; 66: 461-484.
- [38] Glowinski R, Pironneau O. On the numerical computation of the minimum-drag profile in laminar flow. *Journal of Fluid Mechanics* 1975; 72: 385-389.
- [39] Huan J, Modi V. Optimum design of minimum drag bodies in incompressible laminar flow using a control theory approach. *Inverse Problems in Engineering* 1994; 1: 1-25.
- [40] Makino K, Himeno Y, Hamasaki J. Optimization of body profiles by nonlinear programming based on numerical Navier - Stokes solutions. *The Kansai Society of Naval Architects, JAPAN* 1994; 222:25-32.
- [41] Katamine E, Azegami H. Domain optimization analysis of viscous flow field. *The Japan Society of Mechanical Engineers* 1995; 61:1646-1653.
- [42] Neittaanmaki P, Rivkind V, Seregin G. About optimal shape design in fluid-dynamics. *Optimal Control Applications & Methods* 1996; 16; 143-148.
- [43] Beichang HE, Ghattas O, Antaki JF. Computational strategies for shape optimization of time dependent Navier-Stokes flows. *Technical Report CMU-CML-97-102* 1997.
- [44] Lund E, Moller H, Jakobsen LA. Shape design optimization of steady fluid-structure interaction problems with large displacements. *AIAA Paper 2001-1624*, 2001.
- [45] Yagi H, Kawahara M. Shape optimization of a body located in low Reynolds number flow. *International Journal for Numerical Methods in Fluids* 2005; 48: 819-833.
- [46] Matsumoto J. Shape identification for Navier-Stokes equation with unsteady flow using bubble function element stabilization method. *WCCM* 2004; 353.
- [47] Srinath DN, Mittal S. A stabilized finite element method for shape optimization in low Reynolds number flows. *International Journal for Numerical Methods in Fluids* 2007; 54: 1451-1471.

- [48] Zhiming G, Yichen M, Hongwei Z. Optimal shape design for the time-dependent Navier-Stokes flow. *International Journal for Numerical Methods in Fluids* 2007; DOI: 10.1002/fld.1673.
- [49] HEC-MW, <http://www.rss21.iis.u-tokyo.ac.jp/en/result/download/>.
- [50] HPC-MW,http://www.ciss.iis.u-tokyo.ac.jp/rss21/en/result/download_fsis/index.php
- [51] Millikan CB. Some problems in the steady motion of viscous incompressible fluids with particular reference to a variation principle. *PhD Theses* 1928.
- [52] (<http://resolver.caltech.edu/CaltechETD:etd-05212003-105955>).
- [53] Millikan CB. On the steady motion of viscous incompressible fluids with particular reference to a VP. *Phil. Mag* 1929; 7: 641-662.
- [54] Usuki S. The application of a variational finite element method to problems in fluid dynamics. *International Journal for Numerical Methods in Engineering* 1977; 11: 563-577.
- [55] Finlayson BA. Existence of variational principles for Navier-Stokes equations. *Physics of Fluids* 1972; 15: 963-967.
- [56] Gunzburger M. Adjoint Equation-Based Methods for Control Problems in Incompressible Viscous Flows. *Flow Turbulence and Combustion* 2000; 65: 249-272.
- [57] Gunzburger M. Sensitivities adjoints and flow optimization. *International Journal for numerical methods in fluids* 1999; 31: 53-78.
- [58] Okumura H, Kawahara M. Shape optimization of a body located in incompressible Navier–Stokes flow based on optimal control theory. *Computer Modeling in Engineering and Sciences* 2000; 1:71–77
- [59] Laporte E, Patrick LT. Numerical Methods in Sensitivity Analysis and Shape Optimization 2003, *Boston Basel Birkhauser*.
- [60] Soto O, Lohner R. A mixed adjoint formulation for incompressible turbulent problems. *AIAA* 2002; 0451.
- [61] Kim HJ, Salim K, Nakahashi K. Surface modification method for aerodynamic design optimization. *AIAA Journal* 2005; 43: 727-740.
- [62] Mavriplis DJ. Multigrid solution of the discrete adjoint for optimization problems on unstructured meshes. *AIAA Journal* 2006; 44: 42-50.
- [63] Canann SA, Liu YC, Mobley AV. Automatic 3D surface meshing to address today's industrial needs, *Finite Elements in Analysis and Design* 1997; 25: 185-198.
- [64] Canann SA, Tristano JR, Staten ML. An approach to combined laplacian and optimization-based smoothing for triangular quadrilateral and quad-dominant meshes. *7th International Meshing Roundtable* 1998; 479-494.
- [65] Freitag LA, Knupp PM. Tetrahedral mesh improvement via optimization of the element condition number. *International Journal for numerical methods in engineering* 2002; 53: 1377-1391.
- [66] Shinohara K, Okuda H, Ito S, Nakajima N, Ida M. Shape optimization using an adjoint variable method in ITBL grid environment. *14th International Conference On Nuclear Engineering* 2006; 14: 89568.
- [67] Frederic JB. Considerations on the spring analogy. *International Journal for Numerical Methods in Fluids* 2000; 32: 647-668.
- [68] Brian TH. Mesh deformation using the biharmonic operator, *International Journal for Numerical Methods in Engineering* 2003; 56: 1007-1021.

- [69] Masud A, Hughes TJR. A space-time Galerkin / least-squares finite element formulation of the Navier-Stokes equations for moving domain problems. *Computer Methods in Applied Mechanics and Engineering*. 1997; 146; 91-126.
- [70] Donea J. Finite element solution of the unsteady Navier-Stokes equations by a fractional step method. *Computer Methods in Applied Mechanics and Engineering* 1982; 30: 53-73.
- [71] Ramaswamy B, Kawahara M. Lagrangian finite element analysis applied to viscous free surface fluid flow. *International Journal for Numerical Methods in Fluids* 1987; 7: 953-984.
- [72] Tezduyar TE, Mittal S, Ray SE, Shih R, Incompressible flow computations with stabilized bilinear and linear equal-order-interpolation velocity-pressure elements. *Computer Methods in Applied Mechanics and Engineering* 1992; 95; 221-242.
- [73] Gerritsma M. Time dependent numerical simulations of a viscoelastic fluid on a staggered grid. *Ph.D. Thesis, University of Groningen, The Netherlands*, 1996.
- [74] Brooks AN, Hughes TJR. Streamline upwind Petrov-Galerkin formulations for convection dominated flows with particular emphasis on the incompressible Navier-Stokes equations. *Computer Methods in Applied Mechanics and Engineering* 1982; 32; 199-259.
- [75] Donea J, Huerta A. Finite element methods for flow problems 2003. *John Wiley & Sons, New York, London, Sydney*.
- [76] Ilinca, F, Hetu, JF, Pelletier D. On Stabilized Finite Element Formulations for Incompressible Advective-diffusive Transport and Fluid Flow Problems. *Computer Methods in Applied Mechanics and Engineering* 2000; 188; 235-255.
- [77] Kakuda K, Miura S, Tosaka N. Finite element simulation of 3D flow around a circular cylinder. *International Journal of Computational Fluid Dynamics* 2006; 20; 193-209.
- [78] Zienkiewicz OC, Taylor RL. Finite Element Method Volume 1 - *The Basis*. *Butterworth Heinemann, London* 2000.
- [79] Kawano K, Kitoh T. Introduction to Optical Waveguide Analysis: Solving Maxwell's Equations and the Schrödinger Equation. *John Wiley, New York* 2001; 267-271.
- [80] Ito S, Okuda H. HPC-MW: A Problem solving environment for developing parallel FEM applications. Applied Parallel Computing. State of the Art in Scientific Computing, *Lecture Notes in Computer Science, Springer Berlin / Heidelberg* 2007; 4699; 694-702.
- [81] METIS, <http://www.cs.umn.edu/~metis>.
- [82] Gilboa G, Sochen N, Zeevi Y. Forward-and-backward diffusion processes for adaptive image enhancement and denoising. *IEEE Transaction on image processing* 2002; 11: 689-703.
- [83] Kirkup SM, Wadsworth M. Solution of inverse diffusion problems by operator-splitting methods. *Applied Mathematical Modeling* 2002; 26: 1003-1018.
- [84] Laporte E, Tallec P. Numerical methods in sensitivity analysis and shape optimization. *Birkhauser* 2003; 127.
- [85] GPPVIEW, http://geofem.tokyo.rist.or.jp/download_en/gppview.html.
- [86] MicroAVS, https://www.kgt.co.jp/viz/dl/mavs_trial/mavs_trial.html.
- [87] Yagi H, Kawahara M. Optimal shape determination of a body located in incompressible viscous fluid flow. *Computer Methods in Applied Mechanics and Engineering* 2007; 196; 5084-5091.

-
- [88] Chun YW, Haug EJ. Two-dimensional shape optimal design. *International Journal for Numerical Methods in Engineering* 1978; 13; 311-336.
 - [89] Nojima K, Kawahara M. Three-dimensional shape identification of body located viscous fluid flow. *Proceedings of the 7th International Conference on HydroScience and Engineering*. 2006; ISBN:0977447405.
 - [90] ADVENTURE (ADVanced ENgineering analysis Tool for Ultra large REal world), <http://adventure.q.t.u-tokyo.ac.jp/>.
 - [91] WARP3D, <http://cern49.cee.uiuc.edu/cfm/software.html>.
 - [92] FEAST, <http://www.feast.uni-dortmund.de/>.
 - [93] PCP, <http://www.aist.go.jp/infobase/pcp/platform/index.html>
 - [94] Manoj Bhardwaj et al., "Salinas: a scalable software for high-performance structural and solid mechanics simulations," Proceedings of the ACM/IEEE conference on Supercomputing table of contents, (2002), pp.1-19.
 - [95] Behr M., Hastreiter D. Mittal S, Tezduyar TE, "Incompressible flow past a circular cylinder: dependence of the computed flow field on the location of the lateral boundaries" *Computer Methods in Applied Mechanics and Engineering* 123(1995), pp.309-316.
 - [96] Meshman_Viewer, <http://www.meshman.jp/english/english.html>.

Chapter 11

NUMERICAL AND EXPERIMENTAL INVESTIGATIONS OF FLUID DYNAMICS OF HIGH SPEED FLOWS

R. C. Mehta

School of Mechanical and Aerospace Engineering,
Nanyang Technological University, Singapore

1. FLOW FIELD OF SUPERSONIC FREE JETS AND JET DEFLECTOR

The phenomenon of supersonic jets and their interaction with deflector surfaces is found in many engineering applications such as impingement of exhaust from a rocket nozzle of launch vehicles during the liftoff phase, during stage separation of multistage rockets, and VTOL/STOL operation of aircraft etc. An interaction between a supersonic jet and a flat plate at atmospheric conditions has been studied [1] as the fundamental problem to the impingement of a rocket exhaust plume on the deflector or plate that of a control jet on the rocket body, etc. Inviscid numerical models can offer fairly good prediction of the impinging jet for moderate plate inclination. The impingement jet is characterized by many discontinuities such as barrel shock, exhaust gas jet boundary, Mach disk, reflected shock, plate shock. The flow structure of an under expanded supersonic jet impinging on an inclined plate has been numerically investigated [2] using a numerical scheme for the Euler equations. The maximum pressure was found to be larger on the inclined plate than on the normal plate. Flow fields of the exit jet Mach number of 2.2 impinging on an inclined plate at various plate angles, nozzle-plate distance and pressure ratios are experimentally investigated using pressure-sensitive paints and schlieren flow visualization [3]. The flow field patterns can be predicted without experiments if the shock cell length in the free jet for various pressure ratios is known in advance. Numerical study of under expanded jet impinging against the solid wall has been presented by Wu et al. [4]. The acoustic efficiency of deflected rocket exhaust is less than that of undeflected rockets. The differences are greatest when the exhaust impinges on a flat plate which is normal to the flow and are least for rockets that are deflected by smooth curved buckets [5].

Flow field features of supersonic free-jets as well as impinging jets over the axisymmetric and double wedge deflector are studied. The differences of the flow field

behavior are obtained in the numerical simulations [6] and [7]. An oscillating phenomena was noticed in the case of free jets operating at sonic exit Mach number and in another case of impinging of the under expanded jets on a flat plate [8]. A non-dimensional parameter has been obtained to characterize the pressure distribution in the jet axis which makes them invariant of the exit to ambient pressure ratio [9].

Figure 1 illustrates, the under expanded flow produced by a supersonic nozzle. First shock cell length L_1 , second shock cell length L_2 and third shock cell length L_3 are the shock cell length as shown in the sketch. The first shock cell length of slightly incorrectly expanded axisymmetric jet was theoretically estimated by Prandtl to vary as $L_1/D_e = k\beta$, where $k = 1.306$ and D_e is nozzle exit diameter as mentioned in Ref. [10]. Abdel-Fattah [11] has measured shock cell lengths for supersonic jets issuing from a conical convergent-divergent nozzle in conjunction with schlieren pictures. He was found experimentally that the first and second shock cell lengths are having a linear dependence on β^2 rather than β . The schlieren pictures of free jets and corresponding isobar contours at jet exit Mach number of 2.2 at various jet exits to ambient pressure ratio (p_e/p_a) are depicted in Fig. 2. The schlieren picture and isobar contours exhibits all the essential flow field features of the supersonic free jets, such as jet boundary, jet shock, Mach disk and reflected shock. The numerical and the schlieren pictures reveals that for a constant exit Mach number, the location of Mach disk moves closer to the nozzle exit plane and the length of the shock-cell length decreases with decreases in the exit to ambient pressure ratios. Moreover, the location of the Mach disk moves away from the nozzle exit plane as the exit Mach number increase while taking same value of (p_e/p_a). A parameter [$\beta^2/(M_e^2 - 1)$] has been employed to characterize the distribution of pressure and also Mach number along the jet axis which makes them invariant of the exit to ambient pressure ratio.

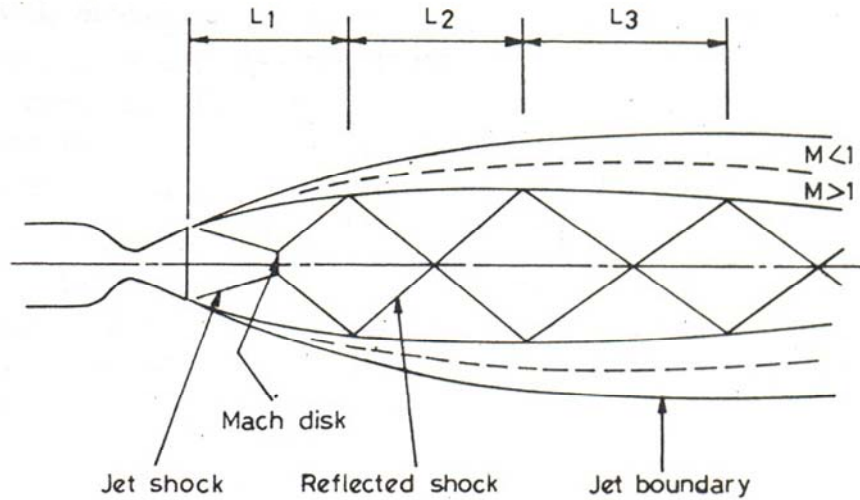


Figure 1. Schematic sketch of a supersonic free jet.

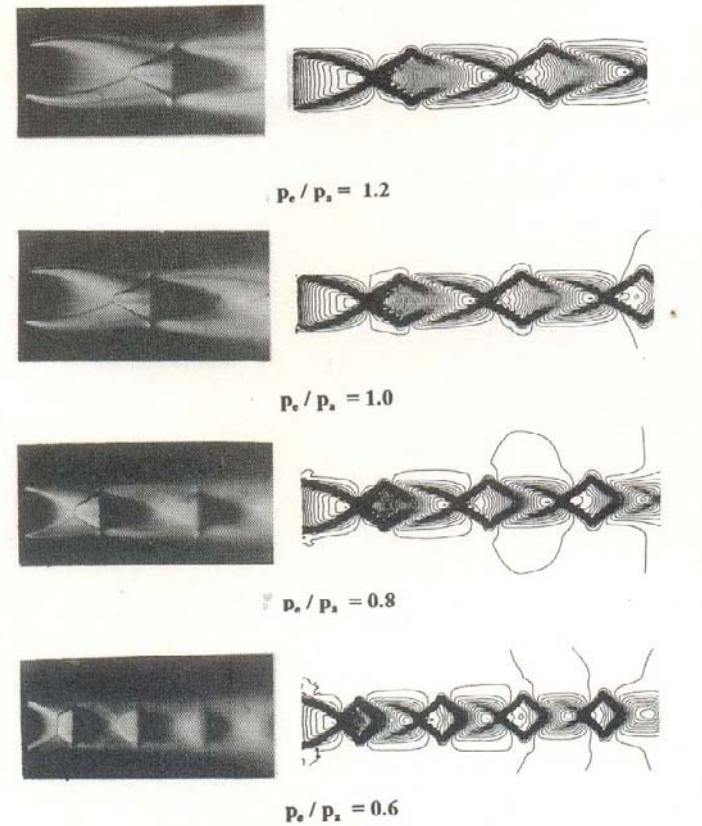


Figure 2. Schlieren photographs and pressure contours at different p_e/p_a for $M_e = 2.2$.

The shock cell lengths were obtained from the numerical and schlieren pictures for jet exit Mach number of 2.20, 2.61 and 3.10 at various jet exit to ambient pressure ratio (p_e/p_a). The L_1/d^* and the L_2/d^* versus β^2 are obtained by solving compressible, axisymmetric Euler equations and the schlieren pictures [9], where β^2 is defined as

$$\beta^2 = \left(\frac{2}{\gamma - 1} \right) \left(\frac{P_0}{p_a} \right)^{\frac{\gamma-1}{\gamma}} - \left(\frac{\gamma + 1}{\gamma - 1} \right)$$

where P_0 is the jet stagnation pressure, p_e is the nozzle exit pressure, γ is ratio of the specific heats. The pitot p_{t2} and the static pressure distribution p_s are measured and the distribution of the local Mach number in the free jets are computed by solving following isentropic equations [12]

$$\frac{p_{t2}}{p_s} = \left[1 + \frac{(\gamma - 1)}{2} M^2 \right]^{\frac{\gamma}{\gamma - 1}} \quad M < 1$$

and

$$\frac{p_{t2}}{p_s} = \left[1 + \frac{(\gamma - 1)}{2} M^2 \right]^{\frac{\gamma}{\gamma-1}} \left[\frac{(\gamma + 1)}{2\gamma M^2 - (\gamma - 1)} \right]^{\frac{1}{\gamma-1}} \quad M \geq 1$$

The variation of the Mach number and versus nondimensional parameter makes Mach number independent of exit to ambient pressure ratio (p_e/p_a). The similarly (p/p_a) versus also became independent of (p_e/p_a). The following linear relationship [13] are obtained by applying least square fit for each nozzle

$$L_1 / D^* = 0.3(M_e + 1)\beta^2 - (2.75M_e - 5.2)$$

The validation of the constants is checked by directly comparing with the results of Abdel-Fattah [11]. The commutated values of second shock cell length from the numerical results show following linear relationship

$$L_2 / D^* = 0.72\beta^2$$

The second shock cell length became independent of M_e . The difference between experimental with computed results may be attributed to the faster jet spreading rate and viscous effects after first shock cell and hence the lower length of second shock cell length. The convergent-divergent nozzles were designed for producing supersonic free jets. D^* is the throat diameter of the nozzle. The exit diameter is designated as D_e and has a semi-divergent angle of 15° . The particulars of the nozzles are as given in Table 1. The A^* and A_e represent the area of the throat and nozzle exit, respectively. Figure 3 depicts the variation of measured and calculated pressure distribution along the jet axis for exit Mach number 2.2 at various ratios of p_e/p_a .

The geometrical detail of the axisymmetric model depicted in Fig. 4 is employed to study the numerical and the experimental simulation of the supersonic jet impinging on a typical jet deflector. Measured and calculated pressure distribution [9] and Mach number [12] along the jet axis for various operating conditions indicate that a nondimensional parameter could be obtained to make axial pressure distribution independent of exit to ambient pressure ratio.

The axisymmetric jet deflector model (Fig. 4) consists of a cone-apex angle of 70° and a tip bluntness radius of R of $0.13 D_e$ is provided at a location of $r = 0.7 D_e$, where r is the distance measured from the deflector axis. The model has a base diameter of $0.8 D_e$. The deflector was carefully aligned with its base perpendicular to the jet axis and the apex was carefully located. The process of centralizing the model was accomplished by equalizing the reading from pressure holes at corresponding position on opposite faces of the deflector. The static pressure distribution in the axial direction of free jets was measured using a miniature static probe. The measurement of surface pressures on the jet deflector is done by pressure transducers. Figure 5 shows schematic the flowfield of the impinging jet. The Mach contours plots shows all the essential flow field features like jet shock, jet boundary, Mach disk, reflected shock and cone shock. The comparison of the schlieren pictures of the free jets and impinging jets reveals that the impinging flow field has similar characteristics of the free jet

up to the cone shock of the deflector's apex. However the vector plots of the impinging free jets differ considerably from the impinging vector plots [6]. The inner mixing layer of the impinging jet is different at different conditions. The difference in the velocity field may be attributed to the formation of the vortex. Centre line pressure variation in the presence of the deflector is shown in Fig. 6 at different operating condition. The static pressure distribution on the centre line of the deflector with respect to nozzle is nondimensionalized by the settling chamber pressure P_o and x is nondimensionalized by the nozzle exit diameter D_e . A sharp rise of the pressure on the deflector (stagnation region) is seen [14]. The centre line variation inside the jets differs in the presence of the jet deflector with the distance, X_c and the nozzle exit Mach number, M_e . Figure 7 shows pressure distribution on the jet deflector for $M_e = 2.2$, $p_e/p_a = 1.2$ and $X_c/D_e = 2.0$. The inviscid simulation of the fluid dynamics equations compares fairly well with the experimental data. A quantity, which is of practical importance is the overall impinging jet loads on the jet deflector surface. This is required for the structural design of the jet deflector. Loads have been obtained by integrating the measured pressure distribution. The axial load distribution Ca over the axisymmetric jet deflector is computed using following relation

$$Ca = \frac{2\pi \int_0^{4D_e} (p - p_a) r \sin \psi ds}{P_o A_e}$$

where ψ is local deflector angle. Table 2 shows the comparison between the measure and calculated axial load over the axisymmetric deflector.

Figure 7 shows pressure distribution on the jet deflector for $M_e = 2.2$, $p_e/p_a = 1.2$ and $X_c/D_e = 2$. It can be seen from the pressure distribution a sharp rise of the pressure on the apex of the deflector and second peak in the pressure is found on the curvature region.

Figure 8 gives geometrical details of the wedge deflector model. The wedge deflector has the same apex angle, radius of curvature and base length as used in the axisymmetric jet deflector. The impingement jet is on the wedge deflector characterized by many discontinuities such as barrel shock wave, exhaust gas jet boundary, Mach disk, reflected shock, plate shock as delineated in Fig. 9. The flow field over the double wedge deflector is obtained by solving three-dimensional compressible Euler equations. Surface Mach distribution over wedge deflector for exit Mach number $M_e = 2.2$, $X_c/D_e = 2.0$ is shown in Fig. 10. The Mach contour plot is shown in Fig. 11. It can be seen from the Mach contour plots that the essential flow features of the impinging supersonic jets on the double wedge deflector are captured very well. Figure 12 shows the comparison between the measured [15] and calculated pressure over the double wedge deflector.

The measured surface pressure distribution were used to obtain overall impinging load coefficient. Integration has been carried out using the trapezoidal rule to calculate the load coefficient and results shows good agreement in Ref. [7]. The numerical and experimental investigations of supersonic free jets and impinging on the axisymmetric deflector and the double jet deflector show good agreement can be employed in the design of the jet deflector during the liftoff the launch vehicle.

Table 1. Nozzle Dimensions.

M_e	D_e , mm	D^* , mm	A_e/A^*
2.2	30.0	21.18	2.005
2.6	14.6	9.20	2.923
3.1	23.0	10.65	4.657

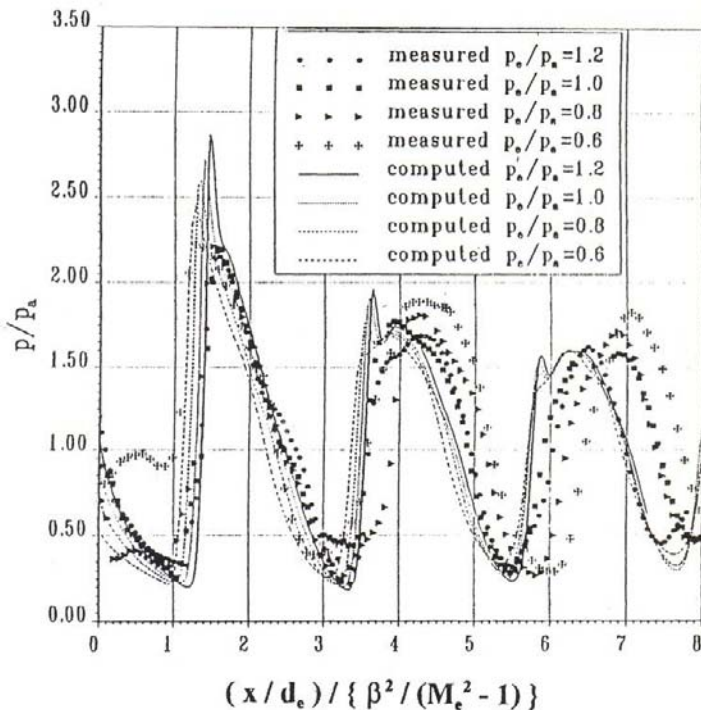
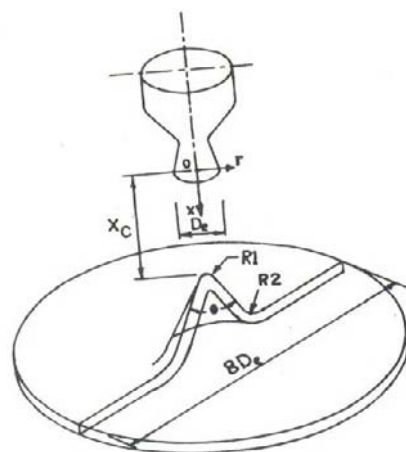
Figure 3. Pressure variation along the jet axis for $M_e = 2.2$ at different values of p_e/p_a .

Figure 4. Coordinate system and axisymmetric model configuration.

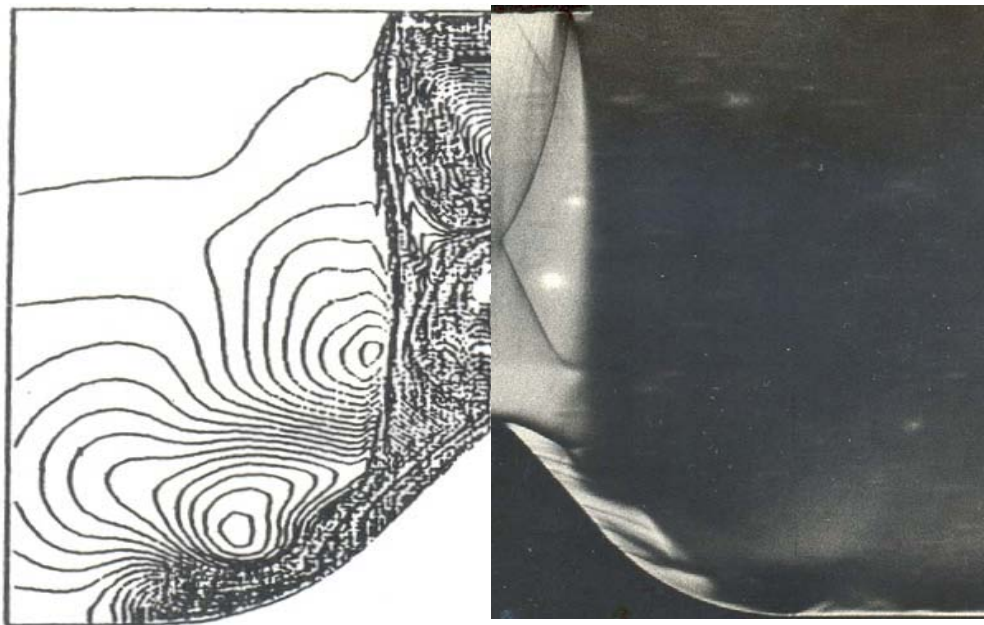


Figure 5. Comparison between density contour plots and schlieren picture over jet deflector ($M_e = 2.2$, $X_c/D_e = 3.0$).

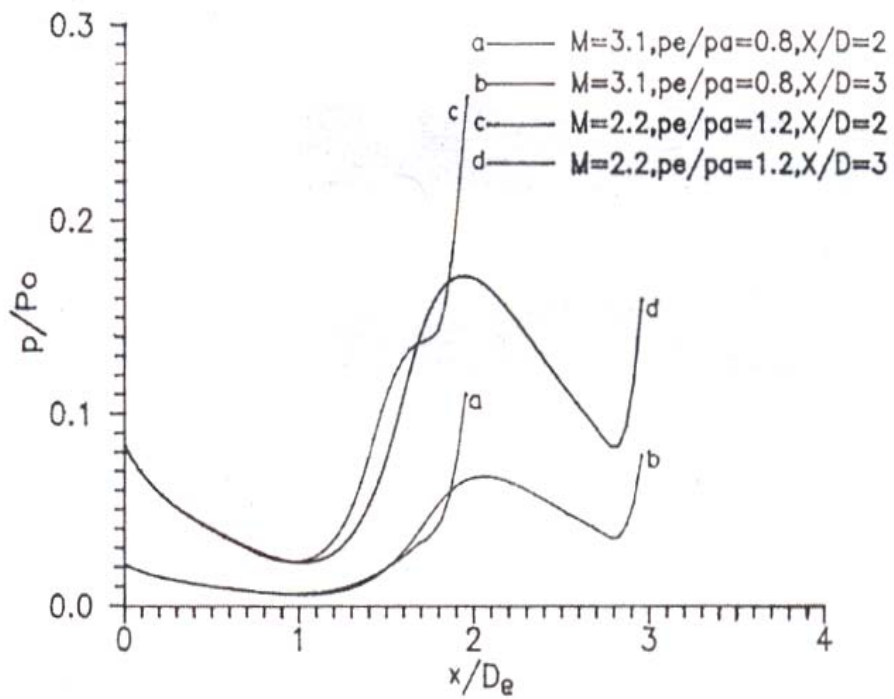


Figure 6. Centre line pressure distribution in the presence of axisymmetric jet deflector.

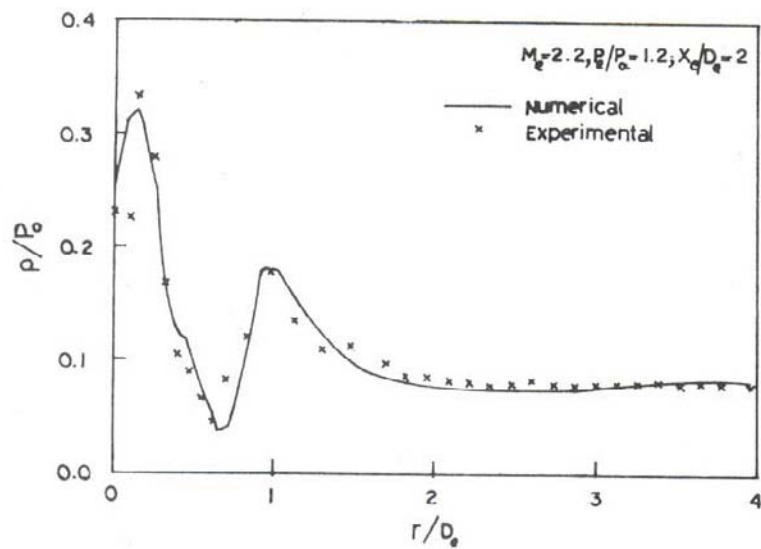


Figure 7. Surface pressure distribution over axisymmetric jet deflector ($M_e = 2.2$, $p_e/p_a = 1.2$, $X_c/D_e = 2.0$).

Table 2. Axial load Over Axisymmetric Deflector.

M_e	$p_e p_a$	$X_c D_e$	Ca	
			Calculated	Measured
2.2	1.2	2	0.70	0.74
2.2	1.2	3	0.65	0.70
3.1	0.8	2	0.75	0.82
3.1	0.8	3	0.63	0.73

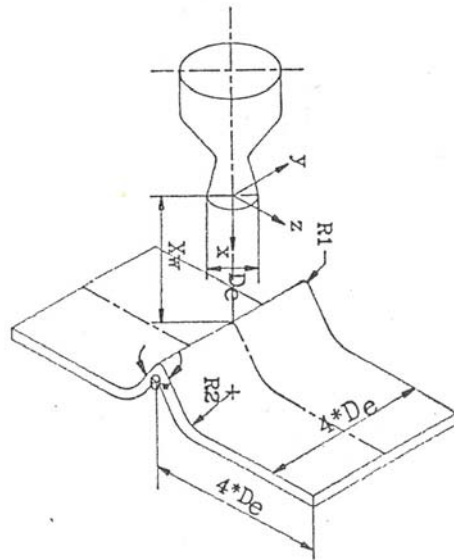


Figure 8. Geometrical detail of the wedge deflector model.

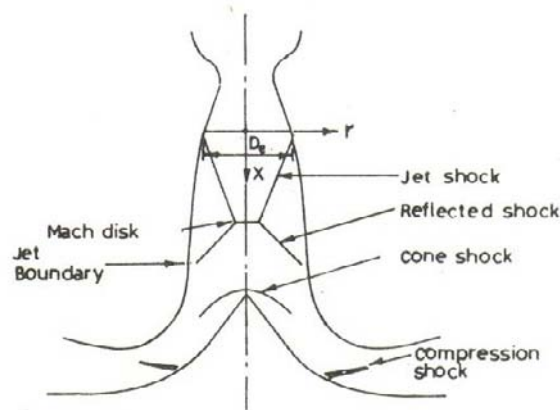


Figure 9. Schematic of the impingement flow field over jet deflector.

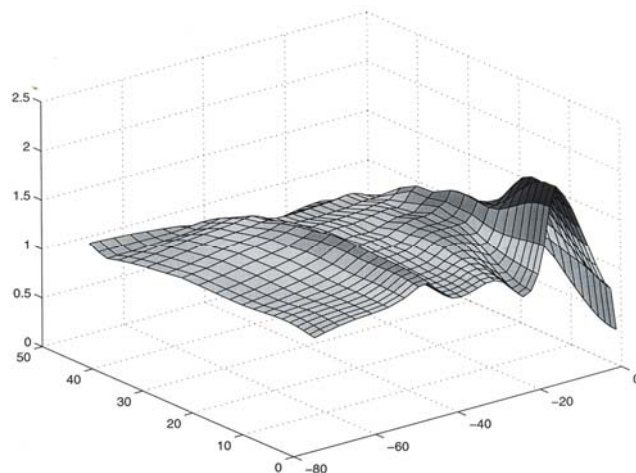


Figure 10. Surface Mach distribution over wedge deflector ($M_e = 2.2$, $X_c/D_e = 2.0$).

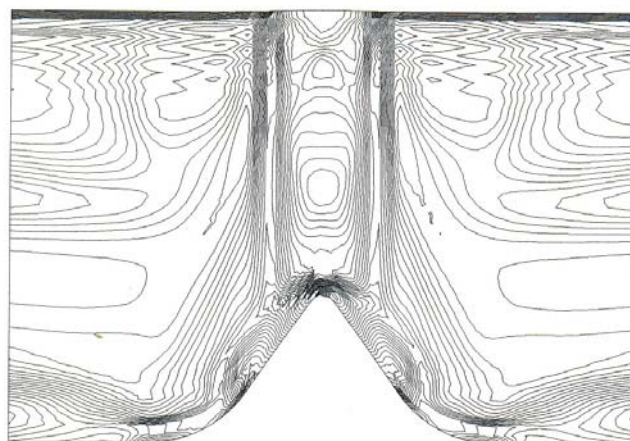


Figure 11. Mach contour plots over wedge deflector ($M_e = 2.2$, $X_c/D_e = 2.0$).

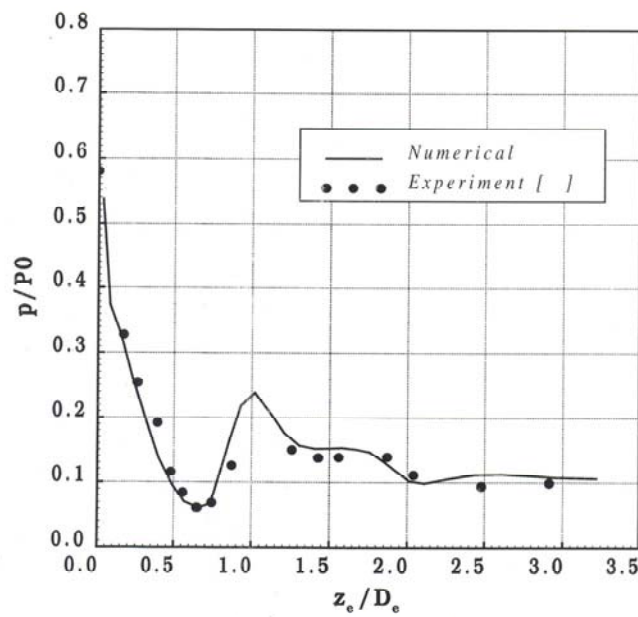


Figure 12. Centre line static pressure distribution over the deflector ($M_e = 2.2$, $X_c/D_e = 2.0$).

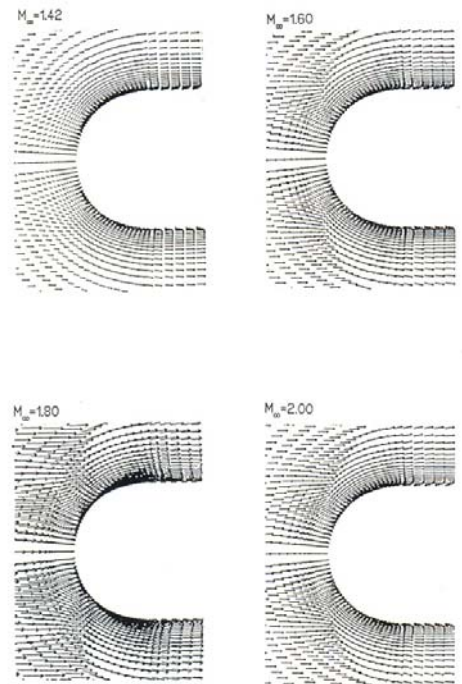


Figure 13. Computed velocity field and shock position over a hemisphere-cylinder.

2. COMPUTATION OF FLOW FIELD OVER PAYLOAD FARING

Hsieh [16 - 17] has conducted wind-tunnel tests of a hemisphere-cylinder model of 2.54 cm diameter at zero angle of incidence and Mach number range of 0.7 – 1.3. The time-dependent axisymmetric Reynolds-averaged turbulent compressible Navier-Stokes equation is solved using finite volume scheme in conjunction with the multi-stage Runge-Kutta time stepping method. The closer of the system of equations is achieved by introducing the turbulence model of Baldwin-Lomax [18]. The bow shock stand off distance is calculated and compared with the available data in Ref. [19]. The velocity field in Fig. 14 shows that the flow becomes parallel to the body after crossing a line perpendicular to the model axis. This line is in the vicinity of the stagnation point of the hemisphere. A schematic sketch of the flow pattern is delineated in Fig. 15 which is constructed based on the observation. The separated flow is observed at the shoulder of the hemisphere-cylinder for freestream Mach number of 0.80 – 0.90. The maximum value of the root-mean-square wall pressure fluctuations is observed at $M_\infty = 0.814$. The numerical analysis shows an interesting finding of the flow past hemispherical-cylinder body.

Table 3 and Fig. 15 depict the dimensions of the heat shield considering for the numerical simulation with the recommended NASA guidelines [20] for the buffet-free configuration. A numerical simulation of the unsteady, compressible, turbulent, axisymmetric Reynolds-averaged Navier-Stokes (RANS) equations is attempted in order to understand the basic fluid dynamics. The governing equations can be written in the following strong conservation form

$$\frac{\partial \mathbf{W}}{\partial t} + \frac{\partial \mathbf{F}}{\partial x} + \frac{\partial \mathbf{G}}{\partial r} + \mathbf{H} = \left[\frac{\partial \mathbf{R}}{\partial x} + \frac{\partial \mathbf{S}}{\partial r} \right]$$

where

$$\mathbf{W} = r \begin{bmatrix} \rho \\ \rho u \\ \rho v \\ \rho e \end{bmatrix}, \quad \mathbf{F} = r \begin{bmatrix} \rho u \\ \rho u^2 + p \\ \rho uv \\ (\rho e + p)u \end{bmatrix}, \quad \mathbf{G} = r \begin{bmatrix} \rho v \\ \rho uv \\ \rho v^2 + p \\ (\rho e + p)v \end{bmatrix}$$

are the \mathbf{W} is conservative state and \mathbf{F} and \mathbf{G} are inviscid flux vectors. x and r are axial and radial coordinate system and t is time. The viscous flux vectors are

$$\mathbf{R} = r \begin{bmatrix} 0 \\ \sigma_{xx} \\ \tau_{xr} \\ u\sigma_{xx} + v\tau_{xr} + q_x \end{bmatrix}, \quad \mathbf{S} = r \begin{bmatrix} 0 \\ \tau_{xx} \\ \sigma_{xr} \\ u\tau_{xr} + v\sigma_{rr} + q_r \end{bmatrix}, \quad \mathbf{H} = \begin{bmatrix} 0 \\ 0 \\ \sigma_+ \\ 0 \end{bmatrix}$$

where R and S are viscous flux vector and S is source vector. σ and τ are components of the stress vector, while q is components of the heat flux vector. Reynolds stresses and turbulent heat fluxes in the mean flow equations are modeled by introducing an isotropic eddy viscosity μ_t . Thus, the viscous terms in the equations became

$$\sigma_{xx} = -\frac{2}{3}(\mu + \mu_t) \nabla \cdot U + 2(\mu + \mu_t) \frac{\partial u}{\partial x}$$

$$\sigma_{rr} = -\frac{2}{3}(\mu + \mu_t) \nabla \cdot U + 2(\mu + \mu_t) \frac{\partial v}{\partial r}$$

$$\tau_{xr} = (\mu + \mu_t) \left(\frac{\partial u}{\partial r} + \frac{\partial v}{\partial x} \right)$$

$$\sigma_+ = -p - \frac{2}{3}(\mu + \mu_t) \nabla \cdot U + 2(\mu + \mu_t) \frac{v}{r}$$

$$\nabla \cdot U = \frac{\partial u}{\partial x} + \frac{\partial v}{\partial r} + \frac{v}{r}$$

$$q_x = -cp \left(\frac{\mu}{Pr} + \frac{\mu}{Pr_t} \right) \frac{\partial T}{\partial x}$$

$$q_r = -cp \left(\frac{\mu}{Pr} + \frac{\mu}{Pr_t} \right) \frac{\partial T}{\partial r}$$

where Pr and Pr_t , the molecular and turbulent Prandtl numbers are assumed to take a constant value of 0.72 and 0.90, respectively. cp is specific heat at constant pressure. The coefficient of molecular viscosity is calculated according to Sutherland's law. The temperature is related to pressure and density by perfect gas equation of state as

$$p = (\gamma - 1) \left[e - \frac{1}{2} \rho (u^2 + v^2) \right]$$

The ratio of the specific heat γ was assumed constant and equal to 1.4. The closure of the system of equations is achieved by introducing the Baldwin-Lomax turbulence model [18]. This model, which utilizes the vorticity distribution to determine the scale lengths, has been extensively used in conjunction with the RANS equations and is reputed to yield acceptable engineering solution.

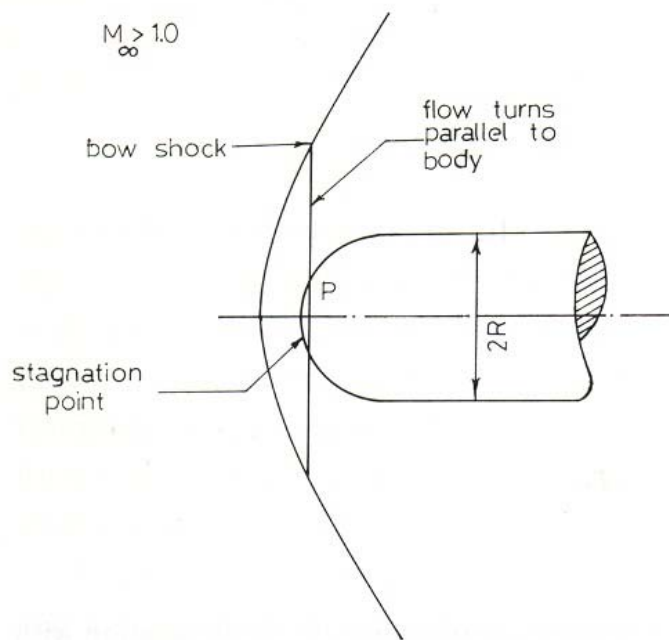


Figure 14. Schematic sketch of the flow over a hemisphere-cylinder.

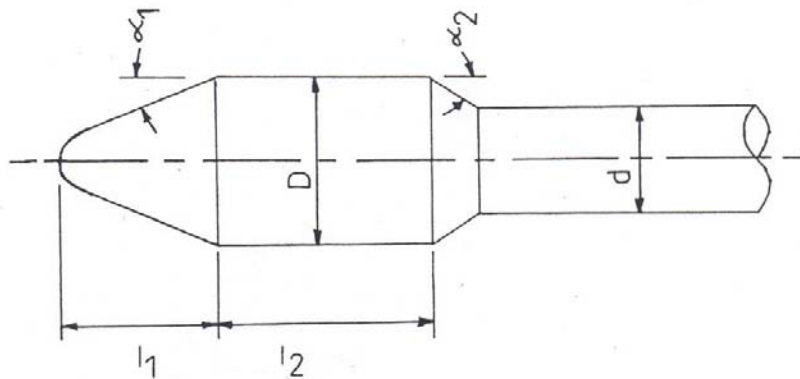


Figure 15. Geometrical parameters of heat shield.

Table 3. Geometrical parameters of heat Shield.

Model	α_1 , deg	l_1/D	L_2/D	d/D	α_2 , deg
M1	20	0.965	1.400	0.875	15
M2	15	1.023	1.117	0.823	30
NASA	≤ 15	≥ 0.80	> 1.50	0.9 - 1.11	Not critical

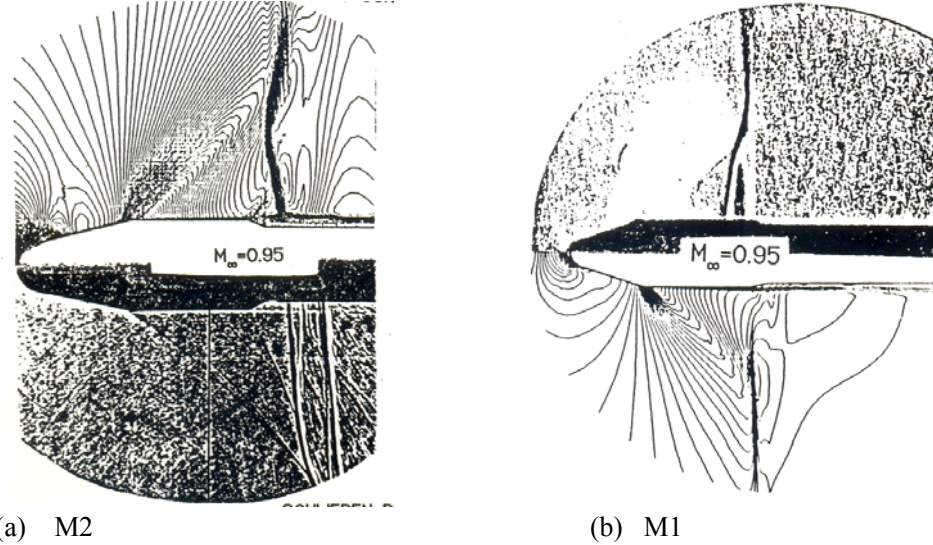


Figure 16. Comparison between density contours and schlieren pictures.

Figure 16 shows all of the essential flow field features of the transonic flow, such as supersonic pocket, terminal shock, and expansion and compression regions are very well captured and compare well with the schlieren photographs. The density contour plots reveal that the supersonic region increases with increasing freestream Mach number, and as a result, the terminal shock moves downstream with increasing freestream Mach number. It is worth to mention here that the terminal shock is just reached at the end of the payload shroud in the case of M1 heat shield, whereas the terminal shock crosses the fore body cylinder in the M2 configuration at the same freestream Mach number. It can be noticed that the M1 model is able to hold the terminal shock, which is attributed to the greater length of the payload shroud. The flow field characteristics are shown in detailed in Refs. [21 – 24].

Comparison between the shock locations of the numerical and experimental results is shown in Fig. 17 for heat shield M1 for freestream Mach number 0.90 and 1.0. It can be seen that the terminal shock crosses the fore body cylinder at $M_{\infty} = 0.97$. The location of the terminal shock is found nonlinear function of Mach number. In the boat-tail region, a local separation results, due to sharp discontinuity in the longitudinal curvature. The separated flow in the boat-tail region is observed for both heat-shield configurations. The flow reattachment length is normalized by the boat tail height, where X_c is the location of the boat-tail shoulder and X_r is the reattachment point as depicted in the insert of Fig. 18. The prediction of X_r was chosen as the point where the axial component of velocity along the downstream wall changed from negative to positive. Figure 18 shows the comparison between measured normalized separation lengths with the computed value. A reasonably good agreement is seen between them. The separation length is function of Mach number. The extent of predicted separation reaches its maximum value when the freestream Mach number reaches unity. A schematic sketch of the separated flow in the boat-tail region at the transonic and supersonic Mach numbers, which are reconstructed from the velocity vector [25] and density contour plots. For the transonic case, a shear layer is formed, and it contains a recirculation region. The down stream boundary layer [24] is found to be thick, which is nearly the boat-tail height. Sketch also shows the flow field features for the supersonic case. The flow turns

downstream of the boat-tail through an expansion fan with a resulting mixing layer that separates fluid above the subsonic recirculating region below it. The pressure in the recirculating region is generally uniform and below that of the freestream pressure. As the mixing layer impinges on the downstream wall, the flow turns back toward the freestream direction and a recompression shock wave is typically found. Comparison between the shock locations of the numerical and experimental results is shown in Figure 19 for the M1 heat shield. The location of the shock is confirmed during the flight of the launch vehicle as depicted in Fig. 20. It is interesting to note that the numerical analysis compares well with the wind-tunnel data as well as the flight measurement.

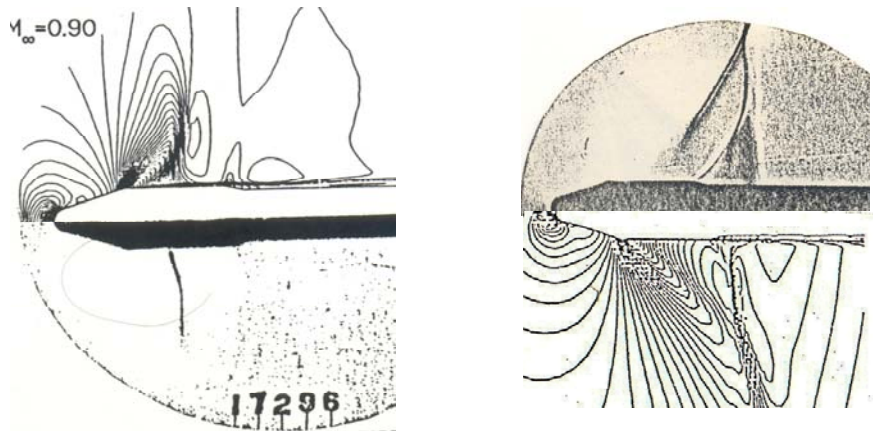


Figure 17. Comparison between density contours and schlieren picture (M1 heat shield).

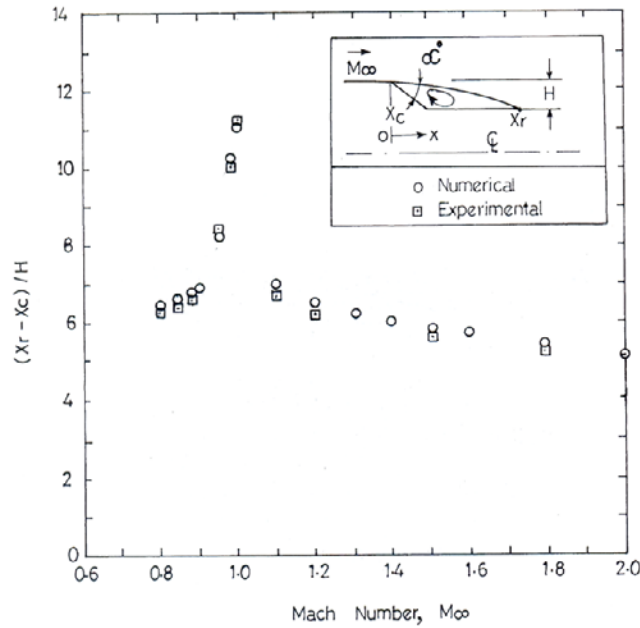


Figure 18. Reattachment distance as a function of Mach number.

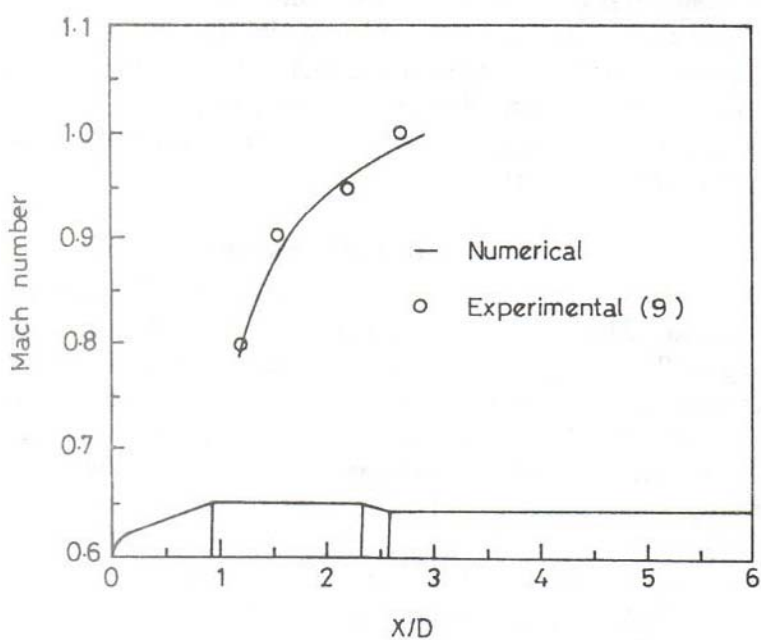


Figure 19. Shock location at various Mach numbers.

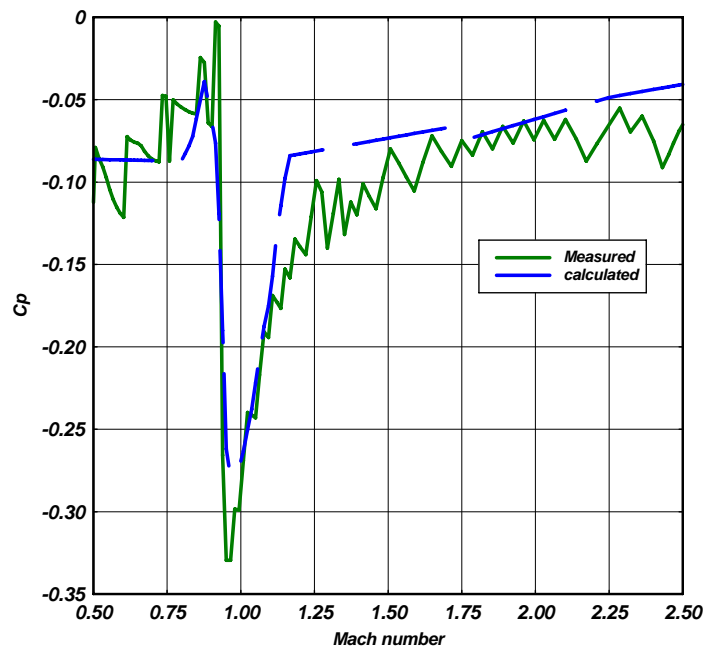


Figure 20. Variation of pressure coefficient on the heat shield.

3. UNSTEADY FLOW OVER PAYLOAD FAIRING

The buffet loads must be considered in the design of the space-vehicle structure. The pressure fluctuations which originated at the location of the normal shock wave within regions of separation can cause buffeting of the space vehicle. The buffet pressures are configuration dependent. Using Gaussian distribution, the appropriate unsteady pressure data are utilized to calculate the sound pressure level and corresponding frequencies. The time-dependent calculation reveals that around the cone-cylinder junction near the shock the SPL values are high and coupled with the low frequencies. The vehicle should be designed to minimize buffeting through the use of favorable configurations. The occurrence of buffeting of vehicle during atmospheric ascent depends primarily on the shape of the vehicle [20].

Coe [26] has investigated pressure fluctuations over hammer head pay load shroud. The buffet pressures are configuration dependent [27]. Self-sustained oscillation [28] of launch vehicles can result during transonic flight if structural responses couple with alternating flow separation forces at the payload fairing cone-cylinder junction. Pressure and heat flux fluctuations due to shock-boundary layer interaction show that the fluctuations in heat flux quantitatively the same feature as those of wall pressure but different quantitatively [29].

Using the unsteady numerical simulation [30] of the RANS, the unsteady flow field analysis is carried out for the heat shield M1 and M2. Figure 21 shows the surface pressure fluctuations for the model M1. A cyclic nature of the surface pressure variation occurs at $x/D = 2.4611$, and with a time period of about 1.5 s for one cycle. A Set of histograms of pressure coefficient for the transonic Mach number range for M2 heat shield is shown in Fig. 22. A spectral analysis was carried out on the computed pressure data for all possible modes of oscillations using fast Fourier transform FFT of MATLAB [31]. The FFT converts the pressure histories from time domain into the frequency domain. A cyclic behavior of the pressure coefficient is observed in the vicinity of the separation and reattachment points. From the spectrum analysis low frequency pressure fluctuations and sound pressure levels are found at freestream Mach number 0.95, whereas high frequency fluctuations are observed at supersonic Mach number 1.20 as presented in Ref. 32.

The inclusion of body flexibility in dynamic loads and stability analyses requires a detailed description of the normal force distribution on body by integrating the running load curve over the length of the body and dividing by a reference area, a total normal force coefficient slope can be obtained. An empirical method based on experimental results for rapidly determining distributed aerodynamic coefficient configuration has been developed. It represents a compilation and correlation of available experimental results into a set of design curves that yield aerodynamic distribution for various geometric components used in launch vehicle design. The tangent-cone method [33] is useful for an estimate of the pressure distribution over slender bodies of revolution at angle of attack. The stability derivatives are in error when they are determined by the tangent-cone method, however, predicts the correct trend of the derivative due to nose blunting but over estimates the magnitude. An experimental investigation [34] and [35] has been made to determine the normal force coefficient slopes, centre of pressure locations, and fore body drag coefficients for several cones with different nose bluntness ratios over a Mach number range from 0.5 to 5.0. The local normal load distribution, CN_α normal force coefficient and centre of pressure X_{CP} are calculated over the sounding rocket using tangent-cone method in-conjunction with numerical

simulation of the compressible axisymmetric Euler equations. The Mach contours plot for freestream Mach numbers 0.9 – 1.5 are shown for typical sounding rocket in Ref. [36]. Table 4 gives the comparison between the experimental data with aerodynamic coefficient obtained using the hybrid method. The hybrid method is simple, computationally efficient for getting preliminary aerodynamic coefficient at supersonic Mach number at moderate angle of attack.

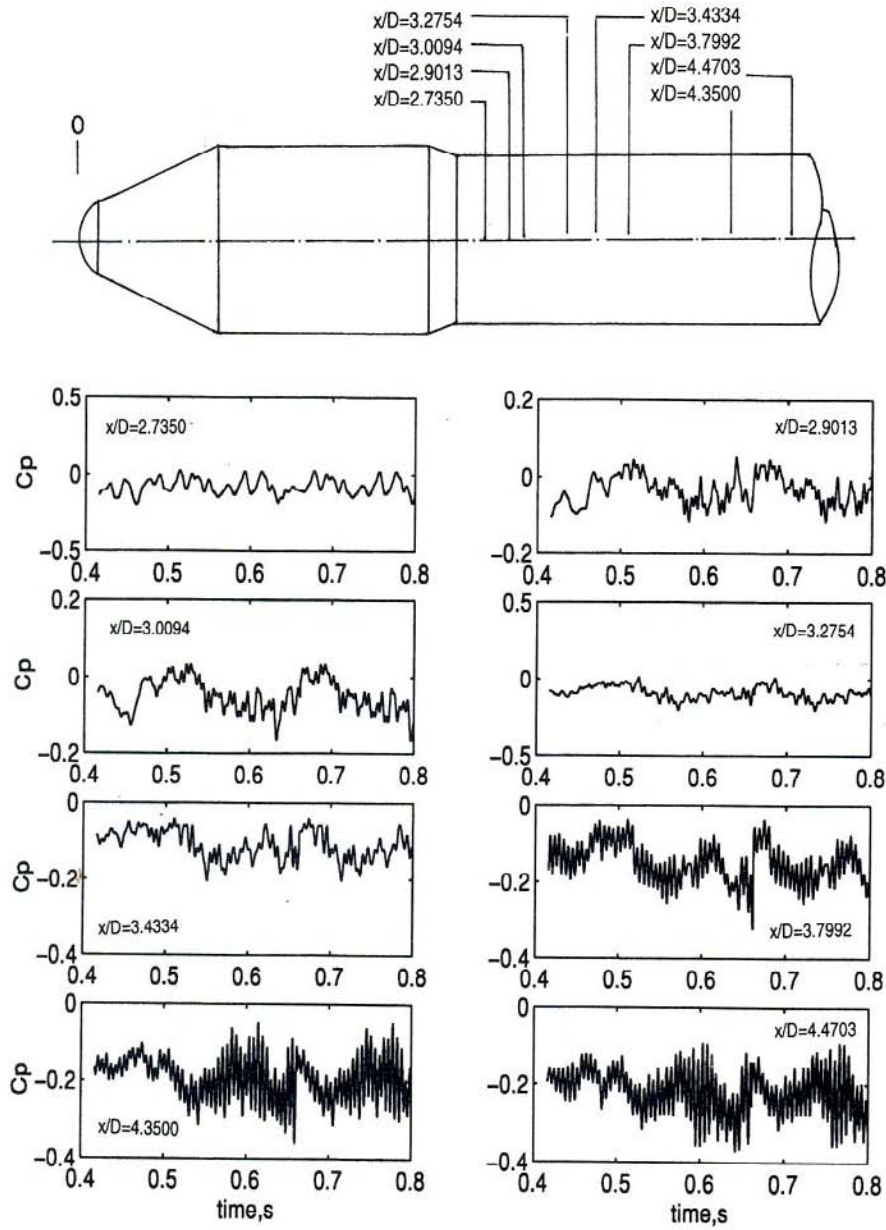


Figure 21. Surface pressure fluctuations for heat shield model M1.

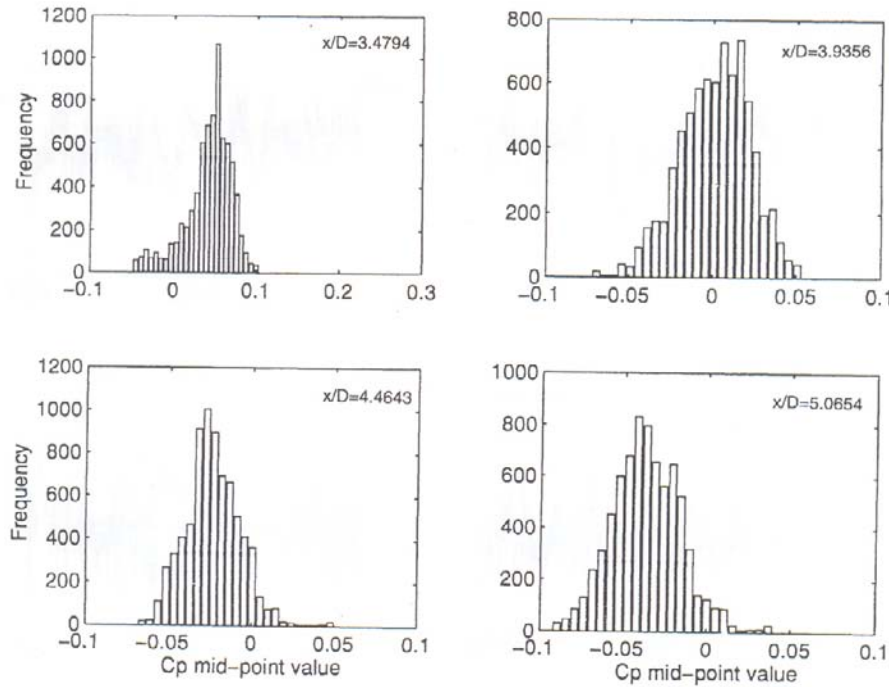


Figure 22. Histogram of pressure coefficient (M2 heat shield).

Table 4. Aerodynamic coefficient for sounding rocket.

Mach Number	Experimental		Calculated	
	CN_α	X_{CP}	CN_α	X_{CP}
2.5	0.058	8.60	0.051	8.50
3.0	0.60	8.70	0.059	8.40

4.FLOW FIELD STUDY OF THE FORWARD FACING SPIKE

A forward facing spike attached to a heat shield creates a region of flow separation over the nose that reduces the aerodynamic drag [37] due to the reducing dynamic pressure in the separated region at supersonic and hypersonic speeds. A summary of experimental investigations up to 1966 has been reported in Ref. [38] for axially symmetric models with nose shapes of hemispheres, flat surfaces, hemispherical flats, ogives and tapered configurations, and cylindrical after bodies in the freestream Mach number range of $1.75 \leq M_\infty \geq 14.0$. A complete flow field over the heat shield with forward facing spike [39] is presented in Fig. 23 for $M_\infty = 1.7$ and compared with schlieren picture. The density contour picture show a complex flow field due to the presence of the spike. The schlieren picture and density contour plots depict all the essential flow field features of the supersonic flow such as formation of the bow shock wave over the spike, reattachment shock wave and expansion fan

over the shoulder of the forward facing spike attached to typical heat shield of launch vehicle. Heat transfer study of the spiked blunt body shows reduction of wall heat transfer [40].

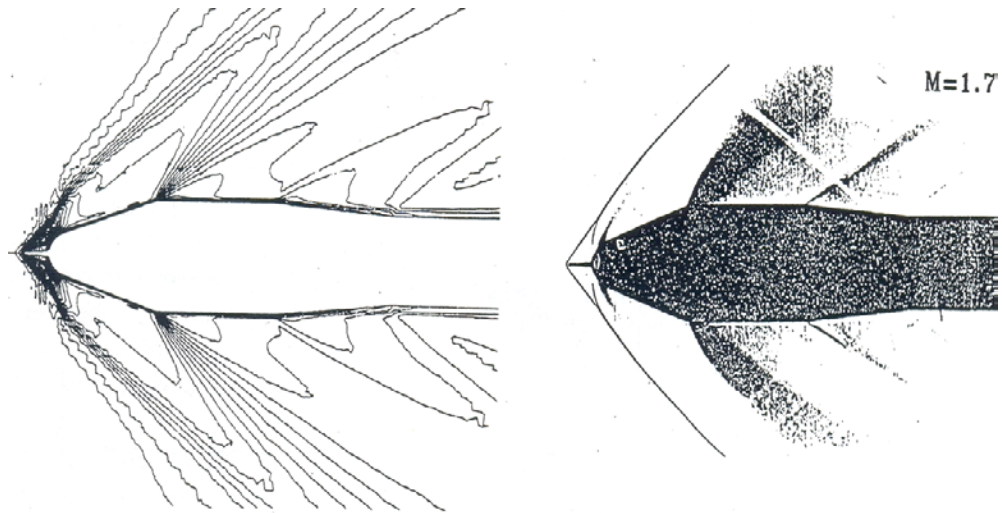


Figure 23. Comparison between density contour and schlieren picture for a forward facing spike attached to heat shield.

Fundamentally the instability was observed in earlier 1950's, when drag reducing spikes considered to be employed on ballistic missiles. The features of the supersonic flow field over a conical spike attached to hemispherical body can be delineated through the experimental investigation. It is characterized by a conical shock wave from the tip of the spike, a reattachment shock wave on the blunt body, and a separated flow region ahead of the blunt body. A schematic of the flow field over the spiked blunt body is shown in Fig. 24 (a). This flow field has also been numerically investigated and physical aspects of the flow field have been found. The dimensions of the spiked blunt body are shown in Fig. 24(b). The model is axisymmetric, the main body has a hemisphere-cylinder nose, and diameter D is 7.62×10^{-2} m. the spike consists of a conical part and a cylindrical part. The angle of the spike's cone is 10° , and the diameter of the cylinder of the spike is $0.1 D$. Spike lengths L of $0.5D$, $1.0D$, and $2.0D$ are considered in the numerical simulation. Figure 25 shows the computed flow field for the spike lengths of $L/D = 0.5$, 1.0 , and 2.0 . At $M_\infty = 6.8$. Computed density contour plots with schlieren photographs are shown in Fig. 25 for different spike lengths. Flow patterns for $L/D = 1.0$ and 2.0 are similar to that of $L/D = 0.5$. However, when the spike length is large, the angle of the oblique shock wave from the spike tip decreases, and flow separation occurs slightly downstream. The angle of the conical shock wave depends on the angle of the shear layer, which gives an effective body shape to the outer freestream. The computed flowfields show agreement with the schlieren photographs taken in the experiment by Crawford [41]. According to these computed flow fields, the angle of the conical shock wave is much larger than that of a single cone of 10 deg. This difference may be attributed to the recirculation region acting as if it were a body boundary. This feature effectively causes the reduction in the drag.

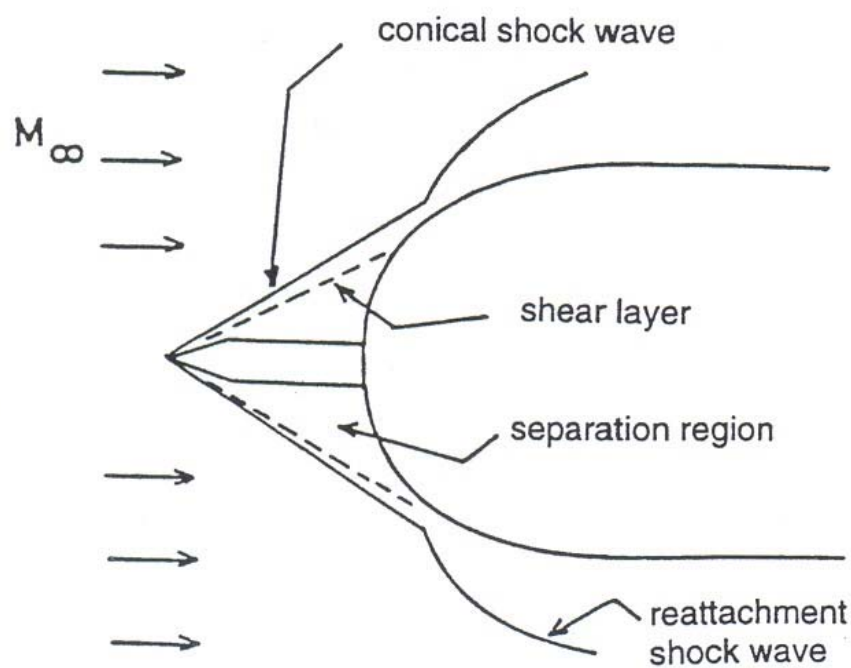


Figure 24(a). Schematic sketch of flow field over spiked blunt body.

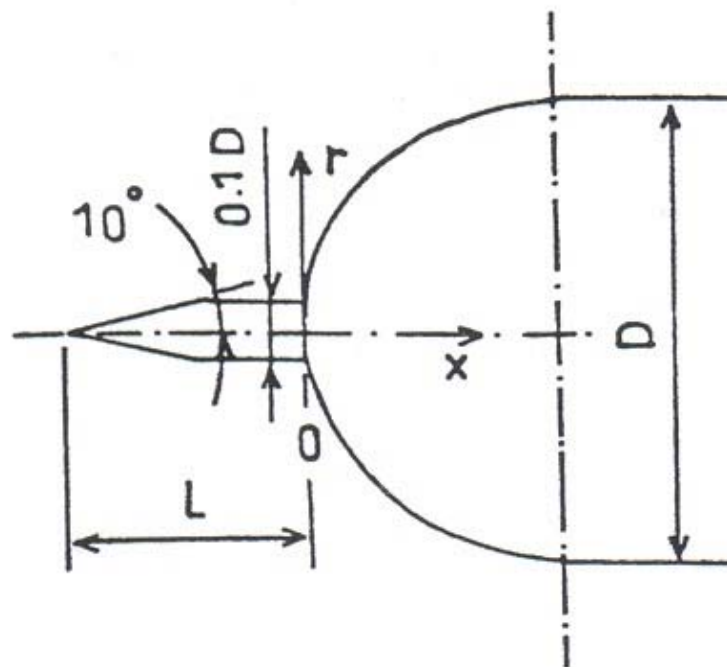


Figure 24(b). Dimension of the spiked blunt body.

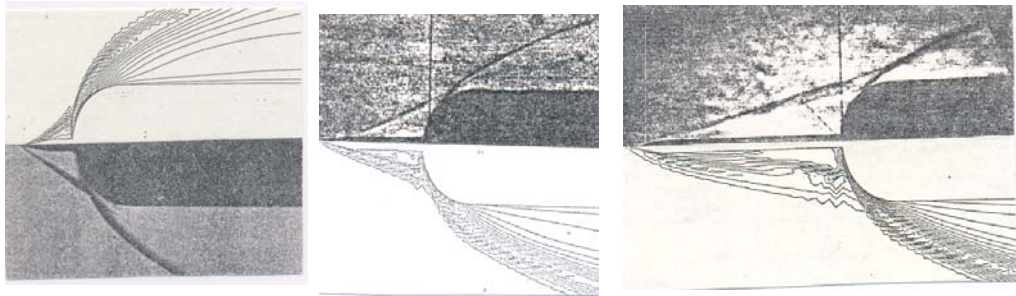


Figure 25. Comparison between density contour and schlieren picture.

The occurrence of buzzing might be critical because it brings about severe pressure oscillations on the surface. Disk on the shaft reduce stable recirculation regions by dividing single separation flow into several critical cavity flows. The aerospike [42] substantially reduces missile fore body drag by creating a low dynamic pressure region of separated flow over the high volume nose fairing. Wind-tunnel tests [43] were conducted to define the fluctuating pressure environment of the telescoping design of the aero spike/nose fairing combinations. The effects of spike length, shape (aero spike or aero disk), spike nose configuration and angle of attack [44] on the reduction of heat flux and drag is experimentally studied at $M_\infty = 7$. These experiments suggest that the aero disk is superior to the aero spike and that the aero disk of appropriate length, diameter, and nose configuration may have the potential for thermal protection and drag reduction. The hysteresis phenomenon occurring in unsteady flows over an axisymmetric spiked cylinder at Mach 2.21 was numerically simulated by Feszty et al. [45]. One of the advantages of CFD in investigation of the unsteady spiked body flows that it can offer a sequence of flow visualization frames from one particular cycle. This could be difficult to achieve in the experimental due to high frequency of the event, varying from 2 kHz up to 7.5 kHz depending on the Mach number [46]. There were few studies directed to reveal the driving mechanisms of unsteady spiked body flows [47]. The phenomenon of self-excited shock oscillations on a spike-tipped body at mach 3 is investigated experimentally. The shock oscillations are symmetric and asymmetrically depend on spike length [48]. Used the fluid dynamic stability analysis to determine flow frequency regimes where the shear layer would admit disturbance amplification. Supersonic flows around a spiked blunt body [49] are numerically simulated to examine the effects of spike length, Mach number, and angle of attack.

Computational Fluid Dynamics used to investigate the flow field characteristics for various types of forward facing spike [50]. The surface pressure oscillations over the spike and phase plots exhibit a behavior analogous to that of the Van der Pol equation [51] for the self-sustained oscillating flow [52]. Numerical simulation is carried out over the forward facing spike and without spike using laminar and turbulent flow. Numerical results [53] are compared with the experimental data [54] as shown in Fig. 25. Peak heating for reattachment of separated flow on a spike is investigated for different length to diameter of the spike in Refs. 55 and 56. Pressure oscillation over the spike for $L/D = 0.5$ and freestream Mach number of 6.8 is shown in Fig. 26.

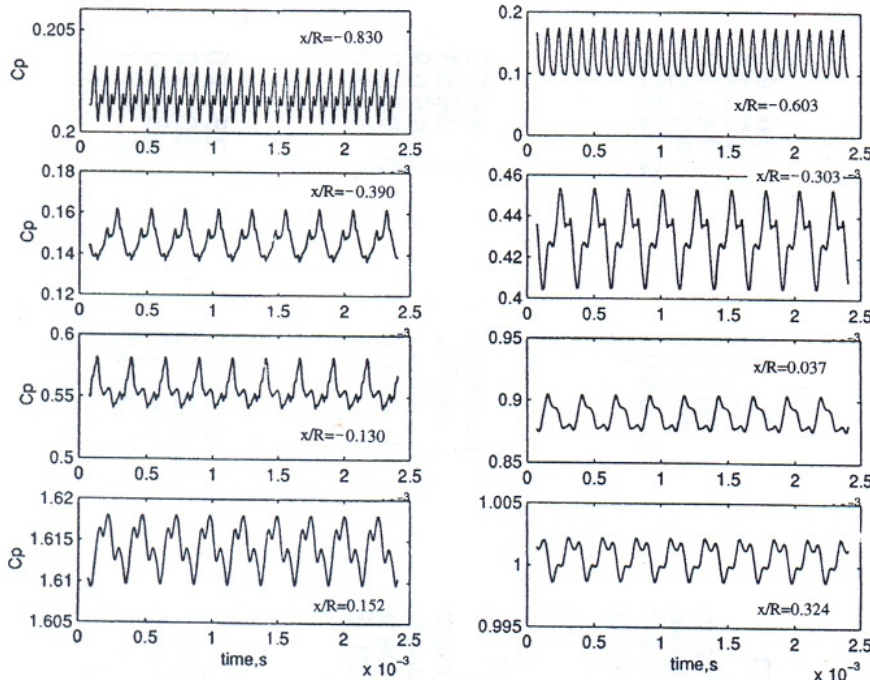


Figure 26. Pressure oscillation over spiked blunt body ($L/D=0.5$).

The self-excited oscillations is self governed or autonomous and drawing its energy from an external source by its own periodic motion. When the motion ceases, the alternating force disappears. The self-excited oscillations occur with frequency very close to the natural frequency of the undamed system. For small oscillations, energy is fed into the system and there is “negative” damping [57]. For large oscillations energy is taken from the system and is therefore damped. To emulate periodic pressure behavior with a differential equation describes the self-sustained oscillation of Van der Pol equation. Assuming that the pressure waves are planar and one-dimensional, the resulting second order, nonlinear differential equation can be written as

$$\frac{d^2 p(t)}{dt^2} - \Lambda(1 - p(t)^2) \frac{dp(t)}{dt} + p(t) = 0 \quad (L > 1)$$

where $p(t)$ is pressure computed numerically at time t and Λ is the damping term. This is having negative value for small oscillations. Figure 27 shows variation of time dependent pressure vs pressure. The phase plane derivative of the pressure coefficient is shown in Fig. 27. The phase portrait is analysed to understand the characteristic of the oscillatory flow. The critical point $(0,0)$ of the van der Pol equation shows that the critical point is stable and attractive [58]. Numerical simulation of wall pressure fluctuations on the hemisphere cylinder for freestream Mach numbers in the range of $0.80 - 0.95$ is analyzed in Ref. [59].

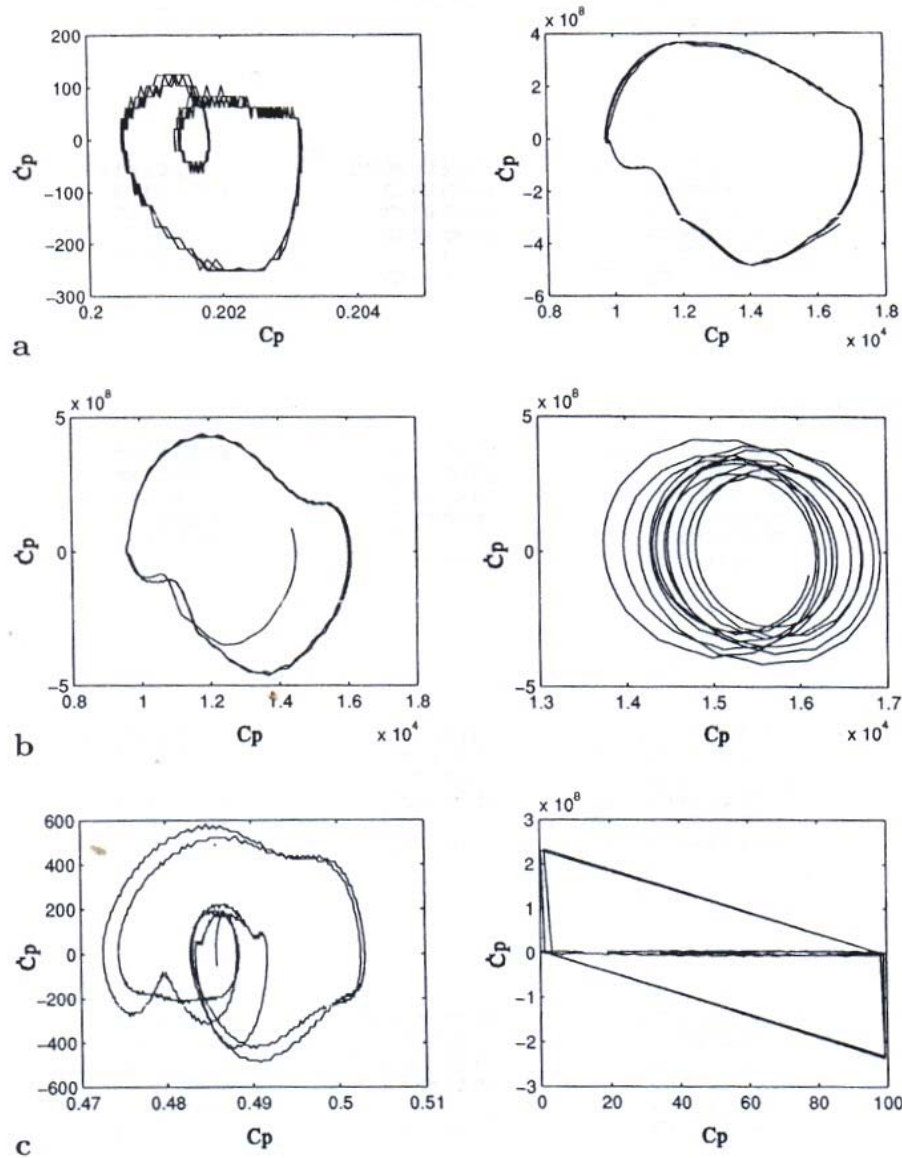


Figure 27. (a) Phase trajectory, $L/D = 0.5$, (b) Phase trajectory, $L/D = 1.0$, (c) Phase trajectory, $L/D = 2.0$.

5. ESTIMATION OF ANGLE OF ATTACK OF LAUNCH VEHICLE

The accurate measurement of air data is critical to the flight control, guidance and post flight analysis of most modern atmospheric flight vehicles. The Flush Air Data Sensing (FADS) concepts relies on a mathematical model that relates measured fore body surface pressure to the air data state. The current method uses a nonlinear pressure model and a nonlinear algorithm to solve for the air data state from the measured pressures. Five hole

probes are used in the space shuttle [60] to estimate flow direction during the ascent period of the flight. The ascent air data system of space shuttle consists of a bi-conic spike, or probe mounted on the tip of the external tank. Out of five probes, four probes are located on the conical region of the spike to measure differential pressure during flight. These pressures probes are sensitive to pitch and yaw angle, total pressure and static pressure. A relationship between the wind tunnel calibration and calibrated corrected flight pressure data are required for the estimation of flow direction. Calibration coefficients and parameters are derived using measured pressure data obtained from the wind-tunnel. In the post flight analysis, the measured pressures obtained through the telemetry are used to estimate the pitch, yaw and total angle of attack in conjunction with the wind tunnel data. Neural network method [61] have been developed and implemented for sensing air data obtained from the multi-hole pressure probes. The calibration of multi-holes requires a large data base of flow cone angles. The artificial neural network needs net work architecture, training and optimization for estimating the flow parameters. The calibration of multi-hole probes used in the neural network method needs large number of blow down of wind tunnel. Therefore, the most economical and computationally efficient way is to simulate flow field over the complex aerodynamic configuration using the Computational Fluid Dynamics.

Figure 28 shows geometry of the heat shield consists of spherical-cone and cylinder. Probes are mounted at 0.77D from the stagnation point of the heat shield on pith (P^+ and P^-) and yaw (Y^+ and Y^-) planes. D is the diameter of the cylinder region of the heat shield. The time-dependent compressible Euler equations are written in the Cartesian coordinate system as

$$\frac{\partial \mathbf{W}}{\partial t} + \frac{\partial \mathbf{F}}{\partial x} + \frac{\partial \mathbf{G}}{\partial y} + \frac{\partial \mathbf{H}}{\partial z} = 0 \quad (1)$$

Where

$$\mathbf{W} = \begin{bmatrix} \rho \\ \rho u \\ \rho v \\ \rho w \\ \rho e \end{bmatrix}, \quad \mathbf{F} = \begin{bmatrix} \rho u \\ \rho u^2 + p \\ \rho u v \\ \rho u w \\ (\rho e + p)u \end{bmatrix}, \quad \mathbf{G} = \begin{bmatrix} \rho v \\ \rho u v \\ \rho v^2 + p \\ \rho v w \\ (\rho e + p)v \end{bmatrix}, \quad \mathbf{H} = \begin{bmatrix} \rho w \\ \rho u w \\ \rho v w \\ \rho w^2 + p \\ (\rho e + p)w \end{bmatrix}$$

are the U state vector conserved quantities with ρ , u , v , w and e denoting the density, Cartesian velocity components, and the specific total internal energy, respectively, and inviscid flux vectors, E, F and G in the Cartesian coordinate. With the ideal gas assumption, the pressure and total enthalpy can be expressed as

$$\rho e = \frac{p}{(\gamma - 1)} + \frac{1}{2} \rho (u^2 + v^2 + w^2) \quad (2)$$

where γ is the ratio of specific heats. Figure 29 depicts grid over the payload fairing. A finite volume scheme in conjunction with multistage Runge-Kutta time stepping is employed to solve the three dimensional compressible Euler equations. Calibration parameters are derived using the computed differential pressure with small increment of freestream Mach number and angle of attack. The pitch and yaw angles are calculated from the calibration parameters derived from the numerical simulation of the flow field over the heat shield. High degree of linearity in the pitch and yaw angles are seen with respect to the angle of attack. The calibration factors span the freestream Mach number range of 0.5 to 3.0 which covers maximum dynamic pressure and transonic region of the vehicle. The calibration factors are validated with wind tunnel results. Initial results from the ascent air data system are compared with reconstructed trajectory data. The differential pressure transducers are in the range of $\pm 13.788 \times 10^3$ Pa. The digitization of the flight pressure data is 0.41×10^3 Pa for absolute pressure and 0.1096×10^3 Pa for differential pressure. Figure 30 shows the variation of flow angles with Mach number over heat shield [62]. The results are compared with the reconstructed trajectory data and found in reasonably good agreement. Numerical analysis is employed to compute angle of attack of the launch vehicle in conjunction with the measured pressure during the flight of the satellite launch vehicle. The measurements of the pressure are done in the conical region of the heat shield. The location of the pressure transducers are selected in the conical region of the heat shield because the flow is attached. The present scheme differs with the previously method of the estimation of angle of attack.

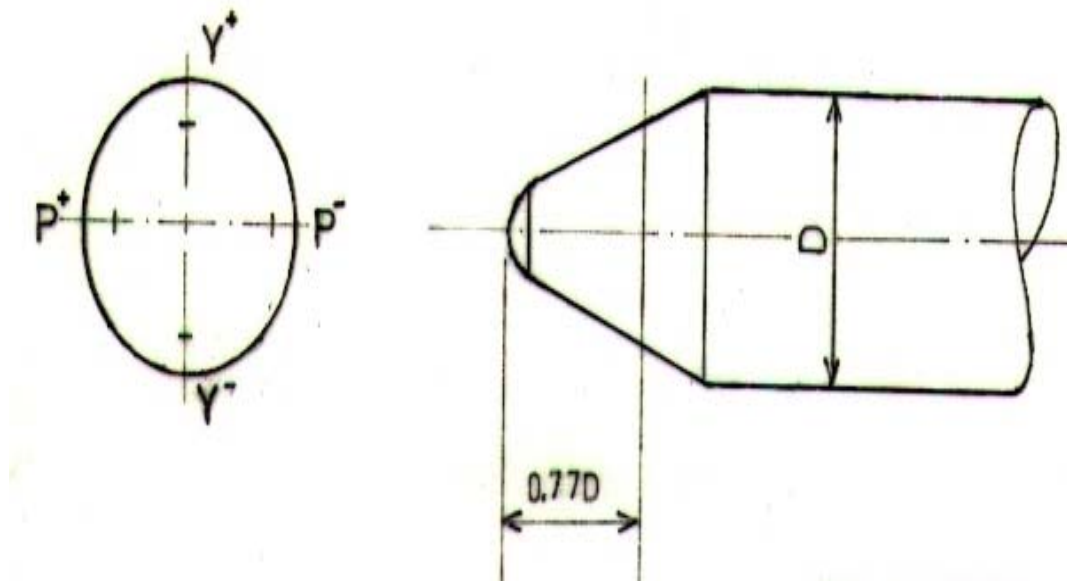


Figure 28. Location of pressure transducers on payload fairing.

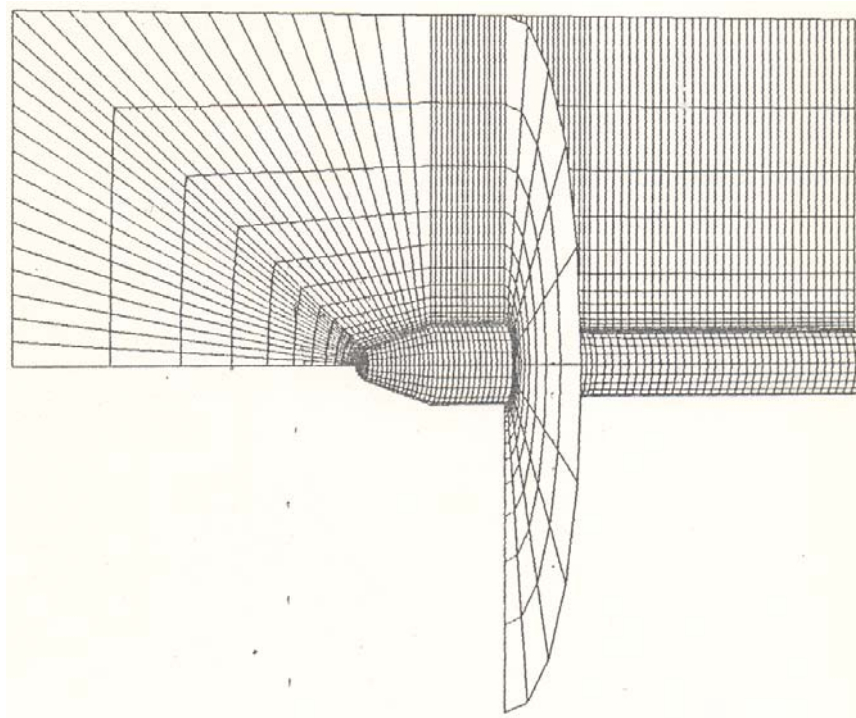


Figure 29. Computational grid over heat shield.

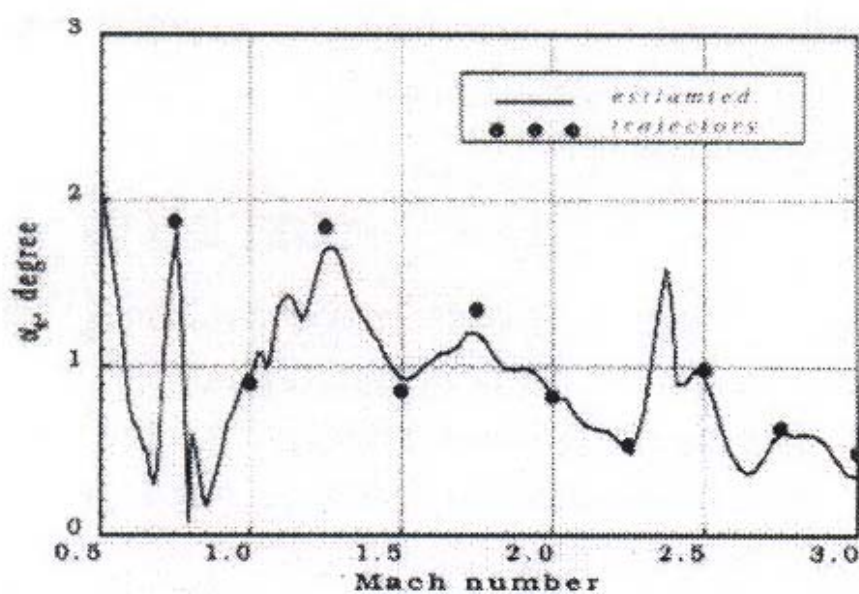


Figure 30. Variation of flow angles with Mach number over heat shield.

6. DEPRESSURIZATION OF PAYLOAD FAIRING

During the atmospheric flight, the heat shield fairing of a satellite launch vehicle needs venting in order to prevent abnormal pressure built-up, this can be detrimental to the structure. Important class of aerodynamically induced loads which must be considered in the design of a sounding rocket are those due to the differential pressure occurring across internal bulk heads and across the vehicle outer surface. Improper design of a spacecraft launch vehicle venting system can result complete mission failure. The static pressure and equivalent dynamic pressures are used in venting analyses and aided in describing the pressure differential predicted along the payload fairing. In order to model the venting process and predict the differential pressure time history reasonably for the design, a compressible flow loss coefficient is essential for the mass flux calculation. International reference guide [63] to space launch gives the maximum differential and rate of change of pressure inside the fairing. The NASA monograph [64] describes the design criteria of compartment venting for space vehicles during ascent and re-entry period. An earlier study was carried out by Mironer and Regan [65] and Murri [66] to determine the venting design criteria for space shuttle payload, using a nominal ascent, payload bay pressure profile. An analytical approach of the discharge process of a compartment into a decreasing time-dependent pressure environment has been published by Sanz-Andres et al. [67]. The effective discharge coefficient for flow through the multi-row payload fairing vents on the Titan IV launch vehicle has been numerically simulated by Huseman [68] using a three-dimensional analysis. The discharge coefficient has been obtained for a range of external flow Mach number and internal-to-external pressure ratios applicable to the Titan IV flight trajectory. Experiments were conducted by Johns and Jones [69] in the 8ft x 6 ft supersonic wind tunnel of the NASA Lewis Centre to find out the effective discharge coefficient for the application of the Titan/Centaur launch vehicle. Fay and Hengel [70] have analyzed the flow through the vent connecting the multi-compartment using a quasi-steady isentropic equation with empirical discharge coefficient. A post flight analysis [71] of the space shuttle showed that the differences between the pre-flight prediction and measured values were primarily due to difference between external pressures, which are based on subscale wind-tunnel test data, and the actual vehicle external pressure measured during the flight. Most of the predictions of the discharge coefficient are based on the flight derived vent port pressure coefficients since the wind tunnel does not adequately define the orbiter ascent pressure environment. An inverse venting problem [72] for estimation of the discharge coefficient in a heat shield fairing carried out in conjunction with the measured internal pressure.

A new reduced-order model of multidimensional payload venting is proposed for numerical simulation of simplified zero-order model. The multidimensional venting analysis is simulated by the solution of the time-dependent compressible-quasi-one-dimensional Euler equations. The governing fluid dynamics equations can be written in conservation law form as follows:

$$\frac{\partial \mathbf{W}}{\partial t} + \frac{\partial \mathbf{F}}{\partial x} + \mathbf{S} = 0 \quad (1)$$

where

$$\mathbf{W} = A \begin{bmatrix} \rho \\ \rho u \\ \rho e \end{bmatrix}, \quad \mathbf{F} = A \begin{bmatrix} \rho u \\ \rho u^2 + p \\ (\rho e + p)u \end{bmatrix}, \quad \mathbf{S} = - \begin{bmatrix} 0 \\ p \frac{\partial A}{\partial x} \\ 0 \end{bmatrix}$$

where \mathbf{W} is conserve vector and \mathbf{F} is flux vector. A is the cross-sectional area of the quasi-one-dimensional depressurization equation for the venting. It is considered that A is a continuously differentiable function that is independent of time. Therefore, the A is function of axial distance, x and can be expressed as $A = A(x)$. The variables ρ , u , p , e and H are the density, velocity, pressure, total specific energy and total enthalpy, respectively. \mathbf{S} is source term due to the area variables. The equation of state for perfect gas is

$$p = (\gamma - 1)\rho(e - \frac{1}{2}u^2) \quad (2)$$

where γ is the ratio of specific heats for air.

The reduced-order model of the venting analysis has several advantages. In contrast to the zero-dimensional models, this approach provides conservation of mass, momentum, and energy. Numerical results demonstrating the accuracy of the new-reduced-order model and its limitations are presented. The low-dimensional depressurization model of venting has a several advantages. First, this approach is fully conservative and provides conservation of mass, momentum, and energy. Second, the new quasi-one-dimensional model is computationally much more efficient compared with two-dimensional or three-dimensional numerical simulations of the orifice flow. Third, the reduced-order model retains some important features of the realistic venting model, such as the area of the vent holes, volume of the compartment. These quantities of the new model and its ability to account for the compressibility effects inherent in the venting analysis make it an efficient tool for quantitative study of the venting performance as a function of trajectory. The proposed reduced-order model is based on the assumption that the multidimensional and viscous effects inside the compartment away from the orifice can be neglected.

An orifice exits between the zero-dimensional models and the full two-dimensional/three-dimensional models of a depressurization loads. To combine the accuracy and conservation properties of the full numerical simulation methods with the efficiency of the simplified boundary conditions, a new reduced-order model of a multidimensional venting from a heat shield of a typical launch vehicle is proposed. In contrast to the methods available in the literature, the new approach uses a reduced-order model to approximate a two-dimensional or three-dimensional venting problem. The multi-dimensional depressurization is simulated by the solution of the time-dependent Euler equations similar to those used for the quasi-one-dimensional nozzle problem. The present numerical simulation is used to compute pressure inside the heat shield during the ascent phase of the launch. The compartment pressure is calculated using following expression [67]:

$$\frac{dp_0}{dt} = -C_D \frac{A_H}{V_C} \left(\frac{2\gamma}{\gamma-1} \right)^{\frac{1}{2}} \left[\left(\frac{p_i}{p_e} \right) \left(\frac{\rho_0}{\rho_i} \right)^n \right] \left[\frac{p_i}{\rho_i^n} \right]^{\frac{1}{2}} \left(\rho_0^{\frac{n+1}{2}} \right) \left[1 - \left\{ \left(\frac{p_i}{p_e} \right) \left(\frac{\rho_0}{\rho_i} \right) \right\}^{\frac{\gamma-1}{\gamma}} \right]^{\frac{1}{2}} \quad (3)$$

where n is polytropic coefficient. Subscripts e , i , and o are condition inside the fairing, initial condition and inside respectively. A_H is the area of the vent hole, V_C is volume of the compartment, ρ is density, C_D is the discharge coefficient, p is pressure, γ is the ratio of specific heats. The variation of discharge coefficient, C_D is shown as function of flight time in Fig. 31 for the fairing of M1 and M2 launch vehicle. The discharge coefficient is defined here as the actual mass flow rate divided by the ideal mass flow rate through the vent hole. The venting analysis leading up to the first Titan IV launch [74] for complete description of the dynamic pressures were combined in determining the skin-pressure differential for the design of pay load fairing. The differential pressure depends mainly on the geometry of the venting holes, the effective volume of air to be evacuated and the trajectory of the launch vehicle.

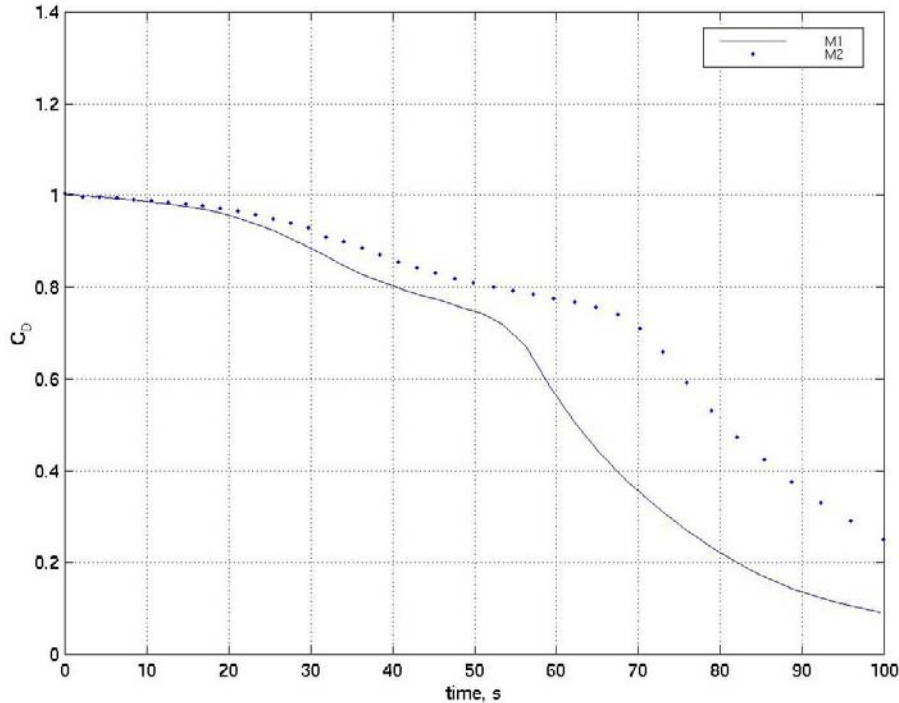


Figure 31. Variation of discharge coefficient as a function of flight time.

6. FLOW FIELD SIMULATION OF THE REENTRY CAPSULES

The primary design consideration of reentry capsules requires large spherical nose radius of their forebody that gives high aerodynamic drag and a short body length for reducing the total structure weight and the ballistic coefficient. The forebody shape of reentry capsules can be selected either employing a spherical cap, or a combination of spherical nose with cone, or

a spherical blunt cone/flare configuration. To ensure the deployment of parachute in the transonic region, the flow field past the capsule must be known at supersonic speeds. The flow field in the wake region of a reentry capsule is complex due to the expansion at the shoulder and the base-shell.

A large number of computational fluid dynamics simulations [75 – 80] have been performed for aerobraking and reentry capsules. Allen and Cheng [78] have carried out the numerical solution of Navier-Stokes equations in the near wake region of the reentry module, which confirms the mechanism of flow separation as, observed experimentally [80]. Base drag represents the loss in recovery of pressure over the base of the capsule [81]. The supersonic and hypersonic laminar flow over a slender cone has been numerically calculated by Tai and Kao [82]. A summary of developments relating to the base pressure prediction is reported in the review paper of Lamb and Oberkampf [83]. An aerodynamic analysis of the Commercial Experiment Transport (COMET) reentry capsule carried out by Wood et al. [84] by solving the laminar thin layer Navier-Stokes equations flow solver LAURA. The flow field past blunt and short reentry capsule has been analyzed in order to understand the mechanism of the instability at supersonic speeds due to decay of base pressure [85]. Yamamoto et al. [86] have computed flow field over the OREX reentry module in conjunction with the in-depth thermal analysis of thermal protection system and results were compared with the flight data. Tam [87] has used LUSGS implicit scheme for flow computation over On-Axis Biconic and Aeroassist Flight Experiment (AFE) reentry vehicles. Liever et al. [88] solved the flow field over Beagle reentry capsule. The flow field and the heat flux computation over the Mars pathfinder vehicle has been numerically carried out by Haas [77] along with fore body and wake flow structure during atmospheric entry of the spacecraft. Flow field simulations are carried out over various reentry configurations such as OREX, Apollo, Apollo-II, Beagle-2, MUSES, CARINA, ARD and spherically blunted cone flare. Figure 32 and Table 5 shows the geometrical details of the various reentry capsules.

The above mentioned reentry geometrical configurations reveal that the forebody shape of reentry capsules can be classified either using as a spherical cap as in the case of Apollo and ARD, or combination of the spherical nose with cone as in the case of OREX and Beagle-2, or a spherical blunt-cone/flare configuration as shown in the figure and semi-cone angle given in the Table 5(b). The significant flow features are described by the following: In the forebody region, the fluid decelerates through the bow shock wave depending upon the cruise speed and altitude. At the shoulder of the capsule, the flow turns and expands rapidly, that the boundary layer detaches, forming a free shear layer that separates the inner recirculating flow region behind the base from the outer flow field. The latter is recompressed and turned back to freestream direction, first by so-called lip shock, and further downstream by recompression shock. At the end of recirculating flow past the neck, the shear layer develops in the wake trail. A complex inviscid wave structure often includes a lip shock wave (associates with the corner expansion) and wake trail (adjacent to the shear layer confluence). The corner expansion process is a modified Prandtl-Mayer pattern distorted by the presence of the approaching boundary layer. Figure 33 shows schematic feature of the flow field over OREX and spherical blunt cone/flare capsules. The sonic line is located on the OREX-type configuration on the shoulder whereas in the case of spherical blunt cone/flare's module, the location of the sonic line is at the junction of the spherical blunt cone. Thus, it is seen that the flow field over the reentry capsule needs a high drag with good static stability margin which leads to the selection of an axisymmetric shape of large angle sphere-cone combination.

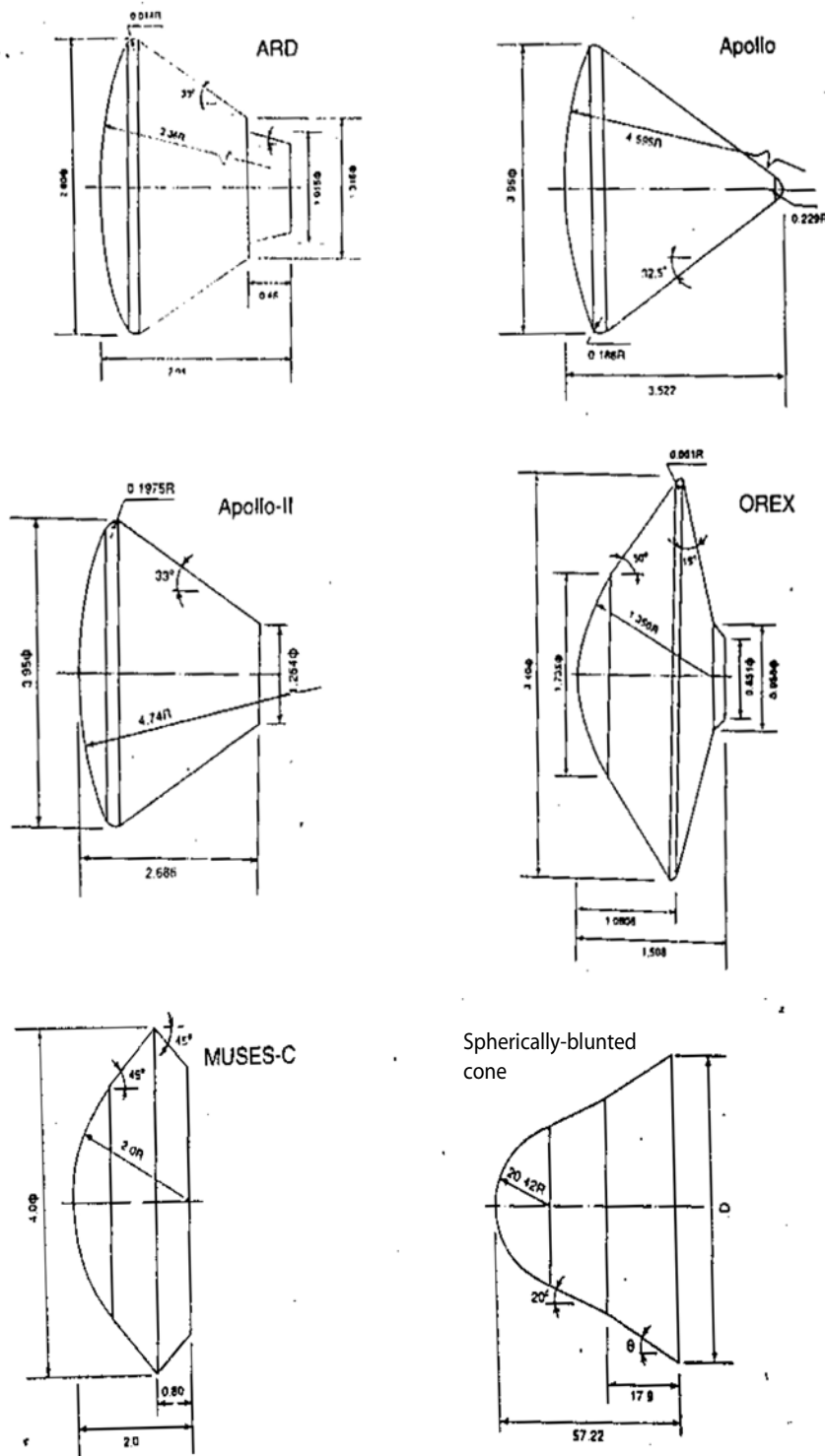


Figure 32. Geometrical details of various reentry configurations.

Figure 34 shows the pressure coefficient [$C_p = 2\{(p/p_\infty) - 1\}/(\gamma M_\infty^2)\}$] variation along the surface for different reentry capsules and freestream Mach numbers. The $s/D = 0$ location is the stagnation point, where s is the distance measured along the surface from the stagnation point D is the maximum diameter of the capsule. The pressure coefficient on the spherical cap of the capsule decreases gradually for a given M_∞ . C_p falls on the sphere-cone junction and remains constant over the cone. In the case of the OREX, the sonic point moves to the corner of the blunt body and affects the pressure distribution throughout the subsonic flow. In the case of the OREX with $\alpha_N = 50^\circ$, the pressure coefficient shows over expanded flow. The spherical blunted cone-flare configuration ($\theta = 20^\circ$) gives under expanded flow as seen in Fig. 34. A sudden drop in C_p is observed on the shoulder of the module followed by a negative C_p variation in the base region. A low pressure is formed immediately downstream of the base which is characterized by a low-speed recirculating flow region which can be attributed to fill-up the growing space between the shock wave and the body. In the region, C_p is decreasing with increasing M_∞ . Computed Mach contours plots around the OREX capsule is shown in Fig. 35 for various free stream Mach number, M_∞ . The Mach contours plots show the formation of vortices at the corner region of the capsule for $M_\infty \leq 3$. Characteristic features of the flow field around the blunt body at supersonic speeds, such as bow shock wave ahead of the capsule, the wake, and the recompression shock waves emanating from the neck point, are observed in the Mach contour plots. The bow shock wave follows the body contour and the forebody is entirely subsonic upto the corner tangency point of the OREX where the sonic line is located. The effects of the sonic line on the aerodynamic design parameters are investigated [90] and [91]. A low pressure is formed immediately down stream of the base which is characterized by a low speed recirculating flow region which can be attributed to fill up growing space between the shock wave and the body.

An oscillating flow over the reentry configuration analyzed using numerical simulation [92]. Flow oscillations over Apollo and OREX are numerically simulated by solving unsteady, axisymmetric, compressible Navier-Stokes equations for $M_\infty = 1.2$. The periodicity of the flow fields in the base region are 8.33 Hz and 1.04 Hz, respectively for the Apollo and the OREX capsules. The cycle of motion of the flow field over the Apollo is 8 times faster as compared the OREX.

Table 5(a). Geometrical parameters of reentry configurations.

Capsule	Overall length, L	Semi-cone angle, α_A deg	Back-shell angle, α_B deg	Spherical radius, R_N	Frontal diameter, D	Corner radius, R_C
ARD	2.04	—	33.0	3.36	2.80	0.014
Apollo	3.522	—	32.5	4.59	3.95	0.186
Apollo-II	2.686	—	33.0	4.74	3.95	0.197
MUSES-C	2.0	45.0	45.0	2.0	4.0	--
OREX	1.508	50.0	75.0	1.35	3.40	0.001

Table 5(b). Geometrical parameters of spherical blunt cone-cylinder configurations.

Base diameter, D mm	Semi-cone angle, θ in deg
73.91	25
77.89	30
82.29	35

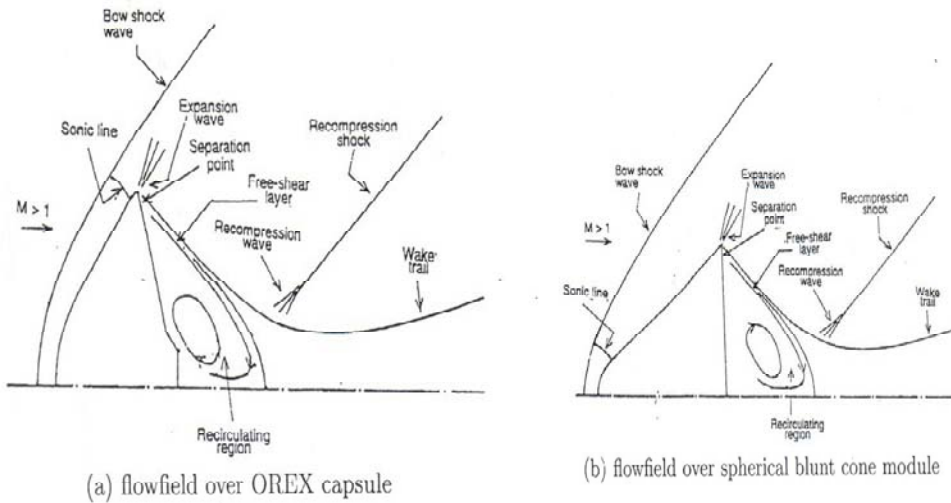


Figure 33. Representation of flow features on reentry capsules at supersonic speeds.

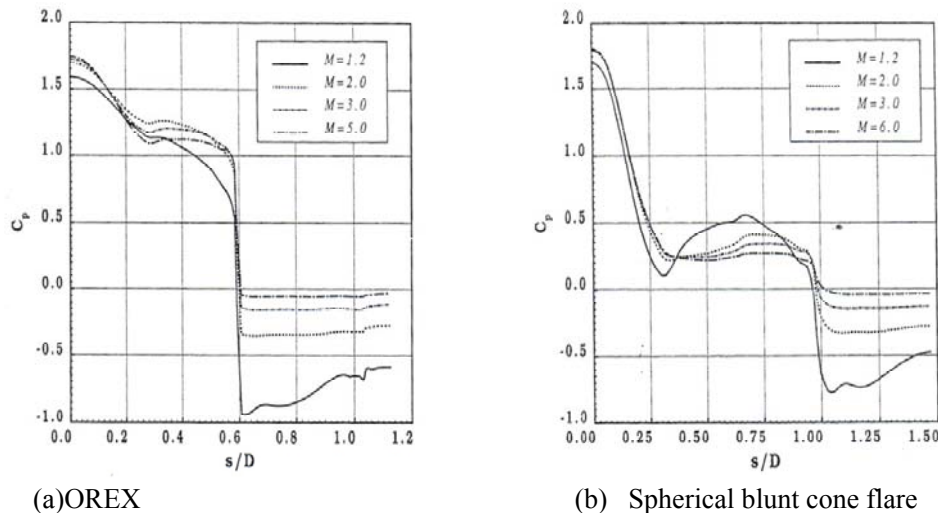


Figure 34. Variation of pressure distribution along the surface of the reentry capsules.

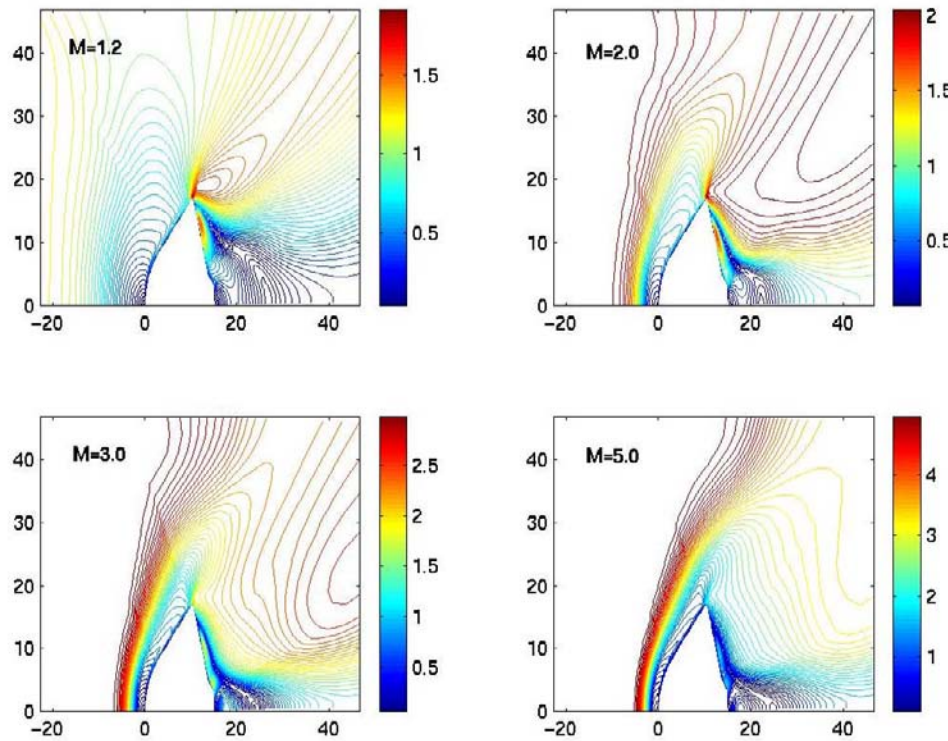


Figure 35. Mach contours over OREX reentry module.

REFERENCES

- [1] Lamont, P. J. and Hunt, B. L., The impingement of under expanded axisymmetric jets on wedges, *Journal of Fluid Mechanics*, Vol. 76, Part 2, 1976, pp. 307 – 336.
- [2] Kim, K.-H. and Chang, K.-S., Three-dimensional structure of a supersonic jet impinging on an inclined plate, *AIAA Journal*, Vol. 31, No.5, 1994, pp. 778 – 782.
- [3] Nakai, Y., Fujimatsu, N., and Fujii, K., Experimental study of under expanded supersonic jet impinging on an inclined plate, *AIAA Journal*, Vol. 44, No. 11, 2006, pp. 2691 – 2699.
- [4] Wu, J., Tang, L., Luke, E. A., Tong, X – L. and Cinnella, P., Comprehensive numerical study of jet flow impingement over flat plates, *Journal of Spacecraft and Rockets*, Vol. 39, No. 3, 2002, pp. 357 – 366.
- [5] Anon, Acoustic loads generated by the propulsion system, NASA Space Vehicle Design Criteria (Structures), NASA SP 8072, June 1971.
- [6] Prasad, J. K., Mehta, R. C. and Sreekanth, A. K., Impingement of supersonic jets on an axisymmetric deflector, *AIAA Journal*, Vo.32, No.7. July 1994, pp.1535-1538.
- [7] Prasad, J. K., Mehta, R. C. and Sreekanth, A. K., Impingement of supersonic jets on a wedge and axisymmetric deflector, in the proceedings of 6th Asian Congress of Fluid Mechanics, Nanyang Technological University, Singapore, pp.983-987, May 22-26, 1995.

- [8] Mehta, R. C., Pandya, M. J. and Jayachandran, T., Euler calculations for diffuser flow field, free jets and impingement jets, *International Journal of Numerical Methods of Heat and Fluid Flows*, Vol.4, No.4, May 1995, pp. 287-300.
- [9] Mehta, R. C. and Prasad, J. K., Investigation of supersonic free jets emanating from convergent-divergent nozzle, *International Journal of Computational Fluid Dynamics*, Vol. 10, 1998, pp. 61-71.
- [10] Park, D.C., A note on Prandtl formula for the wave length of supersonic gas jet, *Quarterly Journal of Mechanics and Applied Mathematics*, Vol. 3, No. 2, 1950, pp. 173 -181.
- [11] Abdel-Fattah, A. M., Discrete tone emission from high pressure ratio supersonic jets from convergent-divergent nozzles, *AIAA Journal*, Vol. 26, No. 3, 1988, pp. 283 – 291.
- [12] Mehta, R. C. and Prasad, J. K., Numerical analysis of flow fields of axisymmetric supersonic free jets, *Computational Fluid Dynamics JOURNAL*, Vol. 12, No. 1, April 2003, pp. 115 – 120.
- [13] Mehta, R. C. and Prasad, J. K., Estimation of shock-cell structure of axisymmetric free jets, *Indian Journal of Engineering & Material Sciences*, Vol. 3, August 1996, pp. 141 – 147.
- [14] Mehta, R. C., Numerical simulation of supersonic turbulent jets impinging on an axisymmetric deflector, *Indian Journal of Engineering & Material Sciences*, Vol. 9, August 2002, pp. 227 – 236.
- [15] Prasad, J. K., Mehta, R. C. and Sreekanth, A. K., Experimental study of overexpanded supersonic jet impingement on a double wedge deflector, *Journal of the Royal Aeronautical Society*, June/July 1993, pp. 209 – 214.
- [16] Hsieh, T., Hemisphere-cylinder in low supersonic flow, *AIAA Journal* Vol. 13, No. 12, Dec. 1973, pp. 1551 – 1552.
- [17] Hsieh, T., Hemisphere-cylinder in transonic flow, $M_\infty = 0.7 \sim 1.0$, *AIAA Journal* Vol. 13, No. 10, 1975, pp. 1411 – 1413.
- [18] Baldwin, B. S. and Lomax, H, Thin layer approximation and algebraic model for separated turbulent flow, AIAA paper 78-257, 1978.
- [19] Mehta, R. C., Numerical investigation of viscous flow over a hemisphere-cylinder, *Acta Mechanica*, Vol. 128, 1998, pp. 49-58.
- [20] Anon., Buffeting During Atmospheric Ascent, NASA Special Vehicle Design Criteria (Structures), NASA SP-8001, Nov. 1970.
- [21] Mehta, R. C., Comparative Study of Surface Pressure Fluctuations Over Bulbous Heat Shield at Mach 0.95, *Computers & Fluids*, Vol. 30, No. 6, June 2001, pp. 689-709.
- [22] Mehta, R. C., Solution of viscous flow over heat shield using structured grid, *Aerospace Science and Technology*, Vol. 2, 1998, pp. 415-423.
- [23] Mehta, R. C., Transonic flow simulation for a bulbous heat shield, *Journal of Spacecraft and Rockets*, Vol.34, No.4, July-Aug. 1997, pp.561-564.
- [24] Mehta, R. C., Flowfield over bulbous heat shield in transonic and low supersonic speeds, *Journal of Spacecraft and Rockets*, Vol. 35, No. 1, Jan-Feb 1998, pp.102-105.
- [25] Mehta, R. C., Numerical studies over a bulbous payload shroud in transonic and low supersonic Mach numbers, AIAA Paper 97-2256, 1997.
- [26] Coe, C. F., The effects of some variations in launch vehicle nose shape on steady and fluctuating pressures at transonic speeds, NASA TM X 645, March 1962.

- [27] Rainey, A. G., Progress on the launch vehicle buffeting problem, *Journal of Spacecraft and Rockets*, Vol. 2, No. 3, 1965, pp. 289 – 299.
- [28] Dotson, K. W., Baker, R. L. and Bywater, R. L., Launch vehicle self-sustained oscillation from aero-elastic coupling, Part 2: Analysis, *Journal of Spacecraft and Rockets*, Vol. 35, No. 3, 1998, pp. 365 - 373.
- [29] Mehta, R. C. and Sastri, V. M. K., Numerical analysis of wall pressure and heat flux fluctuations in shock/turbulent boundary layer interaction, *International Journal of Numerical Methods in Fluids*, Vol.16, No.8, April 1993, pp.739-753.
- [30] Mehta, R. C., Unsteady pressure fluctuations in the boat tail region of a heat shield, *Aerospace Science and Technology*, Vol. 4, 2000, pp. 91 – 102.
- [31] Marple Jr., S. L., Digital Spectral Analysis with applications, Prentice-Hall inc., NJ, 1987.
- [32] Mehta, R. C., Wall pressure fluctuations over a bulbous heat shield of a satellite launch vehicle, *Acta Mechanica*, Vol. 137, 1999, pp. 13 – 31.
- [33] Friberg, E. G. and Walchner, O., Pressure correlation for blunted slender cones, *AIAA Journal*, Vol. 7, No. 8, 1969, pp.1618 – 1619.
- [34] Owens, R. V., Aerodynamic characteristics of spherical blunted cones at Mach numbers from 05 to 5.0, NASA TN D 3088, 1965.
- [35] Muraca, R. J., External and internal air loads on sounding rockets, *Journal of Spacecraft and Rockets*, Vol. 4, No. 9, 1967, pp. 1207 – 1210.
- [36] Mehta, R. C. and Sastry, M. S., Computation of Aerodynamic load and coefficient for satellite launch vehicle, *Indian Journal of Engineering & Material Sciences*, Vol. 4, April 1997, pp. 41 – 48.
- [37] Reding, J. P., Guenther, R., and Richer, B. J., Unsteady aerodynamic considerations in the design of a drag reduction spike, *Journal of Spacecraft and Rockets*, Vol. 14, 1977, pp. 705 – 710.
- [38] Zorea, C. and Rom, J., Effects of a spike on the drag and on the aerodynamic stability of blunt bodies in supersonic flow, *Journal of Spacecraft and Rockets*, Vol. 7, 1990, pp. 1017 – 1019.
- [39] Mehta, R. C. and Jayachandran, T., Navier Stokes solution for a heat shield with and without a forward facing spike, *Computers & Fluids*, Vol. 26, No. 7, 1997, pp. 741 – 754.
- [40] Mehta, R. C., Heat transfer study of high speed flow over a spiked blunt body, *International Journal of Numerical Methods in Heat & Fluid Flow*, Vol. 10, No. 7, 2000, pp. 750 – 769.
- [41] Crawford D. H., Investigation of flow over a spiked-nose hemisphere-cylinder at a Mach number of 6.8, NASA TN D 118, 1959.
- [42] Kobayashi, H., Maru, Y. and Fukiba, K., Experimental study on aerodynamic characteristics of telescopic aerospikes with multiple disks, *Journal of Spacecraft and Rockets*, Vol. 44, No. 1, 2007, pp. 33 – 41.
- [43] Reding, J. P., Guenther, R. A., and Jecmen, D. M., Scale effects on fluctuating pressures in spike-induced flow separation, *Journal of Spacecraft and Rockets*, Vol. 17, No. 2, 1980, pp. 112 – 118.
- [44] Motoyama, N., Mihara, K., Miyajima, R., Watanuki, T. and Kubota, H., Thermal protection and drag reduction with use of spike in hypersonic flow, AIAA paper 2001-1828, 2001.

- [45] Feszty, D., Badcock, K. J. and Richards, B. E., Numerical simulation of hysteresis phenomenon in high-speed spiked body, AIAA paper 2000 – 0141, 2000.
- [46] Calarese, W. and Hankey, W. L., Modes of shock wave oscillations on spike-tipped bodies, AIAA Journal, Vol. 23, No. 2, 1985, pp. 185 – 192.
- [47] Shang, J. S., Smith, R. E. and Hankey, W. L., Flow oscillations of spike-tipped bodies, AIAA paper 80 – 0062, 1980.
- [48] Raleigh, L., On the stability or instability of certain fluid motion, Scientific papers, Vol. 1, Cambridge University Press, 1880, pp. 474 -487.
- [49] Yamauchi, M., Fujii, K. and Higashino, F., Numerical investigation of supersonic flows around spiked blunt body, *Journal of Spacecraft and Rockets*, Vol. 32, No. 1, 1995, pp. 32 - 42.
- [50] Mehta, R. C., Kalimuthu, R. and Rathakrishnan, E., Numerical simulation of flow field over aerodisc at Mach 6, 34th National Conference on Fluid Mechanics & Fluid Power, BIT Mesra, Ranchi, India, Dec. 10-12, 2007.
- [51] Kreyszig, E., Advanced Engineering mathematics, 5th Ed. Wiley, New Delhi, p. 135.
- [52] Mehta, R. C., Numerical analysis of pressure oscillations over axisymmetric spiked blunt bodies at Mach 6.8, Shock Waves, Vol. 11, No. 6, May 2002, pp. 431-440.
- [53] Mehta, R. C., Pressure oscillations over a spiked blunt body at hypersonic Mach number, *Computational Fluid Dynamics Journal*, Vol. 9, No. 2, July 2000, pp. 88-95.
- [54] Mehta, R. C., Limit cycle of oscillating flow over a spiked blunt body, in the proceedings of the 4th Asian Computational Fluid Dynamics Conference, Mianyang, Sichuan, China, September 19-21, 2000.
- [55] Mehta, R. C., Numerical heat transfer study over spiked blunt bodies at Mach 6.8, *Journal of Spacecraft and Rockets*, Vol. 37, No. 5, 2000, pp. 700 – 703.
- [56] Mehta, R. C., Peak heating for reattachment of separated flow on a spiked blunt body, *Heat and Mass Transfer*, Vol. 36, 2000, pp. 277 – 283.
- [57] Mehta, R. C., Numerical analysis of pressure oscillations over axisymmetric spiked blunt bodies at Mach 6.8, Shock Waves, Vol. 11, No. 6, May 2002, pp. 431-440.
- [58] Mehta, R. C., Pressure oscillations over a spiked blunt body at hypersonic Mach number, *Computational Fluid Dynamics Journal*, Vol. 9, No. 2, July 2000, pp. 88-95.
- [59] Mehta, R. C., Numerical simulation of wall pressure fluctuations on hemisphere cylinder at transonic Mach numbers, *Computational Fluid Dynamics JOURNAL*, Vol. 8, No. 4, 2000, pp. 511 – 520.
- [60] Hillije, E. R., and Nelson, R. L., Ascent air data system results from the space shuttle flight test program – Lessons learned, compiled by J. P. Arrington, NASA CR 2283, 1983.
- [61] Rediniotis, O. K. and Vijaygopal, R., Miniature muti-hole pressure probes and their neural network based calibrations, AIAA Journal, Vol. 37, No. 6, June, 1999, pp. 666 – 674.
- [62] Mehta, R. C., Flow direction estimation based on computed and flight measured surface pressure, *Computational Fluid Dynamics JOURNAL*, Vol. 12, No. 3, Oct. 2003, pp. 555-561.
- [63] Payload Accommodation in International Reference Guide to Space Launch Systems, Edited by S. J. Isakowitz, J. B. Hopkins, J. P. Hopkins, Jr., Fourth Edition, AIAA Publication, July 2004.

- [64] Anon. Compartment Venting: Space Vehicle Design Criteria (Structures), NASA SP-8060, Nov. 1970.
- [65] Mironer, A., and Regan, F., Venting of Space-Shuttle Payloads, AIAA paper 83-2600 (1983).
- [66] Murri, B. W., Payload Venting in Worst Case Shuttle Environments, AIAA paper 87-1598 (1987).
- [67] Sanz-Andres, A., Satiago-Prowald, J., and Ayuso-Berea, A., Spacecraft Launch Depressurization loads, *Journal of Spacecraft and Rockets* Vol. 34, No.6, 1997, pp.805 - 810.
- [68] Huseman, P. G., and Chern, S-Y., Discharge Coefficient Analysis for Titan IV Payload Fairing Vents, AIAA paper 97-2068 (1997).
- [69] John, A. L., and Jones, M. L., Venting characteristics of gaseous helium and nitrogen discharging into a freestream at Mach number from 0.60 to 1.57, NASA TM X-2995 (1974).
- [70] Fay, J. F., and Hengel, J. E., Pressure Dither in Venting Analyses, AIAA paper 93-3014 (1993).
- [71] Lutfi, H. S., and Nieder, R. L., Space Shuttle Obiter Venting – Lesson Learned, complied by J. P. Arrington, NASA CR 2283, 1983.
- [72] Mehta, R. C., Inverse Venting Problem for Estimation of the Discharge Coefficient in a Satellite Launch Vehicle, *Journal of Aerospace Engineering*, Vol. 217, No. G6, 2003, pp. 277-281.
- [73] Mehta, R. C., Quasi-one-dimensional numerical analysis of payload venting of satellite launch vehicle, *Journal of Spacecraft and Rockets*, Vol. 45, No. 2, 2008, pp.412-414.
- [74] Brower, T. L., Titan launch vehicle: Ground Test History, *Journal of Spacecraft and Rockets*, Vol. 43, No. 1, 2006, pp. 147 - 160.
- [75] Gnoffo, P.A., Price, J.M. and Braum, R.D., On the computation of near wake aerobrake flow fields, AIAA paper 91-1371, June 1991.
- [76] Grasso, F. and Marinir, M., Solution of hypersonic flows with total variation diminishing multigrid techniques, *Computer & Fluids*, Vol. 23, No. 5, 1995, pp. 571-592.
- [77] Venkatapathy, E., Palmer, G., and Prabhu, D. K., AFE base computations, AIAA paper 91-1372, June 1991.
- [78] Allen, J.S. and Cheng, S.I., Numerical solution of the compressible Navier-Stokes equations for the near wake, *Physics of Fluids*, Vol. 13, No. 1, 1970, pp. 37-52.
- [79] Weinbaum, S., Rapid expansion of a supersonic boundary layer and its applications to the near wake, *AIAA Journal*, Vol. 4, No. 2, 1966, pp. 217-226.
- [80] Osu, H., Abe, T., Ohnishi, Y., Sasoh, A. and Takayama, K., Numerical investigation of high enthalpy flow generated by expansion tube, *AIAA Journal*, Vol. 40, No. 12, 2002, pp. 2423-2430.
- [81] Grasso, F. and Pettinelli, C., Analysis of laminar near wake hypersonic flow, *Journal of Spacecraft and Rockets*, Vol. 32, No. 6, 1995, pp. 970-980.
- [82] Tai, C-S. and Kao, A.F., Navier-Stokes solver for hypersonic flow over a slender cone, *Journal of Spacecraft and Rockets*, Vol. 31, No. 1, 1994, pp. 215-222.
- [83] Lamb, J.P. and Oberkampf, W.L., Review and development of base pressure and base heating correlations in supersonic flow, *Journal of Spacecraft & Rockets*, Vol. 32, No. 1, 1995, pp. 8-23.

- [84] Wood, A.W., Gnoffo, P.A. and Rault, D.F.G., Aerodynamic analysis of commercial experiment transport reentry capsule, *Journal of Spacecraft & Rockets*, Vol. 33, No. 5, 1996, pp. 643-646.
- [85] Teramoto, S., Hiraki, K., and Fujii, K., Numerical analysis of dynamic stability of a reentry capsule at transonic speed, *AIAA Journal*, Vol. 39, No. 4, April 2001, pp. 646-653.
- [86] Yamamoto, Y. and Yoshioka, M., CFD and FEM coupling analysis of OREX aero-thermodynamic flight data, AIAA 95-2087, 1995.
- [87] Tam, L.T., LU-SGS implicit scheme for entry vehicle flow computation and comparison with aerodynamic data, AIAA 92-2671 CP, 1992.
- [88] Liever, P.A., Habchi, S.D., Burnell, S. I. and Lingard, J.S., Computational fluid dynamics prediction of the Beagle 2 aerodynamic data base, *Journal of Spacecraft and Rockets*, Vol. 40, No. 5, 2003, pp. 632-638.
- [89] Haas, B.L. and Venkatapathy, E., Mars path finder computations including base heating predictions, AIAA 95-2086, 1995.
- [90] Mehta, R. C., Numerical simulation of supersonic flow past reentry capsules, *Shock Waves*, Vol. 15, No. 1, March 2006, pp. 31-41.
- [91] Mehta, R. C., Computation of flow field over reentry capsules at supersonic Mach numbers, *Computational Fluid Dynamics JOURNAL*, Vol. 13, No. 3, Oct. 2004, pp. 585-596.
- [92] Mehta, R. C., Computational investigation of flow oscillation over reentry capsules, *Computational Fluid Dynamics JOURNAL*, Vol. 15, No. 2, July 2006, pp. 247-260.

Chapter 12

AERODYNAMIC RESEARCH AND DEVELOPMENT OF VERTICAL-AXIS WIND TURBINES WITH ROTARY BLADES*

Victor V. Cheboxarov¹ and Valery V. Cheboxarov²

¹Institute of Automation and Control Processes, FEB RAS, Russia

²Far Eastern State Technical University, Russia

ABSTRACT

Nowadays, offshore wind power engineering quickly grows and becomes the leading branch of renewable energy. However, offshore turbines differ from the onshore turbines essentially only in towers and foundations. So the well-known drawbacks and limitations of propellers still remain offshore. We note the limited unit power capacity, infrasound emission, and harmful effects on birds and animals. The following tasks were set: to increase substantially unit capacity of wind power plants, to work safely under extra wind loads, to enhance wind speed range, to reduce wind energy cost, to eliminate infra sound emission and fatal injury of birds due to turbine rotation. They can be reached with the recently suggested concept of wind turbines called Wind Energy Marine Unit (WEMU). All WEMU turbines feature large-scale (more than 100m in diameter) circular floating rotors. A circular pontoon bears vertical columns with a circular deck and rotary blades. In this way, water supports the rotor during slow rotation about vertical axis. Here we present approaches, methods, and important results of aerodynamic research of the WEMU turbines. Well-verified CFD-methods with full-scale domains are chosen for research. Flow through the turbine is described by RANS equations with chosen turbulent models. Numerical aerodynamic experiments are carried out using the finite volume method with several geometrical models of the rotor. Discretization, grid, and calculation conditions are described. As a rule, the computation domain is presented by a non-conformal grid of hexahedral elements and is divided into rotary and stationary zones. The vertical wind profile on the velocity-inlet boundary at height above 10 m is described according to the Monin-Obukhov theory with parameters which are typical to sea surface. At first, several symmetric airfoils are analyzed. Slightly convex airfoil with two flaps is found out as optimal for rotary blades. Maximum of power capacity is achieved for

* This study is financially supported by the Russian Foundation of Basic Research (grant No. 06-01-89505)

nondimensional blade speed as $0.7 \sim 0.8$. Aerodynamic efficiency of the WEMU turbine about 50% is guaranteed by an optimal control of rotation of vertical blades. Vertical circulation in cross-flow turbines is described. Stiffened design of the turbine with two face rings is proposed and investigated. It is shown that a slope of the plane of the floating turbine's rotation cannot change the air flow significantly. Additionally, new design of cross-flow turbine with partially free rotating blades is investigated. Turbine's parameters are found out which provide positive torque for most blade positions.

INTRODUCTION

Wind power engineering has biggest installed capacities among all renewables. Current crisis in fuel prices, growing energy demands, lack of cheaply extractable reserves of oil, and the problem of global warming all give a good chance for wind energy to grow much quickly. But well-known limitations of modern wind power plants exist and already prevented some wind energy projects from realization. Offshore wind power plants seem to be the most promising and quickly growing branch of wind power engineering. They have obvious advantages over installed inland. First of all, they have softer ecological demands, higher blade speed, and therefore, increased efficiency. Thus an offshore wind energy cost could be rather reduced. However, offshore turbines differ from the onshore turbines essentially only in towers and foundations. So the well-known drawbacks and limitations of propellers still remain offshore. We note the limited unit power capacity, infrasound emission, and harmful effects on birds and animals.

Until now, wind energy cost is higher than that from conventional power plants. It came down for years but now seems stopped. Unit power capacity of wind power plants is still much lower than that in conventional ones. And some research have showed [14, 15] that the 10MW limit is hardly reasonable to achieve with one propeller.

Our aims are to increase substantially unit capacity of wind power plants, to work safely under extra wind loads, to enhance wind speed range, to reduce wind energy cost, to eliminate infra sound emission and fatal injury of birds due to turbine rotation. They can be reached with the recently suggested concept of wind turbines called Wind Energy Marine Unit (WEMU) [4, 5]. The WEMU turbine features a large-scale (more than 100m in diameter) circular floating rotor (see Figures 1, 2). The rotor consists of a semi-submerged toroidal pontoon which bears vertical columns with a circular deck and rotary blades. In this way, water supports the rotor during slow rotation about vertical axis. For maximum turbine torque, the angular position of each blade is adjusted according to the local wind direction. Top and lower rings support vertical blade axles. The rings are also linked by raking props. A set of cables connects the rings with tower and transfers turbine's torque.

Here we present approaches, methods, and important results of aerodynamic research of the WEMU turbines. Results of recent hydrodynamic research of rotary pontoon of the WEMU turbines can be found in paper [13].

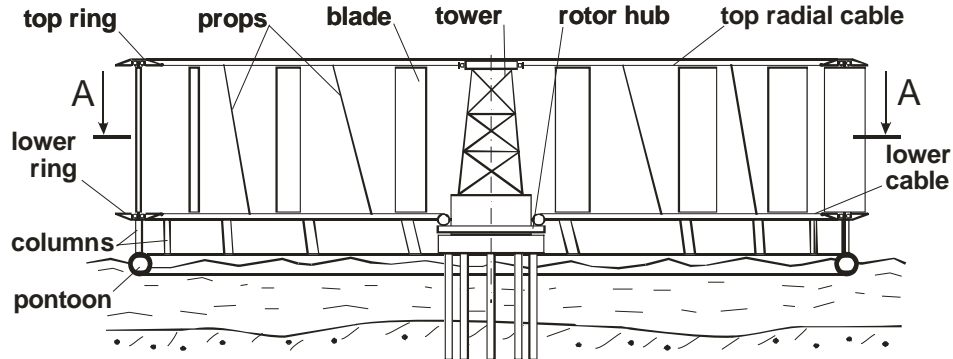


Figure 1. Layout of the WEMU turbine.

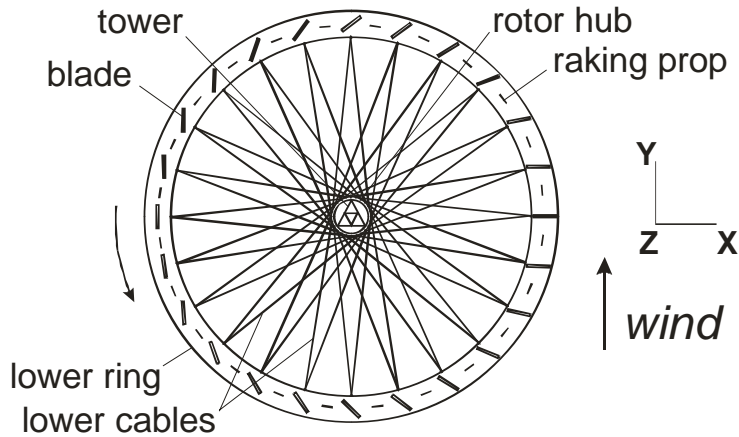


Figure 2. A-A section in Figure 1.

WEMU BLADE AIRFOILS

At first, let us investigate what airfoils are appropriate for WEMU blades. One of the main features of the WEMU concept is a relatively low linear speed of blades v , less than a uniform wind velocity far from the turbine u_∞ . In this case infra sounds are not emitted by blades and hydrodynamic resistance of rotary pontoon becomes smaller even for large rotors [13]. Unfortunately, then an angle of attack α_i of a blade i ($i = 1 \dots n$) varies widely with its azimuth angle θ_i if the blades are fixed to the rotor. However, positive torque from most blades i can be guaranteed through an optimal control of the blade pitch angles β_i when angles of attack α_i are kept optimal for all blade local positions.

One can trace in Figure 2 that during one turn of the WEMU rotor, all blades should be half-turned around their vertical axes as opposed to the rotor. For this time each leading edge of the blade becomes trailing, while each trailing edge becomes leading. Hence, to prevent worsening of the blade aerodynamic quality during rotation, the blade cross section must have central symmetry. It is clear that the simplest decision is to develop a plain airfoil without a

camber. But its aerodynamic quality is low, so it can not be adopted for multi-megawatt wind turbines. Convex-concave airfoils have much higher lift coefficient and, hence, better aerodynamic quality than the plain one.

Some designs of blades with variable camber are suggested for the WEMU. They are similar to design of an aircraft wing with a flap. First version of blade should consist of two hinged semi-blades (Figure 3a). By virtue of the requirement of symmetry, the hinge should coincide with axis of blade rotation at the rotor. As the blade turns, the sign of the angle between semi-blades is changing. Hence, the concavity arises on the other side of the blade. It must be noted that an additional motor for the semi-blade turning is not necessary. The semi-blades could be driven from the motor of the blade rotation through a power train.

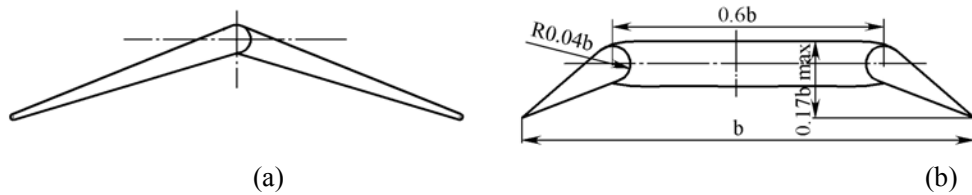


Figure 3. Possible cross sections of a WEMU blade

Unfortunately, this airfoil has very short convex zone which is located near the centre only. Any expanding of the convex zone by an increase in diameter of the blade axle leads to undesirable shrinking of the stagnation zone on the concave airfoil side. Hence, if $\alpha_i > 20^\circ$, the flow stalls just behind the axis and the lift force drops dramatically.

Let us expand the convex zone by dividing airfoil into three parts (Figure 3b). The central part must have two wide surfaces with slight convexity. Two other parts are connected with central one by hinges similarly to aircraft wing flaps. When the leading-edge and the trailing-edge flaps are turned, wide stagnation zone arises between them on one blade side, and quite big zone of low pressure occurs on the other side. Hence, circulation about the airfoil grows considerably. This airfoil with dimensions shown in Figure 3b is chosen for blades in further aerodynamic analysis of the full WEMU turbine. It is easy to show that this design also allows the flaps to be driven from the motor of the blade rotation. The flaps must be aligned with the central part moving upwind [7].

NUMERICAL METHOD

Governing Equations

Large dimensions of the WEMU turbines prevent our research from the full-scale experimental tests in a wind tunnel. Any experiments with prototypes reduced of many times will suffer serious similarity problems especially in Reynolds number. Hence, CFD-methods well verified by numerous experiments were adopted for this study with full-scale computation domains.

The three-dimensional analysis of the incompressible fluid flow through the WEMU rotor in steady state of its rotation is performed. The Reynolds-averaged continuity and momentum equations in Cartesian tensor form are given as follows:

$$\rho \frac{\partial u_i}{\partial x_i} = 0 \quad (1)$$

$$\rho u_j \frac{\partial u_i}{\partial x_j} = -\frac{\partial p}{\partial x_i} + \mu \frac{\partial^2 u_i}{\partial x_j \partial x_j} + \frac{\partial}{\partial x_j} (-\rho \bar{u}_i' \bar{u}_j') \quad (2)$$

where (x_1, x_2, x_3) is a position in stationary coordinate system; (u_1, u_2, u_3) is a mean absolute velocity; (u'_1, u'_2, u'_3) is a fluctuating component of velocity; p is a pressure; ρ is air density; μ is air viscosity.

The Reynolds stress can be expressed as:

$$-\rho \bar{u}_i' \bar{u}_j' = -\rho \frac{2}{3} k \delta_{ij} + \mu_t \left(\frac{\partial u_i}{\partial x_j} + \frac{\partial u_j}{\partial x_i} \right) \quad (3)$$

where k is a turbulence kinetic energy; μ_t is turbulent viscosity; δ_{ij} is Kronecker delta.

In the relative reference frame fixed to the rotor, Eqs. (1) and (2) are then transformed to the following:

$$\rho \frac{\partial U_i}{\partial X_i} = 0 \quad (4)$$

$$\rho U_j \frac{\partial U_i}{\partial X_j} = -\frac{\partial p}{\partial X_i} + \mu \frac{\partial^2 U_i}{\partial X_j \partial X_j} + \frac{\partial}{\partial X_j} (-\rho \bar{U}_i' \bar{U}_j') + \rho (A_{ij} X_j + B_{ij} U_j) \quad (5)$$

where (X_1, X_2, X_3) is a position in coordinate system fixed to rotor; (U_1, U_2, U_3) is a mean relative velocity; (U'_1, U'_2, U'_3) is a fluctuating component of relative velocity.

The Reynolds stress in the relative reference frame fixed to the rotor can be expressed as:

$$-\rho \bar{U}_i' \bar{U}_j' = -\rho \frac{2}{3} k \delta_{ij} + \mu_t \left(\frac{\partial U_i}{\partial X_j} + \frac{\partial U_j}{\partial X_i} \right) \quad (6)$$

Here the transformation from absolute coordinates and velocities to their relative values is expressed by Eqs. 7~8.

$$X_i = C_{ij} x_i \quad (7)$$

$$U_i = C_{ij} u_i + D_{ij} X_2 \quad (8)$$

In Eqs. 5, 7~8, the matrices of conversion are $[A_{ij}] = \begin{pmatrix} \omega^2 & 0 & 0 \\ 0 & \omega^2 & 0 \\ 0 & 0 & 0 \end{pmatrix}$,

$$[B_{ij}] = \begin{pmatrix} 0 & -2\omega & 0 \\ 2\omega & 0 & 0 \\ 0 & 0 & 0 \end{pmatrix}, [C_{ij}] = \begin{pmatrix} \cos\theta & -\sin\theta & 0 \\ \sin\theta & \cos\theta & 0 \\ 0 & 0 & 1 \end{pmatrix}, [D_{ij}] = 0.5[B_{ij}]$$

where ω is a rotor angular velocity; θ is azimuth angle ($\theta=0$ corresponds to a downwind (+Y-axis) moving blade).

Standard k - ε turbulence model is used in this research. So in addition to Eqs.1~8, the equations for the transport of turbulence kinetic energy k and its dissipation rate ε are

$$\rho u_i \frac{\partial k}{\partial x_i} = \mu_t \left(\frac{\partial u_j}{\partial x_i} + \frac{\partial u_i}{\partial x_j} \right) \frac{\partial u_j}{\partial x_i} + \frac{\partial}{\partial x_i} \left\{ (\mu_t / \sigma_k) \frac{\partial k}{\partial x_i} \right\} - \rho \varepsilon \quad (9)$$

$$\rho u_i \frac{\partial \varepsilon}{\partial x_i} = C_{1\varepsilon} \frac{\varepsilon}{k} \mu_t \left(\frac{\partial u_j}{\partial x_i} + \frac{\partial u_i}{\partial x_j} \right) \frac{\partial u_j}{\partial x_i} + \frac{\partial}{\partial x_i} \left\{ (\mu_t / \sigma_\varepsilon) \frac{\partial \varepsilon}{\partial x_i} \right\} - C_{2\varepsilon} \rho \frac{\varepsilon^2}{k} \quad (10)$$

Turbulent viscosity

$$\mu_t = \rho C_\mu \frac{k^2}{\varepsilon} \quad (11)$$

The constants ($C_{1\varepsilon}$, $C_{2\varepsilon}$, σ_k , σ_ε , C_μ) in Eqs. 9~11 are assigned to the standard values of the k - ε turbulence model: (1.44, 1.92, 1.0, 1.3, 0.09).

Discretization and Grid

Eqs. 1~11 are solved using finite volume method. Standard pressure interpolation scheme and SIMPLE scheme of pressure-velocity coupling are chosen. The second-order upwind discretization is used because it provides better calculation accuracy for generated grid. Commercially available software Fluent is used in this CFD-research.

Geometric models of the WEMU turbines are simplified for computation efficiency. Aerodynamic drags of the cables, the raking props, the pontoon with vertical columns, and the central tower are not taken into account. The computation domain is composed of two zones: the ring-shaped rotary zone, which wraps up the blades, and the stationary zone located between the first domain and the box with a dimension of 1000m×1100m×150m (see Figure 4)

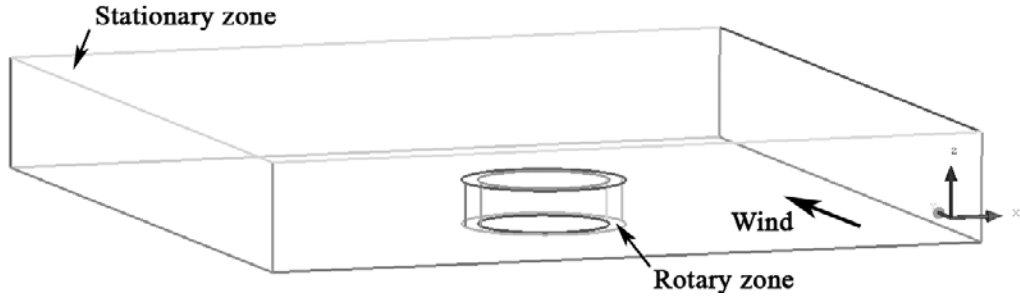


Figure 4. Computation domain.

Pitch angular positions of blades $\beta_i(\theta)$, turbine's solidity σ , and an optimal range of the non-dimensional blade speed $\lambda = \omega R / u_\infty$ are the main research topics at initial aerodynamic experiments (R is radius of rotor, u_∞ is uniform wind velocity far from the turbine). Here we neglect the top and lower rings and assume that the cantilever blades rotate quite high above the sea, so it is possible to neglect the interaction between water surface and air streams deflected down by the blades. Therefore, as a first approximation the flow through the rotor can be considered mirror symmetrical as related to the middle horizontal plane, which divides all blades in half. Symmetry boundary condition is assigned to this plane. Only space above the plane is used. Tetrahedral grids are generated at this initial research stage (see Figure 5). Following parameters of the blade set are used: the radius of rotor $R = 100$ m, the chord length of blade $b = 8$ m, the height of blade $H_b = 40$ m, the number of blades $n = 30\dots60$.

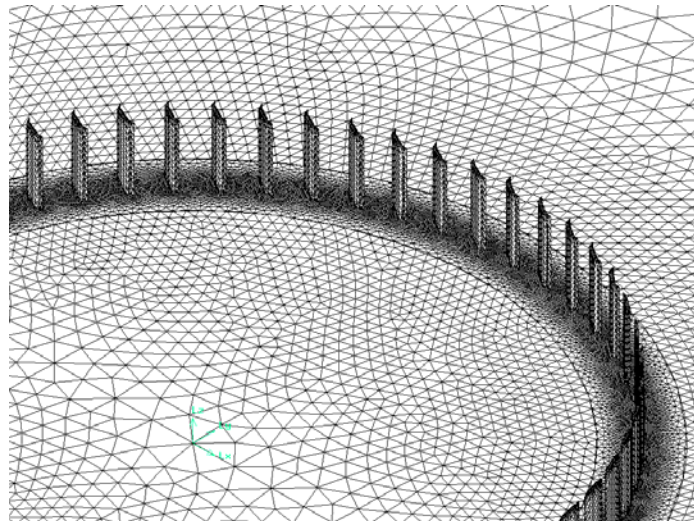


Figure 5. Face meshes on blades and on the middle horizontal plane (initial aerodynamic experiments).

At the second research stage we pay more attention to the accuracy of calculation results. For this purpose an influence of both rings, near sea surface flow, and vertical stratification of wind velocity all should be taken into account. So in this case full height blades and rings are included in the geometric models. The symmetry boundary is excluded. The height of rotor hub and lower ring $h_0 = 10$ m.

Moreover, viscous-affected flows in near-wall layers should be correctly treated. Therefore, hexahedral grid is generated at the second research stage. The distance from the first cell center to blade surface is only 5 mm height, so that the required near-wall treatment by the standard wall function is guaranteed. Because the number of blades n is big, the grid becomes extremely huge for time-limited calculations. Non-conformal grid highly clustered near the blades (see Figure 6) is adopted to solve this problem. Then, the grid reduces to about 4 million hexahedral cells which is acceptable for calculations using an 8-processors cluster.

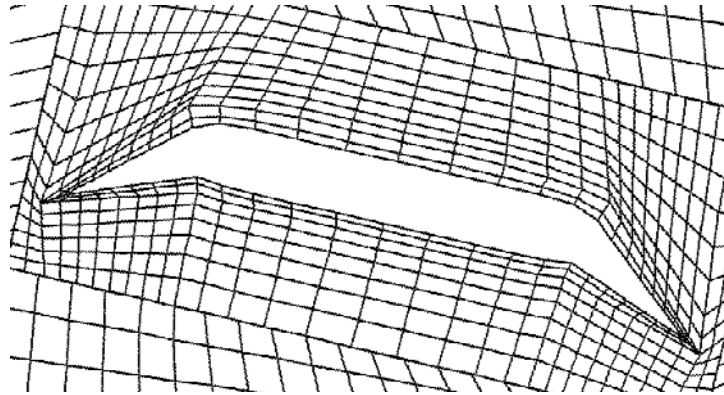


Figure 6. Coarsened view of near-blade hexahedral grid (second research stage)

Wind Conditions

At initial research stage following parameters are assigned at velocity-inlet boundary: $u_2 = u_\infty = \text{const}$, $u_1 = u_3 = 0$. Numerical experiments are carried out with several u_∞ values up from 7 m/s. Initial turbulence is included to reflect real wind conditions better. Turbulence intensity $I = 5\%$, turbulent viscosity ratio $\mu_t/\mu = 2$.

At the second research stage extreme wind conditions are considered and specified as the velocity condition at the inlet boundary (uniform velocity profile): $u_2 = u_\infty = 25$ m/s and $u_1 = u_3 = 0$. Typical turbulent parameters for sea surface are chosen: turbulence intensity $I = 12\%$ and $\mu_t/\mu = 10$. Moreover, the vertical logarithmic wind velocity profile according to the Monin-Obukhov theory with parameters given in [1] is used in calculations. In that case, the velocity at the velocity-inlet boundary at the height above 10 m from the sea surface is described as follows:

$$u_2(x_3) = u_{10} + u_* \ln(x_3/10)/0.4 \quad (12)$$

where mean wind velocity at 10 m height $u_{10} = 25$ m/s and the friction velocity u_* is defined as

$$u_* = u_{10} \sqrt{0.001 \cdot (1.5 \cdot (1 + \exp(-(u_{10} - 12.5)/1.56))^{-1} + 1.04)} \quad (13)$$

BLADE ANGLES CONTROL

Angular positions of blade $\beta_i(\theta)$ ($i = 1 \dots n$) which provide maximum efficiency of the WEMU turbine are variable and depend on several factors. Strictly speaking, they cannot be described by analytic expressions. However, let us use the method proposed in [5] to calculate $\beta_i(\theta)$ preliminarily assuming stability of the absolute wind velocity:

$$\beta_i = \alpha_i - \theta + \arcsin \frac{\lambda \cdot \sin \theta}{\sqrt{\lambda^2 + 2\lambda \cdot \cos \theta + 1}} \quad (14)$$

Here angle of attack α_i is derived from

$$C_L(\alpha_i) \cdot \sin \theta - C_D(\alpha_i) \cdot (\cos \theta + \lambda) = \max \quad (15)$$

where C_L and C_D are lift and drag coefficients of the airfoil, respectively.

Results of calculations of Eq. 14 for several λ were presented in [6, 7]. They were used to develop geometric models of the WEMU blade system for the first computation domains. Then, initial numerical experiments were carried out. Derived velocity vector maps show that the flow is deflected and partly by-passes the rotor. The flow also comes into stagnation zone and is deflected significantly within the rotor. So the angular positions β_i should be corrected for several i . Improved version of Eq. (14) is proposed in [6] taking into account the variability of absolute velocity in vicinity of blade i . Then, let us calculate new values of $\beta_i(\theta)$, set the blades in these angular positions, generate mesh again, and repeat CFD experiment. The results show some increase of blade torque $M_i(\theta)$ for most blades with re-calculated angles $\beta_i(\theta)$. However, many turbine blades still work badly. For instance, upwind moving blades ($\theta = 180^\circ \dots 240^\circ$) give essential negative torque. So it seems more suitable to use manual method of correction of blade angles as described below.

Turbulence must grow sharply in the wakes of all blades which have wrong angle of attack. Therefore such blades can be easily found on the diagram of the turbulence kinetic energy k (see Figure 7). A real angle of attack α_i of blade i can be derived from the relative velocity map (Figure 8). It is clearly seen in Figures 7~8 that high turbulence occurs due to the wrong sign of the angle of attack.

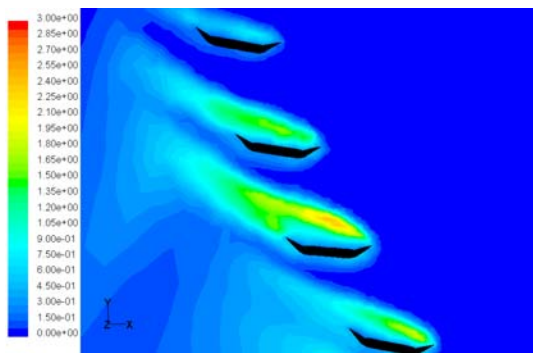


Figure 7. Growth of turbulent kinetic energy k in wakes of some blades.

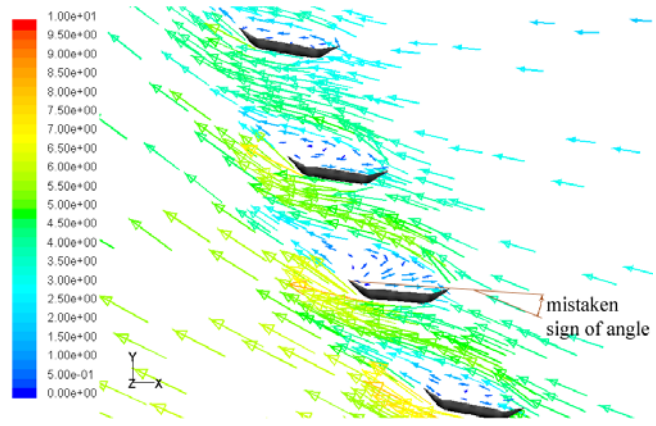


Figure 8. An example of relative velocity vectors.

Let us measure the angles as shown in Figure 8, calculate and execute the necessary additional turn of the blades. As a result of two iterations calculation-correction, we get near-optimal blade positions $\beta_i(\theta, \lambda)$ which guarantee smooth flow on all blades. Figure 9 presents the final positions of blades along the turbine's perimeter for $\lambda = 0.7$ derived at the second research stage.

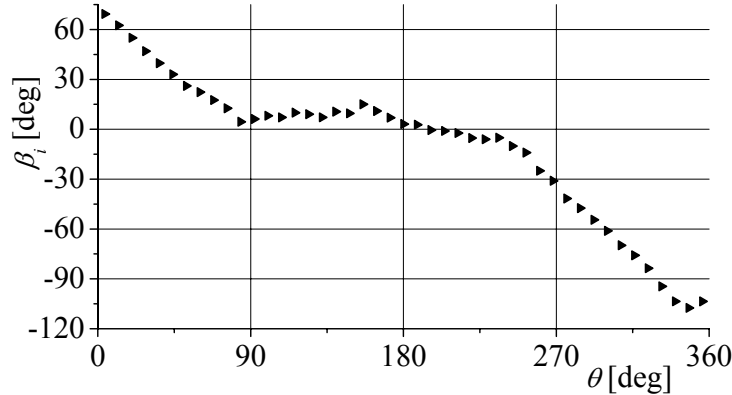


Figure 9. Angle of blade rotation β_i versus azimuth angle θ finally for $\lambda = 0.7$.

WEMU TURBINE'S EFFICIENCY

The curve shown in Figure 9 is quite smooth so the pitch control assuming $\lambda = \text{const}$ does not require powerful drives [9]. In fact, wind velocity is variable. Because of a huge WEMU turbine's moment of inertia, non-dimensional blade speed λ will also change inversely the wind velocity. It should be noted that during a short-term gust/calm a wideband control $\beta_i(\theta, \lambda)$ is possible but hardly appropriate. A number of CFD calculations were carried out to verify this point with $\lambda = \text{var}$ but keeping the blade angular positions found for $\lambda = 0.8$. Figure 10 presents curves of the turbine's power coefficient $C_P(\lambda)$ calculated at the initial research stage

(tetrahedral grids). One can see that the curves for $n = 45\dots60$ have practically flat tops. It means that the aerodynamic efficiency of the WEMU turbine remains high under the significant speed changes for $n = 45\dots60$. Maximum C_P equals 54% when $\lambda = 0.7$, $n = 45$. Then, more accurate calculations with hexahedral grids yield maximum $C_P = 49\%$. This value is already close to the theoretic Betz limit ($C_{P\max} \approx 0.59$) despite of relatively low rotor velocity.

The total aerodynamic power of WEMU turbine with described parameters reaches 37.7 MW for the uniform velocity profile and 51.4 MW for the log velocity profile.

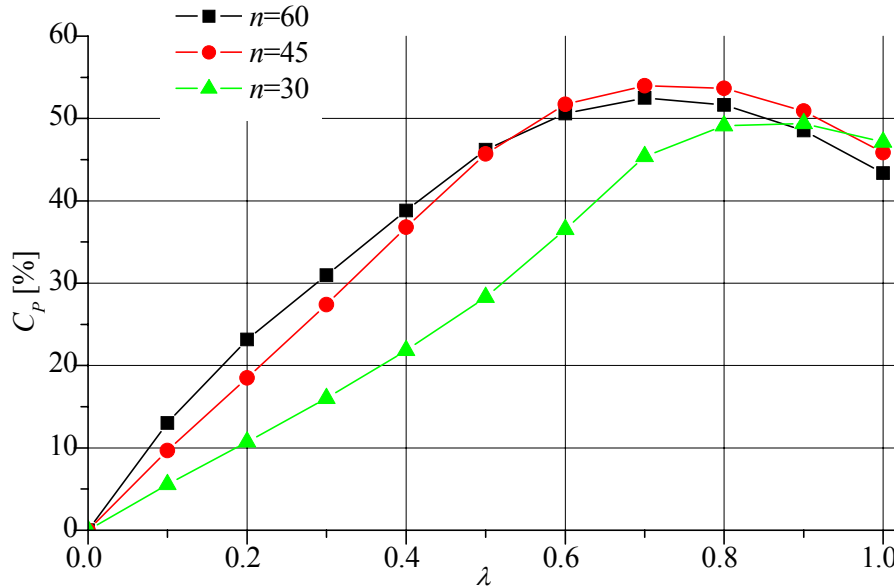


Figure 10. Power coefficient of the turbine.

Figure 10 also helps us to analyze effects of the WEMU turbine's solidity. In general, WEMU turbines require bigger conventional turbine's solidity σ (calculated assuming $\beta_i = 0$ for all i) than common wind turbines due to lower rotational velocity. A decrease of the number of blades n (or decrease of σ) reduces turbine's efficiency at the zone of low λ , and we must use higher rotor velocity to reach the maximum value of power coefficient C_P . However in whole, the turbine with $n = 45\dots60$ has significantly higher efficiency than the turbines with lower solidity. The turbine with $n = 45$ ($\sigma = 58\%$) seems the optimal combination of highest power efficiency and reduced cost.

3D deformations of the floating wind turbine can be investigated by research method proposed in paper [9]. Taking into account aerodynamic forces calculated at the initial research stage [8], proposed method yields drastically big deflections of blades if their axles are cantilevers. Therefore, the stiffened design of the WEMU turbine has been proposed in paper [11]. It has the two rings with bearings as shown in Figure 1. The rings significantly change the airflow near the ends of all blades. The other influencing factor is a slope of the floating turbine due to the aerodynamic forces. As a result of coupled calculations "aerodynamics – structural stability" for revised aerodynamic computation domains with hexahedral grids and simplified models of stress in the floating rotor, it occurs [9, 12] that top

ring in connection with the central tower provides sufficient structural stability of the floating wind turbine even under extreme wind conditions. The blade deflections become quite small. The turbine's slope is less than 0.5 deg which has negligible influence on the airflow.

VERTICAL CIRCULATION IN WEMU TURBINE

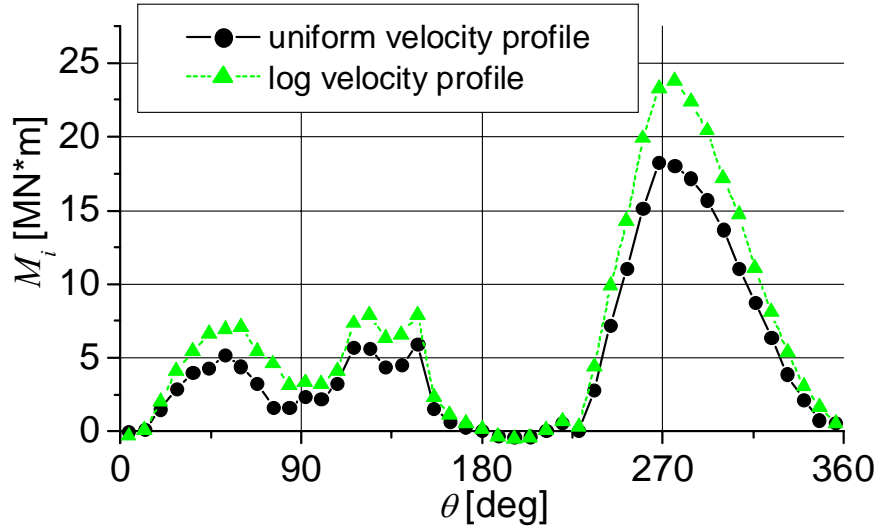


Figure 11. Blade torque M_i versus azimuth angle θ .

Distributions of blade torque $M_i(\theta)$ for the uniform and logarithmic velocity profiles are shown in Figure 11. It is seen that blades on the weather side of turbine ($\theta > 180^\circ$) provide large torque, so these blades utilize most of the incoming wind energy. But blades on the lee side of turbine ($\theta < 180^\circ$) also operate quite effectively despite their sheltering by blades of the weather side of turbine. Obviously, torque values M_i for lee blades depend on the turbine's solidity σ . Indeed, as the number of blades n decreases keeping $b = \text{const}$, the distributions of M_i over blades on the weather and lee sides of the WEMU turbine exhibit gradual leveling. However, it occurs that even at a quite large number of blades n (very high density of the weather side), the lee blades still produce a significant torque. It means that this cross-flow wind turbine features an essential circulation in the axial (vertical) direction, which contributes to the turbine efficiency.

Let us consider the phenomenon of vertical circulation in detail. At first, the pattern of pathlines shows (see Figure 12) that the flow passing blades on the weather side strongly deviates toward the upwind moving blades and a considerable fraction of decelerated streams (shown in light-green and cyan) leaves the turbine before reaching lee blades. Undoubtedly, faster streams must enter the inner space instead the leaving fraction of streams.

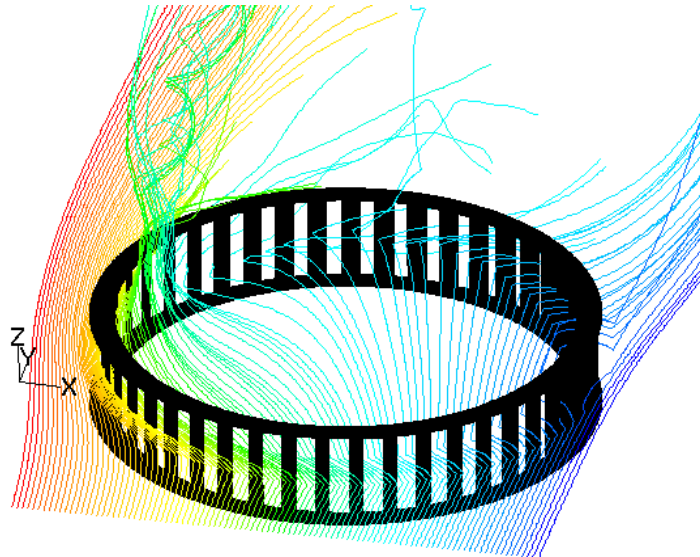


Figure 12. Pathlines of airflow approaching the WEMU turbine in horizontal intermediate plane.

Figure 13 shows the contours of vertical velocity as projected onto a horizontal plane at the top ring level ($x_3 = H_b + h_0 = 50$ m). In this pattern, yellow/green region 1 (corresponding to positive velocities) indicates the site where slow streams leave the inner space of the turbine and dark blue region 2 (negative velocities) shows the site where fast streams enter the inner space. These streams are significantly extended in the flow direction.

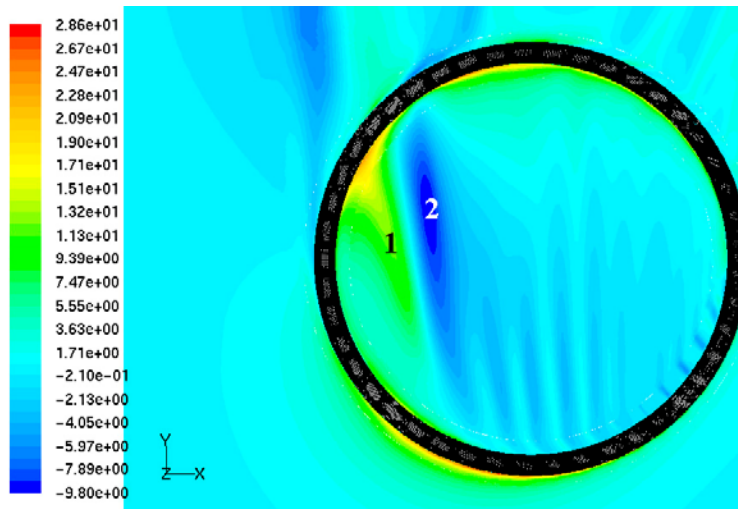


Figure 13. Contours of vertical velocity at the top ring level.

Figure 14 shows the distribution of absolute velocity vectors near upwind moving blades (on the right), as viewed in the transverse plane passing through the regions of maximum vertical circulation ($x_2 = 20$ m). The color palette indicates the vertical velocity component magnitudes. The pattern clearly reveals two vortices formed above and below the wind turbine. The lower vortex is compressed across due to the presence of adjacent water surface

from below, while the upper vortex has the shape of an almost regular cylinder. The intensity in the upper vortex is rather higher, which is due to the logarithmic stratification of velocities. The vertical component of the vortex velocity reaches about half of the unperturbed wind flow velocity (u_∞). The indicated vortices constitute a channel through which additional energy is supplied to the wind turbine from the adjacent (upper and lower) air layers, thus increasing the power coefficient C_P by several percents.

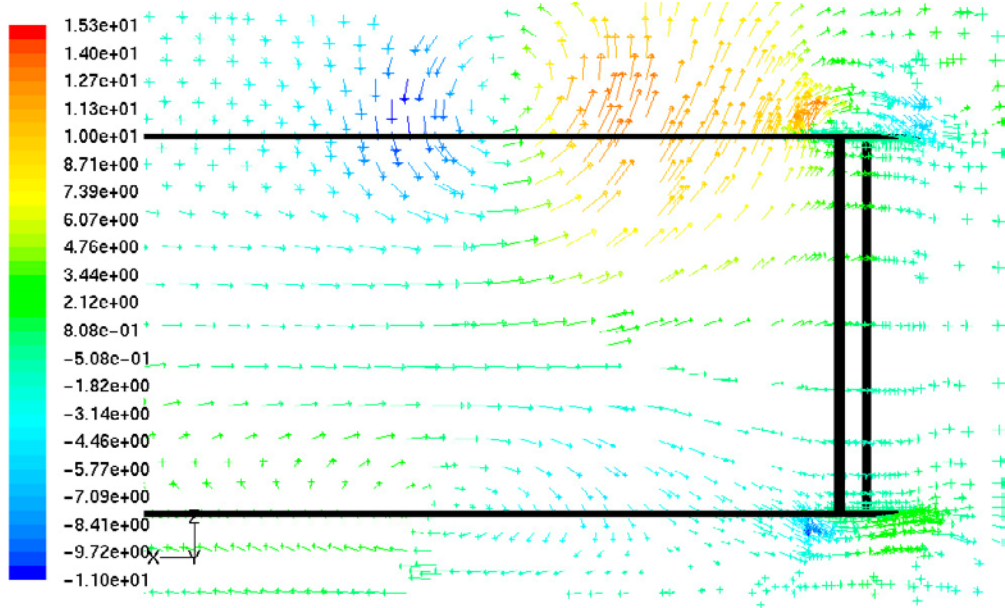


Figure 14. Absolute velocity vectors in rotor's cross-section $x_2 = 20$ m near upwind moving blades.

The vortices are originated in deviation of the airflow streaming down trailing-edge flaps of the weather blades toward these blades. As a result, an increased pressure zone appears beside the upwind moving blades, which are relatively tight here due to the zero angle of attack. Then the streams partly leave this zone upwards and downwards twisting the flow.

The observed phenomenon of vertical circulation must have important practical implications in turbine design. This factor can be used to increase the power and efficiency of cross-flow turbines by means of increasing diameter rather than axial dimensions.

PARTIALLY FREE ROTATING BLADE TURBINE

The WEMU turbine as described has active individual control of all blade positions. It provides maximum power output but turbine's cost becomes a bit higher due to blade motors. So the above-described design can hardly be recommended for small wind turbines. However, the methods and approaches used in the WEMU research help us also to develop an enhanced low-speed turbine with passively rotating blades [10]. Preliminary results of aerodynamic research of new turbine are presented in this section.

Variable-pitch turbines have been proposed and used mostly in marine applications. The cycloidal blade system in turbines [e.g. 3] works as the reverse well-known Voith-Schneider

propeller where all rotary blades are connected to single specific mechanism. The Kobold concept of water turbines [2] was also inspired by the Voith-Schneider propellers. But it features a set of blades, partially free rotating (self-adjusting) between fixed stops. All these turbines have blades with invariable airfoils.

Our new wind turbine (Figure 15) can be considered as an enhanced version of the Kobold turbine. In this concept, the much more flexible airfoil with leading- and trailing-flaps (see Figure 3b) is used. There are two zones of free blade rotation in the turbine. The first one is where the blades move upwind (positions *h*, *a*, and *b* in Figure 15). Here, two flaps of each blade are smoothly rotated together with their respective central part through a simple mechanism. The blade in position *a* has both flaps strictly aligned along the wind direction. Then, at the weather turbine's side (positions *c*, *d*, and *e*) blades are set against the fixed stop. After that, at the second zone of rotation, the aerodynamic forces quickly shift a downwind moving blade to the second fixed stop because all blades are asymmetrical relatively to their axes of rotation. The leading flap becomes the trailing one and vice versa. Both flaps are also rotated at the same time. Therefore, the camber position is changed. All blades situated at the lee turbine's side (positions *f*, *g*, and *h*) have cambers which should provide a positive torque. It must improve turbine's efficiency even during slow rotation.

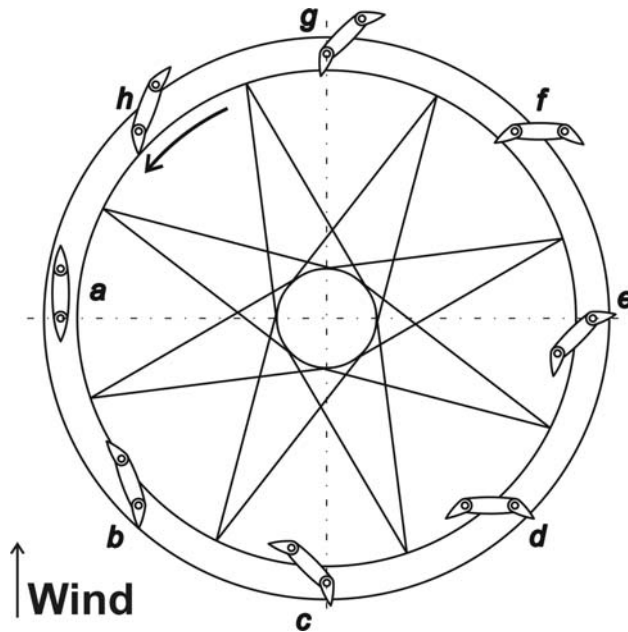


Figure 15. Blade positions during rotation of the turbine.

Let us analyze the pitch angle β_i distribution in the WEMU turbine (see Figure 9). Three separate segments can be recognized at the curve where the pitch angle is linearly changing or occurs relatively stable and small. If we approximate this curve by a jogged line, then it becomes similar to changing of the pitch angle in the turbine with free rotating blades and fixed stops. That is why the above described new design with passively rotating blades seems theoretically feasible for small-scale turbines.

Let us investigate airflow through this turbine with following dimensions: $R = 7.5$ m, $b = 1$ m, $H_b = 5$ m, $n = 16$. Moderate wind conditions are adjusted on the velocity inlet boundary: $u_2 = u_\infty = 7$ m/s. The turbine rotates slowly: $\lambda = 0.75$. Symmetry boundary condition is assigned to the middle horizontal plane, which divides all blades in half. Only space above this plane is meshed. Computation domain sizes are $40\text{m} \times 50\text{m} \times 10\text{m}$. It consists of about 1.4 million tetrahedral cells. Other calculation parameters are the same as above described for the initial aerodynamic experiments for the WEMU turbine (tetrahedral grids).

The first aim of calculations is to find out good positions of the stops by numeric aerodynamic experiments. Above described step-by-step approach is used when the computation domain is regenerated according to results of the previous calculation. However, here we apply different criteria to adjust blade angular positions β_i . For all free rotating blades located at the upwind zone, following equation is verified: $M_{ip} = 0$ where M_{ip} is torque of blade i about its pivotal axis. For all other blades we set $\beta_i = \gamma_1$ or $\beta_i = \gamma_2$ where γ_1 and γ_2 are angular positions of the stops. A blade position where this blade quickly shifts to the opposite stop is identified through changing of the M_{ip} sign. Preliminarily, γ_1 and γ_2 are chosen to provide best angles of attack α found in [6] for blades moving with maximum relative velocity.

After two iterations we get $\gamma_1 = -45^\circ$ and $\gamma_2 = 40^\circ$. Figure 16 presents derived map of static pressure contours on the middle horizontal plane. Distribution of the blade torque M_i along the turbine's perimeter is shown in Figure 17. It is clearly seen that, in comparison with the WEMU turbine (see Figure 11), we have some loss of blade torque M_i for several blades of the new turbine due to passive pitch control. However, for most blades M_i is positive and quite big. In comparison with the Kobold turbines [2], here blade angles β_i change in the wide range. It can be explained by relatively low non-dimensional blade speed λ .



Figure 16. Static pressure contours.

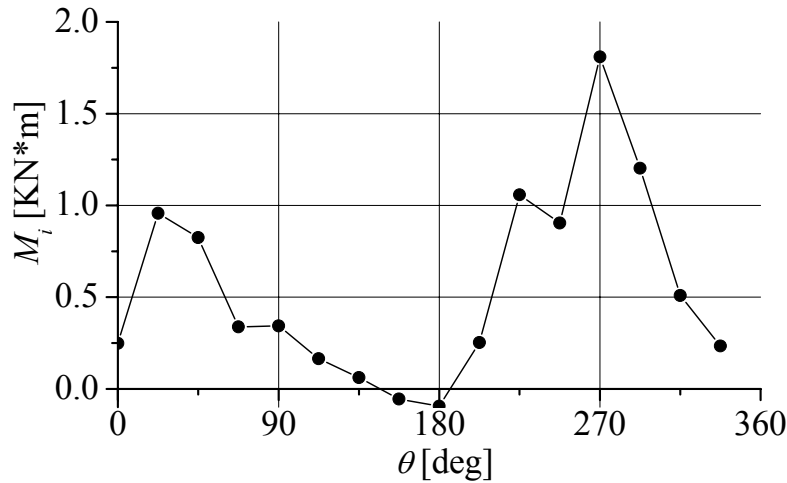


Figure 17. Blade torque M_i versus azimuth angle θ ,

Moreover, nonrigid fixed stops can be used to enhance the pitch control [10]. It will be investigated in our future research. The criterion $\sum_{i=1}^n M_i = \max$ will be applied to find out optimal angular positions of the stops γ_1 and γ_2 .

CONCLUSION

New types of vertical-axis variable-pitch wind turbines were proposed. The floating WEMU turbine with individual control of blade positions is intended for large-scale offshore wind power engineering. The second turbine has passive partially free rotating blades. Airflow through these turbines was investigated by CFD-methods.

Despite of low speed of rotation, the WEMU turbine has very good aerodynamic performance. Its power coefficient is as high as 49%. Rated power capacity can reach dozens of MW. We have some loss of blade torque M_i for several blades of the second turbine due to passive pitch control. However, for most blades M_i is positive and quite big.

The new effect of essential vertical circulation in WEMU turbines was found out and clarified.

REFERENCES

- [1] Amoroch, J.; Vrees, de J. *J. Geophys. Res.* 1980, 85(NC1), 435-442.
- [2] Calcagno, G., Salvatore, F., Greco, L., Moroso, A., Eriksson, H. (2006). In *Proc. 16th Int Offshore and Polar Eng Conf*; ISOPE, San-Francisco, CA, USA, 2006; Vol. 1, pp 323-330

- [3] Camporeale, S. M.; Magi, V. *Energy Convers. Manag.* 2000, 41(16), 1811-1827.
- [4] Cheboxarov, V.V., & Cheboxarov, V.V. (2002). In *Proc. World Wind Conf.*, Berlin, Germany, [CD-ROM].
- [5] Cheboxarov, V.V. et al. (2002). In *Proc. 12th Int Offshore and Polar Eng. Conf.*, ISOPE, KitaKyushu, Japan, 2002, Vol.1, pp 700-706.
- [6] Cheboxarov, V.V.; Cheboxarov, V.V.; Bekker, A.T. *Int. J. Offshore Polar Eng.* 2004, 14(3), 233 - 238.
- [7] Cheboxarov, V.V., Cheboxarov, V.V., & Bekker, A.T. (2004). In *Proc. 14th Int Offshore and Polar Eng Conf*, ISOPE, Toulon, France, 2004, Vol. 1, pp 150-157.
- [8] Cheboxarov, V.V., & Cheboxarov, V.V. (2004). In *Proc. 6th Pacific/Asia Offshore Mechanics Symp*, ISOPE, Vladivostok, Russia, 2004, pp 216 - 221.
- [9] Cheboxarov, V.V., & Cheboxarov, V.V. (2005). In *Proc. EXPO World Conference on Wind Energy, Renewable Energy, Fuel Cell & Exhibition*, Hamamatsu, Japan, [CD-ROM].
- [10] Cheboxarov, V.V., & Cheboxarov, V.V. (2005). Windmill [Russian patent No 2290533]. Bulletin of inventions No 36, 2006.
- [11] Cheboxarov, V.V., & Cheboxarov, V.V. (2006). In *Proc. Int. Conf. "Renewable Energy-2006"*, Makuhari Messe, Japan, 2006, pp 759 – 762.
- [12] Cheboxarov, V.V. et al. (2007). In *Proc. ISES Solar World Congress 2007*, Beijing, China, 2007 – Tsinghua Univ. and Springer, Vol. 5, pp. 2324-2328.
- [13] Cheboxarov, V.V. et al. (2008). In *Proc. 4th Asia-Pacific Workshop on Marine Hydodyn.*, APHydro2008: Taipei, Taiwan, 2008, pp 315-322.
- [14] Henderson, A.R. et al. (2004). In *Proc. 14th Int Offshore and Polar Eng Conf*, ISOPE, Toulon, France, 2004; Vol.1, pp 120-127.
- [15] Klinger, F. et al. (2002). In *Proc. World Wind Conf.*, Berlin, Germany, [CD-ROM].

Chapter 13

THE DETERMINATION OF AERODYNAMIC FORCES ON SAILS – CHALLENGES AND STATUS

William C. Lasher

School of Engineering, Penn State Erie, The Behrend College,
Erie, Pennsylvania, USA

ABSTRACT

It is important to be able to determine the forces on the sails of racing yachts and square-rigged historical vessels, as well as for potential commercial vessel applications. This problem is very complicated due to qualities of the sailing environment, viscous flow physics, and the need for accuracy. Three methods are currently being used to determine these forces – full-scale testing, wind tunnel testing, and computational fluid dynamics. Each of these methods has advantages and disadvantages relative to the sail aerodynamics problem, and these are discussed. Advances in our understanding of sail aerodynamics will require continued research using all three methods, and some suggestions for future research are presented.

INTRODUCTION

Sailing has been a major mode of transport for thousands of years and consists solely of subsonic flow. Given this history, one might think that there was little to learn about the aerodynamics of sails. There is, however, a significant amount of research currently being done on sailing vessel performance and sail aerodynamics. There are several reasons for this, including the complexity of the problem, a lack of quantitative data from the historical record, innovations in experimental and computational technology, and increasing competition at the grand prix level of sailing yacht racing.

There are several primary functional areas in which knowledge of sail aerodynamics can be applied, such as yacht racing, innovative rigs for non-racing sailing yachts, the safety of passenger/historical vessels, and sail-assisted commercial transport. Some of these applications are discussed below. While there are a myriad of technical issues that can be

investigated for sailing vessels, the focus of this article is on one aspect of sailing – the determination of the aerodynamic forces on sails.

The Need for Speed

Most of the recent research on sail aerodynamics has been related to the demands of yacht racers, where small changes in performance can have a huge effect on the outcome. Milgram et al. (1993) point out that a 0.3% variation in speed can be the difference between a winner and an “also ran”, and that speed differences of 0.1% can be meaningful, especially at the Grand Prix level such as the America’s Cup.

The prediction of aerodynamic forces is required for several aspects of yacht design and sailing. Optimization of sail design is one obvious aspect; however, there are other reasons that the forces must be known such as predicting the performance of yachts, learning how to optimize trim of a particular sail, identifying the best collection of sails for a particular yacht under specific environmental conditions, and heightened interest in breaking the mythical 50 knot barrier.

Yacht performance prediction is usually based upon a Velocity Prediction Program (VPP) (Kerwin, 1978), which balances the aerodynamic forces on the sails with the hydrodynamics forces on the hull to determine actual sailing speed. In addition to simply predicting the performance of a yacht, many sailors race under a handicapping system, where boats of different sizes and designs are given “ratings” that, in theory, predict the speed of the boat, and are used to correct actual finish times to determine the winner. The most sophisticated of these handicapping systems are based upon VPP results.

Another application of sail aerodynamics is exploring advantageous sailing tactics. A sailboat creates a wind shadow, which can influence the performance of another yacht in that shadow. For example, Cowles et al. (2003) used a Computational Fluid Dynamics (CFD) code to investigate the interactions between two America’s Cup yachts as an aid in making tactical decisions regarding boat position on the course.

Safety First

It is estimated that over 300 traditionally-rigged sailing vessels exist world-wide. These vessels, which are also known as tall ships or square-rigged ships, are typically reconstructions and are used today primarily for historical reasons. Examples include the Japanese sailing trader *Naniwa-maru* (Masuyama et. al, 2003) and the U.S. Brig *Niagara* (Figure 1).



Figure 1. – U.S. Brig *Niagara* is a reconstruction of the ship that was credited with winning the Battle of Lake Erie during the War of 1812.

While movies often paint a picture of square-rigged sailing as being romantic, it was in fact quite uncomfortable and dangerous (Apollonio, 2000). Modern square-rigged sailing vessel crews can simply not accept the kind of risk that was commonly tolerated during the peak of commercial sailing. As a result of this, researchers have begun to focus on a scientific analysis of what it takes to capsize a traditionally-rigged vessel (Miles, et al., 2007; Lasher et al., 2007). This requires a thorough knowledge of the aerodynamic forces on the sails.

Going Green

The advent of steam power first reduced, and then eliminated, the need for shippers to tolerate the risk and uncertainty of sail power, and this led to the virtual elimination of sail as a primary means of commercial transport by the mid-1900's. Concerns over climate change and the increasing costs of fossil fuels have resurrected an interest in the use of sail, at least as a supplemental power source. Fujiwara et al. (2005) assessed the operation of a hybrid sail-assisted bulk carrier and concluded that the economic benefits of the driving forces from the sails are greater than the overhead of equipping the ship with a system of hybrid-sails. Several groups have recently been testing concepts of sail-assisted ships, such as the Wing Systems tests on the model tanker *Massachusetts* (Figure 2).



Figure 2. Tests of a concept for sail-assisted shipping on a scale-model of the tanker *Massachusetts* (photo courtesy of Wing Systems).

In addition to calculating the cost/benefit ratio of sail-assisted power, the sail aerodynamic forces are needed to assess vessel stability and route optimization (i.e., it may be more economical to take a longer route if it results in more favorable winds). Depending on the type of sail deployed (some groups are looking at kite-type systems) ease of handling could also be an issue, and an analysis of this would require an understanding of the dynamic forces on the sails.

Overview of Article

The benefits of improving our knowledge of sail aerodynamics are clear. To help the non-sailor better understand the issues, the article will first explain the sailing environment and some of the terminology. This will be followed by a discussion of what makes sailing aerodynamics so complex. The three primary means of determining sail forces – full-scale testing, wind tunnel testing, and computational simulation – will be discussed, and the state-of-the-art as it relates to sail aerodynamics in each of these will be described. The article will finish with suggested directions for future research.

PRIMER ON SAILING

Points of Sail and Aerodynamic Forces

A sailboat can sail at various angles to the wind, from about 40° to 180° . The approximate angle between the boat and the wind is referred to as a *point of sail*, as shown in Figure 3. While a boat cannot sail directly into the wind, it can effectively sail towards the wind by *tacking*, or sailing a zig-zag course on an *upwind* point of sail. When a boat is sailing either upwind or on a *close reach*, the sails are pulled in tight to the boat and are relatively flat, so they act very much like traditional airfoils. In these conditions, the flow over the sails is mostly attached, and traditional inviscid aerodynamic and boundary layer theory can be used with reasonable confidence.

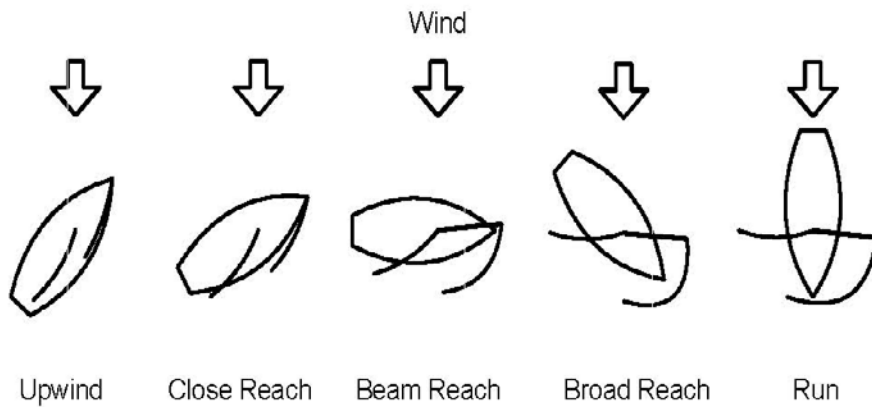


Figure 3. Points of sail (originally published in Lasher et al. 2005).

The aerodynamic objective on all points of sail is to maximize the driving force and minimize the side force (see Figure 4). These force components are referenced to *body axes*, which are aligned with the boat. Aerodynamic lift and drag, however, are referenced to *wind axes*, which are aligned with the wind. The angle between the wind axes and the body axes varies depending on the point of sail, and the lift and drag forces must be resolved into driving and side forces. When sailing upwind, on a close reach, or on a *beam reach*, this means it is desirable to maximize lift and minimize drag. However, when the wind is at an angle of greater than 90° (*broad reach* or *run*), drag becomes beneficial. Under these conditions racing sailors use a *spinnaker* (Figure 5) because it is more effective. At these higher sailing angles the flow over the sails is largely separated, and drag is of the same order as lift.

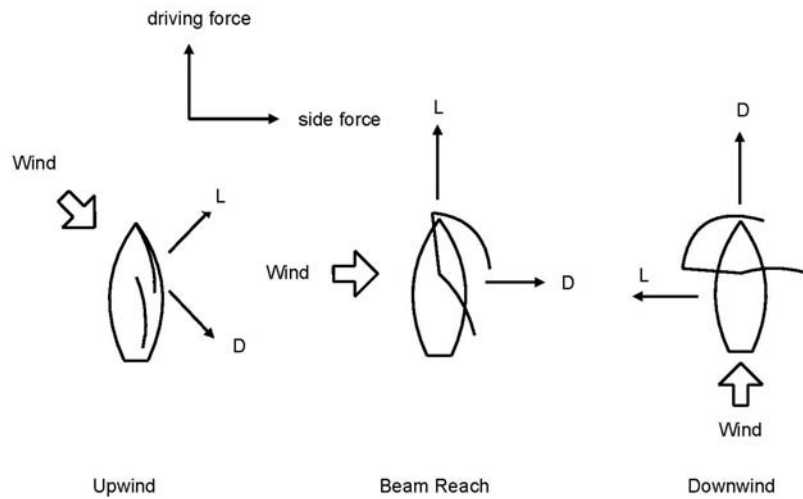


Figure 4. Driving force and side force are determined by lift and drag, which must be resolved from wind axes to body axes.



Figure 5. Alinghi leads Team New Zealand on a run in the final race of the 2003 America's Cup. The sail in the front is the spinnaker.

Apparent Wind and Twist

Since a sailboat is moving with respect to the water, the wind as seen on the boat is a vector combination of the actual (or *true*) wind and the wind generated by the motion of the boat. The wind as seen on a reference frame attached to the boat is known as the *apparent*

wind, and this is what is important for determining sail aerodynamics. Boats sail in an atmospheric boundary layer (Figure 6), where the true wind speed is zero at the water surface and increases with height at a rate that can vary dramatically from place to place and over time. Since the boat's speed is constant with distance from the water surface, this means that the apparent wind changes both speed and direction as the distance from the water surface increases (Figure 7). The change in wind direction is known as *twist*, and presents a complication for determining aerodynamic forces. When sailing upwind the amount of twist tends to be small (typically a few degrees), but when sailing downwind the amount of twist in the apparent wind can be significant (on the order of 15-20 degrees).

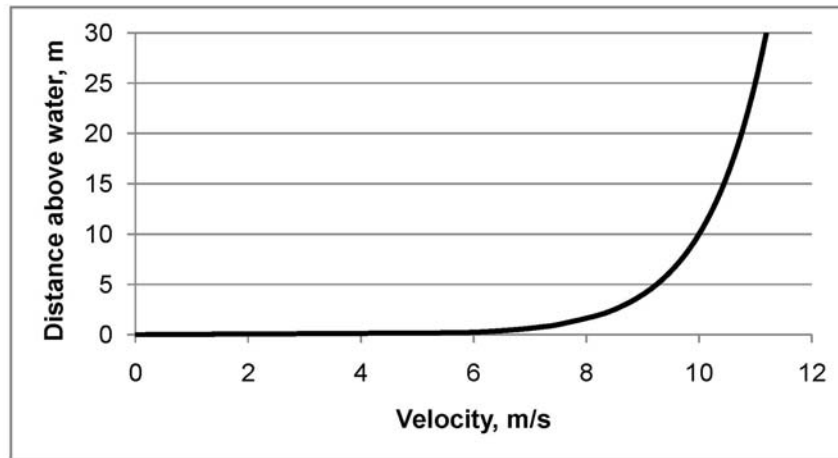


Figure 6. Typical atmospheric boundary layer velocity profile with a velocity of 10 m/s at a reference elevation of 10 m above the water surface.

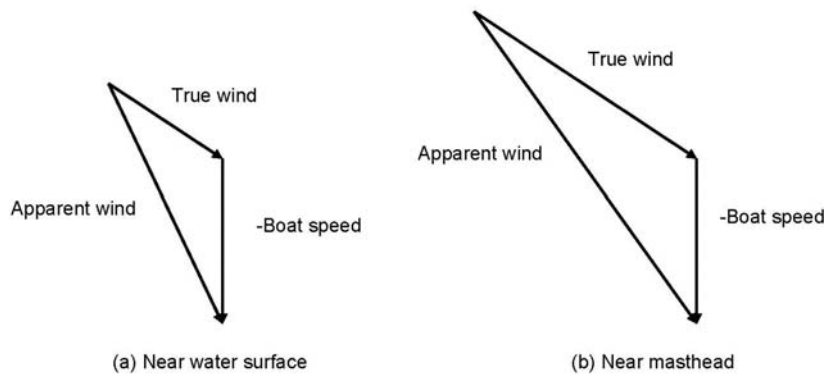


Figure 7. Apparent wind, which is a combination of true wind and wind due to motion of the boat, changes both speed and direction as distance increases from near water surface (a) to the masthead (b). The change in direction is known as *twist*.

Flying Sails

Unlike wings on an aircraft, sails are not rigid surfaces. Depending on the type of sail, they may be supported along one or two edges, or in some cases only at the corners. For example, in Figure 8 the spinnaker is supported at the head by the mast and at the tack by a pole. The sail is free to “fly”; that is, it can change shape depending on how the pole and tension in the “sheet” (a control line on one of the corners of the sail) are set. In fact, sailors have significant control over the shape of sails while on the water. By adjusting various controls, it is possible to change the camber (both amount and location) and the geometric twist of the sail, within limits. Additionally, the sail shape changes with wind speed, since sails act as membranes. Sail designers can provide an envelope of shapes that the sail can be trimmed to, and the sailors must work within that envelope to optimize performance.

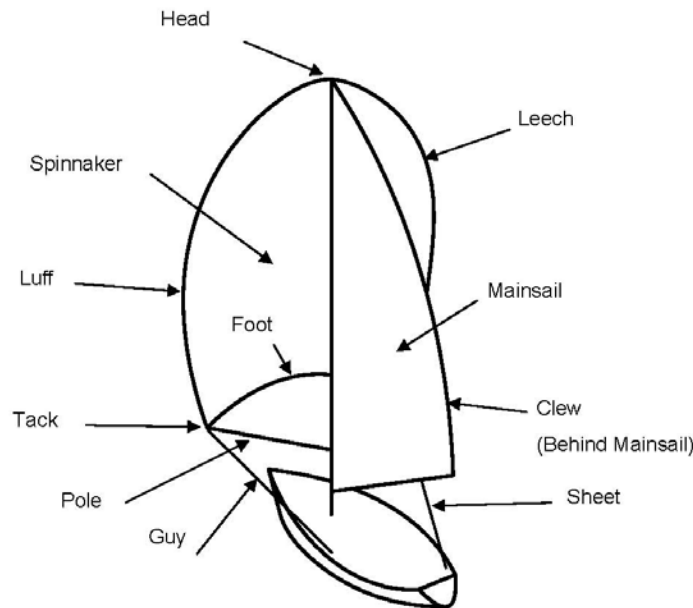


Figure 8. Spinnaker terminology and controls. The pole can be moved vertically (up or down), forward, or aft, giving the sailor significant control over camber, twist and projected area (originally published in Lasher et al. 2005).

Sails as Part of a System

The performance of a sailboat is determined by a complex interaction of the forces on the sails and on the hull and appendages. The lift and drag on the sails can be resolved into driving and side forces, and these are balanced by the hydrodynamic drag and lift (Figure 9) due to the hull and an underwater appendage (usually a *keel* or *centerboard*, which acts like an underwater wing). The side force also causes the boat to *heel* (or tip), and this heeling moment is counteracted by a *righting moment* due to a lateral shift in the center of buoyancy of the hull as well as an opposing shift in the center of gravity of any weighted appendages. There are additional moments due to the sails about the vertical and transverse axis, and these

are counteracted by other hydrodynamic forces on the hull and appendages which will not be described in this article. The final sailing condition of the boat is determined when all of the forces and moments are balanced.

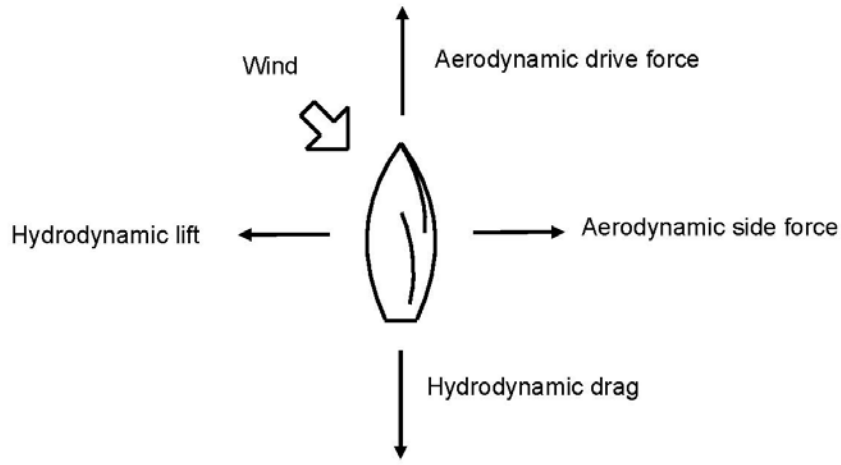


Figure 9. Aerodynamic lift and drag are resolved into drive and side forces. These are balanced by hydrodynamic lift and drag generated by the hull and an underwater appendage. In addition, moments about all three axes must be in balance.

A complete discussion of sailing is beyond the scope of this article; however, there are several excellent references that the interested reader may refer to, such as Marchaj (1979) and Whidden and Levitt (1990).

Complexities of Sail Aerodynamics

The sailing environment discussed above makes sail aerodynamics complex. The flow field alone presents numerous challenges – it is not constant in either speed or direction due to the atmospheric boundary layer and twist. It is (generally) highly turbulent, with typical turbulence intensities of 10-20% (compared to intensities on the order of 0.1% for a wind tunnel). The length scale of the turbulent eddies in the atmospheric boundary layer is also very large, which can produce significant transient effects beyond what is normally seen in a laboratory environment. This flowfield presents challenges not only for wind tunnel testing but for CFD as well, since turbulence model coefficients are generally tuned to flows with much smaller length scales, and thus much lower effective viscosities. In addition, the unsteady nature of the flow field is completely overlooked in most analyses.

The shapes of the sails and ranges of angle of attack also present challenges. When sailing upwind the sails are very thin foils operating at low to moderate angles of attack, whereas when sailing downwind the sails are more like parachutes and the flow is highly separated. This means that analysis techniques that are optimum for one point of sail may not be optimum for another. The aero-elastic nature of the sails can also be a problem, because the shape of the sail and the aerodynamic loading depend on each other. In some cases

simply determining the actual shape of a sail on a wind tunnel model or full-size yacht can be quite difficult. Computationally, it would be ideal to perform a fully-coupled solution of the sail shape and flow field.

The sail-sail and sail-hull interactions mean that simple models and theories for performance are difficult to develop. For example, *Niagara* typically might carry a dozen sails at one time, and any individual sail can be strongly influenced by as many as 4 or 5 of the other sails. The fact that a sailboat is a system also complicates the analysis. For example, when sailing upwind a high lift-drag ratio is generally preferred; however, this can generate an excessive heeling moment, so under some conditions it might be preferable to use a lower lift-drag ratio if it results in a lower heel angle.

In most cases a sailboat can be considered a quasi-equilibrium system, but not always. Wind is never truly steady, and sometimes the changes in wind speed and direction can be quite large. When sailing in waves a boat will pitch and roll, which induce significant unsteadiness on the sails. Sailboats must also maneuver, which will create rapid changes in wind direction. An analysis of unsteady aerodynamics, either through model testing or computational methods, adds another layer of complexity to an already complex problem.

APPROACHES TO DETERMING SAIL FORCES

Full-Scale Testing

The earliest attempts at determining sail force coefficients using full-scale experiments were based on the equilibrium concepts discussed earlier (Gerritsma et al., 1975). Hydrodynamic lift and drag coefficients for the hull can be determined from model testing in a towing tank. If the full-size yacht's speed, heel angle and rudder angle at a given sailing condition are measured, the hydrodynamic forces on the hull can be found. These forces are in turn balanced by the aerodynamic forces on the sails, so the sail forces can be determined. If the wind speed and direction are also measured, force coefficients can be computed as a function of apparent wind angle.

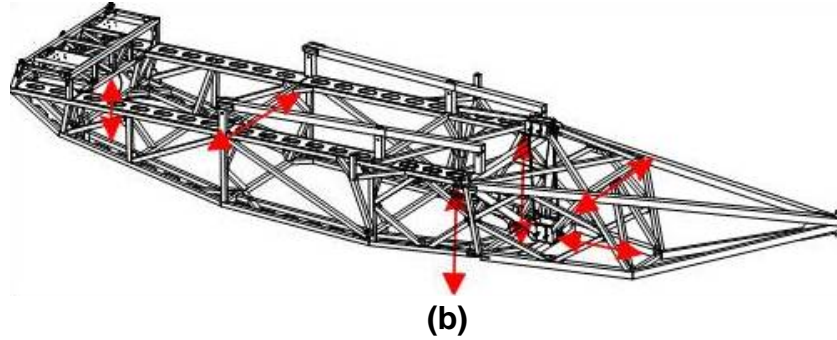
In addition to measurement uncertainty that will be discussed later, an obvious problem with this approach is the accuracy of the hull force coefficients. Since boats sail at the water-air interface, both the Reynolds number (viscous resistance) and Froude number (wave-making resistance) are important for similitude. Since Reynolds number scales with length and Froude number scales with the inverse of the square-root of the length, it is not possible to match both of these parameters in a scale model. As a result, models are tested at equivalent Froude number and the viscous contribution is estimated.

In recent years several researchers have built sailing dynamometers, which are specially constructed boats where the mast and rigging are attached to a rigid frame that is structurally separate from the hull. This allows for direct measurement of the sail forces without having to estimate the hull hydrodynamic forces. The earliest of these dynamometers was reported by Milgram et al. (1993). Additional dynamometers have since been reported by Masuyama and Fukasawa (1997) and by Hochkirch and Brandt (1999) (Figure 10). While a sailing dynamometer is a major improvement over the force-balance approach, there are still significant problems determining accurate force coefficients. Due to problems associated

with accurately measuring boat speed, wind speed near the boat (the sails influence the incoming free stream), sail shape, and the inherent fluctuations in both wind speed and direction, there is a tremendous amount of scatter in the data. For example, Milgram et al. show drag coefficient vs. lift coefficient for upwind sailing. At a lift coefficient of 1.0, the mean experimental drag coefficient is near 0.19, with a standard deviation of 0.025 and a range from 0.14 to 0.22. Masuyama and Fukasawa show even more scatter in the data. As an example of the sensitivity of the force coefficients to measured data, Milgram et al. state that one degree of error in the measured apparent wind angle produces a 10% error in the lift coefficient. Since the induced drag is proportional to the lift coefficient squared, the error in drag is even larger (roughly 20%).



(a)



(b)

Figure 10. (a) DYNA sailing. (b) The internal frame to which the mast and all rigging are attached (photo and drawing courtesy of Technical University of Berlin).

Milgram et al. addressed the sail shape problem by locating a high-resolution video camera on a trailing motorboat and having the motorboat maneuver around the dynamometer through a series of eight pre-set locations to provide sufficient views for determining perspective. The video was then analyzed to determine the shapes of the sails. This is time

consuming, but may be the most effective means of getting downwind sail shape based on current technology. By contrast, most America's Cup teams now use on-board camera systems, at least for upwind sail shape analysis.

While full-scale testing is expensive and the accuracy challenges are numerous, it is important that it be conducted. Continued refinements in technique and technology should reduce the variation in the data, and this is the only way to measure sail forces in the actual sailing environment.

Wind Tunnel Testing

While full-scale testing provides the most realistic environment, wind tunnel testing is much more controlled and the data scatter is accordingly smaller. There are other advantages, including cost, speed with which testing can be done (there is no waiting for good winds), the ability to perform flow visualization, and the ability to measure details of the flow field in areas of interest.

Two of the major problems with wind tunnel testing for sail aerodynamics are well known – similitude and blockage. When fabric sails are being tested it is desirable to match wind speed to cloth weight, which will produce Reynolds numbers much lower than what is seen on the water. Whether this is a significant limitation is not clear. Fallow (1996) states that wind tunnel data compared well with full-scale testing, in spite of the fact that no attempt was made to match Reynolds number. Hansen et al. (2002) compare wind tunnel data to full-scale experiments from a sailing dynamometer, and in some cases the agreement between the wind tunnel and full-scale results was excellent; however, in some instances the differences were as large as 50%. It is not known if these differences are attributable to Reynolds number or other factors.

Given the size of sailboats, a wind tunnel must be large to maintain a reasonable Reynolds number and minimize blockage. Model sail tests performed at the Wolfson Unit at the University of Southampton (US Sailing, 1995) indicated that blockage corrections for downwind sailing, where the flow is separated and there is a large recirculation region, were on the order of 40%. Ranzenbach and Mairs (1997) used an advanced blockage correction technique for flow normal to a flat plate and found that they could adequately correct for blockage ratios of up to 10%. The same authors (1999) then applied this technique to the testing of downwind sails at the Glenn L. Martin Wind Tunnel at the University of Maryland.

The problems induced by the presence of the atmospheric boundary layer have been addressed at the Yacht Research Unit of the University of Auckland. Flay (1996) describes the development of a twisted flow wind tunnel, where an untwisted atmospheric boundary layer is developed through the use of roughness elements, then the flow is twisted using adjustable vanes (Figure 11). While flow field equilibrium is not achieved, the boundary layer profile at the test section is a reasonable approximation of what is actually found on the water. Whether the benefits of modeling twist offset this lack of equilibrium is unclear.



Figure 11. Model of rigid fiberglass sails in twisted flow wind tunnel at the University of Auckland. The vanes in the background re-direct the flow so that it changes with elevation (photo courtesy of Peter Richards, Yacht Research Unit, University of Auckland).

The nominal objective when adjusting sails is to maximize the driving force. However, the previously described interaction between the sail aerodynamics and hull hydrodynamics means that there are cases where maximum drive is not desirable, as it may produce too much side force and heeling moment. The advent of VPP's has allowed this interaction to be examined in the wind tunnel. For example, Ranzenbach and Teeters (2001) utilized a VPP to create a virtual sailing environment, using the wind tunnel measurements as input to the VPP for the sail forces. The VPP would compute the boat's equilibrium speed, and the sails in the wind tunnel could be adjusted to maximize this speed. This process allows for rapid optimization of performance. For example, an experienced sailor could find the optimum sail trim for a given wind condition and apparent wind angle in less than an hour, as opposed to days of testing on the water.

Measurement of sail shape in a wind tunnel is much easier than on the water. Ranzenbach and Kleene (2002) showed how both photogrammetry and a Coordinate Measuring Machine (CMM) could be used to determine the flying shape of spinnakers. These measurements can be used to compare the “design shape”, which is the nominal shape determined by the sail designers, with the “flying shape” that is actually realized in the wind tunnel. Measurement of actual sail shape is important, especially if the results are to be compared with CFD simulations.

While not perfect, wind tunnel testing has been shown to correlate reasonably well with full-scale experimentation, and has provided much useful guidance in understanding sail aerodynamics. On a cost-benefit ratio it is probably the best alternative currently available.

Computational Simulation

CFD has been used in sail design for some time. Milgram (1968) first employed panel techniques to sail aerodynamics with some success, and Charvet and Huberson (1992) used vortex particle methods on this problem. These inviscid techniques work reasonably well for upwind sailing, where the sails are flat and separation is at a minimum. If the presence of the mast is neglected and the sails are operating close to their ideal angle of attack, the viscous drag can be estimated using boundary layer techniques. Jackson and Fiddes (1995) used a panel method and an integral boundary layer method with a weak viscous-inviscid interaction on two-dimensional sails and showed good agreement with experiment.

These inviscid techniques cannot be applied to downwind sails due to large areas of separated flow (Richards, 1997), nor can they be used if the influence of the mast on the sails is to be considered (Ciortan and Soares, 2007). Hedges, Richards and Mallinson (1996) were among the first to use Reynolds-Averaged Navier Stokes (RANS) simulation for downwind sail aerodynamics. Lasher and Richards (2007) compared the results from RANS simulations to wind tunnel data for spinnakers in an untwisted atmospheric boundary layer, and in general the lift and drag coefficients were predicted with reasonable accuracy (Figure 12). Lasher and Sonnenmeier (2008) performed a more comprehensive analysis of various spinnaker shapes in uniform flow; in most cases the agreement with experiment was very good; however, the simulations failed to correctly predict the effect of camber on sail performance under certain circumstances. Specifically, wind tunnel results showed that a low camber spinnaker would produce more drive force when the boat was on a broad reach, whereas the CFD simulations sometimes showed that a high camber sail was better. A sail designer using the results of this type of simulation would be led to the wrong conclusion about which of two candidate shapes was the fastest.

The inability of the CFD simulations to predict the effects of camber on performance is not a surprise. It is well known that none of the turbulence models currently available are capable of predicting separation, reattachment and reformation of the boundary layer (Collie, 2005). Since these phenomena are strongly influenced by camber, one should not expect a high degree of accuracy for predicting the force coefficients for sails of different cambers. Improvements in the prediction of sail forces using RANS will have to wait for better turbulence models.

The fluid-structure interaction of sails has also been investigated computationally. Letcher (1986) developed a linear theory for inextensible membrane sails. Jackson and Christie (1986) used a vortex lattice simulation of potential flow and a finite element representation of the membrane, along with an interactive scheme to couple to the two simulations, to determine the pressure and deformed shape of a membrane sail. More recently, Cioro et al. (2002) used a vortex lattice method coupled to a two-dimensional boundary layer solution to obtain the pressure, and a finite element code to obtain the sail shape. Ranzenbach and Xu (2004) computed the shape of a code zero sail (a very flat spinnaker) as well as the loads acting upon the boat. This aero-structural calculation was based upon a vortex lattice code with a directly coupled boundary layer solver and a modified, commercially available FEA code. One key contribution to the state of the art in this area was that the calculation included the impact of membrane wrinkling, which is critical to correctly calculating aero-structural coupling of sails.

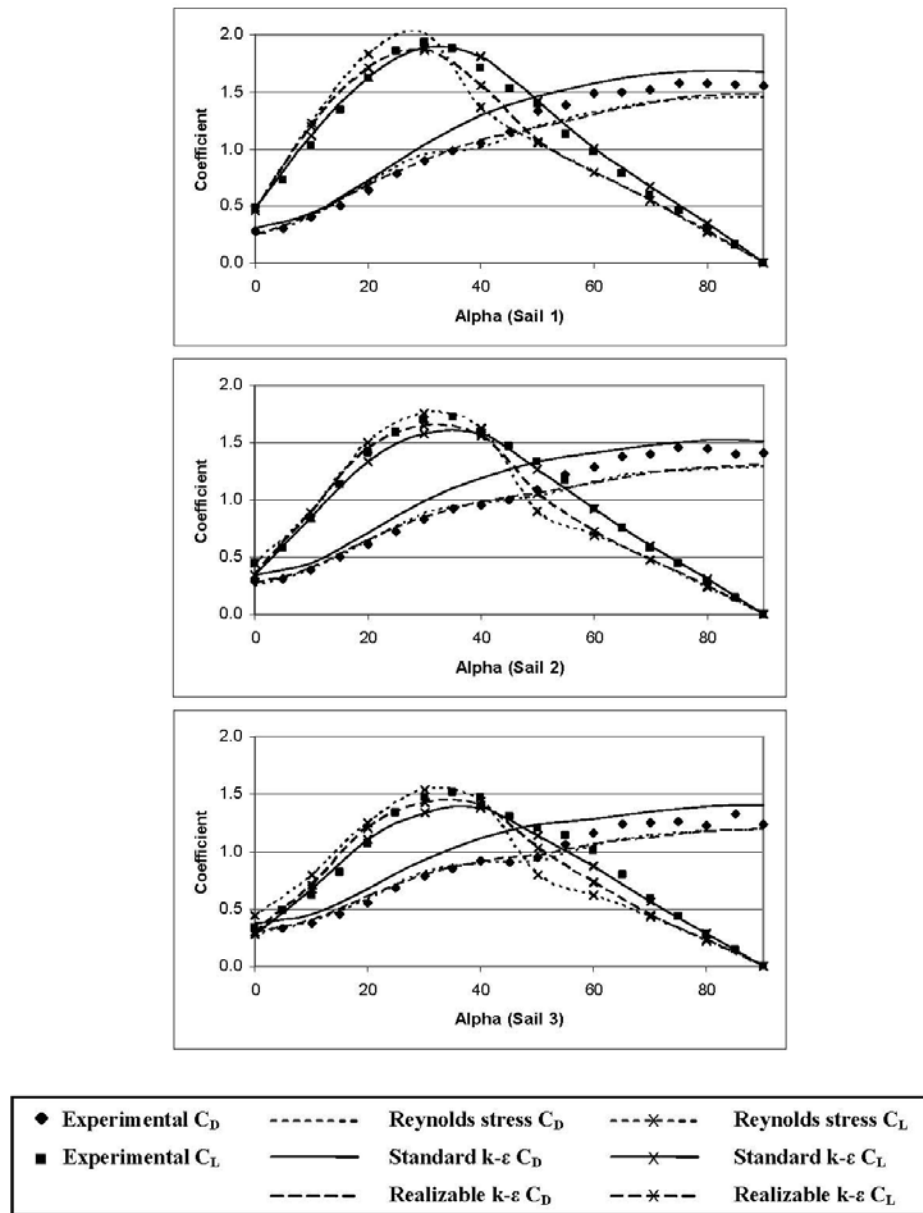


Figure 12. Lift and drag coefficients predicted by three different turbulence models for three different sail models, compared to wind tunnel results (originally published in Lasher and Richards, 2007).

Richter et al. (2003) was among the first to report the linking of a RANS simulation with a finite element solver to calculate the flow and shape of spinnakers, and called their system a “Virtual Wind Tunnel”. They did not compare their results to any experiments, but did find that the predicted drive force was about 4% higher than that given by a Velocity Prediction Program, indicating that the simulations were reasonable. They used a coarse mesh to keep simulation times low, and this work should thus be viewed as a “proof of concept”. Mairs (2003) used a commercial RANS code and a membrane code originally developed by the

Army, Tension 9, to calculate the flying shapes of spinnakers and validated his computations against wind tunnel tests. The results were promising but highlighted the challenges of RANS codes to capture the viscous flow physics of offwind sails. The Virtual Wind Tunnel is clearly the holy grail of computational analysis of sails; several researchers are currently working on a fully coupled solver which would minimize the computation time, but to the best of the author's knowledge no results from this work have been published.

CFD is arguably the least expensive of the three approaches, but the accuracy of the turbulence models and the relatively high computation times are still a problem. Nevertheless, the ability to accurately model the boundary conditions and to determine the details of the flow field everywhere are advantages that make this technology useful.

CONCLUSION

This article has only been able to touch the surface of this important and complex problem. The determination of aerodynamic forces on sails is clearly a challenge. Each of the three approaches currently being used has strengths and weaknesses; it is the opinion of the author that all three must be used to advance the state of the art. Suggested areas for future research include:

- Continued development of experimental databases of lift and drag coefficients, including measurement and reporting of flying shape. This will be helpful in improving our understanding of sail aerodynamics, modeling of sail forces for velocity prediction programs, and verification of computational simulations.
- As with all turbulent flows, better accuracy in computational simulations will have to await improvements in turbulence modeling or improved computational horsepower to replace RANS codes with other viscous flow solution approaches, such as Large Eddy Simulation (LES) or even Direct Numerical Simulation (DNS). This is especially true for high-camber shapes typically found in downwind sails.
- Development of computational techniques for a fully-coupled solution of the fluid-structure interaction problem, especially for spinnakers.
- Unsteady sail aerodynamics. Researchers are beginning to model sailing dynamics, including tacking (Battistin and Ledri, 2007) and sailing in waves (Harris, 2005), but only use steady-state aerodynamic models for the sails. Very little research has been done in this area; to the best of the author's knowledge there has only been one publication (Fitt and Lattimer, 2000) on unsteady sail aerodynamics.

REFERENCES

- [1] Apollonio, S. (Ed.) *The Last of the Cape Horners*, Brassey's, Washington, DC, 2000.
- [2] Battistin, D.; Ledri, M. *Proc, 18th Chesapeake Sailing Yacht Symposium*, Annapolis, MD, 2007, 95-118.
- [3] Charvet, T.; Huberson, S. *European J. Mech, B/Fluids*, 1992, vol. 11, no. 5, 559-610.

- [4] Cioro, D.P.; Nicolosi, F.; Scherillo, F.; Maisto, U. *Proc, High Performance Yacht Design Conference*, Auckland, NZ, 2002.
- [5] Ciortan, C.; Soares, C.G. *Ocean Engin*, 2007, vol. 34, 2198-2206.
- [6] Collie, S. *PhD Dissertation, University of Auckland*, Auckland, NZ, 2005.
- [7] Cowles, G.; Parolini, N.; Sawley, M.L. *Proc, 16th Chesapeake Sailing Yacht Symposium*, Annapolis, MD, 2003, 73-89.
- [8] Fallow, J.B. *J. Wind Eng Ind Aerodyn*, 1996, vol. 63, 183-192.
- [9] Flay, G.J. *J. Wind Eng Ind Aerodyn*, 1996, vol. 63, 171-182.
- [10] Fitt, A.D.; Lattimer, T.R.B. *IMA J. Applied Math*, 2000, vol. 65, 147-171.
- [11] Fujiwawa, T.; Hearn, G.E.; Kitamura, F.; Ueno, M.; Minami, Y. *J. Marine Science Tech*, 2005, vol. 10, 131-146.
- [12] Gerritsma, J.; Kerwin, J.E.; Moeyes, G. *Determination of Sail Forces Based on Full Scale Measurements and Model Tests*, MIT Dept of Ocean Engineering, Boston, MA 1975.
- [13] Harris, D.H. *Proc, 17th Chesapeake Sailing Yacht Symposium*, Annapolis, MD, 2005, 13-32.
- [14] Hansen, H.; Jackson, P.; Hochkirch, K. *Proc, High Performance Yacht Design Conference*, Auckland, NZ, 2002.
- [15] Hedges, K.L.; Richards, P.J.; Mallinson, G.D. *J. Wind Eng Ind Aerodyn*, 1996, vol. 63, 95-110.
- [16] Hochkirch, K.; Brandt, H. *Proc, 14th Chesapeake Sailing Yacht Symposium*, Annapolis, MD, 1999, 33-44.
- [17] Jackson, P.S.; Christie, G.W. *AIAA J.*, 1986, vol. 25, no. 5, 676-682.
- [18] Jackson, P.S.; Fiddes, S.P. *Aeronautical J.*, 1995, June/July, 217-225.
- [19] Kerwin, J.E. *A Velocity Prediction Program for Ocean Racing Yachts Revised to June, 1978*, MIT Dept of Ocean Engineering, Boston, MA, 1978.
- [20] Lasher, W.C.; Musho, T.D.; McKee, K.C.; Rybka, W. *Proc, 18th Chesapeake Sailing Yacht Symposium*, Annapolis, MD, 2007, 185-197.
- [21] Lasher, W.C.; Richards, P.J. *J. Ship Research*, 2007, vol. 51, no. 1, 22-38.
- [22] Lasher, W. C.; Sonnenmeier, J. R.; Forsman, D. R.; Tomcho, J. *The Aerodynamics of Symmetric Spinnakers*, *J. Wind Eng and Ind Aerodyn*, 2005, vol. 93, 311-337.
- [23] Lasher, W.C.; Sonnenmeier, J.R. *J. Wind Eng Ind Aerodyn*, 2008, vol. 96, no. 2, 143-165.
- [24] Letcher, J.S., *Proc, AIAA/SNAME 16th Symposium on the Aero/Hydronautics of Sailing*, Long Beach, CA, 1986, 120-128.
- [25] Mairs, C. *PhD Dissertation, University of Maryland*, Auckland, College Park, Maryland, 2003.
- [26] Marchaj, C.A. *Aero-Hydrodynamics of Sailing*, Dodd, Mead and Co., New York, NY, 1979.
- [27] Masuyama, Y.; Fukasawa, T. *Proc, 13th Chesapeake Sailing Yacht Symposium*, Annapolis, MD, 1997, 23-36.
- [28] Masuyama, Y.; Nomoto, K.; Sakuri, A. *Proc, 16th Chesapeake Sailing Yacht Symposium*, Annapolis, MD, 2003, 179-186.
- [29] Miles, J.C.; Johnson, B.; Womack, J.; Franzen, I. *Proc, 18th Chesapeake Sailing Yacht Symposium*, Annapolis, MD, 2007, 165-184.
- [30] Milgram, J.H. *SNAME Transactions*, 1968.

- [31] Milgram, J.H.; Peters, D.B.; Eckhouse, D.N. *Proc, 11th Chesapeake Sailing Yacht Symposium*, Annapolis, MD, 1993, 65-73.
- [32] Ranzenbach, R.; Kleene, J. *Proc, High Performance Yacht Design Conference*, Auckland, NZ, 2002.
- [33] Ranzenbach, R.; Mairs, C. *Proc, 13th Chesapeake Sailing Yacht Symposium*, Annapolis, MD, 1997, 245-259.
- [34] Ranzenbach, R.; Mairs, C. *Proc, 14th Chesapeake Sailing Yacht Symposium*, Annapolis, MD, 1999, 171-179.
- [35] Ranzenbach, R.; Teeters, J. *Proc, 15th Chesapeake Sailing Yacht Symposium*, Annapolis, MD, 2001, 181-191.
- [36] Ranzenbach, R.C.; Xu, Z. *Proc, MDY'04 International Symposium on Yacht Design and Production*, Madrid, Spain, 2004.
- [37] Richards, P.J. *J. Wind Eng Ind Aerodyn*, 1997, vol. 67 & 68, 313-321.
- [38] Richter, H.J.; Horrigan, K.C.; Braun, J.B. *Proc, 16th Chesapeake Sailing Yacht Symposium*, Annapolis, MD, 2003, 19-27.
- [39] US Sailing Association, *Wind Tunnel Tests of a Sailing Yacht Rig Aerodynamics*, Report No. 1234, 1995.
- [40] Whidden, T.; Levitt, M. *The Art and Science of Sails, A Guide to Modern Materials, Construction, Aerodynamics, Upkeep and Use*, St. Martin's Press, New York, 1990.

Reviewed by Robert Ranzenbach

Chapter 14

LARGE-EDDY SIMULATION OF FREE SHEAR AND WALL-BOUNDED TURBULENT FLOWS

Konstantin N. Volkov*

Fluids Research Centre, Faculty of Engineering and Physical Sciences,
University of Surrey, Guildford, Surrey, GU2 7XH, United Kingdom

Abstract

The main objectives of the chapter are to show possibilities of large-eddy simulation to predict properties of free shear and wall-bounded turbulent flows, to test widely used sub-grid scale eddy viscosity models against selected benchmark problems identifying range of applicability and limitations of the models used, to help accurately predict flows in channels, mixing layers, free and impingement jets. The cases considered include fully developed turbulent flow in the channel, turbulent flow in the channel induced by wall injection, free mixing layer, free non-isothermal turbulent jet, unsteady-state heat transfer in the region of interaction of turbulent jet with flat target. The data obtained from large-eddy simulation are used to predict aero-optical effects in the turbulent boundary layers and free shear turbulent flows. Comparisons are made with well-documented experimental data, benchmark cases and computations from other CFD codes.

Nomenclature

- a Speed of sound
- c_p Specific thermal conductivity at constant pressure
- C Constant

*Email: k.volko@surrey.ac.uk

- C_f Friction coefficient
- D Diameter
- e Total energy per unit mass
- f Damping function
- h Width of channel
- k Turbulent kinetic energy
- L Length
- M Mach number
- Nu Nusselt number
- p Pressure
- Pr Prandtl number
- q Heat flux
- Re Reynolds number
- Ri Richardson number
- S Strain rate tensor
- t Time
- T Temperature
- x, y, z Cartesian coordinates
- x, r, θ Cylindrical coordinates
- u, v, w Velocity components
- v_x, v_y, v_z Velocity components in Cartesian frame of reference
- v_x, v_r, v_θ Velocity components in cylindrical frame of reference
- γ Specific heat ratio
- δ Thickness
- Δ Filter width
- ε Dissipation rate

- θ Intensity of turbulence
- ϑ Degree of preheating
- λ Thermal conductivity
- μ Dynamic viscosity
- ν Kinematic viscosity
- ρ Density
- τ Shear stress
- Ω Rotation tensor
- c Centreline
- eff Effective
- i, j, k Tensor indexes
- m Maximal
- sgs Sub-grid scale
- t Turbulent
- w Wall
- 0 Stagnation point
- ∞ Infinity
- n Time layer
- + Non-dimensional near-wall value
- CDS Central Difference Scheme
- CFD Computational Fluid Dynamics
- DES Detached Eddy Simulation
- DNS Direct Numerical Simulation
- HRN High-Reynolds Number
- LES Large-Eddy Simulation
- LRN Low-Reynolds Number
- PDF Probability Density Function
- PPM Piecewise-Parabolic Method

- RANS Reynolds-Averaged Navier–Stokes
- RK Runge–Kutta
- RNG Re-Normalization Group
- SGS Sub-Grid Scale

1. Introduction

Despite intense development of computational technologies, achievements in the field of construction of numerical methods and development of appropriate software, the problem of numerical simulation of turbulence remains one of the most complicated and important problems of computational fluid dynamics (CFD). In contrast to laminar flows whose computation has already become a routine procedure, reliable prediction of turbulent flows is more art than rigorous science for numerous reasons, e.g., three-dimensional character of the flow, stochastic nature and wide spatial and temporal spectrum of scales.

The quality of CFD calculations of the flows and heat transfer in boundary layers, free mixing layers, and free and impinging jets strongly depends on the proper prediction of turbulence phenomena. Investigations of heat transfer, skin friction, flow separation and re-attachment effects demand a reliable simulation of the turbulence, reliable numerical methods, accurate programming, and robust working practices.

The methods of numerical simulation of turbulent flows include Direct Numerical Simulation (DNS), Large-Eddy Simulation (LES), and solution of Reynolds-Averaged Navier–Stokes equations (RANS). There are also hybrid approaches that combine these or those features of DNS, RANS, and LES, in particular, Detached Eddy Simulation (DES).

DNS implies solving the full (e.g., unsteady and three-dimensional) Navier–Stokes equations, which allows obtaining instantaneous characteristics and resolving all scales of a turbulent flow, if numerical and other types of errors can be avoided. The resultant statistics is used to validate turbulence models, to develop methods of turbulent flow control, and to study the laminar–turbulent transition. As the capabilities of measurement equipment are limited, DNS is considered as a source of experimental data, e.g., pressure fluctuations, vorticity, and dissipation rate of turbulent kinetic energy.

Limitations in the use of DNS are high requirements to difference schemes, satisfaction of initial and boundary conditions, and limited resources of computational engineering. Time and mesh steps are of the order of Kolmogorov’s scales of time and length and decrease with increasing Reynolds number [1]. Obtaining a statistically steady flow pattern requires tens and hundreds of hours of processor time. The use of unstructured meshes also contributes to consumption of computer memory and processor time. Because of the requirements listed above, it is difficult to implement computations that involve DNS except for low Reynolds numbers and simple flow geometry.

Solution of RANS equations requires much lower computational resources and is successfully used in practice. The issues of closure are solved at different levels of complexity. Turbulence models are classified in terms of the number of equations introduced in addition to the RANS equations. An increase in the number of equations requires additional semi-empirical information to be involved, which spoils model universality. Available turbulence

models do not possess acceptable universality and, therefore, cannot be used to solve a wide range of applied problems.

The absence of a universal turbulence model suitable for computing all or at least most turbulent flows shifted the focus in turbulence research. Improved capabilities of CFD tools stimulated the search for and application of approaches that are more rigorous and universal than RANS.

LES is a compromise between DNS and solution of RANS equations. LES implies solution of filtered Navier–Stokes equations. Large eddies, being under a direct action of boundary conditions and carrying the maximum Reynolds stresses, are computed. Small eddies have a more universal structure and are modelled by sub-grid scale (SGS) models based on the eddy viscosity or other rational approximations of transport processes. SGS models are normally characterized by significant diffusion and dissipation, which allows one to overcome computational problems caused by presentation of small eddies on a chosen mesh and to stabilize numerical computations.

As LES excludes direct computations of small eddies, the time and mesh steps are much greater (approximately by an order of magnitude) than Kolmogorov's scales of length and time. Higher Reynolds number than that in the DNS can be achieved with a fixed computational memory.

A large number of SGS models, filters, boundary conditions, and finite-difference schemes have been tested in numerous computations [2, 3]. Nevertheless, neither is the optimal choice of the SGS model clear nor is the choice, if made, justified. There are no universal near-wall functions providing a decrease in the number of nodes in the near-wall region, therefore it is difficult to use LES for computing flows with small separation regions and transition points [4]. Yet, LES is a promising direction in the development of methods for computing turbulent flows and seems to be a serious alternative to DNS and RANS.

The main objectives of the chapter are to show the possibilities of LES to predict properties of free shear and wall-bounded turbulent flows, to test widely used SGS models against selected benchmark problems identifying range of applicability and limitations of the models used, to help accurately predict flows in channels, mixing layers, and free and impingement jets.

Basic equations, SGS models used and discussion of some modifications made to the SGS models, and summary of the CFD method are given in sections 2, 3 and 4. Results are then presented in sections from 5 to 10, and the main conclusions are given in section 11.

The basic equations formally coincide with unsteady RANS equations but are written for filtered quantities (section 2).

The Smagorinsky model with and without a Van Driest correction and Richardson number correction for a curvature of streamlines, the re-normalization group (RNG) model, the dynamic model, and the one-equation model are considered (section 3). Weaknesses in the models are identified and suggestions made for possible improvements.

The numerical calculations are based on finite volume structured compressible flow code (section 4). The solver works in an explicit time-marching fashion based on a three-step Runge–Kutta (RK) stepping procedure. The piecewise-parabolic method (PPM) and Chakravarthy–Osher scheme are used for discretization of inviscid fluxes, and central difference scheme (CDS) of second order is used for discretization of viscous fluxes.

The cases considered include a fully developed turbulent flow in the channel (section

5), turbulent flow in the channel induced by wall injection (section 6), free mixing layer (section 7), free non-isothermal turbulent jet (section 8), unsteady-state heat transfer in the region of interaction of turbulent jet with flat target (section 9). The statistical data obtained from LES are used to predict aero-optical effects in the turbulent boundary layers and free shear turbulent flows (section 10). Comparisons are made with well-documented experimental data, benchmark cases and computations from other CFD codes.

2. Basic equations

In Cartesian coordinates (x, y, z) , an unsteady-state flow of a viscous compressible fluid is described by the following equation written relative to filtered quantities

$$\frac{\partial Q}{\partial t} + \frac{\partial F}{\partial x} + \frac{\partial G}{\partial y} + \frac{\partial H}{\partial z} = 0. \quad (1)$$

Equation (1) is complemented with the equation of state for perfect gas,

$$p = (\gamma - 1)\rho \left[e - \frac{1}{2} (v_x^2 + v_y^2 + v_z^2) \right].$$

The vector of conservative variables Q and the flux vectors F , G , and H have the following form

$$Q = \begin{pmatrix} \rho \\ \rho v_x \\ \rho v_y \\ \rho v_z \\ \rho e \end{pmatrix},$$

$$F = \begin{pmatrix} \rho v_x \\ \rho v_x v_x + p - \tau_{xx} \\ \rho v_x v_y - \tau_{xy} \\ \rho v_x v_z - \tau_{xz} \\ (\rho e + p)v_x - v_x \tau_{xx} - v_y \tau_{xy} - v_z \tau_{xz} + q_x \end{pmatrix},$$

$$G = \begin{pmatrix} \rho v_y \\ \rho v_y v_x - \tau_{yx} \\ \rho v_y v_y + p - \tau_{yy} \\ \rho v_y v_z - \tau_{yz} \\ (\rho e + p)v_y - v_x \tau_{yx} - v_y \tau_{yy} - v_z \tau_{yz} + q_y \end{pmatrix},$$

$$H = \begin{pmatrix} \rho v_z \\ \rho v_z v_x - \tau_{zx} \\ \rho v_z v_y - \tau_{zy} \\ \rho v_z v_z + p - \tau_{zz} \\ (\rho e + p)v_z - v_x \tau_{zx} - v_y \tau_{zy} - v_z \tau_{zz} + q_z \end{pmatrix}.$$

The components of viscous stress tensor and components of heat flux vector are found from the relations

$$\tau_{ij} = \mu_{\text{eff}} \left(\frac{\partial v_i}{\partial x_j} + \frac{\partial v_j}{\partial x_i} - \frac{2}{3} \frac{\partial v_k}{\partial x_k} \delta_{ij} \right), \quad q_i = -\lambda_{\text{eff}} \frac{\partial T}{\partial x_i}.$$

Here, t is the time, ρ is the density, v_x , v_y , and v_z are the velocity components in the coordinate directions x , y , and z , p is the pressure, e is the total energy per unit mass, T is the temperature, and γ is the specific heat ratio.

The equation (1) is suitable for both laminar and turbulent flows, and it formally coincides with unsteady RANS equations. The effective viscosity, μ_{eff} , is calculated as the sum of molecular viscosity, μ , and eddy viscosity, μ_{sgs} , and the effective thermal conductivity, λ_{eff} , is expressed in terms of viscosity and Prandtl number,

$$\mu_{\text{eff}} = \mu + \mu_{\text{sgs}}, \quad \lambda_{\text{eff}} = c_p \left(\frac{\mu}{\text{Pr}} + \frac{\mu_{\text{sgs}}}{\text{Pr}_{\text{sgs}}} \right),$$

where c_p is the specific heat capacity at constant pressure. For air, $\text{Pr} = 0.72$ and $\text{Pr}_{\text{sgs}} = 0.9$. The Sutherland's law is used to obtain molecular viscosity as a function of temperature

$$\frac{\mu}{\mu_*} = \left(\frac{T}{T_*} \right)^{3/2} \frac{T_* + S_0}{T + S_0},$$

where $\mu_* = 1.68 \times 10^{-5}$ kg/(m s), $T_* = 273$ K and $S_0 = 110.5$ K for air.

Modelling of unsteady subsonic flows faces the problem of setting the boundary conditions for the fluid outflow containing intense vortex structures. Possible non-physical effects of generation and reflection of acoustic waves on the outlet boundary distort the real pattern of the flow. All sought functions on the outlet boundary are subjected to the non-reflecting boundary conditions.

Cylindrical coordinates (x, r, θ) are used for specifying the boundary conditions and for post-processing the results computed instead of Cartesian coordinates (x, y, z) . The radial and tangential velocity components are related to Cartesian velocity components by the relations

$$v_r = \frac{v_y y + v_z z}{(y^2 + z^2)^{1/2}}, \quad v_\theta = \frac{v_z y - v_y z}{(y^2 + z^2)^{1/2}}.$$

In view of the symmetry of computational domain and boundary conditions, the time-averaged tangential velocity is zero.

3. Sub-grid scale models

To close the filtered Navier–Stokes equations, written in the form (1), we use the hypothesis of eddy viscosity. The inclusion of compressibility in the SGS model affects the results of numerical simulation only slightly [5].

3.1. Smagorinsky model

In the Smagorinsky model [6], the eddy viscosity is calculated as

$$\mu_{\text{sgs}} = \rho (C_S \Delta)^2 |S|, \quad (2)$$

where

$$|S| = (2S_{ij}S_{ij})^{1/2}, \quad S_{ij} = \frac{1}{2} \left(\frac{\partial v_i}{\partial x_j} + \frac{\partial v_j}{\partial x_i} \right).$$

It is usually assumed that $C_S \sim 0.1$.

To take into account the influence of the wall on the mixing length, $C_S \Delta$, the equation (2) is supplemented by the Van Driest damping function

$$f_\mu = 1 - \exp \left[- \left(\frac{y^+}{25} \right)^3 \right].$$

Here, $y^+ = \rho u_\tau y / \mu$, $u_\tau = (\tau_w / \rho)^{1/2}$, and τ_w is the wall shear stress.

To incorporate the effects of curvature of streamlines, the eddy viscosity is multiplied by the damping function dependent on the Richardson number [7]

$$f(\text{Ri}) = (1 - \alpha \text{Ri})^{1/2} \quad (\alpha \sim 0.1).$$

The Richardson number is found by the formula

$$\text{Ri} = \frac{|\Omega|}{|S|} \left(1 + \frac{|\Omega|}{|S|} \right),$$

where

$$|\Omega| = (2\Omega_{ij}\Omega_{ij})^{1/2}.$$

3.2. RNG model

The RNG model is simple and efficient from the computational viewpoint, and in contrast to the Smagorinsky model correctly predicts the behavior of eddy viscosity in the laminar flow region without any additional modifications ($\mu_{\text{sgs}} \rightarrow 0$ as $\text{Re} \ll 1$).

In the RNG model, the calculation of effective viscosity reduces to the solution of non-linear equation [8]

$$\mu_{\text{eff}} = \mu \left[1 + H(X - C) \right]^{1/3}, \quad X = \frac{\mu_{\text{sgs}}^2 \mu_{\text{eff}}}{\mu^3}. \quad (3)$$

In the equation (3), $H(X)$ is the Heaviside function, $C = 100$. The eddy viscosity is found from the relation

$$\mu_{\text{sgs}} = \rho (C_R \Delta) |S|^2, \quad (4)$$

where $C_R = 0.157$. At $X \ll C$, the equation (4) yields the Smagorinsky formula (2), and

$$C_S = \frac{(2C_R)^{1/4}}{2\pi} = 0.119.$$

3.3. Dynamic model

The dynamic model [9] involves information contained in resolvable scales to estimate the Smagorinsky parameter.

The formulation of the dynamic model starts from the Smagorinsky eddy viscosity approximation (2). The so-called probe or test filter is introduced, the transmission band of this filter $\hat{\Delta}$ being greater than the width of the grid filter Δ used for filtering the Navier–Stokes equations (it is normally assumed that $\hat{\Delta} = 2\Delta$). Density is considered as a function of time only, but not as a function of spatial coordinates. The Smagorinsky constant, C_S , is assumed to be unchanged during secondary filtration.

We introduce a second-order tensor L_{ij} (the so-called Leonard stress tensor) whose components are equal to the difference between the components of SGS stress tensors T_{ij} and τ_{ij}

$$L_{ij}^* = L_{ij} - \frac{1}{3}\delta_{ij}L_{kk} = \frac{1}{\rho}(T_{ij} - \hat{\tau}_{ij}) = \widehat{v_i v_j} - \widehat{v_i} \widehat{v_j} = -2C_S \hat{\Delta}^2 M_{ij},$$

where

$$M_{ij} = \left(\frac{\hat{\Delta}}{\Delta}\right)^2 |\hat{S}| \hat{S}_{ij} - |S| S_{ij}.$$

The L_{ij} is the contribution of edies whose sizes vary from Δ to $\hat{\Delta}$ to the Reynolds stresses.

The parameter $C_S \Delta$ is chosen by minimizing the error given by the quantity

$$Q = E_{ij}E_{ij}, \quad (5)$$

where

$$E_{ij} = L_{ij}^* - T_{ij} + \hat{\tau}_{ij} = L_{ij}^* + 2C_E M_{ij}, \quad C_E = (C_S \Delta)^2.$$

Using the least squares method to (5), and averaging over the volume, we can write

$$\frac{\partial E^2}{\partial C_E} = \frac{\partial \langle E_{ij}E_{ij} \rangle}{\partial C_E} = 2 \left\langle E_{ij} \frac{\partial E_{ij}}{\partial C_E} \right\rangle = 0.$$

Taking into account that $\partial E_{ij}/\partial C_E = 2M_{ij}$, we obtain

$$C_E = -\frac{1}{2} \frac{\langle L_{ij}M_{ij} \rangle}{\langle M_{kl}M_{kl} \rangle}. \quad (6)$$

The Smagorinsky's constant calculated from (6) by the dynamic procedure significantly oscillates in space and time. A specific difficulty resulting from these oscillations is a possibly negative eddy viscosity, $C_S < 0$. This feature means energy transfer from small eddies to resolvable scales [10] (back-scatter). In principle, such a process may occur in an unsteady flow, but it usually leads to computational instability [11]. To prevent this, C_S is averaged over uniform directions, which damps high-frequency harmonics. At the $n+1$ th time step, we use the low-relaxation, which suppresses high-frequency oscillations

$$C_S^{n+1} = (1 - \omega)C_S^n + \omega C_S^*,$$

where ω is the relaxation coefficient, $\omega \sim 10^{-3}$.

3.4. One-equation model

Eddy viscosity is expressed in terms of the SGS kinetic energy

$$\nu_{\text{sgs}} = C_\nu k_{\text{sgs}}^{1/2} \Delta,$$

where $C_\nu = 0.067$.

The SGS kinetic energy is found by solving the equation [12]

$$\frac{\partial k_{\text{sgs}}}{\partial t} + \frac{\partial v_i k_{\text{sgs}}}{\partial x_i} = \frac{\partial}{\partial x_i} \left[(\nu + \nu_{\text{sgs}}) \frac{\partial k_{\text{sgs}}}{\partial x_i} \right] + P - D. \quad (7)$$

The terms P and D take into account production and dissipation of turbulence. They are modeled in the form

$$P = -\tau_{ij} \frac{\partial v_i}{\partial x_j} = 2\nu_{\text{sgs}} |S|^2, \quad D = C_\varepsilon \frac{k_{\text{sgs}}^{3/2}}{\Delta},$$

where $C_\varepsilon = 0.916$. The components of the SGS stress tensor are found from the expression

$$\tau_{ij} = -2\nu_{\text{sgs}} \left(S_{ij} - \frac{1}{3} S_{kk} \delta_{ij} \right) + \frac{2}{3} k_{\text{sgs}} \delta_{ij}.$$

3.5. Filter width

The filter width, Δ , is related to the mesh step size

$$\Delta = V^{1/3} = (\Delta x \Delta y \Delta z)^{1/3},$$

where V is the volume of cell, Δx , Δy , and Δz are mesh steps in the coordinate directions x , y , and z , respectively.

In the boundary layer, the mesh step in the direction normal to the wall, Δx , is replaced by the $\widehat{\Delta}x$, and the filter width is found as

$$\Delta = \left(\widehat{\Delta}x \Delta y \Delta z \right)^{1/3}.$$

So, $\widehat{\Delta}x = \Delta x$ near the wall, and $\widehat{\Delta}x = \overline{\Delta}x$ far from the wall. The Δx smoothly changes between the above-indicated values. The $\overline{\Delta}x$ is the average value of Δx in the near-wall region, and $\widehat{\Delta}x$ is found from the formula

$$\widehat{\Delta}x = \left[\left(\frac{1}{\Delta x} \right)^\alpha + \left(\frac{1}{\overline{\Delta}x} \right)^\alpha \right]^{-1/\alpha} \quad (\alpha = 3).$$

A smaller width of the filter allows reproduction of a wider frequency range of fluctuations of flow parameters, whereas an increase in Δ facilitates smoothing of the solution (LES transforms to DNS as $\Delta \rightarrow 0$).

4. Numerical method

Nonlinear interactions with resolved scales and corresponding wavenumbers produce waves with wavenumbers higher than the critical wavenumber that can be interpreted numerically (so-called compatibility). If no special precautions are taken, this effect can be interpreted as a fictitious energy transfer to low wavenumbers (negative eddy viscosity).

Discretization of the equation (1) is performed by the finite-volume method on an structured mesh and by using high resolution difference schemes. In contrast to the mean velocity, the accuracy of prediction of velocity fluctuations strongly depends on the order of the difference scheme [11].

Equation (1) is written in the form

$$\frac{dQ_{i,j,k}^n}{dt} + L(Q_{i,j,k}^n) = 0,$$

where

$$\begin{aligned} L(Q_{i,j,k}^n) = & \frac{F_{i+1/2,j,k}^n - F_{i-1/2,j,k}^n}{\Delta x_{i,j,k}} + \frac{G_{i,j+1/2,k}^n - G_{i,j-1/2,k}^n}{\Delta y_{i,j,k}} + \\ & + \frac{H_{i,j,k+1/2}^n - H_{i,j,k-1/2}^n}{\Delta z_{i,j,k}}. \end{aligned}$$

The three-step RK method is used for discretization in time [13]

$$\begin{aligned} Q_{i,j,k}^{(1)} &= Q_{i,j,k}^{(n)} + \Delta t L(Q_{i,j,k}^{(n)}), \\ Q_{i,j,k}^{(2)} &= \frac{3}{4} Q_{i,j,k}^{(n)} + \frac{1}{4} \left[Q_{i,j,k}^{(1)} + \Delta t L(Q_{i,j,k}^{(1)}) \right], \\ Q_{i,j,k}^{(n+1)} &= \frac{1}{3} Q_{i,j,k}^{(n)} + \frac{2}{3} \left[Q_{i,j,k}^{(2)} + \Delta t L(Q_{i,j,k}^{(2)}) \right]. \end{aligned}$$

The flux vector is divided into the inviscid and viscous components. The discretization of inviscid fluxes is performed using the PPM and the Chakravarthy–Osher scheme [14] based on the approximate solution of the problem on breakup of arbitrary discontinuity. The discretization of viscous fluxes involves the CDS of the second order. The method of discretization of viscous fluxes affects the technical aspect of implementation of the approach. A lower order of discretization of viscous terms is interpreted as a small inaccuracy in presenting viscous forces, which is admissible if eddy viscosity is calculated by an approximate model.

The computational procedure is implemented as a sequence of the following steps.

1. Reconstruction of the solution in each control volume and extrapolation of the unknowns to find the state of the flow on the control-volume faces from values prescribed in the center.
2. Solving the Riemann problem for each face of the control volume with allowance for the local flow direction (normal to the control-volume face).
3. Evolution of the time step.

The use of LES also imposes some specific requirements to computational meshes. As the effective viscosity is proportional to the mesh step, an increase in the cell size in any direction can increase the scheme viscosity and distort the results. That is why it is

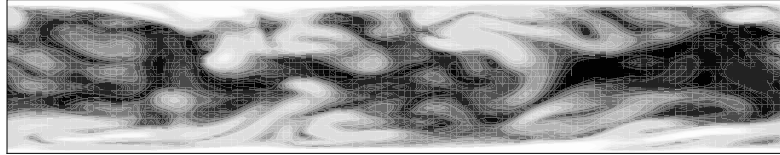


Figure 1. Vortex flow pattern in a channel at $t = 0.32$ s.

reasonable to use computational meshes whose cells have approximately identical sizes in all coordinate directions, independent of the direction of gradients of the mean flow parameters.

The computational procedure is implemented as a computer code in the Fortran and C/C++ programming languages. Parallelization of the computational procedure is performed by a message passing interface (MPI).

5. Fully developed turbulent channel flow

The accuracy and computational efficiency of some SGS models (Smagorinsky model, RNG model, dynamic model and one-equation model) are compared with the experimental data and results of DNS.

No-slip and no-penetration boundary conditions are specified for the velocity on the wall, as well as the uniform wall temperature, T_w . Periodic boundary conditions are specified in streamwise direction.

The calculations are performed for the Reynolds number, $\text{Re} = \rho u_0 h / \mu$, from 100 to 6000. The fluid velocity on the inlet boundary is fixed at $u_0 = 180$ m/s, and the Reynolds number varies by appropriate changes in dynamic viscosity. The Reynolds number based on dynamic velocity, $\text{Re}_\tau = \rho u_\tau h / \mu$, varies from 10 to 600. In main computational variant $\mu = 0.039$ kg/(m s) and $\text{Re}_\tau = 360$.

The mesh contains $150 \times 65 \times 65$ nodes, and it is refined towards the walls of the channel. The time step is $\Delta t = 2.5 \times 10^{-4}$ s, and 40 000 time steps are performed.

The instantaneous flow pattern in the channel is visualized by using the absolute value of vorticity

$$\Omega = |\nabla \times \mathbf{v}| = (\Omega_x^2 + \Omega_y^2 + \Omega_z^2)^{1/2},$$

where Ω_x , Ω_y and Ω_z are the vorticity components. The channel flow pattern in the symmetry plane of the channel is presented in the Figure 1.

The profile of streamwise velocity in the channel cross section is shown in the Figure 2. The results obtained show that the Smagorinsky model yields a less filled profile of velocity than other models. Introduction of the Van Driest damping function improves the computed results, that become almost identical to those computed by the dynamic model.

The profile of velocity in the near-wall region based on dynamic model is in good agreement with the Reihardt law [15] based on the experimental data and covering the viscous

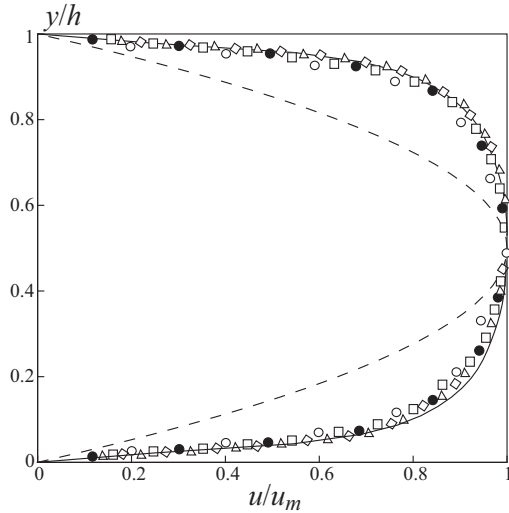


Figure 2. Profiles of streamwise velocity based on Smagorinsky model (symbols \circ), Van Driest model (symbols \bullet), RNG model (symbols \triangle), dynamic model (solid line), one-equation model (symbols \diamond), DNS data of [1] (symbols \bullet). Dashed line corresponds to profile of streamwise velocity in laminar flow [15].

sub-layer, the buffer region and logarithmic region of the boundary layer (see Figure 3).

The turbulent kinetic energy is compared to DNS data of [1, 16] in the Figure 4, and profiles of root-mean-square velocities in the channel cross section are plotted in the Figures from 5 to 7 compared to data of [16, 17]. Though the Smagorinsky model and the Van Driest model underpredict the fluctuations of streamwise velocity, the fluctuations of velocity in y and z directions based on different models are in a fairly good agreement with each other. The role of SGS modeling becomes more important with the increasing Reynolds number.

The Figure 8 shows the profiles of Reynolds stresses and SGS stresses. The eddy viscosity in the boundary layer as a function of the distance from the wall is plotted in the Figure 9. The Smagorinsky model and the Van Driest model underpredict the eddy viscosity. The best agreement with the experimental data is provided by the dynamic and one-equation models.

The Smagorinsky constant as a function of the distance from the wall, predicted by the dynamic model, is shown in the Figure 10.

The use of the RNG model, the dynamic model and one-equation model increases the computational time by 18, 30, and 35% compared to the time spent on a calculation without any SGS model.

6. Turbulent flow in channel induced by wall injection

Modeling of turbulent flows in channels with the intensive distributed uniform fluid injection is carried out using LES with RNG model and RANS closed with the $k-\varepsilon$ turbulence model. Calculations are performed for various ratios of fluid injection velocities from the channel walls. The results of LES for the one-sided injection channel agree well with the

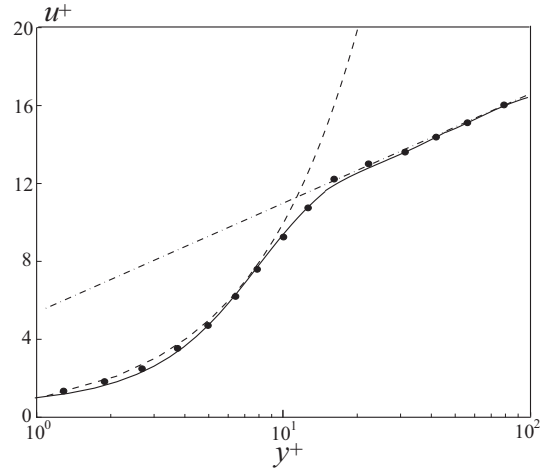


Figure 3. Profile of velocity in the boundary layer (solid line) compared to Reihardt law (symbols ●). Dotted and dash-dotted lines correspond to liner and logarithmic velocity profiles.

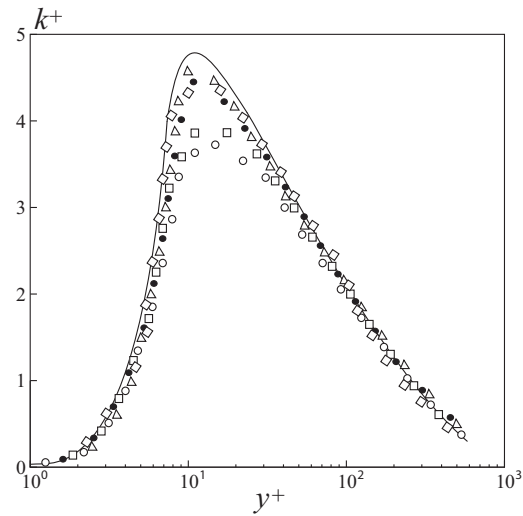


Figure 4. Profiles of turbulent kinetic energy near the wall. Symbols ● correspond to DNS data of [1] for $\text{Re}_\tau = 395$.

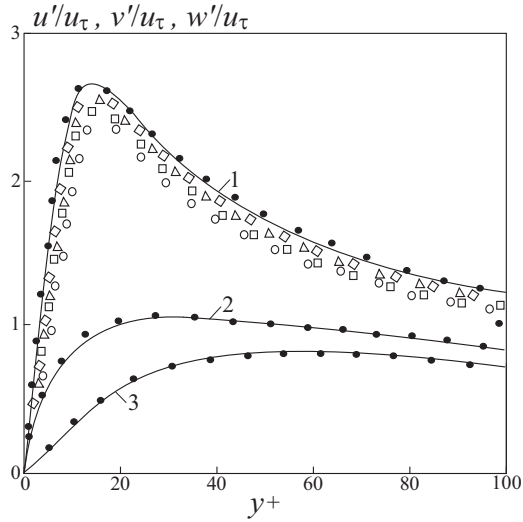


Figure 5. Profiles of root-mean-square velocities u (line 1), v (line 2) and w (line 3) for $\text{Re}_\tau = 180$. The symbols \bullet correspond to the data of [16, 17].

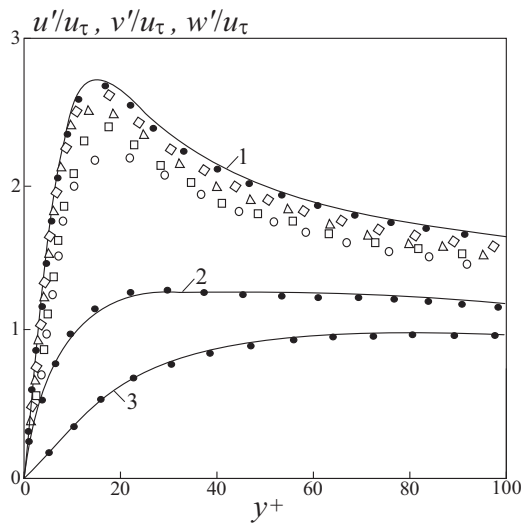


Figure 6. Profiles of root-mean-square velocities u (line 1), v (line 2) and w (line 3) for $\text{Re}_\tau = 360$. The symbols \bullet correspond to the data of [16, 17].

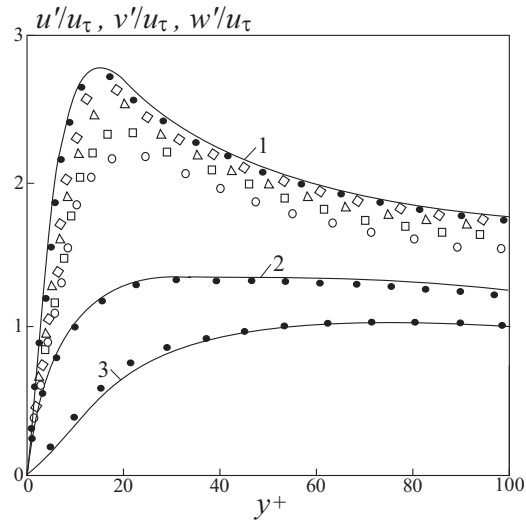


Figure 7. Profiles of root-mean-square velocities u (line 1), v (line 2) and w (line 3) for $\text{Re}_\tau = 590$. The symbols \bullet correspond to the data of [16, 17].

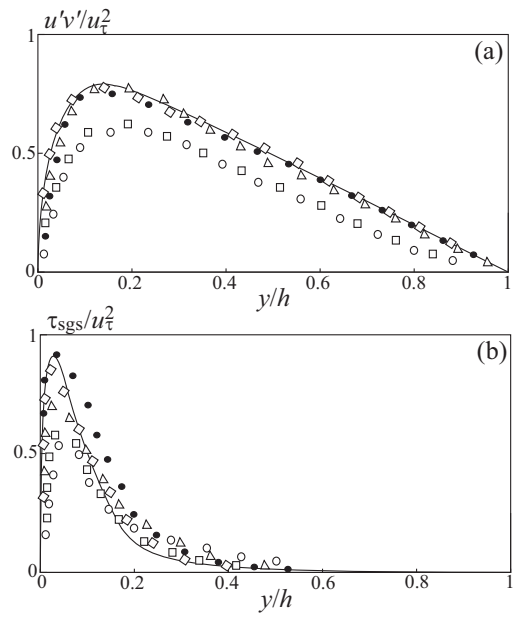


Figure 8. Profiles of Reynolds stresses (a) and SGS stresses (b). The symbols \bullet correspond to Smagorinsky model.

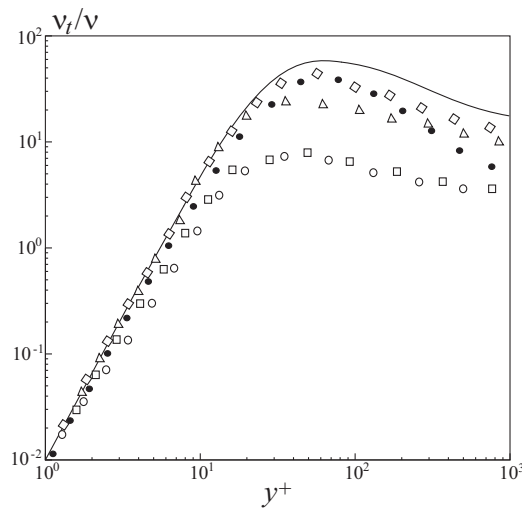


Figure 9. Profile of eddy viscosity near the wall. The symbols \bullet correspond to the data of [17].

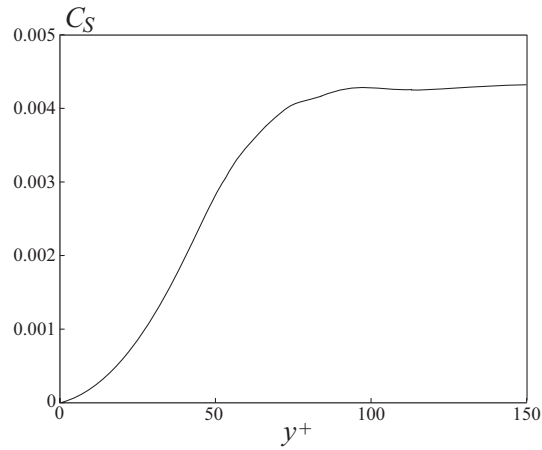


Figure 10. Distribution of Smagorinsky's constant as a function of distance from wall.

experimental data whereas the $k-\varepsilon$ model gives a less filled velocity profile in the cross section and a substantial error in definition of the wall shear stress on the impermeable wall. In case of a two-sided injection, the results based on LES and $k-\varepsilon$ model agree with one another and with the experimental data.

6.1. Methods of simulation

The flow in the channel with distributed fluid injection serves as a model for flow of products of solid fuel decomposition in the solid rocket motors, which reflects the essential side of the process — injection of the mass from the burning surface.

Investigation of flows in channels with permeable walls is extensively covered in the literature [18, 19, 20, 21, 22, 23, 24, 25, 26]. The paper of [18] is devoted to the experimental study of flow modes in injection channels with different cross sections of the channel (square, round, star-shaped). Physical and mathematical models of various degrees of complexity are applied for numerical calculations in [19, 20]. Considering physical features of the flow, it is possible to simplify the problem substantially [18, 19]. The simplified mathematical models, whose calculating efficiency is achieved by neglecting the influence of certain factors, is substantiated by appropriate assessment and comparison of different approaches [20].

Equations that describe the flow of a viscous incompressible fluid between two parallel flat plates, one of them is permeable, have the exact solution [19]. Suggesting that the streamwise velocity depends on x coordinate according to the linear law, $u \sim xf(y)$, and the transverse velocity does not depend on the streamwise coordinate, $v \sim g(y)$, the calculation of the flow field comes down to integration of the equation

$$g^{(4)} - \text{Re} (gg''' - g'g'') = 0. \quad (8)$$

Functions f and g are connected by the continuity equation, $f = -g'$. Boundary conditions are specified on the walls of the channel ($g = 0$, $g' = 0$ at $y = 0$, and $g = -1$, $g' = 0$ at $y = 1$). The characteristic parameter of the problem is the Reynolds number $\text{Re} = \rho v_w h / \mu$, where v_w is the injection velocity, and h is the distance between the plates.

For intensive injection, $\text{Re} \rightarrow \infty$, the solution of the equation (8) is expressed in the form [19]

$$g = -\sin\left(\frac{\pi}{2}y\right). \quad (9)$$

The intensive injection means that the injection velocity considerably, by the order of magnitude, exceeds the velocity in the boundary layer near the impermeable surface, and the injection velocity is considerable lower than the average flow velocity in the channel. In such conditions, the flow in the injected fluid layer turns out inviscid, and the boundary layer is pushed away from the surface and transformed into the mixing layer between the injected layer and the flow in the channel. The thickness of this layer turned out to be small compared to the thickness of the layer of the injected fluid.

Experimental and computational data [18, 19, 20] show that the solution (9) describes well the velocity distribution in turbulent channel flow at $\text{Re} > 80$. Model of flow of

inviscid incompressible fluid leads to large errors in the simulation of turbulent flows in long and narrow channels [21, 22].

The $k-\varepsilon$ turbulence model gives accurate results for the channels with two-sided uniform fluid injection [20, 21, 22, 23, 24]. For the one-sided injection, the discrepancy of the computed and experimental data on turbulence intensity near the solid wall reaches 15–20% [24]. The three- and four-equation turbulence models, e.g. v^2-f model, produce more consistent computational results [21, 25].

The LES of turbulent flow with wall injection is performed in [26] based on structure function model. The two-dimensional formulation of the problem used in [26] conflicts with the fundamental concept of LES.

6.2. Boundary conditions

The x axis of Cartesian frame of reference is directed along the lower wall of channel, and y and z axes are connected with cross section of channel. Lower and upper walls of channel are permeable with the fluid injection velocities v_{w1} and v_{w2} normal to walls.

The velocity distribution described by the relation (9) is specified at initial time, $t = 0$. The velocity in z direction is zero.

The boundary conditions of normal fluid injection from lower and upper walls, and uniform temperature of walls are specified ($u = w = 0, v = v_{w1}, T = T_{w1}$ at $y = 0$, and $u = w = 0, v = -v_{w2}, T = T_{w2}$ at $y = h$). The left boundary of channel is non-permeable and adiabatic ($u = v = w = 0, \partial T / \partial n = 0$ at $x = 0$).

Non-reflecting boundary conditions are applied to the outlet boundary of the channel at $x = L$. Periodic boundary conditions are specified in z direction.

Injection velocity is constant in space, and changes in time according to Gaussian law with imposed random fluctuations in the form of white noise [22].

For the calculations based on the $k-\varepsilon$ model, the turbulent kinetic energy and its dissipation rate are $k \sim 10^{-3} \text{ m}^2/\text{s}^2$ and $\varepsilon \sim 10^{-2} \text{ m}^2/\text{s}^3$. The results of [20] demonstrate a weak sensitivity of the flow pattern in the channel to the inlet turbulent kinetic energy and its dissipation rate. The wall functions are applied to specify turbulent kinetic energy and its dissipation rate on the non-permeable wall of the channel if the $k-\varepsilon$ model is used.

6.3. Results and discussion

The mesh contains $400 \times 100 \times 50$ nodes. The mesh is refined towards the left boundary (in x direction) and wall (in y direction) of channel. Minimal and maximum mesh steps are $\Delta x_{\min} = 1.5 \times 10^{-5} \text{ m}, \Delta x_{\max} = 1.2 \times 10^{-4} \text{ m}, \Delta y_{\min} = 1.8 \times 10^{-5} \text{ m}, \Delta y_{\max} = 2 \times 10^{-4} \text{ m}, \Delta z = 10^{-4} \text{ m}, \Delta t = 2.5 \times 10^{-6} \text{ s}$, and 50000 time steps are performed.

The width and length of the channel are $h = 0.01 \text{ m}$ and $L = 0.6 \text{ m}$ respectively. Injection velocities from lower and upper wall are varied in calculations.

At high Reynolds numbers, the flow region in the channel with wall injection is divided into sub-region of singularity influence of viscosity near the walls and sub-region of vortical flow in the core.

The re-circulation regions above and below plane of symmetry of the channel in the case of two-sided uniform injection and near the lower wall of the channel in the case of

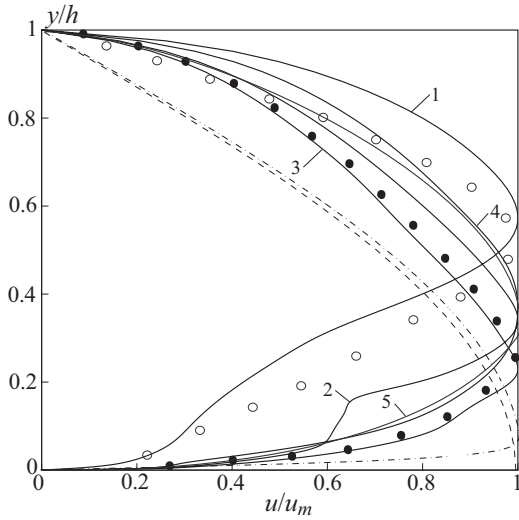


Figure 11. Profiles of streamwise velocity at $x/h = 40$, $v_{w1} = 0$ and $v_{w2} = 0.1$ (line 1), 0.55 (line 2), 1 (line 3), 2.75 (line 4), 5 (line 5) m/s compared to experimental data of [22] (symbols \bullet) and solution of the $k-\varepsilon$ model (symbols \circ) at $v_{w2} = 1$. The dashed line corresponds to cosine profile (9), and dot-dashed line corresponds to velocity profile from (8) at $Re = 10^3$.

one-sided injection are formed at some distance from left butt-end. Viscous forces play negligible role compared to inertial forces at all x except for small region near the left wall at $x/h < 12$. The size of re-circulation regions does not change at $Re > 10^4$.

The maximum of streamwise velocity comes towards the solid wall of the channel, near which the zone of viscous flow in the likeness of boundary layer on a flat plate is developed (see Figure 11). With increase in distance from left butt-end of the channel, the profile of streamwise velocity takes a more filled shape than a profile computed from the $k-\varepsilon$ model.

The solution is independent on Reynolds number at two-sided injection with the same intensity and Reynolds number higher than 10^3 . The profiles of streamwise velocity are more filled than before compared to those based on the model of vortical flow of incompressible fluid in the channel with wall injection or $k-\varepsilon$ turbulence model (see Figure 12). The profile of streamwise velocity differs from the profiles describing by the solution of the equation (8) or formula (9).

Profiles of transverse velocity demonstrates a weak dependency on the injection velocity in the wide interval of parameters of the problem.

Distribution of streamwise velocity along x coordinate is close to linear dependence (see Figure 13). The profiles of transverse velocity have universal behavior, and depend on x coordinate weakly. Starting from $x/h \sim 30$, the profiles of transverse velocity become independent on x coordinate. The results based on $k-\varepsilon$ model show divergence of distribution of streamwise velocity from linear dependence at $x/h > 35$ [20].

Laminar-turbulent transition is defined by the distribution of friction coefficient along solid wall of the channel (see Figure 14), $C_f = 2\tau_w/\rho U^2$, where τ_w is wall shear stress,

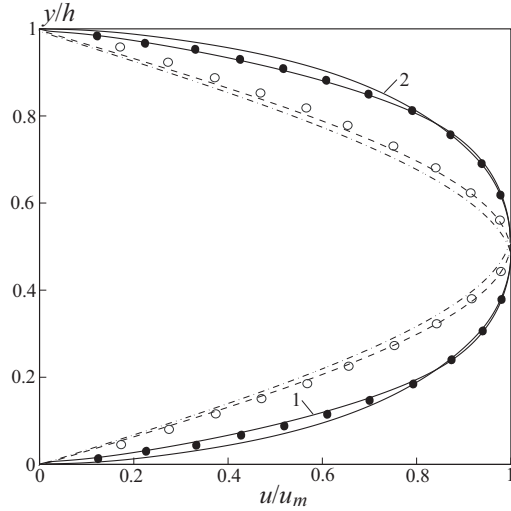


Figure 12. Profiles of streamwise velocity at $v_{w1} = v_{w2} = 2.75$ m/s and $x/h = 20$ (line 1), 60 (line 2). The legend is presented in the Figure 11.

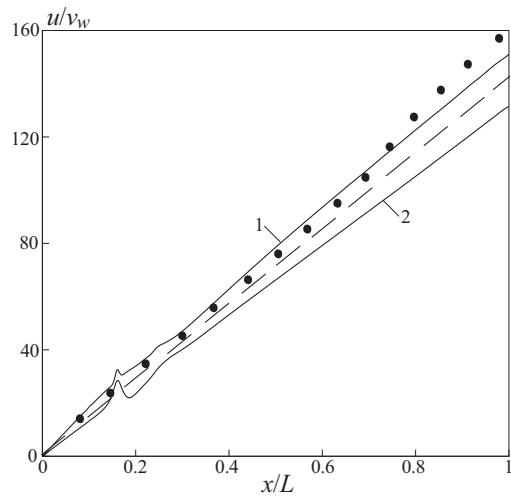


Figure 13. Distributions of streamwise velocity along x coordinate at $v_{w1} = v_{w2} = 2.75$ m/s and $y/h = 0.5$ (line 1), 0.75 (line 2). The dashed line corresponds to theory, and symbols \bullet correspond to the results based on the $k-\varepsilon$ model.

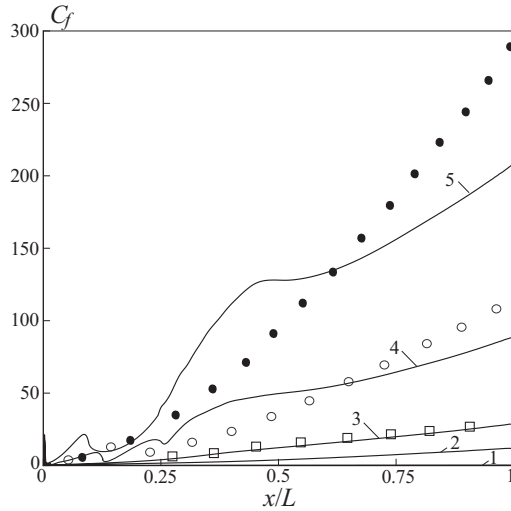


Figure 14. Distributions of friction coefficient along solid wall at $v_{w1} = 0$ and $v_{w2} = 0.1$ (line 1), 0.55 (line 2), 1 (line 3), 2.75 (line 4), 5 (line 5) m/s. The symbols \bullet , \circ , and \square correspond to the results based on the $k-\varepsilon$ model for conditions defined by lines 3, 4 and 5.

U is average velocity. The results computed show that the $k-\varepsilon$ model gives satisfactory prediction of friction coefficient at small injection velocities (line 3). The discrepancy of the results based on LES and $k-\varepsilon$ model increases moving from left boundary of the channel.

Increase in friction coefficient, starting with $x/L \sim 0.2$, corresponds to the laminar-turbulent transition. Location of transition point depends on parameters of the problem, and is sensible to fluctuations of velocity on a permeable wall. The transition point is moved downstream with increase in the injection velocity. Coordinate of the transition point agrees with the data of [24]. The flow pattern computed allows marking the following flow regimes

- Region with considerable influence of viscous forces, $x/h < 1/\text{Re}$
- Region of laminar flow with cosine profile of streamwise velocity, $1 \leq x/h < 5$
- Transition region, $5 < x/h < 10-15$
- Region of turbulent flow, $10-15 < x/h$

The length of laminar flow depends on Reynolds number. The coordinate of transition point decreases with increasing relative amplitude of perturbations at $k_m^{1/2}/u_m > 4\%$.

The feature of the flow in the channel with fluid injection is a negative gradient of pressure. The pressure distribution along the x coordinate presented in the Figure 15 is consistent with the results of [20] based on $k-\varepsilon$ model and data of [21] based on v^2-f model. It is described well by the parabolic dependence, which follows from the equation (9). The pressure distribution demonstrates a weak dependence on fluid injection velocity. The discrepancy of the results presented and data of [20] is explained by the fluid compressibility at $x/h > 30$. The pressure variation along y coordinate is small.

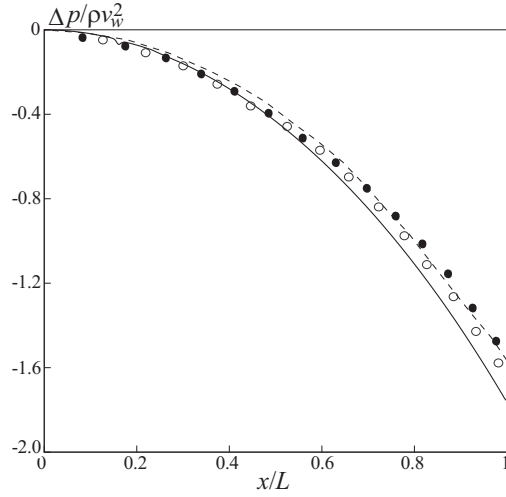


Figure 15. Distributions of pressure along middle line at $v_{w1} = v_{w2} = 2.75$ m/s. The legend is presented in the Figure 11.

The maximum of turbulent kinetic energy is displaced from the wall to the core of channel flow (see Figure 16). The profile of turbulent kinetic energy has two maxima, located near the walls of channel. The intensity of turbulence increase takes place in the region of shear flow on some distance from the permeable wall, where fluid particles, moving normal to the wall, are forced to turn round in the narrow near-wall region. The maximum of turbulent kinetic energy located near the solid wall of the channel is almost 2 times as small. The results computed are consistent with the experimental data of [22], except for near-wall region, where calculations overestimate turbulence intensity [24]. For the two-sided injection, production of turbulence in the central region of channel does not occur, and its level is very small.

The results of [20] based on $k-\varepsilon$ model predict maximum of turbulent kinetic energy far from the permeable wall of the channel and overpredict a turbulence intensity near the walls compared to experimental data and results of DNS presented in [22, 24].

For a two-sided fluid injection, the distribution of turbulent kinetic energy and its dissipation rate along x coordinate is well described by the dependencies $k \sim x^2 k(y)$ and $\varepsilon \sim x^3 \varepsilon(y)$ (see Figure 17). These dependencies were used to construct a simplified model of the turbulent flow in the channel with wall injection and arbitrary shape of cross section [20]. Increase of turbulent kinetic energy at $x/L \sim 0.2$ corresponds to the transition point.

Contribution of the fluctuations of streamwise and transverse velocities to the balance of turbulent kinetic energy is approximately the same.

7. Free mixing layer

Comparison of accuracy and computational effectiveness of some SGS models (Smagorinsky model, RNG model, dynamics model and one-equation model) are performed for free

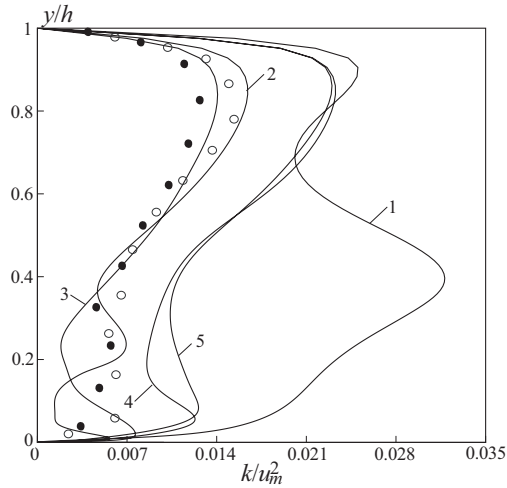


Figure 16. Profiles of turbulent kinetic energy at $x/h = 40$. The legend is presented in the Figure 11.

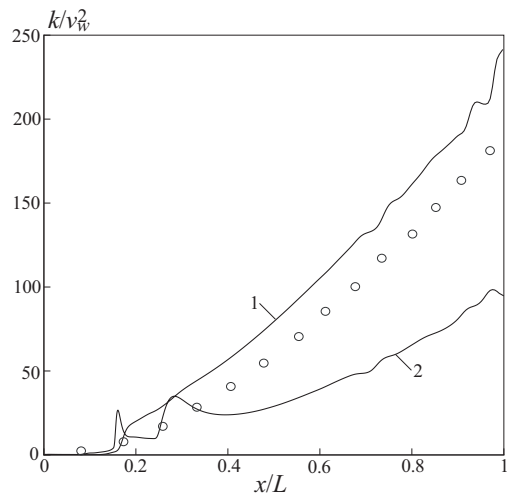


Figure 17. Distributions of turbulent kinetic energy along x coordinate at $v_{w1} = v_{w2} = 2.75$ m/s and $y/h = 0.5$ (line 1), 0.75 (line 2). The legend is presented in the Figure 11.

mixing layer.

7.1. Self-similar solutions

A fully developed turbulent flow in a free mixing layer is semi-similar with a linear growth of width of mixing zone. The width of the turbulent mixing region is commonly presented as

$$L = \frac{1}{2} \alpha_u f (\rho_1/\rho_2) |u_1 - u_2| t,$$

where α_u is constant ($\alpha_u \sim 0.38$), t is interaction time of mixing flows, f is function defining dependence of mixing width on density ratio. Indexes 1 and 2 correspond to mixing flows.

In practice, the change of variable $x = u_c t$ is used for studying of the mixing layer, and the spatial problem is transformed into the temporal problem. The width of the mixing region is recorded as

$$L = \frac{1}{2} \alpha_u f (\rho_1/\rho_2) |u_1 - u_2| \frac{x}{u_c},$$

where u_c is characteristic velocity connecting spatial and temporal formulations of the problem.

The effective velocity is defined by different ways [27], e.g.

$$\begin{aligned} u_c &= \frac{1}{2} (u_1 + u_2), \\ u_c &= \frac{1}{2} (u_1 + u_2) \left[1 + \frac{1}{3} \left(\frac{u_1 - u_2}{u_1 + u_2} \right)^2 \right]^{1/2}, \\ u_c &= \frac{1}{2} (u_1 + u_2) \left[1 + \frac{8}{15\pi} \left(\frac{u_1 - u_2}{u_1 + u_2} \right)^2 \right]. \end{aligned}$$

In mixing of flows of various density, the following correlation is used

$$u_c = \frac{\rho_1 u_1 + \rho_2 u_2}{\rho_1 + \rho_2}.$$

With high drops in density of mixing substances, the integral definition of effective velocity is preferable

$$u_c = \int_{y_1}^{y_2} \rho u dy / \int_{y_1}^{y_2} \rho dy,$$

where y_1 and y_2 are boundaries of the mixing region.

The inapplicability of the Taylor hypothesis for the transition from the spatial to the temporal problem in the three-dimensional case is demonstrated in [29, 28].

In [30], the data based on some nonlinear turbulence models are compared to the data obtained with the $k-\varepsilon$ model and the Reynolds stress model. The results show that nonlinear models appear more sensitive to the impact of the curvature of streamlines in calculations of shear flows.

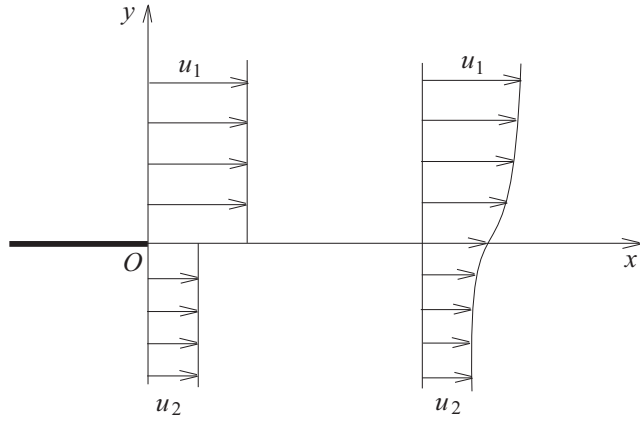


Figure 18. Free mixing layer.

Boundary conditions at the inlet are specified using results for turbulent boundary layer on a flat plate [31, 32]. In order to reduce computational expenses, an approximate method of calculation of boundary layer is applied, similar to the Karman–Paulauzen method [33].

In works [34, 35] evolution over time of the mixing layer is considered. Periodic boundary conditions are specified in the streamwise direction. This allows saving on computational resources yet does not account for effect of curvature of streamline and spatial inhomogeneity of the flow.

Simulation of the mixing layer's spatial evolution is performed in [36, 37, 38]. It is noted that the three-dimensional nature of the flow must be taken into account when increasing the effective Mach number at the inlet [39, 40]. Solution of the problem in a two-dimensional formulation leads to overestimation of intensity of the velocity fluctuations [41].

7.2. Boundary conditions

Let us consider two semi-infinite fluid flows moving in the same direction with the velocities u_1 and u_2 relative to one another in the same plane, $x < 0, y = 0$. In the point $x = 0$ the flows come into contact and further on (with $x > 0$) the boundary between them is turbulentised (see Figure 18).

Unsteady-state boundary conditions defined by the fluctuation pattern of flow need to be assigned in the inlet section. Free shear flows are unstable, and oscillation in these flows arises in the absence of external sources of disturbances.

The profile of streamwise velocity is defined as [41]

$$u(y) = \frac{1}{2} (u_1 + u_2) + \frac{1}{2} (u_1 - u_2) \tanh \left[\frac{y}{2\delta_m(0)} \right],$$

where $\delta_m(0)$ is momentum thickness at the point $x = 0$.

In order to set boundary conditions on the inlet boundary, the profiles of velocity and other flow parameters should be defined, which were obtained from the calculation of turbulent boundary layer on a flat plate (with the same mesh resolution). This way seems

quite expensive from the computational point of view, and other methods of formulation of non-stationary boundary conditions on the inlet boundary are applied.

1. The flow interface is disturbed at random with given amplitude. The transverse velocity is changed according to the law

$$v = v_a \sin \omega t,$$

where v_a is amplitude, and ω is frequency ($v_a \sim 2$ m/s and $\omega \sim 400$ rad/s in calculations).

2. Uniform profiles of streamwise velocity, density and pressure are specified on the inlet boundary with imposed random oscillations (white noise). Root-mean-square velocity is selected as 0–8% from the effective velocity u_c .

Non-reflecting boundary conditions are applied to the outlet boundary. Slip boundary conditions are specified on the remote boundaries of fluid domain in y direction

$$\frac{\partial u}{\partial y} = v = \frac{\partial w}{\partial y} = 0.$$

Periodic boundary conditions are specified in z direction.

7.3. Parameters of flow

The flow in the free mixing layer is characterized by the following parameters:

- Difference of velocities of mixing flows

$$\Delta u = u_2 - u_1$$

- Effective Mach number

$$M_c = \frac{u_1 - u_2}{a_1 + a_2}$$

- Momentum thickness

$$\delta_m(x) = \frac{1}{(\Delta u)^2} \int_{-\infty}^{+\infty} \rho (u - u_1) (u_2 - u) dy$$

- Reynolds numbers based on difference of velocities and effective velocity

$$Re_m = \frac{\Delta u \delta_{m0}}{\nu}, \quad Re_c = \frac{u_c \delta_{m0}}{\nu}$$

- Vorticity thickness

$$\delta_\omega(x) = \frac{u_{\max} - u_{\min}}{\max_y(\partial u / \partial y)}.$$

- Reynolds number based on vorticity thickness

$$Re_\omega = \frac{\Delta u \delta_{\omega 0}}{\nu}, \quad \delta_{\omega 0} = \left(\frac{\Delta u}{\partial u / \partial y} \right)_{x=0}$$

To compare the results computed with experimental data, the defect of velocity and the transformed coordinate normal to flow direction are introduced

$$\Delta u(\xi) = \frac{u(\xi) - u_2}{u_1 - u_2} \in [0, 1], \quad \xi = \frac{y - y_1}{y_2 - y_1} \in [0, 1].$$

The initial velocity profiles are re-calculated depending on the ξ coordinate for all x and then they are averaged over the x coordinate.

7.4. Mesh

The mesh is refined to the edge of the plate, near the flow separation plane and by the remote boundaries of the computational domain. The coordinates of nodes in y direction are obtained from the correlation [41]

$$y = \begin{cases} \Delta y_0 (a^{j-1} - 1) / (a - 1) & \text{for } j \leq j_p \\ y_p + \Delta y_p (b^{j-j_p}) / (b - 1) & \text{for } j > j_p \end{cases},$$

where $\Delta y_p = \Delta y_0 a^{j_p-1}$, $j = 1, 2, \dots, N$. The node with y_p coordinate is located on the border between the internal and external sub-regions, and its index is

$$j_p = 1 + \ln [1 + y_p(a - 1)/\Delta y_0] / \ln a.$$

The a and b determine the closeness of mesh nodes with $y < y_p$ and $y > y_p$ respectively, and they are $\Delta y_{j+1}/\Delta y_j$. The maximum aspect ratio of cell is

$$A_m = \frac{\max_{j=0,\dots,N} \Delta y_j}{\min_{j=0,\dots,N} \Delta y_j} = \frac{\Delta y_N}{\Delta y_0}.$$

In computations, $\Delta x = 0.25$, $y_p/L_y = 0.125$, $\Delta y_0 = 0.12$, $a = 1.0$, $b = 1.02$, $A_m = 4.8$.

The stretch function is applied to the nodes located above the flow separation plane, up to the upper boundary of the computational domain. The node distribution obtained is then mirror-reflected from the flow separation plane.

The calculations are performed on the mesh $500 \times 80 \times 80$. The length of the domain is $25\delta_{\omega 0}$ and its width is $6\delta_{\omega 0}$, the y coordinate changes from $-3\delta_{\omega 0}$ to $+3\delta_{\omega 0}$. In the z direction, the domain spreads by $5\delta_{\omega 0}$. Refinement of mesh is achieved in such a way that the filter width is approximately in the order of length of Taylor's micro-scale near the flow separation aline.

The time step is $\Delta t = 1.5 \times 10^{-3}$ s, and 50 000 time steps are performed.

7.5. Results and discussion

The velocities of mixing flows are $u_1 = 78$ m/s and $u_2 = 200$ m/s. The working fluid is air. For these parameters, $\delta_{\omega 0} = 0.021$ m and $\text{Re}_{\omega} = 21600$, which corresponds to fully developed turbulent flow.

The profiles of streamwise velocity are presented in the Figure 19. The symbols \circ correspond to Smagorinsky's model, symbols \triangle correspond to RNG model, symbols \bullet

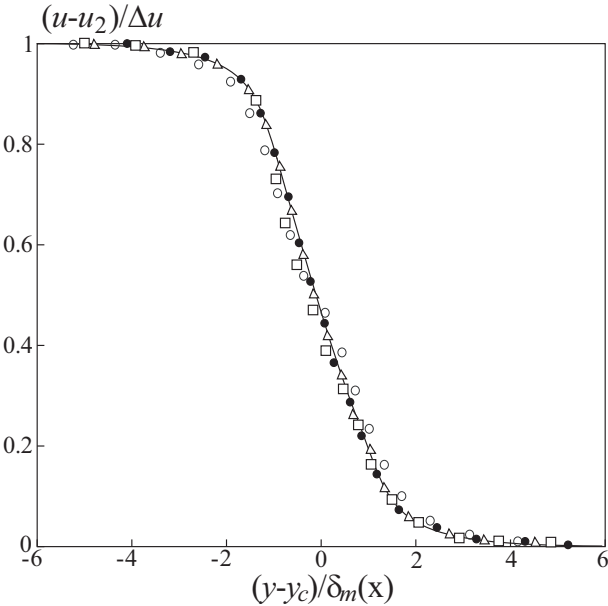


Figure 19. Profiles of streamwise velocity based on different SGS models.

correspond to dynamic model, and symbols correspond to one-equation model. The solid line shows a theoretical profile of streamwise velocity.

The Smagorinsky model predicts a less filled profile of streamwise velocity, while RNG model and dynamic model have approximately the same accuracy. The one-equation model gives a small error in the low-velocity region of mixing layer.

The Figure 20 demonstrates influence of features of specification of inlet boundary conditions on the results computed (RNG model is used), where σ_u is root-mean-square streamwise velocity. The solid lines correspond to the results obtained with uniform profile of streamwise velocity at the inlet and imposed random oscillations (white noise). The symbols \bullet correspond to the results obtained with sinusoidal velocity oscillator at point $x = 0$.

The profiles of streamwise and transverse velocities are in a good agreements with universal dependencies for wide interval of effective Mach number (see Figure 21). The profiles of streamwise velocity in x direction and at fixed inlet Mach number coincide in transformed coordinates.

The central streamline is defined by the y_c coordinate so that, with the increase in effective Mach number, M_c , the line $u(y = y_c) = u_c$ moves to the region of the low-velocity flow (see Figure 22).

Distribution of intensity of fluctuations of streamwise and transverse velocities as well as distribution of shear stress and the asymmetry coefficient, $s_u = \langle u'^3 \rangle / \sigma_u^3$, are shown in the Figure 23 and Figure 24 at $M_c = 0.42$.

The results agree quite well with the experimental data [40] for $M_c = 0.46$, excluding distribution of fluctuations of transverse velocity (see Figure 25). The measurements demonstrate a lower level of intensity of fluctuations of transverse velocity. It must be

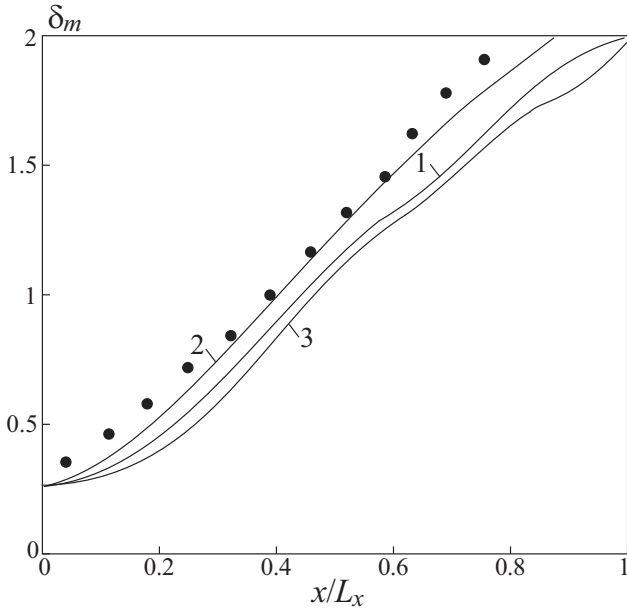


Figure 20. Dependence of momentum thickness on formulation of inlet boundary conditions at $\sigma_u/u_c = 0.01$ (line 1), 0.03 (line 2), 0.08 (line 3).

noted that such an effect (overestimation of the level of the fluctuations of transverse velocity) is observed in [37] and can be explained by the energy transfer from small-scale eddies to large-scale ones. The author of [39] mentions that overestimation of the level of fluctuations takes place when different SGS models of eddy viscosity are used.

When passing through the central streamline, the asymmetry coefficient changes the sign. Local extremum occurs when $y = \pm 2\delta_m$ and $y = \pm 6\delta_m$. Computational results agree qualitatively with the data of [39], excluding the boundaries of the mixing zone, which can be explained by influence of initial disturbances of the transverse component of velocity.

Momentum thickness decreases with increasing effective Mach number (see Figure 26), which corresponds to the data of [39, 40, 42].

8. Free turbulent jet

LES of a subsonic non-isothermal turbulent round submerged jet is performed. The calculations are produced for different degrees of jet preheating. The post-processing of the results computed enables one to obtain the distributions of correlation moments of density, velocity and temperature along the axis and in cross sections of the jet. The results obtained are compared with the available data obtained using the solution of RANS equations closed with the $k-\varepsilon$ turbulence model, as well as with the experimental data.

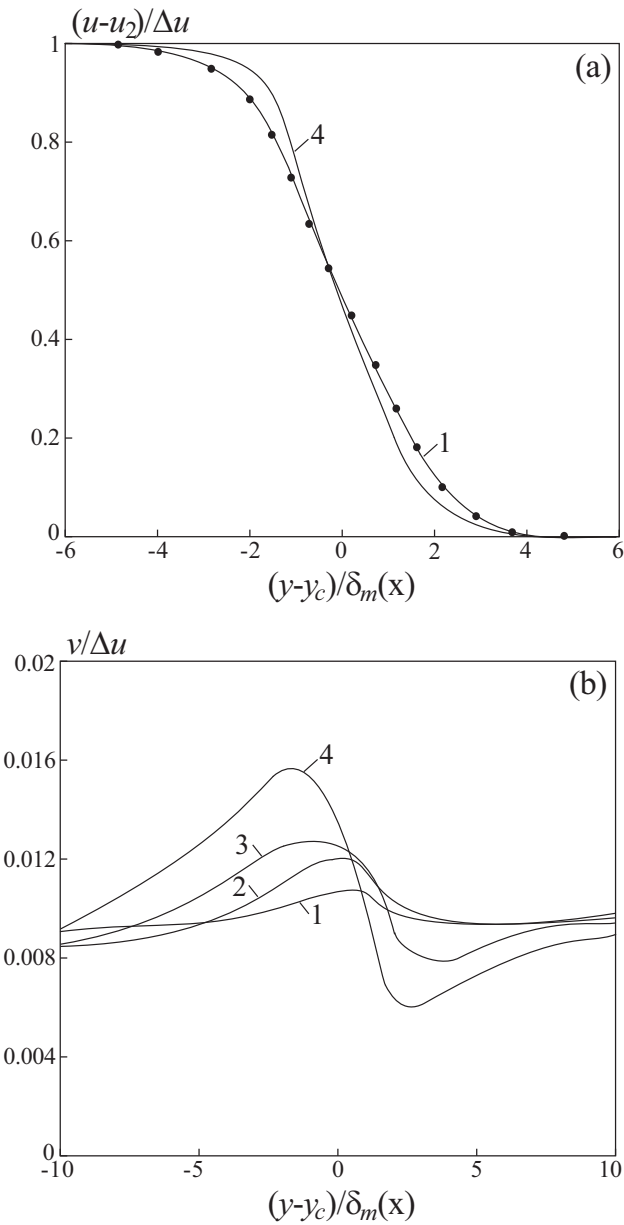


Figure 21. Profiles of streamwise (a) and transverse (b) velocities at $M_c = 0.2$ (line 1), 0.4 (line 2), 0.6 (line 3), 0.8 (line 4). Symbols \bullet correspond to data of [39].

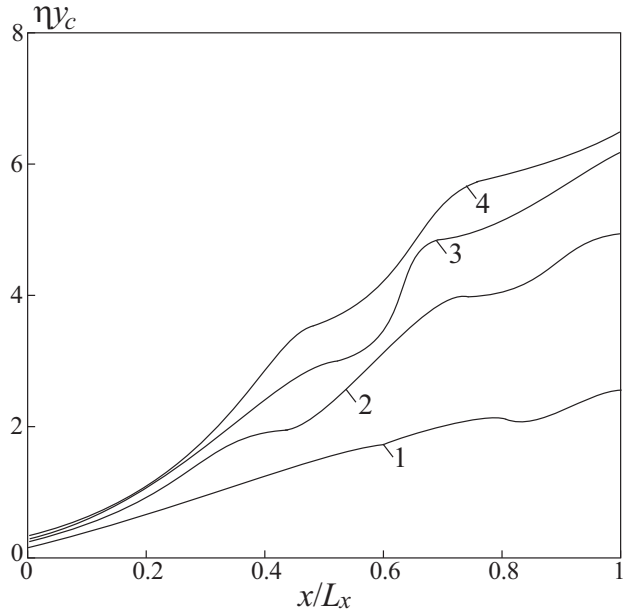


Figure 22. Dependence of central streamline on effective Mach number at $M_c = 0.2$ (line 1), 0.4 (line 2), 0.6 (line 3), 0.8 (line 4).

8.1. Methods of simulation

Considerable attention is given in the literature to physical and numerical simulation of subsonic turbulent jets. The characteristics of non-isothermal jets were measured in [43, 44, 45, 46, 47, 48, 49, 50, 51]. Main attention in [48, 49, 50, 51] was given to the investigation of the degree of preheating on the turbulent structure of jet flow.

Various turbulence models were employed for numerical calculations [52, 53] as well as DNS and LES [54, 55, 56, 57, 58, 59, 60]. Referred to in [54] as DNS were approaches, in which the eddy viscosity depends on the mesh step. The calculations on a coarse mesh without using any SGS model were performed in [55, 56]. The dissipative mechanism was introduced using a difference scheme (Monotonically Integrated LES).

The solution obtained using DNS or LES carries more information compared to the solution of RANS equations. It contains information both on the characteristics of mean flow (e.g. velocity, temperature and pressure) and on the spectral characteristics, two-point moments and higher-order moments, and distributions of turbulent Prandtl number and constant in the formula for eddy viscosity

The Smagorinsky model [57, 58] and the structure function model [59], as well as the dynamic model [60] and similarity scale model [57], were used in practice. In [58], the emphasis was on the processes of formation of a mixing layer in the initial region of the jet and of its development downstream, as well as on the impact made by the Smagorinsky constant on the characteristics of the jet. The discrepancy between the computational and experimental data is explained by the intermittency of flow and reverse transition of energy from small to large eddies [57] (back-scatter).

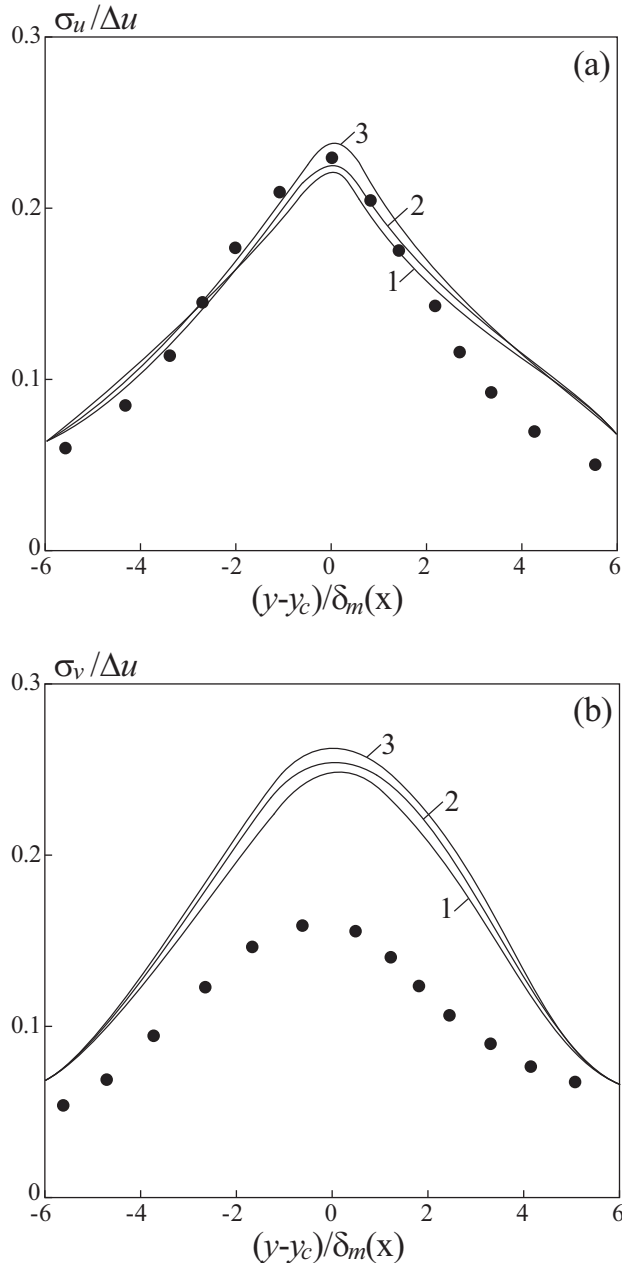


Figure 23. Distributions of root-mean-square streamwise (a) and transverse (b) velocities compared to experimental data of [40] (symbols \bullet) at $x/L_x = 0.6$ (line 1), 0.7 (line 2), 0.8 (line 3).

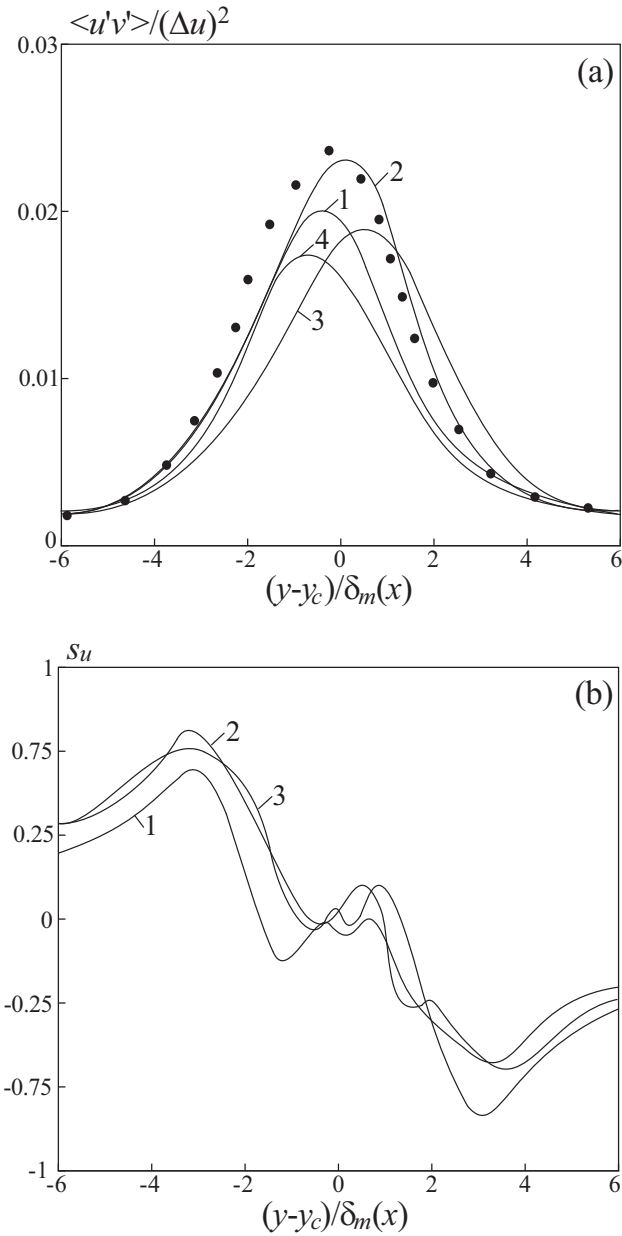


Figure 24. Distributions of shear stress (a) and asymmetry coefficient (b) compared to experimental data of [40] (symbols \bullet) at $x/L_x = 0.6$ (line 1), 0.7 (line 2), 0.8 (line 3), 0.9 (line 4).

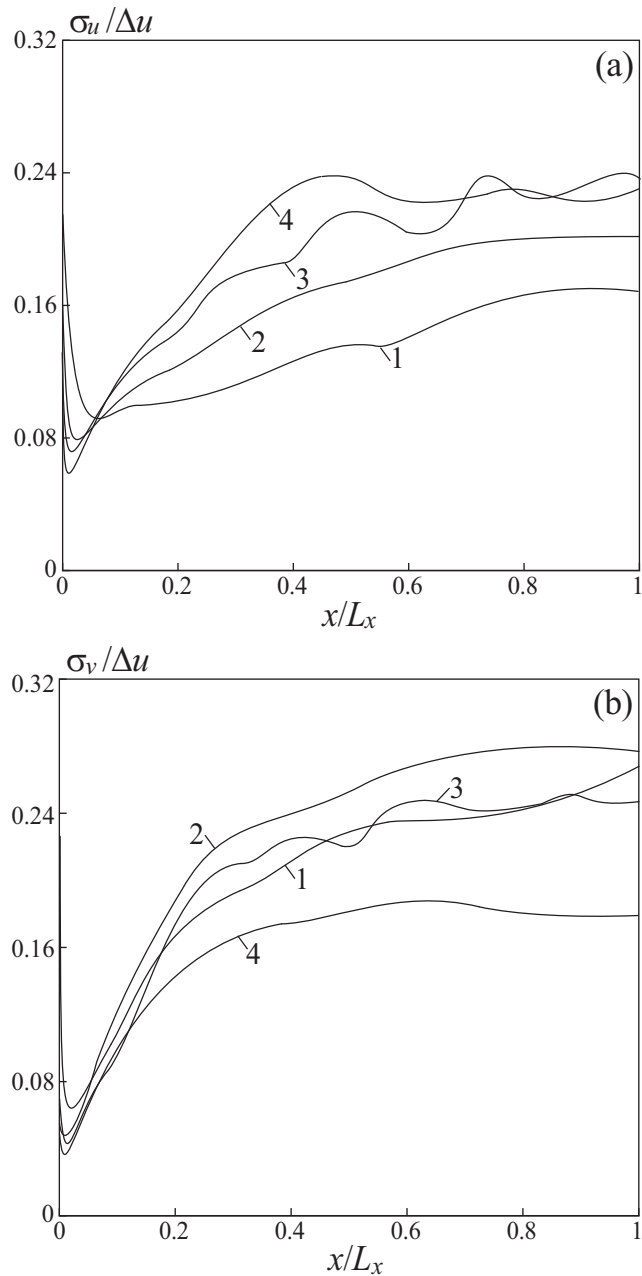


Figure 25. Distributions of maximum of fluctuations of streamwise (a) and transverse (b) velocities along x coordinate at $M_c = 0.2$ (line 1), 0.4 (line 2), 0.6 (line 3), 0.8 (line 4).

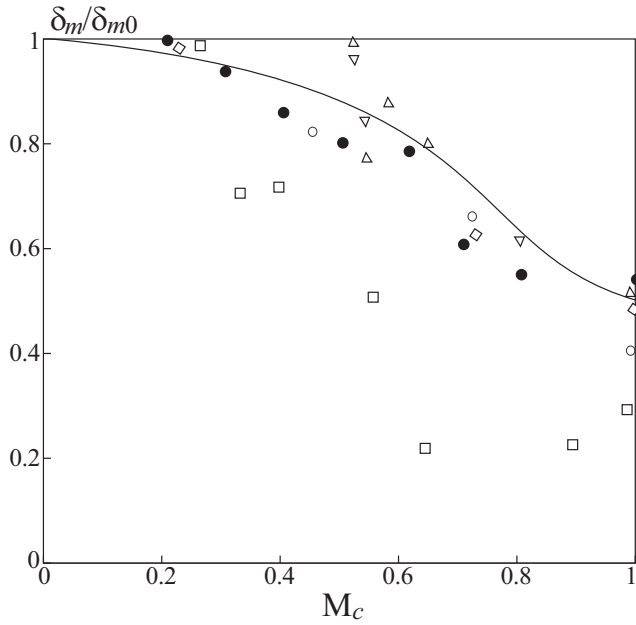


Figure 26. Dependence of momentum thickness on effective Mach number. Symbols \bullet correspond to computational data, symbols \square correspond to data of [42], symbols \diamond , and \triangledown correspond to data of [39], symbols \circ correspond to data of [40].

Some researchers employed the axisymmetric formulation of the problem [57]. This conflicts with the concept of LES, which presumes the solution of unsteady-state three-dimensional equations.

8.2. Boundary conditions

We will consider a turbulent jet of heated gas, which flows out of a round nozzle into submerged space. The origin of point is located at the nozzle outlet. The positive reading of x coordinate is made in the direction of propagation of the jet. The radius of nozzle, r_a , is the characteristic scale for variables with the dimensionality of length. The velocity u_a and temperature T_a at the nozzle outlet are the characteristic scales for variables with the dimensionality of velocity and temperature. The temperature of surrounding fluid is T_∞ . The flow in the jet is characterized by the preheat parameter, $\vartheta = T_a/T_\infty$ (for isothermal jet, $\vartheta = 1$) and by the intensity of turbulence, $\theta = u'/u_a$, where u' is the fluctuation velocity.

Correct assignment of boundary conditions calls for the calculation of flow in the pipe and in the boundary layer on the external surface of the nozzle [56] (a part of the nozzle is included in the computational domain). No calculation of flow in pipe is performed, and a velocity profile is preassigned at the nozzle outlet section at $|r| \leq r_a$, on which random sinusoidal oscillations are imposed [60]

$$v_x(r, t) = \frac{u_a}{3} \left[1 + \tanh \left(\frac{0.5 - |r|}{2\delta} \right) \right] [1 + \alpha \sin(\text{Sh } t)],$$

where δ is the momentum thickness, α is the amplitude of disturbances, and Sh is the Strouhal number. It is assumed that $\delta/r_a \sim 0.1$, $\alpha = 2.1 \times 10^{-3}$, and $\text{Sh} = 0.42$. Small random oscillations are further imposed on the radial distribution of circumferential velocity

$$v_\theta(r, t) = 0.025 \exp \left[-3(1 - |r|)^2 \right] \phi,$$

where ϕ is a random number from uniform distribution in $[0.5, 0.5]$. The radial velocity at the nozzle exit is taken to be zero.

The boundary conditions away from a jet flowing out into submerged space are defined by the ejection properties of the jet, and an induced potential flow directed towards the jet exists away from the jet exists. The properties and parameters of this flow are not known in advance and are defined by the jet proper. The calculations of steady-state flows reveal that the best results are produced by the boundary conditions based on the exact solution which describes a potential flow outside of a round turbulent jet [54].

Non-reflecting boundary conditions are used on the outflow boundary.

8.3. Results and discussion

The calculations are performed for $r_a = 5$ mm, $u_a = 80$ m/s, $\rho_a = 0.58\text{--}1.26$ kg/m³, $T_a = 280\text{--}600$ K, $\rho_\infty = 0.58\text{--}1.26$ kg/m³, $T_\infty = 280\text{--}600$ K. The parameters at the nozzle outlet correspond to Reynolds number $\text{Re} = 1.2 \times 10^5$, which is maintained constant owing to proper variation of dynamic viscosity, and to the range of variation of degree of preheating $\vartheta = 0.48\text{--}2.15$.

The calculations are performed in the domain $[0, L_x] \times [-L_y, L_y] \times [-L_z, L_z]$, where the length of domain is $L_x = 100r_a$, and its width and height in the inlet and outlet sections are $L_y = L_z = 10r_a$ and $L_y = L_z = 40r_a$.

The mesh contains $350 \times 150 \times 150 = 7\,875\,000$ nodes. In the initial region of the jet, the mesh is uniform up to $x \sim 10r_a$, then mesh is refined, so $\Delta x_{\min} = 0.08r_a$ and $\Delta x_{\max} = 0.15r_a$. In the cross section, the mesh nodes are concentrated towards the nozzle outlet, so $\Delta y_{\min} = \Delta z_{\min} = 0.03r_a$ and $\Delta y_{\max} = \Delta z_{\max} = 0.09r_a$.

The time step is $\Delta t = 0.08r_a/u_a = 5.8 \times 10^{-5}$ s. A statistically reliable averaged pattern of flow is obtained by making 10^5 time steps.

The contours of the vorticity are presented in the Figure 27 at $\vartheta = 1.2$. Large-scale eddy structures are present in the shear layer of the jet in the form of toroidal axisymmetric eddies arising at some distance from the nozzle outlet. In the initial region of the jet, the size of eddy structures is fairly small. Downstream of the initial region, the size of eddy structures increases, and the momentum exchange between the jet and surrounding fluid is intensified. The contours of coherent structure are ellipses, which implies the anisotropy of turbulent fluctuations.

The results computed demonstrate that the velocity and temperature profiles in the flow cross sections exhibit a typical jet pattern, as well as a kink in the middle part. The profiles become wider with increasing axial coordinate, which points to the increase in the thickness of the zone of jet mixing with the surrounding fluid. Near the jet boundary, the profiles become sloping.

As a result of the impact made by non-isothermality on the turbulent structure of the jet, the maximum of intensity of fluctuations of axial velocity at $\vartheta < 2.1$ increases with

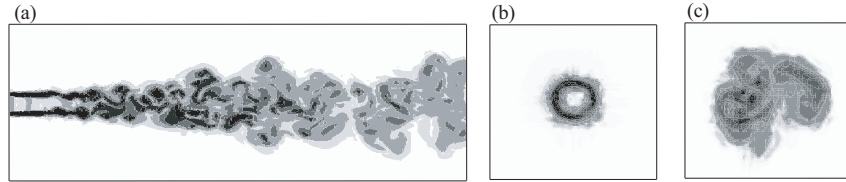


Figure 27. Contours of vorticity at $t = 2.32$ s in the axial plane of the jet (a), and radial planes at $x/r_a = 10$ (b) and $x/r_a = 80$ (c).

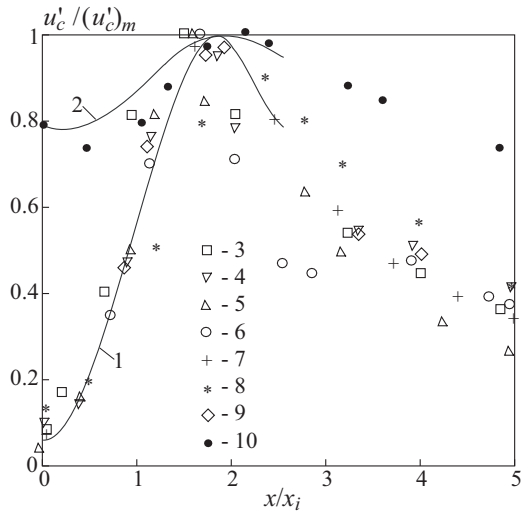


Figure 28. Profiles of turbulence intensity along axial coordinate. Lines 1 and 2 correspond to jets with natural ($\theta = 2\%$) and increased ($\theta = 8\%$) levels of turbulence, — data of [50] ($\vartheta = 2.6$), ∇ — data of [50] ($\vartheta = 3.9$), Δ — data of [50] ($\vartheta = 5$), \circ — data of [48] ($\vartheta = 2$), $+$ — data of [51] ($\vartheta = 1, \theta = 1.5\%$), $*$ — data of [49] ($\vartheta = 2.32, \theta = 1.5\%$), — data of [43] ($\vartheta = 1, \theta = 9.3\%$), \bullet — data of [43] ($\vartheta = 1, \theta = 20.9\%$).

the degree of preheating and amounts to about 25% of velocity at the nozzle outlet (see Figure 28). This is much higher than the respective values in a jet of cold gas, where they do not exceed 16% [50, 51].

As the degree of preheating of the jet increases, the maximum of fluctuations of axial velocity shifts towards the nozzle outlet. A further increase in the degree of preheating causes a qualitative variation of the pattern of this impact (according to the data of [51]), and the maximum of fluctuations of axial velocity decreases. A similar impact is made by the non-isothermality of flow on the distribution of intensity of temperature fluctuations, the maximum of which is of the order of 13% of the temperature difference at the nozzle outlet.

The results of [43, 49, 51] demonstrate that the maximum of fluctuations of axial velocity occurs at $x/r_a \sim 16$. In the region of the core of constant velocity, the intensity

of turbulence, while remaining almost constant in the transverse direction, increases from 1.5–2% at the nozzle outlet to a value of the order of 6% at the end of the initial region with increasing distance from the nozzle. Because no turbulent mixing is present within the jet core, the effect of the increase in the degree of turbulence is associated with the penetration of pressure fluctuations from the mixing zone into the core. The fluctuations of velocity on the jet axis reach a maximum at a distance equal to two lengths of initial region, x_i (see Figure 28, subscript c indicates the jet axis). This value remains almost constant for both isothermal and non-isothermal jets and depends relatively weakly on the conditions of outflow [51].

The increase in the intensity of turbulence at the nozzle at $\theta > 5\%$ causes the rearrangement of the microstructure of flow, the intensification of the mixing of jet with surrounding fluid, and the decrease in the range of the jet [43] (down to complete disappearance of the initial segment). A significant difference is observed in the pattern of variation of turbulent kinetic energy along the jet axis at low and high levels of initial turbulence. At a low degree of turbulence in the nozzle, the turbulent kinetic energy increases, reaches a maximum, and then slowly decreases. In the case of a high intensity of turbulence in the nozzle, the turbulent kinetic energy decreases along the jet axis, increases and reaches a maximum. Then it decreases downstream by the power law. At the very high initial degree of turbulence, the turbulent kinetic energy continuously decreases downstream.

The Figure 29 gives the distribution of root-mean-square axial velocity, $\langle v_x'^2 \rangle$, radial velocity, $\langle v_r'^2 \rangle$, and temperature, $\langle T'^2 \rangle$, as well as of the correlation moment of axial velocity and temperature, $\langle v_x' T' \rangle$, along axial coordinate. Line 5 from [47] corresponds to the approximate solution based on the model of [52]. The results are normalized to $10u_a$ and the temperature difference of $10\Delta T_a$. In the initial segment of the jet, the fluctuation parameters assume values typical of fully developed turbulent flow in a round pipe. In the far field of jet, these vary by a close-to-power law. The increase in temperature fluctuations begins from a distance $x/r_a \sim 6$, while the fluctuations of axial and radial velocities start increasing at $x/r_a \sim 8$. These values of axial coordinate, which correspond to the lengths of the thermal and dynamic initial regions, are close to values corresponding to the minimum of distributions of skewness and flatness factors of temperature and velocity.

The profiles of correlation moment of axial velocity and temperature, $\langle v_x' T' \rangle$, and correlation moment of radial velocity and temperature, $\langle v_r' T' \rangle$, are presented in the Figure 30. Radial coordinate is normalized to the half radius of the jet, r_u . The data of [44] correspond to cross section $x/r_a = 118$, and the data of [45, 46] correspond to cross section $x/r_a = 30$.

The radial coordinate, at which the correlation moments of velocity and temperature reach a maximum, almost coincide in sections $x/r_a = 10$ and $x/r_a = 30$, and correspond to the position of maximum of turbulent kinetic energy ($r/r_u = 0.8$ according to the data of [45] and $r/r_u = 0.7$ according to the data of [46]). However, the maximum and shape of the profiles computed of the moment of axial velocity and temperature differ from those obtained experimentally. Apparently, this is explained by the impact of the outflow conditions. The results for the moment $\langle v_r' T' \rangle$ better agree with the experimental data than those for the moment $\langle v_x' T' \rangle$.

In the near field of jet at $x/r_a \sim 10$, the heat transfer occurs along axial coordinate, because $\langle v_x' T' \rangle / \langle v_r' T' \rangle \sim 2$ at $0.2 < r/r_u < 1.4$. Downstream at $x/r_a \sim 30$, the

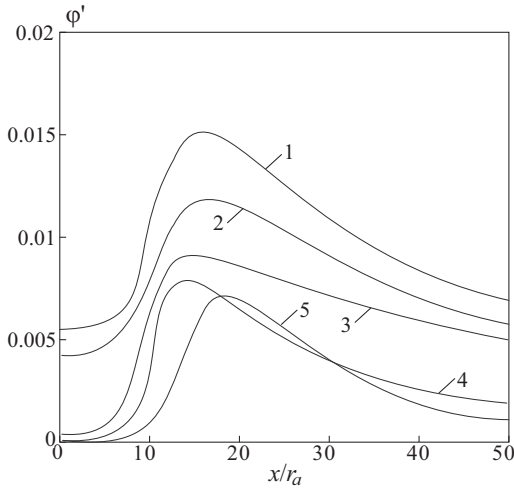


Figure 29. Profiles of root-mean-square axial velocity (line 1), radial velocity (line 2), temperature (line 3), and correlation moment of axial velocity and temperature (line 4) along the jet axis at $\vartheta = 1.2$. Line 5 corresponds to the data of [47].

contributions made by the axial and radial heat fluxes become approximately equal, so that $\langle v'_x T' \rangle / \langle v'_r T' \rangle \sim 1.1$ at $0.5 < r/r_u < 1.8$. In a plane jet, $\langle v'_x T' \rangle / \langle v'_r T' \rangle \sim 2$ at $x/r_a = 80$ and $0.4 < r/r_u < 1.3$ [44] ($Re = 7.9 \times 10^3$ and $\Delta T = 25$ K). In an axisymmetric jet, the measurements of [44] give $\langle v'_x T' \rangle / \langle v'_r T' \rangle \sim 1$ downstream of section $x/r_a \sim 100$ and at $0.3 < r/r_u < 1.3$.

The profiles of correlation moments of density and velocity along the jet axis, which characterize the anisotropy of mass flow, are shown in the Figure 31 (calculations are normalized to $\rho_a u_a$). The results are in qualitative agreement with the data of [53] based on $k-\varepsilon$ turbulence model which does not include the anisotropy of turbulent fluctuations of velocity but enables one to estimate the anisotropy of diffusion flow of mass. The anisotropy is observed at $4 < x/r_a < 40$. Downstream, we have $\langle \rho' v'_r \rangle / \langle \rho' v'_x \rangle \sim 1$ at $x/r_a > 40$.

The discrepancy of PDF from Gaussian distribution is characterized by the skewness factor (third moment), S_φ , and flatness factor (fourth moment), F_φ . The coefficient of n th moment is defined as

$$M_n(\varphi) = \frac{\langle \varphi'^n \rangle}{\langle \varphi'^2 \rangle^{n/2}}.$$

In so doing, $S_\varphi = M_3$ ($n = 3$) and $F_\varphi = M_4$ ($n = 4$). For Gaussian distribution, $S_\varphi = 0$ and $F_\varphi = 3$.

The results obtained demonstrate that the distributions of skewness and flatness factors along the jet axis are non-monotonic. At small distances from the nozzle (at $x/r_a < 6$), the fluctuations of velocity and temperature approximately satisfy the normal probability distribution, which is reflective of the respective normal distribution of velocity and temperature fluctuations at the nozzle outlet. High skewness and flatness factors are found at the end of potential core. At $x/r_a > 40$, non-Gaussian probability distribution is observed.

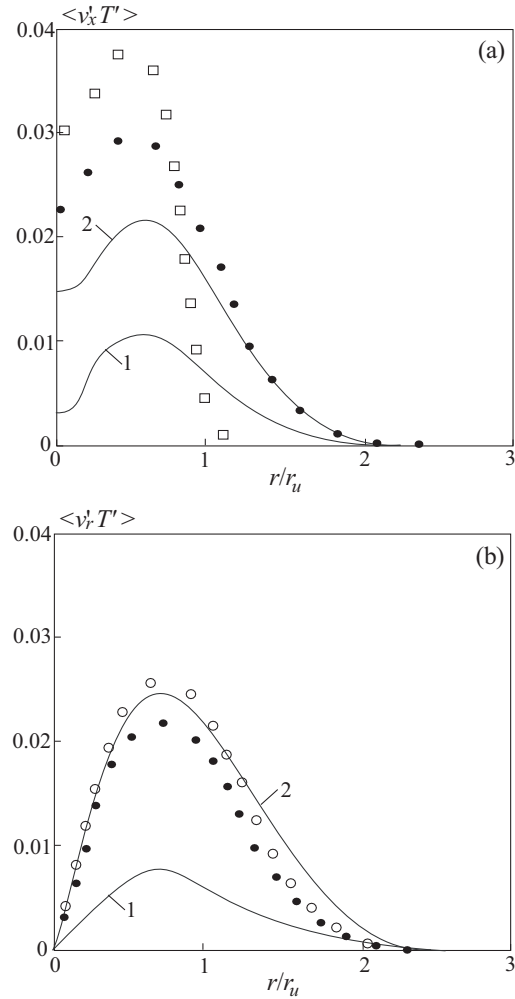


Figure 30. Profiles of the correlation moments of axial velocity and temperature (a), and correlation moment of radial velocity and temperature (b) at $\vartheta = 1.2$ in cross sections $x/r_a = 10$ (line 1) and $x/r_a = 30$ (line 2) compared to the data of [44] (symbols), [45] (symbols ●), and [46] (symbols ○).

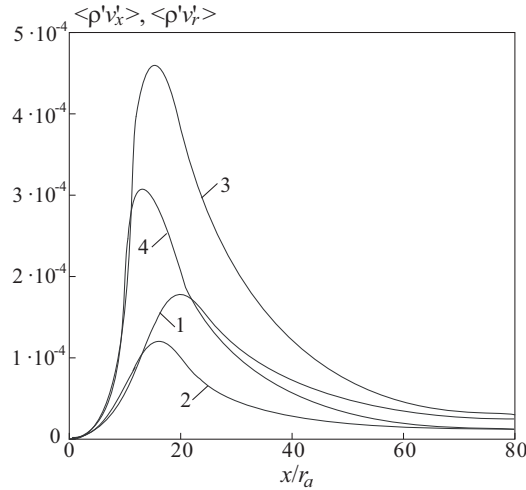


Figure 31. Profiles of correlation moment $\langle \rho' v'_x \rangle$ (lines 1, 3) and correlation moment $\langle \rho' v'_r \rangle$ (lines 2, 4) along the jet axis at $\vartheta = 0.6$ (lines 1, 2) and $\vartheta = 2$ (lines 3, 4).

The axial distributions of the skewness and flatness factors of the velocity and temperature are given in the Figure 32. While the distributions of the third and fourth moments of velocity and temperature are qualitatively and quantitatively similar in the far flow of the jet, they significantly differ at $0.4 < x/r_a < 16$. The rearrangement of S_T and F_T distributions is faster than that of S_v and F_v . In particular, the factors S_T and F_T reach maximum at $x/r_a \sim 6$, while S_v and F_v reach maximum at $x/r_a \sim 10$. Their maximum corresponds to the jet section in which the mixing layers reach the jet axis. In so doing, the maximum S_T and F_T significantly exceed the respective values for the velocity. Similar tendencies are observed in [47], where $S_T \sim 8$ at $x/r_a \sim 8$ for a plane jet. The minimum of the correlation of axial velocity and temperature, $R_{v_x T}$, is 0.2 and is reached in the same section where the maximum of S_T and F_T were observed (at $x/r_a \sim 6$). In the far field of jet, the S_v and F_v distributions are described by Gaussian distribution, $S_T \sim -0.5$ and $F_T \sim 3.3$.

The PDF of velocity fluctuations exhibits a symmetric shape, which is close to Gaussian at $x/r_a \sim 10$. The PDF of temperature fluctuations differs from Gaussian. At $x/r_a \sim 30$, their qualitative behavior does not vary. However, the skewness (asymmetry) of PDF of temperature fluctuations becomes appreciable.

The distributions of constants (e.g. c_μ constant and turbulent Prandtl number) are of great importance from the standpoint of verification and validation of the results obtained using the RANS equations closed with the $k-\varepsilon$ model.

The experimental data for flows in tubes and boundary layers demonstrate that the wall shear stress turns out to be proportional to the turbulent kinetic energy with the proportionality factor confined in a rather narrow range. This substantiates the assignment of the relevant value to the constant in the formula for eddy viscosity.

The variation of constant in the $k-\varepsilon$ model along the jet axis for different degrees of preheating is shown in the Figure 33. The results are normalized to the standard constant

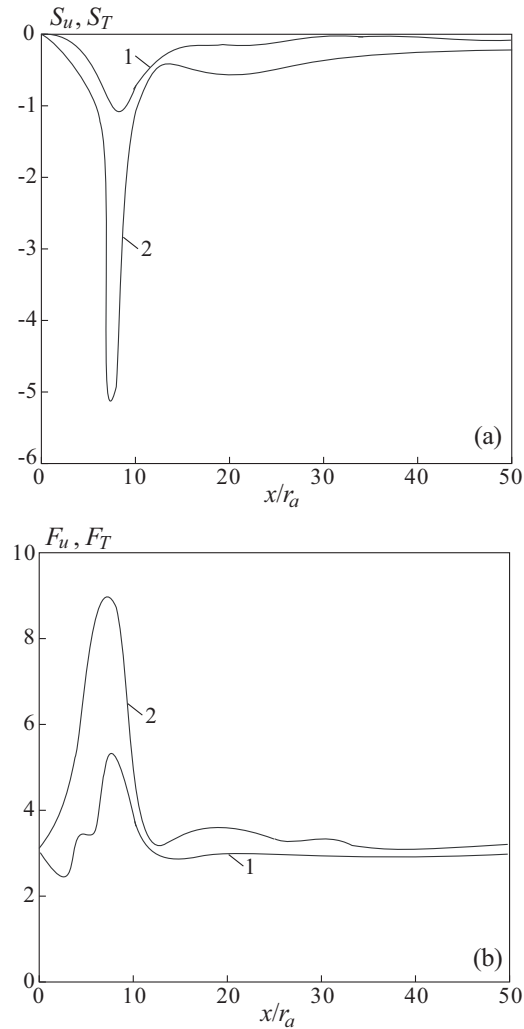


Figure 32. Distributions of skewness (a) and flatness (b) factors of velocity (line 1) and temperature (line 2) along the jet axis at $\vartheta = 1.2$.

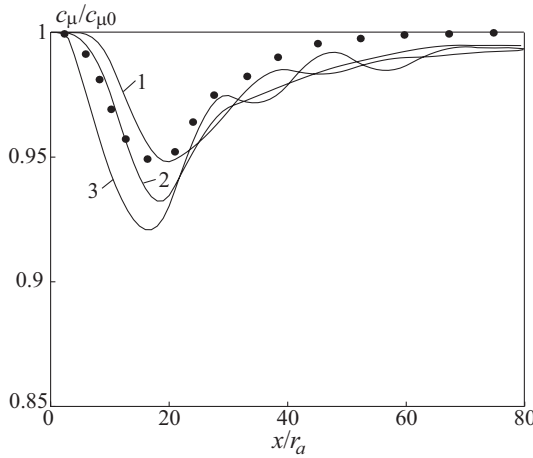


Figure 33. Distributions of constant c_μ along the jet axis at $\vartheta = 0.6$ (line 1), 1 (line 2), 1.8 (line 3). The symbols \bullet correspond to the correlation of [52].

$c_{\mu 0} = 0.09$. The maximal deviation from the standard value is observed at $12 < x/r_a < 20$ and exhibits a tendency to shifting towards the nozzle with increasing degree of preheating of the jet. The deviation from the standard value is 5.2% at $\vartheta = 0.6$, 6.2% at $\vartheta = 1$, and 7.9% at $\vartheta = 1.8$.

The results obtained for isothermal jet agree quite well with the correlation of [52]

$$c_\mu = 0.09 - 0.04f, \quad f = \left| \frac{\delta}{2\Delta U} \left(\frac{dU_c}{dx} - \left| \frac{dU_c}{dx} \right| \right) \right|,$$

where δ is the thickness of the mixing zone, and ΔU is the characteristic variation of velocity in the mixing layer. The differences are observed in the far field of jet, where the calculations produce lower values of the constant. The minimum of the constant is likewise lower than the value obtained by the data of [52].

The turbulent Prandtl number is calculated as

$$\text{Pr}_t = \langle v'_x v'_r \rangle \frac{\partial \langle T \rangle}{\partial r} \left(\langle v'_r T' \rangle \frac{\partial \langle v_x \rangle}{\partial r} \right)^{-1}.$$

The l'Hospital rule is employed on the axis for overcoming the indeterminacy.

The distributions of turbulent Prandtl number are presented in the Figure 34. The Prandtl number reaches the maximum on the jet axis. In the far field of jet, the Prandtl number slightly varies. The minimum of Prandtl number is located at $r/r_u \sim 0.62$ and exhibits a weak dependence on the parameters at the nozzle outlet section. When r/r_u varies from 0 to 0.6, the turbulent Prandtl number decreases by a factor of almost 3 (from 1.5 on the jet axis to 0.5 in the mixing layer).

9. Turbulent impingement jet

Unsteady-state heat transfer in the region of interaction of a round turbulent jet with a normally positioned flat target is considered. The symmetry condition is not employed,

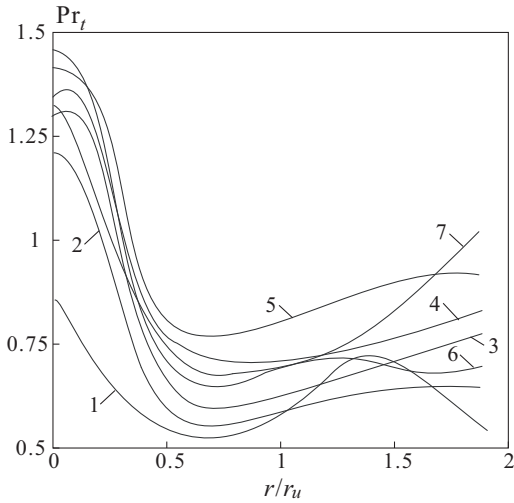


Figure 34. Distribution of turbulent Prandtl number at $\vartheta = 1.6$ and $x/r_a = 10$ (line 1), 14 (line 2), 16 (line 3), 18 (line 4), 24 (line 5), 28 (line 6), 80 (line 7).

and the stagnation point is not fixed. The calculations are performed for different relative distances from the nozzle to the target and Reynolds numbers. The correlation between distribution of Nusselt number along target and eddy structure of the jet is discussed.

9.1. Methods of simulation

The flow structure and heat transfer in the jet–target interaction region are affected by the dimensionless distance from the nozzle to the target, conditions of jet outflow (e.g. Reynolds number and turbulence intensity), angle of impingement onto the target.

In the case of the normal impact of the jet onto the flat target, the overall flow region is divided into several sub-regions (see Figure 35).

In the free jet flow region at $r/D < 1$ (region 1), the source of turbulence is the mixing layer separating the potential core of the flow (region 5) from a constant axial velocity of the jet and the surrounding fluid (region 6). If the distance from the nozzle to the target is small, no significant mixing of the jet with the surrounding fluid occurs. The velocity at the jet axis remains unchanged at the distance $x/H = 0.4$. The intensity of turbulence increases approximately by 5% compared to its value at the nozzle outlet.

In the region of flow deceleration at $1 < r/D < 2$ (region 2), the jet velocity on the wall vanishes, and the streamlines are substantially curved in the region of flow turning at $r/D \sim 1$. The effect of curvature of streamlines leads to the stabilization of flow and the decrease in the turbulent kinetic energy. In terms of the x coordinate, the region of flow deceleration extends to cross section located at a distance from the target $x/H = 0.25$. For $H/D = 8$, the intensity of turbulence near the target is approximately 25% higher than that at the nozzle outlet section. For $H/D = 2$, the maximum of eddy viscosity is located at the point $x/H = 0.18$ for $Re = 2.3 \times 10^4$ and at the point $x/H = 0.12$ for $Re = 7 \times 10^4$.

The shear layer formed owing to jet mixing with the surrounding fluid reaches the target

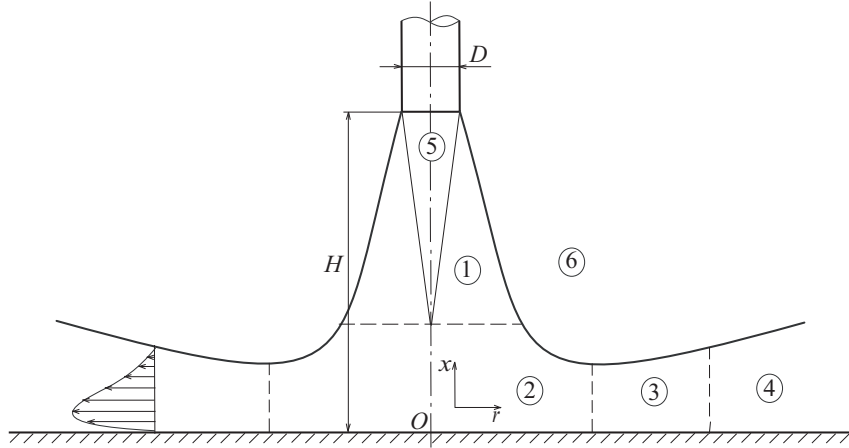


Figure 35. Regions of flow.

when it still has a rather high level of turbulence. The level of fluctuations of normal velocity is higher than the level of fluctuations of tangential velocity. The length scale of turbulence depends on the flow history determined by jet outflow conditions.

In the wall region at $r/D > 2$ (region 3), shear stresses become predominating compared to normal stresses, and this causes an increase in the generation of turbulence.

Flowing along the target, the jet loses some momentum, and the boundary-layer thickness increases. In region 4, the flow separation occurs, and large eddies are broken into a number of secondary vortices.

The experimental data of [61] (heat transfer) and [62] (flow field) were obtained for different Reynolds numbers, $\text{Re} = (2.3\text{--}7) \times 10^4$, and distances from the nozzle to the obstacle, $H/D = 2\text{--}10$. For the same conditions, the data on the Nusselt number disagree by 20–25%, which is attributed to the effect of conditions of jet outflow [63]. Local properties of the flow (e.g. distributions of wall shear stress) are described in [64, 65].

To describe the flow in the interaction region, solution of RANS equations is usually used [66, 68, 71, 72, 73, 74, 75, 76]. The HRN and LRN $k-\varepsilon$ models overestimate the turbulent kinetic energy by approximately 55%, and the heat flux is overestimated by almost 41% [66]. In the standard $k-\varepsilon$ model, the degree of jet expansion is overestimated, and a too rapid decrease in temperature along axial coordinate is assumed [68]. The Kato–Launder correction is used for a more accurate prediction of generation of turbulence. Additional source terms are introduced into the transport equation of turbulent kinetic energy [68], and the time scale of turbulence is restricted [71]. The use of differential source terms causes problems with regard to stability of iteration process. The foregoing corrections fail to improve the results relating to heat transfer, and the level of turbulence turns out to be higher than that observed experimentally [61, 62].

Further disadvantages of the $k-\varepsilon$ model are associated with the wall functions [72, 73]. At $H/D = 2$ and $\text{Re} = 2 \times 10^4$, the predicted turbulent kinetic energy is higher than the real value almost by a factor of nine [72]. The predictability of the model is improved by solving simplified equations for the turbulent kinetic energy and its dissipation rate in the

near-wall control volume [73]. More accurate results are given by zonal models, e.g. the two-layer model and the SST-model [74].

Nonlinear eddy viscosity models produce more accurate results compared to the $k-\varepsilon$ model [68]. Nevertheless, the data on heat transfer turn out to be 10% higher than the measured values. These models overestimate the turbulent stresses at $1 < r/D < 2.5$ and underestimate the turbulence stresses at $r/D > 2.5$.

For $H/D \leq 2$, the exact solution for laminar boundary layer is used for estimating friction and heat flux at the stagnation point [15]. When the distance from the nozzle to the obstacle increases, the data on heat transfer deviate from the exact solution, which is attributed to the mixing of jet with the surrounding fluid.

The results computed with the $k-\varepsilon-f_\mu$ model [75] and the v_2-f model [76] show that the distribution of Nusselt number has maximum at the stagnation point, $r = 0$, and its minimum is observed in the region of turning of flow at $r/D \sim 1$. The maximum of Nusselt number in the stagnation point is reached at $H/D = 6-8$. For low relative distances from the nozzle to the target and high Reynolds numbers, the secondary maximum of the heat transfer coefficient is observed in time-averaged distributions at $r/D \sim 1.5-2$ [61, 62]. Some experiments, e.g. [69] and [70], show that there is a local minimum of the heat transfer coefficient and a ring hump with a maximum at $r/D \sim 0.5$ in the case of low H/D and moderate level of turbulence.

There may be several reasons for the local maximum of the Nusselt number. In particular, it may be caused by the laminar–turbulent transition in the boundary layer [77], by increase in the turbulent kinetic energy in the near-wall jet [63, 76] or with generation of large-scale eddy structures [67].

Applicability of DNS is limited by low Reynolds numbers [67] ($\text{Re} < 5 \times 10^3$). The use of LES is a compromise option between the solution of RANS and DNS [78, 79]. The computations performed in [80] at $\text{Re} = 10^4$ and $H/D = 4$ use the dynamic model and the modified scale similarity model. The results obtained confirm the existence of secondary vortices in the near-wall region and their relation to the primary vortex formed in the mixing layer of the free jet with the surrounding fluid. The primary vortex near the wall has a helical shape. The discrepancy of the results based on different SGS models is less than 10%.

9.2. Boundary conditions

We will consider a submerged turbulent jet interacting along a normal with a flat obstacle. The point of origin is located at the stagnation point (see Figure 35).

No-slip and no-penetration boundary conditions and wall temperature are specified on the target surface. Slip boundary conditions are applied to the upper boundary of the computational domain except for the nozzle outlet section. These boundaries are adiabatic.

The profile of axial velocity is specified on the nozzle outlet boundary [15]

$$u(x) = \frac{U_a}{3} \left[1 + \tanh \left(\frac{0.5 - |x|}{2\delta} \right) \right],$$

where U_a is the velocity on the jet axis, and δ is the momentum thickness ($\delta/D \sim 0.05$). Random oscillations in the form of a white noise are imposed on the profile of axial velocity.

The root-mean-square velocity of disturbances is taken proceeding from the preassigned level of turbulence on the inlet boundary, $v_a = 0.05k_a^{1/2}$.

Non-reflecting boundary conditions are used on the outlet boundary.

9.3. Results and discussion

The computational domain is $[0, H] \times [-L_y, L_y] \times [-L_z, L_z]$, where $L_y = L_z = 10D$ and $D = 0.008$ m. The distance from the nozzle to the obstacle and the Reynolds number vary in the calculations, $H/D = 1\text{--}12$ and $\text{Re} < 10^5$. The working fluid is air, $T_a = 400$ K and $T_w = 320$ K.

The potential core of the jet propagates to a distance of the order of four to eight diameters of the nozzle, so calculations partly correspond with fully developed turbulent flow ($H/D \sim 10$), and partly — with the case where the obstacle is within the potential core of the jet.

The mesh contains $240 \times 200 \times 200$ nodes at $H/D = 12$, so $\Delta x_{\max} = 0.18H$ near the inlet boundary and $\Delta x_{\min} = 0.0012H$ near the target ($\Delta x^+ = 0.16$). The mesh is refined towards jet centerline, so $\Delta y_{\min} = \Delta z_{\min} = 0.0038H$. When the distance from the nozzle to the obstacle varies, the number of mesh nodes along x coordinate is reduced in order to obtain an acceptable aspect ratio of the cells.

The time step is $\Delta t = 1.22 \times 10^{-6}$ s, and 50 000 time steps are performed. When the Reynolds number varies, the time step is estimated as $\Delta t \sim 10^{-3}D/U_a$.

The Nusselt number and the wall heat flux are defined by the formulas

$$\text{Nu}(y) = \frac{q(y)D}{\lambda(T_w - T)}, \quad q(y) = \lambda \left(\frac{dT}{dx} \right)_w.$$

The deviation of the Nusselt number at the stagnation point from its averaged value is calculated by the formula

$$\Delta \text{Nu}_0 = \frac{\text{Nu}_0 - \langle \text{Nu}_0 \rangle}{\langle \text{Nu}_0 \rangle}.$$

The angle brackets indicate time averaging, and the subscript 0 indicates the parameters at the stagnation point.

The shear layer of the flow contains large eddies in the form of toroidal axisymmetric vortices incipient at a certain distance from the nozzle (approximately 1–2 nozzle diameters) and propagating in the mixing layer downstream. The generation of the primary eddy is associated with the Kelvin–Helmholtz instability of the shear layer. The maximum and minimum of vorticity approximately correspond to the centers of eddies. At low Reynolds numbers, $\text{Re} \sim 10^3$, the jet is almost axisymmetric. With increasing Reynolds number to $\text{Re} \sim 10^4$ and distance from the nozzle, a weak sine mode arises, and the stagnation point moves about the geometric center of the obstacle. As a result of further increase in Reynolds number, the flow becomes fully three-dimensional and turbulent.

The level of velocity fluctuations at the stagnation point remains unchanged as long as the target is in the potential core of the jet. The distribution of velocity fluctuations has a minimum at the stagnation point, and its maximum is located at a point where the shear layer reaches the obstacle and depends on H/D .

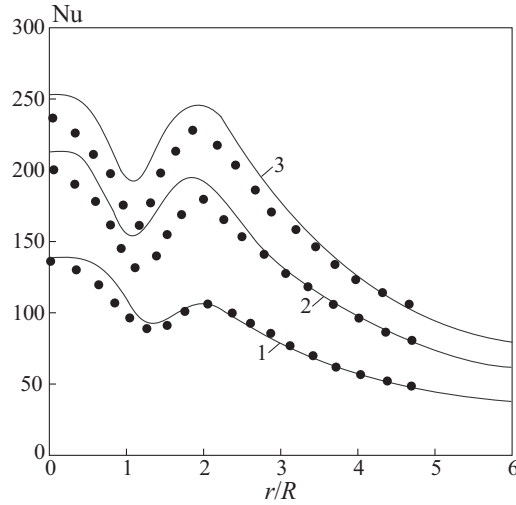


Figure 36. Distributions of the Nusselt number along obstacle based on computations at $H/D = 2$ and $Re = 2.3 \times 10^4$ (line 1), $Re = 5 \times 10^4$ (line 2), $Re = 7 \times 10^4$ (line 3). The symbols \bullet correspond to experimental data of [61, 62].

The distribution of time-averaged Nusselt number along the obstacle is presented in the Figure 36 compared to the experimental data of [61, 62] (symbols \bullet) for different Reynolds numbers. The Nusselt number has two maximums, one of which is located at the stagnation point, and the position of the other one depends on the distance from the nozzle to the obstacle. In the diagram $(r/D, Nu)$, the maximums of the Nusselt number corresponding to different H/D are located almost on one straight line.

For low H/D , the Nusselt number at the stagnation point is adequately described by the dependence $Nu_0 \sim Re^{1/2}$, which follows from the solution for a laminar boundary layer in the vicinity of the stagnation point [15]. This dependence is validated by experimental data for rather high Reynolds numbers as well [63].

The results computed at the stagnation point are shown in the Figure 37 and Figure 38 for different Reynolds numbers and distances from the nozzle to the obstacle.

As a result of generation of large-scale eddy structures, the temperature and heat transfer coefficient comes to be dependent on time. The Figure 39 shows the time history of temperature at $H/D = 10$ and $Re = 10^3$.

The temperature oscillations begin at the time when the primary vortex reaches the obstacle (line 1). This time depends rather slightly on the Reynolds number, $t \sim 16$ at $Re < 10^3$. The temperature oscillations downstream of the stagnation point (line 2) is associated with the displacement of eddy structures in the direction parallel to the wall. The decrease in the oscillation amplitude is caused by the mixing of the wall jet with the surrounding fluid.

The temperature oscillations are not strictly periodic, and their amplitude increases with the Reynolds number, because the intensity of eddy structures at low Reynolds numbers is low due to the low impact of viscous effects on the instability of shear layer. As a result of the decrease in the distance from the nozzle to the obstacle, there is not enough time for

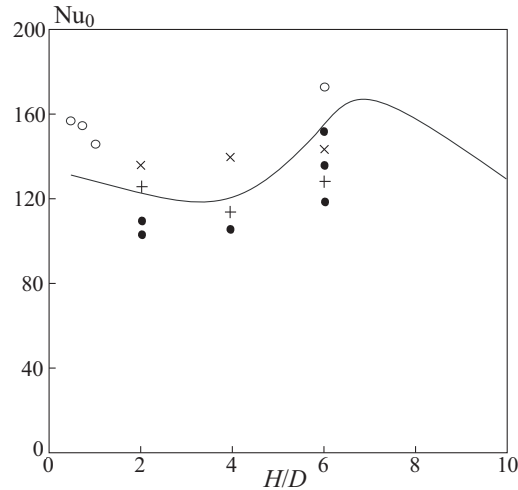


Figure 37. Nusselt number at the stagnation point as a function of distance from the nozzle to the obstacle at $\text{Re} = 2.3 \times 10^4$. The solid line corresponds to calculations, the symbols \bullet correspond to data of [61], symbols \circ correspond to data of [63], symbols \times correspond to calculations based on the $k-\varepsilon$ model [74], the symbols $+$ correspond to calculations based on the SST model [74].

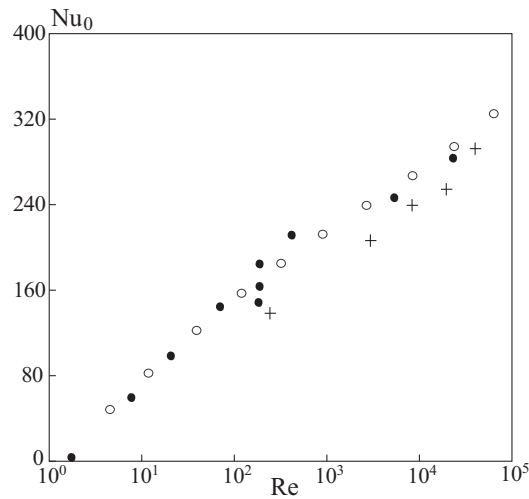


Figure 38. Nusselt number at the stagnation point as a function of Reynolds number at $H/D = 6$. The symbols \circ correspond to calculations, symbols \bullet correspond to data of [61, 62], symbols $+$ correspond to calculation based on the SST model [74].

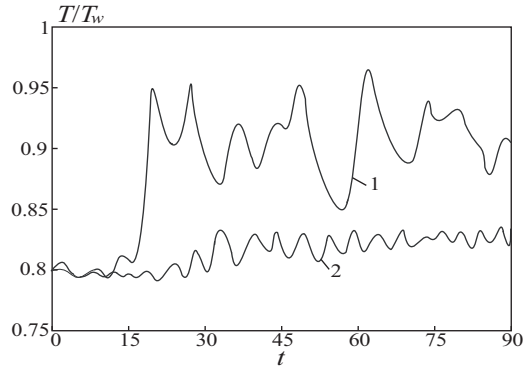


Figure 39. Temperature history at $x/D = 0.02$ from the obstacle. The lines 1 and 2 indicate sections $r = 0$ and $r = 4H$.

the eddies to form completely, and the amplitude and frequency of temperature oscillations decrease.

The maximum of the Nusselt number is always located at the stagnation point, in spite of the fact that its value varies in time significantly (see Figure 40). The distributions of Nusselt number along wall at different times have a local maximum, while the time-averaged Nusselt number varies monotonically along wall.

The Nusselt number at the stagnation point slightly depends on the eddy intensity. At the same time, the position of the primary eddy has a significant effect on heat transfer downstream. The increase in the heat transfer coefficient is associated with the extension of eddies in the direction parallel to the wall. The development of flow under conditions of adverse pressure gradient and its separation from the wall leads to the formation of secondary eddies responsible for the second maximum of the Nusselt number.

Fluctuations of the Nusselt number near the stagnation point are caused by the interaction of the primary eddy with the wall. At high r/D , the distribution of heat transfer coefficient depends on the structure of secondary eddies arising due to the interaction of primary eddy with boundary layer of wall jet. The unsteady-state pattern of this interaction and the variation of the structure of thermal boundary layer result in the emergence of the second local minimum of the Nusselt number (see Figure 41).

Because the fluctuations of the Nusselt number are not strictly periodic, it makes sense to consider the time interval between its two successive maximums. During this time period ($\text{Re} \sim 500$), the Nusselt number varies from maximum at $t \sim 34$ to minimum at $t \sim 38$, and then again to maximum at $t \sim 41$.

As the primary eddy P_1 moves downstream along the wall, the thickness of thermal boundary layer increases. The time variation of the position of the primary eddy causes the local minimum of heat flux to shift. During the time the eddy moves downstream, the next eddy P_2 fails to reach the wall (local minimum of Nu). A secondary eddy S arises downstream at $r/D \sim 3$, which rotates in the same direction as the primary eddy (clockwise). This time corresponds to the local minimum of the Nusselt number on the wall.

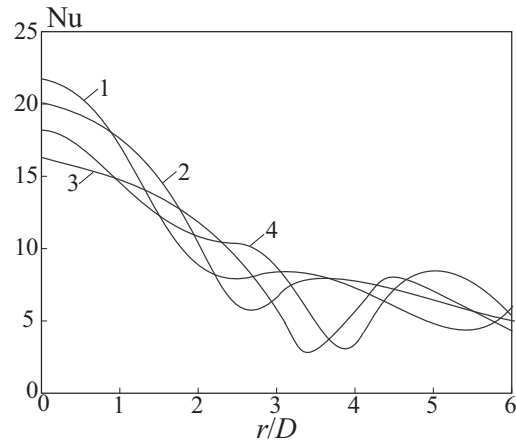


Figure 40. Nusselt number history at $H/D = 5$, $\text{Re} = 500$ and $t = 10$ (line 1), 20 (line 2), 30 (line 3), 40 (line 4).

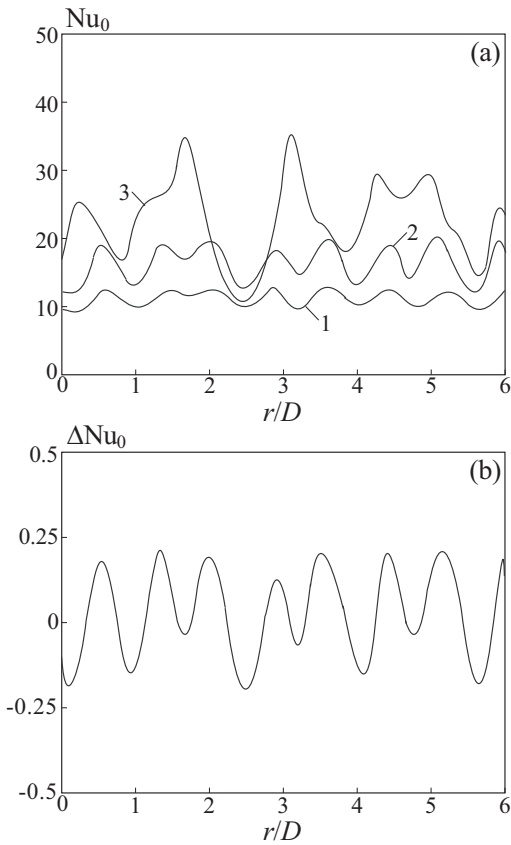


Figure 41. Nusselt number history at the stagnation point (a) and deviation of Nusselt number from averaged value (b) at $H/D = 5$ and $\text{Re} = 300$ (line 1), 500 (line 2), 1000 (line 3).

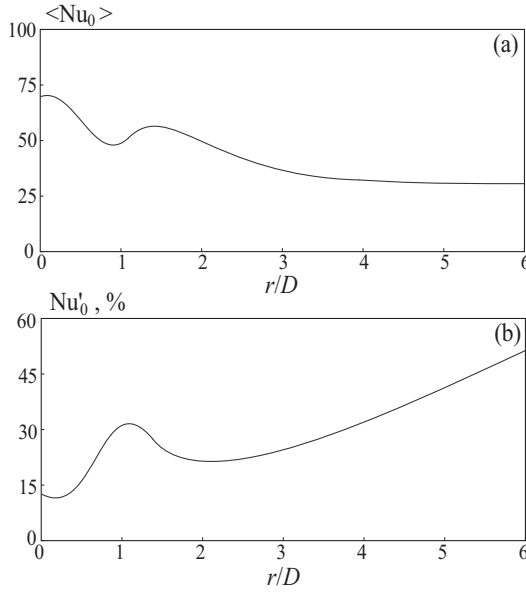


Figure 42. Distributions of time-averaged (a) and fluctuating (b) Nusselt number along the wall at $H/D = 1$ and $\text{Re} = 10^4$.

When the eddy P_2 reaches the wall, the heat flux starts increasing again. At this time, the eddy P_1 is located quite far away from the stagnation point and produces no significant effect on heat transfer. The effect of eddy P_2 increases with approaching the wall. During the cycle, the extension of eddy decreases by approximately 10% because of viscous effects.

Fluctuation component of the Nusselt number is comparable with its time-averaged value even at low Reynolds numbers, $\text{Nu}'_0 / \langle \text{Nu}_0 \rangle = 0.4$ at $\text{Re} \sim 500$. At $r = \pm 3H$, these low Reynolds numbers come to be of the same order of magnitude as the time-averaged Nusselt number (see Figure 42).

For high r/D , the distribution of the heat transfer coefficient depends on the structure of secondary eddies arising owing to interaction of the primary eddy with the boundary layer of the near-wall jet. The unsteady character of this interaction and change in the structure of the thermal boundary layer are responsible for a local maximum in the Nusselt number.

At $\text{Re} \sim 500$, the asymmetry of the distribution of Nusselt number along the wall on both sides of the stagnation point is about 0.5%, and reaches 2% at $\text{Re} \sim 10^3$.

The increase in Reynolds number causes increase in fluctuations of Nusselt number at the stagnation point (see Figure 41). The amplitude of fluctuations is about 20% of the time-averaged value at $\text{Re} = 5 \times 10^3$, and it reaches 35% at $\text{Re} = 2.5 \times 10^4$. The Strouhal numbers based on the velocity at the jet centerline and nozzle diameter are $\text{Sh} = 0.20$ and 0.32.

The fluctuations of velocity at the stagnation point does not vary for as long as the wall is in the potential core of the jet. The distribution of velocity fluctuations has a minimum at the stagnation point, and its maximum is located at the point where the shear layer reaches the surface (this position depends on H/D). At $H/D > 3$, the velocity fluctuations are

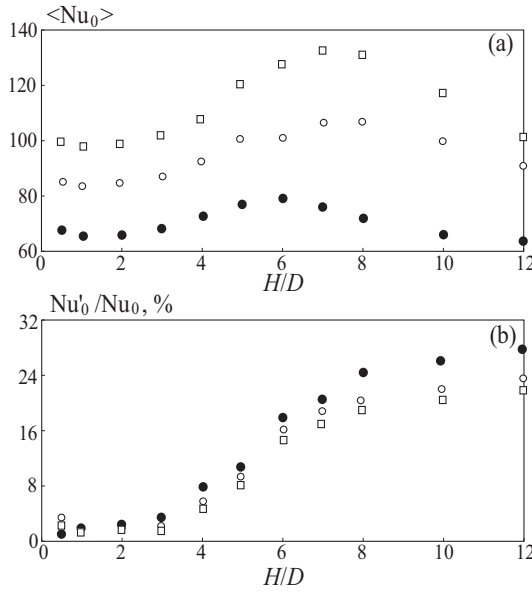


Figure 43. Averaged (a) and fluctuating (b) Nusselt number as function of distance from nozzle to obstacle at $\text{Re} = 10^4$ (symbols ●), $\text{Re} = 2 \times 10^4$ (symbols ○), and $\text{Re} = 3 \times 10^4$ (symbols □).

fairly uniformly distributed along the wall, and no local maximum of the Nusselt number is observed. The local maximum of fluctuations of Nusselt number is located somewhat farther away from the stagnation point than the local maximum of fluctuations of velocity.

For low H/D , the fluctuations of Nusselt number are insignificant (see Figure 43). The length of potential core increases with Reynolds number. This explains the reason for the emergence of a maximum of Nusselt number at $H/D \sim 2$ and $\text{Re} = 10^4$, and high H/D at $\text{Re} = 2 \times 10^4$. At $H/D = 2.5$, the fluctuations of Nusselt number increase and vary from 6% to 27% of its averaged value if H/D increases from one to eight.

10. Aero-optic effects in turbulent flows

Large-scale eddies and related aero-optic effects in turbulent boundary layer on a flat plate, free mixing layer, and free round jet are considered and simulated. The flow field computed is used to investigate the distortions produced in the phase function of a coherent beam by turbulent fluctuations. The results obtained are compared with the experimental data and results of solution of RANS equations.

10.1. Methods of simulation

A coherent beam propagating through a randomly inhomogeneous medium (e.g. turbulent boundary layer or shear flow) feels optical aberrations. While the periphery of the boundary layer produces relatively small aberrations of a regular character, processes in the inner

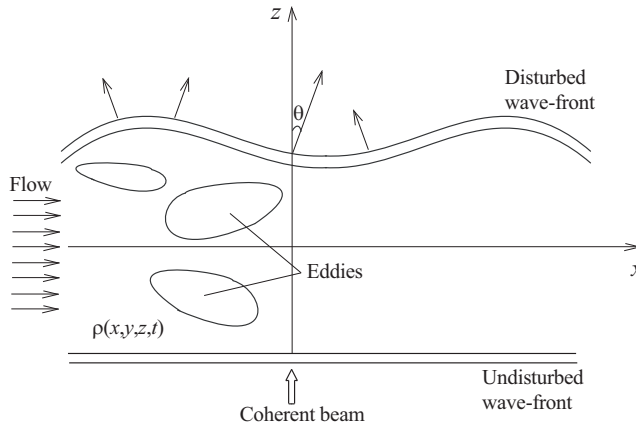


Figure 44. Propagation of coherent beam through a randomly inhomogeneous medium.

region of the boundary layer determine the electromagnetic wave propagation.

Problems of coherent beam propagation through a substance have received a lot of consideration in the literature. Most results are obtained for the propagation of laser beam in the turbulent atmosphere [81]. Almost in any part of the atmosphere, the major phase distortions are introduced by large-scale eddy structures (with the exception of the near-earth boundary layer, where optical distortions are determined by small-scale eddies). The influence of the atmospheric effects on coherent beam propagation is associated with relatively low frequencies and can well be revealed by contemporary experimental tools. The influence of turbulent mixing is due to fast (high-frequency) changes in the flow field. Since the spatial scales and characteristic frequencies of turbulent flows may vary within several orders of magnitude, serious difficulties may be anticipated in direct measurements and numerical calculations [82, 83].

The turbulent mixing causes refractive index fluctuations in space and time. A relation between the refractive index and the medium density can be taken on the basis of the Gladstone–Dale law [82, 84]

$$n(\mathbf{x}, t) = 1 + G(\lambda) \frac{\rho(\mathbf{x}, t)}{\rho_0},$$

where ρ_0 is a characteristic density (e.g. the density of an undisturbed medium). The Gladstone–Dale constant, G , depends on the wavelength of the propagating beam and the working fluid. Weak dependence on wavelength is ignored, and $G = 0.223 \times 10^{-3}$ for air.

As coherent beam propagates through a randomly inhomogeneous medium, its amplitude and phase are subjected to fluctuations corresponding to the structural changes (broadening, deflection, and splitting) of the beam (see Figure 44). The distortions produced in the amplitude characteristics of the beam are negligibly small as compared to fluctuations of the refractive index [82, 84].

Because of the beam broadening, it cannot be focused at a large distance from the radiation source. As the diameter of the wave source grows, the diffraction spot at the focal

point decreases to a certain finite radius (saturation size), rather than behaving as predicted in the optics of homogeneous media.

Fluctuations of the coherent beam's propagation direction shift the geometrical center of the beam in relation to the observation point.

The beam splitting shows up in a complex structure of the light spot at a small distance from the wave source. At a large distance in the region of strong fluctuations, the coherent beam splits into thin threads with round or crescent-shaped cross sections. The optical energy is redistributed over the beam cross section, while the average power remains the same.

Scattering by random inhomogeneities of the medium also adds to the fluctuations of the intensity of electromagnetic radiation.

The effect of the refractive index fluctuations depends on the ratio D/L , where D is the beam diameter and L is the spatial period of the refractive index variations. At $D \ll L$, the refraction gradient is the same over the cross section of the beam and the beam deviates as a whole. At $D \sim L$, turbulence acts as a lens, which restructures the wave. At $D \gg L$, the turbulence deflects different elements in the cross section by different angles (light scattering).

In contrast to flows produced by turbulent mixing of medium (e.g. mixing layers and jets), atmospheric turbulent flows have a considerably large characteristic length and their losses for turbulent scattering are only insignificant [81].

10.2. Dispersion of phase fluctuations

Dispersion of small-scale fluctuations of density, σ_ρ^2 , and the corresponding correlation length scale, l_ρ , are related to the dispersion of wave phase, σ_φ^2 , by the expression

$$\sigma_\varphi^2 = \alpha \beta^2 \int_0^L \sigma_\rho^2 l_\rho dy, \quad \beta = \frac{2\pi}{\lambda} \frac{dn}{d\rho} = kG(\lambda), \quad (10)$$

where L is the optical path length, and the integral is taken across the boundary layer. The constant α depends on the form of the correlation function assumed for the density fluctuations (e.g. $\alpha = 2$ for the exponential correlation function and $\alpha = \pi$ for the Gaussian correlation function). According to (10), this leads to an 11% difference in the dispersion of phase fluctuations.

Length scale l_ρ is found by integrating the correlation function

$$l_\rho = \int_{-\infty}^{+\infty} R_{\rho\rho}(y) dy.$$

In the conditions of local equilibrium, the correlation length scale l_ρ coincides with the correlation scale of velocity fluctuations, $l_u \sim k^{3/2}/\varepsilon$. This assumption is not applicable near the wall, where velocity fluctuations turn to zero, therefore $k = 0$ and $l_u = 0$ but $l_\rho \neq 0$.

To estimate the phase fluctuations in the near-wall region, the formula (10) is usually replaced with a semi-empirical formula [84]

$$\sigma_\varphi^2 = \beta^2 l_y \delta \sigma_\rho^2, \quad (11)$$

where l_y is the integral turbulence scale in the direction normal to the wall. It is assumed that $l_y \sim 0.1\delta$, where δ is the boundary layer thickness. The dispersion of the density fluctuations can be estimated as

$$\sigma_\rho^2 = A^2 (\rho_w - \rho_\infty)^2,$$

where ρ_w and ρ_∞ are the density at the wall and the density in the free flow, and $A = 0.1 - 0.2$. At $l_y \ll \delta$, formula (11) is refined by integrating across the boundary layer [84, 85],

$$\sigma_\varphi^2 = \beta^2 \int_0^L \sigma_\rho^2(y) l_y(y) dy. \quad (12)$$

Optical aberrations have been the subject of extensive experimental investigations [86, 87, 88, 89].

LES of turbulent shear flows makes it possible to determine fluctuating parameters of a turbulent flow, including the field of density fluctuations [82, 90]. To this end, a number of semi-empirical models of different complexity have been elaborated. The most popular models are those described in [84] for homogeneous turbulence and in [91] for inhomogeneous turbulence. In models of [84, 85, 91] based on formulas (11) and (12), the dispersion of density fluctuations is determined as the difference between the densities near the wall and at the periphery region of the boundary layer. The applications of the models of [84, 91] are discussed in [85]. In the methods of [92, 93], the density fluctuations are found by solving the transport equation of a passive scalar.

If pressure fluctuations are disregarded, density fluctuations can be related to temperature fluctuations via the state equation [92, 93]. The temperature fluctuations are determined using the Reynolds analogy between the velocity and temperature fluctuations and the Prandtl mixing model [94], whilst the accounting for the fact that the corresponding linear scales obey the relationship $l_u/l_T = \text{Pr}_t$, where the turbulent Prandtl number is taken to be constant.

Unlike solving the RANS equations, the use of DNS and LES makes it possible to obtain the field of density fluctuations, as well as the distributions of parameters σ_ρ^2 and l_ρ by solving the full (in DNS) or filtered (in LES) Navier–Stokes equations [90].

A method for numerical simulation of the aero-optic characteristics of a subsonic air flow near a flat rectangular cave with regard to the field of turbulent pulsations of the refractive index is proposed in [95]. The Reynolds equations are closed using the Cockley model and the hypothesis of frozen stationary locally homogeneous and isotropic turbulence with the Kolmogorov spectrum. The optical characteristics of the turbulence are determined upon the local values of average aerodynamic fields. Fluctuations of pressure are neglected as compared to temperature fluctuations. However, in aerodynamic applications, this condition fails for the largest scale eddies [86] and the fluctuation parameters of the flow along with their average values are to be determined neglecting the microstructure of the turbulent flow.

10.3. Phase function of wave front

The propagation of electromagnetic wave is described by Maxwell equations. Let us assume that the time scale related to the wave propagation is much smaller than the time scale of

turbulence, refractive index is time-independent, and the medium is nonconducting and has a constant magnetic susceptibility. Then, the wave equation has the form

$$\nabla^2 \mathbf{E} - \frac{n^2}{c_0^2} \frac{\partial^2 \mathbf{E}}{\partial t^2} = 0, \quad (13)$$

where \mathbf{E} is the electric field strength. The refractive index is given by $n = c_0/c$, where c and c_0 are the velocities of light in the medium and free space, respectively. For a monochromatic sinusoidal wave with frequency ω , the equation (13) has an exact solution

$$\mathbf{E}(\mathbf{r}, t) = \mathbf{E}_0 \exp[\varphi(\mathbf{k}, \mathbf{r}) - \omega t], \quad (14)$$

where \mathbf{E} is the field strength at point \mathbf{r} at time moment t , and \mathbf{E}_0 is the field strength at the point $\mathbf{r} = 0$. The wave number, frequency, and wavelength are coupled by well-known relationships $k = \omega c = 2\pi/\lambda$.

The phase function of the wave front is given by

$$\varphi = \int \mathbf{k}(\mathbf{x}, t) \cdot d\mathbf{x},$$

where $\mathbf{k} = 2\pi\mathbf{l}/\lambda$ is the wave vector, and \mathbf{l} is a unit vector specifying the wave propagation direction.

When a plane monochromatic wave passes through a layer with a varying refractive index, its amplitude remains almost constant and the phase is changed, so that $\varphi = \varphi_0 + \Delta\varphi$, where $\Delta\varphi$ is the phase shift due to the inhomogeneity of the medium.

The field strength of a perturbed wave can be obtained by multiplying solution (14) by factor $\exp(i\Delta\varphi)$, where $\Delta\varphi(x, y)$ denotes the phase shift along the optical path length, $L = z_2 - z_1$. The phase distribution is found by integrating the distribution of the refractive index over the layer thickness

$$\Delta\varphi(x, y, t) = k \int_{z_1}^{z_2} \Delta n(x, y, z, t) dz,$$

where $\Delta n(x, y, z, t)$ is the variation of the refractive index along the propagation direction, z (across the flow).

In case the perturbations of the wave vector are small, the beam deflections can be neglected and the integral appears in the form

$$\varphi(x, y, t) = k_0 \int_{z_1}^{z_2} n(x, y, z, t) dz, \quad (15)$$

where $\varphi(x, y, t)$ is the phase distribution in plane (x, y) normal to the direction of the wave propagation, z , at time t .

The results of these calculations are usually represented in the following form [86]

$$\tilde{\varphi}(x, y, t) = \frac{\varphi(x, y, t)}{k_0 L \Delta n} \simeq \frac{1}{L \Delta n} \int_{z_1}^{z_2} [n(x, y, z, t) - n_\infty] dz. \quad (16)$$

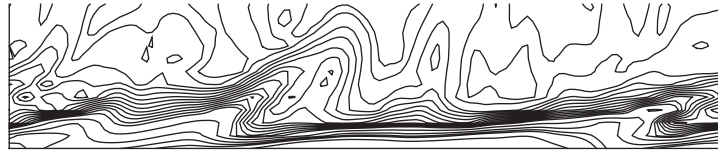


Figure 45. Contours of vorticity in the boundary layer on a flat plate at $t = 0.85$ s.

Along the direction of the beam propagation, we have

$$\psi(x) = L \frac{\partial \tilde{\varphi}}{\partial x} = \frac{1}{\Delta n} \int_{z_1}^{z_2} \frac{\partial n}{\partial x} dz,$$

where L is the size of the region of turbulent mixing. The corresponding spectra follow the relationship

$$S_\psi(k_x L) \sim (k_x L)^2 S_\varphi(k_x L).$$

For the mixing layer, we assume that $\Delta n = |n_1 - n_2|$ and $L = 2\delta$, where δ is the local width of the shear region and subscripts 1 and 2 refer to the flows involved in mixing. The values calculated for the jet are normalized to $\Delta n = |n_a - n_\infty|$ and $L = 2r_a$, where the subscripts a and ∞ refer to the parameters at the nozzle outlet and in submerged space.

10.4. Results and discussion

A non-stationary flow of a viscous compressible fluid is described by filtered Navier–Stokes equations closed with the RNG model [8].

A root-mean-square density can be found from the expression

$$\langle \rho'^2 \rangle^{1/2} = \left\{ \frac{1}{N} \sum_{i=1}^N \left[\rho(x, y, z, t_i) - \langle \rho(x, y, z) \rangle \right]^2 \right\}^{1/2},$$

where N is the number of time steps (in calculations $N \sim 5 \times 10^4$). Angle brackets denote time averaging.

Calculations for the boundary layer on a flat plate are performed at a $180 \times 90 \times 90$ mesh. In this case, $x^+ = 45$, $y_{\min}^+ = 1$ and $z^+ = 14$, where

$$y^+ = \left(\frac{u_\tau}{\nu_w} \right) y, \quad u_\tau = \left[\frac{\mu_w}{\rho_w} \left(\frac{\partial \langle u \rangle}{\partial y} \right)_w \right]^{1/2}.$$

Under these conditions, $\text{Re}_\delta = 2.6 \times 10^4$ (as calculated from boundary layer thickness, $\delta = 18$ mm) and $\text{Re}_{\delta_m} = 2.8 \times 10^3$ (as calculated from momentum thickness, $\delta_m = 2.2$ mm). Vortex structure of the flow in the boundary layer on a flat plate is shown in the Figure 45.

The resulting density fluctuations are by 10–20% higher than the experimental values (see Figure 46). The maximum of the y axis distribution of the density fluctuations is

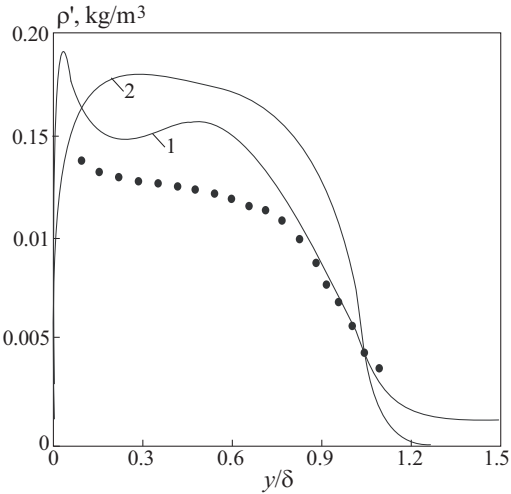


Figure 46. Density fluctuations in the boundary layer. The line 1 corresponds to the data computed, line 2 corresponds to the numerical data of [85], and symbols • correspond to the experimental data of [85] at $M = 0.88$.

located well close to the wall. At $0.2 < y/\delta < 0.6$, the root-mean-square density remains nearly constant and the dispersion of phase fluctuations is virtually uniform in this region.

Comparison of the length scales l_u and l_ρ shows that they are equal only in the interval $0.1 < y/\delta < 0.22$. In the rest of the boundary layer, the correlation scale of the velocity fluctuations is considerably smaller than that of the density fluctuations.

The results of calculations concerning the boundary layer on a flat plate are shown in the Figure 47 (it is assumed that $\alpha = 2$). The plate has a constant temperature, $T_w = 300$ K. The dispersions obtained from formula (12) (line 4) are overestimated as compared to those calculated in accordance with model of [84] by formula (11) (lines 2 and 3). Unlike line 4, the dispersion of the wave phase provided by the LES calculations (line 1) has a kink point.

Following the Reynolds analogy, we assume that the correlation factor between the pulsations of velocity and temperature is $R_{u'T'} = -1$. The results computed for large eddies indicate that, in the interval $0.12 < y/\delta < 0.86$, the correlation factor is nearly constant, $R_{u'T'} = -0.5$, which is in line with the data of [85].

Calculations for the mixing layer have been carried out for $Re = 2 \times 10^5$ (the Reynolds number is calculated from the momentum thickness) within the range $M_c = 0.15\text{--}0.8$, where $M_c = (u_1 - u_2)/(a_1 + a_2)$, and a is the velocity of sound. At $M_c = 0.15$, compressibility has no effect on the properties of the flow ($\rho_2/\rho_1 = 1$), while at $M_c = 0.9$ the density difference is $\rho_2/\rho_1 = 4$.

The profiles of the density fluctuations in the mixing layer are shown in the Figure 48 at $M_c = 0.8$. It is seen that the distributions of the density and pressure fluctuations in the cross sections of the mixing layer are similar with a maximum at the line separating the mixing flows. The profiles of pressure fluctuations are filled to a greater extent, and the maximal amplitude of the pressure fluctuations is close to a linear dependence on the

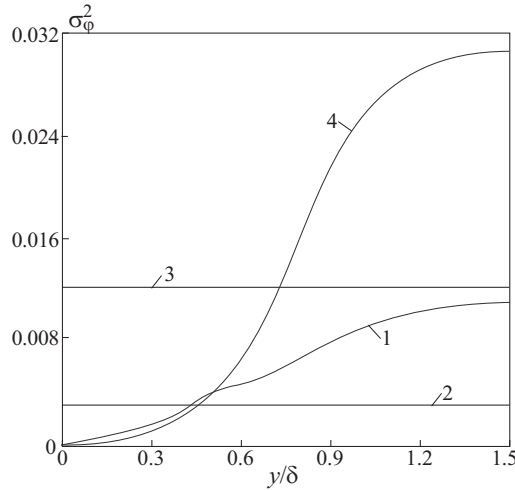


Figure 47. Dispersion of phase fluctuations in the boundary layer. Line 1 corresponds to the data computed, lines 2 and 3 correspond to the calculations based on model (11) at $A = 0.1$ and $A = 0.2$, and line 4 corresponds to the calculations based on model (12).

streamwise coordinate. Small deviations from the linear dependence occur only at $x/L > 0.68$. The dependence of the maximal density fluctuations on the x coordinate is non-monotonic (see Figure 49). At $x/L < 0.6$, it is close to a linear one and, after that, shows a peak and a smooth decay.

In the intermediate range of wave numbers, the wave spectrum in the mixing layer shows the power dependence

$$S_\varphi(k_x L) \sim (k_x L)^{-q},$$

where $q \sim 2$ (see Figure 50). The compressibility only has a weak influence on the spectrum behavior (this influence is largely displayed at large wave numbers).

The density fluctuations grow with an increase in the effective Mach number. Calculations yields $l_\rho \sim 4l_u$, where $l_u = 0.2k^{3/2}/\varepsilon$.

Calculations of flow in the submerged round jet are carried out in the range $10^3 \leq \text{Re} \leq 10^5$ (Reynolds number is found from the velocity at the nozzle outlet and the nozzle diameter).

Large-scale eddy structures present in the shear layer have the form of toroidal axially symmetric eddies nucleating certain distance apart from the nozzle outlet (of the order of one to two section diameters).

Eddy structures existing in the initial part of the jet are fairly small. The typical eddy size gradually increases from the start point downstream, thus, intensifying the exchange of momentum between the layer and the ambient fluid. The ellipsoidal shape of the coherent structure points to the anisotropy of turbulent pulsations in the region where large-scale eddies exist.

The generation of eddies is due to the Kelvin–Helmholtz instability of the shear layer. The maximum and minimum of the vorticity approximately correspond to the eddy centers.

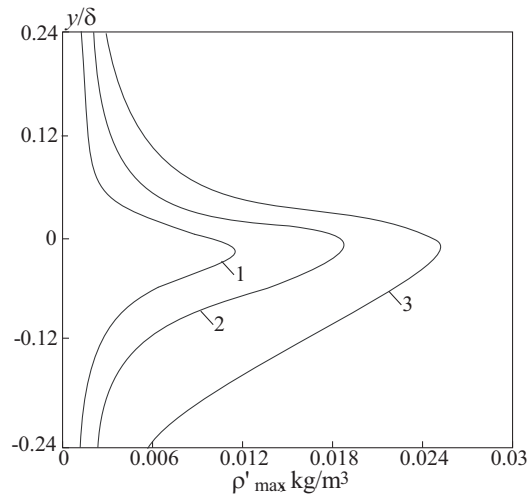


Figure 48. Density fluctuations in the cross section of the mixing layer at $x/L = 0.25$ (line 1), $x/L = 0.5$ (line 2), and $x/L = 0.75$ (line 3).

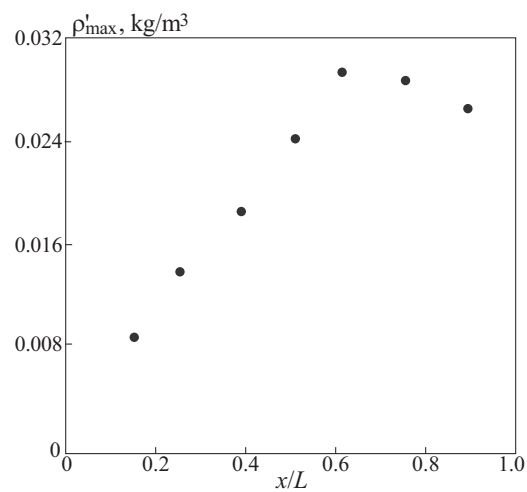


Figure 49. Dependence of the maximal density fluctuations in the mixing layer on streamwise coordinate.

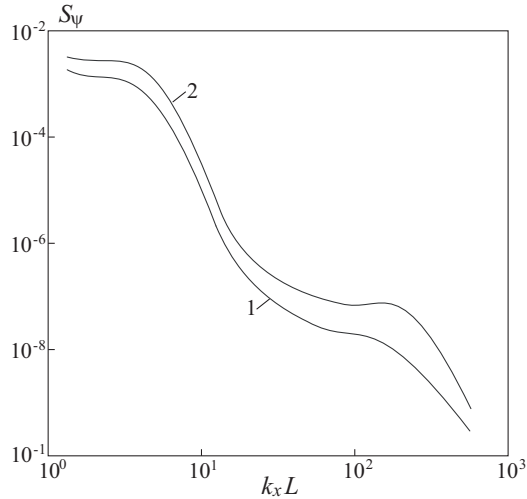


Figure 50. Spectrum of phase fluctuations in the free mixing layer at $M_c = 0.2$ (line 1) and $M_c = 0.2$ (line 2).

At low Reynolds numbers, $\text{Re} \sim 10^3$, the jet at the nozzle outlet is nearly axially symmetrical. As the Reynolds number increases with distance from the nozzle outlet (to $\text{Re} \sim 10^4$), a weak sinusoidal mode appears.

In the free jet at $\text{Re} = (2-8) \times 10^4$ and high wave numbers, $2r_a k_x > 1$, the wave spectrum is described by a

$$S_\varphi(k_x L) \sim (2r_a k_x)^{-q},$$

where $q \sim 2.5$ (see Figure 51). The spectrum for the jet is steeper than that for the mixing layer because of a stronger turbulent mixing, and is almost independent of the Reynolds number calculated from the parameters at the nozzle section.

11. Conclusion

Computational modeling of flows is vital for understanding and controlling processes relevant to aeronautical, environmental and numerous engineering problems. Most flows are turbulent, this dynamic complexity generally is being treated using inexpensive deterministic mathematical models (e.g., RANS) requiring calibration and validation against measurements. The increasing power of computers is allowing much less model-dependent approaches, in particular LES. This chapter contains the details of implementation of an LES model based on finite-volume method and high resolution difference schemes. The LES model has been quantitatively validated on several test cases, by comparing results with experimental data and DNS results as well as with the results based on solution of RANS equations.

The cases computed have included a fully developed turbulent flow in the channel (SGS modeling), turbulent flow in the channel induced by wall injection (relative injection veloc-

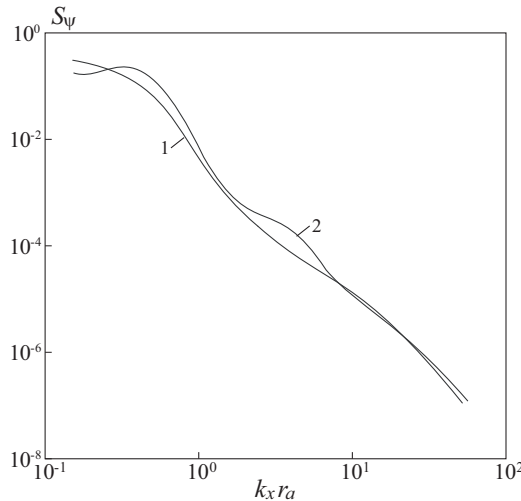


Figure 51. Spectrum of phase fluctuations in the round jet for $\text{Re} = 5 \times 10^3$ (line 1) and $\text{Re} = 1.5 \times 10^4$ (line 2).

ity varies), free mixing layer (SGS modeling, inlet boundary conditions vary), free non-isothermal turbulent jet flowing out from a round nozzle into submerged space (degree of preheating and turbulence intensity at the nozzle outlet vary), unsteady-state flow and heat transfer in the region of interaction of turbulent round jet with a flat target (distance from the nozzle to the obstacle and Reynolds number vary). The data obtained from LES have been used to predict aero-optical effects in the turbulent boundary layers and free shear turbulent flows. The local and integral properties of the flow and heat transfer were compared with the available experimental and numerical data.

The accuracy and computational efficiency were compared for a number of SGS models (Smagorinsky model, Van Driest model, RNG model, dynamic model and one-equation model). By comparing the computed data with the experimental data and results of DNS for fully developed turbulent channel flow, it was demonstrated that the use of the Smagorinsky model and the Van Driest model leads to rather large errors in predicting the fluctuating characteristics of the flow. The models examined offer fairly accurate estimates of the mean flow parameters. The role of SGS modelling becomes more important with the increasing Reynolds number.

The results obtained for the turbulent flow in a channel induced by wall injection predict a more filled profile of velocity than the theoretical cosine solution or results based on the $k-\varepsilon$ turbulence model. The maximum of turbulent kinetic energy was located nearer to the porous wall than it was predicted with the $k-\varepsilon$ turbulence model. For two-sided uniform fluid injection from the walls, the flow properties become independent from the Reynolds number.

The results for free mixing layer were not sensitive to the specification of unsteady boundary conditions on the inlet boundary (imposed oscillations in the form of white noise and sinusoidal oscillator were considered).

The distributions of correlation moments of density, velocity and temperature, as well

as the distributions of turbulent Prandtl number and the constant in the formula for eddy viscosity, were obtained along the axis and in cross sections of free round jet. The increase in the degree of preheating of the jet causes a reduction in the length of initial region and an increase in the degree of expansion of the jet. The damping of the fluid dynamics, thermal and fluctuation parameters in the region of jet expansion is more intensive than that in the case of isothermal jet or jet with a lower degree of preheating. The maximum of fluctuations of axial velocity in the mixing zone is of the order of 15–17% of the fluid velocity at the nozzle outlet, and is located at a distance approximately equal to two lengths of the initial region. The radial distribution of velocity fluctuations in the mixing zone is characterized by a maximum shifting towards the jet axis away from the nozzle outlet.

Large-scale eddy structures have a significant effect on the properties of friction and heat transfer in the region of interaction of round turbulent jet with a flat target. The fluctuations of Nusselt number near the stagnation point are caused by the interaction of the primary eddy with the wall. The variation of heat transfer downstream is associated with the extension of eddies in the direction parallel to the wall. The development of flow under conditions of adverse pressure gradient and its separation lead to the formation of secondary eddies responsible for the local maximum of the Nusselt number. The temperature oscillations are not strictly periodic, and their amplitude increases with the Reynolds number. The fluctuation of Nusselt number is comparable with its average value even at low Reynolds number.

The simulation of aero-optic effects in the boundary layer on a flat plate, free mixing layer, and round turbulent jet indicate that the spectrum of phase fluctuations is only a weak function of the input parameters, and the dependence is stronger at large wave numbers. It is also shown that the use of semi-empirical turbulence models leads to inaccurate values for the dispersion of phase fluctuations.

Acknowledgments

Special thanks go to my wife, Elena Volkova, for proofreading this work. I would like to express my sincere thanks to Professor Vladislav Emelyanov for the review of this work.

References

- [1] Moin P.; Mahesh K. *Annu Rev Fluid Mech.* 1998, *30*, 539–578.
- [2] Piomelli U. *Progr Aero Sci.* 1999, *35*, 335–362.
- [3] Spalart P.R. *Int J Heat Fluid Flow.* 2000, *21*, 252–263.
- [4] Strelets M. *AIAA P.* 2001, 2001-0879.
- [5] Martin M.P.; Piomelli U.; Candler G.V. *Theor Comput Fluid Dynam.* 2000, *13*, 361–376.
- [6] Smagorinsky J. *Monthly Weather Review.* 1963, *91*, 99–164.
- [7] Shen S.; Ding F.; Han J.; Lin Y.-L.; Arya S.P.; Proctor F.H. *AIAA P.* 1999, 99-0755.
- [8] Yakhout A.; Orszag S.A.; Yakhout V.; Israeli M. *SISC.* 1986, *1*, 1–51.

- [9] Germano M.; Piomelli U.; Moin P.; Cabot W.H. *Phys Fluids*. 1991, *3*, 1760–1765.
- [10] Horiuti K. *JPSJ*. 1997, *66*, 91–107.
- [11] Fureby C. *Phys Fluids*. 1995, *8*, 1301–1311.
- [12] Yoshizawa A.; Horiuti K. *JPSJ*. 1985, *54*, 2834–2839.
- [13] Osher S. *SINUM*. 1984, *21*, 217–235.
- [14] Chakravarthy S.R.; Osher S. *AIAA P*. 1985, 85-0363.
- [15] Schlichting H.; Gersten K. *Boundary layer theory*; Springer Verlag: Berlin, DE, 2000.
- [16] Moser R.D.; Kim J.; Mansour N.N. *Phys Fluids*. 1999, *11*, 943–945.
- [17] Temmerman L.; Leschziner M.A.; Mellen C.P.; Frohlich J. *Int J Heat Fluid Flow*. 2003, *24*, 157–180.
- [18] Benderskiy B.Ya.; Tenenev V.A. *Fluid Dynamics*. 2001, *36*, 336–340.
- [19] Eroshenko V.M.; Zaichik L.I. *Hydrodynamics and heat and mass transfer on porous surfaces*; Science Publishing House: Moscow, RU, 1984.
- [20] Emelyanov V.N.; Volkov K.N. *Mathematical Simulation*. 2004, *16*, 41–63.
- [21] Ciucci A.; Iaccarino G.; Moser R.; Najjar F.; Durbin P. In *Center for Turbulence Research*; University of Stanford: Stanford, US, 1998, 245–266.
- [22] Chaouat B. *AIAA P*. 2000, 2000-0992.
- [23] Chung Y.M.; Sung H.J.; Krogstad P.A. *AIAA J*. 2002, *40*, 1529–1535.
- [24] Kourta A. *Comput Fluid*. 2004, *33*, 155–178.
- [25] Nikitin N.V.; Pavel'ev A.A. *Fluid Dynamics*. 1998, *33*, 826–832.
- [26] Vuillot F.; Lupoglazoff N. *AIAA P*. 1996, 96-0884.
- [27] Brown G.L.; Roshko A. *J Fluid Mech*. 1974, *64*, 775–816.
- [28] Bernal L.P.; Roshko A. *J Fluid Mech*. 1986, *170*, 499–525.
- [29] Leboeuf R.L.; Mehta R.D. *Phys Fluids*. 1995, *7*, 1516–1518.
- [30] Bauer W.; Haag O.; Hennecke D.K. *Int J Heat Fluid Flow*. 2000, *21*, 312–319.
- [31] Chung Y.M.; Sung H.J. *AIAA J*. 1997, *35*, 269–274.
- [32] Li N.; Balaras E.; Piomelli U. *Phys Fluids*. 2000, *12*, 935–938.
- [33] Tenaud C.; Pellerin S.; Dulieu A.; Ta Phuoc L. *Comput Fluid*. 2005, *34*, 67–96.
- [34] Ladeinde F.; Liu W.; O'Brien E.E. *J Fluid Eng*. 1998, *120*, 48–53.
- [35] Vreman A.W.; Sandham N.D.; Luo K.H. *J Fluid Mech*. 1996, *320*, 235–258.
- [36] Lele S.K. *AIAA P*. 1989, 89-0374.
- [37] Stanley S.; Sarkar S. *Theor Comput Fluid Dynam*. 1997, *9*, 121–147.
- [38] Wilson R.V.; Demuren A.O. *Numer Heat Tran*. 1996, *29*, 485–509.
- [39] Elliott G.S.; Samimy M. *Phys Fluids*. 1990, *2*, 1231–1240.

- [40] Goebel S.G.; Dutton J.C. *AIAA J.* 1991, **29**, 538–546.
- [41] Li Q.; Fu S. *Comput Fluid.* 2003, **32**, 1357–1377.
- [42] Papamoschou D.; Roshko A. *J Fluid Mech.* 1988, **197**, 453–477.
- [43] Ginevsky A.S. *The theory of turbulent jets and wakes.* Science Publishing House: Moscow, RU, 1969.
- [44] Antonia R.A.; Prabhu A.; Stephenson S.E. *J Fluid Mech.* 1975, **72**, 455–480.
- [45] Chevray R.; Tutu N.K. *J Fluid Mech.* 1978, **88**, 133–160.
- [46] Chua L.P.; Antonia R.A. *Int J Heat Mass Tran.* 1990, **33**, 331–339.
- [47] Pietri L.; Amielh M.; Anselmet F. *Int J Heat Fluid Flow.* 2000, **21**, 22–36.
- [48] Kukes V.I.; Yarin L. In *Proceedings of the 5th Conference on Heat and Mass Transfer;* Minsk, BY, 1976; Vol. 1, pp 167–171.
- [49] Lau J.C. *J Fluid Mech.* 1981, **105**, 193–218.
- [50] Ustimenko B.P.; Zmeikov V.N.; Shishkin A.A.; Rivin B.O. In *Turbulent Jet Flows;* Tallinn, ES, 1985, 21–26.
- [51] Gorshkov G.F. In *Dynamics of Inhomogeneous and Compressible Mediums;* Leningrad State University: Leningrad, RU, 1984, 164–174.
- [52] Launder B.E.; Morse A.; Rodi W.; Spalding D.B. *NASA Report.* 1973, SP-321, 361–422.
- [53] Gazzah M.H.; Sassi M.; Sarh B.; Gokalp I. *Int J Therm Sci.* 2002, **41**, 51–62.
- [54] Lyubimov D.A. *AGD.* 2003, 14–20.
- [55] Shur M.L.; Spalart P.R.; Strelets M.Kh.; Travin A.K. *Int J Heat Fluid Flow.* 2003, **24**, 551–561.
- [56] Tucker P.G. *Int J Heat Fluid Flow.* 2004, **25**, 625–635.
- [57] Yan H.; Su M. *Comm Nonlinear Sci Numer Simulat.* 1999, **4**, 12–19.
- [58] Ilyushin B.B.; Krasinskii D.V. *TA.* 2006, **13**, 49–61.
- [59] Salinas-Vazquez M.; Vicente W.; Espinosa A.; Barrios E. *Am J Appl Sci.* 2005, **2**, 1270–1273.
- [60] Boersma B.J.; Lele S.K. In *Center for Turbulence Research;* University of Stanford: Stanford, US, 1999, pp 365–377.
- [61] Baughn J.; Hechanova A.; Yan X. *J Heat Tran.* 1991, **113**, 1023–1025.
- [62] Cooper D.; Jackson D.; Launder B.; Liao G. *Int J Heat Mass Tran.* 1993, **36**, 2675–2684.
- [63] Lytle D.; Webb B. *Int J Heat Mass Tran.* 1994, **37**, 1687–1697.
- [64] Alekseenko S.V.; Kulebyakin V.V.; Markovich D.M.; Pokryvailo N.A.; Tovchi-grechko V.V. *JEPTER.* 1996, **69**, 615–624.
- [65] Phares D.J.; Smedley G.T.; Flagan R.C. *J Fluid Mech.* 2000, **418**, 351–375.
- [66] Heyerichs K.; Pollard A. *Int J Heat Mass Tran.* 1996, **39**, 2385–2400.

- [67] Chung Y.M.; Luo K.H.; Sandham N.D. *Int J Heat Fluid Flow.* 2002, *23*, 592–600.
- [68] Craft T.J.; Iacovides H.; Yoon J.H. *FTC.* 2000, *63*, 59–80.
- [69] Gardon R.; Cobonpue J. In *International Development in Heat Transfer.* ASME: New York, 1963, 454–460.
- [70] Hoogendoorn C.J. *Int J Heat Mass Tran.* 1977, *20*, 1333–1338.
- [71] Durbin P.A. *Int J Heat Fluid Flow.* 1996, *17*, 89–90.
- [72] Ashforth-Frost S.; Jambunathan K. *Int J Numer Meth Fluid.* 1996, *23*, 295–306.
- [73] Amano R.; Sugiyama S. *JSME.* 1985, *28*, 74–79.
- [74] Vieser W.; Esch T.; Menter F. *CFX Validation Report.* 2002, CFX-VAL10/0602.
- [75] Park T.S.; Sung H.J. *Int J Heat Fluid Flow.* 2001, *22*, 10–18.
- [76] Behnia M.; Parneix S.; Durbin P.A. *Int J Heat Mass Tran.* 1998, *41*, 1845–1855.
- [77] Collucci D.W.; Viskanta R. *Exp Therm Fluid Sci.* 1996, *13*, 71–80.
- [78] Voke P.R.; Gao S. *Int J Heat Mass Tran.* 1998, *41*, 671–680.
- [79] Tsubokura M.; Kobayashi T.; Taniguchi N.; Jones W. *Int J Heat Fluid Flow.* 2003, *24*, 500–511.
- [80] Olisson M.; Fuchs L. *Phys Fluids.* 1998, *10*, 476–486.
- [81] Zuev V.E. *Propagation of visible and infrared radiation in the atmosphere.* Wiley & Sons: Ney York, US, 1974.
- [82] Jumper E.J.; Fitzgerald E.J. *Progr Aero Sci.* 2001, *37*, 299–339.
- [83] Gordeyev S.; Jumper E.J. *AIAA P.* 2005, 2005-4657.
- [84] Sutton G.W. *AIAA J.* 1985, *23*, 1525–1537.
- [85] Tromeur E.; Garnier E.; Sagaut P. *J Fluid Eng.* 2006, *128*, 239–246.
- [86] Dimotakis P.E.; Catrakis H.J.; Fourguette D.C. *J Fluid Mech.* 2001, *433*, 105–134.
- [87] Wyckham C.M.; Zaidi S.H.; Miles R.B.; Smits A.J. *AIAA P.* 2003, 2003-4308.
- [88] Carroll B.F.; Boulos E.; Sytsma M.; Cattafesta L.N.; Hubner J.P.; Sheplak M. *AIAA P.* 2004, 2004-0936.
- [89] Catrakis H.J.; Aguirre R.C.; Nathman J.C.; Garcia P.J. *JoT.* 2006, *7*, 1–21.
- [90] Volkov K.N.; Emelyanov V.N. *TP.* 2008, *53*, 217–223.
- [91] Sutton G.W. *Applied Optics.* 1994, *33*, 3972–3976.
- [92] Truman C.R. *AIAA P.* 1992, 92-2817.
- [93] Wei H.; Chen C. *Int J Heat Mass Tran.* 1996, *39*, 3989–3991.
- [94] Huang P.G.; Coleman G.N.; Bradshaw P. *J Fluid Mech.* 1995, *305*, 185–218.
- [95] Koterov V.N.; Savelev A.D.; Tolstykh A.I. *Mathematical Simulation.* 1997, *9*, 27–39.

Reviewed by Professor Vladislav N. Emelyanov, Head of Department of Gas and Plasma Dynamics, Physical and Mechanical Faculty, Baltic State Technical University, ul. 1-aya Krasnoarmeyskaya, 1, 190005 Saint Petersburg, Russia, e-mail: vlademelyanov@gmail.com.

Chapter 15

GRAND COMPUTATIONAL CHALLENGES FOR PREDICTION OF THE TURBULENT WIND FLOW AND CONTAMINANT TRANSPORT AND DISPERSION IN THE COMPLEX URBAN ENVIRONMENT

Fue-Sang Lien¹, Eugene Yee², Bing-Chen Wang² and Hua Ji³

¹University of Waterloo, Canada

²Defence R & D Canada - Suffield, Canada

³Waterloo CFD Engineering Consulting, Inc., Canada

Abstract

A comprehensive overview of the prognostic physics-based urban microscale models for flow and dispersion that have been developed as part of a four-year research and development effort is described. The effort was funded by the Chemical, Biological, Radiological and Nuclear (CBRN) Research and Technology Initiative (CRTI) under a project entitled “An Advanced Emergency Response System for CBRN Hazard Prediction and Assessment for the Urban Environment”. The primary objective of this project was to develop an advanced, high-fidelity, fully validated, state-of-the-science modeling system for the prediction of urban flows and the dispersion of CBRN agents released in these highly disturbed flows. This chapter describes the progress on one of the components of the project. This component focuses on (1) the development and implementation of a computational fluid dynamics (CFD) model for the simulation of the aerodynamics of the extremely complex turbulent wind flow in an arbitrary cityscape; (2) the development of a grid generation capability for the automatic generation of grids in the computational domain when provided with detailed geometric information on the shapes and locations of buildings; and, (3) the provision of predictive models for transport and turbulent diffusion of contaminants released in an urban area. The predictive accuracy of the urban microscale models for flow and dispersion have been validated by comparing model predictions with comprehensive experimental data obtained from laboratory studies of flow and dispersion over idealized obstacle arrays and from a full-scale urban field experiment conducted in Oklahoma City, Oklahoma in July 2003 (Joint Urban 2003, or JU2003 experiment).

1. Introduction

The environmental and toxicological impact of the downwind transport and diffusion of contaminants released into the atmosphere has become increasingly important in recent years. Considerable interest has been focused on the prediction of mean concentration levels downwind of contaminant sources in the turbulent atmospheric boundary layer. Consequently, atmospheric transport and diffusion models have played an important role in emergency response systems for toxic releases and have been used in calculating the transport, diffusion, and deposition of toxic chemical, biological, or radiological materials released (either accidentally or deliberately) into the turbulent atmospheric boundary layer over relatively smooth and horizontally homogeneous surfaces. For example, military and civilian (government and commercial) emergency response models commonly use standard Gaussian plume or puff models which employ semi-empirical relationships for plume or puff growth with the mean wind and turbulence field obtained either from similarity theory or from the use of simple diagnostic wind fields constructed from interpolation and/or extrapolation of sparse observational data. The advantages of these approaches for wind flow specification are their simplicity, general applicability in simple atmospheric conditions, and most importantly, their limited computational requirements. While this approach is useful for a landscape that is relatively flat and unobstructed, it is wholly inadequate for surface-atmosphere interactions over “complex” surfaces (viz., most of the real world) such as cities and other built-up areas.

It needs to be emphasized that as the fraction of the World’s population that live in cities continues to grow, it is becoming increasingly important to address the urgent problem of modeling of the dispersion of toxic releases in the urban environment, characterized by extremely diverse length and time scales and complex geometries and interfaces. Indeed, a typical urban canopy consists of a large collection of buildings and other obstacles (e.g., cars lining a street, treed areas in city green spaces, etc.) that are aggregated into complex structures. When this rough surface interacts with the atmospheric flow within and above it, the disturbed flow field can become extremely complex (e.g., curved mean streamlines, large velocity gradients, sharp velocity discontinuities, flow separations and reattachments, cavity regions, recirculation zones, and strongly inhomogeneous turbulence). Understanding the complex flow of the wind through and above the urban environment and the dispersion of contaminants released into that flow is both necessary and important. In view of this, we require physically-based urban wind models that can provide the needed spatial-temporal pattern of urban wind statistics required to “drive” modeling of dispersion of contaminants within the street canyons of an urban environment (where it is venting of these street canyons that is important for determination of the contaminant concentrations).

This identified capability gap was the motivation for the development of an advanced emergency response system for chemical, biological, radiological and nuclear (CBRN) hazard prediction and assessment for the urban environment sponsored by Chemical, Biological, Radiological and Nuclear Research and Technology Initiative (CRTI) under Project 02-0093RD entitled “An Advanced Emergency Response System for CBRN Hazard Prediction and Assessment for the Urban Environment”. The principal objective of this project was to develop an advanced, fully validated, state-of-the-science modeling system for the prediction of urban flow (i.e., turbulent flow through cities) and the concomitant problem of

the modeling of the dispersion of CBRN agents released into these complex flows. This system will allow the dispersion of CBRN materials to be modeled over a vast range of length scales at the appropriate resolution for each scale: namely, in the near field (up to about 2 km) where dispersion is governed by the micro-scale regime of the planetary boundary layer; to the intermediate field between about 2 and 20 km where dispersion is governed by the local or meso- γ scale; through the far field covering the range from about 20-200 km (meso- β scale) and from about 200-2000 km (meso- α scale) which correspond to dispersion at the regional scale; and, finally out to the very far field encompassing scales greater than about 2000 km corresponding to dispersion on the large (synoptic and global) scales.

The development of this proposed high-fidelity, multi-scale and multi-physics modeling system will provide a real-time modeling and simulation tool for prediction of injuries, casualties, and contamination resulting from the release of a CBRN agent in an urban area. This, in turn, will provide the key-enabling technology that will enable emergency managers and decision makers to make the informed decisions (based on the strongest technical and scientific foundations) required in the support of Canada's more broadly based efforts at advancing CBRN counter-terrorism planning and operational capabilities.

The multi-scale modeling system for emergency response consists of five major components shown in the schematic diagram of Figure 1. These five components can be described briefly as follows. Component 1 involves the development of models to predict the mean flow and turbulence in the urban complex at the microscale (from the building and street scale up to a length scale of about 2 km). Two kinds of models have been developed for this purpose: namely, high-resolution building-aware models for urban flow where buildings are explicitly resolved; and, virtual building models for urban flow where groups of buildings are represented simply in terms of a distributed drag force.

Component 2 involves the inclusion of the effects of urban terrain on the subgrid scales of a mesoscale meteorological model (Global Environmental Multi-scale Local Area Model, or GEM LAM – see Côté et al., 1998) through an urban parameterization. This parameterization (Masson, 2000) is required to account properly for the area-averaged effects of form drag, increased turbulence production, heating and surface energy budget modification due to the presence of buildings/obstacles and urban land use within the urban environment. Component 3 involves coupling the urban microscale flow models developed in Component 1 with the “urbanized” mesoscale model developed in Component 2. The interface between the urban microscale flow models and the “urbanized” GEM LAM model is demanding in that the information transfer between the two models must honor physical conservation laws, mutually satisfy mathematical boundary conditions, and preserve numerical accuracy, even though the corresponding meshes might differ in structure, resolution, and discretization methodology.

Component 4 involves using the mean flow and turbulence predicted by the multi-scale flow model developed in Component 3 to “drive” a Lagrangian stochastic (LS) model for the prediction of urban dispersion of CBRN agents. The application of LS models to atmospheric dispersion in general (and, urban dispersion in particular) is recommended because LS models (1) are (in principle) the most flexible and the most easily able to incorporate all the known statistical details on the complex urban flow and (2) are physically transparent, and easily adapted to handle particulates, biological or radioactive decay, dry and wet deposition, and other relevant source and sink mechanisms. Finally, Component 5 involves

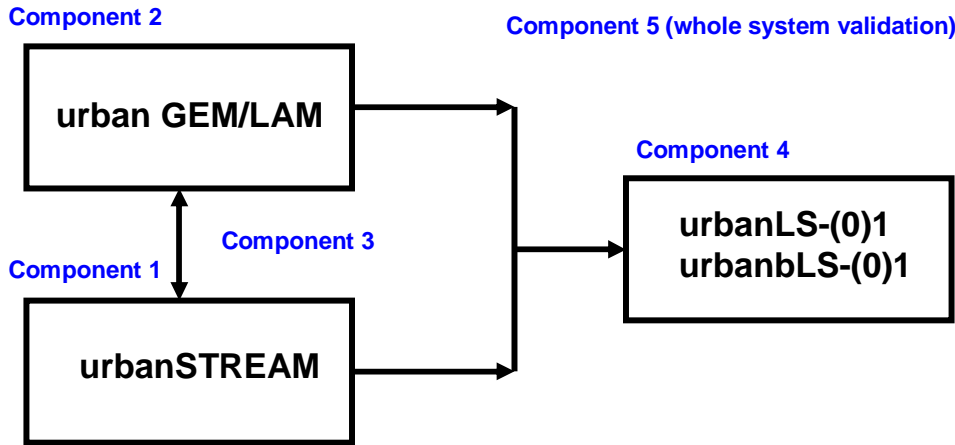


Figure 1. Relationships between various components of CRTI Project 02-0093RD.

the validation of the multi-scale modeling system for both the urban flow and dispersion components.

The primary objective of this chapter is to describe the current status (and, more specifically, the technical formulation) of the ongoing model development conducted under Component 1 of the project. In addition, the predictive capabilities of the urban microscale flow and dispersion models developed in Component 1 and applied in stand-alone mode are demonstrated by presenting results from case studies involving the comparison of model predictions with experimental data obtained from a laboratory study of flow and dispersion over an idealized obstacle array and from a comprehensive full-scale urban field experiment conducted in Oklahoma City, Oklahoma in July 2003 (Joint Urban 2003, or JU2003 field experiment).

1.1. Overview of the urban microscale modeling system

The urban modeling system developed for Component 1 of CRTI Project 02-0093RD includes five main modules: urbanGRID, urbanSTREAM, urbanEU, urbanAEU, and urbanPOST. These modules and how they interface with each other and with other project components are shown in Figure 2.

In the simplest terms, urbanGRID imports building information encoded in Environmental Systems Research Institute (ESRI) Shapefiles and uses this data to generate a structured grid over a user-selected computational domain in a given cityscape. Furthermore, urbanGRID imports three-dimensional meteorological fields (e.g., mean wind, turbulence kinetic energy, etc.) provided by urban GEM LAM and uses this information to provide inflow boundary conditions for the urban microscale flow model.

The structured grid and inflow boundary conditions provided by urbanGRID are used as input by urbanSTREAM which is a computational fluid dynamics (CFD) model for the numerical simulation of the flows within and above the complex geometries of buildings in the cityscape. The flow solver urbanSTREAM provides the high-resolution wind and tur-

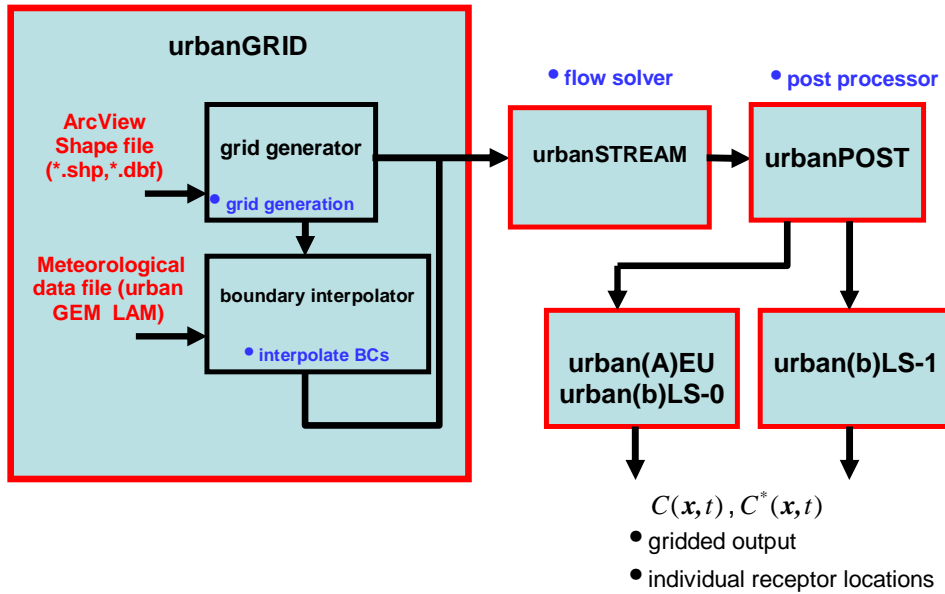


Figure 2. Various modules of Component 1 and their relationship to other components of CRTI Project 02-0093RD.

bulence fields used by the two Eulerian grid dispersion models urbanEU (source-oriented) and urbanAEU (receptor-oriented) to simulate the dispersion of contaminants in the urban area. These two urban dispersion models are based on the numerical solution of a K -theory advection-diffusion equation or its adjoint. Finally, urbanPOST is used to post-process the primary output files from urbanSTREAM to provide an appropriate specification of wind statistics required as input by either the two Eulerian urban dispersion models urbanEU and urbanAEU or, alternatively, by the urban Lagrangian stochastic particle trajectory model urbanLS (forward dispersion model) or urbanbLS (backward dispersion model) developed under Component 4 of CRTI Project 02-0093RD. Both zeroth-order forward and backward Lagrangian stochastic models (or, random displacement models) involving the evolution of the position of a “marked” fluid particle (urban(b)LS-0 – see Figures 1 and 2) and first-order forward and backward Lagrangian stochastic models involving the joint evolution of the position and velocity of a “marked” fluid particle (urban(b)LS-1 – see Figures 1 and 2) have been formulated.

The memory management scheme used in urbanSTREAM, urbanEU, and urbanAEU is full dynamic array allocation which allows the maximum array dimensions in these models to be easily adjusted to match the requirements of a particular problem. The size of the grid for a specific application is determined in urbanGRID, which provides an external parameter file that specifies the required array sizes for all the major arrays in urbanSTREAM. The latter model then dynamically allocates only the amount of memory required for the specific problem.

2. Technical Description of Modules

2.1. Grid generator: urbanGRID

urbanGRID is a program that is concerned with the automatic generation of structured grids (or meshes) in the computational domain for numerical solutions involving the complex geometry of buildings and other obstacles in the urban environment (real cityscape). This program provides a predetermined mesh which fills the entire computational domain, and serves as the input data for spatial discretization required to “drive” the flow solver program urbanSTREAM. The mesh determines the location in the domain at which the flow quantities will be evaluated as well as where boundary conditions need to be applied at all the walls and roofs of arbitrary-shaped buildings (and other solid surfaces) in the domain.

The geometric information on shapes and locations of buildings in the computational domain (corresponding to a region of a real city) is assumed to be available in form of ESRI Shapefiles (ESRI, 1998). An ESRI Shapefile is a digital vector storage format that stores non-topological information and spatial features in a data set, with the geometry for each feature comprising a set of vector coordinates and associated attribute information. A Shapefile is actually a set of files. Three individual files are mandatory and these store the core data, although in general a Shapefile may also include up to eight further optional individual files. urbanGRID only requires Shapefile information stored in the three mandatory files. These three individual files have the following file extensions in their name: (1) *.shp is the main file and is a direct-access, variable record-length file whose records store the feature geometry (for our current application, the key features are area features corresponding to building “footprints” encoded as closed-loop double-digitized polygons); (2) *.shx is the file that stores the index of the feature geometry and contains the offset of the main file record from the beginning of the main file; and, (3) *.dbf is a file in the form of a dBASE table that contains feature attributes (e.g., height of buildings) with one record per feature, there being a one-to-one correspondence between the geometry and attributes based on record number.

The computational domain where the flow field will be calculated is specified by the user who provides the x and y coordinates (easting and northing coordinates, respectively) of the southwest ($x_{\text{SW}}^{\text{outer}}$, $y_{\text{SW}}^{\text{outer}}$) and northeast ($x_{\text{NE}}^{\text{outer}}$, $y_{\text{NE}}^{\text{outer}}$) corners of the domain in the Universal Transverse Mercator (UTM) coordinate system. Additionally, the user provides the easting and northing coordinates of the southwest ($x_{\text{SW}}^{\text{inner}}$, $y_{\text{SW}}^{\text{inner}}$) and northeast ($x_{\text{NE}}^{\text{inner}}$, $y_{\text{NE}}^{\text{inner}}$) corners for an inner domain which lies strictly inside the computational domain, where buildings are explicitly resolved (building-aware region) in the sense that appropriate boundary conditions are imposed on all the building surfaces (e.g., wall, roofs). For the region that lies outside the inner domain but inside the computational domain, the buildings are treated as virtual in the sense that the effects of these unresolved buildings on the flow are represented simply as a distributed mean-momentum sink in the mean momentum equation (which is described later in this report). urbanGRID uses the Shapefile C Library Version 1.2 (Warmerdam, 1998) for reading ESRI Shapefiles, and of greatest interest here, are the vector coordinates of all the vertices (ordered in a counter-clockwise direction) that define the footprints of the buildings (which are represented in UTM coordinates) and the attribute corresponding to the heights of the buildings in the inner domain. Finally, the

height z_d of the computational domain is provided as a user input to urbanGRID.

Once the computational domain has been defined, a structured Cartesian mesh is generated over the domain. The implicit grid structure alleviates the need to store the mesh connectivity, and permits the use of rapid iterative solution algorithms for the computation of the flow, which makes use of sparse matrix solvers. urbanGRID generates a Cartesian mesh over the computational domain by defining an arrangement of discrete grid points that define the cell faces (grid lines). In any given coordinate direction, the spacing of the grid points starting from a solid surface (e.g., ground surface, wall or roof of a building, etc.) is stretched as one moves away from the surface along the coordinate direction. The stretching function used in urbanGRID has the form

$$x_{s,i}[j] = L_i \frac{(\beta + 2\alpha)((\beta + 1)/(\beta - 1))^{(x_i[j]-\alpha)/(1-\alpha)} - \beta + 2\alpha}{(2\alpha + 1)\left(1 + ((\beta + 1)/(\beta - 1))^{(x_i[j]-\alpha)/(1-\alpha)}\right)}, \quad (1)$$

($j = 1, 2, \dots, N_i$) where L_i is the length of the domain in the i -th coordinate direction, N_i is the number of grid points in the i -th coordinate direction, $x_i[j]$ is the j -th grid point coordinate in the i -th coordinate direction for a uniform grid spacing, and $x_{s,i}[j]$ is the corresponding j -th grid point coordinate in the i -th direction for the stretched grid. In Equation (1), $\alpha \in \{0, \frac{1}{2}, 1\}$ and $\beta \in (1, \infty)$ are parameters of the stretching function that are used to determine, respectively, the direction (positive, negative, or in both directions) of stretching along the coordinate axis and the magnitude of the stretching. More specifically, if $\alpha = 0$ the spacing between the grid points is stretched along the positive direction of the x_i -axis, if $\alpha = 1$ the stretching is applied along the negative direction of the x_i -axis, and if $\alpha = \frac{1}{2}$ the stretching is along both the negative and positive directions of the x_i -axis. Finally, the stretching of the spacing between grid points along a coordinate axis increases as $\beta \rightarrow 1^+$, whereas $\beta \rightarrow \infty$ results in a uniform spacing between grid points.

In the inner region of the computational domain, the buildings are explicitly resolved and it becomes imperative to define an appropriate data structure to encode information about whether a control volume (grid cell) is a fluid cell (which lies mostly or completely within the fluid region) or an obstacle cell (which lies mostly or completely inside a building), and if a fluid cell whether any face of this cell abuts against a wall or roof of a building (the latter information being required for the implementation of the wall function boundary condition in urbanSTREAM). To this purpose, urbanGRID uses an 8-bit integer `FLAG` array to encode this information as follows:

	high								low	
FLAG	C_D on/off	C_O on/off	C_B on/off	C_T on/off	C_S on/off	C_N on/off	C_W on/off	C_E on/off	1 ON	0 OFF
	128	64	32	16	8	4	2	1		

If bit number 7 (C_O bit) of the FLAG array is set for a cell with indices (i, j, k) (viz., $\text{FLAG}(i, j, k) = \text{C_O} = 64$), then this cell is an obstacle cell; otherwise, it is a fluid cell. Bit number 8 (C_D bit) of the FLAG array determines whether the cell lies in the region where buildings are considered to be virtual and, hence, represented as a distributed momentum drag force in the mean momentum equation. More specifically, if bit 8 is switched on in the FLAG array for cell (i, j, k) then this cell lies within the “virtual building” region of

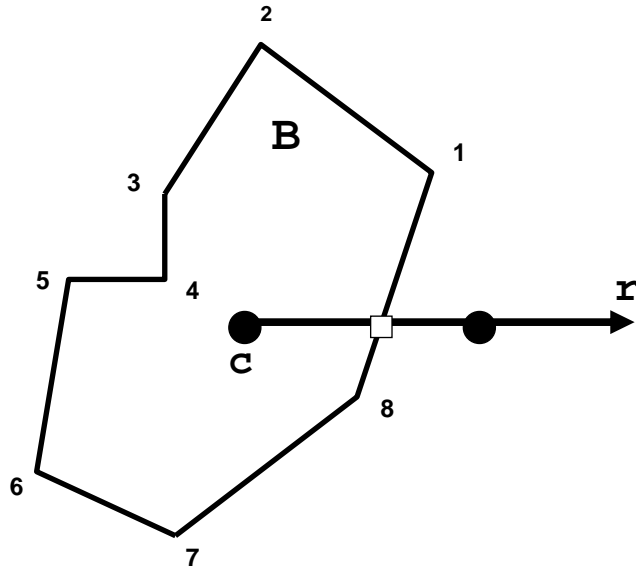


Figure 3. Illustration of ray-casting approach to determine if a grid cell with centroid c lies inside the building B .

the computational domain. The remaining lower-order bits of the FLAG array determine whether a fluid cell is also a boundary cell in the sense that one or more faces of this cell borders an obstacle cell. For example, a fluid cell for which the lowest bit (or, C_E bit) of the FLAG array is ON signifies that the east face of the corresponding fluid cell abuts against a building surface. Similarly, the second (C_W), third (C_N), fourth (C_S), fifth (C_T), or sixth (C_B) bits of the FLAG array if switched ON imply that the west, north, south, top, or bottom faces of the associated fluid cell borders on a building surface.

Because each building extracted from an ESRI Shapefile has a constant height attribute, it is computationally more efficient to consider the intersection of the projection of the cell in the horizontal x - y plane with the building footprint (represented by a closed-loop polygon in the Shapefile) in order to determine whether a particular grid cell is a fluid cell or an obstacle cell. To this end, a bounding box (or, smallest rectangle that completely surrounds the building footprint and has sides that are parallel to the x -axis and y -axis) is constructed for each building within the inner (or, building-aware) region. Clearly, only grid cells that intersect any of these bounding boxes in the inner region can possibly be classified as obstacle cells (with the appropriate bit in the associated FLAG array set); otherwise, the grid cell must necessarily be classified as a fluid cell.

For the grid cells that intersect one of the bounding boxes in the inner region, the determination of whether these cells are obstacle or fluid cells depends on whether the centroid of the cell lies inside or outside the building, respectively. A ray-casting approach is used to ascertain this condition. As shown in Figure 3, the ray-casting approach for determination of whether a grid cell should be classified as a fluid cell or an obstacle cell involves casting a ray r from the cell centroid c and simply counting the number of intersections of r with the

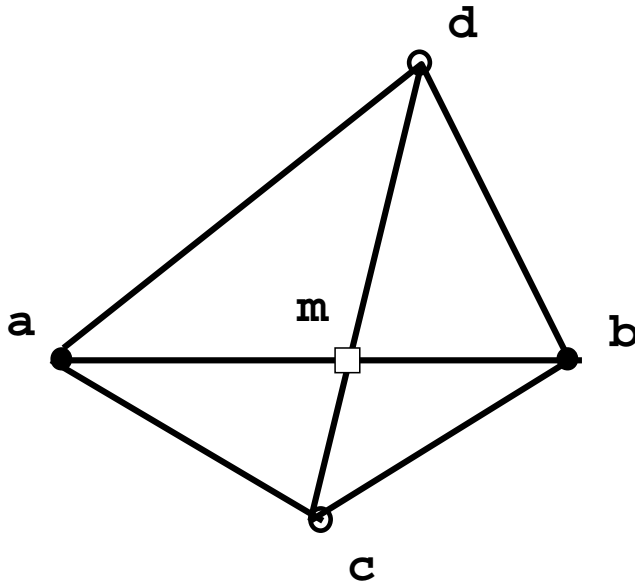


Figure 4. Determination of whether two line segments intersect each other.

various faces of the building enclosed by the bounding box that the grid cell overlaps. If the grid cell centroid lies inside a building (labeled B in Figure 3), the number of intersections of r with the building faces must be odd. Because the building footprint is encoded as a list of vector coordinates of vertices forming a number of line segments that constitute a closed polygon, we need to determine if there is an intersection of ray r with each of these line segments and then count the total number of intersections.

The determination of whether two line segments intersect is based on the computation of a signed area. To this purpose, let us focus on whether line segment \overline{ab} intersects line segment \overline{cd} as depicted in Figure 4. To ascertain this, we calculate the signed areas for the following four triangles: $\Delta(acd)$, $\Delta(bcd)$, $\Delta(acb)$ and $\Delta(adb)$. The signed area for a triangle $\Delta(abc)$ whose three vertices are a, b and c (ordered in either a clockwise or counter-clockwise direction) is given by

$$A_{abc} = \det \begin{pmatrix} a_x & a_y & 1 \\ b_x & b_y & 1 \\ c_x & c_y & 1 \end{pmatrix}, \quad (2)$$

where $a = (a_x, a_y)$, $b = (b_x, b_y)$ and $c = (c_x, c_y)$. With reference to Figure 4, the two line segments \overline{ab} and \overline{cd} intersect each other if and only if the following two conditions are verified:

$$\begin{aligned} A_{acd} \times A_{bcd} &< 0, \\ A_{acb} \times A_{adb} &< 0. \end{aligned} \quad (3)$$

While the test for intersection of two line segments provided by Equation (3) is straightforward, its implementation on the necessarily finite precision of the hardware on a digital

computer is not. Problems can arise when a zero-area triangle is encountered, corresponding to the case when the vertices of a triangle are exactly collinear. Given the finite precision of a digital computer, distinguishing between the case of a zero-area triangle occurring because of round-off error and precision problems or because of an exact collinearity is difficult and needs to be handled carefully. To deal with this possibility, urbanGRID uses an adaptive exact arithmetic procedure developed by Schewchuk (1996) in its computation of signed areas. The procedure used in urbanGRID for this is as follows. We first calculate the signed area given by Equation (2) using floating point arithmetic, and then estimate the maximum possible value for the round-off error using the error bound derived in Schewchuk (1996). If this error is larger than the computed signed area, then the area is re-calculated using adaptive precision floating point arithmetic. If this result is identically zero too, then we resolve the degeneracy in the signed area computation by using a “tie-breaking” algorithm based on a virtual perturbation approach advocated by Edelsbrunner and Muncke (1990). The basic idea underpinning this approach is to resolve “ties” in the vector coordinates of the triangular vertices that result in an “exact” zero signed area by breaking this degeneracy through the introduction of a unique and ordered perturbation of the vertices. This results in a non-degenerate signed area. Since the perturbation is virtual, no geometric data is modified. It is noted that this refinement is merely a technicality needed to resolve possible finite precision collinearity of vertices of a triangle. The virtual perturbation of the vertices never affects the actual coordinates of these vertices (which are always held to finite precision), but nevertheless enables an unambiguous calculation of the signed area.

The distribution of flow variables needs to be specified (viz., Dirichlet boundary conditions need to be defined) at the inflow boundary planes for the computational domain used for flow calculation in urbanSTREAM. To this purpose, urbanGRID interpolates the gridded mean velocity and turbulence fields provided by urban GEM LAM (a prognostic mesoscale model with an urban parameterization developed by Environment Canada for CRTI Project 02-0093RD). The gridded mean velocity and turbulence kinetic energy fields provided by urban GEM LAM in a large domain that includes the computational domain defined in urbanGRID are linearly interpolated to the grid nodes in the inflow boundary planes for urbanSTREAM. This corresponds to a one-way coupling between the mesoscale flow model urban GEM LAM and the microscale (building-aware) flow model urbanSTREAM.

2.2. Flow solver: urbanSTREAM

The computational fluid dynamics (CFD) code urbanSTREAM was developed specifically in a general non-orthogonal (curvilinear) coordinate system in order to compute specifically the flow through and above an urban canopy on arbitrary terrain. The curvilinear coordinate system allows the terrain to be described accurately. However, for simplicity of exposition, the relevant governing flow equations will be stated in a Cartesian orthogonal coordinate system, despite the fact that the flow solver has been implemented in a general curvilinear coordinate system.

The prediction of the complex flow (mean wind and turbulence quantities), through and above an urban canopy consisting of groups of buildings in various configurations that are representative of a real cityscape, is based on the Reynolds-averaged Navier-Stokes (RANS)

equations whereby the turbulent flow is considered as consisting of two components: a fluctuating part and a mean or average part. The Reynolds-averaged continuity and momentum equations for an incompressible adiabatic (i.e., not buoyancy-affected) fluid are a system of partial differential equations governing mass and momentum conservation and can be expressed in Cartesian coordinates as follows:

Continuity

$$\frac{\partial \bar{u}_i}{\partial x_i} = 0, \quad (4)$$

Momentum

$$\frac{\partial \bar{u}_i}{\partial t} + \frac{\partial \bar{u}_j \bar{u}_i}{\partial x_j} = -\frac{\partial \bar{p}}{\partial x_i} + \nu \frac{\partial^2 \bar{u}_i}{\partial x_j^2} - \frac{\partial}{\partial x_j} (\bar{u}'_i \bar{u}'_j) - 2\epsilon_{ijk} \Omega_j \bar{u}_k, \quad (5)$$

where the Reynolds averaging of a quantity is denoted by drawing a bar over the quantity. Summation is implied by repeated indices. Here, \bar{u}_i and u'_i are the mean and fluctuating velocities in the x_i -direction, respectively, with $i = 1, 2$, or 3 representing the west-east x , south-north y , or vertical z directions; $x_i = (x, y, z) \equiv \mathbf{x}$; t is time; $u_i = (u, v, w)$; $\bar{u}_i = (\bar{u}, \bar{v}, \bar{w})$; ν is the kinematic viscosity and \bar{p} is the kinematic mean pressure (with p' used to denote pressure fluctuations). The last term on the right-hand-side (RHS) of Equation (5) is the Coriolis acceleration term (caused by the Coriolis force) where Ω_j is the Earth's rotation vector and ϵ_{ijk} is the permutation symbol [which has the value zero if any pair of subscripts is identical, and is $(-1)^q$ otherwise where q is the number of subscript transpositions required to bring (ijk) to the natural order (123)]. Rotation is defined by the right-hand rule where positive is clockwise when looking in the direction of Ω_j . Note that the Cartesian coordinate system fixed on the Earth's surface can have any orientation with respect to Ω_j .

Reynolds-averaging the Navier-Stokes equation gives rise to the so-called kinematic Reynolds stresses which are defined as the tensor $\bar{u}'_i \bar{u}'_j$. The Reynolds stresses depend on the velocity fluctuations u'_i , and introduce new unknown quantities in the RANS equations. In consequence, these equations no longer constitute a closed system. In order to close the system of equations, we need further equations describing the relationship between $\bar{u}'_i \bar{u}'_j$ and the quantities \bar{u}_i and \bar{p} that we seek to determine. This is known as the closure problem in turbulence modeling. One of the simplest turbulence models for $\bar{u}'_i \bar{u}'_j$ involves approximating the Reynolds stress components by analogy with a Newtonian type of linear constitutive relationship between the turbulence stress and the mean strain-rate tensor. This model uses the Boussinesq eddy-viscosity approximation (which is perhaps the simplest coordinate invariant relationship between stresses and strains) and is given by

$$\bar{u}'_i \bar{u}'_j = \frac{2}{3} k \delta_{ij} - \nu_t \left(\frac{\partial \bar{u}_i}{\partial x_j} + \frac{\partial \bar{u}_j}{\partial x_i} \right), \quad (6)$$

where ν_t is the kinematic eddy viscosity, $k \equiv \frac{1}{2} \bar{u}'_i \bar{u}'_i$ is the turbulence kinetic energy (TKE), and δ_{ij} is the Kronecker delta function. It is interesting to note that with the adoption of the Boussinesq eddy-viscosity approximation, the RANS equations have the same form as the

¹with the implied Reynolds decomposition $u_i = \bar{u}_i + u'_i$.

Navier-Stokes equations except that the kinematic molecular viscosity ν is replaced by an effective kinematic viscosity $\nu_{\text{eff}} = (\nu + \nu_t)$ and provided the mean pressure is interpreted to be a modified mean pressure.²

The CFD code urbanSTREAM also implements a more sophisticated turbulence closure scheme for the kinematic Reynolds stresses $\overline{u'_i u'_j}$. To this purpose, there is an option in the code to approximate $\overline{u'_i u'_j}$ using an explicit nonlinear algebraic Reynolds stress model proposed originally by Speziale (1987): namely,

$$\begin{aligned} \overline{u'_i u'_j} &= \frac{2}{3} k \delta_{ij} - \nu_t \left(\frac{\partial \bar{u}_i}{\partial x_j} + \frac{\partial \bar{u}_j}{\partial x_i} \right) + \frac{k^3}{\epsilon^2} \left[C_{\tau 1} \left(\frac{\partial \bar{u}_i}{\partial x_k} \frac{\partial \bar{u}_j}{\partial x_k} \right)^* \right. \\ &\quad \left. + C_{\tau 2} \left(\frac{\partial \bar{u}_i}{\partial x_k} \frac{\partial \bar{u}_k}{\partial x_j} + \frac{\partial \bar{u}_j}{\partial x_k} \frac{\partial \bar{u}_k}{\partial x_i} \right)^* + C_{\tau 3} \left(\frac{\partial \bar{u}_k}{\partial x_i} \frac{\partial \bar{u}_k}{\partial x_j} \right)^* \right], \end{aligned} \quad (7)$$

where an asterisk is used to indicate the deviatoric part of a tensor (viz., $(\cdot)_{ij}^* \equiv (\cdot)_{ij} - (\cdot)_{kk} \delta_{ij} / 3$), and ϵ denotes the viscous dissipation rate for TKE. The three model coefficients appearing in this equation have the following values: $C_{\tau 1} = 0.041$, $C_{\tau 2} = 0.014$ and $C_{\tau 3} = -0.014$. Note that the first two terms in the nonlinear Reynolds stress model of Equation (7) are simply the Boussinesq approximation for $\overline{u'_i u'_j}$.

For both the linear (or, Boussinesq) and nonlinear models for the Reynolds stresses, the task of turbulence closure reduces to the determination of the eddy viscosity. Dimensional analysis dictates that the eddy viscosity ν_t be determined by the product of a turbulence velocity scale u_0 and a turbulence length scale l_0 , so $\nu_t = u_0 l_0$, where u_0 and l_0 can vary significantly in space and time for a given turbulent flow (and, in particular, for an urban flow). In the most common approach, the turbulence velocity and length scales are based on the turbulence kinetic energy k and its dissipation rate ϵ (i.e., rate at which TKE is converted into thermal internal energy), with the turbulence velocity and length scales chosen to be

$$u_0 = C_{\mu}^{1/4} k^{1/2}, \quad l_0 = \frac{u_0^3}{\epsilon}. \quad (8)$$

Hence, in this so-called k - ϵ modeling framework at high-Reynolds (high-Re) numbers, the eddy viscosity is given by (on combining turbulence velocity and length scales)

$$\nu_t = C_{\mu} \frac{k^2}{\epsilon}, \quad (9)$$

where C_{μ} is a closure constant.

The modeled transport equation for the turbulence kinetic energy k is

$$\frac{\partial k}{\partial t} + \frac{\partial \bar{u}_j k}{\partial x_j} = \frac{\partial}{\partial x_j} \left[\left(\nu + \frac{\nu_t}{\sigma_k} \right) \frac{\partial k}{\partial x_j} \right] + P_k - C_{\epsilon_0} \epsilon, \quad (10)$$

where P_k is the production of k defined as

$$P_k \equiv -\overline{u'_i u'_j} \frac{\partial \bar{u}_i}{\partial x_j}. \quad (11)$$

²When Equation (6) is inserted into Equation (5), the term $\frac{2}{3} k \delta_{ij}$ in the Boussinesq approximation for the Reynolds stresses is usually incorporated with the pressure \bar{p} to define a modified pressure $\bar{p} + \frac{2}{3} k$ (so, $\bar{p} \rightarrow \bar{p} + \frac{2}{3} k \equiv \bar{p}^{\text{mod}}$ in the RANS equations).

The terms in the modeled TKE transport equation [Equation (10)] are from left to right: local rate of change of k , transport of k by mean advection, transport of k by viscous and turbulent diffusion, rate of production of k , and rate of destruction of k . Within the framework of a two-equation turbulence closure scheme, the combination of the turbulent transport and pressure-velocity correlation terms in the exact transport equation for TKE is modeled using a gradient diffusion hypothesis as

$$\bar{D}_j^t \equiv - \left[\frac{1}{2} \bar{u}'_i \bar{u}'_i \bar{u}'_j + \bar{p}' \bar{u}'_i \delta_{ij} \right] = \frac{\nu_t}{\sigma_k} \frac{\partial k}{\partial x_j}, \quad (12)$$

where σ_k is a constant that functions like an effective Schmidt number for the turbulent diffusion of k [see Equation (10)]. Note that, with this model, both the turbulent and molecular diffusion terms can be combined into a gradient transport model with effective viscosity $(\nu + \nu_t/\sigma_k)$. This resulting simple form of the modeled transport equation for k is the obvious appeal of this formulation.

Equation (10) represents the standard transport equation for TKE, except that an additional coefficient C_{ϵ_0} has been incorporated in this transport equation to adjust the balance between the production and dissipation of TKE. If $C_{\epsilon_0} = 1$, the transport equation for TKE reduces to the standard form. The coefficient C_{ϵ_0} was introduced because it can be demonstrated (see later) that a non-unity value for C_{ϵ_0} can provide significantly improved predictions of the turbulence energy levels in obstacle arrays that exhibit skimming flow over the buildings (with concomitant limited penetration of the flow aloft into the spaces between the buildings).³

An exact transport equation for ϵ can be written, but this equation is not useful owing to the fact that most of the terms in the equation are not in closed form. In its most usual form, the modeled equation for the TKE dissipation rate ϵ is

$$\frac{\partial \epsilon}{\partial t} + \frac{\partial \bar{u}_j \epsilon}{\partial x_j} = \frac{\partial}{\partial x_j} \left[\left(\nu + \frac{\nu_t}{\sigma_\epsilon} \right) \frac{\partial \epsilon}{\partial x_j} \right] + \frac{\epsilon}{k} (C_{\epsilon 1} P_k - C_{\epsilon 2} \epsilon), \quad (13)$$

where $C_{\epsilon 1}$, $C_{\epsilon 2}$ and σ_ϵ are closure constants to be determined. In Equation (13), the turbulent diffusion of dissipation (which has been grouped with the molecular diffusion term) is given by

$$\bar{D}_\epsilon^t = \frac{\partial}{\partial x_j} \left[\frac{\nu_t}{\sigma_\epsilon} \frac{\partial \epsilon}{\partial x_j} \right], \quad (14)$$

where σ_ϵ is a constant that acts like an effective Schmidt number for the turbulent diffusion of TKE dissipation. In Equation (13), the term on the RHS that involves $C_{\epsilon 1}$ is the production of dissipation term, whereas the term involving $C_{\epsilon 2}$ is the destruction of dissipation term. The factor ϵ/k in the production and destruction terms makes these terms dimensionally correct in the transport equation for ϵ .

Within the Boussinesq type of eddy-viscosity approximation, the Reynolds stresses appearing in the production P_k [cf. Equation (11)] are modeled in accordance with Equation (6) resulting in the following modeled form for P_k :

$$P_k = \nu_t \left(\frac{\partial \bar{u}_i}{\partial x_j} + \frac{\partial \bar{u}_j}{\partial x_i} \right) \frac{\partial \bar{u}_i}{\partial x_j} = C_\mu \epsilon |\bar{S}|^2, \quad (15)$$

³The k - ϵ model with $C_{\epsilon_0} \neq 1$ will be referred to as the modified k - ϵ model. When $C_{\epsilon_0} = 1$, the modified k - ϵ model reduces to the standard k - ϵ model.

where

$$|\bar{S}| = \frac{k}{\epsilon} (2\bar{S}_{ij}\bar{S}_{ij})^{1/2}, \quad \bar{S}_{ij} \equiv \frac{1}{2} \left(\frac{\partial \bar{u}_i}{\partial x_j} + \frac{\partial \bar{u}_j}{\partial x_i} \right). \quad (16)$$

Here, \bar{S}_{ij} is the mean rate-of-strain tensor (or, equivalently, the symmetric part of the mean velocity gradient tensor).

Together, the transport equations for k and ϵ contain five closure constants (C_μ , σ_k , σ_ϵ , $C_{\epsilon 1}$, and $C_{\epsilon 2}$) which must be determined before the equations can be solved. Two different high-Re number k - ϵ models are considered here. The first is the standard k - ϵ model and following the recommendation of Launder and Spalding (1974), the closure coefficients for this turbulence model are

$$C_\mu = 0.09, \quad \sigma_k = 1, \quad \sigma_\epsilon = 1.3, \quad C_{\epsilon 1} = 1.44, \quad C_{\epsilon 2} = 1.92. \quad (17)$$

Here, $C_{\epsilon 2}$ is determined from the experiment on the decay of isotropic turbulence, and $C_{\epsilon 1}$ is determined experimentally based on the local equilibrium wall shear flow. The value of σ_ϵ is chosen to ensure the correct log-law behaviour in boundary-layer flows. The second k - ϵ model implemented is the limited-length-scale k - ϵ model proposed by Apsley and Castro (1997). In this limited-length scale k - ϵ model, the length-scale determining equation (i.e., ϵ -transport equation) is modified in order to acknowledge the upper bounds on the turbulence length scale imposed by the finite depth of the atmospheric boundary layer. The modification is both simple and elegant; namely, the coefficient $C_{\epsilon 1}$ in the production of dissipation term is replaced by

$$C_{\epsilon 1} \rightarrow C_{\epsilon 1} + (C_{\epsilon 2} - C_{\epsilon 1}) \frac{l_0}{l_{0,\max}}, \quad (18)$$

where $l_{0,\max} = h/3$ is the maximum turbulence length scale imposed by the depth h of the atmospheric boundary layer [and l_0 is defined in Equation (8)]. It is noted that with the exception of $l_{0,\max}$, the modification introduces no new closure constants into the model (viz., the closure constants C_μ , σ_k , σ_ϵ , $C_{\epsilon 1}$, and $C_{\epsilon 2}$ assume exactly the same values as in the standard k - ϵ model).

A closed-form solution for the modified k - ϵ model can be obtained for the neutral wall shear layer. The solution gives

$$\bar{u} = \frac{u_*}{k_v} \log z + B, \quad k = \frac{u_*^2}{\sqrt{C_\mu}}, \quad \epsilon = \frac{u_*^3}{k_v z}, \quad (19)$$

where $u_* \equiv (-\overline{u'w'})^{1/2}$ is the friction velocity and B is a constant of integration. For this analytical solution, we find an implied value for the von Kármán constant, k_v , of

$$k_v^2 = \sqrt{C_\mu} (C_{\epsilon 2} - C_{\epsilon 1} C_{\epsilon 0}) \sigma_\epsilon / C_{\epsilon 0}. \quad (20)$$

It should be noted that for the standard k - ϵ model, $C_{\epsilon 0} = 1$. Using the closure coefficient values for the standard k - ϵ model, k_v assumes a value of 0.43. The experimental values for k_v are primarily in the range 0.41 ± 0.2 , so the implied value of k_v in the k - ϵ model is consistent with these measurements. The stress-intensity ratio, u_*^2/k , is predicted to be 0.3

(using $C_\mu = 0.09$) which agrees well with experimental measurements of this quantity in many industrial shear flows (Townsend, 1980).⁴

The technical details of urbanSTREAM used in the high-resolution computational fluid dynamics simulation of urban flow, where all the buildings in the computational domain are explicitly resolved in the sense that appropriate boundary conditions are imposed at all the building surfaces (e.g., walls, roofs), have been described. However, the computational demands of such an approach are high and, as a consequence, sufficiently prohibitive as to preclude the simulation of flow through and above all buildings over a relatively large computational domain in a typical city environment.

In lieu of imposing correct boundary conditions on the true (but usually complex, three-dimensional) geometry of the building surfaces and fully resolving the detailed intricate flow around every individual building in a computational domain, it is convenient to consider the prediction of statistics of the mean wind and turbulence in an urban canopy that are obtained by averaging horizontally the flow properties over an area that is larger than the spacings between the individual roughness elements comprising the urban canopy, but less than the length scale over which the roughness element density changes. Towards this objective, we consider the use of a virtual building concept in urbanSTREAM whereby groups of buildings are unresolved and the aggregate of these individual buildings is treated simply as a porous medium. Here, the effects of the unresolved buildings (or, virtual buildings) on the flow are represented through a distributed mean-momentum sink in the mean momentum equation. Furthermore, the additional source/sink terms in the supporting transport equations for k and ϵ are included in order to model the effects of the virtual buildings on the turbulence.

The foundations of a systematic mathematical formulation for the derivation of the governing equations for flow through an urban canopy where the individual buildings are unresolved (virtual buildings) and the aggregate of various groups of buildings (and other obstacles) is treated simply as a porous medium is described in Lien et al. (2005). Details of the implementation of this distributed drag force model can be found in Lien and Yee (2005). The representation of groups of buildings as a porous medium requires an additional modeling effort. The transport equation for the mean momentum is modified with the inclusion of a mean drag force $\bar{f}_{d,i}$ due to the effects of the virtual buildings on the flow, so

$$\frac{\partial \bar{u}_i}{\partial t} + \frac{\partial \bar{u}_j \bar{u}_i}{\partial x_j} = -\frac{\partial \bar{p}}{\partial x_i} + \nu \frac{\partial^2 \bar{u}_i}{\partial x_j^2} - \frac{\partial}{\partial x_j} (\bar{u}'_i \bar{u}'_j) - 2\epsilon_{ijk} \Omega_j \bar{u}_k + \bar{f}_{d,i}, \quad (21)$$

where $\bar{f}_{d,i}$ is parameterized as follows:

$$\bar{f}_{d,i} = -\widehat{C_D} \hat{A} \left(Q \bar{u}_i + \frac{\bar{u}_j}{Q} \bar{u}'_i \bar{u}'_j + \frac{\bar{u}_i k}{Q} \right), \quad (22)$$

where $\widehat{C_D}$ is the drag coefficient, \hat{A} is the frontal area density (frontal area of buildings exposed to the wind per unit volume), and $Q \equiv (\bar{u}_i \bar{u}_i)^{1/2}$ is the magnitude of the (spatially-averaged) time-mean wind speed. Utilizing the eddy viscosity model for turbulent stresses

⁴For the case where $C_{\epsilon_0} \neq 1$, the coefficient σ_ϵ is assigned the value $\sigma_\epsilon = k_v^2 C_{\epsilon 0} / [C_\mu^{1/2} (C_{\epsilon 2} - C_{\epsilon 1} C_{\epsilon 0})]$ in order to be consistent with the compatibility condition for flow in a neutrally-stratified wall shear layer given by Equation (20).

of Equation (6) in Equation (22) yields the following final form for the mean drag force imposed by the virtual buildings on the flow:

$$\bar{f}_{d,i} = -\widehat{C_D} \hat{A} \left[\left(Q + \frac{5}{3} \frac{k}{Q} \right) \bar{u}_i - \nu_t \left(\frac{\partial \bar{u}_i}{\partial x_j} + \frac{\partial \bar{u}_j}{\partial x_i} \right) \frac{\bar{u}_j}{Q} \right]. \quad (23)$$

Standard turbulence models need additional modifications when applied to urban flows where buildings are treated as virtual (and represented as a distributed mean-momentum sink). Additional modifications required in the transport equations for k and ϵ were derived in Lien et al. (2005) and are simply summarized here. The k - and ϵ -equations require additional source/sink terms and now take the following form:

$$\frac{\partial k}{\partial t} + \frac{\partial \bar{u}_j k}{\partial x_j} = \frac{\partial}{\partial x_j} \left[\left(\nu + \frac{\nu_t}{\sigma_k} \right) \frac{\partial k}{\partial x_j} \right] + (P_k + F) - C_{\epsilon_0} \epsilon, \quad (24)$$

and

$$\frac{\partial \epsilon}{\partial t} + \frac{\partial \bar{u}_j \epsilon}{\partial x_j} = \frac{\partial}{\partial x_j} \left[\left(\nu + \frac{\nu_t}{\sigma_\epsilon} \right) \frac{\partial \epsilon}{\partial x_j} \right] + \frac{\epsilon}{k} (C_{\epsilon 1} (P_k + F) - C_{\epsilon 2} \epsilon). \quad (25)$$

The term F in Equation (24) can be interpreted as an additional physical mechanism for the production/dissipation of k , and as shown in Lien et al. (2005) can be approximated as

$$F = -\widehat{C_D} \hat{A} \left[2Qk + \frac{1}{Q} \left(\bar{u}_i \bar{u}_k \overline{u'_i u'_k} \right) + \frac{3}{2Q} \left(\bar{u}_k \overline{u'_i u'_i u'_k} \right) \right], \quad (26)$$

where the triple correlation term $\overline{u'_i u'_i u'_k}$ here is modelled, following Daly and Harlow (1970), as

$$\overline{u'_i u'_i u'_k} = 2C_s \frac{k}{\epsilon} \left[\overline{u'_k u'_l} \frac{\partial k}{\partial x_l} + \overline{u'_i u'_l} \frac{\partial \overline{u'_i u'_k}}{\partial x_l} \right], \quad (27)$$

where the closure constant $C_s \approx 0.3$ is used. The double correlation (turbulent stress) $\overline{u'_i u'_j}$ in Equations (26) and (27) are modeled using either the Boussinesq stress-strain relationship in Equation (6) or the explicit nonlinear stress-strain relationship in Equation (7).

2.3. Urban dispersion: urbanEU and urbanAEU

Prediction of the wind field statistics using urbanSTREAM is in principle pre-requisite to or co-requisite with prediction of the simpler (but nevertheless complex) problem of scalar (contaminant) dispersion within the urban environment. In particular, the prediction of turbulent flow statistics through a built-up area is required to provide the input information needed to “drive” a physically-based model for urban dispersion. Within the context of Component 1 of CRTI Project 02-0093RD, two different (but complementary) models for urban dispersion from the Eulerian perspective have been developed, and will be described in this sub-section. Furthermore, within Component 4 of CRTI Project 02-0093RD, a three-dimensional LS trajectory model urbanLS for urban dispersion has also been developed. This model, which is described in Wilson (2007) and will not be discussed in this chapter, computes forward or reverse time paths of “marked” fluid parcels released from transient or continuous sources and is “driven” using the fully three-dimensional building-resolving wind field provided by urbanSTREAM.

The first urban dispersion model within the Eulerian framework, referred to as urbanEU, uses a source-oriented dispersion modeling technique. The model estimates dispersion of scalars within and above the urban canopy (viz., at the street and neighborhood scale). In consequence, the mean momentum equation is decoupled from the scalar transport equation with the velocity field independent of the scalar concentration field. More specifically, the additional transport equation required for the conservation of the scalar (the contaminant) has the following form:

$$\frac{\partial C}{\partial t} + \frac{\partial \bar{u}_j C}{\partial x_j} = \frac{\partial}{\partial x_j} \left[K \frac{\partial C}{\partial x_j} \right] - \frac{\partial}{\partial x_j} \overline{u'_j c'} + Q, \quad (28)$$

where C is the concentration of a contaminant, K is the molecular kinematic diffusivity of the contaminant in air, Q is the source density distribution for the contaminant, and $\overline{u'_j c'}$ is the turbulent concentration (scalar) flux in the coordinate direction j (c' is the fluctuating concentration).

In Equation (28), a gradient diffusion model can be used as perhaps the simplest closure model for the turbulent concentration fluxes, although this assumption has not been rigorously justified for urban dispersion. In particular, within this popular framework the turbulent concentration fluxes are modeled as

$$\overline{u'_j c'} = -K_t \frac{\partial C}{\partial x_j}, \quad (29)$$

where K_t is the turbulent (or, eddy) kinematic diffusivity which is obtained from the turbulent viscosity ν_t (predicted by urbanSTREAM) in combination with a turbulent Schmidt number Sc_t in the following manner:

$$K_t = \frac{\nu_t}{Sc_t}. \quad (30)$$

In urbanEU, we adopt this concept using a constant turbulent Schmidt number Sc_t with a value of 0.63. This value for Sc_t was chosen with reference to Project Prairie Grass (Barad, 1958), a benchmark field experiment documenting turbulent dispersion from a continuous point source near the ground into the atmospheric surface layer. It has subsequently been shown that an Eulerian dispersion model is in excellent conformance with these high-quality experimental measurements, provided the turbulent Schmidt number has a value $Sc_t \approx 0.63$ (Wilson, 2007). With the closure for the turbulent scalar fluxes given by Equations (29) and (30), the modeled transport equation for the mean concentration C reduces to the following advection-diffusion equation:

$$\frac{\partial C}{\partial t} + \frac{\partial \bar{u}_j C}{\partial x_j} = \frac{\partial}{\partial x_j} \left[(K + K_t) \frac{\partial C}{\partial x_j} \right] + Q, \quad (31)$$

In addition to using a simple gradient diffusion hypothesis to model the turbulent scalar fluxes, urbanEU also allows the option of more sophisticated closures for $\overline{u'_j c'}$. To this purpose, the tensor diffusivity model of Yoshizawa (1985) has been implemented in urbanEU as an alternative closure for the turbulent scalar fluxes. This model has the following form:

$$\overline{u'_j c'} = -D_{jk} \frac{\partial \bar{c}}{\partial x_k}, \quad (32)$$

where the tensor diffusivity D_{jk} is defined as

$$D_{jk} = C_{s1} \frac{k^2}{\epsilon} \delta_{jk} + C_{s2} \frac{k^3}{\epsilon^2} \left(\frac{\partial \bar{u}_j}{\partial x_k} + \frac{\partial \bar{u}_k}{\partial x_j} \right). \quad (33)$$

Here, $C_{s1} = 0.134$ and $C_{s2} = -0.032$ are two model coefficients.

In the source-oriented dispersion model implemented in urbanEU, the goal of the dispersion modeling is to calculate the mean concentration ‘seen’ by a detector at a given receptor location when provided the source distribution (source term) Q of the contaminant. In other words, in the source-oriented approach the advection-diffusion equation given by Equation (31) is solved forward in time for a given source distribution of contaminant $Q(\mathbf{x}, t)$ to obtain the mean concentration field $C(\mathbf{x}, t)$. Then, the concentration of contaminant ‘seen’ by a detector at a given receptor, denoted $\Phi(C)$, can be defined as the following integral of concentration $C(\mathbf{x}, t)$ filtered in space and time by the spatial-temporal filtering function $h(\mathbf{x}, t)$ corresponding to the response function of the detector:

$$\Phi(C) = \int C(\mathbf{x}, t) h(\mathbf{x}, t) d\mathbf{x} dt \equiv (C, h). \quad (34)$$

Therefore, this integral is simply a linear functional of C and expresses averaging of the concentration field over the spatial volume and averaging time imposed by the detector at the receptor location. This linear functional of C is defined by the inner product (C, h) given in Equation (34), and allows one to calculate detector concentrations at any number of receptors located within the computational domain. However, for any new release scenario involving a different source distribution Q , the solution of Equation (31) needs to be calculated again in order to determine Φ .

Alternatively, when the detector concentration at a fixed receptor is of principal interest for a range of different emission scenarios, the alternative receptor-oriented dispersion modeling approach is useful. As a result, we have implemented a receptor-oriented dispersion model in urbanAEU, which solves the following adjoint advection-diffusion equation for the influence (or, adjunct) function C^* (with dimensional units of inverse volume):

$$-\frac{\partial C^*}{\partial t} - \frac{\partial \bar{u}_j C^*}{\partial x_j} = \frac{\partial}{\partial x_j} \left[(K + K_t) \frac{\partial C^*}{\partial x_j} \right] + h, \quad (35)$$

where h is the space-time filtering function of the detector at the fixed receptor location. It is important to note that Equation (35) is the adjoint of Equation (31), with C and C^* related to each other through the source function Q and detector (receptor) function h as follows:

$$\Phi(C) = \int C^*(\mathbf{x}, t) Q(\mathbf{x}, t) d\mathbf{x} dt \equiv (C^*, Q) = (C, h). \quad (36)$$

Equation (36) is a duality relation that relates C with C^* through Q and h and, in this sense, C and C^* can be interpreted as dual quantities. In the receptor-oriented approach, Equation (35) is solved backwards in time for a given receptor, and the concentration ‘seen’ by a detector at this receptor can now be calculated directly using Equation (36) once the source distribution Q has been specified. It should be noted that these computations can be repeated for any source distribution Q to obtain the concentration at the given receptor without having to re-solve Equation (35) for C^* . However, a new adjunct function C^*

needs to be determined if the concentration is desired for a different receptor. The adjoint transport equation for C^* has been applied primarily in the context of source reconstruction (viz., the determination of the source location and emission rate using a finite number of noisy concentration data obtained from an array of sensors). To this purpose, a Bayesian inferential methodology used in conjunction with the adjoint method (in which the transport and diffusion of matter in turbulent flows was solved using either partial or stochastic differential equations backwards in time in an Eulerian or Lagrangian description of turbulent dispersion, respectively) was proposed by Yee (2006), Keats et al. (2007a, 2007b), Yee (2007, 2008a, 2008b), and Yee et al. (2008).

In addition to the prediction of the mean concentration C , urbanEU provides the user the option to predict the concentration variance $\overline{c'^2}$. Undoubtedly, knowledge of fluctuating scalar concentration variance is valuable in situations where instantaneous or short time-averaged concentrations are important; for example, the assessment of risk from the release of certain highly toxic materials (e.g., industrial chemicals, chemical warfare agents) in which there is a nonlinear relationship between concentration and duration of exposure for a given level of harmful effect (ten Berge et al., 1986), the prediction of the probability of visibility through obscurant clouds, and the characterization of the perception of odours required to evaluate the nuisance due to malodorous substances. The transport equation for the concentration variance $\overline{c'^2}$ has the form

$$\frac{\partial \overline{c'^2}}{\partial t} + \frac{\partial (\bar{u}_j \overline{c'^2})}{\partial x_j} = \frac{\partial}{\partial x_j} \left(K \frac{\partial \overline{c'^2}}{\partial x_j} - \overline{u'_j c'} \right) - 2 \overline{u'_j c'} \frac{\partial \bar{c}}{\partial x_j} - \epsilon_c, \quad (37)$$

where ϵ_c is the molecular dissipation of $\overline{c'^2}$. As in the case of the transport equation for the mean concentration, the turbulent flux of $\overline{c'^2}$ is modeled using either a simple gradient diffusion hypothesis or tensor diffusivity model as follows:

$$\overline{u'_j c'} = -K_t \frac{\partial \overline{c'^2}}{\partial x_j} \quad \text{or} \quad \overline{u'_j c'} = -D_{jk} \frac{\partial \overline{c'^2}}{\partial x_k}, \quad (38)$$

where K_t and D_{jk} are determined in accordance to Equations (30) and (33), respectively.

The critical term that requires modeling in the transport equation of $\overline{c'^2}$ is the scalar dissipation ϵ_c . This term is modelled as $\epsilon_c = k^{1/2} \overline{c'^2} / \Lambda_c$, where Λ_c is a characteristic dissipation length scale for the concentration variance. Following Wang et al. (2007, 2008), the scalar dissipation length scale is determined as follows:

$$\Lambda_c = \Lambda_c(x) = \max \left[\Lambda_0, \min \left(\frac{\Lambda_{c2D}}{C_{\chi_{21}}}, \frac{\Lambda_{k2D}}{C_{\chi_{22}}} \right) \right], \quad (39)$$

where $C_{\chi_{21}} = C_{\chi_{22}} = 1.45$ are two model constants, and Λ_0 is the initial plume size taken to be $\Lambda_0 = d_0/2$ (d is the source diameter). In Equation (39), $\Lambda_{c2D}(x)$ is the characteristic plume size at a fixed downwind distance x from the source, determined from

$$\Lambda_{c2D} = \Lambda_{c2D}(x) = \left(\sigma_y(x) \sigma_z(x) \right)^{1/2}, \quad (40)$$

where $\sigma_y(x)$ and $\sigma_z(x)$ are the crosswind and vertical plume spreads, respectively, at a downwind distance x from the source.

The crosswind plume spread, $\sigma_y(x)$, is computed as

$$\sigma_y(x) = \left(\frac{\iint (y - \bar{y})^2 C(x, y, z) dy dz}{\iint C(x, y, z) dy dz} \right)^{1/2}, \quad (41)$$

with the crosswind plume centroid in the y - z plane (at a fixed downwind distance x from the source) determined from

$$\bar{y} = \bar{y}(x) = \frac{\iint y C(x, y, z) dy dz}{\iint C(x, y, z) dy dz}. \quad (42)$$

The vertical plume spread, $\sigma_z(x)$, is defined in a manner analogous to Equations (41) and (42). Finally, in Equation (39), Λ_{k2D} is the integral length scale of turbulence averaged over a vertical cross-section of the plume at downwind distance x from the source, viz.

$$\Lambda_{k2D} = \Lambda_{k2D}(x) = \frac{\iint \Lambda_k C(x, y, z) dy dz}{\iint C(x, y, z) dy dz}, \quad (43)$$

where $\Lambda_k \equiv k^{3/2}/\epsilon$.

2.4. Concentration probability density function

The model urbanEU allows the prediction of the mean concentration C and concentration variance $\overline{c'^2}$ for a plume dispersing in an urban area. However, these two concentration statistics do not provide an adequate description of the plume concentration fluctuation statistics without also specifying the form of the probability density function (PDF) of concentration.⁵ More specifically, the statistical description of the natural random fluctuations in the instantaneous concentration of a plume dispersing in the atmosphere is conveniently embodied in the concentration PDF. In order to investigate and model concentration fluctuation phenomenology, it is useful to know the concentration PDF which necessarily embodies all the higher-order concentration moments of the stochastic process. Chatwin (1982) discusses the importance of the concentration PDF with reference to the assessment of hazards posed by the release of flammable and toxic gases. In particular, he emphasizes the need to characterize precisely the upper tail of the probability density function in order to determine exceedances of critical threshold levels by peak concentrations.

For a fixed point in space \mathbf{x} and a given instant in time t , the random concentration field $\chi(\mathbf{x}, t) > 0$ of a hazardous pollutant dispersing in the atmosphere, can be characterized by the one-point concentration PDF $f(c; \mathbf{x}, t)$ defined by

$$f(c; \mathbf{x}, t) dc \equiv \Pr\{c \leq \chi(\mathbf{x}, t) < c + dc\}. \quad (44)$$

Here, the right-hand side denotes the probability that the random variable $\chi(\mathbf{x}, t)$ falls in the interval of sample space values between c and $c + dc$ for different realizations of the turbulent dispersion of the hazardous cloud or plume. In Yee and Chan (1997), a new

⁵Indeed, from a knowledge of the mean and variance of a probability law, one cannot in general determine the probability law.

concentration PDF model corresponding to a clipped-gamma distribution, was proposed. In this model, the concentration PDF has the form

$$f(c; \mathbf{x}, t) = \left(\frac{c + \lambda}{s} \right)^{k-1} \frac{\exp(-(c + \lambda)/s)}{s\Gamma(k)} + (1 - \gamma)\delta(c), \quad (45)$$

with $k = k(\mathbf{x}, t) > 0$, $s = s(\mathbf{x}, t) > 0$, $\lambda = \lambda(\mathbf{x}, t) \geq 0$, $\gamma = \gamma(\mathbf{x}, t) \in [0, 1]$, $\Gamma(x)$ is the gamma function, $\delta(x)$ is the Dirac delta function and the range for c is $0 \leq c < \infty$. The total PDF of concentration in Equation (45) is composed of a mixed fluid part (first term on right-hand side of equation) that results from in-plume mixing of eddies that contain the scalar contaminant, and an unmixed ambient fluid part (second term on right-hand side of equation) that is produced by plume meandering producing intermittent periods of zero concentration for a fraction of time $(1 - \gamma)$. Alternatively, $\gamma = \Pr\{\chi(\mathbf{x}, t)\} > 0$ is the intermittency factor that determines the probability of observing a non-zero concentration χ at a point (\mathbf{x}, t) in space-time.

The concentration PDF in Equation (45) is completely determined by four parameters: namely, γ , k , s and λ . However, for practical applications, we require a simple concentration PDF that predicts an arbitrary moment of the concentration given information on only the two lowest-order moments of concentration; namely, the mean concentration (first-order moment) and the concentration variance (second-order moment). In other words, we require a simple PDF form that can be specified with no more than two parameters, and yet is capable of fitting observed cloud or plume concentration data over a wide range of atmospheric conditions (various diabatic conditions) and terrain types (level, unobstructed terrain, urban terrain, etc.). This constraint arises from the fact our urban dispersion models can only predict the two lowest-order concentration moments.

To provide a special form of the clipped-gamma distribution that is determined by two (rather than four) parameters, Yee and Chan (1997) introduced two additional constraints. Firstly, it was assumed that γ can be uniquely determined as the area remaining under the gamma PDF curve for $c > 0$ after a left-shift of c by the amount λ , so

$$\gamma = \gamma(k, s, \lambda) = \int_{\lambda}^{\infty} \left(\frac{c}{s} \right)^{k-1} \frac{\exp(-c/s)}{s\Gamma(k)} dc = \frac{\Gamma(k; \lambda/s)}{\Gamma(k)}, \quad (46)$$

where $\Gamma(\nu; x)$ denotes the complementary incomplete gamma function. With this assumption, we have $\gamma \rightarrow 1^-$ (i.e., non-intermittent plume concentration) when $\lambda \rightarrow 0^+$ (i.e., no left-shift).⁶ Secondly, concentration data measured in the CONFLUX project (Yee et al., 1994; Yee et al., 1995) was used to provide a simple relation between the normalized mean-square concentration and plume intermittency:

$$\langle (\chi/C)^2 \rangle \equiv \frac{\overline{C'^2}}{C^2} + 1 = 3/\gamma, \quad (47)$$

where $\langle \cdot \rangle$ denotes the ensemble average (viz., average over a number of independent realizations of a process).⁷

⁶Note that $x \rightarrow a^-$ and $x \rightarrow a^+$ denotes the approach to x to the limiting value a from the left (viz., from values of x smaller than a) and from the right (viz., from values of x larger than a), respectively.

⁷Note that $\langle \chi \rangle = C$ and $\langle (\chi - C)^2 \rangle = \overline{C'^2}$.

```
[Clipped-gamma      parameter      λ]
figure=clipped-gamma-parms-
lambda.eps,width=65mm

[Clipped-gamma      parameter      k] [Clipped-gamma      parameter      s]
figure=clipped-gamma-parms-
k.eps,width=65mm                      figure=clipped-gamma-parms-
s.eps,width=65mm
```

Figure 5. Dependence of the parameters (k , s , and λ) of a clipped-gamma distribution on the normalized mean-square concentration $\langle(\chi/C)^2\rangle$.

Note that with the parameterization for γ given by Equation (47), the plume concentration is implicitly assumed to be non-intermittent (viz., $\gamma = 1$) for $\langle(\chi/C)^2\rangle \in [1, 3]$ ⁸ because γ cannot exceed unity in value. For a non-intermittent plume concentration, the concentration PDF of Equation (45) reduces to a simple gamma PDF as $\gamma = 1$ and $\lambda = 0$ (which occurs when $\langle(\chi/C)^2\rangle \in [1, 3]$); viz., the concentration PDF reduces to

$$f(c; \mathbf{x}, t) = \left(\frac{c}{s}\right)^{k-1} \frac{\exp(-c/s)}{s\Gamma(k)}, \quad (48)$$

when $\langle(\chi/C)^2\rangle \in [1, 3]$. More succinctly, this special form of the clipped-gamma distribution is defined with γ determined as

$$\gamma = \min\left(1, \frac{3}{\langle(\chi/C)^2\rangle}\right), \quad (49)$$

so that when $\langle(\chi/C)^2\rangle \in [1, 3]$, $\gamma \equiv 1$ and $\lambda = 0$; and, the clipped-gamma distribution simplifies to the simple gamma distribution in this case.

The n -th concentration moment of Equation (45) is given by

$$\begin{aligned} \langle\chi^n\rangle &= \int_0^\infty c^n f(c; \mathbf{x}, t) dc \\ &= \sum_{j=0}^n \binom{n}{j} (-\lambda)^j s^{n-j} \frac{\Gamma(n-j+k; \lambda/s)}{\Gamma(k)}, \quad n \in \mathbb{N}. \end{aligned} \quad (50)$$

With the constraints given by Equations (46) and (49), the model concentration PDF parameters k , s and λ in Equation (45) can be obtained by solving the following system of transcendental equations:

$$\frac{1}{s} = \left(-\frac{\lambda}{s} + k\right)\gamma + \frac{1}{\Gamma(k)} \left(\frac{\lambda}{s}\right)^k \exp(-\lambda/s); \quad (51)$$

$$\left\langle\left(\frac{\chi}{C}\right)^2\right\rangle = \frac{((\lambda/s)\gamma + (-\lambda/s + k + 1)/s)}{[(-\lambda/s + k)\gamma + (\lambda/s)^k \exp(-\lambda/s)/\Gamma(k)]^2}; \quad (52)$$

⁸The concentration variance $\langle\chi'^2\rangle = \langle\chi^2\rangle - C^2 \geq 0$ ($\chi' \equiv \chi - C$), so $\langle\chi^2\rangle \geq C^2$ or, equivalently, $\langle(\chi/C)^2\rangle \geq 1$ is the lower bound for the normalized mean-square concentration.

and

$$\gamma = \min \left(1, 3 \left\langle \left(\frac{\chi}{C} \right)^2 \right\rangle^{-1} \right) = \frac{\Gamma(k; \lambda/s)}{\Gamma(k)}. \quad (53)$$

Thence, for a specified value of $\langle (\chi/C)^2 \rangle$, Equations (52) and (53) can be solved for k and (λ/s) ,⁹ and these values can be subsequently substituted into Equation (51) to obtain s , after which the value of λ can be deduced. The solution of these equations for k , s and λ as a function of $\langle (\chi/C)^2 \rangle$ is exhibited in Figure 5. These are the parameters that define the clipped-gamma probability law for the normalized concentration, χ/C [viz., determine the functional form for the clipped-gamma distribution $f(c/C; \mathbf{x}, t)$].

3. Numerical Implementation

3.1. Finite-volume discretization

The coupled, nonlinear system of six partial differential equations which models unsteady, three-dimensional turbulent flow field in urbanSTREAM and the partial differential equations describing scalar transport in urbanEU and urbanAEU are solved using a finite-volume method. All these partial differential equations have the following generic form:

$$\frac{\partial \phi}{\partial t} + \frac{\partial \bar{u}_j \phi}{\partial x_j} = \frac{\partial}{\partial x_j} \left(\Gamma_\phi \frac{\partial \phi}{\partial x_j} \right) + S_\phi, \quad (54)$$

for a scalar ϕ (which can be identified with any of the mean Cartesian velocity components \bar{u}_i , turbulence kinetic energy k , viscous dissipation ϵ , mean concentration C , or influence function C^* , concentration variance $\overline{c'^2}$); Γ_ϕ is the diffusivity and S_ϕ represents the source/sink term. If the current time level for ϕ is denoted by the superscript $n+1$ and the time increment by Δt , a two- or three-level time discretization can be used to approximate the local rate of change of ϕ as follows:

$$\left(\frac{\partial \phi}{\partial t} \right)^{n+1} \approx \frac{1}{2\Delta t} (a_0 \phi^{n+1} + a_1 \phi^n + a_2 \phi^{n-1}), \quad (55)$$

where $a_0 = -a_1 = 2$, $a_2 = 0$ for first-order accuracy (using only two time levels) and $a_0 = 3$, $a_1 = -4$, $a_2 = 1$ for second-order accuracy. Both options are available in urbanSTREAM and urban(A)EU for approximating temporal derivatives. Finally, in the discretization to follow, it is assumed that the source/sink term S_ϕ , which may be a nonlinear function of ϕ , is linearized as follows:

$$S_\phi \approx S_P \phi + S_C, \quad (56)$$

where it is implicitly assumed that S_P is chosen to be unconditionally negative.

Integration of the transport equation governing the flow property ϕ in Equation (54) over the finite volume (or, control volume) shown in Figure 6, use of the time discretization

⁹Note that the factor $1/s$ in Equation (52) can be expressed as a function of only k and (λ/s) using Equation (51).

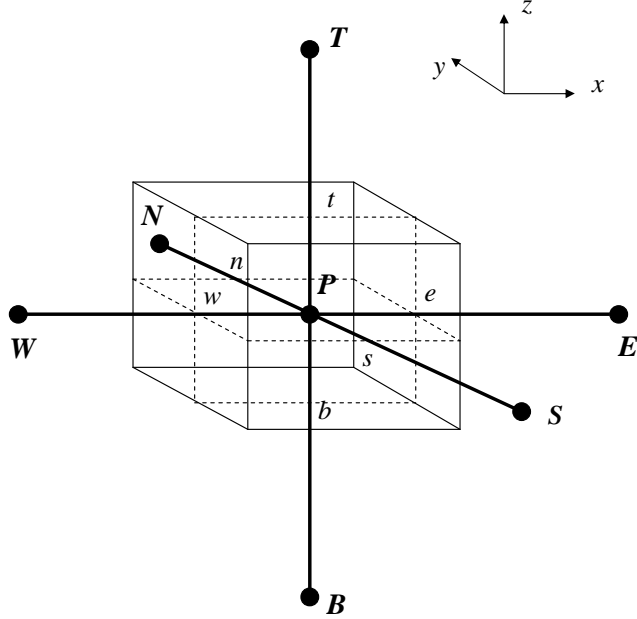


Figure 6. Finite volume and storage arrangement.

of Equation (55) to approximate the local tendency term, and application of the divergence theorem results in a discretized transport equation for ϕ that expresses a balance of local flow property change, advective and diffusive fluxes of the flow property across the cell faces, and generation/destruction of ϕ embodied by the volume-integrated net source/sink term. The resulting fully implicit time-discrete version of Equation (54) takes the following form [on insertion of the linearization of S_ϕ given by Equation (56)]:

$$a_P \phi_P^{n+1} = \sum_{\text{nb}} a_{\text{nb}} \phi_{\text{nb}}^{n+1} + Q_C, \quad (57)$$

where

$$Q_C = S_C \Delta \Omega - \frac{\Delta \Omega}{2 \Delta t} [a_1 \phi^n + a_2 \phi^{n-1}] \quad (58)$$

($\Delta \Omega$ is the volume of the cell with center node P); nb refers to the six neighbors of cell center P associated with nodes at the cell centers to the west (W), east (E), south (S), north (N), bottom (B) and top (T) of the center node P ; and, the six surfaces (faces) of the control volume centered at P will be denoted using lower-case letters corresponding to their direction (w, e, s, n, b and t) with respect to P (see Figure 6). The surface area of a cell face in direction κ relative to the cell center P will be denoted by A_κ ($\kappa \in \{w, e, s, n, b, t\}$).

The influence coefficients (not to be confused with the influence function C^*) a_{nb} ($\text{nb} \in \{W, E, S, N, B, T\}$) of the neighboring unknowns of the flow property ϕ take the following form, assuming that the diffusive fluxes have been approximated by central differences and the advective fluxes have been approximated using a first-order upwind scheme:

$$a_W = \left[\frac{\Gamma_{\phi,w} A_w}{\delta x_{WP}} \right] + \max(\bar{u}_w A_w, 0),$$

$$\begin{aligned}
a_E &= \left[\frac{\Gamma_{\phi,e} A_e}{\delta x_{\overline{PE}}} \right] + \max(-\bar{u}_e A_e, 0), \\
a_S &= \left[\frac{\Gamma_{\phi,s} A_s}{\delta y_{\overline{SP}}} \right] + \max(\bar{v}_s A_s, 0), \\
a_N &= \left[\frac{\Gamma_{\phi,n} A_n}{\delta y_{\overline{PN}}} \right] + \max(-\bar{v}_n A_n, 0), \\
a_B &= \left[\frac{\Gamma_{\phi,b} A_b}{\delta z_{\overline{BP}}} \right] + \max(\bar{w}_b A_b, 0), \\
a_T &= \left[\frac{\Gamma_{\phi,t} A_t}{\delta z_{\overline{PT}}} \right] + \max(-\bar{w}_t A_t, 0),
\end{aligned} \tag{59}$$

where $\delta x_{\overline{WP}} \equiv x_P - x_W$ denotes the distance along the x -coordinate direction from the west neighbor node W to the cell center node P , with analogous definitions for other similar quantities in Equation (59). Finally, the central coefficient a_P is

$$a_P = \sum_{\text{nb}} a_{\text{nb}} + \frac{a_0 \Delta \Omega}{2 \Delta t} - S_P \Delta \Omega. \tag{60}$$

urbanSTREAM employs a fully-collocated, cell-centered storage arrangement for all transported flow properties as well as for pressure. Furthermore, urbanSTREAM allows two user-selected options for the approximation of the advective fluxes across a cell face; namely, the upwind scheme summarized above and the Upstream Monotonic Interpolation for Scalar Transport (UMIST) scheme (Lien and Leschziner, 1994a). The UMIST scheme is a total variation diminishing (TVD) variant of the higher-order quadratic upwind interpolation for convective kinematics (QUICK) scheme developed originally by Leonard (1979) to approximate volume-face fluxes. This second-order scheme for the discretization of the net advective flux through a control volume combines the second-order accuracy of a central differencing scheme, with the stability inherent in an upwind differencing scheme, by using in each direction separately a quadratic upstream interpolation. The second-order accuracy of the QUICK scheme minimizes numerical diffusion errors that are characteristic of first-order accurate discretization schemes such as the upwind scheme. The UMIST scheme generalizes QUICK by introducing a limiter to give a monotonic version of QUICK that satisfies TVD constraints. In urbanSTREAM, the higher-order advection scheme UMIST is implemented simply as a first-order upwind approximation (described above) augmented with deferred corrections that constitute additional contributions to the source term \mathcal{Q}_C given in Equation (58).

To this purpose, an additional source contribution (deferred corrector ‘source’) $\mathcal{Q}_C^{\text{DC}}$ is added to \mathcal{Q}_C ($\mathcal{Q}_C \rightarrow \mathcal{Q}_C + \mathcal{Q}_C^{\text{DC}}$) in the implementation of UMIST. This deferred corrector source has the following explicit form:

$$\begin{aligned}
\mathcal{Q}_C^{\text{DC}} &= 0.5 \left\{ \left[(\bar{u})_e^+ \vartheta(r_e^+) - (\bar{u})_e^- \vartheta(r_e^-) \right] (\phi_E - \phi_P) \right. \\
&\quad \left. - \left[(\bar{u})_w^+ \vartheta(r_w^+) - (\bar{u})_w^- \vartheta(r_w^-) \right] (\phi_P - \phi_W) \right\}
\end{aligned}$$

$$\begin{aligned}
& + \left[(\bar{v})_n^+ \vartheta(r_n^+) - (\bar{v})_n^- \vartheta(r_n^-) \right] (\phi_N - \phi_P) \\
& - \left[(\bar{v})_s^+ \vartheta(r_s^+) - (\bar{v})_s^- \vartheta(r_s^-) \right] (\phi_P - \phi_S) \\
& + \left[(\bar{w})_t^+ \vartheta(r_t^+) - (\bar{w})_t^- \vartheta(r_t^-) \right] (\phi_T - \phi_P) \\
& - \left[(\bar{w})_b^+ \vartheta(r_b^+) - (\bar{w})_b^- \vartheta(r_b^-) \right] (\phi_P - \phi_B) \Big\}, \quad (61)
\end{aligned}$$

where $\vartheta(r)$ is defined as

$$\vartheta(r) \equiv \max \left[0, \min(2r, 0.25 + 0.75r, \underbrace{0.75 + 0.25r}_{\text{QUICK}}, 2) \right], \quad (62)$$

in which the term singled out by the underbrace is the contribution from the QUICK scheme (viz., if $\vartheta(r)$ were exactly equal to the term highlighted by the underbrace in Equation (62), then the advective flux approximation reduces exactly to Leonard's QUICK scheme). Furthermore, in Equation (61), the following definitions have been used:

$$(\bar{u})^\pm = (\bar{u} \pm |\bar{u}|)/2, \quad (\bar{v})^\pm = (\bar{v} \pm |\bar{v}|)/2, \quad (\bar{w})^\pm = (\bar{w} \pm |\bar{w}|)/2; \quad (63)$$

and, r_κ^\pm ($\kappa \in \{w, e, n, s, t, b\}$) are

$$r_e^+ = \frac{\phi_P - \phi_W}{\phi_E - \phi_P}, \quad r_e^- = \frac{\phi_E - \phi_{EE}}{\phi_P - \phi_E}, \quad r_w^+ = \frac{\phi_W - \phi_{WW}}{\phi_P - \phi_W}, \quad r_w^- = \frac{\phi_P - \phi_E}{\phi_W - \phi_P}, \quad (64)$$

$$r_n^+ = \frac{\phi_P - \phi_S}{\phi_N - \phi_P}, \quad r_n^- = \frac{\phi_N - \phi_{NN}}{\phi_P - \phi_N}, \quad r_s^+ = \frac{\phi_S - \phi_{SS}}{\phi_P - \phi_S}, \quad r_s^- = \frac{\phi_P - \phi_N}{\phi_S - \phi_P}, \quad (65)$$

$$r_t^+ = \frac{\phi_P - \phi_B}{\phi_T - \phi_P}, \quad r_t^- = \frac{\phi_T - \phi_{TT}}{\phi_P - \phi_T}, \quad r_b^+ = \frac{\phi_B - \phi_{BB}}{\phi_P - \phi_B}, \quad r_b^- = \frac{\phi_P - \phi_T}{\phi_B - \phi_P}, \quad (66)$$

where EE refers to the node east of node E , WW refers to the node west of node W , and so forth. It is noted that the higher-order UMIST scheme for approximation of advective volume-face fluxes uses a twelve-point molecule, with the neighborhood of a cell center P consisting of $W, E, S, N, B, T, WW, EE, SS, NN, BB$ and TT .

3.2. Pressure-correction algorithm

For an incompressible flow, there is no direct method for specifying an equation for pressure. In this case, pressure needs to be interpreted as a kinematic variable (Lagrange multiplier) which is determined indirectly so as to satisfy the continuity equation [cf. Equation (4)]. Indeed, the lack of a temporal derivative in the continuity equation implies that this equation can be interpreted as a constraint for the pressure (rather than a transport or evolution equation). In urbanSTREAM, the continuity equation is enforced indirectly by solving a pressure-correction equation which, as part of the iterative sequence, steers the pressure towards a state in which all mass residuals in the cells are negligibly small. The two iterative schemes available in urbanSTREAM to enforce mass conservation through a pressure-correction algorithm are the Semi-Implicit Method for Pressure-Linked Equations

(SIMPLE) described in detail by Patankar (1980) and the SIMPLEC (SIMPLE-Consistent) algorithm of Van Doormal and Raithby (1984).

The SIMPLE(C) algorithm provides a method for connecting the discretized forms of the momentum and continuity equations to give an equation linking the pressure correction at a node to its neighboring nodes. In this iterative solution sequence, \bar{u}_i ($i = 1, 2, 3$) are initially obtained with an estimated pressure field. This is continuously updated by reference to the local mass residuals, which are used to steer the pressure field towards the correct level. However, the fully collocated variable storage used in urbanSTREAM, in combination with a central differencing for pressure, is known to provoke checkerboard oscillations, reflecting the pressure-velocity decoupling. More specifically, if a linear interpolation scheme is used to determine the pressure on cell faces, the pressure gradient across a cell depends on the pressure at the nodes in the neighboring cells and is independent of the pressure in the current cell, leading to the above mentioned checkerboard pattern in the pressure. To avoid this, the widely used interpolation practice of Rhie and Chow (1983) is adopted to interpolate cell-face velocities from the nodal values. This method for interpolation essentially introduces a fourth-order smoothing term based on the pressure, and prevents the occurrence of spurious pressure modes. The interpolation scheme of Rhie and Chow for removing checkerboard pressure oscillations within a collocated scheme for solving the RANS equations in a generalized curvilinear coordinate system has been presented in detail by Lien and Leschziner (1994b).

The key concept underlying Rhie and Chow's interpolation for avoidance of checkerboard oscillations in the pressure within a collocated storage arrangement can be seen as follows. To this purpose, let us consider the discretized \bar{u} -momentum transport equation, which by virtue of Equation (57) [with the identification $\phi \equiv \bar{u}$], is given by

$$\bar{u}_P = \underbrace{\frac{\sum_{nb} a_{nb} \bar{u}_{nb} + Q_C}{a_P}}_{H_P} - (\bar{p}_e - \bar{p}_w) \underbrace{\frac{A_P}{a_P}}_{D_P^{\bar{u}}}, \quad (67)$$

where the discretized pressure gradient term contribution to Q_C has been split out, and A_P is the cross-sectional area of the cell at P . Equation (67) can be re-arranged as follows:

$$\bar{u}_P = H_P - D_P^{\bar{u}}(\bar{p}_e - \bar{p}_w). \quad (68)$$

A corresponding expression can be written for the neighboring node to the east, so

$$\bar{u}_E = H_E - D_E^{\bar{u}}(\bar{p}_{ee} - \bar{p}_e), \quad (69)$$

where ee denotes the eastern face of the cell that has node E at its center. Similarly, the velocity at the eastern face of the cell that has node P at its center is given by

$$\bar{u}_e = H_e - D_e^{\bar{u}}(\bar{p}_E - \bar{p}_P). \quad (70)$$

The critical point to note is that the face velocity \bar{u}_e is evaluated by a linear interpolation of the nodal velocities \bar{u}_P and \bar{u}_E from which then the pressure-gradient terms are subtracted and to which a compensating pressure-gradient fragment is added, the last formed only with

the two nodal pressures that straddle the face velocity \bar{u}_e . The result gives

$$\begin{aligned}\bar{u}_e &= \frac{1}{2}(H_P + H_E) - \frac{1}{2}(D_P^{\bar{u}} + D_E^{\bar{u}})(\bar{p}_E - \bar{p}_P) \\ &= \frac{1}{2}[\bar{u}_P + D_P^{\bar{u}}(\bar{p}_e - \bar{p}_W) + \bar{u}_E + D_E^{\bar{u}}(\bar{p}_{ee} - \bar{p}_e)] \\ &\quad - \frac{1}{2}(D_P^{\bar{u}} + D_E^{\bar{u}})(\bar{p}_E - \bar{p}_P),\end{aligned}\quad (71)$$

which can be recast into the following more perspicuous form:

$$\begin{aligned}\bar{u}_e &= \underbrace{\frac{1}{2}(\bar{u}_P + \bar{u}_E)}_{\text{linear interpolation}} \\ &\quad + \underbrace{\frac{1}{2}[D_P^{\bar{u}}(\bar{p}_e - \bar{p}_w) + D_E^{\bar{u}}(\bar{p}_{ee} - \bar{p}_e) - (D_P^{\bar{u}} + D_E^{\bar{u}})(\bar{p}_E - \bar{p}_P)]}_{\text{pressure smoothing}}.\end{aligned}\quad (72)$$

Equation (72) implies that the Rhie and Chow interpolation practice consists of two parts: a centered approximation for \bar{u}_e and a stabilizing pressure smoothing term which is a function of pressure at the neighboring nodes. Note that \bar{u}_e in Equation (72) depends on the values of pressure at four nodes, two on either side of the cell face.

The pressure-correction equation now arises by decomposing the correct pressure field \bar{p} into an approximate (guessed) pressure field \bar{p}^* and a corrective pressure perturbation \bar{p}' , so that

$$\bar{p} = \bar{p}^* + \bar{p}'.\quad (73)$$

Similarly, the correct face velocity \bar{u}_e is decomposed into an estimated (or, guessed) value \bar{u}_e^* and a correction \bar{u}'_e :

$$\bar{u}_e = \bar{u}_e^* + \bar{u}'_e,\quad (74)$$

where $\bar{u}'_e \approx d_e^{\bar{u}}(\bar{p}'_P - \bar{p}'_E)$, with $d_e^{\bar{u}}$ denoting the value of $d^{\bar{u}}$ at cell face e obtained as a centered average of the values of $d^{\bar{u}}$ at the two neighboring nodes on either side of the face (viz., at nodes P and E). The form for $d^{\bar{u}}$ depends on the pressure-based algorithm used. In the SIMPLE algorithm, $d_e^{\bar{u}} = A_e/a_e = D_e^{\bar{u}}$. However, for the SIMPLEC algorithm which provides a better approximation for the corrective velocity perturbation, $d_e^{\bar{u}} = A_e/(a_e - \sum a_{nb})$. Substitution of Equation (74) along with analogous expressions for the other cell face velocities into the continuity equation, and integrating over the volume of a cell, yields the following discretization equation for \bar{p}' :

$$a_P^{\bar{p}} \bar{p}'_P = \sum_{nb} a_{nb}^{\bar{p}} \bar{p}'_{nb} + b^{\bar{p}},\quad (75)$$

where

$$\begin{aligned}a_E^{\bar{p}} &= d_e^{\bar{u}} A_e, & a_W^{\bar{p}} &= d_w^{\bar{u}} A_w, \\ a_N^{\bar{p}} &= d_n^{\bar{v}} A_n, & a_S^{\bar{p}} &= d_s^{\bar{v}} A_s, \\ a_T^{\bar{p}} &= d_t^{\bar{v}} A_t, & a_B^{\bar{p}} &= d_b^{\bar{v}} A_b,\end{aligned}\quad (76)$$

and

$$a_P^{\bar{p}} = a_W^{\bar{p}} + a_E^{\bar{p}} + a_S^{\bar{p}} + a_N^{\bar{p}} + a_B^{\bar{p}} + a_T^{\bar{p}}, \quad (77)$$

with the mass imbalance $b^{\bar{p}}$ given by

$$b^{\bar{p}} = (\bar{u}_w^* A_w - \bar{u}_e^* A_e) + (\bar{v}_s^* A_s - \bar{v}_n^* A_n) + (\bar{w}_b^* A_b - \bar{w}_t^* A_t). \quad (78)$$

We note that if $b^{\bar{p}}$ vanishes identically, then the starred velocity field satisfies the continuity equation and no pressure correction is needed. The term $b^{\bar{p}}$ can be interpreted as a “mass source” which the pressure corrections must annihilate (through the associated velocity corrections) in order for the continuity equation to be exactly satisfied.

The pressure-correction equation for \bar{p}' is susceptible to divergence unless some under-relaxation is applied during the iterative process. In view of this, only a fraction of \bar{p}' is added to \bar{p}^* in Equation (73) to give the corrected pressure \bar{p} , so that

$$\bar{p} = \bar{p}^* + \alpha_p \bar{p}', \quad (79)$$

where $\alpha_p \in (0, 1]$. For the SIMPLE algorithm, α_p is typically chosen to have a value of about 0.7. However, it is important to note that under-relaxation of the pressure is not required for the SIMPLEC algorithm, so in this case $\alpha_p = 1.0$. Similarly, we also under-relax the corrections for velocity (cf. Equation (74) and analogous expressions for the other velocity components). The under-relaxation of the velocity does not need to be computed directly, but rather it is more convenient (and elegant) to implement this under-relaxation while solving the discretized equations for \bar{u}_i ($i = 1, 2, 3$). With reference to Equation (57) with $\phi \equiv \bar{u}_i$, the under-relaxation of the discretized \bar{u}_i -momentum equation takes the following form:

$$\frac{a_P^{\bar{u}_i}}{\alpha_{\bar{u}_i}} \bar{u}_i = \sum_{\text{nb}} a_{\text{nb}}^{\bar{u}_i} \bar{u}_i + \mathcal{Q}_C^{\bar{u}_i} + \left[(1 - \alpha_{\bar{u}_i}) \frac{a_P^{\bar{u}_i}}{\alpha_{\bar{u}_i}} \right] \bar{u}_i^*, \quad (80)$$

where $\alpha_{\bar{u}_i} \in (0, 1]$ is the under-relaxation factor for \bar{u}_i ; and, \bar{u}_i^* is the value of \bar{u}_i from the previous iteration. Ferziger and Perić (2002) recommend $\alpha_p + \alpha_{\bar{u}_i} \approx 1.1$ for the SIMPLE algorithm. In Equation (80), the contribution of the pressure gradient term has been absorbed in $\mathcal{Q}_C^{\bar{u}_i}$ and the effect of the under-relaxation of the momentum equation is to introduce an additional contribution to the source term. Its effect, therefore, is to increase the diagonal dominance of the coefficient matrix through the inclusion of this additional source term. Finally, we note that the pressure-correction equation is also affected by the under-relaxation of the \bar{u}_i -momentum equations in the sense that the $d^{\bar{u}_i}$ -terms in the pressure-correction equation [cf. Equations (76), (77) and (78)] need to be replaced as follows:

$$d^{\bar{u}_i} \rightarrow d^{\bar{u}_i} \alpha_{\bar{u}_i}, \quad i = 1, 2, 3. \quad (81)$$

The solution procedure for the velocity field in urbanSTREAM is as follows. For each time step, the following procedure is undertaken: (a) Guess the pressure field \bar{p}^* and solve the mean momentum equations to obtain the provisional Cartesian velocity components \bar{u}_i^* ($i = 1, 2, 3$); (b) With the provisional velocity \bar{u}_i^* ($i = 1, 2, 3$), solve the pressure-correction equation to obtain \bar{p}' ; (c) Update the provisional velocities and pressure to \bar{u}_i ($i = 1, 2, 3$) and \bar{p} using the velocity-correction and pressure-correction formulae; (d) Solve all the other

discretized transport equations (e.g., k and ϵ); (e) Treat the corrected pressure \bar{p} as the new guessed pressure \bar{p}^* ; and, (f) Return to Step (a) until a converged solution is obtained at which point proceed to the next time step.

Within this scheme, the transport equations for \bar{u}_i ($i = 1, 2, 3$), k , and ϵ and the pressure-correction equation are solved sequentially and iterated to convergence, defined by reference to L1-residual norms for the mass and momentum components. Here, the L1-residual norm is defined as the sum of absolute residuals over all grid points of the flow domain. The residual norm provides a quantitative measure of how perfectly the discretization equations are satisfied by the current values of the dependent variables. The L1-residual norms for the mass and momentum components were normalized by the mass and momentum fluxes at the inflow plane. A convergent solution was assumed after each normalized L1-residual norm decreased below 0.001 (although this level for declaration of convergence can be chosen by the user). In urbanSTREAM, the discretized equations are solved using an iterative method called the strongly implicit procedure (SIP) that was proposed by Stone (1968). The SIP method uses an incomplete lower-upper (LU) decomposition and was specifically designed for solving algebraic equations that arise from the discretizations of partial differential equations (e.g., those that arise in various CFD applications). For these types of problems, Stone's SIP method generally converges in a small number of iterations.

3.3. Boundary condition implementation

The boundary conditions used in urbanSTREAM (flow solver) and urban(A)EU (urban dispersion) pertain to physical situations described by partial differential equations of either a parabolic or elliptic character. For the mean concentration C , influence function C^* and concentration variance $\bar{c'^2}$, at all solid boundaries (e.g., ground surface, walls and roofs of buildings, etc.) in the computational domain, zero Neumann conditions were used, implying no flux of C , C^* and $\bar{c'^2}$ across the solid boundary (viz., $\partial C / \partial n|_B = 0$, $\partial C^* / \partial n|_B = 0$ and $\partial \bar{c'^2} / \partial n|_B = 0$ where n refers to the direction normal to the solid boundary B). At the computational (flow) domain boundaries, zero Neuman conditions were applied for C and $\bar{c'^2}$, but convective boundary conditions were used for C^* (viz., $K_{\text{eff}} \partial C^* / \partial n + \mathbf{u} \cdot \mathbf{n} C^* = 0$ where $K_{\text{eff}} \equiv (K + K_t)$ and \mathbf{n} is the unit outward normal vector to the flow domain boundary).¹⁰

The boundary conditions imposed on the flow field are more complex. At the inflow boundaries of the computational domain, all transported flow properties need to be prescribed (i.e., Dirichlet boundary conditions apply here). With the velocity prescribed, no boundary conditions are needed for the pressure. In urbanSTREAM, the mean velocity components \bar{u}_i ($i = 1, 2, 3$) and the turbulence kinetic energy k at the inflow boundary planes are provided by urbanGRID which imports four-dimensional (3-space dimensions plus 1-time dimension) meteorological fields from urban GEM LAM and interpolates these field quantities on the grid nodes of the inflow planes. Alternatively, measured profiles of mean velocity and turbulence kinetic energy (e.g., obtained from sodars, radiosondes, radars, etc.) can also be used by urbanSTREAM to define the boundary conditions for mean flow and turbulence on the inflow boundary planes, if these are available. Unfortu-

¹⁰The convective boundary conditions need to be used for C^* to ensure that C^* is the adjoint of C , verifying the duality relationship of Equation (36).

nately, the viscous dissipation rate ϵ is not available from urban GEM LAM and is virtually never available from experimental measurements. In urbanSTREAM, ϵ is prescribed on the inflow boundary planes using the assumption of local equilibrium of the turbulent flow (so that the rates of production and destruction of turbulence are in near balance) to give

$$\epsilon = \frac{C_\mu^{3/4} k^{3/2}}{\min(k_v z, h/3)}, \quad (82)$$

where z is vertical distance from the ground and h is the atmospheric boundary-layer height.¹¹

Far downstream, at the outflow boundary planes, the flow was assumed to reach a fully-developed state where no changes occur in the flow direction (approximately or better). Hence, at the outflow boundary, the horizontal gradients of all flow variables are assumed to be zero; viz., $\partial \bar{u}/\partial x_i = \partial \bar{v}/\partial x_i = \partial \bar{w}/\partial x_i = \partial k/\partial x_i = \partial \epsilon/\partial x_i = 0$ ($i = 1, 2$). At the upper boundary, we used free-slip conditions for all flow variables. Furthermore, at the outflow boundaries, a mass flux correction is undertaken to ensure that the total mass flux that exits through the outflow boundary planes is equal to the total mass flux that enters through the inflow boundary planes (and, in fact, the imposition of this condition enhances convergence of the iterative flow solver). During iterations of the pressure-based algorithm (either SIMPLE or SIMPLEC), there is no guarantee that the exit velocities through the outflow boundary planes will conserve mass over the computational domain as a whole. To ensure that the continuity is satisfied globally, the total mass flux $M_{\text{in}}^{x_i}$ entering into the domain and total mass flux $M_{\text{out}}^{x_i}$ going out of the domain in the x_i -coordinate direction ($i = 1, 2$) are first calculated as follows:

$$M_{\text{in}}^{x_i} = \sum_{j \in \mathcal{I}^{x_i}} (\bar{u}_i)_j \Delta A_j; \quad M_{\text{out}}^{x_i} = \sum_{j \in \mathcal{O}^{x_i}} (\bar{u}_i)_j \Delta A_j, \quad i = 1, 2, \quad (83)$$

where \mathcal{I}^{x_i} and \mathcal{O}^{x_i} denote the inflow and outflow boundary planes normal to the x_i -coordinate direction, respectively; and, $(\bar{u}_i)_j$ corresponds to the inlet (exit) velocity through inlet (exit) cell j whose inlet (exit) face area is ΔA_j . There is no unique procedure for ensuring that the mass flux out $M_{\text{out}}^{x_i}$ is equal to mass flux in $M_{\text{in}}^{x_i}$ for $i = 1, 2$. One method to ensure overall continuity is to add a constant velocity correction \bar{u}_i^c given by

$$\bar{u}_i^c = \frac{(M_{\text{in}}^{x_i} - M_{\text{out}}^{x_i})}{\sum_{j \in \mathcal{O}^{x_i}} \Delta A_j}, \quad i = 1, 2, \quad (84)$$

to the outlet velocity component $(\bar{u}_i)_j$, $j \in \mathcal{O}^{x_i}$ ($i = 1, 2$). Alternatively, global continuity in the computational domain can also be ensured by multiplying the outflow plane velocities $(\bar{u}_i)_j$ ($j \in \mathcal{O}^{x_i}$) by the ratio $M_{\text{in}}^{x_i}/M_{\text{out}}^{x_i}$. Currently, urbanSTREAM uses the first method for ensuring that mass is conserved over the entire computational domain.

At all the solid boundaries (ground, obstacle walls, obstacle roofs), standard wall functions are applied for the mean velocities and turbulence quantities. Wall functions are used to reduce the computational cost associated with the alternative of using a low-Reynolds number turbulence model to numerically integrate the solution through the entire near-wall

¹¹The upper limit of $h/3$ in the turbulence length scale used in Equation (82) is consistent with that used in the limited-length-scale k - ϵ turbulence model.

region, including the viscous sublayer up to the wall where no-slip and impermeability conditions can be applied. Typically, this will require a very fine grid near the wall because spatial variations in near-wall turbulence structure are large here due to the combined influence of viscosity and wall-induced anisotropy. Log-law based ‘wall laws’ are adopted in conjunction with high-Reynolds number turbulence models to bridge the viscous sublayer. Basically, the flow quantities at the first grid point above the solid surface, which is located outside the viscous sublayer, are related to the wall friction velocity based on the assumption of a semi-logarithmic velocity distribution.

The implementation of a wall function boundary condition for the mean velocity tangential to the wall first requires the evaluation of the normalized distance perpendicular to the wall:

$$z^+ = \frac{z_P}{\nu} \left(\frac{\tau_w}{\rho} \right)^{1/2}, \quad (85)$$

where z_P is the distance from the near-wall node P to the solid surface, τ_w is the wall shear stress, and ρ is fluid density. If $z^+ \leq 11.6$, the flow at near-wall node P is assumed to be in the laminar sublayer where the flow is linear; otherwise, the flow is turbulent, lying in the log-law region where a logarithmic variation in the tangential velocity is assumed to prevail and a wall function is used. For the velocity component \bar{u}_3 normal to the wall, the impermeability condition that $\bar{u}_3 = 0$ at the wall is used.

More specifically, if $z^+ \leq 11.6$, the wall shear stress in the x_i -coordinate direction ($i = 1, 2$) is obtained from $\tau_w^{x_i} = \rho\nu(\bar{u}_i)_P/z_P$, where $(\bar{u}_i)_P$ is the tangential velocity at the near-wall node P (assuming a linear variation of velocity with distance from the wall). The shear force F_s on the bottom face of the near-wall cell (with center node P) is given by $F_s = -\rho\nu(\bar{u}_i)_P A_b/z_P$ (A_b is the wall (bottom) area of the near-wall cell). The link to the wall in the discretized \bar{u}_i -momentum equation ($i = 1, 2$) is suppressed by setting $a_B = 0$ and the wall function contribution $S_P^{\text{wf}} = -\rho\nu A_b/z_P$ is added to S_P [cf. Equation (60)]. If, however, $z^+ > 11.6$, the near-wall node P is considered to lie in the log-law region of the turbulent flow and a wall function is utilized. To this purpose, one calculates the wall shear stress τ_w and the associated wall shear force F_s from the log-law velocity profile with properties evaluated at the near-wall node P . Again, the coefficient a_B in the discretized \bar{u}_i -momentum equation ($i = 1, 2$) is nullified and the source \mathcal{Q}_C [cf. Equation (58)] is modified to explicitly include the contribution from the shear force acting on the bottom near-wall cell face as follows:

$$\mathcal{Q}_C \rightarrow \mathcal{Q}_C - \frac{\rho k_P^{1/2} C_\mu^{1/4} k_v}{\ln(Ek_P^{1/2} z_P/\nu)} (\bar{u}_i)_P A_b, \quad i = 1, 2, \quad (86)$$

where $E = 9.793$ is a constant.

To implement the wall function of Equation (86), a correct value for k_P (TKE at the near-wall node) is required. A local equilibrium of turbulence (where the volume-averaged production and dissipation of turbulence are in balance) is assumed to prevail near the wall. The average production of k in a near-wall cell is given by

$$\overline{P_k} = |\tau_w| \cdot |\mathbf{u}_P^t| / z_P, \quad (87)$$

where $|\tau_w| = ((\tau_w^{x_1})^2 + (\tau_w^{x_2})^2)^{1/2}$ and $|\mathbf{u}_P^t| \equiv ((\bar{u}_1)_P^2 + (\bar{u}_2)_P^2)^{1/2}$ are the magnitudes of the wall shear stress and the tangential velocity (at near-wall node P), respectively. With

respect to implementation, the net k -source per unit volume in Equation (87) is included in the near-wall cells in the discretized k -transport equation by suppressing the link to the wall boundary ($a_B = 0$) and augmenting the source term \mathcal{Q}_C with the additional contribution $\mathcal{Q}_C^{\text{prod}} = |\tau_w| \cdot |\mathbf{u}_P^t| \Delta\Omega / z_P$ ($\Delta\Omega$ is the volume of the near-wall cell). Finally, the viscous dissipation ϵ at a near-wall cell with center node P has the nodal value set at (with an assumed local equilibrium condition persisting in the near-wall cell)

$$\epsilon_P = C_\mu^{3/4} k_P^{3/2} / (k_v z_P). \quad (88)$$

4. Parallelization of urbanSTREAM

In this section, we describe how the CFD code urbanSTREAM is parallelized on a distributed-memory computer system using the Message-Passing Interface (MPI) library, in conjunction with the “domain-decomposition” approach.

4.1. Multiblock algorithm

The first step in the parallelization of urbanSTREAM involves the generalization of the single-block algorithm used in the code to a multiblock strategy. The numerical details of this generalization are described in this sub-section. This includes the formulation of the connectivity matrix, the exchange of ‘halo data’ between the various blocks, and the construction of the required data structures.

The multiblock algorithm (Lien et al., 1996) involves the subdivision of the computational domain into an arbitrary number of contiguous, non-overlapping blocks, each having its own grid and associated local coordinate system. The grid for each block is generated separately by use of any suitable grid-generation procedure (e.g., urbanGRID). The only constraint that needs to be imposed in this grid generation is that the grid lines need to be continuous across the block boundaries. Each block, when viewed in isolation, is surrounded by an ‘auxiliary’ layer of two control volumes originating from the neighboring blocks. In effect, a block is designed to overlap its neighboring blocks to the extent of two control volumes along each block boundary in order to accommodate ‘halo data’ corresponding to the boundary data required in the solution within the block in question. The choice of a block boundary layer with a thickness of two control volumes is linked to the nature of the higher-order convection scheme and the Rhie and Chow (1983) nonlinear interpolation scheme [cf. Equations (61) and (72)].

Although the coordinate systems of neighboring blocks can be quite different in orientation, as illustrated in Figure 7, all the geometric data pertaining to the auxiliary layer attached to the parent block, including the metric tensors and Jacobian (for curvilinear coordinate systems), are treated in terms of the coordinate system for the parent block and are stored as if the layer were part of this block. This arrangement obviates the need for any one block to directly access the ‘foreign’ geometric information and mass fluxes residing in the neighboring blocks during the solution process within the parent block.

Interblock connectivity is handled using a connectivity matrix in the form of a two-dimensional (2-D) array MCONEC(BLOCK,FACE), where BLOCK is the block number

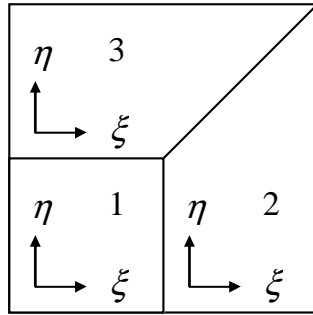


Figure 7. Multiblock arrangement with different local coordinate systems in a two-dimensional computational domain expressed in terms of the curvilinear (non-orthogonal) coordinate system (ξ, η).

being considered, FACE identifies the block face (ranging from 1 to 6, with 1 denoting the eastern face, 2 the western face, 3 the northern face, 4 the southern face, 5 the top face and 6 the bottom face), and MCONEC denotes the block sharing FACE with BLOCK. The coordinate system relating to any one block is stored in the form of COORD(BLOCK,FACE), representing all possible coordinate permutations in the neighboring block sharing the face ‘FACE’. To convey the basic idea without introducing a significant loss of generality, a typical 2-D example for COORD is illustrated in Figure 8. The neighboring right-hand-side block can take any one of eight combinations of coordinates, signified by the integers 1 to 8. Another example illustrating the use of both MCONEC and COORD is given below by reference to Figures 7 and 8, where

$$\begin{aligned} \text{MCONEC}(3,1) &= 2, \quad \text{MCONEC}(3,2) = 0, \\ \text{MCONEC}(3,3) &= 0, \quad \text{MCONEC}(3,4) = 1, \end{aligned}$$

and

$$\begin{aligned} \text{COORD}(3,1) &= 8, \quad \text{COORD}(3,2) = 0, \\ \text{COORD}(3,3) &= 0, \quad \text{COORD}(3,4) = 1. \end{aligned}$$

In these specifications, the value ‘0’ signifies that the neighboring block is a physical (real) boundary of the computational domain, rather than an artificial boundary resulting from the multiblock strategy.

With reference to Equations (72) and (76), it is seen that the coefficients of the pressure-correction equation are obtained as centered averages of the values of $d\bar{u}_i A$ at the two neighboring nodes on either side of a control volume face in any coordinate direction $i = 1, 2, 3 \equiv x, y, z$. Therefore, the coefficients of the pressure-correction equation depend on the values of a_P [cf. Equation (67)] associated with the mean momentum equations applied to the control volume over which mass conservation is to be satisfied, as well as on the two neighboring control volumes on either side in any coordinate direction. In consequence, it is crucial to transmit this quantity from the neighboring blocks into the auxiliary two control-volume layer when solving the mean momentum equation in the parent block. This transfer is greatly facilitated by the fact that a_P is coordinate-invariant (viz., a_P is independent of the block-local coordinate system).

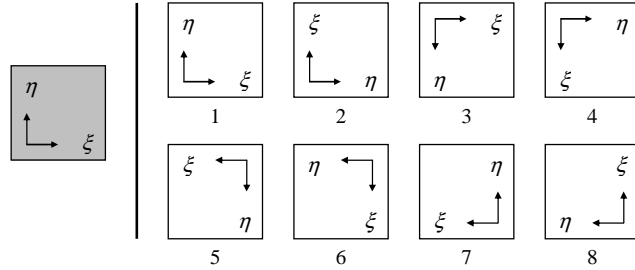


Figure 8. All possible permutations of local coordinate systems in blocks adjacent to any reference block.

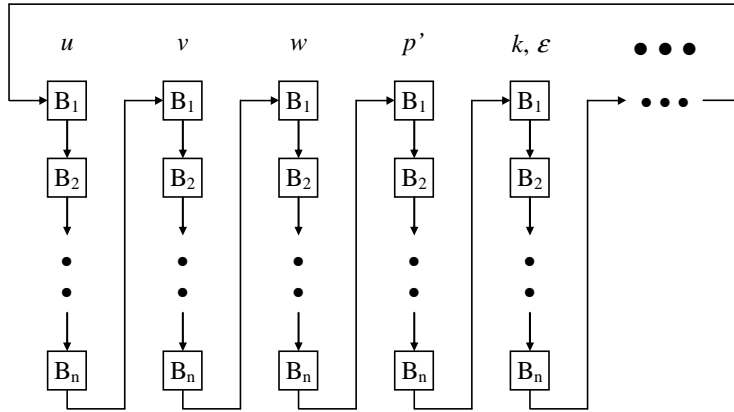


Figure 9. Solution sequence of SIMPLE algorithm within a multiblock scheme.

Once the coefficients for the transport and pressure-correction equations have been assembled for each block, the resulting system of equations is solved in a segregated manner as illustrated in Figure 9. Each set of equations pertaining to any one block is solved within an ‘inner iteration’ by Stone’s (1968) SIP method, concurrently with the temporarily ‘frozen’ block boundary conditions in the ‘halo’ region. Then, an update of boundary conditions is effected through the connectivity matrix and the identifiers of the coordinate systems in the neighboring blocks, in order to establish the interblock coupling. An ‘outer iteration’ consists of solving any one set of equations over all blocks and the associated exchange of data across block boundaries. This sweep is arranged as a *Block Jacobi* method.

4.2. Parallelization of multiblock code

Parallelization of the multiblock version of urbanSTREAM to run on a parallel computer with a distributed-memory system will be described in this sub-section.

Firstly, a data file containing the coordinate information for a computational mesh generated by urbanGRID is read into a grid partitioning program. This program automatically partitions the grid for a single block generated by urbanGRID into NBLOC partitions of approximately equal size in order to achieve near optimal load-balancing. Here, $\text{NBLOC} = \text{I_MAX} \times \text{J_MAX} \times \text{K_MAX}$, in which I_MAX, J_MAX and K_MAX cor-

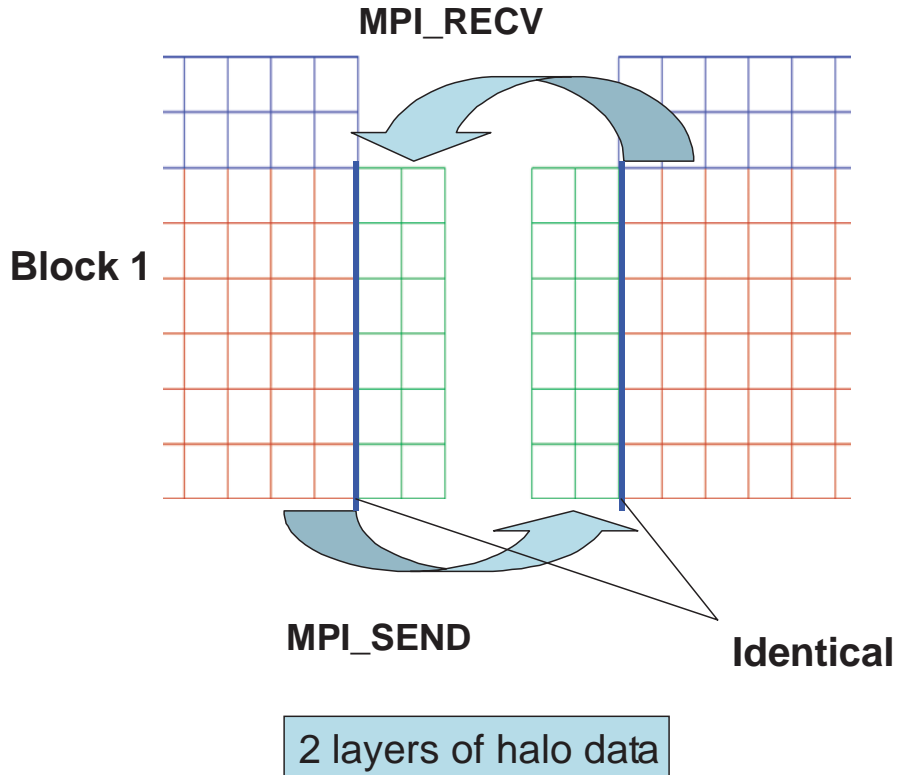


Figure 10. Illustration of block boundary data swapping between two adjacent ‘halo data’ regions. The data swapping is implemented on a distributed memory parallel computer using the Message Passing Interface directives MPI_RECV and MPI_SEND.

respond to the number of partitions in the I-, J- and K-directions (coordinate directions), respectively. Note that NBLOC is equal to the number of central processing units (CPUs) on the parallel computer (e.g., Beowulf cluster) that will be used to execute urbanSTREAM. An example of the partitioning of a computational domain is illustrated in Figure 10, which also shows the ‘halo data’ regions that will be used to pass block boundary information between two adjacent blocks (or, equivalently, from one CPU to another since the blocks in the partitioning are mapped in one-to-one correspondence to the CPUs on the parallel computer).

A subroutine OVEL_Q is used to swap the boundary data information in the ‘halo data’ regions. Two MPI directives are used in OVEL_Q to accomplish this data swapping; namely, MPI_SEND and MPI_RECV which send messages to and receive messages from the neighboring blocks, respectively (see Figure 10). The index of the neighboring block (or, equivalently, the node number in the parallel computer system) is identified by the connectivity matrix MCONEC as explained previously. The indexing system used for a block in question and four neighboring halo data regions in a 2-D environment is presented in Figure 11.

It is important to note that MPI_SEND is “blocking”. This means that it does not return

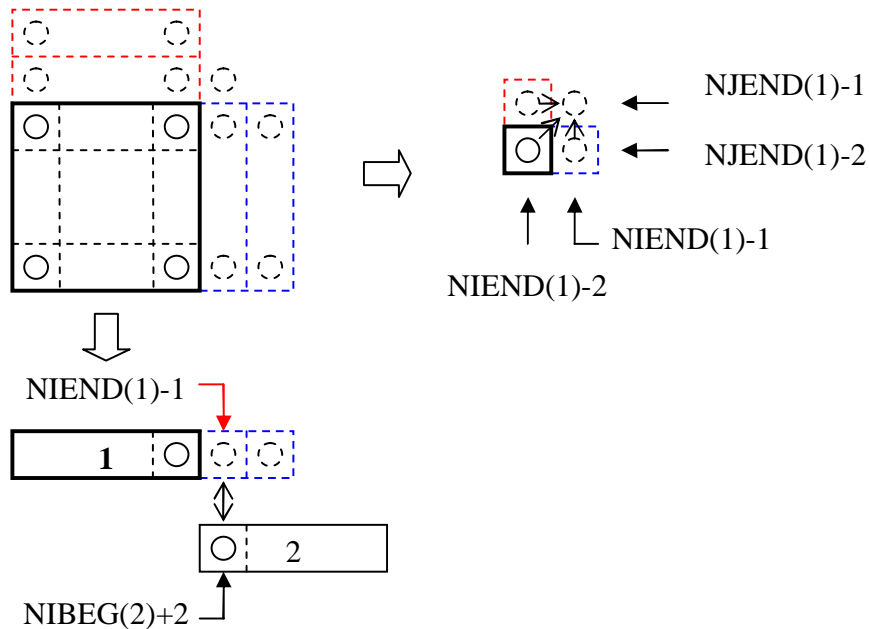
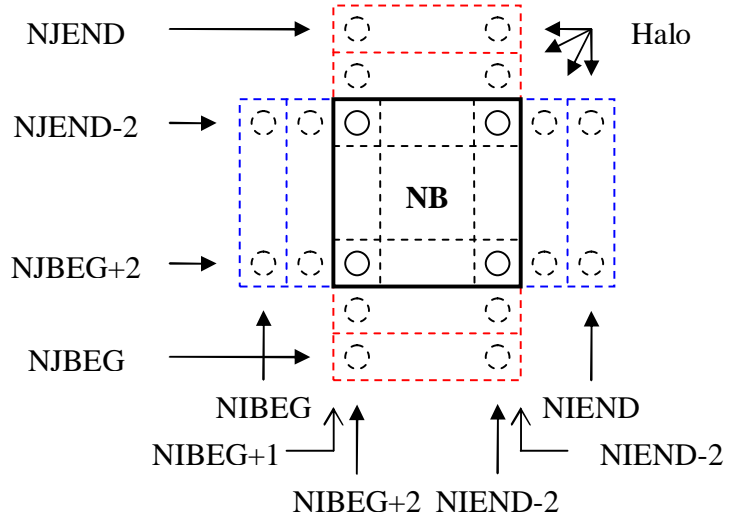


Figure 11. The indexing system used for a reference block and its four neighboring blocks in a 2-D computational domain.

until the message data have been received, so that the sender is free to access and overwrite the send buffer. Similarly, MPI_RECV is also blocking. It returns only after the receive buffer contains the newly received message. Message buffering decouples the send and receive operations. A blocking send might complete as soon as the message was buffered, even if no matching receive has been acknowledged by the receiver. On the other hand,

message buffering can be expensive, as it entails additional memory-to-memory copying, and it requires the allocation of memory. In a poorly designed program, blocking may lead to a “deadlock” situation, where all processes are blocked (deadlocked), and no further progress can then occur. Such programs may complete when sufficient buffer space is available, but will fail on parallel computer systems that use less buffering, or when message sizes are increased. Since any system will exhaust buffer resources as the message sizes are increased, a “safe programming style” is adopted in our current implementation. This implementation will not result in deadlock even when no buffer space is available and, therefore, is safe and will always complete execution correctly.

5. Application to Idealized Obstacle Array

In this section, we illustrate the predictive accuracy of urbanSTREAM and urbanEU by presenting the results of a detailed comparison of the flow and turbulent dispersion between a comprehensive water channel experiment and the model predictions. For the simulations in this section, urbanSTREAM was used with a nonlinear stress-strain model for the Reynolds stresses and the modified k - ϵ turbulence model was applied with $C_{\epsilon_0} = 0.7$. The Eulerian dispersion model urbanEU was used with a tensor diffusivity model for the turbulent concentration fluxes.

5.1. Water channel experiment

The water channel experiment is fully described in Hilderman and Chong (2007), and only the important details of the experiment will be presented here. The experiment was conducted in the boundary-layer water channel at Coanda Research & Development Corporation (Burnaby, British Columbia, Canada). The water channel had a working section of 10 m length, 1.5 m width and 0.9 m height.

The water channel experiment simulated a neutrally-stratified atmospheric boundary-layer flow over a regular array of three-dimensional (3-D) buildings. A schematic drawing of the 3-D building array is shown in Figure 12. The array consists of sharp-edged cubes with a characteristic dimension $L = W = H = 31.75$ mm, where L , W and H are the length, width and height of the obstacles. A total of 256 cubes was placed in an aligned array consisting of 16 rows of 16 cubes. The array filled the entire spanwise dimension (width) of the water channel. The streamwise and spanwise face-to-face spacings between cubes was H giving frontal and plan area indices (λ_f and λ_p , respectively) of 0.25.¹²

The building array was immersed in a simulated neutral atmospheric boundary layer that was created in the water channel using the combination of a “turbulence” grid made of square bars 19 mm \times 19 mm placed at the start of the channel inlet and a sawtooth fence, with a base width equal to that of the channel and a height of 70 mm, placed 200 mm downstream of the square bar array. The boundary-layer thickness, δ , taken to be the height where the mean wind speed reached 99% of the free stream value, was found to be 275 mm. At this point, the mean wind speed \bar{u}_δ was 0.375 m s⁻¹. The friction velocity u_* determined

¹²The frontal area index of an obstacle array is defined as $\lambda_f \equiv A_f/A_L$, where A_f is the frontal (windward) area of an obstacle and A_L is the lot area (surface area within which a single obstacle sits in the array). The plan area index is defined as $\lambda_p = A_p/A_L$, where A_p is the plan (floor) area of the obstacle.

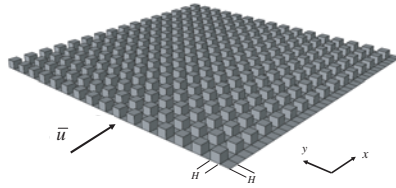


Figure 12. A three-dimensional perspective view showing the geometry of the regular and aligned array of cubes and the Cartesian coordinate system used. Here, x is in the streamwise direction and y is in the spanwise direction.

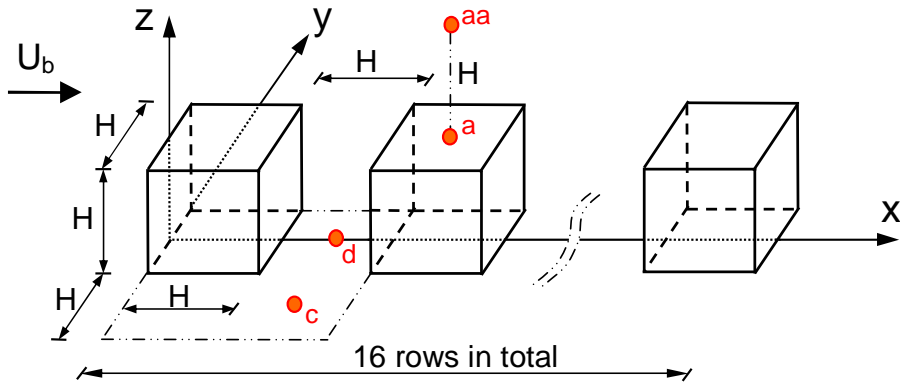


Figure 13. Geometry of the regular and aligned array of cubes in the water channel depicting the eighth column of the obstacles. The location of the ground-level source is marked by d.

from measurements of the shear stress in the constant stress layer near the surface of the upstream fetch was 0.0255 m s^{-1} , giving $u_*/\bar{u}_\delta = 0.068$ for the water channel simulations. A least-squares fit of the usual log-law profile for the mean wind speed in a regular rough-wall boundary layer, $\bar{u}/u_* = k_v \log[(z - d)/z_0]$, where z_0 is the roughness length, d is the zero-plane displacement, and $k_v \approx 0.4$ is von Kármán's constant gave the following results: $z_0 = 0.35 \pm 0.05 \text{ mm}$, assuming a zero-plane displacement d of 2.8 mm (using the common rule of thumb that d should be approximately 70% of the height of the roughness elements). The reference Reynolds number of the flow was approximately $Re_H = 12,005$ (based on H and the free stream velocity $U_b = 0.375 \text{ m s}^{-1}$).

Measurements of the velocity components were made using a 4-beam, 2-component fibre-optic laser Doppler velocimeter (LDV). The velocity time series were sampled for 500 s, which was found to be sufficiently long to give statistically converged estimates for the various velocity statistics. For the water channel simulations of dispersion in the obstacle array, a ground-level point source consisting of a vertical stainless steel tube (2.8 mm I.D. and 3.1 mm O.D.) was used, with the outlet of the tube placed just above the wire mesh that served as the ground roughness elements. The source emitted a sodium fluorescein dye tracer at a constant flow rate of $12 \times 10^{-3} \text{ l min}^{-1}$ with low discharge momentum (weak vertical jet). The source was located between the first and second rows of obstacles in the spanwise-oriented street canyon at a position lying at the intersection of the first row

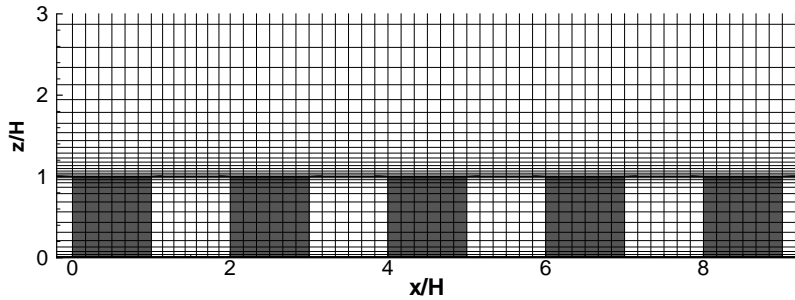


Figure 14. A partial x - z view at $y = 0$ of the computational grid used for the prediction of flow over the aligned array of cubes.

and eighth column of obstacles (where the rows are numbered in increasing order in the streamwise direction from the leading (windward) edge of the array and the columns are numbered in increasing order in the spanwise direction from the right-hand side of the array when looking in the flow direction – see Figure 12). This source location will be referred to as location d as shown in Figure 13. The instantaneous concentration field in the dispersing dye plume was measured using the laser-induced fluorescence (LIF) technique.

5.2. Flow domain discretization

For the simulations to be reported, the model domain used to simulate the flow within and over the 3-D building array spanned $-15 \leq x/H \leq 46$ with the windward face of the first row of cubes placed at $x/H = 0$. The spanwise extent of the domain was $18H$ (spanning 9 columns of cubes in the spanwise direction with $-9 \leq y/H \leq 9$) and the domain height was $11H$ ($0 \leq z/H \leq 11$), where z is the vertical coordinate direction measured from ground level. The domain height was sufficiently deep to provide an appropriate computational domain within which the flow changes near the surface can occur without being moulded by the boundary conditions (i.e., free slip conditions) imposed at the outer boundary layer.

The discretization of the computational domain is displayed in Figure 14. A non-uniform coarse grid of $228 \times 111 \times 48$ control volumes (in the streamwise, spanwise and vertical directions, respectively) was used for the discretization of the computational domain. As shown in Figure 14, the grid lines were preferentially concentrated in the vicinity of every solid surface (e.g., walls, rooftops, ground) where the gradients in the flow properties are expected to be greatest. The spacing between the grid lines was gently stretched with increasing distance from the solid surface in accordance to Equation (1).

5.3. Comparison of velocity statistics

Detailed measurements of vertical velocity profiles were made at 12 locations in two unit cells of the cubic array. The two unit cells were taken at two streamwise locations along the eighth column of cubes (near the centerline of the array). In the aligned array of cubes

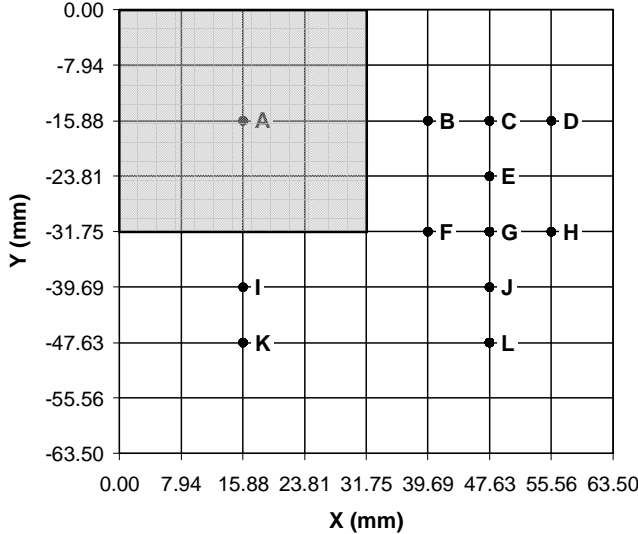


Figure 15. Sampling locations for velocity measurements in a unit cell of the cubic array. Each unit cell of the array was $2H \times 2H$, with $H = 31.75$ mm.

shown in Figure 12, a unit cell of the array occupies a plan area of $2H \times 2H$ in the $x-y$ plane as shown in Figure 15. In this figure, the 12 locations for the measurements of the velocity profiles are labelled A through K. Note that the cubical obstacle occupies the upper-left quadrant of the unit cell (with location A situated at the center of this obstacle). The location of the cubical obstacle is marked by the shaded region shown in Figure 15. Measurements of vertical profiles of the velocity were made in the first (cell 1) and sixth (cell 6) cells in the streamwise direction along the eighth column of cubes in the array.

Figure 16 compares model predicted vertical profiles of the mean streamwise velocity \bar{u} (normalized by the free-stream velocity U_b) at two locations C and G in cells 1 and 6. The model predictions shown here were generated with $C_{\epsilon_0} = 0.7$. The mean streamwise velocity profiles corresponding to locations C and G in cell 1 are located in the adjustment zone where the undisturbed upstream flow is adjusting to the presence of the urban canopy. In contrast, the mean streamwise velocity profiles corresponding to locations C and G in cell 6 are located in the equilibrium zone where the mean velocity appears to have reached streamwise equilibrium (viz., the mean streamwise velocity is fully developed). At all these locations, it is seen that the mean streamwise velocity is well predicted by the model results. In particular, a very strong shear layer forms at the top of the urban canopy, whose signature is revealed by the inflection point in $\bar{u}(z)$ at or near the building height H . Note that the large values of mean shear $\partial\bar{u}/\partial z$ just above the building height are predicted well by the model. Furthermore, at location C, the magnitude of the reverse velocity in the spanwise-oriented street canyon is correctly reproduced by the model predictions.

Figure 17 presents vertical profiles of turbulence kinetic energy, k , at the same locations as the mean streamwise velocity profiles displayed in Figure 16. The model predictions shown here were obtained with the standard $k-\epsilon$ model with $C_{\epsilon_0} = 1$ and the modified $k-\epsilon$ model with $C_{\epsilon_0} = 0.7$. Generally speaking, the turbulence energy levels in the roughness

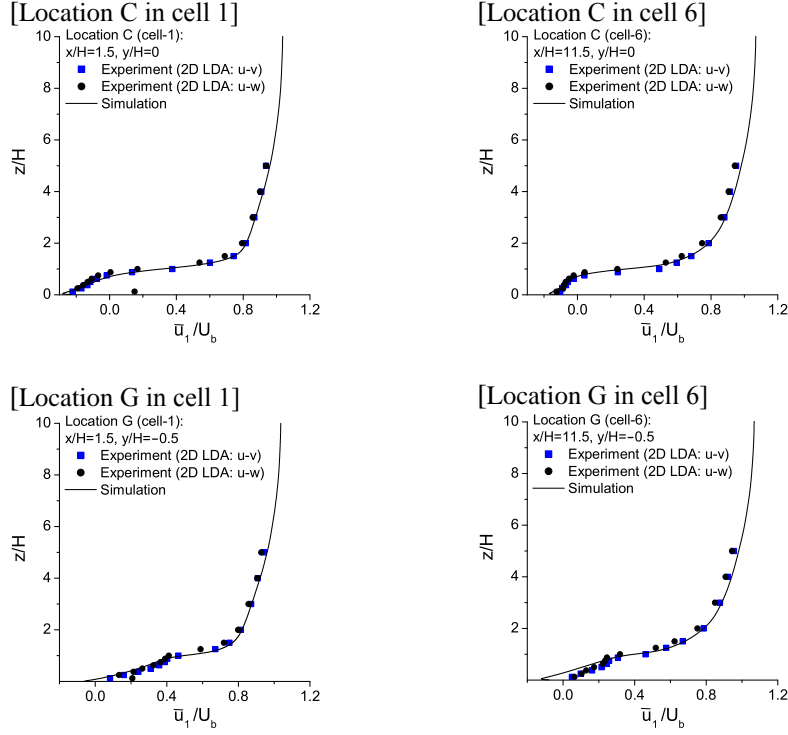


Figure 16. Comparison of measured and predicted vertical profiles of mean streamwise velocity, $\bar{u}_1 \equiv \bar{u}$, (normalized by U_b) at locations C and G in cells 1 and 6 ($C_{\epsilon_0} = 0.7$). Two different configurations of the LDV have been used to measure \bar{u} (namely, the u - v and u - w configurations).

sublayer ($z/H < 2$) are under-predicted by the standard k - ϵ model. The modified k - ϵ improves the prediction of the turbulence energy levels for $z/H < 2$. In particular, note that the observed large peak in TKE at location C in cell 1 (which is just above the first building rooftop) is well predicted using the modified k - ϵ model, whereas it is significantly under-predicted (by about a factor of two) using the standard k - ϵ model. This observed large peak in the TKE may arise from an oscillation of the high shear layer by the larger-scale upstream turbulence which would enhance the streamwise velocity variance (and, hence, k). Furthermore, the position and magnitude of the prominent nose in the k -profile at location C in cell 6 (which lies just above the street canyon top in the equilibrium zone) is largely reproduced by the modified k - ϵ model, but poorly predicted by the standard k - ϵ model. The peak value of k at location C (which occurs at or near the canopy top at $z/H \approx 1$) decreases monotonically in the streamwise direction from the first street canyon (cell 1) and reaches a near constant value at the sixth street canyon (cell 6). This feature in the behaviour of the TKE is correctly captured by the modified k - ϵ model.

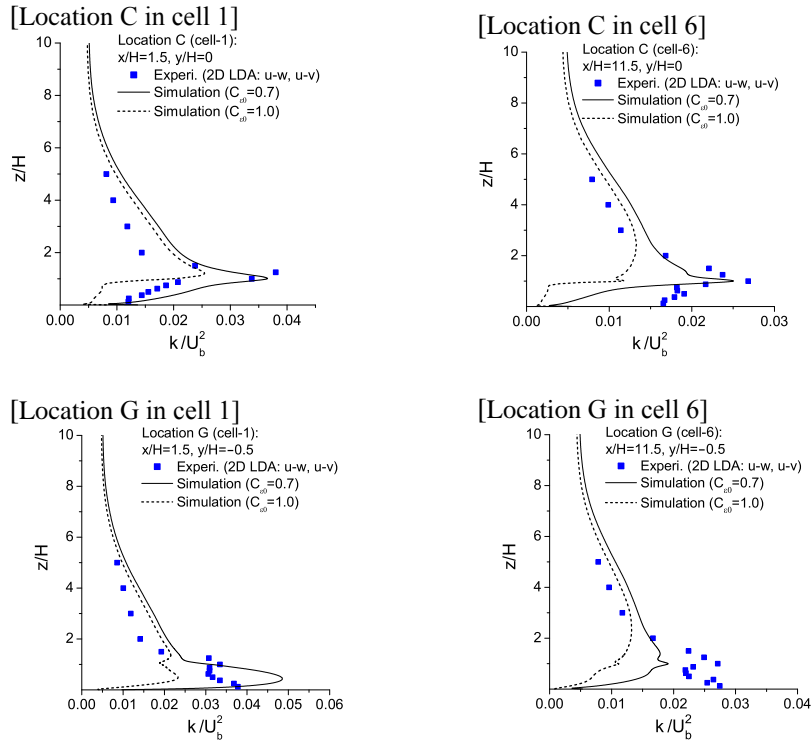


Figure 17. Comparison of measured and predicted vertical profiles of turbulence kinetic energy, k , (normalized by U_b^2) at locations C and G in cells 1 and 6 (for $C_{\epsilon 0} = 1$ and 0.7).

5.4. Comparison of concentration statistics

Figure 18 exhibits comparisons of model predictions with observations for crosswind (horizontal) profiles of the normalized mean concentration, C/C_s , and the normalized concentration standard deviation, $(\bar{c}^2)^{1/2}/C_s$, at the streamwise location $x/H = 5.5$ at half canopy height ($z/H = 0.5$). Here, C_s is the source concentration. This x -location lies midway between rows 3 and 4 in the cubic obstacle array, corresponding to a downwind fetch of $(x - x_s)/H = 4.0$ (where $x_s/H = 1.5$ is the streamwise location of the source – labelled d in Figure 13). The agreement between the predictions (obtained using urbanEU) and the experimental data for the first two concentration moments is very good.

Note that the model predicts correctly the bimodal non-Gaussian form observed in the crosswind mean concentration profile. This non-Gaussian form for the crosswind mean concentration profile is due to splitting of the plume into two by the horseshoe vortex that forms around the base of the cube immediately downwind of the source (viz., the cube whose windward face is located at $x/H = 2.0$). The locations of the local minimum and two local maxima in the horizontal mean concentration profile at $y/H \approx 0$ and $\approx \pm 1$, respectively, are correctly predicted by the model, although the model over-predicts the magnitude of the mean concentration at each of these three locations by about 15%. Similarly, the model correctly predicts the locations of the off-axis peaks in the concentration

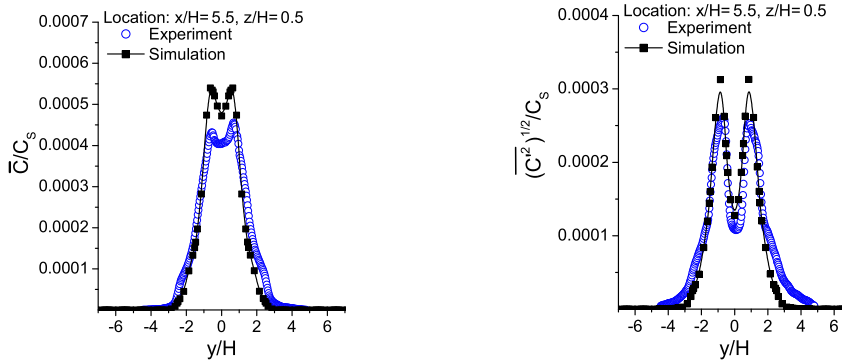


Figure 18. Comparison of measured and predicted crosswind profiles of (a) the normalized mean concentration, C/C_s , and (b) the normalized concentration standard deviation, $(\bar{C}'^2)^{1/2}/C_s$, obtained at half canopy height ($z/H = 0.5$) and at $x/H = 5.5$. Here, C_s is the source concentration.

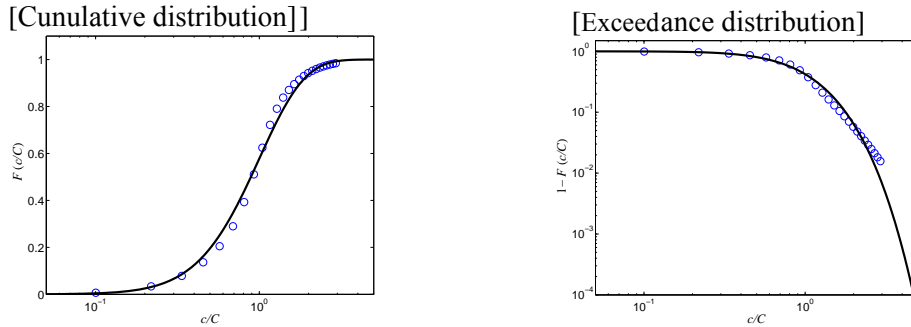


Figure 19. Comparison of measured (circles) and model (solid line) cumulative and exceedance probability distributions for normalized concentration, c/C , at location $(x, y, z)/H = (5.5, 0, 0.5)$. The model cumulative and exceedance probability distributions were for the clipped-gamma form. The parameters for the clipped-gamma distribution were computed from the predicted values for C and \bar{C}'^2 obtained for this position using urbanEU (see Figure 18).

standard deviation at $y/H \approx \pm 1$ (which are located roughly along the centerlines of the two streamwise-oriented street canyons, one on either side of the eighth column of cubes).

Given predictions of C and \bar{C}'^2 , the prediction of probability of exceedances of critical concentration levels can be obtained using a pre-specified form of the concentration PDF. Earlier, we suggested the application of the clipped-gamma PDF for the concentration since the parameters for this PDF are uniquely defined given the information embodied in C and \bar{C}'^2 . To this end, we compare the modeled and measured cumulative and exceedance proba-

bility distributions¹³ of the normalized concentration in Figure 19 at a location on the plume centerline ($y/H = 0$) at $x/H = 5.5$ and $z/H = 0.5$. Note that the concentration has been normalized by the (local) mean concentration C . The mean concentration and concentration standard deviation at this location obtained from the model predictions (cf. Figure 18) were used to determine the parameters k , s , and λ for the clipped-gamma distribution, and the cumulative and exceedance distributions for the clipped-gamma form determined in this manner are compared to the corresponding measured quantities in Figure 19.

The clipped-gamma distribution is seen to be in excellent conformance with the measured concentration CDF. Because it is the prediction of the likelihood of extreme events that is important in the hazard assessment of toxic gas releases, it is important to examine the upper tail of the concentration distribution. To that purpose, the exceedance distribution is displayed in Figure 19 on a logarithmic scale in order to emphasize the upper tails. Figure 19 indicates that the clipped-gamma distribution predicts the upper tail extremely well.

6. Application to Real Urban Environment

Here, a computational study is performed in which the capabilities of urbanSTREAM for urban flow prediction and urban(A)EU for urban dispersion predictions are examined by reference to a full-scale experimental study of flow and dispersion in a real cityscape (Oklahoma City, Oklahoma). For the simulations in this section, urbanSTREAM was used with a linear Boussinesq approximation for the Reynolds stresses and the standard $k-\epsilon$ was applied (viz., $C_{\epsilon_0} = 1.0$). The Eulerian dispersion model urbanEU was used with a simple gradient diffusion hypothesis for representation of the turbulent concentration fluxes.

6.1. Joint Urban 2003

Joint Urban 2003 (JU2003) experiment was a major urban study that was conducted in Oklahoma City, Oklahoma during the period from June 28 to July 31, 2003 (Allwine et al., 2004). The principal objective of JU2003 was to obtain high-quality meteorological and tracer data sets documenting urban flow and dispersion in a real city on a range of scales: namely, from flow and dispersion in and around a single city block (street canyon at building scale), to that in and around several blocks in the central business district (CBD) of downtown Oklahoma City (neighborhood scale), and finally to that in the suburban area several kilometers from downtown Oklahoma City (urban scale). Additionally, JU2003 included measurements of indoor flow and dispersion in four buildings in the CBD that were coordinated and conducted in conjunction with the outdoor urban field experiments in order to study physical mechanisms involved in indoor-outdoor exchange rates.

¹³The cumulative distribution of concentration, $F(c; \mathbf{x}, t)$, at location \mathbf{x} and time t is defined as

$$F(c; \mathbf{x}, t) \equiv \int_{0^-}^c f(c'; \mathbf{x}, t) dc',$$

and the exceedance distribution of concentration is simply $1 - F(c; \mathbf{x}, t)$. In the case of a steady continuous plume releasing into a statistically stationary turbulent flow (as in our current example), we note that $F(c; \mathbf{x}, t)$ is independent of time t .

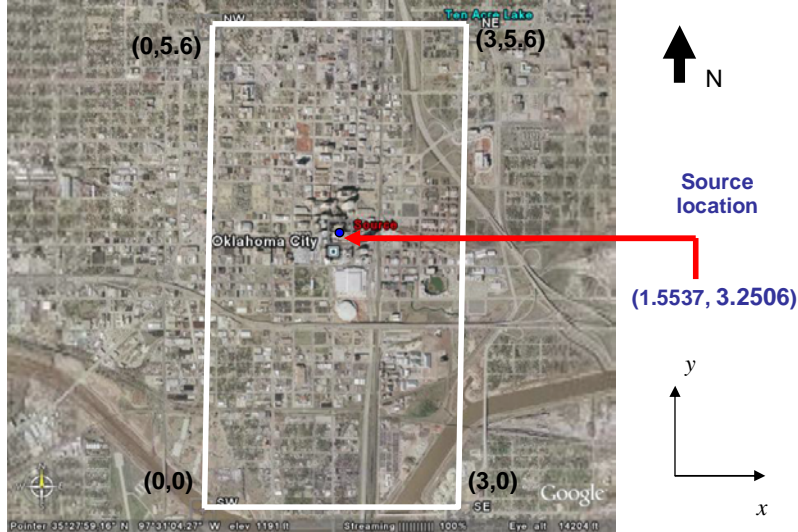


Figure 20. Computational domain used for simulation of flow in Oklahoma City.

A large number of meteorological measurements in Oklahoma City were obtained during JU2003. These included detailed measurements of wind and turbulence characteristics in the urban atmospheric boundary layer obtained with remote sensing instruments such as Doppler lidars, Doppler sodars (acoustic wind profiler) and radar profilers; and, measurements of wind, temperature, and turbulence in the urban canopy layer (including, within a street canyon) using fast-response in-situ meteorological sensors such as sonic anemometers and infrared thermometers. Furthermore, tracer bag samplers were used to measure mean concentration data obtained from the release of a sulfur hexafluoride (SF_6) tracer in downtown Oklahoma City, Oklahoma at three different locations. To this purpose, ten intensive observation periods (IOPs) were undertaken during JU2003, during each of which there was typically three 30-minute (continuous) tracer gas releases as well as four puff (instantaneous) releases where balloons filled with tracer gas were “popped”.

For all the IOPs, each of the three 30-minute continuous releases was separated by 90 minutes and this set of three continuous releases was either preceded or followed by a set of four instantaneous releases with a 20-minute interval between each release. The release rates for the continuous source was constant (generally to within about 5%) during each experiment, and the release rates from the various experiments ranged over the interval from $2\text{--}5 \text{ g s}^{-1}$. The tracer masses released from the instantaneous source varied over the range from 300–1000 g. The tracer gas from all releases was sampled in and around downtown Oklahoma City on the regular CBD sampler grid and as far downwind as four kilometers from the release along various sampling arcs. The first six IOPs were conducted during the day from 08:00 CST to 16:00 CST, whereas the last four IOPs were conducted during the night from 22:00 CST to 06:00 CST.

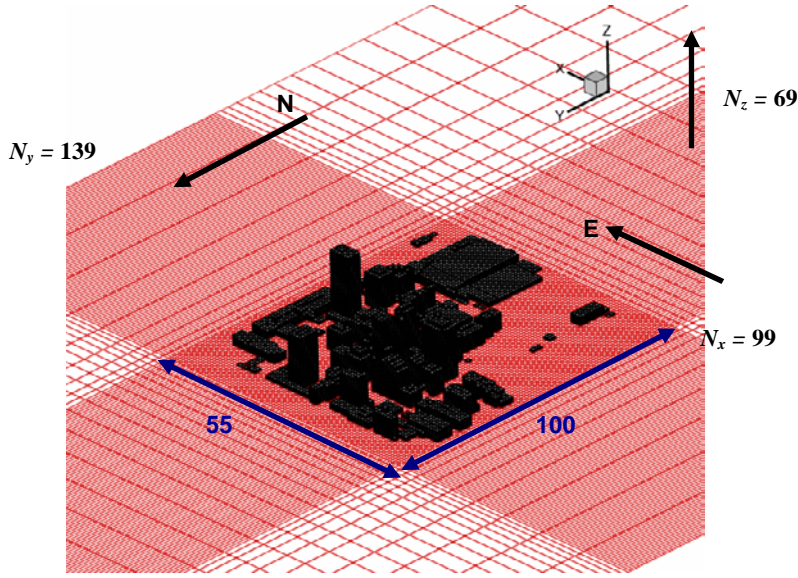


Figure 21. Computational grid generated by urbanGRID for Oklahoma City.

6.2. Grid generation for Oklahoma City

Some capabilities of the modeling system are presented with the aid of numerical simulations performed for a built-up (urban) region in Oklahoma City, Oklahoma. The modeling domain with the extent of $1,934.25\text{ m} \times 3,610.6\text{ m} \times 800.0\text{ m}$ in the x - (or, W-E), y - (or, S-N) and z - (or, vertical) directions, respectively, covers the CBD of Oklahoma City and surrounding environs. At ground level where $z = 0$, the southwest corner of the modeling domain (see Figure 20) is at the following coordinates in the Universal Transverse Mercator (UTM) coordinate system¹⁴: zone = 14, $x_0 = 633,683$ UTM easting and $y_0 = 3,923,940$ UTM northing (or, equivalently, in the geodetic coordinate system this location is 35.449959° N and -97.52694° E). The internal coordinate system used in urbanSTREAM is shown in Figure 20, where the southwest corner of the modeling region is chosen as the origin $(0, 0)$ in the x - y (horizontal) plane. All distances shown here have been normalized by a reference length scale which is chosen in this case to be $\Lambda_{\text{ref}} = 644.75\text{ m}$. Hence, in this internal coordinate system, the northeast corner of the modeling region is referenced as $(3, 5.6)$. A proper subset within this modeling region is chosen as the region in which buildings will be explicitly resolved in the flow simulation; for this example, this rectangular building-aware region ($644.75\text{ m} \times 709.23\text{ m}$) has its southwest corner at $(1, 2.5)$ and its northeast corner at $(2, 3.6)$. In the portion of the modeling region lying outside the building-aware region, all buildings are treated as virtual and their effects on the flow are modeled using a distributed drag force representation in the mean momentum equations.

ESRI Shapefiles of the shapes, locations and heights of buildings in Oklahoma City are

¹⁴The UTM easting coordinate reported here and elsewhere in this report is referenced relative to the central meridian of the zone.

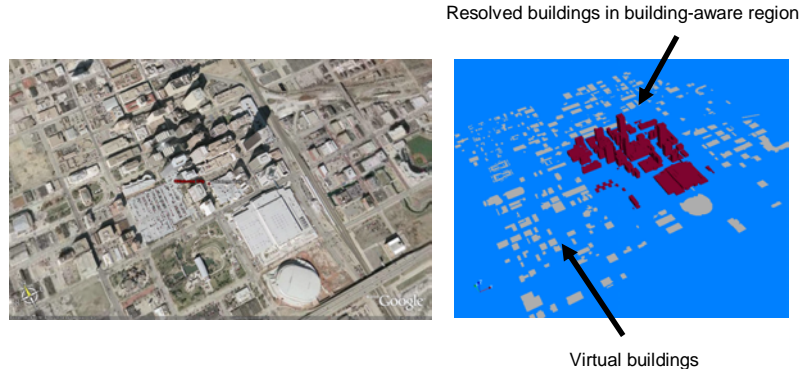


Figure 22. Satellite photograph of downtown Oklahoma City and 3-D computer rendering of buildings in building-aware region of the computational domain.

available from the Joint Urban 2003 archival database (<https://ju2003-dpd.dpg.army.mil>). These Shapefiles were used in urbanGRID to generate automatically a grid mesh over the modeling region as shown in Figure 21. The simulation was carried out in a three-dimensional Cartesian framework, and curved surfaces on buildings or planar building surfaces that are not aligned with the grid lines are approximated by stepwise surfaces. A mesh of $99 \times 139 \times 69$ grid lines in the x -, y -, and z -directions, respectively, was used to accommodate all the necessary geometrical details. The interior building-aware region was covered with a fine calculation grid of $55 \times 100 \times 69$ grid lines to better approximate the building features in this region. The grid arrangement adopted here is shown in the x - y plane in Figure 21. Hence, the fine grid used for the building-aware region contains 379,500 nodes, whereas the entire computational domain was covered with a mesh of 945,509 nodes. The grid lines were preferentially concentrated near the solid surfaces (ground, building rooftops and walls) where the gradients in the flow properties are expected to be greatest, and the spacing between the grid lines was gently stretched with increasing distance from the solid surfaces.

Figure 21 shows the finite-volume approximation of the explicitly resolved buildings in the building-aware region, and these approximated buildings should be compared to the actual (true) buildings in this area given in Figure 22 in the form of a satellite photograph and a three-dimensional computer rendering of the buildings from the ESRI Shapefile. As can be seen, there is very little difference between finite volume approximated buildings and the actual (true) buildings and therefore the stepwise approximation of the building surfaces is not expected to undermine the accuracy of the subsequent flow simulation.

6.3. Flow field

The flow field in the computational domain was computed using urbanSTREAM in a stand-alone mode (viz., this flow model was not coupled to the urban GEM LAM model). In consequence, at the inflow (inlet) boundary of the computational domain, the measured profiles of the undisturbed mean velocity and turbulence kinetic energy are used. The flow simulation conducted here was for IOP-9 for the time period from 06:00–06:30 UTC (01:00–01:30

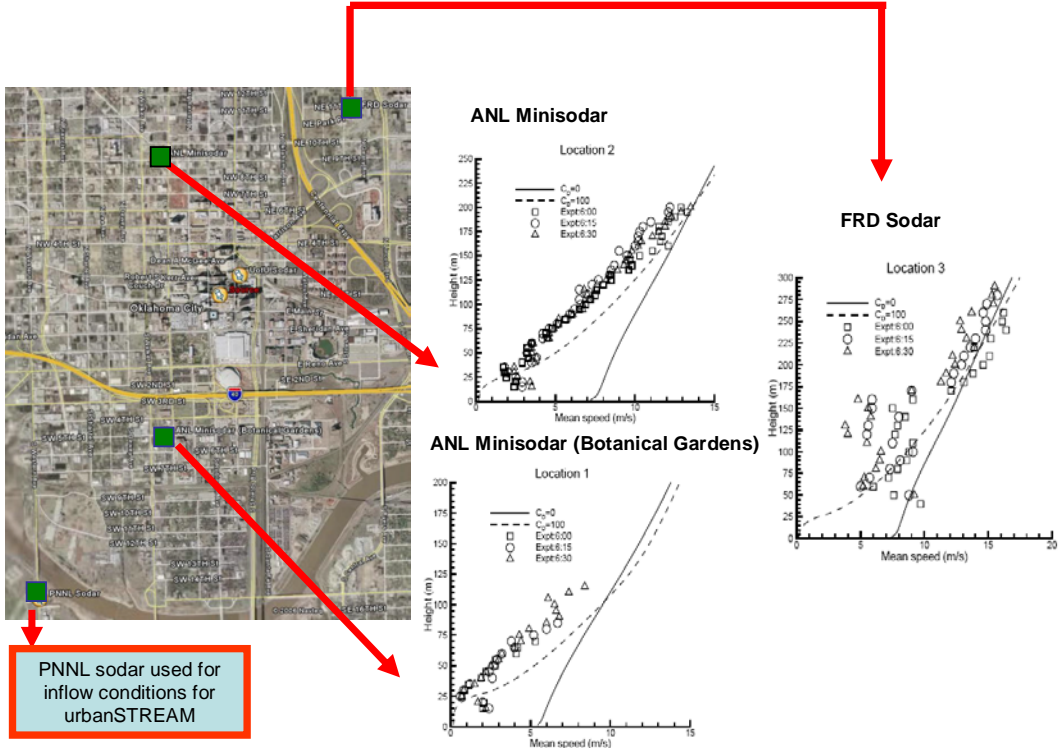


Figure 23. Comparison of mean wind speed measured at three locations in the computational domain with model predictions. The inflow conditions for the model were obtained from measurements made by the PNNL sodar.

CDT) on 28 July 2003 when the prevailing winds were from the south at about 6.8 m s^{-1} at 50-m above ground level at the southern edge of the computational domain shown in Figure 20. As a result, the inflow mean velocity and turbulence kinetic energy profiles (required for the inflow specification) were obtained from the Scintec Multi-frequency Flat Array Antenna Series (MFAS) sodar operated by a team of investigators from Pacific Northwest National Laboratory (PNNL). The Scintec MFAS sodar has an operating frequency in the 2 kHz band allowing for a spatial resolution of 10 m with a measurement range of up to 1000 m. This sodar was located 2 km south of the central business district of Oklahoma City in a parking lot at the Traffic Maintenance Yard (latitude 35.45° N ; longitude -97.53° E) which is on the south edge of Wheeler Park. The area south of this sodar was covered with low-rise (less than three stories) buildings, houses, and trees. The PNNL sodar was located very near the upwind (southern) edge of the computational domain, and measurements of mean wind velocity and turbulence were used to define the inflow conditions for urbanSTREAM.

The flow simulation in the computational domain was carried out using urbanSTREAM in the unsteady RANS mode. The effects of the buildings outside the building-aware region were represented by a distributed drag force approximation in the mean momentum

equation with a normalized drag coefficient of $C_d \equiv \hat{C}_d \hat{\Lambda} \Lambda_{\text{ref}} = 100$ (where Λ_{ref} is the reference length scale). For the simulations, a constant time step $\Delta t = 30$ s was used. The predicted wind statistics were averaged over 500 time steps after the flow had achieved a (pseudo) steady state. We compared the predicted vertical profiles of the mean horizontal wind speed with associated measured values obtained at three different locations in the computational domain. These comparisons are shown in Figure 23.

The measurements of wind speed were obtained from three different sodars: two minisodars deployed by Argonne National Laboratory (ANL) and one sodar operated by National Atmospheric and Oceanic Administration (NOAA) Atmospheric Research Laboratory Field Research Division (ARLFRD). One ANL minisodar was located near the southern edge of the central business district in the Oklahoma City Botanical Garden (latitude 35.46° N; longitude -97.52° E). The CBD of Oklahoma City, which includes many high-rise buildings, was immediately north of this sodar. The second ANL sodar was located approximately 1 km north of the CBD of Oklahoma City near the Minor building (latitude 35.48° N; longitude -97.52° E). The ARLFRD sodar (Radian 600PA phased-array Doppler sodar) was located about 1.5 km northeast of the CBD of Oklahoma City at the campus of the Oklahoma School of Science and Mathematics on the southwest corner of Lincoln and NE 13th Street (latitude 35.48147° N ; longitude -97.5051° E). Both ANL minisodars were operated with the first range gate at 5 m, a range gate spacing of 5 m with the top gate at 200-m above ground level (AGL), and an averaging (integration) time of 15 min. The ARLFRD sodar was operated with the first range gate at 40 m, a range gate spacing of 10 m with the top gate at 300-m AGL, and an averaging (integration) time of 15 min.

From Figure 23, it is seen that the model with the inclusion of the drag force representation for virtual buildings (dashed curves) correctly reproduces the overall qualitative trends in the horizontal wind speeds at the three locations in the computational domain. At the locations of the ANL minisodars, the wind speeds predicted by the model were slightly larger than the measured wind speeds over most of the range between about 25 m and 200 m AGL. The predicted wind speeds agreed well with those measured at the location of the ARLFRD sodar, although the measurements here from one 15-min averaging period to another showed greater variability than those measured at the two ANL minisodar locations. Figure 23 also shows model predictions of horizontal wind speed without the inclusion of a distributed drag force approximation for the virtual buildings (solid lines). Note in this case that the wind speed is greatly overestimated by the model owing to the fact that without a distributed mean-momentum sink within the urban canopy to represent the effects of the unresolved buildings on the flow, there cannot be a deceleration of the flow in this region leading to the overprediction of the wind speed.

6.4. Plume dispersion in Oklahoma City

The flow field statistics predicted by urbanSTREAM were next used to “drive” an urban dispersion model in both the source-oriented (urbanEU) and receptor-oriented (urbanAEU) modes within the Eulerian framework. Furthermore, these wind field statistics were also used to “drive” a first-order Lagrangian stochastic model for urban dispersion (urbanLS, or more precisely urbanLS-1). The simulations were conducted for the second continu-

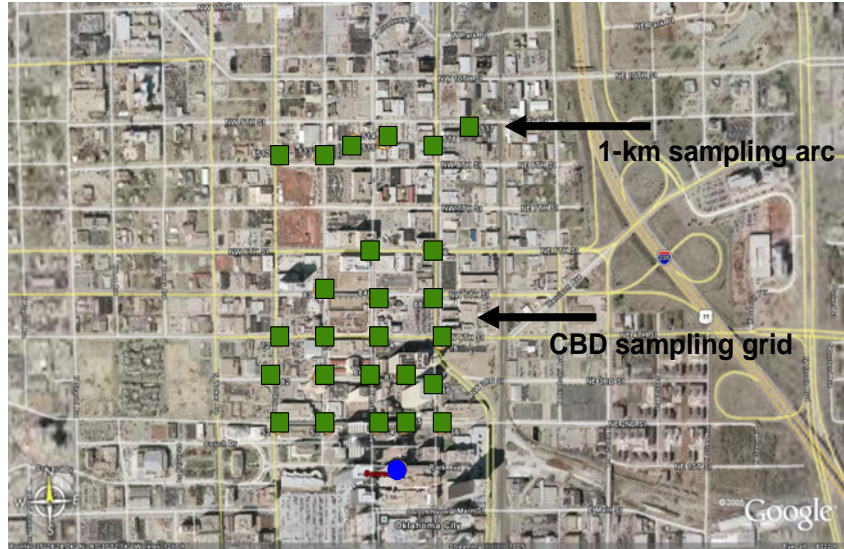


Figure 24. Detectors (squares) were positioned in the CBD sampling grid and at the 1-km sampling arc for measurement of the time-averaged tracer concentrations released from the indicated source (solid circle).

ous 30-min release of SF₆ in IOP-9, which occurred in the period from 06:00–06:30 UTC (01:00–01:30 CDT) on 28 July 2003. The SF₆ tracer gas was released at a point from a specially designed gas dissemination system that included a mass flow controller attached to a Campbell Scientific CR-23 data logger (Clawson et al., 2003). The dissemination point was located on the south side of Park Avenue (latitude 35.4687° N; longitude –97.5156° E) with a release height of 1.9 m. This source location was near the center of the computational domain (see Figure 20). The constant gas release rate for this experiment was 2.0 g s^{−1}.

The SF₆ plume concentrations were measured using Programmable Integrating Gas Samplers (PIGS) deployed by ARLFRD. The subsequent analysis of the samples was performed using an Automated Tracer Gas Analysis System (ATGAS) which used gas chromatography (GC) analysis techniques along with autosampler capabilities to give time-integrated concentration measurements. The sampling system was designed to provide average SF₆ plume concentrations over specific time intervals at given receptor locations. The PIGS collected 12 samples by pumping air into 12 individual Tedlar bags. Subsequently, the bag samples were analyzed using the ATGAS. The grid of sampling stations at which predictions of SF₆ plume concentrations were compared with measurements is shown in Figure 24 in relationship to the location of the source. The samplers used for comparison include 19 samplers located on the CBD sampling grid and six samplers located along the 1-km sampling arc.

Figure 25 displays various isolopleths (on a logarithmic scale) of the predicted mean concentration field C at ground level in the computational domain obtained using urbanEU (source-oriented approach). Figure 26 shows isolopleths (on a logarithmic scale) of the influence function C^* (viz., adjunct of the concentration C) at ground level corresponding to one

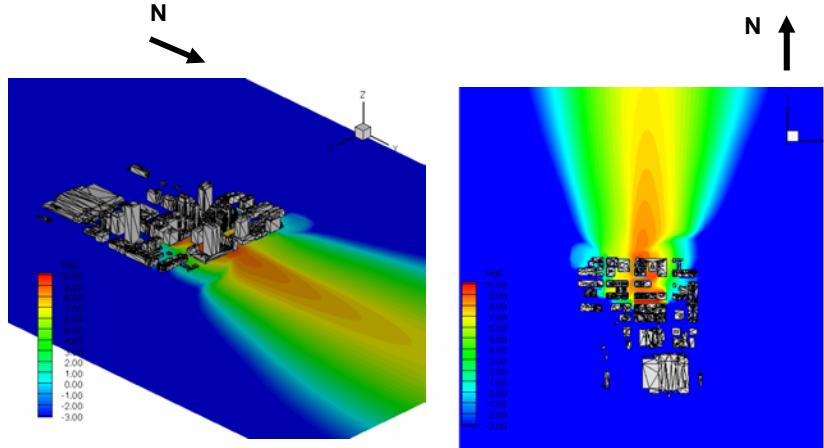


Figure 25. Mean plume concentration isopleths (logarithmic scale) at ground level for tracer release on south side of Park Avenue (Oklahoma City).

of the sampling locations (receptors) along the 1-km sampling arc. This result was obtained using urbanAEU (receptor-oriented approach). The influence function C^* characterizes the concentration “seen” at the given receptor through the duality relationship of Equation (36) for an arbitrary source distribution Q . In essence, the value of C^* at a given spatial position provides information on the contribution of a point source with a unit emission rate to the concentration at the receptor.

Figure 27 compares predictions of the mean concentration [in parts-per-trillion by volume (pptv)] obtained using urbanEU, urbanAEU and urbanLS-1 with the experimental concentration data measured at 10 different sampling locations along Kerr Avenue and McGee Avenue. Similarly, Figure 28 shows comparisons of mean concentration obtained using the three dispersion models with experimental concentration measurements made at eight sampling stations located along 4th Street and 5th Street. Finally, Figure 29 exhibits predicted and observed mean concentration obtained at two sampling locations along 6th Street and six sampling stations along the 1-km sampling arc. The experimental concentration data shown here is for a 30-min averaging time.

Generally speaking, the predictions for mean concentration at or near the mean plume centerline were quite good, with predictions within a factor of two of the observed concentration. However, the predicted concentrations at sampling locations 56, 66, and 76 were more than a factor of five lower than the experimentally measured values, suggesting that either the predicted plume was too narrow or the eastern edge of the predicted plume was too far west at these locations. Furthermore, it is interesting to note that the 30-min average concentration at the receptor calculated using the influence function (receptor-oriented approach) generally agrees well with the concentration predicted using the source-oriented approach. The discrepancy in the predictions using these two approaches is due to the non-uniform grid utilized in the simulations (the mesh was finer in the region surrounding the source and coarser generally in the region downwind of the source where the receptors were located).

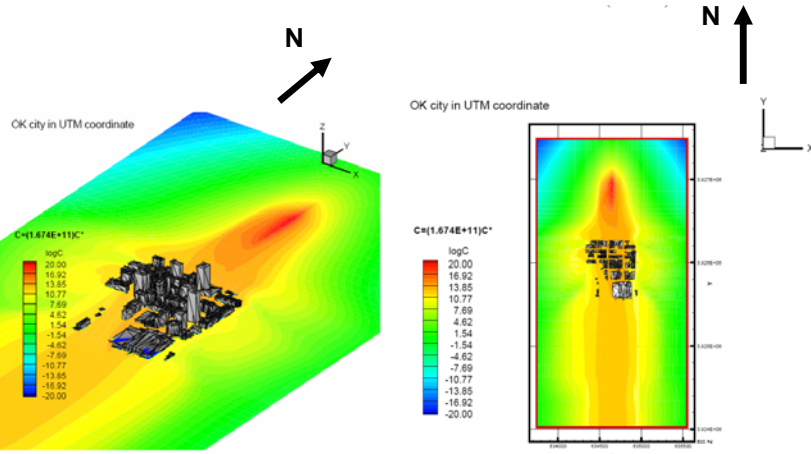


Figure 26. Influence function isopleths (logarithmic scale) at ground level associated with a receptor (#515) at the 1-km sampling arc (Oklahoma City).

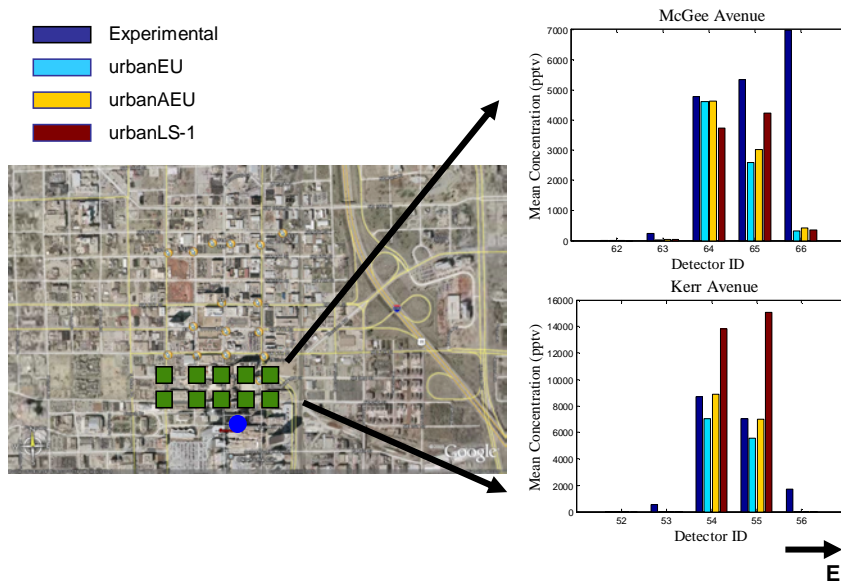


Figure 27. Comparison of predicted mean concentrations obtained from urbanEU, urbanAEU and urbanLS-1 with experimental measurements obtained with detectors along Kerr Avenue and McGee Avenue.

7. Conclusion

This chapter provides a technical description of the models that comprise Component 1 of CRTI Project 02-0093RD whose principal objective is the development of an advanced, fully validated, state-of-the-science modeling system for the prediction of urban flow (i.e., turbulent flow through cities) and the concomitant problem of modeling the dispersion of

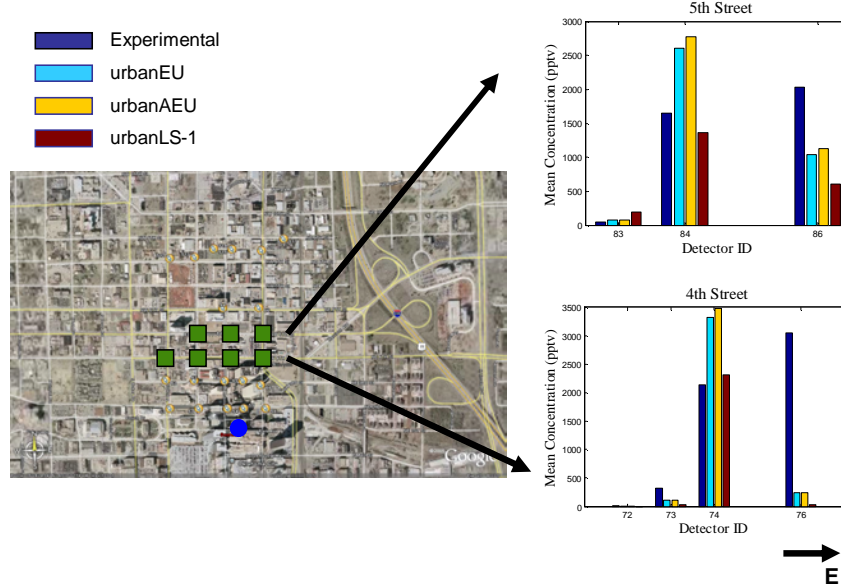


Figure 28. Comparison of predicted mean concentrations obtained from urbanEU, urbanAEU and urbanLS-1 with experimental measurements obtained with detectors along 4th Street and 5th Street.

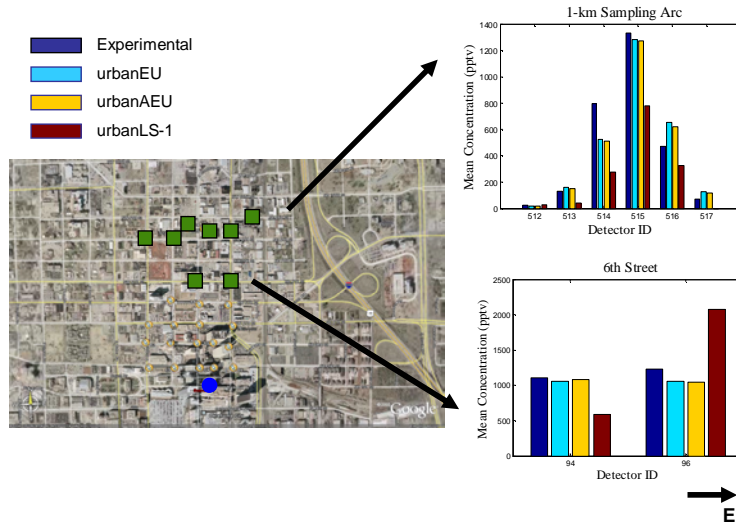


Figure 29. Comparison of predicted mean concentrations obtained from urbanEU, urbanAEU and urbanLS-1 with experimental measurements obtained with detectors along 6th Street and the 1-km sampling arc.

CBRN agents released in a populated urban complex. Component 1 focuses on the development of an urban microscale building-aware flow model and Eulerian-based urban dispersion models. This capability has been developed because almost all current dispersion

models employ simple diagnostic wind fields and Gaussian diffusion techniques to predict plume (cloud) dispersion which are not applicable in the highly disturbed flows present in an urban environment.

The principal module of Component 1 is urbanSTREAM, which is a general second-order accurate finite-volume code designed for the simulation of urban flow using a two-equation turbulence closure model (namely, the standard $k-\epsilon$ model and limited-length-scale $k-\epsilon$ model). This is perhaps the simplest complete turbulence model (in the sense that no advance knowledge of any property of the turbulence is required for the simulation other than the initial and/or boundary conditions for the problem) that is available currently as a general purpose simulator for urban flows. The modeling scheme used here is simple enough to be tractable numerically and, hence, not require excessive computing time which is important if the system is to be employed for emergency response applications. In addition, Component 1 incorporates a module (urbanGRID) for the automatic generation of grids in the computational domain when provided with detailed geometric information on the shapes and locations of buildings in the urban environment in the form of ESRI Shapefiles. Finally, Component 1 also includes modules for the prediction of urban dispersion in the Eulerian framework: namely, urbanEU which is an Eulerian grid dispersion model based on numerical solution of a K -theory advection-diffusion equation (source-oriented approach) and urbanAEU which is a receptor-oriented dispersion model based on numerical solution of the adjoint of the K -theory advection-diffusion equation.

The microscale urban flow and dispersion modeling system of Component 1 has been applied in stand-alone mode to simulate flow and tracer dispersion in a water channel experiment involving an idealized obstacle array and in a full-scale experiment in Oklahoma City, Oklahoma. Certainly, the numerical simulations of IOP-9 in the Joint Urban 2003 experiment provide an initial demonstration that the developed modeling system can correctly reproduce many features of the flow and dispersion in a real cityscape. While the results from this preliminary case study are certainly not definitive, they do suggest that the urban dispersion modeling system has the potential to improve the predictive performance capabilities for emergency response in built-up areas where the flow is highly disturbed.

The numerical models included in Component 1 require further improvements and evaluation against data from full-scale meteorological and dispersion field experiments in the urban environment. In particular, an evaluation of the predictive performance of the urban microscale flow and dispersion models when fully coupled with urban GEM LAM will be required. An improvement of the modeling system developed under Component 1 can be expected from: (a) the inclusion of more sophisticated turbulence closure schemes (e.g., second-moment closure which potentially can reproduce effects of streamline curvature, rotation and swirl, secondary motion, and other effects in highly disturbed complex flows better than with an eddy-viscosity concept); (b) application of hybrid Reynolds-averaged Navier-Stokes/large-eddy simulation (RANS/LES) approach which allows very large, coherent, or deterministic structures in the urban flow to be resolved rather than modeled; and, (c) inclusion of thermal effects on flow and contaminant dispersion in the urban street canyons.

To further improve the computational efficiency, in particular when thermal stratification effects are important and the coupling between velocity and temperature fields is strong, the fully-coupled multigrid (MG) method (Lien and Leschziner, 1994c) should be

implemented. Here, the primary task is to compute corrections of variables for a system of transport equations, including momentum, pressure-correction, energy and turbulence equations (rather than the correction of a variable for each transport equation separately) on a sequence of meshes of different sizes. The main challenge in the application of MG to turbulent flows is that the TKE can potentially become negative (or, physically non-realizable) at the prolongation (coarse-to-fine grid interpolation) stage during MG cycles.

The inclusion of an adaptive mesh refinement capability in the models would allow a dynamic tracking of the urban flow features as the computation proceeds, giving complete control of grid resolution with an expected concomitant computational savings over a static grid approach. A simpler alternative to a full adaptive mesh refinement capability would be to implement a local grid refinement (LGR) capability in the code. LGR would allow sufficient grid resolution to be provided in regions of interest, such as the clusters of buildings surrounding the contaminant source. In addition, the computational cost, which is closely related to the total number of grid points, is significantly reduced compared to the case where a sufficiently fine grid is used throughout the entire solution domain. However, parallelizing an LGR method can be challenging. A near optimal load balancing would be required in order to minimize the total CPU time on a parallel (distributed-memory or shared-memory) computer system. One avenue to address this problem would be to use a Hilbert space-filling-curve (HSFC) approach (Ji et al., 2006) for load balancing on a massively parallel system.

Acknowledgments

This work has been partially supported by Chemical Biological Radiological Nuclear Research and Technology Initiative (CRTI) program under project number CRTI-02-0093RD. The calculations reported here were made possible by the facilities of the Shared Hierarchical Academic Research Computing Network (SHARCNET) and Western Canada Research Grid (WESTGRID).

References

- Allwine, K. J., Leach, M. J., Stockham, L. W., Shinn, J. S., Hosker, R. P., Bowers, J. F. & Pace, J. C. (2004). Overview of Joint Urban 2003 – An Atmospheric Dispersion Study in Oklahoma City. *Symposium on Planning, Nowcasting, and Forecasting in the Urban Zone*. Seattle, Washington: American Meteorological Society.
- Apsley, D. D. & Castro, I. (1997). A Limited-Length-Scale k - ϵ Model for the Neutral and Stably-Stratified Atmospheric Boundary-Layer. *Boundary-Layer Meteorol.*, 83, 75–98.
- Barad, M.I. (1958). *Project Prairie Grass, a Field Program in Diffusion: Vols I and II*. Geophysics Research Paper No. 59, Geophysics Research Directorate, Air Force Cambridge Research Center, Bedford, MA.
- Chatwin, P. C. (1982). The Use of Statistics in Describing and Predicting the Effects of Dispersing Gas Clouds. *J. Haz. Mat.*, 6, 213-230.
- Clawson, K. L., Carter, R. G., Lacroix, D. J., Hukari, N. F. & Allwine, K. J. (2004). Joint Urban 2003 Vertical SF₆ Real-Time Analyzer and Time-Integrated Sampler Data Char-

- acteristics. *Fifth Conference on Urban Environment*. Vancouver, British Columbia: American Meteorological Society.
- Côté, J., Gravel, S., Méthot, A., Patoine, A., Roch, M. & Staniforth, A. (1998). The Operational CMC–MRB Global Environmental Multiscale (GEM) Model, Part I: Design Considerations and Formulation. *Mon. Weather Rev.*, 126, 1373–1395.
- Daly, B. J. & Harlow, F. H. (1970). Transport Equations of Turbulence. *Phys. Fluids*, 13, 2634–2649.
- Edelsbrunner, H. & Mucke, E. P. (1990). Simulation of Simplicity: A Technique to Cope with Degenerate Cases in Geometric Algorithms. *ACM Trans. Graph.*, 9, 66–104.
- ESRI (1998). *ESRI Shapefile Technical Description: An ESRI White Paper*. ESRI, 380 New York Street, Redlands California, USA.
- Ferziger, J. H. & Perić, M. (2002). *Computational Methods for Fluid Dynamics, 3rd edition*. Berlin: Springer-Verlag.
- Hilderman, T. & Chong, R. (2007). *A Laboratory Study of Momentum and Passive Scalar Transport and Diffusion Within and Above a Model Urban Canopy*. DRDC Suffield CR 2008-025, Defence R&D Canada – Suffield, Ralston, Alberta.
- Ji, H., Lien, F.-S. & Yee, E. (2006). Parallel Adaptive Mesh Refinement Combined With Multigrid for a Poisson Equation. *Proc. 14th Annual Conference of the CFD Society of Canada*. Kingston, Ontario.
- Keats, A., Yee, E. & Lien, F.-S. (2007a). Bayesian Inference for Source Determination With Applications to a Complex Urban Environment. *Atmos. Environ.*, 41, 465–479.
- Keats, A., Yee, E. & Lien, F.-S. (2007b). Efficiently Characterizing the Origin and Decay Rate of a Non-conservative Scalar Using Probability Theory. *Ecol. Modeling*, 205, 437–452.
- Launder, B. E. & Spalding, D. B. (1974). The Numerical Computation of Turbulent Flows. *Comp. Meth. Appl. Mech. Eng.*, 3, 1112–1128.
- Leonard, B. P. (1979). A Stable and Accurate Convective Modeling Procedure Based on Quadratic Upstream Interpolation. *Comp. Meth. Appl. Mech. Eng.*, 19, 59–98.
- Lien, F.-S. & Leschziner, M. A. (1994a). Upstream Monotonic Interpolation for Scalar Transport with Applications to Complex Turbulent Flows. *Int. J. Numer. Methods Fluids*, 19, 527–548.
- Lien, F.-S. & Leschziner, M. A. (1994b). A General Non-Orthogonal Collocated Finite-Volume Algorithm for Turbulent Flow at all Speeds Incorporating Second Moment Closure, Part 1, Computational Implementation. *Comp. Meth. Appl. Mech. Eng.*, 114, 123–148.
- Lien, F.-S. & Leschziner, M. A. (1994c). Multigrid Acceleration for Turbulent Flow with a Non-Orthogonal, Collocated Scheme. *Comp. Meth. Appl. Mech. Eng.*, 118, 351–371.
- Lien, F.-S., Chen, W. L. & Leschziner, M. A. (1996). A Multi-Block Implementation of Non-Orthogonal Collocated Finite-Volume Algorithm for Complex Turbulent Flows. *Int. J. Num. Meth. Fluids*, 23, 567–588.
- Lien, F.-S. & Yee, E. (2005). Numerical Modeling of the Turbulent Flow Developing Within and Over a 3-D Building Array, Part III: A Distributed Drag Force Approach, Its Implementation and Application. *Boundary-Layer Meteorol.*, 114, 287–313.
- Lien, F.-S., Yee, E. & Wilson, J. D. (2005). Numerical Modeling of the Turbulent Flow Developing Within and Over a 3-D Building Array, Part II: A Mathematical Foundation

- for a Distributed Drag Force Approach. *Boundary-Layer Meteorol.*, 114, 245–285.
- Masson, V. (2000). A Physically-Based Scheme for the Urban Energy Budget in Atmospheric Models. *Boundary-Layer Meteorol.*, 94, 357–397.
- Patankar, S. V. (1980). *Numerical Heat Transfer and Fluid Flow*. New York: Hemisphere Publishing Corporation.
- Rhie, C. M. & Chow, W. L. (1983). Numerical Study of the Turbulent Flow Past an Airfoil With Trailing Edge Separation. *AIAA J.*, 21, 1525–1532.
- Schewchuk, J. R. (1996). *Adaptive Precision Floating Point Arithmetic and Fast Robust Geometric Predicates*. Technical Report, School of Computer Science, Carnegie Mellon University, Pittsburg, PA.
- Speziale, C. G. (1987). On Nonlinear $k-l$ and $k-\epsilon$ Models of Turbulence. *J. Fluid Mech.*, 178, 459–475.
- Stone, H. L. (1968). Iterative Solution of Implicit Approximations of Multidimensional Partial Differential Equations. *SIAM J. Numer. Anal.*, 5, 530–558.
- ten Berge, W. F., Zwart, A. & Appelman, L. M. (1986), Concentration-Time Mortality Response Relationships of Irritant and Systemically Acting Vapours and Gases. *J. Haz. Mat.*, 13, 301–309.
- Townsend, A.A. (1980). *The Structure of Turbulent Shear Flows*. Cambridge: Cambridge University Press.
- Van Doormal, J. P. & Raithby, G. D. (1984). Enhancements of the SIMPLE Method for Predicting Incompressible Fluid Flows. *Numer. Heat Transfer*, 7, 147–163.
- Wang, B.-C., Yee, E. & Lien, F.-S. (2007). Study of Turbulent Passive Scalar Dispersion Within a Regular Array of Obstacles. *Proceedings of 5th International Symposium on Turbulence and Shear Flow Phenomena (TSFP5)*, Munich, Germany, 797–802.
- Wang, B.-C., Yee, E. & Lien, F.-S. (2008). Experimental and Numerical Study of Contaminant Dispersion in an Array of Cubic Obstacles. *Proceeding of 7th International ERCOFTAC Symposium on Engineering Turbulence Modeling and Measurements*, Limassol, Cyprus, 6 pp.
- Warmerdam, F. (1998). Shapelib C Library V1.2. <http://shapelib.maptools.org>.
- Wilson, J. D. (2007). *Technical Description of Urban Microscale Modeling System: Component 4 of CRTI Project 02-0093RD*. J. D. Wilson & Associates, Edmonton, Alberta.
- Yee, E. (2006). A Bayesian Approach for Reconstruction of the Characteristics of a Localized Pollutant Source From a Small Number of Concentration Measurements Obtained by Spatially Distributed “Electronic Noses”. Russian-Canadian Workshop on Modeling of Atmospheric Dispersion of Weapon Agents, Karpov Institute of Physical Chemistry, Moscow, Russia.
- Yee, E. (2007). Bayesian Probabilistic Approach for Inverse Source Determination From Limited and Noisy Chemical or Biological Sensor Concentration Measurements. *Chemical and Biological Sensing VIII* (Augustus W. Fountain III, ed), Proc of SPIE Vol. 6554, 65540W, doi:10.1117/12.721630, 12 pp.
- Yee, E. (2008a). Inverse Dispersion of an Unknown Number of Contaminant Sources. *15th Joint Conference on the Applications of Air Pollution Meteorology with the A&WMA*, New Orleans, LA, Paper 7.1, 17 pp.
- Yee, E. (2008b). Theory for Reconstruction of an Unknown Number of Contaminant Sources Using Probabilistic Inference. *Boundary-Layer Meteorol.*, 127, 359–394.

- Yee, E., Chan, R., Kosteniuk, P. R., Chandler, G. M., Biltoft, C. A. & Bowers, J. F. (1994). Experimental Measurements of Concentration Fluctuations and Scales in a Dispersing Plume in the Atmospheric Surface Layer Obtained using a Very Fast-Response Concentration Detector. *J. App. Meteorol.*, 33, 996-1016.
- Yee, E., Chan, R., Kosteniuk, P. R., Chandler, G. M., Biltoft, C. A. & Bowers, J. F. (1995). The Vertical Structure of Concentration Fluctuation Statistics in Plumes Dispersing in the Atmospheric Surface Layer. *Boundary-Layer Meteorol.*, 76, 41-67.
- Yee, E. & Chan, R. (1997). A Simple Model for the Probability Density Function of Concentration Fluctuations in Atmospheric Plumes. *Atmos. Environ.*, 31, 991–1002.
- Yee, E., Lien, F.-S., Keats, A. & D'Amours, R. (2008). Bayesian Inversion of Concentration Data: Source Reconstruction in the Adjoint Representation of Atmospheric Diffusion. *J. Wind Eng. Ind. Aerodyn.*, 96, 1805–1816.
- Yoshizawa, A. (1985). Statistical Analysis of the Anisotropy of Scalar Diffusion in Turbulent Shear Flows. *Phys. Fluids*, 28, 3226–3231.

Chapter 16

A SEMI-ANALYTIC MODEL OF FOG EFFECTS ON VISION

Eric Dumont¹, Nicolas Hautière¹ and Romain Galle^{1,2}

¹ Laboratoire Central des Ponts et Chaussées,
Division Exploitation Signalisation Eclairage,
Paris, France

² Laboratoire sur les Interactions Véhicules Infrastructure Conducteurs,
unité mixte de l'INRETS et du LCPC,
Versailles, France

Abstract

Fog is often considered as a mere nuisance rather than a hazard. However, reduced meteorological visibility conditions cause accidents and transportation delays, with substantial financial consequences. The visibility loss results from minute airborne droplets which scatter light, causing drastic alterations in the image of the environment perceived by vision systems, both human and artificial. Modeling the visual effects of dense fog makes it possible to simulate foggy conditions, in order to design and test countermeasures for improved safety and mobility. First, we introduce basic notions about the nature of fog and we briefly review the microphysical models which usually serve to describe its droplet size distribution. Second, we explain how light interacts with fog droplets, and we present the optical descriptors which describe scattering and extinction phenomena. Third, we analyze how contrast is impaired by these phenomena in the image of the environment perceived by a vision system, and we propose and discuss a semi-analytic model of the visual effects of fog. Finally, we show applications of this model to the monitoring of the meteorological visibility through use of charge-coupled device cameras operating in the visible light range.

1 Introduction

Dense fog drastically impairs visibility, causing important traffic safety issues, particularly in the field of ground transportation. In order to design and assess solutions for detecting

and counterbalancing the loss of visual information in foggy weather conditions, the use of simulation can hardly be avoided, since field experiments are made very difficult by the lack of control over the time and place where fog will occur.

Two approaches are possible for simulating the image of a scene observed in fog: computer graphics and image processing. The first consists in simulating all radiative transfers between emitting and reflecting surfaces, taking into account the interactions with the participating medium [34]. It involves global illumination calculations which are generally time-consuming. The other approach consists in simulating the perturbations caused in the image of the environment by the interactions of light with the scattering medium [7]. Originally designed for remote sensing, this approach has only recently found applications for horizontal visibility problems because of the depth-dependency of fog visual effects [29, 35].

This chapter shows how fog effects on vision can be simulated by image processing through a combination of depth-dependent (2D1/2) operations. First, we examine the nature and origin of fog, and we introduce its microphysical characteristics. Secondly, we consider the optical interactions between visible light and fog droplets, and we present the optical parameters characterizing the scattering phenomenon. Then we analyze the distance-dependent effects of light scattering on human or camera vision, and we propose a unified photometric model for simulating foggy weather conditions by image processing. Finally, we show applications of the model to the monitoring of the meteorological visibility through use of charge-coupled device cameras operating in the visible light range.

2 Fog Nature and Microstructure

2.1 Meteorological Phenomenon

The atmosphere always contains some concentration of sub-micron hygroscopic particles, with higher quantities in polluted areas (smoke, dust) or sea coasts (salt). These particles serve as condensation nuclei and support the condensation of water vapor when the air temperature approaches dew point. This may happen in two ways: either as the air cools or as the humidity rises. The most stable fogs are those which are caused by an inversion of temperature between the air and the ground. Such conditions usually lead to the formation of radiation or advection fog.

- Radiation fog (sometimes called ground fog) is the most common type of fog. It usually happens in late fall or early winter, when the land cools by thermal radiation after sunset, in calm conditions with clear sky.
- Advection fog happens when moist air moves over a cooler surface. It often happens when a cold marine layer is pushed or drawn to the coastline.

There are other types of fog, more localized or less stable, such as valley fog (which is essentially a confined radiation fog), evaporation or steam fog (caused by cold air standing

over warm water or moist land), upslope fog (caused by moist air cooling as it is pushed upslope by the wind) or ice fog (which only occurs at extremely low temperatures). Fog is usually classified after the mechanism which lead to its formation, but it should be noted that several mechanisms may actually work simultaneously in the process.

Fog often dissipates naturally at sunrise, as the ground warms up, or when turbulences lift it and break it up into clouds. It may also be caused to break up artificially. Spreading salt or ice crystals, depending on the temperature, causes fog droplets to transform into raindrops or snowflakes, and forces their precipitation. Only large airports can afford this technique, because it is not cost-effective: it only works in certain conditions, and there is no guaranty that fog will not reappear later on.

2.2 Fog Microstructure

Dispersed media may contain various sorts of solid or liquid particles, characterized by their numbers, their sizes, their shapes, and in some complex cases by their orientations, their chemical compositions and their structures [23]. Fog contains both water droplets formed around condensation nuclei and non-active sub-micron particles, but the latter have relatively little effect on light propagation. Therefore, fog is ordinarily assumed to contain spherical water droplets in different numbers and sizes [24, 36, 37].

2.2.1 Particle Size Distribution

Fog microstructure is characterized by a particle size distribution $n(r) = dN(r)/dr$, where $N(r)$ is the number of water droplets with a radius between r and $r + dr$ per unit volume.

The droplet size distribution of fog has been observed to be unimodal [22]. It is generally characterized by the mode radius r_m , but other granulometric descriptors such as the mean radius \bar{r} , the effective radius r_e and the standard deviation σ are often used. Disperse media with different particle size distributions but identical effective radii and standard deviations are considered optically equivalent [23].

$$\bar{r} = \int_0^\infty r n(r) dr \quad (1a)$$

$$r_e = \frac{\int_0^\infty r^3 n(r) dr}{\int_0^\infty r^2 n(r) dr} \quad (1b)$$

$$\sigma = \sqrt{\int_0^\infty (r - \bar{r})^2 n(r) dr} \quad (1c)$$

2.2.2 Fog Granulometry

Theoretically, fog is in the same category of aerosols as clouds, with particle sizes between 2 and $50 \mu\text{m}$ [22]. In reality, different types of fog have different particle size distributions which evolve during their life-cycle [12]. According to Shettle and Fenn [36], who refer to

several granulometric measurement campaigns, developing fogs contain 100 and 200 particles per cm^3 in the 1 to $10 \mu\text{m}$ radius range with mean radius of 2 to $4 \mu\text{m}$, but as fog thickens droplet concentration may fall under 2 particles per cm^3 while the mean radius increases from 6 to $12 \mu\text{m}$. More recent measurements reported by Guédalia and Bergot [14] seem to agree with these observations.

2.2.3 Granulometric Models

Measurements in natural fog are extremely difficult, mainly because it is almost impossible to ensure repeatable thermodynamic and photometric conditions. Artificial fog is an interesting alternative, but many studies simply use simulation, often validating their results by measurements in a mock-up scattering medium such as diluted milk in a transparent tank. Among the various laws which serve to model the particle size distribution of a natural dispersed medium [22], the modified Γ -distribution proposed by Deirmendjian [6] is the most popular to study fog [23, 24, 37]:

$$n(r) = A r^\alpha e^{-b r^\gamma} \quad (2)$$

where $n(r)$ is the number of droplets per unit volume, r is the droplet radius and A , α , b and γ are the parameters which allow to fit the model to observations. Shettle and Fenn proposed a four-class fog typology based on this model [36]; the parameter sets to be used with (2) are presented in Tab. 1, and the particle size distributions are plotted in Fig. 1. Models 1 and 2 are characteristic of respectively heavy and moderate advection fogs, while models 3 and 4 are characteristic of respectively heavy and moderate radiation fogs, but Shettle and Fenn note that scaling the total particle number N is a relevant way to model other fog concentrations.

Fog	Model	A	α	b	γ	$r_m (\mu\text{m})$	$N(\text{cm}^{-3})$
Advection	1	0.027	3	0.3	1	10.0	20
	2	0.066	3	0.375	1	8.0	20
Radiation	3	2.373	6	1.5	1	4.0	100
	4	607.5	6	3.0	1	2.0	200

Table 1: Size distribution parameters of the fog granulometric models reported by Shettle and Fenn [36]: r_m is the mode radius, N is the total particle number, A , α , b and γ are the parameters of the modified Γ -law (2).

3 Light Scattering in Fog

3.1 Single scattering

What we perceive as light is actually a combination of monochromatic electromagnetic radiations with wavelengths between 380 and 780 nm, the visible spectrum of the human

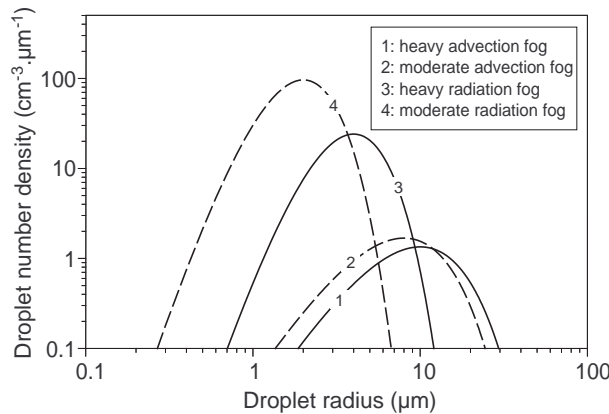


Figure 1: Fog droplet size distribution models reported by Shettle and Fenn [36].

visual system. When passing through fog, these electromagnetic waves interact with air-borne droplets, losing energy at every interaction. This extinction effect results from two phenomena:

- absorption, which transforms part of the luminous energy into thermal energy;
- scattering, which spreads the luminous energy from the incident direction into other directions.

3.1.1 Influent Parameters: Size and Wavelength

The relative importance of absorption in the extinction phenomenon depends on the chemical nature of the particle through the complex refractive index $m(\lambda)$ of the material it is made of, an index which depends on the wavelength λ . In the case of fog, formed exclusively of water droplets, it is roughly constant and equal to 1.33 for all wavelengths in the visible spectrum.

The spatial distribution of the energy scattered by a droplet depends on its radius, as well as on the wavelength. The ratio of the droplet radius to the wavelength determines the type of scattering which occurs:

- Rayleigh scattering is prominently caused by air molecules. It happens when the wavelength is much higher than the droplet radius ($r < \lambda/10$). The scattered luminous energy is then proportional to the fourth power of the wavelength. It causes the blue color of clear skies, but it is negligible in fog [22].
- Mie scattering concerns bigger particles such as water droplets. The spatial distribution of scattered energy then strongly depends on the refractive index $m(\lambda)$ and on its so called size parameter x :

$$x = 2\pi r/\lambda \quad (3)$$

3.1.2 Mie Scattering Theory

The importance of the extinction phenomenon is proportional to the section of space in which the wave interacts with the particle. This section, $C_{\text{ext}}(r)$, is called the extinction cross section. It is related to the particle cross section πr^2 by means of the factor $Q_{\text{ext}}(r)$, called the extinction efficiency:

$$C_{\text{ext}}(r) = Q_{\text{ext}}(r) \pi r^2 \quad (4)$$

The scattering efficiency $Q_{\text{sca}}(r)$ has an equivalent definition, allowing the characterization of scattering separately from absorption:

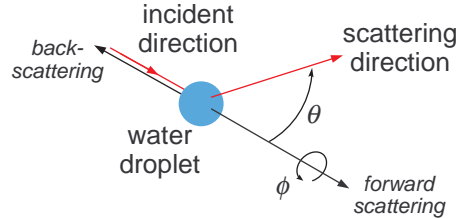


Figure 2: Light scattered by a water droplet.

The radiation scattered by the particle is characterized by its intensity, i.e. the energy flux per unit solid angle in the propagation direction. The scattered intensity thus depends on the scattering direction, defined by the angles θ and ϕ relative to the incident direction of the wave, as illustrated in Fig. 2.

The spatial distribution of scattered intensity is defined by the scattering diagram, more often called the phase function, $P(\theta, \phi)$. As fog droplets are spherical, their phase function is independent of angle ϕ , and only varies as a function of angle θ , or its cosine:

$$\mu = \cos \theta \quad (5)$$

Starting from Maxwell equations for electromagnetic waves, Lorenz expressed the efficiency factors for extinction, $Q_{\text{ext}}(r)$, and for scattering, $Q_{\text{sca}}(r)$, of a transparent sphere with a radius r , and the intensity scattered by this particle when it interacts with a planar monochromatic wave with a wavelength λ . His solution was later and independently

generalized by Mie and by Debye. Here are the resulting equations [38]:

$$Q_{\text{ext}}(r) = \frac{2}{x^2} \sum_{n=1}^{\infty} (2n+1) \Re(a_n + b_n) \quad (6a)$$

$$Q_{\text{sca}}(r) = \frac{2}{x^2} \sum_{n=1}^{\infty} (2n+1) (|a_n|^2 + |b_n|^2) \quad (6b)$$

$$S_1(\mu) = \sum_{n=1}^{\infty} \frac{2n+1}{n(n+1)} [a_n \pi_n(\mu) + b_n \tau_n(\mu)] \quad (6c)$$

$$S_2(\mu) = \sum_{n=1}^{\infty} \frac{2n+1}{n(n+1)} [a_n \tau_n(\mu) + b_n \pi_n(\mu)] \quad (6d)$$

S_1 and S_2 are the complex scattering amplitudes in both orthogonal incident polarization directions. The scattered intensity is proportional to the phase function:

$$P(r, \mu) = \frac{\lambda^2}{8\pi^2} (|S_1(\mu)|^2 + |S_2(\mu)|^2) \quad (7)$$

Mie complex coefficients a_n and b_n depend on the size parameter and the refractive index. They are expressed in terms of primary and secondary Riccati-Bessel functions and their derivatives. Function τ_n and π_n are expressed in terms of Legendre polynomials and their derivatives. The approximate number of terms of these series which need to be computed in order to obtain accurate results is of the same order as the size parameter x of the considered particle [40]. The full details of these calculations are reported in [39].

3.2 Multiple Scattering

3.2.1 Monodispersed Medium

Extinction is proportional to the concentration of particles on the path of the radiation. The consequent attenuation of luminous energy per unit distance is characterized by the extinction coefficient $K_{\text{ext}}(r)$. For a monodispersed medium formed of N particles of radius r per unit volume, $K_{\text{ext}}(r)$ is related to the extinction efficiency as follows:

$$K_{\text{ext}}(r) = NC_{\text{ext}}(r) = \pi N Q_{\text{ext}}(r) r^2 \quad (8)$$

The scattering coefficient $K_{\text{sca}}(r)$ is similarly related to the scattering efficiency.

3.2.2 Polydispersed Medium

A polydispersed medium can be characterized as an “equivalent” monodispersed medium, formed of one-sized particles which confer the same extinction and scattering properties to the equivalent medium as those of the actual medium. The equivalent extinction and

scattering coefficients can be computed by convoluting the size-dependent extinction and scattering cross sections with the particle size distribution $n(r)$:

$$K_{\text{ext}} = \pi N \int_0^{\infty} Q_{\text{ext}}(r) n(r) r^2 dr \quad (9a)$$

$$K_{\text{sca}} = \pi N \int_0^{\infty} Q_{\text{sca}}(r) n(r) r^2 dr \quad (9b)$$

The equivalent phase function can be calculated in the same way:

$$P(\mu) = \pi N \int_0^{\infty} Q_{\text{ext}}(r) P(r, \mu) n(r) r^2 dr \quad (10)$$

3.3 Fog Optical Properties

3.3.1 Extinction Coefficient

Thus, a monochromatic luminous wave undergoes extinction and scattering along its path in a dispersed medium, because of the particles which absorb and scatter its energy. The transmissivity T , i.e. the proportion of luminous energy transmitted along a path of length d , is given by Beer-Lambert law:

$$T = e^{-K_{\text{ext}} d} \quad (11)$$

where K_{ext} is the extinction coefficient of the medium, expressed in m^{-1} .

The relative part played by scattering in this extinction phenomenon is characterized by the albedo a :

$$a = \frac{K_{\text{sca}}}{K_{\text{ext}}} \quad (12)$$

In the case of fog, in which the particles are water droplets, absorption of visible light is negligible. It follows that extinction is entirely caused by scattering. With an albedo equal to one, the extinction coefficient suffices to characterize the energy loss of light transmitted through fog. It is simply noted K :

$$K = K_{\text{ext}} \simeq K_{\text{sca}} \quad (13)$$

The extinction phenomenon along a path of length d may also be described by means of the optical depth τ :

$$\tau = Kd \quad (14)$$

3.3.2 Phase Function

In the visible light spectrum and in the size range of fog droplets, Mie scattering does not vary much with the wavelength. Therefore, fog optical properties can be calculated for a wavelength of 550 nm, where the human visual system is most sensitive in photopic conditions, and reasonably generalized to other visible wavelengths.

Because of the complexity of Mie equations, the phase function is often approximated by means of analytic expressions [13]. Nishita separated “hazy” and “murky” media, and proposed the following analytic expressions for their phase functions [2]:

$$P_{\text{hazy}}(\mu) = \frac{1}{2} + \frac{9}{2} \left(\frac{1+\mu}{2} \right)^8 \quad (15a)$$

$$P_{\text{murky}}(\mu) = \frac{1}{2} + \frac{33}{2} \left(\frac{1+\mu}{2} \right)^{32} \quad (15b)$$

Despite the fact that it was originally destined to the characterization of interstellar dust [21], the analytic phase function proposed by Henyey and Greenstein is very often used for scattering in the atmosphere:

$$P_{\text{HG}}(\mu, g) = \frac{1 - g^2}{(1 + g^2 - 2g\mu)^{3/2}} \quad (16)$$

The parameter $g \in]-1, 1[$ of this function is called the asymmetry factor:

$$g = \frac{1}{2} \int_{-1}^1 P(\mu) \mu d\mu \quad (17)$$

Its variations describe different scattering behaviors: when g is close to 1, scattering in the forward direction predominates; when g is close to -1 , it is back-scattering (scattering in the backward direction) which predominates; and when g is close to 0, scattering is almost isotropic. A simpler analytic form of Henyey-Greenstein phase function was proposed by Schlick [2]:

$$P_S(\mu, k) = \frac{1 - k^2}{(1 - k\mu)^2} \quad (18)$$

where k is equivalent to the asymmetry factor g in (17). Schlick also showed that it was possible to produce phase functions resembling those of (15) or (16) by means of a linear combination of two of his phase functions:

$$P_{2S}(\mu, \alpha, k, k') = \alpha P_S(\mu, k) + (1 - \alpha) P_S(\mu, k') \quad (19)$$

where $(\alpha, k, k') \in [0, 1] \times]-1, 1[^2$

Cornette and Shanks [5] proposed an analytic phase function which is similar to that of Henyey-Greenstein, only more physically-based and without the need for the extra weighting parameter of (19):

$$P_{CS}(\mu, g) = \frac{3}{2} \frac{1 - g^2}{2 + g^2} \frac{1 + \mu^2}{(1 + g^2 - 2g\mu)^{3/2}} \quad (20)$$

Fig. 3 illustrates the limits of analytic models. Even with equal asymmetry factor, none of the listed expressions suitably accounts for the shape of the phase function computed

for a given particle size distribution with Mie equations (6-7). The models tend to underestimate back-scattering, and to over-estimate scattering at intermediate angles, around 90° . The most important discrepancy lies in the forward-scattering “peak” caused by diffraction. Therefore, the Mie phase function should be preferred to analytic models when the granulometric data is available.

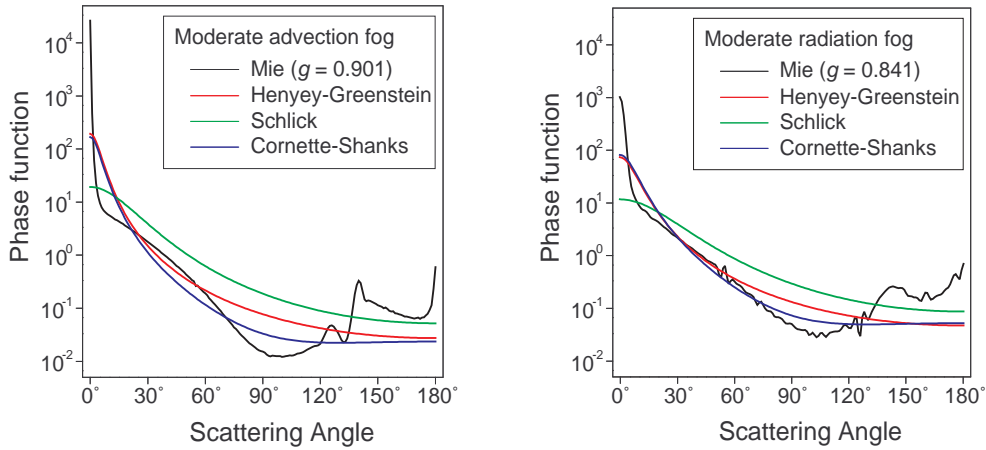


Figure 3: Comparison between Mie phase functions (computed from the fog granulometric models in Tab. 1) and different analytic models.

3.4 Visibility in Fog

Visibility is a complex notion, usually referring to the greatest distance at which an object can be detected or recognized. It depends on the geometric and photometric characteristics of the observed object and its background. In the presence of fog, visibility is affected on both geometric and photometric aspects because of the distance-dependent extinction effect.

Fog opacity is ordinarily characterized by means of the meteorological visibility V_{met} , defined as the visibility distance of a black object of “suitable” dimensions by day against the horizon sky [4]. However, meteorological visibility is a perceptual notion which cannot be easily measured. Fog opacity is more easily characterized by means of the meteorological optical range, defined as the length of the path in the atmosphere which is required to attenuate by 95% the luminous flux from a collimated light source [4]. This attenuation value was chosen because 5% is considered as the minimum visual contrast required to recognize an object against its background, in order to set an equivalence between the

meteorological optical range and the meteorological visibility.

$$\begin{aligned} T &= e^{-KV_{\text{met}}} = 0.05 \\ V_{\text{met}} &\simeq \frac{3}{K} \end{aligned} \quad (21)$$

Hence, meteorological visibility is in fact a more intuitive expression of the extinction coefficient K . Therefore, it is only an indication of fog opacity, and it should never be confused with the actual visual range of anything except a black object on the horizon sky in daytime.

4 Modeling Fog Effects on Vision

4.1 Fog Effects on the Visual Signal

4.1.1 Composition of the Visual Signal

As shown in Fig. 4, the image of the visual environment is formed by the luminance distribution which is projected into the eyes of an observer (or the aperture of a camera) by the elements of the observed scene. The luminance comes from the luminous energy emitted by the sky on the one hand, and by artificial light sources on the other hand. In normal visibility conditions, a small part of this energy reaches the observer directly, and the rest illuminates the surfaces throughout the scene. These surfaces then become secondary light sources, and a small part of the luminous energy is reflected toward the observer. Hence, the visual signal is composed of primary and secondary zones, depending whether light followed a single path or multiple paths to reach the observer.

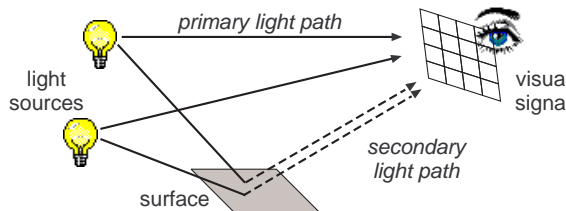


Figure 4: The visual signal is formed of the luminance which is either emitted by light sources (primary zones) or reflected by surfaces (secondary zones). Scattering by fog droplets occurs along light paths between the light sources, the surfaces and the observer.

4.1.2 Effects of Light Scattering

As seen in the previous section, light interacts with the airborne particles along its path. In fog, which is formed of water droplets with diameters ranging from several tenths to a few tens of microns, visible wavelengths are scattered without absorption. According to Mie

theory, the directional distribution of scattered energy depends on the size of the droplets: the bigger droplets of advection or heavy radiation fog yield stronger forward scattering.

The main effect of fog on the visual signal is the attenuation of luminance caused by transmission through scattering droplets. This extinction effect is described by Beer-Lambert law (11), which results in an exponential attenuation of luminance with distance. It should be noted that extinction not only occurs between the elements in the scene and the observer, but also between the light sources and the surfaces.

$$L(d) = e^{-Kd} L(0) \quad (22)$$

Since water droplets do not absorb visible light, scattered energy does not simply disappear: it is re-distributed throughout the scene. Part of it reaches the observer, causing further alterations to the visual signal. Scattered light thus produces two major visual effects, illustrated in Fig. 5.

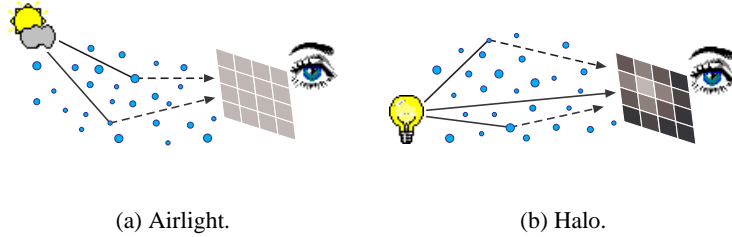


Figure 5: Airlight and halos are the two major alterations caused by scattered light in the visual environment of an observer in fog.

The first effect is caused by fog droplets scattering daylight toward the observer. According to Koschmieder theory of horizontal visibility, later generalized to slant visibility by Duntley (as reported in details by Middleton [28]), the resulting atmospheric veil L_v which is superimposed on the image of an object at a distance d is related to the luminance L_f of the fog at the horizon:

$$L_v = (1 - e^{-Kd}) L_f \quad (23)$$

This effect is often referred to as airlight, and sometimes as path luminance. Koschmieder model provides a very simple and elegant expression for the luminance $L(d)$ of a non-luminous object at a distance d in daytime fog:

$$L(d) = e^{-Kd} L(0) + (1 - e^{-Kd}) L_f \quad (24)$$

The luminance at close range $L(0)$ is generally called the intrinsic luminance.

The second effect is caused by fog droplets scattering the light they receive from artificial light sources toward the observer. According to the atmospheric modulation transfer

function (MTF) theory [26], the resulting halo (or glow) effect is equivalent to the convolution of the image of the light source with the point spread function (PSF) of the fog. The PSF is the inverse Fourier transform of the MTF, which is distance-dependent. But using the analogy between a slab of fog and an optical filter, the MTF $M(K, d)$ of a homogeneous slab of fog of width d and extinction coefficient K can be derived from the MTF M of a slab of unit optical depth, called the frequency contrast operator (FCO) [9]:

$$M(K, d) = M^{Kd} \quad (25)$$

It should be noted that the FCO not only depends on the particle size distribution, as shown in Fig. 6, but also varies with the divergence of the considered light beam, because the halo comes essentially from light emitted outside of the observer's direction. Narrow beams (like those used in transmissometers) produce a negligible halo, especially in small droplet fogs.

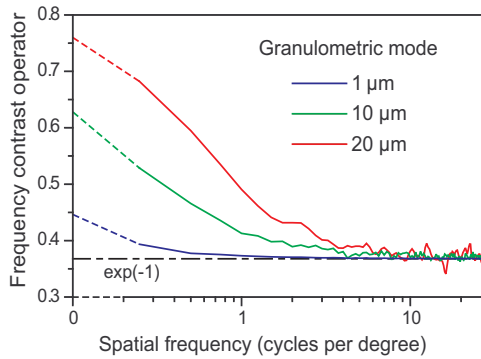


Figure 6: MTF of three types of fog with different droplet size distributions, computed by Monte-Carlo light tracing [9].

4.2 Modeling Fog Visual Effects

4.2.1 Combining Extinction, Halos and Airlight

Based on the previous analysis of the mechanisms underlying visibility impairment, a unified model for the effects of fog on the visual signal can be proposed. The altered visual signal is computed in three steps: attenuation of secondary zones, convolution of primary zones and addition of airlight.

In the first step, the intrinsic luminance of visible surfaces must be decomposed in two parts: L_0 coming from daylight, and $L_{s \in [1, n]}$ issued by n artificial light sources present in the scene. The transmitted luminance of the secondary zones, L_{sec} , is computed by applying Beer-Lambert attenuation factor, first to the paths of lengths d_s from every light sources to

the surface, and then to the path of length d from the surface to the observer:

$$L_{\text{sec}} = e^{-Kd} \left(L_0 + \sum_{s=1}^n e^{-Kd_s} L_s \right) \quad (26)$$

In the second step, the intrinsic luminance L_s of each luminous object is “spread” onto the neighboring zones of the visual signal using the range dependent PSF of fog as a convolution kernel. The PSF is obtained by taking the inverse Fourier transform of the MTF of the slab of length d separating the object from the observer. The MTF is derived from the specified FCO M using (25). Thus, the transmitted luminance L_{pri} of primary zones can be expressed as follows:

$$L_{\text{pri}} = L_s * \mathcal{F}^{-1} \left\{ M^{Kd} \right\} \quad (27)$$

In the final step, the path luminance, expressed in (23), is added to the result of the two previous steps, and yields the apparent luminance L perceived by the observer:

$$L = L_{\{\text{pri}|\text{sec}\}} + \left(1 - e^{-Kd} \right) L_f \quad (28)$$

where $L_{\{\text{pri}|\text{sec}\}}$ is either L_{pri} for primary zones or L_{sec} for secondary zones in the visual signal, and L_f is the fog luminance.

4.2.2 Pros and Cons

Equations (26-28) constitute a unified photometric model of fog visual effects. It is in fact a generalization of Koschmieder law which accounts for artificial lighting, extending the field of applications to luminous objects and night-time or twilight situations.

However, very detailed photometric and geometric information is needed for its implementation. Moreover, the model retains some of the hypotheses and approximations of the theories on which it is based: in Koschmieder theory, fog is assumed to be homogeneous; in the atmospheric MTF theory, light sources are assumed to emit isotropically toward the observer.

Also, the model does not deal with hidden light sources, though their halo may actually be visible. Finally, the scattered energy from the light sources is not taken into account in the intrinsic luminance of the surfaces. But getting past these limitations would require global illumination calculations, which are far less versatile than the presented image processing approach. And the model can be customized to overcome particular problems. For instance, when the observer is driving in fog, light from the headlamps of his motor-vehicle is scattered back into his field of vision as illustrated in Fig. 7: as the resulting back-scattered veil is independent of the scene, it can be pre-computed and then simply added to the foggy image of the scene [10, 11].

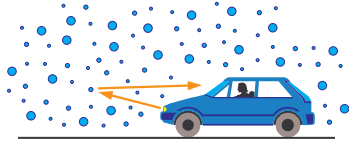


Figure 7: When driving in fog, light from the headlamps is back-scattered toward the driver, producing an additional veil in the driver's field of vision.

4.3 Implementation

4.3.1 Input

In order to use the proposed model to compute the bi-dimensional luminance distribution $L(i, j)$ seen by an observer looking at a scene in foggy weather conditions, detailed geometric and photometric information is needed. For each direction (i, j) in the visual field (which corresponds to a pixel in the image of the scene), the distance $d(i, j)$ of the pointed element in the scene, as well as its intrinsic luminance $L_0(i, j)$ as produced by ambient lighting, must be known. Furthermore, the distance $d_s(i, j)$ between the pointed element and each artificial light source s in the scene must be known, as well as the luminance $L_s(i, j)$ produced on the element by this light source. Hence, if n light sources are present in the scene, $n + 1$ luminance and range distributions are needed as input to the simulation, as described in Fig. 8.

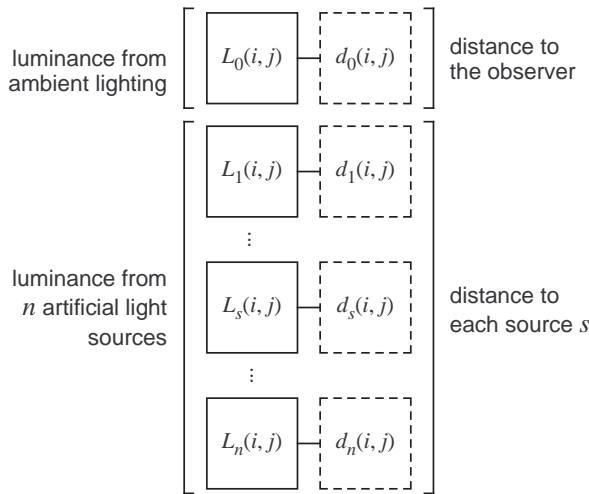


Figure 8: Detailed geometric and photometric description of the visual environment of an observer is needed to implement the photometric model of fog visual effects.

The extinction coefficient K and the FCO M of the fog must also be specified in order

to apply the proposed model, as well as the fog luminance L_f . The extinction coefficient is directly related to the meteorological visibility using (21). The FCO may be approximated from a model MTF [1] or from a model PSF [27]. As for fog luminance, Paulmier showed that it varies greatly with the altitude of the sun (and thus the hour of the day), the height of the fog layer and the type of fog, as well as the direction of observation with respect to the position of the sun [33].

4.3.2 Semi-analytic Model

With the visual signal represented by the bidirectional luminance distribution $L(i, j)$ in the observer's field of vision, the model can be summarized in one equation, here including the back-scattered veil $L_b(i, j)$ mentioned earlier:

$$L(i, j) = \begin{cases} e^{-Kd(i,j)} (L_0(i, j) + \sum_{s=1}^n e^{-Kd_s(i,j)} L_s(i, j)) \\ L_s(i, j) * \mathcal{F}^{-1} \{ M^{Kd(i,j)} \} \\ + (1 - e^{-Kd(i,j)}) L_f + L_b(i, j) \end{cases} \quad (29)$$

4.3.3 Sample Results

To demonstrate the implemented model, it was applied to compute photometric images of a simple rural road scene in night-time and daytime foggy weather conditions. The 2D1/2 description of the driver's visual environment is presented in Fig. 9.

Radiation and advection types of fog were simulated. The computed luminance values were mapped to gray levels in order to produce the images presented in Fig. 10 for the night-time situation, and in Fig. 11 for the daytime situation.

It can be noted from the results that the relative importance of fog visual effects strongly depends on the lighting conditions (night or day) and on the microphysical nature of the fog (droplet size). The extinction effect yields the most important perturbations in the image of the scene. In night-time, particularly, every details vanish except the front- and rear-lamps of other vehicles, whereas they quickly fade into the distance in daytime because of the atmospheric veil. The halo effect around the light sources is much "smoother" with radiation fog, more like a veiling effect than with advection fog. As a consequence, the importance of the halos is greatly reduced by daytime airlight: they even seem negligible in radiation fog.

Although the images in Figs. 10&11 are only a tone-mapped representation of what the observer actually perceives, this example illustrates the complexity of fog effects on vision.

5 Application to the Validation of a Fog Observation Test Bench

5.1 Objectives

To improve road safety or the comfort of future vehicles, methods are being developed to detect the presence of fog and estimate the meteorological visibility distance through use

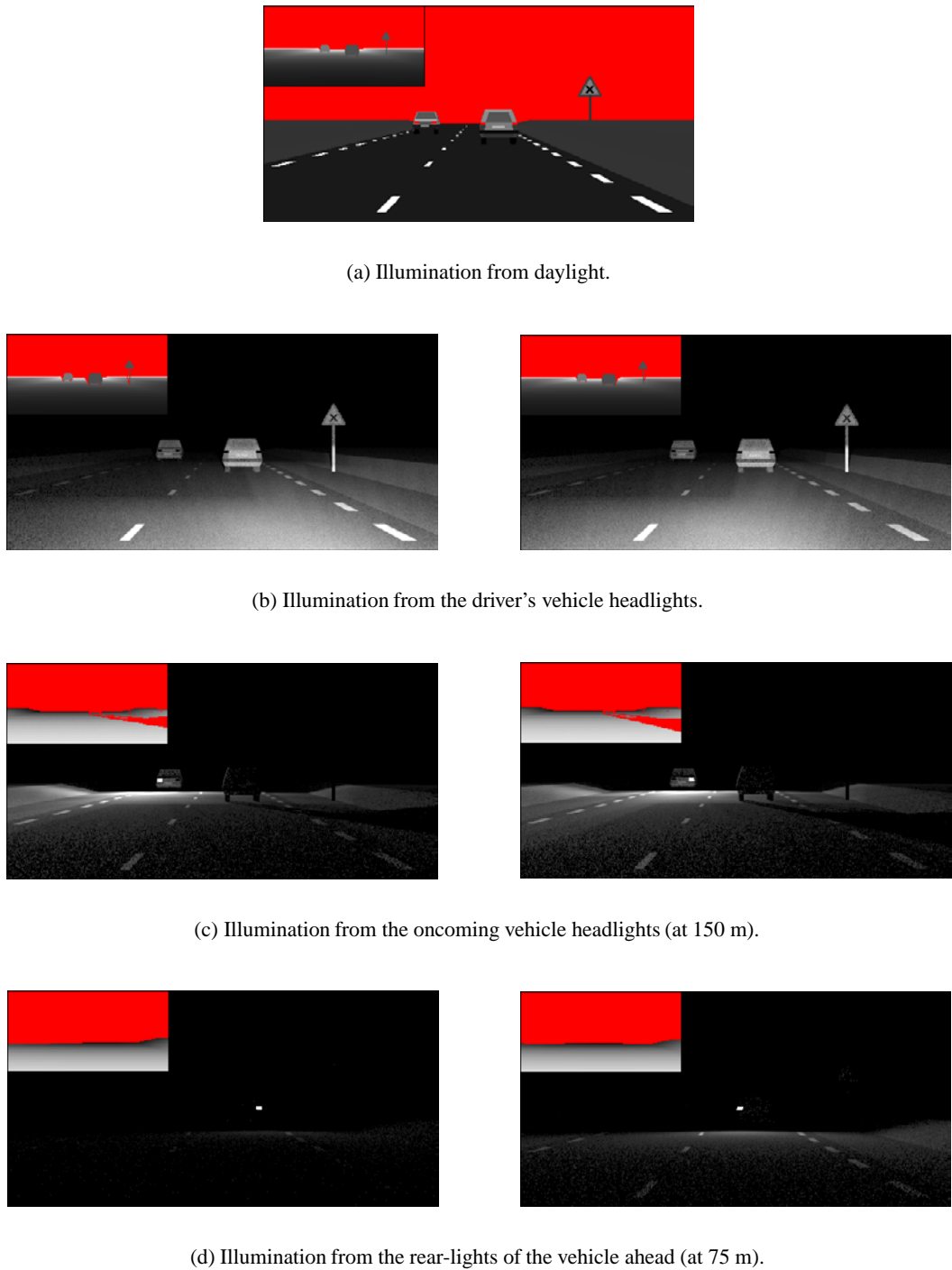
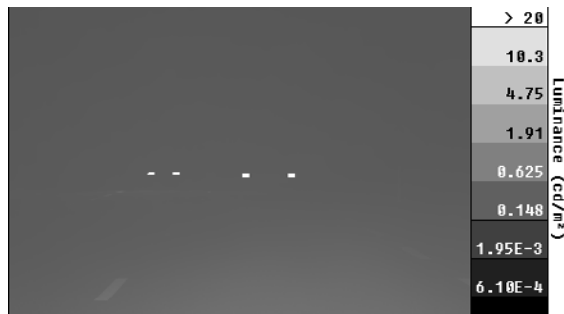


Figure 9: Luminance and depth maps characterizing a rural road scene as described in Fig. 8, computed by Monte-Carlo light tracing [8]. Zones with indefinite depth from the observer (sky) or a light source (shadows) are shown in red.



(a) Without fog.



(b) Radiation fog.



(c) Advection fog.

Figure 10: Computed luminance maps in the field of vision of a driver in a foggy rural scene during night-time (the meteorological visibility is 100 m).

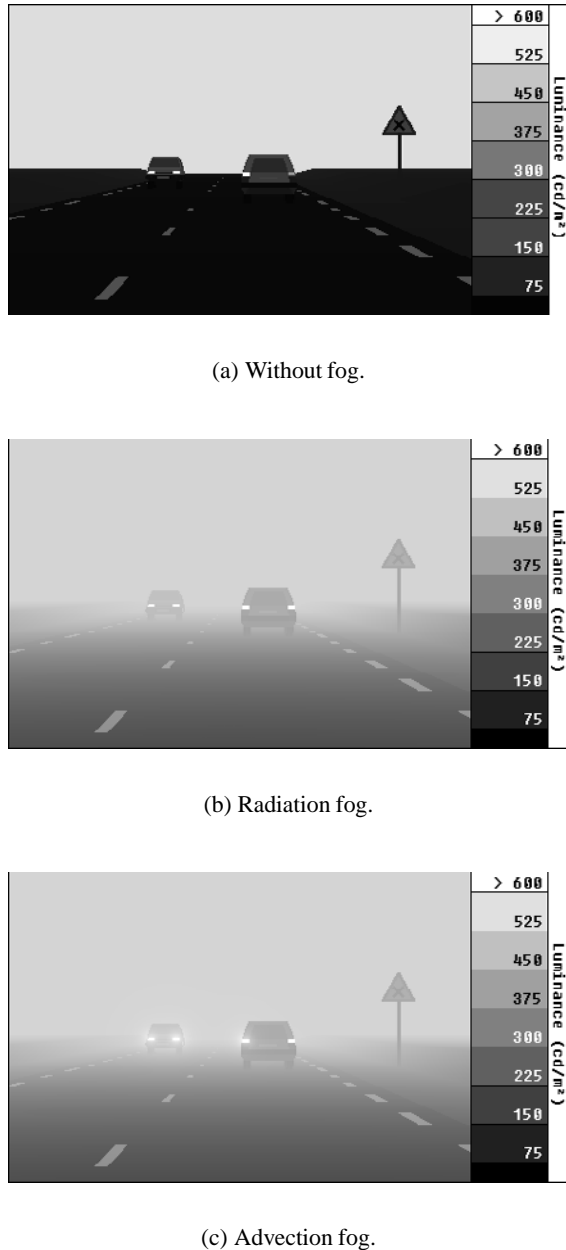


Figure 11: Computed luminance maps in the field of vision of a driver in a foggy rural scene during daytime (the meteorological visibility is 100 m, and the fog luminance is 500 cd.m^{-2}).

of either in-vehicle [3, 19, 20] or roadside cameras [16, 17]. A major issue of this research is the quantitative evaluation of the methods [15]. To perform this task, the classical approach is to test the methods against a reference database [32]. The problem is to build the ground truth on the images in the database, usually by means of reference sensors. This involves some sort of visibilitymeter. Unfortunately, transmissometers are very expensive and scatterometers have some drawbacks, which make them unsuited to our needs [18].

To overcome this problem, we have thus proposed to build a fog observation test bench. This test bench is composed of a road track equipped with photometric targets which constitute a reference for assessing the meteorological visibility distance. They are passive targets for daytime and artificial light sources for nighttime, as already proposed in [25]. The fog model presented in the previous section is used to simulate the visual appearance of the test bench in foggy weather. We can then propose and test meteorological visibility distance estimation methods relying on the reference objects. It allows to predict the theoretical maximum accuracy of these methods, and to check if they are relevant to validate other methods which do not rely on any reference targets.

5.2 The Test Bench

For the daytime situation, our goal is to assess the contrast reduction in the reference targets, in order to estimate the value of the meteorological visibility distance. We equipped our test track in Versailles (France) with five large specific targets (cf. Fig. 12), located between 65 m and 200 m from the cameras onboard a vehicle stationed at a reference position (cf. Tab. 2a). For a maximum intrinsic contrast, we have designed black and white targets. To avoid aliasing effects, we have designed the targets so that they have the same apparent size in the images. An additional mobile target is used at a closer range when the fog is very dense.

For the nighttime situation, our goal is to assess the luminance reduction of artificial light sources. These light sources are set on top of the previous targets. Another mobile light source is set on the left side of the test track (see Fig. 12b). We use signal lights which ordinary serve in work zone areas. A typical configuration of the light sources in night tests is given in Tab. 2b.

Finally, based on the measurements given in Tab. 2, a virtual mockup of the test bench has been built. Fig. 13 shows this mockup in clear weather in full daylight. We have all the necessary geometric and photometric information concerning this mockup to simulate foggy weather on the test bench with the model presented previously.

5.3 Daytime Situation

In this section, we first propose a process to measure the meteorological visibility distance using the black and white passive targets. Secondly, we check if this process is relevant by applying it on simulated images of the observation test bench in daytime fog.

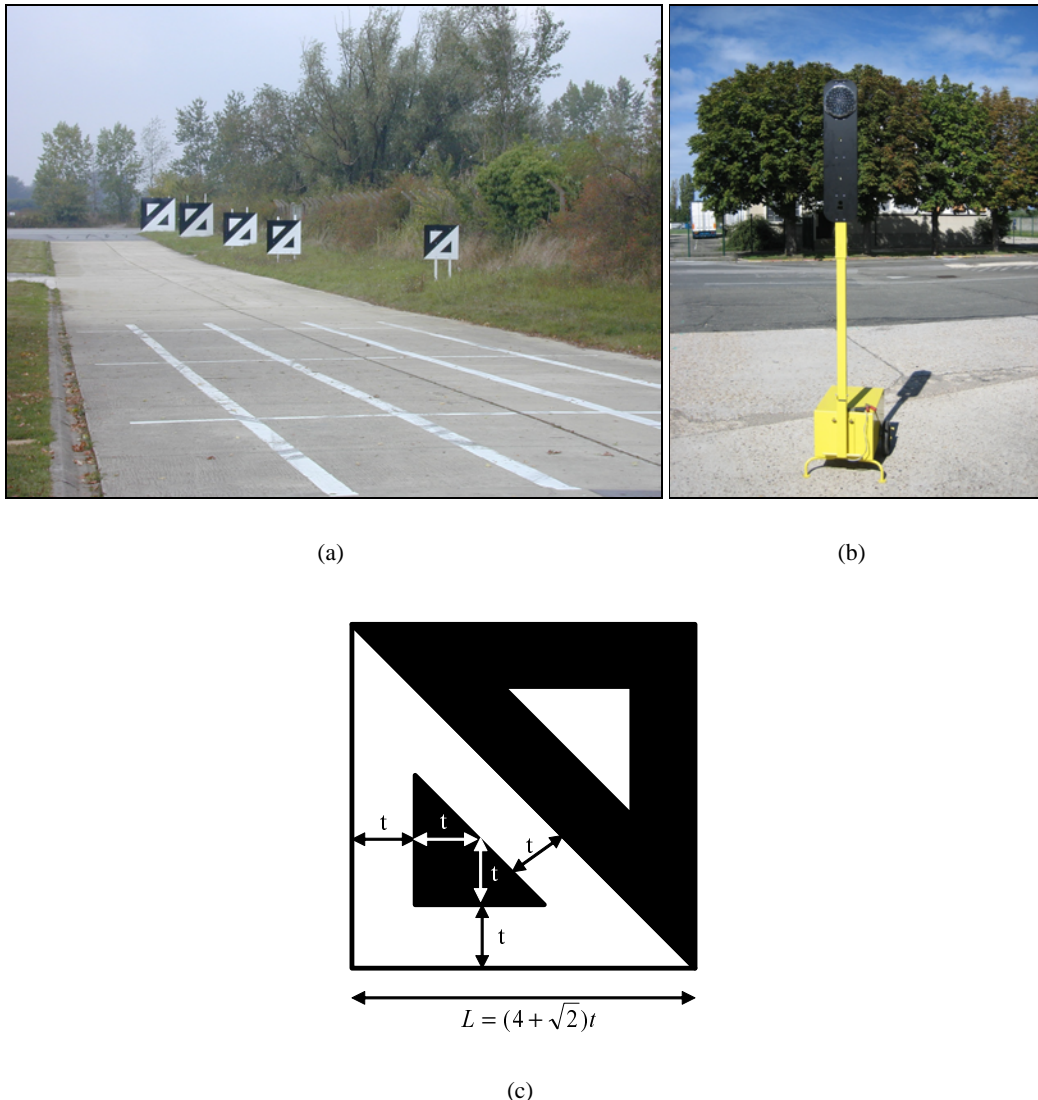


Figure 12: (a) Actual picture of the fog observation test bench dedicated to visibility measurement, taken in sunny weather conditions; (b) the mobile light source used in nighttime tests; (c) graphic design of the reference targets.

Target index	1	2	3	4	5	6
Distance [m]	0-35	65.2	97.6	130.7	162.4	195
L [m]	0.5	1	1.5	2	2.5	3
t [m]	0.1	0.19	0.28	0.37	0.47	0.56

Target index	1'	2'	3'
Distance [m]	35	35-200	200

Table 2: (a) Index, distance and dimensions L, t (see Fig. 12c) of the different reference targets on the test bench for the daytime use. (b) Index and distance of the different light sources on the test bench for the nighttime use.

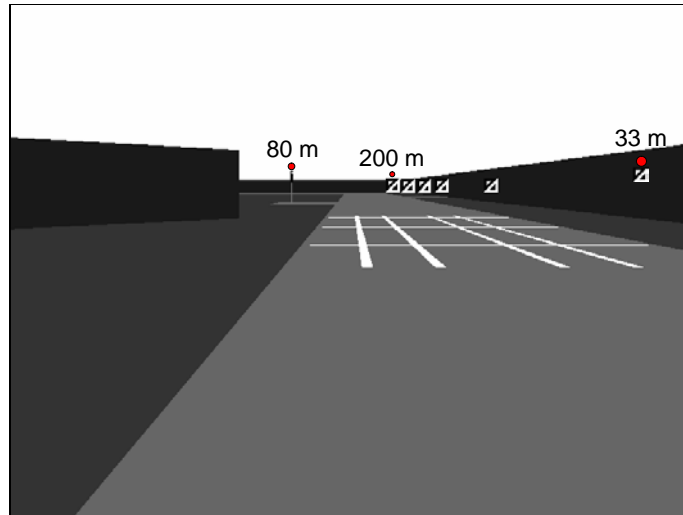


Figure 13: Image of the virtual mockup of the fog observation test bench. The signal lights are marked in red, and their relative positions are specified.

5.3.1 Measurement Process

In daytime, with the sky as only light source, the model (29) simply comes down to Koschmieder law (24). Based on this equation, we can build two methods to estimate the meteorological visibility distance. The first method only uses the black part of the targets. The second one uses the black part as well as the white part of the targets.

- Using the black part of the targets

We consider the black part of two black targets located at distances d_1 and d_2 from the camera. We assume that they have a negligible intrinsic luminance ($L_b(0) = 0$). According to (24), their apparent luminances are:

$$\begin{cases} L_b(d_1) &= (1 - e^{-Kd_1})L_f \\ L_b(d_2) &= (1 - e^{-Kd_2})L_f \end{cases} \quad (30)$$

Taking the ratio $r_b = \frac{L_b(d_1)}{L_b(d_2)}$ of these values, we obtain the following equation, which we need to solve for K :

$$r_b = \frac{1 - e^{-Kd_2}}{1 - e^{-Kd_1}} \quad (31)$$

(31) admits analytical solutions for certain values of the ratio $\frac{d_2}{d_1}$. We deduce the value of the extinction coefficient K in different ways:

$$K = \begin{cases} -\frac{1}{d_1} \log(r_b - 1) & \text{if } d_2 = 2d_1 \\ -\frac{1}{d_1} \log\left(\frac{\sqrt{4r_b-3}-1}{2}\right) & \text{if } d_2 = 3d_1 \\ -\frac{1}{d_1} \log\left(\frac{(r_b-1)(\sqrt{r_b+3}-\sqrt{r_b-1})^2}{4}\right) & \text{if } d_2 = \frac{3}{2}d_1 \end{cases} \quad (32)$$

- Using both black and white parts of the targets

An alternative technique consists in using the white and the black parts of the targets, whose apparent luminances $L_w(d)$ and $L_b(d)$ are given by (24):

$$\begin{cases} L_w(d_1) - L_b(d_1) &= e^{-Kd_1}L_w(0) \\ L_w(d_2) - L_b(d_2) &= e^{-Kd_2}L_w(0) \end{cases} \quad (33)$$

Again taking the ratio r_{bw} of these values, we have:

$$r_{bw} = e^{-K(d_1-d_2)} \quad (34)$$

We deduce the value of extinction coefficient K :

$$K = \frac{1}{d_2 - d_1} \log(r_{bw}) \quad (35)$$

- Averaging the measurements

(32) and (35) each gives a single estimate of the meteorological visibility distance. By fusing the different estimates, we can have a more accurate overall estimate. In this aim, we must take into account the relative accuracy of each estimate. An estimation $\mathcal{V}(K)$ of the variance of K is thus associated with each formula (32) or (35). $\mathcal{V}(K)$ is expressed by:

$$\mathcal{V}(K) \approx \mathcal{V}_I \sum \left(\frac{\partial K}{\partial L_{b,w}(d_{1,2})} \right)^2 \quad (36)$$

where \mathcal{V}_I is the variance on the pixel value due to the digitalization of the pictures, assuming a Gaussian centered distribution with a standard deviation of $\frac{1}{2}$. From (21), we deduce the variance of V_{met} :

$$\mathcal{V}(V_{met}) \approx \left(\frac{V_{met}}{K} \right)^2 \mathcal{V}(K) \quad (37)$$

Assuming that the measurements are not correlated, these estimates are optimally averaged using the variances:

$$\widehat{V}_{met} = \frac{\sum_i \frac{V_{met_i}}{\mathcal{V}(V_{met_i})}}{\sum_i \frac{1}{\mathcal{V}(V_{met_i})}} \quad (38)$$

We deduce the variance of this estimator:

$$\mathcal{V}(\widehat{V}_{met}) = \left(\sum_i \frac{1}{\mathcal{V}(V_{met_i})} \right)^{-1} \quad (39)$$

5.3.2 Process Validation on Photometric Simulations

To check the measurement process presented in the previous paragraph, we must ensure that the equations are relevant for estimating the meteorological visibility distance. In this aim, using the model of fog effects on vision given in section 4.3.2, we simulated pictures of the virtual mockup of our test bench in daytime fog, for different values of V_{met} : 33 m, 66 m, 100 m, 133 m, 166 m and 200 m. These pictures are shown in Fig. 14.

Tab. 3a gives the values of \widehat{V}_{met} obtained thanks to averages of estimates (32). Tab. 3b gives the values of \widehat{V}_{met} obtained thanks to averages of (35). First, some results at the bottom of the tables are bad. The reason for that is the round-off caused by the digital nature of the simulated images. Thereafter, the logarithmic formula is more sensitive to the small intensity differences on the distant targets, than with the large intensity differences of closer targets. The estimated visibility distance is thus necessarily worst using the most distant targets. All these considerations are confirmed by the standard deviation values, which are given between brackets in Tab. 3. Second, the standard deviations in Tab. 3a are smaller than in Tab. 3b. Unfortunately, the method seems to be biased, because the estimated visibility distance is biased and always smaller than the ground truth. This may

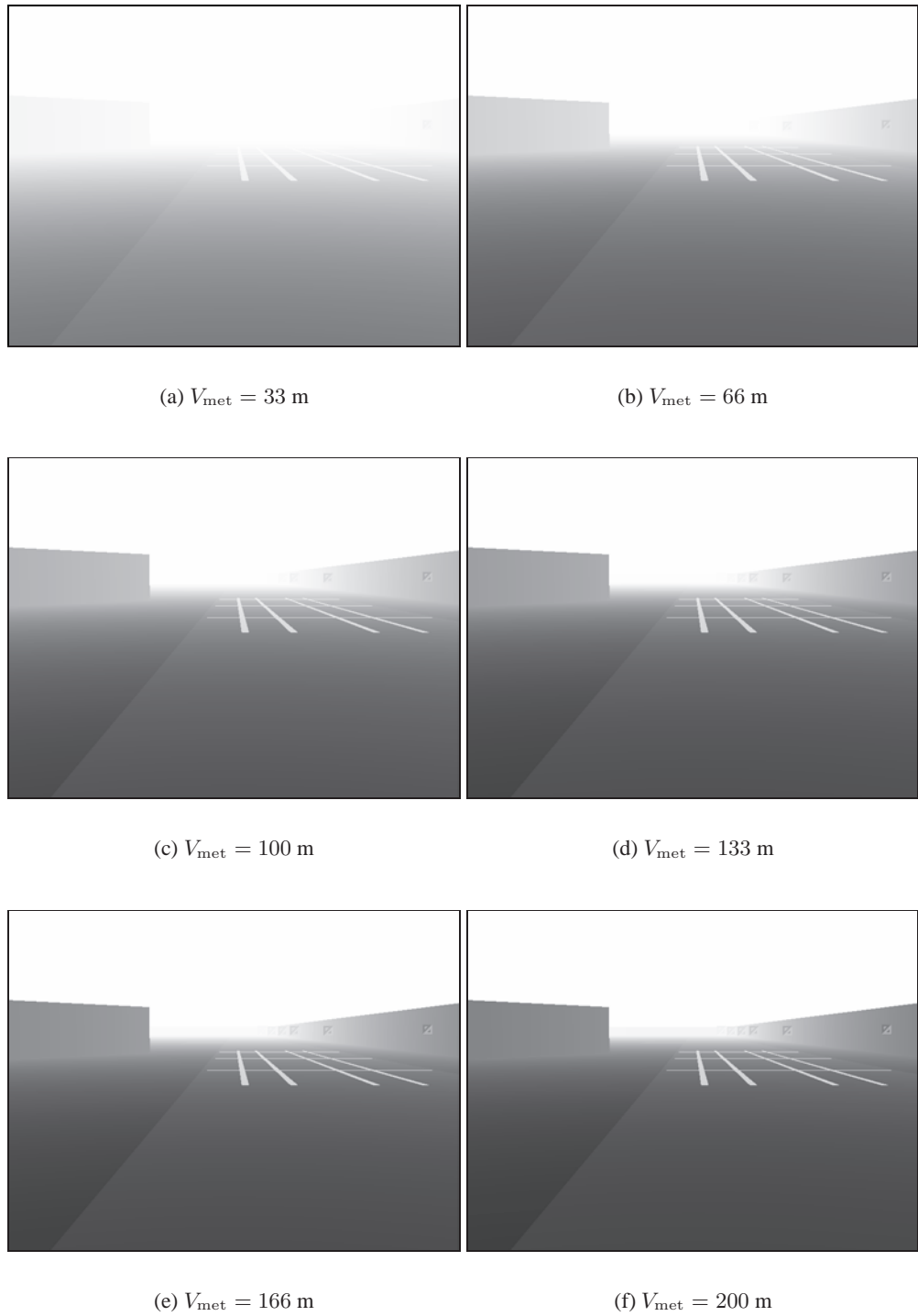


Figure 14: Photometric simulations of the test bench in daytime fog for different meteorological visibility distances.

$\hat{V}_{\text{met}}(\sigma) [\text{m}]$		(a)				
		200	166	133	100	66
couple of targets	1 → 2	172 (2.2)	144 (1.7)	119 (1.4)	92 (1.4)	61 (1)
	1 → 3	183 (1.7)	151 (1.4)	124 (1.4)	-	-
	2 → 3	199 (2.2)	161 (2)	132 (1.7)	100 (1.4)	-
	2 → 4	197 (1.7)	162 (1.4)	132 (1.4)	-	-
	2 → 6	198 (1.4)	-	-	-	-
	3 → 6	197 (1.7)	-	-	-	-
	4 → 6	199 (2)	-	-	-	-
	V_{met}	194 (1)	155 (1)	126 (1)	95 (1)	61 (1)

$\hat{V}_{\text{met}}(\sigma) [\text{m}]$		(b)				
		200	166	133	100	66
couple of targets	1 → 2	203 (3.7)	170 (3.5)	138 (3.2)	103 (3)	74 (3.3)
	1 → 3	198 (3.2)	173 (3.2)	135 (3.2)	103 (3.3)	-
	1 → 4	201 (3.3)	162 (3.3)	138 (3.6)	-	-
	1 → 5	189 (3.6)	172 (3.9)	-	-	-
	1 → 6	203 (4.1)	-	-	-	-
	2 → 3	194 (4.6)	176 (4.8)	133 (4.5)	103 (4.8)	-
	2 → 4	200 (4)	158 (4)	138 (4.5)	-	-
	2 → 5	184 (4.1)	172 (4.5)	-	-	-
	2 → 6	203 (4.6)	-	-	-	-
	3 → 4	206 (6.2)	143 (5.4)	142 (6.8)	-	-
	3 → 5	180 (5)	170 (5.6)	-	-	-
	3 → 6	207 (5.5)	-	-	-	-
	4 → 5	160 (6.5)	210 (10.2)	-	-	-
	4 → 6	207 (6.8)	-	-	-	-
	5 → 6	294 (14.6)	-	-	-	-
	V_{met}	197 (2)	168 (2.2)	137 (2.4)	103 (2.6)	74 (3.3)

Table 3: Estimated meteorological visibility distance and standard deviation (between brackets) on simulated pictures using the reference targets and (a) average estimates (32) or (b) average estimates (35).

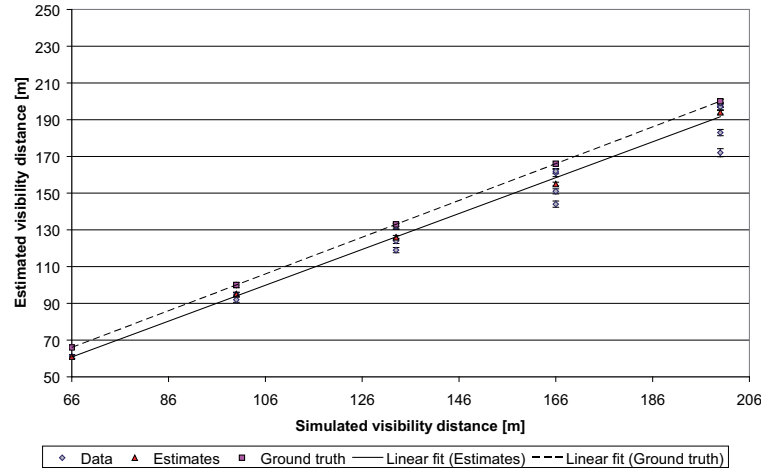
be due to the fact that the targets are not really black, as is assumed for establishing (32). In our simulations, we implemented a reflectance factor of 1% in order to stick to reality.

To confirm these statements, we plotted in Fig. 15 the estimated meteorological visibility distances with respect to the simulated meteorological visibility distances as well as the averaged estimates (32) and (35). In addition, linear regression lines are plotted using a black line for the averaged estimates and a dashed line for the ground truth. By looking at Fig. 15a, we have the confirmation that the method relying on the averaged estimates (32) is biased. However, the bias seems to be constant, which is a somehow interesting. By looking at Fig. 15b, it seems that the method relying on the averaged estimates (35) is relevant to estimate the meteorological visibility distance. Indeed, the regression line of the averaged estimates seems to merge with that of the ground truth for the highest meteorological visibility distances, where there are enough points to compute reliable averaged estimates.

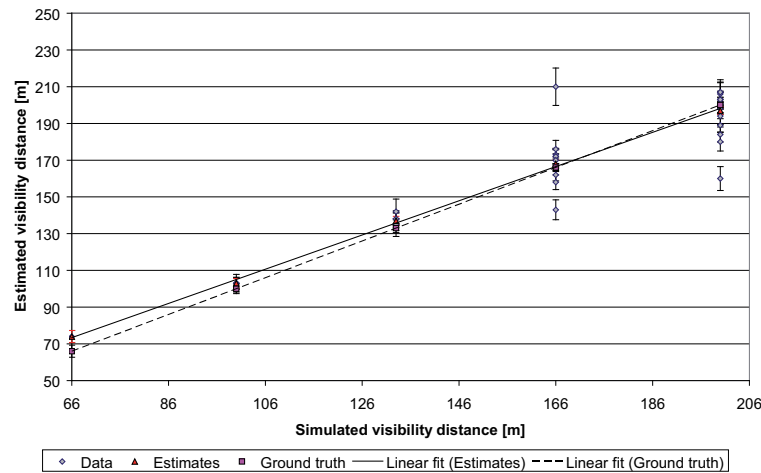
Consequently, based on Tabs. 3a&b and Figs. 15a&b, it seems reasonable to only rely on the averages of (35) to compute the reference measurement \hat{V}_{met} . This reference measurement can then be used to assess the performances of methods which detect and estimate the fog density in daytime without any reference.

5.4 Nighttime Situation

In this section, we first propose a process to measure the meteorological visibility distance using artificial light sources. Second, we check if this process is relevant by applying it on



(a)



(b)

Figure 15: Plots of estimated vs. simulated meteorological visibility distances in daytime fog using the reference targets and (a) average estimates (32) or (b) average estimates (35). Linear regression lines are plotted using a black line for the averaged estimates and a dashed line for the ground truth.

simulated images of the observation test bench in nighttime fog.

5.4.1 Measurement Process

In nighttime, the light sources are the single visible objects in the test bench. Based on (29), the luminance of these light sources is given by:

$$L_s(d) = L_s(0) * \mathcal{F}^{-1} \left\{ M^{Kd} \right\} \quad (40)$$

This equation models both the luminance attenuation effect and the halo effect of night fog. We can split the model in two parts, where each part is related to each visual effect:

$$L_s(d) = L_s(0) * \mathcal{F}^{-1} \left\{ M^{Kd} - e^{-Kd} \right\} + L_s(0) * \mathcal{F}^{-1} \left\{ e^{-Kd} \right\} \quad (41a)$$

$$= L_s(0)e^{-Kd} + L_s(0) * \mathcal{F}^{-1} \left\{ M^{Kd} - e^{-Kd} \right\} \quad (41b)$$

The first term of (41b) is related to the luminance attenuation effect, whereas the second term models the halo visual effect. Let us consider two targets located at two distinct distances d_1 and d_2 . We can again take the ratio r_s of their luminances:

$$r_s = \frac{L_{s1}(d_1)}{L_{s2}(d_2)} = \frac{L_{s1}(0)e^{-Kd_1} + L_{s1}(0) * \mathcal{F}^{-1} \left\{ M^{Kd_1} - e^{-Kd_1} \right\}}{L_{s2}(0)e^{-Kd_2} + L_{s2}(0) * \mathcal{F}^{-1} \left\{ M^{Kd_2} - e^{-Kd_2} \right\}} \quad (42)$$

In [30], the authors neglect the contribution of the halos to r_s . Based on this assumption, they compute the relative depth of light sources. This measurement process is rather simple since measuring the maximum luminance of the light sources is enough to compute fog density. We propose to use this assumption and thus (42) becomes:

$$r_s = \frac{L_{s1}(0)}{L_{s2}(0)} e^{-K(d_2 - d_1)} \quad (43)$$

Assuming that the light sources are identical, their intrinsic luminances are equal. We obtain finally:

$$K = \frac{1}{d_2 - d_1} \log(r_s) \quad (44)$$

Since we have more than two light sources in the test bench, we can, like in section 5.3, fuse the different estimates obtained using (44). An estimation $\mathcal{V}(K)$ of the variance of K is thus associated with (44). $\mathcal{V}(K)$ is expressed by:

$$\mathcal{V}(K) \approx \mathcal{V}_I \sum \left(\frac{\partial K}{\partial L_{s1,2}(d_{1,2})} \right)^2 \quad (45)$$

where \mathcal{V}_I is the variance on the pixel value due to the digitalization of the pictures, assuming a gaussian centered distribution with a standard deviation of $\frac{1}{2}$. From (21), we deduce the variance of V_{met} :

$$\mathcal{V}(V_{\text{met}}) \approx \left(\frac{V_{\text{met}}}{K} \right)^2 \mathcal{V}(K) \quad (46)$$

Assuming again that the measurements are not correlated, these estimates are optimally averaged using the variances:

$$\widehat{V}_{\text{met}} = \frac{\sum_i \frac{V_{\text{met}_i}}{\mathcal{V}(V_{\text{met}_i})}}{\sum_i \frac{1}{\mathcal{V}(V_{\text{met}_i})}} \quad (47)$$

The variance of this estimator is again:

$$\mathcal{V}(\widehat{V}_{\text{met}}) = \left(\sum_i \frac{1}{\mathcal{V}(V_{\text{met}_i})} \right)^{-1} \quad (48)$$

5.4.2 Process Validation on Photometric Simulations

In the previous section, we assume that the halos can be neglected to compute the meteorological visibility distance. In this section, we propose to check if this assumption is valid. Based on the model of fog effects on vision given in section 4.3.2, we have performed photometrical simulations of the test bench in nighttime. We simulated different meteorological visibility distances (33 m, 66 m, 100 m, 133 m, 166 m and 200 m) and droplet size distributions using moderate advection and radiation fogs from Tab. 1. Some samples of simulated pictures are shown in Fig. 16. One can see that the visual appearance of the light sources differ even if the meteorological visibility distance is the same, as it was already mentioned in section 4.3.3. The halos seem to be more intense for advection fog than for radiation fog. One can see also that the most distant light source (index 3') is no longer visible for very low meteorological visibility distances. The intermediate source (index 2') is also barely visible.

Tab. 4a gives the values of \widehat{V}_{met} obtained thanks to averages of estimates (44) in advection fog (denoted G2). Tab. 4b gives the values of \widehat{V}_{met} obtained thanks to averages of estimates (44) in radiation fog (denoted G4).

First, we can see that the variances of the averaged estimates are bigger than those obtained in daytime. This can be related to the fact that fog effects are more complex in nighttime than in daytime. Indeed, the model used in nighttime is semi-analytic whereas in daytime it is completely analytic. The non-analytic part of the model is noise sensitive, which partly explains the higher variances of the measurements.

Second, we can see that the averaged estimates are far from the ground truth in advection fog (see Tab. 4a), whereas they are quite close to the ground truth in radiation fog (see Tab. 4b). This can be directly related to the droplet size distributions. For the moment, we can state that the halo effect cannot be neglected to estimate the meteorological visibility distance. (44) is thus questionable.

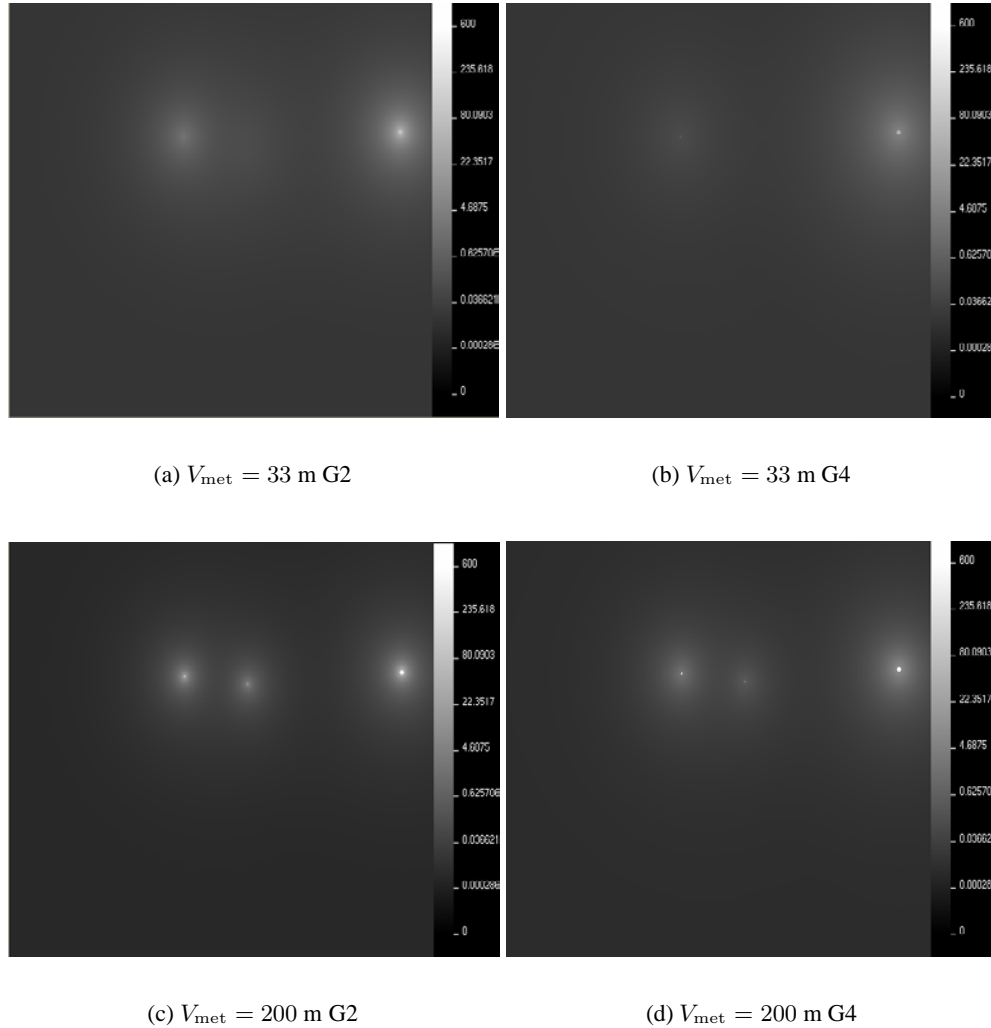
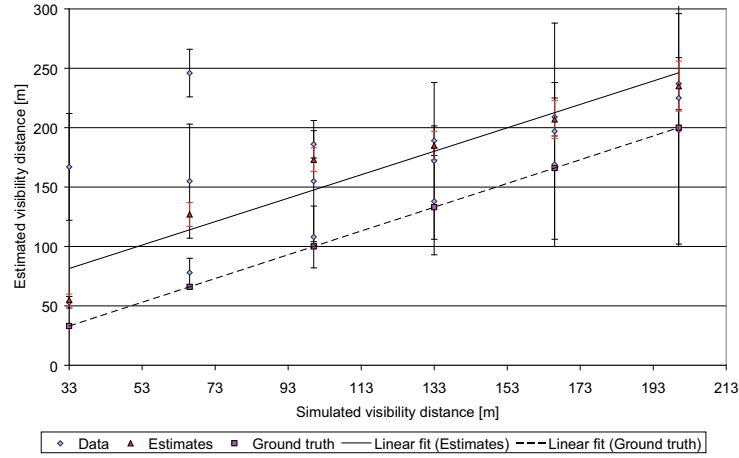
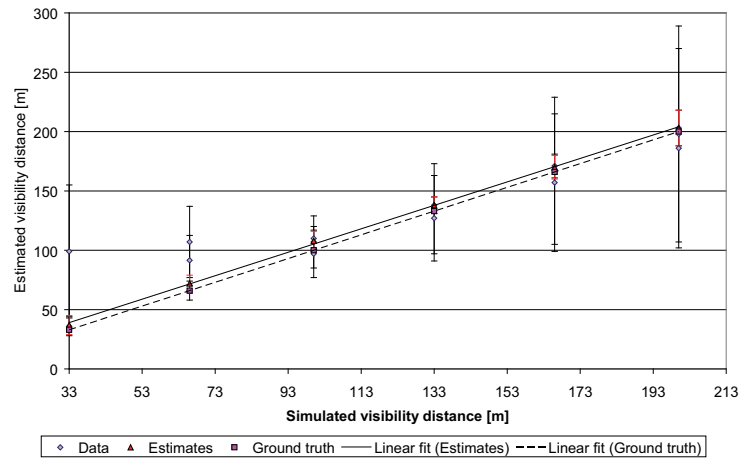


Figure 16: Samples of the photometric simulations of the test bench in nighttime fog for different meteorological visibility distances and different droplet size distributions (G2 moderate advection fog; G4 moderate radiation fog).



(a)



(b)

Figure 17: Plots of estimated vs. simulated meteorological visibility distances in nighttime (a) advection and (b) radiation fog using the artificial light sources and average estimates (44). Linear regression lines are plotted using a black line for the averaged estimates and a dashed line for the ground truth.

$\hat{V}_{\text{met}}(\sigma) [\text{m}]$		(a)					
		200	166	133	100	66	33
couple of targets	$1' \rightarrow 2'$	198 (98)	169 (69)	138 (45)	108 (26)	78 (12)	53 (4.8)
	$1' \rightarrow 3'$	225 (123)	197 (91)	172 (66)	155 (51)	155 (48)	167 (45)
	$2' \rightarrow 3'$	237 (22)	209 (16)	189 (12.5)	186 (11.5)	246 (20)	846 (389)
V_{met}		235 (21)	207 (16)	185 (12)	173 (10)	127 (10)	55 (5)

$\hat{V}_{\text{met}}(\sigma) [\text{m}]$		(b)					
		200	166	133	100	66	33
couple of targets	$1' \rightarrow 2'$	186 (84)	157 (58)	127 (36)	97 (20)	66 (8)	36 (8)
	$1' \rightarrow 3'$	198 (91)	167 (62)	135 (38)	107 (22)	91.5 (21)	99 (56)
	$2' \rightarrow 3'$	203 (15)	171 (10)	138 (7)	110 (10)	107 (30)	294 (699)
V_{met}		203 (15)	170 (10)	138 (7)	108 (8)	72 (7)	37 (8)

Table 4: Estimated meteorological visibility distance and standard deviations (between brackets) on simulated pictures using the artificial light sources and (44) in (a) moderate advection fog and (b) moderate radiation fog.

To go further in the details, we plotted in Fig. 17 the estimated meteorological visibility distances with respect to the simulated meteorological visibility distances as well as the averaged estimates (44). In addition, linear regression lines are plotted using a black line for the averaged estimates and a dashed line for the ground truth. These plots are given for advection fog in Fig. 17a, as well as for radiation fog in Fig. 17b. By looking at these plots, we have the confirmation that the proposed measurement process is biased, since it overestimates the meteorological visibility distance. However, the bias seems to be constant thanks to the proposed averaging process, which is rather interesting. Indeed, it provides a practical solution to correct the bias. In this aim, with approximate knowledge of the granulometry of the fog, i.e. the type of fog, we can correct the bias to get a better estimate \hat{V}_{met} of the meteorological visibility distance. We can also ignore this bias if radiation fog is encountered.

In the future, it would be relevant to not only use the luminance attenuation of the light sources, but also to use the shape of the halos to estimate the granulometry of the fog and thus correct the bias. [27, 31] are good examples of such a process, but for the fact that they both rely on the Henyey-Greenstein phase function (16), which we saw was not the best model for fog.

5.5 Partial Assessment

In this section, we have shown an application of the proposed model of fog effects on vision to the validation of a fog observation test bench. First, we have described the test bench, in particular the photometric references which are used. Second, we have tackled the daytime fog situation. It has been shown that using both black and white parts of the passive targets leads to a good estimation of the meteorological visibility distance. Third, we have tackled the nighttime fog situation. It has been shown that the contribution of halos to the visual appearance of light sources cannot be neglected to estimate the meteorological visibility distance. Indeed, it leads to underestimate the fog density. However, in the specific case of radiation fog, which is the most typical type of fog, the proposed measurement process

provides quite good results.

6 Conclusion

After examining the microphysical and optical characteristics of fog, and the resulting effects on the visual environment perceived by an observer or recorded by a camera, one thing at least appears obvious: there is more to fog than just the meteorological visibility distance. Indeed, we found that there are different kinds of fog, radiation and advection fogs being the most common, which appear and dissipate in different places and at different times. And we saw that these fogs are formed of water droplets which come in different sizes, between several tenths of a micron for radiation fog to several microns for advection fog. Then we showed that each droplet scatters visible light in an angular distribution which depends on its size, bigger droplets favoring the forward scattering. And when light travels through fog, scattered by multiple droplets along the way, it is exponentially attenuated with distance (Beer-Lambert law). This phenomenon is characterized by the extinction coefficient, which describes fog density. The meteorological visibility distance was conventionally defined as a more intuitive way to express the extinction coefficient. But extinction does not entirely describe the visual effects of fog. Some of the light scattered along light paths reaches the field of vision, adding two kinds of veils. The most obvious is the airlight, caused by the scattering of daylight: it adds a distance dependent veiling luminance to the visual signal (Koschmieder law). But artificial light sources also contribute some scattered light to the visual signal, only in a more localized way, under the form of halos which strongly depend on the type of fog because of the influence of droplet size on light scattering.

When investigating visual perception in fog, or when designing solutions to detect, measure or remove fog in digital images, one should not forget that extinction, airlight and halos happen simultaneously, with different relative effects. This is what led us to propose a unified model of fog effects on vision, applicable for both dark and luminous objects, under both daytime and night-time, as well as in twilight. It is a semi-analytic model because of the halo effect, modeled as a distance dependent PSF. Its implementation requires detailed geometric and photometric knowledge on the scene. But despite its limitations, it offers a convenient and versatile tool to predict fog effects, or to extract information about the scene or the fog by image processing.

To demonstrate the benefit of using the model, we show how it helped us validate a fog observation test bench for camera-based fog monitoring applications. The test bench consists of black and white targets for daytime fog and light sources for nighttime fog. Several targets are installed at different distances from a reference observation point along a test track. A virtual mockup of this test bench was built, and the model of fog effects on vision was applied to compute digital images of the scene in different daytime and nighttime visibility conditions (with radiation and advection fog, and meteorological visibility distances between 30 m and 200 m). Different methods were tested to estimate the meteorological visibility distance from the reference objects in the images, and the estimated values were compared to the simulated values. It allowed us to prove that evaluating fog density directly

in the images, using the reference objects, was a valid alternative to the deployment of an expensive visibilitymeter. It also allowed to reveal that neglecting the halo effect may lead to an underestimation of the meteorological visibility distance in advection fog.

References

- [1] L.R. Bissonnette. Imaging through the atmosphere: Practical instrumentation-based theory and verification of aerosol modulation transfer function: Comment. *Journal of the Optical Society of America A*, 11(3):1175–1179, March 1993.
- [2] P. Blasi, B. Le Saëc, and C. Schlick. A rendering algorithm for discrete volume density objects. In *Rendering Techniques '93*, pages 201–210, Vienna, 1993. Springer-Verlag.
- [3] C. Boussard, N. Hautière, and B. d'Andréa Novel. Vehicle dynamics estimation for camera-based visibility range estimation. In *Proceedings of the IEEE/RSJ International Conference on Intelligent RObots and Systems, Nice France*, September 2008.
- [4] CIE. *International Lighting Vocabulary*. Number 17.4. 1987.
- [5] W. M Cornette and J. G. Shanks. Physically reasonable analytic expression for the single-scattering phase function. *Applied Optics*, 31(16):3152–3160, 1992.
- [6] D. Deirmendjian. *Electromagnetic Scattering on Spherical Polydispersions*. American Elsevier, New York, 1969.
- [7] A. S. Drofa and I. L. Katsev. Certain problems of seeing through clouds and fogs. *Meteorologiya i Gidrologiya*, 11:101–109, 1981.
- [8] E. Dumont. Semi-monte-carlo light tracing for the study of road visibility in fog. In *Monte Carlo and Quasi-Monte Carlo Methods 1998*, pages 177–187, Berlin, 1999. Springer-Verlag.
- [9] E. Dumont. *Caractérisation, modélisation et simulation des effets visuels du brouillard pour l'usager de la route*. PhD thesis, Université Paris V, Novembre 2002.
- [10] E. Dumont and V. Cavallo. Extended photometric model of fog effects on road vision. *Transportation Research Record*, (1862):77–81, 2004.
- [11] E. Dumont, G. Paulmier, P. Lecocq, and A. Kemeny. Assessment of the simulation of low-beams backscattering in fog. In *Proceedings of the 6th International Symposium on Automotive Lighting (Darmstadt, Germany, September 27-28, 2005)*, pages 880–889, 2005.
- [12] T. Elias, M. Haeffelin, P. Drobinski, J.-C. Dupont, C. Fesquet, H. Holin, E. Dupont, L. Musson-Genon, T. Bergot, and L. Gomes. The fog life cycle described by the parisfog field experiment. *Geophysical Research Abstracts*, 10, 2008.

- [13] Andrew S. Glassner. *Principles of Digital Image Synthesis*. Morgan Kaufmann Pub., San Francisco, CA, 1995.
- [14] D. Guédalia and T. Bergot. Premiers résultats de la campagne «lille 88» d'étude du brouillard. *La Météorologie*, 42:11–20, 1992.
- [15] N. Hautière, D. Aubert, E. Dumont, and J.-P. Tarel. Experimental validation of dedicated methods to in-vehicle estimation of the atmospheric visibility distance. *IEEE Transactions on Instrumentation and Measurement*, 27(10), October 2008.
- [16] N. Hautière, E. Bigorgne, and D. Aubert. Daytime visibility range monitoring through use of a roadside camera. In *Proceedings of the IEEE Intelligent Vehicles Symposium, Eindhoven, The Netherlands*, June 2008.
- [17] N. Hautière, E. Bigorgne, J. Bossu, and D. Aubert. Meteorological conditions processing for vision-based traffic monitoring. In *IEEE International Workshop on Visual Surveillance, Marseille, France*, October 2008.
- [18] N. Hautière, R. Labayrade, and D. Aubert. Estimation of the visibility distance by stereovision: a generic approach. *IEICE Transactions on Information and Systems*, E89-D(7):2084–2091, July 2006.
- [19] N. Hautière, R. Labayrade, and D. Aubert. Real-time disparity contrast combination for onboard estimation of the visibility distance. *IEEE Transactions on Intelligent Transportation Systems*, 7(2):201–212, June 2006.
- [20] N. Hautière, J.-P. Tarel, J. Lavenant, and D. Aubert. Automatic fog detection and estimation of visibility distance through use of an onboard camera. *Machine Vision and Applications Journal*, 17(1):8–20, April 2006.
- [21] L. C. Henyey and J. L. Greenstein. Diffuse radiation in the galaxy. *Astrophysical Journal*, 93:70–83, 1941.
- [22] Rudolf B. Husar. Physics and chemistry of atmospheric aerosols. A course given at the University of Stockholm (Department of Meteorology), fall semester 1976.
- [23] Alex A. Kokhanovsky. *Optics of Light Scattering Media - Problems and Solutions*. John Wiley & Sons, 1999.
- [24] Christos Kontogeorgakis. Millimeter through visible frequency waves through aerosols -particle modeling, reflectivity and attenuation. Master's thesis, Virginia Polytechnic Institute and State University, Blacksburg, VA, 1997.
- [25] T. M. Kwon. Atmospheric visibility measurements using video cameras: Relative visibility. Technical report, University of Minnesota Duluth, July 2004.
- [26] R.F. Lutomirsky. Atmospheric degradation of electrooptical system performance. *Applied Optics*, 17(24):3915–3921, 1978.

- [27] S. Metari and F. Deschênes. A new convolution kernel for atmospheric point spread function applied to computer vision. In *Proceedings of the IEEE International Conference on Computer Vision, Rio de Janeiro, Brazil*, October 2007.
- [28] W.E.K. Middleton. *Vision through the atmosphere*. University of Toronto Press, 1952.
- [29] N. Nameda. Fog modulation transfer function and signal lighting. *Lighting Research & Technology*, 24(2):103–106, 1992.
- [30] S. G. Narasimhan and S. K. Nayar. Vision and the atmosphere. *International Journal of Computer Vision*, 48(3):233–254, July-August 2002.
- [31] S. G. Narasimhan and S. K. Nayar. Shedding light on the weather. In *Proceedings of the IEEE Computer Society Conference on Computer Vision and Pattern Recognition, Madison, Wisconsin, USA*, June 2003.
- [32] S. G. Narasimhan, C. Wang, and S. K. Nayar. All the images of an outdoor scene. In *Proceedings of the European Conference on Computer Vision, Copenhagen, Denmark*, May 2002.
- [33] Giselle Paulmier. Fog luminance evaluation in daytime. *Transportation Research Record*, (1862):82–88, 2004.
- [34] Frederic Pérez, Xavier Pueyo, and François-Xavier Sillion. Global illumination techniques for the simulation of participating media. In *Rendering Techniques '97*, pages 309–320, New-York, June 1997. Springer-Verlag.
- [35] Zi-qin Sang, Ming-yue Ding, and Tian-xu Zhang. Imaging for outdoor scene in rain and fog. *Acta Electronica Sinica*, 28(3):131–133, March 2000.
- [36] Eric P. Shettle and Robert W. Fenn. Models for the aerosols of the lower atmosphere and the effectsof humidity variations on their optical properties. AFGL-TR 79-0214, Air Force Geophysics Laboratory, Hanscom Air Force Base, MA, 1979.
- [37] Robert E. Turner and Peter F. Lambeck. Natural and artificial illumination in optically thick atmospheres. Final report 108300-4-F, Environment Research Institute of Michigan, Ann Arbor, MI, 1975.
- [38] Hendrik C. van de Hulst. *Scattering by Small Particles*. Structure of matter. Dover, New York, 1981.
- [39] Warren J. Wiscombe. Mie scattering calculations: Advances in technique and fast, vector-speed computer codes. NCAR/TN 140+STR, National Center for Atmospheric Research, Boulder, CO, June 1979. Edited/revised August 1996.
- [40] Warren J. Wiscombe. Improved mie scattering algorithms. *Applied Optics*, 19(9):1505–1509, May 1980.

SHORT COMMENTARIES

Short Commentary A

ON PARAMETERIZING INCLINED STABLE BOUNDARY LAYERS

Branko Grisogono

AMGI, Department of Geophysics, Faculty of Science,
University of Zagreb, Croatia

Atmospheric boundary layer (ABL) is the lowest layer of the ocean, called the atmosphere, being continuously governed by frictional and thermal effects due to the presence of the Earth surface. Most of life on the Earth takes place in or around this layer. Its fate is too important and hence, it should be forecasted or at least guessed for close and distant future. Current numerical meteorological models often simulate stable atmospheric boundary layers (SABL) inadequately in terms of the SABL depth, near-surface inversion characteristics, low-level wind and mixing properties (e.g. Mahrt, 1998; King et al., 2001; Söderberg and Parmhed, 2006; Mauritsen et al., 2007; Steeneveld et al., 2007; Gohm et al., 2008). Typical numerical weather prediction (NWP) models produce too much mixing in the SABL by superficially enhancing vertical diffusion which emulates turbulent processes (for e.g. sufficient filling of cyclones). Consequently, other erroneous effects in the simulations are encountered too, like cold bias in the boundary layer against observations, so-called frictional decoupling, etc. (e.g. Gohm et al., 2008; Jerićević and Grisogono, 2006). These are only a few among the reasons for why the stably stratified turbulence processes and the SABL as such are still in the focus of scientific research (e.g. Baklanov and Grisogono, 2007; Mahrt, 2007, 2008; Monti et al., 2002; Weng and Taylor, 2003; Renfrew and Anderson, 2006; Cuxart and Jiménez, 2007; Esau and Byrkjedal, 2007; Mauritsen et al., 2007; Zilitinkevich et al., 2007; Zilitinkevich and Esau, 2007; Grisogono et al., 2007). A recent comprehensive overview, ranging from theory and observations to performances of several NWP models can be found in dissertation of Steeneveld (2007). Almost needless to say, inadequate treatment of SABL affects our simulations of future climate scenarios, allowing for undesired extra uncertainties in our predictions; moreover, the shallow and dry SABL, pertaining to e.g. polar regions, is particularly susceptible to errors in turbulent fluxes. The latter greatly affects precipitation, cloud and radiation estimations, hence adding to future climate uncertainties.

In this short commentary I assess the mixing length-scale for the SABL, i.e. that in the “z-less” regime, as often parameterized in mesoscale models with higher-order closure turbulence parameterization schemes. At some height above the surface in the SABL, turbulent eddies become sufficiently far from the surface so that they do not sense directly their distance from the surface; their overall mixing properties are described conveniently by the z-less mixing length-scale which depends on the local flow properties. This length-scale needs improvements accommodating various subtle and changeable processes that may dominate the mixing; for example to include shear effects explicitly. Such modifications have been only tackled or mentioned by e.g. Hunt et al. (1988), Tjernström (1993), Schumann and Gerz (1995), Grisogono and Enger (2004), etc. These works abided imprecise with regard to the relative weight between buoyancy and shear-dominated frequencies, N and $|S|$ respectively, in dividing the local turbulence characteristic wind speed, $u_{*LOC} \approx (TKE)^{1/2}$, where TKE appears as the turbulent kinetic energy. When this turbulence speed is divided by the frequencies introduced, the z-less mixing length-scale for the SABL is ensued. Numerical modelers need this length-scale for the higher-order closure turbulence parameterization schemes where the appropriate mixing length-scale under stable stratification is chosen each time-step, namely when $0 < Ri < \infty$, $Ri \equiv (N/S)^2$, Ri being the gradient Richardson number. In the models Ri is typically based upon calculations using vertical finite differences; depending on the value of Ri , either N or $|S|$ is chosen for determining the mixing length-scale.

Finding the relative ratio between buoyancy- and shear-dominated mixing length-scales has been recently conducted for slightly sloped SABL by Grisogono and Belušić (2008). They compare a mesoscale numerical model from Uppsala University, so-called MIUU model (e.g. Enger, 1990a, b; Enger and Grisogono, 1998; Abiodun and Enger, 2002; Grisogono and Enger, 2004), with a theory (arguably weakly non-linear, see Stiperski et al., 2007) which applies to finite-amplitude perturbations (e.g. Kavčič and Grisogono, 2007). The importance of this detailed subject is manifold, ranging from improving NWP, moisture exchange estimations over complex terrain (e.g. Weigel et al., 2007) to betterment of air-pollution and wind-energy related calculations (e.g. Bergström and Juuso, 2006; Baklanov and Grisogono, 2007). A next step will be e.g. including entrainment properties in such drainage-type of flows, having distinctly different character than the entrainment in laboratory flows (Princevac et al., 2005). Nowadays we know very little about vertical and horizontal mixing and transport properties of moderately-to-strongly stratified SABL (Mahrt, 1998, 2007, 2008; Princevac et al., 2005; Baklanov and Grisogono, 2007; Weigel et al., 2007, Zilitinkevich et al., 2007). As mentioned above, some minor improvements have been already made toward better parameterizations of the processes poorly treated in the NWP models (e.g. Grisogono et al., 2007, Zilitinkevich et al., 2007).

At the same time, it appears appropriate to re-derive the higher-order-closure for turbulence parameterization schemes used in the current numerical mesoscale models. Namely, all these are based on Mellor and Yamada (1974) scheme, see e.g. Andrén (1990), Enger (1990a), Abiodun and Enger (2002), Enger and Grisogono (1998). However, these schemes rely heavily on the assumption of horizontal homogeneity, the next one being the hydrostatic assumption, etc. These assumptions are justified most of times when the resolution is about several kilometers (or worse) in the horizontal. Nonetheless, these assumptions fail in many situations when this resolution is finer than a few kilometres. This

short note is a call for those improvements which appear necessary nowadays having increasingly refined horizontal and vertical resolution in NWP models.

ACKNOWLEDGMENT

This work is supported by the Croatian Ministry of Science, Education and Sports, project BORA, 119-1193086-1311, and by EMEP4HR project number 175183/S30 provided by the Research Council of Norway.

REFERENCES

- [1] Abiodun, B.J. and L. Enger, 2002: The role of advection of fluxes in modelling dispersion in convective boundary layers. *Quart. J. Roy. Meteorol. Soc.* 128, 1589-1608.
- [2] Andrén, A., 1990: Evaluation of a turbulence closure scheme suitable for air-pollution applications. *J. Appl. Meteor.* 29, 224-239.
- [3] Baklanov, A. and B. Grisogono (editors), 2007: *Atmospheric Boundary Layers: Nature, Theory and Applications to Environmental Modelling and Security*. Springer, New York, 241 pp.
- [4] Bergström, H. and N. Juuso, 2006: A study of valley winds using the MIUU meso-scale model. *Wind Energy*, 9, 109-129.
- [5] Cuxart, J. and M.A. Jiménez, 2007: Mixing processes in a nocturnal low-level jet, an LES study. *J. Atmos. Sci.* 64, 1666-1679.
- [6] Enger, L., 1990a: Simulation of dispersion in moderately complex terrain -Part A. The fluid dynamics model. *Atmos. Environ.* 24A, 2431-2446.
- [7] Enger, L., 1990b: Simulation of dispersion in moderately complex terrain -Part C. A dispersion model for operational use. *Atmos. Environ.* 24A, 2457-2471.
- [8] Enger, L. and B. Grisogono, 1998: The response of bora-type flow to sea surface temperature. *Quart. J. Roy. Meteorol. Soc.* 124, 1227-1244.
- [9] Esau, I.N. and Ø. Byrkjedal, 2007: Application of a large-eddy simulation database to optimization of first-order closures for neutral and stably stratified boundary layers. *Bound.-Layer Meteorol.* 125, 207-225.
- [10] Gohm, A., G.J. Mayr, A. Fix and A. Giez, 2008: On the onset of bora and the formation of rotors and jumps near a mountain gap. *Quart. J. Roy. Meteorol. Soc.* 134, 21-46.
- [11] Grisogono, B. and L. Enger, 2004: Boundary-layer variations due to orographic wave-breaking in the presence of rotation. *Quart. J. Roy. Meteorol. Soc.* 130, 2991-3014.
- [12] Grisogono, B., A. Jerićević and L. Kraljević, 2007: The low-level katabatic jet height versus Monin-Obukhov height. *Quart. J. Roy. Meteorol. Soc.* 133, 2133-2136.
- [13] Grisogono, B. and D. Belušić, 2008: Improving mixing length-scale for inclined stable boundary layers. *Quart. J. Roy. Meteorol. Soc.* 134, 2185-2192.
- [14] Hunt, J.C.R., D.D. Stretch and R.E. Britter, 1988: Length scales in stably stratified turbulent flows and their use in turbulence models. *Stably stratified flow and dense gas dispersion*. Edited by J.S. Puttock, Oxford, United Kingdom, 285-321.

- [15] Jeričević, A. and B. Grisogono, 2006: The critical bulk Richardson number in urban areas: verification and application in a numerical weather prediction model. *Tellus*, 58A, 19-27.
- [16] Kavčič I. and B. Grisogono, 2007: Katabatic flow with Coriolis effect and gradually varying eddy diffusivity. *Bound.-Layer Meteorol.* 125, 377-387.
- [17] King, J.C., W.M. Conneley and S.H. Derbyshire, 2001: Sensitivity of modelled Antarctic climate to surface and boundary-layer flux parameterizations. *Quart. J. Roy. Meteorol. Soc.* 127, 779-794.
- [18] Mahrt, L., 1982: Momentum balance of gravity flows. *J. Atmos. Sci.* 39, 2701-2711.
- [19] Mahrt, L., 1998: Stratified atmospheric boundary layers and breakdown of models. *Theoret. Comput. Fluid Dyn.* 11, 263-279.
- [20] Mahrt, L., 2007: The influence of small-scale nonstationarity on the turbulent flux for stable stratification. *Bound.-Layer Meteorol.* 125, 245-264.
- [21] Mahrt, L., 2008: Bulk formulation of the surface fluxes extended to weak-wind stable conditions. *Quart. J. Roy. Meteorol. Soc.* 134, 1-10.
- [22] Mauritzen, T., G. Svensson, S. Zilitinkevich, I. Esau, L. Enger and B. Grisogono, 2007: A total turbulent energy closure model for neutral and stably stratified atmospheric boundary layers. *J. Atmos. Sci.* 64, 4113-4126.
- [23] Mellor, G.L. and T. Yamada, 1974: A hierarchy of turbulence closure models for planetary boundary layers. *J. Atmos. Sci.* 31, 1791-1806.
- [24] Monti, P., H.J.S. Fernando, M. Princevac, W.C. Chan, T.A. Kowalewski and E.R. Pardyjak, 2002: Observations of flow and turbulence in the nocturnal boundary layer over a slope. *J. Atmos. Sci.* 59, 2513-2534.
- [25] Pielke, R.A., 1984: *Mesoscale Numerical Modeling*. Academic Press, 612 pp.
- [26] Princevac, M., H. J. S. Fernando and C.D. Whiteman, 2005: Turbulent entrainment into natural gravity-driven flows. *J. Fluid Mech.* 533, 259-268.
- [27] Renfrew, I. A., and Anderson, P. S., 2006, Profiles of Katabatic Flow in Summer and Winter over Coats Land, Antarctica, *Quart. J. Roy. Meteorol. Soc.* 132: 779-882.
- [28] Schumann, U. and T. Gerz, 1995: Turbulent mixing in stably stratified shear flows. *J. Appl. Meteor.* 34, 33-48.
- [29] Steeneveld, G.J, 2007: Understanding and prediction of stable atmospheric boundary layers over land. *PhD thesis, Wageningen Univ.*, the Netherlands, 199 pp.
- [30] Steeneveld, G.J, B.J.H. van de Wiel and A.A.M. Holtslag, 2007: Diagnostic equations for the stable boundary layer height: evaluation and dimensional analysis. *J. Appl. Meteor. Clim.* 46, 212-225.
- [31] Stiperski, I., I. Kavčič, B. Grisogono and D. R. Durran, 2007: Including Coriolis effects in the Prandtl model for katabatic flow. *Quart. J. Roy. Meteorol. Soc.* 133, 101–106.
- [32] Söderberg S. and O. Parmhed, 2006: Numerical modelling of katabatic flow over melting outflow glacier. *Bound.-Layer Meteorol.* 120, 509-534.
- [33] Tjernström, M., 1993: Turbulence length scales in stably stratified free shear flow analyzed from slant aircraft profiles. *J. Appl. Meteor.* 32, 948-963.
- [34] Weigel, A.P., F.K. Chow and M.W. Rotach, 2007: The effect of mountainous topography on moisture exchange between the “surface” and the free atmosphere. *Boundary-Layer Meteorol.* 124: 227-244.

-
- [35] Weng, W., and Taylor, P. A., 2003, On modelling the one-dimensional atmospheric boundary layer, *Boundary-Layer Meteorol.* 107: 371–400.
 - [36] Zilitinkevich, S.S., T. Elperin, N. Kleeorin and I. Rogachevskii, 2007: Energy- and flux-budget (EFB) turbulence closure model for stably stratified flows. Part I: steady-state, homogeneous regimes. *Bound.-Layer Meteorol.* 125, 167-191.
 - [37] Zilitinkevich, S.S. and I. Esau, 2007: Similarity theory and calculations of turbulent fluxes at the surface for the stably stratified atmospheric boundary layer. *Bound.-Layer Meteorol.* 125, 193-205.

Short Commentary B

AMBIENT AIR TEMPERATURE INTERPOLATION IN INHOMOGENEOUS REGIONS

Klemen Zakšek^{1,2,*} and Daniel Joly^{3,†}

¹ZRC SAZU, Slovenia

²University of Hamburg, Germany

³ThéMA, France

ABSTRACT

The importance of climatic data for the society increased in the last years due to the global climate change. But spatial representation of climatic data is also a key point in many applications. The estimation of the spatial distribution of ambient air temperature (AAT) measured 2 m above the ground is a GIS application that is especially problematic in mountainous countries with low autocorrelation among measurements. Kriging (usually optimal interpolation method) is not adapted to inhomogeneous areas, thus a statistical method based on multiple regression is proposed.

Within the presented case study, AAT was measured at 20 synoptic stations in Slovenia three times a day (7:00, 14:00 and 21:00) throughout 2005, which means that there are 1095 situations to be interpolated in total. The measurements were linked with the data stored in GIS: firstly, with the DEM and from it derived layers such as relief slope, relief aspect, etc., and secondly with the land cover including derived layers such as distance from the sea. Some of this data has a micro-local and some has a regional influence. Therefore, some explanatory variables were estimated within spatial analyses windows of seven different sizes and only the analysis window, where the attributes were the highest correlated to AAT, was considered in the following procedure.

The novelty of the presented study is inclusion of satellite data – MODIS is an instrument on board Terra and Aqua satellite that observes the land and sea surface from the polar orbit four times per day. Recorded images are used to derive land surface temperature, surface albedo, normalized difference vegetation index and enhanced vegetation index that were introduced into the case study and used within the multiple regression. Systematic correlations between temperature and explanatory variables introduced into the GIS showed that, next to the relief aspect, especially land surface temperature is a significant and easy obtainable data for AAT interpolation. The standard

deviation of all the results improved after MODIS data inclusion from 1.7 to the final 1.5 °C.

Keywords: ambient air temperature, interpolation, multiple regression, inhomogeneous areas, MODIS.

INTRODUCTION

The estimation of the spatial distribution of ambient air temperature (AAT) is necessary because it is used within many application applications like agriculture management, environmental research, energy meteorology, transport managment, etc. However, the AAT estimation is also difficult because AAT close to the ground is measured at meteorological stations (at the standard height of 2 m above ground level) which are often far apart (20–30 km). Physical causes for AAT spatial distribution, which usually form spatial gradients, can be statistically described with appropriate tools. Many studies have shown that relief and land cover attributes play an important role in the spatial distribution of AAT (Anquetin et al., 1999; Benichou and Le Breton, 1987; Bolstad et al., 1998; Bootsma, 1976; Joly et al., 2003; Geiger, 1965; Tveito and Førland, 1999). Therefore, the AAT variation as a function of elevation is a strong rule of spatial distribution. In the same way many other rules that explain AAT spatial distribution exist, thus they have to be identified and estimated.

A continuous AAT field can be estimated by one of the several spatial interpolation techniques (Anderson, 2002) applied to AAT measured at meteorological stations. Notably kriging (Courault and Monestiez , 1999; Matheron, 1970), a geostatistic interpolation (usually used in combination with one of the trend determination techniques, is often used for meteorological purposes. However, kriging, inverse distance, splines, etc., perform under expectations when interpolating a variable with low spatial autocorrelation, because all these techniques are based on the assumption that objects that are close to each other are more similar than objects far apart (Kanveski and Maignan, 2004).

The low autocorrelation issue requires other solutions – spatial distribution of AAT can also be explained with environmental parameters/attributes of the meteorological station. These attributes can be used to explain the AAT spatial distribution if a correlation between them and the AAT is statistically significant. This means that the attributes determine the behaviour of the AAT spatial distribution. Therefore, they are first used to generate a rule, which determines the AAT behaviour as regards the explanatory attributes. Later, this rule is applied to the regularly gridded data (which contains the spatial distribution of the attributes) in order to determine the AAT spatial distribution of the entire study area. This method, which is in statistics referred to as multiple regression, can be generally used to determine the relationship between any kind of variables. The rule used to explain the unknown variable with the explanatory variables, is mathematically defined as a polynomial function of explanatory attributes; the evaluated value is usually a linear combination of the explanatory attributes.

The presented study describes an interpolation experience based on the previously stated principles. Therefore, it uses a deductive approach in order to confirm our findings and estimate the general parameters that influence the AAT spatial distribution. The defined

spatial climatology requires a database of appropriate data and a set of appropriate tools. The novelty of the presented study, which uses similar methods as for example Brossard et al. (2002) or Joly et al. (2003), is the introduction of remote sensing data as explanatory variables. In the end, the results can be mapped or even used as a model input in some other applications. The method was applied to Slovenia using AAT measurements at 20 meteorological stations over the whole year 2005. The theoretical background is described in the second chapter and the case study is presented in third chapter. Finally, the results are discussed in the fourth chapter.

THE METHOD

The interpolation can begin once the GIS database containing the data able to explain the AAT spatial variation. The following procedure for the determination of AAT spatial distribution consists of six steps (figure 1):

1. computation of the AAT spatial autocorrelation (Moran's index I ; if the autocorrelation index is not close to 0, it is better to use a geostatistic or deterministic interpolation than the proposed procedure),
2. systematical computation of Pearson correlation index r between AAT and all the explanatory variables stored in the GIS and then selection of the significantly correlated explanatory attributes,
3. multiple regression using the previous selected variables,
4. evaluation of the results by computing the residuals and cross validation,
5. interpolation of the residuals (by a geostatistic or deterministic interpolation if they are autocorrelated),
6. mapping the results.

The first two steps are usually preformed smoothly. The problems might arise in step number three (multiple regression), if insufficient measurements are available. Multiple regression should be performed only on those explanatory attributes that are independent and statistically significant. Therefore, the correlations between AAT and explanatory attributes are systematically estimated by the correlation index r (step 2). However, if the number of measurements is small, the computed correlation index might be a consequence of chance. Therefore, one needs to set a threshold that shows which correlation can be considered as a real correlation and not as a coincidence. Only variables that show a significant correlation index (not coincidental) are then kept for the second step, since statistically insignificant data often represents a source of errors. The significance of the correlation index was tested for all explanatory attributes using the equation following a Student t -distribution (Lowry, 2007):

$$t = \frac{r \cdot \sqrt{n - 2}}{\sqrt{1 - r^2}}$$

where n is the number of measurements and t is the t -distribution value. There are 18 degrees of freedom (to describe a linear relationship) when using 20 uncorrelated

measurements, which means that if one is interested in a 95% (90%) confidence interval, the statistics t should be larger than 2.10 (1.73). In this case all correlation indexes larger than 0.38 (0.30) are statistically significant (not coincidental) and the corresponding explanatory attributes can be used within the multiple regression. All the possible combinations of statistically significant explanatory attributes are then tested within a stepwise procedure (Efroymson, 1960). The final model corresponds to the equation that explains the most AAT variance.

No input data is usually left out for validation (step 4) of the deterministic or geostatistic interpolation method; the accuracy is then estimated by the k-fold cross or leave-one-out cross validation (Kanevski and Maignan, 2004). In the presented study the validation was especially problematic because data for only 20 meteorological stations was available (insufficient measurements to make a stable model, because if some measurements are left out of the model calibration in order to use them for the validation, the model can change significantly). Therefore, leave-one-out cross-validation was used; it involved using a single observation from the original sample as validation data, and the remaining observations as training data. This was repeated 20-times per situation so that each observation was used once as validation data – each measurement is left out once, the model is calibrated on the other 19 measurements and the standard deviation σ is computed from the 20 residuals res_i in order to estimate the result accuracy.

$$\sigma = \frac{\sqrt{\sum_{i=1}^n res_i}}{n-1}$$

Furthermore, step number five is interesting because multiple regression can already be the final step in the procedure. However, the results might be enhanced with additional interpolation if the residuals are spatially correlated even if the variable to be interpolated was not autocorrelated at the beginning of the process. On the end, the results are finally mapped using parameters estimated in step 3 and 5.

CASE STUDY

The proposed procedure was tested in Slovenia which covers approximately 20 000 km². Its topography features a small coastal strip on the Adriatic Sea, the Alpine region in the north-west, hills in the central part and the Pannonia plain in the east. Due to its position on the crossing of various climatic regions, Slovenia has a number of different climate types. In order to describe this variety one needs various data (the datasets are introduced into the GIS as raster datasets at a 100 m resolution projected to UTM, zone 33N):

1. Environmental Agency of the Republic of Slovenia provided the AAT measurements (ARSO, 2007; measured at the height of 2 m measured at 7:00, 14:00 and 21:00 for the year 2005),
2. Surveying and Mapping Authority of the Republic of Slovenia provided the digital elevation produced from various sources (Podobnikar, 2005; slope, slope N-S

- direction, aspect, quasi-global solar radiation, topographic roughness and down-up position were derived from elevation data),
3. land cover data and its derivates (distance from the forest, distance from the sea) was prepared by Kokalj and Oštir (2006), and
 4. MODIS satellite data averaged to the whole year 2005 (land surface temperature – LST and surface albedo in 1000 m resolution, normalized difference vegetation index – NDVI and enhanced vegetation index – EVI in 250 m resolution) was acquired from NASA (DAAC, 2006).

WINDOWING PROCEDURE

AAT spatial distribution is influenced by many parameters that might have a micro-local or a regional influence. Therefore, some explanatory variables (elevation, slope, roughness, aspect, solar radiation, down-up position and MODIS NDVI, but not other MODIS data, distance to the forest and to the sea and slope in the N–S direction) were estimated within spatial analyses windows of seven different sizes centred on each meteorological station (table 1). The various sizes of spatial analyses windows made it possible to consider the effect of the surrounding area on the measured AAT at different scale levels.

Table 1. Size of spatial analyses windows used during data preparation.

Window number	1	2	3	4	5	6	7
Size [pixel]	3	11	29	51	101	151	201
Size [km]	0.3	1.1	2.9	5.1	10.1	15.1	20.1

The modelling was applied for each of the available temperature situations. The example for the first set of measurements in the AAT dataset (01. 01. 2005 at 7:00) was used to show how correlation indices between AAT and explanatory variables vary with scale. Figure 1 shows the correlation index r values for different window sizes for some chosen variables. The elevation effect remains constant from the first to the seventh analysis window (the curve is almost flat), reflecting that the correlation between the elevation and AAT changes gradually in the case study area. This non-scalar pattern was already described by Joly and Brossard (2007). The correlation between AAT and elevation measures the intensity of the vertical thermal gradient. These calculations show that the elevation induces a uniform influence on this gradient (the higher the elevation is, the lower the AAT is).

On the other hand, the remaining explanatory attributes exhibit a strong scale effect. The scale of the explanatory variables indicates the hierarchy of variables that can explain the AAT distribution in a random situation. The optimal window size varies from one situation to another and might differ completely from those in the example presented for 01.01.2005. When the conditions are similar for the entire study area (for example on a clear night), large window sizes are more suitable for the analysis.

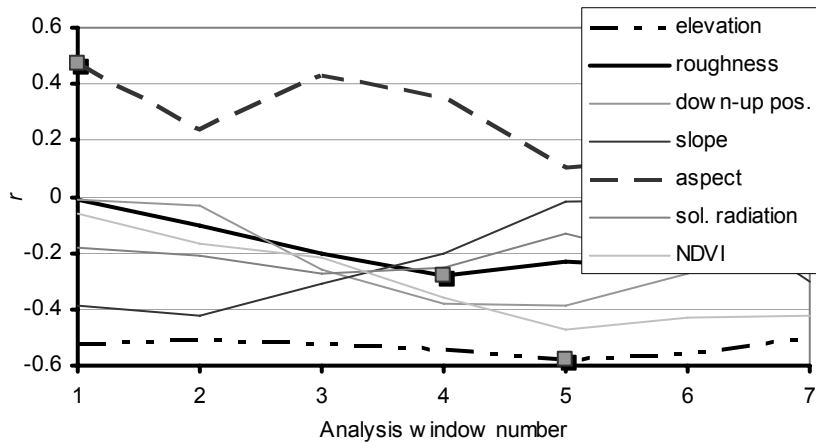


Figure 1. Correlation index r for six explanatory variables and the seven window sizes; situation on the 01.01.2005 at 7:00.

Among the available variables introduced in the systematic linear correlation, only four of them were characterised by a significant correlation index and then used within the multiple regression:

1. elevation (window 5; $r = -0.59$),
2. LST ($r = -0.58$),
3. aspect (window 1; $r = 0.47$), and
4. roughness (window 4; $r = -0.30$).

Some variables had also a significant correlation with AAT but their use did not increase the final accuracy: slope (window 2; $r = -0.42$), down-up position (window 5; $r = -0.39$) and NDVI (window 4; $r = -0.36$). Solar radiation (window 3; $r = -0.27$), slope in the N-S direction ($r = 0.11$), EVI ($r = 0.11$), albedo ($r = -0.08$) and distance to the sea ($r = 0.00$) were not significantly correlated with AAT. The standard deviation of residuals for the 01. 01. 2005 at 7:00 situation equals $2.2\text{ }^{\circ}\text{C}$.

STANDARD DEVIATION OF RESIDUALS

All of the remaining 1095 situations for the year 2005 (365 days, three records per day) are systematically analyzed in the same way as the previous example. The standard deviation of the residuals for the entire 1095 situations equals $1.5\text{ }^{\circ}\text{C}$. The minimum and the maximum residuals are respectively $-10.5\text{ }^{\circ}\text{C}$ and $11.0\text{ }^{\circ}\text{C}$ (perhaps a consequence of gross errors in the measurements). Over 50% of the residuals can be found between $-1\text{ }^{\circ}\text{C}$ and $1\text{ }^{\circ}\text{C}$ (figure 2 left). The time in the day has only a small influence on the estimation quality. High residuals occur notably during winter time: from October to March (figure 2 below). The accuracy was for comparison estimated also without using the MODIS images which yielded to the standard deviation of $1.7\text{ }^{\circ}\text{C}$. The additional data has therefore improved the results.

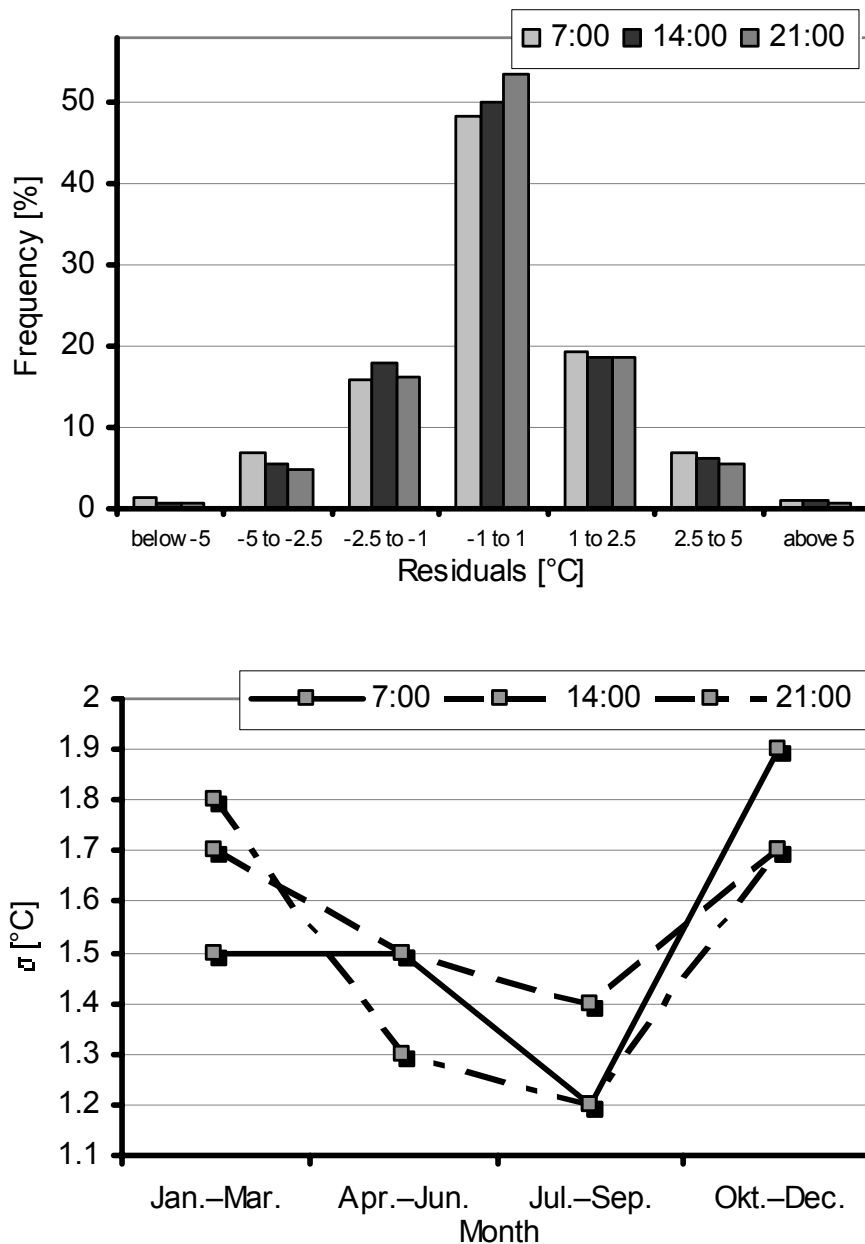


Figure 2. Statistical evaluation of the results – histogram of final residuals for 7:00, 14:00 and 21:00 on the left, accuracy according to time of the year and time of the day (365 days; 20 stations).

EXPLANATORY VARIABLES SIGNIFICANCE

Table 2 shows the frequencies of using explanatory variables introduced in the multiple regressions. It reveals that aspect, elevation, and distance from the sea, slope in the N–S direction, solar energy and albedo2005 were often selected at 14:00 when AAT is the highest.

In opposite, down-high position, roughness, slope, LST2005, NDVI2005 and EVI2005 were selected to explain the AAT distribution usually in morning and evening most likely because of the micro-local scale effects.

Aspect was the most frequently chosen as a significant explanatory variable AAT – more than 1000 situations (91.4%). The second most frequent variable used in the regressions is elevation (79.8%). EVI (MOD13Q1 product) and albedo (MOD43B3 product) with 3.3 and 2.8% frequency were recognized as the least statistically significant parameters, which is surprisingly at least for albedo that influences the amount of the solar radiation to be accepted by the surface.

The other two MODIS datasets played more significant role. The frequency of MODIS NDVI (MOD13Q1) is comparable to other explanatory variables (25.1%). One can also observe that the MODIS and artificial NDVI are well correlated in window 1 due to their similar spatial resolution, thus this combination of data was not used in the study. Furthermore, MODIS LST (MOD11A2 product) is a significant attribute for AAT distribution in 47.9% of all situations. Because of its low spatial resolution (1000 m) it has only a regional influence but it is still the third most frequent explanatory variable.

Table 2. Frequency [%] of explanatory variables introduced in the multiple regression.

Variable	7:00	14:00	21:00	Average
Aspect	91.3	95.6	87.4	91.4
Elevation	74.1	87.6	77.8	79.8
Distance from the sea	18.4	43.4	20.3	27.4
Slope in N–S direction	22.8	33.2	24.1	26.7
Solar radiation	12.6	22.2	12.1	15.6
Albedo2005	2.7	5.0	2.2	3.3
LST2005	61.9	37.8	44.1	47.9
Down-up position	34.0	13.5	42.5	30.0
NDVI2005	26.8	15.4	33.2	25.1
Roughness	21.7	19.4	24.4	21.8
Slope	14.6	10.7	27.2	17.5
EVI2005	3.0	1.9	3.3	2.8

INTERPOLATED RESULTS

Figures 3 and 4 show an example of the interpolated results for January 4 at 7:00 and July 7 at 14:00. The areas in white are nodata areas that occur where the selected explanatory variable is out of range given by the attribute values on the meteorological stations (in order to prevent extrapolation that can lead to gross errors).

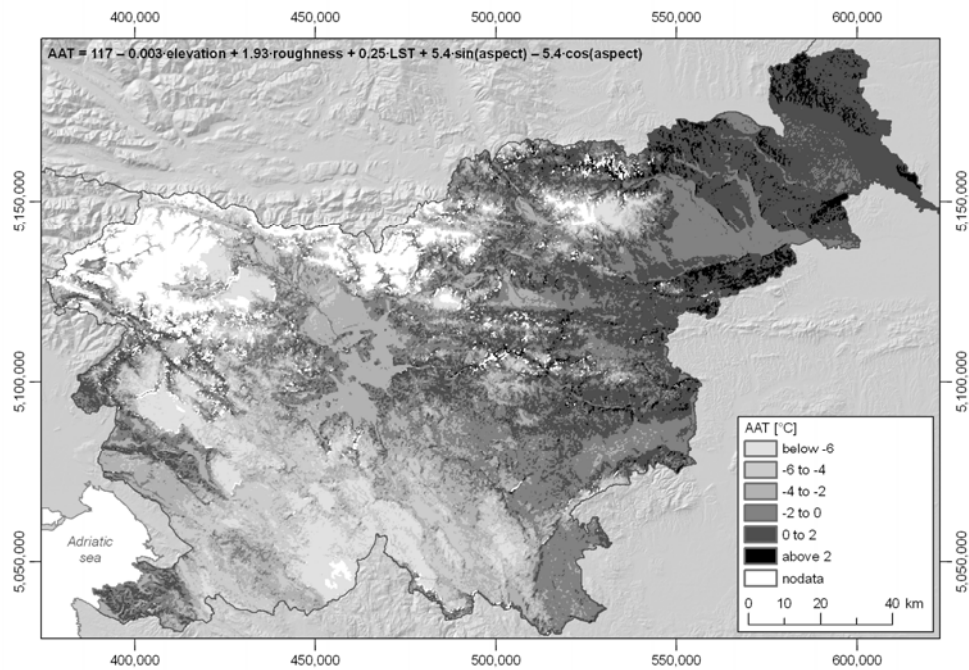


Figure 3. Interpolated AAT field in 100 m spatial resolution; example for 04. 01. 2005 at 7:00). The relief roughness has a large influence on the AAT in the morning as it can explain the thermal inversion.

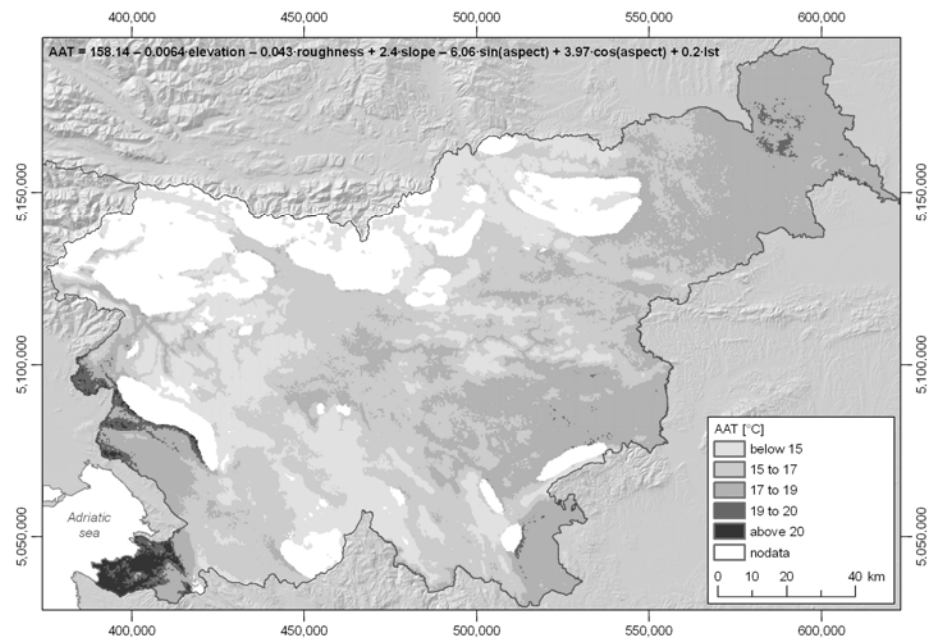


Figure 4. Interpolated AAT field in 100 m spatial resolution; example for a cloudy day – 07. 07. 2005 at 14:00). It can be seen that the elevation has a great influence in the case of cloudy weather.

CONCLUSION

The results of the presented study, which were not validated with independent data because of the low number of measurements (cross validation was therefore used), are comparable with previous studies. Anderson (2002) tested various interpolation methods in the Phoenix metropolitan area, where the density of measurements was approximately ten-times larger than in the presented study; the best results were obtained by kriging interpolation ($\text{RMSE} = 1.62 \text{ }^{\circ}\text{C}$). The presented results are also better than the 24 hour weather forecast (ARSO, 2007), but they cannot be compared to the results of the AAT high resolution interpolation on Svalbard (Joly et al., 2003) where the AAT was determined with the accuracy of $0.3 \text{ }^{\circ}\text{C}$ based on 50 measurement stations covering the area of merely 8 km^2 . In addition to the low density of the meteorological stations, the origin of the rather poor results quality in the case study is mountainous study area which can be characterized also by climatically quasi independent climate valleys (Sevruk and Miegltz, 2002).

Aspect, elevation and LST are often among the significant attributes that can explain the AAT spatial distribution. Solar radiation, distance from the sea or slope in the N–S direction are also usually significant during daytime in clear-sky conditions. NDVI, EVI, LST, albedo, down-high position and slope are significant in night and by cloudy conditions. Therefore, many attributes are correlated to AAT but the connection between these attributes and the measured AAT is different for different weather situations. Furthermore, the scale has an effect on the results, which makes AAT interpolation a difficult task.

The presented method can be successfully applied for any case study area once GIS database is prepared, which gives one a possibility to do even nowcasting for example in traffic management or agriculture. It was shown that data from a greater number of meteorological stations is necessary in order to obtain a high accuracy AAT field. But it is not just the number of stations that should be higher – the new stations should be situated on such locations that would cover also those combinations of explanatory variables that were not considered within the presented case study.

A novelty of this study was the inclusion of MODIS data – EVI and surface albedo are not correlated with AAT but LST and NDVI have proved to have a significant influence on AAT and therefore their use improves the overall accuracy for $0.2 \text{ }^{\circ}\text{C}$. Moreover, LST is the third most frequent used data for the interpolation, which confirms its usability.

REFERENCES

- [1] Anderson S. 2002. An Evaluation of Spatial Interpolation Methods on Air Temperature in Phoenix, AZ. Available from: URL: <http://www.cobblestoneconcepts.com/ucgis2summer/anderson/anderson.htm> (12.12.2006).
- [2] Anquetin S., Guilbaud C., Chollet JP, 1999. Thermal valley inversion on the dispersion of a passive pollutant in a complex mountainous area. *Revue Atmospheric Environment* 33: 3953–3959.
- [3] ARSO 2007. Članek o verifikaciji regionalnih vremenskih napovedi na ARSO. Available from: URL: http://www.ars.si/podro~cja/vreme_in_podnebje/poro~cila_in_projekti/Clanek_verifikacija.pdf (12. 3. 2007).

- [4] Benichou P., Le Breton O., 1987. Prise en compte de la topographie pour la cartographie des champs pluviométriques statistiques. *La météorologie* 7/19: 22–34.
- [5] Bolstad P., Swift L., Collins F., Regniere J., 1998. Measured and predicted air temperatures at basin to regional scales in the southern Appalachian mountains. *Agricultural and forest meteorology* 91: 161–176.
- [6] Bootsma A., 1976. Estimating minimum temperature and climatological freeze risk in hilly terrain. *Agricultural Meteorology* 16: 425–443.
- [7] Brossard T., Elvebakk A., Joly D., Nilsen L. 2002. Modelling index of thermophily by means of a multi-source database on Broggerhalvoya Peninsula (Svalbard). *International Journal of Remote Sensing* 23: 4683–4698.
- [8] Courault D., Monestiez P. 1999. Spatial interpolation of air temperature according to atmospheric circulation patterns in southeast France. *International Journal of Climatology* 19: 365–378.
- [9] DAAC, 2006. Available from: URL: <http://edcimswww.cr.usgs.gov/pub/imswelcome/> (12.12.2006).
- [10] Efroymson M.A. 1960. Multiple regression analysis. In Ralston A & Wilf HS (Eds.): *Mathematical Methods for Digital Computers*. New York: Wiley.
- [11] Geiger R. 1965. *The climat near the ground*. Cambridge: Harvard University Press.
- [12] Joly D., Brossard T. 2007. Contribution of environment factors to the temperature distribution at different resolution levels on the forefield of the Loven glaciers, Svalbard. *Polar Record* 43/227: 353–359.
- [13] Joly D., Nilsen L., Fury R., Elvebakk A., Brossard T. 2003. Temperature interpolation at a large scale: test on a small area in Svalbard. *International Journal of Climatology* 23/13: 1637–1654.
- [14] Kanevski M, Maignan M. 2004. *Analysis and modelling of spatial environmental data*. Lausanne: EPFL Press.
- [15] Kokalj Ž, Oštir K. 2006. Ugotavljanje pokrovnosti Slovenije iz satelitskih posnetkov Landsat. *Geografski vestnik* 78/2: 85–95.
- [16] Lowry R. 2007. The Significance of a correlation coefficient. Available from: URL: <http://faculty.vassar.edu/lowry/ch4apx.html> (12.3.2007).
- [17] Matheron G. 1970. *Traité de géostatistique appliquée, Tome 1*. Mémoires du bureau de recherches géologiques et minières, n°14. Paris: Technip.
- [18] Podobnikar T. 2005. Production of integrated terrain model from multiple datasets of different quality. *International Journal of Geographical Information Science* 19/1: 69–89.
- [19] Sevruk B., Miegltz K. 2002. The effect of topography, season and weather situation on daily precipitation gradients in 60 Swiss valleys. *Water Science Technology*, 45/2: 41–48.
- [20] Tveito O., Førland EJ. 1999. Mapping temperatures in Norway applying terrain information, geostatistics and GIS. *Norsk geografisk tidskrift* 53: 202–212.

Short Commentary C

**PEAT MOISTURE IN RELATION TO
METEOROLOGICAL FACTORS: MONITORING,
MODELLING, AND IMPLICATIONS FOR THE
APPLICATION OF THE CANADIAN FOREST FIRE
WEATHER INDEX SYSTEM**

***Vladimir Krivtsov¹, G. Matt Davies¹, Colin Legg¹,
Teresa Valor¹ and Alan Gray²***

¹The University of Edinburgh, Scotland, UK.

²Centre for Ecology and Hydrology, Bush Estate, Penicuik, Scotland, UK

ABSTRACT

Underground fires in peatlands are relatively rare events but when active they can smoulder for very long periods and cause significant environmental damage. They emit large quantities of combustion products, including greenhouse gases, into the atmosphere causing deterioration in air quality and public health. These fires are fed by small but continuous quantities of air diffusing through the peat and flowing through fractured strata, cracks and soil pipes. Reduced heat losses and high thermal inertia of the ground, combined with the continual fuel availability and small oxidizer flow, promote long-term smouldering combustion and creeping propagation that can be extensive in both depth and area. These fires are difficult to detect and frustrate most efforts to extinguish them. Here we present a case study of variation in peat soil water potential in relation to changes in meteorological variables and indices of the Canadian Forest Fire Weather Index System (CFFWIS). Duff Moisture Code (DMC) values appeared to correspond relatively well to modelled changes in soil moisture deficit (SMD), as well as to the soil water potential (SWP), thus giving certain credibility to this component of the CFFWIS in relation to the probability of occurrence of an underground fire. It should be noted, however, that the fit between SWP and DMC was somewhat weaker than the fit between SWP and the modelled values of SMD ($r = 0.76$ and 0.85 respectively). It has previously been shown (Davies et al. 2006) that the CFFWIS is unable to predict the rate of fire spread in heather (*Calluna vulgaris*) stands, because the moisture content of live and dead

Calluna was not accurately predicted by any of the moisture codes of the CFFWIS. Considering the results presented here, the standard method to estimate soil moisture deficit might be a good starting point for developing an index specifically catering for the British conditions.

INTRODUCTION

Wild fire is a serious problem in the terrestrial environment. In the UK, major wildfires are sporadic, but may cause serious environmental impacts. In particular, underground fires in peatlands are currently relatively rare events but when active they can smoulder for long periods of time causing significant ecological damage, and emit large quantities of combustion products (Rein *et al.* 2008b). In other locations, particularly in the tropics, this can cause a deterioration in air quality with public health concerns (Page *et al.* 2002).

Peat fires spread slowly at rates of approximately 3 cm hr^{-1} (Frandsen 1991). They are fed by small but continuous quantities of air diffusing through the peat and flowing through fractured strata, cracks and groundwater pipe networks. Particularly important for smouldering behaviour is moisture content - the critical factor influencing the likelihood of ignition and the rate of fire spread (Rein *et al.* 2008a). A combination of ecological and hydrological assessment of peatlands is therefore required for the understanding of fire hazard and risk and the sustainable management of peatland ecosystems (Zaidel'man & Romanov 2007).

Belowground, reduced heat losses and the high thermal inertia of the peat, together with continuous fuel availability and reduced oxygen supply, promote long-term smouldering combustion and allow for a creeping propagation extensive in both depth and area. These fires are difficult to detect and frustrate most efforts to extinguish them. Smouldering fires may be caused by, for example, transition from a flaming wildfire or management fire or from an incompletely extinguished camp fire.

The Met Office (2005) have recently introduced a fire danger rating system known as the Met Office Fire Severity Index (MOFSI) to forecast exceptional fire weather (i.e. conditions that would normally be expected roughly every four years) for England and Wales. MOFSI is based on the Canadian Forest Fire Weather Index System (CFFWIS). The index performs well for the specific and rather limited function for which it was designed but has limited applicability for forecasting actual fire occurrence or hazard in important British fuel types. We examine the moisture indices of the CFFWIS with regards to the peat soil water potential (SWP) and comment on their applicability for use in the UK. The CFFWIS has been widely adopted in many geographical locations (including in tropical peatlands where wildfires are a significant problem) and the results presented here are thus likely to be important not only in the local, but also in the global context.

Materials and Methods

A weather station was set up in the Pentland Hills (near Edinburgh, approximate position $55^{\circ} 51' \text{ N}$, $3^{\circ} 18' \text{ W}$) recording changes in net solar radiation, wind speed and direction, air temperature, relative humidity, surface wetness, rainfall, and soil temperature and resistance

every 30 seconds. SWP was calculated from soil resistance using standard equations (Campbell Scientific 1996). Realised soil moisture deficit (SMD) was modelled (see Appendix) using data on rainfall and potential evapotranspiration; the latter was calculated using Penman's method (Shaw 1983). Handling and analysis of the data were carried out using Matlab software, and the details can be viewed in the relevant script listed in the Appendix. Calculations of the Drought Code (DC), Fine Fuel Moisture Code (FFMC), Buildup Index (BUI), and Duff Moisture Code (DMC) of the Canadian Forest Fire Weather Index System (CFFWIS) were carried out using a custom program written in Delphi, which implements the standard published methodology (Van Wagner & Pickett 1985). It should be noted that the input data for the calculations of the DC use meteorological data 100 days prior to the investigations period. As our field measurements started only in Aug 2007, the national forecast data were used for the spin-up prior to that. However, among the data needed, the air temperatures and relative humidity were not freely available for any location close to the study site prior to August 2007. Therefore, we have used multiple regression technique to model the air temperature in terms of the surface temperature, wind speed and cloud cover (which were available). Humidity was deduced from the available data on rainfall, surface T, cloud cover and potential evaporation. These simulated air T and relative humidity were subsequently used as inputs for part of the spin-up calculations of DC.

Results

The data presented here span through Aug to Nov 2007 and include a three-week dry spell in late August to early September. There is a notable (and indeed expected) diurnal variation in changes of a number of variables, including e.g. air and soil temperature, and net radiation. This variation, however, is superimposed on longer-term changes and seasonal trends; for example air T during the study period was negatively correlated to decimal day (Table 1).

During the dry period values of soil resistance were seen to gradually increase, but plummeted after the intensive rainfall on Sep 16 (Day 259 – see Fig. 1).

Changes in the values of indices of the CFFWIS are shown in Fig. 2, whilst the strengths of their relationships with soil water potentials and the modelled values of SMD could be judged from the relevant correlations listed in Table 1. The outline of the CFFWIS is given in Fig. 3.

Changes in the modelled SMD (Fig. 4) appear to correspond to the observed changes in the soil water potential (e.g. for SWP1, $r=0.85$). Among the examined indices of the CFFWIS, the Duff Moisture Code (designed to reflect changes in the moisture content of loosely compacted duff and surface organic soils in the boreal forest) showed the best fit both to the modelled changes in SMD ($r=0.91$) and to the observed water potentials (e.g. for SWP1, $r=0.76$). The BUI also corresponded relatively well to these variables ($r=0.91$ and 0.75 respectively).

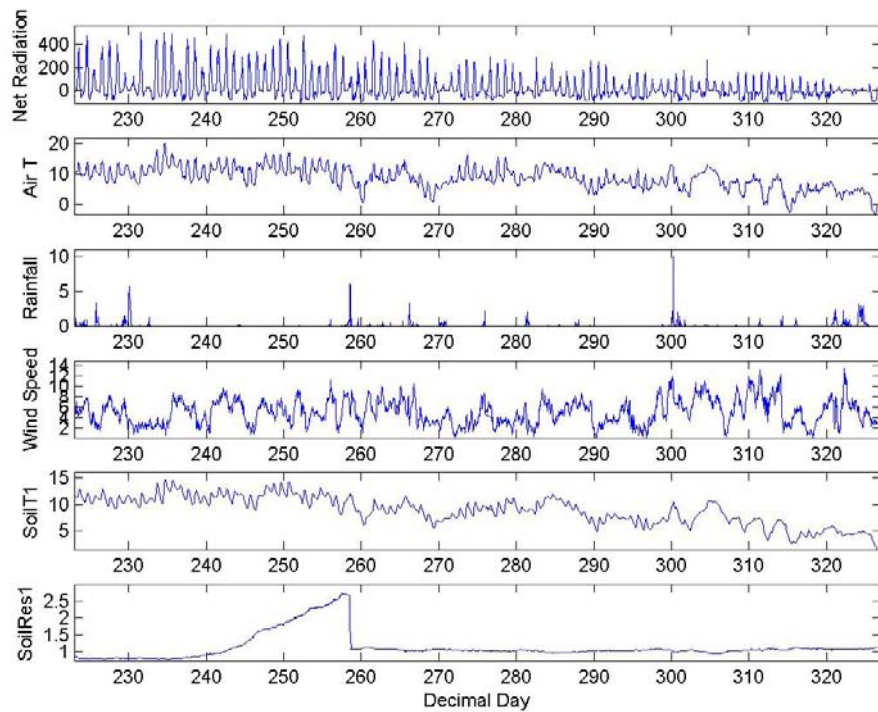


Figure 1. Selected summary of monitoring data.

Table 1. Summary of correlation analysis between selected monitoring and modelling data. Only significant ($p \leq 0.05$) correlation coefficients are shown.

Vars	T	RH	Wind	Rain	FFMC	DMC	DC	ISI	BUI	FWI	DSR	DecDay	SMD
T	1					0.44	-0.45	0.23	0.44	0.34	0.31	-0.67	0.37
RH		1	0.3	0.22	-0.37			-0.31		-0.28	-0.27		
Wind		0.3	1					0.23					
Rain		0.22		1	-0.55		-0.28	-0.34		-0.23			
FFMC		-0.37		-0.55	1	0.58	0.26	0.91	0.59	0.7	0.48		0.34
DMC	0.44				0.58	1		0.7		1	0.85	0.74	-0.45
DC	-0.45				-0.28	0.26	1						0.74
ISI	0.23	-0.31	0.23	-0.34	0.91	0.7		1	0.7	0.87	0.68		0.47
BUI	0.44				0.59	1		0.7	1	0.85	0.73	-0.45	0.91
FWI	0.34	-0.28		-0.23	0.7	0.85		0.87	0.85	1	0.94	-0.28	0.68
DSR	0.31	-0.27			0.48	0.74		0.68	0.73	0.94	1	-0.27	0.62
DcDy	-0.67					-0.45	0.74		-0.45	-0.28	-0.27	1	-0.44
SMD	0.37				0.34	0.91		0.47	0.91	0.68	0.62	-0.44	1
SWP1					0.23	0.76	0.23	0.33	0.75	0.56	0.54		0.85
SWP2	0.33				0.34	0.87		0.49	0.87	0.69	0.63	-0.31	0.89
SWP3	0.32				0.4	0.89		0.55	0.88	0.73	0.65	-0.27	0.89
SWP4	0.25				0.27	0.81		0.41	0.81	0.63	0.6	-0.21	0.84
SWP5						0.54			0.53	0.34	0.39		0.62
SWP6	0.38					0.42	0.9		0.59	0.9	0.76	0.67	-0.37
SWP7	0.33					0.42	0.88		0.59	0.87	0.74	0.65	-0.3
SWP8						0.56	0.42		0.55	0.36	0.36		0.67

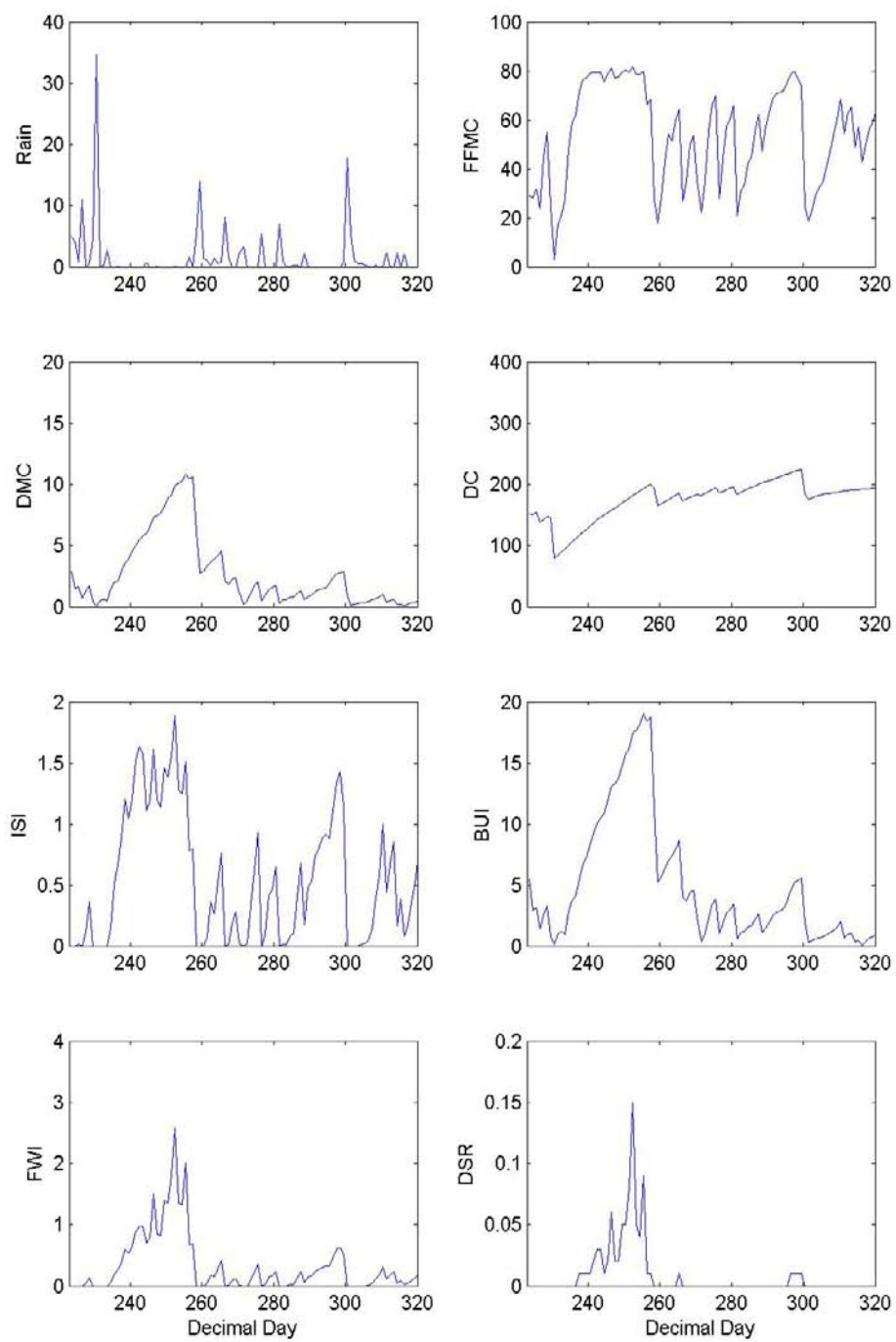


Figure 2. Summary of the CFFWI simulation.

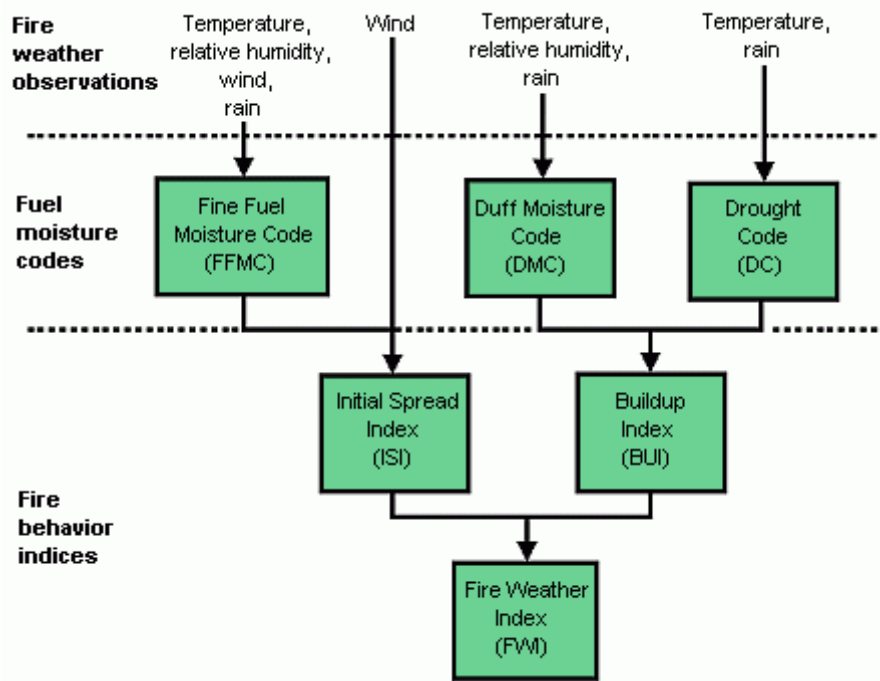


Figure 3. Outline of the Canadian Forest Fire Weather Index (CFFWI) System (Van Wagner 1987). The system was originally designed for jack pine, but has since been adapted to many different locations throughout the world, even in the tropics.

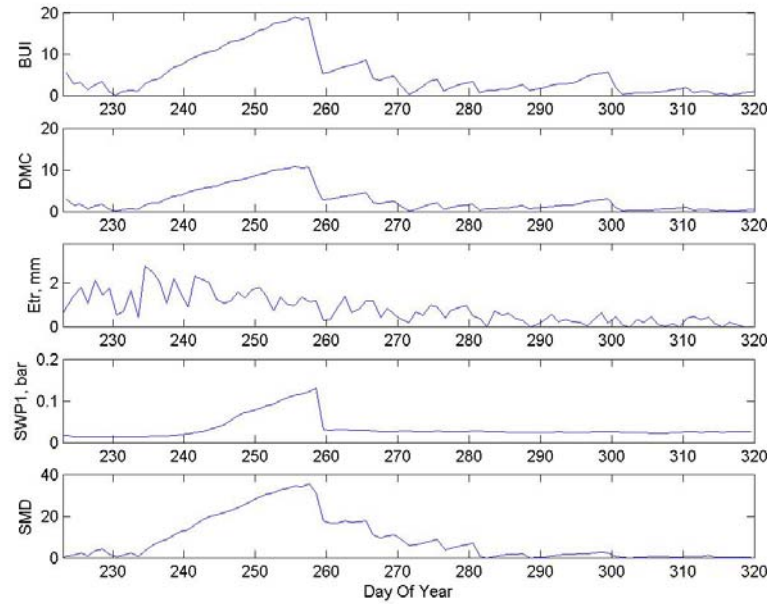


Figure 4. CWFI estimates of Drought Code (DC) and Duff Moisture Code (DMC) are plotted together with estimates of Soil Water Potential (SWP), Evapotranspiration (Etr), and Soil moisture Deficit (SMD).

DISCUSSION

The UK holds approximately 10 – 15% of the world's land area of blanket peat, and these areas are recognised as being of considerable global conservation interest (Lindsay 1995). Fire is widely used as a management tool in these areas and wildfires are not uncommon. When peat fires occur they cause significant ecological damage leaving some areas bare for decades if not centuries and can release significant quantities of carbon. The results presented here are therefore important in both the local and the global context. Indeed globally the future of the peatlands is increasingly uncertain due to climate change. In the UK, climate change scenarios suggest increases in mean temperature and decreases in rainfall in summer (Jenkins et al. 2007) that are likely to result in lowered water tables and a consequent increase hazard of peat fires. Furthermore, laboratory experiments have shown that elevated temperatures promote decomposition of peat samples exposed to drying cycles but have little effect on decomposition of continuously flooded samples (Hogg et al. 1992), with subsequent effects on the balance between emissions of greenhouse gasses such as methane and carbon dioxide (Nakano et al. 2006).

CFFWIS uses meteorological data to calculate fuel moisture codes, and subsequently uses those for estimation of indices characterising the behaviour of a potential wild fire (Fig. 3). The UK is in the process of developing a fire danger rating system and the current prediction system, the Met Office Fire Severity Index (MOFSI) is an almost direct implementation of the CFFWIS (Kitchen et al. 2006). Existing research has highlighted the problems associated with applying the CFFWIS to vegetation types which it was never designed to represent (Anderson 2006; Davies et al. 2006) and this includes *Calluna vulgaris*-dominated peatlands in the UK. The results of the previous research have shown that CFFWIS (in particular the drought code – DC) showed an unsatisfactory performance in relation to the shrub fires in the UK (Davies et al. 2006), being unable to predict the rate of fire spread in the stands of *Calluna* shrubs. This failure was caused by the fact that the moisture content of live and dead *Calluna* was not accurately predicted by any of the moisture codes of the CFFWIS.

As has been shown here, however, both DMC and BUI values appeared to correspond relatively well to the modelled changes in SMD (see Fig.4), as well as to the SWP, thus giving certain credibility to these components of the CFFWIS in relation to the probability of occurrence of an underground fire. It should be noted, however, that even the best fits between the Canadian indices and SWP were somewhat weaker than the fit between SWP and the modelled values of SMD (Table 1); the latter therefore might be a good candidate for a starting point in developing an index specifically catered for the British conditions.

The current MOFSI system is designed for a very specific purpose: to detect “exceptional fire weather conditions” that may result in unacceptably high levels of ecological damage should a fire occur (Kitchen et al. 2006). If the system does indeed reflect changes in the moisture content, and therefore flammability, it will successfully capture one of the main controls governing when truly severe fires occur. Considering the above, the results presented here provide specific information which may be helpful in informing future improvements to MOFSI and the development of the weather prediction system designed specifically for the British conditions.

REFERENCES

- [1] Anderson S. A. J. (2006) Future option for fire behaviour modelling and fire danger rating in New Zealand. In: *Proceeding of the Bushfire Conference 2006: Life in a fire-prone environment: Translating science into practice*, Brisbane.
- [2] Campbell Scientific (1996) *257 and 253 Soil Moisture Sensors. User Guide*. Campbell Scientific Ltd.
- [3] Davies G. M., Legg C. J., Smith A. & Macdonald A. J. (2006) Developing shrub fire behaviour models in an oceanic climate: Burning in the British uplands. *Forest Ecology and Management* 234S.
- [4] Frandsen W. H. (1991) Burning Rate of Smoldering Peat. *Northwest Science* 65: 166-172.
- [5] Hogg E. H., Lieffers V. J. & Wein R. W. (1992) Potential Carbon Losses from Peat Profiles - Effects of Temperature, Drought Cycles, and Fire. *Ecological Applications* 2: 298-306.
- [6] Jenkins G. J., Perry M. C. & Prior M. J. (2007) *The climate of the United Kingdom and recent trends*. Met Office Hadley Centre, Exeter, UK.
- [7] Kitchen K., Marno P., Legg C. J., Bruce M. & Davies G. M. (2006) Developing a fire danger rating system for the United Kingdom. *Forest Ecology and Management* 234S.
- [8] Lindsay R. A. (1995) *Bogs: the Ecology Classification and Conservation of Ombrotrophic Mires*. Scottish Natural Heritage, Battleby.
- [9] Met Office (2005) *The Met Office Fire Severity Index for England and Wales*. Met Office, Exeter.
- [10] Nakano T., Takeuchi W., Inoue G., Fukuda M. & Yasuoka Y. (2006) Temporal variations in soil-atmosphere methane exchange after fire in a peat swamp forest in West Siberia. *Soil Science and Plant Nutrition* 52: 77-88.
- [11] Page S. E., Siegert F., Rieley J. O., Boehm H.-D. V., Jaya A. & Limin S. (2002) The amount of carbon released from peat and forest fires in Indonesia during 1997. *Nature* 420: 61-65.
- [12] Rein G., Cleaver N., Ashton C., Pironi P. & Torero J. L. (2008a) The severity of smouldering peat fires and damage to the forest soil. *Catena* 74: 304-309.
- [13] Rein G., Cohen S. & A. Simeone. (2008b) Carbon emissions from smouldering peat in shallow and strong fronts. *Proceedings of the Combustion Institute* 38.
- [14] Shaw E. M. (1983) *Hydrology in practice*. Van NostrandReinhold (UK) Co. Ltd., Wokingham.
- [15] Van Wagner, C. E. (1987) *The Development and Structure of the Canadian Forest Fire Weather Index System*. Canadian Forestry Service Publications FTR-35.
- [16] Van Wagner, C. E. & Picket, T. L. (1985). *Equations and FORTRAN program for the Canadian Forest Fire Weather Index System*. Canadian Forestry Service, Ottawa.
- [17] Zaidel'man F. R. & Romanov S. V. (2007) Ecological-hydrothermal assessment of pyrogenic soils of cutover peatlands. *Eurasian Soil Science* 40: 82-92.

APPENDIX 1. MATLAB SCRIPT 1.

```

%%%a script by VK to plot measurements from the Meteostation%%%%%
%also calls the Penmanf function to calculate SMD and Evaporation
%NB: use SummaryPlot2 for easy replotting!
clear all; close all;

%Input section%
TotalVar=36;
DataDir='\\geoshome5.geos.ed.ac.uk\\vkrivtso\\FireParadoxCommon\\MatlabPeat';
XLSfile2write='PeatCanadaCorrelations.xls';

fname='CombinedAutumnData';%input file with combined meteo data
FileExt='.txt';

CWFISfname='Blackhill_edited';%input file with combined meteo data
CWFISfileExt='.txt';

StrtTime=223;EndTime=320
SMDstart=0;%i.e. SMD just BEFORE StrtTime

%%Changes the Switches below between 1 and 0 if you want/do not want a
%%relevant printout
IndPlotSwitch=0;Sum1PlotSwitch=0;Sum2PlotSwitch=0;SWPplotsSwitch=0;PenmanPlotSwitch
h=0;
CanadaPlotSwitch=1;
%NB: use SummaryPlot2 for easy replotting!

%end of inputs%
%%%%%%%%%%%%%
str2eval=['cd ' DataDir]; eval(str2eval);
str2eval=['load ' fname FileExt]; eval(str2eval);
str2eval=['data=' fname]; eval(str2eval);

VarLabels={'RecN', 'SampleYear', 'DayOfYear', 'HHMM', 'SS', 'Wind Speed',
'Wind Direction', 'WDIrSD', 'WspdSD', 'Net Radiation', 'NetRadSD', 'Air
T', 'Humidity', 'Tsd', 'RHsd', 'Tmax', 'Rhmax', 'Tmin', 'Rhmin',
'Rainfall', 'Wetness', 'WetSD', 'WetMax', 'WetMin', 'SoilT1', 'SoilT2',
'SoilT3', 'SoilT4', 'SoilRes1', 'SoilRes2', 'SoilRes3', 'SoilRes4',
'SoilRes5', 'SoilRes6', 'SoilRes7', 'SoilRes8'};

%block below calculates decimal day, starting from 0
SampleHr=fix(data(:,4)/100); SampleMin=data(:,4)-SampleHr*100; SampleSS=data(:,5);
DecDay=data(:,3)-1+SampleHr/24+SampleMin/60/24+SampleSS/3600/24;
keepTime=find(DecDay(:,1)>StrtTime);

%block below converts the soil resistances (upper-lower) into water potentials
using the
%following soil T: for soilRes2(upper?) and soilRes1(Lower?) T1, for
%soilRes3 and soilRes4 T2, for soilRes6 and soilRes5 T3, and for soilRes7
%and soilRes8 - T4. The new Var stored as SWP(:,1:8) - using conversion by the
default
%method recommended by the company (bottom of p.6 instructions for SMS253 manual),
%and also as SWPthompson(:,1:8) using the conversion from the top of that
%page. The the units are bars in both cases, divide by 0.01 to get kPa.
jj=0;%will be used for counting SWP columns
for ii=25:1:28;%i.e. for soilT in Cols 25-28
    %below will have a double increment/calculation; first solRes in col 29
    jj=jj+1; SWP(:,jj)=(data(:,jj+28)./(1-0.018*(data(:,ii)-21)))*0.07407-0.03704;

```

```

SWPthompson(:,jj)=0.01*data(:,jj+28)./(0.01306*(1.062*(34.21-
data(:,ii))+0.0106*data(:,ii).^2)-data(:,jj+28)));
jj=jj+1; SWP(:,jj)=data(:,jj+28)./(1-0.018*(data(:,ii)-21))*0.07407-0.03704;
SWPthompson(:,jj)=0.01*data(:,jj+28)./(0.01306*(1.062*(34.21-
data(:,ii))+0.0106*data(:,ii).^2)-data(:,jj+28)));
end; % for ii=...

%the block below caLCULATES average daily values of variables, e.g. wind
DecDays=StartTime:1:EndTime;
CurrentAverages=[];DailyAverages=[];DailySWP=[];CurrentDailySWP=[];
CurrentDailySWPthompson=[];DailySWPthompson=[];DailyTotals=[];CurrentDailyTotals=[];
];
MinRH=[];AllNoon=[];
for kk=1:1:length(DecDays);
    %CurrentDay=find(data(:,3)==DecDays(kk));
    %the above has been altered in May 2008 to reflect the requirement of
    %Canadian FWI, i.e. the day now end in noon!
    if kk>1
        CurrentDay=find((data(:,3)==DecDays(kk) & data(:,4)<=1200) |
(data(:,3)==DecDays(kk-1) & data(:,4)>1200)) ;
    else
        CurrentDay=find(data(:,3)==DecDays(kk));
    end;% if kk>1

    Noon=find(data(:,3)==DecDays(kk) & data(:,4)<=1300 & data(:,4)>1130);
    CurrentNoonValues=mean(data(Noon,:),1);
    AllNoon=[AllNoon;CurrentNoonValues];
    CurrentAverages=mean(data(CurrentDay,:),1);
    DailyAverages=[DailyAverages;CurrentAverages];
    CurrentMinRH=min(data(CurrentDay,13));
    MinRH=[MinRH;CurrentMinRH];
    CurrentDailyTotals=sum(data(CurrentDay,:));%e.g. need a sum, not average for
the rain
    DailyTotals=[DailyTotals;CurrentDailyTotals];
    CurrentDailySWP=mean(SWP(CurrentDay,:),1);
    DailySWP=[DailySWP;CurrentDailySWP];
    CurrentDailySWPthompson=mean(SWP(CurrentDay,:),1);
    DailySWPthompson=[DailySWPthompson;CurrentDailySWPthompson];

end;%for kk=1:1:length(DecDays);

DataForColin=[DailyAverages(:,2),DailyAverages(:,3),DailyAverages(:,16),AllNoon(:,13),AllNoon(:,6), DailyTotals(:,20)];
%this will be the data to calculate the canadian DMC and DC staff
save MeteoData4ColinProgram DataForColin -ASCII -TABS;

if IndPlotSwitch==1
for ii=1:1:TotalVar
    figure(ii);
    plot(DecDay,data(:,ii)); ylabel(VarLabels(ii));% xlabel('Decimal Day');
    xlabel('Day of Year');
    MinY=nanmin(data(keepTime,ii))-0.05*abs(nanmin(data(keepTime,ii)));
    axis([StartTime EndTime MinY 1.1*nanmax(data(keepTime,ii))]);
end %for ii...
end %if IndPlotSwitch==1
[Etrc75, SMDrc75,
PotSMD,PotentialE,Eo,JulDay,SatVapour,Wind24,VapourP,H,Ea]=PenmanF(DailyAverages,D
ailyTotals,SMDstart);

if Sum1PlotSwitch==1;
figure(40);

```

```

subplot(6,1,1)
ii=10
plot(DecDay,data(:,ii)); ylabel(VarLabels(ii)); xlabel('Decimal Day');
MinY=nanmin(data(keepTime,ii))-0.05*abs(nanmin(data(keepTime,ii)));
axis([StrtTime EndTime MinY 1.1*nanmax(data(keepTime,ii))]);

subplot(6,1,2)
ii=12;
plot(DecDay,data(:,ii)); ylabel(VarLabels(ii)); xlabel('Decimal Day');
MinY=nanmin(data(keepTime,ii))-0.05*abs(nanmin(data(keepTime,ii)));
axis([StrtTime EndTime MinY 1.1*nanmax(data(keepTime,ii))]);
subplot(6,1,3)
ii=20
plot(DecDay,data(:,ii)); ylabel(VarLabels(ii)); xlabel('Decimal Day');
MinY=nanmin(data(keepTime,ii))-0.05*abs(nanmin(data(keepTime,ii)));
axis([StrtTime EndTime MinY 1.1*nanmax(data(keepTime,ii))]);
subplot(6,1,4)
%ii=21
ii=6;%windspeed
plot(DecDay,data(:,ii)); ylabel(VarLabels(ii)); xlabel('Decimal Day');
MinY=nanmin(data(keepTime,ii))-0.05*abs(nanmin(data(keepTime,ii)));
axis([StrtTime EndTime MinY 1.1*nanmax(data(keepTime,ii))]);

subplot(6,1,5)
ii=25
plot(DecDay,data(:,ii)); ylabel(VarLabels(ii)); xlabel('Decimal Day');
MinY=nanmin(data(keepTime,ii))-0.05*abs(nanmin(data(keepTime,ii)));
axis([StrtTime EndTime MinY 1.1*nanmax(data(keepTime,ii))]);

subplot(6,1,6)
ii=29
plot(DecDay,data(:,ii)); ylabel(VarLabels(ii)); xlabel('Decimal Day');
MinY=nanmin(data(keepTime,ii))-0.05*abs(nanmin(data(keepTime,ii)));
axis([StrtTime EndTime MinY 1.1*nanmax(data(keepTime,ii))]);

FigureFileName=['Sum1Plot' '.jpg']
h=gcf; saveas(h,FigureFileName) %saves current figure

end%if Sum1PlotSwitch==1;

%%%%%%%
if Sum2PlotSwitch==1;
JJ=[6 10 13 20 28 35 12 36 ];
figure(41); % ii=25;
for jj=1:1:8 %i.e. 12 subplots
    subplot(4,2,jj);
    ii=JJ(jj);
    plot(DecDay,data(:,ii)); ylabel(VarLabels(ii));
    MinY=nanmin(data(keepTime,ii))-0.05*abs(nanmin(data(keepTime,ii)));
    axis([StrtTime EndTime MinY 1.1*nanmax(data(keepTime,ii))]);
    ii=ii+1;
end %for jj...
xlabel('Decimal Day');
subplot(4,2,7); xlabel('Decimal Day'); hold on;
orient tall;
FigureFileName=['Sum2Plot' '.jpg']
h=gcf; saveas(h,FigureFileName) %saves current figure

end %if Sum2PlotSwitch==1

%%%%%%%Now the SWP plotting bit%%%%%%

```

```

if SWPplotsSwitch==1;
figure(42); jj=0;
for ii=1:1:8;
    jj=jj+1;
    subplot(4,2,jj);
    plot(SWP(keepTime,ii),SWPthompson(keepTime,ii),'k.');//hold on;
    plot(SWP(keepTime,ii),SWP(keepTime,ii));legend('2methods','y=x',2);

    xlabel(['SWP' num2str(ii) ', bars']); ylabel(['SWPthompson' num2str(ii) ', bars']);
end;%for ii=1:1:8;
figure(42); orient tall;

figure(43); jj=0;
for ii=1:1:8;
    jj=jj+1;
    subplot(4,2,jj);
    plot(data(keepTime,ii+28),SWPthompson(keepTime,ii),'k.');//%SoilRes 1 in Col1 29
    xlabel(['SoilRes' num2str(ii) ', kOm']); ylabel(['SWPthompson' num2str(ii) ', bars']);
end;%for ii=1:1:8;
FigureFileName=['SWPplot' '.jpg']
h=gcf; saveas(h,FigureFileName) %saves current figure

figure(43); orient tall;
end;%if SWPplotsSwitch==1;

if PenmanPlotSwitch==1;
    figure(44);
    subplot(4,2,1); plot(JulDay, Eo); ylabel('Eo, mm');
    axis([StartTime EndTime min(Eo) 1.1*nanmax(Eo)]);

    subplot(4,2,2); plot(JulDay, PotentialE); ylabel('PotentialE, mm');
    CurrentAxis=axis; CurrentAxis(1)=StartTime;
    CurrentAxis(2)=EndTime;axis(CurrentAxis);
    subplot(4,2,3); plot(JulDay, DailyAverages(:,29)); ylabel('SoilRes1,kOm');
    CurrentAxis=axis; CurrentAxis(1)=StartTime;
    CurrentAxis(2)=EndTime;axis(CurrentAxis);
    subplot(4,2,4); plot(JulDay, DailyAverages(:,30)); ylabel('SoilRes2,kOm');
    CurrentAxis=axis; CurrentAxis(1)=StartTime;
    CurrentAxis(2)=EndTime;axis(CurrentAxis);
    subplot(4,2,5); plot(JulDay, DailySWP(:,1)); ylabel('SWP1, bar');
    CurrentAxis=axis; CurrentAxis(1)=StartTime;
    CurrentAxis(2)=EndTime;axis(CurrentAxis);
    subplot(4,2,6); plot(JulDay, DailySWP(:,2)); ylabel('SWP2, bar');
    CurrentAxis=axis; CurrentAxis(1)=StartTime;
    CurrentAxis(2)=EndTime;axis(CurrentAxis);
    subplot(4,2,7); plot(JulDay,DailyAverages(:,25)); ylabel('SoilT1');
    CurrentAxis=axis; CurrentAxis(1)=StartTime;
    CurrentAxis(2)=EndTime;axis(CurrentAxis);

    subplot(4,2,8); plot(JulDay, DailyAverages(:,12)); ylabel('AirT');
    CurrentAxis=axis; CurrentAxis(1)=StartTime;
    CurrentAxis(2)=EndTime;axis(CurrentAxis);

figure(45);
subplot(4,2,1); plot(JulDay, Eo); ylabel('Eo, mm');
CurrentAxis=axis; CurrentAxis(1)=StartTime;
CurrentAxis(2)=EndTime;axis(CurrentAxis);
subplot(4,2,2); plot(JulDay, PotentialE); ylabel('PotentialE, mm');


```

```

CurrentAxis=axis; CurrentAxis(1)=StartTime;
CurrentAxis(2)=EndTime; axis(CurrentAxis);
    subplot(4,2,3); plot(JulDay, DailyAverages(:,29)); ylabel('SoilRes1,kOm');
    CurrentAxis=axis; CurrentAxis(1)=StartTime;
CurrentAxis(2)=EndTime; axis(CurrentAxis);
    subplot(4,2,4); plot(JulDay, Wind24); ylabel('Wind24');
    CurrentAxis=axis; CurrentAxis(1)=StartTime;
CurrentAxis(2)=EndTime; axis(CurrentAxis);
    subplot(4,2,5); plot(JulDay, DailySWP(:,1)); ylabel('SWP1, bar');
    CurrentAxis=axis; CurrentAxis(1)=StartTime;
CurrentAxis(2)=EndTime; axis(CurrentAxis);
    subplot(4,2,6); plot(JulDay, PotSMD); ylabel('PotSMD');
    CurrentAxis=axis; CurrentAxis(1)=StartTime;
CurrentAxis(2)=EndTime; axis(CurrentAxis);
    subplot(4,2,7); plot(JulDay, SMDrc75); ylabel('SMDrc75');
    xlabel('Decimal Day');
    CurrentAxis=axis; CurrentAxis(1)=StartTime;
CurrentAxis(2)=EndTime; axis(CurrentAxis);

    subplot(4,2,8); plot(JulDay, EtRC75); ylabel('EtRC75'); xlabel('Decimal Day');
    CurrentAxis=axis; CurrentAxis(1)=StartTime;
CurrentAxis(2)=EndTime; axis(CurrentAxis);
    FigureFileName=['Penamn1Plot' '.jpg']
    h=gcf; saveas(h,FigureFileName) %saves current figure

figure(46);
subplot(2,1,1);plot(JulDay,H);xlabel('JulDay');ylabel('H');
CurrentAxis=axis; CurrentAxis(1)=StartTime;
CurrentAxis(2)=EndTime; axis(CurrentAxis);
    subplot(2,1,2);plot(JulDay,Ea);xlabel('JulDay');ylabel('Ea');
    CurrentAxis=axis; CurrentAxis(1)=StartTime;
CurrentAxis(2)=EndTime; axis(CurrentAxis);
    FigureFileName=['Penamn2Plot' '.jpg']
    h=gcf; saveas(h,FigureFileName) %saves current figure

end;%if PenmanPlotSwitch==1;

%%%%%%%Now the bit related to CWF1
if CanadaPlotSwitch==1;
CWF1labels={'T','RH','Wind', 'Rain', 'FFMC', 'DMC', 'DC', 'ISI', 'BUI', 'FWI',
'DSR', 'DecDay'};

str2eval=['load ' CWF1Sfname CWF1SfileExt]; eval(str2eval);
str2eval=['CWF1data=' CWF1Sfname]; eval(str2eval);

keepCanada=find(CWF1data(:,12)>=StartTime & floor(CWF1data(:,12))<=EndTime);
CWF1selected=CWF1data(keepCanada,:);

figure(47);
    subplot(5,1,1);plot(CWF1selected(:,12), CWF1selected(:,9)); ylabel('BUI');
    CurrentAxis=axis; CurrentAxis(1)=StartTime;
CurrentAxis(2)=EndTime; axis(CurrentAxis);
    subplot(5,1,2);plot(CWF1selected(:,12), CWF1selected(:,6));ylabel('DMC');
    CurrentAxis=axis; CurrentAxis(1)=StartTime;
CurrentAxis(2)=EndTime; axis(CurrentAxis);

    subplot(5,1,3); plot(JulDay, EtRC75); ylabel('Etr, mm');
    axis([StartTime EndTime min(Eo) 1.1*nanmax(Eo)]);

    subplot(5,1,4); plot(JulDay, DailySWP(:,1)); ylabel('SWP1, bar');

```

```

CurrentAxis=axis; CurrentAxis(1)=StartTime;
CurrentAxis(2)=EndTime;axis(CurrentAxis);

subplot(5,1,5); plot(JulDay,SMDrc75); ylabel('SMD');%meaning SMDrc75
    xlabel('Day Of Year');
CurrentAxis=axis; CurrentAxis(1)=StartTime;
CurrentAxis(2)=EndTime;axis(CurrentAxis);

%%%%%%%%%%%%%
FigureFileName=['CompareIndices' '.jpg']
h=gcf; saveas(h,FigureFileName) %saves current figure

JJ=[4:1:11];
figure(48);
for jj=1:1:8 %i.e. all subplots
    subplot(4,2,jj);
    ii=JJ(jj);
    plot(CWFISelected(:,12),CWFISelected(:,ii)); ylabel(CWfIlabels(ii));
    CurrentAxis=axis; CurrentAxis(1)=StartTime;
CurrentAxis(2)=EndTime;axis(CurrentAxis);
    ii=ii+1;
end %for jj...
xlabel('Decimal Day');
    subplot(4,2,7); xlabel('Decimal Day'); hold on;
orient tall;
FigureFileName=['CanadianIndicies' '.jpg']
h=gcf; saveas(h,FigureFileName) %saves current figure

%Now the stats bit
Data4stats=[CWFISelected SMDrc75 DailySWP(:,1:8)];
SWPnames={};
for nn=1:1:8
    SWPnames(1,nn)={['SWP' num2str(nn)}];
end %for nn-1:1:8
NamesCor=[CWfIlabels'; {'SMD'}; SWPnames'];
ColNumberCor=[1:1:21];
Fcorrelations(Data4stats,ColNumberCor,NamesCor,'AllCor','A3',XLSfile2write);

pack;

end %if CanadaPlotSwitch==1

```

INDEX

A

- AAT, xv, xvi, 679, 680, 681, 682, 683, 684, 685, 686, 687, 688
absorption, 214, 336, 639, 640, 642, 645
absorption coefficient, 214
acceleration, 9, 62, 63, 171, 585
accidents, xv, 635
accounting, 48, 561
ACE, 610
acetone, 279
achievement, 64
ACM, 427, 631
acoustic, xiii, 171, 175, 188, 197, 422, 429, 511, 620
acoustic waves, 511
adaptation, xii, 295, 329, 334
ADC, 118
adiabatic, 26, 43, 115, 124, 214, 523, 551, 585
adjustment, 142, 307, 616
advection-diffusion, 124
aeronautical, 567
aerosol, 279, 668
aerosols, 637, 669, 670
age, 32, 106, 627
agent, 577
agents, xiv, 575, 577, 594, 629
agriculture, 680, 688
aid, 488, 621
Air Force, 108, 630, 670
air pollution, 278
air quality, xvi, 278, 288, 292, 691, 692
airborne particles, 645
Aircraft, 54, 237
airports, 637
Airship, 423, 424
Alaska, 8, 19, 35
Alberta, 631, 632
Algeria, 293, 294, 296, 300, 310, 312, 316, 322
alluvial, 173
alternative, xi, 104, 115, 150, 159, 278, 291, 293, 297, 298, 302, 316, 320, 499, 509, 592, 593, 607, 630, 638, 657, 668
alters, 48
amalgam, 333
ambient air, xi, xv, 217, 277, 279, 284, 679, 680
ambient air temperature, xv, 679, 680
ambient pressure, xiii, 430, 431, 432
ambiguity, 171
ammonia, 279
amplitude, 8, 50, 112, 119, 152, 154, 155, 156, 175, 177, 179, 183, 186, 190, 192, 193, 194, 195, 196, 198, 200, 526, 531, 541, 553, 555, 557, 559, 562, 564, 569, 674
AMS, 51, 282
Amsterdam, 55, 107, 163, 164, 201, 203
analog, 210
anemometers, 249
angular velocity, 8, 474
animals, xiii, 469, 470
anisotropy, viii, 111, 112, 114, 116, 119, 135, 150, 151, 153, 157, 161, 183, 541, 544, 565, 608
Anisotropy, 633
ANN, 298, 300, 301, 302, 303, 304, 305, 307, 309, 312, 314, 315, 323
annealing, 344
anomalous, 114, 115, 117, 122, 125, 145, 150, 154, 161
anomalous diffusion, 154
Antarctic, 19, 53, 54, 55, 57, 676
Arabia, 296, 299, 305, 308, 326
Arctic, vii, 3, 4, 5, 6, 7, 8, 11, 12, 13, 16, 18, 19, 20, 21, 23, 24, 25, 26, 27, 28, 29, 30, 31, 32,

35, 36, 37, 38, 39, 41, 43, 45, 47, 48, 49, 50,
 51, 52, 53, 54, 55, 56, 57, 58
 Arctic Ocean, vii, 3, 5, 18, 19, 21, 25, 36, 39, 45,
 49, 50, 51, 52, 56, 57
 argon, 216
 arid, 294, 321
 Army, 502
 artificial intelligence, 293, 294, 300, 302, 324,
 325
 ash, 51, 339
 Asia, 486
 Asian, 19, 463, 466
 aspect ratio, 223, 532, 552
 assessment, xi, 6, 210, 239, 294, 522, 576, 594,
 595, 619, 692, 698
 assignment, 540, 546
 assumptions, 10, 63, 72, 126, 128, 157, 159, 674
 astrophysics, 112, 115
 asymmetry, 5, 43, 171, 179, 533, 534, 538, 546,
 557, 643
 Athens, 300, 324
 Atlantic, 5, 8, 16, 18, 21, 23, 25, 32, 33, 35, 37,
 43, 44, 47, 48, 49, 50
 Atlas, 6, 7, 8, 53, 54, 57, 296
 atmospheric pressure, 67, 218, 309
 Australia, 167, 169, 170, 172, 173, 175, 179, 180,
 181, 182, 183, 184, 185, 186, 187, 188, 189,
 190, 191, 192, 194, 198, 199, 200, 201, 202,
 203, 204
 Austria, 338, 340
 autocorrelation, xv, 176, 216, 305, 679, 680, 681
 automata, 65
 autoregressive model, 305

B

backscattering, 668
 Bahrain, 295, 321
 ballistic missile, 448
 ballistic missiles, 448
 bandwidth, 390
 barrier, 147, 488
 battery, 249, 266
 Bayesian, 302, 594, 631, 632, 633
 beam radiation, 296, 305
 beams, 647, 668
 behavior, xiii, 61, 65, 105, 112, 116, 117, 120,
 130, 134, 136, 154, 297, 356, 430, 445, 450,
 451, 512, 524, 546, 565
 Beijing, 107, 162, 236, 486
 benchmark, xiv, 297, 300, 505, 509, 510, 592
 benchmarking, x, 205, 207, 209, 210, 212, 222,
 234
 bending, 114

benzene, 278
 Bessel, 641
 bias, 14, 18, 48, 180, 278, 288, 660, 666, 673
 bifurcation, 118
 binomial distribution, 141
 biomass, 101
 birds, xiii, 469, 470
 blocks, 609, 610, 611, 612, 613, 620
 boats, 65, 488, 496
 body shape, 448
 body temperature, 25
 bogs, 19
 Bohr, 64, 106
 boreal forest, 693
 Boston, 425, 503
 Botanical Garden, 623, 624
 Botswana, 296
 boundary conditions, 40, 116, 123, 125, 169, 210,
 211, 244, 275, 382, 457, 502, 508, 509, 511,
 516, 523, 530, 531, 540, 541, 551, 552, 568,
 577, 578, 580, 589, 606, 611, 616, 629
 bounds, 116, 588
 Boussinesq, 212, 585, 586, 587, 591, 620
 brass, 216
 Brazil, 296, 322, 670
 breakdown, 47, 48, 55, 676
 British Columbia, 614, 631
 broad spectrum, ix, 167
 Brownian motion, 112, 127, 130, 154
 bubble, 346, 424
 buffer, 517, 613, 614
 buildings, xiv, 294, 575, 576, 577, 578, 580, 581,
 584, 587, 589, 591, 606, 614, 620, 621, 622,
 623, 624, 629
 burn, 209
 burning, 218, 522

C

C++, 516
 cables, 470, 474
 CAD, 344, 397
 calculus, 64, 345, 351, 410, 412
 calibration, ix, 94, 167, 240, 282, 453, 454, 567,
 682
 campaigns, vii, 3, 5, 6, 11, 13, 16, 18, 19, 49, 638
 Canada, 203, 205, 222, 235, 238, 315, 322, 327,
 575, 577, 584, 614, 630, 631
 capsule, 459, 461, 468
 carbon, 279, 697, 698
 carbon dioxide, 697
 Cartesian coordinates, 506, 510, 511, 585
 case study, xv, xvi, 629, 679, 681, 683, 688, 691
 casting, 582

- cation, 630
causality, 155
cavities, 280
CDT, 623, 625
cell, xiii, 21, 43, 45, 50, 140, 251, 282, 375, 429, 430, 431, 432, 464, 476, 514, 515, 532, 581, 582, 583, 599, 600, 601, 602, 603, 607, 608, 609, 616, 617
Centaur, 456
ceramic, 223, 224
CH₄, 214
channels, xiv, 118, 182, 183, 241, 275, 505, 509, 517, 522, 523
chaos, 64, 87, 119, 164, 337
chemical composition, 637
chemical kinetics, 214
chemicals, 594
chemiluminescence, 282
China, 59, 106, 236, 466, 486
circulation, vii, xiv, 3, 4, 5, 18, 20, 21, 32, 38, 45, 49, 50, 51, 53, 55, 76, 77, 275, 470, 472, 480, 481, 482, 485, 523, 524, 689
CISM, 275
classical, vii, viii, ix, 59, 60, 64, 112, 113, 114, 127, 161, 167, 300, 301, 308, 654
classical physics, vii, viii, 59, 64
classification, 7, 125
climate change, xii, 5, 7, 54, 55, 57, 65, 329, 333, 337, 339, 340, 341, 489, 697
climatology, vii, 3, 4, 5, 6, 7, 8, 10, 11, 12, 13, 14, 18, 19, 27, 31, 32, 35, 36, 38, 41, 43, 48, 49, 50, 327, 332, 681
closure, xv, 18, 64, 71, 73, 74, 77, 101, 107, 208, 210, 212, 215, 440, 508, 585, 586, 587, 588, 591, 592, 629, 674, 675, 676, 677
clouds, 5, 20, 28, 29, 31, 43, 49, 51, 58, 305, 594, 637, 668
clusters, 385, 630
CMC, 631
CML, 424
CO₂, 55, 214, 223
coastal areas, 32
codes, 115, 502, 505, 510, 670, 692, 697
cofactors, 364
cognition, 64
coherence, 81, 152
coil, 118
collisions, 116
Columbia, 614, 631
combustion, x, xvi, 205, 206, 208, 210, 213, 214, 215, 216, 222, 223, 224, 225, 232, 233, 234, 691, 692
combustion chamber, 222, 223, 224, 225, 233
common rule, 615
communication, 41, 387
communities, 60, 105
community, 63
compatibility, 515, 590
competition, 64, 87, 115, 124, 487
complex systems, xi, 293
complexity, 65, 243, 487, 496, 508, 561, 567, 643, 650
composites, 337
compounds, 278, 318
compressibility, 457, 511, 526, 564, 565
computation, xiii, 65, 159, 275, 345, 385, 408, 423, 424, 459, 467, 468, 469, 472, 474, 477, 479, 484, 502, 581, 583, 584, 630, 681
computational fluid dynamics, xiv, 459, 487, 508, 578, 584
Computational Fluid Dynamics (CFD), 422, 426, 450, 453, 464, 466, 468, 488, 507
computational grid, 616
computer simulations, 113
computer systems, 614
computing, 126, 207, 208, 288, 301, 315, 316, 327, 354, 383, 385, 397, 509, 629, 681
conception, 154, 241
condensation, 636, 637
conductance, xi, 277, 284, 286, 287
conduction, 26, 63, 64, 70, 102, 229
conductive, vii, 3, 21, 37, 38, 39, 50
conductivity, 62, 63, 102, 157, 179, 215, 505, 507, 511
confidence interval, 682
configuration, x, 118, 206, 233, 234, 307, 312, 318, 434, 439, 442, 445, 450, 453, 459, 461, 654
confinement, 112, 114, 123, 145, 162
conflict, 100
conformity, 268
Congress, 324, 463, 486
connectionist, 315, 326, 327
connectionist models, 315, 327
connectivity, 375, 389, 392, 394, 581, 609, 611, 612
conservation, 128, 153, 155, 210, 211, 278, 439, 456, 457, 577, 585, 592, 601, 610, 697
constraints, 171, 348, 358, 596, 597, 600
construction, 154, 279, 382, 508, 609
consumption, 218, 508
contaminant, ix, 55, 167, 192, 576, 591, 592, 593, 596, 630
contaminants, xiv, 575, 576, 579
contamination, 65, 290, 577

continuity, 90, 91, 102, 240, 335, 349, 409, 473, 522, 585, 601, 602, 603, 605, 607
control, xi, xiii, xiv, 101, 293, 296, 306, 307, 325, 336, 341, 344, 349, 423, 424, 425, 429, 452, 470, 471, 478, 482, 484, 485, 494, 508, 515, 551, 581, 598, 599, 600, 609, 610, 616, 630
convection, vii, 3, 5, 25, 28, 29, 31, 33, 42, 43, 49, 60, 62, 99, 100, 101, 102, 231, 352, 418, 426, 609
convective, 10, 17, 18, 19, 21, 25, 32, 36, 38, 39, 43, 45, 48, 50, 99, 100, 102, 103, 104, 233, 351, 352, 362, 366, 367, 383, 396, 408, 600, 606, 675
convergence, viii, 36, 40, 59, 92, 99, 100, 102, 103, 104, 106, 215, 408, 606, 607
conversion, 282, 321, 322, 387, 474, 699
convex, xiv, 126, 130, 469, 472
cooling, 4, 5, 17, 20, 26, 27, 29, 31, 36, 38, 41, 44, 55, 208, 297, 637
Copenhagen, 670
Coriolis effect, 676
correlation analysis, 176, 694
correlation coefficient, 95, 97, 98, 186, 300, 301, 302, 304, 312, 314, 317, 689, 694
correlation function, 120, 122, 560
correlations, xv, 112, 114, 145, 161, 274, 294, 321, 322, 335, 467, 679, 681, 693
cosine, 524, 526, 568, 640
cost-effective, 278
countermeasures, xv, 635
coupling, viii, 4, 6, 38, 48, 49, 59, 65, 66, 69, 70, 71, 72, 77, 89, 90, 91, 92, 93, 94, 95, 96, 97, 98, 99, 105, 106, 159, 213, 215, 465, 468, 474, 500, 577, 584, 611, 630
covering, 20, 50, 516, 577, 688
Cp, 206, 266, 461
CPU, 612, 630
CRC, 164
Croatia, 673
cross-sectional, 281, 457
cross-validation, 682
CRS, 387, 393, 397
crystals, 28, 29, 637
CST, 620, 621
cultural heritage, 278
cumulative frequency, 296
cycles, ix, 48, 75, 168, 173, 179, 181, 183, 184, 189, 200, 630, 647, 697
cyclone, 77
cyclones, 32, 673
Cyprus, 302, 320, 632

D

damping, 451, 512, 516, 569
danger, 692, 697, 698
data analysis, vii, 3, 29, 38, 298
data availability, 5
data collection, 302, 330, 334
data generation, 308
data set, 8, 12, 13, 21, 23, 44, 47, 52, 54, 55, 175, 177, 178, 189, 190, 192, 193, 194, 198, 200, 301, 302, 305, 312, 314, 580, 620
data structure, 375, 581, 609
database, 6, 53, 209, 216, 222, 229, 297, 621, 654, 675, 681, 688, 689
decay, 50, 61, 73, 120, 141, 154, 459, 565, 577, 588
decision makers, 577
decisions, 330, 488, 577
decomposition, 154, 155, 385, 386, 387, 522, 585, 606, 609, 697
decoupling, vii, 3, 4, 21, 32, 38, 48, 49, 52, 602, 673
deficit, xvi, 40, 691, 693
definition, vii, 3, 61, 72, 127, 140, 177, 206, 207, 522, 529, 640
deformation, 131, 344, 356, 358, 359, 360, 378, 379, 397, 406, 425
degenerate, 126, 130, 584
degradation, 55, 147, 669
degrees of freedom, 65, 66, 112, 137, 681
denoising, 426
density fluctuations, 120, 121, 122, 124, 125, 131, 561, 563, 564, 565, 566
dependent variable, 124, 606
deposition, 43, 118, 576, 577
derivatives, 154, 243, 246, 262, 323, 352, 445, 598, 641
designers, 494, 499
destruction, 587, 599, 607
detachment, 405
detection, 176, 290, 669
detection techniques, 176
deviation, 61, 123, 130, 132, 133, 136, 141, 143, 151, 154, 156, 158, 159, 224, 308, 482, 548, 552, 556, 684
diamonds, 151
differential equations, 164, 212, 240, 242, 245, 264, 594
differentiation, 244, 354, 375, 376
diffraction, 559, 644
diffusion process, 278, 287, 426
diffusion time, 153
diffusivities, 53

diffusivity, 19, 40, 41, 125, 206, 210, 213, 215, 592, 593, 594, 598, 614, 676
digital images, 667
digitization, 454
dimensionality, 113, 540
Dirac delta function, 596
direct action, 509
direct measure, 43, 287, 299, 300, 323, 496, 559
direct observation, 68
directives, 612
Dirichlet boundary conditions, 606
discharges, 117, 147
discontinuity, 26, 442, 515
discretization, 245, 374, 474, 509, 515, 577, 580, 598, 600, 603, 615, 616
discriminant analysis, 340
disorder, 64, 82
dispersion, ix, xiv, 141, 167, 168, 192, 200, 275, 339, 560, 561, 564, 569, 575, 576, 577, 578, 579, 591, 592, 593, 594, 595, 596, 614, 615, 620, 625, 626, 629, 630, 675, 688
displacement, 94, 116, 159, 162, 356, 357, 359, 377, 378, 383, 553, 579, 615
dissipative structure, viii, 111, 114, 116, 138, 141, 142, 143, 145, 149, 150, 151, 152, 157, 158, 161
dissipative structures, viii, 111, 114, 116, 138, 141, 142, 143, 145, 149, 150, 151, 152, 157, 158, 161
dissociation, 213, 214
distilled water, 282
distortions, 558, 559
distributed memory, 387, 612
distribution function, 112, 137, 140, 160, 197, 198
divergence, viii, 59, 73, 92, 99, 100, 102, 103, 104, 105, 106, 264, 361, 524, 599, 605, 647
divertor, 117, 118, 120, 123, 134, 149
Doppler, 18, 171, 175, 188, 201, 221, 222, 237, 615, 620, 623
download, 396, 425, 426
draft, xi, 277, 283, 284, 423
drainage, 32, 674
drought, 697
Drought, 693, 696, 698
drying, 43, 697
duality, 593, 606, 626
dust, 60, 636, 643
dynamic loads, 445
dynamic theory, 87
dynamic viscosity, 242, 243, 247, 253, 256, 258, 516, 541

E

earth, viii, 36, 59, 62, 66, 101, 106, 330, 559
Earth Science, 277
ecological, 335, 339, 470, 692, 697
ecological damage, 692, 697
ecologists, 330
ecology, 332, 335, 339
economics, 63
ecosystems, ix, xii, 5, 167, 329, 692
eddies, vii, 5, 61, 75, 114, 116, 119, 133, 157, 169, 185, 192, 495, 509, 513, 534, 536, 541, 550, 552, 555, 557, 558, 559, 561, 564, 565, 569, 596, 674
education, 162, 675
Egypt, 303
electric field, 117, 562
electricity, 5, 63
electrodes, 118
electromagnetic, 344, 559, 560, 561, 638, 639, 640
electromagnetic wave, 559, 561, 639, 640
electron, 115, 117, 124, 279
electronic systems, 317
emergency response, 576, 577, 629
emission, xiii, 209, 335, 339, 464, 469, 470, 593, 594, 626
energy supply, 61, 73, 105
energy transfer, 114, 116, 157, 161, 513, 515, 534
England, 56, 236, 692, 698
Enthalpy, 237
entropy, viii, 59, 67, 69, 71, 89, 129
environmental conditions, 488
environmental factors, 332
environmental impact, 692
EPA, 204
equality, 150
equilibrium, viii, 9, 25, 26, 27, 33, 36, 58, 59, 63, 67, 68, 89, 90, 106, 107, 214, 215, 496, 498, 499, 560, 588, 607, 608, 609, 616, 617
equilibrium state, 68
ERA, 13, 16, 18, 21, 25, 32, 33, 34, 37, 43, 45, 49, 57
estimating, xii, 293, 294, 295, 296, 301, 302, 303, 304, 305, 309, 310, 311, 314, 318, 320, 321, 322, 324, 325, 453, 551, 658
estimation process, 314
estimator, 658, 663
estuaries, ix, 167, 168, 169, 171, 173, 183, 186, 188, 189, 190, 192, 199, 200, 204
estuarine, ix, 167, 169, 170, 173, 176, 177, 179, 183, 188, 189, 190, 191, 197, 198, 200

estuarine systems, ix, 167, 188, 189, 200
 ethylbenzene, 278
 Euler equations, xiii, 429, 431, 433, 446, 453, 454, 456, 457
 Eulerian, 119, 135, 176, 579, 591, 592, 594, 614, 620, 625, 629
 Eurasia, 46, 54
 Europe, 19, 332, 333, 334, 338
 European Commission, 291
 evaporation, 13, 29, 36, 48, 57, 58, 79, 281, 283, 284, 285, 636, 693
 evapotranspiration, 693
 evening, 686
 evolution, xii, 8, 128, 175, 329, 337, 338, 345, 530, 579, 601
 exceedance, 619
 exchange rate, 620
 exchange rates, 620
 execution, 614
 experimental condition, 80
 exposure, 278, 282, 283, 285, 288, 290, 594
 external validation, 335
 extinction, xv, 61, 73, 105, 635, 639, 640, 641, 642, 644, 645, 646, 647, 649, 650, 657, 667
 extraction, 282
 extrapolation, 12, 101, 106, 189, 515, 576, 686

F

family, 332, 335, 350
 farmers, 330
 faults, 240
 feedback, 48, 317
 FEM, 343, 426, 468
 FFT, 445
 fidelity, xiv, 575, 577
 filament, ix, 111, 145, 150, 161
 filters, 282, 509
 filtration, 513
 financial support, 51, 422
 finite differences, 251, 252, 674
 finite element method, 244, 424, 425
 finite volume, xiii, 241, 244, 245, 263, 273, 439, 454, 469, 474, 509, 598, 622
 finite volume method, xiii, 241, 245, 263, 273, 469, 474
 fire, xvi, 691, 692, 697, 698
 fire hazard, 692
 fires, xvi, 691, 692, 697, 698
 first principles, 114
 flame, x, 205, 206, 209, 212, 213, 214, 215, 216, 218, 220, 221, 222, 223, 224, 225, 229, 230, 234
 flammability, 697

flare, 459, 461, 462
 flatness, 131, 543, 544, 546, 547
 flexibility, xi, 293, 445
 flight, 443, 445, 452, 454, 456, 458, 459, 466, 468
 floating, xiii, 469, 470, 479, 485, 584
 flood, ix, 167, 169, 179, 180, 181, 183, 188, 190, 191, 192, 200
 flow rate, 224, 458, 615
 FLUENT, xi, 239, 241, 264, 268, 274
 fluid mechanics, 204, 240, 241, 423
 fluorescence, 615
 focusing, 122
 FOG, 635
 foils, 495
 forecasting, xi, 293, 294, 297, 298, 299, 300, 301, 306, 307, 309, 313, 314, 315, 318, 320, 323, 324, 325, 326, 330, 333, 337, 338, 339, 340, 692
 forest fire, 698
 forest fires, 698
 Forestry, 698
 formaldehyde, 279
 Fortran, 516
 fossil, 489
 fossil fuel, 489
 fossil fuels, 489
 Fourier, viii, 59, 63, 64, 66, 69, 70, 77, 81, 105, 107, 120, 121, 152, 294, 297, 321, 445, 647, 648
 Fourier analysis, 121, 294, 321
 Fox, 291
 FPGA, xii, 293, 294, 317, 318, 319, 320, 327
 FPGAs, 317
 fractal analysis, 330
 fractal dimension, 140, 141, 159
 fractal properties, 113
 fractality, 122, 155
 France, 164, 337, 486, 635, 654, 668, 669, 679, 689
 free energy, 129, 214
 freedom, 64, 66, 87, 112, 114, 137, 288, 681
 freezing, 49
 frequency distribution, 321
 freshwater, 58, 173, 179
 friction, 32, 40, 50, 78, 79, 81, 82, 93, 94, 96, 98, 211, 476, 508, 524, 526, 551, 569, 588, 608, 615
 FTC, 572
 fuel, xvi, 209, 213, 214, 216, 218, 222, 223, 224, 225, 229, 231, 470, 522, 691, 692, 697
 fuel type, 692
 Fur, 601

fusion, viii, 111, 113, 114, 115, 116, 117, 118, 119, 121, 122, 124, 136, 144, 145, 152, 154, 159, 160, 161, 162, 587
fuzzy logic, 302, 309, 310, 320

G

G4, 663, 664
galactic, 60, 66
Gamma, 141
gas, vii, xi, xiii, 64, 67, 118, 208, 209, 214, 222, 229, 233, 235, 277, 279, 280, 281, 284, 286, 429, 433, 440, 453, 457, 464, 510, 540, 542, 619, 620, 625, 675
gas jet, xiii, 429, 433, 464
gas turbine, 208, 209, 233, 235
gases, 64, 282
Gaussian, viii, 111, 112, 113, 115, 123, 128, 131, 135, 137, 160, 169, 171, 183, 192, 200, 295, 321, 445, 523, 544, 546, 560, 576, 618, 629, 658
GCC, 20, 40, 42
gene, xii, 329, 334
generalization, xi, 138, 293, 304, 609, 648
generation, xiv, 31, 78, 80, 294, 300, 301, 306, 307, 308, 316, 321, 323, 325, 326, 360, 511, 550, 551, 552, 553, 565, 575, 580, 599, 609, 621, 629
genetic algorithms, 344
genetics, 63
Geographic Information System, 334, 340
geometrical parameters, 241
Georgia, 327
Germany, 167, 203, 326, 486, 632, 668, 679
GH, 215
Gibbs, 214
Gibbs free energy, 214
GIS, xii, xv, 329, 334, 335, 337, 679, 681, 682, 688, 689
glaciers, 39, 689
glass, 281, 283, 284, 285
global climate change, xv, 679
global warming, 56, 330, 470
GPS, 296
grains, 338
graph, 181, 243, 252, 262, 265, 282, 387
graphite, 118
grass, 27, 55, 333, 338, 340, 341
grasses, 332, 333, 335, 337, 340
grassland, 336
gravity, 9, 39, 40, 62, 66, 89, 91, 356, 494, 676
Greece, 324, 325, 326
greed, 624
greenhouse, xvi, 691, 697

Greenhouse, 54
greenhouse gas, xvi, 691, 697
greenhouse gases, xvi, 691
Greenland, 5, 7, 8, 16, 20, 31, 33, 39, 40, 41, 42, 53, 54, 57
grid environment, 425
grid generation, xiv, 575, 579, 609
grid resolution, 630
grids, xiv, 217, 223, 475, 479, 484, 575, 580, 629
groundwater, 692
groups, 20, 63, 72, 145, 489, 490, 577, 584, 589
growth, 54, 119, 240, 252, 262, 271, 332, 333, 336, 529, 576
guidance, 452, 499
guidelines, 208, 274, 282, 439

H

H1, 370
H₂, 214, 238, 370
habitation, 60
halos, 646, 650, 662, 663, 666, 667
Hamiltonian, 126, 130
handling, 104, 290, 490
harmful effects, xiii, 469, 470
harmonics, 513
haze, viii, 4, 29, 31
HDL, 317
hearing, 159
heat capacity, 49
heat conductivity, 62
heat loss, xvi, 37, 50, 214, 222, 691, 692
heat release, 222
heat shield, 439, 441, 442, 443, 444, 445, 446, 447, 448, 453, 454, 455, 456, 457, 464, 465
heat storage, 25, 101
heat transfer, xiv, 63, 209, 210, 211, 223, 233, 274, 275, 448, 466, 505, 508, 510, 543, 548, 549, 550, 551, 555, 557, 568, 569
heating, 4, 21, 25, 29, 31, 43, 50, 56, 112, 210, 297, 450, 466, 467, 468, 577
heating rate, 21, 50, 56
helicity, 115, 153
heliosphere, 145
helium, 117, 209, 216, 467
hemisphere, 438, 439, 441, 448, 451, 464, 465, 466
heterogeneity, viii, 9, 13, 29, 49, 59, 101, 103, 106
heterogeneous, viii, 8, 60, 92, 99, 102, 104, 106
heuristic, 355, 377
high pressure, 464
high resolution, 55, 355, 356, 377, 397, 515, 567, 688

- high temperature, 229
 high-risk, 333
 high-speed, 466
 Hilbert, 125, 630
 Hilbert space, 630
 histogram, 123, 192, 195, 445, 685
 Holland, 55, 56, 107, 163
 homogeneity, 19, 101, 106, 121, 674
 Hong Kong, 323
 horizon, 33, 296, 323, 623, 644, 645, 646
 House, 107, 278, 570, 571
 HPC, 346, 385, 425, 426
 hub, 475
 human, xv, 6, 60, 105, 635, 636, 638, 642
 human activity, 6
 humans, 107, 108
 humidity, vii, xii, 3, 4, 9, 12, 17, 20, 21, 23, 29,
 31, 43, 44, 47, 67, 71, 79, 91, 94, 106, 293,
 294, 298, 300, 301, 304, 305, 315, 316, 317,
 320, 325, 332, 636, 670, 692
 hybrid, 311, 312, 313, 316, 320, 446, 489, 508,
 629
 hydro, 163
 hydrocarbon, 214
 hydrodynamic, ix, 111, 112, 113, 114, 115, 136,
 137, 138, 150, 153, 157, 158, 161, 345, 470,
 471, 494, 495, 496
 hydrodynamics, 138, 161, 488, 499
 hydrogen, 215, 216, 220, 279
 hydrologic, 57
 hydrological, 4, 49, 692
 hydrological cycle, 4, 49
 hydrothermal, 698
 hypothesis, 29, 31, 101, 114, 117, 119, 123, 125,
 128, 147, 154, 208, 212, 334, 511, 529, 561,
 587, 592, 594, 620
 hysteresis, 450, 466
- I
- Iberian Peninsula, 334, 337, 339, 340
 ice, vii, 3, 4, 6, 11, 12, 13, 18, 19, 20, 21, 25, 26,
 28, 29, 31, 36, 37, 39, 42, 43, 45, 48, 49, 50,
 51, 52, 53, 54, 55, 57, 637
 identification, xi, 60, 293, 316, 321, 424, 427,
 602
 identification problem, 316
 IGRA, 6, 12, 13, 14, 21, 23, 24, 32, 45, 49
 Illinois, 7, 202, 237
 illumination, 636, 648, 670
 IMA, 503
 imagery, 45
 images, xv, 55, 302, 337, 650, 654, 658, 662,
 667, 668, 670, 679, 684
 implementation, xii, xiv, 106, 293, 294, 318, 319,
 377, 385, 515, 567, 575, 581, 583, 589, 600,
 606, 608, 609, 614, 667, 697
 imports, 578, 606
 impurities, 20
 in situ, 12, 17, 18, 43, 49, 594
 incidence, 299, 303, 304, 325, 439
 inclusion, xv, 445, 511, 577, 589, 605, 624, 629,
 630, 679, 688
 incompressible, x, 73, 90, 91, 115, 120, 123, 125,
 157, 239, 240, 241, 242, 274, 275, 345, 360,
 424, 425, 426, 473, 522, 523, 585, 601
 independence, 123, 125, 217, 224
 independent variable, 330
 indeterminacy, 548
 indexing, 612, 613
 India, 197, 295, 301, 322, 466
 Indian, 203, 303, 424, 464, 465
 indication, 645
 indicators, 7, 295, 310
 indices, xvi, 347, 366, 375, 581, 585, 614, 683,
 691, 692, 693
 Indonesia, 698
 industrial, 235, 241, 343, 425, 589, 594
 industrial chemicals, 594
 industry, 240, 345
 inert, 215
 inertia, xvi, 478, 691, 692
 infinite, 100, 114, 530
 Information System, 334, 340
 infrared, 304, 309, 336, 337, 572, 620
 infrared light, 336, 337
 infrastructure, 5
 inhomogeneities, 53, 560
 inhomogeneity, 113, 138, 562
 initiation, 33
 injection, xiv, 168, 505, 510, 517, 522, 523, 524,
 526, 527, 567, 568
 injuries, 577
 injury, xiii, 469, 470
 insertion, 599
 insight, 13, 28, 152
 instabilities, 112, 159, 171
 instability, 33, 50, 52, 448, 459, 466, 513, 552,
 553, 565
 instruments, 5, 18, 171, 297, 320, 620
 insulation, 223, 224
 integration, 77, 366, 522, 588, 623, 624
 intelligence, xi, 293, 302, 325
 interaction, xii, xiv, 8, 103, 112, 116, 123, 125,
 153, 193, 197, 222, 346, 424, 429, 445, 465,
 475, 494, 499, 500, 502, 505, 510, 529, 548,
 549, 550, 555, 557, 568, 569, 639

interactions, x, 28, 205, 212, 231, 234, 337, 488, 496, 515, 576, 636
 interdependence, 152
 interface, 496, 516, 531, 577, 578
 interfacial layer, 49
 Intergovernmental Panel on Climate Change (IPCC), 5, 6, 48, 54, 57, 337
 interplanetary, 116, 118, 119, 136, 145, 153
 interval, 7, 45, 146, 154, 160, 175, 177, 232, 361, 394, 524, 533, 555, 564, 595, 620
 intrinsic, 40, 118, 646, 647, 648, 649, 654, 657, 662
 invariants, 115, 125
 inventions, 486
 inversion, 5, 21, 26, 27, 28, 43, 45, 46, 48, 49, 50, 379, 636, 673, 687, 688
 inversions, vii, 4, 27, 29, 31, 37, 45, 55, 57
 Investigations, 429, 508
 investment, 330
 ions, 282
 IOP, 623, 625, 629
 irradiation, 294, 295, 296, 297, 299, 300, 301, 304, 305, 309, 310, 311, 315, 317, 321, 322, 323, 324, 325, 326
 island, 118
 isolation, 5, 152, 609
 isothermal, xiv, 27, 209, 215, 505, 510, 534, 536, 540, 543, 548, 568, 569
 isotropic, 61, 73, 74, 105, 112, 113, 114, 116, 119, 135, 139, 142, 145, 150, 151, 169, 200, 212, 213, 440, 561, 588, 643
 isotropy, 61
 Italy, 204, 293
 iteration, 356, 359, 550, 605, 611
 iterative solution, 581, 602

J

Jacobian, 414, 609
 Japan, xi, 108, 172, 173, 174, 175, 179, 180, 181, 182, 183, 184, 185, 186, 187, 199, 200, 277, 279, 282, 286, 287, 288, 289, 343, 385, 424, 486
 Japanese, 282, 290, 488
 Jordan, 51, 294, 321

K

kernel, 127, 252, 648, 670
 kinematics, 60, 124, 600
 kinetic equations, 154
 kinetics, 214, 278
 King, 56, 673, 676

Kolmogorov, 61, 62, 64, 112, 113, 114, 116, 120, 123, 125, 126, 135, 136, 137, 138, 141, 142, 144, 147, 154, 156, 158, 161, 162, 163, 164, 314, 508, 509, 561

L

L1, 430, 431, 606
 L2, 430, 431, 441
 laboratory studies, xv, 575
 lack of control, 636
 Lagrange multipliers, 348
 Lagrangian, 119, 426, 577, 579, 594, 625
 lakes, 19, 28
 lambda, 597
 lamina, vii, 60, 62, 113, 168, 207, 208, 225, 232, 271, 279, 283, 424, 450, 459, 467, 508, 511, 512, 517, 526, 551, 553, 608
 laminar, vii, 60, 62, 113, 168, 207, 208, 225, 232, 271, 279, 283, 424, 450, 459, 467, 508, 511, 512, 517, 524, 526, 551, 553, 608
 land, xv, 54, 55, 57, 77, 101, 102, 103, 104, 106, 335, 337, 577, 636, 637, 676, 679, 680, 683, 697
 land use, 577
 Langmuir, 117, 118, 120, 136
 language, 126, 152, 317, 318
 large-scale, xiii, 56, 116, 118, 123, 125, 152, 157, 171, 179, 233, 469, 470, 485
 laser, 216, 221, 222, 559, 615
 lattice, 65, 500
 laws, viii, 9, 59, 63, 66, 77, 105, 112, 113, 114, 119, 125, 138, 145, 162, 577, 608, 638
 learning, 307, 315, 318, 326, 327, 488
 Lebanon, 235
 lens, 560
 Lie group, 164
 LIF, 615
 life cycle, 668
 life span, 196
 life-cycle, 75
 lifetime, 208
 lift, 345, 472, 477, 491, 492, 494, 495, 496, 497, 500, 502, 637
 light beam, 647
 light scattering, 636, 667
 likelihood, 302, 619, 692
 limitation, ix, 65, 115, 168, 205, 211, 234, 247, 498
 limitations, x, xiii, xiv, 116, 117, 177, 206, 234, 457, 469, 470, 505, 509, 648, 667
 Lincoln, 623
 linear dependence, 430, 524, 564, 565
 linear function, 90, 95, 113, 265, 271, 273, 593

linear law, 522
 linear model, 296
 linear regression, 286, 288, 303, 325, 660, 666
 loading, 495
 location information, 387, 389, 391
 LOD, 290
 logic rules, 306
 logistics, 5, 18
 London, 55, 106, 107, 108, 109, 162, 164, 275,
 338, 340, 424, 426
 long period, ix, xvi, 168, 189, 200, 691, 692
 losses, xvi, 114, 117, 145, 162, 222, 229, 560,
 691, 692
 low temperatures, 4, 29, 33, 637
 low-level, 20, 28, 29, 31, 36, 44, 45, 49, 50, 673,
 675

M

M1, 441, 442, 443, 445, 446, 458
 machines, viii, 111, 122
 Madison, 670
 magnetic, viii, 111, 112, 113, 114, 115, 116, 117,
 118, 124, 125, 132, 135, 136, 142, 147, 149,
 151, 153, 157, 159, 161, 171, 562
 magnetic field, viii, 111, 112, 113, 114, 115, 116,
 117, 118, 124, 125, 135, 136, 147, 151, 153,
 157, 159, 161
 magnetic field effect, 153
 magnetic fusion, 136
 magnetic structure, 118, 159
 magnetization, 60
 magnetosphere, 145
 maiming, 100
 Maintenance, 623
 Malaysia, 295
 management, 204, 292, 330, 579, 680, 688, 692,
 697
 manifold, 674
 mapping, 324, 335, 340, 681
 marine environment, 58
 maritime, 18, 21, 28, 29, 32, 35, 45, 50, 56
 Markov, 153, 154, 294, 297, 298, 311, 312, 321,
 326
 Markov chain, 294, 297, 298, 311, 312
 Markov process, 154, 321
 Markovian, 294, 321
 Mars, 459, 468
 marshes, 19
 Maryland, 498, 503
 mass loss, 283
 mass transfer, xi, 188, 189, 277, 279, 281, 283,
 570
 Massachusetts, 58, 341, 489, 490

Mathematical Methods, 689
 mathematics, 126, 466
 matrices, 326
 matrix, 73, 243, 366, 367, 368, 369, 370, 371,
 372, 374, 378, 379, 380, 381, 382, 383, 387,
 389, 390, 391, 392, 393, 394, 395, 396, 581,
 605, 609, 611, 612
 Maxwell equations, 561, 640
 MBE, 302, 303, 304, 305
 mean-square deviation, 133
 measures, 117, 118, 127, 129, 336, 683
 media, 63, 113, 145, 279, 560, 637, 643, 670
 median, 182, 184, 186, 189, 190, 191, 193, 196
 mediation, 37
 medicine, xi, 293
 Mediterranean, 332, 333, 337, 340
 Mediterranean climate, 340
 megawatt, 472
 melt, 20, 25
 melting, 20, 21, 29, 36, 40, 42, 49, 50, 676
 membranes, 494
 memory, 112, 120, 161, 271, 319, 387, 508, 509,
 579, 609, 611, 612, 614, 630
 meridian, 621
 mesh node, 532, 541, 552
 message passing, 385, 516
 messages, 612
 meteorological measurements, 5, 11, 620
 methane, 216, 697, 698
 metric, 609, 649
 metropolitan area, 688
 Mexico, 307, 323, 325
 MHD, 115, 116, 117, 118, 119, 125, 136, 138,
 145, 150, 153, 157, 161, 163
 micrometeorological, 18
 microscope, 279
 microstructure, 543, 561, 637
 microwave, 13
 migration, 64
 military, xi, 293, 576
 Ministry of Education, 385
 Ministry of Environment, 282
 Minnesota, 669
 mirror, 155, 475, 532
 misinterpretation, 13, 18
 misleading, 154
 missiles, 448
 missions, 698
 MIT, 108, 163, 237, 503
 mobility, xv, 635
 modality, 60
 modulation, 646, 668, 670
 modules, 65, 249, 296, 578, 579, 629

modulus, 129, 242
 moisture, xvi, 4, 10, 28, 29, 31, 674, 676, 691, 692, 693, 696, 697
 moisture content, xvi, 691, 692, 693, 697
 mole, 207, 214, 229
 molecular dynamics, 65, 105
 molecular weight, 213, 287
 molecules, xi, 63, 65, 277, 278, 279, 281, 291, 639
 monofractal, 127, 130, 132
 monsoon, 32
 Monte Carlo, 668
 morning, 296, 686, 687
 Morocco, 310
 mosaic, 103
 Moscow, 57, 111, 117, 163, 164, 570, 571, 632
 motivation, 576
 motors, 482, 522
 mountains, 689
 mouth, 172, 173
 movement, 61, 66, 279, 283, 356, 400, 401
 MPI, 516, 609, 612, 613
 multidimensional, 456, 457
 multifractal, 114, 116, 119, 123, 125, 126, 127, 128, 129, 130, 137, 154, 155, 160, 161
 multifractal formalism, 116, 119, 123, 125, 126, 128, 130
 multifractality, viii, 111, 117, 127, 130, 131, 132, 133, 136, 160, 162
 multiple regression, xv, 330, 679, 680, 681, 682, 684, 685, 686, 693
 multiplier, 176
 multivariate, 300
 mutation, 316

N

Nanyang Technological University, 429, 463
 naphthalene, 281, 284, 285
 NASA, 439, 441, 456, 463, 464, 465, 466, 467, 571, 683
 National Research Council, 205, 222
 natural, vii, viii, ix, 59, 60, 87, 105, 111, 114, 117, 118, 145, 167, 169, 191, 283, 334, 340, 362, 423, 451, 542, 585, 595, 638, 676
 natural environment, 283
 Navier-Stokes, ix, 65, 66, 115, 124, 125, 128, 205, 208, 240, 263, 345, 349, 351, 352, 383, 395, 424, 425, 426, 439, 459, 461, 467
 Navier-Stokes equation, 65, 66, 115, 124, 125, 240, 345, 349, 351, 352, 383, 395, 424, 425, 426, 439, 459, 461, 467
 Navy, 43
 Nb, 194, 196
 Netherlands, 201, 202, 203, 338, 340, 426, 669, 676
 network, xii, 12, 19, 173, 293, 294, 298, 300, 301, 302, 304, 305, 306, 307, 308, 309, 310, 311, 312, 313, 314, 315, 316, 317, 318, 320, 323, 324, 325, 326, 327, 330, 340, 453, 466
 Neumann condition, 606
 neural network, xii, 293, 294, 298, 299, 300, 301, 302, 304, 305, 306, 307, 308, 309, 310, 311, 312, 313, 314, 315, 316, 317, 318, 320, 323, 324, 325, 326, 327, 330, 340, 453, 466
 Neural Network Model, 325
 neural networks, 299, 300, 302, 304, 306, 308, 309, 313, 315, 316, 318, 320, 323, 324, 325, 326, 330, 340
 neurons, 303
 New Jersey, 340
 New Orleans, 633
 New York, 54, 55, 107, 108, 163, 164, 165, 201, 202, 203, 235, 236, 237, 238, 275, 338, 426, 503, 504, 631, 632, 668, 670, 675, 689
 New Zealand, 203, 277, 492, 698
 Newton, viii, 59, 63, 64, 66, 73, 77, 81, 89, 105
 Newtonian, 585
 Nielsen, 203
 NIST, 214, 237
 nitrate, 282
 nitrogen, xi, 277, 278, 467
 nitrogen dioxide, xi, 277, 278
 NOAA, 32, 53, 337, 623
 nodes, xii, 217, 250, 316, 343, 355, 356, 357, 359, 375, 378, 380, 383, 385, 397, 400, 401, 509, 516, 523, 532, 541, 552, 584, 599, 602, 603, 606, 610, 621
 noise, xi, 175, 282, 293, 523, 531, 533, 551, 568, 663
 nonequilibrium, viii, 59, 60, 66, 68, 71, 74, 75, 77, 82, 85, 86, 87, 89, 92, 99, 105
 non-Gaussian, 544, 618
 non-linear equations, 9
 non-uniform, 63, 82, 99
 non-uniformities, 99
 non-uniformity, 82
 normal distribution, 114, 141, 197, 544
 normalization, 509
 norms, 606
 North America, 52
 North Atlantic, 49
 Northern Hemisphere, 5, 35
 Norway, 3, 675, 689
 NOS, 14
 nose, 445, 447, 448, 450, 458, 459, 464, 465, 617
 novelty, xv, 679, 681, 688

nuclear, 576
 nuclei, 636, 637
 numerical analysis, 345, 439, 443, 467
 numerical computations, 509
 Nusselt, 506, 549, 550, 551, 552, 553, 554, 555, 556, 557, 558, 569

O

observations, vii, 3, 5, 7, 11, 17, 18, 19, 20, 32, 37, 38, 40, 41, 43, 47, 49, 50, 51, 53, 54, 60, 71, 75, 80, 136, 138, 162, 181, 182, 183, 192, 194, 233, 336, 618, 638, 673, 682
 OCs, 278
 offshore, xiii, 469, 470, 485
 oil, 470
 Oklahoma, xv, 575, 578, 620, 621, 622, 623, 625, 626, 627, 629, 630
 olive, 338, 339
 Oman, 295, 301
 one dimension, 79, 387
 on-line, 5, 318
 opacity, 644, 645
 operator, 425, 426, 647
 opposition, 47
 optical, xiv, xv, 222, 223, 282, 284, 505, 510, 558, 559, 560, 561, 562, 568, 635, 636, 642, 644, 645, 647, 667, 670
 optical parameters, 636
 optical properties, 642, 670
 optics, 560
 optimization, xi, xii, 53, 232, 233, 234, 293, 316, 343, 344, 345, 346, 348, 352, 355, 356, 359, 383, 384, 385, 397, 401, 404, 408, 422, 423, 424, 425, 426, 453, 490, 499, 675
 optimization method, 344, 346, 383, 408
 oral, 335
 orbit, xv, 679
 order statistic, 296, 310, 322
 Oregon, 51
 organic, 278, 279, 280, 693
 organic compounds, 278
 orientation, 158, 585
 oscillation, 45, 188, 397, 445, 450, 451, 465, 468, 530, 553, 617
 oscillations, 45, 130, 136, 179, 180, 192, 362, 412, 445, 450, 451, 461, 466, 513, 531, 533, 540, 551, 553, 555, 568, 602
 oscillator, 533, 568
 outliers, 304
 oxygen, 692
 ozone, 278

P

Pacific, 8, 18, 48, 173, 486, 623
 parabolic, 296, 509, 526, 606
 parallel computers, 387
 parallelism, 318
 parallelization, 609
 Paris, 107, 423, 635, 668, 689
 partial differential equations, 125, 585, 598, 606
 particles, ix, xi, 119, 159, 167, 175, 277, 278, 279, 527, 636, 637, 638, 639, 641, 642, 645
 partition, 129
 passenger, 487
 passive, xi, 13, 113, 197, 277, 278, 279, 280, 282, 284, 285, 286, 288, 290, 291, 484, 485, 561, 654, 666, 688
 pathways, 55
 patients, 330
 PBL, vii, 3, 4, 5, 6, 7, 8, 9, 10, 11, 12, 13, 14, 16, 18, 19, 20, 21, 22, 25, 26, 27, 28, 29, 31, 32, 33, 34, 35, 36, 37, 38, 39, 40, 41, 43, 44, 45, 46, 47, 48, 49, 50
 PCP, 385, 427
 peak concentration, 595
 peat, xvi, 691, 692, 697, 698
 peatland, 692
 perception, 301, 594, 667
 percolation, 153, 159
 perfect gas, 440, 457, 510
 periodic, 193, 398, 451, 553, 555, 569
 periodicity, 461
 permafrost, 4, 19, 25, 28, 55
 permeability, 279
 personal communication, 41
 perturbation, 117, 411, 414, 584, 603
 perturbations, 526, 562, 636, 650, 674
 phase space, 64, 87
 phenomenology, 115, 116, 137, 151, 157, 161, 595
 phonological, 332, 338
 photographs, 431, 442, 448
 photolysis, 278
 photoperiod, xii, 329, 332, 333
 photovoltaic, 296, 321, 322, 323, 325
 physical mechanisms, 620
 physics, vii, viii, ix, xiv, 28, 59, 63, 64, 87, 100, 104, 112, 115, 124, 136, 138, 161, 205, 207, 423, 487, 502, 575, 577
 pitch, 453, 454, 471, 478, 482, 483, 484, 485, 496
 pith, 453
 planar, 451, 621
 planetary, vii, 3, 4, 58, 60, 577, 676
 planning, 330, 577

- plants, xii, xiii, 329, 330, 332, 333, 334, 336, 337, 469, 470
- plasma current, 117, 147
- plasma physics, 136, 138, 161
- plasticity, xii, 329, 334
- point of origin, 551
- point spread function, 647
- Poisson, viii, 111, 112, 113, 114, 117, 136, 137, 138, 140, 141, 142, 144, 145, 146, 147, 148, 149, 151, 152, 153, 154, 155, 157, 158, 159, 160, 161, 162, 361, 370, 631
- Poisson distribution, 114, 141
- Poisson equation, 361, 370
- Poland, 239, 341
- polarization, 641
- pollen, 330, 332, 333, 334, 335, 337, 338, 339, 340, 341
- pollination, 338, 340
- pollutant, 214, 595
- pollution, 65, 278, 674, 675
- polyethylene, xi, 277, 278, 279, 291
- polygons, 580
- polymer, 280
- polynomial, 127, 271, 316, 327, 680
- polynomials, xi, 214, 239
- polyolefin, 280
- pore, 279, 287
- porosity, 279, 287
- porous, xi, 63, 277, 279, 280, 281, 283, 284, 285, 287, 291, 568, 570, 589
- porous media, 63
- powder, 278
- powders, 279
- power generation, 307, 325
- power plant, xiii, 469, 470
- power plants, xiii, 469, 470
- power-law, 61, 73, 113, 117, 120, 121, 122, 123, 125, 136, 154, 160
- PPM, 507, 509, 515
- Prandtl, ix, x, 39, 41, 64, 108, 205, 206, 207, 208, 210, 211, 215, 216, 218, 220, 222, 233, 234, 236, 240, 275, 430, 440, 459, 464, 506, 511, 536, 546, 548, 549, 561, 569, 676
- precipitation, 298, 299, 637, 673, 689
- predicate, 81
- predictability, 550
- prediction models, 47
- predictive accuracy, xiv, 575, 614
- predictive model, xiv, 575
- predictive models, xiv, 575
- preprocessing, 326, 390
- press, 299, 323, 325, 326, 335
- prevention, 278
- principal component analysis, 323
- probability density function, 122, 123, 127, 135, 154, 160, 213, 215, 216, 294, 321, 595
- probability distribution, 65, 112, 113, 126, 171, 183, 193, 195, 197, 198, 200, 544, 619
- probability theory, 112, 141, 165
- probe, 117, 118, 120, 126, 134, 147, 148, 149, 152, 223, 432, 453, 513
- production, 67, 69, 71, 89, 216, 242, 335, 339, 343, 514, 527, 577, 586, 587, 588, 591, 607, 608
- prognosis, 330
- program, xii, 19, 108, 201, 241, 245, 249, 263, 264, 268, 271, 291, 316, 343, 385, 396, 422, 466, 580, 611, 614, 630, 693, 698
- programming, 317, 354, 424, 508, 516, 614
- programming languages, 516
- propagation, xvi, 540, 559, 560, 561, 562, 563, 637, 640, 691, 692
- propane, 222
- property, x, 65, 66, 93, 94, 105, 113, 114, 115, 117, 118, 119, 125, 128, 136, 137, 138, 145, 147, 158, 160, 162, 171, 181, 239, 241, 244, 246, 251, 261, 263, 265, 268, 598, 599, 629
- prophylaxis, 337
- propriety, 252
- propulsion, 208, 463
- protection, 450, 459, 465
- proxy, 11, 13, 19, 175
- pseudo, 177, 196, 623
- public, xvi, 282, 691, 692
- public health, xvi, 691, 692
- pulse, 192, 209
- pumping, 625
- PUs, 215
- Q**
- quality control, 12, 13, 49, 107
- quality research, 273
- quartz, 282
- quasi-equilibrium, 114, 496
- quasilinear, 112
- quasi-periodic, 193
- Quercus, 331, 333, 334, 339, 340
- Quercus ilex, 334, 339
- R**
- radar, 16, 620
- Radial Basis Function, 317, 324
- radial distribution, 541, 569
- radio, 5, 12, 26
- radiological, 576

- radius, 117, 118, 126, 132, 133, 152, 159, 287, 432, 433, 458, 461, 475, 540, 543, 560, 637, 638, 639, 640, 641
 rail, 117
 rain, 189, 282, 670, 700
 rainfall, 332, 692, 693, 697
 Raman spectroscopy, 209
 random, 64, 112, 123, 126, 128, 135, 140, 141, 144, 149, 154, 157, 161, 162, 169, 171, 288, 308, 523, 531, 533, 540, 541, 560, 579, 595, 683
 randomness, 207
 Rayleigh, viii, 59, 60, 62, 66, 73, 74, 75, 78, 81, 87, 105, 108, 639
 RBF, 300, 301, 302, 306
 RCI, 303
 reaction rate, 213
 reading, 262, 290, 387, 432, 540, 580
 reagent, 281, 282
 real time, 318
 reality, 637, 660
 reasoning, xi, 27, 293
 receptors, 593, 626, 627
 reconstruction, vii, 3, 5, 8, 12, 13, 49, 50, 118, 489, 594
 recovery, 41, 459
 reference frame, 114, 473, 492
 reflection, 5, 336, 511
 reflectivity, 669
 refraction gradient, 560
 refractive index, 559, 560, 562, 639, 641
 refractive index variation, 560
 regional, xii, xv, 7, 12, 13, 20, 25, 56, 295, 329, 334, 336, 577, 679, 683, 686, 689
 regression, 130, 286, 287, 288, 295, 300, 302, 303, 325, 341, 660, 661, 665, 666, 681, 689
 regression analysis, 287, 288, 341, 689
 regression line, 130, 660, 661, 665, 666
 regressions, 685, 686
 regular, vii, 3, 5, 11, 12, 13, 19, 20, 62, 482, 558, 614, 615, 620
 regulation, 57
 relationship, vii, xii, 3, 4, 83, 84, 85, 127, 152, 175, 198, 214, 286, 288, 297, 329, 333, 432, 453, 561, 563, 579, 585, 591, 594, 606, 626, 680, 681
 relationships, 11, 32, 68, 81, 240, 262, 282, 562, 576, 693
 relaxation, 9, 513, 605
 relaxation coefficient, 513
 relevance, 302
 reliability, 285, 339, 343
 remote sensing, xii, 329, 330, 336, 337, 620, 636, 681
 renewable energy, xiii, 294, 299, 300, 324, 469
 renormalization, 112
 repeatability, 284
 reproduction, 48, 332, 514
 Research and Development (R&D), 469
 reserves, 470
 residual error, 84, 86, 87, 95, 97, 98
 residuals, 288, 321, 601, 602, 606, 681, 682, 684, 685
 resistance, 9, 63, 224, 284, 345, 360, 471, 496, 692, 693
 resolution, viii, ix, xi, 4, 5, 11, 12, 18, 20, 21, 47, 48, 52, 55, 56, 168, 171, 222, 278, 355, 356, 377, 397, 398, 408, 497, 515, 530, 567, 577, 578, 589, 623, 630, 674, 682, 683, 686, 687, 688, 689
 resources, 322, 508, 530, 614
 returns, 359, 384, 613
 Reynolds stress model, 212, 234, 529, 586
 Riemann problem, 515
 rifting, 19
 rings, xiv, 470, 475, 479
 risk, 333, 489, 594, 689, 692
 rivers, vii, 19, 60
 road safety, 650
 Romania, 295, 322
 room temperature, 224
 root-mean-square, 133, 439
 rotations, 125
 roughness, 9, 10, 20, 32, 35, 42, 51, 93, 94, 96, 98, 190, 275, 498, 589, 615, 617, 683, 684, 686, 687
 Royal Society, 108, 424
 runoff, ix, 167, 179
 rural, 650, 651, 652, 653
 Russia, 19, 52, 54, 111, 327, 469, 486, 573, 632
 Russian, 6, 7, 19, 37, 53, 108, 163, 469, 486, 632
- S**
- safety, xv, 487, 635, 650
 salt, 636, 637
 saltwater, 199
 sample, 118, 175, 176, 192, 193, 194, 196, 278, 282, 283, 300, 326, 335, 595, 682
 sampling, xi, 41, 118, 169, 172, 173, 174, 175, 177, 186, 188, 189, 191, 192, 193, 200, 222, 223, 277, 278, 279, 280, 282, 283, 284, 285, 286, 288, 290, 291, 330, 620, 625, 626, 627, 628
 sand, 336

- satellite, vii, xv, 3, 5, 7, 11, 12, 13, 28, 35, 43, 44, 45, 49, 299, 302, 305, 325, 336, 337, 454, 456, 465, 467, 622, 679, 683
satellite imagery, 45
saturation, 29, 51, 117, 118, 119, 136, 560
Saudi Arabia, 296, 299, 305, 308, 326
savings, 630
scalable, 385, 427
scalar field, 124, 208, 211
scaling, 113, 114, 116, 119, 120, 125, 126, 127, 128, 129, 130, 135, 136, 137, 138, 139, 140, 141, 142, 144, 145, 147, 148, 149, 150, 152, 154, 155, 156, 157, 158, 159, 160, 161, 638
scaling law, 125, 140
scarcity, vii, 3, 6
scatter, xv, 5, 497, 498, 513, 536, 635, 642
scattered light, 646, 667
scattering, xv, 114, 147, 159, 216, 223, 560, 635, 636, 638, 639, 640, 641, 642, 643, 644, 646, 667, 668, 670
schema, 318
Schmidt number, ix, x, 205, 206, 207, 209, 215, 216, 218, 220, 222, 233, 234, 587, 592
scientific community, 63
sea ice, 4, 6, 18, 42, 48, 50, 51, 52, 53, 54, 55
search, 113, 344, 355, 358, 377, 509, 630
seasonal variations, 37, 42
second generation, 13, 49
sediment, ix, 167, 175, 177, 188, 189, 190, 192, 195, 196, 200
self-organization, 29, 43
self-organized criticality, 154
self-similarity, viii, 111, 113, 114, 117, 121, 122, 123, 124, 126, 127, 135, 136, 137, 159, 160, 161
SEM, 281, 287
sensing, xii, 329, 330, 336, 337, 453, 620, 636, 681
Sensitivity Analysis, 239, 241, 246, 251, 268, 271, 425
sensors, 20, 101, 249, 319, 336, 337, 594, 620, 654
separation, xiii, 119, 135, 275, 429, 442, 445, 447, 448, 450, 459, 465, 500, 508, 509, 532, 550, 555, 569
severity, 338, 340, 698
shaping, 4, 424
sharing, 610
shipping, 490
shock, xiii, 429, 430, 431, 432, 433, 438, 439, 442, 445, 447, 448, 450, 459, 461, 464, 465, 466
shock waves, 461
short period, ix, 168
short-term, 341, 478
shoulder, 439, 442, 448, 459, 461
shrubs, 337, 697
Siberia, 16, 19, 35, 698
sign, 32, 47, 102, 171, 177, 255, 412, 472, 477, 484, 534, 635
signals, 117, 118, 119, 123, 126, 127, 130, 133, 135, 136, 142, 145, 147, 152, 156, 175
signs, 48, 83
silica, 222, 278
similarity, viii, 8, 10, 11, 19, 61, 64, 79, 80, 81, 82, 83, 84, 85, 86, 93, 94, 99, 101, 106, 111, 113, 114, 115, 117, 121, 122, 123, 124, 126, 127, 135, 136, 137, 138, 145, 153, 159, 160, 161, 208, 472, 536, 551, 576
sine, 552
Singapore, 203, 429, 463
singular, viii, 111, 114, 116, 127, 130, 138, 140, 149, 150, 152
singularities, 129, 155
sintering, 279
sites, xi, 6, 7, 32, 169, 172, 277, 282, 286, 288, 289, 295, 297, 298, 305, 309, 310, 320, 326, 334, 338
skeleton, 129
skewness, 131, 171, 183, 223, 543, 544, 546, 547
skimming, 587
skin, 458, 508
Slovenia, xv, 679, 681, 682
Smithsonian, 338
Smithsonian Institution, 338
smoke, 52, 636
smoothing, 355, 356, 357, 359, 425, 514, 602, 603
SO₂, xi, 277, 279, 280
SOC, 154
sodium, 282, 615
software, 215, 249, 318, 344, 385, 422, 427, 474, 508, 693
soil, xvi, 19, 26, 36, 101, 102, 103, 691, 692, 693, 698, 699
soils, 693, 698
solar, xii, 21, 25, 35, 42, 116, 293, 294, 295, 296, 297, 298, 299, 300, 301, 302, 303, 304, 305, 309, 310, 311, 312, 313, 314, 318, 319, 320, 321, 322, 323, 324, 325, 326, 327, 683, 685, 686, 692
solar energy, 298, 299, 301, 323, 324, 685
solar wind, 116
solid state, 60
solid surfaces, 580, 621
sorption, 286

- sounds, 471
 Soviet Union, 54
 space shuttle, 453, 456, 466
 space-time, 126, 155, 426
 space-time, 593, 596
 Spain, 301, 324, 329, 331, 333, 334, 337, 338, 339, 340, 504
 spatial analysis, xii, 329, 335, 337
 spatial heterogeneity, viii, 13, 49, 59, 101, 103, 106
 spatiotemporal, 152
 species, xii, 115, 207, 208, 210, 211, 213, 214, 215, 216, 218, 222, 223, 233, 287, 329, 330, 332, 333, 334
 specific heat, 9, 67, 102, 206, 214, 431, 440, 454, 457, 458, 511
 spectral analysis, 297, 445
 spectrum, ix, 61, 65, 113, 114, 115, 116, 120, 121, 125, 126, 127, 128, 129, 130, 132, 133, 142, 143, 151, 152, 154, 157, 158, 161, 167, 445, 508, 561, 565, 567, 569, 638, 639, 642
 spheres, 138
 sporadic, 173, 692
 springs, 356, 357
 St. Petersburg, 54
 stability, vii, 3, 5, 8, 10, 21, 27, 29, 31, 32, 33, 43, 45, 50, 80, 81, 82, 84, 94, 412, 445, 450, 459, 465, 466, 468, 477, 479, 490, 550, 600
 stabilization, 362, 371, 424, 549
 stabilize, 509
 stages, 335, 336
 stainless steel, 222, 223, 280, 615
 standard deviation, xvi, 36, 38, 49, 119, 120, 123, 131, 154, 155, 176, 181, 182, 183, 186, 188, 192, 284, 285, 290, 497, 618, 619, 637, 658, 660, 663, 666, 680, 682, 684
 standards, 278, 288
 statistical analysis, 135, 302, 335
 statistical mechanics, 119
 statistics, viii, 28, 64, 111, 112, 113, 115, 124, 126, 128, 135, 150, 154, 171, 193, 296, 304, 310, 322, 323, 508, 576, 579, 589, 591, 595, 615, 616, 618, 623, 625, 680, 682
 steady state, 118, 140, 383, 473, 623
 steel, 222, 223, 280, 615
 stiffness, 357, 360
 stochastic model, 294, 295, 296, 322, 579, 625
 storage, 5, 25, 101, 290, 307, 334, 387, 408, 580, 599, 600, 602
 storms, 189
 strain, 212, 242, 585, 588, 591, 614
 strains, 585
 strategies, 345, 385, 424
 stratification, 5, 21, 26, 27, 40, 43, 50, 62, 76, 78, 79, 80, 81, 82, 84, 85, 87, 88, 90, 155, 475, 482, 674, 676
 streams, 475, 480, 481, 482
 strength, 4, 6, 27, 28, 48, 82, 118, 150, 209, 233, 562
 stretching, 164, 169, 581
 structural changes, 559
 structure formation, 124
 submarines, 65
 subsonic, 443, 461, 487, 511, 534, 536, 561
 substances, 529, 594
 suburban, xi, 278, 282, 290, 620
 Sudan, 295, 322
 sulfur, 620
 sulphur, 279
 superiority, 304
 superposition, 379
 SUPG, 362
 supplemental, 489
 supply, 5, 222, 278, 319, 692
 suppression, 49, 78, 80, 221, 222
 surface area, 173, 189, 345, 375, 413, 599, 614
 surface energy, 42, 51, 56, 57, 101, 102, 577
 surface friction, 8
 surface layer, 4, 5, 43, 71, 79, 81, 83, 93, 94, 99, 101, 106, 592
 surface roughness, 32, 42
 surface water, 51
 surprise, 500
 susceptibility, 562
 suspensions, 189
 Sweden, 235
 Switzerland, 324, 338
 symbolic, xi, 293
 symbols, 147, 517, 518, 519, 520, 521, 524, 525, 526, 532, 533, 537, 538, 540, 545, 548, 553, 554, 558, 564
 symmetry, 69, 71, 72, 74, 75, 113, 115, 116, 125, 135, 136, 153, 155, 161, 207, 231, 471, 472, 475, 511, 523, 548
 synthesis, 317
 systematics, 338
- T**
- tactics, 488
 taiga, 19, 35, 50, 58
 Taiwan, 486
 targets, 654, 655, 656, 657, 658, 660, 661, 662, 666, 667
 taxa, 338
 Taylor series, 69
 temperate zone, 338

- temperature gradient, 21, 27, 38, 40, 45, 50, 62, 64, 71, 72, 73, 74, 75, 78, 81, 90, 93, 97, 105
temporal, ix, 6, 49, 55, 114, 155, 168, 171, 183, 334, 508, 529, 576, 593, 598, 601
temporal distribution, 171, 183
tension, 494
terrorism, 577
test data, 456
thawing, 28
theoretical assumptions, 101
thermal analysis, 459
thermal conduction, 63, 70, 102
thermal energy, 639
thermal expansion, 9, 62
thermal load, 294
thermal properties, 215
thermodynamic, viii, 58, 59, 64, 65, 66, 67, 68, 69, 71, 72, 77, 89, 91, 92, 96, 105, 106, 468, 638
thermodynamic equilibrium, 68
thermodynamics, viii, 37, 50, 59, 60, 64, 66, 68, 71, 74, 75, 76, 77, 81, 82, 85, 86, 87, 89, 91, 92, 99, 100, 101, 103, 104, 105, 126, 129, 130
third order, 136
three-dimensional, 62, 114, 116, 124, 150, 169, 191, 211, 216, 423, 433, 456, 457, 473
three-dimensional model, 124, 457
threshold, 62, 119, 154, 176, 177, 332, 595, 681
threshold level, 595
thresholds, 332
throat, 216, 432
tides, ix, 168, 169, 173, 179, 180, 181, 182, 183, 184, 188, 190, 191, 194, 196, 200
time consuming, 498
time increment, 361, 598
time periods, 13, 49
time series, 13, 28, 120, 126, 127, 154, 155, 156, 192, 249, 294, 300, 305, 306, 307, 314, 316, 321, 324, 325, 326, 340, 615
timing, 333, 334
Titan, 456, 458, 467
tokamak, 113, 117, 118, 120, 123, 132, 133, 134, 135, 136, 143, 144, 151, 152, 153, 155, 156, 157, 158, 159, 160
Tokyo, 343, 385
toluene, 278
top-down, 5
topographic, 101, 683
topological, 141, 580
topological structures, 141
topology, viii, 111, 117, 125, 142, 145, 147, 152, 314, 345, 355, 383
torque, xiv, 470, 471, 477, 480, 483, 484, 485
total energy, 61, 511
toxic, 576, 594, 595, 619
toxic gases, 595
toxicological, 576
tracking, 119, 630
traction, 344, 345, 348, 402, 403, 404, 411
traffic, 635, 669, 688
training, 300, 301, 304, 305, 307, 313, 316, 453, 682
trajectory, 64, 87, 452, 454, 456, 457, 458, 579, 591
trans, 553, 576, 589, 594
transformation, 21, 128, 129, 140, 157, 308, 313, 314, 334, 353, 354, 409, 473
transformations, 125, 295, 320
transition, 60, 62, 75, 321, 326, 508, 509, 524, 526, 527, 529, 536, 551, 692
transmission, 330, 513, 646
transparency, 247
transparent, 60, 278, 638, 640
transpiration, 35, 48, 50
transport phenomena, 62, 64, 105, 159
transport processes, viii, 59, 92, 105, 159, 509
transportation, ix, xv, 65, 66, 69, 71, 105, 205, 212, 216, 225, 635
trees, 35, 333, 338, 623
troposphere, 14, 18, 21, 25, 48
tundra, 13, 20, 40, 46
tungsten, 118
turbulent flows, ix, xiv, 64, 116, 125, 126, 145, 167, 168, 200, 207, 213, 226, 240, 274, 275, 502, 505, 508, 509, 510, 511, 517, 523, 558, 559, 560, 594, 675
turbulent mixing, ix, 4, 5, 7, 9, 10, 18, 19, 20, 26, 27, 29, 32, 36, 40, 43, 45, 48, 49, 50, 167, 190, 200, 208, 213, 215, 229, 529, 543, 559, 560, 563, 567
Turkey, 296, 301, 305, 309, 322, 324, 325
two-dimensional (2D), 114, 116, 124, 150, 209, 211, 241, 275, 345, 424, 457, 500
typhoon, 77
typology, 638

U

- Uganda, 304
ultraviolet, 7, 304, 309
uncertainty, 6, 43, 49, 288, 289, 291, 489, 496
uniform, 32, 61, 63, 113, 152, 157, 216, 229, 250, 283, 443, 471, 475, 476, 479, 480, 500, 513, 516, 517, 523, 533, 541, 564, 568, 581, 616, 627, 683
United Kingdom, 54, 291, 505, 675, 698
United States, 65

univariate, 295
 universality, 117, 122, 136, 145, 508, 509
 updating, 356
 urban areas, 676
 urbanized, 577
 USSR, 57

V

vacuum, 112, 117
 Valencia, 338, 339
 validation, ix, 106, 167, 209, 212, 216, 301, 302, 304, 305, 312, 314, 316, 323, 432, 546, 567, 578, 666, 669, 681, 682, 688
 validity, 115, 119, 157, 335
 vapor, 29, 51, 57, 67, 69, 70, 71, 79, 89, 91, 92, 100, 102, 103, 104, 106, 300, 636
 variability, vii, ix, 3, 4, 5, 6, 7, 13, 21, 32, 37, 49, 55, 56, 168, 332, 477, 624
 variance, 49, 61, 73, 80, 85, 86, 87, 213, 215, 216, 314, 340, 594, 595, 596, 597, 598, 606, 617, 658, 662, 663, 682
 vegetation, xv, 35, 50, 101, 103, 336, 337, 679, 683, 697
 vehicles, xiii, 429, 445, 452, 456, 459, 650
 vessels, xiv, 487, 488
 vibration, 344, 355, 423
 Victoria, 201, 204, 277
 violent, 252
 viscose, 74
 visible, xv, 40, 169, 253, 256, 262, 265, 268, 273, 336, 337, 572, 635, 636, 638, 639, 642, 645, 646, 647, 648, 662, 663, 667, 669
 vision, xv, 66, 635, 636, 648, 649, 650, 652, 653, 658, 663, 666, 667, 668, 669, 670
 visual environment, 645, 646, 649, 650, 667
 visual field, 649
 visual perception, 667
 visual system, 639, 642
 visualization, xiii, 216, 429, 450, 498
 vortex, 61, 66, 75, 76, 152, 169, 252, 433, 481, 500, 511, 551, 553, 618
 vortices, 152, 157, 161, 207, 252, 400, 461, 481, 482, 550, 551, 552

W

Wales, 692, 698
 wall temperature, x, 206, 209, 222, 223, 224, 232, 233, 234, 516, 551
 War of 1812, 489
 warfare, 594
 warm air, 25
 Warsaw, 323
 wastewater, ix, 167
 water quality, 204
 water table, 697
 water vapor, 29, 51, 57, 102, 636
 waterways, ix, 167
 wave number, 562, 565, 567, 569
 wave propagation, 559, 561, 562
 wave vector, 116, 562
 wavelengths, 101, 169, 337, 638, 639, 642, 645
 wavelet, 129, 130, 154, 155, 160, 297, 306, 308, 313, 314, 315, 326
 wavelet analysis, 306, 313, 314, 326
 Wavelet Transform, 129
 weather prediction, 47, 673, 676, 697
 Weibull, 308
 wildfires, 692, 697
 wind farm, 307
 wind speeds, 279, 283, 624
 wind tunnels, 240
 wind turbines, xiii, 469, 470, 472, 479, 482, 485
 windows, xv, 222, 679, 683
 winter, 11, 20, 21, 27, 28, 32, 36, 37, 38, 40, 45, 49, 50, 51, 54, 55, 333, 636, 684
 wintertime, vii, 4, 25, 28, 32, 35, 36, 38, 39, 41, 43, 49, 50, 52

X

xylene, 278

Y

Y-axis, 474
 yield, 153, 338, 440, 445, 479, 646